Lisa Bodei
Jason S. Lewis
Brian M. Zeglis   *Editors*

Radiopharmaceutical Therapy

Springer

Radiopharmaceutical Therapy

Lisa Bodei • Jason S. Lewis •
Brian M. Zeglis
Editors

Radiopharmaceutical Therapy

Editors
Lisa Bodei
Memorial Sloan Kettering
Cancer Center
New York, NY, USA

Jason S. Lewis
Memorial Sloan Kettering
Cancer Center
New York, NY, USA

Brian M. Zeglis
Hunter College - CUNY
New York, NY, USA

Foreword

It is my pleasure to write the foreword for this exciting new textbook that explores the fascinating world of radiopharmaceutical therapy (RPT). RPT is a unique approach to cancer treatment that harnesses the power of ionizing radiation, often with laser-like precision. Over the last two decades, RPT has emerged as one of the most promising strategies for the treatment of many cancers, and this innovative technology is increasingly making a real difference in patient outcomes.

I have spent my entire career . . . nearly 60 years(!) . . . in nuclear medicine. And over this time, I have worked steadfastly to study its trends and advances. I observed the field's humble beginnings with ^{131}I and the Cassen scanner; its transformation—fueled by ^{99m}Tc and the gamma camera—into the clinical mainstream; the advent of personalized diagnoses and treatments in oncology via [^{18}F]FDG PET; and the emergence of the plethora of targeted agents that have given rise to the era of 'molecular imaging' as we know it today. Indeed, these advances in molecular imaging have laid the foundation for what I believe to be the most exciting period of growth and expansion that our field has ever seen: the era of radiopharmaceutical therapy.

The science, technology, and practice of nuclear medicine are constantly improving, especially in the context of RPT. In order to serve our community, Professors Bodei, Lewis, and Zeglis have created a reference work that is impeccably timed to coincide with the field's unprecedented growth. The book offers a thorough overview of topics relevant to the scientific study and clinical application of RPT, from the leading edge of preclinical research to the latest clinical trials to its increasing acceptance by the medical establishment. With contributions from many of the world's leaders in radiochemistry, radiopharmacy, medical physics, nuclear medicine, and radiology, the work as a whole admirably captures the foundation of RPT as well as its present and future.

I am confident that the deep expertise and experience that is on display throughout the book will quickly make it an essential guide for anyone seeking a comprehensive understanding of RPT. With its informed insights, engaging style, and useful references, it is sure to become an invaluable resource for clinicians and scientists alike. As the field continues to expand and welcomes new blood, it is my sincere hope that this work becomes a touchstone covering the origins of our discipline, where it is now, and where it is going to take us.

In the end, I am incredibly grateful for the opportunity to witness—and participate in—the evolution of nuclear medicine over my long career, and I am excited to see what the future holds for RPT.

Memorial Sloan Kettering Cancer Center   Steven M. Larson
(Emeritus), New York City, NY, USA

Preface

Radiopharmaceutical therapy (RPT) is not new: it has been deployed for over 80 years, ever since Dr. Saul Hertz first attempted to treat thyroid cancer patients with radioiodine. In 1946, Dr. Hertz was quoted as saying "…demand is expected in the fields of cancer and leukemia for other radio-active medicines." He was right, but it took a while. Since then, RPT has traversed rejection, indifference, oblivion, ascendance, and finally, acceptance.

The last decade has played witness to a remarkable surge in the discipline of RPT, with trailblazing explorations into basic science, the clinical translation of an expanding array of new agents, and the ever-quickening regulatory approval of novel radiotherapeutics. With this advent in mind, we felt now was the moment to create a textbook that could become both a teaching resource as well as a primary reference for those interested in RPT and its applications. Sir Winston Churchill—who moonlighted as an author and was awarded the 1953 Nobel Prize in Literature—wrote, "Writing a book is an adventure. To begin with, it is a toy and an amusement. Then it becomes a mistress; then it becomes a master; then it becomes a tyrant. The last phase is that just as you are about to be reconciled to your servitude, you kill the monster and fling him to the public." This quote roughly approximates our experience (though perhaps we've had a bit less drama), and, in the interest of full disclosure, we are writing this preface sometime between the "tyrant" and "killing the monster" phases.

The book is divided into three overarching sections: Fundamentals, Deeper Dives, and Special Topics. In the first section, we cover several foundational issues in the field, such as the history of RPT, the radiobiology underpinning the discipline, and the radiopharmaceutical chemistry of therapeutic radionuclides. In the second section, we take a more in-depth look at specific radiotherapeutics. Here, we have used a two-tiered approach, with both broader chapters that cover different scaffolds for agents (i.e., antibodies, peptides, and small molecules) as well as more focused "Case Study" chapters on individual radiotherapeutics. In the final section, we cover a number of areas that are important but do not necessary fit in either of the two previous sections, including the therapeutic potential of radionuclides that emit Auger electrons, the promise of pretargeted radioimmunotherapy, theranostic imaging in the context of RPT, and the regulatory review process for radiotherapeutics. Ultimately, we believe that this textbook will provide

both scientists and physicians with a comprehensive yet accessible introduction to this rapidly growing discipline. We further hope that this book will serve as a critical introduction for those wanting to enter the field.

The three of us have dedicated our careers to radiochemistry and nuclear medicine; this book is the manifestation of our desire to grow the field we love. This work would not have been possible without extraordinary contributions from our dear friends and colleagues who make this field what it is today. Their efforts and work (especially after some serious nagging on our part) are very much appreciated. We would also like to recognize the editors at Springer Nature for their hard work and patience. Finally, our friends, families, and colleagues deserve thanks for their support during this process: the African proverb "it takes a village to raise a child" is an apt description for creating a book like this—from conception to realization.

New York, NY, USA   Lisa Bodei
                                                                           Jason S. Lewis
                                                                           Brian M. Zeglis

Contents

Part III   Special Topics

Part I

Fundamentals

Introduction: The Case for Radiopharmaceutical Therapy

Kelsey L. Pomykala and Ken Herrmann

1.1 The Fundamentals

Radiopharmaceutical therapy (RPT) is an approach to cancer treatment that employs injectable radiopharmaceuticals. It has been utilized for over 70 years [1] but has continued to advance over time with impressive progress in the last decade due to the discovery of novel vectors and targets. This textbook will first review the fundamentals of radiopharmaceutical therapy, including its history, biology, chemistry, and physics. Then, it will offer both broader discussions and specific case studies focused on treatments using three different types of targeting vectors: antibodies, peptides, and small molecules. Finally, it will address several special topics in the field of radiopharmaceutical therapy including pretargeting, next-generation therapeutic radionuclides, artificial intelligence, and regulation.

1.2 The Details

In this introductory chapter, we focus on the unique properties and benefits of radiopharmaceutical therapy. Radiopharmaceutical therapy uses similar biological properties as external beam radiation, but instead of the need for physician-guided localized therapy, radiopharmaceutical therapy is delivered systemically and reaches the target throughout the entire body. Next, it is important to note that these radiotargeted treatments are often guided by the imaging of the same target, conveniently linking diagnostic imaging and therapeutic intervention (Fig. 1.1). Additional advantages of RPT include the simple, often intravenous, systemic administration of radiopharmaceuticals as well as the comparably lower number of reported side-effects, primarily consisting of fatigue and nausea. Finally, perhaps the main distinguishing factor of radiopharmaceutical therapy is the significant increase in the quality of life of patients, in addition to tumor response and impact on survival parameters [2–8].

The first major example of radiopharmaceutical therapy was the use of $[^{131}I]I^-$ for the treatment of both benign and malignant thyroid diseases [9, 10]. This remains a therapeutic mainstay today. Currently, the majority of new indications for radiopharmaceutical therapy are

K. L. Pomykala
Institute for Artificial Intelligence in Medicine, University Hospital Essen, Essen, Germany

K. Herrmann (✉)
Department of Nuclear Medicine, University Hospital Essen, Essen, Germany
e-mail: Ken.Herrmann@uk-essen.de

Fig. 1.1 Schematic of radiopharmaceutical therapy
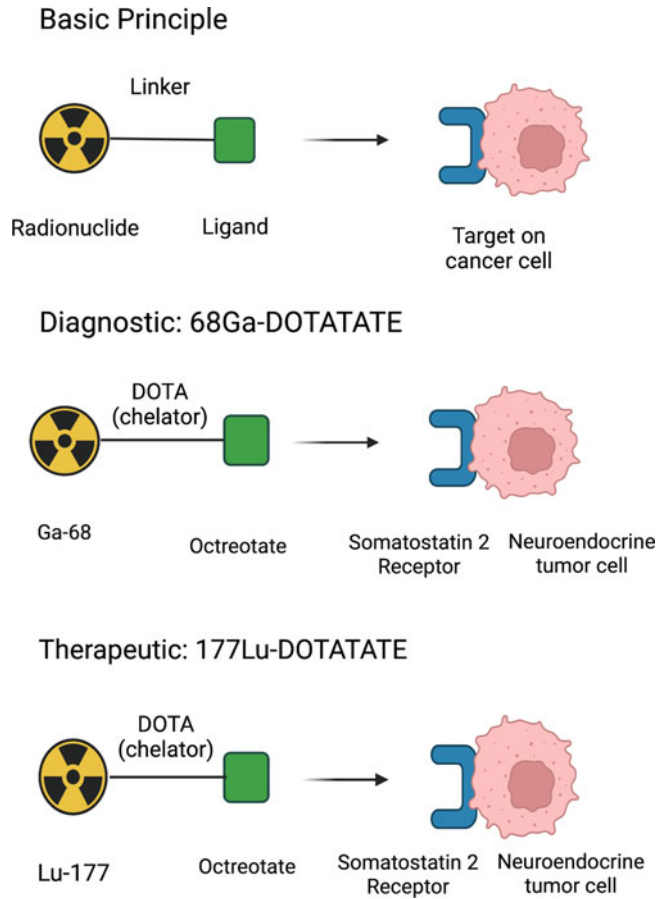
to stabilize end-stage disease that is resistant to other treatments and improve quality of life. However, in the future, the hope is to move these therapies to earlier lines, treating even early-stage cancer through targeted intervention and thereby reducing the side-effects of systemic therapies.

1.2.1 Current Uses

Studies have shown that radiopharmaceutical therapy is successful. To wit, therapy with radioactive iodine transformed well-differentiated iodine-avid thyroid cancer from a disease with poor outcome to a disease with about 85% overall survival [11]. Treatment with [^{177}Lu]Lu-DOTATATE has resulted in longer progression-

free survival, a significantly higher response rate, and higher quality of life in patients with advanced midgut neuroendocrine tumors compared to high-dose octreotide acetate [6, 12] and has shown benefits in patients with pancreatic neuroendocrine tumors as well [13–17] (Fig. 1.2). Targeted radiotherapy with [^{177}Lu] Lu-PSMA-617 has been shown to decrease prostate-specific antigen (PSA) levels, reduce pain, and produce few side-effects in patients with metastatic castrate-resistant prostate cancer [19, 20] (Fig. 1.3). Moreover, the approach to therapy produces prolonged imaging-based progression-free survival and overall survival when added to standard care in patients with advanced prostate-specific membrane antigen (PSMA)-positive metastatic castration-resistant prostate cancer [22].
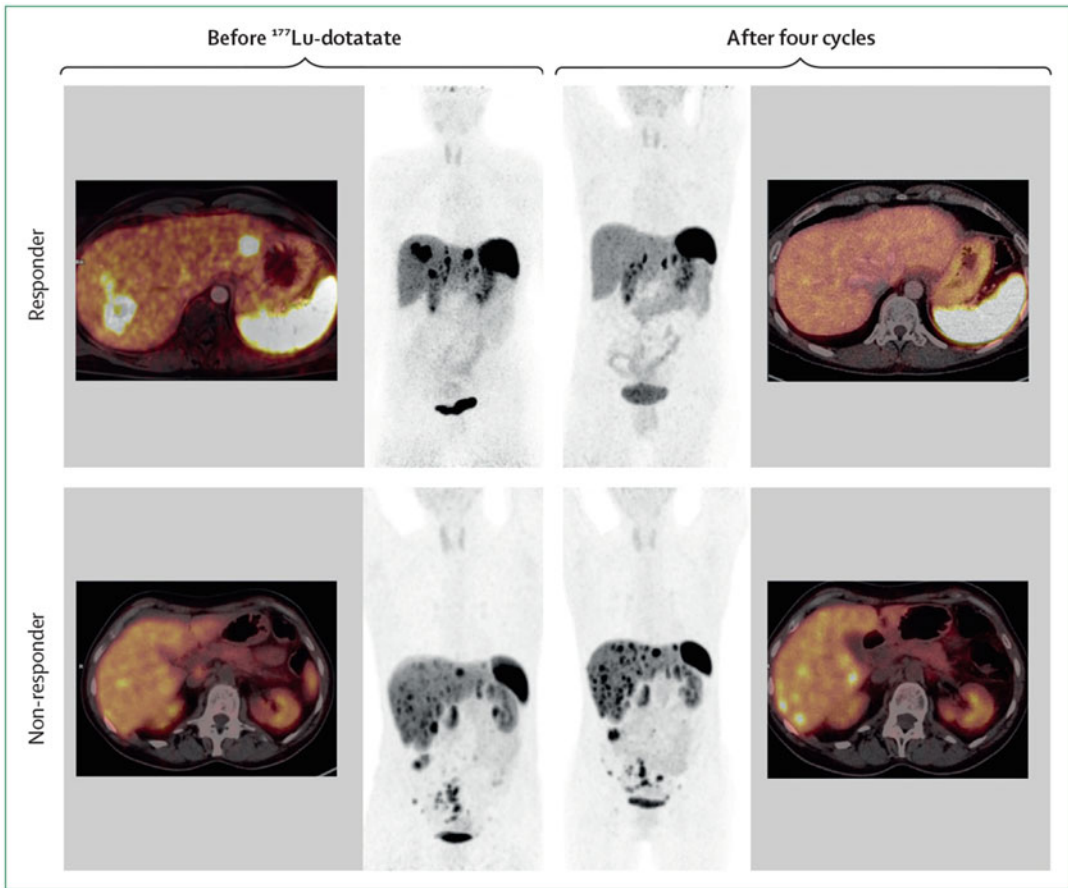
Fig. 1.2 A [^{68}Ga]Ga-DOTATATE PET/CT scan performed ten months after four cycles of [^{177}Lu]Lu-DOTATATE therapy reveal (top) remission in a responder with a pancreatic neuroendocrine tumor (Ki-67 = 20%) and (bottom) progression in a non-responder with a well-differentiated ileal neuroendocrine tumor (Ki-67 = 1%). (This research was originally published in *Lancet Oncology*; Herrmann et al. [18])

1.2.2   Combination Treatments

A promising route for improving the therapeutic effectiveness of radiopharmaceutical therapy is the use of combination treatments that offer synergistic effects. For example, clinical trials are underway for the treatment of small-cell lung cancer with a combination of [^{177}Lu]Lu-DOTATATE (Lutathera) and nivolumab, with the phase I study demonstrating that the therapy is well tolerated and has antitumor activity [23, 24]. The combination of [^{177}Lu]Lu-DOTATATE and carboplatin, etoposide, and tislelizumab is also being investigated for extensive-stage small-cell lung cancer (NCT05142696). For the treatment of metastatic prostate cancer with [^{177}Lu]Lu-PSMA-617 and pembrolizumab, preliminary results in two patients show PSA stabilization after three therapy cycles, and for [^{177}Lu]Lu-PSMA-617 with Olaparib, radiological and biochemical response was seen [25]. Both patients tolerated the combination therapy without significant hematological toxicity [25]. Additionally, patients with castration-resistant prostate cancer who underwent therapy with [^{177}Lu]Lu-PSMA-617
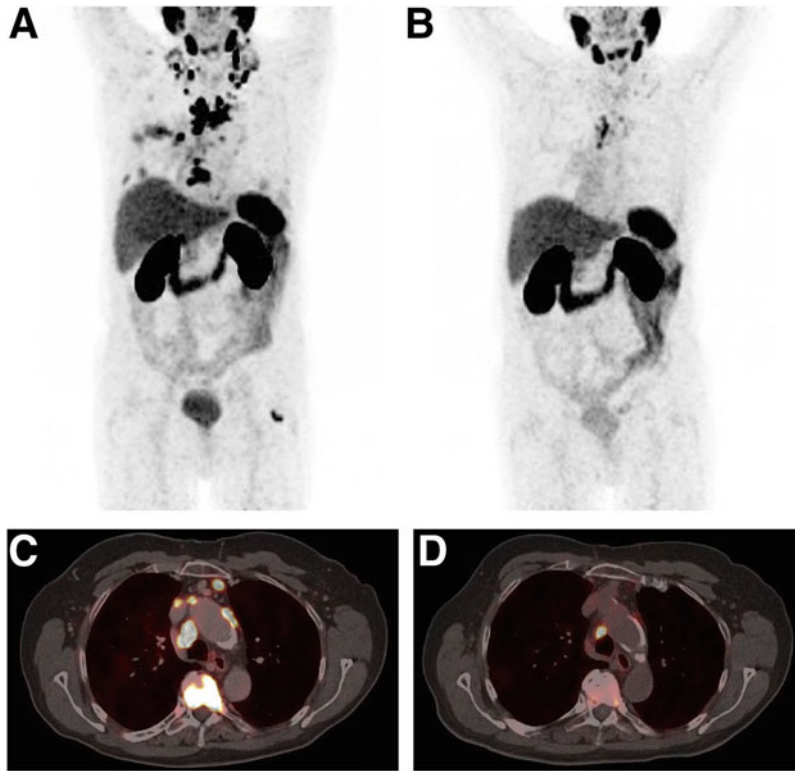
Fig. 1.3 [^{68}Ga]Ga-PSMA-11 PET/CT scans obtained at baseline and after two cycles of [^{177}Lu]Lu-PSMA-617 therapy in a patient with metastatic castrate-resistant prostate cancer. Whole-body [^{68}Ga]Ga-PSMA-11 PET maximum-intensity projections (**a** and **b**) and axial PET/CT scans (**c** and **d**) of thorax are shown at baseline (**a** and **c**) and after therapy (**b** and **d**). [^{68}Ga]Ga-PSMA-11 PET demonstrates considerable reduction of PSMA-expressing metastases in the lymph nodes and bones after two cycles, each with 6.0 GBq of [^{177}Lu]Lu-PSMA-617. The patient's serum PSA level decreased from 11.5 to 1.2 ng/mL. (This research was originally published in *JNM*; Fendler et al. [21]. © SNMMI)

and pembrolizumab in the PRINCE trial had a PSA response rate of 76%, a median radiological progression-free survival of 11.2 months, and a median overall survival of 17.8 months [26]. Furthermore, the combination of [^{177}Lu]Lu-DOTATATE and metronomic capecitabine has been investigated for patients with advanced neuroendocrine tumors showing that the therapy is well tolerated [27] and leads to prolonged overall survival and progression-free survival (Fig. 1.4) [28]. The same combination was studied in a patient with metastatic mediastinal paraganglioma who showed partial response and a significantly improved quality of life [29].

1.2.3   New Targets

The therapeutic concepts outlined above are just the beginning. There are endless possibilities for radiopharmaceutical therapy, which makes it an exciting field destined for growth. For example, targeting somatostatin receptors has proven effective for neuroendocrine tumors, but there are other cancers that overexpress somatostatin receptor type 2, including breast cancer, small-cell lung cancer, pheochromocytoma, and meningioma [30–34]. Similarly, PSMA is also expressed in hepatocellular carcinoma and renal cell carcinoma [35–37].
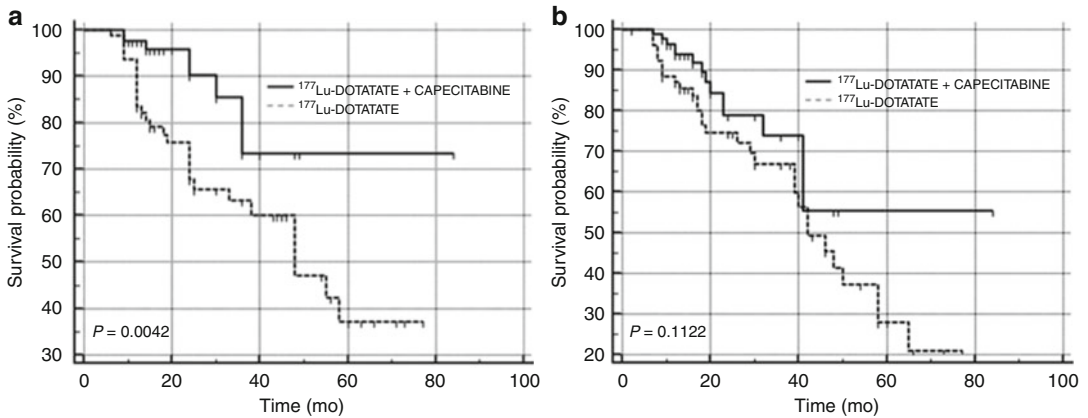
Fig. 1.4 Kaplan-Meier plots of overall survival (**a**) and progression-free survival (**b**) for patients with advanced neuroendocrine tumors who underwent treatment with [177Lu]Lu-DOTATATE with and without capecitabine. (This research was originally published in *Clinical Nuclear Medicine*; Ballal et al. [28])

Innovation is also possible with new biological targets such as the C-X-C chemokine receptor type 4 (CXCR-4)–stromal cell-derived factor 1 (SDF-1) axis [38–40] for hematological malignancies, fibroblast activation protein (FAP) [41–44] for several cancers including many gynecological tumors, neurotensin receptor 1 (NTR1) for pancreatic adenocarcinoma [45–47], cholecystokinin B receptor (CCK2-R) [48, 49], the gastric-releasing peptide receptor (GRP-R) [50], and integrin receptors [51–54]. A wide variety of vectors could be leveraged for these targets and others, including monoclonal antibodies—e.g., [131I]I-Omburtamab for central nervous system neuroblastomas and brain stem gliomas and [177Lu]Lu-Lilotomab satetraxetan for lymphoma [55–57]—nanobodies, engineered proteins, peptides, and small molecules [18].

1.2.4 Innovations in Radionuclides and Dose

Two opportunities for growth lie in broadening the range of therapeutic radionuclides harnessed for therapy and expanding the use of alpha-particle-emitting radionuclides such as 225Ac, 213Bi, 212Pb, and 211At. Alpha-emitting radionuclides are advantageous because the range of alpha particles in human tissue corresponds to only a few cell diameters (< 0.1 mm), allowing for the selective killing of the targeted cancer cells while sparing the surrounding healthy tissue. In addition, the higher energy of alpha particles affords the ability to kill cells that otherwise exhibit resistance to treatment with beta- or gamma-emitting radionuclides or chemotherapeutics [58]. Furthermore, most targeted radionuclide therapies are restricted to a single or a few administrations due to a lack of prospective studies demonstrating the tolerability of higher doses and more cycles/administrations. Therefore, the exploration of both dose escalation and fractionation represents areas for expansion and innovation as well [18, 59, 60].

1.2.5 Clinical Trials and Training

As the number of options for cancer therapeutics increases, the optimal choice, timing, and combination of interventions will become the principal aim of precision oncology. In this spirit, well-designed, step-wise, multicenter prospective clinical trials will be highly important for radiopharmaceutical therapy—and all therapeutics, for that matter—as we move forward. These trials will be especially important in the

context of expanding the focus of radiopharmaceutical therapy from advanced metastatic disease to a first-line treatment in certain cancers. For example, the low-toxicity profile and favorable dosimetry of PSMA-targeted endoradiotherapy paired with the radiosensitivity of early localized prostate cancer may combine to yield a curative therapy [18].

In order to best implement the upcoming advances in radiopharmaceutical therapy, emphasis must be placed on the continued high-level training of physicians, physicists, radiochemists, and radiopharmacists. For example, the formulation and safe dispensation of these radiotherapeutics requires additional expertise and training in radiopharmacy. This expert knowledge is particularly important when handling large quantities of β- and α-emitting radionuclides. Furthermore, all members of the care team should understand radiation safety and dosimetry. Finally, well-trained nuclear medicine physicians and radiologists will be needed to bridge the gap between radiochemistry, pharmacy, medical physics, radiation protection, and the different fields of clinical oncology [18, 61].

1.3   Controversial Issues

Radiopharmaceutical therapy is often deployed hand-in-hand with theranostic imaging in order to select the patients most likely to respond to treatment. Whereas this personalized concept is logical, a group of clinicians recently questioned the predictive value of a baseline PSMA-PET (PSMA-positron emission tomography) for the clinical benefit of [^{177}Lu]Lu-PSMA-617 treatment [62]. However, this question was recently investigated in 301 metastatic castrate-resistant prostate cancer patients treated with [^{177}Lu]Lu-PSMA-617 as a part of the VISION trial. Patients were classified as eligible or "screen failure" based on their baseline PSMA-PET/CT (PSMA-PET/computed tomography). PSA response rates (decline of ≥50%), PSA–progression-free survival, and overall survival were also compared.

The results illustrated that patients who did not meet the PSMA PET/CT criteria in the VISION trial showed worse outcomes after [^{177}Lu]Lu-PSMA-617 therapy than those who were eligible [63], demonstrating the utility of PSMA-PET/CT for patient selection.

An additional controversy in the field stems from the question of which medical specialty will administer the treatments. In Europe, in many countries such as Germany, Switzerland, and Austria, among others, it is clear that nuclear medicine departments will treat these patients. Whereas in other countries, such as Italy and Belgium, even thyroid treatments were often performed by radiation oncology. In the United States both radiation oncology and nuclear medicine/radiology departments are expressing interest in administering radiopharmaceutical therapy. In 2017 and more recently last fall, the American Society for Radiation Oncology prioritized the development of a radiopharmaceutical therapy curriculum that can be integrated into radiation oncology resident education [64, 65]. Therefore, the nuclear medicine community, while currently dealing with the rapid expansion of targeted radionuclide therapies, will need to adapt and face the demands of the larger radiation oncology competition. Building on the 80 plus years of experience, nuclear medicine should embrace multidisciplinary collaborations to secure the competitive edge of its field in theranostics [66].

1.4   The Future

In the future, we predict that radiopharmaceutical therapy will also be utilized for early-stage cancer treatment; however, prospective clinical trials are needed to test this hypothesis. In addition, it will be very important to identify the complementary role of RPT with antibody–drug conjugates as well as in other combination therapies. In summary, RPT is an exciting expanding field that will be invaluable for the application of precision oncology and the improvement of treatments for a multitude of different cancers.

1.5 The Bottom Line

- Radiopharmaceutical therapy is predicated on the use of injectable radiopharmaceuticals for the treatment of cancer.
- Radiopharmaceutical therapy has been shown to increase the survival parameters of patients with metastatic thyroid cancer treated with $[^{131}I]I^-$ (overall survival), patients with advanced midgut neuroendocrine tumors treated with $[^{177}Lu]Lu$-DOTATATE (progression-free survival), and patients with metastatic prostate cancer treated with $[^{177}Lu]$ Lu-PSMA-617 (overall and progression-free survival).
- Innovation is possible with new targets such as the C-X-C chemokine receptor type 4–SDF-1 axis, fibroblast activation protein, neurotensin receptor 1, cholecystokinin B receptor, gastric-releasing peptide receptor, and integrin receptors as well as new vectors like antibodies, nanobodies, engineered proteins, peptides, and small molecules.
- Combining radiopharmaceutical therapy with other therapeutic modalities offers a way to create synergistic effects and drive the clinical acceptance of RPT.
- The development of well-designed, step-wise, multicenter prospective clinical trials and the implementation of specialized endoradiotherapy training programs are imperative as the field moves forward.

References

1. Seidlin SM, Marinelli LD, Oshry E. Radioactive iodine therapy; effect on functioning metastases of adenocarcinoma of the thyroid. J Am Med Assoc. 1946;132(14):838–47.
2. Nilsson S, Cislo P, Sartor O, Vogelzang NJ, Coleman RE, O'Sullivan JM, et al. Patient-reported quality-of-life analysis of radium-223 dichloride from the phase III ALSYMPCA study. Ann Oncol. 2016;27(5):868–74.
3. Lange R, Overbeek F, de Klerk JMH, Pasker-de Jong PCM, van den Berk AM, Ter Heine R, et al. Treatment of painful bone metastases in prostate and breast cancer patients with the therapeutic radiopharmaceutical rhenium-188-HEDP. Clinical benefit in a real-world study. Nuklearmedizin. 2016;55(5):188–95.
4. Fendler WP, Reinhardt S, Ilhan H, Delker A, Böning G, Gildehaus FJ, et al. Preliminary experience with dosimetry, response and patient reported outcome after 177Lu-PSMA-617 therapy for metastatic castration-resistant prostate cancer. Oncotarget. 2017;8(2):3581–90.
5. Hofman MS, Violet J, Hicks RJ, Ferdinandus J, Thang SP, Akhurst T, et al. [177Lu]-PSMA-617 radionuclide treatment in patients with metastatic castration-resistant prostate cancer (LuPSMA trial): a single-centre, single-arm, phase 2 study. Lancet Oncol. 2018;19(6):825–33.
6. Strosberg J, Wolin E, Chasen B, Kulke M, Bushnell D, Caplin M, et al. Health-related quality of life in patients with progressive midgut neuroendocrine tumors treated with 177Lu-Dotatate in the phase III NETTER-1 trial. J Clin Oncol. 2018;36(25):2578–84.
7. Marinova M, Mücke M, Fischer F, Essler M, Cuhls H, Radbruch L, et al. Quality of life in patients with midgut NET following peptide receptor radionuclide therapy. Eur J Nucl Med Mol Imaging. 2019;46(11):2252–9.
8. Waissi F, Kist JW, Lodewijk L, de Wit AG, van der Hage JA, van Dalen T, et al. Fast-track radioiodine ablation therapy after thyroidectomy reduces sick leave in patients with differentiated thyroid cancer (FASTHYNA Trial). Clin Nucl Med. 2019;44(4):272–5.
9. Fahey FH, Grant FD, Thrall JH. Saul Hertz, MD, and the birth of radionuclide therapy. EJNMMI Phys. 2017;4(1):15.
10. Hertz B. A tribute to Dr. Saul Hertz: the discovery of the medical uses of radioiodine. World J Nucl Med. 2019;18(1):8–12.
11. Luster M, Clarke SE, Dietlein M, Lassmann M, Lind P, Oyen WJG, et al. Guidelines for radioiodine therapy of differentiated thyroid cancer. Eur J Nucl Med Mol Imaging. 2008;35(10):1941–59.
12. Strosberg J, El-Haddad G, Wolin E, Hendifar A, Yao J, Chasen B, et al. Phase 3 trial of 177Lu-Dotatate for midgut neuroendocrine tumors. N Engl J Med. 2017;376(2):125–35.
13. Kaemmerer D, Prasad V, Daffner W, Hörsch D, Klöppel G, Hommann M, et al. Neoadjuvant peptide receptor radionuclide therapy for an inoperable neuroendocrine pancreatic tumor. World J Gastroenterol. 2009;15(46):5867–70.
14. Sansovini M, Severi S, Ambrosetti A, Monti M, Nanni O, Sarnelli A, et al. Treatment with the radiolabelled somatostatin analog Lu-DOTATATE for advanced pancreatic neuroendocrine tumors. Neuroendocrinology. 2013;97(4):347–54.
15. Ezziddin S, Lauschke H, Schaefers M, Meyer C, van Essen M, Biersack HJ, et al. Neoadjuvant downsizing by internal radiation: a case for preoperative peptide receptor radionuclide therapy in patients with pancreatic neuroendocrine tumors. Clin Nucl Med. 2012;37(1):102–4.
16. Delpassand ES, Samarghandi A, Zamanian S, Wolin EM, Hamiditabar M, Espenan GD, et al. Peptide receptor radionuclide therapy with 177Lu-DOTATATE for patients with somatostatin receptor-expressing neuroendocrine tumors: the first US phase 2 experience. Pancreas. 2014;43(4):518–25.

17. van Schaik E, van Vliet EI, Feelders RA, Krenning EP, Khan S, Kamp K, et al. Improved control of severe hypoglycemia in patients with malignant insulinomas by peptide receptor radionuclide therapy. J Clin Endocrinol Metab. 2011;96(11):3381–9.

18. Herrmann K, Schwaiger M, Lewis JS, Solomon SB, McNeil BJ, Baumann M, et al. Radiotheranostics: a roadmap for future development. Lancet Oncol. 2020;21(3):e146–56.

19. Hofman MS, Lawrentschuk N, Francis RJ, Tang C, Vela I, Thomas P, et al. Prostate-specific membrane antigen PET-CT in patients with high-risk prostate cancer before curative-intent surgery or radiotherapy (proPSMA): a prospective, randomised, multicentre study. Lancet. 2020;395(10231):1208–16.

20. Kim YJ, Kim YI. Therapeutic responses and survival effects of 177Lu-PSMA-617 radioligand therapy in metastatic castrate-resistant prostate cancer: a meta-analysis. Clin Nucl Med. 2018;43(10):728–34.

21. Fendler WP, Rahbar K, Herrmann K, Kratochwil C, Eiber M. 177Lu-PSMA radioligand therapy for prostate cancer. J Nucl Med. 2017;58(8):1196–200.

22. Sartor O, de Bono J, Chi KN, Fizazi K, Herrmann K, Rahbar K, et al. Lutetium-177-PSMA-617 for metastatic castration-resistant prostate cancer. N Engl J Med. 2021;385(12):1091–103.

23. Kim C, Subramaniam D, Liu S, Giaccone G. P2.12-03 phase I/II trial of 177Lu-DOTA0-Tyr3-Octreotate (Lutathera) and nivolumab for patients with extensive-stage small cell lung cancer (ES-SCLC). J Thorac Oncol. 2018;13(10):S791.

24. Kim C, Liu SV, Subramaniam DS, Torres T, Loda M, Esposito G, et al. Phase I study of the 177Lu-DOTA0-Tyr3-Octreotate (lutathera) in combination with nivolumab in patients with neuroendocrine tumors of the lung. J Immunother Cancer. 2020;8(2):e000980.

25. Prasad V, Zengerling F, Steinacker JP, Bolenz C, Beer M, Wiegel T, et al. First experiences with 177Lu-PSMA therapy in combination with pembrolizumab or after pretreatment with olaparib in single patients. J Nucl Med. 2021;62(7):975–8.

26. Sandhu S, Joshua AM, Emmett L, Spain LA, Horvath L, Crumbaker M, et al. PRINCE: phase I trial of 177Lu-PSMA-617 in combination with pembrolizumab in patients with metastatic castration-resistant prostate cancer (mCRPC). JCO. 2022;40 (16_suppl):5017.

27. Nicolini S, Bodei L, Bongiovanni A, Sansovini M, Grassi I, Ibrahim T, et al. Combined use of 177Lu-DOTATATE and metronomic capecitabine (Lu-X) in FDG-positive gastro-entero-pancreatic neuroendocrine tumors. Eur J Nucl Med Mol Imaging. 2021;48 (10):3260–7.

28. Ballal S, Yadav MP, Damle NA, Sahoo RK, Bal C. Concomitant 177Lu-DOTATATE and capecitabine therapy in patients with advanced neuroendocrine tumors: a long-term-outcome, toxicity, survival, and quality-of-life study. Clin Nucl Med. 2017;42(11): e457–66.

29. Ashwathanarayana AG, Biswal CK, Sood A, Parihar AS, Kapoor R, Mittal BR. Imaging-guided use of combined 177Lu-DOTATATE and capecitabine therapy in metastatic mediastinal paraganglioma. J Nucl Med Technol. 2017;45(4):314–6.

30. Bartolomei M, Bodei L, De Cicco C, Grana CM, Cremonesi M, Botteri E, et al. Peptide receptor radionuclide therapy with (90)Y-DOTATOC in recurrent meningioma. Eur J Nucl Med Mol Imaging. 2009;36 (9):1407–16.

31. Savelli G, Zaniboni A, Bertagna F, Bosio G, Nisa L, Rodella C, et al. Peptide Receptor Radionuclide Therapy (PRRT) in a patient affected by metastatic breast cancer with neuroendocrine differentiation. Breast Care (Basel). 2012;7(5):408–10.

32. Mak IYF, Hayes AR, Khoo B, Grossman A. Peptide receptor radionuclide therapy as a novel treatment for metastatic and invasive phaeochromocytoma and paraganglioma. Neuroendocrinology. 2019;109(4): 287–98.

33. Jaiswal SK, Sarathi V, Memon SS, Garg R, Malhotra G, Verma P, et al. 177Lu-DOTATATE therapy in metastatic/inoperable pheochromocytoma-paraganglioma. Endocr Connect. 2020;9(9):864–73.

34. Mirvis E, Toumpanakis C, Mandair D, Gnanasegaran G, Caplin M, Navalkissoor S. Efficacy and tolerability of peptide receptor radionuclide therapy (PRRT) in advanced metastatic bronchial neuroendocrine tumours (NETs). Lung Cancer. 2020;150: 70–5.

35. Raveenthiran S, Esler R, Yaxley J, Kyle S. The use of 68Ga-PET/CT PSMA in the staging of primary and suspected recurrent renal cell carcinoma. Eur J Nucl Med Mol Imaging. 2019;46(11):2280–8.

36. Kesler M, Levine C, Hershkovitz D, Mishani E, Menachem Y, Lerman H, et al. 68Ga-PSMA is a novel PET-CT tracer for imaging of hepatocellular carcinoma: a prospective pilot study. J Nucl Med. 2019;60(2):185–91.

37. Hirmas N, Leyh C, Sraieb M, Barbato F, Schaarschmidt BM, Umutlu L, et al. 68Ga-PSMA-11 PET/CT improves tumor detection and impacts management in patients with hepatocellular carcinoma. J Nucl Med. 2021;62(9):1235–41.

38. Herrmann K, Schottelius M, Lapa C, Osl T, Poschenrieder A, Hänscheid H, et al. First-in-human experience of CXCR4-directed endoradiotherapy with 177Lu- and 90Y-labeled pentixather in advanced-stage multiple myeloma with extensive intra- and extramedullary disease. J Nucl Med. 2016;57(2): 248–51.

39. Kircher M, Herhaus P, Schottelius M, Buck AK, Werner RA, Wester HJ, et al. CXCR4-directed theranostics in oncology and inflammation. Ann Nucl Med. 2018;32(8):503–11.

40. Schottelius M, Herrmann K, Lapa C. In vivo targeting of CXCR4-new horizons. Cancers (Basel). 2021;13 (23):5920.

41. Altmann A, Haberkorn U, Siveke J. The latest developments in imaging of fibroblast activation protein. J Nucl Med. 2021;62(2):160–7.

42. Dendl K, Koerber SA, Finck R, Mokoala KMG, Staudinger F, Schillings L, et al. 68Ga-FAPI-PET/CT

in patients with various gynecological malignancies. Eur J Nucl Med Mol Imaging. 2021;48(12):4089–100.

43. Kratochwil C, Flechsig P, Lindner T, Abderrahim L, Altmann A, Mier W, et al. 68Ga-FAPI PET/CT: tracer uptake in 28 different kinds of cancer. J Nucl Med. 2019;60(6):801–5.

44. Sollini M, Kirienko M, Gelardi F, Fiz F, Gozzi N, Chiti A. State-of-the-art of FAPI-PET imaging: a systematic review and meta-analysis. Eur J Nucl Med Mol Imaging. 2021;48(13):4396–414.

45. Schulz J, Rohracker M, Stiebler M, Goldschmidt J, Stöber F, Noriega M, et al. Proof of therapeutic efficacy of a 177Lu-labeled neurotensin receptor 1 antagonist in a colon carcinoma xenograft model. J Nucl Med. 2017;58(6):936–41.

46. Baum RP, Singh A, Schuchardt C, Kulkarni HR, Klette I, Wiessalla S, et al. 177Lu-3BP-227 for neurotensin receptor 1-targeted therapy of metastatic pancreatic adenocarcinoma: first clinical results. J Nucl Med. 2018;59(5):809–14.

47. Langbein T, Weber WA, Eiber M. Future of theranostics: an outlook on precision oncology in nuclear medicine. J Nucl Med. 2019;60(Suppl 2): 13S–9S.

48. Roosenburg S, Laverman P, van Delft FL, Boerman OC. Radiolabeled CCK/gastrin peptides for imaging and therapy of CCK2 receptor-expressing tumors. Amino Acids. 2011;41(5):1049–58.

49. Sauter AW, Mansi R, Hassiepen U, Muller L, Panigada T, Wiehr S, et al. Targeting of the cholecystokinin-2 receptor with the minigastrin analog 177Lu-DOTA-PP-F11N: does the use of protease inhibitors further improve in vivo distribution? J Nucl Med. 2019;60(3):393–9.

50. Chastel A, Vimont D, Claverol S, Zerna M, Bodin S, Berndt M, et al. 68Ga-radiolabeling and pharmacological characterization of a kit-based formulation of the Gastrin-Releasing Peptide Receptor (GRP-R) antagonist RM2 for convenient preparation of [68Ga] Ga-RM2. Pharmaceutics. 2021;13(8):1160.

51. Debordeaux F, Chansel-Debordeaux L, Pinaquy JB, Fernandez P, Schulz J. What about αvβ3 integrins in molecular imaging in oncology? Nucl Med Biol. 2018;62–63:31–46.

52. Rangger C, Haubner R. Radiolabelled peptides for positron emission tomography and endoradiotherapy in oncology. Pharmaceuticals (Basel). 2020;13(2): E22.

53. Minamimoto R, Karam A, Jamali M, Barkhodari A, Gambhir SS, Dorigo O, et al. Pilot prospective evaluation of (18)F-FPPRGD2 PET/CT in patients with cervical and ovarian cancer. Eur J Nucl Med Mol Imaging. 2016;43(6):1047–55.

54. Li L, Ma L, Shang D, Liu Z, Yu Q, Wang S, et al. Pretreatment PET/CT imaging of angiogenesis based on 18F-RGD tracer uptake may predict antiangiogenic response. Eur J Nucl Med Mol Imaging. 2019;46(4): 940–7.

55. Modak S, Kramer K, Gultekin SH, Guo HF, Cheung NK. Monoclonal antibody 8H9 targets a novel cell surface antigen expressed by a wide spectrum of human solid tumors. Cancer Res. 2001;61(10): 4048–54.

56. Kaplon H, Muralidharan M, Schneider Z, Reichert JM. Antibodies to watch in 2020. MAbs. 2020;12(1): 1703531.

57. Yerrabelli RS, He P, Fung EK, Kramer K, Zanzonico PB, Humm JL, et al. IntraOmmaya compartmental radioimmunotherapy using 131I-omburtamab-pharmacokinetic modeling to optimize therapeutic index. Eur J Nucl Med Mol Imaging. 2021;48(4):1166–77.

58. Morgenstern A, Apostolidis C, Kratochwil C, Sathekge M, Krolicki L, Bruchertseifer F. An overview of targeted alpha therapy with 225Actinium and 213Bismuth. Curr Radiopharm. 2018;11(3):200–8.

59. Garske-Román U, Sandström M, Fröss Baron K, Lundin L, Hellman P, Welin S, et al. Prospective observational study of 177Lu-DOTA-octreotate therapy in 200 patients with advanced metastasized neuroendocrine tumours (NETs): feasibility and impact of a dosimetry-guided study protocol on outcome and toxicity. Eur J Nucl Med Mol Imaging. 2018;45(6): 970–88.

60. Eberlein U, Cremonesi M, Lassmann M. Individualized dosimetry for theranostics: necessary, nice to have, or counterproductive? J Nucl Med. 2017;58(Suppl 2):97S–103S.

61. Czernin J. Toward independent nuclear medicine, molecular imaging, and theranostic programs. J Nucl Med. 2019;60(8):1037.

62. Hussain M, Carducci MA, Clarke N, Fenton SE, Fizazi K, Gillessen S, et al. Evolving role of prostate-specific membrane antigen-positron emission tomography in metastatic hormone-sensitive prostate cancer: more questions than answers? J Clin Oncol. 2022; https://doi.org/10.1200/JCO2200208.

63. Hotta M, Gafita A, Czernin J, Calais J. Outcome of patients with PSMA-PET/CT screen failure by VISION criteria and treated with 177Lu-PSMA therapy: a multicenter retrospective analysis. J Nucl Med. 2022; https://doi.org/10.2967/jnumed.121.263441.

64. Kiess AP, Hobbs RF, Bednarz B, Knox SJ, Meredith R, Escorcia FE. ASTRO's framework for radiopharmaceutical therapy curriculum development for trainees. Int J Radiat Oncol Biol Phys. 2022. https://www.sciencedirect.com/science/article/abs/pii/S0360301622002516.

65. Meredith R, Howell R. RPT radiobiology, theranostics pharmacokinetics [Internet]. Available from: https://bluetoad.com/publication/?i=780120&article_id=4490646&view=articleBrowser.

66. Dierckx R, Herrmann K, Hustinx R, Lassmann M, Wadsak W, Kunikowska J. European Association of Nuclear Medicine (EANM) response to the proposed ASTRO's framework for radiopharmaceutical therapy curriculum development for trainees. Eur J Nucl Med Mol Imaging. 2022;50(1):1–3.

A Brief History of Radiopharmaceutical Therapy

2

Gustav Y. Cederquist and Freddy E. Escorcia

2.1 Molecular Lock and Key: Ehrlich and His Magic Bullets

Until the twentieth century, cancer was a surgical problem. For centuries, anatomists and pathologists had illustrated the organization of human tissues and the ways in which cancer spreads through it. This understanding equipped surgeons with the knowledge of how to best remove cancer from the human body. Aseptic technique permitted cleaner and more extensive surgeries that included the removal of not only the visible cancer but also the lymphatic channels through which cancer invisibly spreads. This strategy is most notably illustrated by Halsted's radical mastectomy, which removed the entire breast, the lymph nodes under the arm, and the chest wall musculature. In 1894, he published his surgical experience of 50 patients [1]. Yet while the titans of surgery were experimenting on the width of anatomical margins needed to eradicate cancer, a revolutionary new way to look at this problem was just over the horizon.

In 1878, Paul Ehrlich was a 24-year-old medical student who had the idea to use textile dyes to stain cells for microscopy. He observed that his textile dyes were discriminant and colored specific subcellular structures in a predictable way (Fig. 2.1). This led him to believe that the cell is composed of a chemical matrix, and each constituent can be accessed with a key of the correct chemical affinity [2]. Ehrlich went on to refine this idea through work with certain protein products of plant and animal cells: toxins. He observed that their activity harbored a peculiar duality. Toxins—such as abrin, ricin, and snake venom—acted as not only poisons but also as stimulators of anti-toxin, or neutralizing receptors. He dissected the molecular anatomy of these neutralizing receptors and ultimately theorized the existence of a lock-and-key mechanism that existed between toxins and anti-toxins [3]. This idea was further refined into the "receptor theory" as he described in his 1908 Nobel lecture [4].

Ehrlich extended this conceptual framework beyond toxins and postulated the existence of "chemoreceptors" with specific affinities for simple chemical structures, far less complex than toxins. For example, he proposed that hemoglobin might contain "ferroreceptors" with specific affinity for iron that endowed the molecule with its oxygen-capturing potential [4]. If such chemoreceptors did exist, they could support the rational development of therapeutics. Drugs could be aimed at chemoreceptors present on

G. Y. Cederquist (✉)
Radiation Oncology, Memorial Sloan Kettering Cancer Center, New York, NY, USA
e-mail: cederqug@mskcc.org

F. E. Escorcia (✉)
Molecular Imaging Branch, Radiation Oncology Branch, National Cancer Institute, Bethesda, MD, USA
e-mail: freddy.escorcia@nih.gov

Fig. 2.1 The use of aniline dyes in microscopy by Paul Ehrlich (date unknown). (Source: Wellcome Collection. Creative Commons Attribution 4.0 International license. https://wellcomecollection.org/works/m5ahupne)
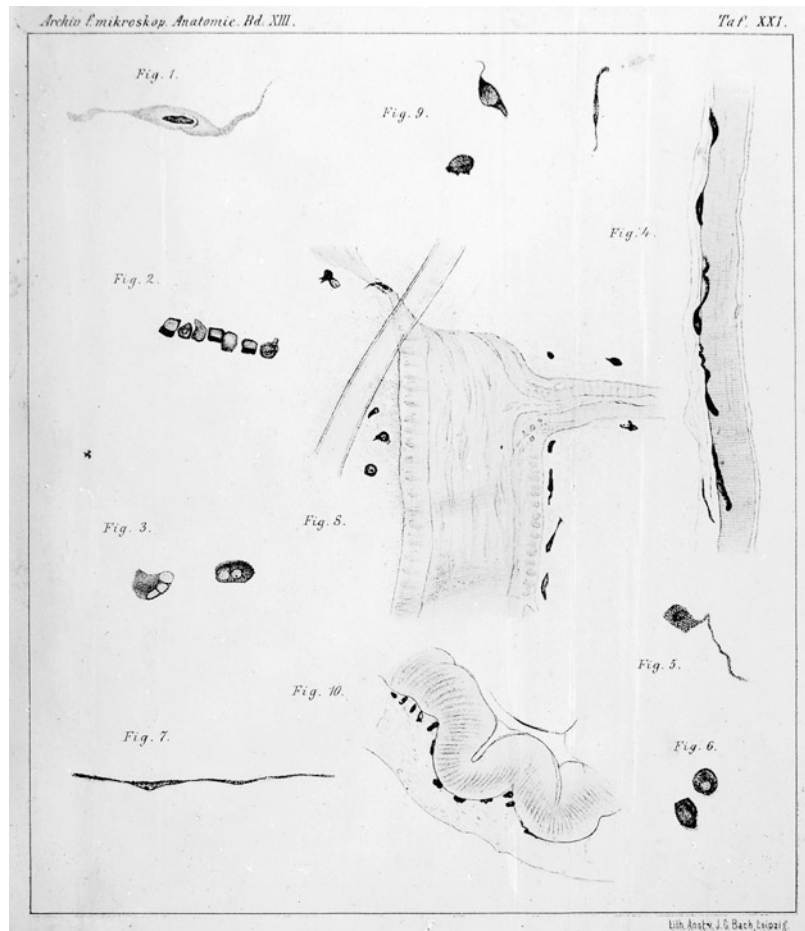
pathogens or cancerous cells while simultaneously remaining invisible to healthy cells. And thus began Ehrlich's search for a therapeutic magic bullet.

But proving the existence of chemoreceptors was not straightforward. Unlike anti-toxins—which were shed into the blood and thus allowed their activity to be isolated—chemoreceptors were stubborn and intrinsically tied to the cell's protoplasm. Evidence for their existence came in a roundabout way. In studying drug-resistant strains of *Trypanosoma*, Ehrlich found that each resistance phenotype develops not just to a specific drug but to the chemical family to which that drug belongs, all while maintaining sensitivity for other distinct classes of drugs [4]. This strict specificity between chemical identity and drug activity could only be explained by the existence of receptors that recognize a specific chemical identity, that is, chemoreceptors.

Ehrlich set his sights on the major public health priority of his day: syphilis. Working with colleague Sahachiro Hata, he screened libraries of chemical derivates for potent anti-syphilitic activity. Compound 606, or Salvarsan, possessed the activity they were looking for [5]. Salvarsan was deployed in the clinic as an intravenous injection, thus marking the development of the first chemotherapy. Ehrlich's fame brought him to Kaiser Wilhelm II's palace in 1908. There, the emperor asked Ehrlich to devote his research to the study of cancer chemotherapy; Ehrlich began to describe the complexity of this task. But the emperor, instead of appreciating this

point of view, became upset and ended Ehrlich's lecture abruptly [2]. Had Ehrlich been in Kaiser Wilhelm II's palace 7 years earlier, he might have run into a fellow hero in the history of radiopharmaceutical therapy: Wilhelm Roentgen.

2.2 I Have Seen My Death: Roentgen and the Discovery of X-Rays

On November 8, 1895, Wilhelm Roentgen was experimenting with cathode rays in a vacuum tube. The experiment was set up such that a cathode wire generates a ray of energy that travels from the negatively charged cathode to the positively charged anode end of the tube. This was done in a vacuum to avoid molecular collisions with air. The tube itself was covered with cardboard to prevent the escape of visible light. The assumption was that by blocking the sides of the tube with cardboard, the cathode rays would only be able to escape through a small aluminum window at the anode end of the tube. But when Roentgen started the apparatus, he noticed something strange, a flickering light on a barium platinocyanide screen next to the ray tube. Because of the cardboard insulation, no visible light should be escaping in that direction(!). The only possible explanation, he surmised, was the existence of a new kind of ray that he called the X-ray [6]. He experimented for a few more weeks to probe the nature of these mysterious rays. He experimented with their transparency through various materials, tested whether prisms could refract them, or probed whether strong magnets could bend them. In every way, the rays appeared to be something novel.

In characterizing the permeability of X-rays through various substances, he asked his wife Bertha to hold a lead plate against the detector screen. What he saw was not only an outline of the lead plate, but also the outline of the bones in her hand (Fig. 2.2). Roentgen observed that bones, like lead, are rather opaque and visible to his new kind of ray. The practical implications of this escaped neither him nor the public. Indeed,

Fig. 2.2 The first medical X-ray of Anna Bertha Ludwig's hand; by Wilhelm Roentgen (December 22, 1895). (Source: Wikimedia Commons. Public Domain: This work is in the public domain in its country of origin and other countries and areas where the copyright term is the author's life plus 100 years or less [70 years in the USA]. https://commons.wikimedia.org/wiki/File:First_medical_X-ray_by_Wilhelm_R%C3%B6ntgen_of_his_wife_Anna_Bertha_Ludwig%27s_hand_-_18951222.gif)

his discovery caught the public's attention like wildfire, and its diagnostic possibilities were quickly exploited. But not everyone shared this enthusiasm. Upon seeing the images of her bones, Bertha reportedly exclaimed, "I have seen my death" [7].

Roentgen published his original paper on December 28, 1895. Just 8 days later, this achievement made newspaper headlines [8] and quickly spread to the media capitals of the world, including Paris, London, and the United States. The diagnostic possibilities of X-rays were immediately put to the test, as we will soon learn.

2.3   Spontaneous Rays: The Discovery of Radioactivity

While X-rays were quickly exploited for medical use, they also spurred new scientific breakthroughs. In 1896, on the first day he heard of the news, Henri Becquerel decided to explore whether Roentgen's mysterious rays might also emanate from phosphorescent materials [9]. He chose to study uranium based on its exceptional emission spectrum. To this end, he placed uranium salts on a developing film protected with black paper and various metal screens, including a Maltese cross. He first exposed the salts to the sun and found that the film darkened near the salts, suggesting that uranium transformed the sun's energy (Fig. 2.3). But when he performed the control experiment—in the absence of sun exposure—he observed the same phenomenon! He discovered that uranium emanates spontaneous radiations [10].

While the world was occupied with X-rays, only a few discerning minds realized the importance of Becquerel's observations. Marie Curie was one of this select few, and she began her studies of uranium in 1897 (Fig. 2.4). She, along with her husband Pierre, developed a very sensitive electrometer that allowed for the measurement of small ionizations of air generated by Becquerel's rays. Curie studied a variety of uranium-containing compounds and found that spontaneous radiation depended only on the presence of uranium. She concluded that this property is inherent to the uranium atom itself, rather than dependent on any physical or chemical arrangement [11]. She later demonstrated the same phenomenon with thorium and termed this property radioactivity. She shared the 1903 Nobel Prize in physics with Becquerel and her husband Pierre.

Curie and her husband noticed that certain minerals were much more radioactive than predicted based on their quantities of uranium or thorium and suspected that these minerals were laced with even more radioactive elements. They then began the arduous process of chemically fractionating the raw material of pitchblende, a uranium-containing ore, into its constituent elements. This led to the discovery of both polonium—an element with similar chemical properties to bismuth—and radium, which is
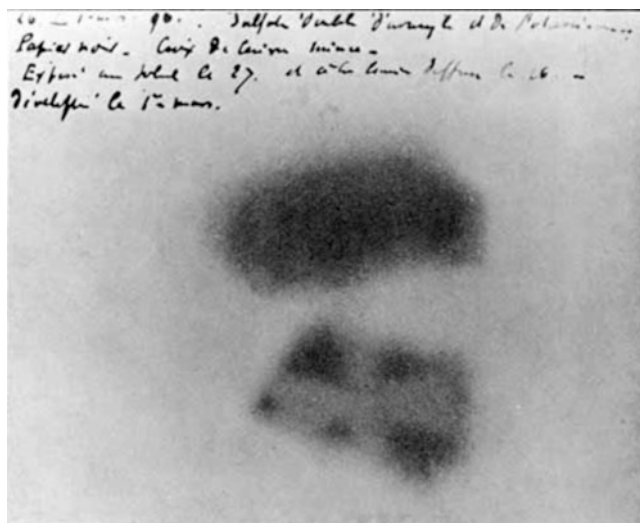
Fig. 2.3 The effect of exposure to radioactivity is demonstrated using a Becquerel plate—a shadow is created by placing a Maltese cross between the radioactive source and plate; by Henri Becquerel (1896). (Source: Wikimedia Commons. Public Domain: This work is in the public domain in its country of origin and other countries and areas where the copyright term is the author's life plus 100 years or less [70 years in the USA]. https://commons.wikimedia.org/wiki/File: Becquerel_plate.jpg)

Fig. 2.4 Pierre and Marie Curie using a specialized electrometer to measure radioactivity; author unknown (circa 1904). (Source: Wikimedia Commons. Public Domain: This image was published more than 70 years ago without a public claim of authorship and no subsequent claim of authorship was made in the 70 years following its first publication. https://commons.wikimedia.org/wiki/File:Pierre_and_Marie_Curie.jpg)
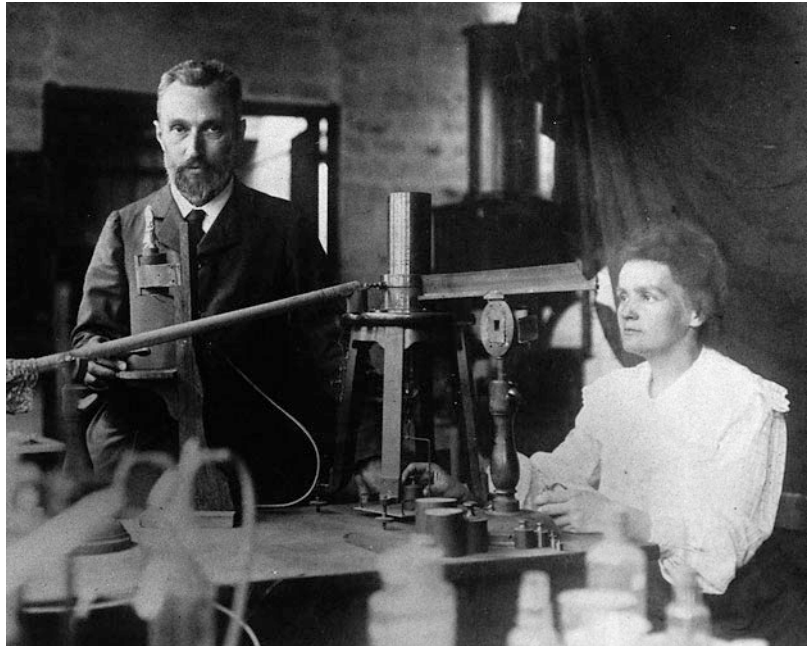
chemically similar to barium [12]. Polonium and radium possessed radioactivity that was orders of magnitude stronger than that of uranium.

These new elements not only solidified the concept of radioactivity as an atomic property but also served as key tools for further study. Researchers were soon able to probe the nature of the different types of emitted rays, identifying alpha, beta, and gamma emissions. They also developed theories on how atoms disintegrate during radioactive decay [13]. Spontaneous radioactivity from radon gas would even be transformed into therapeutic radiation, as Curie witnessed while visiting Memorial Hospital during her 1921 tour of the United States. It was the X-ray, however, that first found its way to the world of medicine.

2.4 Epilation and Epiphany: Discovering the Therapeutic Effect of Radiation

Roentgen published his original article in December 1895, and X-rays were being exploited around the world for diagnostic imaging the next month [14]. By February 1896, John Daniel, a researcher in Nashville, was asked to use X-rays to locate a bullet in the head of a boy who had been accidentally shot [15]. Daniel first made a preliminary test on his acquaintance William Dudley. Dudley wedged a coin between his head and a detector screen and placed a Crookes tube X-ray source on the other side of his head. The coin was visualized. Twenty-one days later, however, Dudley noticed a bald spot form at the very site where the Crookes tube was placed (Fig. 2.5). Daniel wrote a letter to the editor of *Science* to describe this observation [15], one of the first reports describing that X-rays interact with cells of the human body. Similar observations were made by Pierre Curie in the conclusion of his 1905 Nobel address, in which he described radiation skin burns from carrying radium salt in one's pocket [12].

Dr. William Allen Pusey was among the first to use radiation for the treatment of cancer. In 1902, Pusey treated two patients with bulky Hodgkin lymphoma using X-rays (Fig. 2.6). He went on to treat women with advanced breast cancers that had invaded the axillary lymphatics causing arm edema. Remarkably, he and his

Fig. 2.5 Cartoon Illustration of John Daniel's experiment using X-rays to image a coin behind William Dudley's head and leading to subsequent hair loss a few weeks later (1896). (Source: Vanderbilt Biomedical Library, the Vanderbilt "Comet." Public Domain: This work is in the public domain because it was published in the United States over 100 years ago, without any known copyright)
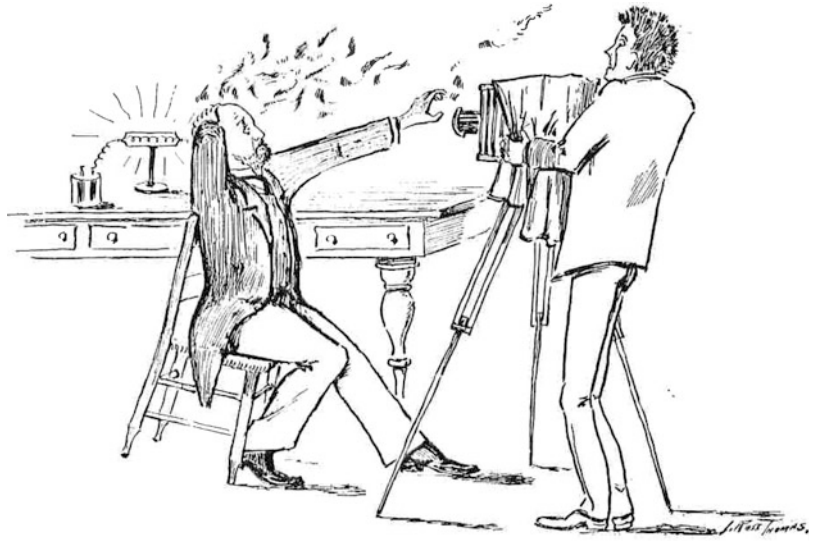
VIEW OF X-RAYS EXPERIMENT BY DRS. DUDLEY AND DANIEL.

Fig. 2.6 A child with Hodgkin lymphoma treated with X-rays, demonstrating an enlarged cervical lymph node (left) that is significantly reduced in size with radiotherapy (right); by William A. Pusey (1902). (Source: *Journal of* *the American Medical Association*. Public Domain: This work is in the public domain because it was published or registered with the U.S. Copyright Office over 100 years ago)

patients watched these tumors and their symptoms melt away [16]. While his early experiments were done with X-rays, he later described similar changes with radium [17]. Pusey regarded X-rays an excellent treatment modality for cancer, "entitled to consideration in all cases of carcinoma." However, as a prelude to the field of radiopharmaceutical therapy, he understood their shortcomings: "it is manifestly impossible to hope for benefit from any remedy which is not capable of selectively destroying carcinoma tissue, no matter where situated in the body. X-rays do not and cannot rise to such requirements; and doubtless no remedy ever well until some specific agent is found which is capable of causing the solution of carcinoma masses in the body in the way that potassium iodide, for example, causes the disappearance of syphilitic gummata" [16]. Importantly, even the first physician to use

radiation to treat carcinoma understood how this technology would be transformed by a method capable of selectively targeting it to cancer cells.

2.5   Nuclear Alchemy: The Artificial Production of Radionuclides

While physicians were bombarding human tissues with radiation, physicists were doing the same with their own test subjects—atomic nuclei. A popular experiment in the early-mid-1900s was to bombard various atoms with alpha particles generated by Marie Curie's radioactive elements. These experiments led to several fundamental insights. In 1919, Ernst Rutherford published his observation on the nuclear disintegration of nitrogen after an alpha-particle collision, ejecting a proton and leaving behind oxygen-17 (Fig. 2.7). Despite centuries of alchemists' claims, this was
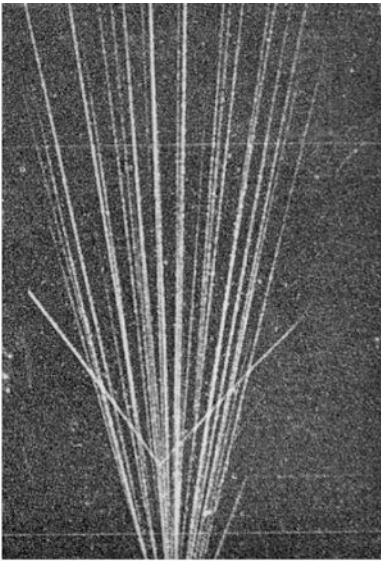
Alpha particle strikes helium nucleus and they part at right angles (Blackett)
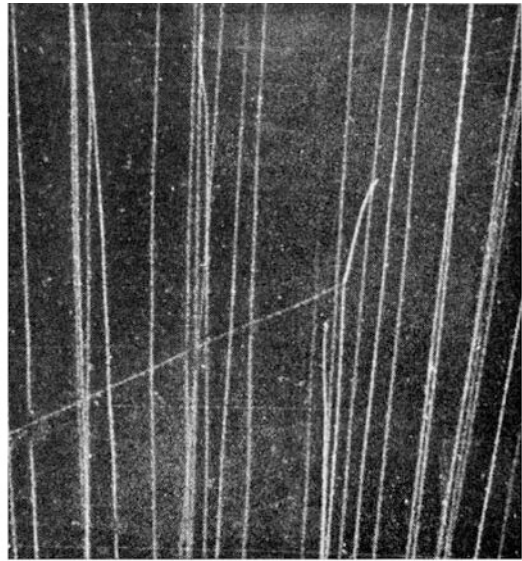
Alpha particle enters nitrogen which ejects proton and becomes oxygen (Blackett)

Fig. 2.7 The use of the Wilson Condensation method to visualize the path of energetic charged particles; by Patrick Maynard Stuart Blackett (February 2, 1925). (Source: Images reproduced in "Being the Life and Letters of the Rt. Hon. Lord Rutherford," by Arthur Stewart Eve 1939; Wellcome Collection. Creative Commons 4.0 International License. https://wellcomecollection.org/works/e7g4fwxx/images?id=yza7cchv)

Fig. 2.8 Irène and Frédéric Joliot-Curie in their laboratory; by Agence de presse Meurisse (1935). (Source: Bibliothèque nationale de France; Wikimedia commons. Public Domain: This image was published more than 70 years ago without a public claim of authorship and no subsequent claim of authorship was made in the 70 years following its first publication. https://commons.wikimedia.org/wiki/File:Ir%C3%A8ne_et_Fr%C3%A9d%C3%A9ric_Joliot-Curie_1935.jpg)

the first demonstration that one element could be artificially transmutated into another [18]. Over a decade later, Irène Curie and Frédéric Joliot-Curie (Fig. 2.8) performed a variation of the same experiment. They bombarded beryllium with polonium-derived alpha particles and observed the production of a strong, lead-penetrating radiation that could, in turn, eject protons from hydrogen-rich materials. Like prior researchers, they interpreted this as high-energy gamma rays but shortly thereafter realized there were contradictions in the interpretation [19, 20]. It was James Chadwick who solved the contradictions and proved that beryllium radiation was in fact a new kind of particle entirely, the neutron [21, 22].

The discovery of the neutron had evaded Irène Curie and Frédéric Joliot-Curie, but their experiments of bombarding elements with alpha particles yielded more Nobel-worthy insights. They observed positron emissions when aluminum was irradiated with polonium, and, strikingly, these emissions continued as an exponential decay even after the polonium irradiation source was removed [23]. It appeared they were artificially producing radioactive aluminum, but the quantity was so small that it could not be directly measured by chemical means. They understood, however, that radioactivity itself could serve as a probe for the subatomic world, a concept that is foundational to the field of nuclear medicine. By obeying the conservation of the number of nucleons, the researchers could deduce the likely radioactive products of their experiments. They could then use chemical separations to isolate the artificial elements and

detect them using their radioactive signatures. For example, the bombardment of aluminum with an alpha particle could release a neutron and produce radioactive phosphorous, which would then be precipitated away [24].

$$^{27}_{13}\text{Al} + ^4_2\text{He} \rightarrow ^{30}_{15}\text{P} + ^1_0 n$$
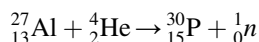
Irène Curie and Frédéric Joliot-Curie were awarded the Nobel Prize for chemistry in 1935, the same year that Chadwick was awarded the same award for physics. Yet somehow, Enrico Fermi brought together their work in an even more substantial way. He believed that Chadwick's neutrons would be able to easily slip past the electrically charged cloud that shields the atomic nucleus, unlike positively charged alpha particles that need to muscle their way through [25]; furthermore, once captured by the nucleus, neutrons could induce an excited state that would release radioactivity upon decay. Fermi's suspicion was correct. Through his method, termed neutron activation, he was able to generate a robust repertoire of approximately 40 artificial radionuclides [26, 27]. This work also allowed Fermi to participate in the ambitious efforts to discover the "trans-uranium" elements with atomic numbers greater than 92. Fermi reasoned that he could achieve this by bombarding uranium with neutrons that would be captured by the uranium nucleus. Surprisingly, it was later found that this process not only produced heavier elements but lighter ones as well. From these discoveries, the theory of nuclear fission was born [28], marking the beginning of the nuclear age [29].

2.6   If You Are Worth Your Salt: Birth of the Radiotracer Principle

Marie and Pierre Curie discovered radium in Paris, but the pitchblende from which it was purified came from the ore mines of Joachimsthal in the former Czechoslovakia. The mines were

Fig. 2.9 Portrait of George de Hevesy; author unknown (circa 1913). (Source: Wikimedia commons. Public Domain: This image was published more than 70 years ago without a public claim of authorship and no subsequent claim of authorship was made in the 70 years following its first publication. https://commons.wikimedia.org/wiki/File:George_de_Hevesy.jpg)

owned by the Austrian government, who supplied Western Europe with radium and its byproducts to perform research in radioactivity. In 1911, George de Hevesy (Fig. 2.9) was in his mid-20s and working in the basement of Rutherford's laboratory. The Austrian government had generously supplied Rutherford with hundreds of kilograms of one of the more important radium byproducts, radium D. However, it came intermixed with substantial quantities of lead that rendered it useless. Rutherford told de Hevesy, "My boy if you are worth your salt, you try to separate radium D from all that nuisance of lead" [30, 31].

de Hevesy undertook this task with youthful optimism. But every time it appeared as though he might succeed, he soon realized otherwise. He

was able to isolate radium E, the disintegration product of radium D, but never the intended element. Yet the inseparability of radium D provided de Hevesy's keen mind with scientific fodder. He thought that the radioactivity of radium D could be carried in minute quantities along with lead, thus serving as an indicator, or radiotracer, of its non-radioactive cousin. He then returned to Vienna, which housed the world's largest radium stores [31].

In Vienna, de Hevesy collaborated with Fritz Paneth to apply the radiotracer principle to chemical analytics by quantifying the solubility of weakly soluble lead compounds using radium D as an indicator. Their experiments were a success, but de Hevesy already had a hunch that the radiotracer principle would work. While working with Rutherford in Manchester in 1911, he was convinced that the cook at his boarding house was recycling food and serving it again a few days later. The cook, naturally, denied this. To prove his point, one night de Hevesy spiked the remnants of his food with radioactive material. A few days later, he brought an electroscope to the table and proved that the food he was eating was radioactive and, indeed, recycled [32].

de Hevesy also applied the radiotracer principle to more scientific pursuits, including clinical medicine. Around 1924, bismuth was becoming a popular treatment for syphilis. One of its major side effects is leaving a blue line on one's teeth, thus marking those who had been previously infected with syphilis. The appearance of this blue line, as well as the other toxic effects of bismuth, could be minimized with preparations that optimize its pharmacokinetics. de Hevesy and colleagues used the isotopic method to trace the biodistribution and excretion of bismuth [33, 34]. Svend Lomholt subsequently tested different bismuth preparations and found that bismuth hydroxide prepared in a glycerin-based suspension had the optimal pharmacokinetic properties [35]. The radiotracer principle was also applied to other radioelements; for example, the biodistribution of radioactive phosphorous was studied in rats and found to selectively accumulate in the bones, muscle, and fat [36].

2.7 Atoms Go To Work: Generating Usable Quantities of Radionuclides

Rutherford's classic paradigm of artificially disintegrating the nucleus with projectiles was a powerful approach to probing the nature of the atom, resulting in two Nobel Prizes in 1935 alone. While fruitful, these experiments were performed with low-energy beams, and the nuclear collisions were rare events. Ernest O. Lawrence reasoned that a more general method to accelerate charged particles would yield new fundamental physical insights. He received inspiration from a paper written by Rolf Wideröe in 1928 in which an oscillating electric field is shown to accelerate sodium and potassium ions to twice the expected speed based on the voltage applied [37]. Lawrence envisioned a machine to repeatedly deflect particles past an electrode in a circular path, thus accelerating the particles to very high speeds. This concept of cyclotron resonance was transformed to reality with the help of his graduate student, M. Stanley Livingston (Fig. 2.10). In 1931 they published a series of papers describing particle accelerations in the MeV range [38, 39], and, shortly thereafter, they were splitting atoms on their own.

On February 24, 1934—the very day Lawrence's lab heard of the Joliot-Curies' artificial production of radioactivity— they used the cyclotron to perform their own version of the experiment, bombarding carbon with deuterons. As coincidence has it, the experimental setup was already in place; they only needed to modify the circuits of their Geiger counter. Within 30 min of hearing of Joliot and Curie's discovery, Lawrence's lab had produced artificial radioactivity with a cyclotron [40].

It was around 1935 that an interest in biology developed in Lawrence's lab. Some of these investigations took the form of de Hevesy's radiotracer experiments. John Lawrence, Ernest's brother and a physician from Yale, came to the laboratory to learn about the exciting work that was being done. As de Hevesy had earlier, he studied the uptake of radiophosphorous but did
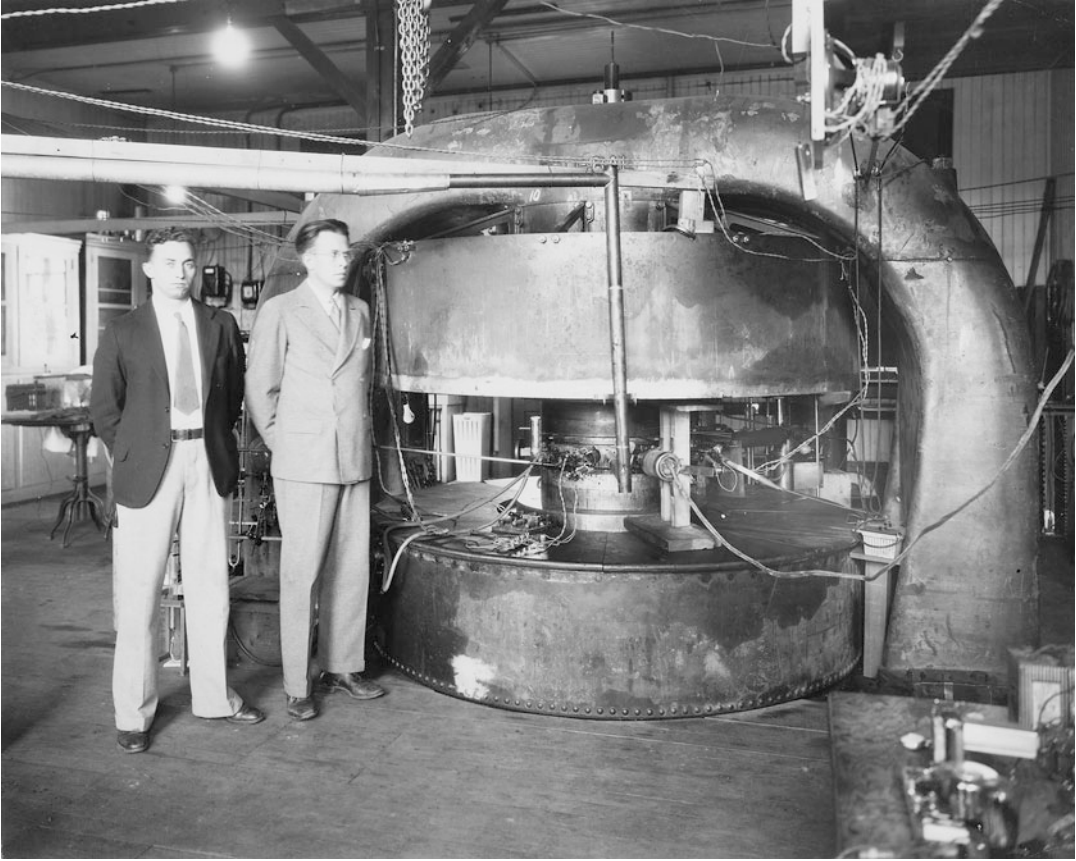
Fig. 2.10 Stanley Livingston and Ernest Lawrence in front of a 27-inch cyclotron at Berkeley; author unknown (1934). (Source: US national Archives and Records Administration. Public Domain: This work is in the public domain in the United States because it is a work prepared by an officer or employee of the United States Government as part of that person's official duties under the terms of Title 17, Chap. 1, Section 105 of the US Code. https://commons.wikimedia.org/wiki/File:M._Stanley_Livingston_(L)_and_Ernest_O._Lawrence_in_front_of_27-inch_cyclotron_at_the_old_Radiation_Laboratory_at_the..._-_NARA_-_558593.tif)

so in leukemic rats. He found that leukemic cells were hungry for phosphorous, consuming and retaining relatively large amounts of the element [41]. He extended these studies to humans and found that phosphorous accumulates in the nuclei of leukemic cells [42]. Based on this biodistribution, he hypothesized that radiophosphorous might be a solution to specifically enrich cancer cells with therapeutic radioactivity, and he even observed some therapeutic effect [43].

World War II put a hold on cyclotron research, as the cyclotron magnets were used for developing methods of isotope enrichment [44]. But after the war, wartime nuclear reactors helped accelerate radionuclide research. At the International Cancer Research Congress in St. Louis in 1947, President Harry Truman announced that the United States would make the radionuclides generated by wartime nuclear reactors available to the world, which the *New York Times* predicted would have "incalculable benefits to humanity" [45]. In an article titled "The Atom Goes To Work For Medicine," *The Times* continued to tout the utility of radioactivity for both diagnostic and therapeutic medical uses [46]. By 1949 the Atomic Energy Commission exported radionuclides to over 450 institutions across the world [47]. Atomic medicine was poised to flourish.

2.8 Trojan Horse: Iodine-131 and the Treatment of Thyroid Cancer

In 1949, *LIFE* magazine published a "before and after" photo of Bernard Brunstein (Fig. 2.11). In the 1942 "before" photo, one sees a ghostly cachectic man with hollow eyes and an expressionless face. In the "after" photo, Mr. Brunstein is an entirely new man, almost unrecognizable from 7 years earlier. He is well built with an energetic smile. This transformation, *LIFE* reported, was brought about by a new radioactive medicine [48].

In 1936, Karl Compton, the President of the Massachusetts Institute of Technology (MIT), gave a lecture at Harvard Medical School titled "What Physics Can Do For Biology And Medicine." Saul Hertz was in attendance that day and asked whether iodine could be made radioactive for the treatment of thyroid disease [49]. This insightful question was predicated on Eugen Bauman's 1896 discovery of the significant enrichment of iodine in the thyroid as well as James Means' 1922 demonstration that radiation could treat toxic goiter [50].

Hertz first reported that the radioactive ^{128}I could be used as a chemical indicator for in vivo thyroid metabolism in 1938 [51]. MIT had recently built a cyclotron dedicated to medical use, providing Hertz with usable amounts of radioiodine. On March 31, 1941, he treated his first patient with hyperthyroidism using 2.1 mCi of an ^{130}I/^{131}I mixture. He published his report including an additional 28 patients in 1946, in which he demonstrated a roughly 80% cure rate for hyperthyroidism [52] (Fig. 2.12). Hertz also pioneered the concept of using radioiodine to treat thyroid cancer. He performed early clinical studies on this topic in 1942, but important questions remained, which led Hertz to initiate a dedicated research program on radioiodine and thyroid cancer [53].

Whether metastatic thyroid cancers would respond to radioiodine was not known. There were conflicting reports in the literature: one suggesting that cancerous thyroid tissue does not take up the tracer, while another found that it could as long as the normal functioning thyroid tissue is removed [54, 55]. So when Sam Seidlin decided to treat Bernard Brunstein with radioiodine, he could not be sure of the outcome. Nevertheless, he purchased $1500 worth of radioiodine from Compton's MIT cyclotron and administered it to Brunstein. Suspecting he had a metastasis in his right parietal area, Brunstein asked that the Geiger counter be held up to this

RADIO-IODINE HALTS ONE TYPE OF CANCER

Radioactive chemical brings about history-making recovery of patient dying from thyroid tumors

The man shown in the contrasting portraits at right is a Brooklyn shoe salesman named Bernard Brunstein who is destined to become one of the most famous patients in medical history. Brunstein is the first person known to be cured (insofar as a cure can be established by medical tests on a living patient) of metastatic cancer, a form of the disease in which the malignancy spreads through the body from an original tumor. Metastatic cancer has always been 100% fatal. But Brunstein's tumors were destroyed in a simple, almost miraculous way: by the drinking of four doses of radioactive iodine. When Brunstein was admitted to New

BERNARD BRUNSTEIN IN 1942 (LEFT); AS HE LOOKS TODAY

iodine is chemically identical with ordinary iodine, it gives off a powerful radiation that can kill any tissue that absorbs it in sufficient concentration. The chemical had never been effectively used as a treatment for cancer, but Brunstein agreed to try it in the hope that it might help. It did. Three months after he drank his first glassful of the tasteless, colorless liquid, his heart began to slow down and he started to put on weight. Geiger counters placed over the tumor sites revealed that there was a heavy concentration of radio-iodine in these areas. After three additional doses the tumors slowly began to diminish in size

Fig. 2.11 Photographs of Bernard Brunstein before and after he was treated with radioiodine; author unknown (October 31, 1949). (Source: *LIFE* magazine; Reproduced in the article "A tribute to Dr. Saul Hertz: The discovery of the medical uses of radioiodine." Barbara Hertz [133] [With permissions from Thieme Publishing])

Fig. 2.12 Saul Hertz using a multicounter to measure radioiodine absorbed by the patient's thyroid gland (1944). (Source: Barbara Hertz [with permissions from Barbara Hertz])

area. Click-click-click-click. The radioiodine was able to find the metastatic deposits! Seidlin published that radioiodine could treat metastatic thyroid cancer, so long as a functioning thyroid gland was removed so as not to act as a sink for the radioactive drug [55, 56].

The development of radioiodine treatment by Hertz and Seidlin is a major milestone as the first successful radiopharmaceutical therapy, and it continues to be one of the most effective oncologic treatments even today. Nonetheless, Brunstein was ultimately not cured of his thyroid cancer. After multiple rounds of radioiodine, he eventually succumbed to an aggressive anaplastic transformation of the disease, suspected to be a result of the cumulative radiation he received. Seidlin also reported on 2 patients from his over

30 patient series who developed subacute myeloid leukemia 4–5 years after radioiodine exposure [57]. Then as now, radiation toxicity was a poorly understood yet critical element of patient care.

2.9 They Would Quite Literally Glow: Radionuclides for Cancer of the Bone

After the emergence of radioiodine, other cancer-seeking radionuclides were developed. Unfortunately, the realization that certain radioactive molecules distribute with tissue specificity came at the cost of human lives.

Fig. 2.13 Photo of women factory workers using radium paint with little to no protection; author unknown (circa 1922). (Source: Rutgers University Libraries; Wikimedia Commons. Public Domain: This media file is in the public domain in the United States. This applies to US works where the copyright has expired, often because its first publication occurred prior to January 1, 1927, and if not then due to lack of notice or renewal. https://commons.wikimedia.org/wiki/File:USRadiumGirls-Argonne.jpg)

When radiation was first discovered it was billed as a panacea, and it was attempted as a cure to over one hundred diseases [14]. The unbridled enthusiasm for and carefree use of radiation is epitomized by the plight of female watch dial painters who worked in factories using radium-laced luminescent paint (Fig. 2.13). They were asked to lick the tip of their paintbrushes to a point and thus ingested large quantities of radioactive material, so much so that an article in the *Atlantic* reported that "They would quite literally glow." In 1929, Harrison Martland published his report of these workers falling ill to diseases of the bones, including infections, fractures, and cancer [58]. Concern for occupational hazards eventually led to experimental studies of the biodistribution of radioactive elements.

As early as 1939, Charles Pecher observed strontium—an analog of calcium—distributes to the bones and performed preliminary studies on the therapeutic use of radioactive strontium for bone metastases [59]. Later in the century, large animal studies using beagles were undertaken to characterize the biodistribution of other radioactive molecules. In 1974, plutonium was show to exhibit an affinity for bones and liver [60]. Likewise, radium was also shown to have a preference for bone, and its uptake was associated with elevated rates of osteosarcoma [61].

Nosrat Firusian built on the earlier work of Pecher, reporting on the use of strontium-89 to

alleviate intractable bone pain in a small but significant number of patients with metastatic prostate cancer [62]. Based on this, a series of studies were undertaken to understand the biodistribution of strontium-89 in patients with painful bone metastases [63]. These studies illustrated that strontium-89 can effectively palliate bone pain in patients with metastatic breast and prostate cancer [64]. The clinical efficacy of strontium-89 was later demonstrated in a randomized phase II trial for metastatic prostate cancer [65]. Similarly, samarium-153 would later prove effective in treating painful bone metastases [66, 67]. This early experience, combined with the biodistribution studies of radium, laid the groundwork for the alpharadin in symptomatic prostate cancer patients (ALSYMPCA) trial demonstrating survival benefit for patients with metastatic prostate cancer limited to the bone when treated with radium-223 [68].

2.10 Cancer's Barcode: Imaging and Attacking Cancer Antigens

Ehrlich had sought a magic bullet to target cancer cells but ultimately concluded that cancer cells were too similar to normal cells [2]. One would need to understand the biology of cancer cells at a deeper level to find some molecular differentiator between them and their normal counterparts. A breakthrough came in 1929 when Ernest Witebsky developed an anti-serum to uterine carcinoma, raising the possibility of antigenic differences between cancer and normal tissue [69]. The first rigorous demonstration of a tumor antigen was discovered for tumors of the gastrointestinal tract. Phil Gold had just completed his medical residency and had the idea to search for cancer-specific antigens, though it was not even clear at the time that such an antigen would exist. Gold approached Sam Freedman with the idea to immunize rabbits with cancer cells of the gastrointestinal tract to induce the production of anti-sera that could bind a cancer antigen. The problem was that immunization with cancer cells would expose the rabbits to foreign antigens that were derived from normal as well as neoplastic

tissue. Gold and Freedman therefore induced immunologic tolerance by exposing fetal rabbits to normal gastrointestinal antigens. When they later exposed the rabbits to cancer cells, the rabbits only recognized cancer antigens as foreign and generated reactive anti-sera [70]. This groundbreaking work was validated when a large-scale cohort study showed that the expression of carcinoembryonic antigen (CEA) was highly associated with patients with gastrointestinal cancers and absent in both healthy controls and patients with non-gastrointestinal cancers [71].

While the studies above demonstrated the utility of CEA as a blood marker, David Goldenberg's group demonstrated in 1973 that radioiodine-labeled antibodies to CEA could be used to image tumors, first in animals [72] and then in humans [73]. Goldenberg's concept of radioimmunodetection was extended to other cancer antigens, such as beta-human chorionic gonadotropin [74], alpha fetoprotein [75], prostatic acid phosphatase [76], and placental alkaline phosphatase [77]. These radioimmunoconjugates illuminated cancer cells in photoscans and provided a proof-of-concept that they could be selectively targeted, as Ehrlich had envisioned.

The conversion of radioimmuno*detection* to radioimmuno*therapy* began with attempts to attach radioactive payloads to known biomolecular carriers. Already in 1947, the *New York Times* reported on research at Memorial Hospital in New York City in which "such drugs as sex hormones and 'nucleic acids' furnished the means of transporting radioactive materials to a specific area of the body where the rays could be directed at cancerous tissue" [78]. In 1951, William Beierwaltes reported the first efforts to treat patient with radiolabeled tumor antibodies, generated from the anti-sera of rabbits immunized with patient-derived melanoma cells. The first subject treated had a remarkable response to treatment: no tumor cells were found on autopsy when he died 9 years later in a car accident [79, 80]. However, the next few patients did not fare as well, and the concept was abandoned for a few decades. Stanley Order revived clinical investigations into radioimmunotherapy targeting

Fig. 2.14 ^{131}I-labeled monoclonal p97 Fab fragments to visualize metastatic melanoma. (Source: Larson et al. [134] [with permissions from Elsevier])

liver cancer with ^{131}I-labeled polyclonal antibodies [81, 82]. The results were promising, but they faced two problems. First was the lack of controlled clinical trials. Second, the method to produce tumor-specific antibodies relied on the inoculation of animals and was thus not a reproducible and scalable approach.

A key achievement in the field of bioengineering antibodies was achieved in 1975 when Georges Kohler and César Milstein reported the hybridoma method of generating cell lines capable of continuously secreting predefined monoclonal antibodies (mAbs) [83]. Naturally, this generated a substantial amount of optimism for the field of radioimmunotherapy. Jean-Pierre Mach capitalized on this achievement and published on the use of monoclonal CEA-targeting antibodies for radioimmunodetection [84]. Shortly thereafter,

Steve Larson and Jorge Carrasquillo used an ^{131}I-labeled conjugate of a monoclonal antibody targeting the p97 protein melanotransferrin for the imaging of metastatic melanoma [85, 86] (Fig. 2.14). They subsequently administered ^{131}I-labeled anti-p97 mAb to patients in a phase I study to characterize the organ distribution and toxicity of the drug, concluding that a therapeutic approach would be safe [79, 87].

At the same time, antibody therapeutics with intrinsic anti-tumor activity were being developed. Ronald Levy led early efforts testing the activity of idiotypic monoclonal antibodies that were uniquely reactive to each patient's tumor [88]. There were some limitations to this strategy, and efforts shifted toward the targeting of cell-type specific antigens, most notably B-cell specific CD20. Clinical studies showed a 48% response rate in low-grade lymphoma [89], and

the CD20-specific rituximab achieved Food and Drug Administration (FDA) approval in 1997. The concept of radioimmunotherapy was applied to anti-CD20 antibodies to test if response rates could be improved. Susan Knox ran one of the first phase I/II dose escalation studies of a ^{90}Y-labeled anti-CD20 antibody in patients with recurrent B-cell lymphoma, showing an encouraging 72% response rate [90]. Furthermore, ^{131}I-labeled anti-CD20 mAbs were tested in the setting of relapsed refractory cancer and initially showed response rates of over 60% and a substantial number of durable responses after just one dose [91–93].

Despite its success in clinical trials, the CD20-targeting radioimmunotherapeutic—^{131}I-tositumomab (Bexxar®)—has since been withdrawn from the market. The production and availability of another agent, ^{90}Y-ibritumomab tiuxetan (Zevalin®), has been limited at the time of this writing. The origins of the market failures of these agents are multifactorial and have been discussed elsewhere [94]. Institutional challenges, namely reimbursements in US health care system, as well as non-radioactive options for the same indications surely contributed. Additional efforts testing alpha-particle-emitting radioimmunotherapy in the preclinical and clinical settings have been pursued. However, none have achieved FDA approval at the time of publication [95].

2.11 Watch and Wait, or Act: Imaging and Attacking Cancer Peptides

In 2007, Josh Mailman was at a routine physical exam when his internist discovered a lump behind his rib cage. He was sent for an ultrasound but otherwise felt completely fine, and no one thought anything of it. The ultrasound was eventually performed while Mailman was sitting in the emergency room for respiratory issues. Even before anyone spoke to him, he knew something was not right. The emergency room doctors were avoiding eye contact and tiptoeing around him; their body language saying it all. He soon learned that there was a mass taking up three-quarters of his liver. It took the next 4–6 weeks to arrive at his diagnosis of pancreatic neuroendocrine tumor (NET).

Mailman was not a foreigner to the medical field. He comes from a family of health care professionals, and while five of his closest acquaintances were doctors, none had ever seen this. Mailman's internist worked hard to arrange a number of consults and secured one with a world-famous pancreatic surgeon. At the end of a marathon day in the clinic, he finally met the surgeon, who told Mailman that his tumor was unresectable. No surgery would be offered. And just like that, his world hit a dead end. He was essentially relegated to a "watch and wait" strategy. But this did not sit well with Mailman, a career technology entrepreneur and avid information seeker, so he did the only thing he could—learn. He dove into the field of neuroendocrine tumors, which led him to the world of radiopharmaceuticals.

The first efforts to image endocrine malignancies date back to the 1970s. Early in the decade, researchers had developed diagnostic tools for adrenocortical disease by discovering agents that specifically deposit in the adrenal cortex [96, 97]. Within the adrenal gland, however, neuroendocrine malignancies originate from a different region: the adrenal medulla. Strategies to specifically image the adrenal medulla capitalized on the biology of neurotransmitter recycling. Nancy Korn successfully radioiodinated bretylium, an adrenergic neuron-blocking agent, and found that this imaging agent had affinity for the tissues where these neurons reside, including the adrenal medulla [98]. This groundbreaking work led medicinal chemists to develop a number of substituted aralkylguanidines with even greater potency, including metaiodobenzylguanidine (MIBG). Donald Wieland and colleagues demonstrated that [^{131}I]MIBG has a remarkable affinity for adrenal medullary cells and could be used to localize tumors like pheochromocytomas that reside there (Fig. 2.15) [99, 100].

In the mid-1980s, the world of radiopharmaceuticals for neuroendocrine tumors
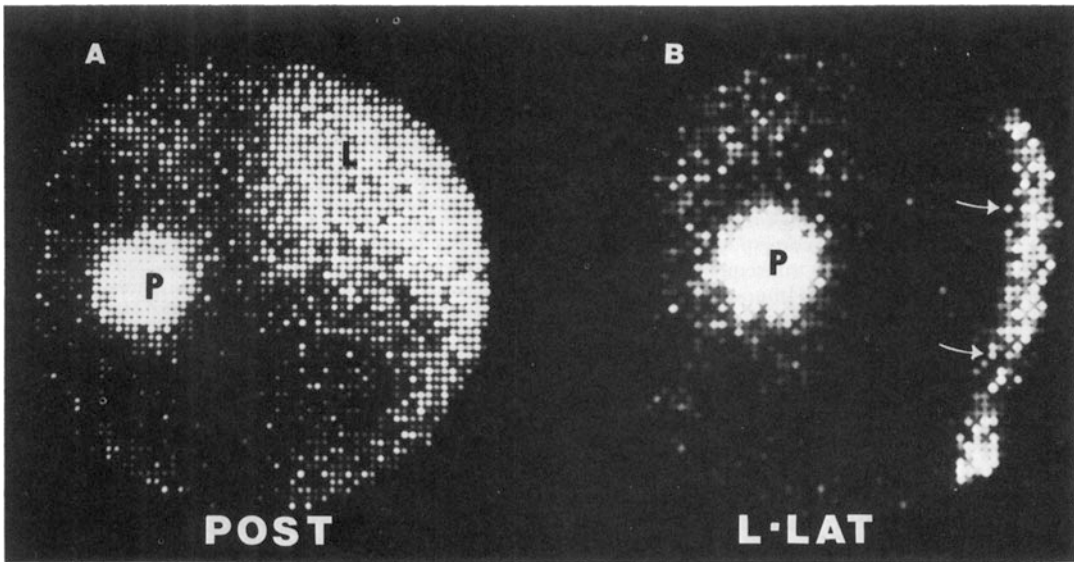
Fig. 2.15 Scintogram after injection of [^{131}I]MIBG in a patient with a pheochromocytoma of the left adrenal gland. The pheochromocytoma (P) is visualized from the posterior (A, Post) and lateral (B, Lat) view. The liver (L) is seen from the posterior view. (Source: Sisson et al. [135] [with permissions from Massachusetts Medical Society])

(NETs) underwent a radical transformation that can be traced back to an endocrinology postdoctoral conference at the University of Erasmus in 1985. The Sandoz Research Institute had recently developed octreotide, a highly potent inhibitor of the somatostatin receptor (SSTR) [101]. At the conference, researchers from Sandoz presented autoradiograms of octreotide conjugated to radioiodine in gastroenteropancreatic neuroendocrine tumors (GEP-NETs). Erasmus was Eric Krenning's home institution. When he saw this work, he wondered whether this conjugate could also be used to localize GEP-NETs in vivo [102]. Krenning worked with the Sandoz Research Institute to tweak the octreotide molecule to alter its biodistribution properties and was soon gaining clinical experience with these agents [103, 104]. By 1993, his team had published on their clinical experience with over 1000 patients, demonstrating that they had developed a sensitive and specific method to label GEP-NETs in humans (Fig. 2.16) [105].

Just as had been done with radioimmunoconjugates, the next logical step was to convert these diagnostic radiopeptides into a therapeutic modality. This was first attempted by infusing higher doses of the diagnostic product [106]. By 1997, Andreas Otte and Helmut Maecke had published on a peptide vector—DOTA-TOC—that could be stably conjugated to the beta-emitter ^{90}Y and began testing this radiopharmaceutical in patients who had no other treatment options [107, 108]. They established a clinical protocol and demonstrated evidence of anti-tumor activity [109]. Through multi-institutional collaboration, additional therapeutic agents were developed, including [^{177}Lu]Lu-DOTA-TATE. Initial studies in NETs showed favorable response profiles [110], which paved the way for a larger multinational phase 3 trial that demonstrated improvement in progression-free survival and led to approval by the U.S. FDA [111, 112].

By 2008, Josh Mailman had immersed himself in the world of neuroendocrine tumors. At one of the international conferences, he was introduced to striking images of new positron emission tomography (PET)-based SSTR tracers [113, 114]. Impressed by these, he later flew himself to Germany to get his own [^{68}Ga]Ga-
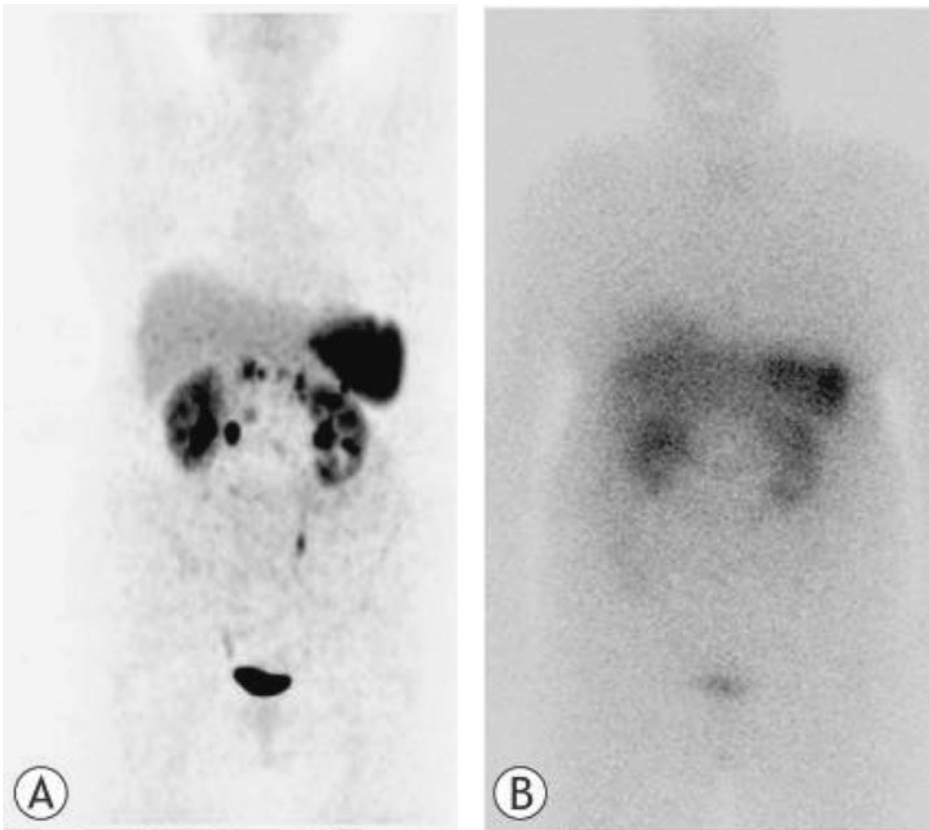
Fig. 2.16 [^{68}Ga]Ga-DOTA-TOC PET (**a**) compared with Octreoscan (**b**). (Source: Modified from Schreiter et al. [136]; Wikimedia Commons. Creative Commons Attribution-Share Alike 3.0)

DOTA-TOC imaging. The images illuminated his cancer clearly and distinctly. By 2009, however, his cancer journey was reaching a critical point. The neuroendocrine tumor cells were revving up, secreting large amounts of vasoactive intestinal peptide (VIP), enough to cause severe secretory symptoms and life-threatening electrolyte imbalances—the Verner-Morrison syndrome. All the while, he was battling with insurance companies to simply access the subcutaneous octreotide needed to manage his symptoms. But even if he could get his hands on it, this drug was losing its efficacy. In search of another solution, he emailed Richard Baum at Zentralklinik Bad Berka to ask if there might be any therapy available to him. Baum told Mailman to show up at the hospital in Bad Berka on May 25, 2009. There, he received a first dose of [^{90}Y]Y-DOTA-TOC on

his birthday in 2009 and a second of [^{177}Lu]Lu-DOTA-TOC on his wedding anniversary. He has not needed subcutaneous octreotide since.

Josh Mailman's story is a clear reminder of the true partnership needed between physician scientists and patients. Without brave patients to demonstrate the promise of novel agents that represent the basis for definitive prospective clinical trials, the advent of radiopharmaceutical therapy would have stagnated. Now, through Mailman's generous efforts to advocate for others, we have an effective treatment option that can improve the quality of life of the many patients living with SSTR-expressing NETs. This success has heralded broader momentum for the radiopharmaceutical field. To wit, by 2018, the FDA had granted [^{131}I]MIBG approval as a therapeutic agent for paragangliomas and

Fig. 2.17 [^{68}Ga]Ga-PSMA PET identifies punctate prostate cancer metastases. The metastasis is visualized as a sclerotic osseous lesion on computed tomography (CT) scan (**a**, left panel) and is avid on [68Ga]Ga-PSMA PET (**b**, right panel). (Source: Rauscher et al. [137]. Creative Commons Attribution 4.0)
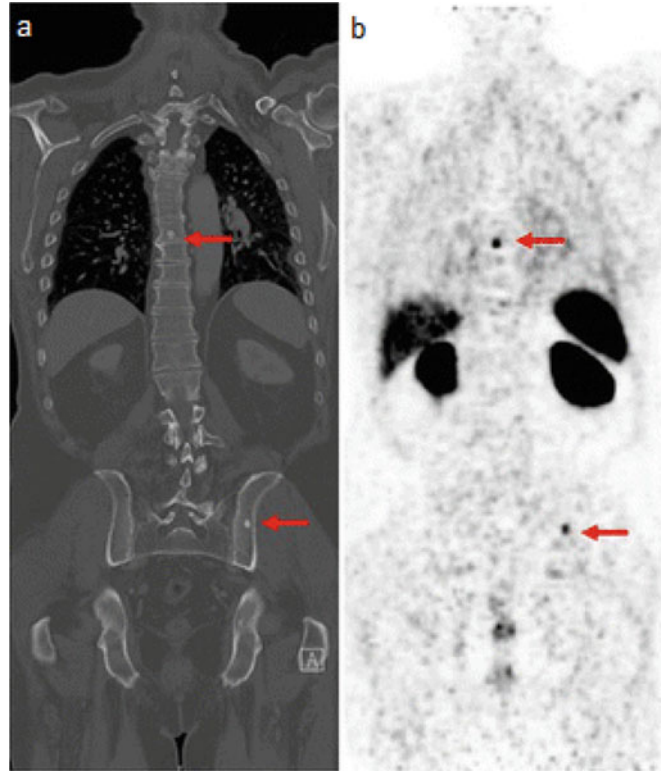
pheochromocytomas based on its clinical efficacy [115].

Around the same time that PET-based tracers were being developed for NETs, a group in Heidelberg was working to develop PET-based imaging ligands for prostate-specific membrane antigen (PSMA), a specific marker for prostate cancer. PSMA was identified by the 7E11-C5 murine hybridoma generated through the immunization of animals with the lymph node carcinoma of the prostate (LNCaP) prostate cancer cell line [116]. William Fair and colleagues later cloned the gene for PSMA [117]. The authors hypothesized that PSMA may be an excellent handle for the detection and targeting of prostate cancer cells, and Fair went on to describe the enzymatic activity of PSMA as a folate hydrolase [118].

The first efforts to target PSMA used antibodies and were met with varying degrees of success. Martin Pomper capitalized on the recent development of simple urea-based carboxypeptidase inhibitors [119] and generated radiolabeled peptides with high affinity for PSMA [120]. Antibodies—which are large, have limited vascular permeability, and slow washout kinetics—may not be ideal carriers for radionuclides. Perhaps short peptides could surmount some of these issues.

The Heidelberg group published their first experiences with PSMA-ligand PET imaging in 2012 and 2013 [121, 122]. Since then, the clinical success of PSMA-targeted PET tracers has been demonstrated across a number of high-profile trials and is making a huge impact on clinical decision-making [123–127] (Fig. 2.17). The PSMA-11 ligand that was originally used for imaging by the Heidelberg group was not suitable for labeling with a therapeutic radionuclide. Therefore, they set out to transform it into one more appropriate for therapeutic use, resulting in the creation of PSMA-617 [128]. A second PSMA inhibitor with therapeutic potential, PSMA I&T, was also simultaneously developed in Germany [129].

Although [^{177}Lu]Lu-PSMA-617 was not published until 2015, clinicians were already eager to gain experience with it as far back as 2013. They had learned from the field's experience with NETs and knew the value of generating prospective clinical trial data. Michael Hofman led a 30-person single-arm prospective phase 2 trial from Australia (LuPSMA Trial), which showed that [^{177}Lu]Lu-PSMA-617 achieved a 57% response rate in men with metastatic castration-resistant prostate cancer (mCRPC) who exhausted standard therapy [130]. These promising results led to the TheraP phase 2 trial comparing [^{177}Lu]Lu-PSMA-617 to cabazitaxel in men with mCRPC whose disease was refractory to first-line taxanes. Investigators found that [^{177}Lu]Lu-PSMA-617 was non-inferior to cabazitaxel and provided a better quality of life for patients [131]. In 2018, The FDA greenlighted VISION, a large, randomized phase 3 study to further test [^{177}Lu]Lu-PSMA-617. The VISION trial showed that in patients with metastatic castrate-resistant prostate cancer who had progressed on at least one course of taxane therapy, [^{177}Lu]Lu-PSMA-617 achieved a 4-month absolute survival benefit compared to study-defined standard of care [132]. This resulted in FDA approval in early 2022. Now, beta- and alpha-particle-emitting versions of both the small molecule- and antibody-based agents are actively being explored in several clinical trials as monotherapies and in combination with other systemic (e.g., immunotherapy, DNA damage repair inhibitors) or local (e.g., stereotactic ablative radiotherapy) therapies. There is no doubt that the regulatory approval of [^{177}Lu]Lu-PSMA-617 represents a historic milestone in the field of radiopharmaceutical therapy.

Taken together, these advances represent the culmination of over a century of discovery. What the next century holds is unknowable. However, earnest efforts by scientists and clinicians can identify the scenarios in which radiopharmaceutical therapy can maximize the survival and quality of life of patients. While cures currently remain elusive, improved patient selection and drug combination strategies may soon bring them within reach.

2.12   Conclusion

In oncology, there is a significant unmet and urgent need to do better for our patients. Stepping back to reflect on the history of radiopharmaceutical therapy, it is quite remarkable to see how far it has come in just over 100 years. At the turn of the last century, radioactivity had not even been discovered. Yet today, the field is grappling with sophisticated questions such as radionuclide selection, coordination chemistry, target identification, dose optimization, personalized dosimetry, normal tissue toxicity, and beyond. One observation that emerges from this historical reflection is the remarkable number of disciplines that have contributed to the success of the field, a phenomenon that is underscored by the number of hands that touch a radiopharmaceutical before it reaches a patient. Perhaps more than any other modality, radiopharmaceutical therapy represents the epitome of a rich, ongoing dialogue between scientific disciplines and the patients with whom and for whom we work.

2.13   Bottom Line

- The twentieth century witnessed a transformation that moved oncology away from a primarily surgical specialty into a multidisciplinary field.
- Early pioneers of radiopharmaceutical therapy made transformative discoveries in their respective scientific disciplines. Notable discoveries include the conception of chemotherapy by Ehrlich, the production and detection of the X-ray by Roentgen, and the exploration of spontaneous and induced radioactivity by two generations of Curies.
- As the century progressed, these distinct streams of scientific inquiry began to collide and produced new paradigms of thought. This is best illustrated by the evolution of de Hevesy's radiotracer principle in which nuclear physics unlocked avenues of exploration in chemistry, metabolism, and clinical medicine.

- The influence of cross-disciplinary collaboration is epitomized by the advent of the first successful radiopharmaceutical therapy. Hertz embraced discoveries in physics, biology, and medicine to conceive of radioiodine therapy, which successfully treated hyperthyroidism and eventually thyroid cancer.
- The modern era of radiopharmaceutical therapy has witnessed technologic innovation to create ever more sophisticated small molecule- and biomolecule-based radiopharmaceuticals.
- Now, as the field looks to translate scientific achievement into effective medicines through prospective clinical trials, the cross-disciplinary dialogue will continue to expand and will importantly include the patients with whom and for whom we work.

References

1. Halsted WS. I. The results of operations for the cure of cancer of the breast performed at the Johns Hopkins Hospital from June, 1889, to January, 1894. Ann Surg. 1894;20(5):497–555.
2. Mukherjee S. The emperor of all maladies : a biography of cancer. New York/London: Scribner; 2011.
3. Ehrlich P. Croonian lecture.—On immunity with special reference to cell life. Proceedings of the royal Society of London. 1900 66(424–433):424–48
4. Ehrlich P. Partial cell functions. Stockholm: Nobel Lecture; 1908.
5. Ehrlich P. Die Behandlung der Syphilis mit dem Ehrlichschen Präparat 606. Dtsch Med Wochenschr. 1910;1893–1896.
6. Rontgen WC. On a new kind of rays. Science. 1896;3(59):227–31.
7. Markel H. 'I have seen my death': how the world discovered the X-Ray: PBS News Hour; 2012. Available from: https://www.pbs.org/newshour/health/i-have-seen-my-death-how-the-world-discovered-the-x-ray.
8. Eine Sensationelle Entderkung. Die Presse. 5 Jan 1896.
9. Becquerel A. On radioactivity, a new property of matter. Stockholm: Nobel Lecture; 1903.
10. Becquerel A. On radioactivity, a new property of matter. Stockholm: Nobel Lecture; 1905.
11. Curie M. Radium and radioactivity. Century magazine. 6 Jan 1904.
12. Curie P. Radioactive substances, especially radium. Stockholm: Nobel Lecture; 1905.
13. Curie M, editor. Radium and the new concepts in chemistry. Stockholm: Nobel Lecture; 1911.
14. Porter R. The greatest benefit to mankind: a medical history of humanity. 1st American ed. New York: W. W. Norton; 1998.
15. Daniel J. The X-Rays. Science. 1896;3(67):562–3.
16. Pusey WA. IX. The use of X-Rays in Carcinoma. Ann Surg. 1905;42(6):910–7.
17. Pusey WA. The biological effects of radium. Science. 1911;33(861):1001–5.
18. Rutherford ELIV. Collision of α particles with light atoms. IV. An anomalous effect in nitrogen. Lond Edinb Dublin Philos Mag J Sci. 1919;37(222):581–7.
19. Joliot-Curie I, Joliot-Curie F. Émission de protons de grande vitesse par les substances hydrogénées sous l'influence des rayons [lambda] tres pénétrants. Gauthier-Villars; 1932.
20. Curie I, Joliot F. Effet d'absorption de rayons γ de tres haute fréquence par projection de noyaux legers. CR Acad Sci Paris. 1932;194:708–11.
21. Chadwick J. The existence of a neutron. Proc R Soc Lond Ser A, Contain Pap Math Phys Character. 1932;136(830):692–708.
22. Chadwick J. Possible existence of a neutron. Nature. 1932;129(3252):312.
23. Joliot F, Curie I. Artificial production of a new kind of radioelement. Nature. 1934;133:2.
24. Joliot F. Chemical evidence of the transmutation of elements. Stockholm: Nobel Lecture; 1935.
25. Fermi E. Artificial radioactivity produced by neutron bombardment. Stockholm: Nobel Lecture; 1938.
26. Fermi E. Radioactivity induced by neutron bombardment. Nature. 1934;133(3368):757.
27. Fermi E, Amaldi E, D'Agostino O, Rasetti F, Segrè E. Artificial radioactivity produced by neutron bombardment. Proc R Soc Lond Ser A, Contain Pap Math Phys Character. 1934;146(857):483–500.
28. Meitner L, Frisch OR. Disintegration of uranium by neutrons: a new type of nuclear reaction. Nature. 1939;143:2.
29. Seaborg GT. Some recollections of early nuclear age chemistry. J Chem Educ. 1968;45(5):278.
30. Hevesy G. Adventures in radioisotope research. Oxford: Pergamon; 1962.
31. De Hevesy G. Some applications of isotopic indicators. Stockholm: Nobel Lecture; 1944.
32. Myers W. Georg Charles de Hevesy: the father of nuclear medicine. J Nucl Med Technol. 1996;24:4.
33. Christiansen JA, Hevesy G, Lomholt S. Recherches, par une methode radiochimique, surla circulation du bismuth dans l'organisme. Compt Rend. 1924;178:1324–1326

34. Lomholt S. Investigations into the circulation of some heavy metals in the organism (mercury, bismuth and lead). Biochem J. 1924;18(3–4):693.

35. Lomholt S. Notes on the pharmacology of bismuth, with reference to its employment in the therapy of syphilis. Br J Vener Dis. 1925;1(1):50.

36. Chieveitz O, Hevesy G. Radioactive indicators in the study of phosphorous metabolism in rats. Nature. 1935;136(136):2.

37. Wideröe R. Über ein neues Prinzip zur Herstellung hoher Spannungen. Archiv für Elektrotechnik. 1928;21(4):387–406.

38. Lawrence EO, Livingston MS. The production of high speed protons without the use of high voltages. Phys Rev. 1931;38(4):834.

39. Lawrence E, Livingston S. The production of high speed light ions without the use of high voltages. Phys Rev. 1932;40:19.

40. Henderson MC, Livingston MS, Lawrence EO. Artificial radioactivity produced by deuton bombardment. Phys Rev. 1934;45(6):428.

41. Lawrence J, Tuttle L, Scott K, Connor C. Studies on neoplasms with the aid of radioactive phosphorus. I. The total phosphorus metabolism of normal and leukemic mice. J Clin Invest. 1940;19(2): 267–71.

42. Tuttle L, Erf L, Lawrence J. Studies on neoplasms with the aid of radioactive phosphorus. II. The phosphorus metabolism of the nucleoprotein, phospholipid and acid soluble fractions of normal and leukemic mice. J Clin Invest. 1941;20(1):57–61.

43. Erf L, Lawrence J. Clinical studies with the aid of radio-phosphorus. III. The absorption and distribution of radio-phosphorus in the blood of, its excretion by, and its therapeutic effect on, patients with polycythemia. Ann Intern Med. 1941;15(2):276–90.

44. Livingston MS, McMillan EM. History of the cyclotron (Part 1, Livingston; Part 2 McMillan). Phys Today. 1959;12(10):18–34.

45. Laurence WL. New peacetime vistas open for atomic energy. New York Times. 14 Sept 1947.

46. Davis H. The atom goes to work for medicine. New York Times. 22 Sept 1946.

47. Atomic peace use triples in 2 years. The New York Times. 14 Nov 1949.

48. Ehrhardt JD Jr, Gulec S. A review of the history of radioactive iodine theranostics: the origin of nuclear ontology. Mol Imaging Radionucl Ther. 2020;29(3): 88–97.

49. Fahey FH, Grant FD, Thrall JH. Saul Hertz, MD, and the birth of radionuclide therapy. EJNMMI Phys. 2017;4(1):15.

50. Means JH, Holmes GW. Further observations on the roentgenray treatment of toxic goiter. Arch Intern Med. 1923;31(3):39.

51. Hertz S, Roberts A, Evans RD. Radioactive iodine as an indicator in the study of thyroid physiology. Proc Soc Exp Biol Med. 1938;38(4):4.

52. Hertz S, Roberts A. Radioactive iodine in the study of thyroid physiology; the use of radioactive iodine therapy in hyperthyroidism. J Am Med Assoc. 1946;131:81–6.

53. Hertz S. A plan for analysis of the biologic factors involved in experimental carcinogenesis of the thyroid by means of radioactive isotopes. Bull New Engl Med Cent. 1946;8(5):220–4.

54. Keston AS, Ball RP, Frantz VK, Palmer WW. Storage of radioactive iodine in a metastasis from thyroid carcinoma. Science. 1942;95(2466): 362–3.

55. Seidlin SM, Marinelli LD, Oshry E. Radioactive iodine therapy; effect on functioning metastases of adenocarcinoma of the thyroid. J Am Med Assoc. 1946;132(14):838–47.

56. Leiter L, Seidlin SM, et al. Adenocarcinoma of the thyroid with hyperthyroidism and functional metastases; studies with thiouracil and radioiodine. J Clin Endocrinol Metab. 1946;6:247–61.

57. Seidlin S, Siegel E, Yalow AA, Melamed S. Acute myeloid leukemia following prolonged iodine-131 therapy for metastatic thyroid carcinoma. Science. 1956;123(3201):800–1.

58. Martland HS. Occupational poisoning in manufacture of luminous watch dials: general review of hazard caused by ingestion of luminous paint, with especial reference to the New Jersey cases. JAMA. 1929;92 (6):8.

59. Pecher C. Biological investigations with radioactive calcium and strontium; preliminary report on the use of radioactive strontium in the treatment of metastatic bone cancer. Berkeley/Los Angeles: University of California press; 1942. 2 p.l., 117–49

60. Bair WJ, Thompson RC. Plutonium: biomedical research. Science. 1974;183(4126):715–22.

61. Raabe OG, Book SA, Parks NJ. Bone cancer from radium: canine dose response explains data for mice and humans. Science. 1980;208(4439):61–4.

62. Firusian N, Mellin P, Schmidt CG. Results of 89strontium therapy in patients with carcinoma of the prostate and incurable pain from bone metastases: a preliminary report. J Urol. 1976;116(6):764–8.

63. Robinson RG, Blake GM, Preston DF, McEwan AJ, Spicer JA, Martin NL, et al. Strontium-89: treatment results and kinetics in patients with painful metastatic prostate and breast cancer in bone. Radiographics. 1989;9(2):271–81.

64. Porter AT, McEwan AJ, Powe JE, Reid R, McGowan DG, Lukka H, et al. Results of a randomized phase-III trial to evaluate the efficacy of strontium-89 adjuvant to local field external beam irradiation in the management of endocrine resistant metastatic prostate cancer. Int J Radiat Oncol Biol Phys. 1993;25(5): 805–13.

65. Tu SM, Millikan RE, Mengistu B, Delpassand ES, Amato RJ, Pagliaro LC, et al. Bone-targeted therapy for advanced androgen-independent carcinoma of the

prostate: a randomised phase II trial. Lancet. 2001;357(9253):336–41.

66. Sartor O, Reid RH, Hoskin PJ, Quick DP, Ell PJ, Coleman RE, et al. Samarium-153-Lexidronam complex for treatment of painful bone metastases in hormone-refractory prostate cancer. Urology. 2004;63(5):940–5.

67. Resche I, Chatal J-F, Pecking A, Ell P, Duchesne G, Rubens R, et al. A dose-controlled study of 153Sm-Ethylenediaminetetramethylenephosphonate (EDTMP) in the treatment of patients with painful bone metastase. Eur J Cancer. 1997;33(10):1583–91.

68. Parker C, Nilsson S, Heinrich D, Helle SI, O'Sullivan JM, Fossa SD, et al. Alpha emitter radium-223 and survival in metastatic prostate cancer. N Engl J Med. 2013;369(3):213–23.

69. Order SE. The history and progress of serologic immunotherapy and radiodiagnosis. Radiology. 1976;118(1):219–23.

70. Gold P, Freedman SO. Demonstration of tumor-specific antigens in human colonic carcinomata by immunological tolerance and absorption techniques. J Exp Med. 1965;121:439–62.

71. Edgington TS, Astarita RW, Plow EF. Association of an isomeric species of carcinoembryonic antigen with neoplasia of the gastrointestinal tract. N Engl J Med. 1975;293(3):103–7.

72. Primus FJ, Wang RH, Goldenberg DM, Hansen HJ. Localization of human GW-39 tumors in hamsters by radiolabeled heterospecific antibody to carcinoembryonic antigen. Cancer Res. 1973;33(11): 2977–82.

73. Goldenberg DM, DeLand F, Kim E, Bennett S, Primus FJ, van Nagell JR Jr, et al. Use of radiolabeled antibodies to carcinoembryonic antigen for the detection and localization of diverse cancers by external photoscanning. N Engl J Med. 1978;298(25):1384–6.

74. Goldenberg DM, Kim EE, DeLand FH, van Nagell JR Jr, Javadpour N. Clinical radioimmunodetection of cancer with radioactive antibodies to human chorionic gonadotropin. Science. 1980;208(4449): 1284–6.

75. Goldenberg DM, Goldenberg H, Higginbotham-Ford E, Shochat D, Ruoslahti E. Imaging of primary and metastatic liver cancer with 131I monoclonal and polyclonal antibodies against alphafetoprotein. J Clin Oncol. 1987;5(11):1827–35.

76. Goldenberg DM, DeLand FH, Bennett SJ, Primus FJ, Nelson MO, Flanigan RC, et al. Radioimmunodetection of prostatic cancer. In vivo use of radioactive antibodies against prostatic acid phosphatase for diagnosis and detection of prostatic cancer by nuclear imaging. JAMA. 1983;250(5): 630–5.

77. Epenetos AA, Snook D, Hooker G, Begent R, Durbin H, Oliver RT, et al. Indium-111 labelled monoclonal antibody to placental alkaline phosphatase in in the detection of neoplasms of testis, ovary, and cervix. Lancet. 1985;2(8451):350–3.

78. Cancer Aids Found IN Radioisotopes. New York Times. 1947 Aug 5, 1957.

79. Larson SM, Carrasquillo JA, Reynolds JC, Hellstrom I, Hellstrom K-E, Mulshine JC, et al. Therapeutic applications of radiolabelled antibodies: current situation and prospects. Nucl Med Biol. 1986;13 (2):207–13.

80. Beierwaltes W. Effects ofsome Ii 31tagged antibod ies in human melanoblastoma: preliminary report. U Mich Med Bull. 1956;20:284â.286:i9.

81. Order SE, Klein JL, Ettinger D, Alderson P, Siegelman S, Leichner P. Phase I–II study of radiolabeled antibody integrated in the treatment of primary hepatic malignancies. Int J Radiat Oncol Biol Physics. 1980;6(6):703–10.

82. Ettinger D, Order S, Wharam M, Parker MK, Klein J, Leichner P. Phase I-II study of isotopic immunoglobulin therapy for primary liver cancer. Cancer Treat Rep. 1982;66(2):289–97.

83. Köhler G, Milstein C. Continuous cultures of fused cells secreting antibody of predefined specificity. Nature. 1975;256(5517):495–7.

84. Mach J-P, Buchegger F, Forni M, Ritschard J, Berche C, Lumbroso J-D, et al. Use of radiolabelled monoclonal anti-CEA antibodies for the detection of human carcinomas by external photoscanning and tomoscintigraphy. Immunol Today. 1981;2(12): 239–49.

85. Larson SM, Carrasquillo JA, Krohn KA, McGuffin RW, Williams DL, Hellstrom I, et al. Diagnostic imaging of malignant melanoma with radiolabeled antitumor antibodies. JAMA. 1983;249(6):811–2.

86. Larson SM, Brown JP, Wright PW, Carrasquillo JA, Hellstrom I, Hellstrom KE. Imaging of melanoma with L-131-labeled monoclonal antibodies. J Nucl Med. 1983;24(2):123–9.

87. Larson SM, Carrasquillo JA, Krohn KA, Brown JP, McGuffin RW, Ferens JM, et al. Localization of 131I-labeled p97-specific Fab fragments in human melanoma as a basis for radiotherapy. J Clin Invest. 1983;72(6):2101–14.

88. Meeker TC, Lowder J, Maloney DG, Miller RA, Thielemans K, Warnke R, et al. A clinical trial of anti-idiotype therapy for B cell malignancy. Blood. 1985;65(6):1349–63.

89. McLaughlin P, Grillo-Lopez AJ, Link BK, Levy R, Czuczman MS, Williams ME, et al. Rituximab chimeric anti-CD20 monoclonal antibody therapy for relapsed indolent lymphoma: half of patients respond to a four-dose treatment program. J Clin Oncol. 1998;16(8):2825–33.

90. Knox SJ, Goris ML, Trisler K, Negrin R, Davis T, Liles T-M, et al. Yttrium-90-labeled anti-CD20 monoclonal antibody therapy of recurrent B-cell lymphoma. Clin Cancer Res. 1996;2(3):457–70.

91. Vose JM, Wahl RL, Saleh M, Rohatiner AZ, Knox SJ, Radford JA, et al. Multicenter phase II study of iodine-131 tositumomab for chemotherapy-relapsed/ refractory low-grade and transformed low-grade

B-cell non-Hodgki's lymphomas. J Clin Oncol. 2000;18(6):1316–23.

92. Kaminski MS, Estes J, Zasadny KR, Francis IR, Ross CW, Tuck M, et al. Radioimmunotherapy with iodine (131)I tositumomab for relapsed or refractory B-cell non-Hodgkin lymphoma: updated results and long-term follow-up of the University of Michigan experience. Blood. 2000;96(4):1259–66.

93. Kaminski MS, Zelenetz AD, Press OW, Saleh M, Leonard J, Fehrenbacher L, et al. Pivotal study of iodine I 131 tositumomab for chemotherapy-refractory low-grade or transformed low-grade B-cell non-Hodgkin's lymphomas. J Clin Oncol. 2001;19(19):3918–28.

94. White JM, Escorcia FE, Viola NT. Perspectives on metals-based radioimmunotherapy (RIT): moving forward. Theranostics. 2021;11(13):6293.

95. King AP, Lin FI, Escorcia FE. Why bother with alpha particles? Eur J Nucl Med Mol Imaging. 2021;49(1):7–17.

96. Lieberman LM, Beierwaltes WH, Conn JW, Ansari AN, Nishiyama H. Diagnosis of adrenal disease by visualization of human adrenal glands with 131I-19-iodocholesterol. N Engl J Med. 1971;285(25):1387–93.

97. Beierwaltes WH, Lieberman LM, Ansari AN, Nishiyama H. Visualization of human adrenal glands in vivo by scintillation scanning. JAMA. 1971;216(2):275–7.

98. Korn N, Buswink A, Yu T, Carr EA, Carroll M, Counsell RE. A radioiodinated bretylium analog as a potential agent for scanning the adrenal medulla. J Nucl Med. 1977;18(1):87–9.

99. Sisson JC, Frager MS, Valk TW, Gross MD, Swanson DP, Wieland DM, et al. Scintigraphic localization of pheochromocytoma. N Engl J Med. 1981;305(1):12–7.

100. Wieland DM, Wu J-l, Brown LE, Mangner TJ, Swanson DP, Beierwaltes WH. Radiolabeled adrenergic neuron-blocking agents: adrenomedullary imaging with [131I] iodobenzylguanidine. J Nucl Med. 1980;21(4):349–53.

101. Bauer W, Briner U, Doepfner W, Haller R, Huguenin R, Marbach P, et al. SMS 201-995: a very potent and selective octapeptide analogue of somatostatin with prolonged action. Life Sci. 1982;31(11):1133–40.

102. Levine R, Krenning EP. Clinical history of the theranostic radionuclide approach to neuroendocrine tumors and other types of cancer: historical review based on an interview of Eric P. Krenning by Rachel Levine. J Nucl Med. 2017;58(Suppl 2):3S–9S.

103. Lamberts S, Barker W, Reubi J-C, Krenning E. Somatostatin-receptor imaging in the localization of endocrine tumors. N Engl J Med. 1990;323(18):1246–9.

104. Krenning EP, Breeman WA, Kooij PP, Lameris J, Bakker WH, Koper J, et al. Localisation of endocrine-related tumours with radioiodinated

analogue of somatostatin. Lancet. 1989;333(8632):242–4.

105. Krenning EP, Kwekkeboom DJ, Bakker WH, Breeman WA, Kooij PP, Oei HY, et al. Somatostatin receptor scintigraphy with [111In-DTPA-D-Phe1]- and [123I-Tyr3]-octreotide: the Rotterdam experience with more than 1000 patients. Eur J Nucl Med. 1993;20(8):716–31.

106. Krenning EP, Kooij PP, Bakker WH, Breeman WA, Postema PT, Kwekkeboom DJ, et al. Radiotherapy with a radiolabeled somatostatin analogue, [111In-DTPA-D-Phe1]-octreotide. A case history. Ann N Y Acad Sci. 1994;733:496–506.

107. Otte A, Mueller-Brand J, Dellas S, Nitzsche E, Herrmann R, Maecke H. Yttrium-90-labelled somatostatin-analogue for cancer treatment. Lancet (London, England). 1998;351(9100):417–8.

108. Otte A, Jermann E, Behe M, Goetze M, Bucher H, Roser H, et al. DOTATOC: a powerful new tool for receptor-mediated radionuclide therapy. Eur J Nucl Med. 1997;24(7):792–5.

109. Otte A, Herrmann R, Heppeler A, Behe M, Jermann E, Powell P, et al. Yttrium-90 DOTATOC: first clinical results. Eur J Nucl Med. 1999;26(11):1439–47.

110. Kwekkeboom DJ, Teunissen JJ, Bakker WH, Kooij PP, de Herder WW, Feelders RA, et al. Radiolabeled somatostatin analog [177Lu-DOTA0,Tyr3]octreotate in patients with endocrine gastroenteropancreatic tumors. J Clin Oncol. 2005;23(12):2754–62.

111. Strosberg J, El-Haddad G, Wolin E, Hendifar A, Yao J, Chasen B, et al. Phase 3 trial of (177)Lu-Dotatate for midgut neuroendocrine tumors. N Engl J Med. 2017;376(2):125–35.

112. Strosberg JR, Caplin ME, Kunz PL, Ruszniewski PB, Bodei L, Hendifar A, et al. (177)Lu-Dotatate plus long-acting octreotide versus highdose long-acting octreotide in patients with midgut neuroendocrine tumours (NETTER-1): final overall survival and long-term safety results from an open-label, randomised, controlled, phase 3 trial. Lancet Oncol. 2021;22(12):1752–63.

113. Fani M, Del Pozzo L, Abiraj K, Mansi R, Tamma ML, Cescato R, et al. PET of somatostatin receptor–positive tumors using 64Cu-and 68Ga-somatostatin antagonists: the chelate makes the difference. J Nucl Med. 2011;52(7):1110–8.

114. Maecke HR, Hofmann M, Haberkorn U. 68Ga-labeled peptides in tumor imaging. J Nucl Med. 2005;46(1 suppl):172S–8S.

115. Pryma DA, Chin BB, Noto RB, Dillon JS, Perkins S, Solnes L, et al. Efficacy and safety of high-specific-activity 131I-MIBG therapy in patients with advanced pheochromocytoma or paraganglioma. J Nucl Med. 2019;60(5):623–30.

116. Horoszewicz JS, Kawinski E, Murphy GP. Monoclonal antibodies to a new antigenic marker in epithelial prostatic cells and serum of

prostatic cancer patients. Anticancer Res. 1987;7 (5B):927–35.

117. Israeli RS, Powell CT, Fair WR, Heston WD. Molecular cloning of a complementary DNA encoding a prostate-specific membrane antigen. Cancer Res. 1993;53(2):227–30.

118. Pinto JT, Suffoletto BP, Berzin TM, Qiao CH, Lin S, Tong WP, et al. Prostate-specific membrane antigen: a novel folate hydrolase in human prostatic carcinoma cells. Clin Cancer Res. 1996;2(9):1445–51.

119. Pomper MG, Musachio JL, Zhang J, Scheffel U, Zhou Y, Hilton J, et al. 11C-MCG: synthesis, uptake selectivity, and primate PET of a probe for glutamate carboxypeptidase II (NAALADase). Mol Imaging. 2002;1(2):96–101.

120. Foss CA, Mease RC, Fan H, Wang Y, Ravert HT, Dannals RF, et al. Radiolabeled small-molecule ligands for prostate-specific membrane antigen: in vivo imaging in experimental models of prostate cancer. Clin Cancer Res. 2005;11(11):4022–8.

121. Eder M, Schäfer M, Bauder-Wüst U, Hull W-E, Wängler C, Mier W, et al. 68Ga-complex lipophilicity and the targeting property of a urea-based PSMA inhibitor for PET imaging. Bioconjug Chem. 2012;23(4):688–97.

122. Afshar-Oromieh A, Malcher A, Eder M, Eisenhut M, Linhart H, Hadaschik B, et al. PET imaging with a [68Ga] gallium-labelled PSMA ligand for the diagnosis of prostate cancer: biodistribution in humans and first evaluation of tumour lesions. Eur J Nucl Med Mol Imaging. 2013;40(4):486–95.

123. Hope TA, Eiber M, Armstrong WR, Juarez R, Murthy V, Lawhn-Heath C, et al. Diagnostic accuracy of 68Ga-PSMA-11 PET for pelvic nodal metastasis detection prior to radical prostatectomy and pelvic lymph node dissection: a multicenter prospective phase 3 imaging trial. JAMA Oncol. 2021;7(11):1635–42.

124. Fendler WP, Calais J, Eiber M, Flavell RR, Mishoe A, Feng FY, et al. Assessment of 68Ga-PSMA-11 PET accuracy in localizing recurrent prostate cancer: a prospective single-arm clinical trial. JAMA Oncol. 2019;5(6):856–63.

125. Hofman MS, Lawrentschuk N, Francis RJ, Tang C, Vela I, Thomas P, et al. Prostate-specific membrane antigen PET-CT in patients with high-risk prostate cancer before curative-intent surgery or radiotherapy (proPSMA): a prospective, randomised, multicentre study. Lancet. 2020;395(10231):1208–16.

126. Morris MJ, Rowe SP, Gorin MA, Saperstein L, Pouliot F, Josephson D, et al. Diagnostic performance of (18)F-DCFPyL-PET/CT in men with biochemically recurrent prostate cancer: results from the CONDOR phase III, multicenter study. Clin Cancer Res. 2021;27(13):3674–82.

127. Pienta KJ, Gorin MA, Rowe SP, Carroll PR, Pouliot F, Probst S, et al. A phase 2/3 prospective multicenter study of the diagnostic accuracy of prostate specific membrane antigen PET/CT with (18)F-DCFPyL in prostate cancer patients (OSPREY). J Urol. 2021;206(1):52–61.

128. Benešová M, Schäfer M, Bauder-Wüst U, Afshar-Oromieh A, Kratochwil C, Mier W, et al. Preclinical evaluation of a tailor-made DOTA-conjugated PSMA inhibitor with optimized linker moiety for imaging and endoradiotherapy of prostate cancer. J Nucl Med. 2015;56(6):914–20.

129. Weineisen M, Schottelius M, Simecek J, Baum RP, Yildiz A, Beykan S, et al. 68Ga-and 177Lu-labeled PSMA I&T: optimization of a PSMA-targeted theranostic concept and first proof-of-concept human studies. J Nucl Med. 2015;56(8):1169–76.

130. Hofman MS, Violet J, Hicks RJ, Ferdinandus J, Thang SP, Akhurst T, et al. [177Lu]-PSMA-617 radionuclide treatment in patients with metastatic castration-resistant prostate cancer (LuPSMA trial): a single-centre, single-arm, phase 2 study. Lancet Oncol. 2018;19(6):825–33.

131. Hofman MS, Emmett L, Sandhu S, Iravani A, Joshua AM, Goh JC, et al. [177Lu] Lu-PSMA-617 versus cabazitaxel in patients with metastatic castration-resistant prostate cancer (TheraP): a randomised, open-label, phase 2 trial. Lancet. 2021;397(10276):797–804.

132. Sartor O, de Bono J, Chi KN, Fizazi K, Herrmann K, Rahbar K, et al. Lutetium-177-PSMA-617 for metastatic castration-resistant prostate cancer. N Engl J Med. 2021;385(12):1091–103.

133. Hertz B. A tribute to Dr. Saul Hertz: the discovery of the medical uses of radioiodine. World J Nucl Med. 2019;18(1):8–12; PMID 30774539; PMCID: PMC6357704.

134. Larson SM, et al. Therapeutic applications of radiolabelled antibodies: current situation and prospects. Nucl Med Biol. 1986;2:207–13.

135. Sisson, et al. Scintigraphic localization of Pheochromocytoma. N Engl J Med. 1981;305:12–7.

136. Schreiter, et al. Searching for primaries in patients with neuroendocrine tumors (NET) of unknown primary and clinically suspected NET: evaluation of Ga-68 DOTATOC PET/CT and In-111 DTPA octreotide SPECT/CT. Radiol Oncol. 2014;48(4):339–47. PMID: 25435846.

137. Rauscher, et al. 68Ga-PSMA ligand PET/CT in patients with prostate cancer: how we review and report. Cancer Imaging. 2016;16:14.

The Nuclear Chemistry of Therapeutic Radionuclides

3

Frank Rösch

3.1 The Fundamentals

3.1.1 Transformations of Unstable Nuclei

In order to understand the origin and character of the individual radioactive emissions accompanying nuclear transformation processes, we should first seek out the answers to four questions:

- What is an unstable nucleus?
- What is its motivation to transform?
- What is the best way to transform?
- What are the radioactive emissions that accompany the transformations?

The following discussions aim to describe phenomena relevant to radiopharmaceutical chemistry and nuclear medicine. Of course, the chapter cannot cover all the important aspects. For a comprehensive review, see the six-volume *Handbook of Nuclear Chemistry* [1]. Alternatively, there is a two-volume teaching book entitled *Nuclear and Radio Chemistry* composed of *Volume I: Introduction* [2] and *Volume II: Modern Applications* [3]. The book entitled *Basics of Nuclear Chemistry and Radiochemistry: An Introduction to Nuclear Transformations and Radioactive Emissions* may be helpful as well [4].

3.1.2 The Composition of an Atomic Nucleus and the Mass Defect

The nomenclature of nuclear chemistry and physics presents the nucleus in the following way: the number of protons (Z) and the number of neutrons (N) as lower indices left and right, respectively, of the symbol of the chemical element, and the overall mass number (A)—i.e., the sum of the number of protons and neutrons—as the upper index on the left. We may believe that the weight of the nucleus is the sum of the masses of the protons and neutrons within it. However, the true result differs from our expectation. The masses of the individual—i.e., *non-bound*—nucleons summed do not reflect the real mass of the nucleus containing exactly the same nucleons *bound* together. The difference is expressed as the *mass defect*: $\Delta m^{\text{defect}} = m^{\text{nucleus}} - m^{\text{sum of individual, non-bound nucleons}}$. The nucleus is lighter than its individual components! This represents one of the most fundamental effects of our material world.

The absolute masses of the nucleons are extremely small and thus not convenient to handle. Accordingly, two other expressions of mass are preferred in nuclear sciences. One is the equivalent of mass in terms of energy according to $E = mc^2$. This yields energy values in units of

F. Rösch (✉)
Institute of Nuclear Chemistry, Johannes Gutenberg-University Mainz, Mainz, Germany
e-mail: froesch@uni-mainz.de

electron Volts (eV). The other approach is to utilize a relative mass parameter, the *atomic mass unit*. For systematics and individual values of atomic mass and other parameters (such as mean nucleon-binding energy), see Refs. Atomic Mass Data Center (AMDC) IAEA Nuclear Data Services [5] and Atomic Mass Evaluations [6, 7]. More data compilations for 2016 are available in Ref. [8].

3.1.3 Binding Energy

Where is that mass—"the mass defect" (Δm)—going? Of course, mass cannot disappear. Instead, it is translated into energy according to $\Delta E = \Delta mc^2$. What happens? Once nucleons approach a very small distance between each other (on the order of fm, i.e., the dimension of the atom nucleus), they are attracted to each other by the "strong force"—the strongest force known in our universe—and combine to form a nucleus. The energy all the nucleons *save* once bound together compared to their former non-bound state is called their "overall binding energy." The equivalents of Δm and ΔE thus reflect the overall binding energy, E_B, of the nucleus. Nucleon-binding energies correlate with mass defect values via $E_B = \Delta E = \Delta mc^2$. A more interesting parameter is the "mean binding energy," which is the average binding energy an individual nucleon contributes: $\bar{E}_B = E_B/A$. It appears that high values of $\bar{E}_B$ reflect highly stable nuclei. $\bar{E}_B$ values for the ~250 stable and more than 3000 unstable nuclei are tabulated in Ref. [5].

A key goal in the nuclear sciences is understanding the correlation between the mass number A (i.e., the total number of nucleons in the nucleus) and $\bar{E}_B$, the mean nucleon-binding energy. The basic theory is the "liquid drop model" (LDM), which is accompanied by a complementary "shell model" (SM). The LDM of the atomic nucleus postulates that all protons are identical, all neutrons are identical, and all nucleons are distributed homogeneously within the nucleus like H_2O molecules within a droplet of water. The semi-empirical mathematics quantifying the experimentally known dependencies is the so-called WEIZSÄCKER equation. The equation may be divided into five (or more) parts for volume, surface forces, Coulomb forces, symmetry, and pairing. Each term of this equation has a physical rationale that describes the various ways in which the two different types of nucleons contribute to binding energy. For some terms, there is a dependency on mass number A exclusively. For others, the individual contributions from either protons or neutrons are reflected in addition to just A. Finally, each of the terms gets a coefficient, a value that is just an adjustment of a polynomial to the "experimental" values of mean nucleon-binding energy. Overall, the result is excellent (with some exceptions!). It appears that high values of $\bar{E}_B$ are achieved in cases when the mixture between protons and neutrons for a given mass number A is well balanced.

For some mass numbers, there are extreme deviations between the real values and the ones predicted by the LDM. This begs for another approach: the "shell model." The "shell model" refers to the arrangement of these protons and neutrons into shell structures in which the balance of the nucleons represents "full" (or "closed") shell occupancies and reflects "magic" numbers. We will come back to this model in the context of γ-emissions.

3.1.4 From Stable to Unstable Nuclei

Both the liquid drop and shell models were developed based on parameters of ~250 stable atoms. One can conclude that the stability of an atomic nucleus of mass A is basically a question of attaining the right mixture between protons and neutrons for a given value of A. If "right," the nucleus owns the optimum value of the mean nucleon-binding energy for that value, reflecting the correlation $\bar{E}_B = f(A)$. If the specific mixture of nucleons in those stable nuclei deviates from the optimum value, $\bar{E}_B$ values are lower, and the nucleus of that value of A is no longer stable. However, not being stable does not mean not existing. To wit, a suboptimal mean nucleon-

binding energy for a given A does not guarantee stability, but it can allow the nucleus to exist for a certain period. The question is, If the nucleus exists but is not stable, what is it doing?

The answer? Such an unstable nucleus tries to stabilize itself! Its intrinsic motivation is to improve the mean nucleon-binding energy by optimizing its existing mixture of protons and neutrons into a better, more stable mixture. *This is the essence of radioactive transformations.* The old unstable nucleus will find a way to form a new one of lower mass that is characterized by increased mean nucleon-binding energy. Consequently, the process is exothermic and spontaneous. The velocity of this transformation (i.e., its half-life, $t_{1/2}$) is proportional to the gain in $\bar{E}_B$.

In the literature, the behavior of an unstable nucleus is typically expressed as "decay." Let us agree on a definition: Does the unstable nucleus really "decay"? The philosophic answer is that nothing decays: it only transforms into something new. An unstable nucleus *K1 thus transforms into a more stable one by optimizing its mean nucleon-binding energy. The absolute mass of the transformation product—nucleus K2, which may be stable or simply "more stable" but still

radioactive and in need of another transformation—is less than the absolute mass of the initial unstable nucleus. This transformation thus proceeds exothermically. The difference in mass is typically related in terms of energy ΔE and is referred to as the Q-value of the transformation; see below.

However, there is a third component to consider: that which is "emitted." This is the "radiation" that is released and accompanies the transformation processes. This kind of emission is generally associated with "radioactivity." At this stage, it is called "x" and subsumes the various kinds of "radiation" to be discussed later in detail (Fig. 3.1).

3.1.5 Primary Transformations vs. Secondary Transitions and Post-Processes

The primary goal of an unstable nucleus is to optimize its nucleon composition. "Radioactivity"—i.e., all of the forms of radioactive emission we observe—is a phenomenon that accompanies the individual processes an unstable
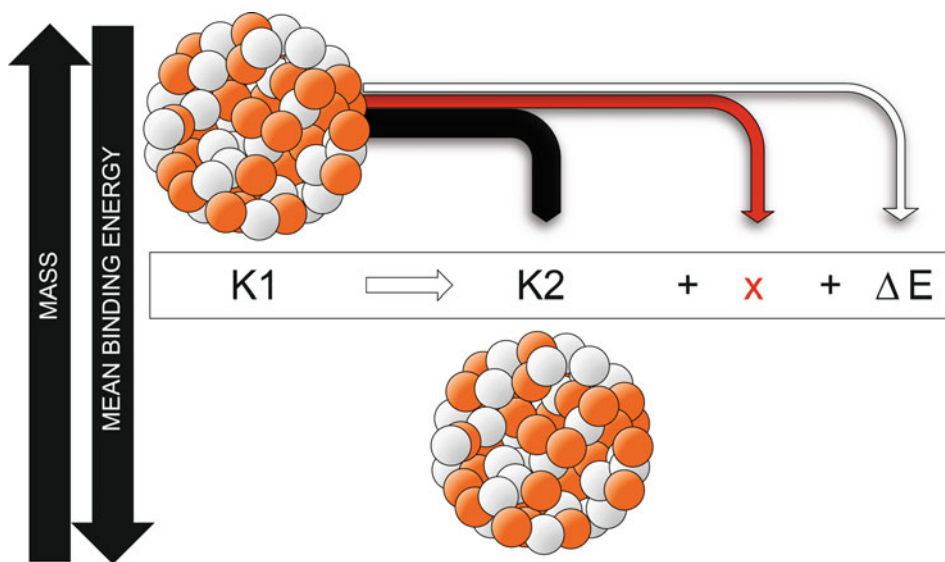
Fig. 3.1 Simplified scheme of the primary transformation of an unstable nuclide K1 into a more stable nuclide K2. This "x" is typically a particle, such as a ^{4}He nucleus (the α-particle) or a beta-electron (as in β-processes)

nucleus undergoes to increase its mean nucleon-binding energy! In the following, let us define a hierarchy of these processes of transformation: Primary ones, secondary ones, and post-processes (Fig. 3.2). (Note: One may include post-effects of type I, which are the origin of Auger-Meitner electrons, yet this will not be discussed here in detail. For the origin and characteristics of Augers electrons, please see Chaps. 5 and 20, and Refs. [2, 4]).

It all begins with a "primary" transformation: changing the nucleon composition of the unstable nucleus K1(A_1,Z_1,N_1). This results in the formation of a new nucleus: K2 (A_2,Z_2,N_2). There are three primary options: β-processes, α-processes, and fission. The three subtypes of primary transformations are β-processes (in which A remains constant with $A_2 = A_1$, and only Z and N change by one unit: $Z_2 = Z_1 \pm 1$, $N_2 = N_1 \pm 1$), α-emission (in which A changes as well: $A_2 = A_1 - 4$, $Z_2 = Z_1$–2, and $N_2 = N_1$–2), and spontaneous fission.

3.1.5.1 The Details

3.1.5.1.1 β-transformations

The β - and α-emitting radionuclides are illustrated and color-coded in the Chart of Nuclides (Fig. 3.3). It is obvious that the neutron-rich β⁻-emitters cover a broad range of proton and mass numbers (i.e., including light, medium, and heavy nuclei), while the α-emitters are heavy nuclides.

Three individual β-transformation processes exist depending on whether they start in neutron-rich or neutron-poor unstable nuclei (see Table 3.1). Only the blue ones representing neutron-rich unstable nuclei that emit β⁻-particles are relevant in a chapter focused on radiopharmaceutical therapy.

Indeed, in the context of therapeutic radionuclides, it is the β⁻ transformation that we should focus on. Accordingly, let us start with a neutron-rich unstable isotope. What should it do to stabilize itself to increase the mean binding
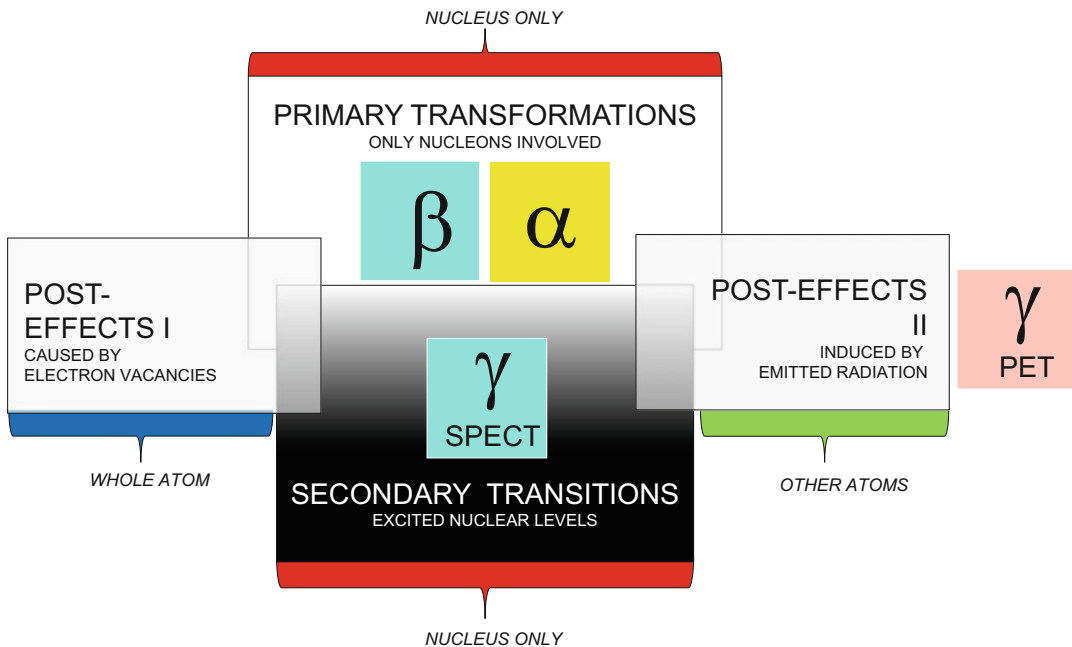
Fig. 3.2 Hierarchy of the primary transformations of unstable nuclei, the subsequent secondary transitions, and the parallel post-processes
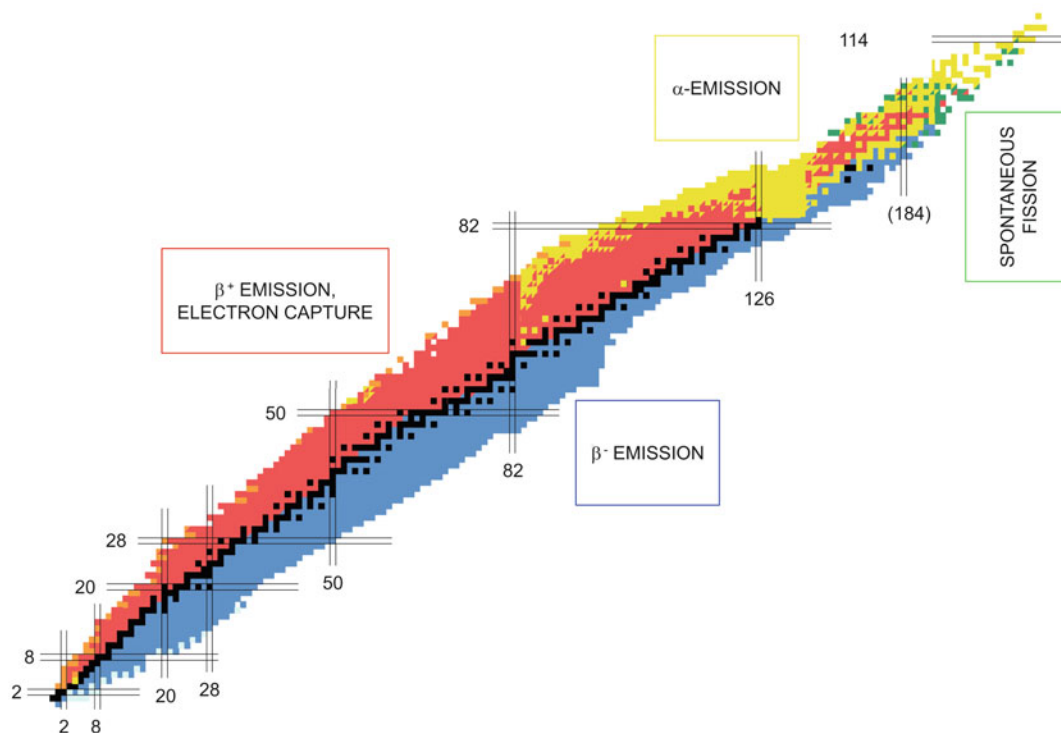
Fig. 3.3 Distribution of radionuclides in the Chart of Nuclides undergoing β-processes, α-emission, and spontaneous fission. According to the Karlsruhe Chart of Nuclides, β-processes are indicated by blue (β⁻) or red (β⁺ or ε), α-emission by yellow, and spontaneous fission by green [9]

Table 3.1 Three individual subtypes of β-transformations

Unstable nucleus	subtype	Emitted particle	Emitted neutrino
Neutron-rich	β^-	Electron	Electron neutrino
Proton-rich	β^+	Positron	Electron anti-neutrino
	EC	None	Electron neutrino

Note: EC = electron capture

energy of its nucleons? The elimination of a neutron seems to be a good idea. However, this would require sufficient energy to eliminate that nucleon from the nucleus, which is not necessarily available. On the other hand: what does it mean to have an "excess" of neutrons? It is tantamount to a "deficit" of protons. Now the clever unstable nucleus comes up with a brilliant idea: converting an (excess) neutron into a (deficient) proton would solve the problem in an elegant way. (The same applies to neutron-deficient isotopes, which are proton-rich, by converting a proton into a neutron.) Converting excess nucleons into deficient nucleons is the foundation of β-processes. As a result, all β-transformations proceed with constant values of A. The conversion of a neutron into a proton via the process $_Z K1 \rightarrow _{Z+1} K2$ is accompanied by the emission of a *negatively charged electron* and is called β⁻-process.

The β-Particle

But what about the emitted β-particle? It is needed for the balance in charge (Fig. 3.4)! For β⁻-processes, a neutral nucleon has changed into a +1 charged nucleon. Where is the missing

LOCATED IN THE OLD AND NEW ATOMIC NUCLEUS | RELEASED AS RADIATION
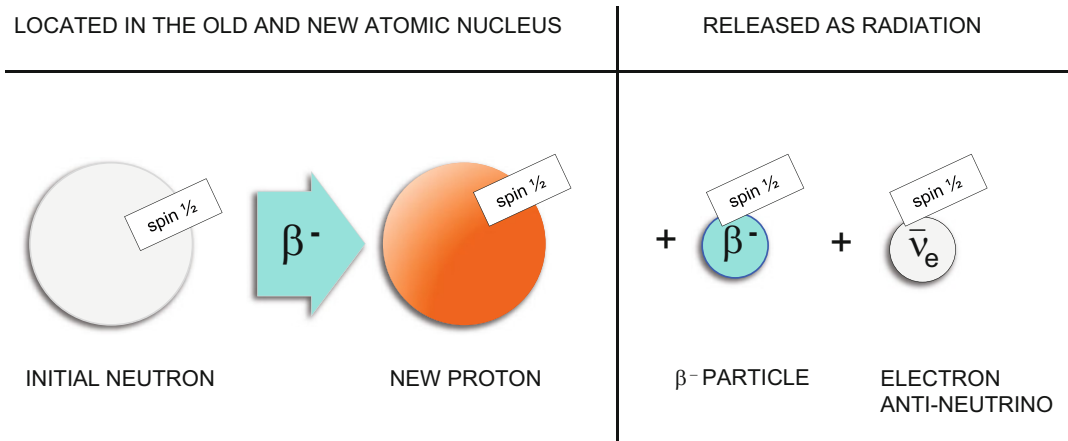
Fig. 3.4 Balancing electric charge and momentum during the nuclear conversion described by the β⁻-subtype of primary β-transformations. The gray and orange circles on the left represent the neutron and the proton, respectively, that remain in the nucleus of the transforming atom. The β⁻-particle (right) handles the balance in charge. For symmetry in momentum, an electron neutrino (also on the right) is emitted as well. It guarantees the conservation of spin. To ensure symmetry in matter vs. anti-matter, the electron neutrino created is an anti-elementary particle. Both the β⁻-electron and the electron anti-neutrino leave the atomic nucleus and carry kinetic energy

charge going? The answer: a new particle that carries a −1 charge! Note that in the present context, this electron is referred to as β⁻-particle. It is the origin of the electron that is responsible for this terminology: The β⁻-particle electron is an electron created within the nucleus. Its rest mass is exactly that of one electron (511 keV).

Yet there appears one more particle! Let us consider the n → p conversion of a neutron. The neutron's spin is ½, so the total spin on the left side of the transformation equation is non-integral. Among the transformation products discussed so far, the spin is ½ for the proton and ½ for the electron. These combine to form an integer. So here comes a problem: The overall spin of the starting particles and product particles differs! A third reaction product is needed to solve the problem. It should have no electric charge (so as not to disturb the symmetry in electric charge) and almost no mass (so as not to disturb the balance in mass). However, it should carry a half-integer spin. The solution is the electron neutrino. Its charge is zero, and its rest mass is close to zero, so it typically is neglected in the context of radiopharmaceutical chemistry and nuclear medicine.

Energetics of β-Transformations: The *Q*-Value

The new nuclide *must* be of lesser mass in order to guarantee an exothermic transformation. Put in a different way, the difference between the masses of the new nuclide and the old one is always positive: $+\Delta m$, which is also $+\Delta E$. The value of ΔE is specified as the *Q*-value of the process. The range of *Q*-values is very large.

Energetics of β-Transformation Products: Atomic Recoil

Let us assume the β-particle is ejected from K2, i.e., the former K_1. The momentum it takes causes an opposite momentum to K2. This is referred to as the "recoil energy" of K2. It is linked with (a) the *Q*-value, (b) its own mass, and (c) the kinetic energy, E_β, of the emitted β-particle and the electron neutrino (or the electron neutrino exclusively in the case of electron capture). In addition, it is influenced by the spatial arrangement of the two elementary particles emitted. K2 recoil energies thus lie between a theoretical maximum value and zero. The maximum kinetic energy $^{\mathrm{RECOIL}}E_{K2}{}^{\max}$ the recoil nucleus may get is:

$$^{\text{RECOIL}}E_{\text{K2}}^{\text{max}} = \left(\frac{E_\beta^{\text{max}}}{2c^2} + m_{\beta^0}\right)\frac{E_\beta^{\text{max}}}{m_{\text{K2}}}$$

Recoil energies of K2 are higher if the kinetic energy of the β-particle emitted is high and the mass number of K2 is low. For example, at mass numbers around 100 and maximum kinetic energies of the emitted β-particle of 1 MeV, values of $^{\text{RECOIL}}E_{\text{K2}}^{\text{max}}$ are about 10 eV (Fig. 3.5).

Energetics of β⁻-Transformation Products: Continuous Spectra of β⁻-Energies

Despite the fact that the electron neutrino is neglected in the context of radiopharmaceutical chemistry and nuclear medicine, it is responsible for an important aspect of RPT using β⁻-emitting radionuclides: the β⁻-particle and the electron neutrino share their fraction of kinetic energy "statistically." As a result, the kinetic energies observed for β⁻-particles and for electron neutrinos exist as a continuous spectrum. The β⁻-particle kinetic energies lie between the theoretical maximum value, E_β^{max}, and zero. Typical maximum energies for β⁻-particles emitted from neutron-rich unstable nuclides range from about 100 keV to a few MeV. However, most of the β⁻-particles show mean energies (E_β^{mean} or $\bar{E}_\beta$) around $1/3E_\beta^{\text{max}}$. Figure 3.6 illustrates the clinically most relevant β⁻-emitters, their maximum β⁻-energies, and their half-lives.

Several β⁻-Emissions Within One Transformation

For many neutron-rich unstable nuclei, several individual β⁻-emissions lead to the formation of the new nucleus. This takes us back to the SM model of the atomic nucleus that defines nucleons existing in separate shells. Accordingly, each nucleon is characterized by a unique set of quantum numbers. This is true for the ground-state of the nucleus. However, within a nuclear

Fig. 3.5 Recoil effects in β-transformations

Fig. 3.6 Clinically most
relevant β⁻-emitters, their
maximum β⁻-energies, and
their half-lives
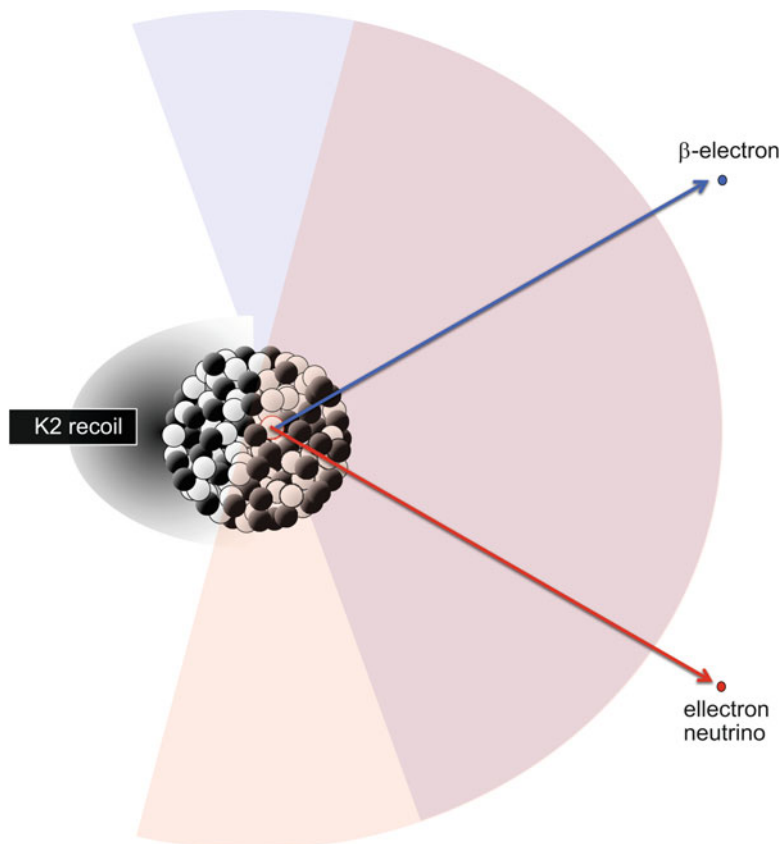
Fig. 3.6 Clinically most relevant β⁻-emitters, their maximum β⁻-energies, and their half-lives
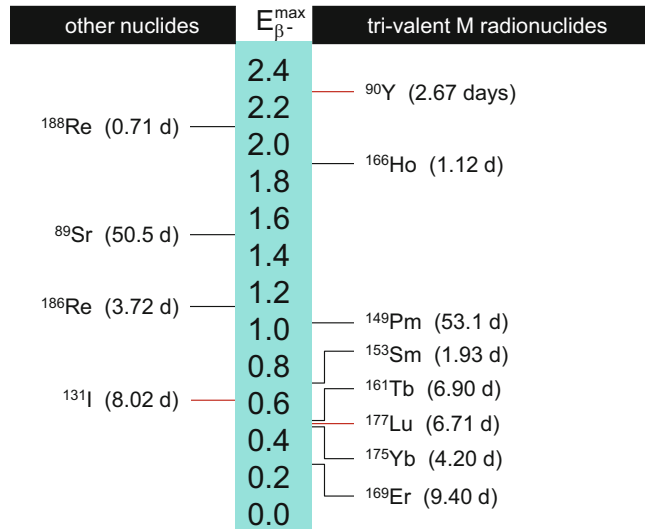
transformation, the newly formed nucleus does not necessarily distribute all its nucleons in their ground-state orbitals. In contrast, several nucleons first arrive at higher-energetic shells, referred to as excited nuclear states. Each nuclear state is defined by its *overall spin J* and its *parity Π*.

Overall Nuclear Spin J Each nucleon in a nucleus owns a characteristic individual orbital spin. The sum of all individual spins creates the overall spin, J, of a given nuclear state. Overall spin values may thus be different between the initial state of the unstable nuclide K_1 and the ground-state of the new nuclide K2. In addition, the new nucleus formed may be the ground-state of K2 or an intermediate excited nuclear state $^\Theta$K2. An excited nuclear level is characterized by individual nucleons populating higher-energy shell positions with quantum numbers different from those of the corresponding ground-state of the same nucleus. Accordingly, the overall nuclear spin numbers J may differ between the excited and ground-state levels of K2.

Parity Π: In quantum physics, parity refers to changes in physical quantities under spatial inversion within a polar coordinate system. Mathematically, parity refers to how wave functions with corresponding eigenvalues and parity operators,

P, change in the course of spatial inversion. While the three coordinates change from, e.g., $(+x,+y,+z)$ to $(-x,-y,-z)$, the quantum parameters in terms of wave functions and eigenvalues may also change or not. Parity is thus indicated as + or −.

Figure 3.7 illustrates the situation for the important therapeutic β⁻-emitter ^{131}I and several of its selected nuclear states. Note that the nuclear states indicated in the gray field all belong to the product nucleus of the primary transformation, namely ^{131}Xe. Each nuclear state has a characteristic energy value and quantum number, J and Π. Accordingly, the probabilities of populating the various levels differ: It is zero for directly populating the ground-state because the difference in overall spin is $\Delta J = 2$ (7/2 for ^{131}I to 3/2 for ^{131g}Xe) and highest for populating the excited nuclear state $^{\Theta 3}$K2 with $J = 5/2$, as $\Delta J = 1$ with both parities the same (i.e., +). Relative to all the other β⁻-emission pathways, more than 89.4% of all β⁻-electrons emitted from ^{131}I populate that particular excited nuclear state.

As each nuclear state corresponds to an energy value, the maximum β⁻-energies of the β⁻-particles emitted upon transformation to these states differ. The β⁻-energy is at its maximum value for the transformation to the ground-state of ^{131}Xe and lowest for the transformation to the
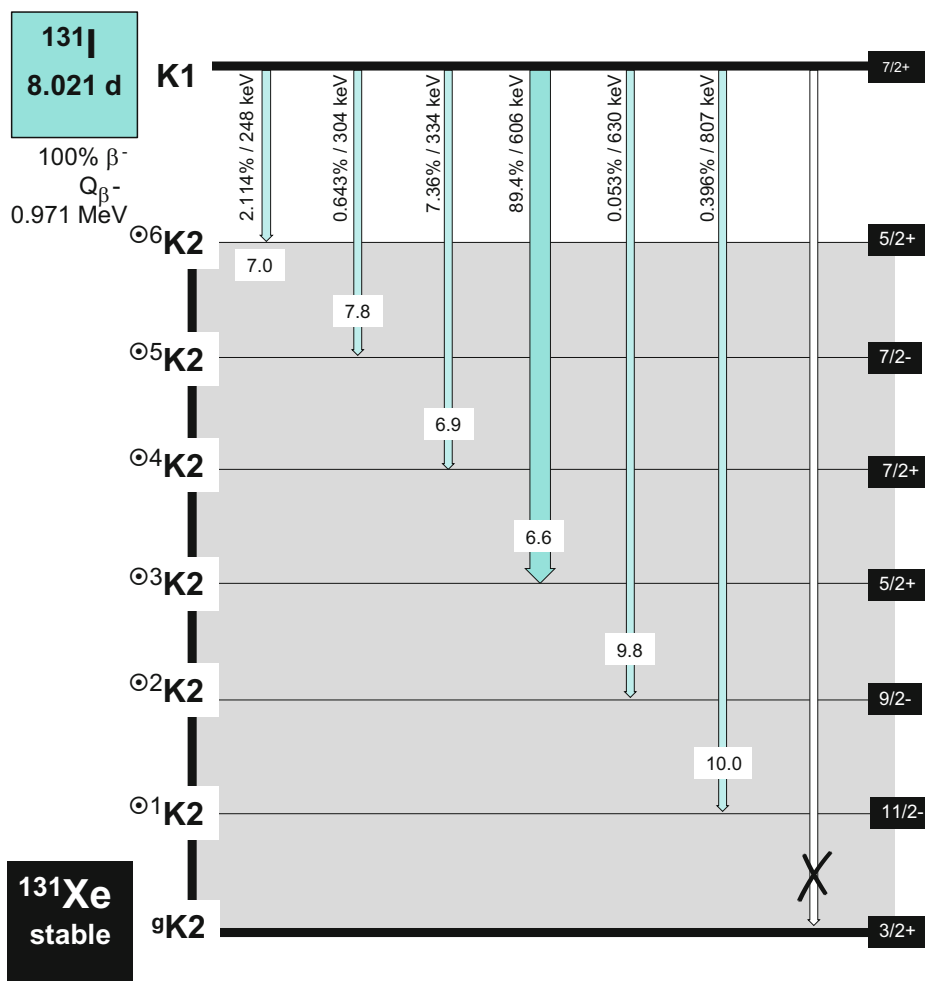
Fig. 3.7 β⁻-transformation pathways of ¹³¹I to the ground-state and several excited states of stable ¹³¹Xe. *JΠ* sets are given on the right edge of the figure. White boxes in the arrows reflect log(ft) values, which also reflect transition probabilities

highest energy excited nuclear state ᴼ⁶K2. What matters most, however, is the β⁻-energy from the most abundant process: 606 keV.

3.2 α-Transformations

3.2.1 From β-Transformation to α-Emission

For all atomic mass numbers from 1 to 209, β⁻-processes yield at least one definite stable nuclide; sometimes, in the case of (odd,odd) nuclei

transforming to (even,even) nuclei and vice versa, two for a given isobar A. This paradigm does not continue above A = 209. Let us consider the mechanism of a β⁻-transformation of the A = 226 isobar. The radium isotope 226 represents its most stable nucleon composition. ²²⁶Ra by far shows the longest half-life of this isobar: 1600 years. The neighbors at Z + i are of much lower stability, as their half-lives are in the range of hours (29 h for ²²⁶Ac), minutes (31 min and 1.8 min for ²²⁶Th and ²²⁶Pa, respectively), and milliseconds (280 ms for ²²⁶U and 31 ms for ²²⁶Np). For the Z-i arm of the parabola,

^{226}Fr and ^{226}Rn show half-lives of 48 s and 7.4 min, respectively. In the present case, the nuclide at the vertex of the isobar parabola of $\bar{E}_B = f(Z)$ is ^{226}Ra, yet it is not stable (Fig. 3.8). Why is this the case? β^{-}-Transformation does its best to build the most stable nuclide of the A = 226 isobar, but these transformations were ultimately not able to create a stable nucleon configuration. Consequently, ^{226}Ra must transform to a more stable nucleon configuration by a mode other than β^{-}-transformation: α-emission.

The emission of an α-particle immediately reduces the mass of the unstable nuclide K_1 and changes both its proton and neutron numbers: it is a primary transformation. The reason the α-particle is preferred (compared to the emission of other clusters of nucleons) lies in its very high "internal" stability. The mean nucleon-binding energy of a ^{4}He nucleus is 7.052 MeV, and the nucleus is further stabilized due to a "double magic" nucleon shell configuration (Z = 2, N = 2). The α-transformation thus balances the
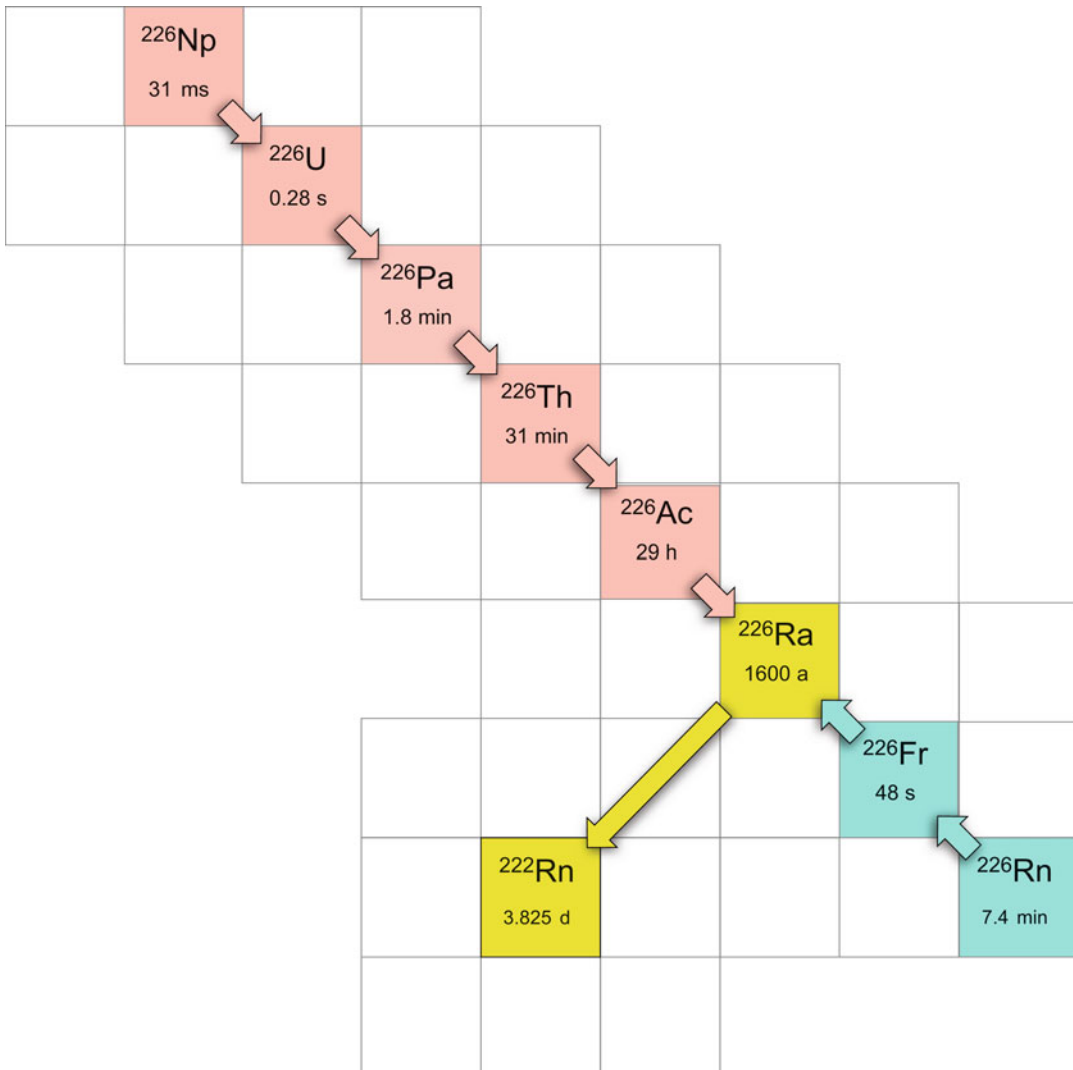
Fig. 3.8 β^{-}-transformation processes along the isobar A = 226. The most stable (but not *really* stable) and longest-lived nuclide is ^{226}Ra. This unstable nuclide of optimum mean nucleon-binding energy along the isobar transforms through α-emission to ^{222}Rn, thereby switching to a new, lower isobar

mass between the initial unstable nuclide K1 and the transformation product nuclide K2 in a clear way: the mass number of the new nuclide is reduced by 4.

The emission of *one* α-particle may generate a stable nucleon mixture but also may result in a nuclide that is "more stable" but *not* actually stable. This effect can be explained following the example given in Fig. 3.9. ^{226}Ra starts to transform by α-emission, following an isodiaphere line to form a product with a Z-2 and N-2 composition. The transformation product is ^{222}Rn, and the process has resulted in an increase in mean nucleon-binding energy: $\bar{E}_B = 7.695$ MeV for ^{222}Rn vs. 7.662 MeV for ^{2226}Ra. Yet this new nuclide is not stable either(!). The transformation may continue via another α-emission. This is exactly the case for ^{226}Ra, as introduced for the natural chain of transformation of the 4*n* + 2 series: ^{226}Ra originates from ^{230}Th by α-emission, and ^{226}Ra itself continues to form

daughters by successive α-emission as ^{226}Ra → α → ^{222}Rn → α → ^{218}Po → α → ^{214}Pb (Fig. 3.9).

With each successive α-emission, the nucleus increases the ratio between the number of its neutrons and protons. The excess of neutrons becomes increasingly dramatic, and β^{-}-transformation processes become increasingly energetically favored. Now, here comes the teamwork between α- and β^{-}-transformations: For ^{214}Pb, the β^{-}-process becomes the only pathway available to further stabilize the nucleus. It happens along the neutron-rich arm of the isobar parabola at A = 214 = constant until a new, local maximum of the mean nucleon-binding energy is reached. This new maximum of $\bar{E}_B$ could represent a stable nuclide, but this is not possible for A = 214, as there is no stable nuclide. If not, a situation occurs like that explained in the beginning for transformations along the isobar A = 226, and another α-emission follows (Fig. 3.9).
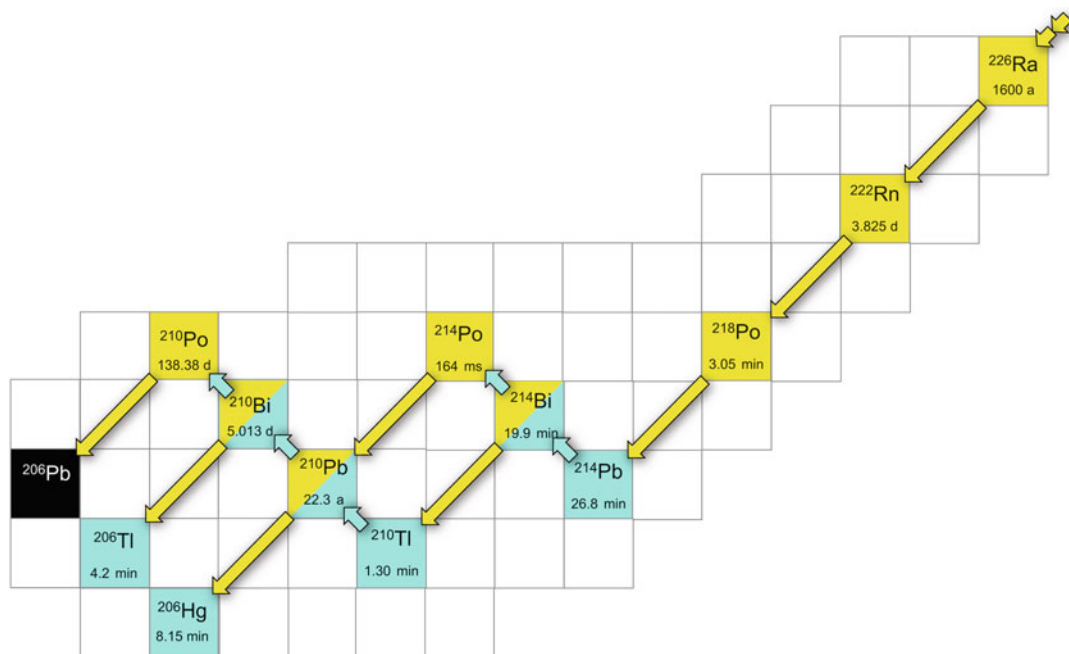
Fig. 3.9 Continuation of the naturally occurring ^{238}U transformation chain after the α-emissions from ^{226}Ra. The direct chain of α-emission terminates at ^{214}Pb, after which the next primary transformations are two β^{-}-processes. At ^{214}Bi, a branched chain starts with simultaneous transformations via β^{-}- and α-emission. Those individual directions finally terminate together at the stable nuclide ^{206}Pb

3.2.2 Simultaneous β- and α-Emission

As indicated in Fig. 3.9, α- and α-transformations not only may alternate from one transformation to the next but also may appear simultaneously for one nuclide! Obviously, ΔE values may be positive for different primary transformation options. In this case, each pathway gets its individual absolute value of Q according to the different balances in mass, illustrated by the notations Q_α and Q_β, respectively. Figure 3.9, for example, illustrates parallel β⁻- and α-emissions for the same radionuclide (^{214}Bi and ^{210}Pb). Another example is ^{213}Bi with both β⁻- and α-emissions (Fig. 3.10), of course leading to different transformation products: ^{213}Po or ^{209}Tl, respectively. In addition, α-emission and electron capture may occur simultaneously, as for ^{211}At, again forming different transformation products (^{207}Bi or ^{211}Po, respectively).

3.2.3 Energetics of α-Emission

3.2.3.1 Absolute Values of Q_α

The α-transformation process occurs spontaneously and, like all the other primary transformation pathways, is non-reversible. The new nuclide
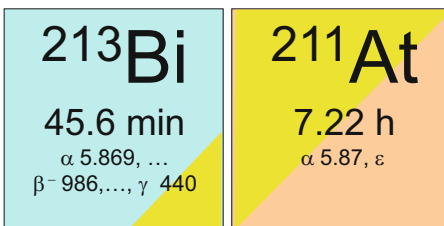
Fig. 3.10 Two examples of parallel options of primary transformations for the same radionuclide. Example #1: ^{213}Bi undergoes 2.1% α-emission (Q_α = 5.982 MeV, main α-energy 6.17 MeV) + 97.9% β⁻-emission (Q_β = 1.427 MeV, main maximum β⁻-energy 0.986 MeV), and main γ-emission 440 keV. Example #2: ^{211}At undergoes 41.8% α-emission (Q_α = 5.982 MeV, main α-energy 5.87 MeV) + 58.2% electron capture (ε) emission (Q_ε = 785 keV). For the individual numbers, see (4–8). The size of the color-coded area only qualitatively indicates the proportions between the different branches of transformation

K2 definitely is of less mass, guaranteeing an exothermic transformation. The absolute value of Q_α depends on the difference between the masses M of the two nuclides and involves the mass of the α-particle. The range of Q_α values is rather small, approximately between 1 and 10 MeV.

3.2.3.2 The Kinetic Energies of Emitted α-Particles and Recoil Nuclei

After an α-emission, the momentum and kinetic energies of the daughter nucleus K2 and the α-particle are balanced according to the equation $m_\alpha \cdot E_\alpha = m_{K2} \cdot E_{K2}$. The overall energy Q_α is allocated to the α-particle and the recoil nucleus K2 according to the following equations. The kinetic energy distributed between the α-particle and K2 directly depends only on the mass number of K2 (the mass of the α-particle is always the same).

$$p_{K2} = p_\alpha$$

$$Q_\propto = {}^{\mathrm{RECOIL}}E_{K2} + E_\propto$$

Because α-transformations produce only a single particle—not two as in β⁻- and β⁺-transformations—α-particles possess discrete kinetic energies. Its value of this energy is nuclide-specific and representative, like a fingerprint. Absolute values of kinetic energies of the α-particle are higher if the Q_α value is high and the mass number of the nuclide is low. The average values of the recoil energy of α-emitters lie between 10 and 100 keV.

$$E_\alpha = \frac{Q_\alpha}{1 + \frac{m_\alpha}{m_{K2}}}$$

3.2.3.3 Excited Nuclear States in α-Transformations

As in β-transformations, α-transformations do not necessarily yield the ground-state of the nuclide K2 directly but may populate excited nuclear levels of this newly formed nucleus. Figure 3.11 shows the pathways of two α-emitting nuclides. In the first (^{212}Po), the α-emission produces the
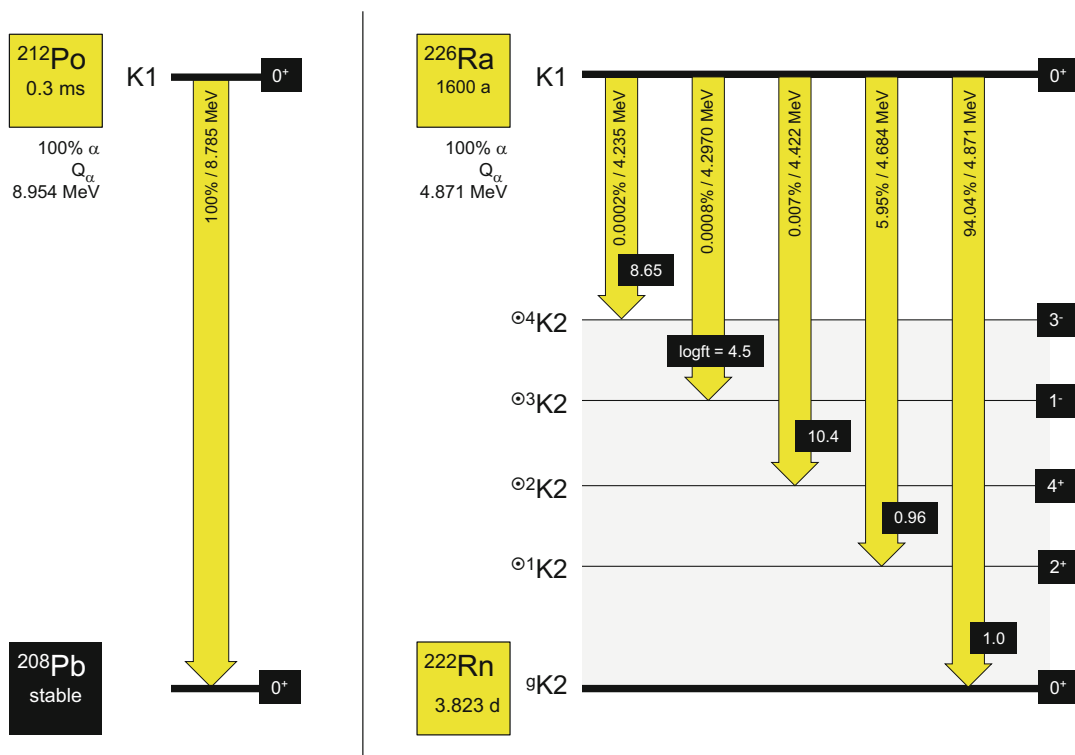
Fig. 3.11 *Left*: α-emission directly into the ground-state of K2 (^{212}Po → ^{208}Pb). The overall spin and parity are indicated for K1 and ^{g}K2. There are no changes. *Right*: α-emissions of ^{226}Ra populating several excited states of ^{222}Rn. Symmetry parameters are indicated for K1, ^{g}K2, and for four excited levels ^{Oi}K2 of ^{222}Rn. Each arrow shows the logft-values for the transformation, the corresponding abundance of the five individual α-emissions, and the corresponding energies of the α-particles emitted. The kinetic energy of the emitted α-particle is maximum for K1 → ^{g}K2 (4.871 MeV). The most probable transformation is K1 → ^{g}K2 (94.04%) because the overall spin and parity values are identical for both nuclei

ground-state of K2 directly and exclusively. In the second (^{226}Ra), the transformation populates through several excited nuclear states of ^{222}Rn.

3.2.4 Secondary Transformations, Excited Nuclear States, and Photon Emission

A primary transformation does not necessarily lead to the ground-state of the new nuclide K2 formed. Instead, individual excited states ^{Oi}K2 are populated. Similar to the excited electrons of an atomic shell, these nucleons "fall" toward lower-energetic nuclear levels. The transitions from a higher-energetic nuclear state may proceed to a lower-energetic excited nuclear state and/or to the final ground-state of the nucleus ^{g}K2. In each case, the specific differences of ΔE between the two nuclear levels involved are carried away by "secondary" transitions. It is the essence of secondary transformations that numbers for Z, N, and A do not change. Only the individual nuclear levels of the newly formed product nucleus K2 are involved.

Transitions between two levels involve a specific amount of energy represented by ΔE. The question is how that specific amount of ΔE is managed by the nucleus. There are three options. The most frequently occurring sort of secondary emission—and, for the molecular imaging of therapeutic radionuclides, very important—

consists in the release of electromagnetic radiation as γ-quanta, i.e., photons with $\Delta E = E_\gamma$. The second option is the conversion of this amount of ΔE into the release of an already existing electron of that nuclide from its inner electron shell, creating a "conversion electron." The third option is the transformation of ΔE directly into matter according to $E = mc^2$. It creates a pair of two particles, representing matter (an electron) and *anti*-matter (a positron). Note that the three pathways may occur simultaneously for the same transition.

Yet here, the photon emission is the most relevant. The energy of those photons is on the order of 100 keV to 1 MeV. For therapeutic radionuclides, it adds a welcome feature that allows for the molecular imaging of the β- or α-emitting radionuclide. Prominent examples of therapeutic nuclides that emit these photons are ^{131}I and ^{177}Lu. Figure 3.12 illustrates the origin of two prominent photons from the most often populated excited nuclear state of ^{131}Xe according to the primary β$^-$-transformation of ^{131}I. The dominant photons created in the
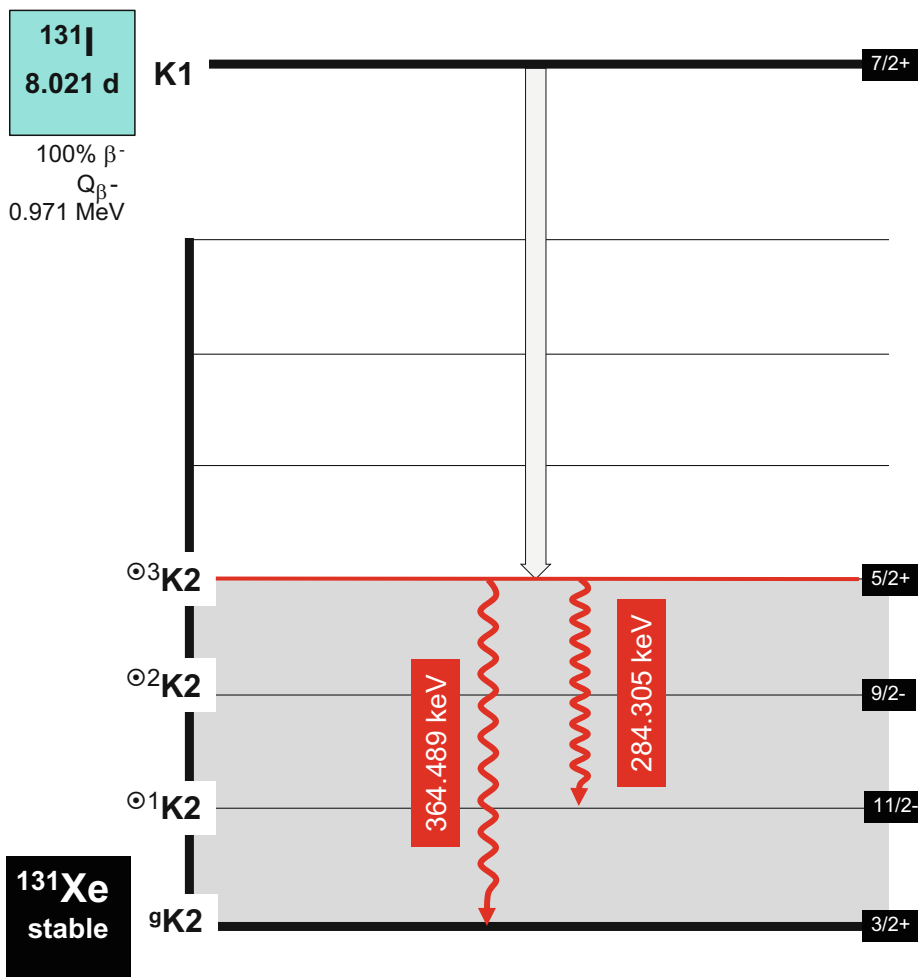
Fig. 3.12 De-excitation between two excited nuclear states defined by quantum physical parameters J and Π for the initial and final states, respectively. The characteristic difference in energy ΔE is released as γ-radiation. The transition via photon emission proceeds for specific values of ΔJ, and the photon must carry away this difference in overall momentum
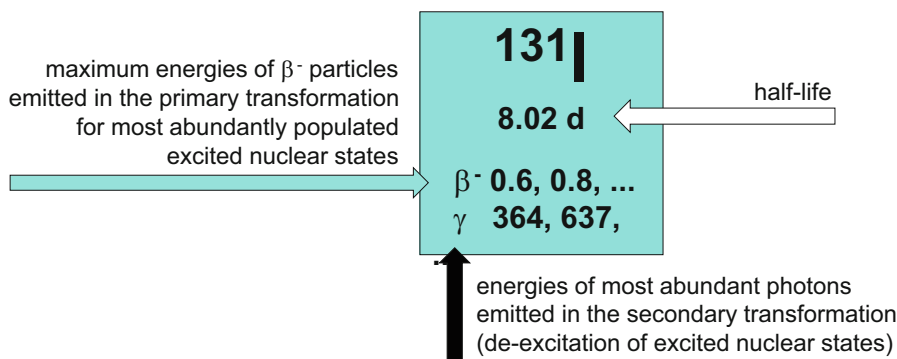
Fig. 3.13 The radionuclide ^{131}I as it appears in the Chart of Nuclides. The illustration conveys the most relevant photons created during the secondary transformations of ^{131}I together with other important nuclear data such as the individual energies of the main β^--transformations populating the excited nuclear states of the product nucleus ^{131}Xe

secondary transformation of therapeutic radionuclides are depicted in the box of the radionuclide within the Chart of Nuclides. Figure 3.13 gives the example for ^{131}I.

3.2.5 Availability of the Most Relevant Therapeutic Radionuclides

Among the many radionuclides within the Chart of Nuclides that emit β^--electrons or α-particles (more than 1000), only about 1% are clinically relevant. The unsuitability of the 99% stems from nuclear parameters that are inadequate for radiopharmaceutical chemistry and nuclear medicine, such as their physical half-life, critical transformation products, suboptimal emission profiles, or lack of sufficient labeling chemistry. Yet even for the 1% that fulfill the desired nuclear requirements, a huge problem remains: availability!

3.2.5.1 β^--Emitters

Almost all of the β^--*emitting* candidate radionuclides for Theranostics have to be produced artificially via nuclear reactions in nuclear reactors or particle accelerators. Many therapeutic isotopes can be produced most economically at medium- and high-flux reactors (neutron flux $> 4 \cdot 10^{14}$ n/cm^2 s^{-1}) in neutron-induced nuclear

reactions. Figure 3.14 illustrates four variants of these nuclear reactions. For all types of *n*-induced processes, production yields are the most important criteria. In addition to direct neutron-capture production pathways, β^--emitters may also be produced via radionuclide generators. The most notable example here is the ^{90}Sr/^{90}Y generator, though generator systems for ^{188}W/^{188}Re and ^{225}Ac/^{213}Bi generators exist as well.

Selected β^--emitters are listed in Table 3.2 by mass number. In the following section, we briefly describe some of the prominent β^--emitting radionuclides used in theranostics and, in some cases, illustrate their production pathways.

^{131}**I**: One production pathway for ^{131}I is the neutron-induced fission of ^{235}U. Here, it is accompanied by the production of other isotopes of iodine—particularly stable forms—and thus contains carrier. This is not an issue when ^{131}I is used for the treatment of thyroid cancer, but it may be problematic in the context of ^{131}I-labeled targeted radiopharmaceuticals. An alternative approach to production relies on the (n,γ) process on tellurium-130 in which the short-lived intermediate ^{131}Te ($t^{1/2} = 25$ min) undergoes β^--transformation to ^{131}I. While this neutron-capture reaction has a very low cross section of 0.19 barn, the strategy yields no-carried-added ^{131}I after separation of the tellurium target material.

^{32}**P**: ^{32}P is readily available from medium-flux reactors via the neutron irradiation of sulfur—the

Fig. 3.14 The main pathways for the production of neutron-rich unstable nuclei
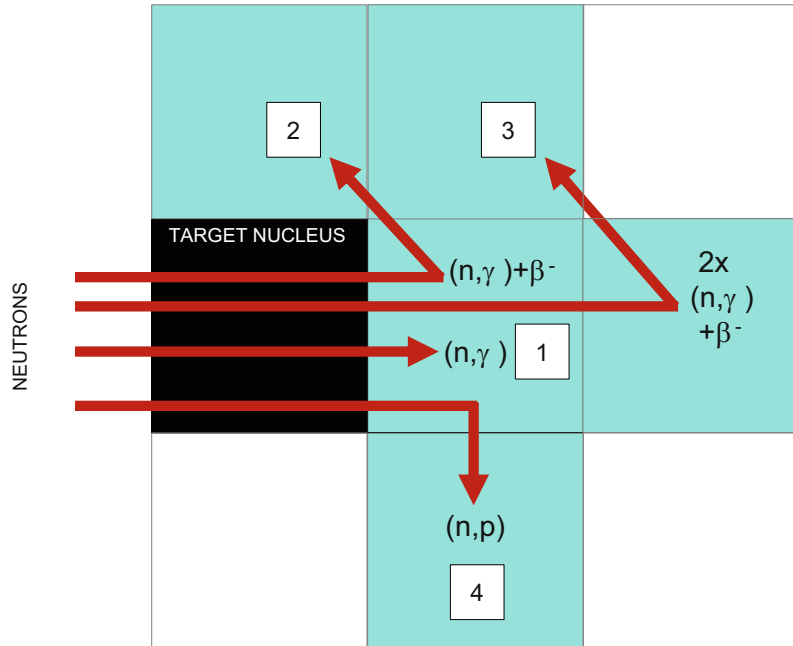
Table 3.2 Radionuclides used for theranostics that transform by β^--emission

Radionuclide	$t\frac{1}{2}$	β^- (E^{max})	Accompanying γ-emission	Mean tissue range
	(h)	(MeV)	(keV (%))	(mm)
^{64}Cu	12.7	0.58	1346 (47.5)	0.19
^{67}Cu	61.9	0.58	184.6 (46.7), 93.3 (16.6)	0.19
^{90}Y	64.1	2.28	–	1.1
^{105}Rh	35.4	0.57	319 (19.6)	0.19
^{131}I	192	0.61	364 (81)	0.21
^{149}Pm	53.1	1.10	286 (3)	0.43
^{153}Sm	46.3	0.81	103 (28.3)	0.30
^{161}Tb	165.8	0.59	48.9 (17), 74.6 (10.2)	0.20
^{166}Ho	26.8	1.86	80.6 (6.2), 1379 (1.1)	0.84
^{177}Lu	161	0.50	208 (11), 113 (6.6)	0.16
^{186}Re	89.2	1.10	137 (9)	0.43
^{188}Re	16.9	2.10	155 (15)	0.98
^{198}Au	64.7	0.96	412 (95.6)	0.38
^{199}Au	75.4	0.45	208 (9.1), 158 (40)	0.14

The table is reproduced from [10]

^{32}S(n,p)^{32}P process—and can be separated chemically from the phosphorus target.

^{89}Sr: One production route for ^{89}Sr is the ^{88}Sr (n,γ)^{89}Sr reaction, though the low cross section of ^{88}Sr (0.0058 barn) results in the formation of ^{89}Sr with low specific activity. A second approach involves the irradiation of ^{89}Y in a fast-flux reactor ^{89}Y(n,p)^{89}Sr, yet this process also suffers from a low cross section (Fig. 3.15).

^{90}Y: The thermal neutron-capture reaction of ^{89}Y is of medium cross section (1.25 barn) and yields ^{90}Y of low specific activity. A better route leverages long-lived ^{90}Sr (half-life 28.64 a) obtained from ^{235}U fission for the creation of a

secular radionuclide generator that produces high specific activity ^{90}Y. Figure 3.16 compares the two pathways.

^{67}**Cu**: ^{67}Cu is produced on a high-energy accelerator through the bombardment of an enriched ^{68}Zn target with 193 MeV high-energy protons via the ^{68}Zn(p,2p)^{67}Cu reaction. This process co-produces ^{64}Cu ($t\frac{1}{2}$ = 12.7 h), ^{61}Cu ($t\frac{1}{2}$ = 3.4 h), and other radionuclides, and production is currently limited to only a few sites worldwide. ^{67}Cu can also be produced in a

nuclear reactor via the irradiation of enriched ^{67}Zn oxide by the ^{67}Zn(n,p)^{67}Cu reaction. However, the yields of this approach are low, and long-lived ^{65}Zn is co-produced. Recently, the production of ^{67}Cu has been performed with an electron accelerator through the photonuclear reaction using bremsstrahlung photons by bombarding an enriched ^{68}Zn target with an e-LINAC at 27 MeV or higher via ^{68}Zn(γ, x)^{67}Cu processes. Using enriched target material avoids the co-production of ^{64}Cu and radioisotopes of zinc, and can thus provide Curie quantities in very high specific activity.

^{64}**Cu**: ^{64}Cu can be produced via the ^{64}Ni(p, n)^{64}Cu reaction using enriched nickel targets, yet the therapeutic potential based on its β$^-$-emission remains rather unclear. The radionuclide is, however, extensively used in PET.

^{177}**Lu**: The direct route to ^{177}Lu is neutron capture by enriched ^{176}Lu. Due to its very large cross section (2100 b), the ^{176}Lu(n,γ)^{177}Lu process converts about 20–30% of the ^{176}Lu atoms to ^{177}Lu even in medium neutron flux. This approach yields specific activities of 740–1110 GBq/mg (20–30 Ci/mg) when utilizing highly enriched ^{176}Lu targets. Higher specific activities of 1850–2405 GBq/mg (50–85 Ci/mg) can be achieved using higher-flux reactors.
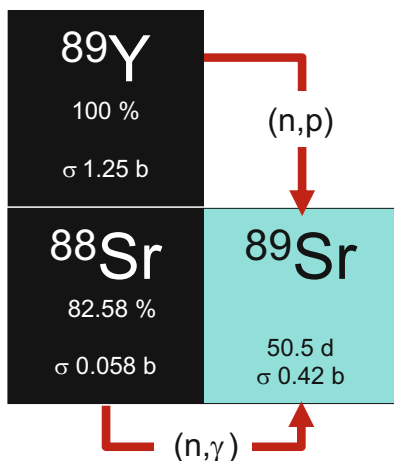
Fig. 3.15 Two *n*-induced pathways leading to ^{89}Sr

Fig. 3.16 Two pathways leading to ^{90}Y via an (n,γ) reaction on ^{89}Y and the use of ^{90}Sr to create a ^{90}Sr/^{90}Y radionuclide generator
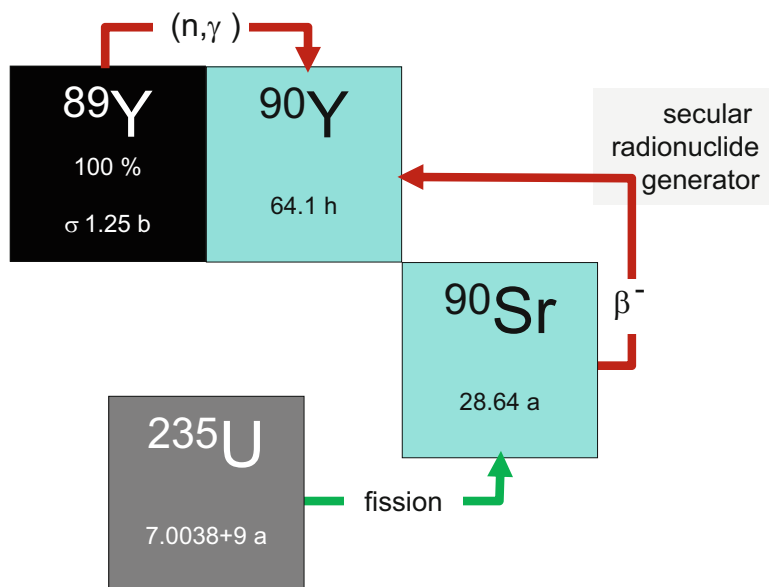
However, the ^{177}Lu is not completely free of stable ^{176}Lu and, in addition, contains the non-separable long-lived metastable isomer ^{177m}Lu ($t\frac{1}{2}$ = 160 days). These two problems in the production of ^{177}Lu are addressed by the neutron activation of enriched ^{177}Yb to produce the short-lived intermediate ^{177}Yb ($t\frac{1}{2}$ = 1.9 h), which then undergoes β-transformation exclusively to the ground-state of ^{177}Lu [11]. The separation of this ^{177}Lu from the Yb target produces a high specific activity product, on the order of 4107 GBq/mg (111 Ci/mg). These days, TBq activities are routinely produced using this approach. Figure 3.17 compares the two neutron-capture pathways.

^{153}Sm: ^{153}Sm is produced using the ^{152}Sm (n,γ)^{153}Sm reaction via the neutron irradiation of an enriched ^{152}Sm target at relatively high cross section (206 b) and, accordingly, yields ^{153}Sm in high specific activity. For example, a specific activity of 222 GBq/mg (6 Ci/mg) was achieved using a 155-h irradiation at a neutron flux of $1.2 \cdot 10^{14}$ n/cm^2 s^{-1} for approximately 155 h.

^{166}Ho: ^{166}Ho is routinely made via the direct neutron irradiation of ^{165}Ho, which is 100% abundant. The cross section of the ^{165}Ho (n,γ)^{166}Ho process is 58 barn. Alternatively, ^{166}Ho can be produced via an indirect route (Fig. 3.18). An enriched ^{164}Dy target undergoes a double (n,γ) reaction to produce ^{166}Dy that

subsequently transforms by β$^-$-emission to ^{166}Ho. The first neutron-capture cross section is very high (2731 barns thermal and 932 barns epithermal) to form ^{165}Dy with a $t_{\frac{1}{2}}$ of 2.3 h. Although the half-life of this intermediate is relatively short, ^{165}Dy has very high thermal and epithermal neutron-capture cross sections (3600 and 22,000 barns, respectively), and thus a significant percentage of the ^{165}Dy atoms capture a second neutron to form ^{166}Dy.

^{161}Tb: ^{161}Tb can be produced by the neutron irradiation of enriched ^{160}Gd to form short-lived ^{161}Gd as an intermediate that proceeds via β$^-$-transformation to ^{161}Tb according to the ^{160}Gd (n,γ)^{161}Gd → ^{161}Tb reaction (exactly as indicated in Fig. 3.17 for ^{177}Lu). Yet unlike ^{177}Lu, ^{161}Tb decays with the co-emission of ~12 Auger and conversion electrons (≤50 keV, vs. ~1 for ^{177}Lu) along with low-energy β$^-$-particles, resulting in a higher total electron-to-photon dose ratio for ^{161}Tb than ^{177}Lu [12].

^{186}Re: ^{186}Re can be produced by the neutron capture of ^{185}Re in low-to-medium specific activity (cross section 110 barn). Alternatively, ^{186}Re can be accelerator-produced via the proton or deuteron bombardment of an enriched ^{186}W target (such as the ^{186}W(p,n)^{186}Re reaction). This strategy can produce ^{186}Re of higher specific activity following the separation of the tungsten target. Although various accelerator approaches

Fig. 3.17 Comparison of the two production pathways leading to ^{177}Lu. For the ^{176}Lu(n,γ) route, long-lived ^{177m}Lu is co-produced at a low level, and neither ^{177}Lu nor ^{177m}Lu can be isolated from the target material. In contrast, neutron capture on ^{176}Yb forms short-lived ^{177}Yb that transforms via β$^-$-transformation to the ground-state of ^{177}Lu exclusively. The latter process requires (and allows) the chemical isolation of almost carrier-free ^{177}Lu from ^{176}Yb
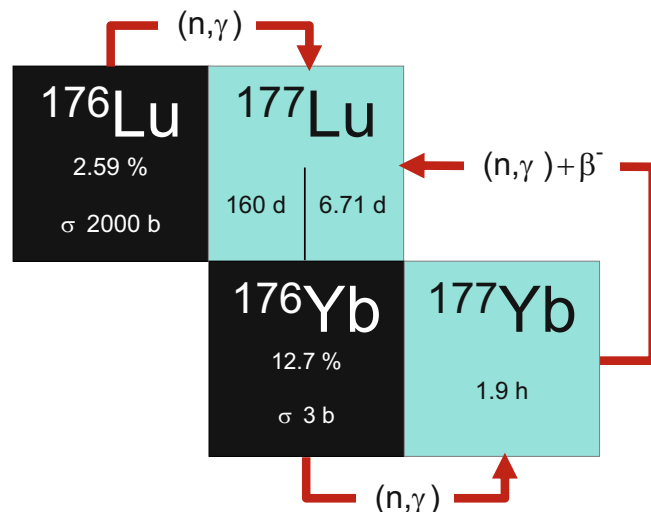
Fig. 3.18 The production of ^{166}Ho via direct and indirect routes. In the direct route, ^{165}Ho is irradiated. In the indirect method, an enriched ^{164}Dy target undergoes a double (n,γ) reaction to produce short-lived ^{166}Dy ($t_½ = 2.35$ h), which immediately transforms by β$^-$-emission to ^{166}Ho
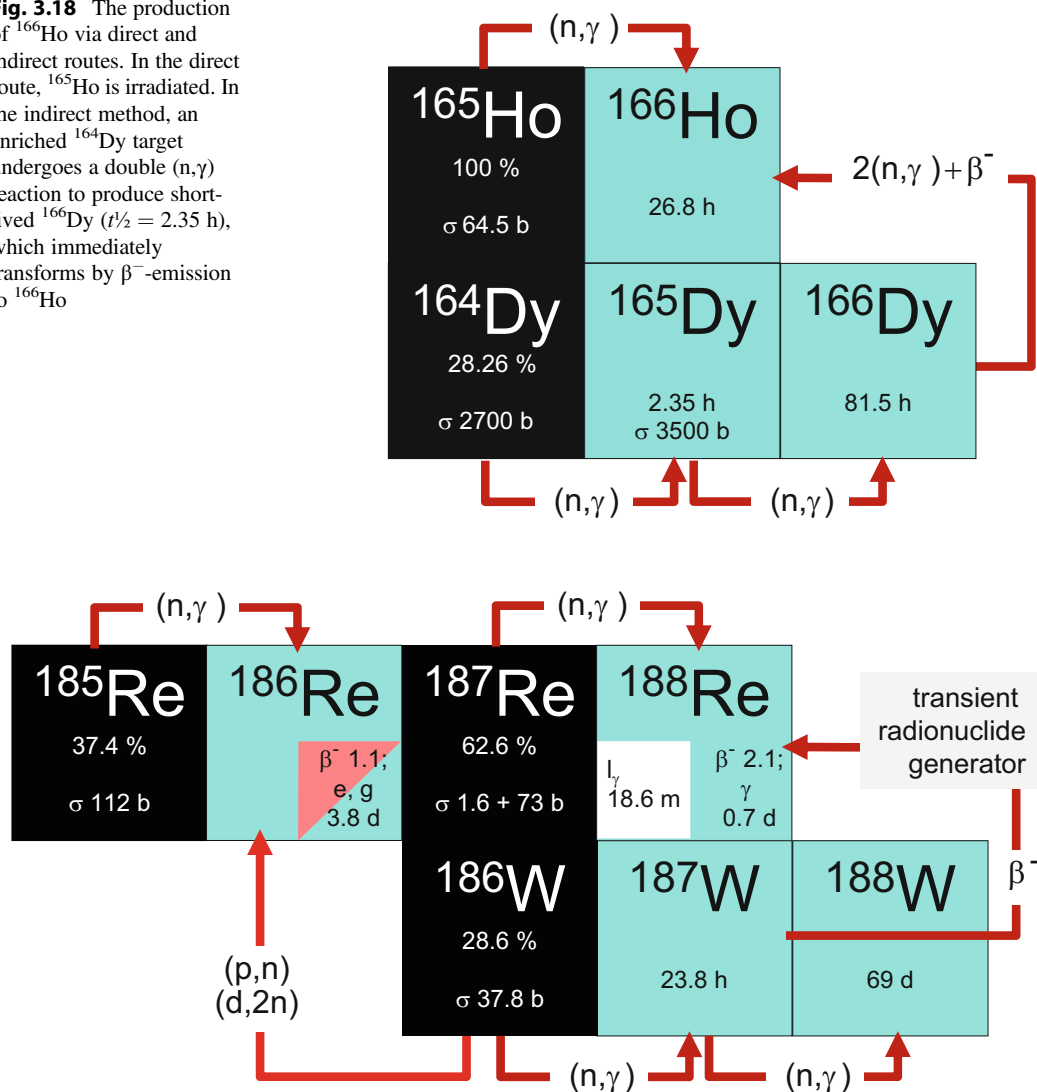
Fig. 3.19 Production pathways of ^{186}Re via the ^{185}Re (n,γ) reactions or p- and d-induced nuclear reactions with ^{188}W. Also shown are the production pathways of ^{188}Re through the ^{187}Re(n,γ)^{188}Re reaction and the double neutron capture of ^{186}W followed by β$^-$-transformation to the short-lived nuclide ^{188}W. The ^{188}W/^{188}Re pair represents a valuable radionuclide generator system

are being explored, regular productions utilizing this option have not yet been established.

^{188}Re: ^{188}Re is obtained from a ^{188}W/^{188}Re generator with very high specific activity. The ^{188}W parent ($t_{½} = 69.4$ d) is produced by the double neutron capture of ^{186}W via the ^{186}W (n,γ)^{187}W(n,γ)^{188}W reaction in a high-flux nuclear reactor (Fig. 3.19). The separation of the parent and daughter radionuclides results in specific activities of ^{188}Re that near the theoretical maximum.

3.2.5.2   α-Emitters

The most common therapeutic α-emitting radionuclides are ^{223}Ra, ^{225}Ac, ^{213}Bi, and ^{211}At (see Table 3.3). Unlike many of the β$^-$-emitting

Table 3.3 A list of α-emitters being used clinically or investigated (gray) for α-theranostics, arranged by increasing mass number

Radionuclide	$t_{1/2}$	$E\alpha$ (keV)	Accompanying γ-emission: energy (keV) and branching (%)
[149]Tb	4.12 h	4077	β^+, γ = 352
[211]At	7.21 h	5867	γ = 79
[212]Bi	60.6 min	8785	γ = 727
[213]Bi	45.7 min	8378	γ = 440
[223]Ra	11.4 d	5348[avg]	γ = 269
[224]Ra	3.62 d	5094[avg]	γ = 241
[225]Ac	10.0 d	5450[avg]	γ = 86
[228]Th	30.9 min	6338[(75%)]	γ = 111 (3%)
[227]Th	18.7 d	5562[avg]	γ = 236 (11.5%)
[255]Fm	20.1 h	7022	γ = 16

"Avg" considers an average energy covering not a single but several successive α-transformations in a transformation chain until reaching the final transformation product (Fig. 3.11). (%) represents the abundance of the main emission given. Table is taken from [10]

therapeutic radionuclides, the candidates here are either produced at particle accelerators or originate from the transformation of long-lived radionuclide precursors.

[211]At: [211]At ($t_{1/2}$ = 7.2 h) simultaneously transforms via 58% electron capture to [211]Po and 42% α-transformation to [207]Bi, a long-lived radionuclide (Fig. 3.20). This provides two possible α-particles with energies of 4.87 and 7.5 MeV, respectively. [211]At is predominantly produced by irradiating natural bismuth with α-particles of not more than 28 MeV. The (α,3n) process must be avoided because it would co-produce long-lived and radiotoxic [210]Po.

[223]Ra: [223]Ra ($t_{1/2}$ = 11.43 days) transforms by four successive α-emissions and two β^--emissions to stable [207]Pb. It is a member of the natural [235]U transformation chain (Fig. 3.21). [227]Ac, a daughter within that chain with a half-life of 21.8 years, represents a potential generator system parent for [223]Ra.

[225]Ac: [225]Ac transforms by successive α-emissions and β^--emissions to stable [207]Pb. It is a member of the natural [237]Np/[233]U transformation chain (Fig. 3.22).

Actinium-225 has traditionally been obtained from long-lived [229]Th ($t_{1/2}$ = 7340 y), for which [233]U has been the only viable source. However, this is limited to a few institutions worldwide, such as the Joint Research Centre (JRC, Karlsruhe, Germany), Oak Ridge National

Laboratory (ORNL, TN, USA), and the Institute of Physics and Power Engineering (IPPE, Kaluga Oblast, Russia). Their estimated total annual production capacity for [225]Ac is approximately 63 GBq (1.7 Ci) [13]. Additional options for the production of [225]Ac include moderate-energy proton-induced reactions on [226]Ra and recently high-intensity photon-induced reactions on radioactive [226]Ra targets [14–19].

[213]Bi: [225]Ac and [213]Bi are linked to each other, as they are daughter nuclides within the same natural transformation chain. [213]Bi represents the last steps of the [225]Ac transformation chain (Fig. 3.22). Once radiochemically separated from [225]Ac in a radionuclide generator system, it can be used as a therapeutic radionuclide despite its short half-life of 45.6 min.

3.3 The Future

In theranostics, the central goal is the particle-induced ionization of tumoral DNA by β^-- and α-emitters. Optimizing this process requires identifying the most successful radionuclide candidates that offer adequate nuclear parameters, specific activities, and production routes (factoring in yield, purity, and cost). The routine clinical availability of therapeutic radionuclides is the key issue. Today, the number of readily available clinical therapeutic isotopes is low. The important
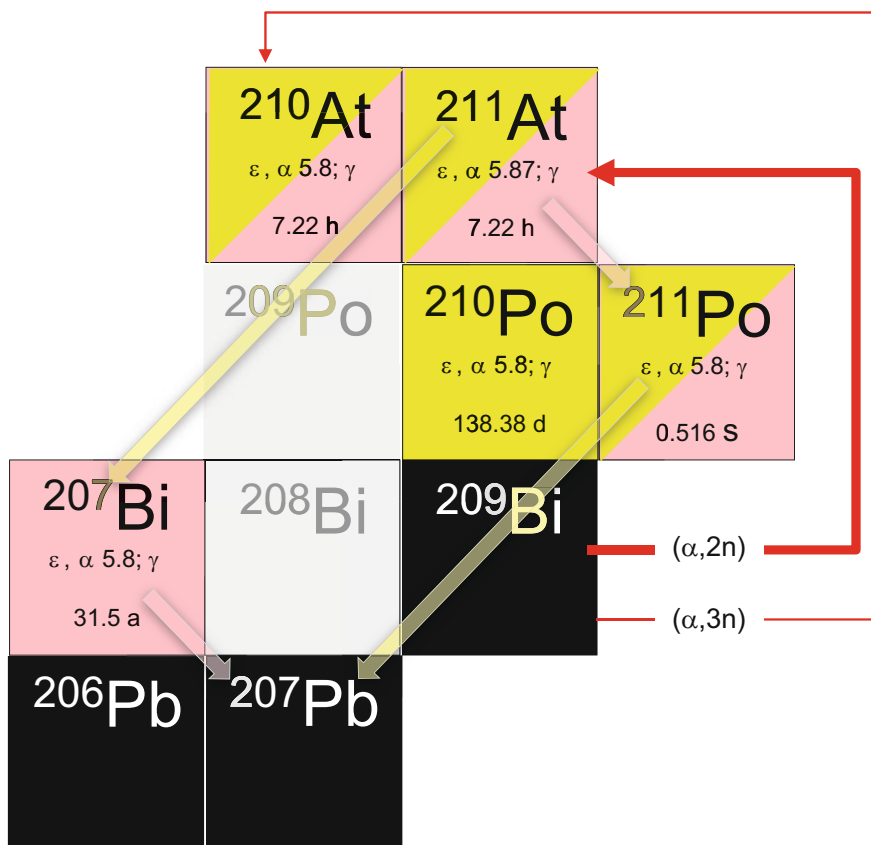
Fig. 3.20 Main production pathways for astatine-211 via the ^{209}Bi(α,2n)^{211}At reaction as well as its complex transformation scheme

carrier-free β⁻-emitters ^{90}Y and ^{177}Lu are available even at a good manufacturing practice (GMP) level, while the availability of ^{225}Ac is limited. However, there is a substantial risk that the supply chain of those radionuclides cannot satisfy the demand created by, for example, radiolabeled prostate-specific membrane antigene (PSMA) inhibitors for prostate cancer theranostics. The growing number of registered theranostic radiopharmaceuticals and the dramatically growing demand for even well-established radionuclides necessitate the upscaling of production capacities. Interestingly, the dual-purposing of nuclear reactors dedicated to nuclear energy for isotope production is a fascinating avenue. In parallel, alternative production routes are being investigated, such as the use of photonuclear reactions. Finally, research into the therapeutic use of new radionuclides must continue, with ^{161}Tb a particularly promising example.

3.4 Conclusion

This chapter focused on the nuclear chemistry of therapeutic radionuclides, while Chaps. 6 and 7 are dedicated to the radiopharmaceutical chemistry of therapeutic radionuclides. It is interesting to note that there are several points of overlap between the two topics. First, it is important to remember that a therapeutic radionuclide identified based on its nuclear transformation profile and production route reflects a chemical element with its own unique chemistry. Not
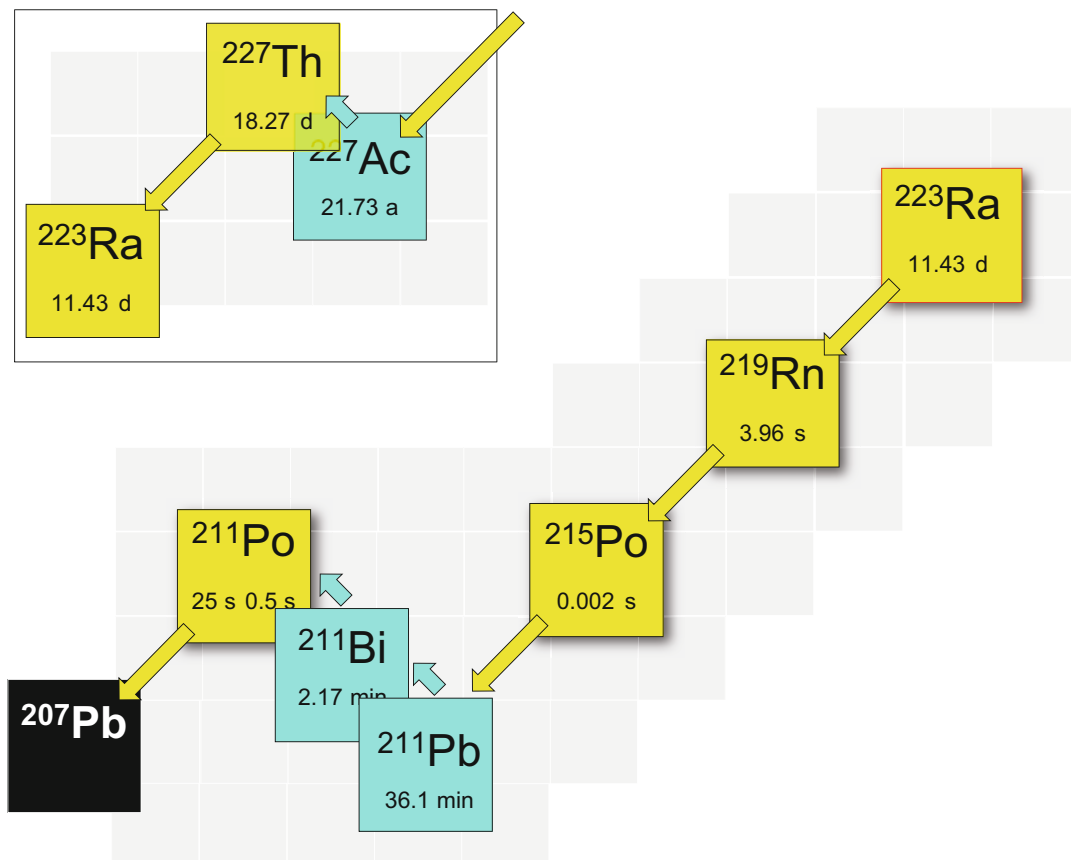
Fig. 3.21 Transformation chain generating ^{223}Ra (insert) and its subsequent transformations

surprisingly, this has dramatic consequences for radiopharmaceutical chemistry. The development of efficient radiolabeling strategies is essential to the creation of effective radiopharmaceuticals, but the chemistry of a certain radionuclide may not be straightforward (take ^{223}Ra, for example). In truth, a chemical profile that allows for facile incorporation into radiopharmaceuticals represents an extra criterion for any emergent therapeutic radionuclide. Second, the specific activity of a novel radionuclide may influence the applications of the isotope, as the isolation of radiopharmaceuticals with high specific activity is more important in some cases (i.e., antigens with low expression) than others (i.e., antigens with high expression). And third, it is important to remember that nuclear transformations may have consequences for the pharmacology of certain

therapeutic radiopharmaceuticals. To wit, the recoil processes of certain α-emitters described in this chapter—for example, ^{223}Ra or ^{225}Ac— can prompt the ejection of daughter radionuclides from chelators and their subsequent off-target accumulation in healthy tissues.

3.5　　The Bottom Line

- The nuclear chemistry of therapeutic radionuclides describes the individual radioactive emissions of these unstable isotopes as well as the production routes used to create them.
- Currently β-electron and α-particle emitting radionuclides dominate the field. These particles originate from primary
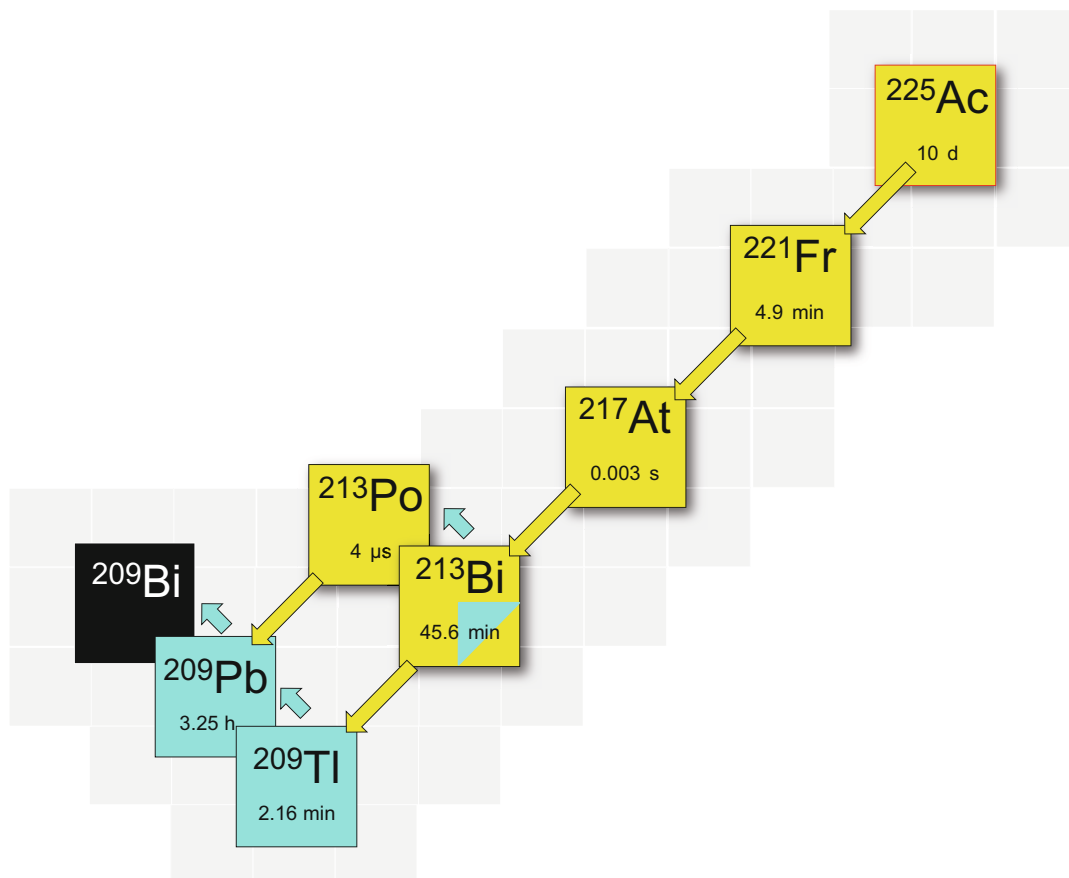
Fig. 3.22 Transformation chain of ^{225}Ac including the ^{213}Bi segment

transformation processes: while β-electrons exhibit a continuous distribution of kinetic energy, α-particles are mono-energetic.

- The molecular imaging of photons emitted from therapeutic radionuclides is an essential feature of theranostics. It is important to understand the two principal origins of emitted photons, which arise via secondary transformations (providing low-energy single γ-photons for SPECT) or positron annihilation (providing high-energy 511 keV photons for PET).

- Therapeutic radionuclides are primarily produced via direct neutron-capture nuclear reactions using nuclear reactors as a neutron source or via charged particle-induced nuclear reactions within particle accelerators. Some therapeutic radionuclides are available from radionuclide generator systems using artificially produced or natural radionuclides as the parents.

References

1. Vértes A, Nagy S, Klencsár Z, Lovas RG. Handbook of nuclear chemistry. Second ed. Berlin-Heidelberg: Springer; 2011.
2. Rösch F. Nuclear-and radiochemistry. Introduction, vol 1. Berlin/Boston: Walter de Gruyter; 2014.
3. Rösch F. Nuclear- and radiochemistry. Modern applications, vol 2. Berlin/Boston: Walter de Gruyter; 2016.
4. Rösch F. Basics of nuclear chemistry and radiochemistry: an introduction to nuclear transformations and radioactive emissions. In: Lewis JS, Windhorst AD, Zeglis B, editors. Radiopharmaceutical chemistry. 1st ed. Springer Cham; 2019. p. 27–61.
5. Atomic Mass Data Center - IAEA Nuclear Data Services. https://www-nds.iaea.org/amdc/.

6. Huang WJ, Audi G, Wang M, Kondev FG, Naimi S, Xu X. The AME2016 atomic mass evaluation (I). Evaluation of input data; and adjustment procedures. Chinese Phys C. 2017;41(3):030002. https://doi.org/10.1088/1674-1137/41/3/030002.

7. Wang M, Audi G, Kondev FG, Huang WJ, Naimi S, Xu X. The AME2016 atomic mass evaluation (II). Tables, graphs and references. Chinese Phys C. 2017;41(3):030003. https://doi.org/10.1088/1674-1137/41/3/030003.

8. Interactive masses and reaction data for all nuclides across the periodic table. www.nndc.bnl.gov/chart.

9. Karlsruhe: Chart of Nuclides, Nuclear Data in Nucleonica. https://www.nucleonica.com/.../8/8a/NuTRoNS-2-ChartofNuclides.pdf. (2010).

10. Culter CS. Life science: Therapy. In: Rösch F, editor. Nuclear- and Radiochemistry. Berlin/Boston: Walter de Gruyter; 2014. p. 505–51.

11. Lebedev NA, Novgorodov AF, Misiak R, Brockmann J, Rösch F. Radiochemical separation of no-carrier-added ^{177}Lu as produced via the ^{176}Yb(n, gamma)^{177}Yb-^{177}Lu process. Appl Radiat Isot. 2000;53(3):421–5. https://doi.org/10.1016/s0969-8043(99)00284-5.

12. Uusijärvi H, Bernhardt P, Rösch F, Maecke HR, Forssell-Aronsson E. Electron- and positron-emitting radiolanthanides for therapy: aspects of dosimetry and production. J Nucl Med. 2006;47(5):807–14.

13. Chérel M, Barbet J, Crcna ICUdNN. Alpha emitting radionuclides and radiopharmaceuticals for therapy. IAEA2013.

14. Nagatsu K, Suzuki H, Fukada M, Ito T, Ichinose J, Honda Y, et al. Cyclotron production of ^{225}Ac from an electroplated ^{226}Ra target. Eur J Nucl Med Mol Imag. 2021;49(1):279–89. https://doi.org/10.1007/s00259-021-05460-7.

15. Griswold JR, Medvedev DG, Engle JW, Copping R, Fitzsimmons JM, Radchenko V, et al. Large scale accelerator production of ^{225}Ac: effective cross sections for 78-192 MeV protons incident on ^{232}Th targets. Appl Radiat Isot. 2016;118:366–74. https://doi.org/10.1016/j.apradiso.2016.09.026.

16. Apostolidis C, Molinet R, McGinley J, Abbas K, Möllenbeck J, Morgenstern A. Cyclotron production of Ac-225 for targeted alpha therapy. Appl Radiat Isot. 2005;62(3):383–7. https://doi.org/10.1016/j.apradiso.2004.06.013.

17. Melville G, Allen BJ. Cyclotron and linac production of Ac-225. Appl Radiat Isot. 2009;67(4):549–55. https://doi.org/10.1016/j.apradiso.2008.11.012.

18. Melville G, Meriarty H, Metcalfe P, Knittel T, Allen BJ. Production of Ac-225 for cancer therapy by photon-induced transmutation of Ra-226. Appl Radiat Isot. 2007;65(9):1014–22. https://doi.org/10.1016/j.apradiso.2007.03.018.

19. Melville G, Fan Liu S, Allen BJ. A theoretical model for the production of Ac-225 for cancer therapy by photon-induced transmutation of Ra-226. Appl Radiat Isot. 2006;64(9):979–88. https://doi.org/10.1016/j.apradiso.2006.05.002.

The Production of Therapeutic Radionuclides

4

Shelbie J. Cingoranelli and Suzanne E. Lapi

4.1 The Fundamentals

4.1.1 Radionuclides for Therapy

Therapeutic radionuclides have emissions capable of directly damaging DNA and producing highly reactive free radicals, both processes that can lead to cell death [1]. Radionuclides that can be used for radiopharmaceutical therapy (RPT) typically decay via the emission of α particles, β- particles, Meitner-Auger electrons, or a combination thereof. The creation and investigation of a therapeutic radiopharmaceutical begins with the production of the therapeutic radionuclide. One of the most valuable tools for understanding the production of radionuclides is the Chart of the Nuclides [2]. It is, in essence, an expanded periodic table that provides information on the different isotopes of each element, their respective half-lives, and their decay emissions. The chart can be used to identify both potentially useful radionuclides for imaging and therapy as well as the nuclear reaction pathways to produce them. Figure 4.1 illustrates a segment of the Chart of Nuclides focused on ^{209}Bi, illustrating some reaction channels to the radionuclide as well as its decay products [2].

Since most medical radionuclides are not naturally occurring, they are produced via nuclear reactions using pathways predicated on bombardment with charged particles and neutrons — (p, x), (n,x), (α,x), (γ,x) —as well as fission events. Specific criteria should also be considered when deciding whether a radionuclide should (or can) be produced for radiopharmaceutical applications:

1. Half-life (i.e., matching the physical half-life of the radionuclide with the biological half-life of the targeting vector)
2. Chemical properties (i.e., the feasibility of labeling a targeting vector)
3. Decay properties (i.e., imaging or therapy; α, β, Meitner-Auger electrons, other emissions)
4. Production route and yields (i.e., reactors, accelerator, or generator requirements; facility needs)
5. Target material (i.e., cost; the need for enrichment)
6. Product recovery and purity (i.e., the purification of the problem from target material, its molar activity, and whether it is carrier-free or carrier-added)
7. Demand (i.e., for preclinical use and, ultimately, clinical trials)

Table 4.1 provides a list of common radionuclides used for therapy, their decay properties, and their production routes.

S. J. Cingoranelli · S. E. Lapi (✉)
Departments of Radiology and Chemistry, University of Alabama at Birmingham, Birmingham, AL, USA
e-mail: lapi@uab.edu

Fig. 4.1 A portion of the chart of nuclides focused on the stable isotope ^{209}Bi as a target for radionuclide production. The reactions in red represent potential reaction channels with ^{209}Bi [2]

4.1.2 Nuclear Reactions

Following are the three main routes used to produce radionuclides:

1. Fission
2. Induced nuclear reactions from the bombardment of a stable target material with charged particles, neutrons, or photons
3. The decay of a parent radionuclide (i.e., a generator)

4.1.3 Fission

Fission is the splitting of a nucleus into two smaller parts with the co-emission of several neutrons. An example of the fission of ^{235}U is shown below in Fig. 4.2.

Here, a uranium ion is bombarded by a neutron. This will cause the formation of ^{236}U, which will subsequently split into smaller components accompanied by the release of neutrons that can

go on and induce other fission events. Many therapeutic radionuclides are obtained through this route, including ^{131}I from the fission of ^{235}U [29].

4.1.4 Equations

A nuclear reaction can be approached like a chemical reaction, with the reactants on one side of the equation and the products on the other. A generic nuclear reaction is shown below in Eq. 4.1 in which a stationary nucleus is hit with an incoming incident particle (reactants), thereby producing a product nucleus as well as secondary particle (products).

$$X + a \rightarrow Y + b \qquad (4.1)$$
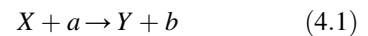
Here, X is the stationary target nucleus with which the incoming particle or photon, a, collides. A new nucleus, Y, is produced from this collision, which can be accompanied by the

Table 4.1 Radioisotopes for therapy

Radionuclide	Half-life	Decay mode	Mean particle energy (keV)	Particle branching (%)	Production route	References
^{32}P	14.268 (5) d	β- (1)	695.03	100	^{31}P(n,γ)^{32}P	[3]
					^{32}S(n,p)^{32}P	[3]
^{47}Sc	3.3492 (6) d	β- (1)	142.6 (7)	68.4 (6)	^{44}Ca(α,p)^{47}Sc	[4]
			203.9 (8)	31.6 (6)	^{47}Ca/^{47}Sc generator	[4]
					^{48}Ti(p,2p)^{47}Sc	[4]
					^{48}Ti(γ,p)^{46}Sc	[4]
					^{47}Ti(n,p)^{47}Sc	[4]
					^{50}Ti(p,α)^{47}Sc	[4]
					^{51}V(p,p + α)^{47}Sc	[4]
^{67}Cu	61.83 (12) h	β- (1)	121 (3)	57 (6)	^{67}Zn(n,p)^{67}Cu	[5]
			154 (3)	22.0 (22)	^{68}Zn(p,2p)^{67}Cu	[5]
			189 (3)	20.0 (20)	^{68}Zn(γ,p)^{67}Cu	[6]
					^{70}Zn(p,α)^{67}Cu	[5]
^{77}As	38.79 (5) h	β- (1)	228.8 (7)	97 (3)	^{76}Ge(n,γ)^{77}Ge->^{77}As	[7]
^{77}Br	57.036 (6) h	ε(1)	Auger/CE		^{77}Se(p,n)^{77}Br	[8]
^{89}Sr	50.563 (25) d	β- (1)	587.1 (11)	99.99036 (5)	Nuclear fission	[9]
^{90}Y	64.053 (2) h	β- (1)	933.7 (12)	99.9885 (14)	^{90}Sr/^{90}Y generator	[10]
^{105}Rh	35.36 (6)	β- (1)	69.9 (10)	19.7 (5)	^{104}Ru(n,γ)^{105}Ru->^{105}Rh	[11]
			73.9 (10)	5.2 (4)		
			179.4 (11)	75.0 (6)		
^{103}Pd	16.991 (19)	ε(1)	Auger/CE		^{102}Pd(n,γ)^{103}Pd	[12]
					^{103}Rh(p,n)^{103}Pd	[12]
^{111}Ag	7.45 (1) d	β- (1)	223.5 (12)	7.1 (5)	^{110}Pd(n,γ)^{111}Pd-^{111}Ag	[12]
			278.9 (12)	1 (20)		
			360.4 (13)	92 (5)		
^{117m}Sn	13.76 (4) d	IT (1)	Auger/CE		^{116}Sn(n,γ)^{117m}Sn	[13]
					^{117}Sn(n,nγ)^{117m}Sn	[13]
^{131}I	8.0252 (6) d	β- (1)	69.36 (25)	2.08 (3)	^{130}Te(n,γ)^{131}Te->^{131}I	[14]
			96.62 (26)	7.23 (1)	^{235}U fission	[15]
			191.58 (30)	89.6 (8)		
^{133}Xe	5.2475 (5) d	β- (1)	75.16 (75)	1.4 (6)	^{235}U fission	[15]
			100.62 (79)	98.5 (13)		
^{149}Tb	4.118 (25) h	α++	3967 (3)	16.7	Proton-induced spallation on natTa	[16]
		ε(0.833)				
^{161}Tb	6.89 (2) d	β- (1)	137.7 (5)	25.7 (16)	^{160}Gd(n,γ)^{161}Gd->^{161}Tb	[17]

(continued)

Table 4.1 (continued)

Radionuclide	Half-life	Decay mode	Mean particle energy (keV)	Particle branching (%)	Production route	References
			157.4 (5)	65 (4)		
			174.6 (5)	5 (5)		
			183.7 (5)	5 (5)		
^{149}Pm	53.08 (5) h	β- (1)	256.2 (15)	3.4 (20)	^{148}Nd(n,γ)^{149}Nd->^{149}pm	[18]
			369.1 (15)	95.9 (3)		
^{153}Sm	46.284 (4) h	β- (1)	199.5 (3)	31.3 (9)	^{152}Sm(n,γ)^{153}Sm	[19]
			225.3 (3)	49.4 (18)		
			264.3 (3)	18.4 (17)		
^{166}Ho	26.824 (12) h	β- (1)	651.33 (38)	49.9 (12)	^{165}Ho (n,γ)^{166}Ho	[20]
			693.96 (39)	48.8 (12)		
^{177}Lu	6.647 (4) d	β- (1)	47.66 (23)	11.61(11)	^{176}Lu(n,γ)^{177}Lu	[21]
			111.69 (26)	9.0 (5)	^{176}Yb(n,γ)^{177}Yb->^{177}Lu	[18]
			149.35 (28)	79.4 (5)		
^{186}re	3.7186 (5) d	β- (0.925)	306.1 (4)	21.54 (14)	^{185}Re(n,γ)^{186}Re	[22]
			359.2 (4)	70.99 (12)	^{186}W(p,n)^{186}Re	[22]
					^{189}Os(p,α)^{186}Re	[22]
^{188}Re	17.003 (3) h	β- (1)	527.78 (17)	1.748 (20)	^{188}W/^{188}Re generator	[10]
			728.88 (18)	26.3 (5)		
			795.41 (18)	70 (5)		
^{195m}Pt	4.01 (5) d	IT (1)	Auger/CE		^{194}Pt(n,γ)^{195m}Pt	[23]
					^{195}(n,n'γ)^{195}mpt	[23]
					^{194}Ir(n,γ)^{195}mIr->^{195}mpt	[23]
					^{192}Os(α,n)^{195}mpt	[23]
^{212}Bi	60.55 (6) min	β- (0.641)	192.6 (6)	1.86 (4)	^{212}Pb/^{212}Bi generator	[24]
			230.8(7)	1.44 (4)		
			533.1 (7)	4.47 (11)		
			834.2 (8)	55.37 (11)		
		α++(0.359)	6050.78 (3)	25.13 (7)		
			6089.88 (3)	9.75 (5)	Ac^{225}/^{213}Bi generator	[25]
^{213}Bi	45.61 (6) min	β- (0.978)	320.4 (19)	30.79 (24)		
			492.2 (20)	65.9 (4)		
		α++(0.022))	5875 (4)	1.959 (9)		
^{211}At	7.214 (7) h	α++(0.418)	5869.5 (22)	41.8	^{209}Bi(α,2n)^{211}At	[26]
		ε(0.582)				
^{212}Pb	10.64 (1) h	α++(1)	41.1 (6)	5.08 (9)	Decay product ^{232}Th	[24]

Table 4.1 (continued)

Radionuclide	Half-life	Decay mode	Mean particle energy (keV)	Particle branching (%)	Production route	References
			93.5 (7)	83.1 (16)		
			171.7 (7)	11.9 (16)		
^{223}Ra	11.43 (5) d	α++(1)	5433.6 (5)	2.22 (20)	Decay product of ^{235}U	[15]
			5501.6 (10)	1 (15)		
			5539.8 (90)	9 (20)		
			5606.73 (30)	25.2 (5)		
			5716.23 (29)	51.6 (13)		
			5747.0 (4)	9 (20)		
			5871.3 (10)	1.00 (20)		
^{225}Ac	10 (1) d	α++(1)	5580 (3)	1.20 (10)	^{225}Ra/^{225}Ac	[25]
			5609 (3)	1.10 (10)	^{229}Th/^{225}Ac	[25]
			5637 (2)	4.4 (3)		
			5682 (2)	1.3 (2)		
			5724 (3)	3.1 (5)		
			5732 (2)	8.0 (5)		
			5732 (2)	1.32 (10)		
			5790.6 (22)	8.6 (9)		
			5792.5 (22)	18.1 (20)		
			5830 (2)	50.7 (15)		
^{230}U	20.8 (21) d	α++(1)	5817.5 (7)	32 (20)		
			5888.4 (7)	67.4 (4)	^{231}Pa(γ,n)^{230}Pa->^{23}U	[27]
					^{231}Pa(p,2n)^{230}U	[28]

Fig. 4.2 A neutron (blue) colliding with ^{235}U (yellow) and inducing a fission event in which the ^{235}U nucleus splits into smaller components: ^{148}La, ^{87}Br, and an additional neutron. This neutron has the possibility of inducing another fission event with another ^{235}U atom

emission of either a photon or particle, *b*. The shorthand notation for nuclear reactions—shown in Eq. 4.2—will be used throughout the chapter:

$$X(a, b)Y \tag{4.2}$$

Take, for example, the ^{209}Bi(α,2n)^{211}At reaction in which an alpha-induced reaction on a stationary ^{209}Bi atom (*X* in Eq. 4.2) results in the emission of two neutrons and yields ^{211}At. An example of a photon-induced reaction is ^{68}Zn (γ,p)^{67}Cu: a high-energy photon collides with a ^{68}Zn atom, prompting the emission of a proton and the production of ^{67}Cu. An example of a neutron-capture reaction is ^{176}Lu(n,γ)^{177}Lu, in

which a thermal neutron collides with ^{176}Lu, prompting the emission of a photon and the creation of ^{177}Lu. These reactions can be induced using either accelerators or nuclear reactors. For example, charged particles are typically produced from either linear accelerators (LINACs) or cyclotrons. Photons are produced from bremsstrahlung gamma radiation from charged particles decelerating from interactions of stationary material. Neutrons are produced from fission events as described above.

4.1.5 Energetics of Nuclear Reactions

As with chemical reactions, understanding the fundamentals of nuclear reactions begins with energetics. We know that the total energy of a reaction must be conserved, and that mass is related to energy via Einstein's equation: $E = mc^2$. As result, we can consider the conservation of total energy as shown in Eq. 4.3.

$$m_x c^2 + E_x + m_a c^2 + E_a = m_Y c^2 + E_Y + m_b c^2 + E_b \tag{4.3}$$

Where the E's are the kinetic energies, and the m's are rest masses. Furthermore, we can calculate Q values, the amount of energy released or consumed in the nuclear reaction, using Eqs. 4.4 and 4.5.

$$Q = (m_{\text{initial}} - m_{\text{final}})c^2$$
$$= (m_X + m_a - m_Y - m_b)c^2 \tag{4.4}$$

$$Q = E_{\text{final}} - E_{\text{initial}} = E_Y + E_b - E_a \tag{4.5}$$

If $Q > 0$, the reaction is exoergic (exothermic). If $Q < 0$, the reaction is endoergic (endothermic). An example of this calculation is the Q value for the ^{209}Bi(α,2n)^{211}At reaction shown in Eqs. 4.6 and 4.7 below.

$$Q = m(\text{amu})_{209_{\text{Bi}}} + m(\text{amu})_\alpha$$
$$- 2m(\text{amu})_n - m(\text{amu})_{211_{\text{At}}} \tag{4.6}$$

$$Q = [((208.9803987 \text{ amu}) + (4.0026 \text{ amu}))$$
$$- (2(1.0086 \text{ amu}) - (210.9875 \text{ amu}))]$$
$$= 0.02183 \text{ amu}$$
$$\tag{4.7}$$

Now, the mass-to-energy conversion can be applied for Eq. 4.8, where 1 amu = 931.48 MeV:

$$Q = \left(0.02183 \text{ amu} \times 931.48 \frac{MeV}{\text{amu}}\right) = -20.33 \text{ MeV} \tag{4.8}$$

Thus, in this example, the Q value is -20.33 MeV,

An additional issue that must be considered in nuclear reactions with positively charged particles is the "coulomb barrier" created by the electrostatic repulsion from the positively charged nucleus. As the incoming particle gets closer to the positively charged nucleus, the particle starts to experience the charge and requires additional energy to overcome this repulsion. A short-form equation that can be used to determine the coulomb barrier is given in Eq. 4.9:

$$V^0 = \frac{Z_X Z_a e^2}{R_x + R_a} = \frac{1.44 Z_x Z_a}{R_x + R_a} \tag{4.9}$$

Where $R = 1.4A^{1/3}$-fm, Z is the number of protons of the projectile and target nuclei, and e^2 is 1.44. Back to our ^{209}Bi(α,2n)^{211}At reaction, the coulomb barrier for our reaction can be calculated as shown in Eq. 4.10:

$$V^0 = \frac{1.44(83)(2)}{1.4\left(209^{\frac{1}{3}} + 4^{\frac{1}{3}}\right)} = 22.69 \text{ MeV} \tag{4.10}$$

Finally, nuclear reactions also follow the law of conservation of linear momentum since there is a velocity transfer from the moving particle onto the stationary particle. This means that not all energy is available for the reaction. Equation 4.11 is the calculated kinetic energy required for a nuclear reaction with the linear momentum taken into consideration.

$$E_{\text{incident}} = \left[\frac{m_a + m_x}{m_x}\right] \times |Q| \tag{4.11}$$

Finally, these equations can be used to determine the projectile energy required for the reaction to occur (i.e., the threshold energy). This calculation of this threshold energy—i.e., the energy required for the reaction to occur—must include a momentum correction to the Q value if the Q value is negative or a momentum correction

to the coulomb barrier correction (whichever is higher). Including the momentum correction for the $^{209}Bi(\alpha,2n)^{211}At$ reaction coulomb barrier (which is larger than the absolute Q value) yields 23.12 MeV, as shown in Eq. 4.12.

$$E_{incident} = \left[\frac{4 + 209}{209}\right][22.69 \text{ MeV}] = 23.12 \text{ MeV}$$
(4.12)

Therefore, the calculated threshold of our nuclear reaction is 23.12 MeV. Put simply, this reaction should only occur if the energy of the incident α[alpha] particles is greater than 23.12 MeV.

Yet experimental findings show that the production of ^{211}At from ^{209}Bi is observed with α particles of a minimum energy of ~21 MeV(!) [26]. While this seems to run counter to the threshold of 23.12 MeV that we have calculated, some production does occur at these slightly lower energies due to quantum effects that are outside the scope of this chapter. This phenomenon clearly illustrates the need for experimental data to fully characterize these reactions.

4.1.6 Cross Sections and Reaction Rates

The cross section (σ) of a nuclear reaction describes the probability of the reaction. The cross section of a reaction is given in units of area (typically barn, where $1b = 10^{-24}$ cm^2) [30]. Cross sections are dependent on the type of incoming particle, the energy of that particle, and the target nucleus [31].

The reaction rate of a nuclear reaction (calculated using the cross section) can be used to predict the amount of product produced, Y. The reaction rate depends on the cross section of the reaction at that energy, the number of incident particles per second (flux), the thickness of the target, and the number of target nuclei. As a reminder before discussing reaction rates, the activity is related to the number of decays per unit time as shown in Eq. 4.13:

$$A = -\frac{dN}{dt}$$
(4.13)

Where A is radioactivity in decays per second, N is the number of parent nuclei, and t is time. Finally, lambda (λ) is the decay constant, in units of s^{-1}, unique for each radionuclide. This equation can be used determine N, the activity at any time point with respect to the starting activity, N_o, as shown in Eq. 4.14.

$$N = N_0 e^{-\lambda t}$$
(4.14)

Referring to Eq. 4.13, where activity is proportional to the number of atoms, the same relationship can be described in Eq. 4.15:

$$A = A_0 e^{-\lambda t}$$
(4.15)

Where A is the activity at time t, A_0 is the activity at time 0, and λ[lambda] is the decay constant. Equation 4.16 can then be used to calculate reaction rates.

$$R = Ix\sigma N_{tgt}$$
(4.16)

Where R is the reaction rate in nuclei produced per second, I is the flux (incident particles per second), x is the target thickness (cm), σ is the cross section (cm^2), and N_{tgt} is number of target atoms per cubic cm (atoms/cm^3) [32].

Once the threshold energy has been determined, the bombardment parameters have been set, and the target material has been selected, the total reaction rate and theoretical yields can be calculated using Eq. 4.14. The generic Eq. 4.14 can be modified slightly to account for other variables present for reactions that occur via charged particles or in nuclear reactors, as shown later in Eqs. 4.17 and 4.35. These modifications take into account the difference in types of incident particles, the particle's energy, and the energy degradation through the target.

The radioactive material produced will inevitably decay during the irradiation time period, leading to a loss of product even during the bombardment. This becomes particularly important at long bombardment times. In these cases, a ratio can explain the effect this decay rate has on the final yield of radionuclide product. As the target bombardment time increases, the ratio of radionuclide product generated to that lost due to nuclide decay will become closer to 1, meaning

that the rate of product loss from decay is approaching the rate of product production. This is called the saturation effect. The change in this ratio over the bombardment time is directly related to the half-life of the produced radionuclide, and this ratio will approach 1 asymptotically. If the target is bombarded for one half-life of the product, the saturation effect will be at 50%, meaning that the amount of radionuclide produced is 50% of saturation (the maximum amount of product possible for this target and bombardment parameter configuration). The saturation effect will reach 75% at two half-lives and 87.5% at three half-lives. As the bombardment time surpasses more half-lives, the saturation effect will near 100%, at which point the rate of production will be essentially equal to the rate of decay. Once the bombardment nears 100% saturation, there is little to be gained in increasing the irradiation time, as the final radioactivity produced will effectively remain the same. The saturation effect can be used to help determine optimal bombardment parameters and can be factored into the prediction of the radioactivity produced in Eq. 4.17 (in which the final term in brackets represents the saturation effect). This equation can be graphed to illustrate the impact of product decay on the production yields as a function of time as shown in Fig. 4.3.

$$A = nIx\sigma\left(1 - e^{-\lambda t}\right) \qquad (4.17)$$
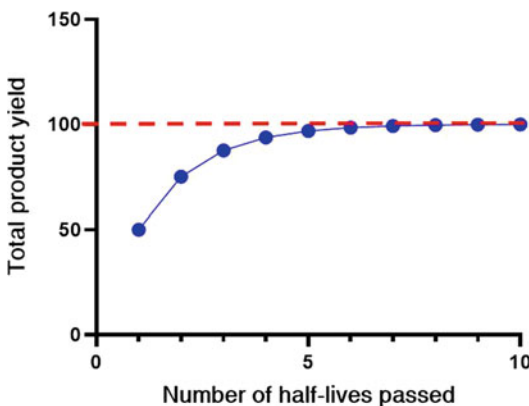
Fig. 4.3 The saturation effect of radionuclide production as a function of irradiation time

4.2 The Details: Radionuclide Production with Reactors and Accelerators

4.2.1 Neutron-Induced Reactions

Many therapeutic nuclides can be produced via neutron bombardment. Neutron-activated reactions will generally produce neutron-rich radionuclides, which commonly decay via β-emission.

4.2.2 Nuclear Reactors

Neutrons used to produce radionuclides are typically generated via the fission of a fissile material, for example ^{235}U, ^{232}Th, or ^{239}Po. Nuclear reactors utilize the fission events of fissile material to produce neutrons. Once a fission event occurs, the neutrons that are produced can induce additional fission events, ultimately creating a self-sustaining process and a flux of neutrons that can be used to induce other nuclear reactions. For example, ^{235}U releases 2.44 neutrons per fission event that can then go on and potentially induce on average two more fission events and so forth. To understand this self-sustaining process, the multiplication factor (k) is defined in Eq. 4.18.

$$k = \frac{\text{Number of neutrons in the } n + 1 \text{ generation}}{\text{Number of neutrons in the } n \text{ generation}}$$

(4.18)

When $k < 1$, the reactor is considered subcritical, $k > 1$ supercritical, and $k = 1$ is critical. To control and maintain the chain reaction, reactors use control rods. These control rods absorb the neutrons, allowing for control over the total number of fission events. Control rods are made from alloys with high neutron-capture cross sections, such as boron and cadmium. The control rods work by insertion into (decreasing the flux) or withdrawal from (increasing the flux) the reactor pool. As the fuel is slowly consumed, the control rods are gradually extracted to maintain constant flux [33, 34].

Neutrons produced by nuclear reactors can be used to induce neutron-capture nuclear reactions. The probability of neutron capture is inversely related to neutron energy. The fast neutrons ($E > 1.5$ MeV) released during a ^{235}U fission event are too high for radionuclide production via neutron capture. Therefore, moderating materials are used to slow down these fast-moving neutrons. Examples of moderating materials are water, deuterated water (D_2O), or graphite. These materials slow down fast neutrons to epithermal (0.025–0.4 eV) or thermal (<0.025 eV) energies. Moderating materials have low neutron-capture cross sections to prevent a decrease in neutron flux within the reactor. One of the more common moderating materials is D_2O, which can be used as a moderating material and as a coolant. A diagram of a nuclear reactor core is provided in Fig. 4.4. Nuclear reactors commonly use ^{235}U as the fission fuel, but ^{235}U has a low natural abundance of 0.72% [35]. This leads to two different types of reactors:

1. Low-enriched uranium (LEU), in which the ^{235}U enrichment is 2–5% and D_2O is typically used as the moderator/coolant.
2. High-enriched uranium (HEU), in which the ^{235}U enrichment is >20% and H_2O is typically used as the moderator/coolant.

4.2.3 Neutron-Induced Reaction Rates and Excitation Functions

Isotope production targets for nuclear reactors are usually submerged into the reactor pool to expose them to neutrons. Therefore, these targets are exposed to a relatively uniform neutron flux. As mentioned in the section before, the probability of neutron capture occurring (the cross section) increases as the neutron energy decreases. This is shown in Fig. 4.5, the neutron-capture excitation function: a plot of the cross section versus the neutron energy for the ^{176}Lu(n,γ)^{177}Lu reaction [36].

As illustrated above, the cross section (σ) decreases as the energy increases with the exception of sharp spike regions. These sharp spikes are called resonance peaks and arise from the different nuclear energy levels of the ^{176}Lu target nucleus that becomes excited from the incoming neutron. The equation for the neutron reaction rate can be adapted from Eq. 4.16 to account for the uniform flux of neutrons, φ, and is shown below in Eq. 4.19:

$$R = \varphi n \sigma \qquad (4.19)$$

Fig. 4.4 A diagram of a nuclear reactor. Here, the fuel rods are submerged within water that acts as both moderator and coolant, and movable control rods are used to control the neutron flux
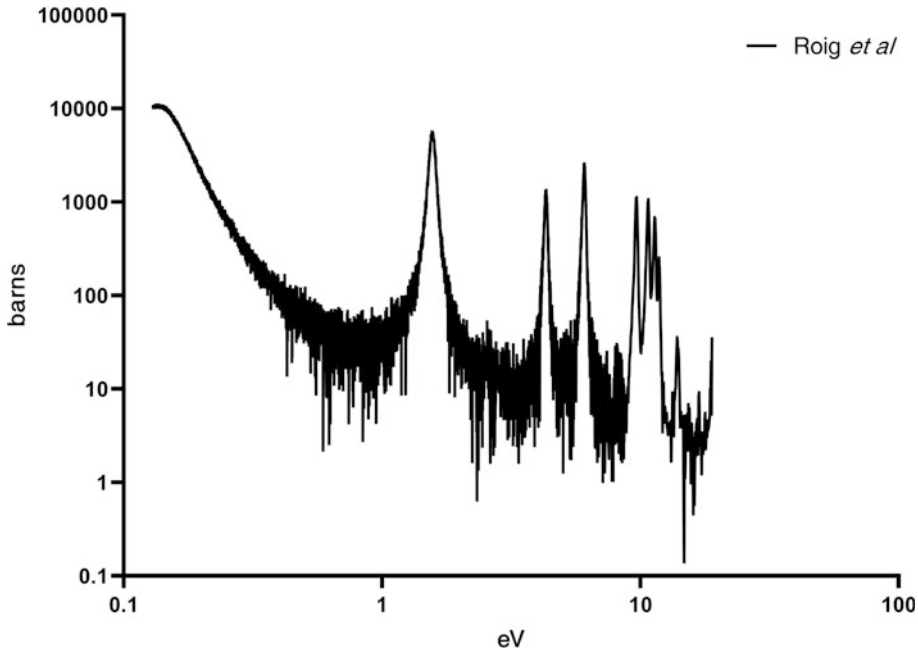
Fig. 4.5 The excitation function for the production of ^{177}Lu via the ^{176}Lu(n,γ)^{177}Lu reaction (Eq. 4.11)

Where φ is the neutron flux (n/cm^2/s), n is the total number of target nuclei, and σ is the cross section (cm^{-2}).

One can calculate the reaction rate for the production of ^{177}Lu from 5 mg of an enriched [^{176}Lu]Lu$_2$O$_3$ target with 72% enrichment. Several things need to be considered in our calculation. First, the percent of ^{176}Lu with respect to all Lu atoms is increased from the natural abundance of 2.59% to 72%. Second, the 5 mg of the target also includes the oxide component, therefore the percent of Lu in the target is 40% Lu atom per Lu$_2$O$_3$. And third, the target is submerged in a neutron flux of 1.00×10^{13} n/cm^2/s with a cross section of 2100 barns for 3 days. After determining the number of target nuclei, the reaction rate can then be calculated as shown in Eqs. 4.20 and 4.21.

$$n = \left(\frac{0.005\text{g}}{397.932\frac{\text{g}}{\text{mol}}} \right)$$
$$\times \left(6.02 \times 10^{23} \frac{\text{atoms}}{\text{mol}} \right)$$
$$\times 0.40 \frac{\text{Lu}}{\text{Lu}_2\text{O}_3} \times 0.72 \frac{176\text{Lu}}{\text{Lu}} = 2.18$$
$$\times 10^{18} \text{ atoms} \qquad (4.20)$$

$$R = \left(\frac{\frac{1.00 \times 10^{13} n}{\text{cm}^2}}{s} \right)$$
$$\times \left(2100b \times \frac{10^{-24}\text{cm}^2}{b} \right)$$
$$\times \left(2.18 \times 10^{18} \text{ atoms} \right) = 4.57$$
$$\times 10^{10} \text{ atoms per second} \qquad (4.21)$$

Referring to Eq. 4.19 and using $A = \lambda N$—where λ is the ^{177}Lu decay constant ($\lambda = \ln(2)/t_{1/2}, = 1.19 \times 10^{-6}$ s^{-1})—we can predict the amount of activity produced during the 3-day neutron bombardment in Eqs. 4.22 and 4.23:

$$A = n\varphi\sigma\left(1 - e^{-\lambda t}\right) \qquad (4.22)$$

$$A = 4.57 \times 10^{10} \text{atoms per second}$$
$$\times \left(1 - e^{-1.19 \times 10^{-6}\text{s}^{-1} \times 259200 \text{ s}} \right)$$
$$= 12.1 \text{ GBq (328 mCi)} \qquad (4.23)$$

Targets for radionuclide production typically have a cool-down period after they are removed from the reactor to allow for the decay of short-lived nuclides. This cool-down time must also be

taken into consideration during the calculation of the theoretical final product yield as shown in Eq. 4.24.

$$A = \varphi \sigma N_{\text{tgt}} \left(1 - e^{-\lambda t_{\text{irr}}}\right) \left(e^{-\lambda t_{\text{post}}}\right) \qquad (4.24)$$

Here, t_{irr} is the irradiation time, and t_{post} is the cool-down time. Back to our ^{177}Lu example: if the cool-down period is 1 day, the final activity is calculated in Eq. 4.25.

$$A = 12.1 \text{ GBq}$$
$$\times \left(e^{\left(-1.19 \times 10^{-6} \text{s}^{-1} 86400 \text{ s}\right)}\right)$$
$$= 10.9 \text{ GBq } (297 \text{ mCi}) \qquad (4.25)$$

4.2.4   Particle Accelerators

Several types of machines accelerate particles via electrical and/or magnetic fields, but they essentially contain the same four components:

1. A source of particles
2. A method of acceleration
3. A method for the extraction of particles
4. A target station (or stations)

Protons are the most common charged particles used for the production of radionuclides, but ^{2}H, ^{3}He, and heavier ions are also used. Ion sources produce the charged particles (typically via ionization of a gas) that are injected into the accelerator. Most instruments typically accelerate a single particle type, but others can accelerate two or more. The next component, which accelerates these particles, relies on a combination of electromagnetic fields to set the particles into motion, provide direction, and increase their kinetic energy. After the particles have achieved the desired energy, they are extracted, which removes them from the accelerating device to strike the desired target. The acceleration takes place in a vacuum to avoid molecular collisions that could result in losses from neutralization, changes of trajectory, and the radioactivation of the accelerator components.

The two most common accelerators for the production of medical radionuclides are linear accelerators and cyclotrons. One example of a linear accelerator (LINAC) is a drift tube LINAC that accelerates particles using alternating charged electrodes of opposite polarity (as shown in Fig. 4.6). Here, the particle is accelerated in the gaps between the drift tubes, which are a set of alternating electrodes. When the particle reaches the end of one drift tube, a radiofrequency (RF) oscillator alters its polarity to induce repulsion. At the same time, the drift tube at the end of the gap has the opposite charge, providing attraction that accelerates the particle across the gap. This is repeated as the particle travels down the linear path. As the particle travels, its energy
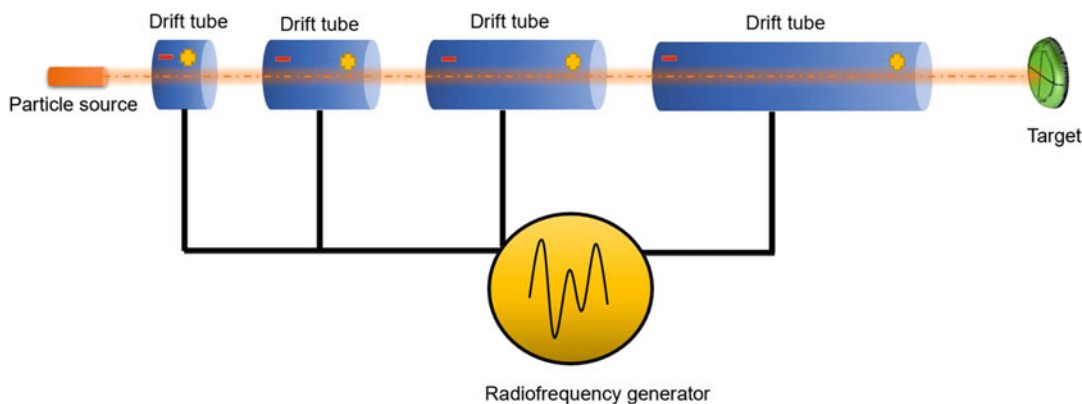
Fig. 4.6 A diagram of a drift tube linear accelerator showing the particle path through drift tubes that increase in length down the charged particle's path. A radionuclide production target is at the end of the LINAC
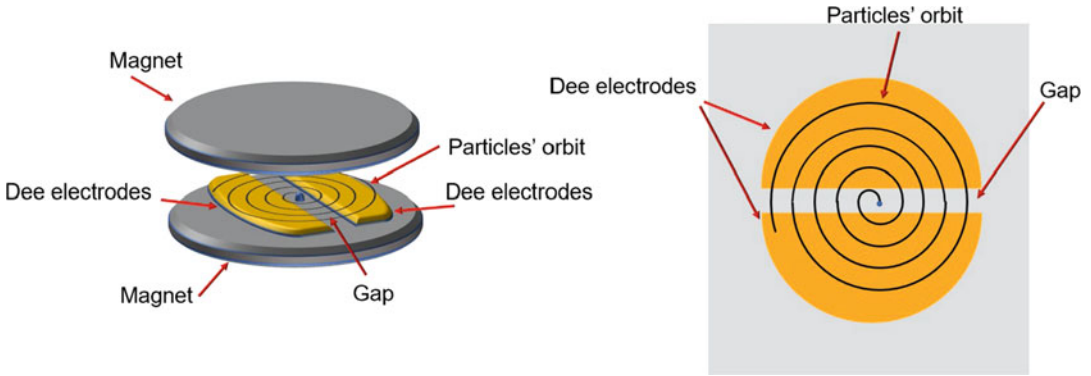
Fig. 4.7 Diagram of a cyclotron showing the accelerating dees between two poles of a magnet. A gap is shown between the dees where the acceleration of particles occurs

increases, but as its velocity increases, so does the length of the drift tubes (and the distance between the gaps) because the frequency of the voltage oscillation must remain the same regardless of where the particle is in the LINAC. Thus, one of the limitations of the drift tube-style LINAC is the length of the particle accelerator.

Cyclotrons, in contrast, accelerate particles within a circular path, allowing for continuous acceleration using the same voltage gaps and a smaller footprint. In a cyclotron, the ions are restricted within the orbit by a magnetic field, and the accelerating electrodes are contained within the magnetic poles [37]. Figure 4.7 is a diagram of a cyclotron.

Here, the ion source injects charged particles into the center region between semicircular hollow disks containing a pair of electrodes (i.e., "dees"). The gap between the dees, so named because of their historical shape, is where the acceleration occurs. As with the LINAC example, a radiofrequency oscillator is used to alter the charge of these dees to accelerate the particles across this gap. The radiofrequency, RF, is the cyclotron voltage oscillation frequency used to accelerate the particles and is typically in the range of 10 s of MHz. This is applied to change the polarity of the dees to maintain the accelerating force. By alternating the voltage at a frequency paired with the orbital frequency, the particle is accelerated. This is referred to as the cyclotron principle. The force associated with the

particle motion can be described starting with the circular motion shown in Eq. 4.26:

$$F = \frac{Mv^2}{r} \tag{4.26}$$

And balancing with the magnetic force Eq. 4.27,

$$F = qvB \tag{4.27}$$

Solving for v yields Eq. 4.28:

$$v = \frac{qBr}{M} \tag{4.28}$$

The time that it takes the particle to complete an orbit is represented in Eq. 4.29

$$t = \frac{2\pi r}{v} \tag{4.29}$$

While the associated period is calculated by Eq. 4.30,

$$t = \frac{2\pi M}{qB} \tag{4.30}$$

And the frequency in Eq. 4.31:

$$f = \frac{qB}{2\pi M} \tag{4.31}$$

Most cyclotrons used for the production of medical radionuclides are isochronous, meaning that the particle arrives at the accelerating gap at the same point in the voltage oscillation

Fig. 4.8 A top view of a cyclotron that uses an extraction foil method. Here, the extraction foil is at the end of a moveable arm that can be used for both directing the particle down a beam line and determining the energy of the extracted particle
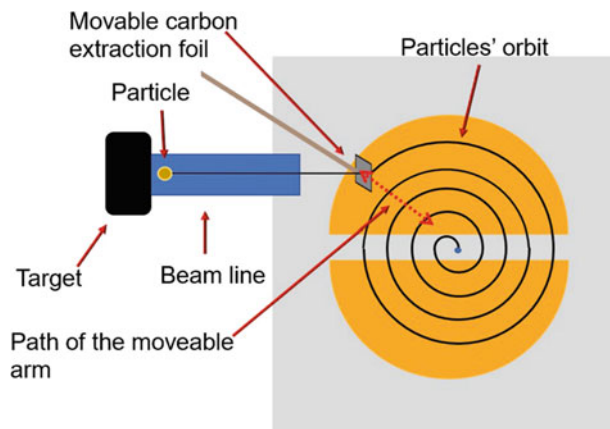
independent of the energy of the particle. The time it takes for the particle to complete an orbit is a constant, which is confirmed by the absence of velocity in Eq. 4.31. At higher energies, relativistic mass increases may also need to be considered as particles are accelerated to significant fractions of the speed of light. Relativistic mass increases, as shown in Eq. 4.32, are typically corrected for by changes in the magnetic field at the outer orbits.

$$M = M_\mathrm{o} / \left(\frac{1 - v^2}{c^2} \right)^{\frac{1}{2}} \qquad (4.32)$$

Here, M is the mass of the particle, v is the speed, and M_o is the rest mass, body measured at rest.

After the particles are accelerated to the desired energy, they must be extracted from the accelerator and directed to the desired target. An extraction foil may be used for the extraction of accelerated negative ions. This extraction foil is typically a carbon foil used to strip the negative electrons, yielding a positive ion. When the ion switches from a negative charge to a positive charge, its trajectory within the magnetic field will also change. This change can be used to direct the particles to the target. The carbon foil may be at the end of a movable arm on variable energy cyclotrons. This movable arm can extend to the inner orbits for the extraction of lower-energy particles or outer orbits for the extraction

of higher-energy particles. This extraction method can have 99% efficiency. Figure 4.8 is a diagram of an extraction foil method.

If the accelerated ions are positive, a deflector can be used for extraction. A deflector creates an electric or magnetic perturbation in the ion's path, which is used to direct the ion toward the target. The efficiency of a typical deflector is between 20% and 30%.

4.2.5 Charged Particles: Cross Sections and Reaction Rates

The cross sections for charged particle reactions differ from neutron excitation functions in part due to the coulomb barrier. This means that there is always a threshold energy for charged particle reactions, whereas for neutron-induced reactions, the threshold may be zero. An example of an α-induced reaction is shown in Fig. 4.9. Here, two reaction channels are depicted for the proton bombardment on $^{209}\mathrm{Bi}$. The $^{209}\mathrm{Bi}$ $(\alpha,2n)^{211}\mathrm{At}$ reaction occurs at lower energies than the $^{209}\mathrm{Bi}(\alpha,3n)^{210}\mathrm{At}$ reaction since the latter will require a higher-energy α for the knockout of an additional neutron.

As demonstrated in Fig. 4.9, the $(\alpha,2n)$ reaction requires lower energies to induce this nuclear reaction than the $(\alpha,3n)$ reaction. But as the energy of the particle increases, the $(\alpha,3n)$ reaction becomes accessible, competition occurs, and
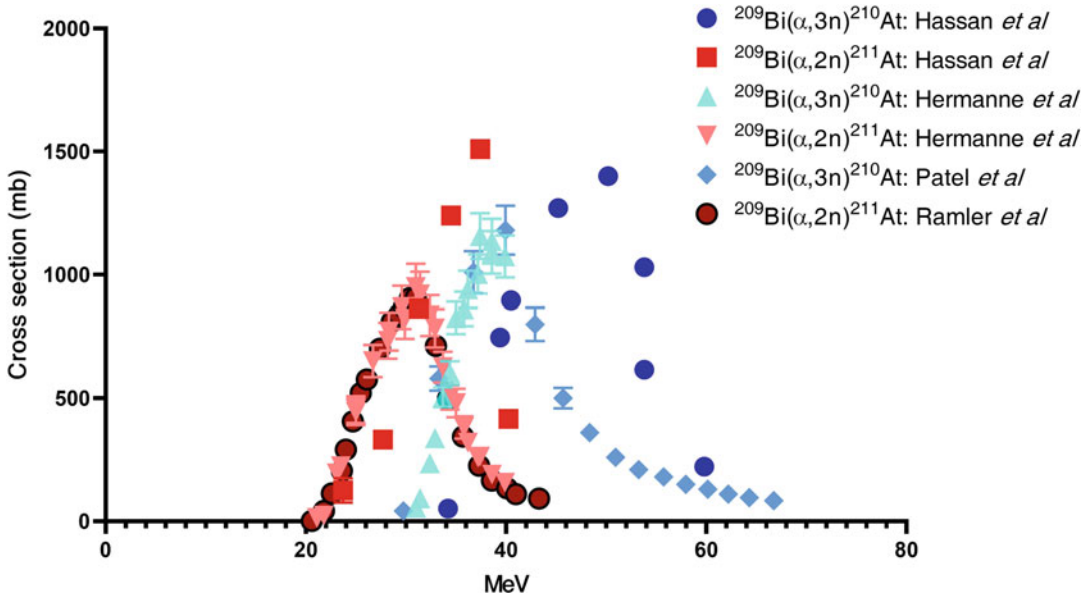
Fig. 4.9 The cross sections of alpha(α)-bombardment on ^{209}Bi atoms at variable energies for the ^{209}Bi(α,2n)^{211}At and ^{209}Bi(α,3n)^{210}At nuclear reactions

the cross section of the (α,2n) reaction starts to decrease. Using the same equations as used previously, the calculated threshold energy for the ^{209}Bi(α,3n)^{210}At is shown below in Eqs. 4.33 and 4.34.

$$Q = [(208.9803987 \text{ amu}) + (4.0026 \text{ amu}) - (3 \times 1.0086 \text{ amu}) - (209.98715 \text{ amu})] \times 931.48 \frac{\text{MeV}}{\text{amu}} = -27.89 \text{ MeV} \tag{4.33}$$

$$\text{Threshold} = \left[\frac{209 + 4}{209} \right] \times 27.89 \text{ MeV} = 28.42 \text{ MeV} \tag{4.34}$$

Therefore, higher-energy α particles will be required to induce the ^{209}Bi(α,3n)^{210}At reaction with a threshold of 28.42 MeV, than for the ^{209}Bi(α,2n)^{211}At reaction. Figure 4.9 displays the experimental excitation functions of the ^{209}Bi(α,2n)^{211}At (in red, with a threshold of ~21 MeV) and ^{209}Bi(α,3n)^{210}At (in blue, with a threshold of ~30 MeV) reactions [26, 38–40]. These values can be leveraged to ensure the production of high-purity ^{211}At by keeping the energy of the α beam below the 28.42 MeV threshold point, thereby preventing the production of ^{210}At. Data for this graph were obtained

from the EXFOR nuclear database from the national nuclear database website (https://www-nds.iaea.org/exfor/) [2, 26, 38–40].

Charged particles will experience energy degradation as they pass through different target materials. Equation 4.14 can be used for thin targets that do not experience significant energy and current degradation. In thick targets, the starting incident energy, or entrance energy, will decrease as it passes through the target, changing the rate of production at each energy value. A thin target is small enough that the entrance energy is essentially equal to the exit energy, resulting in a simplified rate of production. To calculate the rate of production using thick targets, one can consider sectioning out the thick target and consider it to be a series of thin targets with different charged particle energies, currents, and cross sections that can be used to predict the overall production rate. Each thin target reaction rate can be calculated individually and then summed to yield the total reaction rate in a thick target. For example, consider the production of ^{67}Cu via the ^{67}Cu(p,2p)^{68}Zn reaction. We will assume a thin target that does not cause significant energy degradation of the proton beam, that ^{68}Zn is in 100%

abundance in a 0.01 cm thick target with a density of 7.13 g/cm^3, a proton current of 1.6×10^{12}, and a cross section of 1.14 b. First, let us calculate the number of target nuclei followed by the reaction rate in Eqs. 4.35 and 4.36

$$n = 7.13 \frac{\text{g}}{\text{cm}^3} \div 65.38 \frac{\text{g}}{\text{mol}} \times 6.023$$
$$\times 10^{23} \text{atoms} = \frac{6.57 \times 10^{22} \text{atoms}}{\text{cm}^3} \qquad (4.35)$$

$$R = \left(1.6 \times 10^{12} \frac{\text{protons}}{\text{s}}\right) \times (0.01 \text{ cm})$$
$$\times \left(1.14 \text{ b} \times \frac{10^{-24} \text{cm}^2}{\text{b}}\right)$$
$$\times \left(6.57 \times 10^{22} \frac{\text{atoms}}{\text{cm}^3}\right) = 1.2$$
$$\times 10^9 \text{ atoms per second} \qquad (4.36)$$

Using this rate, we can predict the radioactivity produced and the saturation effect from the decay of ^{67}Cu over the time of the irradiation using Eq. 4.16, where ^{67}Cu λ[lambda] is 3.11×10^{-6} s^{-1} and the irradiation time was 48 h as shown in Eq. 4.37:

$$A = \left(1.2 \times 10^9 \text{ atoms per second}\right)$$
$$\times \left(1 - e^{-\left(\left(3.11 \times 10 - 6 \text{ s}^{-1}\right) \times 444960 \text{ s}\right)}\right)$$
$$= 499 \text{ MBq}(13.5 \text{ mCi})$$
$$\qquad (4.37)$$

Thus, we learn that if we were to bombard our ^{68}Zn target for 48 h, we would produce 499 MBq of ^{67}Cu.

4.2.6 Photonuclear Reactions

Photonuclear reactions are induced by photons, typically of energies between 15 and 30 MeV. These nuclear reaction notations include $X(\gamma, x)Y$, in which x can be any particle. This nuclear reaction can be accomplished by taking advantage of the giant dipole resonance (GDR) that occurs when enough energy is added to a nucleus to induce an excited state [41]. While there are different types of electron accelerators that can be used to generate photons, the example used herein will be a linear electron accelerator (eLINAC).

4.2.7 The Production of Photons for Nuclear Reactions

For photonuclear reactions, electrons are typically accelerated toward a high-Z radiator converter such as tungsten or tantalum [42–44]. The electrons will interact with the converter, resulting in bremsstrahlung radiation producing a continuous shower of photons with a range of energies as shown in Fig. 4.10 [43].

These photons are used for nuclear reactions such as (γ,n) or (γ,p) reactions [45]. These routes require high-current electron accelerators to produce high-intensity photon radiation and have been less explored than other routes for the production of radionuclides. High-intensity photon beams of sufficient energy are hard to produce and will cause heating of the target. Another route for producing these gamma rays is through
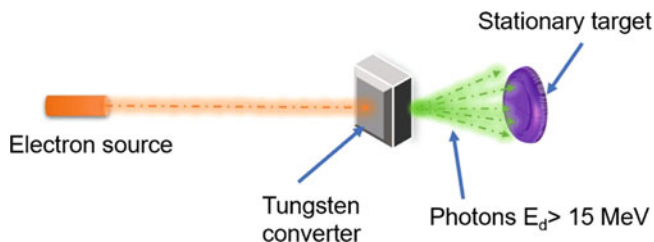
Fig. 4.10 A diagram of an accelerated electron colliding with a tungsten converter that creates a cone of variable energy photons from this interaction. The stationary target is placed behind this converter for the bombardment by the photon beam
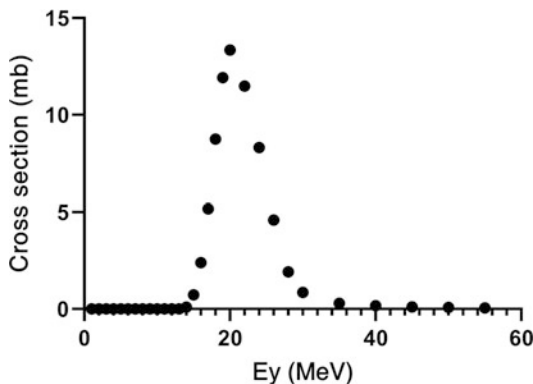
Fig. 4.11 The TENDL-2019: TALYS-based evaluated nuclear data library theoretical cross section plot for the ^{48}Ti(γ,p)^{47}Sc reaction

Compton backscattering, in which a low-energy photon is bounced off a high-energy electron. Compton backscattering requires higher electron energy beams (i.e., up to GeV) compared to the lower electron energy beam needed for the production of bremsstrahlung radiation discussed above. However, Compton backscattering can produce mono-energetic photons, while Bremsstrahlung radiation requires high current and results in photons with a range of energies [46]. An advantage of photonuclear production is the potential for compact, lightweight, and relatively inexpensive accelerators. An example of a photonuclear cross section can be seen in Fig. 4.11, in which the theoretical cross section of the ^{48}Ti(γ,n)^{47}Sc reaction is shown (https://tendl.web.psi.ch/tendl_2019/tendl2019.html).

Similar to charged particle reactions, photonuclear reactions have a threshold energy required to induce a nuclear reaction. Furthermore, the cross section of a reaction increases to a maxima and decreases as the energy of the incident photon increases, similar to charged particle reactions. A difference between photonuclear reactions and charged particle reactions, however, is that the photon flux density and energy are variable, as mentioned above. Calculations of the rates of production of photonuclear reactions must take into account the photon energy range used for these irradiations, as shown in Eq. 4.38 [43]:

$$A = n \int_{E_{\text{th}}}^{E_{\text{max}}} \varphi(E)\sigma(E)dE\left(1 - e^{-\lambda t_i}\right)\left(e^{-\lambda t_c}\right)$$

(4.38)

Where n is the number of target nuclei, E_{max} is the maximum photon energy, E_{th} is the threshold energy, $\varphi(E)$ is flux density of photons, $\sigma(E)$ is the cross section, λ is the decay constant, and t_i and t_c are the irradiation and cooling times respectively [43]. As with nuclear reactors, larger targets are required for photonuclear reactions compared to methods that rely upon charged particles. This impacts the chemical processing techniques that can be used for the purification of the radionuclide. Targets for photonuclear radionuclide production also experience high target heating from photons that must be taken into consideration during the design of the targets [43].

4.2.8 Radionuclide Generators

Radionuclide generators are typically composed of a longer-lived parent radionuclides bound to a solid support. This parent isotope decays to the desired radioactive daughter nuclide that is chemically different from the parent. Chemical separation is employed to elute the daughter while the parent nuclide remains bound to the resin. After the elution, the parent radionuclide will continue to decay to the daughter radionuclide, and at later time points—after the daughter radionuclide has built up—it can be eluted from the generator again. This elution of the daughter radionuclide with the parent radionuclide remaining bound to the resin is depicted in Fig. 4.12 below.

Radionuclide generators may provide a source of radionuclides for hospitals, clinics, and research facilities that may not be in close proximity to a reactor or accelerator. Radionuclide generators also provide consistent access to a desired radionuclide over the course of the half-life of the parent, with availability at different time points based on the in-growth of the daughter. Four examples of radionuclide generators that
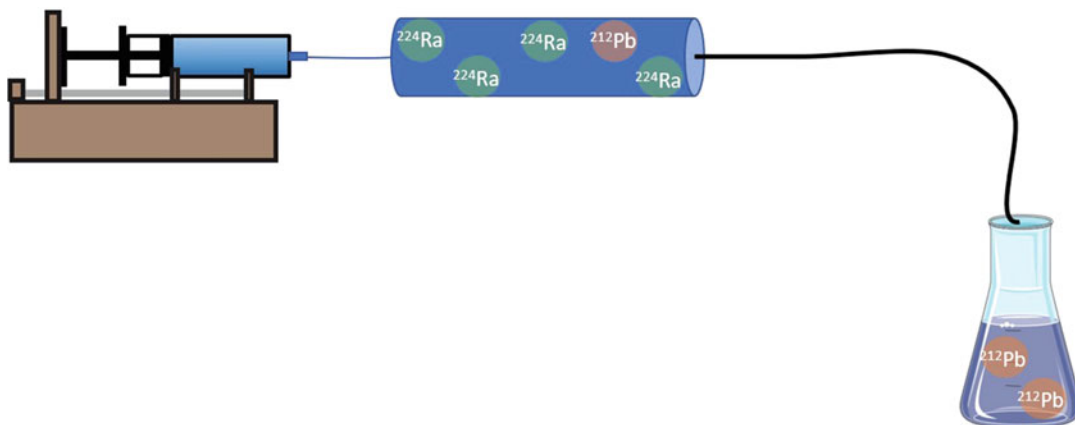
Fig. 4.12 Generator schematic of a chromatography column with the parent radionuclide, ^{224}Ra, bound to the column as well as the daughter, ^{212}Pb, that is produced from the decay of ^{224}Ra. A solution administered through the syringe elutes the ^{212}Pb into a separate vial while leaving the ^{224}Ra on the column [47]

produce therapeutic radionuclides are ^{188}W/^{188}Re, ^{229}Th/^{225}Ac, ^{225}Ra/^{225}Ac, and ^{228}Th/^{212}Pb [24, 25, 47, 48].

The development of therapeutic radionuclide generators requires the consideration of several factors. Many of the desired therapeutic radionuclides are obtained from the decay chain of longer-lived radionuclides, for example ^{232}U. The decay of the parent radionuclide can lead to the radiolytic degradation of the generator material. Radiolytic degradation occurs when emissions, such as α particles, cause damage to the solid support columns. This is concerning because these parent radionuclides are bound to these columns for extended times. As time passes, the parent radionuclide may leach (or become unbound) and end up in the desired daughter collection fraction. This presents dosimetry concerns, can complicate downstream chemistries required for radiopharmaceutical synthesis, and can lead to a decrease in the functionality and quality of the generator. Thus, careful thought and chemistry must be taken into account when selecting and producing both the parent and daughter of these generators.

An example of a generator-produced isotope is lead-212 (^{212}Pb $t_{1/2}$ = 10.62 h). Lead-212 is a particularly promising radionuclide for radiopharmaceutical therapy due to its β- decay and two α-emitting daughters that make it, in essence, an in vivo generator of α particles [49]. The predominate route of obtaining ^{212}Pb is through the decay of ^{228}Th ($t_{1/2}$ = 1.9 y), and the formation of a ^{224}Ra generator. The shipped generator contains ^{224}Ra isolated from ^{228}Th stockpiles. The ^{224}Ra is extracted first and chemically adhered to an extraction column as the parent radionuclide. However, ^{228}Th is necessary for the production of ^{224}Ra. One route to the production of ^{228}Th arises during the production of ^{225}Ac (another α emitter). During this process, the reaction of high-energy protons with ^{232}Th targets can produce ^{228}Th as a byproduct of the reaction intended to produce ^{225}Ac [24, 47]. Another route for obtaining ^{228}Th is through the decay chains of ^{233}U or ^{232}Th. During these long-lived decay chains, ^{228}Th can be chemically separated from other radionuclides. Figure 4.13 shows three different decay schemes used to produce medically used α emitters [24, 47, 49].

As was stated, radionuclide generators are based on the decay of a parent radionuclide to a daughter radionuclide, and understanding the decay of the parent in relation to the daughter is essential to understanding the longevity of a generator system and the number of times the daughter can be eluted. The equation used for determining this relationship is shown in Eq. 4.39.
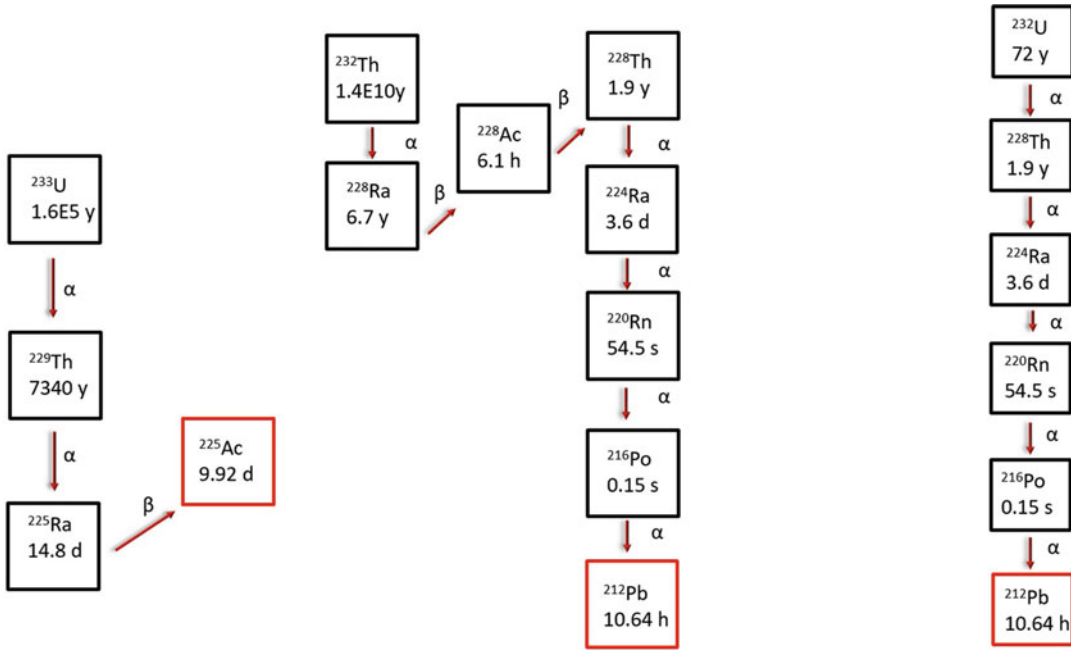
Fig. 4.13 The decay schemes of ^{232}U, ^{232}Th, and ^{233}U that provide medically relevant α-daughters (red boxes) that can be chemically separated

$$A_2 = \frac{\lambda_2}{\lambda_2 - \lambda_1} A_1^o \left(e^{-\lambda_1 t} - e^{-\lambda_2 t}\right) + A_2^o e^{-\lambda_2 t} \quad (4.39)$$

Where A_1 is the radioactivity of the parent, and A_2 is the radioactivity of the daughter. There are two equilibrium types based on the difference between the half-lives of the parent and daughter: transient and secular equilibrium [50]. Transient equilibrium occurs when the half-life of the parent is only a few times greater than that of the daughter, for example ^{225}Ra ($t_{1/2}$ = 14.9 d) and ^{225}Ac ($t_{1/2}$ = 9.9 d). In this case, Eq. 4.39 can be rearranged and simplified to determine the activity of the daughter if $\lambda_2 > \lambda_1$ shown in Eq. 4.40.

$$A_2 = \frac{\lambda_2}{\lambda_2 - \lambda_1} \times A_1 \quad (4.40)$$

Secular equilibrium, in contrast, occurs when the half-life of the parent is much longer than that of the daughter, $\lambda_2 >> \lambda_1$. In this case, the in-growth of the daughter reaches a saturation value due to the significantly longer half-life of the parent. An example of this scenario is provided by ^{188}W ($t_{1/2}$ = 69.4 d) that decays to ^{188}Re ($t_{1/2}$ = 17.0 h) [48].

4.3 Targetry: Target Materials and the Design of Target Holders

4.3.1 Target Materials

The design of targets is dependent upon both the intended nuclear reaction and the target material. Targets can be solid, liquid, or gas, and the selection of a target material is often predicated on its thermal conductivity, melting point, and physical state. The intended nuclear reaction, the possibility of producing byproducts, and future separation methods should be considered as well. For example, we have already determined that the bombardment of a ^{209}Bi target with alpha particles with energies between 21 and 40 MeV can produce ^{211}At. While the cross section for the nuclear reaction starts at 21 MeV, as the particle energy increases, different reaction channels become accessible, introducing the production of radiocontaminates. For example, the ^{209}Bi (p,3n)^{210}At reaction has a threshold of 28.42 MeV. Current methods consider this

energy range by bombarding targets at energies of ~28 MeV to prevent the production of ^{210}At [51–53]. Clearly, understanding all the nuclear reactions that may occur on a specific target material can aid in selecting bombardment parameters that maximize production yield while minimizing the production of radiocontaminates, especially those that cannot be separated by chemical means.

Targets may also be designed with a degrader in front of the target. A degrader is a section of the target apparatus placed in front of the target material that modifies the energy of the incident particles from a higher (undesired) energy down to a lower (desired) energy. This is useful at sites that have fixed beam energies or where the lowest beam energy available is still higher than required. In the ^{209}Bi example, the degrader must be thick enough to reduce the energy of the beam to an energy of ~28 MeV to remain below the threshold of the ^{210}At reaction. One must also consider the thickness of the target material. There is typically no need to make a target so thick that it degrades the energy of the beam to 0, for this would complicate subsequent purification processes. As we previously calculated, the threshold energy for the production of ^{211}At is 21 MeV α particles, so a bismuth target thickness that degrades the entrance particle beam from 28.8 MeV down to 21 MeV will enable the maximum production of ^{211}At while concomitantly using the minimal amount of target material. A software package called *Stopping and Range of Ions in Matter* (SRIM) can be used to help determine this. Using SRIM, a 0.09 mm thick bismuth target will degrade a 28.8 MeV alpha beam down to 20.2 MeV, which is within the desired cross section [54]. Some types of machines do not need a degrader if the energy of the extracted particles is within the desired range [51, 53].

4.3.2 The Design of Target Holders

While we have already discussed the different routes for producing radionuclides including target material considerations, the introduction of these target materials to the neutron flux or particle beam must be carefully designed as well. Most, if not all, of these targets must be contained within a holder, referred to from here on as a target holder, to maintain both the integrity of the target and its introduction and retrieval. The design of a target holder must consider effective cooling, the physical properties of the target, and the physical constraints of the space available for target irradiation by the accelerator or reactor. The material of the target holder must also be carefully selected based on its thermal conductivity, machinability, chemical inertness, and low activation. The latter property refers to the number of secondary radionuclides that may be produced by the interaction of the particle beam with the holder. Furthermore, the target material should not interact with the target holder, which may result in possible complications during purification. Commonly used materials in target holders include gold, niobium, and tantalum [37].

Sites with access to lower-energy charged particles may use coins (i.e., target holders used in smaller cyclotrons in which small amounts of target material are required and can be electroplated or otherwise adhered to a disk-shaped backing) as target holders, while sites that produce isotopes using high-energy charged particles may use a fully encapsulated target. In the latter, the target is typically in contact with the target holder on all surfaces, and the target holder is submerged in water for enhanced heat dissipation. The target should not experience phase changes during irradiation, which may result in the loss of target material, decreased yields, and/or more complicated separations. For example, bismuth has a low melting point of 271.4°C. For the production of ^{211}At from ^{210}Bi, the target design must have efficient cooling during bombardment in order to keep the target below this temperature and avoid the production of ^{211}At$_{(g)}$ [53].

4.3.3 Gaseous Targets

Gaseous targets can be cylindrical or conical. They are typically cooled with water on the outside of the contained gas. This is important because increased pressure upon heating could

rupture the beam window that separates the target material from the cyclotron vacuum. Alongside water-cooling of the target holder, heat dissipation can also be controlled with helium-cooling in front of gas target material. Gaseous targets are not typically used for the production of therapeutic radionuclides.

4.3.4 Liquid Targets

A liquid target may be 1–4 mL in volume and requires both an isolation foil between the target volume and helium-cooling and a vacuum isolation foil [55]. For example, liquid targets containing $^{18}O[H_2O]$ are commonly used for the production of the diagnostic radionuclide ^{18}F. As with gas targets, the optimization of a liquid target focuses on the dissipation of heat and power, and the liquid target holder is designed with materials with low activation such as niobium or tantalum [56]. Gas and liquid target materials can be easily transferred from the production area to shielded hot cells for further chemistry. Recent developments in the production of radionuclides via the irradiation of liquid targets containing dissolved salts have attracted interest due to the easy transfer of these target materials and the elimination of a dissolution step that is needed with solid targets, which are more common for the production of radiometals. An example of this strategy is the use of an enriched $[^{68}Zn]Zn(NO_3)_2$ liquid target for the production of ^{68}Ga via the $^{68}Zn(p,n)^{68}Ga$ reaction [57]. Another example of production using a liquid target is an unconventional method of harvesting the off-gas of an irradiated water target to produce $^{76/77}Kr$. In this case, a water-filled target is bombarded with a ^{78}Kr beam that produces $^{76/77}K$. The $^{76/77}Kr$ is then collected by purging the target with gas, upon which the $^{76/77}Kr$ gas is pushed into a gas trap in an isotope harvesting system [58]. After the $^{76/77}Kr$ is initially cryotrapped, this trap is connected with another trapping system in which $^{76/77}Kr$ is pushed through and its $^{76/77}Br$ daughters are trapped [58].

4.3.5 Solid Targets

Most therapeutic radionuclides are produced using solid targets. As many therapeutic radionuclides have longer half-lives than their diagnostic counterparts, the targets may be irradiated for extended time periods (hour to days). As a result, heat conductivity becomes an especially important consideration. In addition, the target design must also consider the bombardment parameters, including the beam energy, current, and beam incident angle.

4.3.6 Solid Targets for Nuclear Reactors

Many radionuclides suitable for radiopharmaceutical therapy are produced via neutron capture on solid targets. These targets are embedded in a neutron flux, and the energy deposited in the target is essentially uniform. The target holders must be able to withstand high temperatures, as targets for neutron capture are typically submerged in the reactor pool. Therefore, the target material should be encased within an inert target holder with a low neutron-capture cross section to prevent the activation of the target holder and the loss of neutrons available for reactions. Most reactor targets are metals or metal oxides encapsulated within a target holder made of aluminum or quartz to withstand temperatures of up to 1000°C.

Neutrons interact with materials to a lesser extent than charged particles. Therefore, reactor targets here are typically larger than those used in accelerators. Some considerations for reactor targets include target burn-up, product burn-up, and self-shielding [33].

1. *Target burn-up* occurs when the target material is irradiated for a long time and has a large cross section, affecting the overall yield due to the significant percentage of the target material that is converted to the product material. This eventually changes the available mass of the target, directly reducing the reaction rates.

Fig. 4.14 The same target is represented in two orientations within the same particle beam
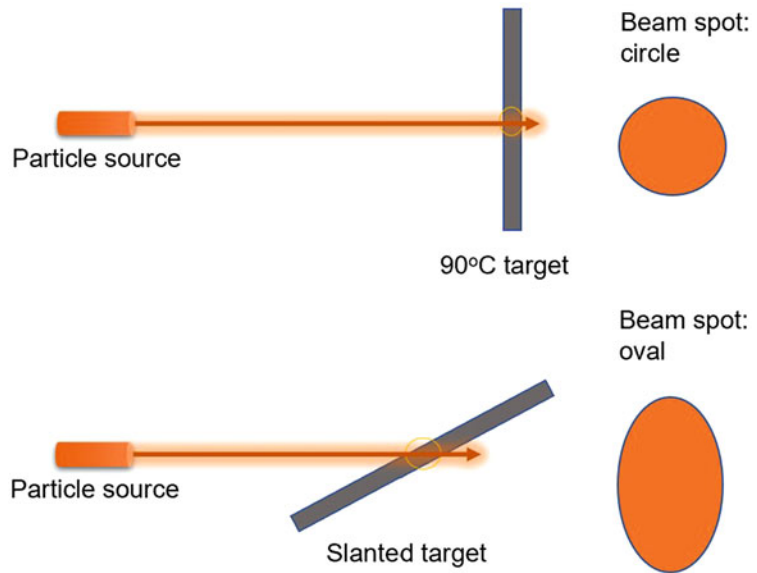
2. *Product burn-up* occurs when the product has a large neutron-capture cross section, meaning that the product *also* undergoes neutron capture, resulting in another reaction and another product, thereby decreasing the final yields of the intended product.

3. *Self-shielding* occurs in large targets with high cross sections. In this phenomenon, the nuclei within the center of the target do not experience the same neutron flux as the outer regions, decreasing the yield.

4.3.7 Solid Targets for Particle Accelerators

Solid targets for the production of radionuclides using an accelerator include powders (oxides and carbonates), electroplated materials, and foils that lay directly in the target holder or are spot-welded into the target holder. Direct contact with the target backing enhances cooling; for example, electroplated targets can be more effectively cooled than foil targets that are simply placed within the holder with less thermal contact.

The beam geometry can impact multiple facets of accelerator-based reactions. One such aspect is the beam spread (or beam spot) on a target,

specifically whether the beam is focused on a smaller section of the target or spread out across a larger portion. Thermal dissipation can be greatly affected by the beam spread: a smaller, more concentrated beam will cause higher heat deposition, while a beam with the same energy and current that is more spread out will cause lower localized heating. One way of spreading out the beam spot is by manipulation of the beam incident angle; targets that are bombarded at 90° have a smaller beam spot and thus higher local heat deposition than targets bombarded at 30°. Figure 4.14 shows the same target within the same particle beam but at different angles.

The slanted target also results in an increase in the effective thickness of the target. A 30° target may withstand longer irradiations and higher energy currents due to its larger surface area and enhanced cooling properties. An example of the increase of effective target thicknesses between a 1 mm target bombarded at 90° and the same target bombarded at 30° is shown in Eqs. 4.41 and 4.42 below:

$$\frac{\text{Target thickness}}{\sin(\sphericalangle)} = \text{effective target thickness}$$

(4.41)
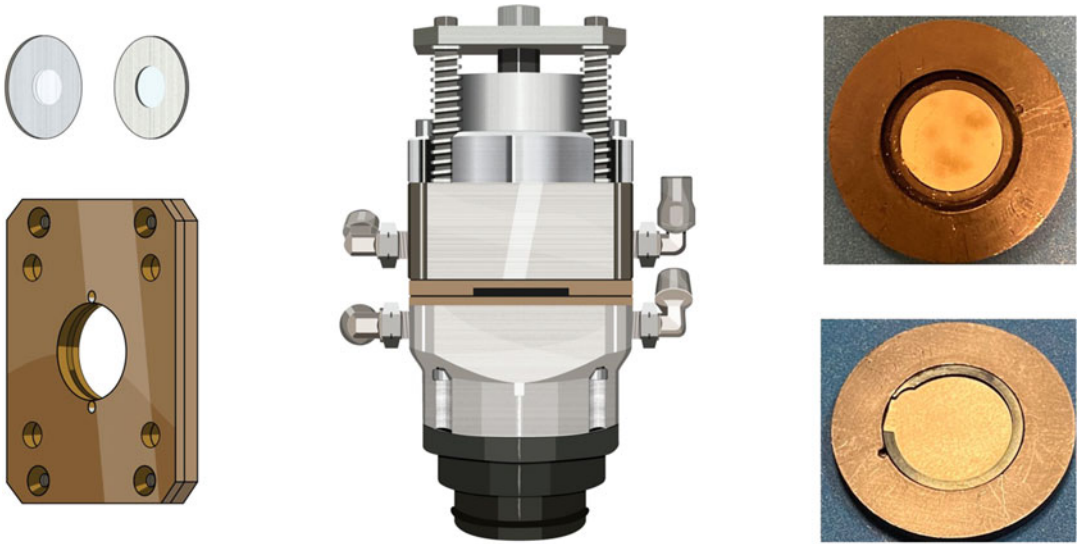
Fig. 4.15 An example of a solid target station (from Pyles et al. [59]). An image of pressed titanium dioxide target for the production of ^{47}Sc via the ^{50}Ti(p,α)^{47}Sc reaction (Eq. 4.36)

$$\frac{1 \text{ mm}}{\sin(30)} = 2 \text{ mm} \qquad (4.42)$$

One practical example of the use a slanted target is the production of ^{211}At from ^{209}Bi. In this case, the enhanced cooling properties that come with a slanted target help mitigate the limitation of using bismuth (which has a low melting point) as a target material [53]. An example of a 90° target station is shown in Fig. 4.15 [59].

Another practical consideration for targetry is the retrieval of the irradiated target. There are two routes of retrieving solid targets. Some facilities have remote systems for the automated removal of targets and their subsequent transfer to shielded processing cells for further downstream chemistry. The alternative requires that personnel physically remove the solid target from the accelerator or reactor and transport it to a separate area for separation chemistry. It is important to consider this issue when assessing potential doses to staff. Solid targets also typically require a dissolution step before separation chemistry can be performed, which may vary depending on the target material.

4.3.8 Natural and Enriched Target Materials

An important factor in the selection of the target material is the natural abundance of the target nuclei. Many solid targets are elements with multiple stable isotopes. For example, ytterbium has seven stable nuclides with different natural abundances: ^{168}Yb(0.123%), ^{170}Yb(2.8%), ^{171}Yb(14.09%), ^{172}Yb(21.68%), ^{173}Yb(16.10%), ^{174}Yb(32.02%), and ^{176}Yb(12.99%). One possible production route for the ubiquitous therapeutic nuclide ^{177}Lu is via an indirect pathway: ^{176}Yb (n,γ)^{177}Yb->^{177}Lu. While the irradiation of a natural ytterbium target can produce ^{177}Lu, other reactions from the other ytterbium nuclei can occur, resulting in the co-production of other radioisotopes of lutetium that cannot be separated via standard chemical techniques. Thus, targets enriched in ^{176}Yb are preferred. Another production route for ^{177}Lu—the ^{176}Lu(n,γ)^{177}Lu reaction—also requires enriched material. There are two naturally abundant isotopes of lutetium: ^{175}Lu (97.40%) and ^{176}Lu (2.59%). The low natural abundance of ^{176}Lu means that it must be

enriched to optimize yields. Enriched material is expensive and may require recycling to offset the cost. Alternatively, the radioactive impurities that are produced using natural abundance targets but cannot be chemically separated must be factored into the production process.

Another example of the importance of isotopic enrichment in the production of radionuclides is provided by the production of ^{47}Sc via the irradiation of titanium targets [60]. There are five naturally occurring isotopes of titanium, all of which could lead to the production of different scandium radionuclides: ^{43,44,46,47,48}Sc. While some of these radioisotopes of scandium could be allowed to decay before the purification of ^{47}Sc, both ^{46}Sc ($t_{1/2} = 83$ d) and ^{48}Sc ($t_{1/2} = 43$ h) pose dosimetry concerns due to their long half-lives. Therefore, the production of high-purity ^{47}Sc requires the utilization of targets enriched in ^{48}Ti or ^{50}Ti that are costly and must be recycled for continued use [61]. Along these lines, there are several criteria that should be considered during the recycling of a target. To name a few, the target material must be collected in a physical state that allows for chemical processing, the target material must have high recoveries with minimal introduction of impurities, and the target should have reproducible radionuclide production yields alongside high recovery of the starting material.

4.3.9 Product Purity

One critical aspect that must be addressed during the production of radionuclides is molar activity. Molar activity is the amount of radioactivity per mole of material: Bq/mol. Both the starting target material and other contaminants can directly impact this parameter. To wit, if the starting material is the same element as the product, this will inevitably decrease the specific activity of the product, as the target material cannot be chemically separated from the product. This becomes prominent during (n,γ) reactions, as these reactions involve the target nuclei capturing a neutron and thus producing different isotopes of the same element. For example, ^{177}Lu can be produced directly by the neutron bombardment

of ^{176}Lu, resulting in a low molar activity product because the ^{177}Lu product is necessarily contaminated with inseparable ^{176}Lu. Another route for the production of ^{177}Lu is the indirect method based on the neutron bombardment of ^{176}Yb to create ^{177}Yb that subsequently decays to ^{177}Lu. This approach results in ^{177}Lu with higher molar because the lutetium can be chemically separated from the ytterbium [62].

4.3.10 Practical Considerations: Simulation Tools

Several different tools can be used to simulate the energy degradation and scatter of particles through various materials. For example, the software *Stopping and Range of Ions in Matter* (SRIM) can be used to simulate a charged particle (e.g., an α particle) within a target material [54]. This software utilizes Monte Carlo simulations to predict how the charged particles interact with matter, the distance the particle will travel in the target, the energy loss within the target material, and how the beam scatters. An example of the use of this software is determining the thickness of a degrader. A degrader can be used in front of target material in accelerators that produce particles with minimum energies higher than the desired energy for a given reaction. In this scenario, the degrader is used to reduce the energy of the incident particles on the target. Using ^{211}At as an example again, suppose we have a particle accelerator that can produce alpha particles with a minimum energy of 40 MeV. However, we only want alpha particles with energies lower than 28.8 MeV incident on the ^{209}Bi target to prevent the production of ^{210}At. We can use SRIM to design a degrader that will decrease the beam energy below 28.8 MeV, thereby optimizing the bombardment parameters. As shown in Fig. 4.16 below, the incoming α particles have an energy of 40 MeV. Panel A displays the simulation of a 0.3 mm Al degrader in front of the target material. In this case, the calculated exit energy from the degrader is 27.4 MeV, below the threshold of the ^{209}Bi (α,3n)^{210}At reaction. Panel B shows the complete
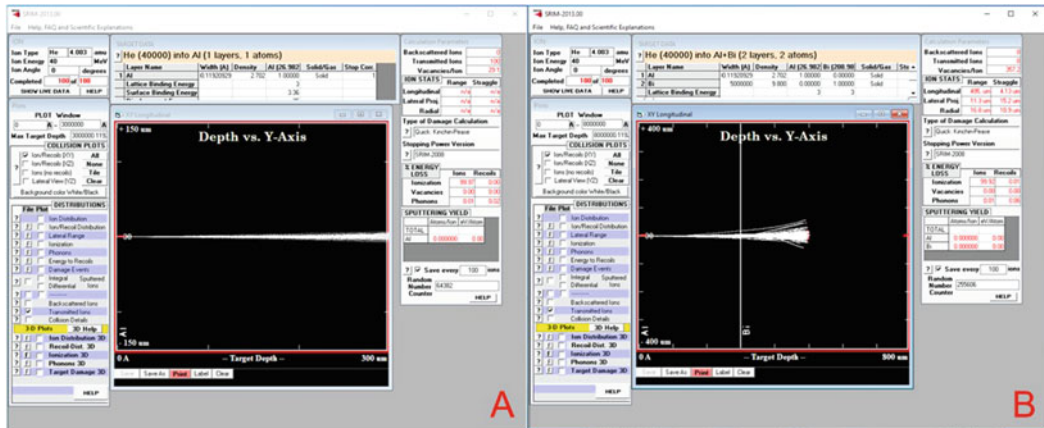
Fig. 4.16 Using *Stopping and Range of Ions in Matter* to simulate an alpha particle at 40 MeV on an Al degrader and a 0.5 mm Bi target. In panel A, the beam is shown to continue through the 0.3 mm thick Al degrader where the output provides the exit energy. Panel B shows the complete target, in which the particles are shown to stop with the Bi target

target assembly, including the aluminum degrader and a 0.5 mm Bi target, with SRIM used to show that the beam is being fully stopped within the assembly.

4.3.11 Theranostic Approaches: The Production of Elementally Matched Diagnostic and Therapeutic Radionuclides

Within the context of nuclear medicine, the principle of theranostics is predicated on the idea of using the same targeting moiety labeled with different radionuclides for both diagnostic imaging and targeted therapy. If we consider a "theranostic radionuclide pair" of the positron-emitting ^{68}Ga and the beta-emitting ^{177}Lu, we can envision the same (or a similar) targeting vector labeled with the former to facilitate imaging and the latter to enable therapy. Two widely used clinical examples of such pairs are [^{68}Ga]Ga-DOTATATE and [^{177}Lu]Lu-DOTATATE for the imaging and therapy of neuroendocrine neoplasms and [^{68}Ga]Ga-PSMA-11 and [^{177}Lu]Lu-PSMA-617 for the imaging and therapy of prostate cancer [63, 64]. In both cases, the examples highlight the value of using

non-invasive imaging both for the selection of patients likely to respond to radiopharmaceutical therapy and for the monitoring of these patient's response to therapy.

The theranostic pair of ^{68}Ga/^{177}Lu has undeniably demonstrated its utility in the clinic. However, ^{68}Ga^{3+} has slightly different coordination chemistry than ^{177}Lu^{3+}, which can lead to differences in the in vitro and in vivo behavior of radiopharmaceuticals labeled with the two radiometals. As a result, when developing radiopharmaceuticals with these nuclides, the dosimetry, in vitro binding, in vivo pharmacokinetics, and toxicity must be determined separately for the radiopharmaceuticals labeled with both nuclides [64]. The difficulty and expense of this process creates an impetus to develop theranostic pairs of radionuclides that are elementally matched.

There is significant interest in the production of chemically identical, isotopologous theranostic pairs in which the nuclear imaging agent and the radiotherapeutic exhibit identical chemical, biological, and pharmacokinetic behavior. Two radionuclides of lead offer one example of such a pair. In this case, ^{203}Pb ($t_{1/2} = 51.9$ h) can be used for Single Photon Emission Computer Tomography (SPECT) imaging while

^{212}Pb ($t_{1/2} = 10.6$ h, β- and α) can be harnessed for radiopharmaceutical therapy. One can easily envision a radiopharmaceutical in which the same chelator-bearing targeting moiety can be labeled with both radioisotopes, since the coordination chemistry of ^{203}Pb is identical to that of ^{212}Pb. In this case, of course, the pharmacokinetic profile of the ^{203}Pb-labeled compound would also match that of the ^{212}Pb-labeled radiopharmaceutical, simplifying clinical translation and the extrapolation of imaging data to therapy [24].

One of the biggest challenges in the investigation of elementally matched theranostic pairs lies in their production, as many of the relevant production routes have yet to be fully explored. Along these lines, investigations into potential routes for the production of these pairs as well as their target preparation, starting target material, and product purity are critical. One of the potential obstacles in the production of isotopologous radionuclides is that in some cases they will be co-produced alongside other radioisotopes of the same element. This would complicate the downstream chemistry, as the desired matched-pair radionuclides could not be chemically separated from any isotopologous byproducts, thereby lowering the radionuclidic purity and specific activity of the desired products. Furthermore, many of these production routes will require expensive enriched materials to help reduce the production of these radiocontaminates. Recycling procedures will thus have to be applied to help offset the cost of these materials. Examples of other elementally matched theranostic pairs are shown in Table 4.2. Investigations into the production of elementally matched theranostic pairs will increase the toolbox available to scientists and physicians for the development of novel targeted radiotherapeutics.

4.4 Future Directions and Conclusion

The expansion of clinically used targeted radionuclide therapies has resulted in a dramatically increased need for robust methods for the production of radionuclides. These include nuclear reactions induced by neutrons, charged particles, and photons that can be accomplished using nuclear reactors and particle accelerators. Finding the optimal production route for a radionuclide begins with understanding nuclear reactions and their energetics. The development of effective production strategies also requires careful considerations related to targetry—especially with respect to the target material, the target holder, and efficient cooling—as well as downstream chemistry. A wide variety of tools are available to facilitate this process, including the Chart of Nuclides, experimental and theoretical cross section databases, and computational applications for particle energy degradation. Radionuclide generators that exploit the long-lived decay chains of some parent radionuclides can provide access to radionuclides for sites that do not have production capabilities. Finally, new developments in the production of elementally matched theranostic pairs are paving the way for the creation of impactful strategies for patient selection and treatment monitoring.

4.5 The Bottom Line

- The Chart of Nuclides can be used to identify potential therapeutic radionuclides as well as possible routes for their production.
- Reaction rates can be calculated based on the threshold values and cross sections of nuclear reactions.
- Nuclear reactors, particle accelerators, and generators are different ways to produce radionuclides.
- The design of a target for the production of a radionuclide must take into account the target material, its melting temperature, its cooling ability, and the chemical processing techniques that will be used to isolate and purify the desired radionuclide.
- There is an urgent need for the identification of new therapeutic radionuclides, the optimization of pathways that produce therapeutic radionuclides in high yield and high purity, and the development of clinically viable elementally matched theranostic pairs.

Table 4.2 Elementally matched theranostic pairs

Radionuclide	Half-life	Decay	Production method	Target nuclei	Medical use	Reference
^{43}Sc	3.89 h	EC + β + (100%)	Accelerator	^{40}Ca(α,p)^{43}Sc	PET	[4]
				^{46}Ti(p,α)^{43}Sc		[4]
^{44}Sc	3.97 h	EC + β + (100%)	Accelerator	^{44}Ca(p,n)^{44}Sc	PET	[4]
				^{45}Sc(p,2n)^{44}Sc		[4]
				^{47}Ti(p,α)^{44} m,gSc		[4]
			Generator	^{44}Ti/^{44}Sc		[4]
^{47}Sc	3.3 d	β- (100%)	Accelerator	^{44}Ca(α,p)^{47}Sc	Therapy	[4]
				^{48}Ti(p,2p)^{47}Sc		[4]
				^{48}Ti(γ,p)^{46}Sc		[44]
				^{50}Ti(p,α)^{47}Sc		[4]
				^{51}V(p,p + α)^{47}Sc		[4]
			Reactor	^{47}Ti(n,p)^{47}Sc		[65]
			Generator	^{47}Ca/^{47}Sc generator		[4]
^{64}Cu	12.7 h	EC+(β+) (61.5%)	Accelerator	^{64}Ni(p,n)^{64}Cu	PET	[5]
		β-(38.5%)		^{67}Zn(p,α)^{64}Cu	Therapy	[5]
^{67}Cu		β- (100%)	Reactor	^{67}Zn(n,p)^{67}Cu	Therapy	[5]
			Accelerator	^{68}Zn(p,2p)^{67}Cu		[5]
				^{68}Zn(γ,p)^{67}Cu		[6]
				^{70}Zn(p,α)^{67}Cu		[5]
^{76}Br		EC + β + (100%)	Accelerator	^{76}Se(p,n)^{76}Br	PET	[8]
^{77}Br		Auger/CE	Accelerator	^{77}Se(p,n)^{77}Br	Therapy	[8]
^{149}Tb		EC(82.3%)	Accelerator	Proton-induced spallation on natTa	Therapy	[66]
		α (17.7%)				[66]
^{152}Tb		EC + β + (100%)	Accelerator	Proton-induced spallation on natTa	PET	[66]
^{155}Tb		EC (100%)	Accelerator	^{155}Gd(p,n)^{155} Tb	SPECT	[66]
				^{156}Gd(p,2n)^{155} Tb		[66]
^{161}Tb		β- (100%)	Reactor	^{160}Gd(n,γ)^{161}Gd->^{161} Tb	Therapy	[67]
^{203}Pb		EC (100%)	Accelerator	^{205}Tl(p,3n)^{203}Pb	SPECT	[49]
^{212}Pb		β- (100%)	Generator	^{228}Th/^{212}Pb	Therapy	[49]

References

1. Yordanova A, Eppard E, Kürpig S, Bundschuh RA, Schönberger S, Gonzalez-Carmona M, et al. Theranostics in nuclear medicine practice. Onco Targets Ther. 2017;10:4821–8.
2. NuDat 2.8 Brookhaven National Laboratory website. https://www.nndc.bnl.gov/nudat2/. Data extracted June 2, 2021. Accessed January 1, 2022 [Internet].
3. Vimalnath KV, Shetty P, Rajeswari A, Chirayil V, Chakraborty S, Dash A. Reactor production of 32P for medical applications: an assessment of 32S(n,p) 32P and 31P(n,γ)32P methods. J Radioanal Nucl Chem. 2014;301(2):555–65.

4. Chernysheva M, Loveless SC, Brossard T, Becker K, Cingoranelli S, Aluicio-Sarduy E, et al. Accelerator production of scandium radioisotopes: Sc-43, Sc-44, and Sc-47. Curr Radiopharm. 2021;14(4):359–73.
5. Mou L, Martini P, Pupillo G, Cieszykowska I, Cutler CS, Mikołajczak R. 67Cu production capabilities: a mini review. Molecules. 2022;27(5):1501.
6. Hovhannisyan GH, Bakhshiyan TM, Dallakyan RK. Photonuclear production of the medical isotope 67Cu. Nucl Instrum Methods Phys Res B Beam Interact Mater At. 2021;498:48–51.
7. Bhike M, Fallin B, Krishichayan TW. Measurement of the neutron-capture cross section of 76Ge and 74Ge below 15 MeV and its relevance to 0νββ decay searches of 76Ge. Phys Lett B. 2015;741:150–4.

8. Ellison PA, Olson AP, Barnhart TE, Hoffman SLV, Reilly SW, Makvandi M, et al. Improved production of (76)Br, (77)Br and (80m)Br via CoSe cyclotron targets and vertical dry distillation. Nucl Med Biol. 2020;80–81:32–6.

9. Vereshchagin YI, Markovskii DV, Pavshuk VA, Ponomarev-Stepnoi NN, Udovenko AN, Khvostionov VE, et al. 89Sr production in a reactor with solution fuel. At Energy. 2006;100(5):350–8.

10. Therapeutic Radionuclide Generators. 90Sr/90Y and 188W/188Re generators. Vienna: International Atomic Energy Agency; 2009.

11. Jai W, et al. Platinum Metals Rev. 2000;44:50.

12. Tárkányi F, Hermanne A, Király B, Takács S, Ditrói F, Csikai J, et al. New cross-sections for production of 103Pd; review of charged particle production routes. Appl Radiat Isot. 2009;67(9):1574–81.

13. Maslov OD, Starodub GY, Vostokin GK, Gustova MV, Dmitriev SN, Shvetsov VN, et al. Production of 117mSn with high specific activity by cyclotron. Appl Radiat Isot. 2011;69(7):965–1.

14. Elom Achoribo AS, Akaho EHK, Nyarko BJB, Osae Shiloh KD, Odame Duodu G, Gibrilla A. Feasibility study for production of I-131 radioisotope using MNSR research reactor. Appl Radiat Isot. 2012;70 (1):76–80.

15. Grummitt WE, Wilkinson G. Fission products of U235. Nature. 1946;158(4005):163.

16. Allen BJ, et al. Appl Radiat Isot. 2001;54:53–8.

17. Lehenberger S, et al. Nucl Med Biol. 2011;38:917–24.

18. Karadag M. Measurement of thermal neutron cross section and resonance integral for 148Nd(n,γ)149Nd reaction by using a 55Mn monitor. Ann Nucl Energy. 2013;62:274–9.

19. Uddin MS, Chowdhury MH, Hossain SM, Latif SA, Islam MA, Hafiz MA, et al. Thermal neutron capture cross sections for the 152Sm(n,γ)153Sm and 154Sm (n,γ)155Sm reactions at 0.0536eV energy. Nucl Instrum Methods Phys Res B Beam Interact Mater At. 2008;266(22):4855–61.

20. Lahiri S, Volkers KJ, Wierczinski B. Production of 166Ho through 164Dy(n,γ)165Dy(n, γ)166Dy(β−) 166Ho and separation of 166Ho. Appl Radiat Isot. 2004;61(6):1157–61.

21. Dash A, et al. Nucl Med Mol Imaging. 2015;49:85–107.

22. Moustapha ME, Ehrhardt GJ, Smith CJ, Szajek LP, Eckelman WC, Jurisson SS. Preparation of cyclotron-produced 186Re and comparison with reactor-produced 186Re and generator-produced 188Re for the labeling of bombesin. Nucl Med Biol. 2006;33 (1):81–9.

23. Knapp FF Jr, Mirzadeh S, Beets AL, Du M. Production of therapeutic radioisotopes in the ORNL HighFlux Isotope Reactor (HFIR) for applications in nuclear medicine, oncologyandinterventional cardiology. J Radioanal Nucl Chem. 2005;263(2):503–9.

24. McNeil BL, Robertson AKH, Fu W, Yang H, Hoehr C, Ramogida CF, et al. Production, purification, and radiolabeling of the (203)Pb/(212)Pb theranostic pair. EJNMMI Radiopharm Chem. 2021;6(1):6.

25. Engle JW. The production of ac-225. Curr Radiopharm. 2018;11(3):173–9.

26. Hermanne A, Tárkányi F, Takács S, Szücs Z, Shubin YN, Dityuk AI. Experimental study of the cross-sections of alpha-particle induced reactions on 209Bi. Appl Radiat Isot. 2005;63(1):1–9.

27. Hashimoto T, et al. Rad Chem Radioanel Lett. 1977;28:385–91.

28. Morgenstern A, et al. Anal Chem. 2008;80:8763–70.

29. Ehmann WD, Vance D. Radiochemistry and nuclear methods of analysis. New York: Wiley; 1991.

30. Chadwick MB, Herman M, Obložinský P, Dunn ME, Danon Y, Kahler AC, et al. ENDF/B-VII.1 nuclear data for science and technology: cross sections, Covariances, fission product yields and decay data. Nucl Data Sheets. 2011;112(12):2887–996.

31. Qaim SM. Nuclear data for production and medical application of radionuclides: present status and future needs. Nucl Med Biol. 2017;44:31–49.

32. Wooten AL, Lewis BC, Lapi SE. Cross-sections for (p, x) reactions on natural chromium for the production of 52,52m,54Mn radioisotopes. Appl Radiat Isot. 2015;96:154–61.

33. International Atomic Energy Agency. Manual for reactor produced radioisotopes. Vienna: International Atomic Energy Agency; 2003.

34. Cyclotron Produced Radionuclides. Principles and practice. Vienna: International Atomic Energy Agency; 2009.

35. Muranaka RG. Conversion of research reactors to low-enrichment uranium fuels. IAEA Bull. 1983;25 (1):18–21.

36. Roig O, Jandel M, Méot V, Bond EM, Bredeweg TA, Couture AJ, et al. Radiative neutron capture cross sections on $^{176}\mathrm{ Lu}$ at DANCE. Phys Rev C. 2016;93(3):034602.

37. Synowiecki MA, Perk LR, Nijsen JFW. Production of novel diagnostic radionuclides in small medical cyclotrons. EJNMMI Radiopharm Chem. 2018;3(1):3.

38. Hassan AE, Lukyanov S, Kalpakchieva R, Penionzhkevich YE, Stabatyan R, Vinsour J, et al. Investigation of nuclear fusion in reactions of 4,6 He and 7 Li on 208 Pb and 208 Bi nuclei. Bull Russ Acad Sci Phys. 2006;7011:1558–63.

39. Patel HB, Shah DJ, Singh NL. Study of (a,xn) reactions on 169Tm, 181Ta and 209Bi up to 70MeV. Nuovo Cimento. 1999;112:1439.

40. Ramler WJ, Wing J, Henderson DJ, Huizenga JR. Excitation functions of bismuth and Lead. Phys Rev. 1959;114(1):154–62.

41. Starovoitova VN, Tchelidze L, Wells DP. Production of medical radioisotopes with linear accelerators. Appl Radiat Isot. 2014;85:39–44.

42. Obodovskiy I. Chapter 19 – Neutron sources. In: Obodovskiy I, editor. Radiation. Elsevier; 2019. p. 289–92.

43. Howard S, Starovoitova VN. Target optimization for the photonuclear production of radioisotopes. Appl Radiat Isot. 2015;96:162–7.

44. Hovhannisyan GH, Bakhshiyan TM, Balabekyan AR, Kerobyan IA. Production of 47Sc in photonuclear reactions on natTi targets at the bremsstrahlung end-point energy of 30 and 40 MeV. Appl Radiat Isot. 2022;182:110138.

45. Hussein EMA. Chapter three – cross sections. In: Hussein EMA, editor. Radiation mechanics. Oxford: Elsevier Science Ltd; 2007. p. 153–245.

46. Habs D, Köster U. Production of medical radioisotopes with high specific activity in photonuclear reactions with γ-beams of high intensity and large brilliance. Appl Phys B. 2011;103(2):501–19.

47. Robertson AKH, Ramogida CF, Schaffer P, Radchenko V. Development of (225)Ac radiopharmaceuticals: TRIUMF perspectives and experiences. Curr Radiopharm. 2018;11(3):156–72.

48. Boschi A, Uccelli L, Pasquali M, Duatti A, Taibi A, Pupillo G, et al. 188W/88 Re generator system and its therapeutic applications. J Chem. 2014;2014:529406.

49. Kokov KV, Egorova BV, German MN, Klabukov ID, Krasheninnikov ME, Larkin-Kondrov AA, et al. (212) Pb: production approaches and targeted therapy applications. Pharmaceutics. 2022;14(1)

50. Production of long lived parent radionuclides for generators. 68Ge, 82Sr, 90Sr and 188W. Vienna: International Atomic Energy Agency; 2010.

51. Lebeda O, Jiran R, Ráliš J, Štursa J. A new internal target system for production of 211At on the cyclotron U-120M. Appl Radiat Isot. 2005;63(1):49–53.

52. Burns JD, Tereshatov EE, Avila G, Glennon KJ, Hannaman A, Lofton KN, et al. Rapid recovery of at-211 by extraction chromatography. Sep Purif Technol. 2021;256:117794.

53. Guérard F, Gestin J-F, Brechbiel MW. Production of [(211)At]-astatinated radiopharmaceuticals and applications in targeted α-particle therapy. Cancer Biother Radiopharm. 2013;28(1):1–20.

54. Ziegler JFBJPZMD. SRIM, the stopping and range of ions in matter. Chester: SRIM Co.; 2008.

55. Peeples JL, Stokely MH, Michael DJ. Thermal performance of batch boiling water targets for 18F production. Appl Radiat Isot. 2011;69(10):1349–54.

56. Nye JA, Avila-Rodriguez MA, Nickles RJ. A grid-mounted niobium body target for the production of reactive [18F]fluoride. Appl Radiat Isot. 2006;64(5):536–9.

57. Pandey MK, Byrne JF, Schlasner KN, Schmit NR, DeGrado TR. Cyclotron production of 68Ga in a liquid target: effects of solution composition and irradiation parameters. Nucl Med Biol. 2019;74-75:49–55.

58. Clause HK, Domnanich KA, Kleinfeldt C, Kalman M, Walker W, Vyas C, et al. Harvesting krypton isotopes from the off-gas of an irradiated water target to generate 76Br and 77Br. Sci Rep. 2022;12(1):1433.

59. Pyles JM, Massicano AVF, Appiah J-P, Bartels JL, Alford A, Lapi SE. Production of 52Mn using a semi-automated module. Appl Radiat Isot. 2021;174:109741.

60. Loveless CS, Blanco JR, Diehl GL, Elbahrawi RT, Carzaniga TS, Braccini S, et al. Cyclotron production and separation of scandium radionuclides from natural titanium metal and titanium dioxide targets. J Nucl Med. 2021;62(1):131–6.

61. Loveless CS, Radford LL, Ferran SJ, Queern SL, Shepherd MR, Lapi SE. Photonuclear production, chemistry, and in vitro evaluation of the theranostic radionuclide 47Sc. EJNMMI Res. 2019;9(1):42.

62. Tarasov VA, Andreev OI, Romanov EG, Kuznetsov RA, Kupriyanov VV, Tselishchev IV. Production of no-carrier added Lutetium-177 by irradiation of enriched Ytterbium-176. Curr Radiopharm. 2015;8 (2):95–106.

63. Jones W, Griffiths K, Barata PC, Paller CJ. PSMA Theranostics: review of the current status of PSMA-targeted imaging and Radioligand therapy. Cancers (Basel). 2020;12(6)

64. Werner RA, Weich A, Kircher M, Solnes LB, Javadi MS, Higuchi T, et al. The theranostic promise for neuroendocrine tumors in the late 2010s – where do we stand, where do we go? Theranostics. 2018;8(22):6088–100.

65. Domnanich KA, Müller C, Benešová M, Dressler R, Haller S, Köster U, et al. 47Sc as useful β-emitter for the radiotheragnostic paradigm: a comparative study of feasible production routes. EJNMMI Radiopharm Chem. 2017;2(1):5.

66. Naskar N, Lahiri S. Theranostic terbium radioisotopes: challenges in production for clinical application. Front Med (Lausanne). 2021;8:6e75014.

67. Gracheva N, Müller C, Talip Z, Heinitz S, Köster U, Zeevaart JR, et al. Production and characterization of no-carrier-added 161Tb as an alternative to the clinically-applied 177Lu for radionuclide therapy. EJNMMI Radiopharm Chem. 2019;4(1):12.

The Radiobiology of Radiopharmaceutical Therapy: The Input of Imaging and Radiomics

Jean-Pierre Pouget, Marion Tardieu, and Sophie Poty

5.1 Introduction

Radiopharmaceutical therapy (RPT) is a modality in which radiolabelled cancer-targeted biomolecules are used to specifically irradiate tumour cells [1]. The approach is particularly useful for the treatment of metastatic or diffuse tumours, i.e. situations in which conventional external beam radiotherapy (EBRT) would expose normal tissues to intolerable doses. Depending on the decay spectrum of the radionuclide, RPT can be categorized as alpha (α), beta (β) or Auger electron (AE) RPT. However, most radionuclides emit a mixture of radiation types that also includes gamma (γ) rays, X-rays or internal conversion electrons (ICE). Unlike EBRT, which uses low linear energy transfer (LET) radiation, RPT offers the possibility of using both low- and high-LET particles with ranges generally below 1.5 cm [2]. In theory, RPT is most suitable for the treatment of small volume tumours because of 'volume effects', i.e. for a same physical absorbed dose, RPT is expected to be more efficient at treating smaller tumours than larger ones. Another distinct feature of RPT irradiation is a heterogeneous dose distribution in time and space that is dependent on (i) the pharmacokinetic profile of the radio-pharmaceutical, (ii) the physical half-life of the radionuclide and (iii) the range of emitted particles. Importantly, RPT generally delivers continuous low dose rate (CLDR) irradiation ($<$ 1 Gy/h), which can be compared to some extent to low dose rate brachytherapy.

Taken together, the distinct features of RPT merit the reconsideration of current radiobiology paradigms that are predominantly based on data from EBRT [3, 4]. After a century of work, the latter is predicated largely on the 'target cell' theory as well as DNA as the primary mediator of radiation-induced cytotoxicity (Fig. 5.1). Yet, it is now clear that subcellular compartments other than the nucleus should be considered to be mediators of cytotoxicity and that cell death mechanisms that originate both close to (i.e. bystander effects) and farther from (i.e. the immune response) irradiated cells are at work as well (Fig. 5.1). As a result, it becomes clear that a more integrated view of radiation biology is needed and that the contribution of non-targeted radiation effects needs to be assessed in patients. While radiobiology is mostly evaluated in vitro or ex vivo, there is a critical need to develop non-invasive approaches that allow for the real-time in vivo monitoring of radiation-induced biological events during RPT. In recent years, molecular imaging has played a critical role in the measurement of molecular and cellular processes in humans and other living systems.

J.-P. Pouget (✉) · M. Tardieu · S. Poty (✉)
Institut de Recherche en Cancérologie de Montpellier (IRCM), INSERM U1194, Université de Montpellier, Institut Régional du Cancer de Montpellier (ICM), Montpellier, France
e-mail: jean-pierre.pouget@inserm.fr;
marion.tardieu@inserm.fr; sophie.poty@inserm.fr
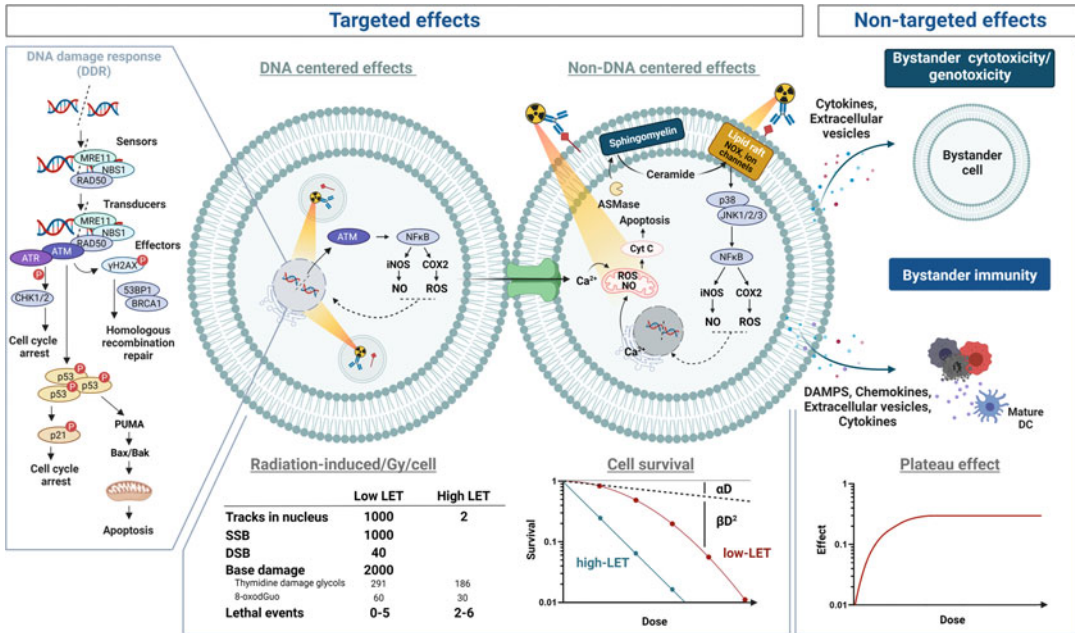
Fig. 5.1 General overview of the targeted and non-targeted effects induced by RPT. (Adapted from [3]). Created with BioRender.com

Indeed, imaging allows for the non-invasive monitoring of anatomical and functional parameters and may offer new resources to improve RPT. From medical images, radiomics extracts a high number of quantitative features and explores potential associations with biology and clinical outcomes when coupled to mathematical methods and artificial intelligence (AI) algorithms. In these pages, we will work to identify established and potential molecular imaging probes that may help delineate radiobiological events and thus augment our understanding of the radiobiology of RPT.

considerations, such as availability and ease of handling. Furthermore, very little concern was devoted to the administration schedule of RPT and its dosimetry. Until recently, in preclinical models but also in the clinic, one single injection was generally performed; the mean absorbed doses to normal tissues or tumours were not systemically calculated; and considerations related to the total absorbed dose, dose fractionation, overall treatment time and volume effects were not considered. Simply put, the concepts of radiobiology have historically been ignored.

5.2 The Fundamentals of Radiobiology

With a few notable exceptions (e.g. radioactive iodide, radium), RPT requires the development of radiopharmaceuticals based on tumour-targeting vectors – e.g. monoclonal antibodies, peptides, small molecules – that are labelled with radionuclides. Since the 1950s, the choice of radionuclide was generally dictated by practical

5.2.1 Overview of EBRT Clinical Radiobiology: An Empirical Experience

While RPT is fundamentally different from EBRT, the former has certainly benefitted from the latter's century of experience. A tremendous number of patients have been treated with a large number of EBRT schemes, allowing for the optimization of various radiotherapy parameters. In

contrast, although increasing, the number of patients treated with RPT remains relatively low.

To better understand what could or should be done in the context of RPT, it is interesting to note that the beginnings of EBRT have been empirical and somewhat random. The first cancer patients were treated with EBRT as early as 1896 by Victor Despeignes in Lyon [5]. Because of the very low output of X-ray tubes, most of the dose was delivered to the skin, then the dose-limiting organ. Skin was shown to have two types of response: (i) erythema and moist desquamation occurring several days/weeks after irradiation (early effects) and (ii) telangiectasia occurring several months after exposure (late effects). As dose rates were not yet calculated, erythema, moist desquamation and telangiectasia were used as the biological endpoints of normal tissue tolerance. Progressively, preclinical studies have been conducted to better understand the effects of radiation at the cellular level.

One of the first principles of radiobiology comes from the studies of Regaud, who irradiated human testis and observed that spermatogonia rather than spermatozoids exhibited the greatest effects [5]. These data were followed by Bergonie and Tribondeau's law that 'the radiosensitivity of a biological tissue is directly proportional to the mitotic activity and inversely proportional to the degree of differentiation of its cells' [5]. The principle of dose fractionation was introduced in 1928 by Krönig and Friedrich, who showed that the dose required to observe a skin reaction is higher when it is fractionated, suggesting that the skin can recover when the dose is delivered over several days [5]. Several years later, Coutard showed that, at specific doses, the reaction of the skin and mucosa depended on the total treatment duration, and the latter parameter became another principle of radiotherapy [5]. Furthermore, Baclesse observed that if the dose is limited to certain levels, skin mucositis and moist desquamation does not take place at 2.5 weeks and 6 weeks [5]. As a result, a second cycle can be given after 6 weeks, and higher doses can be given over a longer period. Treatments were then progressively optimised by varying the dose, the dose fraction and the intervals between fractions

so that the treatment duration was longer. Finally, Coutard arrived at dose-time-fractionation schedules close to those that are now regarded as a standard fractionation schedule: 2 Gy per fraction with daily fractionation over 6–7 weeks [5].

In the 1980s, the question of tissue radiosensitivity was first raised. The response of early- and late-responding normal tissues to each fraction was shown to differ. Therefore, dose hyperfractionation – e.g. the administration of 1.15 Gy per fraction three times per day with 4–6 h between fractions over 7–8 weeks – was adopted to exploit the differences in sensitivity between early-responding tissues (e.g. tumour, skin [erythema], bone marrow or kidney) and late-responding tissues (e.g. skin [telangiectasia], lung, jejunum, colon). This difference is due to the greater ability of some cells to repair damage at the molecular level between fractions.

5.2.2   The Linear Quadratic (LQ) Model of EBRT: Can We Extrapolate to RPT?

As EBRT aims at eradicating clonogenic tumour cells, the clonogenic assay developed by Puck and Marckus in the 1950s was immediately considered the reference technique for measuring the ability of irradiated cells to form colonies (i.e. determining clonogenic survival) [6]. In mammalian cells exposed to low-LET radiation, the curve of clonogenic survival vs. dose is a biphasic exponential (Fig. 5.1). In a semi-logarithmic plot, this survival curve is composed of a linear slope (i.e. the α parameter) followed by a curvature or shoulder at increasing doses (i.e. the β parameter). The parameter α (expressed in Gy^{-1}) corresponds to the intrinsic radiosensitivity of the cell (i.e. the probability per Gy for a cell to be killed when its sensitive target is crossed by a particle). The parameter β (expressed in Gy^{-2}) is related to the ability of the cell to repair radiation-induced damage (i.e. β decreases and survival increases when cells have time to repair, for example, between fractions). In contrast, as complex lesions of high-LET

particles are not repaired, survival curves are only fitted by the α parameter. The α/β ratio is a powerful tool to predict the radiosensitivity of tissues. To wit, both tumours and early-responding tissues generally have low α/β ratios since they cannot repair damage efficiently. Late-responding tissues, in contrast, have higher α/β ratios since they can repair their lesions between fractions if given enough time.

However, it is not clear whether the clonogenic survival of cells exposed to therapeutic radiopharmaceuticals (i.e. for RPT) can be evaluated using this LQ model. To answer this question, we first need to investigate the relationships between cell absorbed dose and clonogenic survival in the context of RPT and see if α and β parameters can be determined. Parameters other than the cell absorbed dose might have to be considered, including the radiopharmaceutical intracellular distribution and the involvement of intercellular communications.

5.2.3 Low Dose Rates Require Higher Absorbed Doses: What Happens During RPT

A low dose rate is often considered the ultimate form of fractionation. Its benefit was highlighted by Coutard in 1919, when he compared the skin reactions in patients with head and neck cancer to which he delivered either one or two low dose rate fractions of X-rays per day for 2 weeks or longer [5]. Shortly thereafter, in 1922, Regaud reported the benefits of low dose rate brachytherapy of cervical cancer using radium [5]. Regaud concluded that 'alternating rhythm of cellular reproduction provides an explanation of the efficacy of prolonged irradiation'.

EBRT is usually delivered at a dose rate between 1 and 5 Gy/min such that a conventional 2 Gy dose only requires few minutes, an amount of time insufficient for cells to repair their damage. Decreasing the dose rate (0.2 Gy/min vs. 1 Gy/min) facilitates the sparing of late-responding healthy tissues (e.g. lung) [7]. Similar sparing is observed when fractionated EBRT is used at 2 Gy/fraction and even more at 1 Gy/

fraction. With decreasing dose rate (< 1 Gy/min), the time required to deliver a given dose increases, and biological process can take place during irradiation and/or between fractions. For example, DNA damage repair, redistribution in the cell cycle, reoxygenation and repopulation progressively take place in the hours and days following irradiation. With low dose rates (e.g. 0.2 Gy/min dose rate, 2 Gy/fraction, 10 min treatment time), the induction of damage and repair occurs at the same time [8]. For many tumours and normal tissues, the repair half-times of sublethal damage are between 0.5 and 2 h, and complete repair generally occurs in less than 24 h (i.e. between 2 fractions of EBRT) [9]. However, some late-responding tissues may have longer repair half-times. At the cellular level, the repair half-time for base damage and DNA single-strand breaks (SSBs) is ~10 min, while that for DNA double-strand breaks (DSBs) is ~20 min. Therefore, irradiations lasting more than 10 min will significantly interfere with DNA repair. Assuming a minimal dose of 2 Gy, this corresponds to dose rates below the 0.2 Gy/min delivered by RPT. Ultimately, this creates the need, at least theoretically, for higher doses to counterbalance repair processes. Repopulation is a much slower process and depends on the doubling time of cells, which typically lies between days and weeks. Long treatment times favour the repopulation of cells from early-responding tissues such as tumours. The process will also be prominent at very low dose rates.

5.3 The Details

5.3.1 Physical Events Associated with α-/β-Particles and Auger Electrons

5.3.1.1 The Biological Effects of α-Particles Outweigh Those of Electrons and Gamma-/X-rays

In EBRT, a well-calibrated absorbed dose and dose rate of X-rays is delivered to target tissue in a collimated field. This scenario stands in stark contrast to RPT, as the decay spectra of
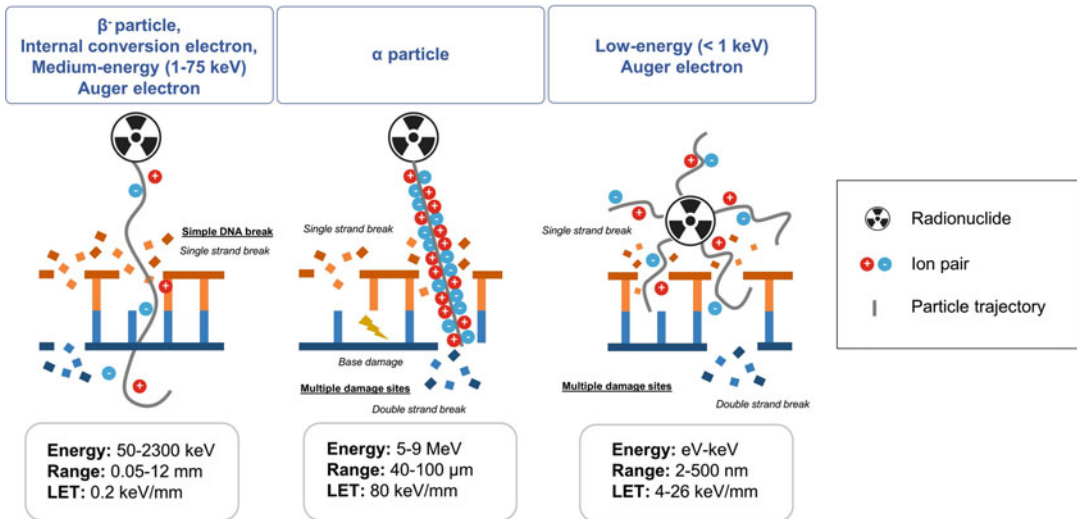
Fig. 5.2 A comparison of the energies, particle ranges and linear energy transfers of α-particles, β-particles and Auger electrons

radionuclides are generally more complex and composed of different types of radiation. Indeed, radionuclides can emit a broad range of particles, including α-particles (i.e. helium nuclei), electrons (β^- particles, internal conversion electrons [ICEs] and AEs), γ-rays and X-rays (Fig. 5.2). Generally, the 'category' of the emitter is determined by its predominant type of cytotoxic or genotoxic radiation. An important parameter for describing and classify radiation is linear energy transfer (LET), which is the average energy released per unit distance travelled by the particle. LET is an average value calculated by assuming a straight path like that of α particles (Fig. 5.2). However, for electrons, the range will be considered rather than the actual path. A distinction is generally made between low ($\sim$0.2 keV/μm) and high (50–230 keV/μm) LET particles (Fig. 5.2). In terms of their biological effects, high LET particles such as α-particles (and to some extent AEs) are more harmful than low LET electrons (β-particles or ICE) (Fig. 5.2). To round out the story, γ- or X-rays (used in EBRT) only have a therapeutic role when their number is high enough to create a significant probability that they will interact with biological tissues.

β^--particles, ICEs and AEs are electrons that differ in their origin and energy. β^--particles originate in the nucleus and can reach energies on the order of MeVs (and, consequently, ranges of cm in tissues) (Fig. 5.2). ICEs, in contrast, are monoenergetic electrons ejected from electronic shells outside the nucleus. AEs are also ejected from electronic shells, but their energy comes from the transition of electrons between two atomic shells following the electron capture of ICE processes. Although some AEs can have maximal energies of tens of keV (e.g. 78.2 keV and maximal range of 87 μm for ^{195m}Pt), most AEs have very low energy ($<$1 keV) that is deposited over distances $<$500 nm in tissues (Fig. 5.2). Moreover, AEs are emitted in cascades that create a variable number of electrons. Because of their very low energy, AEs can deposit massive amounts of energy in small volumes: up to 10^9 Gy in a 40 nm diameter sphere. While it is true that both β-particles and ICEs will behave like AEs at the end of their tracks, only one of the former is usually emitted per decay compared to up to 35 AEs. As a result, neither β-particles nor ICEs are likely to be as cytotoxic as their AE counterparts.

In RPT, radionuclides are referred as AE-emitters depending on the number of AEs they emit per decay as well as whether the other radiation types associated with their decay could reduce the benefit of their emitted AEs. Due to the volume effects previously defined in the introduction and the lack of cross-fire irradiation (due to their short range), AE-emitters must be administered in far higher activities than β-emitters. So far, there is no consensus on what yield of AEs is required to have a 'significant' therapeutic effect. However, since iodine-125 has long been the reference AE-emitter with 20–23 AEs/decay, it is safe to assume that ∼20 AEs/decay is a 'reasonable' threshold [10].

In conclusion, the biological effects of α-particles outweigh those of electrons and of gamma-/X-rays. The effects of AEs take precedence over those of other electrons if they are emitted in high numbers near radiation-sensitive targets (e.g. nuclear DNA, cell membrane, mitochondria).

5.3.1.2 Physical Interactions with Biological Matter

One general principle of physical interactions is that as charged particles interact with matter, their energy decreases, and the probability of their interactions with traversed matter increases. α-Particles, β-particles, ICEs and AEs emitted by radionuclides are all charged particles that will interact with matter according to electrostatic collisions, leading to ionizations and excitations of atoms constituting the matter. Consequently, electrons ejected during ionization processes (called secondary electrons) can in turn lead to a cascade of ionizations/excitations within the molecules with which they collide. This leads to the formation of clusters of ionizations before the electrons are finally stopped.

Beyond their nature and energy, the range and ionization power of particles must also be considered. The standard metric for this discussion is LET. The more the particle interacts with matter, the shorter its path, and the higher its LET. α-Particles are heavy and charged and thus strongly interact with matter such that their linear range in tissue is about 45–100 μm (Fig. 5.2). β-Particles

and ICEs, in contrast, are light particles that produce fewer ionizations/excitations per μm; their range can reach up to 12,000 μm. AEs have variable energies (few eV to tens of keV), and those having the highest energies can have a range similar to that of α-particles (e.g. 76 μm for AE emitted by ^{195m}Pt) but a low LET. Indeed, AEs with energies above 1 keV typically produce sparse and isolated ionizations and behave like low LET particles, while AEs with energies below 1 keV interact more with matter and produce dense ionizations (Fig. 5.2). Therefore, those low-energy (< 1 keV) AEs have a higher LET (4–26 keV/μm) over a short distance (< 500 nm). It is worth noting that while α-particles and low-energy AEs are both considered to have high LET, the cytotoxicity of AEs is only observed if they are emitted in the vicinity of sensitive subcellular targets. This is not a problem for α particles, which have a longer range than low-energy AEs and can reach targets at a distance greater than several cell diameters.

The track structure and energy deposition of these particles have been simulated using Monte Carlo approaches. For low-LET particles – i.e. β-particles, γ-rays, X-rays and high-energy AEs – sparse ionizations are produced in a rather large volume, and the energy deposition is somewhat homogenous on the cellular scale [11]. Conversely, high-LET particles (i.e. α-particles) produce high density ionizations along their linear track with little ionization farther afield. This, naturally, renders their energy deposition more heterogeneous. It is generally considered that 1000 sparse tracks are produced per Gy of absorbed low-LET radiation, while a mean number of 4 α-particle tracks is enough to deliver the same dose (Fig. 5.1).

5.3.2 Chemical Steps

The ionization and excitation of molecules described above leads to the breaking of chemical bonds between atoms and to the generation of free radicals. Two types of substrate molecules in cells are considered; on the one hand water, and on the other hand all the other cellular constituents.

5.3.2.1   Indirect Effects

In living beings, water is considered the first target of radiation. The radiolysis of water – generally referred as an 'indirect effect' of radiation – leads to the production of reactive oxygen species (ROS) including hydroxyl radicals, superoxide and hydrogen peroxide [2]. Hydroxyl radicals are exceptionally reactive and are thus responsible for most of the DNA damage [12, 13]. However, $HO^{\bullet}$ has a very short life, reacts within a few nm range from its origin, and thus cannot be transmitted to neighbouring cells. H_2O_2; however, can diffuse through the cell membrane. Because radiation-induced ROS are similar to those endogenously produced, they can be neutralized by the natural enzymatic and chemical antioxidant defences of the cell such as catalase, glutathione peroxidase, superoxide dismutase, glutathione, vitamin E and thioredoxin [14].

5.3.2.2   Direct Effects

In addition to the radiolysis of water, charged particles can directly ionize or excite biomolecules such as lipids, proteins and nucleic acids [15]. These so-called 'direct effects' are expected to predominate with high-LET particles because the high density of radicals produced from water leads to their recombination and thus the abrogation of indirect effects. That said, the situation might not be quite so straightforward, since radical scavengers or antioxidant enzymes have been shown to reduce the cytotoxic effects of high LET particles, indicating that radicals generated from water could be involved too. This could be explained by the fact that the effects of high LET particles result both from targeted effects (involving direct ionization of cellular compounds) and from non-targeted (secondary) effects observed in adjacent cells that would involve free radical mediated mechanisms.

5.3.2.3   Oxygen Effect

Oxygen was identified very early on as an important modulator of radiation response, particularly in the context of the radioresistance of poorly vascularized large tumours. Indeed, the radiosensitizing effect of oxygen has been known since the 1950s [16, 17]. This can be observed using clonogenic assays in which cells exposed to radiation in the presence of oxygen show an increased response. Subsequently, the oxygen enhancement ratio (OER) was introduced to quantify the radiosensitizing effects of oxygen. The OER is the ratio between the dose required to produce a given effect in the presence and absence of oxygen. At the molecular level, oxygen interacts with radiation-induced radicals to produce peroxyl radicals, thereby preventing the recombination of radicals that would decrease radiation cytotoxicity. For example, the yield of DNA lesions upon low LET irradiation was shown to decrease at low oxygen concentration. Low oxygen concentrations also increase the lifetime of radicals that can recombine or interact with radical scavengers. Because α-particles mainly act via direct effects, the concentration of oxygen within a tissue has only a weak influence on their effects; put differently, with α-particles, an OER is typically not observed. However, the bystander effects associated with α-particle irradiation *do* involve radical species, so some dependence on oxygen concentrations is inevitable.

5.3.2.4   Imaging Key Chemical Features: Oxygen and pH

5.3.2.4.1   Oxygen

Nuclear imaging probes capable of delineating tumour oxygenation levels could be particularly valuable in RPT for identifying tumours that are more (or less) likely to response to treatment. Not surprisingly, several probes have been developed and evaluated in a variety of contexts (Fig. 5.6a).

Hypoxia-targeted radiotracers have been explored in the context of EBRT. The most studied PET tracers for hypoxia are ^{18}F-labeled derivatives of 2-nitroimidazole. First developed as radiosensitizers for hypoxic cells, nitroimidazoles undergo an intracellular six-electron reduction in hypoxic cells, leading to the formation of a highly reactive intermediate that binds to macromolecules and traps the radiotracer within cells. ^{18}F-Fluoromisonidazole ([^{18}F] F-MISO), for example, was used in head-and-neck cancer patients to monitor tumour hypoxia and predict treatment outcome before and during

chemo-radiotherapy [18]. Tumour hypoxic sub-volume was shown to decrease in 64% of patients at week 2 post-treatment and in 80% of patients at week 5 post-treatment compared to the baseline scan (i.e. scan performed before the treatment initiation). Moreover, an analysis of 130 radiomic parameters allowed the identification of predictive features. Among them, 35 were able to predict treatment outcome at week 2, and the predictive value of 18 of them was confirmed at week 5. For example, low grey-level zone emphasis (LGZE), a texture feature that quantifies tracer distribution heterogeneity by emphasizing regions with low concentration, was able to differentiate between patients with and without local recurrence. While [^{18}F]F-MISO is the most commonly used hypoxia PET tracer, its high lipophilicity and slow passive diffusion result in relatively low tumour uptake and moderate contrast at best. Therefore, a second generation of nitroimidazole derivatives have been developed – e.g. ^{18}F-[1-(5-fluoro-5-deoxy-α-D-arabinofuranosyl)-2-nitroimidazole)] [^{18}F]F-FAZA – which have displayed enhanced hydrophilicity and improved signal-to-noise contrast ratios in clinical studies.

Another widely studied radiotracer for the imaging of hypoxia is radiocopper-labelled diacetyl-bis(N4-methylthiosemicarbazone) (ATSM). The mechanism of this radioligand's specific accumulation in hypoxic cells remains controversial. Briefly, it is believed that Cu(II)-ATSM diffuses rapidly into cells due to its high membrane permeability and low redox potential. Once internalized, Cu(II)-ATSM is reduced to Cu(I)-ATSM by microsomal and cytosolic enzymes including NADH/NADPH. Under normoxic conditions, Cu(I)-ATSM is reversibly oxidized back to Cu(II)-ATSM and diffuses out of the cell. But under hypoxic conditions, Cu(I)-ATSM is retained within the cell, upon which Cu(I) dissociates from the ligand and remains trapped. [^{60}Cu]Cu-ATSM was evaluated in clinical trials as a predictor of chemoradiotherapy response in patients with cervical cancer and rectal carcinomas [19, 20]. In both studies, patients with high tumour-to-muscle activity concentration ratios that indicated highly hypoxic tumours

exhibited poorer survival than those with lower ratios and thus more normoxic tumours. More recently, [^{64}Cu]Cu-ATSM was found to predict the efficacy of carbon ion radiotherapy [21]. More specifically, the in vitro uptake of [^{64}Cu]Cu-ATSM in different cell lines correlated to the relative biological effectiveness (RBE) of carbon ions over X-rays: high RBE cell lines showed greater uptake of [^{64}Cu]Cu-ATSM. This observation was later confirmed in mice xenografted with high and low RBE cell lines.

Finally, one can also highlight hypoxia via the targeted imaging of endogenous markers such as carbonic anhydrase IX (CA-IX) or hypoxia-inducible factor 1-alpha (HIF-1α) [22–24]. Ultimately, despite the promising results shown by these tracers in the context of EBRT and carbon ion radiotherapy, there have yet to be any clinical studies in which hypoxia-targeted probes have been used as theranostic imaging agents for RPT.

5.3.2.4.2 pH Imaging

The pH of a tissue is intimately related to its oxygen concentration, yet pH has not received much attention in the context of radiotherapy. Most normal tissues maintain a stable extracellular pH of around 7.4, while tumours typically have an acidic microenvironment (5.6–6.8). This phenomenon is connected to the increased anaerobic glycolysis (fermentation) of tumours known as the Warburg effect. The Warburg effect is associated with the breakdown of glucose into pyruvate which is in turn converted into lactate by lactate dehydrogenase. This process leads to the expulsion of lactate by monocarboxylate transporters and contributes to the acidification of the microenvironment. An acidic microenvironment is indicative of metabolically aggressive cancer cells and can also be associated with the inhibition of the anti-tumour immune response.

Several recent studies have reinforced the ties between tissue pH and the effects of irradiation. For example, the pH of irradiated skin (7.0 ± 0.3) has been shown to differ from non-irradiated skin (6.5 ± 0.2) [25]. In this study, the authors highlighted that a high pH (7.5 ± 0.3) combined with a low oxygen saturation in irradiated wounds created an unfavourable environment for efficient

wound healing post-radiation. Finally, pH has also been shown to be involved in the gene regulation in irradiated cells. Notably, an acidic microenvironment was shown to enhance the radiation-induced expression of p53 [26]. Altogether, pH modulation remains under-investigated in the context of (targeted) radiotherapy, and molecular imaging could offer a non-invasive approach to evaluate this physiochemical parameter (Fig. 5.6a).

In a recent study, Pereira et al. showed that external beam radiation activates the sodium/hydrogen exchanger isoform 1 (NHE1) upon radiation-induced glycolytic upregulation [27]. The activation of NHE1 leads to a reversal of the plasma membrane gradient, which in turn results in an alkaline intracellular pH and an acidic extracellular pH. In this same study, Pereira et al. validated the use of a radiolabelled peptide capable of selectively inserting into the membrane of cells under low pH conditions (pHLIP) for monitoring changes in the pH of the extracellular microenvironment following radiotherapy in mice bearing orthotopic pancreatic ductal adenocarcinoma xenografts [27]. The radiotracer – [^{67}Ga]Ga-NO2A-cysVar3 – produced an activity concentration of $8.6 \pm 0.7\%$ IA/g in irradiated tumours compared to $3.6 \pm 1.9\%$IA/g in non-irradiated control animals. This study highlights the potential of pH-sensitive molecular probes for the non-invasive assessment of response to radiotherapy.

5.3.3 Molecular Radiobiological Effects

5.3.3.1 DNA
All cellular substrates interact with low- and high-LET radiation, but nuclear DNA has long been identified as the main target because damage DNA is directly related to oncogenic transformation or cell death [28]. For example, hydroxyl radicals produced via the radiolysis of water can produce SSBs by reacting with the sugar or phosphate groups within the DNA backbone. The yield per cell and per Gy of DNA lesions in mammalian cells exposed to EBRT was found to be about 40 DSBs, 1000 SSBs, ~10,000 base modifications and 150 protein DNA crosslinks [11, 29].

If unrepaired or mis-repaired DSBs are the most deleterious form of DNA damage and can be involved in creating both genomic instability and chromosomal aberrations. Persistent DNA damage is also a hallmark of senescence. In EBRT, lesions can be repaired after treatment, and the repair of DNA lesions has been identified as a crucial parameter for radiosensitivity. In RPT, the issue of DNA repair is complicated because the low dose rate means that DNA lesions are repaired while new ones are being produced. Several studies have investigated the yield of DNA damage in vitro as well as in blood cells of patients treated with ^{131}I or [^{223}Ra]RaCl$_2$. However, no relationship could be established between the absorbed dose to the blood and the level of DNA DSBs in blood cells. Furthermore, while the activity in the blood decreased over time, the number of radiation-induced lesions per nucleus and per absorbed dose rate increased over time, suggesting a slowing down of DNA repair or, on the contrary, increased de novo formation [30–34]. Moreover, high LET radiation can produce several DNA modifications at the same site, referred to as 'multiple damage sites' or 'clustered DNA lesions' (MDS, defined as 2+ modifications per turn) (Fig. 5.2) [35–40]. These can include base damage, SSBs and DSBs. MDS cannot be measured by simple methods, and their nature makes them difficult to identify and classify. Due to an increased probability of radical recombination, the number of DNA lesions per dose unit (Gy) decreases when radiation LET rises. However, the probability of MDSs increases with increasing LET [37]. Whether AEs can produce complex DNA lesions will depend on the proximity of the emitter to the DNA, with the highest probability occurring when the radionuclide is incorporated into the DNA itself.

5.3.3.1.1 A Brief Overview of DNA Repair
DNA lesions are continuously produced in cells as the result of endogenous oxidative stress and of errors during DNA replication. As irradiated cells

are generally distributed in the different phases of the cell cycle, the presence of DNA lesions will lead to cell cycle arrest in G1 or G2/M-phase cells or to replication fork progression stalling in S-phase cells. For example, endogenous oxidative lesions (e.g. thymine glycols) on the most prominent oxidized bases in irradiated cells may hinder replication fork progression and generate DNA breaks.

Several DNA Damage Repair (DDR) Pathways

DNA lesions can be repaired by: (i) base excision repair (BER) for base damage, abasic sites and DNA single-strand breaks (SSBs); (ii) nucleotide excision repair (NER) for SSBs and DNA adducts; (iii) mismatch repair for base mismatches, small insertions and deletions and (iv) nonhomologous end-joining (NHEJ) or homologous recombination repair (HRR) for DNA double-strand breaks (DSBs) and crosslinks. Several homologous recombination pathways exist [41]. The major one is the error-free 'synthesis-dependent strand annealing' pathway that implicates RAD51 filaments (detailed below). The presence of single-strand DNA tails – as observed, for example, during DNA synthesis at replication forks, in telomeres or during NER – is not considered by the cell to be a 'normal' situation. Therefore, their presence/absence during the repair of DSBs is a key determinant in the choice between NHEJ and HRR.

Alternative DSB repair mechanisms can be involved when NHEJ and HRR do not operate. The first one is single strand annealing, an error-prone RAD51-independent pathway that joins two homologous 3′-ssDNA ends through annealing. Alternative end homology joining, or microhomology-mediated end joining, also uses 3′-ssDNA, like NHEJ but without NHEJ factors. Finally break-induced replication is involved when there is only one DSB end in RAD51-dependent mechanisms.

Considering now NHEJ, the system is also called 'classical' NHEJ (cNHEJ). It is an error-prone system that requires minimal sequence homology and rapidly joins two DNA ends. Conversely, the error-free HRR mechanism is slower and requires large sequence homology between the broken DNA and the donor DNA molecule, such as a sister chromatid in duplicated DNA [42].

From DNA Damage Recognition to DNA Repair

After DNA lesion recognition and the initiation of a cellular signalling cascade to promote DDR, cell cycle progression is blocked to facilitate DNA repair. For the recognition step, DNA DSBs are detected by the MRE11–RAD50–NBS1 (MRN) and Ku70/Ku80/DNA-PKcs (DNA-PK) complexes [43, 44]. This triggers the DDR through the recruitment and activation of the two major surveillance proteins belonging to the phosphatidylinositol-3-kinase (PI3K)-like kinase family: the serine/threonine protein kinase ataxia telangiectasia mutated (ATM; the main sensor of DNA damage), ATM- and Rad3-related (ATR) and DNA-dependent protein kinase (DNA-PK) [45–47] (Figs. 5.1 and 5.3).

ATR recognizes DSBs and is primarily involved in DNA DSB repair via HRR because it requires duplicated DNA. It occurs in S-phase cells with stalled replication forks or after the G2 phase. ATR recruitment requires ssDNA, for instance obtained after nuclease activation by ATM. Thus, ATR intervenes after ATM action and can in turn phosphorylate proteins, such as checkpoint kinase 1 (CHK1; essential for the intra-S and G2-M checkpoint response) and also BRCA1 to trigger HRR [46].

ATM full activation requires non-resected DNA ends. Its activation leads to the dissociation of ATM homodimers into monomers that phosphorylate and activate downstream protein kinases. These molecules act as transducers and effectors and phosphorylate their own substrate(s). Among them, the core Ku70 and Ku80 proteins (also known as XRCC6–XRCC5) bind to the ends of DNA DSBs before recruiting DNA-dependent protein kinase catalytic subunit (DNA-PKcs). This leads to the formation of a large synapse consisting of two DNA molecules brought into close proximity with the assistance of other associated proteins. Then, the two DNA ends are closely aligned into shorter synapses using XRCC4–DNA ligase IV (LIG4), the XRCC4-like factor (XLF) and DNA-PKcs. The
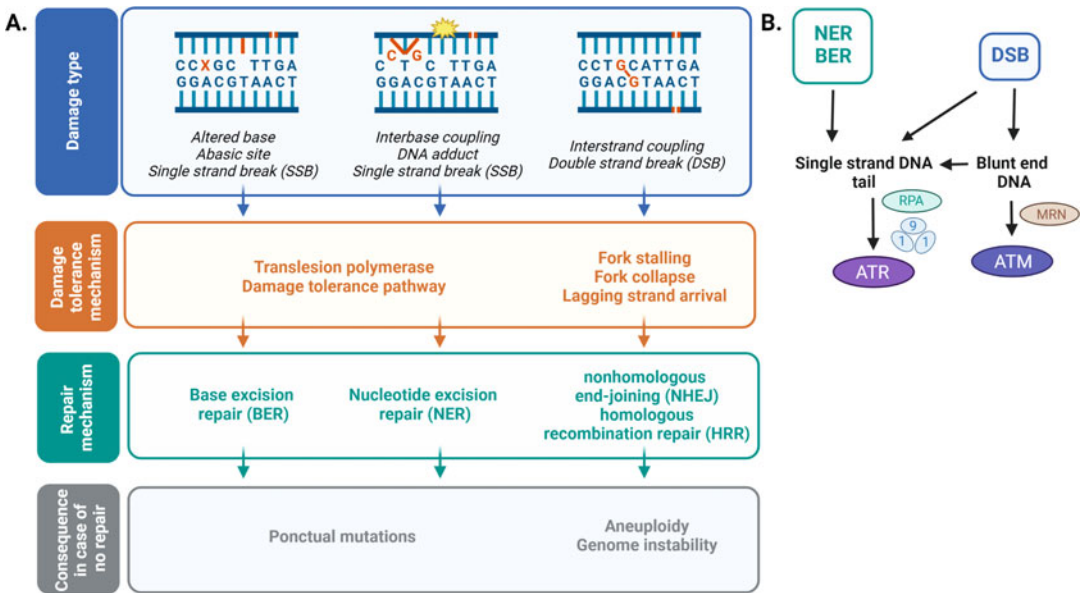
Fig. 5.3 Main radiation-induced DNA damage types. (**a**) Tolerance and repair mechanisms; (**b**) Main damage signalling pathways. Created with BioRender.com

ligation process is terminated by the nuclease Artemis and the DNA polymerases λ and μ. The default engagement of cNHEJ can be avoided by DNA end resection enzymes like MRN.

Phosphorylation of histone H2A (γH2AX) by ATM also is an essential step in the repair process. It allows the remodelling of the chromatin surrounding DSBs and the recruitment of other repair proteins, such as breast cancer type 1 (BRCA1), and p53-binding protein 1 (53BP1) that are involved in HRR promotion and repression, respectively (Fig. 5.1). BRCA1 and 53BP1 participate in the interaction between NBS1 and ATM that is essential for maintaining ATM at DSB sites [47].

Considering now the HRR pathway, it involves the core proteins MRE11, BRCA1 and BRCA2 but also the recombinase RAD51 and replication protein A (RPA). Typically, after Ku70-80 binding to DNA ends, an extended 3'-ssDNA is generated by the 3'-5' endonuclease resection activity of MRE11, which is part of the MRN complex. This generates ssDNA that is further extended up to 300 nucleotides away from the breakpoint by MRE11 3'−5' exonuclease activity. Long-range DNA resection is

terminated by the 5-3' exonuclease activity of exonuclease 1 (EXO 1). Then, RPA coats the new ssDNA to prevent pairing with other ssDNA molecules. To allow HRR, RPA must be replaced through the binding of BRCA2 to ssDNA and the formation of RAD51 nucleoprotein filaments. Such filaments are dynamic structures that, in association with BRCA1 and BRCA1-associated RING domain protein 1 (BARD1), participate in RAD51-mediated DNA strand exchange during HRR. It must be noted that homologous recombination deficiency (e.g. in BRCA-mutated tumours) increases sensitivity to PARP inhibitors. PARP recognizes ssDNA and is involved in the repair of SSBs and some base damage. Upon PARP inhibition, DNA breaks accumulate and are converted into DSBs, thus theoretically promoting HRR. In the absence of HRR, the error-prone NHEJ system is involved and contributes to cell killing [48].

DNA End Resection Triggers HRR in the S and G2 Phases

Interestingly, cell cycle-dependent kinase (CDK) activation in cells that enter the S or G2 phase also leads to the phosphorylation and activation of

proteins involved in HRR and of DNA resection proteins required for HRR. Conversely, 53BP1 favours cNHEJ (during the G1 phase) by protecting DSB ends from resection by the DNA end-resection machinery in the G1 phase. 53BP1 is recruited to chromatin via binding to histone H4 monomethylated or demethylated at lysine 20 (H4K20me1 and H4K20me2) and to histone H2A. Therefore, cNHEJ operates throughout the cell cycle, whereas HRR is mainly restricted to the S and G2 phases. DDR is reduced in cells in the late G2 phase and mid-prophase to allow for progression through mitosis.

ATM and ATR Downstream Proteins

ATM phosphorylates and activates downstream protein kinases that act as transducers and effectors and in turn phosphorylate their own substrate(s). For instance, p53 is stabilized by phosphorylation and accumulates to activate other proteins, including p21 that acts on CDKs. CDKs in turn control cell cycle arrest (i.e. G1-S, intra-S and G2-M checkpoints) to give cells time to repair lesions before entering mitosis or to engage in the intrinsic apoptosis process that involves mitochondria and the activation of pro-apoptotic molecules of the BCL2 family (Fig. 5.1).

If the level of damage is too high, p53 can also participate in the induction of apoptosis in the irreversible arrest of proliferation (i.e. senescence). Indeed, p53, which is mutated in 50% of cancers, is one of the many key proteins in the response to RPT. However, p53's role in RPT is not clearly defined because of the heterogeneity of RPT models (radionuclide, vector and cancer type). For example, our group reported that AE-based RPT using ^{125}I-labeled mAbs is p53-independent [49]. Conversely, other authors suggested that the p53-stabilizing peptide VIP116 might potentiate β-RPT [50].

Other ATM substrates include proteins involved in the G1-S (p21), intra-S (FANCD2, BRCA1, SMC1) and G2-M (CHK2) cell cycle arrest, DNA repair poly(ADP-ribose) polymerase 1 (PARP1) and DNA-PK as mentioned above. These factors enable DNA repair through the NHEJ pathway before replication and mitosis.

As patients resistant to prostate-specific membrane antigen (PSMA)-targeted RPT often present mutations in DDR genes, Privé et al. retrospectively investigated 40 tumour biopsies from patients with metastatic castration-resistant prostate cancer (mCRPC) to explore the impact of the DDR on the response to PSMA-targeted RPT. Surprisingly, they *did not* find a correlation between pathogenic DDR gene alterations and higher response to RPT [51]. Conversely, van der Doelen et al. showed in 13 patients with mCRPC treated with [225]Ac]Ac-PSMA-617 that higher PSMA expression and DDR gene alterations (determined by immunohistochemistry) were associated with longer patient overall survival [52]. Zhu et al. also reported in one patient with a neuroendocrine tumour that HRR defects may predict treatment response to [^{177}Lu]Lu-DOTATATE [53].

Many preclinical studies have combined RPT with DDR inhibitors. A synergistic effect was observed for a mesothelin-targeted [227]Th-labeled radioconjugate and ATR or PARP inhibitors in ovarian cancer xenograft models [54]. PARP inhibitors also were successfully used in combination with α-, β- or AE-RPT in preclinical models [55–59] and in several clinical trials with [^{177}Lu]Lu-DOTATATE, [^{177}Lu]Lu-PSMA-617 and [223]Ra]Ra-dichloride.

5.3.3.1.2 Imaging DNA Damage Signalling

The imaging and quantification of DNA damage in cells and tissues has been investigated in the context of aging, mutagenesis, genotoxicity and the response to radiotherapy. With respect to the latter, pulsed field gel electrophoresis (PFGE) and neutral comet assays have historically been used to demonstrate the linear correlation between DNA damage and irradiation dose during acute EBRT. Although very precise, PFGE suffers from a lack of sensitivity and is thus not used anymore. Therefore, alternative approaches allowing for the longitudinal and non-invasive imaging of DNA lesions are desirable. Radiotherapy does not cause DNA damage events – either SDBs or DSBs – in sufficient numbers for direct molecular imaging. Therefore, alternative molecular imaging targets

have been explored, most notably the imaging of DDR proteins such as 53BP1, γH2AX and PARP.

In clinical studies, the quantification of DDR proteins is performed by immunohistochemistry/immunofluorescence on biopsied samples. However, biopsy can only offer the examination of a few tumour sites and can be biased by tumour heterogeneity. Molecular imaging, however, offers the major advantage of in vivo longitudinal studies on a high number of lesions as well as non-targeted healthy organs. Several fluorescence and nuclear imaging approaches for visualizing the DDR have been developed. However, such indirect downstream strategies inevitably raise concerns, for example whether the expression of the detected protein can be correlated to the number of DNA lesions. Furthermore, the presence of these repair markers does not necessarily indicate whether the break repair is complete, and repair foci can also exist in the absence of DSBs [60]. The nature of the DDR as a target also presents several design challenges for radiopharmaceuticals: for example (i) how can probes be driven within cell nucleus when most molecular probes target membrane bound receptors? and (ii) will nuclear probes themselves induce the DDR? Finally, in the specific context of RPT, complex lesions (e.g. MDS) are not properly recognized by DNA sensors (e.g. H2A), which might lead to an underestimation of radiation-induced damages using DDR-targeted probes. The continuous low dose rate of RPT might not induce sufficient DDR to be detected by molecular probes and repair processes will occur while the irradiation is on-going. However, our group showed in colorectal cancer cell lines that DNA damage induced by AE-mediated RPT was effectively detected by the DDR [61]. It is also likely that the biological response to RPT is more complex than after EBRT and will involve signalling pathways between cells that can generate delayed, non-dose-related DNA damage.

Despite the caveats discussed above, two DDR proteins have attracted particular attention as targets for molecular imaging: γH2AX and PARP1 (Fig. 5.4a) [62]. Notably, both SPECT

(^{111}In) and PET (^{89}Zr) probes for the in vivo quantification of γH2AX were developed based on an anti-γH2AX antibody. Cornelissen et al. appended a TAT peptide to the antibody in hopes of solving the problem of γH2AX's intranuclear localization [63]. The latter peptide combines cell penetrating properties for trans-membrane movement and a nuclear localizing signal (NLS) to bind importins for nucleocytoplasmic trafficking. The authors demonstrated the colocalization of an AF488-anti-γH2AX-TAT with γH2AX foci in cells post-external beam irradiation using confocal microscopy. While the fluorescent probe demonstrated membrane and cytoplasmic uptake 1 h post-irradiation, that accumulation disappeared by 23 h, and a focal nuclear uptake was solely observed. In vivo, the uptake of [^{111}In]In-DTPA-anti-γH2AX-TAT and [^{89}Zr]Zr-DFO-anti-γH2AX-TAT was demonstrated to be proportional to the number of γH2AX foci per cell observed by immunohistochemistry as well as the tumour absorbed dose by external beam radiation (Fig. 5.4b) [63, 64]. As we have noted above, the use of radionuclides to image DDR is a controversial issue, as the ionizing radiation could itself cause further DNA damage and therefore the accumulation of DDR proteins. Thus, it was important for the authors to show that at the specific activity used for imaging (i.e. 0.1–1.0 MBq/μg) with [^{111}In]In-DTPA-anti-γH2AX-TAT and [^{89}Zr]Zr-DFO-anti-γH2AX-TAT did not significantly decrease the cell surviving fraction in a clonogenic assay. However, [^{111}In]In-DTPA-anti-γH2AX-TAT was shown to amplify DNA damage at specific activities >3 MBq/μg [65].

In the context of RPT, [^{111}In]In-DTPA-anti-γH2AX-TAT facilitated the non-invasive visualization of the DNA damage response after [^{177}Lu]Lu-DOTATATE treatment in a preclinical mouse model of pancreatic neuroendocrine cancer [66]. O'Neill et al. underscored the correlations between ^{177}Lu distribution, local absorbed dose heterogeneity and the uptake of [^{111}In]In-DTPA-anti-γH2AX-TAT using a dual isotope SPECT imaging strategy (Fig. 5.4c) [66]. [^{111}In]In-DTPA-anti-γH2AX-TAT showed increased
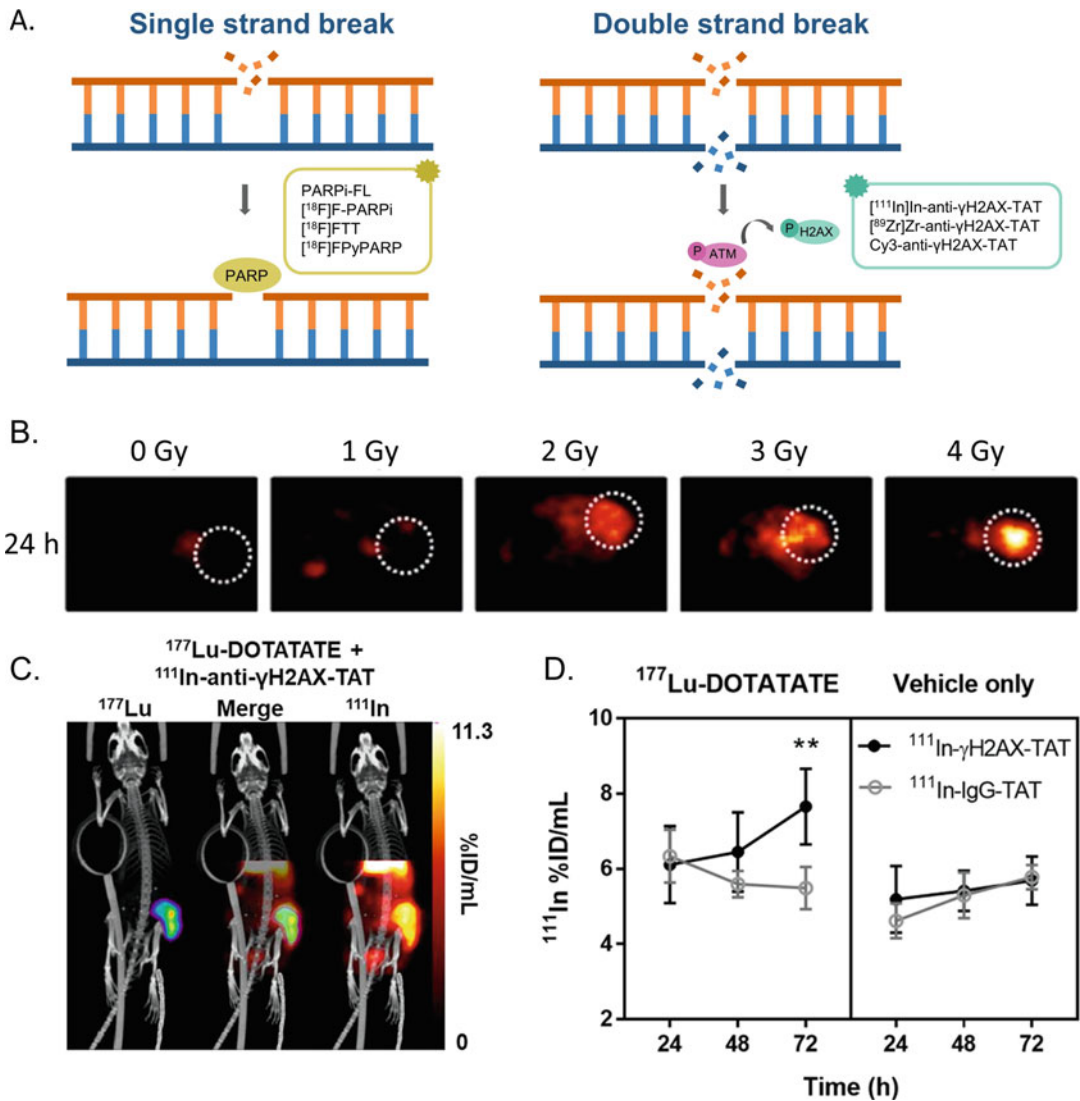
Fig. 5.4 Imaging DNA damage signalling. (**a**) Brief overview of DNA damage biomarkers for molecular imaging and their corresponding targeted molecular probes; (**b**) Transverse SPECT images acquired 24 h after the administration of [^{111}In]In-anti-γH2AX-TAT to mice bearing subcutaneous MDA-MB-468 xenografts that had been subjected to external beam irradiation. The white circles indicate the tumour; (**c**) Dual-isotope SPECT/CT images of mice bearing CA20948 tumours that had been treated with [^{177}Lu]Lu-DOTATATE (20 MBq, 0.33 μg) and were subsequently injected with [^{111}In]In-anti-γH2AX-TAT (5 MBq, 5 μg) 72 h post-RPT. The images were acquired 71 h after the administration of [^{111}In]In-anti-γH2AX-TAT; (**d**) Tumour uptake of [^{111}In]In-anti-γH2AX-TAT and isotype control [^{111}In]In-IgG-TAT at various times after the treatment of mice bearing CA20948 tumours with [^{177}Lu]Lu-DOTATATE (20 MBq, 0.33 μg) or vehicle control

uptake in tumours treated with [^{177}Lu]Lu-DOTATATE compared to animals treated with an isotype control radioimmunoconjugate ([^{111}In]In-DTPA-IgG-TAT) or vehicle alone (Fig. 5.4d). Poty et al. further confirmed the potential of [^{89}Zr]Zr-DFO-anti-γH2AX-TAT for the early monitoring of the DDR following ^{225}Ac- and ^{177}Lu-RPT in a preclinical mouse model of pancreatic adenocarcinoma [67]. However, this study showed no difference in [^{89}Zr]Zr-DFO-anti-γ

H2AX-TAT tumour uptake after α- and β-RPT when the former resulted in prolonged animal survival compared to the latter. This lack of correlation between survival and early DDR highlights that DNA damage is not the sole radiobiology paradigm of merit and that other radiation-induced biological effects (including bystander effects) should be considered.

Both PARPi-FL and [^{18}F]F-PARPi – a fluorescent and ^{18}F-radiolabeled PARP1-targeted small molecule derived from the structure of Olaparib – have been evaluated for the in vivo molecular imaging of PARP1, a DDR protein that is over-expressed in a wide array of cancers. It was shown that the replacement of the cyclopropane group in Olaparib with a BODIPY-based fluorophore or a prosthetic group for ^{18}F-labeling did not affect significantly affect the affinity or specificity of the l small molecule for its target [68]. The preclinical evaluations of both probes in human xenograft models validated their specific accumulation in tumour tissues and led to their clinical translation. PARPi-FL is currently under investigation for the early detection of oral squamous cell carcinoma after topical application [69]. [^{18}F]F-PARPi, in contrast, is currently being evaluated for the imaging of primary and metastatic head and neck cancer lesions [70].

While PARP1 molecular probes have been validated for the imaging of malignant tissue at the preclinical and clinical stage, their application for the evaluation of tumour response to (radio)-therapy remains under-explored. Kossatz et al. used PARPi-FL to visualize a correlation between external irradiation and DNA damage response in a murine model of oral cancer [71]. The probe showed an increased in median radiant efficiency in FaDu tumours within the first 48 h post-external irradiation, $3.2 \pm 0.6 \times 10^8$ for tumour-bearing mice versus $2.3 \pm 0.7 \times 10^8$ for controls. These results were correlated to an increase in PARP1 expression ex vivo, suggesting that PARP1 expression can be measured using PARPi-FL at the whole tumour level. Despite no reports in the context of RPT, this study highlighted the potential of PARPi-FL as a molecular imaging probe of the radiation-induced DNA damage response. Clearly, further studies in the context of RPT are warranted.

5.3.3.2 Lipid Peroxidation and Cell Membrane

DNA is not the only biomolecule subject to radiation-induced damage. Indeed, lipids constituting cellular membranes – specifically their polyunsaturated fatty acids (PUFAs) – can also be oxidized by direct and indirect (i.e. ROS) radiation effects [72]. The resulting carbon-centred radicals participate in chain reactions that can oxidize other PUFAs before leading to lipid-derived metabolites, namely malonedialdehyde (MDA) or 4-hydroxyl-2-nonenal (4HNE). In addition, Haimovitz et al. showed in endothelial cells the role of ceramide as an apoptosis messenger after exposure to high EBRT doses [73]. Ceramide is a sphingolipid that can be formed during the hydrolysis of sphingomyelin (another member of the sphingolipid family) upon the activation of acidic sphingomyelinase by hydroxyl radicals (Fig. 5.1). The coalescence of ceramide into an enriched large domain at the cell surface leads to the activation of signalling pathways involved in cell death or the activation of ion channels. Our group showed that this phenomenon takes place during α- and AE-RPT, suggesting that the local deposition of high levels of energy is required to activate this pathway [72]. In the context of AE-emitters targeting the cell membrane, we demonstrated that signalling pathways turned on by ceramide-enriched large domains activate cyclooxygenase-2 (COX-2) and nitric oxide synthase (NOX), which generate a second wave of ROS and RNS in cells. Those species can then cause further damages to cellular constituents including DNA.

5.3.3.3 Other Extranuclear Targets and Intracellular Communications

Since the first studies focused on the irradiation of the cell cytoplasm [74, 75], the role of this compartment in radiotherapy has been reconsidered. Indeed, the development of α-(external) microbeams that allow for the specific irradiation of subcellular compartments has facilitate the further study of effects of radiation on different cellular compartments. Along these lines, it has

been shown that cytoplasmic irradiation induces oxidative DNA damage and lipid peroxidation, as shown by the increased formation of 4HNE [76–78]. In the cytoplasm, mitochondria – organelles that play a central role in cell metabolism, energy homeostasis and apoptosis – represent up to 25% of the cell volume, which means that the probability that they will be hit by particles is high. Mitochondria contain a circular double-stranded genome (mitochondrial DNA, mtDNA) that encodes proteins and ribosomal RNAs. Reports indicated that the number of mitochondria, their biogenesis and their function were all modified by irradiation with α-particles [79–82]. High-LET irradiation was also shown to cause mitochondrial depolarization and fragmentation [79, 83]. This was accompanied by the participation of the mitochondrial fission regulator, dynamin-related protein 1 (DRP1) in the degradation of dysfunctional mitochondria through induction of autophagy to maintain cellular energy homeostasis. However, mitochondrial fission activated the phosphorylation of the AMP-activated protein kinase (AMPK) and next of ERK1/2 signalling pathways leading to autophagy inhibition and to cell death [84]. Radiation-induced mitochondria damage leading to the dysfunction of respiratory complex I was also observed and created persistent oxidative stress through the increased production of intracellular ROS and further mitochondrial DNA damage. Not surprisingly, the mitochondria are not the only cytoplasmic organelle shown to be impacted by irradiation. Indeed, cells exposed to gadolinium nanoparticles and irradiated have also been shown to contain altered lysosomes (unpublished results). Finally, the expression of tyrosine kinases (e.g. epidermal growth factor receptor), protein kinase C, MAPKs, JNKs, phospholipase C, NF-κB-mediated COX-2 and cytokines as well as the activation of nitric oxide synthase and mechanisms responsible for cytoplasmic Ca^{2+} homeostasis have also been shown to be modulated by radiation (reviewed in [85]).

5.3.3.4   Cellular Cycle Arrest

The activation of the DDR leads to cell cycle arrest of the damaged cells at four specific checkpoints [42, 86, 87]. First, cells irradiated during the G1 phase will stop their progression according to mechanisms under the control of ATM, p53 and p21, preventing entry into S phase. Second, irradiated cells can slow down their progression through S phase with the involvement of ATM, Chk1/Chk12, CDC25A/CDC25C, BRCA1 and BRCA2. Third, irradiated cells can be blocked in early G2 phase to prevent mitosis, a process that is ATM, Chk1/Chk12, CDC25A/CDC25C, BRCA1 and BRCA2 dependent. And fourth, cells are blocked into late G2 (an ATR, Chk1 and CDC25A/CDC25C dependent process).

The progression through the cell cycle is under the control of cyclin-dependent kinases (CDKs) and cyclins that will control those cell cycle checkpoints. In cancer, they are disrupted such that cells can proliferate after the activation of growth-promoting oncogenes, leading to replicative stress and subsequent DNA damage. However, while it is generally thought that cell cycle arrest during EBRT allows the cell more time to repair its DNA, this arrest seems to influence the *quality* of repair rather than the repair itself, as the cell's fundamental radiosensitivity does not seem to be affected. Studies have investigated the role of RPT on cell cycle progression [88–91]. For example, in a lymphoma model, our group showed that cell cycle arrest inhibitors (e.g. MK-1775 and PD-166285 that inhibit G2/M cell cycle progressions) sensitize tumour cells to [^{177}Lu]Lu-lilotomab [89]. This is likely generalizable to tumours with reduced inhibitory CDK1 phosphorylation, such as transformed follicular lymphoma. In ovarian cancer, a ^{177}Lu-labelled variant of the anti-L1CAM antibody chCE7 was also successfully combined with MK1775 [91]. In contrast, others showed that blocking myeloma cells in G2/M phase by combining α-RPT with paclitaxel and doxorubicin led to radiosensitization [90].

5.3.3.5   Cell Proliferation

Despite the induction of DNA damage, cell can repair their damage and continue to proliferate. In the clinic, the assessment of cell proliferation status is largely performed by staining of biopsy
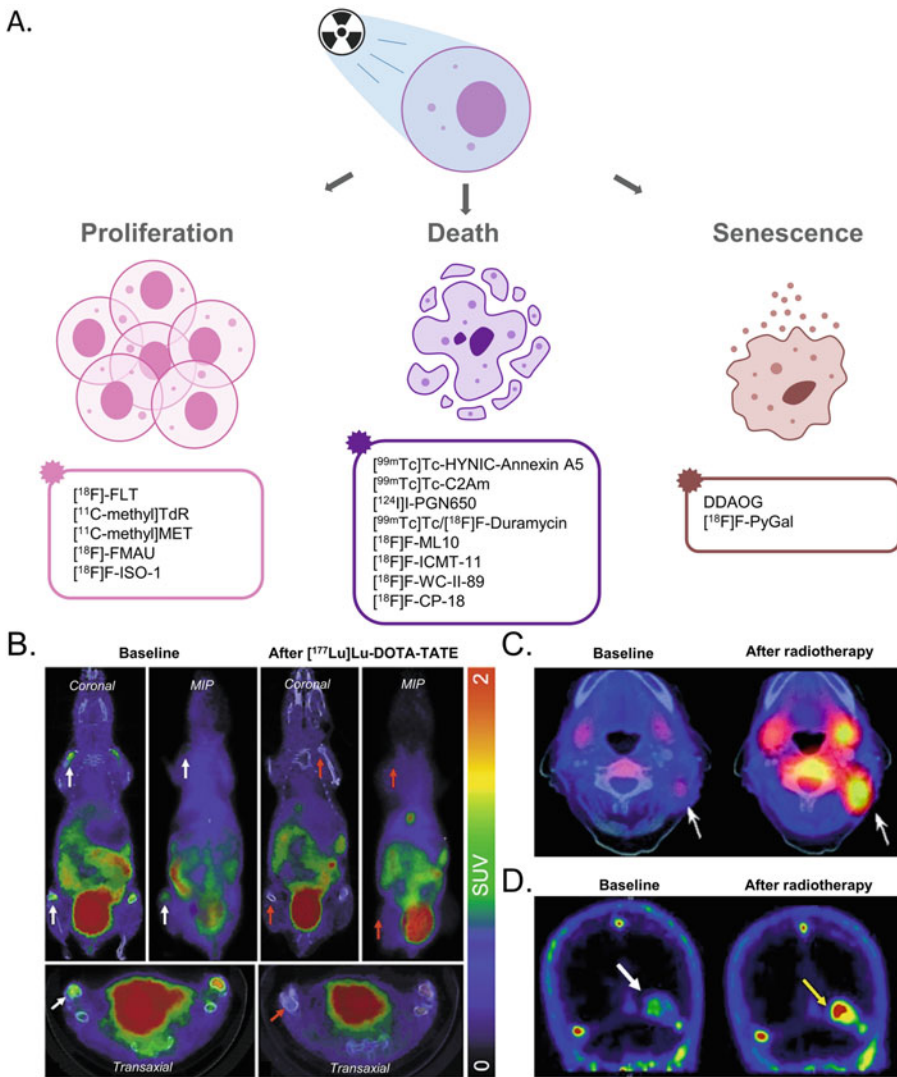
Fig. 5.5 Imaging cell vitality. (**a**) A brief overview of molecular probes for the imaging of cell vital status after irradiation; (**b**) [^{18}F]FLT PET/CT imaging in healthy Balb/cJBomtac mice. [^{18}F]FLT uptake was detected in the bone marrow cavities (white arrows) of the baseline scan. The mice were then treated with 150 MBq of [^{177}Lu] Lu-DOTATATE and imaged again with [^{18}F]FLT. The uptake of [^{18}F]FLT in the marrow cavities (red arrows) was abolished after [^{177}Lu]Lu-DOTATATE therapy, indicating a marked decrease in proliferation. (**c**) [^{99m}Tc] Tc-HYNIC-Annexin A5 SPECT/CT imaging in a 60-year old patient with non-Hodgkin lymphoma. Low-dose radiotherapy induced an increase in [^{99m}Tc]Tc-HYNIC-Annexin A5 uptake in the tumour (white arrow), salivary gland and cervical bone marrow compared to the baseline scan. (**d**) [^{18}F]F-ML-10 PET imaging in a patient with brain metastases treated with whole-brain radiation therapy at 30 Gy in ten daily fractions. While the baseline scan showed a basal apoptotic load, the treated area demonstrated increased [^{18}F]F-ML-10 uptake, reflecting radiation-induced apoptosis

samples for Ki-67, an invasive method that limits the longitudinal follow-up of the proliferative index of multiple tumour lesions. Therefore, the use of molecular imaging probes to assess cell proliferation in vivo could be a useful tool for monitoring the radiobiological response to RPT (Fig. 5.5a).

One established molecular probe for the in vivo assessment of cell proliferation is 3′-deoxy-3′-[^{18}F]fluorothymidine ([^{18}F]-FLT). *In cellulo*, [^{18}F]-FLT is phosphorylated by cytosolic thymidine kinase 1 (TK1) to create FLT-monophosphate and subsequently into the corresponding diphosphate and triphosphates. TK1, a key enzyme in DNA precursor synthesis, is upregulated during cell cycle S phase and is an indicator of active cell proliferation. The substitution of the hydroxyl group at the 5′-end of thymidine with fluorine prevents its binding to DNA. Moreover, once in a triphosphate state, [^{18}F]-FLT remains trapped intracellularly due to its high hydrophilicity. It follows that cancer cells with high proliferative index should exhibit high uptake of [^{18}F]-FLT, and a significant decrease in [^{18}F]-FLT uptake should be observed after therapy.

In preclinical models, Pan et al. used PET/CT to demonstrate that the kinetics of [^{18}F]-FLT were impacted 1-day post-external beam irradiation at doses of 5 Gy and higher [92]. In the clinic, [^{18}F]-FLT uptake in patients with non-small cell lung cancers was shown to correlate with Ki-67 score [93]. Tumour proliferation after curative-intent radiotherapy (46 Gy) in non-small cell lung cancer was further evaluated using [^{18}F]-FLT in 5 patients and compared to [^{18}F]-FDG (metabolism) and [^{18}F]F-MISO (hypoxia). The authors reported a significant decrease in the SUV_{max} of [^{18}F]-FLT in both tumours and nodes, while no statistical differences were observed for [^{18}F]-FDG and [^{18}F]F-MISO [94].

The application of [^{18}F]-FLT imaging to RPT has been very limited. Ahlstedt et al. reported the use of [^{18}F]-FLT to evaluate radiation damage to the bone marrow of mice following treatment with [^{177}Lu]Lu-DOTATATE (Fig. 5.5b) [95]. Compared to mice treated with vehicle alone, mice treated with [^{177}Lu]Lu-DOTATATE showed a marked decrease in [^{18}F]-FLT SUV_{max} from baseline in the different marrow cavities. Despite the lack of tumour-bearing mice, this study highlights the potential of [^{18}F]-FLT to non-invasively image RPT-induced changes in cell proliferation.

5.3.3.6 Cell Death

Cells can die in a variety of ways. The mechanisms of cell death include apoptosis, mitotic death, necrosis, senescence, pyroptosis (an inflammatory form of lytic programmed cell death), ferroptosis (an alteration of the cellular redox metabolism) and anoikis (an extracellular matrix anchorage-independent cell death). DDR proteins play a central role in these outcomes. The diversity and complexity of cell death pathways raise the questions of how cell death can be quantified and whether the different mechanisms can be distinguished. Because radiation-induced cell death can be delayed in time and occur after several rounds of the cell cycle, clonogenic assays were the first gold standard method for measuring cell death [96]. Clonogenic assays describe the ability of cells to form a new colony after several cell divisions (12 days at least). However, the clonogenic survival of senescent cells is equal to zero while the cells are alive and can still secrete factors that can influence the growth or death of neighbouring cells. Clonogenic assays are also limited to in vitro evaluation.

Not surprisingly, imaging probes have been evaluated in this context. Established molecular probes for cell death allow for the monitoring of key cell death features, including cell membrane asymmetry and permeability, changes in mitochondrial transmembrane potential and increased proteolysis (caspase activation). As these phenomena are not restricted to one mechanism of cell death, the imaging probes do not delineate only a single pathway of cell death. Therefore, changes in the uptake of a cell death-targeting probe may result from multiple mechanisms.

The disturbance of cell membrane asymmetry is a feature of apoptosis, pyroptosis, mitotic catastrophe and anoikis. It is characterized by the translocation of phospholipids, specifically phosphatidylethanolamine (PE) and phosphatidylserine (PS), from the inner to the outer leaflet of the cell membrane. Consequently, PE and PS appear as potential target for cell death imaging. Along these lines, it is also important to note that both PE and PS might become accessible during necrosis after integrity of the cell

membrane has been lost. Annexin A5 (also commonly referred as Annexin V) is a protein isolated from the human placenta that has been studied for its Ca^{2+}-dependent binding of negatively charged PS. Derivatives of annexin A5 for nuclear, MR and fluorescence imaging have been developed and evaluated at the preclinical and clinical stages. For example, $[^{99m}Tc]Tc$-HYNIC-Annexin A5 showed increased uptake in subcutaneous lymphoma xenografts as external beam radiation dose increased [97]. In this same study, the uptake of the SPECT tracer was found to have a linear correlation with the number of apoptotic (i.e. TUNEL-positive) cells.

In the clinic, studies in 33 patients with malignant lymphoma, leukaemia, non-small cell lung cancer and head and neck squamous cell carcinoma reported a marked increase in $[^{99m}Tc]Tc$-HYNIC-Annexin A5 uptake after radiotherapy compared to baseline in patients with complete or partial response (Fig. 5.5c) [98]. Yet despite promising results, probes based on Annexin A5 probes failed to meet clinical expectations due to their low signal-to-noise ratios related to their slow clearance and high non-specific accumulation in healthy organs especially the liver and kidneys. Moreover, the evaluation of a patient's response to therapy with an Annexin A5-based imaging agent would require multiple scans after treatment, a complex protocol that hampered clinical enthusiasm.

Altered cell membrane permeability is a hallmark of apoptosis. This phenomenon is accompanied by the permanent acidification of the external plasma membrane leaflet and cytosol and an activation of γ-scramblase. The APOSENSE family of compounds have been developed to detect these apoptosis-related alterations. These small molecules possess an amphiphatic (both hydrophilic and hydrophobic) structure that serve as a membrane anchor as well as a charged moiety that prevents the crossing of the healthy cell membrane. Fortuitously, all of the compounds in the group contain an inherently fluorescent dansyl group, and one was labelled with ^-F to create a probe – $[^{18}F]F$-ML10 – for apoptosis imaging. In ten patients with brain metastases treated with whole-brain irradiation (30 Gy), a significant increase in $[^{18}F]F$-ML10 uptake was observed in the tumour lesions after radiotherapy (Fig. 5.5d) [99]. This early assessment of response also correlated with later changes in anatomical dimensions as observed by MRI. However, to the best of our knowledge, no evaluation of $[^{18}F]F$-ML10 in the context of RPT has yet to be reported despite the probe's clear promise.

Cell death is associated with a proteolytic cascade mediated in large part by caspases. Caspase-3 is a key player in apoptosis and has attracted a lot of attention as a target for molecular imaging. However, the design of caspase-targeted probes is a challenge, as caspases are highly homologous and share a high percentage of structural and active site identity. Moreover, any caspase-targeted radiopharmaceutical must be able to cross the plasma membrane because caspases are located in the cytoplasm. For caspase-3 imaging, both small molecule and peptide-based nuclear probes have been evaluated. The small molecule-based radiotracer, $[^{18}F]F$-ICMT-11, showed higher uptake in chemotherapy-treated tumours compared to controls in murine cancer models [100]. The subsequent clinical investigation of $[^{18}F]F$-ICMT-11 in healthy volunteers as well as patients with breast and lung cancer revealed a suboptimal mixed renal and hepatobiliary excretion profile that leads to high tumour-to-background activity concentration ratios [101]. Low tumour uptake was reported in cancer patients after first-line chemotherapy, which was imputed to poor apoptosis induction and the heterogeneous response within the tumours [102].

A different imaging agent – $[^{18}F]F$-CP-18, a caspase-3/-7 substrate based on the pentapeptide DEVDA – demonstrated contrasting results in preclinical evaluations. Specifically, increased uptake was reported in apoptotic tumours in murine cancer models [103]. However, low absolute uptake values were reported for $[^{18}F]F$-CP-18, raising doubts regarding the level of apoptosis induced and the specificity of the tracer for its target. A phase II clinical trial with $[^{18}F]F$-CP-18 was initiated in 2012, but this trial was rapidly withdrawn without official explanation. To our knowledge, no evaluation of the radiopharmaceutical has been performed in the context of RPT.

5.3.3.7 Senescence

Cellular senescence is characterized by permanent cell cycle arrest and the activation of a senescence-associated secretory phenotype (SASP). Senescence attracted a great deal of attention in oncology during last decade, and its ambivalent (protective and stimulatory) role has been highlighted in the context of cancer. Recent investigations have led to the addition of senescence to Hanahan's Hallmarks of Cancer in 2022 [104]. While senescence remains under-investigated in the context of RPT, it is well shown that ionizing radiation from EBRT can induce senescence. Therefore, there is a current need for molecular probes for the non-invasive imaging of cell senescence.

Senescent cells present an overexpression of lysosomal beta-galactosidase, a biomarker that is widely used for the in vitro characterization of senescent cells via histochemical staining. Fluorescent probes for the senescence-associated activation of beta-galactosidase were reported first, most notably a far-red fluorescent beta-galactosidase substrate developed by the Weissleder laboratory [105]. The enzymatic cleavage of this fluorescent probe by beta-galactosidase resulted in a 50 nm red shift that allowed for the specific detection of the cleaved probe against the background fluorescence of the intact probes. In vivo imaging in a model of glioma expressing beta-galactosidase validated the potential of the probe for the real-time in vivo monitoring of beta-galactosidase activity. More recently, a beta-galactosidase-targeting PET radiotracer, [^{18}F]F-PyGal, was evaluated in tumour-bearing mice in which senescence had been induced by chemotherapy [106]. Compared to controls, the uptake of the tracer increased in the chemotherapy-treated animals. Furthermore, the ex vivo comparison of the uptake of the radiotracer (via autoradiography) to the expression of beta-galactosidase (via histochemical staining) showed a strong correlation. These probes should definitely be evaluated in the context of RPT-induced senescence.

5.3.4 The Role of Tissue Microenvironment and Intercellular Communications

5.3.4.1 Bystander and Abscopal Effects

The use of α-microbeam irradiation was a major step forward in understanding the role of intercellular communications, as it allowed for the irradiation of specific cells within a population [107]. More specifically, this technology facilitated the evaluation of both targeted effects in cells traversed by particles as well as so-called non-targeted effects (a.k.a. bystander effects) in neighbouring non-irradiated cells (Fig. 5.1). For example, in one experiment, chromosomal aberrations were observed in 30% of cells, while less than 1% of cells were effectively irradiated [76]. This observation led to a plethora of publications in the field of EBRT. Generally observed at low EBRT doses (<0.5 Gy) when all the cells are not traversed by particles, bystander effects could play a more prominent role in RPT given its lower 'routine' dose-rate irradiation and its heterogeneous dose distribution. To date, bystander effects have been reported after high-LET radiation (α-particles and AEs) but not with β-particles. However, this should be investigated further. Our group reported that RPT-induced bystander effects could be initiated at the cell membrane level (e.g. by a ^{125}I-radiolabelled non-internalizing mAb) through the formation of lipid rafts and also when the radionuclide was located in the DNA (e.g. 5-[^{125}I]I-2'-deoxyuridine, IdUrd) [49, 72, 108]. With α-particles, we showed that 70% of cells were killed by targeted effects, while 30% were killed by bystander effects. Similar proportions of cell killing were obtained with AE-emitters located in the DNA (IdUrd), but these values changed to 15% and 45%, respectively, when AE-emitters were located at the cell membrane level. Finally, bystander effects were observed ex vivo on tumour slices as revealed by immunofluorescence staining in which γH2AX

was shown to be produced over 1 mm from the radiation source as observed using digital autoradiography.

While bystander effects are short range non-targeted effects, systemic effects – also referred as 'abscopal effects' in EBRT – can be observed at longer distances. Abscopal effects are mediated by circulating factors or actors like immune cells. Radiation-induced immunogenic cell death is mediated by the release of danger-associated molecular patterns (DAMPS) like ATP, HMGB1, calreticulin or other molecules like nucleic acids. Through the presence of toll-like receptors, the latter danger signals can next be recognized by phagocytic cells, including macrophages and immature dendritic cells that participate in innate immunity through the generation of a local inflammatory microenvironment. This environment in turn will facilitate the recruitment of other immune cells and the secretion of cytokines, co-stimulating molecules (CD40, CD80, CD86, MHC-I and -II), and chemokine receptors (CCR7) that will drive mature antigen-presenting cells to the lymph nodes where they will cross-present tumour-derived antigens to $CD8^+$ and $CD4^+$ T cells to prime an adaptive immune response [109–111]. Therefore, there has recently been increased interest in the development and evaluation of the radiation-induced anti-tumour immune response.

Several reports in the field of RPT indicate that the immunostimulatory effects of radiation could convert immunologically 'cold' tumours into 'hot' tumours with the hope of increasing the response to immunotherapies [112, 113]. However, so far, RPT parameters that could affect the immune response have not been clearly identified. Radiation nature, absorbed dose, dose rate and dose fractionation may be the major actors, as they will modulate DNA damage and repair and can differentially trigger the cGAS/STING pathway [114–117].

5.3.4.2 Immuno-imaging

Monitoring the immune response in vivo is of major interest not only in the context of RPT but for cancer therapies in general. Several approaches exist for the non-invasive in vivo tracking of immune cells, including the (i) direct labelling of immune cells by in vitro incubation with a radiotracer, (ii) the use of reporter genes and (iii) the use of immunoPET probes directed against immune cell surface receptors (Fig. 5.6). For the sake of brevity, we will only cover a few molecular probes that have been evaluated in the context of the radiation-induced immune response.

$CD8^+$ cytotoxic lymphocytes are key players in the anti-tumour immune response, and a large range of CD8-targeted molecular probes have been developed and evaluated in preclinical and clinical studies. Among them, a $F(ab)'_2$ fragment targeting murine $CD8a^+$ was radiolabelled with copper-64 and evaluated as a tool to evaluate the response of immunocompetent mice bearing colon adenocarcinoma to a combination of CTLA-4 immune checkpoint inhibition and EBRT (Fig. 5.6b) [118]. Notably, the authors reported a significant increase in the tumour-to-heart activity concentration ratios of [^{64}Cu]Cu-NOTA-CD8a in mice receiving EBRT and anti-CTLA-4 therapy as compared to controls. Interestingly, two distinct groups of responding and non-responding mice were observed in the combination therapy cohort in a survival study. A retrospective analysis of [^{64}Cu]Cu-NOTA-CD8a PET imaging highlighted the predictive value of the tracer: the tumour-to-heart activity concentration ratio increased significantly in treated responders compared to treated non-responders and controls.

Tumour-associated macrophages have also drawn the attention of the molecular imaging community, as their number in the tumour micro-environment is known to affect both treatment outcome and cancer prognosis. Therefore, a variety of molecular probes have been explored for the non-invasive imaging of tumour-associated macrophages. For example, Luo et al. developed a dextran-indocyanine green (DN-ICG) nanoprobe for the imaging of tumour-associated macrophages in the second near-infrared window (1000–1700 nm) [119]. The probe was evaluated in a subcutaneous murine model of pancreatic cancer after low-dose radiotherapy (5 Gy) or chemotherapy (zoledronic acid). The fluorescent
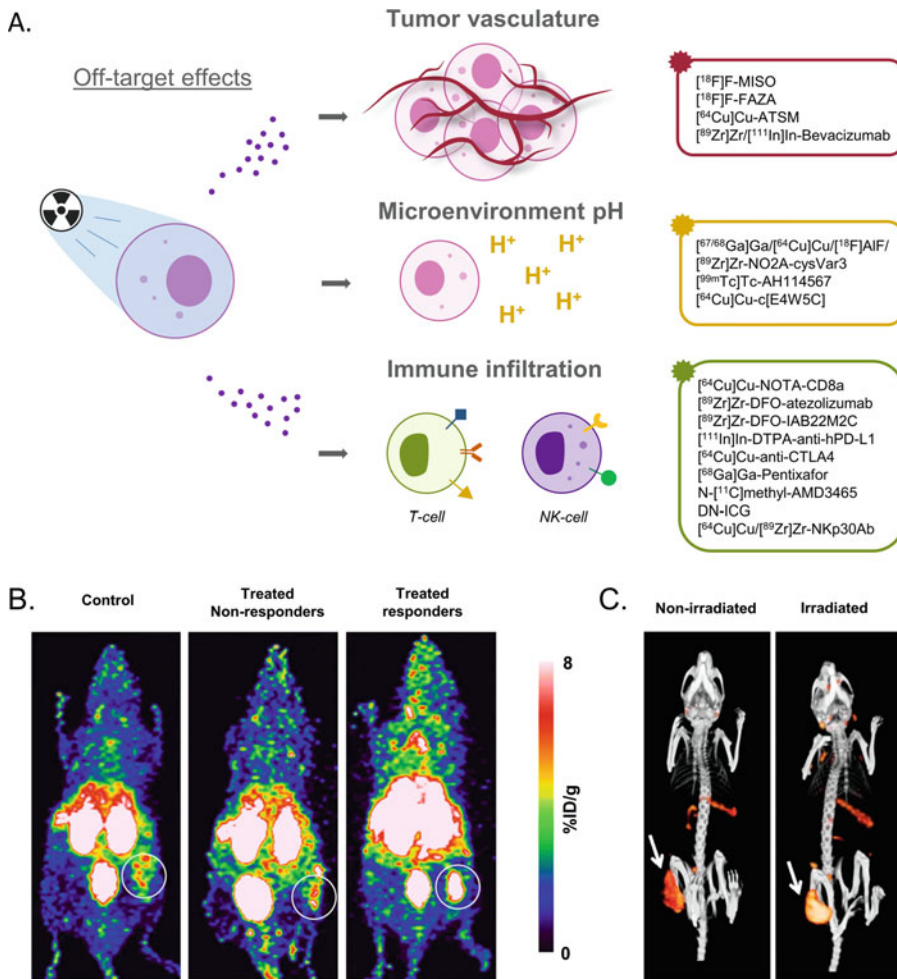
Fig. 5.6 Imaging radiation-induced effects in the tumour microenvironment. (**a**) Examples of radiation-induced off-target effects and their corresponding targeted molecular probes. (**b**) Representative maximum intensity projection of [^{64}Cu]Cu-NOTA-CD8a PET imaging in mice bearing subcutaneous CT26.WT xenografts that had been treated with external beam radiotherapy and anti-CTLA-4 therapy. The mice were retrospectively classified into responders and non-responders to investigate the accuracy of [^{64}Cu]Cu-NOTA-CD8a for therapy monitoring and response prediction. The circles indicate tumours. (**c**) Representative maximum intensity μSPECT/CT projections acquired with [^{111}In]In-anti-mPD-L1 in mice bearing subcutaneous CT26 xenografts that had either been irradiated (10 Gy) or not. The tumours are indicated by arrows

signal in the tumour increased twofold in the case of low-dose radiotherapy and decreased by 50% in the cohort treated with chemotherapy. Importantly, these post-treatment changes were shown to match changes in macrophage infiltration by flow cytometry.

Immune checkpoints are an important component of the immune response, and immune checkpoint inhibitors have – to say the least – garnered a great deal of attention in oncology over the last decade. Programmed death protein ligand 1 (PD-L1) has been found to be upregulated in irradiated tissues. Using a human PD-L1 targeted antibody (atezolizumab) radiolabelled with zirconium-89, Ehlerding et al. assessed the upregulation of PD-L1 in mice bearing subcutaneous lung cancer xenografts receiving two EBRT regimens: 1×5 Gy and 5×2 Gy [120]. [^{89}Zr]Zr-DFO-atezolizumab enabled the clear visualization of the entire lymph node

network. One day after irradiation, [^{89}Zr]Zr-DFO-atezolizumab produced tumour activity concentrations of 2.4 ± 1.2%IA/g in the 1 × 5 Gy cohort, 4.4 ± 1.5%IA/g in the 5 × 2 Gy and 2.1 ± 0.5%IA/g in the control cohort. Interestingly, this study validated both the potential of the radiotracer to monitor in vivo PD-L1 expression as well as dose fractionation to induce PD-L1 expression.

Since PD-L1 is also expressed by subsets of immune cells, Heskamp et al. validated the potential of [^{111}In]In-DTPA-anti-hPD-L1 for SPECT imaging in tumour-bearing humanized mice [121]. Compared to non-humanized mice, humanized mice exhibited an increased accumulation of [^{111}In]In-DTPA-anti-hPD-L1 in the spleen and lymph nodes. Interestingly, despite high levels of uptake in the lymphoid tissues and the presence of PD-L1-expressing immune cells, the uptake of the tracer in the tumour was not negatively affected by the use of humanized mice. In this same study, the investigators also used SPECT to explore the upregulation of PD-L1 after radiotherapy. Indeed, 24 h after irradiation with 10 Gy, the uptake of [^{111}In]In-DTPA-anti-mPD-L1 was significantly higher in irradiated tumours (26.3 ± 2.0%IA/g) compared to their non-irradiated counterparts (17.1 ± 3.1% IA/g) (Fig. 5.6c).

Finally, the CXCR4-CXCL12 signalling pathway is involved in oncogenesis and the treatment-induced recruitment of CXCR4$^+$ cytotoxic immune cells. Therefore, CXCR4 is also an attractive biomarker for both cancer diagnosis and treatment monitoring. Numerous molecular imaging probes have been developed for the non-invasive imaging of CXCR4 expression. Amongst them, a ^{68}Ga-cyclic pentapeptide known as [^{68}Ga]Ga-Pentixafor has been widely evaluated in clinical trials for the imaging of a broad range of CXCR4-expressing cancers. AMD3100 (Plerixafor®) has also been used as a scaffold for the development of CXCR4-targeted radiopharmaceuticals. To wit, Hartimath et al. validated the use of N-[^{11}C]methyl-AMD3465 for monitoring radiation-induced changes in the expression of CXCR4 by tumours [122]. Tumour-bearing mice were irradiated

with a single-fraction 14 Gy dose of external beam radiation. Seven days after irradiation, PET imaging revealed a 2.5-fold higher uptake of the radiotracer in irradiated tumours compared to sham-treated tumours (1.1 ± 0.3%IA/g vs. 0.4 ± 0.1% IA/g, respectively). This study justifies the further evaluation of CXCR4 as an imaging biomarker for the radiation-induced immune response.

5.3.5 Controversial Issues

5.3.5.1 Dose-Response During RPT

One controversial issue of RPT is whether dosimetry is necessary and useful for predicting the efficacy and side effects of RPT. The purpose of radiotherapy is increasing patient survival through local tumour control. The latter is theoretically obtained when all of the tumour's clonogenic cells, which may proliferate and cause recurrence, have been inactivated [123]. The first mathematical models describing the probability of local control referred as 'tumour control probability' (TCP) were introduced one century ago during EBRT. TCP curves describe tumour control progression as a function of tumour absorbed dose and require defining a certain biological endpoint (e.g. based on RECIST criteria). TCP curves show a 'dose threshold' below which no tumour control is observed, followed by an increase in tumour control which correlates with the increasing dose, and finally a tumour control plateau. In EBRT, the absorbed dose is more easily determined as it depends only on the external source of X-rays. Moreover, the field of irradiation is well defined, and dose is considered as homogeneous.

Normal tissue complication probability (NTCP) can also be established for healthy tissues in a manner similar to TCP [124]. As mentioned above, the LQ model was introduced in the 1980s to explain TCP and NTCP. However, RPT faces several challenges. First, absorbed dose determination is not as straightforward as in EBRT, and absorbed doses are still rarely available in either preclinical or clinical models. As a consequence, corresponding alpha and beta values – determined

from dose-response curves – are not available under RPT such that the LQ model has not been validated yet. Another difficulty is that RPT generally aims at treating multiples nodules in metastatic disease. Subsequently, a strong heterogeneity in radiopharmaceutical uptake (and in absorbed doses) can be observed between nodules, even within the same patients. Moreover, for the same absorbed dose, tumour response can be different, suggesting heterogeneity in tumour biology between nodules. Subsequently, the correlation between absorbed dose (and absorbed dose rate) and tumour response can vary dramatically within a single patient from one metastatic lesion to another (unpublished results), suggesting that the relationship between dose and response depends also on other parameters as well. Such observations were also reported by Bodei et al. with respect to the long-term effects of RPT patients with neuroendocrine tumours [125, 126]. For some nodules, an 'inverse dose rate effect' may be also observed, i.e. RPT could be more efficient per Gy than EBRT [127]. It is also likely that continuous low dose rate may be more favourable than high doses and high dose rates for stimulating an immune response [128]. The contribution of non-targeted effects to the final outcome of patients was already highlighted in the literature beginning 20 years ago [129, 130].

In spite of these aspects, some clinical studies including dosimetry (unpublished results) seem to indicate that an absorbed dose threshold, above which tumours don't progress, exists in RPT. This dose threshold now needs to be appreciated regarding toxicity towards healthy tissues.

5.3.5.2 PET Imaging Gold Standard: [^{18}F]F-FDG

[^{18}F]2-fluoro-2-deoxy-D-glucose ([^{18}F]F-FDG) is the most widely used radiotracer in oncology. Because of its high clinical availability and its wide applicability, [^{18}F]F-FDG is the primary molecular imaging probe used in radiation oncology for treatment planning and the evaluation of the efficacy of radiotherapy. [^{18}F]F-FDG is taken up by tumour cells as a result of glucose transport proteins (GLUT1). Once internalized, [^{18}F]F-FDG is phosphorylated into [^{18}F]F-FDG-6-phosphate and is thus metabolically trapped within the cell due to the fluorine substitution. Generally speaking, the uptake of [^{18}F]F-FDG in tumour cells is higher compared to normal tissues due to the high glycolytic rates of tumours. Relative changes in the standard uptake values of [^{18}F]F-FDG (SUVs) are evaluated for the assessment of response to treatment (i.e. chemotherapy, radiotherapy) and the classification of patients into different response categories according to the guidelines of the European Organization for Research and Treatment of Cancer, the National Cancer Institute and the PET Response Criteria in Solid Tumours (PERCIST).

Numerous clinical studies have demonstrated the utility of [^{18}F]F-FDG for the early (during radiotherapy) or late (after radiotherapy) assessment of the metabolic response of tumour tissue in a range of diseases, including lung, head and neck, rectal, oesophageal or cervical cancers [131]. However, the use of [^{18}F]F-FDG to assess response to radiotherapy suffers from a major limitation: the high uptake of [^{18}F]F-FDG in areas of radiation-induced inflammation and the infiltrating macrophages that surrounds the tumour. While the metabolic activity of tumour cells decreases progressively during radiotherapy, this decrease can be counterbalanced by an increase in inflammation. Taken together, this significantly complicates the interpretation of imaging results. Therefore, the timing of the [^{18}F]F-FDG scan is critical. Sufficient tumour cells should be viable in order to extract information, and the surrounding inflammation should be limited. One should also highlight that the quantification of changes in [^{18}F]F-FDG uptake is difficult and sometimes impossible in organs with high baseline metabolic activity such as the brain. To overcome these issues, a shift to more specific biomarkers of radiation-induced biological events – discussed in Sects. 5.2.1, 5.2.2 and 5.2.3 – should be considered. At present, however, this shift remains limited by the availability of the radiotracers.

5.4 The Future of RPT Radiobiology: Imaging and Radiomics Input

Several reports and opinion papers have highlighted the need to specifically investigate the radiobiology of RPT [4, 132]. Beyond preclinical experiments, the collection of data on RECIST and PERCIST criteria, and the analysis of dosimetry data, there is a need to develop the field of clinical RPT radiobiology. This is now possible, as the number of patients treated with RPT is increasing. Clinical samples before and after therapy (i.e. liquid biopsies and tumour samples from patients) together with standard, clinical parameters such as the patient's age, sex, tumour type, tumour grade, previous treatments, lifestyle and environmental factors should be collected and analysed.

Furthermore, in the preceding pages, we have highlighted a broad range of molecular imaging probes that could offer non-invasive approaches to evaluate radiobiology during and after RPT. The collection of images through a broad range of techniques can allow (even in a retrospective manner) for the mining of quantitative features thanks to radiomics. Using mathematical models and artificial intelligence (AI) methods, radiomics entails the exploration of potential associations between imaging features and biological clinical outcomes [133]. The general idea is that standard medical images can provide a large amount of additional information about tumours directly related to their biology [134].

Radiomics could be described in five main steps: image acquisition, post-acquisition image processing, segmentation, radiomic feature extraction and radiomic modelling. However, image pre-processing steps are also needed to homogenize the images in order to reduce noise, enhance quality and facilitate reproducible and comparable radiomic analyses [135]. Segmentation – which consists of contouring regions of interest (ROI) – is a non-negligible step, as radiomic results will differ significantly depending on the ROI delineation (e.g. contouring method or observer). From these ROIs, several hundred radiomic features

can extracted, including descriptors of size, shape, volume, intensity distribution (extracted from the histogram) and texture patterns [136]. Texture features refer to a variety of mathematical descriptors that evaluate the grey-level intensity as well as the position of the pixels within the ROI and can thus provide a measure of tumour heterogeneity [137].

The aim of radiomic modelling is to investigate the relationship between image features and an investigated clinical outcome in order to create a model that will provide clinical decision support for diagnosis, prognosis, treatment response prediction or overall survival prediction. This part involves three major steps: feature selection, modelling methodology (training step) and validation [138]. In order to make the model as robust as possible, a hundred input data (i.e. patients or animals), whose investigated outcome is known are required to produce a dataset [139]. This dataset is randomly divided into two cohorts: one for feature selection and training (70%), and the other for validation (30%). The aim of feature selection is to reduce the risk of overfitting by excluding irrelevant or redundant features. Several machine learning algorithms are generally applied to train the model, such as random forests, support vector machines and neural networks. Finally, each model is evaluated using the validation cohort and by measuring the confusion matrix. Ultimately, the model with the best performance is selected.

We strongly believe that the generation of large data banks with biological samples and medical images in tandem with the coalition of researchers and clinicians with a broad range of expertise have the power to drive major breakthroughs in the radiobiology of RPT.

5.5 The Bottom Line

- RPT offers a unique opportunity to irradiate all tumour sites in metastatic disease with low- or high-LET radiation.
- The radiobiology of RPT cannot strictly be extrapolated from the radiobiology of EBRT.

- Non-targeted effects – including short-distance communications (bystander cytotoxicity) and long-distance systemic effects (including immune system activation) – should be considered alongside the effects to targeted tissues.
- Clinical radiobiology using patient data and samples needs to be more deeply and widely explored.
- Molecular imaging probes for the non-invasive monitoring of radiation-induced biological events have already been developed, but only a very limited number have been evaluated in the context of RPT.
- The use of imaging in radiobiology remains under-investigated and is faced by numerous challenges, including (i) the availability of appropriate and relevant radiotracers, (ii) the appropriate timing of follow-up scans, (iii) the accumulation of the radiotracer in areas surrounding the tumour or normal tissues and (iv) poor signal-to-noise ratios.
- The combination of radiomics and artificial intelligence methods may entail the exploration of both preclinical and clinical radiobiology.

References

1. Herrmann K, Schwaiger M, Lewis JS, Solomon SB, McNeil BJ, Baumann M, et al. Radiotheranostics: a roadmap for future development. Lancet Oncol. 2020;21(3):e146–56.
2. Pouget JP, Lozza C, Deshayes E, Boudousq V, Navarro-Teulon I. Introduction to radiobiology of targeted radionuclide therapy. Front Med (Lausanne). 2015;2:12.
3. Pouget JP, Constanzo J. Revisiting the radiobiology of targeted alpha therapy. Front Med (Lausanne). 2021;8:692436.
4. EANM Radiobiology Working Group, Pouget JP, Konijnenberg M, Eberlein U, Glatting G, Gabina PM, et al. An EANM position paper on advancing radiobiology for shaping the future of nuclear medicine. Eur J Nucl Med Mol Imaging. 2022; https://doi.org/10.1007/s00259-022-05934-2.
5. Holsti LR. Development of clinical radiotherapy since 1896. Acta Oncol. 1995;34(8):995–1003.
6. Puck TT, Marcus PI. Action of X-Rays on mammalian cells. J Exp Med. 1956;103(5):653–66.
7. Turesson I. Radiobiological aspects of continuous low dose-rate irradiation and fractionated high dose-rate irradiation. Radiother Oncol. 1990;19(1):1–15.
8. Van Der Kogel AJ. The dose-rate effect. In: Joiner M, van der Kogel A, editors. Basic clinical radiobiology. London: Hodder Arnold; 2009.
9. Thames HD. Repair kinetics in tissues: alternative models. Radiother Oncol. 1989;14(4):321–7.
10. Ku A, Facca VJ, Cai Z, Reilly RM. Auger electrons for cancer therapy – a review. EJNMMI Radiopharm Chem [Internet]. 2019 [cited 2021 Jun 8];4(1):27. Available from: https://ejnmmipharmchem.springeropen.com/articles/10.1186/s41181-019-0075-2.
11. Goodhead DT. Spatial and temporal distribution of energy. Health Phys [Internet]. 1988 [cited 2021 Jul 6];55(2):231–40. Available from: http://journals.lww.com/00004032-198808000-00015.
12. Halliwell B, Gutteridge JMC. Oxygen toxicity, oxygen radicals, transition metals and disease. Biochem J [Internet]. 1984 [cited 2022 Dec 10];219(1):1–14. Available from: https://portlandpress.com/biochemj/article/219/1/1/15857/Oxygen-toxicity-oxygen-radicals-transition-metals.
13. Cadet J, Delatour T, Douki T, Gasparutto D, Pouget JP, Ravanat JL, et al. Hydroxyl radicals and DNA base damage. Mutat Res. 1999;424(1–2):9–21.
14. Laurent C, Voisin P, Pouget JP. DNA damage in cultured skin microvascular endothelial cells exposed to gamma rays and treated by the combination pentoxifylline and α-tocopherol. Int J Radiat Biol [Internet]. 2006 [cited 2022 Dec 9];82(5):309–21. Available from: http://www.tandfonline.com/doi/full/10.1080/09553000600733150.
15. Cadet J, Douki T, Ravanat JL. One-electron oxidation of DNA and inflammation processes. Nat Chem Biol [Internet]. 2006 [cited 2022 Dec 10];2(7):348–9. Available from: http://www.nature.com/articles/nchembio0706-348.
16. Gray LH, Conger AD, Ebert M, Hornsey S, Scott OCA. The concentration of oxygen dissolved in tissues at the time of irradiation as a factor in radiotherapy. BJR [Internet]. 1953 [cited 2021 Jun 1];26(312):638–48. Available from: http://www.birpublications.org/doi/10.1259/0007-1285-26-312-638.
17. Wright EA, Howard-Flanders P. The influence of oxygen on the radiosensitivity of mammalian tissues. Acta Radiol. 1957;48(1):26–32.
18. Carles M, Fechter T, Grosu AL, Sörensen A, Thomann B, Stoian RG, et al. 18F-FMISO-PET hypoxia monitoring for head-and-neck cancer patients: radiomics analyses predict the outcome of chemoradiotherapy. Cancers (Basel). 2021;13(14):3449.

19. Dietz DW, Dehdashti F, Grigsby PW, Malyapa RS, Myerson RJ, Picus J, et al. Tumor hypoxia detected by positron emission tomography with 60Cu-ATSM as a predictor of response and survival in patients undergoing Neoadjuvant chemoradiotherapy for rectal carcinoma: a pilot study. Dis Colon Rectum. 2008;51(11):1641–8.

20. Dehdashti F, Grigsby PW, Lewis JS, Laforest R, Siegel BA, Welch MJ. Assessing tumor hypoxia in cervical cancer by PET with 60Cu-Labeled Diacetyl-Bis(N4-Methylthiosemicarbazone). J Nucl Med. 2008;49(2):201–5.

21. Nachankar A, Oike T, Hanaoka H, Kanai A, Sato H, Yoshida Y, et al. 64Cu-ATSM predicts efficacy of carbon ion radiotherapy associated with cellular antioxidant capacity. Cancers. 2021;13(24):6159.

22. Huizing FJ, Garousi J, Lok J, Franssen G, Hoeben BAW, Frejd FY, et al. CAIX-targeting radiotracers for hypoxia imaging in head and neck cancer models. Sci Rep. 2019;9(1):18898.

23. Ueda M, Kudo T, Mutou Y, Umeda IO, Miyano A, Ogawa K, et al. Evaluation of [125I]IPOS as a molecular imaging probe for hypoxia-inducible factor-1-active regions in a tumor: comparison among single-photon emission computed tomography/X-ray computed tomography imaging, autoradiography, and immunohistochemistry. Cancer Sci. 2011;102 (11):2090–6.

24. Huang Y, Fan J, Li Y, Fu S, Chen Y, Wu J. Imaging of tumor hypoxia with radionuclide-labeled tracers for PET. Front Oncol [Internet]. 2021 [cited 2022 May 13];11. Available from: https://www.frontiersin.org/article/10.3389/fonc.2021.731503.

25. Auerswald S, Schreml S, Meier R, Blancke Soares A, Niyazi M, Marschner S, et al. Wound monitoring of pH and oxygen in patients after radiation therapy. Radiat Oncol. 2019;14:199.

26. Choi EK, Roberts KP, Griffin RJ, Han T, Park HJ, Song CW, et al. Effect of pH on radiation-induced p53 expression. Int J Radiat Oncol Biol Phys. 2004;60(4):1264–71.

27. Pereira PMR, Edwards KJ, Mandleywala K, Carter LM, Escorcia FE, Campesato LF, et al. iNOS regulates the therapeutic response of pancreatic cancer cells to radiotherapy. Cancer Res. 2020;80(8): 1681–92.

28. Frankenberg-Schwager M. Review of repair kinetics for DNA damage induced in eukaryotic cells in vitro by ionizing radiation. Radiother Oncol [Internet]. 1989 [cited 2021 Jul 6];14(4):307–20. Available from: https://linkinghub.elsevier.com/retrieve/pii/0167814089901436.

29. Goodhead DT. Initial events in the cellular effects of ionizing radiations: clustered damage in DNA. Int J Radiat Biol [Internet]. 1994 [cited 2021 May 31];65 (1):7–17. Available from: http://www.tandfonline.com/doi/full/10.1080/09553009414550021.

30. Signore A, Campagna G, Marinaccio J, de Vitis M, Lauri C, Berardinelli F, et al. Analysis of short term and stable DNA damage in patients with differentiated thyroid cancer treated with [131] I in hypothyroidism or with rhTSH for remnant ablation. J Nucl Med [Internet]. 2022 [cited 2022 Aug 31]. Available from: http://jnm.snmjournals.org/lookup/doi/10.2967/jnumed.121.263442.

31. Lassmann M, Hänscheid H, Gassen D, Biko J, Meineke V, Reiners C, et al. In vivo formation of γ-H2AX and 53BP1 DNA repair foci in blood cells after radioiodine therapy of differentiated thyroid cancer. J Nucl Med [Internet]. 2010 [cited 2022 Aug 31];51(8):1318–25. Available from: http://jnm.snmjournals.org/lookup/doi/10.2967/jnumed.109.071357.

32. Schumann S, Scherthan H, Pfestroff K, Schoof S, Pfestroff A, Hartrampf P, et al. DNA damage and repair in peripheral blood mononuclear cells after internal ex vivo irradiation of patient blood with 131I. Eur J Nucl Med Mol Imaging. 2022;49(5): 1447–55.

33. Schumann S, Eberlein U, Lapa C, Müller J, Serfling S, Lassmann M, et al. α-Particle-induced DNA damage tracks in peripheral blood mononuclear cells of [223Ra]RaCl2-treated prostate cancer patients. Eur J Nucl Med Mol Imaging [Internet]. 2021 [cited 2022 Aug 31];48(9):2761–70. Available from: https://link.springer.com/10.1007/s00259-020-05170-6.

34. Eberlein U, Scherthan H, Bluemel C, Peper M, Lapa C, Buck AK, et al. DNA damage in peripheral blood lymphocytes of thyroid cancer patients after radioiodine therapy. J Nucl Med [Internet]. 2016 [cited 2022 Aug 31];57(2):173–9. Available from: http://jnm.snmjournals.org/lookup/doi/10.2967/jnumed.115.164814.

35. Lomax EM, Gulston KM, O'Neill P. Chemical aspects of clustered DNA damage induction by ionising radiation. Radiat Protect Dosim [Internet]. 2002 [cited 2021 Mar 3];99(1):63–8. Available from: https://academic.oup.com/rpd/article-lookup/doi/10.1093/oxfordjournals.rpd.a006840.

36. Eccles LJ, O'Neill P, Lomax ME. Delayed repair of radiation induced clustered DNA damage: friend or foe? Mutat Res. 2011;711(1–2):134–41.

37. Pouget JP, Frelon S, Ravanat JL, Testard I, Odin F, Cadet J. Formation of modified DNA bases in cells exposed either to gamma radiation or to high-LET particles. Radiat Res [Internet]. 2002 [cited 2021 May 31];157(5):589–95. Available from: http://www.bioone.org/doi/abs/10.1667/0033-7587%282002%29157%5B0589%3AFOMDBI%5D2.0.CO%3B2.

38. Sasaki MS. Advances in the biophysical and molecular bases of radiation cytogenetics. Int J Radiat Biol [Internet]. 2009 [cited 2022 Dec 9];85(1):26–47. Available from: http://www.tandfonline.com/doi/full/10.1080/09553000802641185.

39. Georgakilas A. Detection of clustered DNA lesions: biological and clinical applications. World J Biol Chem. 2011;2(7):173–6.

40. Sage E, Shikazono N. Radiation-induced clustered DNA lesions: repair and mutagenesis. Free Radic Biol Med. 2017;107:125–35.

41. Amoretti M, Amsler C, Bonomi G, Bouchta A, Bowe P, Carraro C, et al. Production and detection of cold antihydrogen atoms. Nature. 2002;419(6906):456–9.

42. Rothkamm K, Krüger I, Thompson LH, Löbrich M. Pathways of DNA double-strand break repair during the mammalian cell cycle. Mol Cell Biol [Internet]. 2003 [cited 2022 Dec 10];23(16):5706–15. Available from: https://journals.asm.org/doi/10.1128/MCB.23.16.5706-5715.2003.

43. Rothkamm K, Krüger I, Thompson LH, Löbrich M. Pathways of DNA double-strand break repair during the mammalian cell cycle. Mol Cell Biol. 2003;23(16):5706–15.

44. Shibata A, Jeggo P, Löbrich M. The pendulum of the Ku-Ku clock. DNA Repair (Amst). 2018;71:164–71.

45. Shiloh Y, Ziv Y. The ATM protein kinase: regulating the cellular response to genotoxic stress, and more. Nat Rev Mol Cell Biol. 2013;14(4):197–210.

46. Marechal A, Zou L. DNA damage sensing by the ATM and ATR kinases. Cold Spring Harb Perspect Biol [Internet]. 2013 [cited 2022 Oct 10];5(9):a012716. Available from: http://cshperspectives.cshlp.org/lookup/doi/10.1101/cshperspect.a012716.

47. Panier S, Boulton SJ. Double-strand break repair: 53BP1 comes into focus. Nat Rev Mol Cell Biol [Internet]. 2014 [cited 2021 May 29];15(1):7–18. Available from: http://www.nature.com/articles/nrm3719.

48. Lord CJ, Ashworth A. PARP inhibitors: synthetic lethality in the clinic. Science. 2017;355(6330):1152–8.

49. Paillas S, Boudousq V, Piron B, Kersual N, Bardiès M, Chouin N, et al. Apoptosis and p53 are not involved in the anti-tumor efficacy of ^{125}I-labeled monoclonal antibodies targeting the cell membrane. Nucl Med Biol. 2013;40(4):471–80.

50. Lundsten S, Berglund H, Jha P, Krona C, Hariri M, Nelander S, et al. p53-Mediated radiosensitization of 177Lu-DOTATATE in neuroblastoma tumor spheroids. Biomol Ther. 2021;11(11):1695.

51. Privé BM, Slootbeek PHJ, Laarhuis BI, Naga SP, van der Doelen MJ, van Kalmthout LWM, et al. Impact of DNA damage repair defects on response to PSMA radioligand therapy in metastatic castration-resistant prostate cancer. Prostate Cancer Prostatic Dis [Internet]. 2022 [cited 2022 Aug 31];25(1):71–8. Available from: https://www.nature.com/articles/s41391-021-00424-2.

52. van der Doelen MJ, Mehra N, van Oort IM, Looijen-Salamon MG, Janssen MJR, Custers JAE, et al. Clinical outcomes and molecular profiling of advanced metastatic castration-resistant prostate cancer patients treated with 225Ac-PSMA-617 targeted alpha-radiation therapy. Urol Oncol: Semin Orig Investig [Internet]. 2021 [cited 2022 Dec 9];39(10):729.e7–16. Available from: https://linkinghub.elsevier.com/retrieve/pii/S1078143920306311.

53. Zhu M, Sonbol MB, Halfdanarson T, Hobday T, Ahn D, Ma WW, et al. Homologous recombination repair defect may predict treatment response to peptide receptor radionuclide therapy for neuroendocrine tumors. Oncologist [Internet]. 2020 [cited 2022 Dec 9];25(8):e1246–8. Available from: https://academic.oup.com/oncolo/article/25/8/e1246/6443870.

54. Wickstroem K, Hagemann UB, Cruciani V, Wengner AM, Kristian A, Ellingsen C, et al. Synergistic effect of a mesothelin-targeted [227] Th conjugate in combination with DNA damage response inhibitors in ovarian cancer xenograft models. J Nucl Med [Internet]. 2019 [cited 2022 Dec 9];60(9):1293–300. Available from: http://jnm.snmjournals.org/lookup/doi/10.2967/jnumed.118.223701.

55. Makvandi M, Lee H, Puentes LN, Reilly SW, Rathi KS, Weng CC, et al. Targeting PARP-1 with alpha-particles is potently cytotoxic to human neuroblastoma in preclinical models. Mol Cancer Ther. 2019;18(7):1195–204.

56. Jannetti SA, Carlucci G, Carney B, Kossatz S, Shenker L, Carter LM, et al. PARP-1–targeted radiotherapy in mouse models of glioblastoma. J Nucl Med. 2018;59(8):1225–33.

57. Fu J, Qiu F, Stolniceanu CR, Yu F, Zang S, Xiang Y, et al. Combined use of [177] Lu-DOTATATE peptide receptor radionuclide therapy and fluzoparib for treatment of well-differentiated neuroendocrine tumors: a preclinical study. J Neuroendocrinol [Internet]. 2022 [cited 2022 Dec 9];34(4). Available from: https://onlinelibrary.wiley.com/doi/10.1111/jne.13109.

58. Purohit NK, Shah RG, Adant S, Hoepfner M, Shah GM, Beauregard JM. Potentiation of 177Lu-octreotate peptide receptor radionuclide therapy of human neuroendocrine tumor cells by PARP inhibitor. Oncotarget. 2018;9(37):24693–706.

59. Pirovano G, Jannetti SA, Carter LM, Sadique A, Kossatz S, Guru N, et al. Targeted brain tumor radiotherapy using an auger emitter. Clin Cancer Res. 2020;26(12):2871–81.

60. Atkinson J, Bezak E, Kempson I. Imaging DNA double-strand breaks — are we there yet? Nat Rev Mol Cell Biol [Internet]. 2022 [cited 2022 Aug 31]. Available from: https://www.nature.com/articles/s41580-022-00513-7.

61. Piron B, Paillas S, Boudousq V, Pèlegrin A, Bascoul-Mollevi C, Chouin N, et al. DNA damage-centered signaling pathways are effectively activated during low dose-rate Auger radioimmunotherapy. Nucl Med Biol. 2014;41:e75–83.

62. Knight JC, Koustoulidou S, Cornelissen B. Imaging the DNA damage response with PET and SPECT. Eur J Nucl Med Mol Imaging. 2017;44(6):1065–78.

63. Cornelissen B, Kersemans V, Darbar S, Thompson J, Shah K, Sleeth K, et al. Imaging DNA damage in vivo using gammaH2AX-targeted immunoconjugates. Cancer Res. 2011;71(13): 4539–49.

64. Knight JC, Topping C, Mosley M, Kersemans V, Falzone N, Fernández-Varea JM, et al. PET imaging of DNA damage using (89)Zr-labelled anti-γH2AX-TAT immunoconjugates. Eur J Nucl Med Mol Imaging. 2015;42(11):1707–17.

65. Cornelissen B, Darbar S, Kersemans V, Allen D, Falzone N, Barbeau J, et al. Amplification of DNA damage by a γH2AX-targeted radiopharmaceutical. Nucl Med Biol. 2012;39(8):1142–51.

66. O'Neill E, Kersemans V, Allen PD, Terry SYA, Torres JB, Mosley M, et al. Imaging DNA damage repair in vivo following 177Lu-DOTATATE therapy. J Nucl Med [Internet]. 2019 [cited 2022 May 16]. Available from: https://jnm.snmjournals.org/content/early/2019/11/21/jnumed.119.232934.

67. Poty S, Mandleywala K, O'Neill E, Knight JC, Cornelissen B, Lewis JS. 89Zr-PET imaging of DNA double-strand breaks for the early monitoring of response following α- and β-particle radioimmunotherapy in a mouse model of pancreatic ductal adenocarcinoma. Theranostics. 2020;10(13): 5802–14.

68. Carney B, Kossatz S, Reiner T. Molecular imaging of PARP. J Nucl Med. 2017;58(7):1025–30.

69. de Souza D, França P, Kossatz S, Brand C, Karassawa Zanoni D, Roberts S, Guru N, et al. A phase I study of a PARP1-targeted topical fluorophore for the detection of oral cancer. Eur J Nucl Med Mol Imaging. 2021;48(11):3618–30.

70. Schöder H, França PDDS, Nakajima R, Burnazi E, Roberts S, Brand C, et al. Safety and feasibility of PARP1/2 imaging with 18F-PARPi in patients with head and neck cancer. Clin Cancer Res. 2020;26(13): 3110–6.

71. Kossatz S, Weber WA, Reiner T. Optical imaging of PARP1 in response to radiation in oral squamous cell carcinoma. PLoS One. 2016;11(1):e0147752.

72. Ladjohounlou R, Lozza C, Pichard A, Constanzo J, Karam J, Le Fur P, et al. Drugs that modify cholesterol metabolism alter the p38/JNK-mediated targeted and nontargeted response to alpha and auger radioimmunotherapy. Clin Cancer Res [Internet]. 2019 [cited 2021 Feb 9];25(15):4775–90. Available from: http://clincancerres.aacrjournals.org/lookup/doi/10.1158/1078-0432.CCR-18-3295.

73. Haimovitz-Friedman A, Kan CC, Ehleiter D, Persaud RS, McLoughlin M, Fuks Z, et al. Ionizing radiation acts on cellular membranes to generate ceramide and initiate apoptosis. J Exp Med [Internet]. 1994 [cited 2021 Mar 26];180(2):525–35. Available from: https://rupress.org/jem/article/180/2/525/50763/Ionizing-radiation-acts-on-cellular-membranes-to.

74. Zirkle RE. Radiation biology. In: Hollaender A, editor. The radiobiological importance of linear energy transfer. New York: McGraw-Hill Book Company; 1954. p. 315–50.

75. Munro TR. The relative radiosensitivity of the nucleus and cytoplasm of Chinese hamster fibroblasts. Radiat Res [Internet]. 1970 [cited 2021 Mar 22];42(3):451. Available from: https://www.jstor.org/stable/3572962?origin=crossref.

76. Nagasawa H, Cremesti A, Kolesnick R, Fuks Z, Little JB. Involvement of membrane signaling in the bystander effect in irradiated cells. Cancer Res. 2002;62(9):2531–4.

77. Shao C, Folkard M, Michael BD, Prise KM. Targeted cytoplasmic irradiation induces bystander responses. Proc Natl Acad Sci [Internet]. 2004 [cited 2021 Mar 26];101(37):13495–500. Available from: http://www.pnas.org/cgi/doi/10.1073/pnas.0404930101.

78. Hong M, Xu A, Zhou H, Wu L, Randers-Pehrson G, Santella RM, et al. Mechanism of genotoxicity induced by targeted cytoplasmic irradiation. Br J Cancer [Internet]. 2010 [cited 2021 Mar 31];103(8): 1263–8. Available from: http://www.nature.com/articles/6605888.

79. Zhang B, Davidson MM, Zhou H, Wang C, Walker WF, Hei TK. Cytoplasmic irradiation results in mitochondrial dysfunction and DRP1-dependent mitochondrial fission. Cancer Res [Internet]. 2013 [cited 2021 Mar 31];73(22):6700–10. Available from: http://cancerres.aacrjournals.org/lookup/doi/10.1158/0008-5472.CAN-13-1411.

80. Leach JK, Van Tuyle G, Lin PS, Schmidt-Ullrich R, Mikkelsen RB. Ionizing radiation-induced, mitochondria-dependent generation of reactive oxygen/nitrogen. Cancer Res. 2001;61(10):3894–901.

81. Kim JG, Chandrasekaran K, Morgan FW. Mitochondrial dysfunction, persistently elevated levels of reactive oxygen species and radiation-induced genomic instability: a review. Mutagenesis [Internet]. 2006 [cited 2021 Mar 23];21(6):361–7. Available from: https://academic.oup.com/mutage/article-lookup/doi/10.1093/mutage/gel048.

82. Kam WWY, Banati RB. Effects of ionizing radiation on mitochondria. Free Radic Biol Med [Internet]. 2013 [cited 2020 Sep 14];65:607–19. Available from: http://www.sciencedirect.com/science/article/pii/S0891584913003687.

83. Walsh DWM, Siebenwirth C, Greubel C, Ilicic K, Reindl J, Girst S, et al. Live cell imaging of mitochondria following targeted irradiation in situ reveals rapid and highly localized loss of membrane potential. Sci Rep [Internet]. 2017 [cited 2021 Mar 23];7(1):46684. Available from: http://www.nature.com/articles/srep46684.

84. Wu J, Zhang B, Wuu YR, Davidson MM, Hei TK. Targeted cytoplasmic irradiation and autophagy. Mutat Res/Fundam Mol Mech Mutagen [Internet]. 2017 [cited 2021 Mar 23];806:88–97. Available from: https://linkinghub.elsevier.com/retrieve/pii/S0027510716301476.

85. Pouget JP, Georgakilas AG, Ravanat JL. Targeted and off-target (bystander and abscopal) effects of radiation therapy: redox mechanisms and risk/benefit analysis. Antioxid Redox Signal [Internet]. 2018 [cited 2021 Mar 23];29(15):1447–87. Available from: https://www.liebertpub.com/doi/10.1089/ars.2017.7267.

86. Kastan MB, Bartek J. Cell-cycle checkpoints and cancer. Nature [Internet]. 2004 [cited 2021 Jun 1];432(7015):316–23. Available from: http://www.nature.com/articles/nature03097.

87. Otto T, Sicinski P. Cell cycle proteins as promising targets in cancer therapy. Nat Rev Cancer. 2017;17(2):93–115.

88. Suman S, Priya R, Kameswaran M. Induction of different cellular arrest and molecular responses in low EGFR expressing A549 and high EGFR expressing A431 tumor cells treated with various doses of ^{177}Lu-Nimotuzumab. Int J Radiat Biol [Internet]. 2020 [cited 2022 Aug 31];96(9):1144–56. Available from: https://www.tandfonline.com/doi/full/10.1080/09553002.2020.1793012.

89. Pichard A, Marcatili S, Karam J, Constanzo J, Ladjohounlou R, Courteau A, et al. The therapeutic effectiveness of 177Lu-lilotomab in B-cell non-Hodgkin lymphoma involves modulation of G2/M cell cycle arrest. Leukemia [Internet]. 2020 [cited 2021 Jun 2];34(5):1315–28. Available from: http://www.nature.com/articles/s41375-019-0677-4.

90. Supiot S, Gouard S, Charrier J, Apostolidis C, Chatal JF, Barbet J, et al. Mechanisms of cell sensitization to α radioimmunotherapy by doxorubicin or paclitaxel in multiple myeloma cell lines. Clin Cancer Res [Internet]. 2005 [cited 2022 Oct 10];11(19):7047s–52s. Available from: https://aacrjournals.org/clincancerres/article/11/19/7047s/190792/Mechanisms-of-Cell-Sensitization-to.

91. Lindenblatt D, Terraneo N, Pellegrini G, Cohrs S, Spycher PR, Vukovic D, et al. Combination of lutetium-177 labelled anti-L1CAM antibody chCE7 with the clinically relevant protein kinase inhibitor MK1775: a novel combination against human ovarian carcinoma. BMC Cancer [Internet]. 2018 [cited 2022 Dec 9];18(1):922. Available from: https://bmccancer.biomedcentral.com/articles/10.1186/s12885-018-4836-1.

92. Pan MH, Huang SC, Liao YP, Schaue D, Wang CC, Stout DB, et al. FLT-PET imaging of radiation responses in murine tumors. Mol Imaging Biol. 2008;10(6):325–34.

93. Vesselle H, Grierson J, Muzi M, Pugsley JM, Schmidt RA, Rabinowitz P, et al. In vivo validation of 3'deoxy-3'-[(18)F]fluorothymidine ([(18)F]FLT) as a proliferation imaging tracer in humans: correlation of [(18)F]FLT uptake by positron emission tomography with Ki-67 immunohistochemistry and flow cytometry in human lung tumors. Clin Cancer Res. 2002;8(11):3315–23.

94. Vera P, Bohn P, Edet-Sanson A, Salles A, Hapdey S, Gardin I, et al. Simultaneous positron emission tomography (PET) assessment of metabolism with 18F-fluoro-2-deoxy-d-glucose (FDG), proliferation with 18F-fluoro-thymidine (FLT), and hypoxia with 18fluoro-misonidazole (F-miso) before and during radiotherapy in patients with non-small-cell lung cancer (NSCLC): a pilot study. Radiother Oncol. 2011;98(1):109–16.

95. Ahlstedt J, Johansson E, Sydoff M, Karlsson H, Thordarson E, Gram M, et al. Non-Invasive imaging methodologies for assessment of radiation damage to bone marrow and kidneys from peptide receptor radionuclide therapy. Neuroendocrinology. 2020;110(1–2):130–8.

96. Constanzo J, Garcia-Prada CD, Pouget JP. Clonogenic assay to measure bystander cytotoxicity of targeted alpha-particle therapy. In: Methods in cell biology [Internet]. Elsevier; 2022 [cited 2022 Dec 10]. Available from: https://linkinghub.elsevier.com/retrieve/pii/S0091679X22001303.

97. Guo MF, Zhao Y, Tian R, Li L, Guo L, Xu F, et al. In vivo99mTc-HYNIC-annexin V imaging of early tumor apoptosis in mice after single dose irradiation. J Exp Clin Cancer Res. 2009;28(1):136.

98. Kartachova M, Haas RLM, Valdés Olmos RA, Hoebers FJP, van Zandwijk N, Verheij M. In vivo imaging of apoptosis by 99mTc-Annexin V scintigraphy: visual analysis in relation to treatment response. Radiother Oncol. 2004;72(3):333–9.

99. Allen AM, Ben-Ami M, Reshef A, Steinmetz A, Kundel Y, Inbar E, et al. Assessment of response of brain metastases to radiotherapy by PET imaging of apoptosis with ^{18}F-ML-10. Eur J Nucl Med Mol Imaging. 2012;39(9):1400–8.

100. García-Argüello SF, Lopez-Lorenzo B, Cornelissen B, Smith G. Development of [18F] ICMT-11 for imaging caspase-3/7 activity during therapy-induced apoptosis. Cancers (Basel). 2020;12(8):E2191.

101. Challapalli A, Kenny LM, Hallett WA, Kozlowski K, Tomasi G, Gudi M, et al. 18F-ICMT-11, a caspase-3-specific PET tracer for apoptosis: biodistribution and radiation dosimetry. J Nucl Med. 2013;54(9):1551–6.

102. Dubash SR, Merchant S, Heinzmann K, Mauri F, Lavdas I, Inglese M, et al. Clinical translation of [18F]ICMT-11 for measuring chemotherapy-induced caspase 3/7 activation in breast and lung cancer. Eur J Nucl Med Mol Imaging. 2018;45(13):2285–99.

103. Kolb H, Walsh J, Mocharla V, Liang Q, Zhao T, Gomez F, et al. 18F-CP18: A novel DEVD containing peptide substrate for imaging apoptosis via Caspase-3 activity. J Nucl Med. 2011;52(supplement 1):350.

104. Hanahan D. Hallmarks of cancer: new dimensions. Cancer Discov. 2022;12(1):31–46.

105. Tung CH, Zeng Q, Shah K, Kim DE, Schellingerhout D, Weissleder R. In Vivo imaging

of β-Galactosidase activity using far red fluorescent switch. Cancer Res. 2004;64(5):1579–83.

106. Krueger MA, Cotton JM, Zhou B, Wolter K, Schwenck J, Kuehn A, et al. Abstract 1146: [18F] FPyGal: a novel ß-galactosidase specific PET tracer for in vivo imaging of tumor senescence. Cancer Res. 2019;79(13_Supplement):1146.

107. Barberet P, Seznec H. Advances in microbeam technologies and applications to radiation biology: Table 1. Radiat Prot Dosimetry [Internet]. 2015 [cited 2021 Mar 23];166(1–4):182–7. Available from: https://academic.oup.com/rpd/article-lookup/doi/10.1093/rpd/ncv192.

108. Paillas S, Ladjohounlou R, Lozza C, Pichard A, Boudousq V, Jarlier M, et al. Localized irradiation of cell membrane by auger electrons is cytotoxic through oxidative stress-mediated nontargeted effects. Antioxid Redox Signal [Internet]. 2016 [cited 2021 Feb 9];25(8):467–84. Available from: http://www.liebertpub.com/doi/10.1089/ars.2015.6309.

109. Formenti SC, Demaria S. Systemic effects of local radiotherapy. Lancet Oncol 2009 [cited 2022 Dec 10];10(7):718–26. Available from: https://linkinghub.elsevier.com/retrieve/pii/S1470204509700828.

110. Demaria S, Ng B, Devitt ML, Babb JS, Kawashima N, Liebes L, et al. Ionizing radiation inhibition of distant untreated tumors (abscopal effect) is immune mediated. Int J Radiat Oncol Biol Phys. 2004 [cited 2019 Nov 2];58(3):862–70. Available from: https://linkinghub.elsevier.com/retrieve/pii/S0360301603019382.

111. Demaria S, Formenti SC. Role of T lymphocytes in tumor response to radiotherapy. Front Oncol [Internet]. 2012 [cited 2021 Nov 1];2. Available from: http://journal.frontiersin.org/article/10.3389/fonc.2012.00095/abstract.

112. Lejeune P, Cruciani V, Berg-Larsen A, Schlicker A, Mobergslien A, Bartnitzky L, et al. Immunostimulatory effects of targeted thorium-227 conjugates as single agent and in combination with anti-PD-L1 therapy. J Immunother Cancer. 2021;9(10):e002387.

113. Patel RB, Hernandez R, Carlson P, Grudzinski J, Bates AM, Jagodinsky JC, et al. Low-dose targeted radionuclide therapy renders immunologically cold tumors responsive to immune checkpoint blockade. Sci Transl Med [Internet]. 2021 [cited 2021 Oct 23];13(602):eabb3631. Available from: https://www.science.org/doi/10.1126/scitranslmed.abb3631.

114. Constanzo J, Galluzzi L, Pouget JP. Immunostimulatory effects of radioimmunotherapy. J Immunother Cancer [Internet]. 2022 [cited 2022 May 30];10(2):e004403. Available from: https://jitc.bmj.com/lookup/doi/10.1136/jitc-2021-004403.

115. Rodriguez-Ruiz ME, Vitale I, Harrington KJ, Melero I, Galluzzi L. Immunological impact of cell death signaling driven by radiation on the tumor microenvironment. Nat Immunol [Internet]. 2020 [cited 2020 Oct 5];21(2):120–34. Available from: https://www.nature.com/articles/s41590-019-0561-4.

116. Vanpouille-Box C, Demaria S, Formenti SC, Galluzzi L. Cytosolic DNA sensing in organismal tumor control. Cancer Cell [Internet]. 2018 [cited 2021 Jul 5];34(3):361–78. Available from: https://linkinghub.elsevier.com/retrieve/pii/S1535610818302277.

117. Ablasser A, Goldeck M, Cavlar T, Deimling T, Witte G, Röhl I, et al. cGAS produces a 2′-5′-linked cyclic dinucleotide second messenger that activates STING. Nature [Internet]. 2013 [cited 2021 Jul 5];498(7454):380–4. Available from: http://www.nature.com/articles/nature12306.

118. Kristensen LK, Christensen C, Alfsen MZ, Cold S, Nielsen CH, Kjaer A. Monitoring CD8+ T cell responses to radiotherapy and CTLA-4 blockade using [64Cu]NOTA-CD8a PET imaging. Mol Imaging Biol. 2020;22(4):1021–30.

119. Luo X, Hu D, Gao D, Wang Y, Chen X, Liu X, et al. Metabolizable near-infrared-II nanoprobes for dynamic imaging of deep-seated tumor-associated macrophages in pancreatic cancer. ACS Nano. 2021;15(6):10010–24.

120. Ehlerding EB, Lee HJ, Barnhart TE, Jiang D, Kang L, McNeel DG, et al. Noninvasive imaging and quantification of radiotherapy-induced PD-L1 upregulation with 89Zr–Df–Atezolizumab. Bioconjug Chem. 2019;30(5):1434–41.

121. Heskamp S, Wierstra PJ, Molkenboer-Kuenen JDM, Sandker GW, Thordardottir S, Cany J, et al. PD-L1 microSPECT/CT imaging for longitudinal monitoring of PD-L1 expression in syngeneic and humanized mouse models for cancer. Cancer Immunol Res. 2019;7(1):150–61.

122. Hartimath S, Draghiciu O, Daemen T, Nijman HW, van Waarde A, Dierckx RAJO, et al. Therapy-induced changes in CXCR4 expression in tumor xenografts can be monitored noninvasively with N-[11C]Methyl-AMD3465 PET. Mol Imaging Biol. 2020;22(4):883–90.

123. Zips D. Tumour growth and response to radiation. In: Joiner M, van der Kogel A, editors. Basic clinical radiobiology. London: Hodder Arnold; 2009.

124. Cremonesi M, Ferrari ME, Bodei L, Chiesa C, Sarnelli A, Garibaldi C, et al. Correlation of dose with toxicity and tumour response to 90Y- and 177Lu-PRRT provides the basis for optimization through individualized treatment planning. Eur J Nucl Med Mol Imaging [Internet]. 2018 [cited 2021 Feb 9];45(13):2426–41. Available from: http://link.springer.com/10.1007/s00259-018-4044-x.

125. Bodei L, Kidd M, Paganelli G, Grana CM, Drozdov I, Cremonesi M, et al. Long-term tolerability of PRRT in 807 patients with neuroendocrine

tumours: the value and limitations of clinical factors. Eur J Nucl Med Mol Imaging [Internet]. 2015 [cited 2019 Nov 2];42(1):5–19. Available from: http://link.springer.com/10.1007/s00259-014-2893-5.

126. Bodei L, Kidd M, Baum RP, Modlin IM. PRRT: defining the paradigm shift to achieve standardization and individualization. J Nucl Med [Internet]. 2014 [cited 2022 Dec 11];55(11):1753–6. Available from: http://jnm.snmjournals.org/lookup/doi/10.2967/jnumed.114.143974.

127. Williams JA, Edwards JA, Dillehay LE. Quantitative comparison of radiolabeled antibody therapy and external beam radiotherapy in the treatment of human glioma xenografts. Int J Radiat Oncol Biol Phys [Internet]. 1992 [cited 2022 Dec 10];24(1):111–7. Available from: https://linkinghub.elsevier.com/retrieve/pii/036030169291029M.

128. Herrera FG, Ronet C, Ochoa de Olza M, Barras D, Crespo I, Andreatta M, et al. Low dose radiotherapy reverses tumor immune desertification and resistance to immunotherapy. Cancer Discov [Internet]. 2021 [cited 2021 Oct 29];candisc.0003.2021. Available from: http://cancerdiscovery.aacrjournals.org/lookup/doi/10.1158/2159-8290.CD-21-0003.

129. Bentzen SM. Preventing or reducing late side effects of radiation therapy: radiobiology meets molecular pathology. Nat Rev Cancer. 2006;6(9):702–13.

130. Prise KM, O'Sullivan JM. Radiation-induced bystander signalling in cancer therapy. Nat Rev Cancer [Internet]. 2009 [cited 2021 Apr 8];9(5):351–60. Available from: http://www.nature.com/articles/nrc2603.

131. Jeraj R, Bradshaw T, Simončič U. Molecular imaging to plan radiotherapy and evaluate its efficacy. J Nucl Med. 2015;56(11):1752–65.

132. Terry SYA, Nonnekens J, Aerts A, Baatout S, de Jong M, Cornelissen B, et al. Call to arms: need for radiobiology in molecular radionuclide therapy. Eur J Nucl Med Mol Imaging. 2019;46(8):1588–90.

133. Kumar V, Gu Y, Basu S, Berglund A, Eschrich SA, Schabath MB, et al. Radiomics: the process and the challenges. Magn Reson Imaging. 2012;30(9):1234–48.

134. Gillies RJ, Kinahan PE, Hricak H. Radiomics: images are more than pictures, they are data. Radiology. 2016;278(2):563–77.

135. Hatt M, Vallieres M, Visvikis D, Zwanenburg A. IBSI: an international community radiomics standardization initiative. J Nucl Med. 2018;59(supplement 1):287.

136. Lambin P, Rios-Velazquez E, Leijenaar R, Carvalho S, van Stiphout RGPM, Granton P, et al. Radiomics: Extracting more information from medical images using advanced feature analysis. Eur J Cancer. 2012;48(4):441–6.

137. Haralick RM, Shanmugam K, Dinstein I. Textural features for image classification. IEEE Trans Syst Man Cybern. 1973;3(6):610–21.

138. Avanzo M, Wei L, Stancanello J, Vallières M, Rao A, Morin O, et al. Machine and deep learning methods for radiomics. Med Phys. 2020;47(5):e185–202.

139. Avanzo M, Stancanello J, El Naqa I. Beyond imaging: the promise of radiomics. Phys Med. 2017;38:122–39.

The Radiopharmaceutical Chemistry of Metallic Radionuclides

6

Aohan Hu and Justin J. Wilson

6.1 The Fundamentals: Overview of the Chemical Properties of Metal Ions

A wide variety of radioisotopes of metallic elements—or radiometals—could be harnessed for radiopharmaceutical therapy (RPT) (Table 6.1) based on their favorable physical decay properties [1–3]. The successful implementation of these radiometals in therapeutic nuclear medicine requires an extensive understanding of their chemical properties. As shown in Table 6.1, these radiometals span nearly the entire periodic table, with key candidates within the main-group elements, transition metals, lanthanides, and actinides. As a result, these radiometals often possess disparate chemical properties, thereby precluding the use of a single chemical strategy for their incorporation into radiotherapeutics. Rather, any approach to the creation of a radiometal-labeled probe must be tailored to the chemical properties of the specific metal ion. The goal of this section is to provide an overview of the coordination chemistry of the main group metals, transition metals, lanthanides, and actinides, thereby providing the reader with a foundational understanding of the radiopharmaceutical chemistry of therapeutic radiometals.

A. Hu · J. J. Wilson (✉)
Department of Chemistry and Chemical Biology,
Cornell University, Ithaca, NY, USA
e-mail: jjw275@cornell.edu

6.1.1 Main Group Metals

6.1.1.1 *s*-Block

The *s*-block metals include the alkali metals (Li, Na, K, Rb, Cs, Fr) and the alkaline earth metals (Be, Mg, Ca, Sr, Ba, Ra). Among these elements, the radionuclides ^{89}Sr and ^{223}Ra are the most important candidates for RPT. Under aerobic and aqueous conditions, alkali metals attain the +1 oxidation state, and alkaline earth elements exist in the +2 oxidation state. In these oxidation states, the electron configurations of these metal ions are closed shell and match those of the nearby noble gas. These *s*-block metal ions are not redox-active and bind with ligands mainly via ionic rather than covalent interactions [4].

6.1.1.2 *p*-Block

The *p*-block metals include the metallic elements in Group 13 (Al, Ga, In, Tl), Group 14 (Sn, Pb), and Group 15 (Bi). Representative therapeutic radionuclides within this category are ^{67}Ga, ^{111}In, and ^{201}Tl (which are used for Auger electron therapy), as well as ^{212}Pb and ^{213}Bi (which can be used for alpha therapy). These *p*-block metals primarily attain two oxidation states. Their higher valent oxidation states arise from the loss of all their valence electrons, yielding a noble gas electron configuration. The lower valent oxidation state corresponds to the loss of only the valence *p* electrons, affording an s^2 valence electron configuration. Accordingly, these oxidation states are +3 and +1 for Group

Table 6.1 Summary of radiometals relevant to radiotherapy

	Half-life	Major decay mode	Therapeutic application
^{47}Sc	3.35 d	β^-	β therapy
^{67}Cu	61.8 h	β^-	β therapy
^{89}Sr	50.6 d	β^-	β therapy
^{67}Ga	3.26 d	electron capture	Auger electron therapy
^{90}Y	64.1 h	β^-	β therapy
^{99m}Tc	6.01 h	internal conversion	Auger electron therapy
^{105}Rh	35.4 h	β^-	β therapy
^{109}Pd	13.7 h	β^-	β and Auger electron therapy
^{111}Ag	7.45 d	β^-	β therapy
^{111}In	67.2 h	electron capture	Auger electron therapy
^{135}La	18.9 h	electron capture	Auger electron therapy
^{153}Sm	46.3 h	β^-	β therapy
^{149}Tb	4.12 h	A	α therapy
^{161}Tb	6.96 d	β^-	β and Auger electron therapy
^{166}Ho	26.8 d	β^-	β therapy
^{177}Lu	6.65 d	β^-	β therapy
^{186}Re	3.72 d	β^-	β therapy
^{188}Re	17.0 h	β^-	β therapy
^{195m}Pt	4.01 d	internal conversion	Auger electron therapy
^{198}Au	2.70 d	β^-	β therapy
^{197m}Hg	23.8 h	internal conversion	Auger electron therapy
^{201}Tl	3.04 d	electron capture	Auger electron therapy
^{212}Pb	10.6 h	β^-	α therapy[a]
^{212}Bi	60.6 min	β^-, α	α therapy[a]
^{213}Bi	45.6 min	β^-	α therapy[a]
^{225}Ac	9.92 d	α	α therapy
^{223}Ra	11.4 d	α	α therapy
^{227}Th	18.7 d	α	α therapy
^{230}U	20.8 d	α	α therapy
^{255}Fm	20.1 h	α	α therapy

[a]These radionuclides – despite their emission of β particles – are categorized as α-therapy candidates because of their α-emitting daughters

13, +2 and +4 for Group 14, +3 and +5 for Group 15. For the lighter p-block elements like Al, Ga, and In, the higher oxidation states are more stable, whereas the heavier p-block elements like Tl, Pb, and Bi tend to adopt the lower oxidation states. The larger preference of the lower oxidation states for the heavy p-block elements is a consequence of the *inert pair effect*. This concept describes enhanced stability of the s^2 electron configuration that arises from relativistic effects, which become important for the heaviest elements on the periodic table.

In many cases of p-block elements with s^2 electron configurations, the lone pair has the potential to be *stereochemically active* [5]. Complexes with a stereochemically active lone pair—which possess what appears to be a vacant coordination site where the lone pair resides—are referred to as *hemidirected*. In some cases, however, the stereochemical activity of the lone pair is not displayed, and the coordination sphere is isotropic, resulting in a *holodirected* complex (Fig. 6.1). In any case, the possibility of lone pair stereochemical activity for the heavy p-block elements needs to be considered when exploring their radiochemistry.

6.1.2 Transition Metals

The transition metals—which belong to the d-block (Groups 3–12) of the periodic table—are

Fig. 6.1 Schematic representation of the two possible coordination modes (holodirected and hemidirected) for metal ions with an s^2 lone pair. (Reproduced from Ref. [6] with permission)
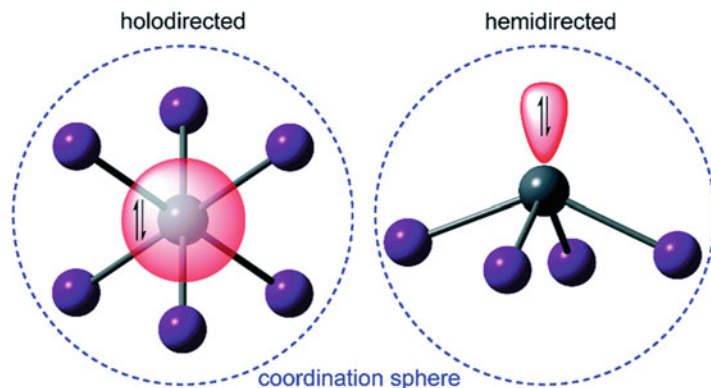
characterized by their valence d electrons. Representative therapeutic radiometals within this category are ^{47}Sc, ^{67}Cu, ^{90}Y, ^{99m}Tc, ^{105}Rh, ^{109}Pd, ^{111}Ag, $^{186/188}Re$, ^{195m}Pt, ^{198}Au, and ^{197m}Hg. In contrast to the main group metal ions discussed above, the d orbitals of transition metal ions can undergo covalent interactions with ligand donors, a property that dictates their overall geometry and stability.

Unlike the main group metal ions, the chemical behavior of the transition metal ions is highly diverse. For example, they can form cations in formal oxidation states ranging from +1 to +8 (as summarized in Fig. 6.2) and possess significantly different ligand donor atom preferences. Thus, it is challenging to summarize the chemistry of transition metal ions as a whole in a few sentences, but some underlying principles and general trends are useful for understanding how they can be employed for radiotherapeutic applications.

In general, there exist several dichotomies between the chemical properties of the transition metals. One such dichotomy is observed between the early (Groups 3–6) and late transition metals (Groups 8–12). The early transition metals are easier to oxidize, typically attaining their highest possible oxidation states by losing all their valence s and d electrons. In contrast, the late transition metals tend to form complexes with lower oxidation states. Furthermore, the cations of early transition metals are usually chemically hard and oxophilic, preferring hard ligands such as O^{2-}, F^-, and Cl^-. Their oxophilicity also

makes them susceptible to hydrolysis. The late transition metals are significantly softer and more polarizable, thus preferring soft ligands like carbonyl (CO), thiols (SR^-), and phosphines (PR_3).

Another dichotomy within the transition metals can be found by comparing those in the second and third rows to those in the first row. Most notably, complexes of the second and third row transition metal ions are significantly more inert than those of the first row metal ions. In addition, the second and third row transition metal ions tend to have more controlled redox chemistry, undergoing primarily two-electron processes with large structural reorganizations. The first row transition metal ions, in contrast, attain a wider range of oxidation states, driven by single-electron processes.

In contrast to the s and p block elements (for which electrostatic interactions predominate), there exists a high degree of covalency in the metal–ligand interactions of transition metal complexes. The bonding, electronic structure, and magnetic properties of the transition metal complexes can be rationalized in the context of *ligand field theory* [7]. Ligand field theory provides a framework for understanding how the degeneracy of the valence d orbitals is lifted as they interact with ligand donor orbitals to form molecular orbitals. The pattern and magnitude of the energetic splitting of the d orbitals are dependent on the geometry around the metal center, the types of ligands present, and the properties of the metal ion itself. Although multiple geometries are possible, arguably the most common one for
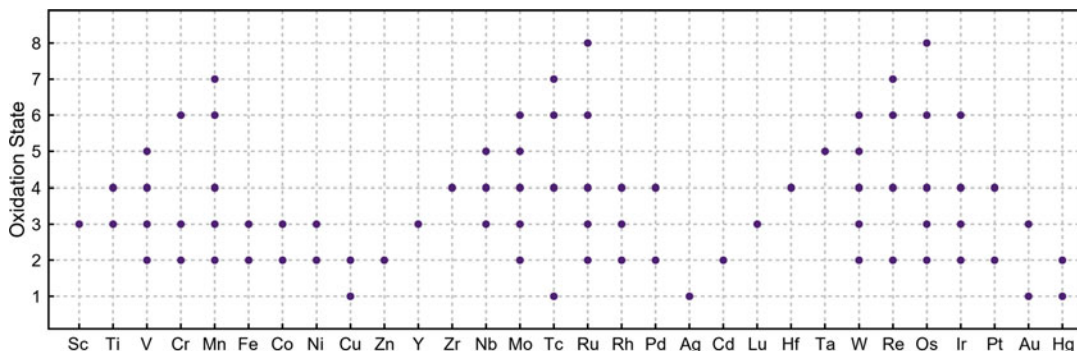
Fig. 6.2 The commonly observed oxidation states of d-block metal ions
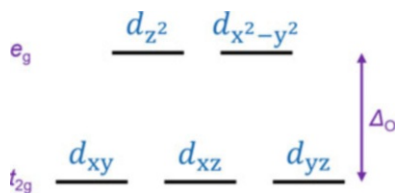

Fig. 6.3 Ligand field splitting for the valence d orbitals in an octahedral complex

transition metal complexes is the 6-coordinate octahedral geometry. Within this geometry, the five valence d orbitals are split into two energy levels, a triply degenerate t_{2g} and a doubly degenerate e_g set that are separated by an energy difference known as the *ligand-field splitting parameter* Δ_O (the subscript "O" indicates octahedral, as depicted in Fig. 6.3). The magnitude of Δ_O depends on the nature of both the metal and ligand. This quantity is important in the context of radiopharmaceutical chemistry because it reflects both the thermodynamic and kinetic stability of a transition metal complex. Generally, transition metal complexes with only the t_{2g} orbitals occupied are significantly more stable than those with electrons in the e_g orbitals, a consequence of the fact that e_g orbitals are primarily σ^* (antibonding).

6.1.3 Lanthanides

The lanthanides (Ln, the 4f-block) consist of the 15 elements from La to Lu in the periodic table, all of which possess stable isotopes except

Pm. Therapeutic radiometals that fall within this group include [135]La, [153]Sm, [149/161]Tb, [166]Ho, and [177]Lu. Due to similarities in their chemical properties and their cooccurrence in natural deposits, the transition metals Sc^{3+} and Y^{3+} are often categorized alongside with lanthanides, forming a larger group referred to as the "rare earth metals." In practice, chemists often use "lanthanides" and "rare earths" interchangeably. Under the aqueous and aerobic conditions required for radiopharmaceutical chemistry, the most stable oxidation state for all Ln is +3 (Ln^{3+}). This oxidation state gives rise to comparable electron configurations across the series of $[Xe]4f^n$, with $n = 0$–14. It should be noted, however, that several members of this series, particularly Ce and Eu, can be stabilized under biologically relevant conditions in +4 and +2 oxidation states, respectively, if appropriate ligands are used. The valence 4f orbitals of the Ln^{3+} are highly contracted and do not expand beyond the core orbitals, minimizing their spatial overlap and covalency with ligand donor orbitals. Thus, Ln^{3+}–ligand interactions are primarily ionic in nature. Ln^{3+} ions are chemically hard, preferring hard donor atoms like O and F. Although the chemical properties of Ln^{3+} ions are similar, the increasing effective nuclear charge across the series leads to a 17 pm decrease in ionic radius from La^{3+} to Lu^{3+} [8], a phenomenon described as the "lanthanide contraction" [9]. As such, the late Ln^{3+} has a larger charge-to-ionic radius ratio, which generally gives rise to more stable electrostatic interactions and stronger Lewis acidic characters.

6.1.4 Actinides

At the very bottom of the periodic table, the radioactive actinides (An, the 5f-block) comprise the 15 elements from Ac to Lr. The therapeutically relevant radioisotopes of the An series are ^{225}Ac, ^{223}Ra, ^{227}Th, ^{230}U, and ^{255}Fm. In contrast to the Ln, the valence electron configurations and preferred oxidation states of the An can vary significantly. For the early An, the 5f and 6d orbitals are of similar energy, and thus electron configurations with occupancy of both orbital types are possible. The 5f and 6d orbitals of the early An are also fairly diffuse, extending beyond the core orbital electrons. As such, the chemistry of the early An (Ac–Pu) somewhat resembles that of transition metals in that the 5f and 6d orbitals can participate in covalent bonding with ligand atoms, and these ions can attain multiple oxidation states. The major oxidation states for these elements are Ac(III), Th(IV), Pa(V), U(VI, IV), Np(V), and Pu(IV). Within these early An, metal–ligand multiple bonding is possible and has particularly important implications for the coordination chemistry of Pa^{5+} and U^{6+}. Indeed, the major forms of these metals under aerobic aqueous conditions are the $[Pa^V{\equiv}O]^{3+}$ and $[O{\equiv}U^{VI}{\equiv}O]^{2+}$ (uranyl) cations. Similarly, Np and Pu can exist in $[O{\equiv}Np^V{\equiv}O]^+$ (neptunyl) and $[O{\equiv}Pu^{VI}{\equiv}O]^{2+}$ (plutonyl) forms. The unique linear geometry of these species needs to be considered when harnessing them in RPT.

As the effective nuclear charge and relativistic effects increase across the series, the 5f orbitals become significantly stabilized and contracted relative to the 6d orbitals such that all valence electrons occupy the former. In the late An, this 5f orbital contraction precludes significant covalent interactions with ligand donor atoms. As such, the late An ions have similar chemical properties to the Ln, forming ionic complexes and existing primarily in +3 oxidation states. However, due to their extremely limited availability and poorly understood chemistry, these metals currently have limited relevance to RPT; only ^{255}Fm has been proposed as a potential candidate. Further efforts to increase their availability and characterize their chemical properties are needed before they can be strongly considered for applications in nuclear medicine.

6.2 The Details: Converting Metallic Radionuclides into Radiopharmaceutical Agents

Both the chemical properties of the radiometal and the desired targeting strategy must be considered prior to the implementation of radiometals into radiopharmaceuticals. In the ensuing section, several different approaches for incorporating radiometals into radiopharmaceuticals are described. Although this book and this chapter are focused on agents for RPT, the principles described also apply to the construction of radiometallated imaging agents.

6.2.1 Standalone Inorganic Salts

Occasionally, free, uncomplexed radiometal ions have properties that are suitable for their standalone use in medicine. This type of application is possible when the radiometal ion has a natural affinity for a specific tissue or organ. In the context of RPT, this phenomenon most frequently manifests in the form of metal ions with bone-seeking properties that facilitate their localization in regions of high bone turnover like bone metastases [10]. Key examples are the alkaline earth radiometals ^{89}Sr^{2+} and ^{223}Ra^{2+}, both heavier analogues of Ca^{2+} (a major constituent of bone matrix). [^{89}Sr]SrCl$_2$ (Metastron™) has been prescribed for the palliative treatment of skeletal metastases [11], and [^{223}Ra]RaCl$_2$ (Xofigo®) is currently used for the management of bone metastases in castration-resistant prostate cancer patients [12] (see Chap. 19 for more details).

6.2.2 Metal–Ligand Complexes

Despite the clinical success of the examples described above, the use of free radiometal ions

for therapeutic applications is very limited because most radiometals do not display inherently useful biodistribution patterns. Indeed, most free radiometal ions accumulate in undesired tissues or organs, giving rise to toxic side effects. Thus, the majority of therapeutic radiometals require the use of ligands to control their chemical and biological properties. Carefully chosen ligands can produce complexes with a number of valuable properties and circumvent the toxic side effects associated with free radiometal ions. In addition to preventing toxicity, the ligands can also be leveraged to enhance tumor-targeting properties. The rational design of ligands with vectors for targeting receptors that are overexpressed on cancer cells is a hallmark of RPT. Finally, before moving on it is important to note that metal ions are almost always bound by ligands in solution. For example, "free" metal ions in an aqueous solution actually form coordination complexes with H_2O molecules. However, in this discussion, we only consider exogenously added ligands.

6.2.2.1 Metal Complexes with a Chelator

Different types of ligands can be used to bind medicinally relevant radiometal ions. Chelating agents—or chelators—are a particularly relevant subset. This class of ligands is generally defined by the presence of multiple donor atoms within a single compound. Although simple bidentate ligands (e.g., ethylenediamine) are chelators in the strictest sense, radiopharmaceuticals typically require chelators with significantly more donor atoms to maximize the thermodynamic and kinetic stability of the resulting complexes. Thus, radiopharmaceutical researchers usually use the word "chelator" to refer to a ligand that provides sufficient donor atoms to enable the formation of a 1:1 complex with the metal ion.

Chelators are effective in radiopharmaceuticals because their multidentate nature leads to the formation of complexes with high thermodynamic and kinetic stability. To elaborate, the ability of a single chelator molecule to bind ions with several donors gives rise to the *chelate effect*, a phenomenon that results in

chelators yielding more stable complexes than those formed by an identical number of analogous monodentate donors [13]. The chelate effect is primarily driven by entropy; the displacement of several monodentate exogenous ligands by a single multidentate chelator is entropically favorable. Moreover, there is a kinetic element in play as well; because the donor atoms of a chelator are confined to the same molecule, the coordination of one donor atom within a chelator makes the coordination of others more kinetically facile.

The suitability of different chelators for therapeutic radiometals can be assessed quantitatively via several experiments. A number of these experiments can be carried out using nonradioactive or longer-lived isotopes of the radiometal of interest, which reduces both their cost and attendant safety considerations. However, differences between the concentrations needed to work at the macroscopic scale with these stable or longer-lived surrogates and the radioisotopic scale with the actual therapeutic radionuclides can, in some cases, give rise to disparities in the efficacy of chelators.

(a) *Facile complex preparation*

Operations involving radionuclides are inherently time sensitive due to their continuous decay. Ideally, the formation of a desired radio metal–ligand complex—*a.k.a.* "*radiolabeling*"—needs to be accomplished in a facile and rapid manner. Although harsh conditions such as higher temperatures can be used to accelerate radiolabeling reactions, the sensitivity of some radiopharmaceutical targeting vectors (like immunoglobulins) precludes heating.

In a typical chelator radiolabeling reaction, the radiometal and chelator are incubated at a well-defined temperature and pH for a pre-set reaction time. The efficiency of this radiolabeling reaction is often described by the *radiochemical conversion* (RCC), which is the percentage of the initial total radioactivity incorporated into the chelator (after correcting for the physical decay of the radionuclide over the course of the experiment). The *radiochemical yield* (RCY), the overall percent of incorporated radioactivity after additional

reaction workup procedures like purification, is another important parameter that can also depend on the chelator. Generally, an excess of the chelator is used to maximize both parameters. The success of a radiolabeling reaction is also often assessed in terms of the amount of radioactivity incorporated per mol or per gram of the chelator, values referred to as the *apparent molar activity* (AMA) or *apparent specific activity* (ASA), respectively. The production source and batch of the radionuclide can also affect the RCC, RCY, and AMA/ASA, as the presence of even small amounts of metal ion impurities can dramatically affect the radiolabeling reaction (see Chap. 8).

(b) *Sufficient complex stability*

Beyond allowing for efficient radiolabeling, a chelator must also form a sufficiently stable complex with the radiometal to prevent its release from the radiopharmaceutical vector in vivo. In principle, both the thermodynamic and kinetic stability of a radiometal–chelator complex should be measured and considered.

(i) Thermodynamic stability

The *thermodynamic stability* of a metal–ligand complex describes the spontaneity of the binding process between the two components. Thermodynamic stability is quantified by the standard free energy change of complexation ($\Delta G°$) and the stability constant (K_{ML}), which are explicitly related to each other. K_{ML} values are used more often due to their more easily interpreted definition. K_{ML} is defined in Eq. 6.1, in which [M], [L], and [ML] are the concentrations of the free metal ion, free ligand in its fully deprotonated state, and metal−ligand complex, respectively, at chemical equilibrium. From this expression, it is clear that a larger K_{ML} indicates stronger binding, which leads to smaller concentrations of the free metal ion at equilibrium. Thus, this quantity is highly useful for assessing ligands in a wide array of research areas [14].

$$K_{ML} = [ML]/[M][L] \qquad (6.1)$$

K_{ML} is a pH-independent quantity, as [L] represents the concentration of the fully deprotonated form of the chelator. Under the aqueous and aerobic conditions relevant to radiopharmaceutical chemistry, H^+ competes with the metal ion to bind to the ligand donor atoms, and OH^- competes with the ligand to hydrolyze the metal center. Thus, the pH of the solution plays an important role in the thermodynamic stability of the complex. As such, *conditional stability constants*—defined at specific pH values—are useful as well. An extension of this concept is the pM value. The pM of a metal–chelator combination is defined as $-\log[M]_{free}$, where the total metal concentration c_M is 10^{-6} M, and the total ligand concentration c_L is 10^{-5} M, at pH 7.4 [15]. Using this scale, large pM values signify smaller quantities of free metal ion present under these conditions and thus reflect more thermodynamically stable chelators at physiological pH.

(ii) Kinetic stability

Although thermodynamic stability quantities K_{ML} and pM are useful for comparing and understanding the metal ion affinity and selectivity of chelators at equilibrium, these values do not contain any information regarding the *rate* of the formation or dissociation of the metal–chelator complex. These parameters fall into the domain of *chemical kinetics*: the study of the rate of chemical reactions. In the context of the stability of a radiometal–chelator complex, the rate of dissociation is an important parameter. The *kinetic stability* (or *inertness*) of a metal–ligand complex describes the dissociation rate of the complex under a thermodynamically unfavored condition. It should be noted that the thermodynamic and kinetic stabilities of metal complexes do not necessarily correlate. In the context of RPT, the kinetic stability of a complex is critical because the conditions encountered in vivo—dilute concentrations of the metal–ligand complex in the presence of much higher concentrations of endogenous competing metal ions and ligands—often lead to unfavorable

thermodynamics. However, the kinetic stability of a radiometal complex is difficult to directly and absolutely quantify. Researchers often employ challenge experiments to assess this property, and three of the most frequently used methods are described below. These methods can be adapted for use with cold or radioactive metal ion complexes by altering the techniques used to determine the dissociation rates of the complexes.

Under low pH conditions, the high H^+ concentrations generally favor the protonation of the chelator and the displacement of the metal ion from a thermodynamic perspective. In such an *acid challenge* experiment, the complex is placed in a strongly acidic condition, and the dissociation kinetics are monitored for the evaluation of complex kinetic stability. Similarly, an excess of competing chelators can be used to create thermodynamically unfavored conditions for the original metal–chelator complex. The pseudo-first-order rate constant for this *transchelation challenge* process can afford a measure for the inertness of the initial complex. Following the same principle, a competing metal ion can also be used for a *transmetallation challenge*, in which an excess of a competing metal is added to displace the original metal, enabling the determination of a pseudo-first-order rate constant for the dissociation of the original complex.

A key similarity of the kinetic studies described above is that none provides an absolute value for this property. In each case, the rate constants obtained are dependent on the experimental conditions, including the concentrations of reagents, pH, and temperature. Thus, these values can only be used in a comparative manner when different complexes are subjected to

identical conditions. Hence, it is prudent to benchmark these experiments using a well-known system when probing the inertness of novel metal−chelator complexes.

(c) *Conjugation with targeting vector*

Once the radiolabeling efficiency and complex stability have been verified for a radiometal–chelator complex, the next step is the development of approaches for attaching the chelator to the targeting vector. There are a few examples of nontargeted radiometal complexes that are used as radiopharmaceuticals, like [^{153}Sm]Sm–EDTMP (Quadramet®, Fig. 6.5) that is used for the treatment of bone metastases [16]. However, most chelator-based radiopharmaceuticals include a targeting vector that is relied upon to deliver the radiometal to tissues in vivo.

Figure 6.4 reflects a general workflow for constructing a chelator-based radiopharmaceutical. After a chelator is revealed to be chemically promising, a derivative of the chelator containing a reactive functional group—a *bifunctional chelator*—is designed and synthesized. This bifunctional chelator is then allowed to react with a targeting vector containing a reactive group, which can be either natural (such as a thiol of cysteine or a primary amine of lysine) or synthetic (such as an azide or an alkyne), a step called *conjugation*. This chelator-modified conjugate is then radiolabeled to yield the completed radiopharmaceutical. Typically, the conjugation of the bifunctional chelator precedes the radiolabeling step because it minimizes the time of handling radioactive materials. Under some circumstances, however, radiolabeling is required *before* the chelator conjugation step. For
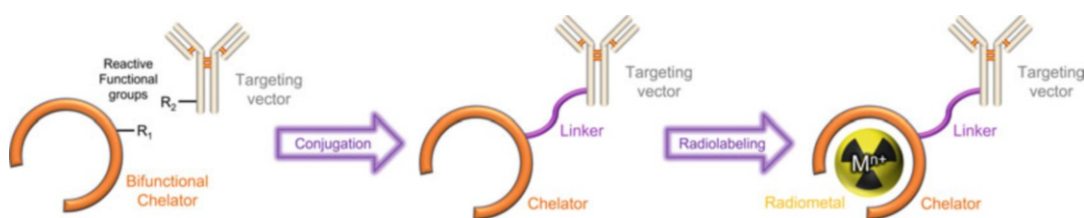

Fig. 6.4 General strategy for the construction of a metal-chelate-based radiopharmaceutical agent
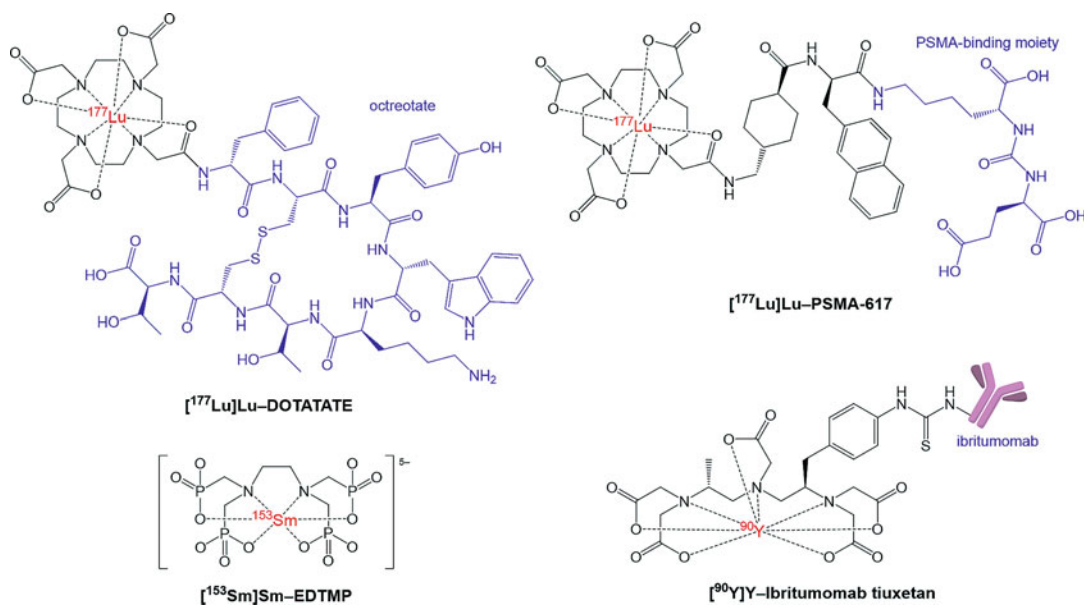
Fig. 6.5 Approved radiometal-based therapeutic agents that use chelators

example, if a high temperature is required for the radiolabeling but the vector is heat-sensitive, the bifunctional chelator needs to be radiolabeled before its attachment to the vector.

The suitability of a chelator in RPT should take into account the synthetic ease with which its bifunctional analogue can be prepared. Moreover, the installation of a reactive functional group to make the bifunctional chelator can potentially alter its metal-binding properties. In some cases, the parent chelator efficiently forms stable radiometal complexes, but its bifunctional analogue or corresponding conjugate does not. Thus, the chelating efficacy should be assessed again after the targeting vector is introduced. These challenges highlight the many different factors that need to be considered during the development of a chelator- and radiometal-bearing radiopharmaceutical.

A variety of molecules can act as targeting vectors. These compounds can be small molecules, short peptides, and macromolecular antibodies or antibody fragments. For instance, the small-molecule moiety Glu–urea–Lys binds to the prostate-specific membrane antigen (PSMA), a zinc glycoprotein that is overexpressed by prostate cancer cells [17]. This

targeting vector has been employed in [^{177}Lu]Lu–PSMA-617 (Pluvitco®, Fig. 6.5), a newly approved drug for the treatment of metastatic castration-resistant prostate cancer [18] that is described in more detail in Chap. 18. Another ^{177}Lu-based RPT agent, [^{177}Lu]Lu-DOTATATE (Lutathera®, Fig. 6.5) [19], is based on a peptide that targets the somatostatin receptor that is frequently overexpressed by gastroenteropancreatic neuroendocrine tumors [20]. A final example of an RPT agent, the non-Hodgkin lymphoma drug [^{90}Y]Y-ibritumomab tiuxetan (Zevalin®, Fig. 6.5) [21], employs the macromolecular monoclonal antibody ibritumomab to target the CD20 antigen expressed on B lymphocytes [22]. These three examples highlight how different types of targeting vectors can be successfully applied in radiotherapeutics, topics that are discussed in a great detail in Chaps. 9, 10, 11, 12, 13, 14, 15, 16, 17, 18, and 19.

(d) *Well-known chelators*

Generally speaking, chelators are classified as either macrocyclic or acyclic. Acyclic chelators have an open-chain or linear structure, whereas macrocyclic chelators have (as their name suggests) a cyclic structure, typically with at

least nine atoms and three donor atoms in their backbones [23]. Several generalizations can be used to compare these two classes of chelators, though they do not necessarily hold true for all systems.

Macrocyclic chelators, unlike acyclic systems, benefit from the *macrocyclic effect*. This effect stems from the restricted conformational freedom of the chelator's cyclic backbone, which gives the chelator a preorganized cavity for the metal. This preorganization diminishes the entropic penalty for complex formation, thus enhancing the thermodynamic stability of complexes formed with macrocyclic chelators when compared to their acyclic analogues [24]. The macrocycle 18-crown-6 provides a key example of this phenomenon. It binds K^+ with high affinity and selectivity compared to linear polyethers. In addition to this thermodynamic advantage, macrocycles also tend to confer complexes with enhanced kinetic inertness due to their conformational inflexibility. A potential limitation of macrocyclic chelators, however, lies in their relatively slow complex formation kinetics, which sometimes necessitates harsh radiolabeling conditions like elevated temperatures.

Acyclic chelators, in contrast, typically form metal complexes rapidly and therefore require milder radiolabeling conditions. From a synthetic chemistry standpoint, the formation of macrocycles is often challenging and low-yielding, whereas acyclic chelators are often easier to synthesize. In many cases, the benefits conferred by the macrocyclic effect cannot be justified in the context of the effort required to prepare macrocycles, especially when an acyclic analogue performs well enough.

Several chelators that have been used extensively in radiopharmaceutical applications are shown in Figs. 6.6 and 6.7. Among them, the macrocyclic 1,4,7,10-tetraazacyclododecane-1,4,7,10-tetraacetic acid (DOTA) [25] and the acyclic diethylenetriaminepentaacetic acid (DTPA) have arguably been used most. Indeed, nearly all approved metal-chelate-based therapeutic and diagnostic agents are derivatives of these two structures.

DOTA (Fig. 6.6) contains a 12-membered macrocyclic cyclen ring with four pendant acetate donor arms. The rigid macrocycle and eight donor atoms of DOTA allow it to form highly inert complexes. The efficacy of DOTA has been demonstrated with a wide range of radionuclides, including the therapeutic $^{47}Sc^{3+}$, $^{90}Y^{3+}$, $^{177}Lu^{3+}$, and $^{225}Ac^{3+}$. Building upon the success of DOTA, a number of derivatives of this chelator—including DO3A, TCMC, DOTMP, and PCTA (Fig. 6.6)—have been synthesized. Close analogs of DOTA are currently used in several clinically approved radiopharmaceuticals, including [^{177}Lu]Lu–DOTATATE and [^{177}Lu]Lu–PSMA-617 (Fig. 6.5). Yet despite its clinical success, DOTA's poor metal-binding kinetics represent a notable limitation. To wit, high temperatures are typically required for efficient radiolabeling. Thus, care must be taken when this chelator is used in conjunction with temperature-sensitive biomolecules.

The solution conformational equilibrium of DOTA complexes has been heavily investigated and discussed over the last few decades. DOTA complexes can adopt two conformations: square antiprismatic (SAP) and twisted square antiprismatic (TSAP), both of which possess a C_4 rotation axis. These two isomers are a consequence of the different conformational chiralities that arise upon metal binding. As illustrated in Fig. 6.8a, the five-membered chelate rings can adopt either δ or λ conformations, depending on their tilt directions. In the most energetically favorable forms, the four chelate rings assume the same conformations, yielding a $\delta\delta\delta\delta$ or a $\lambda\lambda\lambda\lambda$ arrangement in the resulting complex. In addition, the four pendant acetate donors of DOTA assume a chiral helical twist about the metal center, which is denoted as being in either a right-handed (Δ) or left-handed (Λ) conformation. Considering these conformational chiralities, four stereoisomers are possible for DOTA complexes: $\Delta(\delta\delta\delta\delta)$, $\Delta(\lambda\lambda\lambda\lambda)$, $\Lambda(\delta\delta\delta\delta)$, and $\Lambda(\lambda\lambda\lambda\lambda)$. The enantiomeric pair $\Delta(\lambda\lambda\lambda\lambda)$ and $\Lambda(\delta\delta\delta\delta)$ result in the SAP conformer, whereas the enantiomeric pair $\Delta(\delta\delta\delta\delta)$ and $\Lambda(\lambda\lambda\lambda\lambda)$ give rise to the TSAP conformer (Fig. 6.8b). These two
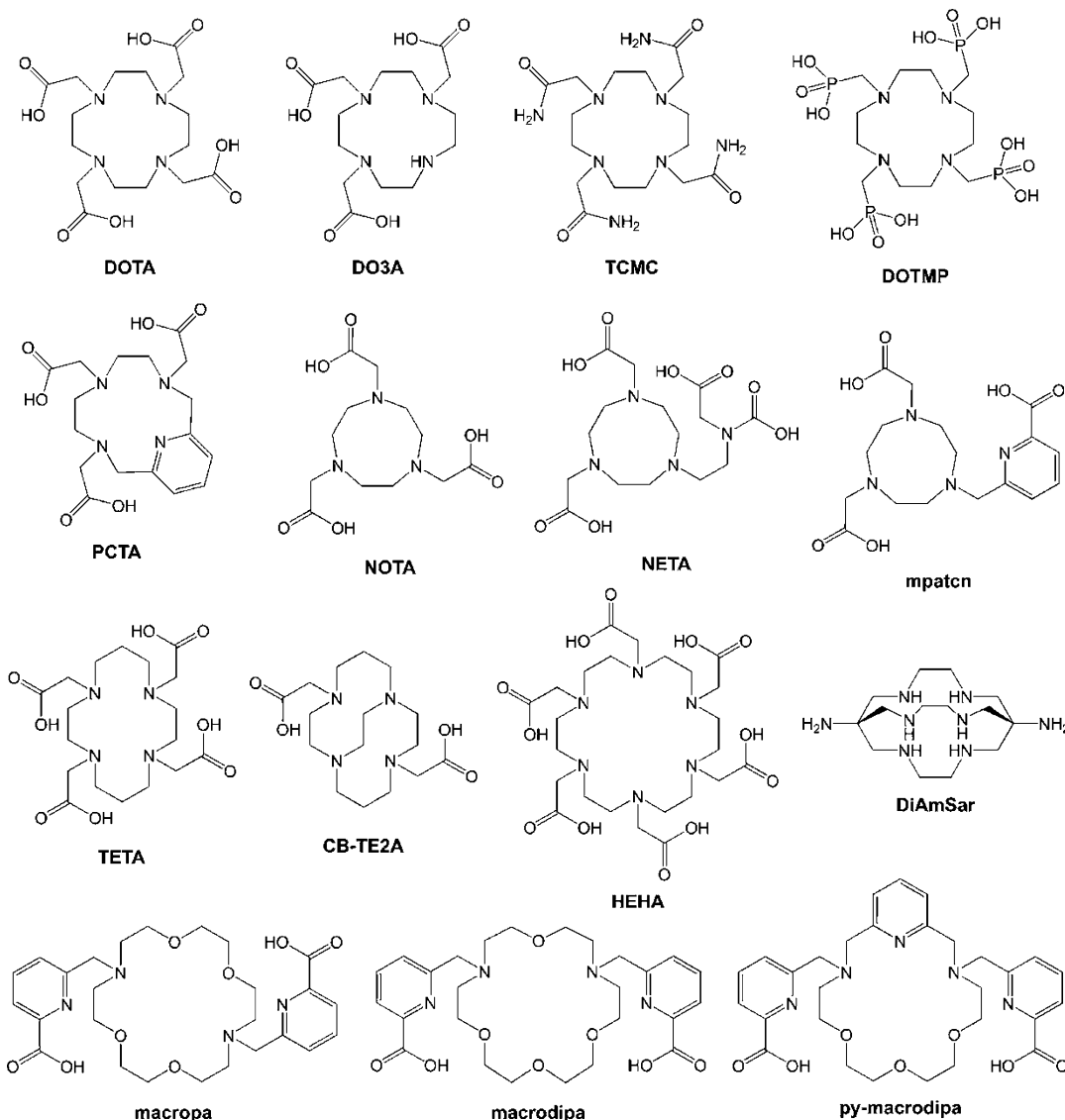
Fig. 6.6 Selected macrocyclic chelators used in the development of radiopharmaceuticals

conformers can interconvert by either an arm rotation or a ring inversion. Generally, the TSAP conformer is usually adopted in thermodynamically less stable complexes of larger ions like La^{3+}, whereas the SAP conformer is preferred for highly stable complexes of smaller ones like Lu^{3+}.

DTPA (Fig. 6.7) is an acyclic chelator with five acetate arms attached to a diethylenetriamine backbone, affording three N donors and five O donors. DTPA is one of the earliest chelators to be applied in radiopharmaceutical chemistry.

Extensive research on the coordination chemistry of DTPA has been undertaken, and this chelator has been revealed to rapidly radiolabel several therapeutic radionuclides under mild conditions, including $^{47}Sc^{3+}$, $^{90}Y^{3+}$, and $^{177}Lu^{3+}$ [26]. A clinical RPT agent that employs an analogue of DTPA is [^{90}Y]Y–ibritumomab tiuxetan (Zevalin®, Fig. 6.5), which is approved for the treatment of non-Hodgkin's lymphoma [21].

Despite their favorable radiolabeling chemistry, DTPA complexes often experience in vivo stability issues due to their structural flexibility.
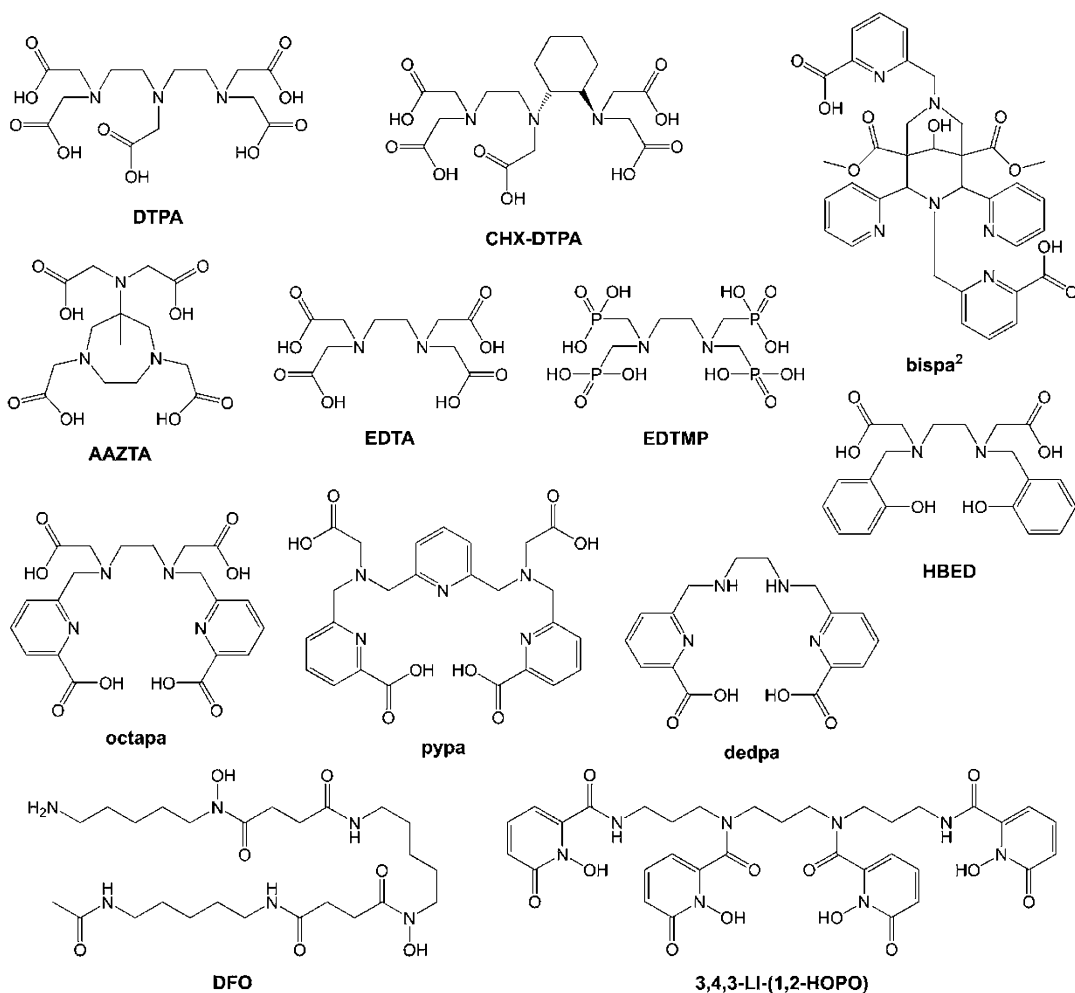
Fig. 6.7 Selected acyclic chelators used in the development of radiopharmaceuticals

Thus, recent efforts have focused on the development of analogues of DTPA that form more inert complexes. One such derivative is CHX-DTPA (Fig. 6.7), which contains a *trans*-diaminocyclohexyl group fused into the backbone. With this rigid group in place, the conformational flexibility of this linear chelator is significantly diminished compared to DTPA, thereby conferring it with a much higher degree of preorganization and giving rise to complexes with greater kinetic stability than those of DTPA. This example highlights a strategy that is commonly applied to improve the kinetic stability of a chelator: the incorporation of rigid moieties into the ligand backbone.

A benzyl isothiocyanate was attached to the backbone of CHX-DTPA, to convert it into a bifunctional chelator. By introducing this group, however, a new chiral center is generated that adds to the existing two chiral centers of the *trans*-diaminocyclohexyl group. Consequently, four possible stereoisomers—the enantiomeric pair CHX-A′-DTPA and CHX-A″-DTPA, as well as the enantiomeric pair CHX-B′-DTPA and CHX-B″-DTPA—are created (Fig. 6.9). These enantiomeric pairs are further distinguished upon their conjugation to chiral targeting vectors, thereby affording four diastereomers with different chemical properties and metal complex stabilities. The Y^{3+} complex of CHX-A-
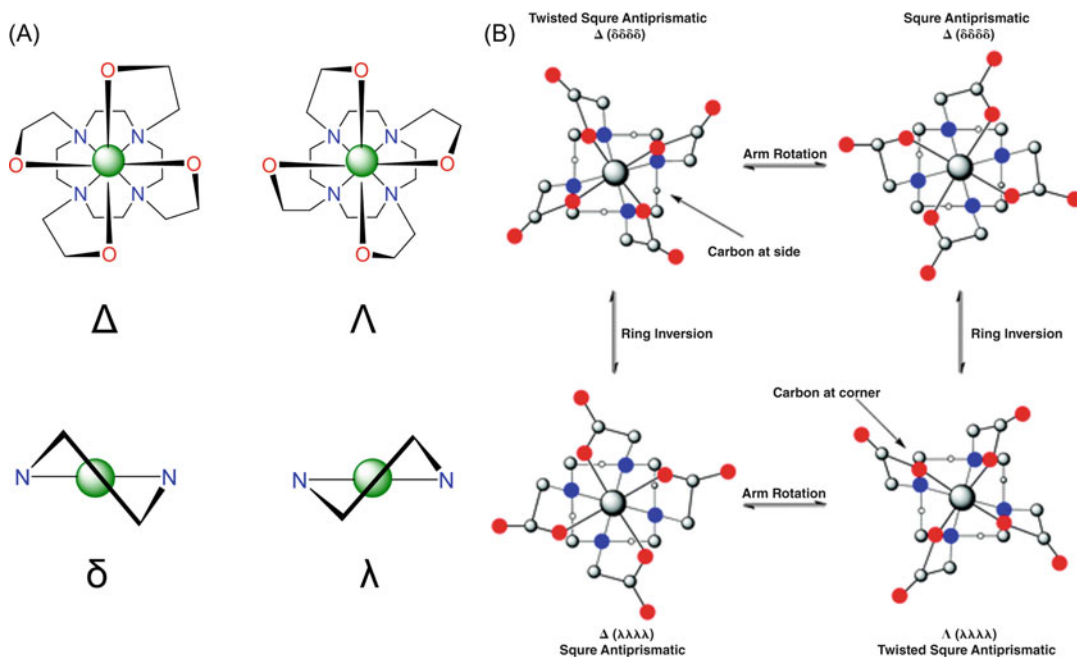
Fig. 6.8 (**a**) Depiction of the sources of chirality in DOTA complexes. (**b**) The stereoisomeric equilibrium for DOTA complexes in solution. (Reproduced from Ref. [25] with permission)

DTPA was found to be significantly more stable than that of CHX-B-DTPA. In an in vivo study in which the four stereoisomers were conjugated to a monoclonal antibody and then radiolabeled with $^{88}Y^{3+}$, the four radioimmunoconjugates exhibited different stability and biodistribution profiles, resulting in different degrees of $^{88}Y^{3+}$ accumulation in the bone with the CHX-B-DTPA analogues displaying more bone uptake than the CHX-A-DTPA complexes [27]. The development of the bifunctional variants of CHX-DTPA demonstrates that subtle structural changes can exert a significant influence on the stability of metal complexes.

(e) *Chelators for large radiometals*

The majority of chelators—such as those shown in Figs. 6.7 and 6.8—preferentially bind and stabilize smaller metal ions. The poor efficacy of these chelators for large radiometals is most likely a consequence of their small cavity sizes and the more charge-diffuse nature of large metal ions that weakens the electrostatic interactions with the ligand donor atoms [28]. Although these types of chelators have been useful for many radiometal ions, large radiometals with promising therapeutic applications have been identified in recent years. For these reasons, there have been substantial efforts to design chelators with a preference for large over small metal ions.

The use of chelators with large macrocycles was found to be an effective strategy for coordinating large radiometal ions. Specifically, macrocyclic chelators containing 1,7-diaza-18-crown-6 were discovered to possess *reverse size selectivity*, a property that describes their greater affinity for large over small metal ions. Among this class of chelators, macropa (Fig. 6.6) has arisen as a promising candidate for RPT. The reverse size selectivity of macropa is demonstrated by its K_{ML} values (Fig. 6.10) with the lanthanides (Ln^{3+}) [29] and alkaline earth metals [30], two classes of metal ions with similar chemical properties but different ionic radii.
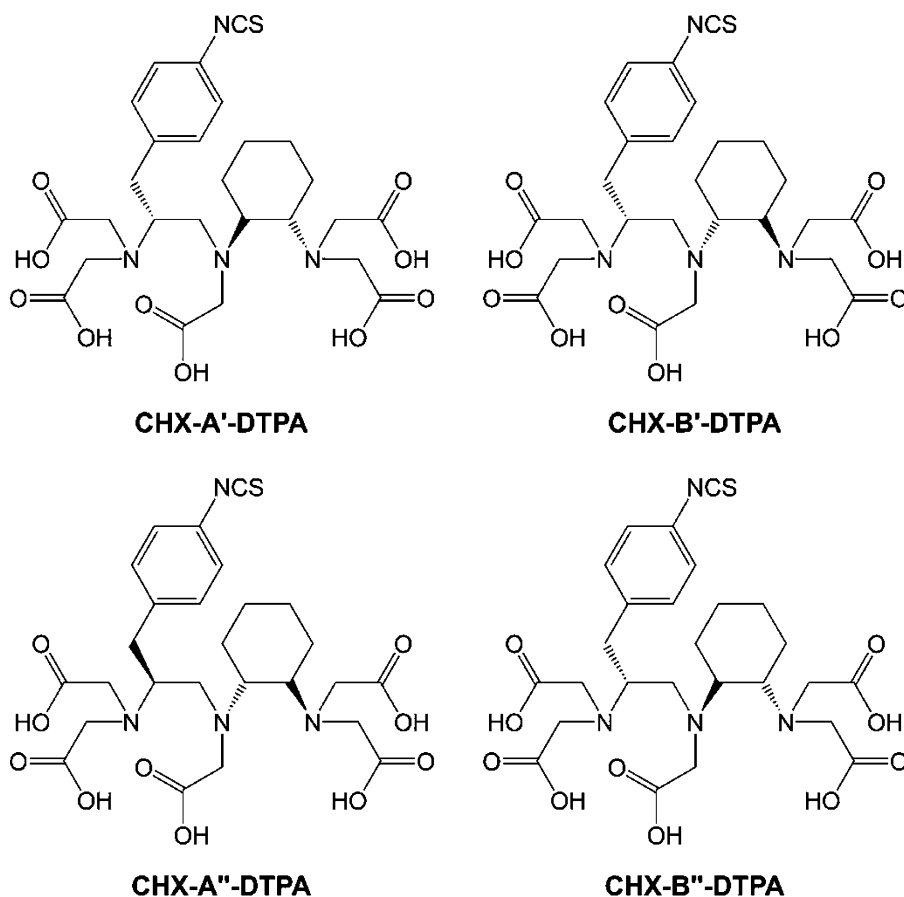
Fig. 6.9 Structures of CHX-A′-DTPA, CHX-A″-DTPA, CHX-B′-DTPA, and CHX-B″-DTPA

Given its high affinity for large metal ions, macropa has been established as an effective chelator for several large radiometals, including $^{135}La^{3+}$, $^{213}Bi^{3+}$, $^{223}Ra^{2+}$, and $^{225}Ac^{3+}$ [28].

(f) *Chelators for both large and small radiometals*

Despite the efficacy of reverse-size-selective chelators with large radiometals, their poor affinity for small radiometals limits their versatility. Recently, a new class of chelators with *dual size selectivity*—a property that reflects a high affinity for both large and small radiometals—was developed. The macrocyclic chelators macrodipa and py-macrodipa (Fig. 6.6) are members of this class, as reflected by the trends in their log K_{ML} values across the Ln^{3+} series (Fig. 6.11a)

[31, 32]. This unique property is a consequence of their ability to toggle between two distinct conformations and thus accommodate both large and small metal ions. Large Ln^{3+} form complexes in the distorted C_2-symmetric, 10-coordinate conformation A, whereas small Ln^{3+} sit in the asymmetric, 8-coordinate Conformation B, as depicted in Fig. 6.11b. In particular, py-macrodipa has been revealed to efficiently form inert complexes with the large therapeutic radionuclides $^{135}La^{3+}$ and $^{213}Bi^{3+}$ as well as the small diagnostic radiometal $^{44}Sc^{3+}$.

6.2.2.2 Metal Complexes with Multiple Low-Denticity Ligands

An alternative approach to chelators is the use of an array of simpler ligands of lower denticity to form coordination complexes. Because lower-

Fig. 6.10 Stability constants of complexes formed by macropa with lanthanide and alkaline earth metal ions plotted versus ionic radii. These plots show the reverse size selectivity of macropa. (Metal ionic radii are taken from Ref. [8])
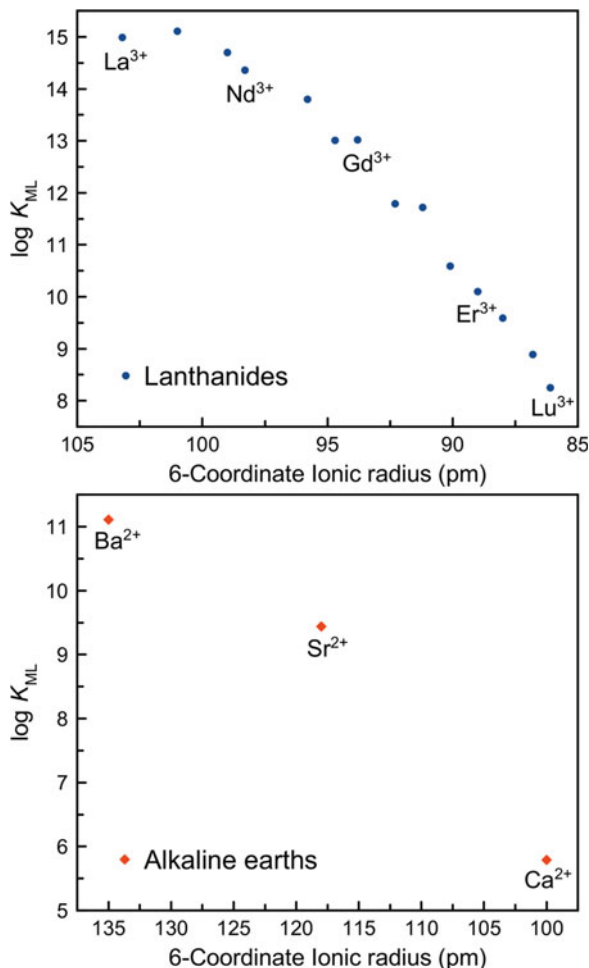
denticity ligands are more dynamic and labile, this strategy can only be applied to radiometal ions that are intrinsically capable of forming inert covalent metal–ligand interactions. These radiometal ions predominately fall within the transition metal series for which ligand field stabilization effects produce inert complexes. Like the chelator strategy described above, this approach requires that the desired radiometal complex be stable in vivo and can be formed with a high specific activity.

The best example of this approach employs ^{99m}Tc. Although this radionuclide has been recently investigated for its potential in Auger electron therapy, it is conventionally used as a diagnostic γ-ray emitter for single-photon emission computed tomography (SPECT). Relatively

simple coordination and organometallic complexes of this radiometal are sufficiently stable for in vivo applications, and many ^{99m}Tc-containing complexes have been approved for clinical use. For example, the homoleptic octahedral complex $[^{99m}$Tc]Tc(I)–sestamibi (Cardiolite®, Fig. 6.12) contains six monodentate methoxyisobutylisonitrile ligands and is sufficiently stable for use as an SPECT imaging agent in cardiology [33]. Furthermore, tricarbonyl complexes of ^{99m}Tc that contain three monodentate carbonyl (CO) ligands are also highly robust in vivo. Like ^{99m}Tc, ^{195m}Pt has also primarily been investigated for SPECT applications but has recently been recognized as a potential radionuclide for Auger-electron-mediated therapy. The intrinsic inertness of Pt^{2+}

Fig. 6.11 (**a**) Stability constants versus ionic radii plotted for rare-earth complexes formed by macrodipa and py-macrodipa. These plots show their dual size selectivity. (Metal ionic radii are taken from Ref. [8]). (**b**) A graphical representation of the conformational toggle of this ligand class upon binding large (Conformation A) and small (Conformation B) ions
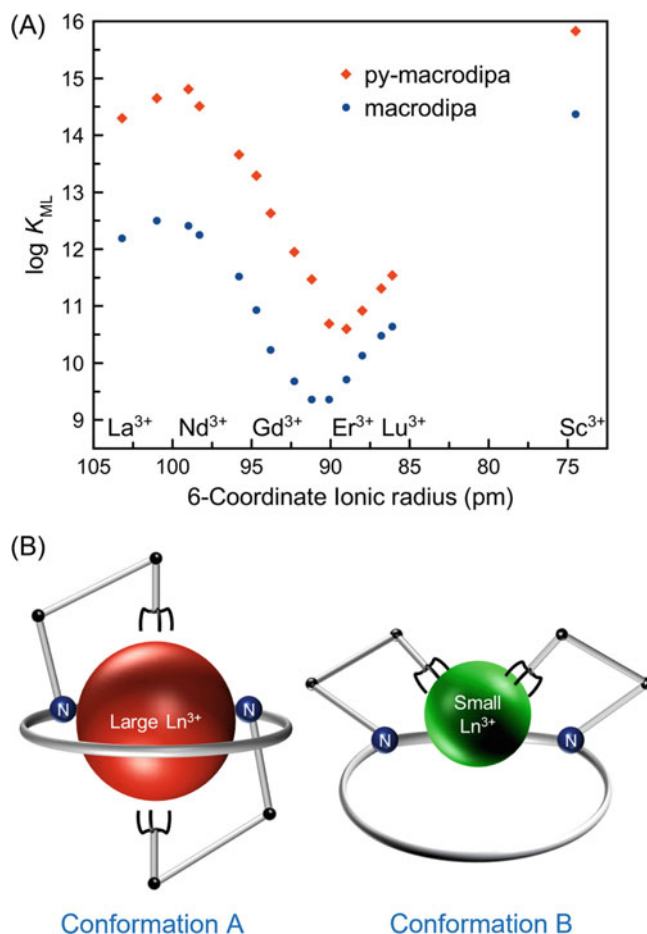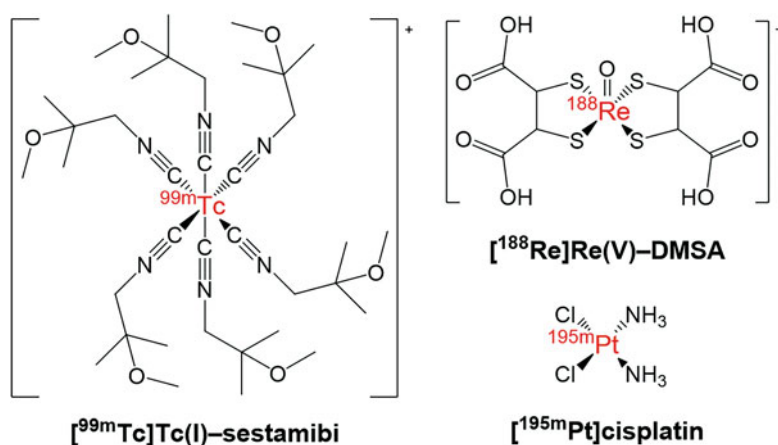

Fig. 6.12 The transition-metal-based radiopharmaceuticals discussed in this chapter

has enabled the assembly of [195mPt]-based radiopharmaceuticals with simple monodentate ligands. A key example is the preparation of [195mPt]-labeled cisplatin (Fig. 6.12), which

contains monodentate ammine and chloride ligands. This labeled compound was ~85% more effective at inhibiting tumor growth compared to nonradioactive cisplatin, demonstrating the

therapeutic potential of the Auger electron emissions of ^{195m}Pt [34].

In principle, this coordination strategy could be employed with other therapeutic radioisotopes of transition metals that preferentially form covalent bonds with ligands, such as the β-emitters $^{186/188}$Re, ^{109}Pd, and ^{105}Rh. Because Re is the heavier Group 7 congener of Tc, the chemistry of these two elements is similar, allowing for radiolabeling strategies employed with ^{99m}Tc to be used for therapeutic $^{186/188}$Re-labeled analogues [35]. For example, [^{99m}Tc]Tc(V)–DMSA (NephroScan™)—in which DMSA is the bidentate ligand *meso*-2,3-dimercaptosuccinic acid—is used for the scintigraphic evaluation of renal parenchymal disorder, whereas its analogue, [^{188}Re]Re(V)–DMSA (Fig. 6.12), has been investigated for RPT. This ^{188}Re complex was tested in prostate cancer patients with disseminated bone metastases and produced high uptake in these malignant lesions but also undesired high renal accumulation [36]. Another low-denticity ligand, the bisphosphonate etidronic acid (1-hydroxyethylidene-1,1-diphosphonic acid, HEDP), has been used in the radiopharmaceutical agent [^{186}Re]Re–HEDP (Etidronate®) for the palliative treatment for bone metastases. Although this drug was approved in Europe, it has since been withdrawn from the market in this region and is currently only found in developing countries.

The major advantage of using these simple low-denticity ligands is that they do not require the lengthy multistep organic syntheses that are often necessary to obtain multidentate chelators. In general, however, it can be argued that chelators are still preferable to lower-denticity ligands for RPT for several reasons. First, the chelate and (in some cases) macrocyclic effects enable chelators to form more stable complexes than lower-denticity ligands. Furthermore, the use of chelators for radiopharmaceutical applications is more widespread across the entire periodic table. Simpler ligands can only be used with transition metal ions that have *d* electron configurations that permit the formation of highly inert complexes. In addition, radiolabeling processes involving chelators are typically more straightforward than those involving multiple simple ligands. Whereas the formation of a radiometal–chelator complex only requires mixing the two components, the formation of coordination complexes with lower-denticity ligands often necessitates other components to modulate the redox state of the metal. Finally, lower-denticity ligands potentially give rise to complexes with constitutional isomers that can have different biological properties.

6.2.3   Nanoparticles

The use of nanoparticles in medicine has expanded significantly over the past several decades. Nanoparticles are generally defined by their size: at least one dimension to be between 1 and 100 nm. A number of properties of nanoparticles have made them attractive as platforms for therapeutic and diagnostic agents. For example, nanoparticles are known for their high relative surface area compared to larger constructs, which enables the modular, multiplexed, and high-density functionalization of their surface (Fig. 6.13). Furthermore, the large size of nanoparticles compared to molecular entities also allows them to encapsulate small molecules. A wide variety of nanoparticles have been leveraged for biomedical applications, and their compositions can be broadly described as either organic or inorganic.

Nanoparticles themselves can act as tumor-targeting vectors by leveraging the *enhanced permeability and retention (EPR) effect* [38]. The rapid angiogenesis in solid tumors often leads to disorganized and flawed neovasculature and enhanced vascular permeability. These irregularities often allow nanoparticles or macromolecules to traverse through the defective blood vessels and accumulate in the tumors. Thus, unmodified nanoparticles of suitable sizes can passively target radionuclides to tumors. In addition, active targeting is also possible for enhanced tumor-seeking properties. In this case, targeting moieties are attached to the nanoparticles via surface modifications, as indicated in Fig. 6.13.
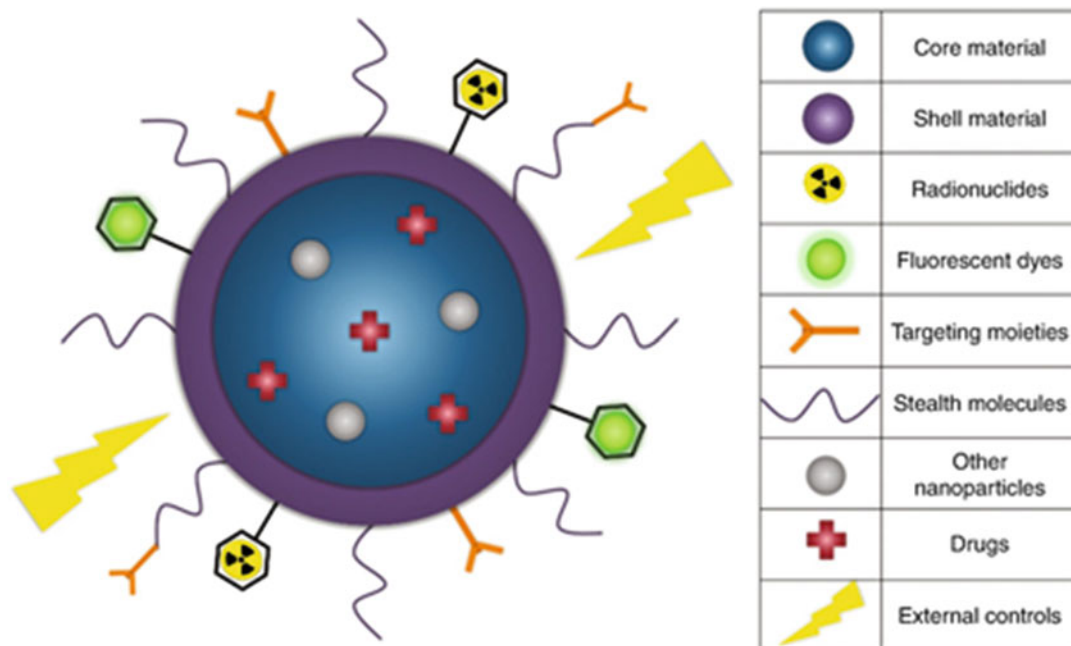
Fig. 6.13 Different cargoes can be appended to nanoparticles for therapeutic and diagnostic applications. (Reproduced from Ref. [37] with permission)

Another potential advantage of nanoparticles for RPT is their ability to handle and retain recoiling daughter nuclides. As detailed in Chap. 5, the conservation of momentum requires that daughter nuclides recoil with an opposite but equal momentum upon the emission of a particle. This phenomenon occurs with all radioactive emissions but is most important in the context of α-decay, in which the recoil energy exceeds that of chemical bonds by orders of magnitude. Thus, the decay of an α-emitting radiometal ruptures the metal–ligand bonds, freeing the daughter nuclide from the radiotherapeutic. In theory, the encapsulation of α-emitting radionuclides in nanoparticles could minimize the release of the recoiled daughter nuclides. This concept has been demonstrated with both inorganic and organic nanoparticles. For example, the incorporation of $^{225}Ac^{3+}$ into $LaPO_4$ nanoparticles led to the retention of ~50% of the ^{221}Fr and ^{213}Bi daughters within the nanoparticle [39]. Similarly, up to 69% of ^{221}Fr and 53% of ^{213}Bi were retained when $^{225}Ac^{3+}$ was encapsulated into polysomes

prepared from a poly(butadiene(1,2 addition)-b-ethylene oxide) block copolymer [40].

The radiolabeling of nanoparticles can be accomplished via two distinct pathways: *derivatization* and *incorporation* (Fig. 6.14) [41]. In derivatization, the nonradioactive nanoparticles are prepared first and then conjugated with the radiometal of interest. This approach is generally applied in conjunction with chelators. Typically, suitable chelators are attached to the nanoparticle surface in advance. For example, an analogue of DOTA (Fig. 6.6) was grafted onto *N,N,N*-trimethyl chitosan-coated magnetic nanoparticles, and the resulting construct was efficiently radiolabeled with $^{68}Ga^{3+}$ [42]. In polymeric nanoparticles, chelators can also be directly incorporated into the polymer backbone. In a recent study, a derivative of NOTA (Fig. 6.6) was attached to the building block of the polymeric chain, and the resulting nanoparticles were effectively radiolabeled with $^{68}Ga^{3+}$ [43].

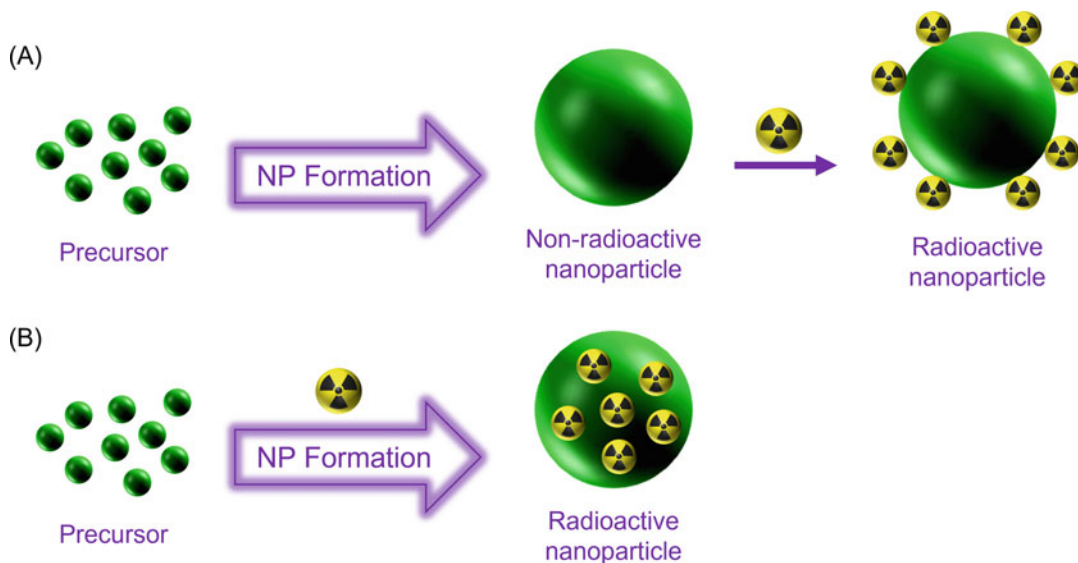The second nanoparticle radiolabeling strategy, *incorporation* or *intrinsic radiolabeling*

Fig. 6.14 Schematic illustration of the difference between the labeling of nanoparticles via (**a**) derivatization and (**b**) incorporation

[44], inserts the radiometal during the formation of the nanoparticle. An example of this approach was the inclusion of [198]Au during the formation of gold nanoparticles that were subsequently functionalized with epigallocatechin gallate (EGCg) to facilitate the targeting of prostate cancer tumors [45].

Despite the increasing research into the use of radiolabeled nanoparticles for RPT, the clinical translation of nanoparticulate radiopharmaceuticals remains at an early stage. One radiolabeled nanoparticle that has undergone clinical trials is [[188]Re]Re–BMEDA-liposome (Fig. 6.15) [46]. Its preparation employs the incorporation method. First, [[188]Re]ReO$_4^-$ is complexed by N,N-bis(2-mercaptoethyl)-N'',N''--diethylethylenediamine (BMEDA), and the radiometal complex is then incorporated into PEGylated liposomes. These liposomes leverage the EPR effect and have shown efficacy for the treatment of advanced solid ovarian tumors [47]. The clinical studies were initiated in 2014 but were terminated in 2020 due to the concerns surrounding the accumulation of radioactivity in the liver and spleen.

6.3   The Future

Harnessing metallic radiometals for RPT is a multidisciplinary endeavor that requires advances across several different fields. As new radiometals are identified as potential tools for RPT, new chemistry will be required to learn how to incorporate them into useful radiopharmaceuticals. Along these lines, the radiometals of unusual elements—including the actinides and transactinides—have driven and will continue to drive efforts to design novel ligands. Since the development and application of conventional chelators like DOTA and DTPA, extensive research has been dedicated to synthesizing and evaluating novel chelating agents. As highlighted in this chapter, these efforts have led to the development of chelators with greater radiolabeling efficiency and complex stability as well as unusual selectivity patterns (such as reverse and dual size selectivity). The use of nanoparticles for radiolabeling also provides intriguing opportunities. For example, the potential of nanoparticles to circumvent the

Fig. 6.15 Schematic
depiction of [188Re]Re–
BMEDA-liposome

[188Re]Re–BMEDA
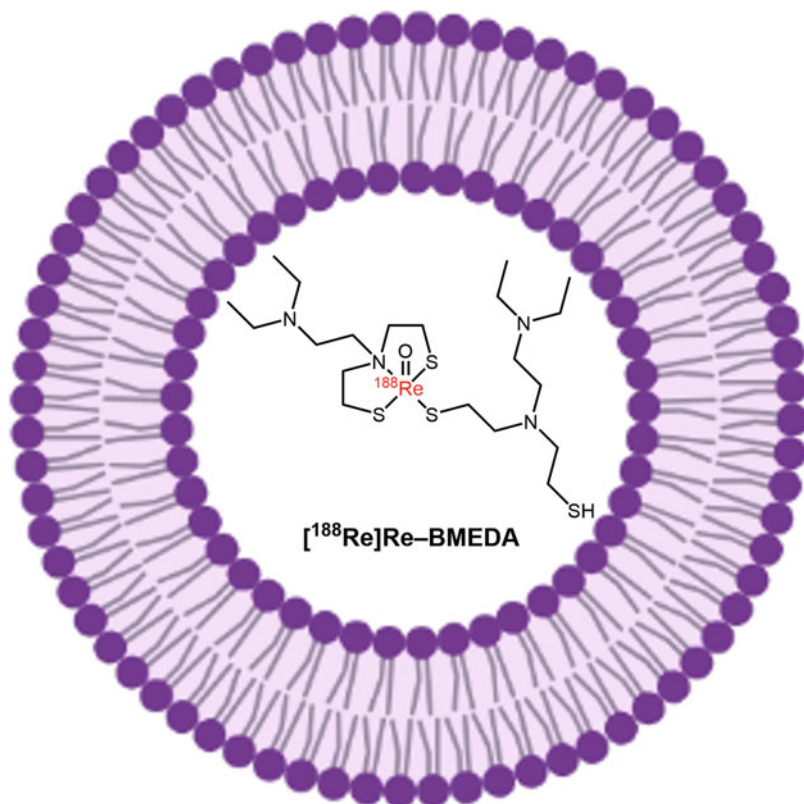
α recoil effect could facilitate the development of safer α-emitting agents for RPT. We also envision that advances in molecular and cellular biology will give rise to new targeting vectors, which will further enhance the selectivity, safety, and efficacy of radiopharmaceutical agents.

6.4 The Bottom Line

- A large number of metallic elements have radioisotopes that are relevant to RPT. These elements span the entirety of the periodic table and thus have distinct chemical properties. It is important to take these properties into account when designing novel radiometallated therapeutic agents.
- Different methods have been applied to leverage the radiometal ions for RPT. The radiometals can be administered as free metal salts or as components of larger radiopharmaceuticals based on small molecules, peptides, proteins, antibodies, or nanoparticles.

- It is often important to attach radiometals to targeting vectors to ensure the delivery of the former to target tissue in vivo. When building radiotherapeutics predicated on metal–ligand complexes, the ligand(s) must efficiently bind the radiometal and form a thermodynamically and kinetically stable complex.
- The successful transformation of a metallic radionuclide into a useful component of a radiotherapeutic requires a careful and lengthy design and assessment process. To this end, expertise in a variety of fields is needed.

References

1. Blower PJ. A nuclear chocolate box: the periodic table of nuclear medicine. Dalton Trans. 2015;44:4819–44. https://doi.org/10.1039/C4DT02846E.
2. Boros E, Packard AB. Radioactive transition metals for imaging and therapy. Chem Rev. 2019;119:870–901. https://doi.org/10.1021/acs.chemrev.8b00281.
3. Kostelnik TI, Orvig C. Radioactive main group and rare earth metals for imaging and therapy. Chem Rev.

2019;119:902–56. https://doi.org/10.1021/acs.chemrev.8b00294.

4. Poonia NS, Bajaj AV. Coordination chemistry of alkali and alkaline earth cations. Chem Rev. 1979;79:389–445. https://doi.org/10.1021/cr60321a002.

5. Shimoni-Livny L, Glusker JP, Bock CW. Lone pair functionality in divalent lead compounds. Inorg Chem. 1998;37:1853–67. https://doi.org/10.1021/ic970909r.

6. Seth SK, Bauzá A, Mahmoudi G, Stilinović V, López-Torres E, Zaragoza G, et al. On the importance of Pb⋯X (X = O, N, S, Br) tetrel bonding interactions in a series of tetra- and hexa-coordinated Pb(II) compounds. CrystEngComm. 2018;20:5033–44. https://doi.org/10.1039/C8CE00919H.

7. Figgis BN, Hitchman MA. Ligand field theory and its applications. New York: Wiley-VCH; 2000.

8. Shannon RD. Revised effective ionic radii and systematic studies of interatomic distances in halides and chalcogenides. Acta Crystallogr Sect A: Found Adv. 1976;32:751–67. https://doi.org/10.1107/S0567739476001551.

9. Seitz M, Oliver AG, Raymond KN. The lanthanide contraction revisited. J Am Chem Soc. 2007;129:11153–60. https://doi.org/10.1021/ja072750f.

10. Lewington VJ. Bone-seeking radionuclides for therapy. J Nucl Med. 2005;46:38S–47S.

11. Nightengale B, Brune M, Blizzard SP, Ashley-Johnson M, Slan S. Strontium chloride Sr 89 for treating pain from metastatic bone disease. Am J Health Syst Pharm. 1995;52:2189–95. https://doi.org/10.1093/ajhp/52.20.2189.

12. Kluetz PG, Pierce W, Maher VE, Zhang H, Tang S, Song P, et al. Radium Ra 223 dichloride injection: U.S. food and drug administration drug approval summary. Clin Cancer Res. 2014;20:9–14. https://doi.org/10.1158/1078-0432.CCR-13-2665.

13. da Silva Frausto JJR. The chelate effect redefined. J Chem Educ. 1983;60:390. https://doi.org/10.1021/ed060p390.

14. Martell AE, Hancock RD. Metal complexes in aqueous solutions. New York: Plenum Press; 1996.

15. Harris WR, Carrano CJ, Raymond KN. Coordination chemistry of microbial iron transport compounds. 16. Isolation, characterization, and formation constants of ferric aerobactin. J Am Chem Soc. 1979;101:2722–7. https://doi.org/10.1021/ja00504a038.

16. Anderson PM, Wiseman GA, Dispenzieri A, Arndt CAS, Hartmann LC, Smithson WA, et al. High-dose samarium-153 ethylene diamine tetramethylene phosphonate: low toxicity of skeletal irradiation in patients with osteosarcoma and bone metastases. J Clin Oncol. 2002;20:189–96. https://doi.org/10.1200/JCO.2002.20.1.189.

17. Wester H-J, Schottelius M. PSMA-targeted radiopharmaceuticals for imaging and therapy. Semin Nucl Med. 2019;49:302–12. https://doi.org/10.1053/j.semnuclmed.2019.02.008.

18. Sartor O, Herrmann K. Prostate cancer treatment: ^{177}Lu-PSMA-617 considerations, concepts, and limitations. J Nucl Med. 2022;63:823–9. https://doi.org/10.2967/jnumed.121.262413.

19. Hennrich U, Kopka K. Lutathera®: the first FDA- and EMA-approved radiopharmaceutical for peptide receptor radionuclide therapy. Pharmaceuticals. 2019;12:114. https://doi.org/10.3390/ph12030114.

20. Rogoza O, Megnis K, Kudrjavceva M, Gerina-Berzina A, Rovite V. Role of somatostatin signalling in neuroendocrine tumours. Int J Mol Sci. 2022;23:1447. https://doi.org/10.3390/ijms23031447.

21. Grillo-López AJ. Zevalin: the first radioimmunotherapy approved for the treatment of lymphoma. Expert Rev Anticancer Ther. 2002;2:485–93. https://doi.org/10.1586/14737140.2.5.485.

22. van Meerten T, Hagenbeek A. CD20-targeted therapy: the next generation of antibodies. Semin Hematol. 2010;47:199–210. https://doi.org/10.1053/j.seminhematol.2010.01.007.

23. Lindoy LF. What is different about macrocyclic ligand complexes? In: The chemistry of macrocyclic ligand complexes. Cambridge: Cambridge University Press; 1989. p. 1–20.

24. Hancock RD, Martell AE. The chelate, cryptate and macrocyclic effects. Comments Inorg Chem. 1988;6:237–84. https://doi.org/10.1080/02603598808072293.

25. Stasiuk GJ, Long NJ. The ubiquitous dota and its derivatives: the impact of 1,4,7,10-tetraazacyclododecane-1,4,7,10-tetraacetic acid on biomedical imaging. Chem Commun. 2013;49:2732–46. https://doi.org/10.1039/C3CC38507H.

26. Price EW, Orvig C. Matching chelators to radiometals for radiopharmaceuticals. Chem Soc Rev. 2014;43:260–90. https://doi.org/10.1039/C3CS60304K.

27. Wu C, Kobayashi H, Sun B, Yoo TM, Paik CH, Gansow OA, et al. Stereochemical influence on the stability of radio-metal complexes in vivo. synthesis and evaluation of the four stereoisomers of 2-(p-nitrobenzyl)-trans-CyDTPA. Bioorg Med Chem. 1997;5:1925–34. https://doi.org/10.1016/S0968-0896(97)00130-2.

28. Hu A, Wilson JJ. Advancing chelation strategies for large metal ions for nuclear medicine applications. Acc Chem Res. 2022;55:904–15. https://doi.org/10.1021/acs.accounts.2c00003.

29. Roca-Sabio A, Mato-Iglesias M, Esteban-Gómez D, Tóth É, de Blas A, Platas-Iglesias C, et al. Macrocyclic receptor exhibiting unprecedented selectivity for light lanthanides. J Am Chem Soc. 2009;131:3331–41. https://doi.org/10.1021/ja808534w.

30. Thiele NA, MacMillan SN, Wilson JJ. Rapid dissolution of baSO$_4$ by macropa, an 18-membered macrocycle with high affinity for Ba^{2+}. J Am Chem Soc. 2018;140:17071–8. https://doi.org/10.1021/jacs.8b08704.

31. Hu A, MacMillan SN, Wilson JJ. Macrocyclic ligands with an unprecedented size-selectivity pattern for the lanthanide ions. J Am Chem Soc. 2020;142:13500–6. https://doi.org/10.1021/jacs.0c05217.

32. Hu A, Aluicio-Sarduy E, Brown V, MacMillan SN, Becker KV, Barnhart TE, et al. Py-macrodipa: a janus chelator capable of binding medicinally relevant rare-earth radiometals of disparate sizes. J Am Chem Soc. 2021;143:10429–40. https://doi.org/10.1021/jacs.1c05339.

33. Nunn AD. New radiopharmaceuticals based on technetium. In: Schubiger PA, Westera G, editors. Progress in radiopharmacy. Dordrecht: Springer Science+Business Media; 1992. p. 55–65.

34. Bodnar EN, Dikiy MP, Medvedeva EP. Photonuclear production and antitumor effect of radioactive cisplatin (^{195m}Pt). J Radioanal Nucl Chem. 2015;305:133–8. https://doi.org/10.1007/s10967-015-4053-1.

35. Lepareur N, Lacœuille F, Bouvry C, Hindré F, Garcion E, Chérel M, et al. Rhenium-188 labeled radiopharmaceuticals: current clinical applications in oncology and promising perspectives. Front Med. 2019;6:132. https://doi.org/10.3389/fmed.2019.00132.

36. Blower PJ, Kettle AG, O'Doherty MJ, Coakley AJ, Knapp FF Jr. ^{99m}Tc(V)DMSA quantitatively predicts ^{188}Re(V)DMSA distribution in patients with prostate cancer metastatic to bone. Eur J Nucl Med. 2000;27: 1405–9. https://doi.org/10.1007/s002590000307.

37. Kamkaew A, Ehlerding EB, Cai W. Nanoparticles as radiopharmaceutical vectors. In: Lewis JS, Windhorst AD, Zeglis BM, editors. Radiopharmaceutical chemistry. Cham: Springer Nature Switzerland AG; 2019. p. 181–203.

38. Fang J, Nakamura H, Maeda H. The EPR effect: unique features of tumor blood vessels for drug delivery, factors involved, and limitations and augmentation of the effect. Adv Drug Deliv Rev. 2011;63:136–51. https://doi.org/10.1016/j.addr.2010.04.009.

39. Woodward J, Kennel SJ, Stuckey A, Osborne D, Wall J, Rondinone AJ, et al. LaPO4 nanoparticles doped with actinium-225 that partially sequester daughter radionuclides. Bioconjug Chem. 2011;22: 766–76. https://doi.org/10.1021/bc100574f.

40. Wang G, de Kruijff RM, Rol A, Thijssen L, Mendes E, Morgenstern A, et al. Retention studies of recoiling daughter nuclides of ^{225}Ac in polymer vesicles. Appl Radiat Isot. 2014;85:45–53. https://doi.org/10.1016/j.apradiso.2013.12.008.

41. Dai W, Zhang J, Wang Y, Jiao C, Song Z, Ma Y, et al. Radiolabeling of nanomaterials: advantages and challenges. Front Toxicol. 2021;3:753316. https://doi.org/10.3389/ftox.2021.753316.

42. Hajiramezanali M, Atyabi F, Mosayebnia M, Akhlaghi M, Geramifar P, Jalilian AR, et al. ^{68}Ga-radiolabeled bombesin-conjugated to trimethyl chitosan-coated superparamagnetic nanoparticles for molecular imaging: preparation, characterization and biological evaluation. Int J Nanomedicine. 2019;14: 2591–605. https://doi.org/10.2147/IJN.S195223.

43. Körhegyi Z, Rózsa D, Hajdu I, Bodnár M, Kertész I, Kerekes K, et al. Synthesis of ^{68}Ga-labeled biopolymer-based nanoparticle imaging agents for positron-emission tomography. Anticancer Res. 2019;39:2415–27. https://doi.org/10.21873/anticanres.13359.

44. Goel S, Chen F, Ehlerding EB, Cai W. Intrinsically radiolabeled nanoparticles: an emerging paradigm. Small. 2014;10:3825–30. https://doi.org/10.1002/smll.201401048.

45. Ravi S, Nripen C, Ajit Z, Anandhi U, Kavita K, Kulkarni RR, et al. Laminin receptor specific therapeutic gold nanoparticles (^{198}AuNP-EGCg) show efficacy in treating prostate cancer. Proc Natl Acad Sci. 2012;109:12426–31. https://doi.org/10.1073/pnas.1121174109.

46. Anselmo AC, Mitragotri S. Nanoparticles in the clinic: an update post covid-19 vaccines. Bioeng Transl Med. 2021;6:e10246. https://doi.org/10.1002/btm2.10246.

47. Chang C-M, Lan K-L, Huang W-S, Lee Y-J, Lee T-W, Chang C-H, et al. ^{188}Re-liposome can induce mitochondrial autophagy and reverse drug resistance for ovarian cancer: from bench evidence to preliminary clinical proof-of-concept. Int J Mol Sci. 2017;18:903. https://doi.org/10.3390/ijms18050903.

The Radiopharmaceutical Chemistry of the Halogen Radionuclides

7

Ganesan Vaidyanathan, Yutian Feng, and Michael R. Zalutsky

7.1 The Fundamentals

Although it is often ignored in contemporary research, it is important to remember that the β (beta)-particle-emitting radiohalogen ^{131}I was responsible for the overwhelming majority of the early success of radiopharmaceutical therapy (RPT). Starting more than 70 years ago, iodine's natural affinity for the thyroid has been exploited for treating both benign and cancerous types of thyroid disease with radioisotopes of the halogen. Unfortunately, the thyroid enzymes that facilitate the uptake of ^{131}I in thyroid also can have a negative effect: dehalogenation, the removal of ^{131}I from molecules like proteins that are radiolabeled directly on tyrosine residues. Because of this in vivo instability, ^{131}I-labeled proteins and compounds with structurally similar iodination sites became an unattractive option for RPT. Furthermore, the increased availability and synthetic simplicity of radiometals fueled their rise as an attractive alternative to radiohalogens for the development of radiotherapeutics. There are also—as discussed in the previous chapter—far more radiometals than radiohalogens, providing a diverse array of options both in terms of coordination chemistry and nuclear decay characteristics.

Two developments have rekindled interest in the radiohalogens in recent years: (1) the development of novel labeling chemistries that have drastically reduced in vivo dehalogenation (*infra vide*) and (2) the advent of theranostics in contemporary nuclear medicine. With respect to the latter, iodine-131 is a true theranostic radionuclide that can be used for both diagnostic SPECT and RPT. Likewise, ^{123}I ($t_{1/2}$ ~ 13.2 h) can also be used for both SPECT and Auger electron therapy (Fig. 7.1). The availability of other radioisotopes of iodine, including ^{124}I ($t_{1/2}$ ~ 4.2 d) for PET and ^{125}I ($t_{1/2}$ ~ 60 d) for Auger electron-mediated RPT, provides still more options to create isotopologous pairs of theranostic radiopharmaceuticals for imaging and RPT. Perhaps the most intriguing radiohalogen for RPT—the α (alpha)-particle emitting heavy halogen ^{211}At ($t_{1/2}$ ~ 7.2 h)—also presents the greatest challenge to the radiochemist. Finally, ^{77}Br ($t_{1/2}$ = 57.0 h) and ^{80m}Br ($t_{1/2}$ = 4.4 h) emit Auger electrons and may prove beneficial in therapeutic situations in which the irradiation of nontargeted cells must be avoided.

There are a few fundamental differences between radiohalogens and radiometals worth noting before we begin. With halogens, the attachment of the radionuclide to the targeting vector involves the formation of a covalent bond, while labeling with radiometals necessitates the use of a chelator. Because chelators are generally large and bear multiple charges, their attachment can inadvertently

G. Vaidyanathan · Y. Feng · M. R. Zalutsky (✉)
Department of Radiology, Duke University Medical Center, Durham, NC, USA
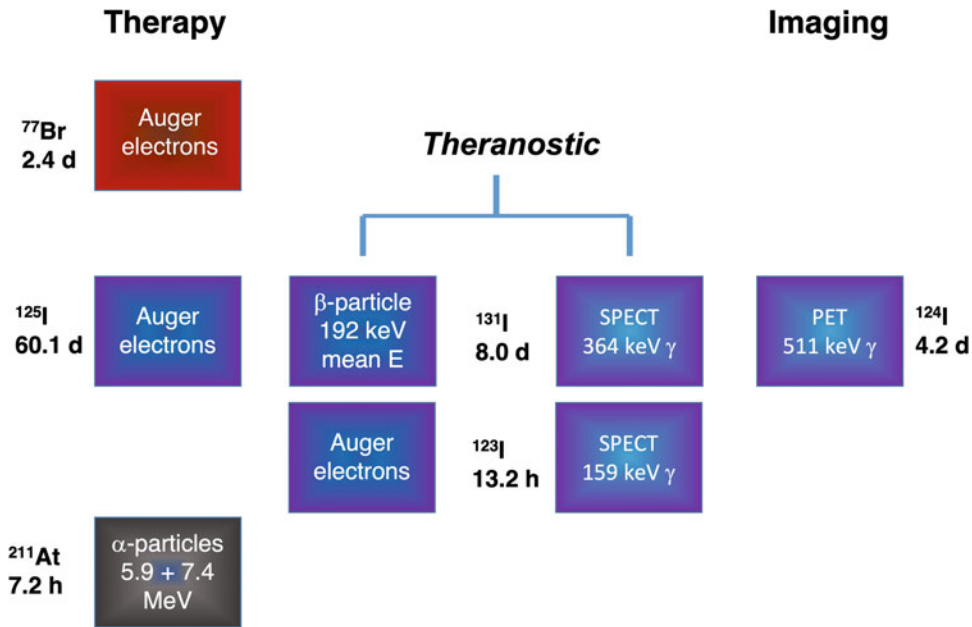e-mail: zalut001@mc.duke.edu

Fig. 7.1 The principal radiohalogens of interest for RPT, imaging and theranostics
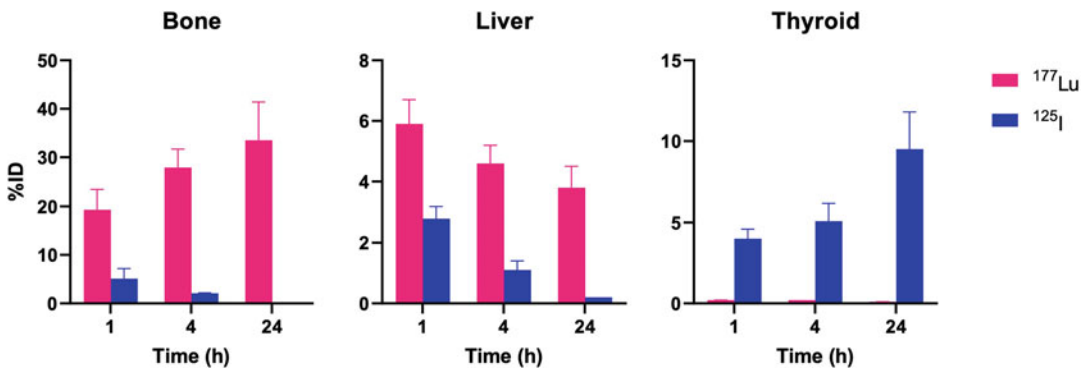

Fig. 7.2 The tissue distribution of ^{177}Lu and ^{125}I [expressed as percent injected dose (%ID)] after the injection of [^{177}Lu] lutetium chloride and sodium [^{125}I]iodide to normal mice. (Data obtained from Ref. [1])

modify the biological properties of the targeting vector. In most cases, this is easier to avoid with radiohalogens, particularly if they can be attached covalently to an existing aromatic ring on the vector. Another important difference between radiometals and radiohalogens is the biological behavior of the radiolabeled degradation products that are generated during the metabolism of the targeted radiotherapeutic. To illustrate this point, we compared the tissue distribution of [^{125}I] iodide and [^{177}Lu]lutetium chloride in normal

mice. Not surprisingly, the uptake of ^{125}I was highest in the thyroid and stomach [1], while that of ^{177}Lu was considerably higher than ^{125}I in both the liver and bone (Fig. 7.2). In practice, one catabolite distribution pattern may have advantages over the other depending on the clinical application and the properties of the targeting vector. However, the radiohalogens do have an important advantage here: supersaturated solutions of sodium iodide and other agents are in routine clinical use to block the uptake of

radiohalogens in the thyroid, stomach, and other tissues. Similar strategies are not available to attenuate the uptake of radiometals in the bones and liver, though infusions of positively charged amino acids can reduce the renal uptake of radiometal-labeled peptides.

In the sections that follow, we shall focus on the extant chemistries for labeling small organic molecules, peptides, and proteins with radiohalogens. We will start with radioiodine because it is the most widely studied of the radiohalogens. In addition, it is generally studied first in many laboratories (including our own) when the final intent is labeling with ^{211}At. The current state of the art for astatine labeling and radiobromination will then be presented, followed by some speculation about future prospects for the radiohalogens in radiopharmaceutical therapy.

7.2 The Details

The primary radiohalogens used in RPT are the β (beta)-emitter ^{131}I, the Auger electron-emitters ^{77}Br, ^{80m}Br, ^{123}I, and ^{125}I, and the α (alpha)-emitter ^{211}At. The chemistry involved in incorporating these radionuclides into radiopharmaceuticals is similar and will be detailed below for each element beginning with iodine.

7.2.1 Radioiodination

A number of excellent and comprehensive reviews on radioiodination have been published recently, and the interested reader is referred to these for additional information on this subject [2, 3].

7.2.1.1 Small Molecules

Due to the lower bond strength of the sp^3 carbon-iodine bond, radioiodination is practically limited to compounds in which the iodine will be attached to an sp^2 carbon. Nonetheless, a few examples of compounds in which radioiodine is attached to an sp^3 or sp carbon have been

reported. However, these are not likely to gain traction as targeted radiotherapeutics because of the aforementioned stability issues; therefore, we will eschew their discussion here.

7.2.1.1.1 Electrophilic Substitution

An oxidizing agent is necessary to convert the commercially available radioiodide to the +1-oxidation state that is needed for electrophilic substitution. To this end, the most commonly used oxidizing agents for radioiodination are iodogen, N-chlorosuccinimide (NCS), hydrogen peroxide, chloramine-T, and peracetic acid. Enzymatic and electrolytic oxidations have also been harnessed for electrophilic radioiodination, though these methods are admittedly seldom used.

The overwhelming majority of compounds synthesized via electrophilic radioiodination are iodoarenes, though a handful of radioiodinated aliphatic compounds have been reported as well. With respect to the former, the radioiodine can be introduced *ortho* or *para* to electron-donating substituents such as OH, NH_2, and OMe in a benzene ring by iododeprotonation (Fig. 7.3a). Although iododeprotonation can be performed on less activated rings (i.e., those lacking electron-donating substituents), the radiochemical yield (RCY) of these reactions will be low; however, the reaction can be accelerated using a metal catalyst. To wit, palladium-mediated C-H activation has been utilized to introduce radioiodine at the adjacent position of a directing group [4].

While activated rings facilitate radiolabeling, their propensity for in vivo deiodination makes them unattractive scaffolds for RPT [5]. This drawback can be overcome by using organometallic precursors that can be radioiodinated via *ipso* substitution in which the radioiodine replaces the metallic substituent (Fig. 7.3b) [6]. Organometallics such as organostannanes, organosilanes, organogermanes, and organomercurials are commonly used for this strategy, with organostannanes used most often. Generally speaking, the radiochemical yields of these substitution reactions are high, and the radioiodinated product can be easily separated
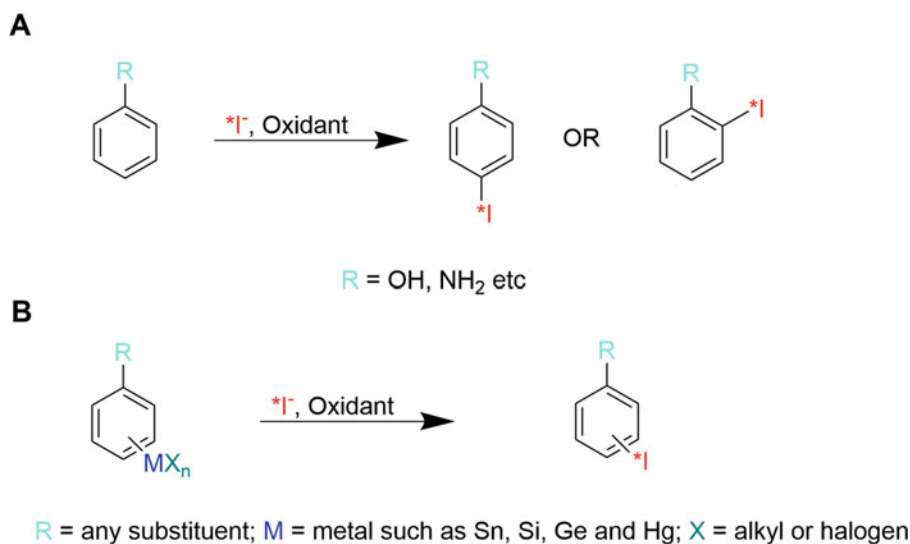
A

R = OH, NH₂ etc

B

R = any substituent; M = metal such as Sn, Si, Ge and Hg; X = alkyl or halogen

Fig. 7.3 The electrophilic radioiodination of aromatic compounds: (**a**) the radioiodination of activated aromatics such as hydroxy- (phenols) and amino-arenes (anilines) by iododeprotonation and (**b**) the radioiododemetallation of organometallics
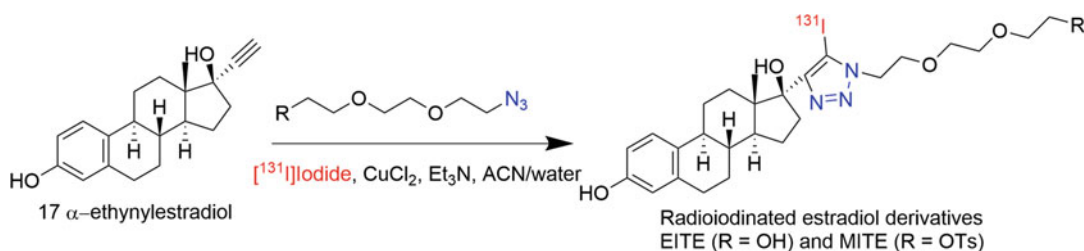

17 α−ethynylestradiol

Radioiodinated estradiol derivatives
EITE (R = OH) and MITE (R = OTs)

Fig. 7.4 The synthesis of estradiol derivatives [131I]EITE and [131I]MITE via a one-pot, three-component radioiodination

from its metallic precursor due to significant differences in polarity. As a result, radioiodinated agents produced via this method can be isolated in very high molar activities. However, some organometallics are very toxic, and thus it is extremely important to ensure that impurities have been removed from the final radiopharmaceutical preparation.

Although not an electrophilic substitution per se, a one-pot, three-component, copper-mediated click reaction has also been developed for the radioiodination of various agents [7]. This strategy was utilized recently for the synthesis of radioiodinated estrogen receptor-targeted agents for the imaging of breast cancer (Fig. 7.4).

7.2.1.1.2 Nucleophilic Substitution

Radioiodinated aliphatic compounds can be synthesized by nucleophilic substitution typically via an S_N2 reaction in which a leaving group is displaced by radioiodide (*a.k.a.* the Finkelstein reaction). Along these lines, commonly used leaving groups are halogens and sulfonates like mesylate, tosylate, and triflate. Higher molar activity can, of course, be obtained using non-iodine leaving groups. Given the remarkable stability imparted by a neopentyl group on an sp^3 carbon-halogen bond, radioiodinated nitrimidazoles bearing a neopentyl glycol were synthesized in high RCY via an S_N2 reaction from a triflate precursor, and the product

demonstrated remarkable inertness to in vivo deiodination [8].

Aromatic compounds also can be radioiodinated by S_NAr substitution reactions. Unlike electrophilic substitution, this reaction is favored for compounds containing aromatic rings with electron-withdrawing groups such as NO_2, or esters or aldehydes positioned *ortho-* and *para-* to the leaving group. Classically, compounds were radioiodinated using homo- or heterohalogen exchange reactions via the displacement of iodine or bromine, though this approach typically produced compounds with lower molar activities. A notable example of this approach is the method used for the synthesis of *meta-*[*I]iodobenzylguanidine ([*I]MIBG) for early clinical trials. Catalysts based on copper and nickel can also accelerate these exchange reactions [9].

Leaving groups other than halogens have been used for S_NAr substitution reactions. Indeed, radioiodinated arenes have been synthesized by adapting the classical Sandmeyer reaction for the synthesis of iodoarenes from aminoarenes via the intermediacy of diazonium salts. There are several drawbacks for this reaction, however, including the instability of the diazonium salt intermediate and the susceptibility of acid-sensitive functional groups to the standard conditions for this type of reaction. Sloan et al. [10] developed an operationally simple one-pot reaction for the radioiodination of arylamines that utilized a polymer-supported nitrite reagent in lieu of the classical sodium nitrite (Fig. 7.5). Excellent RCY was obtained even for compounds with electron-donating substituents. Triazenes are a stable alternative to diazonium salts; however, they are typically synthesized via diazonium salts. A few radioiodinated compounds have been synthesized from triazenes via the Wallach reaction, including *N*-succinimidyl 4-[^{125}I] iodobenzoate (*para-*[^{125}I]SIB), a reagent often used for the labeling of proteins and peptides.

In a method akin to their use in nucleophilic ^{18}F-labeling, diaryl iodonium salts and aryl iodonium ylides can also be employed for the
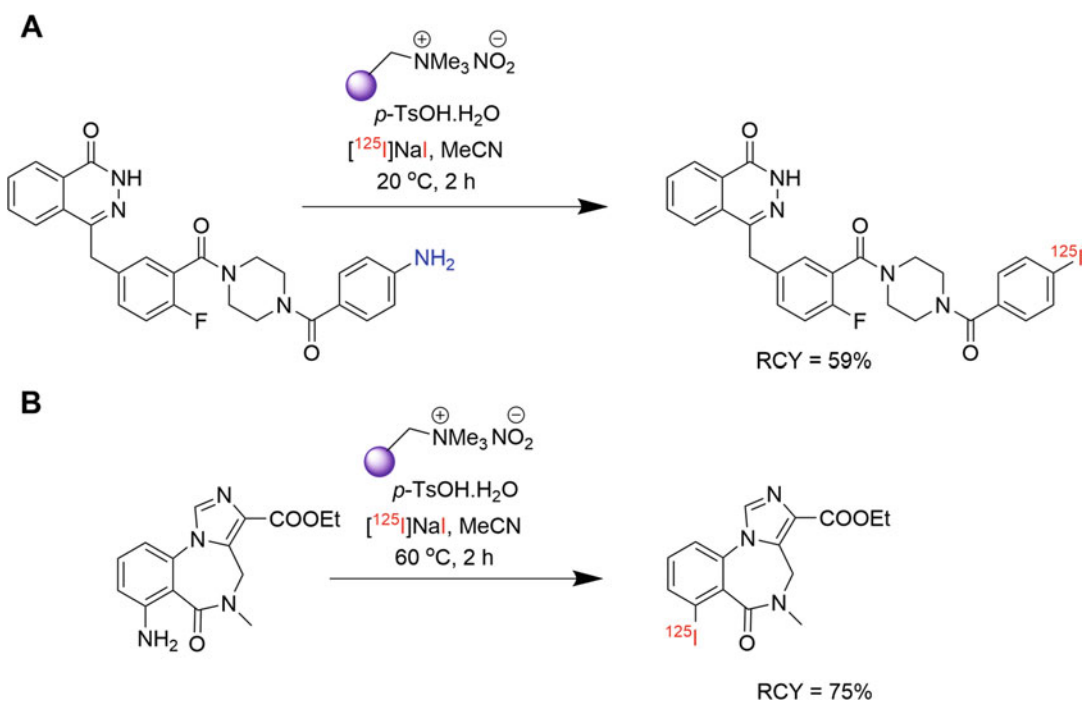

Fig. 7.5 The nucleophilic displacement of a diazonium salt for the synthesis of radioiodinated arenes: (**a**) the synthesis of a radioiodinated derivative of olaparib, a PARP-1 inhibitor, and (**b**) the radiosynthesis of [^{125}I] iomazenil, a central benzodiazepine receptor-targeting agent

Aryl iodonium salt precursor
Desired and Expendable rings
are shown in blue and green, respectively
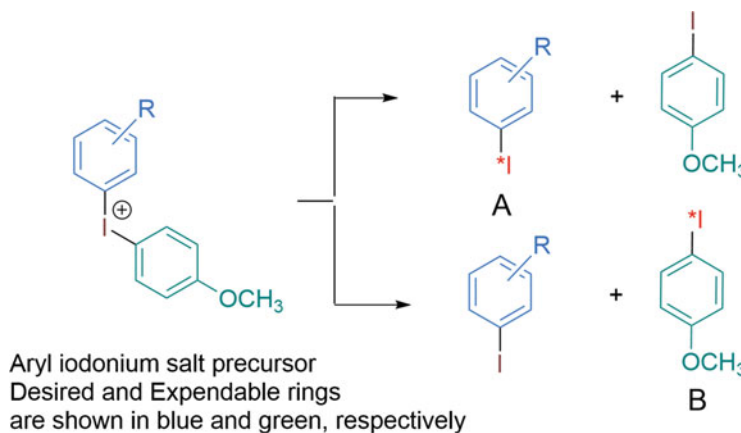
synthesis of radioiodinated compounds (Fig. 7.6). Guerard and colleagues first reported the utility of the iodonium salt strategy, which they adapted for the synthesis of *meta*-[^{125}I]SIB in excellent RCY and RCP [11]. Although both possible products—substitution on the desired ring and on the expendable (undesired) ring—can be formed, the substitution occurs predominantly on the ring bearing the electron-withdrawing substituents. When substitution occurs on the expendable ring, unlabeled carrier of the desired product results, which can decrease molar activity (Fig. 7.6, bottom scheme). The synthesis of *N*-succinimidyl 3-(4-hydroxy-3-[*I]iodophenyl) propanoate (the Bolton-Hunter reagent), which is used for the conjugation labeling of proteins and peptides, was accomplished using this method, but the RCY was not reported [12]. Because iodonium salts are ionic, HPLC can be avoided for the purification of the labeled products: a simple filtration through a silica cartridge will suffice (see below). Finally, iodonium ylides, which are more stable than iodonium salts, have been utilized for ^{18}F-labeling, and this technique has been adapted for radioiodination and astatination [13].

Once upon a time, boron-bearing precursors were used for electrophilic radioiodinations; however, this approach never was used beyond a few labs. However, in light of their efficacy for nucleophilic ^{18}F labeling, aryl boronic acids and boronates recently have been used for copper-mediated nucleophilic radioiodinations (i.e., the

Chan-Evans-Lam cross-coupling). At first, Cu_2O, $Cu(OCOCF_3)_2$, or other copper salts were used as the copper catalyst with 1,10-phenanthroline as a ligand [14]. Kondo et al. [15] reported the synthesis of several radioiodinated compounds in excellent yields from boronic acid or boronate precursors. While they used $Cu(pyridine)_4(OTf)_2$ as the catalyst, the reactions were performed without the phenanthroline ligand. These reactions could be performed in the presence of water and were equally efficient with either unprotected boronic acids or boronate esters. Furthermore, the reaction worked well with substrates containing both electron-withdrawing and electron-donating substituents, and no differences in radiochemical conversion (RCC) were seen between positional isomers. Active ester-containing agents such as *meta*- and *para*-[^{125}I] SIB were obtained in high RCC. As shown in Fig. 7.7, a radioiodinated silicon-rhodamine derivative was synthesized in high RCC and RCY using this approach [16].

7.2.1.2 Approaches to Avoid HPLC Purification in the Synthesis of Radioiodinated Compounds

HPLC purification is usually necessary to obtain a pure radiopharmaceutical. However, it is often time-consuming and requires skilled personnel. In addition, HPLC purification procedures can result in additional radiation dose to the radiochemist and can negatively affect the molar activity of the final product. A potential approach to
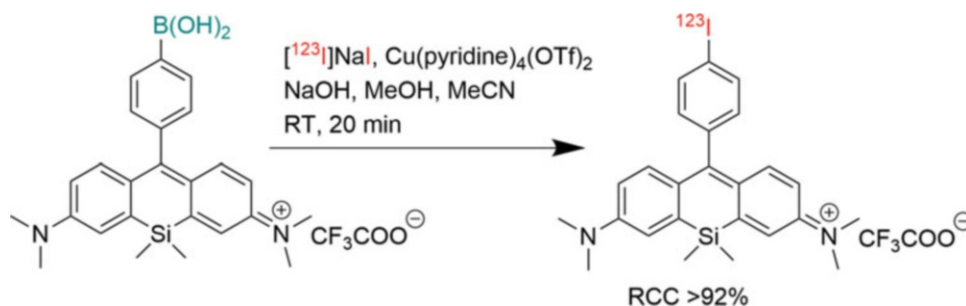
Fig. 7.7 The synthesis of an ^{123}I-labeled silicon-rhodamine derivative via the iododeboronation of the corresponding boronic acid precursor

circumvent HPLC purification is to develop kit-based synthetic methods that use immobilized precursors. After the radioiodination reaction, the labeled product is freed from the insoluble support and can be easily separated from unreacted precursor and byproducts that still remain attached to the support. For example, as shown in Fig. 7.8a, the synthesis of no-carrier-added [^{131}I]MIBG was achieved in >90% RCY and excellent radiochemical purity (RCP) using poly-(3-[dibutyl[2-(3-and-4-vinylphenyl)ethyl] stannyl]-benzylguanidinium acetate)-co-divinylbenzene, a tin precursor anchored to an insoluble resin [17]. The product was isolated by filtration and subsequent solid-phase extraction with a C18 cartridge. A similar strategy has been used for the synthesis of *meta*-[^{125}I]SIB and *meta*-[^{125}I]iodobenzoic acid [18]. Up to 75% RCY was obtained for the free acid, while the mean RCY for the ester was 35%. Analytical HPLC of the isolated product indicated the presence of a major peak with a retention time corresponding to the desired radioiodinated compound.

Unfortunately, the approach described above suffers from a couple of drawbacks: (1) it is generally not possible to synthesize the precursor with consistent loading of the tin moiety and (2) reaction rates are typically lower when the reaction is performed under heterogeneous conditions.

Fluorous (fluorine-rich) compounds can be separated from non-fluorous compounds using fluorous silica gel chromatography, in which fluorous compounds are retained preferentially on the fluorous stationary phase compared to nonfluorous compounds. In addition, fluorous compounds are relatively small, can be synthesized in a pure form, and can be characterized by standard techniques such as NMR and mass spectrometry. Valliant and colleagues as well as others have exploited this strategy for radioiodination (Fig. 7.8b) [19]. Radioiodinated compounds could be synthesized in high RCP and RCY by passing the reaction mixture through a fluorous solid-phase cartridge. An extension of this approach was reported by Rajerison et al. [20] in which an ionic liquid was used as the support (Fig. 7.8c). As with fluorous precursors, ionic liquid-based tin precursors can also be synthesized in a pure form and can be characterized by common analytical techniques. Again, the radioiodinated products can be isolated from the ionic liquid-bound precursor and byproducts by passing the mixture through a silica cartridge. For example, *meta*-[^{125}I]SIB was obtained in 67% RCY and excellent RCP using this method.

Precursors based on metals other than tin have also been utilized for kit-based syntheses of radioiodinated compounds. The synthesis of [^{123}I]iodometamidate from a silicon polymer precursor has been reported [21]. The polymer was heated at 40 °C for 6 min with [^{123}I]iodide and NCS in trifluoroacetic acid (TFA), and the TFA was neutralized with a polymer-bound amine. The reaction mixture was diluted with dichloromethane (DCM), and the resultant solution was passed through a silica cartridge to remove the polymers. The elution of the cartridge
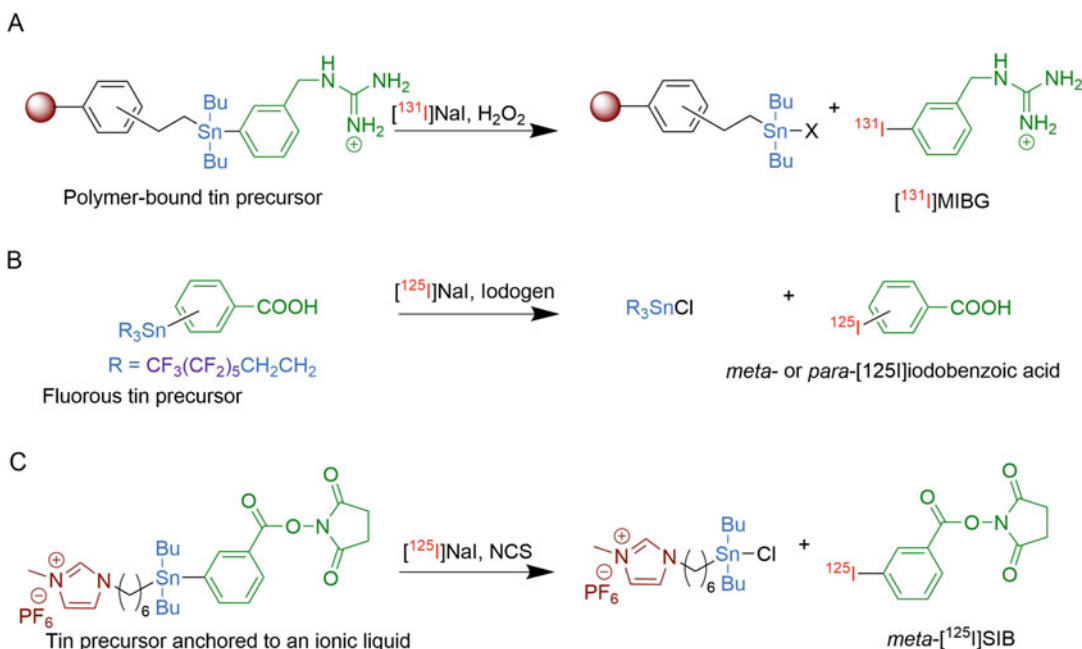
Fig. 7.8 The synthesis of (**a**) no-carrier-added [^{131}I]MIBG from a polymer-bound tin precursor, (**b**) *meta*- and *para*-[^{125}I]iodobenzoic acid from their respective fluorous tin precursors, and (**c**) *meta*-[^{125}I]SIB from ionic liquid tin precursor

with 10% methanol in DCM delivered the radiolabeled product in 85% RCY, and TLC analysis indicated that the product had a RCP of 94%. Kabalka and colleagues have synthesized several radioiodinated compounds from corresponding Dowex-supported organotrifluoroborates [22].

As noted above, diaryl iodonium salts are extremely polar and will be retained efficiently on a silica stationary phase. This property has been exploited for the purification of high RCP *meta*-[^{125}I]SIB synthesized from an iodonium salt precursor using a silica cartridge rather than with HPLC [11].

7.2.1.3 Radioiodination of Peptides and Proteins

Proteins, and to a certain degree peptides, generally cannot withstand the harsh conditions typically used for the radioiodination of small molecules. As a result, the conventional method for the radioiodination of peptides and proteins is direct electrophilic labeling using oxidants such as Iodogen and NCS. Under these conditions, the tyrosines of the biomolecule are radiolabeled,

though other amino acid residues such as histidine can be iodinated as well. Radiochemical yields are typically high, and the labeling procedure can be performed by nonskilled personnel. However, this direct labeling approach has a major drawback: biomolecules labeled this way are susceptible to in vivo deiodination. This results in escape of the radioiodine from the targeting vector after injection, decreasing tumor dose and increasing radiation dose to normal tissues that accumulate free iodide such as the stomach and thyroid. To circumvent this problem, prelabeled prosthetic agents or other strategies are employed. In most of the work cited below, the agents are labeled with ^{125}I and in some cases with ^{123}I, but the methods have frequently been used for labeling with ^{131}I and other radioisotopes of iodine as well.

7.2.1.3.1 Peptides

In some cases, peptides are amenable to the relatively harsh conditions of many radioiodination methods, such as the use of organic solvents, higher temperature, and oxidants. In addition,

HPLC purification is more practical with peptides than proteins. Some radioiodinated peptides can be purified via solid-phase extraction, predominantly using reversed-phase cartridges. Direct radioiodination is a possibility if there are constituent tyrosines within the peptide and the iodination of these tyrosines will not affect the biological activity of the peptide. Alternatively, one or more tyrosine residues—either L or D, the latter more inert to deiodination—can be incorporated within the peptide as long as the incorporation does not affect peptide function. In addition, there are several extant examples of

the radioiodination of peptides via nucleophilic substitution using copper-mediated exchange radioiodination [23] or iododediazoniation [24].

Peptides have also been radioiodinated using prelabeled prosthetic agents. Archetypally, amino (N-terminus and lysine side chain; Fig. 7.9a) and sulfhydryl groups (cysteine; Fig. 7.9b) on the peptide are utilized for conjugation. If some constituent amino acids—i.e., lysines or cysteines—are important for the biological function of the peptide, it is necessary to protect those residues before the conjugation reaction. Alternatively, noncanonical amino acids can be incorporated
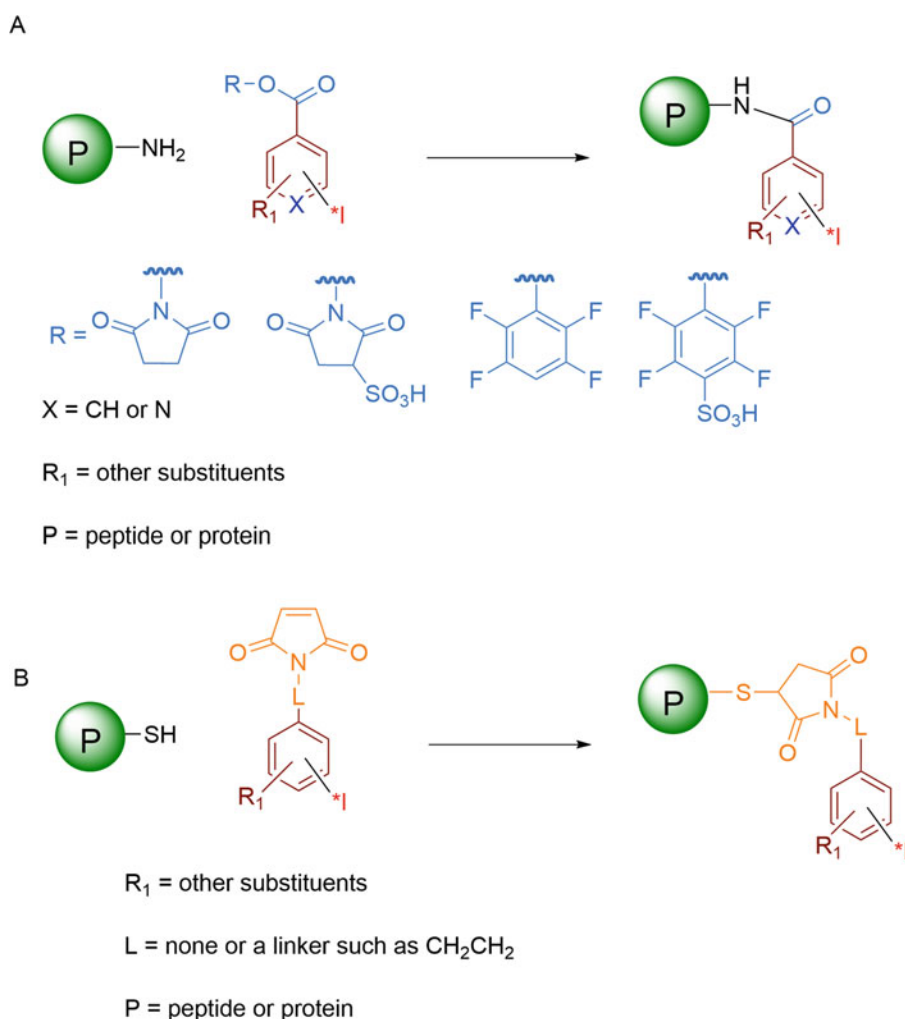

Fig. 7.9 Approaches for the radioiodination of peptides and proteins using pre-labeled prosthetic agents: the modification of amine (**a**) and sulfhydryl groups (**b**)

into peptides for labeling using biorthogonal chemistry. The most commonly used prosthetic agents for lysine-based radioiodination are *para*- and *meta*-[*I]SIB. Other prosthetic agents for acylation include 2,3,5,6-tetrafluorophenyl 4-fluoro-3-[*I]iodobenzoate [16], 5-[*I]iodo-3-pyridine carboxylate, and [*I]iodo-BODIPY-NHS [25]. Conjugation reactions with these prosthetic groups are typically performed in DMF or acetonitrile in the presence of a tertiary amine or, if the peptide is water soluble, in buffers of moderately basic pH.

As alluded to above, several prosthetic groups have also been used to label biomolecules via the modification of sulfhydryl groups generated by the reduction of disulfide linkages, the conversion of amines to thiols via treatment with iminothiolane (Traut's reagent), or the recombinant incorporation of cysteine residues. The most commonly used thiol-reactive group is the maleimide, which is typically conjugated to peptides and proteins under physiological conditions [26]. The generalized structure for these iodinated maleimides is shown in Fig. 7.9b, with 3- and 4-iodophenyl, and 3- and 4-iodophenylethyl maleimides being most frequently used. A radioiodinated 2-cyanobenzothiazole has been used as an alternative to a maleimide to label an RGD peptide containing a cysteine (Fig. 7.10) [27].

The HPLC purification of the prelabeled prosthetic group can be avoided by first attaching precursors of prosthetic agents to peptides and subsequently radioiodinating the resultant conjugate. For example, stannylated active esters have been conjugated to peptide amino groups and then subsequently radioiodinated [28]. Similarly, Kondo et al. conjugated a boronic acid-bearing active ester prosthetic agent to an amino group in an RGD peptide and then radioiodinated this conjugate [15]. In yet another example, an aminooxy-functionalized RGD peptide was conjugated with *para*-trimethylstannyl benzaldehyde via an oxime linkage to facilitate the direct radioiodination of the peptide [29]. The preconjugation of a tin moiety-bearing maleimide agent to a sulfhydryl group on a peptide has also been proposed as a strategy for radioiodination [30]. Finally, a tributyltin-containing phenylalanine has been incorporated into the peptide sequence for subsequent radioiodination [31].

Bioorthogonal chemistry—exemplified by the copper-catalyzed azide-alkyne cycloaddition (CuAAC) reaction, the strain-promoted azide-alkyne cycloaddition (SPAAC), and inverse electron demand Diels-Alder (IEDDA) reaction—have also been used for the radioiodination of peptides (Fig. 7.11) [32]. Similar approaches, such as the copper-mediated oxidative *ortho*-phenylene diamine-aldehyde condensation [33] and the strain-promoted oxidation-controlled cyclooctyne-1,2-quinone cycloaddition reaction (SPOCQ), have been harnessed for radioiodinations as well [34]. In these cases, the peptide is first modified to include one of the two partner moieties and then labeled with a radioiodinated variant of the complementary group.

7.2.1.3.2 Proteins

In general, proteins are much more sensitive than peptides to pH, temperature, and nonaqueous solvents. Because of this, radiolabeling conditions for proteins need to be very mild: reactions need to be performed in buffers at or near physiological pH and at or near room temperature. As noted above, proteins can be radioiodinated under such conditions by the direct electrophilic method albeit in the presence of an oxidizing agent. However, this approach produces radioconjugates that are highly susceptible to in vivo deiodination, and the tumoral accumulation probes radioiodinated in this way, particularly internalizing monoclonal antibodies (mAbs), can be very low due to the rapid washout of the principal radiolabeled metabolite, 3-[*I] iodotyrosine. Prelabeled prosthetic agents (as described in the *Peptides* section) are also routinely used for the radioiodination of proteins. An advantage of this approach is that the use of prosthetic groups avoids subjecting the protein to oxidizing and reducing conditions. However, skilled chemists are needed for this methodology, and RCYs are typically considerably lower than those obtained for the direct radioiodination of proteins. As with peptides, specialized

Fig. 7.10 A benzothiazole-based prosthetic agent for modifying sulfhydryl groups on peptides and proteins, exemplified by the radioiodination of a cysteine-bearing derivative of the RGD peptide
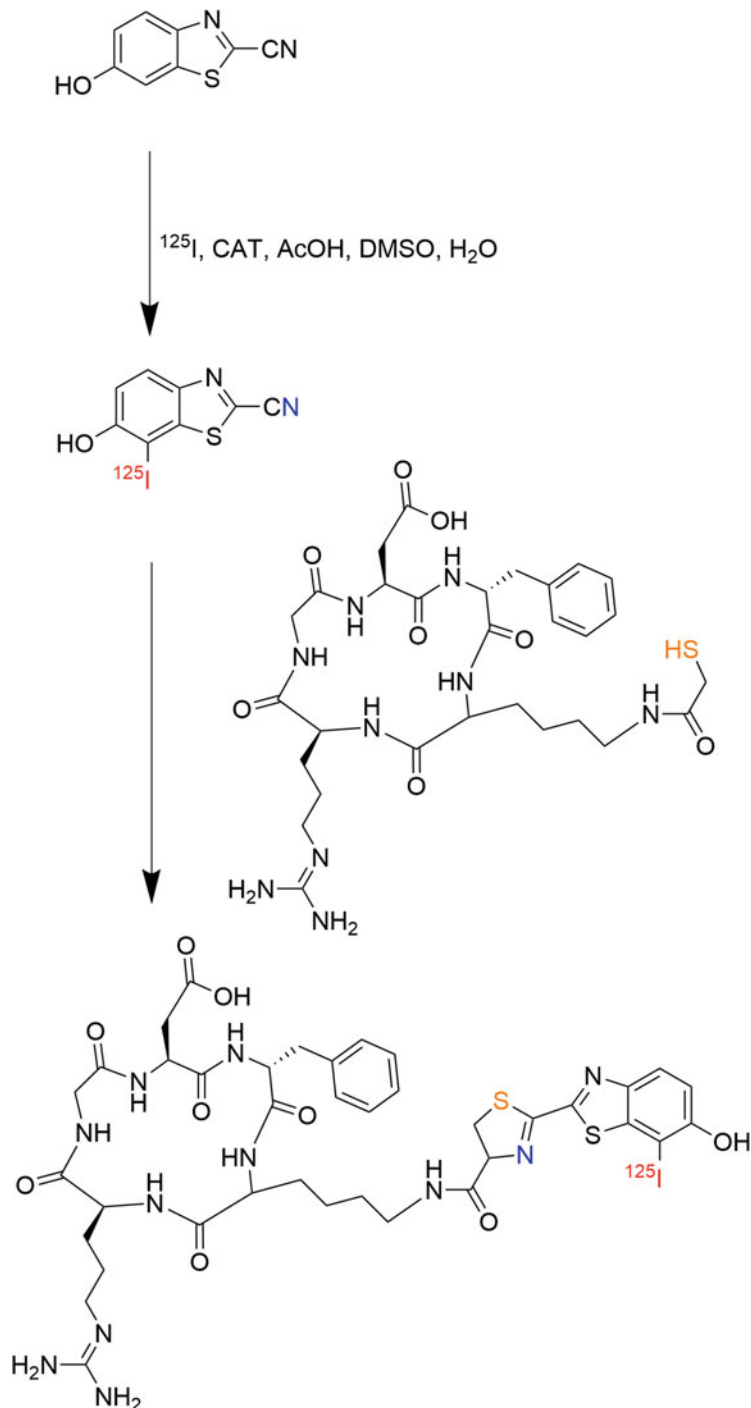
radiolabeling prosthetic groups and biorthogonal chemistry can be used for radiolabeling in the context of proteins as well.

Primary amines—either of lysine residues or at the *N*-terminus of the protein—are typically leveraged for the radioiodination of proteins using prelabeled prosthetic groups. This is generally accomplished using agents containing active esters, with *N*-hydroxysuccinimidyl (NHS) or tetrafluorophenyl (TFP) esters the most
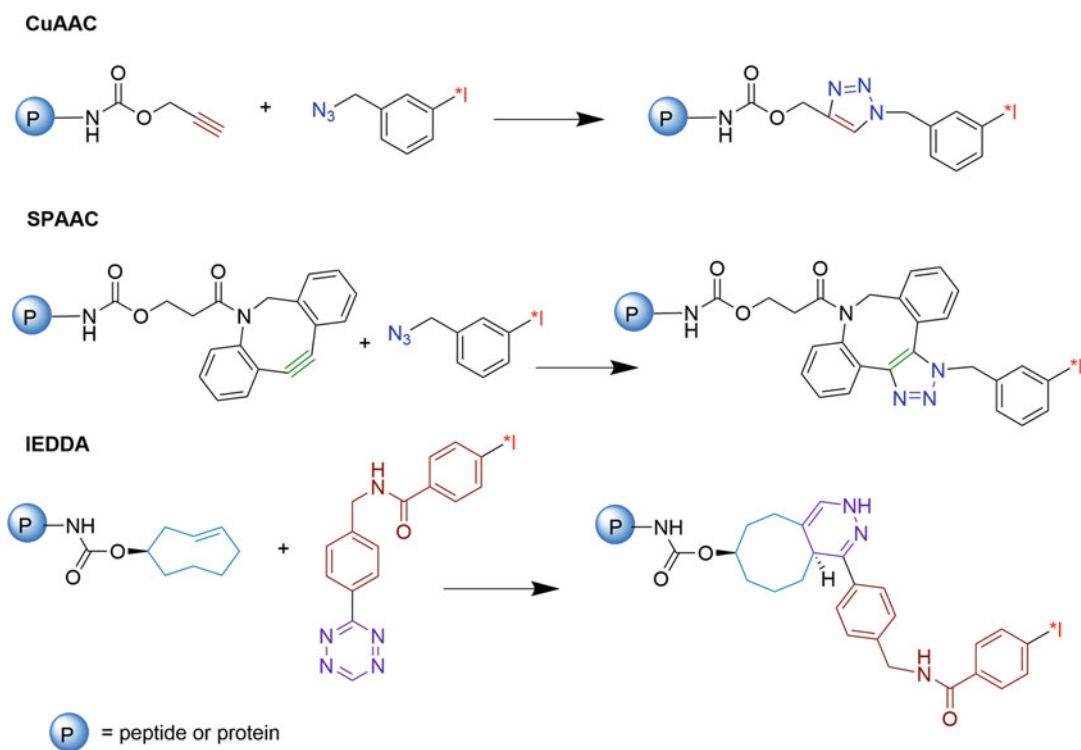
CuAAC

SPAAC

IEDDA

P = peptide or protein

Fig. 7.11 General schemes for the CuAAC, SPAAC, and IEDDA ligations. The complementary reactive groups in the biomolecule and the radioiodinated prosthetic agent potentially can be swapped

commonly used. Other amine-reactive groups include isothiocyanates, imidate esters, and aldehydes. The conjugation of an active ester with proteins is performed in buffers of pH 8–9 to ensure that the primary amine is in the reactive, deprotonated state, and conjugation yields are directly proportional to the protein concentration. In other cases, prelabeled prosthetic groups can target sulfhydryl groups created via the reduction of dithiols or the use of Traut's reagent. Alternatively, for site-specific labeling, cysteines can be introduced into proteins recombinantly at sites that ensure protein function after conjugation.

The classical prosthetic agent for the radioiodination of proteins is the Bolton-Hunter reagent. Because the iodine is positioned *ortho* to a hydroxyl group, it bears some structural similarity to thyroid hormones, making it susceptible to in vivo deiodination. To overcome this, *meta*- and *para*-[*I]SIB reagents that lack a phenolic hydroxyl group were developed. Indeed, when an antibody fragment was radioiodinated using *meta*-[^{125}I]SIB, radioiodine uptake in the thyroid—a convenient indicator of the degree of in vivo deiodination—was about 100-fold lower than that observed for the same fragment labeled directly with ^{131}I on its tyrosine residues using the Iodogen method. Since the introduction of radioiodinated SIB, multiple other prosthetic agents for the modification of amines have been reported. For example, Billaud et al. developed a TFP ester that can be labeled with radioiodine or ^{18}F [19]. Dual optical and nuclear prosthetic agents containing an NHS ester have also been synthesized, and their use in labeling a mouse mAb has been evaluated [35]. Finally, an ^{123}I-labeled prosthetic agent containing a fluorescent BODIPY scaffold was conjugated with the anti-HER2 mAb trastuzumab for the SPECT and fluorescence imaging of HER2-positive tumors [25].

Maleimides are the most commonly used reactive groups in sulfhydryl-targeted prosthetic groups. These come with the advantage that the conjugation reaction can be performed under physiological conditions [36]. As with active

ester-based prosthetic agents, maleimide-containing synthons bearing both radioiodine and fluorophores have been developed [35]. Another sulfhydryl-reactive moiety—phenyloxadiazolyl methyl sulfone (PODS)—has been used for the site-specific labeling of proteins with radiometals [37]. Indeed, a recent publication from our group has extended the PODS approach to radiohalogenation with iodine and astatine, ultimately yielding radioimmunoconjugates with more favorable properties than those created using maleimides (Fig. 7.12) [38].

The tumoral retention of radioactivity from directly radioiodinated antibodies and other proteins that undergo extensive cellular internalization is often very low. This is due to the rapid washout of the labeled catabolites generated from protein degradation within the lysosomal compartment, namely 3-[*I]iodotyrosine and free [*I]iodide. For this reason, direct radioiodination is referred to as a "non-residualizing" approach to radiolabeling. This stands in stark contrast to probes labeled with radiometals, which are considered "residualizing" labels. Several strategies have been investigated to increase the retention of radioiodine and its related catabolites in cancer cells (Fig. 7.13). The first generation of residualizing radiohalogenation reagents contained carbohydrates and was developed based on the hypothesis that the polarity of carbohydrates would minimize their passage through lysosomal and cellular membranes [39]. While this approach increased the tumoral retention of radioactivity, it produced radioimmunoconjugates with poor RCYs, reduced immunoreactivity, increased protein cross-linking, and resulted in high liver accumulation [40]. The next generation of residualizing prosthetic groups was based on short peptides containing positively or negatively charged D-amino acids [41, 42]. Peptides derived from D-amino acids do not undergo hydrolysis by peptidases, and peptides with more than 3 amino acids cannot traverse lysosomal and cellular membranes. Small molecule prosthetic agents bearing groups that will remain positively charged at lysosomal pH were also pursued as residualizing agents. Although the tumoral residualization of activity has been observed when mAbs were radioiodinated using *N*-succinimidyl 5-[*I]iodo-3-pyridine carboxylate ([*I]SIPC), it was transient [43]. Based on the fact that guanidine has a pKa of ~13 and is thus
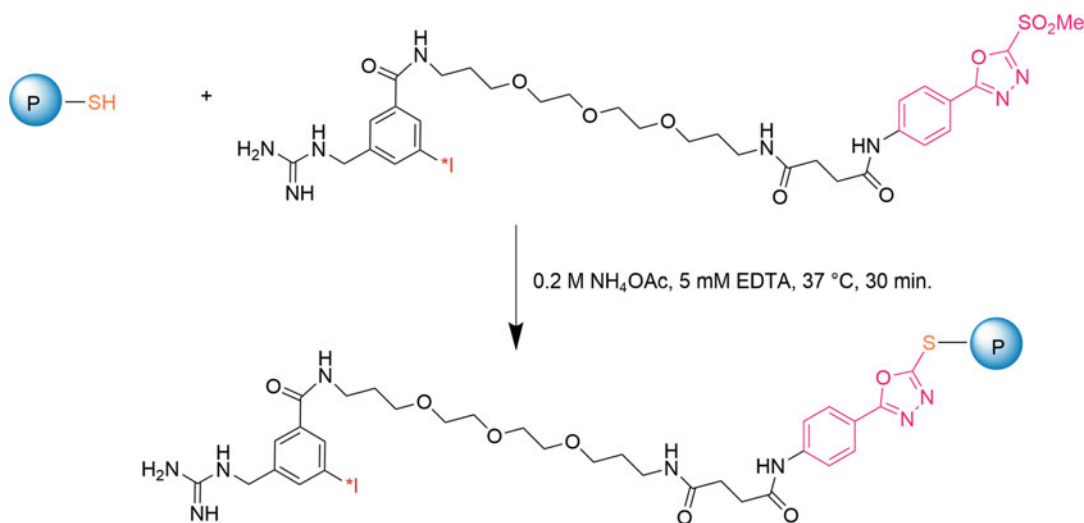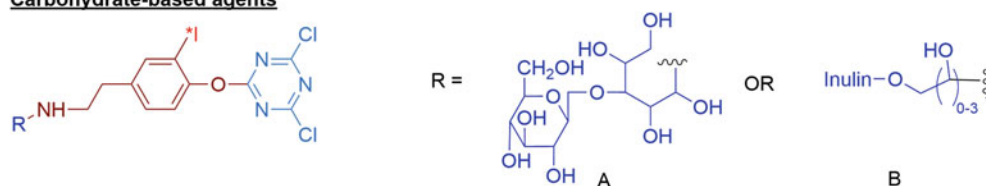

Fig. 7.12 The site-specific radioiodination of a protein via the conjugation of a PODS-based agent (in this case containing a guanidine-bearing residualizing moiety) to a sulfhydryl group

Carbohydrate-based agents

A) Cellobiose-[*I]Iodo-Tyramine-Cyanuric chloride; B) Inulin-[*I]Iodo-Tyramine-Cyanuric chloride

Positive or negative charge-bearing agents

[*I]SIPC   [*I]SGMIB/iso-SGMIB   [*I]SIPMB
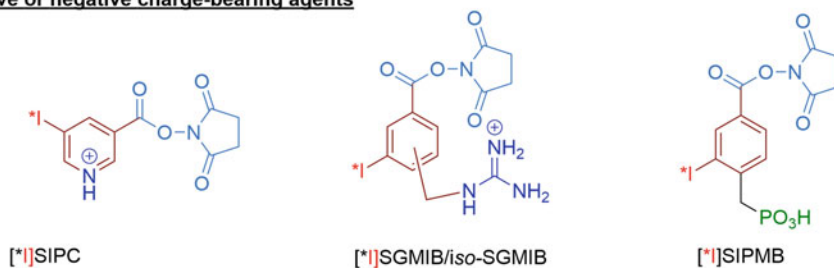
Chelator-bearing agents

[*I]SIB-DOTA   [*I]HIP-DOTA
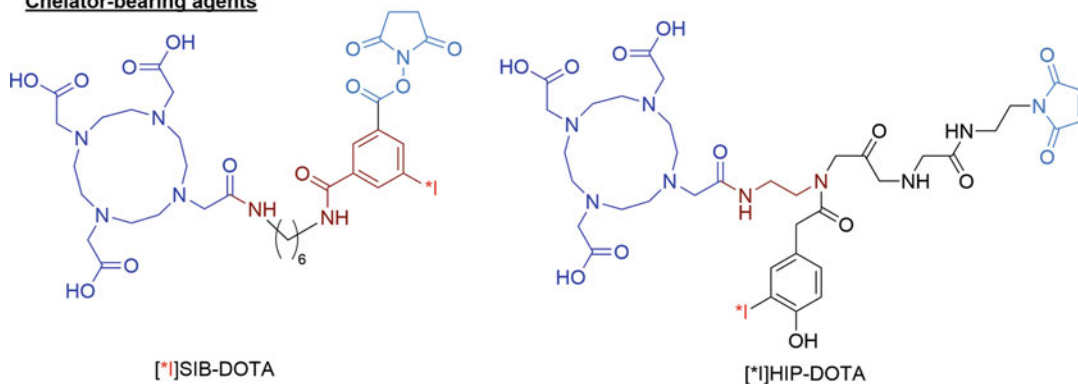
D-Amino acid peptide-containing agents with or without a chelator

MalGeeek-IB   IMP-R1
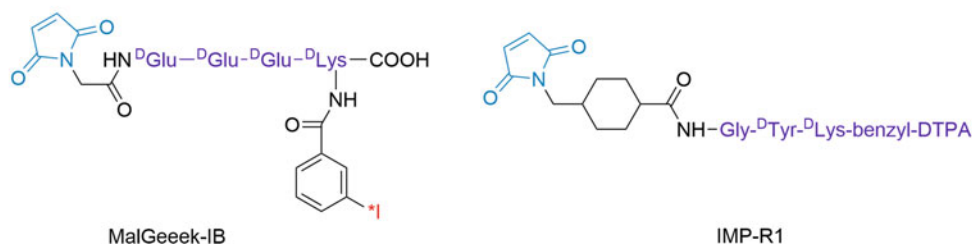
Fig. 7.13 Residualizing prosthetic agents for radiohalogenation

expected to remain exclusively positively charged at lysosomal pH, another residualizing prosthetic agent—*N*-succinimidyl 4-guanidinomethyl-3-[*I]iodobenzoate ([*I]SGMIB)—was developed

[44, 45]. This reagent has produced very promising results in retaining radioactivity in tumors when used to label internalizing mAbs and mAb fragments. Recently, a Phase I trial of

an anti-HER2 single domain antibody fragment (sdAb, a.k.a. V_HH or nanobody) labeled using [^{131}I]SGMIB has been initiated [46]. An isomer of this agent, N-succinimidyl 3-guanidinomethyl-5-[*I]iodobenzoate (iso-[*I]SGMIB) was developed with the goal of improving radiochemical yields compared to the original [*I]SGMIB isomer by decreasing steric interference [47, 48]. The synthesis of iso-[^{131}I]SGMIB and its use for labeling an anti-HER2 sdAb at higher radioactivity levels without the need for the HPLC purification of the labeled prosthetic agent were recently reported [49]. An agent similar to [*I]SGMIB but containing a negatively charged PO_3H group in lieu of the guanidine group has also been synthesized and has shown some promise [50]. In addition, prosthetic agents bearing chelators can be residualizing, and several radioiodination residualizing agents containing a chelator have been developed (see, for example, Bosewell et al.) [51].

There are a handful of instances in which biorthogonal chemistry has been used for the radioiodination of antibodies and proteins. For example, Albu et al. [52] modified an anti-VEGF antibody with a trans-cyclooctene (TCO) moiety, and the resultant conjugate was then reacted with a radioiodinated tetrazine under mild conditions via the IEDDA ligation. The RCY for this reaction was 69%, and the labeled mAb retained immunoreactivity and was very stable in vivo. This group has also reported the development of a radioiodinated carborane-containing tetrazine for labeling mAbs. A similar strategy was used to label human serum albumin in excellent RCY, producing a radioconjugate with high inertness to in vivo deiodination. Other biorthogonal chemical approaches, including the SPAAC reaction, have also been used for the radioiodination of proteins [29–31]. Such approaches may be useful for the in vivo labeling of pretargeted mAbs with short-lived iodine radionuclides such as ^{123}I.

Unlike with peptides, the strategy of attaching unlabeled prosthetic groups to proteins for subsequent radiohalogenation has mostly been limited to astatination (see below). However, Berdal et al. [53] achieved the radioiodination of an anti-CD138 mAb preconjugated with an arylboronic acid scaffold in excellent RCY. In addition, the radioiodination of a F(ab)' molecule conjugated with an anionic boron cage pendant group has been described [54]. However, the stability of this construct to in vivo deiodination was low, most likely due to the fact that some iodination of the constituent tyrosines also occurred.

7.2.2 Astatination

Astatine-211 emits high-LET α- (alpha) particles (Fig. 7.1) that have several advantages over β-(beta) particles for radiopharmaceutical therapy. The potential advantages of α (alpha)-particles for RPT have been discussed in Chap. 5, and the specific advantages of ^{211}At as a radionuclide will be addressed in the final section of this chapter. In the sections that follow, we shall focus on ^{211}At labeling chemistry. Because astatine is a halogen, methods used for radioiodination can be adapted for astatination. However, astatine also exhibits some metallic character, and some radiolabeling methods have been developed that exploit this property. The carbon–astatine bond is weaker than the carbon–iodine bond, and hence, ^{211}At is almost exclusively introduced on sp^2 carbons (i.e., to aromatic and vinylic compounds). Also, because boron–halogen bond strengths are higher than those for carbon–halogen bonds, astatinated carboranes have been developed as well.

7.2.2.1 Small Molecules

7.2.2.1.1 Electrophilic Substitution
An oxidizing agent is required for most electrophilic astatine substitution reactions with astatodemetallation being the primary approach for the synthesis ^{211}At-labeled compounds from electrophilic ^{211}At. While astatodemercuration was used in early work, methods using silicon- and tin-bearing precursors have been developed, with the latter the most common [31, 55, 56]. Generally, astatodestannylation is performed under mild conditions, resulting in moderate-to-high

RCY. As with radioiodinated compounds, [211]At-labeled compounds can be easily separated from their tin-containing precursors by HPLC. In addition, the synthesis of 4-[211]At]astato-L-phenylalanine via astatodeborylation under aqueous conditions in excellent RCY has been reported [57]. Although there is some ambiguity, this was considered an electrophilic substitution reaction because an oxidant was used. However, the reaction also was successful when the oxidant was replaced with carrier sodium iodide. The one-pot three-component reaction described above for radioiodination also has been adapted for labeling with [211]At, and several compounds—including labeled tetrazines—have been synthesized in good RCY [58].

7.2.2.1.2 Nucleophilic Substitution

Astatine is not very stable in the +1 state, especially in the presence of oxidants [11]. On the other hand, the nucleophilic astatide anion is stable and easier to handle. Along these lines, astatodeiodination has been used in the synthesis of [211]At-labeled compounds, including those in which [211]At is attached to an sp^3 carbon. The neopentyl glycol strategy for radioiodination described above has also been adapted for astatation [8]. A nitroimidazole derivative labeled with [211]At using this approach remained stable toward both nucleophilic substitution and cytochrome P-450-mediated metabolism and exhibited a pharmacokinetic profile similar to that of its radioiodinated analogue.

Several aromatic compounds have been labeled with [211]At via nucleophilic substitution reactions. As with radioiodination, nucleophilic astatation has been performed via copper-catalyzed nucleophilic astatodeiodination and astatodediazoniation as well as the use of diaryl iodonium salts and iodonium ylides as substrates.

Pioneering work on astatation using diaryl iodonium salts was reported by Guerard et al. [11, 59]. Although better RCYs were obtained for radioiodination in acetonitrile, the RCYs for astatation were considerably higher in other solvents. However, transesterification was a problem for active ester-containing compounds when methanol was used as the solvent. This behavior was attributed to the highly electron-withdrawing nature of the iodonium ion substituent. Not surprisingly, electron-withdrawing substituents in the desired ring enhanced RCY.

The use of an aryl iodonium ylide precursor for astatation was first reported by Matsuoka [60] (Fig. 7.14). The reaction conditions in this case—100 °C for 30 min in the presence of tetraethyl ammonium bicarbonate, triphenyl phosphine, and DMF—were admittedly somewhat harsh, but RCYs of up to 99.5% were obtained. The RCY was dependent on the type of ylide auxiliary, with a cyclopentyl-containing variant giving the best result. In a subsequent study, the efficiency of astatation and radioiodination was compared [13]. Astatation gave high RCY at room temperature while higher temperatures proved necessary for radioiodination. The use of a radical scavenger—2,2,6,6-tetramethylpiperidine-1-oxyl (TEMPO)—was necessary in some cases to prevent degradation of the ylide precursor. Again, likely due to stability concerns, RCY depended on the auxiliary, and diglyme was found to be the preferred solvent. Several compounds, including those bearing active esters and tetrazines, were synthesized in good to excellent RCY. Dithiothreitol (DTT), the reducing agent initially used in the reaction to keep astatine in its anionic At⁻ form, was found to be detrimental for compounds with the above functionalities;

Fig. 7.14 A general scheme for the synthesis of astatinated compounds using iodonium ylide precursors
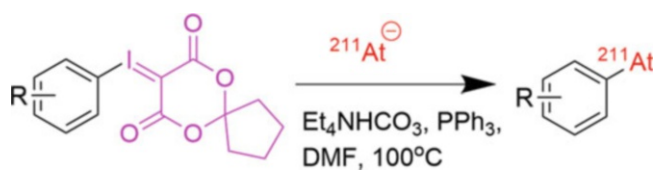
fortunately, higher RCY was achieved by substituting sodium metabisulfite for DTT.

Copper-mediated halodeboronation of boronates and boronic acids have been studied for the synthesis of various [211]At-labeled small molecules, including *N*-succinimidyl 4-[[211]At] astatobenzoate (4-[[211]At]SAB) and [211]At-labeled analogues of poly(ADP-ribose) polymerase-1 (PARP-1) inhibitors [61]. In these cases, the labeling conditions were mild, and high RCC and RCY were obtained; however, the amount of precursor used was considerably higher than that typically used for electrophilic astatodestannylations. Also, a mixture of organic solvents was used for the reaction. To avoid organic solvents, a method of performing the reaction under aqueous conditions was developed, as illustrated by the synthesis of 4-[[211]At] astato-L-phenylalanine [57]. However, as we noted above, some uncertainty remains as to whether this is indeed an electrophilic or nucleophilic substitution reaction.

7.2.2.2   Astatination Methods Without the Use of HPLC Purification

As alluded to in Sect. 7.2.1.2. for radioiodinated compounds, avoiding HPLC purification has considerable benefits for astatinated compounds as well, especially considering the short half-life of [211]At. The same polymer-immobilized tin precursor used for the synthesis of no-carried-added [^{131}I]MIBG could provide *meta*-[[211]At] astatobenzylguanidine ([[211]At]MABG), the astatinated analogue of MIBG, in 63% RCY [62]. The product was isolated by ion-exchange solid-phase extraction in >90% RCP. Similarly, 3-[[211]At]SAB has been synthesized from a tin precursor attached to an ionic liquid in about 65% RCY (though the RCYs were dependent on the amount of both NCS and the precursor) [20]. Purification was achieved by simple filtration through a silica cartridge, and the final RCP was 91%. Another strategy to avoid HPLC purification is the use of ionic diaryl iodonium salt precursors, as any leftover iodonium salt can be efficiently removed via silica cartridge purification [11]. While byproducts, such as 4-[[211]At] astatoanisole, resulting from the astatine

substitution in the expendable (i.e., undesired) ring could not be separated, they could be removed along with unreacted astatide via evaporation, resulting in >98.5% RCP for the desired product.

7.2.2.3   Astatination of Peptides and Proteins

Two important considerations when labeling peptides and proteins with [211]At are (i) whether the half-lives of the biomolecule align with that of the radiohalogen and (ii) whether the biomolecule can withstand the reaction conditions necessary for astatination. While the pharmacokinetic profiles of peptides make them good candidates for [211]At-labeling, smaller format proteins are most relevant. A notable exception are clinical settings in which rapid tumor delivery and reduced normal tissue exposure can be achieved using nonintravenous delivery. Intact mAbs have been labeled with [211]At and even clinically evaluated, albeit only in cases of locoregional (rather than systemic) administration [63]. Unlike radioiodination, the direct electrophilic labeling of peptides and proteins with [211]At is not practical due to the nearly complete instability of the radiolabeled products. Initially, this problem was attributed to the weak C-At bond in 3-astatotyrosine and 5-astatohistidine, which would be created by the direct astatination of tyrosine and histidine residues. However, later it was demonstrated that the astatination of these residues is highly unlikely in the presence of oxidants, and in fact, it is cysteine residues that are labeled instead in a manner that is highly unstable [64]. In summary, the [211]At labeling of proteins and peptides by direct methods is not a viable option, making indirect labeling approaches the only practical approach.

The first indirect method for the labeling of proteins with [211]At utilized 4-[[211]At] astatobenzoic acid. This prosthetic group was synthesized from a diazonium precursor and then conjugated to the protein using a mixed anhydride. At present, the most widely utilized prosthetic groups for the astantination of proteins are 3- and 4-[[211]At]SAB, which are both synthesized from organometallic precursors.

Other active ester-containing prosthetic agents for [211]At-labeling have been reported and can provide conjugates with good in vivo stability [65]. Prosthetic agents based on boron cages have also been developed due to the higher stability of boron-astatine bonds compared to carbon-astatine bonds [64]. As with radioiodine, prosthetic agents bearing moieties that will remain positively charged at lysosomal pH have been used for labeling internalizing biomolecules with [211]At. Notable examples of these constructs include *N*-succinimidyl 5-[[211]At]astato-3-pyridinecarboxylate ([[211]At]SAPC), *N*-succinimidyl 3-[[211]At]astato-4-guanidinomethyl benzoate ([[211]At]SAGMB), and *N*-succinimidyl 3-[[211]At]astato-5-guanidinomethyl benzoate (*iso*-[[211]At]SAGMB) [47].

Several peptides have been labeled with [211]At. The first was the somatostatin receptor-targeted octreotide, which was labeled via a 3-[[211]At] astatobenzoyl moiety [66]. Given the importance of the Lys^5 residue for the recognition of the receptor, its ε (epsilon)-amino group was protected before acylation with [[211]At]SAB and subsequently deprotected. This approach, unfortunately, meant that the radiosynthesis involved three HPLC purifications and took 6 h to complete. To shorten this timeline, the Lys^5 Boc-protected peptide was conjugated with a tin-bearing precursor of the prosthetic agent. In this way, the [211]At-labeled peptide could be synthesized in 50% RCY in 1 h with a single HPLC purification. A glycosylated analogue of octreotate was labeled with [211]At using a precursor bearing a tri-(*n*-butyl)stannyl benzoyl moiety and lacking a Lys^5 protecting group (Fig. 7.15) [28]. In this case, an additional Lys was appended to the *N*-terminus of the peptide for the attachment of both the sugar and the tin-containing prosthetic group. A similar approach was taken to synthesize an [211]At-labeled octreotate conjugate using the 3-[[211]At]astato-4-guanidinomethyl benzoyl prosthetic group. In another example, VP2—a peptide targeting vasoactive intestinal peptide receptor VPAC1—was labeled with [211]At in one step from a precursor containing a 5-(tri-*n*-butylstannyl)-pyridine-3-carbonyl moiety [67]. Finally, an [211]At-labeled variant of the RGD

peptide was synthesized from a precursor peptide that included a 4-(tri-*n*-butylstannyl) phenylalanine residue to facilitate labeling [31].

Bioorthogonal ligations—including the CuAAC, SPAAC, and IEDDA reactions—have also been used to label peptides and proteins with [211]At. In a study comparing five different biorthogonal strategies for the labeling of a model peptide with [211]At, it was reported that all gave RCY of >99% for conjugation with the IEDDA reaction being the fastest [32]. When a mAb was labeled via the SPAAC reaction under conditions similar to those used for the peptide, a 90% RCY was obtained. Although biorthogonal conjugation was not involved in the labeling reaction per se, trastuzumab has been modified with a *closo*-decaborate(2-) via a one-pot three-component click reaction, and the resulting immunoconjugate was subsequently labeled with [211]At [68]. To accomplish this, a decaborate-bearing tetrazine and an aldehyde with a TCO group were reacted with trastuzumab. The resultant decaborate-functionalized trastuzumab was labeled with [211]At using chloramine-T. Although a 78% RCY was obtained, the molar activity was very low. Increasing the initial activity of [211]At increased the molar activity but at the expense of RCY. It is not clear whether this method offers any advantages compared to the [211]At labeling of a mAb that has been directly modified with decaborate.

The direct labeling of a mAb that has been conjugated with radiohalogenation precursor has been investigated in order to help avoid the HPLC purification of radiolabeled prosthetic groups. Lindegren et al. first reported labeling trastuzumab with [211]At using this approach, which is often referred to as "pre-conjugation" [69]. In this study, trastuzumab was first reacted with *N*-succinimidyl 3-(trimethylstannyl) benzoate (3-STB) at a STB:mAb molar ratio of 6:1, and the resulting immunoconjugate was labeled with [211]At under mild conditions using *N*-iodosuccinimide (NIS) as the oxidant. Compared with the standard two-step labeling approach—which takes about an hour and results in 30–60% overall RCY—this one-step method
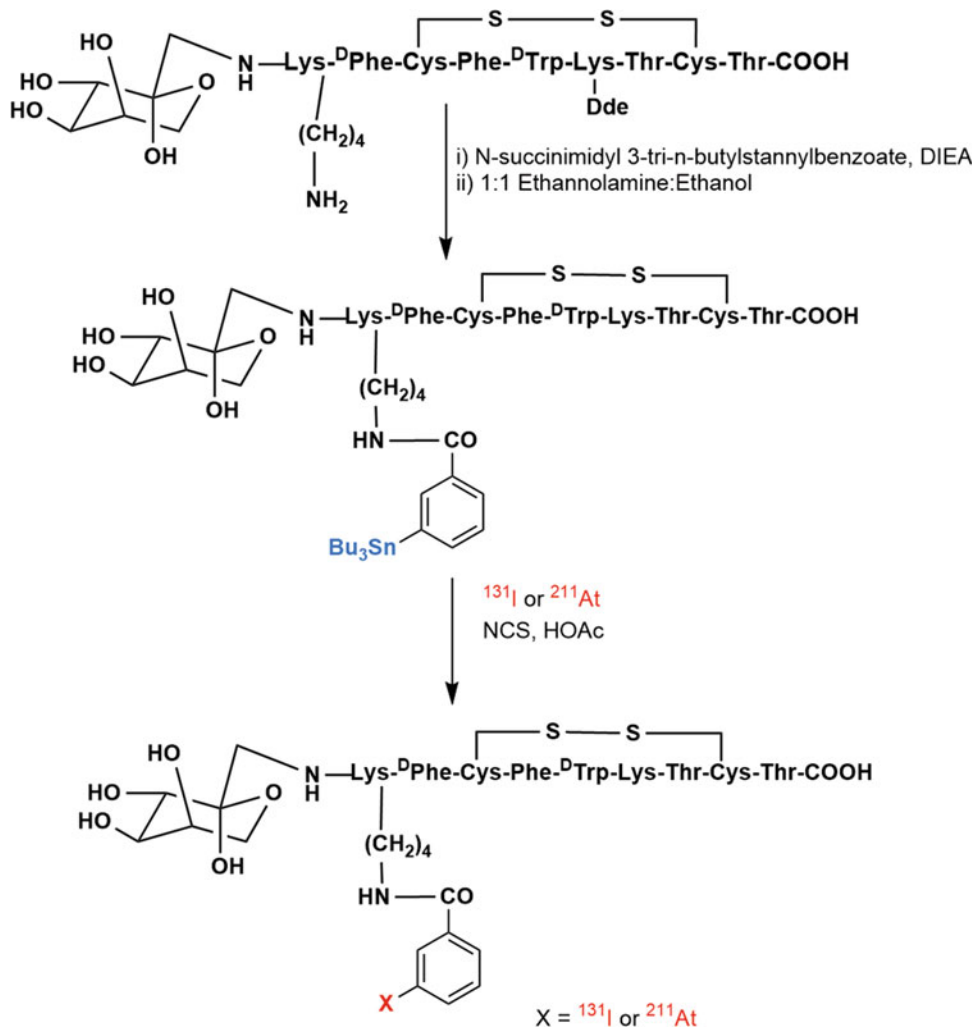
Fig. 7.15 The synthesis of radioiodinated and astatinated glycosylated octreotate analogues from a peptide bearing a tin precursor

was instantaneous and gave 60–80% RCYs and very high molar activities. Importantly, any remaining unreacted trimethylstannyl moieties on the protein could be replaced by iodine via treatment with NIS after labeling. It was demonstrated that the ^{211}At-labeled mAb retained immunoreactivity under optimized conditions. However, when unconjugated trastuzumab was subjected to the same reaction conditions, 30% of the added ^{211}At activity bound to the protein likely due to reactions with its cysteine sulfhydryl groups (see above), which readily deastatinate in vivo. After further refinement, this

pre-conjugation strategy has been applied to other proteins by the Gothenburg group as well as others. That said, this method still has two potential drawbacks: (1) the toxicity of tin compounds and (2) the use of relatively unstable At$^+$ in the labeling reaction.

A preconjugation approach that could potentially address these issues has been reported recently [53]. In this case, the protein was modified with a boronic acid-bearing moiety (instead of a tin-containing compound) and was labeled with ^{211}At using nucleophilic [^{211}At] astatide (Fig. 7.16). Along these lines, a mouse

Fig. 7.16 The astatination of a mAb preconjugated with a boronic acid-bearing precursor
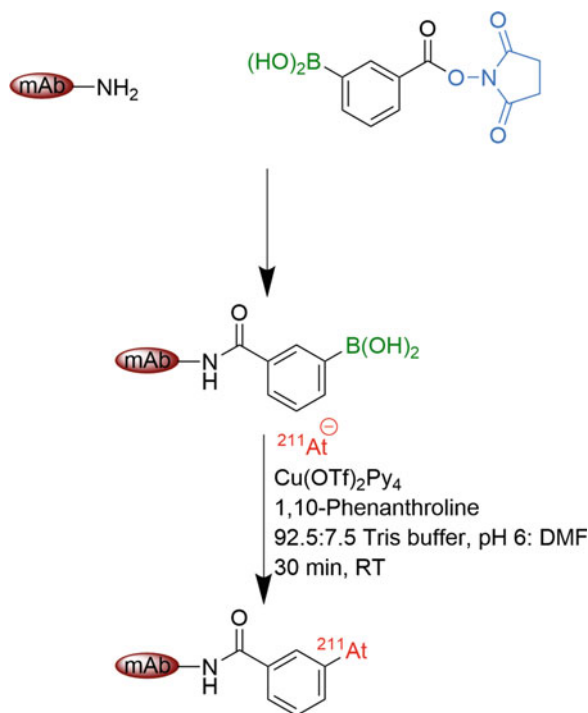
anti-CD138 mAb (9E7.4) was first reacted with 3-(succinimidyloxycarbonyl)-phenylboronic acid to generate an immunoconjugate with an average of 3–4 boronic acid moieties per mAb. This conjugate was then radiolabeled with sodium [^{211}At] astatide (up to 40 MBq), Cu(OTf)$_2$Py$_4$, 1,10-phenanthroline in 92.5:7.5 mixture of Tris buffer (pH 6) and DMF at room temperature for 30 min. The RCY, molar activity, and immunoreactive fraction of the resultant ^{211}At-labeled radioimmunoconjugate were > 95%, 18 GBq/μmol, and 88%, respectively. However, the suitability of this labeling strategy using clinically relevant levels of ^{211}At activity remains to be determined.

Site-specific approaches have been investigated for labeling immunoglobulins with different radionuclides including ^{211}At. These approaches guarantee that the label resides at a site on the protein distant from the areas needed for antigen recognition. Moreover, site-specific bioconjugation yields more homogeneous radioimmunoconjugates, making them more appealing for clinical translation. Generally, this has been done via the modification of free sulfhydryls with radiolabeled maleimide-bearing agents. In the case of ^{211}At, N-maleimidoethyl 3-(trimethylstannyl)benzamide (MSB) has been attached to a mAb that has been pretreated with DTT to reduce its interchain disulfide bonds and then labeled in a single step via astatodestannylation [70]. But because a full-length mAb has several disulfide linkages, this approach is not strictly site-specific, even with exquisite control over the reduction conditions. We have taken a different approach: the recombinant introduction of a free cysteine residue. With sdAbs, this involves the addition of a GGC tail to the C-terminus of the fragment, thereby providing a single point for attachment that is far from the antigen-binding CDR regions. This strategy worked well for the radioiodination of an anti-HER2 sdAb with a maleimide-bearing residualizing prosthetic agent [36]. However, when the same procedure was attempted using ^{211}At, a stable sdAb radioimmunoconjugate could not be obtained. Recently, we employed a PODS synthon for the ^{211}At-labeling of this same 5F7-GGC sdAb with much more favorable results (^{211}At instead of radioiodine in Fig. 7.12) [38],

making this PODS reagent the method of choice for the site-specific labeling of proteins with [211]At.

7.2.3 Radiobromination

Unlike the radioisotopes of iodine and astatine, the radioisotopes of bromine are not commonly used in the development of radiopharmaceuticals. Nonetheless, bromine holds some advantages over iodine, such as its higher carbon-halogen bond strength, lower susceptibility to in vivo dehalogenation, and lack of uptake in thyroid [71]. Most of the radiobrominated agents in the literature have been labeled with [76]Br, but those procedures should be adaptable for use with the Auger electron-emitting [77]Br and [80m]Br as well.

7.2.3.1 Small Molecules

Electrophilic bromination is the most commonly used method for the labeling of molecules with radiobromine. However, due to the high reactivity of electrophilic bromine, several side products can result when radiobrominations are carried out at no-carrier-added levels [71, 72]. Bromodeprotonation has been conducted using both activated and unactivated compounds. In most cases, however, electrophilic radio-bromination has involved bromodemetallation [3], especially using organotin compounds [73]. Similar to radioiodinations, radiobromination is typically conducted using [*Br]bromide, an oxidant such as CAT or NCS, and acetic acid. Moderate to excellent RCYs have been reported for many compounds.

Nucleophilic substitution also has been employed for radiobromination. Along these lines, copper-catalyzed bromodeiodination has been used for the synthesis of a few radiobrominated radiopharmaceuticals. For example, *meta*-[76]Br]bromobenzylguanidine ([76]Br]MBBG) was synthesized from unlabeled MIBG in 60–65% RCY and a molar activity of 20 MBq/nmol. As with radioiodination and astatination, radiobromination has also been performed using diaryl iodonium salt precursors. Several model compounds have been synthesized

using this approach in RCY ranging from moderate to almost quantitative [72]. Both the so-called minimalist approach (typically used for ^{18}F-labeling) and base-free conditions have been utilized. For unknown reasons, a COOH substituent was not tolerated in the minimalist approach, but it was not a problem for the base-free method. Unlike in ^{18}F-labeling, it was possible to elute the activity from a cartridge using DMSO under minimalist conditions, though HPLC purification was necessary to remove the iodo byproduct.

Bromodeboronation also has been used for radiobromination. The synthesis of several radiobrominated compounds—including *N*-succinimidyl 4-[76]Br]bromobenzoate and an olaparib derivative—could be performed using boronic- acid or ester precursors in >95% RCC in most cases [71]. In contrast to the analogous radiofluorination chemistry, the reaction was tolerant to water and could be performed with lower amounts of substrate and copper catalyst and at lower temperatures without sacrificing RCC. Also, DMSO was found to be the best solvent instead of dimethyl acetamide (DMA), which is used for radiofluorination. Free carboxylic acid groups were found to be detrimental. In addition, a radiobrominated analogue of the anti-tuberculosis compound bedaquiline has been synthesized from a boronate ester precursor; however, the RCC was only 20%, and the isolated RCY was 6% [74].

Peptides and proteins also have been labeled with radioisotopes of bromine. For example, octreotide was labeled with [76]Br via conjugation with *N*-succinimidyl 4-[76]Br]bromobenzoate or *N*-succinimidyl 5-[76]Br]bromo-3-pyridinecarboxylate; the labeled prosthetic agents themselves were synthesized from their corresponding tin precursors. Three different approaches have been used to label analogues of RGD with 76Br [75]. Direct labeling on a constituent tyrosine residue using either CAT or peracetic acid gave an RCY of about 50%. The peptide was also labeled using the prosthetic agent *N*-succinimidyl-3-[76]Br]bromo-2,6-dimethoxybenzoate ([76]Br]SBDMB) in >70% RCY; [76]Br]SBDMB itself was synthesized from its des-bromo precursor via
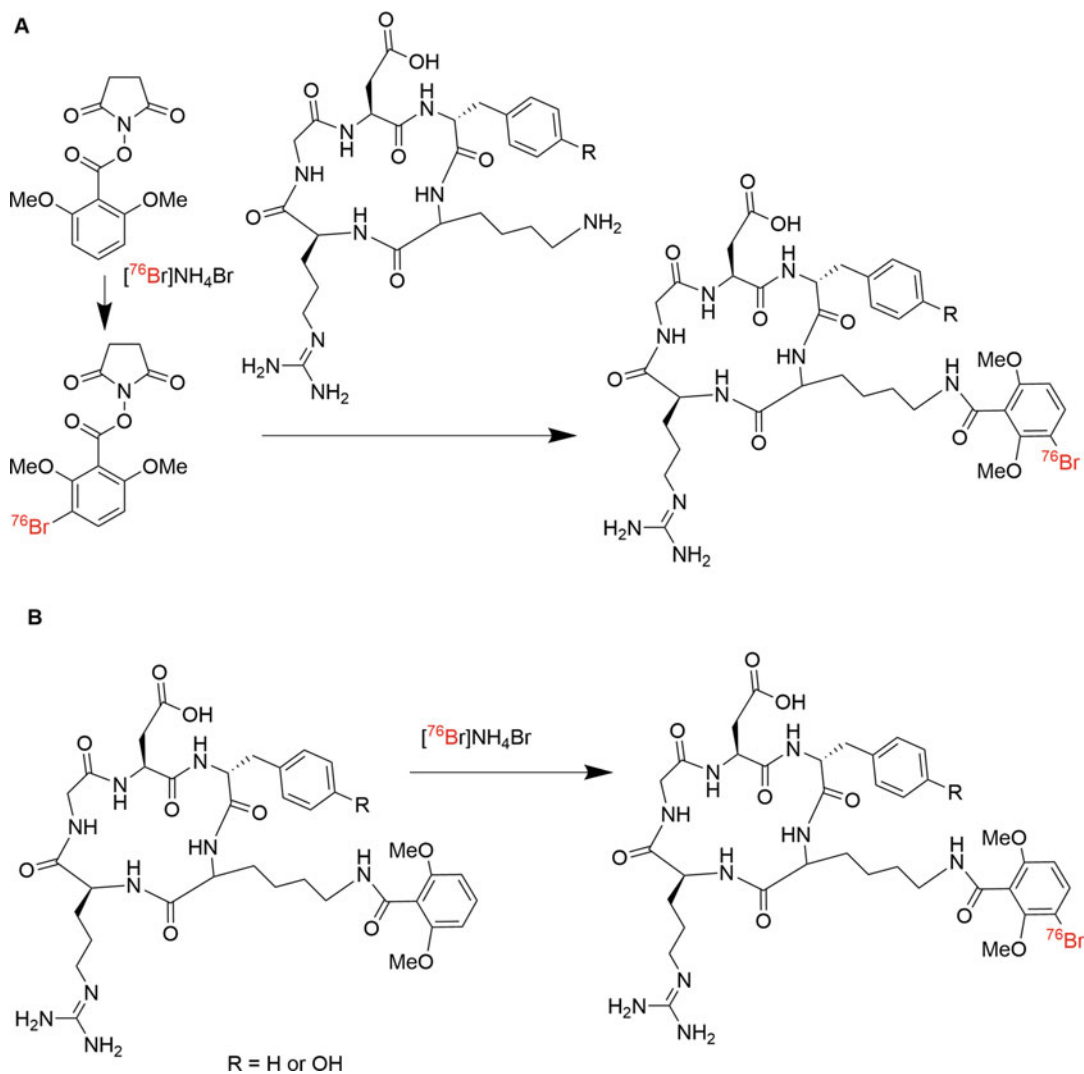
Fig. 7.17 The radiobromination of an RGD peptide using (**a**) a prelabeled prosthetic agent and (**b**) a desbromo precursor

bromodeprotonation in ~60% RCY (Fig. 7.17a). Finally, peptide that was first conjugated with this des-bromo precursor was labeled in >50% RCY (Fig. 7.17b). A byproduct, in which the bromine was attached to the tyrosine phenolic ring, was also generated in 5% yield.

While the direct radiobromination of proteins using chemical oxidants is problematic, enzyme-mediated labeling has been performed. For example, an antibody fragment targeted to the ED-B domain of fibronectin was labeled with ^{76}Br using bromoperoxidase [76]. There are also a few

extant reports of labeling proteins with radiobrominated prosthetic agents. An anti-melanoma antibody was labeled with *N*-succinimidyl 4-[^{77}Br]bromobenzoate—itself synthesized from a tin precursor—in 20% overall RCY. Likewise, trastuzumab was labeled with *N*-succinimidyl 5-[^{76}Br]bromo-3-pyridinecarboxylate in an overall labeling efficiency of 45% [77]. A maleimide moiety-bearing agent, 1-[2-(3-[bromo-4-hydroxyphenyl)ethyl]-1H-pyrrole-2,5-dione, has been synthesized in 83% RCY and used for the site-specific

radiobromination of an affibody in 65% RCY [78]. Finally, the synthesis of a *para*-isothiocyanato derivative of [^{76}Br]undecahydrobromo-7,8-dicarba-*nido*-undecaborate(1-) ion and its conjugation to trastuzumab has been reported [79]. An overall labeling yield of 57% was obtained, and the radiolabeled protein was stable in vitro under physiological and denaturing conditions, including lipophilic and high-ionic-strength solutions, as well as when challenged with a large excess of unlabeled bromide.

7.3 The Future

For much of the last 20 years, interest in using radiohalogens in radiopharmaceutical therapy has taken a distant back seat to radiometals except in a few laboratories including our own. With all due respect to our editors, the originally proposed subject of this chapter was "non-metallic" radionuclides, thus describing them by what they are not rather than what they are. Admittedly, radiometals offer significant advantages over radiohalogens, including chemistries that are readily adaptable to routine use and scalable to clinically relevant activity levels. The availability of numerous radiometals with diverse properties, both nuclear and chemical, provides hundreds of options, and there are many settings in which exploiting these characteristics may be the best strategy. Nonetheless, even though the number of radiohalogens is considerably lower, there are at least three areas where radiohalogens have a bright future: (i) small molecules (~500–1500 molecular weight), (ii) small protein scaffolds, and (iii) targeted alpha-particle therapy with ^{211}At (which will frequently utilize these two types of targeting vectors).

With respect to the former, some small molecules have structures that fortuitously offer sites for labeling with radiometals while simultaneously preserving biological function. Two notable examples of this scenario are currently the focus of much research in RPT: inhibitors of prostate-specific membrane antigen and fibroblast activation protein. However, this is not always the case, as exemplified by unsuccessful attempts to create functional analogues of MIBG labeled with radiometals. The importance of MIBG in the RPT armamentarium is reflected by its approval by the FDA as Azedra® for the treatment of patients with pheochromocytoma and paraganglioma. The development of MIBG as a commercial product is also a good example of another area of importance for future work, namely the progression from a low specific activity synthesis by isotope exchange to a no-carrier-added approach to an immobilized precursor method suitable for industrial scale-up. There are other examples of small organic molecules that have been more successfully labeled with radiohalogens than radiometals, including estrogen receptor-targeted agents and thymidine analogues. As new targets and new targeting vectors emerge, there will undoubtedly be situations where the use of radiohalogens may again prove to be the more prudent approach.

One emerging area of research is the use of small proteins—either derived naturally or created synthetically—as scaffolds for targeted radiotherapeutics. Some of the promising work with sdAbs targeting HER2 was described earlier in this review, and sdAbs are being developed for many of the molecular targets of interest for RPT, including epidermal growth factor receptor, folate receptor, and PSMA [80]. In parallel, a variety of synthetic protein scaffolds in the 5–20 kDa range have been developed, including knottins, DARPins, adnectins, affibodies, and anticalins [81]. All these platforms have excellent chemical and thermal stability and can be generated with sub-nanomolar affinities for relevant biological targets.

For the most part, the work on exploiting these synthetic platforms for RPT is only just beginning. However, based on their molecular size, maximizing the therapeutic potential of these small-protein synthetic scaffolds will require labeling strategies that minimize renal uptake and retention to avoid dose-limiting toxicity to the kidneys. When sdAbs are labeled with an appropriately designed radiohalogenated prosthetic agent, the retention of radioactivity in the kidneys is significantly lower than when they are labeled with radiometals [82]. This is best
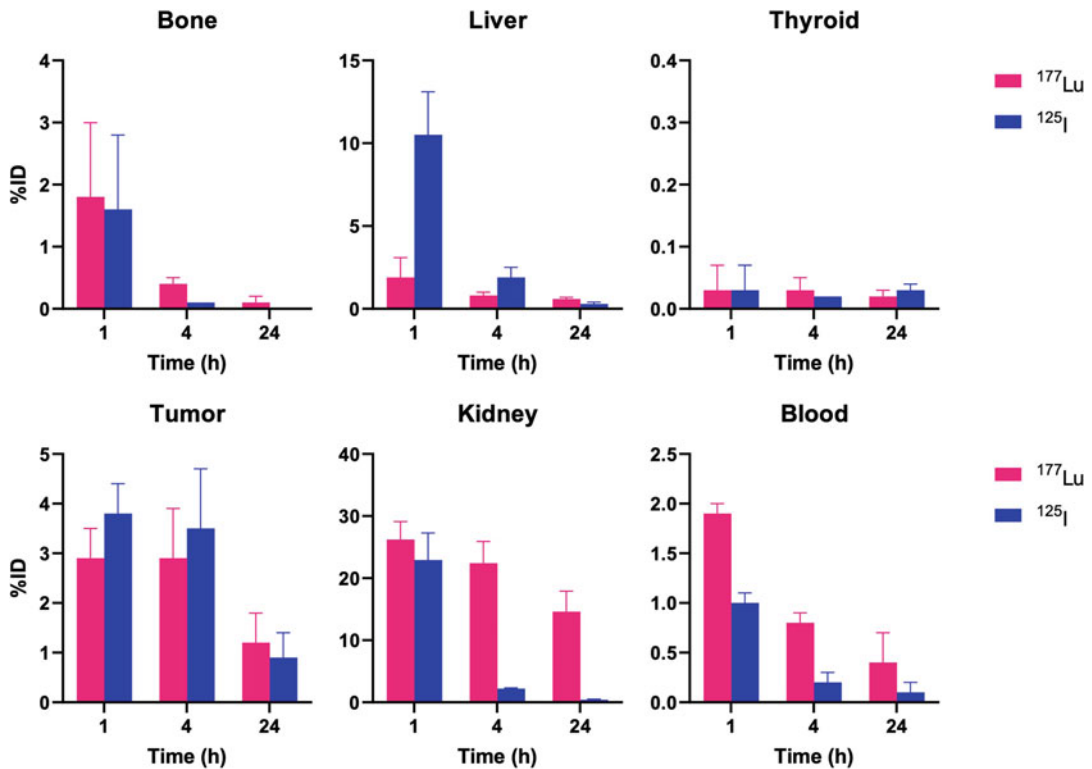
Fig. 7.18 The tissue distribution of ^{177}Lu and ^{125}I after the administration of two anti-HER2 sdAb radioimmunoconjugates—[^{177}Lu]Lu-DOTA-PODS-5F7GGC and *iso*-[^{125}I]GMIB-PODS-5F7GGC—to athymic mice bearing subcutaneous HER2-expressing BT474 xenografts. (Data obtained from Ref. [37])

illustrated by a recent paired-label study directly comparing the tissue distribution of an anti-HER2 sdAb labeled with ^{177}Lu and ^{125}I in the same mice [38]. As shown in Fig. 7.18, the uptake of the two radionuclides in HER2-positive BT474 xenografts was similar, as was the uptake in the kidney at 1 h after injection. However, the radioiodine cleared rapidly from the kidney, while the ^{177}Lu was retained: at 24 h, the renal activity of ^{125}I was about 40-fold lower than that of ^{177}Lu. For this reason, we believe that radiohalogens will play an increasingly important role in the development of small protein scaffolds as targeted radiotherapeutics.

Although this is certainly not limited to halogen radionuclides, most scientists and clinicians currently believe that the most promising direction for future work in RPT is targeted alpha particle therapy (TAT). Astatine-211 differs from the multiple α-particle emitting radiometals

not only in its labeling chemistry but also in its nuclear decay scheme properties, which may offer significant advantages for many applications. Because ^{211}At emits a single α (alpha)-particle per decay, we refer to it as a "kinder, gentler α (alpha)-emitter" that offers greater control over the molecular targeting of the therapeutic radiation. In contrast, long-lived α (alpha)-emitters like ^{225}Ac, ^{227}Th, and ^{223}Ra decay with the emission of multiple α (alpha)-particles, creating several daughter radionuclides along the way. This potentially creates two problems. First, because the half-lives of these radiometals are greater than 10 days (compared with 7.2 h for ^{211}At), the in vivo stability of their radiolabeling chemistry becomes all the more important, and their compatibility with fast-clearing targeting vectors is not ideal. Second, the α (alpha)-decay of the parent radiometal causes the nucleus to recoil, disrupting the

chemical bonds of the chelator and leading to the release of the α (alpha)-emitting daughters from the targeting vector. This leads to the uncontrolled redistribution of the α (alpha)-emitting daughters, resulting in the unintended irradiation of normal tissues such as the kidneys. An additional advantage of [211]At for TAT is that it emits polonium K x-rays that can be used to image patients. In this way, one can determine the distribution of a new [211]At TAT agent in a Phase 0 study. These data can be used to determine human radiation dosimetry and intelligently select starting doses for a therapy trial.

Despite the potential advantages of [211]At for TAT, progress in this area has been slow due to the limited availability of this radionuclide. This is because a cyclotron with a ≥ 28-MeV α (alpha)-particle beam is needed for the efficient production of [211]At, and the scarcity of these machines—combined with the short half-life of [211]At—has limited the radionuclide's use to only a few centers. Fortunately, this situation is changing: new accelerators optimized for the production of [211]At are being built; [211]At production consortia are being set up in the European Union, Japan, and the US; and it is expected that the first commercial source for [211]At will go on line in early 2023 [83]. These developments have already begun to have a positive effect on the use of [211]At in RPT. At least two new agents entered clinical trials in 2022—[[211]At]astatide for differentiated thyroid cancer (University of Osaka, Japan) and [[211]At]MABG for pheochromocytoma (Fukushima Medical University, Japan)—and a trial of a [211]At-labeled PSMA inhibitor is planned for 2024 at our institution. We fully expect the impact of [211]At to grow in the near future, particularly when used in tandem with small organic molecules and small protein scaffolds.

7.4   The Bottom Line

- There are far fewer radiohalogens than radiometals. Nonetheless, there are radiohalogens with properties that are excellent and, in some cases, superior for RPT.

- With radiohalogens, it is all about covalent bond formation.
- Both electrophilic and nucleophilic substitution reaction strategies are available for radiohalogenation.
- Dehalogenation can be avoided with the judicious design of radiopharmaceuticals.
- Small organic molecules, small protein scaffolds, and the α (alpha)-particle emitting [211]At are predicted to be the three most promising areas for future work with radiohalogens.

References

1. Yordanov AT, Hens M, Pegram C, Bigner DD, Zalutsky MR. Antitenascin antibody 81C6 armed with [177]Lu: in vivo comparison of macrocyclic and acyclic ligands. Nucl Med Biol. 2007;34:173–83.
2. Dubost E, McErlain H, Babin V, Sutherland A, Cailly T. Recent advances in synthetic methods for radioiodination. J Org Chem. 2020;85:8300–10.
3. Kumar K. Radioiodine labeling reagents and methods for new chemical entities and biomolecules. Cancer Biother Radiopharm. 2022;37:173–85.
4. Dubost E, Babin V, Benoist F, Hebert A, Pigree G, Bouillon JP, et al. Improvements of C-H radio-Iodination of N-acylsulfonamides toward implementation in clinics. Synthesis-Stuttgart. 2019;51:4393–400.
5. Cavina L, van der Born D, Klaren PHM, Feiters MC, Boerman OC, Rutjes F. Design of radioiodinated pharmaceuticals: structural features affecting metabolic stability towards in vivo deiodination. Eur J Org Chem. 2017;2017:3387–414.
6. Moerlein SM, Coenen HH. Regiospecific no-carrier-added radiobromination and radioiodination of aryltrimethyl group Ivb organometallics. J Chem Soc Perk T 1. 1985;9:1941–7.
7. Liu H, Lin X, Xu D, Li J, Fang J, Li J, et al. Radioiodinated ethinylestradiol derivatives for estrogen receptor targeting breast cancer imaging. ACS Med Chem Lett. 2022;13:203–10.
8. Suzuki H, Kaizuka Y, Tatsuta M, Tanaka H, Washiya N, Shirakami Y, et al. Neopentyl glycol as a scaffold to provide radiohalogenated theranostic pairs of high in vivo stability. J Med Chem. 2021;64:15846–57.
9. Eersels JLH, Mertens J, Herscheid JDM. New insights into the Cu plus -assisted nucleophilic radioiodination of bromopyridine and iodopyridine analogues. J Labelled Compd Rad. 2012;55:135–9.
10. Sloan NL, Luthra SK, McRobbie G, Pimlott SL, Sutherland A. A one-pot radioiodination of aryl amines via stable diazonium salts: preparation of ^{125}I-imaging agents. Chem Commun (Camb). 2017;53:11008–11.

11. Guerard F, Navarro L, Lee YS, Roumesy A, Alliot C, Cherel M, et al. Bifunctional aryliodonium salts for highly efficient radioiodination and astatination of antibodies. Bioorg Med Chem. 2017;25:5975–80.

12. Kothari P, De BP, He B, Chen A, Chiuchiolo MJ, Kim D, et al. Radioiodinated capsids facilitate in vivo non-invasive tracking of adeno-associated gene transfer vectors. Sci Rep. 2017;7:39594.

13. Maingueneau C, Berdal M, Eychenne R, Gaschet J, Cherel M, Gestin JF, et al. ^{211}At and ^{125}I-Labeling of (hetero)aryliodonium ylides: astatine wins again. Chemistry. 2022;28:e202104169.

14. Wilson TC, McSweeney G, Preshlock S, Verhoog S, Tredwell M, Cailly T, et al. Radiosynthesis of SPECT tracers via a copper mediated ^{123}I iodination of (hetero)aryl boron reagents. Chem Commun (Camb). 2016;52:13277–80.

15. Kondo Y, Kimura H, Fukumoto C, Yagi Y, Hattori Y, Kawashima H, et al. Copper-mediated radioiodination reaction through aryl boronic acid or ester precursor and its application to direct radiolabeling of a cyclic peptide. J Labelled Comp Radiopharm. 2021;64:336–45.

16. Kanagasundaram T, Laube M, Wodtke J, Kramer CS, Stadlbauer S, Pietzsch J, et al. Radiolabeled silicon-rhodamines as bimodal PET/SPECT-NIR imaging agents. Pharmaceuticals (Basel). 2021;14(11).

17. Hunter DH, Zhu XZ. Polymer-supported radiopharmaceuticals: [I-131]MIBG and [I-123] MIBG. J Labelled Compd Rad. 1999;42:653–61.

18. Gifford AN, Kuschel S, Shea C, Fowler JS. Polymer-supported organotin reagent for prosthetic group labeling of biological macromolecules with radioiodine. Bioconjug Chem. 2011;22:406–12.

19. Billaud EM, Vidal A, Vincenot A, Besse S, Bouchon B, Debiton E, et al. Development and preliminary evaluation of TFIB, a new bimodal prosthetic group for bioactive molecule labeling. ACS Med Chem Lett. 2015;6:168–72.

20. Rajerison H, Faye D, Roumesy A, Louaisil N, Boeda F, Faivre-Chauvet A, et al. Ionic liquid supported organotin reagents to prepare molecular imaging and therapy agents. Org Biomol Chem. 2016;14:2121–6.

21. Nakagawa C, Toyama M, Takeuchi R, Takahashi T, Tanaka H. Synthesis of [I-123]-iodometomidate from a polymer-supported precursor with a large excluded volume. RSC Adv. 2016;6:12215–8.

22. Yong L, Yao M-L, Green JF, Kelly H, Kabalka GW. Synthesis and characterization of polymer-supported organotrifluoroborates: applications in radioiodination reactions. Chem Commun. 2010;46:2623–5.

23. Terriere D, Chavatte K, Ceusters M, Tourwe D, Mertens J. Radiosynthesis of new radio neurotensin (8-13) analogues. J Labelled Compd Rad. 1998;41:19–27.

24. Pickett JE, Nagakura K, Pasternak AR, Grinnell SG, Majumdar S, Lewis JS, et al. Sandmeyer reaction repurposed for the site-selective, non-oxidizing radioiodination of fully-deprotected peptides: studies on the endogenous opioid peptide alpha-neoendorphin. Bioorg Med Chem Lett. 2013;23:4347–50.

25. Ono M, Watanabe H, Ikehata Y, Ding N, Yoshimura M, Sano K, et al. Radioiodination of BODIPY and its application to a nuclear and optical dual functional labeling agent for proteins and peptides. Sci Rep. 2017;7:3337.

26. Kondo N, Temma T, Shimizu Y, Ono M, Saji H. Radioiodinated peptidic imaging probes for in vivo detection of membrane type-1 matrix metalloproteinase in cancers. Biol Pharm Bull. 2015;38:1375–82.

27. Mushtaq S, Choi DS, Jeon J. Radiosynthesis of ^{125}I-labeled 2-cyanobenzothiazole: a new prosthetic group for efficient radioiodination reaction. J Radiopharm Mol Probes. 2017;3:44–51.

28. Vaidyanathan G, Affleck DJ, Schottelius M, Wester H, Friedman HS, Zalutsky MR. Synthesis and evaluation of glycosylated octreotate analogues labeled with radioiodine and ^{211}At via a tin precursor. Bioconjug Chem. 2006;17:195–203.

29. Thumshirn G, Hersel U, Goodman SL, Kessler H. Multimeric cyclic RGD peptides as potential tools for tumor targeting: solid-phase peptide synthesis and chemoselective oxime ligation. Chemistry. 2003;9:2717–25.

30. Aneheim E, Foreman MRS, Jensen H, Lindegren S. N-[2-(maleimido)ethyl]-3-(trimethylstannyl)-benzamide, a molecule for radiohalogenation of proteins and peptides. Appl Radiat Isot. 2015;96:1–5.

31. Ogawa K, Takeda T, Mishiro K, Toyoshima A, Shiba K, Yoshimura T, et al. Radiotheranostics coupled between an At-211-Labeled RGD peptide and the corresponding radioiodine-labeled RGD peptide. ACS Omega. 2019;4:4584–91.

32. Navarro L, Berdal M, Cherel M, Pecorari F, Gestin JF, Guerard F. Prosthetic groups for radioiodination and astatination of peptides and proteins: a comparative study of five potential bioorthogonal labeling strategies. Bioorg Med Chem. 2019;27:167–74.

33. Mushtaq S, Nam YR, Kang JA, Choi DS, Park SH. Efficient and site-specific ^{125}I-Radioiodination of bioactive molecules using oxidative condensation reaction. ACS Omega. 2018;3:6903–11.

34. Mushtaq S, Park SH. Efficient ^{125}I-radiolabeling of biomolecules using a strain-promoted oxidation-controlled cyclooctyne-1,2-quinone cycloaddition reaction. Chem Commun (Camb). 2020;56:415–8.

35. Yan R, Sander K, Galante E, Rajkumar V, Badar A, Robson M, et al. A one-pot three-component radiochemical reaction for rapid assembly of ^{125}I-labeled molecular probes. J Am Chem Soc. 2013;135:703–9.

36. Feng Y, Zhou Z, McDougald D, Meshaw RL, Vaidyanathan G, Zalutsky MR. Site-specific radioiodination of an anti-HER2 single domain antibody fragment with a residualizing prosthetic agent. Nucl Med Biol. 2021;92:171–83.

37. Sharma SK, Adumeau P, Keinanen O, Sisodiya V, Sarvaiya H, Tchelepi R, et al. Synthesis and comparative in vivo evaluation of site-specifically labeled radioimmunoconjugates for DLL3-targeted immunoPET. Bioconjug Chem. 2021;32:1255–62.

38. Feng Y, Sarrett SM, Meshaw RL, Vaidyanathan G, Cornejo MA, Zeglis BM, et al. Site-specific radiohalogenation of a HER2-targeted single domain antibody fragment using a novel residualizing prosthetic agent. J Med Chem. 2022;65:15358–73.

39. Tolmachev V, Bruskin A, Sjoberg S, Carlsson J, Lundqvist H. Preparation, radioiodination and in vitro evaluation of a nido-carborane-dextran conjugate, a potential residualizing label for tumor targeting proteins and peptides. J Radioanal Nucl Ch. 2004;261: 107–12.

40. Reist CJ, Archer GE, Kurpad SN, Wikstrand CJ, Vaidyanathan G, Willingham MC, et al. Tumor-specific anti-epidermal growth factor receptor variant III monoclonal antibodies: use of the tyramine-cellobiose radioiodination method enhances cellular retention and uptake in tumor xenografts. Cancer Res. 1995;55:4375–82.

41. Pruszynski M, Kang CM, Koumarianou E, Vaidyanathan G, Zalutsky MR. D-amino acid peptide residualizing agents for protein radioiodination: effect of aspartate for glutamate substitution. Molecules. 2018;23(5).

42. Foulon CF, Reist CJ, Bigner DD, Zalutsky MR. Radioiodination via D-amino acid peptide enhances cellular retention and tumor xenograft targeting of an internalizing anti-epidermal growth factor receptor variant III monoclonal antibody. Cancer Res. 2000;60:4453–60.

43. Reist CJ, Archer GE, Wikstrand CJ, Bigner DD, Zalutsky MR. Improved targeting of an anti-epidermal growth factor receptor variant III monoclonal antibody in tumor xenografts after labeling using N-succinimidyl 5-iodo-3-pyridinecarboxylate. Cancer Res. 1997;57:1510–5.

44. D'Huyvetter M, De Vos J, Xavier C, Pruszynski M, Sterckx YGJ, Massa S, et al. 131I-labeled anti-HER2 camelid sdAb as a theranostic tool in cancer treatment. Clin Cancer Res. 2017;23:6616–28.

45. Vaidyanathan G, Zalutsky MR. Synthesis of *N*-succinimidyl 4-guanidinomethyl-3-[*I]iodobenzoate: a radio-iodination agent for labeling internalizing proteins and peptides. Nat Protoc. 2007;2:282–6.

46. D'Huyvetter M, Vos J, Caveliers V, Vaneycken I, Heemskerk J, Duhoux FP, et al. Phase I Trial of 131I-GMIB-Anti-HER2-VHH1, a new promising candidate for HER2-targeted radionuclide therapy in breast cancer patients. J Nucl Med. 2021;62:1097–105.

47. Choi J, Vaidyanathan G, Koumarianou E, Kang CM, Zalutsky MR. Astatine-211 labeled anti-HER2 5F7 single domain antibody fragment conjugates: radiolabeling and preliminary evaluation. Nucl Med Biol. 2018;56:10–20.

48. Choi J, Vaidyanathan G, Koumarianou E, McDougald D, Pruszynski M, Osada T, et al. *N*-Succinimidyl guanidinomethyl iodobenzoate protein radiohalogenation agents: influence of isomeric substitution on radiolabeling and target cell residualization. Nucl Med Biol. 2014;41(10):802–12.

49. Feng Y, Meshaw R, McDougald D, Zhou Z, Zhao XG, Jannetti SA, et al. Evaluation of an 131I-labeled HER2-specific single domain antibody fragment for the radiopharmaceutical therapy of HER2-expressing cancers. Sci Rep. 2022;12:3020.

50. Shankar S, Vaidyanathan G, Affleck DJ, Peixoto K, Bigner DD, Zalutsky MR. Evaluation of an internalizing monoclonal antibody labeled using *N*-succinimidyl 3-[131I]iodo-4-phosphonomethylbenzoate ([131I]SIPMB), a negatively charged substituent bearing acylation agent. Nucl Med Biol. 2004;31:909–19.

51. Boswell CA, Marik J, Elowson MJ, Reyes NA, Ulufatu S, Bumbaca D, et al. Enhanced tumor retention of a radiohalogen label for site-specific modification of antibodies. J Med Chem. 2013;56:9418–26.

52. Albu SA, Al-Karmi SA, Vito A, Dzandzi JP, Zlitni A, Beckford-Vera D, et al. 125I-tetrazines and inverse-electron-demand Diels-Alder chemistry: a convenient radioiodination strategy for biomolecule labeling, screening, and biodistribution studies. Bioconjug Chem. 2016;27:207–16.

53. Berdal M, Gouard S, Eychenne R, Marionneau-Lambot S, Croyal M, Faivre-Chauvet A, et al. Investigation on the reactivity of nucleophilic radiohalogens with arylboronic acids in water: access to an efficient single-step method for the radioiodination and astatination of antibodies. Chem Sci. 2020;12:1458–68.

54. Wilbur DS, Chyan MK, Hamlin DK, Vessella RL, Wedge TJ, Hawthorne MF. Reagents for astatination of biomolecules. 2. Conjugation of anionic boron cage pendant groups to a protein provides a method for direct labeling that is stable to in vivo deastatination. Bioconjug Chem. 2007;18:1226–40.

55. Watanabe S, Azim MA, Nishinaka I, Sasaki I, Ohshima Y, Yamada K, et al. A convenient and reproducible method for the synthesis of astatinated 4-[211At]astato-l-phenylalanine via electrophilic desilylation. Org Biomol Chem. 2018;17:165–71.

56. Vaidyanathan G, Mease RC, Minn I, Choi J, Chen Y, Shallal H, et al. Synthesis and preliminary evaluation of 211At-labeled inhibitors of prostate-specific membrane antigen for targeted alpha particle therapy of prostate cancer. Nucl Med Biol. 2021;94–95:67–80.

57. Shirakami Y, Watabe T, Obata H, Kaneda K, Ooe K, Liu Y, et al. Synthesis of [211At]4-astato-L-phenylalanine by dihydroxyboryl-astatine substitution reaction in aqueous solution. Sci Rep. 2021;11:12982.

58. Denk C, Wilkovitsch M, Aneheim E, Herth MM, Jensen H, Lindegren S, et al. Multifunctional cickable reagents for rapid bioorthogonal astatination and radio-crosslinking. ChemPlusChem. 2019;84:775–8.

59. Guerard F, Lee YS, Baidoo K, Gestin JF, Brechbiel MW. Unexpected Behavior of the heaviest halogen astatine in the nucleophilic substitution of aryliodonium salts. Chemistry. 2016;22:12332–9.

60. Matsuoka K, Obata H, Nagatsu K, Kojima M, Yoshino T, Ogawa M, et al. Transition-metal-free nucleophilic [211]At-astatination of spirocyclic aryliodonium ylides. Org Biomol Chem. 2021;19: 5525–8.

61. Reilly SW, Makvandi M, Xu K, Mach RH. Rapid Cu-catalyzed [211At]astatination and [125I]iodination of boronic esters at room temperature. Org Lett. 2018;20:1752–5.

62. Vaidyanathan G, Affleck DJ, Alston KL, Zhao XG, Hens M, Hunter DH, et al. A kit method for the high level synthesis of [211At]MABG. Bioorg Med Chem. 2007;15:3430–6.

63. Andersson H, Cederkrantz E, Back T, Divgi C, Elgqvist J, Himmelman J, et al. Intraperitoneal alpha-particle radioimmunotherapy of ovarian cancer patients: pharmacokinetics and dosimetry of [211]At-MX35 F(ab')₂--a phase I study. J Nucl Med. 2009;50:1153–60.

64. Guerard F, Gestin JF, Brechbiel MW. Production of [211At]-astatinated radiopharmaceuticals and applications in targeted alpha-particle therapy. Cancer Biother Radiopharm. 2013;28:1–20.

65. Talanov VS, Garmestani K, Regino CA, Milenic DE, Plascjak PS, Waldmann TA, et al. Preparation and in vivo evaluation of a novel stabilized linker for [211]At labeling of protein. Nucl Med Biol. 2006;33: 469–80.

66. Vaidyanathan G, Affleck D, Welsh P, Srinivasan A, Schmidt M, Zalutsky MR. Radioiodination and astatination of octreotide by conjugation labeling. Nucl Med Biol. 2000;27:329–37.

67. Liu WH, Ma H, Tang Y, Chen Q, Peng SQ, Yang JJ, et al. One-step labelling of a novel small-molecule peptide with astatine-211: preliminary evaluation in vitro and in vivo. J Radioanal Nucl Chem. 2018;316(2):451–6.

68. Fujiki K, Kanayama Y, Yano S, Sato N, Yokokita T, Ahmadi P, et al. [211]At-labeled immunoconjugate via a one-pot three-component double click strategy: practical access to alpha-emission cancer radiotherapeutics. Chem Sci. 2019;10:1936–44.

69. Lindegren S, Frost S, Back T, Haglund E, Elgqvist J, Jensen H. Direct procedure for the production of [211]At-labeled antibodies with an epsilon-lysyl-3-(trimethylstannyl)benzamide immunoconjugate. J Nucl Med. 2008;49:1537–45.

70. Aneheim E, Gustafsson A, Albertsson P, Back T, Jensen H, Palm S, et al. Synthesis and evaluation of astatinated N-[2-(Maleimido)ethyl]-3-(trimethylstannyl)benzamide immunoconjugates. Bioconjug Chem. 2016;27:688–97.

71. Zhou D, Chu W, Voller T, Katzenellenbogen JA. Copper-mediated nucleophilic radiobromination of aryl boron precursors: convenient preparation of a radiobrominated PARP-1 Inhibitor. Tetrahedron Lett. 2018;59:1963–7.

72. Zhou D, Kim SH, Chu W, Voller T, Katzenellenbogen JA. Evaluation of aromatic radiobromination by nucleophilic substitution using diaryliodonium salt precursors. J Labelled Comp Radiopharm. 2017;60: 450–6.

73. Mishiro K, Nishii R, Sawazaki I, Sofuku T, Fuchigami T, Sudo H, et al. Development of radiohalogenated osimertinib derivatives as imaging probes for companion diagnostics of osimertinib. J Med Chem. 2022;65:1835–47.

74. Ordonez AA, Carroll LS, Abhishek S, Mota F, Ruiz-Bedoya CA, Klunk MH, et al. Radiosynthesis and PET bioimaging of [76]Br-bedaquiline in a murine model of tuberculosis. ACS Infect Dis. 2019;5:1996–2002.

75. Lang L, Li W, Jia HM, Fang DC, Zhang S, Sun X, et al. New Methods for Labeling RGD Peptides with Bromine-76. Theranostics. 2011;1:341–53.

76. Rossin R, Berndorff D, Friebe M, Dinkelborg LM, Welch MJ. Small-animal PET of tumor angiogenesis using a [76]Br-labeled human recombinant antibody fragment to the ED-B domain of fibronectin. J Nucl Med. 2007;48:1172–9.

77. Mume E, Orlova A, Malmstrom PU, Lundqvist H, Sjoberg S, Tolmachev V. Radiobromination of humanized anti-HER2 monoclonal antibody trastuzumab using N-succinimidyl 5-bromo-3-pyridinecarboxylate, a potential label for immunoPET. Nucl Med Biol. 2005;32:613–22.

78. Mume E, Orlova A, Larsson B, Nilsson AS, Nilsson FY, Sjoberg S, et al. Evaluation of ((4-hydroxyphenyl) ethyl)maleimide for site-specific radiobromination of anti-HER2 affibody. Bioconjug Chem. 2005;16:1547–55.

79. Winberg KJ, Persson M, Malmstrom PU, Sjoberg S, Tolmachev V. Radiobromination of anti-HER2/neu/ErbB-2 monoclonal antibody using the p-isothiocyanatobenzene derivative of the [76Br] undecahydro-bromo-7,8-dicarba-nido-undecaborate (1-) ion. Nucl Med Biol. 2004;31:425–33.

80. Piramoon M, Khodadust F, Hosseinimehr SJ. Radiolabeled nanobodies for tumor targeting: from bioengineering to imaging and therapy. BBA Rev Cancer. 1875;2021:188529.

81. Gebauer M, Skerra A. Engineering of binding functions into proteins. Curr Opin Biotech. 2019;60: 230–41.

82. Küppers J, Kürpig S, Bunndschuh RA, Essler M, Lütje S. Radiolabeling strategies of nanobodies for imaging applications. Diagnostics (Basel). 2021;11: 1530.

83. Feng Y, Zalutsky MR. Production, purification and availability of [211]At: near term steps toward global access. Nucl Med Biol. 2021;100–101:12–23.

Dosimetry in Radiopharmaceutical Therapy

8

Lukas M. Carter and Adam L. Kesner

8.1 The Fundamentals

8.1.1 The Importance of Dosimetry in Radiopharmaceutical Therapy

The study of radiation dosimetry has evolved alongside the uses of radiation in diagnostic and therapeutic nuclear medicine. While radiation cannot be seen with the naked eye, the modes of its origination, interaction with tissue, and detection have been well studied and characterized, providing the tools we need to tailor its safe and efficacious use. As scientists, we can model irradiation scenarios in media or tissue, quantify the energy that the radiation imparts, and predict the biological impact of the radiation exposure. These models can be simulated with computers and/or studied with physical measurements.

The field of radiotherapeutic dosimetry is most established in the domain of external beam radiation therapy (EBRT). As described in its name, EBRT procedures involve directing a field of radiation that originates outside a patient through the patient, selectively aiming to irradiate target tissue. A careful dosimetry plan is always prepared for each treatment, and this plan essentially dictates the amount of source radiation required to achieve the established threshold doses in the patient to elicit the desired tissue response. In the case of modern EBRT, personal dosimetry is a requirement for every treatment.

In the practice of radiopharmaceutical therapy (RPT), dosimetry can be calculated in a similar manner to EBRT, but the calculations are more complex. Whereas the source of the radiation is clearly defined in EBRT, RPT, and all radiopharmaceutical dosimetry—the source of the radiation is distributed throughout a patient and changes with time as illustrated in Fig. 8.1. These additional variables, combined with nuances relating to differing the differing decay spectra of radionuclides—make dosimetry calculations for RPT challenging. But the dose calculations *can* be modeled and help guide treatments. A comparison of these dosimetric principles is shown in Fig. 8.2.

8.1.2 Physical Dosimetry Basics

The most biologically relevant interaction between radiation and tissue is damage to cellular DNA, as this correlates strongly with cell death or sterilization. As different types of radiation traverse tissue, they deposit energy. The most basic unit of radiation dose is known as the gray [Gy], defined by the International System of Units (SI) as the energy imparted to a tissue per unit mass, as shown in Eq. 8.1.

L. M. Carter · A. L. Kesner (✉)
Department of Medical Physics, Memorial Sloan Kettering Cancer Center, New York, NY, USA
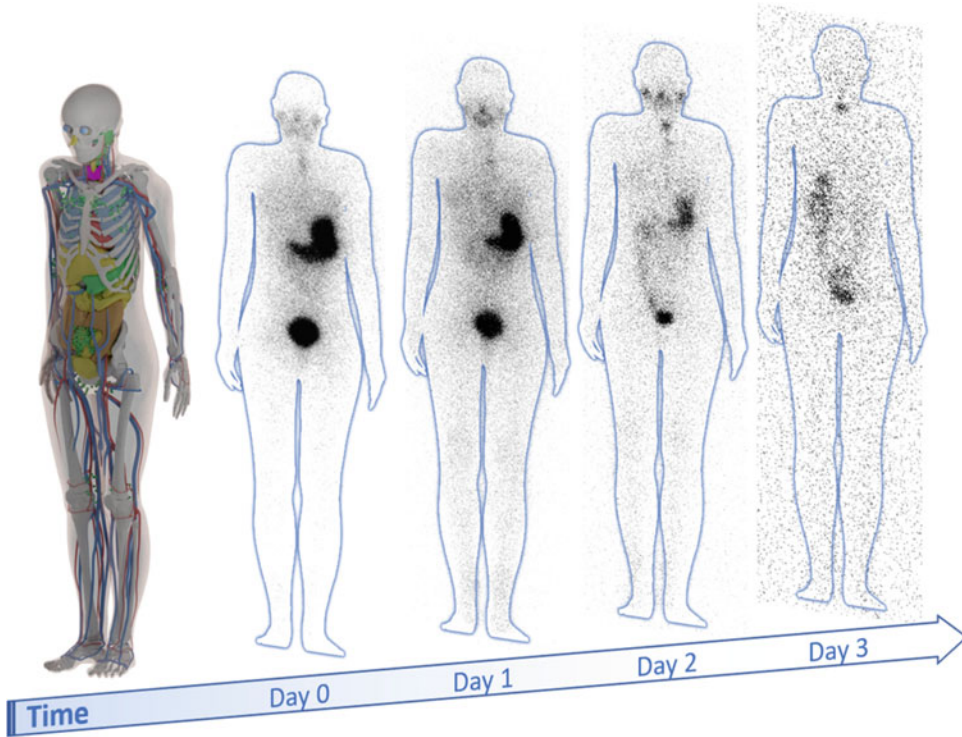e-mail: kesnera@mskcc.org

Fig. 8.1 Gamma camera images of a patient after the administration of ^{131}I for the irradiation of the thyroid. The image illustrates the changing biodistribution of the radiopharmaceutical over time

$$1 \text{ Gy} = 1 \frac{\text{J}}{\text{kg}} \qquad (8.1)$$

The unit of gray is used to quantify radiation dose and is often referred to as "absorbed dose" to remove ambiguity with other uses of the word "dose" (e.g., radioactivity measurements). Because of the clarity, conciseness, and universality of this quantity of absorbed dose, it is the most often reported representation of radiation dose used in RPT. For example, treatment protocols or healthy organ dose limits are often prescribed by the treating physician in units of gray.

Radiations relevant to RPT sometimes call for more descriptive characterizations than absorbed dose. This is because different radionuclides have different rates of decay, types of emitted particles, and energies of their emissions. Along these lines, it is worth noting that two scenarios in which the same amount of absorbed dose to a target can lead to different tissue reactions. For example, the absorbed dose quantity of 2 Gy delivered to lung tissue by a photon beam from a 6 MeV linear accelerator over the course of a few seconds will affect the tissue differently than the delivery of 2 Gy from an internalized alpha-emitting isotope over the course of a few days. Accordingly, we have seen other variables introduced to describe tissue interactions with radiation. Other units include—but are not limited to— *equivalent dose*, a modified form of absorbed dose that has been weighted to account for the cytotoxic effectiveness of the radiation; *biologically effective dose*, which may be thought of as the total physical dose required for a specified biologic effect when it is delivered at a very low dose rate or in many small-dose fractions; and *equivalent uniform dose*, a model that takes into account the possible heterogeneity of radiation source uptake and extrapolates the spatially varying absorbed dose distribution to an equivalent
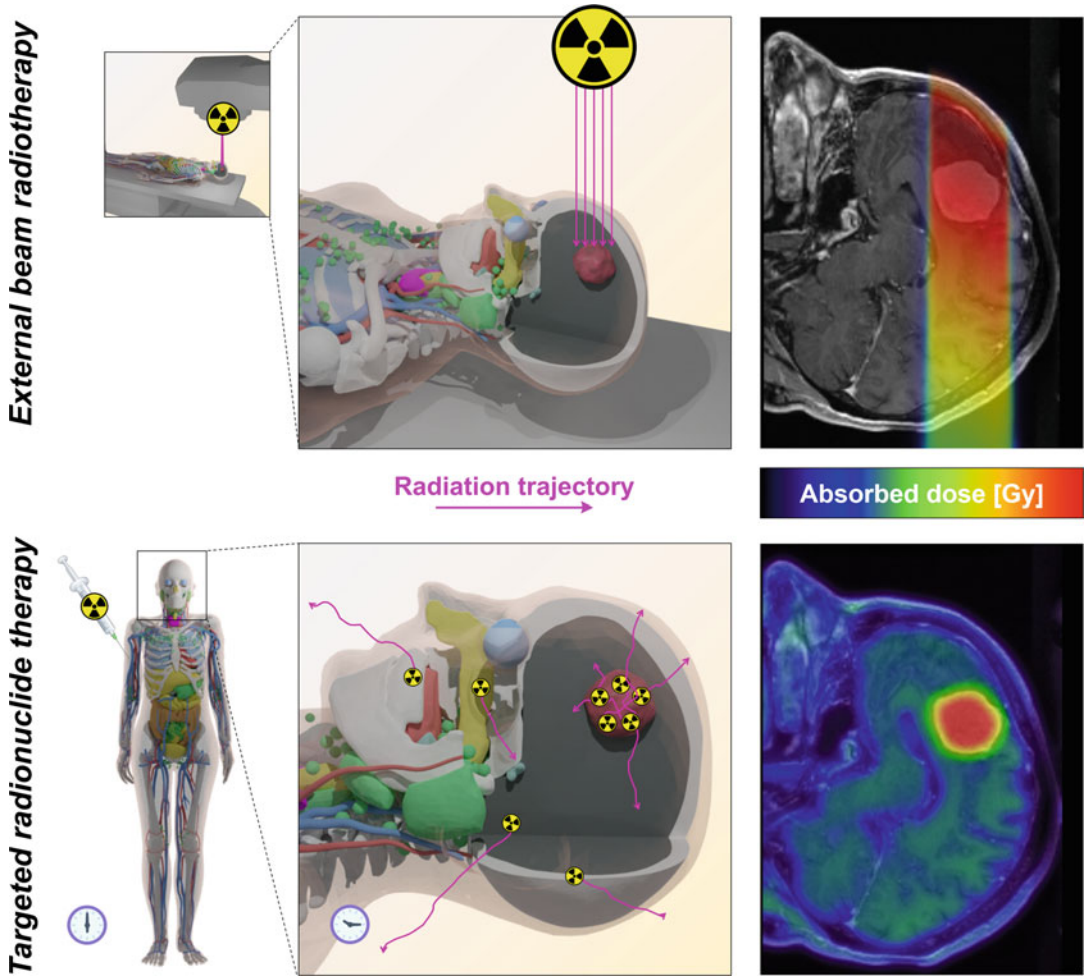
Fig. 8.2 Principles of different radiation sources and target absorbed dose distributions for external beam radiotherapy (top) and radiopharmaceutical therapy (bottom). It should be noted that the external beam illustration shows a single radiation field for illustrative purposes, whereas clinical treatments often utilize multiple fields delivered from multiple angles to better conform the radiation dose on the target

uniform absorbed dose value, which would yield a similar biologic response. Recent concise definitions of the types of units used in dosimetry can be found in the literature [1].

8.1.3 Tissue Response to Radiation

The effects of radiation exposure on humans can be classified into two categories: stochastic effects and tissue reactions (also called deterministic effects or nonstochastic effects). Stochastic effects are defined as the longer-term risks of radiation exposure and stem from possible cell damage that may or may not ultimately manifest as injury. The probability of stochastic effects is usually considered to increase with increasing damage to DNA. For example, contracting cancer from a health screening imaging protocol is considered a stochastic risk (and is usually very low). In contrast, tissue reactions occur when specific levels of exposure to radiation have been surpassed and are usually organ specific. Tissue reactions occur at high doses when enough cells

in an organ or tissue are killed or prevented from reproducing. The onset of tissue reactions is usually immediate (hours to weeks) upon exposure, and their severity increases with the radiation dose [2]. In radiopharmaceutical therapy, we are primarily concerned with tissue reactions, as they are more relevant for high radiation doses and more appropriate to patient-specific treatment plans.

8.1.4   Dosimetry in Contemporary and Novel Clinical Targeted Radionuclide Therapies

At present, the field of radiopharmaceutical therapy is growing, and we are seeing a surge of clinically relevant radiopharmaceuticals moving from the research and development space into the clinic. For preclinical research and development, dosimetry is crucial for understanding the cytotoxic irradiation of target tissue in relation to the risk to healthy tissues as well as for establishing a safe pathway for bringing a new radiotherapeutic to market. Preclinical testing in animals and then the careful transition into small (and later larger) human trials are essential steps in the development of a radiopharmaceutical drug. Ultimately, treatment approvals depend in part on dosimetry characterizations that inform efficacy and safety. Furthermore, drug developers are required to demonstrate that radiation doses that result from their treatments will remain below certain established thresholds.

8.1.4.1   Radioiodine

One of the first established and most successful examples of radiopharmaceutical therapy is the use of radioactive iodine to treat thyroid diseases, including hyperthyroidism and thyroid cancer. When administered to a patient, the iodide anion has a very specific uptake in the patient's thyroid. Iodine-131 (^{131}I) is an isotope of iodine that has a radioactive half-life of approximately 8 days and emits a variety of emissions during its decay. One of these emissions is a beta particle, which deposits its energy/radiation dose within 2 mm of the site of decay. Iodine-131 is used widely in the management of thyroid diseases and has high rates of success. The American Thyroid Association (ATA), an authority on the clinical management of thyroid disease, has published guidelines for its use [3].

Dosimetry may or may not be used in the planning of radioiodine treatments. For some applications, for example, to quell hyperthyroidism, a relatively low activity is administered, typically 10 mCi–15 mCi. In the case of thyroid cancer—in which the radiopharmaceutical is used to ablate any residual cancerous or healthy thyroid tissues—larger activities are administered, typically >100 mCi. While the activity ranges administered are generally agreed upon, there is no clear consensus with respect to the selection of the activity to administer in each case. For example, the ATA guidelines state that therapy can be given for several indications with either empirically chosen activities *or* dosimetry-based (i.e., personalized) activities [3]. Part of the reason for this ambiguity is that ^{131}I-based treatments are "too successful", boasting high rates of successful outcomes with generally very little toxicity. Since the use of ^{131}I within suggested ranges has robust efficacy, there is limited literature justifying increased efforts for personalized dosimetry. However, such literature *does* exist. The Society of Nuclear Medicine and Molecular Imaging has published guidelines for physicians who want to escalate radiation doses in hopes of treating thyroid cancer more aggressively [4]. These guidelines are designed to limit damage to the lungs and bone marrow by keeping doses <2 Gy to the marrow and < 26 Gy to the lungs. More recent literature suggests that treatment planning based on patient-specific dosimetry may indeed provide improvements in outcomes [5].

8.1.4.2   Yttrium-90 Microsphere (Theraspheres™ or Sirtex™)

Yttrium-90 (^{90}Y) labeled microspheres are one of the first internal emitter devices for which internal dosimetry is utilized to personalize treatments in standard clinical workflows. The principle of implanting radioactive microspheres for the treatment of liver disease exploits the distinctive

vasculature of the liver and liver malignancies to target the latter with beta radiation. The actual spheres are micrometers in diameter. When strategically injected into a patient's hepatic artery, the spheres become lodged in the blood vessels of the malignant disease and liver [6].

The administration of ^{90}Y microspheres is technically a brachytherapy procedure, but in practice, it is often treated as an unsealed radiation source and handled by nuclear medicine departments. This is because the millions of small spheres used in a treatment resemble a (traditional) liquid radiopharmaceutical solution. The dosimetry calculation methods provided by the vendors and approved by regulatory agencies differ across the two principal vendors (Theraspheres™ and Sirtex™), but both use dosimetry based on organ-level dosimetry calculations (vide infra) and the principle of prescribing greater radiation dose to patients who have greater volumes of disease. Furthermore, because the ^{90}Y microspheres are implanted (and do not redistribute once administered), their dosimetry does not need to account for changes in tracer kinetics and only requires a single imaging timepoint. They thus offer a simpler scenario for internal dosimetry calculations. Accordingly, the emergence of ^{90}Y microspheres has provided an ideal platform for the development of dosimetry software tools. This has been the case for several companies that first developed software for ^{90}Y microsphere dosimetry and have since modified their software to handle new radiopharmaceuticals and more complex kinetic modeling. Recently, the superiority of the dosimetry-guided prescription of ^{90}Y microspheres has been demonstrated by the DOSISPHERE trial [7].

8.1.4.3 ^{177}Lu-Labeled DOTATATE (Lutathera™)

Peptide receptor radionuclide therapy (PRRT) is a subset of RPT that utilizes radiolabeled peptides to target receptors that are overexpressed in certain tumors with high affinity and specificity. The somatostatin receptor agonists DOTATOC and DOTATATE labeled with the therapeutic radionuclides ^{90}Y or ^{177}Lu provide quintessential

examples of this approach (see Chap. 14) [8]. [^{177}Lu]Lu-DOTATATE—also known commercially as Lutathera®—gained EMA (European Medicines Agency) and FDA (Food and Drug Administration) approvals for the treatment of somatostatin receptor-positive gastroenteropancreatic neuroendocrine tumors in 2017 and 2018, respectively [9]. This approval was influenced by the NETTER-1 trial, a multicenter, randomized, phase-III study [10]. The study demonstrated improved progression-free survival in the treatment cohort compared to a control arm. A more recent analysis has also shown improved overall survival but with less statistical power, though this post-study analysis is limited by cross-over patients switching to the radioligand therapy [11].

Lutetium-177 is a theranostic isotope with a 6.7 d half-life and emits a β-particle as well as imageable gamma rays (113 and 208 keV) that can be exploited for biodistribution and dosimetry [12]. PRRT is a two-step process. Prior to receiving the radiotherapeutic, patients are screened for receptor overexpression using SPECT or PET using analogs of the therapeutic peptide labeled with ^{111}In or [68]Ga. Once receptor expression/potential treatment efficacy is confirmed, the radiotherapeutic is used. [^{177}Lu]Lu-DOTATATE itself has primary uptake in tumors, kidneys, liver, and spleen, and the kidneys and bone marrow have been identified as the healthy organs most at risk [13]. The vendor-recommended treatment schedule consists of four infusions of 7.4 GBq [^{177}Lu]Lu-DOTATATE at intervals of 8 weeks [8, 10]. These approved protocols are conservative dosing regimens; the total activity administration will likely not cause adverse effects across the general population. However, several research groups have demonstrated variability in the dosimetry across the population and demonstrated the possibility of tailoring treatments through personalized dosimetry calculations, ensuring that the respective dose limits to organs at risk are not exceeded [13–15]. It has been shown that patient-tailored treatments can vary among populations, with individuals potentially receiving 2–10 cycles of 7.4 GBq each [13] while maintaining doses to the

critical organs that are below the limits. Moreover, PRRT patients frequently undergo retreatments or alternative treatments (e.g., radioembolizations), therefore warranting the calculation of the cumulative dose to organs at risk. Most [^{177}Lu]Lu-DOTATATE dosimetry research is performed using biodistribution data acquired via multi-timepoint imaging [15].

8.1.4.4 ^{177}Lu-Labeled PSMA-617 (Pluvicto™)

The most recently approved RPT (at the time of writing) is the use of [^{177}Lu]Lu-PSMA-617 for prostate cancer. The treatment was approved under the brand name Pluvicto™ in 2022. The approval was largely based on the results of the VISION and TheraP trials [16, 17], in which it was shown that the therapeutic intervention was able to prolong progression-free survival in patients with advanced PSMA-positive metastatic castration-resistant prostate cancer. This new treatment is predicted by the medical community to become widely used in the treatment of prostate cancer [18].

In the case of [^{177}Lu]Lu-PSMA-617, dosimetry was used for its development and translation and for determining quantities of radioactivity appropriate for its safe use. A robust summary of these dosimetry-related publications is presented by Jackson and colleagues [19]. The literature shows relatively consistent patterns of retention among normal tissues and high specificity for metastatic prostate cancer phenotypes. The organs with notable tracer updates are the liver, kidneys, spleen, salivary glands, and bladder. The potential at-risk and administration activity-limiting organs include the kidneys, bone marrow, and salivary glands. The vendor-recommended treatment schedule for Pluvicto™ consists of 6 infusions of 7.4 GBq (200 mCi) at intervals of 6 weeks with built-in pauses if patients exhibit adverse reactions. While dosimetry was pivotal in the development of the treatment, it has not been integrated into the clinical protocols to support patient-specific treatment optimization.

8.1.5   Strategies for Dosimetry Utilization

Dosimetry provides a means to quantify delivered or anticipated radiation doses. But the quantities need to be contextualized to meaningfully impact a workflow or regimen. The field continues to work at developing best practices for utilizing dosimetry information. The two main categories and/or paradigms in which dosimetry is used to tailor prescriptions for administered activity in RPT are enumerated as follows:

- The *maximum tolerable dose* (MTD) strategy: This is a radioactivity prescription strategy in which the calculated absorbed dose to each organ is compared to the organ absorbed dose limits. Since radiopharmaceuticals have characteristic uptake, there are usually a small number of organs that are determined to be the organs at risk in a given treatment. The administered activity can then be determined by selecting the maximum activity that maintains acceptable absorbed doses to the organs at risk.
- *Tumor target dose* strategy: This is a radioactivity prescription strategy in which the calculated absorbed dose to the patient's tumor is tailored for response effect. This strategy can be used to enhance the probability of favorable treatment outcomes with respect to tumor suppression.

In practice, research and clinical workflows often aim to characterize dosimetry in both diseased and healthy tissues, and both calculations are taken into consideration when planning prescription doses. However, the MTD method has an advantage in that it errs on the "do no harm" side of treatment planning and is thus more likely to avoid unintended radiotoxicity to a patient. Further rationale for using the MTD method is that radiation doses to organs are often easier to calculate accurately than doses to lesions. This is because a patient's tumor burden can change significantly during treatment. Furthermore, a

patient's tumor burden is often distributed throughout the body in seemingly random geometric shapes and patterns. Finally, the uptake of radiopharmaceuticals in lesions is harder to quantify from imaging procedures, as measurements of radiopharmaceutical uptake in small lesions suffers from limitations related to the spatial resolution of clinical PET or SPECT scanners.

8.1.5.1   Dose Limits for Normal Organs

Because uptake occurs in both healthy and diseased tissue, radiopharmaceuticals are developed and screened to ensure that they can be utilized without delivering excessive radiation doses to healthy tissue organs. Common dose-limiting organs for clinical RPT include the bone marrow, liver, kidneys, salivary glands, and lungs. For these organs, radiation dose limits have been established in research studies. A select summary of dose-limiting organs and their associated dose limits is presented in Table 8.1. These limits are not absolute and can be modified if additional clinical considerations are warranted. For a more thorough description of contemporary radiation dose limits to organs, readers are referred to Wahl et al. [20].

8.1.5.2   Standardization

The workflow for performing radiopharmaceutical dosimetry generally includes several design factors, measurements, and assumptions. The timing and types of measurements and the computational models used to calculate dose will impact the final dose estimation. While the field has standard units to report radiation dose (i.e., Gy), the procedures from which dose estimates are derived often vary across sites and treatments. Standardizing dose calculations is important for establishing dose-response relationships and optimizing treatment workflows. The need for the standardization of internal dose calculations is commonly articulated in the literature, and efforts to improve this standardization span equipment quality control, imaging protocols, and dosimetry calculation models.

One challenging aspect of standardizing dosimetry is standardizing protocols for measurements and processing. The variety of radionuclides used in RPT means that different protocols are needed to accommodate varying half-lives and radiation safety considerations. Furthermore, different centers have different equipment and must also adhere to local practicalities for providing imaging services. For example, patients may be imaged serially on different machines at large centers, and scheduling times may be variable for patients at small centers. Fig. 8.3 shows various types of radiation measurement equipment commonly found in nuclear medicine clinics.

Efforts to establish standards for dosimetry calculation methods have been presented. The Medical Internal Radiation Dose (MIRD) Committee of the Society of Nuclear Medicine has published *MIRD pamphlet no. 16: Techniques for quantitative radiopharmaceutical biodistribution data acquisition and analysis for use in human radiation dose estimates*, which aims to set standards for measurements and their documentation [21]. More recently, the European Association of Nuclear Medicine published *Dosimetry Committee guidance document: good practice of clinical dosimetry reporting*. We are now seeing robust software tools— including artificial intelligence-assisted tools—enter the field, which also helps improve standardization through automation.

Table 8.1 Typical normal tissue radiation dose limits used in dosimetry-based treatment planning for RPT

Organ	Dose limit	Clinical toxicity
Bone marrow	2 Gy	Myeloablation, myelosuppression
Liver	30 Gy	Liver failure
Kidneys	25 Gy	Nephropathy
Salivary glands	25 Gy	Hypofunction, xerostomia
Lungs	30 Gy	Pneumonitis
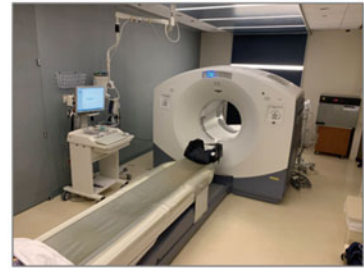
Fig. 8.3 Common radiation measuring equipment found in a nuclear medicine clinic: detectors, probes, and cameras

8.2 The Details

Dosimetry in nuclear medicine is challenging because the source of radiation (the radiopharmaceutical) is nonuniformly distributed throughout a patient, and this distribution is usually time variant. Methods for computing radiopharmaceutical dosimetry have evolved gradually since the 1950s. For a comprehensive discussion of the methods and nomenclature relevant to internal dosimetry assessment, we refer the reader to the MIRD schema for internal dosimetry [22]. The MIRD schema provides a robust general framework for addressing numerous physical phenomena, technical challenges, details, and nuances that may be dosimetrically relevant. In this section, we look at the most central concepts of internal dosimetry through the lens of the MIRD formalism. The consideration of these central concepts is useful for many reasons, including understanding relationships between radiopharmaceutical properties/biokinetics on toxicity/efficacy and understanding the implications of experimental design on dosimetric accuracy. Moreover, meaningful dosimetric assessments can often be made strictly using the basic concepts we look at here.

For a given tissue, the calculation of the mean absorbed dose requires the determination of the energy absorbed in a tissue per unit mass of that tissue. In RPT, of course, the sources of this energy are radionuclides distributed within the tissues (Fig. 8.1). Generally, dosimetry estimation requires the following elementary information:

- *Anatomical information*: The spatial relationships between the tissues of interest and the makeup (i.e., elemental composition, density) of these tissues. A computerized representation of this information is called a *computational phantom* and will be discussed later.
- *Radionuclide decay and radiation transport information*: The radionuclide's decay radiations with corresponding energies and yields as well as knowledge of how these radiations deposit energy in tissue.
- *Biodistribution*: How the distribution of activity of the radionuclide(s) changes in the subject over time. The biodistribution may be

described in terms of *effective*[1] uptake/clearance or *biological*[2] uptake/clearance.

8.2.1 Simple Absorbed Dose Calculation: Local Energy Absorption

If we make the simplifying assumptions that for each decay occurring in a given tissue, *weakly-penetrating radiations*[3] are completely locally absorbed (i.e., absorbed where the decay occurred), *penetrating radiations*[4] are not absorbed, and the anatomy is invariant, then the absorbed dose calculation becomes conceptually trivial. To this end, we need only the number of decays occurring in the tissue, $\tilde{A}$, the equilibrium absorbed dose constant for the weakly penetrating radiations (i.e., the mean energy deposited per decay), Δ_{wp}, and the tissue mass, M:

$$D\ [\text{Gy}]$$
$$= \frac{\tilde{A}\ [\text{\#of decays}] \times \Delta_{wp}\ [\text{J/decay}]}{M\ [\text{kg}]} \qquad (8.2)$$

The number of decays can be calculated if it is known how the activity, $A(t)$ [#of decays/s; Bq], varies with time, t [s], in the tissue. This relationship is often called a *time-activity curve*. If the activity was constant over the irradiation period, we would simply take the product of A with the irradiation time to obtain the number of decays. Realistically, the activity is not constant: it varies as the radiopharmaceutical distributes among different tissues and the radionuclide decays.

Therefore, we must determine the area under the time-activity curve by integrating $A(t)$ over the irradiation period, T, to obtain the number of decays:

$$\tilde{A}\ [\text{\#of decays}] = \int_0^T A(t)dt \qquad (8.3)$$

The number of decays that occur, $\tilde{A}$, is also called the *time-integrated activity*. It is often given in units of Bq·s, which can logically be interpreted as one decay (if one disregards the stochastic nature of radioactive decay, which is unimportant here). Sometimes $\tilde{A}$ is given in other units which differ by a proportionality factor, e.g., Bq·h, MBq·h, and μCi·h. If $\tilde{A}$ is normalized to the administered activity, it is given the lowercase symbol $\tilde{a}$ [Bq·s/Bq, or, s] and is called the *time-integrated activity coefficient* (formerly known as the *residence time*).

Often, a modified form of Eq. 8.2 is used in which $\tilde{A}$ is replaced by the time-integrated activity coefficient, $\tilde{a}$, to obtain an absorbed dose coefficient, $d(r_T)$ [Gy/Bq]. The absorbed dose coefficient is simply the absorbed dose normalized to the administered activity:

$$d[\text{Gy/Bq}] =$$
$$\frac{\tilde{a}[\text{\#of decays per unit administered activity}] \times \Delta_{wp}[\text{J/decay}]}{M[\text{kg}]}$$
$$(8.4)$$

The remaining variables of Eq. 8.2 are straightforward to obtain; Δ_{wp} may be looked up in a prior generated database, and M may be estimated or measured, for example, via anatomical imaging. In RPT, the integration period is usually assumed to be infinite.

Despite their simplicity, Eqs. 8.2 and 8.4 have practical uses in RPT. Namely, they are useful where the main contributors to the absorbed dose are weakly penetrating radiations that have short ranges relative to the dimensions of the target tissue. A specific case is given in the following *Example*.

---

[1] Effective uptake/clearance considers the activity of the radionuclide (or proportional parameter, e.g., the activity concentration) and is a function of both radioactive decay and biological translocation mechanisms.

[2] Biological uptake/clearance considers the activity of a radionuclide that has been decay-corrected back to the time of administration. Thus, biological uptake/clearance is only a function of biological translocation.

[3] Alpha particles, beta particles, and monoenergetic electrons (Auger and conversion electrons) are considered weakly penetrating due to their short tissue ranges

[4] Photons (X-rays, γ-rays) are considered penetrating radiations.

Example 3.1 *Preclinical Radiopharmaceutical Therapy*

In a preclinical radiopharmaceutical therapy experiment, a mouse was administered a ^{177}Lu-labeled monoclonal antibody and then monitored by serial SPECT/CT. Its liver was determined to have a mass of 1.1 g, and the liver activity was found to follow the function: $A[\mathrm{Bq}] = 0.15 \times 10^6\, e^{-\left(3.10 \times 10^{-6}\right)t}$ where time is in seconds. Calculate the absorbed dose to the liver assuming local energy deposition and ignoring the contribution of photons. Hint: $\Delta_{\mathrm{wp}} = 0.146\ \mathrm{MeV}/_{\mathrm{Bq \cdot s}}$ for ^{177}Lu.

Solution 3.1

- Calculate $\tilde{A}$
  We assume the dose integration period to be infinite, as is the usual case. Substituting the expression for the activity into Eq. 8.3, we have:

$$\tilde{A} = \int_0^\infty 1.5 \times 10^5\, e^{-\left(3.10 \times 10^{-6}\right)\mathrm{t}} dt = 4.8$$

$$\times 10^{10}\ \mathrm{Bq \cdot s}$$

- Calculate D
  The absorbed dose follows from Eq. 8.2. We must convert the units of Δ_{wp} and M to arrive at the absorbed dose in units of gray:

$$4.8 \times 10^{10}[\mathrm{Bq \cdot s}] \times$$

$$D = \frac{\left(0.146\left[\mathrm{MeV}/_{\mathrm{Bq \cdot s}}\right] \times \dfrac{1.60 \times 10^{-13}[\mathrm{J}]}{1[\mathrm{MeV}]}\right)}{1.1[\mathrm{g}] \times \dfrac{1[\mathrm{kg}]}{1000[\mathrm{g}]}}$$

$$= 1.0[\mathrm{Gy}]$$

A Closer Look Lutetium-177 is considered a low-energy beta emitter and has a low abundance of energetic photons. Beta emissions from ^{177}Lu have a maximum soft tissue range of about 1.8 mm, but most of these betas—as well as monoenergetic electron emissions—have much shorter ranges. In contrast, the murine liver has dimensions on the order of about a centimeter. Because the dimensions of the liver are large compared to the range of the particles, most particles will lose all their kinetic energy before they escape the liver (i.e., most of the energy lost is deposited locally). This simple approach to absorbed dose calculation is often used preclinically, when reasonable accuracy may be achieved given radionuclides with short-range particulate emissions.

8.2.2 General Absorbed Dose Calculation: Organ-Level MIRD Method

In §3.1, we considered the theoretical situation of complete local absorption. When radiation energy is completely locally absorbed, a tissue only receives a dose stemming from decays that occur within that tissue (i.e., *self-dose*). Realistically, a tissue usually receives both self-dose and *cross-dose*, the latter stemming from decays occurring in the other tissues (vide infra). As one might expect, radionuclides that emit penetrating radiations may create significant cross-dose contributions to distant tissues. Here we consider this more general situation under the assumption the subject's anatomy does not change over time.

The famous *MIRD schema* is a mathematical formalism for modeling the interplay of radiation and tissues within the body. The MIRD schema utilizes the concept of *source regions*, r_S, wherein a spatially uniform distribution of radioactive decays occurs, and *target regions, r_T*, wherein the dose accumulates. The source and target regions may coincide or may be different. In the case of self-dose, the source and target regions are the same (e.g., activity in the liver irradiating the liver). In the case of cross-dose, the source and target regions are different (e.g., activity in the contents of the bladder irradiating the liver). Usually, we consider the source and target regions to be gross anatomical structures (e.g., whole organs, organ contents, tumors); this approach is

known as *organ-level dosimetry*. We will briefly discuss some other ways to define the sources and targets further on.

Conceptually, the task is still simple: to calculate the mean absorbed dose to a target region, we must sum each of the cross-dose contributions to the target with the self-dose. However, it is nontrivial to estimate these individual contributions, as they depend on the potentially complex spectra of the radionuclide, the subject's anatomy, and the biodistribution. In practice, this is facilitated via detailed Monte Carlo simulations, in which millions of possible decay coordinates, radiation trajectories, and dose deposition events are sampled within a computerized anatomical model of a patient/subject. The reward at the end of this complex processing is another central concept in the MIRD schema: a set of *S-values*.

An *S*-value, $S(r_T \leftarrow r_S)$ [Gy/Bq·s], quantifies the mean absorbed dose contribution to a target region, r_T, per unit decay occurring in the source region, r_S.[5] S-values implicitly account for geometry (anatomy) and the radionuclide's decay spectrum, but S-values are independent of biodistribution. The spatial distribution of decays is assumed to be uniform within r_S. For a given source-target combination, we can multiply the S-value by the number of decays occurring in the source to obtain the dose contribution to the target from that source. We can repeat for all the other sources (taking care to account for all decays occurring in the subject) and then sum the dose contributions from each source to obtain the total absorbed dose to the target. Continuing with our use of the liver for example:

$$D(\text{liver}) = \overbrace{\tilde{A}(\text{liver})S(\text{liver} \leftarrow \text{liver})}^{\text{Self} - \text{dose contribution}}$$
$$+ \underbrace{\tilde{A}(\text{spleen})S(\text{liver} \leftarrow \text{spleen}) + \tilde{A}(\text{lungs})S(\text{liver} \leftarrow \text{lungs}) + \ldots}_{\text{Cross} - \text{dose contributions}}$$
$$(8.5)$$

For an arbitrary target region, the absorbed dose [Gy] can be generalized with the following equation:

$$D(r_T) = \sum_{r_S} \tilde{A}(r_S)S(r_T \leftarrow r_S) \qquad (8.6)$$

Analogous to Eq. 8.4, Eq. 8.6 can be normalized by the administered activity to yield the absorbed dose coefficient [Gy/Bq]:

$$d(r_T) = \sum_{r_S} \tilde{a}(r_S)S(r_T \leftarrow r_S) \qquad (8.7)$$

Finally, we need to apply Eq. 8.6 for all target tissues considered to be dosimetrically relevant.

S-values for all the source-target combinations can be amalgamated as a 2-dimensional data table (i.e., a spreadsheet), and Eq. 8.6 can be evaluated by a simple multiplication followed by column summing. Part of the elegance of the MIRD method is that an S-value database can be generated in advance with computationally intensive Monte Carlo simulations that model radiation transport in computational phantoms, computerized models of patient anatomy. The S-value database can be stored in software enabling rapid spreadsheet-style dose calculations appropriate for high-throughput dosimetry workflows.

Example 3.2 *Clinical Radioiodine Treatment.*

An adult male patient is administered 750 MBq of $[^{131}I]$I-NaI for the treatment of hyperthyroidism. Time-integrated activities were estimated in the thyroid, bladder contents, and the *rest of body*[6] via serial imaging and probe measurements:

Source region	Time-integrated activity, $\tilde{A}$ [MBq·s]
Thyroid	2.7E+08
Bladder contents	5.4E+06
Rest of body	3.2E+07

---

[5] S-values can be usefully defined in several ways. MIRD Pamphlet 21 defines the S-value as the absorbed dose rate per unit activity in the specified source region. Due to the stochastic nature of decay and dose deposition, all interpretations should consider the S-value to be a mean value averaged over many interactions.

[6] In dosimetry calculations, the *rest of body* represents a combination of all other tissues, in which the activity is assumed to be uniformly distributed. Tissues without pronounced uptake are often considered collectively as "rest of body" tissues, as it is impractical to segment (via imaging) or harvest (for ex vivo counting) every individual tissue.

Using the following table of S-values in units of *mGy/MBq·s* for the reference adult, estimate the absorbed dose received by the thyroid, bladder wall, and whole body.

		Target region		
		Thyroid	Bladder wall	Whole body
Source region	Thyroid	1.5E-03	1.2E-09	7.4E-07
	Bladder contents	1.1E-09	8.9E-05	3.0E-07
	Rest of body	7.4E-07	8.0E-07	7.5E-07

Solution 3.2

- Find the absorbed dose contributions for each source-target combination.

  For each source-target combination, we need to apply Eq. 8.6; we must multiply the S-value for each source-target combination by the $\tilde{A}$ for the corresponding source and then sum over all sources. Let us start out by finding the absorbed dose contributions:

		Target regions		
		Thyroid	Bladder wall	Whole body
Source regions	Thyroid	2.7E+08 × 1.5E-03	2.7E+08 × 1.2E-09	2.7E+08 × 7.4E-07
	Bladder contents	5.4E+06 × 1.1E-09	5.4E+06 × 8.9E-05	5.4E+06 × 3.0E-07
	Rest of body	3.2E+07 × 7.4E-07	3.2E+07 × 8.0E-07	3.2E+07 × 7.5E-07

Next, we find the total dose to each target by summing the contributions from the sources:

Target regions		
Thyroid	Bladder wall	Whole body
2.7E+08 × 1.5E-03	2.7E+08 × 1.2E-09	2.7E+08 × 7.4E-07
+	+	+
5.4E+06 × 1.1E-09	5.4E+06 × 8.9E-05	5.4E+06 × 3.0E-07
+	+	+
3.2E+07 × 7.4E-07	3.2E+07 × 8.0E-07	3.2E+07 × 7.5E-07
=	=	=
4.1E+05 [mGy]	**5.1E+02 [mGy]**	**2.3E+02 [mGy]**

A Closer Look *In* clinical radiopharmaceutical therapy, we are often interested in assessing absorbed dose to many organs to ensure their respective thresholds for radiation toxicity are not exceeded. This necessitates large tables of S-values, which can be used for calculations in a straightforward manner in spreadsheet software like Microsoft Excel. As such calculations are routinely needed, computer programs are available to assist researchers and clinicians (www. mirdsoft.org).

8.2.2.1 Specialized Uses of the MIRD Method

Until now we have considered organ-level dosimetry, in which source regions and target regions comprise gross anatomical structures, and we assess the mean absorbed dose within each target tissue. There are some limitations to this approach, and here we consider a couple of examples. First, we are sometimes interested in the absorbed dose to microscopic anatomy, namely cells or subcellular structures. Second, organ-level methods generally do not assess nonuniform doses within individual organs. Sometimes, tissues possess highly nonuniform distributions of activity, which in turn create non-uniformity in the absorbed dose; this may have implications for dose-response or dose-toxicity relationships.

8.2.2.1.1 Cell-Level Dosimetry Using the MIRD Method

For internal radionuclide sources, it has been shown that the mean absorbed dose to tissue in some cases does not reliably correlate with biological effects. Because damage to cellular DNA is the main driver of biological effects, a logical hypothesis would be that the absorbed dose to cells—or cell nuclei, which contain the biologically sensitive target DNA—would correlate better with biological effect than the absorbed dose to bulk tissue.

Analogous to the organ-level dosimetry approach, cellular- and sub-cellular scale tissue models can be devised for *cell-level dosimetry* calculations using the MIRD schema. The salient difference is that instead of a human/animal body comprised of source and target organs, we instead consider a cell or group of cells composed of a cellular source and target compartments (e.g., the nucleus, cytoplasm). MIRDcell is a computer

program recently developed to perform this type of calculation; we refer the reader to MIRDcell's webpage for further information (www.mirdsoft. org/mirdcell).

8.2.2.1.2 Voxel-Level Dosimetry Using the MIRD Method

The MIRD S-value approach is a suitable framework for *voxel-level dosimetry*. PET or tomographic SPECT images exemplify the format of a voxel dataset, in which a repeating array of regularly sized volume elements (voxels) is assigned a numeric property. For PET or quantitative SPECT images, this property is usually the activity concentration [Bq/mL]. Such an image could be re-expressed in units of activity per voxel [Bq] by multiplying each voxel by its volume. In serial imaging, multiple voxel images are acquired over several time points. If the serial images can be aligned in space such that the voxels coincide, we can consider individual voxels as the fundamental anatomical regions over which to perform time integration (i.e., we can apply Eq. 8.2 to each voxel to obtain the number of decays occurring in each voxel). Therefore, we can treat each voxel as a source region. Similar to the organ-level case, an S-value database can be generated via Monte Carlo simulations that quantify the absorbed dose contributions of the voxels; the absorbed dose for a given voxel follows from Eq. 8.6.

8.2.3 Dosimetry Workflow

A dosimetry workflow consists of all the steps involved in measuring the biodistribution of a radiopharmaceutical, performing the absorbed dose calculation, interpreting and communicating the results, and, finally, archiving the data.

8.2.3.1 Activity Measurements and Biodistribution

Several factors must be considered together when selecting the method(s) for the quantitative determination of the activity (or activity distribution) within a sample. A comprehensive review of such methods is outside the scope of this chapter.

However, Table 8.2 briefly outlines the modalities commonly used with clinical and preclinical radiopharmaceuticals.

Taken together, the radionuclide, subject, and analysis requirements dictate the appropriate modality or modalities used for measurements. In the clinic, orthogonal techniques are often used together. For example, organ activity measurements in living subjects generally require in vivo imaging. With image data, regions of interest can be defined (e.g., by manual contouring or using automated methods), and the activity within each region can be computed as an average over the voxels comprising said region. These processes are usually called *image segmentation* and *segment quantification*, respectively. In contrast to organs, the activity in blood or urine may be assessed via non- or minimally invasive sampling (e.g., blood draws or urine collection), allowing for quantitatively superior ex vivo counting techniques for these regions. In preclinical research involving small animals, organ activity measurements are usually done by post-mortem ex vivo counting from animals euthanized at different time points.

Radionuclides for RPT often lack optimal characteristics (i.e., photon energy or yield) for quantitative imaging. For therapeutic agents labeled with such radionuclides, there often exists a surrogate agent which is suitable for quantitative imaging. The availability of an imaging surrogate enables a *theranostic*[7] approach to dosimetry in which the imaging agent facilitates the prediction of the biodistribution of the therapeutic agent and therefore allows for the estimation of its dosimetry.

8.2.3.2 Time-Activity Curve Integration

In Example 3.1, we demonstrated how the number of decays occurring in a source region (i.e., the area under the time-activity curve) can be determined using Eq. 8.3 if the effective biodistribution is described by a simple monoexponential function of the form $A(t) = ae^{-bt}$. In practice, a function describing

---

[7] Theranostics are discussed in detail in Chap. 22.

Table 8.2 Common techniques used for activity measurements in clinical and preclinical radiopharmaceutical science

Modality	Description	Spatial information	Resolution	Sensitivity	Quantitative accuracy	Comments
Positron emission tomography; PET	Volumetric activity distribution in living subject reconstructed via positron annihilation photon coincidence counting with ring-shaped detector array	3D	Good; ~1–5 mm (preclinical), ~5 mm (clinical)	Moderate	Good	Positron-emitters only, the partial volume effect limits accuracy for small regions
Single-photon emission computed tomography; SPECT (tomographic)	Volumetric activity distribution in living subject reconstructed via single-photon counting with rotating collimated detector array	3D	Good; ~1–5 mm (preclinical), ~5–10 mm (clinical)	Poor	Moderate-good	Limited photon energy range (100–200 keV) for optimal resolution, partial volume effect limits accuracy for small regions
Gamma camera (planar)	Areal activity distribution in living subject measured via single-photon counting with fixed collimated detector array	2D	Poor	Moderate	Poor	Poor resolution
Probe (in vivo)	Activity in region of living subject measured with single detector	N/A	N/A	Excellent	Moderate-good	Attenuation, inconsistent geometry
Well scintillation (gamma) counter	Activity in small tissue or fluid sample measured non-destructively	N/A	N/A	Excellent	Excellent	Ex vivo only
Liquid scintillation counting	Activity in small tissue or fluid sample measured destructively (dissolution)	N/A	N/A	Excellent	Excellent	Useful for pure beta/alpha emitters, ex vivo only, complex sample preparation
Ion chamber (dose calibrator)	Activity in tissue or fluid sample measured non-destructively	N/A	N/A	Moderate	Very good	Usually used for radiochemistry or syringe measurements, or quality control
Autoradiography	Areal activity distribution measured in thin tissue section (microtome sectioning)	2D	Excellent (submillimeter)	Excellent	Moderate-good	Ex vivo only

the activity in an organ is rarely known ab initio. Instead, the activity is usually measured at specific time points (e.g., via serial imaging). Several strategies exist for estimating the area under a time-activity curve defined by discrete time points; by far the most common are regression-based integration and trapezoidal integration.

In nonlinear regression, an equation that plausibly characterizes the organ activity is fit to the measured time-activity data. This process involves successively guessing the parameters in the equation until the deviations between the model and data are minimized or optimized. Once the best-fit parameter values are known, the integral in Eq. 8.3 can be evaluated analytically or numerically. The equations used for dosimetric modeling of time-activity data from RPT are usually simple sums of exponentials (usually 1 or 2 phases of clearance and/or uptake). There are several reasons for this simplistic approach. First, radioactive decay follows first-order kinetics, and biological elimination is also commonly observed to be first-order process (or a combination of first-order processes). Second, the number of time points that are practical to assess is usually small, both clinically and preclinically. Clinically, imaging cost, throughput, and patient availability/ inconvenience usually permit only 3–5 time points. Similar logistical challenges accompany preclinical imaging and ex vivo tissue harvesting. The small number of time points precludes fitting with detailed models with many parameters.

In trapezoidal integration, the area under the time-activity curve is approximated by dividing the area into small trapezoids. Each trapezoid is defined by two consecutive data points and their projections onto the abscissa. After the last time point, clearance is usually assumed to occur via radioactive decay only, or the biological clearance rate may be extrapolated from the last few time points.

It should be evident that there is some uncertainty in the time-integrated activity, especially considering the different integration methods and their various inherent assumptions. These uncertainties can be minimized by the selection of appropriate time points. Ideally, the time points will be selected to cover about three effective half-lives of the radiopharmaceutical in the potential dose-limiting organs. Furthermore, the time points should be spaced in time to capture the salient phases of uptake and clearance.

8.2.3.3   Dose Calculation

In §3.2, the basic theoretical underpinning for organ-level absorbed dose calculations was discussed. In practice, the dose calculation portion of a dosimetry workflow is usually done using dedicated software programs based on the MIRD (or equivalent) formalisms or based on direct Monte Carlo simulation. Table 8.3 highlights several such programs that have been or continue to be widely used. In each of these programs, one can simply input the time-integrated activity coefficients for the source regions of the subject, and the absorbed dose coefficients for target organs will be the output.

8.2.3.4   Communication and Archiving of Results

Uncertainties and assumptions present in each step of the dosimetry workflow contribute to the overall uncertainty in dose estimates. These uncertainties can vary in magnitude across radiopharmaceuticals, researchers, instrumentation, centers, subjects, and so on. Moreover, the magnitude of these uncertainties often changes as improved methods, instrumentation, etc. become

Table 8.3 Software for clinical and preclinical organ-level dosimetry

Software	Methodology	Availability	References
MIRDcalc	S-value (MIRD)	Free	[23]
OLINDA (1.0)	S-value	Free	[24]
OLINDA (2.0)	S-value	Paid license	[25]
IDAC-dose 2.1	S-value	Free	[26]
PARaDIM	Direct Monte Carlo	Free	[27]

available. In light of this, the specific methods, assumptions, and raw data used in any dosimetry workflow should be clearly documented and archived. The ability to mine these data is valuable in establishing reliable dose-response or dose-toxicity relationships.

8.3 Controversial Issues

8.3.1 Relevance of Dosimetry: Cost vs Benefit

The implementation of dosimetry in RPT requires dedicated tasks, including measurements, processing, and data analysis. The intention is that these added efforts will translate into improved, more personalized care; however, they will also inevitably require additional resources.

Radiopharmaceutical dosimetry necessarily entails many steps and variables. The safe use of dosimetry, even with new software platforms, requires on-site personnel that has a sufficient understanding of dosimetry principles and dose calculation techniques and can provide oversight over the input of data, the dose calculation itself, and, ultimately, its interpretation. Acquiring dose estimates and using them in a clinical setting is a team effort with contributions from technologists (data acquisition), medical physicists (data analysis), and clinicians (interpretation and use). It is difficult to estimate the exact time commitments required for implementing dosimetry since they depend on specific treatments and protocols.

Over the last few decades, the collection of dosimetry data and its analysis have been implemented using site-specific in-house protocols and have depended on in-house expertise. In recent years, however, a multitude of vendors have begun to bring commercial dosimetry solutions to the marketplace. While the solutions differ in scope, they ultimately make clinical workflows and the integration of standardized dosimetry calculations more feasible. Through advanced image processing tools, automating tasks, and workflow establishment, along with reliable vendor support, these new tools are leveraging advanced image processing tools, automated tasks and workflows, and reliable vendor support to usher in a new era of quality internal dosimetry for the field. This can aid in academic efforts to establish clinical efficacy and help provide clinics with reliable tools for the establishment of community-wide standards.

The clinical benefits of personalization through dosimetry are becoming more apparent in the literature [28, 29] but remain largely unestablished in standard-of-care protocols. The gold-standard phase three clinical trials that most agree are needed to establish and justify shifts in practice are resource-intensive and remain relatively scarce. As a result, most US regulatory-approved uses of radiopharmaceuticals require minimal-to-no dosimetry. The uncertain role of dosimetry is exemplified by the recent American Thyroid Association guidelines for the treatment of thyroid disease that cite the theoretical advantages to dosimetric approaches but label the use of dosimetry with "no recommendation, insufficient evidence," leaving it optional for a provider to perform [3]. However, this stands in stark contrast to standards in Europe. The basic safety standards of the European Union provide a much more sweeping statement that dictates that all exposure of patients for radiotherapeutic purposes shall be individually planned and appropriately verified [28]. It is likely the RPT field will continue to refine the role of dosimetry as its infrastructure continues to mature.

8.4 The Future

Dosimetry-guided RPT has always been an attractive integrational element for the field. Just as imaging-based dosimetry supports external beam radiotherapy, imaging-based dosimetry should similarly complement and support RPT facilitating the balance between absorbed dose to the target and toxicity to healthy tissue.

In the coming years, our field is poised to establish new standards for the use of dosimetry in RPT, aided by new software, and new methodological solutions. In its simplest embodiment,

first-order dosimetry estimates can be extracted from single whole-body probe measurements acquired after treatment [30]. At the other end, characterizing the biodistribution of radiopharmaceuticals can be much more detailed (e.g., with multi-timepoint imaging and complex dose modeling) and can support more personalized dose calculations. The main challenges with adopting the latter have been the difficulties associated with performing and standardizing the measurements.

In the last few years, support for the field has gained so much momentum that we are seeing multiple vendors presenting sophisticated software solutions that streamline, and in many instances automate full dosimetry workflows. At the same time, the capacity of software to perform traditionally tedious and highly variable tasks—like organ segmentation—has been supported by newly accessible artificial intelligence-aided frameworks. Thus, recent developments in infrastructure have put the field in an exciting new position that brings us closer to the promise of ubiquitous dosimetry-guided RPT: complex dose calculation workflows can now be performed with relative ease and standardization, facilitating wider access and reliability.

8.5   The Bottom Line

- Dosimetry is the practice of quantifying the interaction of radiation with tissue and can be used to tailor patient treatments.
- RPT regimens can be tailored with patient-specific dosimetry-informed treatment plans.
- The MIRD schema is a robust, well-documented formalism for radiation dose estimation.
- Dosimetry calculation workflows span image acquisition, data processing/modeling, interpretation, and reporting.
- There remains more work to be done in establishing best practices for dosimetry in support of RPT.

References

1. Bolch WE, Eckerman KF, Sgouros G, Thomas SR. MIRD pamphlet No. 21: A generalized schema for radiopharmaceutical dosimetry—standardization of nomenclature. J Nucl Med. 2009;50(3):477–84.
2. International Atomic Energy Agency. Health effects and medical surveillance. Vienna: International Atomic Energy Agency; 2004.
3. Haugen BR, Alexander EK, Bible KC, Doherty GM, Mandel SJ, Nikiforov YE, et al. 2015 American thyroid association management guidelines for adult patients with thyroid nodules and differentiated thyroid cancer: the american thyroid association guidelines task force on thyroid nodules and differentiated thyroid cancer. Thyroid. 2016;26(1):1–133.
4. Silberstein EB, Alavi A, Balon HR, Clarke SEM, Divgi C, Gelfand MJ, et al. The SNMMI practice guideline for therapy of thyroid disease with 131I 3.0. J Nucl Med. 2012;53(10):1633–51.
5. Hammes J, van Heek L, Hohberg M, Reifegerst M, Stockter S, Dietlein M, et al. Impact of different approaches to calculation of treatment activities on achieved doses in radioiodine therapy of benign thyroid diseases. EJNMMI Phys. 2018;5(1):32.
6. Dezarn WA, Cessna JT, DeWerd LA, Feng W, Gates VL, Halama J, et al. Recommendations of the American association of physicists in medicine on dosimetry, imaging, and quality assurance procedures for 90Y microsphere brachytherapy in the treatment of hepatic malignancies. Med Phys. 2011;38(8):4824–45.
7. Garin E, Tselikas L, Guiu B, Chalaye J, Edeline J, de Baere T, et al. Personalised versus standard dosimetry approach of selective internal radiation therapy in patients with locally advanced hepatocellular carcinoma (DOSISPHERE-01): a randomised, multicentre, open-label phase 2 trial. Lancet Gastroenterol Hepatol. 2021;6(1):17–29.
8. Zaknun JJ, Bodei L, Mueller-Brand J, Pavel ME, Baum RP, Hörsch D, et al. The joint IAEA, EANM, and SNMMI practical guidance on peptide receptor radionuclide therapy (PRRNT) in neuroendocrine tumours. Eur J Nucl Med Mol Imaging. 2013;40(5):800–16.
9. Hennrich U, Kopka K. Lutathera(®): The first FDA- and EMA-approved radiopharmaceutical for peptide receptor radionuclide therapy. Pharmaceuticals (Basel). 2019;12(3):114.
10. Strosberg J, El-Haddad G, Wolin E, Hendifar A, Yao J, Chasen B, et al. Phase 3 Trial of 177Lu-dotatate for midgut neuroendocrine tumors. N Engl J Med. 2017;376(2):125–35.
11. Strosberg JR, Caplin ME, Kunz PL, Ruszniewski PB, Bodei L, Hendifar AE, et al. Final overall survival in

the phase 3 NETTER-1 study of [177]lutetium-DOTATATE in patients with midgut neuroendocrine tumors. J Clin Oncol. 2021;39(15_suppl):4112.

12. Ljungberg M, Celler A, Konijnenberg MW, Eckerman KF, Dewaraja YK, Sjögreen-Gleisner K. MIRD pamphlet No. 26: Joint EANM/MIRD guidelines for quantitative ^{177}Lu SPECT applied for dosimetry of radiopharmaceutical therapy. J Nucl Med. 2016;57 (1):151.

13. Sandstrom M, Garske-Roman U, Granberg D, Johansson S, Widstrom C, Eriksson B, et al. Individualized dosimetry of kidney and bone marrow in patients undergoing ^{177}Lu-DOTA-octreotate treatment. J Nucl Med. 2013;54(1):33–41.

14. Sandström M, Freedman N, Fröss-Baron K, Kahn T, Sundin A. Kidney dosimetry in 777 patients during ^{177}Lu-DOTATATE therapy: aspects on extrapolations and measurement time points. EJNMMI Phys. 2020;7 (1):73.

15. Schuchardt C, Kulkarni HR, Prasad V, Zachert C, Müller D, Baum RP. The bad berka dose protocol: comparative results of dosimetry in peptide receptor radionuclide therapy using ^{177}Lu-DOTATATE, ^{177}Lu-DOTANOC, and ^{177}Lu-DOTATOC. In: Theranostics, gallium-68, and other radionuclides. Berlin: Springer; 2013.

16. Sartor O, de Bono J, Chi KN, Fizazi K, Herrmann K, Rahbar K, et al. Lutetium-177–PSMA-617 for metastatic castration-resistant. Prostate Cancer. 2021;385 (12):1091–103.

17. Hofman MS, Emmett L, Sandhu S, Iravani A, Joshua AM, Goh JC, et al. [177Lu]Lu-PSMA-617 versus cabazitaxel in patients with metastatic castration-resistant prostate cancer (TheraP): a randomised, open-label, phase 2 trial. The Lancet. 2021;397 (10276):797–804.

18. Czernin J, Sonni I, Razmaria A, Calais J. The future of nuclear medicine as an independent specialty. J Nucl Med. 2019;60(Suppl 2):3s–12s.

19. Jackson P, Hofman M, McIntosh L, Buteau JP, Ravi KA. Radiation dosimetry in 177Lu-PSMA-617 therapy. Semin Nucl Med. 2022;52(2):243–54.

20. Wahl RL, Sgouros G, Iravani A, Jacene H, Pryma D, Saboury B, et al. Normal-tissue tolerance to radiopharmaceutical therapies, the knowns and the unknowns. 2021;62(Supplement 3):23S–35S.

21. Siegel JA, Thomas SR, Stubbs JB, Stabin MG, Hays MT, Koral KF, et al. MIRD pamphlet no. 16: techniques for quantitative radiopharmaceutical biodistribution data acquisition and analysis for use in human radiation dose estimates. J Nucl Med. 1999;40(2):37S–61S.

22. Committee MIRD, Primer MIRD. Society of nuclear medicine and molecular imaging. Reston: In-press; 2022.

23. Kesner A, Olguin E, Zanzonico P, Bolch W. MIRDCalc V 1.0 – A community spreadsheet tool for organ-level radiopharmaceutical absorbed dose calculations. Journal of Nuclear Medicine. 2018;59(supplement 1):473.

24. Stabin MG, Sparks RB, Crowe E. OLINDA/EXM: the second-generation personal computer software for internal dose assessment in nuclear medicine. J Nucl Med. 2005;46(6):1023–7.

25. Stabin M, Farmer A. OLINDA/EXM 2.0: The new generation dosimetry modeling code. J Nucl Med. 2012;53(supplement 1):585.

26. Andersson M, Johansson L, Eckerman K, Mattsson S. IDAC-Dose 2.1, an internal dosimetry program for diagnostic nuclear medicine based on the ICRP adult reference voxel phantoms. EJNMMI Res. 2017;7(1):88.

27. Carter LM, Crawford TM, Sato T, Furuta T, Choi C, Kim CH, et al. PARaDIM: A PHITS-based Monte Carlo tool for internal dosimetry with tetrahedral mesh computational phantoms. J Nucl Med. 2019;60 (12):1802–11.

28. Strigari L, Konijnenberg M, Chiesa C, Bardies M, Du Y, Gleisner KS, et al. The evidence base for the use of internal dosimetry in the clinical practice of molecular radiotherapy. Eur J Nucl Med Mol Imaging. 2014;41(10):1976–88.

29. Graves SA, Hobbs RF. Dosimetry for optimized, personalized radiopharmaceutical therapy. Semin Radiat Oncol. 2021;31(1):37–44.

30. Hindorf C, Glatting G, Chiesa C, Lindén O, Flux G. EANM dosimetry committee guidelines for bone marrow and whole-body dosimetry. Eur J Nucl Med Mol Imaging. 2010;37(6):1238–50.

Part II

Deeper Dives

Antibodies as Vectors for Radiopharmaceutical Therapy

John E. Shively, Kirstin Zettlitz, Paul Yazaki, Anna Wu, and Jeffrey Wong

9.1 Fundamentals

Why Monoclonal Antibodies? Antibodies are an important arm of the immune system that can neutralize or eliminate toxins and pathogens that are recognized by the immune system as foreign. Since tumors arise from normal tissue, they do not usually elicit an antibody response. The advent of monoclonal antibodies that can be produced by immunizing a mouse with a human tumor raised the possibility that monoclonal antibodies could be used to directly treat tumors. In spite of this possibility, the majority of anti-tumor monoclonal antibodies is not sufficiently cytotoxic by themselves and must therefore be conjugated with drugs or radionuclides to elicit effective tumor killing. The choice of monoclonal antibodies as vehicles for targeted radiotherapy (RPT) is supported by an enormous knowledge base encompassing their formation, structure, function, and chemical or genetic modifications. First, it is informative to review the basic structure of an antibody from the viewpoint of a student or practitioner of radioimmunotherapy.

Several different parts of an immunoglobulin's structure can be harnessed in the construction of a radioimmunoconjugate. In Fig. 9.1, we depict what many will recognize as a typical immunoglobulin G (IgG) composed of two heavy and two light chains. These chains are held together by both non-covalent interactions and covalent bonds. The latter are disulfides that can be reduced under mild conditions without destroying the overall structure of the immunoglobulin. Once reduced, the free thiols present convenient sites for the attachment of prosthetic groups or chelators for radionuclides (vide infra). Alternatively, radionuclides may be attached to surface residues such as lysines, of which there are up to 80 per biomolecule. When attaching radionuclides to an antibody, it is important to remember that the antigen binding sites are at the N-terminal distal ends of the molecule and that perturbing these regions can affect antigen binding. Since there are two antigen-binding sites, the overall affinity of the antibody for its antigen is increased via an effect called *avidity*. Thus, smaller, monovalent antibody fragments such as Fabs may exhibit reduced affinities for their target antigens compared to their full-length monoclonal antibody parent. Finally, the clearance of antibody from the circulation is controlled by many factors, including the molecular size of the antibody or its fragments and its ability to bind FcRn, a receptor on endothelial cells that promotes the transport of the immunoglobulin out of the vascular bed and into surrounding

J. E. Shively (✉) · K. Zettlitz · P. Yazaki · A. Wu
Department of Immunology and Theranostics, Beckman Research Institute of City of Hope, Duarte, CA, USA
e-mail: jshively@coh.org

J. Wong
Department of Radiation Oncology, City of Hope National Medical Center, Duarte, CA, USA

tissues. These important topics will be discussed in more detail later.

Before we move on, it is important to ask a fundamental question: why use antibodies for RPT? First off, antibodies are natural targeting molecules that are easy to generate from many starting points using techniques that will be briefly mentioned later. In theory, one can generate antibodies to almost any antigen, whether a protein, carbohydrate, lipid, or small molecule. The theoretical number of possible different antibodies is estimated as high as a million trillion. In large molecules like proteins, antibodies may recognize an epitope composed of a linear sequence of amino acids or a three-dimensional structure that includes amino acids that are distant from one another in the protein's primary sequence. Knowledge of an antibody's target epitope is important since it may be masked by post-translational modifications or be disrupted by denaturation (the latter is especially germane in the case of three-dimensional epitopes).

Natural antibodies come in different isotypes such as IgG, IgM, IgA, and IgE, and each class has subclasses with different molecular sizes, half-lives, and functions. For example, the structure of the antibody shown in Fig. 9.1 is typical of a human IgG1 that has two disulfide bonds in the lower hinge connecting the two heavy chains and two additional disulfides in the upper hinge connecting the heavy and light chains. This arrangement of disulfide bridges varies between both isotypes and species. Since most clinically available antibodies are derived from natural antibodies from non-human sources, they can be engineered to more closely resemble human sequences (humanized) and tailor their blood clearance and effector functions (vide infra).

All of this structural and functional information must be considered when determining which type of antibody is most appropriate for RPT. For example, an antibody of the most appropriate isotype with a high affinity/avidity for its antigen is desirable. Care must also be taken to choose the suitable antigen, specifically one that is expressed at high levels in target tissues and at low levels in most (if not all) normal tissues.

Antibody Selection and Production It is unlikely that someone interested in developing a therapeutic radioimmunoconjugate would start a project with the goal of developing a new antibody by screening clones or using expression libraries, a time-consuming process that has been reviewed by others [1]. Therefore, we will start a discussion of the possible sources of antibodies for researchers seeking to create a novel radioimmunoconjugate.
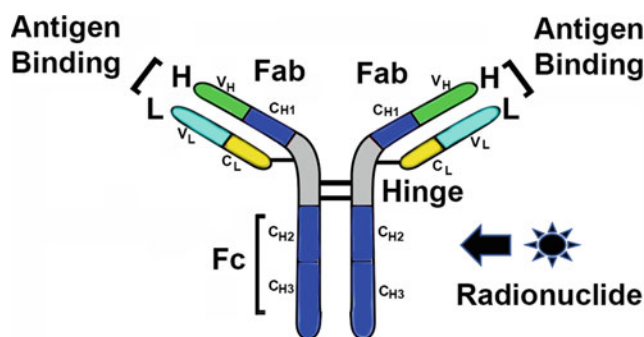

Fig. 9.1 Basic features of an antibody. An antibody has two heavy (H) and two light (L) chains with variable (V) and constant (C) domains. The two antigen binding sites comprise the N-terminal variable regions of the H and L chains, designated as V_H and V_L. Both sites contribute to antigen binding, thereby increasing binding in a process termed *avidity*. The two heavy chains are connected to each other and the light chains by disulfide bridges (thick lines) called the hinge region. The Fc region below the hinge region plays a role in the circulation half-life of the antibody and immune effector functions. The radionuclide can be appended almost anywhere on the antibody depending on the attachment chemistry

- Radiolabeled antibodies that have already been in the clinic but have not yet proven effective for RPT. These may be antibodies that were used for imaging only or ones that did not yield impressive results within a RPT trial but could be improved by choosing another radionuclide, dose, disease, or combination therapy.
- Antibodies approved for human use that are potential candidates for RPT but have not yet been used as radioimmunoconjugates in the clinic. These antibodies may include those that demonstrated impressive clinical results that justify their use as radioimmunoconjugates, or ones that failed to achieve their goals but can be improved with a therapeutic radionuclide payload. These antibodies can be rapidly radiolabeled, and their performance in imaging and/or therapy studies can be rapidly tested in preclinical studies.
- Antibodies that have shown promising results in preclinical studies that may or may not have included nuclear imaging trials.
- Antibodies that shown promising target specificity and efficacy in in vitro studies. These antibodies may not have entered animal studies and thus may require a great deal of in vivo development.

The list above is not comprehensive. It simply suggests several starting points—in order of increasing effort needed—from which radiolabeled antibodies can be developed for the clinic. The time, resources, and expertise available for a given project will also help guide the selection of an antibody. Since target specificity is of paramount importance for a radioimmunoconjugate, researchers should make tissue staining a critical early step in the selection and validation of a candidate antibody. This can be done by staining tissues blocks in a pathology core with expert opinions rendered by a seasoned pathologist. An example of the staining of the anti-CEA (carcinoembryonic antigen) antibody M5A [2] for normal vs. tumor tissue is shown in Fig. 9.2. In general, if an antibody stains a low percentage of cells in the target tissue or stains them with low intensity—or, conversely, stains normal tissues strongly—one can reasonably predict poor outcomes in human trials. It is important to remember than most animal models for growing human xenografts do not express the human variants of the antigen of interest. This can give false hope that an antibody is specific for the targeted tumor antigen and not the normal antigen also expressed in human organs. In addition, screening human cell lines can be misleading because they may or may not express the antigen of interest at the same level as normal or malignant tissue.

The amount of antibody required for a therapeutic study is an important consideration. Often

Fig. 9.2 Immunostaining of normal vs. malignant colon with anti-CEA antibody. Normal colon (left) and malignant colon (right) stained with anti-CEA antibody conjugated to HRP and counterstained with hematoxylin. The results are representative of over 10 normal specimens and 50 colon tumor specimens
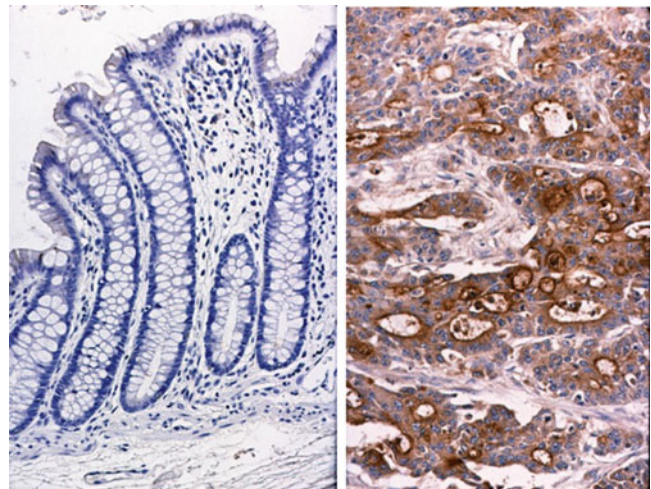
as little as 5 mg of the radioimmunoconjugate will be needed per dose assuming a sufficient specific activity can be achieved. However, some antibodies are rapidly cleared in humans, necessitating the addition of a so-called "cold" dose. Here, it is important to remember that only a small fraction of the antibody molecules is actually radiolabeled. Thus, each injected dose contains mostly unlabeled antibody. If the systemic concentration of antibody is too low for it to bind its target based on its affinity and clearance properties, then more cold (unlabeled) antibody may need to be added to the radiolabeled dose. This is usually done via an initial infusion of the unlabeled antibody followed soon thereafter by the administration of the radioimmunoconjugate. If this is the case, then the amount of antibody required for a clinical trial may be greatly increased. The good news is that the cold antibody need not be chemically modified.

The production of clinical grade antibodies requires a trained staff operating under SOPs in a GMP facility. If the antibody is already a commercially approved agent, an IND is still required for the radiolabeled version, since it is considered a new agent. A summary of the details for the GMP production of an antibody and its journey through the IND process are shown below:

- Selection of a stable, high-expressing mammalian cell culture clone
- Generation of a master and working cell bank
- Production in a bioreactor (grams to kilo scale)
- Purification, including viral inactivation/removal steps
- Bioconjugation in the case of radiometal-labeled immunoconjugates
- Formulation
- Vialing the final product
- Viral validation studies
- Lot release testing
- Toxicity studies
- Preclinical studies
- IND submission

Antibody Fragments and Engineered Antibodies Since intact antibodies clear rather slowly from circulation due to their molecular size (150 kDa) and the presence of their Fc domain that binds FcRn, there has been significant interest in building radioimmunoconjugates out of antibody fragments that retain the antigen-binding portion of mAbs but have a lower mass and lack an Fc domain (Fig. 9.3). The clearance rates of antibody fragments depend on their molecular size and the molecular weight cutoff of kidney filtration, about 60 kDa. Indeed, experimental measurements have shown that that diabodies—with a molecular weight of 55 kDa—are still cleared by the kidney. Figure 9.3 illustrates 6 antibody fragments in decreasing order of molecular size. The clearance of radioimmunoconjugates through the kidneys is a potential concern, because the retention of the radiolabel within the kidneys can lead to the kidneys becoming a dose-limiting organ due to their intrinsic radiosensitivity [3]. For this reason, radiolabeled antibody fragments that clear to the kidney are not favored for RPT. A second consideration surrounding the pharmacokinetics of radiolabeled antibody fragments is that their rapid clearance from circulation may mean substantially less absolute uptake in the target tissue which can translate into lower radiation doses. For these reasons, it is important to optimize the pharmacokinetic profile of a radioimmunoconjugate, whether it is a full-length antibody or a fragment.

The examples of antibody fragments shown in Fig. 9.3 were taken from our work on an anti-CEA antibody that began with the screening of murine hybridomas [4, 5], followed by engineering a half-murine, half-human chimeric version [6], and finally generating a fully humanized antibody [2]. The enzymatic production of divalent F(ab')$_2$ and monovalent Fab fragments was later described [7], as well as the engineering of scFv and diabody constructs [8–11]. Thus, starting from an intact murine monoclonal antibody, it is possible to generate antibody fragments that are entirely murine or—by genetic engineering—to convert monoclonal antibodies to chimeric or fully human mAbs and fragments. Since monoclonal antibodies arise from two genes, the heavy and light chains (Fig. 9.1), genetic engineering,
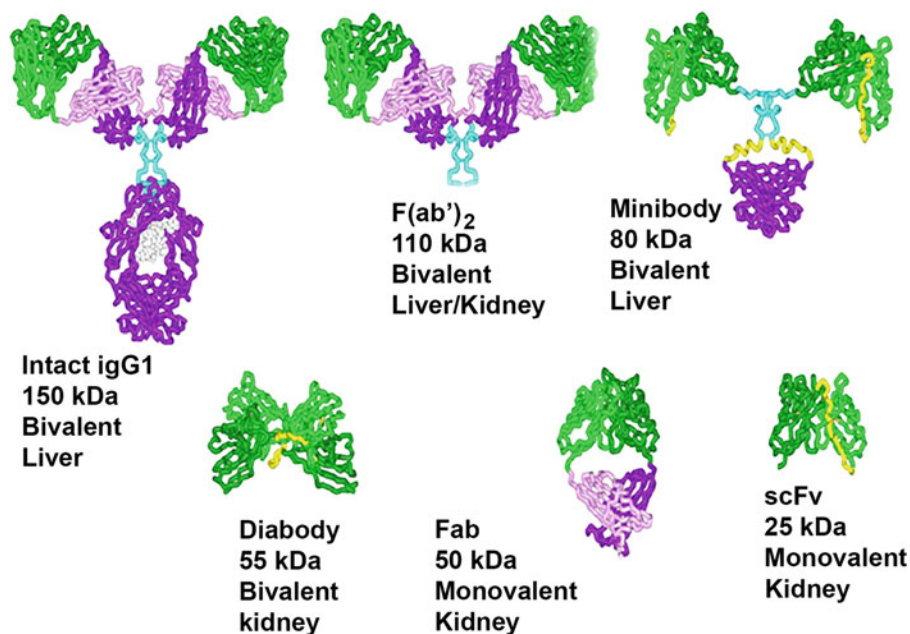
Fig. 9.3 Schematic structures of an intact antibody vs. antibody fragments. For each construct, the molecular size, valency, and route of clearance are shown. Each of the domains is color coded to allow for comparisons of their structures. The variable regions are shown in green, constants regions in magenta, and hinge region in cyan. F(ab')$_2$ and Fab fragments are usually made via the enzymatic digestion of intact IgGs, while the diabodies, minibodies, and scFv fragments are genetically engineered

and expression of intact antibodies are rather complicated. The production of engineered antibodies from a single gene construct has advantages over approaches that require separate genes for the heavy and light chains. An example of such a construct is the minibody, in which an scFv is fused to the C_H3 domain of a heavy chain [11].

Before we move on, it is important to touch upon the use of unusual immunoglobulins from other species in RPT. Camelid antibodies or nanobodies are antibodies that originate from the *Camelidae* family that includes llamas, camels, and alpacas [12]. These nanobodies are attractive in that they are heavy-chain only constructs that don't require light chains. However, they are inherently foreign and likely to produce immune responses when given to humans. This drawback may limit the repeat administrations of these constructs or necessitate humanization. A recent review of the use of nanobodies in the clinic is given by Yang et al. [13].

9.2 Details

Imaging with Radiolabeled Antibodies Although this chapter is focused on RPT, nuclear imaging is a logical complementary approach that can allows one to determine the extent of antibody targeting prior to therapy, monitor the response of a patient to therapy, and, most importantly, perform dosimetry calculations in advance of RPT. The relatively new field of *theranostics* refers to the use of different versions of the same agent for both imaging and therapy. In this context, an antibody radiolabeled with a gamma emitting radionuclide could be an imaging agent for the same mAb when radiolabeled with a beta- or alpha-emitting radionuclide. Several imaging modalities are available in the clinic, including planar imaging, single photon emission computerized tomography (SPECT), and positron emission tomography (PET). Although the ability to do three-dimensional imaging with SPECT and PET is

Table 9.1 Radionuclides for radioimmunoimaging

Radionuclide	Half life	Emission	Modality	Production
Ga-68	68 min	Positron	PET	Generator
F-18	109.7 min	Positron	PET	Cyclotron
Tc-99 m	6 h	Gamma	SPECT	Generator
Cu-64	12.7 h	Positron	PET	Cyclotron
I-123	13.2 h	Gamma	SPECT	Cyclotron
In-111	2.8 da	Gamma	SPECT	Cyclotron
Zr-89	3.3 da	Positron	PET	Cyclotron
I-124	4.2 da	Positron	PET	Cyclotron

preferred, it should be noted that considerable information can be obtained from planar imaging, too. Since it is very likely that the reader is familiar with all three modalities, they will not be discussed here. Instead, we will focus on the some of the most commonly used radionuclides for radioimmunoimaging.

The radionuclides most commonly used for radioimmunoimaging are presented in increasing order of their half-lives in Table 9.1. Since both SPECT and PET instruments are available at most institutions, the first consideration in choosing of radionuclide is typically its half-life. The general rule is to match the biological half-life of the agent with the radiological half-life of the radionuclide. Thus, Ga-68 and F-18 are typically restricted to rapidly clearing antibody fragments, while In-111, Zr-89 and I-124 are most suitable for intact antibodies or larger fragments. In contrast, Cu-64 and I-123 have been successfully used to image tumors with both intact antibodies *and* antibody fragments [14, 15].

One advantage of radioimmunoimaging prior to radioimmunotherapy is the ability to predict the clearance and retention of the radiolabeled antibody, which can affect targeting and dosimetry. Surrogate radioimmunoimaging describes the concept of choosing a positron-emitting radionuclide with similar/comparable characteristics (half-life, metabolism) to the radionuclide that will be used for therapy. Surrogate radioimmunoimaging can be used to profile the pharmacokinetics, biodistribution, and clearance of the mAb and thereby provide support in assembling the best radionuclide, labeling chemistry, and antibody or antibody fragment for RPT.

Several good examples of radioisotopic pairs for surrogate imaging and RPT are I-124/I-131; Cu-64/Cu-67 and Zr-89/Lu-177. Figure 9.4 depicts surrogate radioimmunoimaging using an anti-prostate stem cell antigen (PSCA) minibody that correctly predicted that the bone marrow would be dose limiting for ^{131}I-based RPT and the kidneys would be dose-limiting for radiometal-RPT [16].

An example of PET imaging with a CEA-positive tumor and metastatic lymph node with a ^{64}Cu-labeled antibody is shown in Fig. 9.5. Both the primary tumor and a metastatic lesion in the lymph node can be visualized as early as 24 h after the administration of the radioimmunoconjugate.

A second example of PET imaging with a ^{64}Cu-labeled anti-Her2 antibody that detected liver metastases is given in Fig. 9.6 [17]. In this case, the physical dose of the antibody played a major role. While 5 mg of the radiolabeled antibody barely distinguished tumor from background tissue, pre-injection of 45 mg of unlabeled antibody dramatically improved imaging, presumably by saturating the non-specific uptake of the antibody-antigen complexes in normal hepatocytes.

Examples of SPECT imaging with a minibody [18] of our anti-CEA antibody are given in Fig. 9.7. Given the reduced clearance time of the minibody compared to its parental mAb, it was possible to use two radionuclides with slightly shorter half-lives: [123]I and [111]In.

The availability of radionuclides is a second issue to consider when choosing a label for an antibody. The production of Ga-68 requires an in-house generator, while the longer half-life of
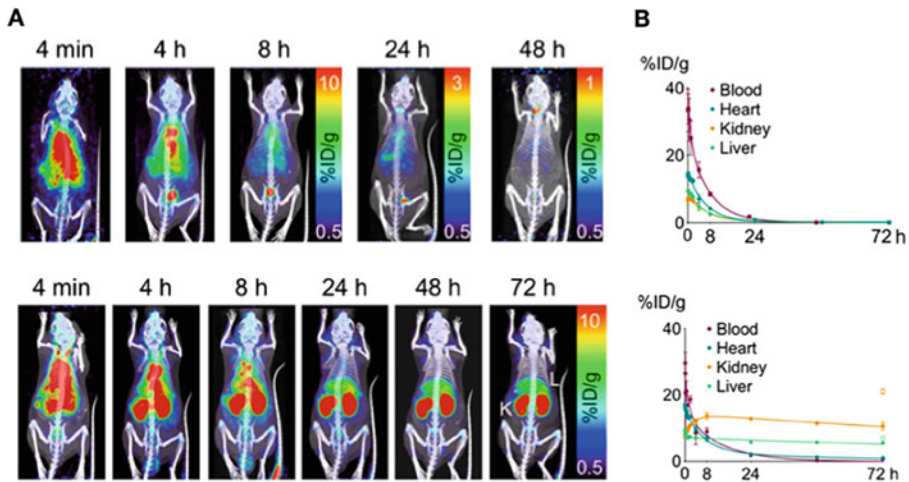
Fig. 9.4 Surrogate PET imaging of prostate cancer with ^{124}I- and ^{89}Zr-labeled anti-PSCA minibodies. (**a**) ImmunoPET images over time. (**b**) Blood clearance curves. *Upper:* The minibody was radio-labeled with I-124 as a surrogate for I-131 therapy. *Lower:* The minibody was radiolabeled with Zr-89 as a surrogate for Lu-177 therapy
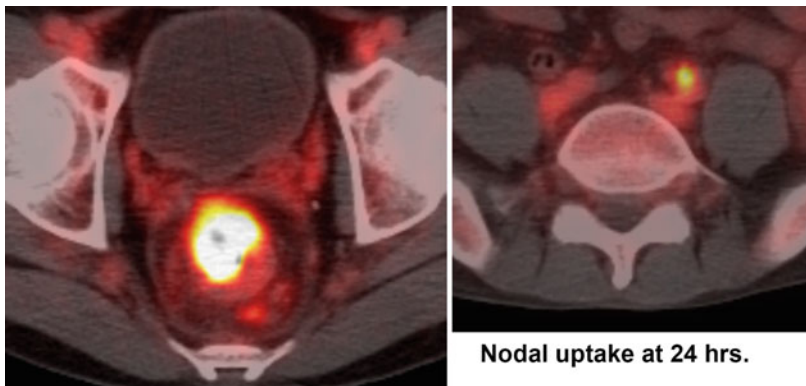

Nodal uptake at 24 hrs.

Fig. 9.5 PET imaging of rectal cancer at 24 h with ^{64}Cu-labeled anti-CEA antibody DOTA-M5A. DOTA-M5A (3 mg) radiolabeled with 555 MBq of Cu-64 was administered and PET imaging performed at 24 and 48 h. The patient had recurrent tumor growth at both the primary site and a lymph node. *Left:* primary site. *Right:* metastatic lymph node. Both sites were confirmed by subsequent biopsies

Tc-99 m means it can be shipped. Both ^{99m}Tc- and ^{18}F-labeled agents can be ordered from a variety of suppliers, and ^{18}F can even be generated in-house using a cyclotron. The remaining radionuclide options—i.e., ^{89}Zr, ^{111}In, etc.—have half-lives that are long enough to allow for shipping that can often take 1–2 days. In this respect, orders of ^{64}Cu can be a bit tricky, as they require shipments of larger amounts to compensate for their significant decay during shipping. Facilities with in-house cyclotrons can produce their own radionuclides, including those for which higher energy beams are required.

A third consideration in the selection of a radionuclide is the possible requirement for preclinical imaging. Preclinical studies are usually a requirement for filing an IND on a new radiotherapeutic. In this respect, access to animal
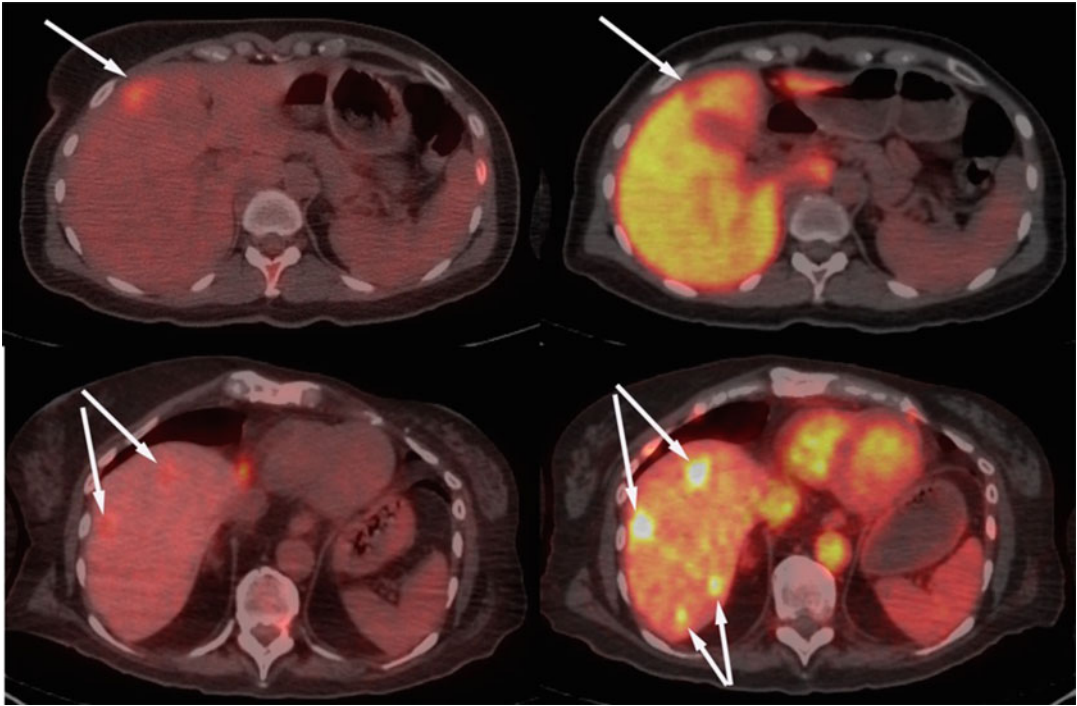
Fig. 9.6 PET imaging of liver metastasis in breast cancer with ^{64}Cu-DOTA-trastuzumab compared to ^{18}F-FDG. (**a, b**): FDG PET/CT of liver metastasis in breast cancer patient at 24 (**a**) and 48 h (**b**). (**c**, **d**): PET/CT at 24 h with 5 mg (551 MBq) radiolabeled trastuzumab (**c**) or 5 mg (551 MBq) radiolabeled trastuzumab plus 45 mg of unlabeled trastuzumab (**d**). Arrows indicate sites of metastasis
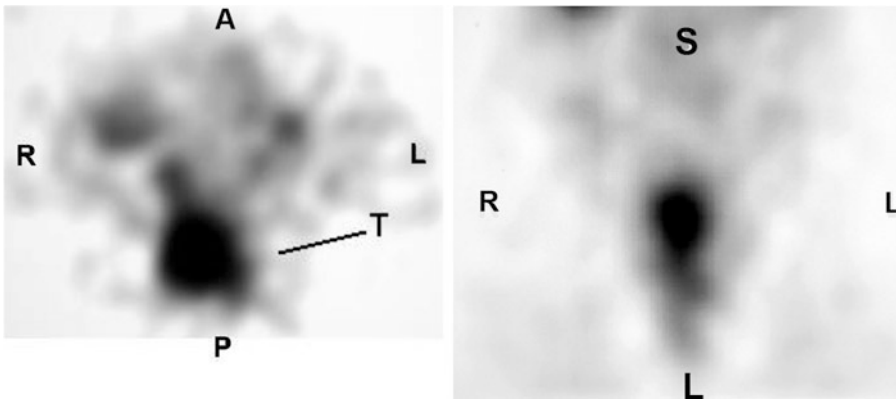

Fig. 9.7 SPECT images of rectal cancer with ^{123}I- or ^{111}In-labeled anti-CEA minibody. *Left:* SPECT image with ^{123}I-labeled antibody. *Right:* ^{111}In-labeled DOTA-antibody

imaging instruments is essential. PET/CT animal imaging instruments are perhaps the most versatile, allowing anatomical imaging with CT alongside PET. Instruments that also allow SPECT are desirable as well, as are PET/MR instruments. An example of preclinical PET images acquired with a ^{64}Cu-labeled anti-CEA antibody is shown in Fig. 9.8. Multiple imaging times can be used to

Fig. 9.8 PET imaging of CEA-positive flank xenografts in a nude mouse with the ^{64}Cu-labeled anti-CEA antibody DOTA-M5A. *Left:* image at 23 h, *Right:* image at 44 h. 30 µg of DOTA-anti-CEA antibody was radiolabeled with 3.7 MBq of Cu-64
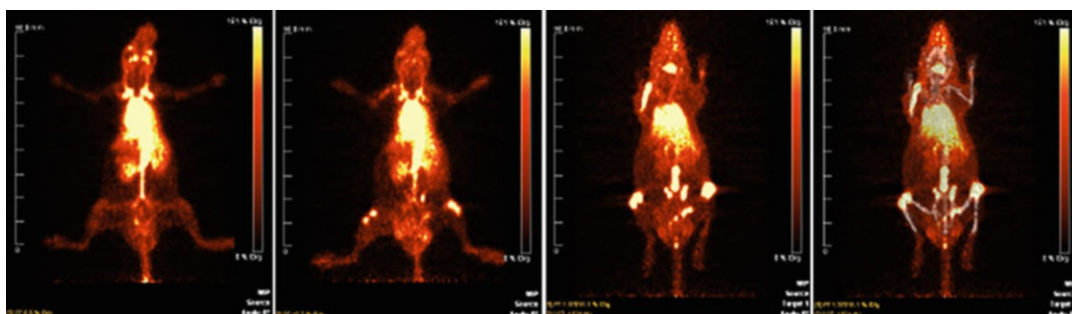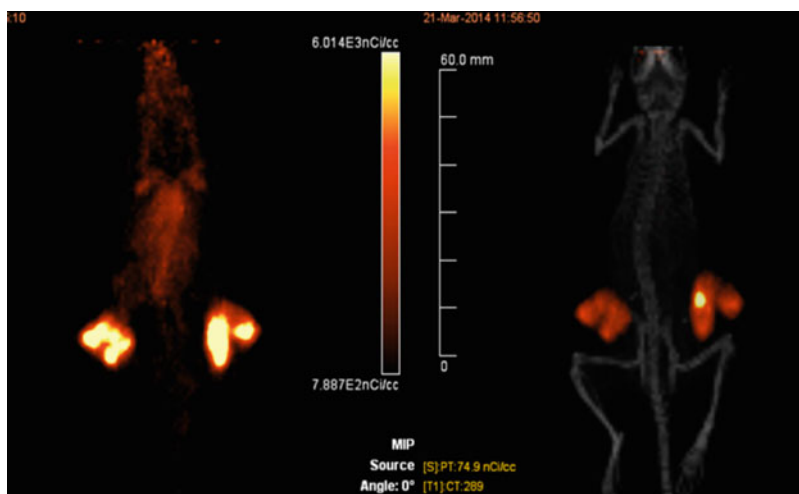

Fig. 9.9 PET imaging of multiple myeloma in NSG mice with [124]I-labeled daratumumab. *Left to right:* PET images at 4, 21, and 44 h as well as a fused PET/CT image from 44 h. The early images show uptake in the blood and liver, while the later images illustrate clearance from the blood and uptake into bony sites

demonstrate the clearance of the radioimmunoconjugate from the blood and liver.

An example of preclinical PET using an [124]I-labeled radioimmunoconjugate of the anti-CD38 mAb daratumumab in systemic model of multiple myeloma (MM) is shown in Fig. 9.9. These preclinical studies helped to demonstrate the utility of imaging with radiolabeled anti-CD38 antibodies. A clinical trial later illustrated the feasibility visualizing MM in patients using ^{64}Cu-labeled DOTA-daratumumab [19].

Conjugation Chemistry of Radionuclides to Antibodies The chemistry of the attachment of radionuclides to antibodies or antibody fragments is similar whether the final

radioimmunoconjugates are used for imaging or RPT. The chief issue with radiolabeling any antibody is the potential loss of immunoreactivity. Thus, an assay must be established to compare the immunoreactivity of the agent before and after radiolabeling. Several potential assays are discussed in the next section. Since traditional methods of bioconjugation introduce the radiolabel at random sites on the immunoglobulins, the most care must be taken with smaller fragments. Concerns regarding the loss of immunoreactivity can be eliminated using site-specific conjugation methods. Along these lines, conjugation into the hinge region of antibodies is popular, since cysteines in this area can be selectively reduced (and then modified) without disturbing the less

Table 9.2 Common methods for the conjugation of radionuclides to antibodies

Radionuclide	Conjugation method	Chelator[a]	Ref
I-131, I-125, I-124, I-123	Iodogen (tyrosine)	None (direct)	[21]
Tc-99 m	Active ester (lysine) Maleimide (cysteine)	SHNH	[22]
Ga-68	Active ester (lysine) Maleimide (cysteine)	NOTA, DOTA	[23]
Cu-64, Cu-67	Active ester (lysine) Maleimide (cysteine)	NOTA, DOTA sarcophagine	[24–26]
In-111	Active ester (lysine) Maleimide (cysteine)	DOTA	[27]
Lu-177	Active ester (lysine) Maleimide (cysteine)	DOTA	[28]
Y-90	Active ester (lysine) Maleimide (cysteine)	DOTA	[29, 30]
Zr-89	Thiourea (lysine) Maleimide (cysteine)	DFO	[31]

[a]SHNH (hydrazino nicotinamide), NOTA (2,2′,2″-(1,4,7-triazacyclononane-1,4,7-triyl)triacetic acid), DOTA (2,2′,2″,2‴-1,4,7,10-tetraazacyclododecane-1,4,7,10-tetrayl)tetraacetic acid), DFO (deferoxamine)

accessible internal disulfides elsewhere in the immunoglobulin. The mild reduction in antibodies usually does not disturb the overall structure or activity of the antibody, with one exception: F(ab')$_2$ fragments will be irreversibly reduced to monovalent Fab' fragments. Since there are a wide variety of conjugation methods that are reviewed well elsewhere [20], only the most common methods will be mentioned here (Table 9.2).

Radioiodination is perhaps the oldest method for the radiolabeling of antibodies. It is still commonly used because it is rapid and several isotopes of iodine are available that differ in their emissions and half-lives (see Chap. 7 for a more detailed discussion). The most common method of radioiodination is the iodogen method, which incorporates radioiodine into tyrosine residues in a matter of minutes at room temperature. Importantly, iodinated tyrosines are targets of tissue-specific metabolic scavenging that is most prevalent in organs such as the liver and kidney. Once the radiolabeled antibody is metabolized, iodotyrosine is rapidly taken up and transported to the thyroid and, less so, the stomach. This process will reduce the amount of radioactivity in the liver, and is an advantage if liver metastases are the target for imaging and/or therapy [32]. However, this process may also reduce the total uptake in the target, requiring

the use of rather high doses of the radioimmunoconjugate for both imaging and therapy. This process also results in unwanted uptake in the thyroid that must be blocked via the co-administration of iodide over several days to reduce the very real prospect of radiodamage to the thyroid. To circumvent some of these problems, alternative methods have been developed in which a prosthetic group is radioiodinated first and *then* conjugated to lysines on the antibody [33].

The use of radiometals requires careful attention to the choice of chelator (see Chap. 6 for a more comprehensive discussion of radiometal chelates). Well-developed methods for labeling immunoglobuliins with Tc-99 m also exist. Given the short half-life of Tc-99 m (6 h), its use is largely limited to labeling antibody fragments. To this end, the unusual chemistry of Tc requires special chelators that can be attached to either lysine or cysteine residues in the antibody. There are also a large number of radiometals that can be coordinated by amine- or thiol-reactive variants of the promiscuous metal ion chelator DOTA. These derivatives are termed "bifunctional chelators," since they facilitate both the coordination of the radiometal and its conjugation to antibodies via lysine or cysteine residues. Since the ionic radius of the radiometal is a factor in stable binding to DOTA, the smaller ring size of NOTA for $^{68}Ga^{3+}$ has been utilized.

Besides DOTA and NOTA, the cage-like chelate sarcophagine has also been used for $^{64}Cu^{2+}$ and $^{67}Cu^{2+}$ (see Table 9.2).

Radiometals—including most of those in Table 9.2—are often termed "residualizing radionuclides" because once they are internalized and metabolized, they are often slowly lost from cells that have no specific mechanisms for their excretion (especially while still bound to a chelate). This retention of radiometals in target tissue is an advantage, as less radioactivity is lost over time compared to radioiodinated probes. On the other hand, the retention of radioactivity in non-target organs like the liver and kidney can lead to a high background signal in the context of imaging and high background dose rates in the context of RPT. The radioisotopes of copper are a possible exception to the trend of residualized radiometals, since it can be metabolically labile in the liver [34]. As a result, the field has worked to develop more metabolically stable chelators for Cu^{2+}, including—but not limited to—the sarcophagine family [35]. Nonetheless, there is a real advantage to the use bifunctional derivatives of DOTA, since DOTA-conjugated antibodies may be radiolabeled with radiometals suitable for either imaging or therapy.

Zr-89, like Tc-99 m, requires a special chelator due to its unique coordination chemistry. The natural iron-chelating siderophore deferoxamine (DFO) has emerged as the chelator of choice for ^{89}Zr and can be conjugated to lysine or cysteine residues via isothiocyanate- or maleimide-bearing bifunctional variants, respectively. These derivatives are more metabolically labile than the active ester derivatives that produce amide bonds within the antibody. Furthermore, the chemical linkage between the chelate and antibody can be fine-tuned to be more or less metabolically stable. This consideration is critically important for antibody-drug conjugates, for which the release of the drug from the antibody may be key to its function [36]. Extensive linker chemistry is available for bifunctional chelates [37].

Once the radionuclide and bioconjugation method are chosen, a number of fundamental steps are required before commencing preclinical or clinical studies with a radioimmunoconjugate. Along these lines, radioiodinated radioimmunoconjugates are simplest as they lack a chelator. In the case of radiometallated radioimmunoconjugates, things are slightly more complicated, as the stability of the chelator-antibody bond must be assessed, and methods must be developed to radiolabel the chelator-bearing immunoconjugate with the radiometal of choice. Further details are described below.

Characterization of Radiolabeled Antibodies The properties of radiolabeled antibodies must be systematically characterized prior to their use in animals or humans. The most important properties to assess are summarized below:

- Percent radiolabeling
- Specific activity (radioactivity/mg)
- Immunoreactivity
- Antibody purity (SEC)
- Radiolabel stability (from production to patient)
- Serum stability (incubation with human serum over time)

The ability of a given radiolabeling method to provide a product in sufficient yield and specific activity will vary with parameters such as antibody concentration, reaction volume, pH, time of incubation and the nature of the radionuclide, especially in the case of a radiometal. The best approach is to first decide on the desired specific activity for the application in mind. For animal studies in which cohorts of 40 mice are imaged or treated with 10–30 μg of antibody per mouse, the amount of antibody to be labeled for a given study may be in the range of 1–2 mg, and the amount of radioactivity required may be in the range 3–15 MBq. In order to optimize a radiolabeling procedure, trials should be executed with a fixed amount of antibody and increasing amounts of radionuclide and monitored via instant thin layer chromatography (iTLC) to determine the efficiency of radiolabeling. In most cases, >95% is the target efficiency at the desired specific activity. An example of a scanned iTLC strip is shown
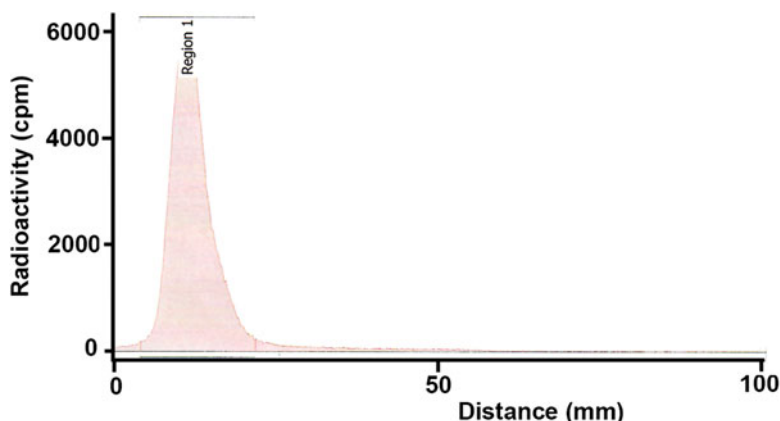
Fig. 9.10 Percent radiolabeling determination by iTLC. DOTA-anti-CEA antibody M5A (5 mg/mL) in 0.25 M pH 6.0 ammonium acetate with 50 mM ascorbic acid was radiolabeled with 16.5 MBq of Ac-225 at 43 °C for 40 min, and excess radiometal was scavenged via the addition of 10 mM DTPA for 10 min. An aliquot was applied to an iTLC strip, developed in saline, and scanned for radioactivity. The counts at the origin (region 1) were > 99% of those applied. Any excess unbound radiometal would appear at the end of the strip

in Fig. 9.10. The concentration of antibody, the volume and pH of the reaction, and the formulation of the radionuclide itself can all affect the radiolabeling reaction and thus must be optimized. In addition, since radiolysis is a potential problem (especially at high concentrations of therapeutic radionuclides), it may be necessary to add a radioprotectant such as ascorbate to the reaction buffer to protect the radioimmunoconjugate [38].

Once a reproducible radiolabeling method has been established, the immunoreactivity of the product must be determined. Along these lines, access to the cognate antigen or a cell line expressing the cognate antigen is essential. In the case of cell surface receptors, many are available as recombinant Fc fusion products or can be prepared by gene synthesis and cell expression systems that include post-translation modifications such as glycosylation. An example of an immunoreactivity assay for CEA is shown in Fig. 9.11a, b. In this assay, the radiolabeled antibody is mixed with a 10- to 20-fold molar excess of CEA, incubated for 1–2 h, and injected on a size exclusion column monitored with a radioactivity detector. Both the radiolabeled antibody and CEA must be diluted in 1% serum albumin to prevent the small amounts of protein present from sticking to the sides of the assay tubes. The size of the antibody-antigen complex will be greater than the starting antibody, thereby allowing one to measure the area under the curves of the bound and unbound antibody. An alternative measure of immunoreactivity is the cell-binding assay. For cell-based immunoreactivity, trace amounts of radiolabeled antibody are incubated with excess antigen-expressing cells (along with antigen-negative controls). The cell-bound and supernatant fractions are separated by centrifugation and gamma counted. A double-reciprocal plot is created by plotting the inverse bound antibody fraction (1/ (bound/[[bound + free]) as a function of the inverse cell number [(1/(cells/mL)] and extrapolated to "infinite antigen excess". The reciprocal of the immunoreactive fraction is given at the y-intercept. The example given in Fig. 9.11c is for an [124]I-labeled cys-diabody binding to human CD20 [39].

Another example can be given for the determination of the immunoreactivity of an anti-CD38 antibody daratumumab to its cognate antigen, the extracellular domain of CD38. An Fc fusion protein with CD38 is commercially available, and since it is fused to a Fc domain, both its valency and molecular size are increased, leading to a

Fig. 9.11
Immunoreactivity of radiolabeled antibodies. (**a, b**) An aliquot of ^{225}Ac-labeled DOTA-anti-CEA (see Fig. 9.10) was injected onto a Superose 200 column and eluted with PBS. Radiochromatograms before (**a**) and after (**b**) mixing with a 20-fold excess of CEA. Note the shift to higher molecular size after the addition of CEA. The percent immunoreactivity = bound/(bound plus unbound) x 100. In this example the % immunoreactivity was >98%. (**c**). An example of a double reciprocal plot stemming from a cell-based immunoreactivity assay in which an ^{124}I-labeled anti-CD20 antibody binds to 38C13 murine B-cell lymphoma cells expressing human CD20
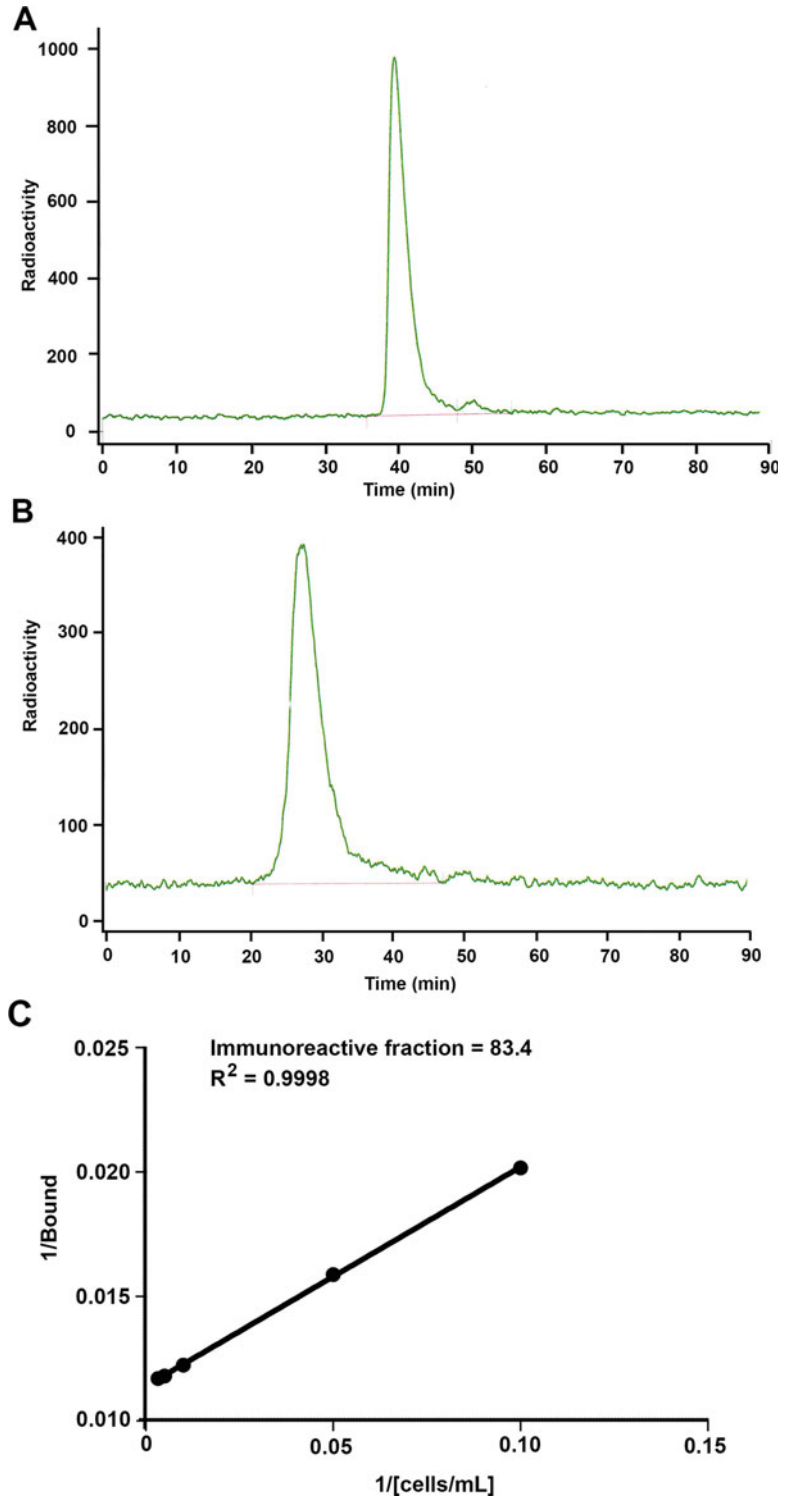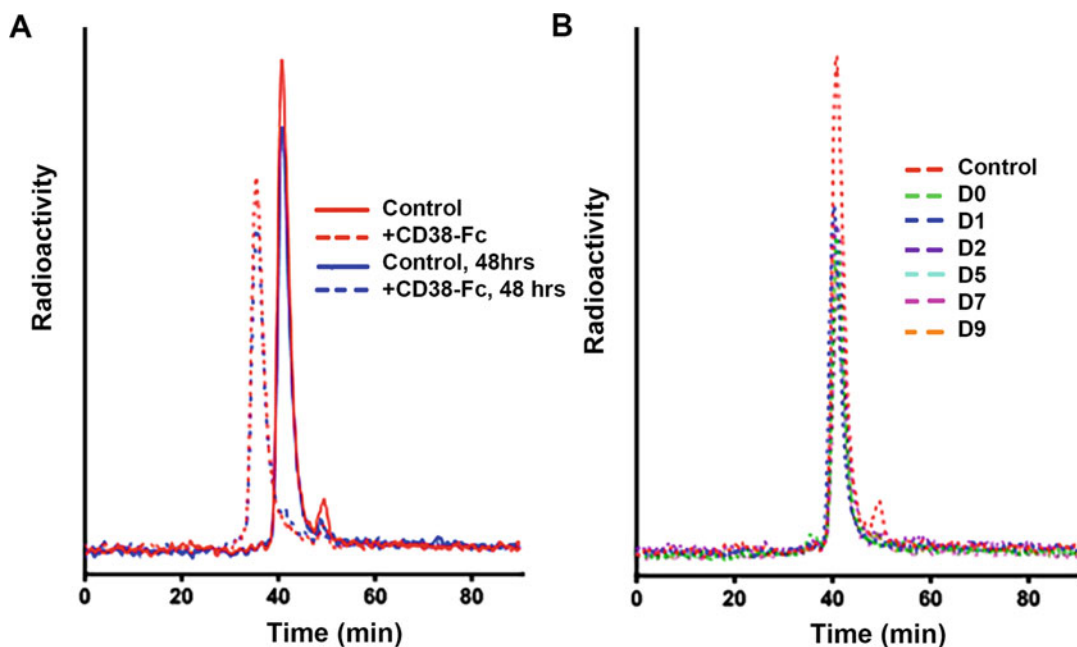
Fig. 9.12 Immunoreactivity and serum stability of ^{225}Ac-labeled DOTA-daratumumab. (**a**). Immunoreactivity: the radioimmunoconjugate was analyzed via SEC before and after incubation with CD38-Fc. (**b**). Serum stability: SEC chromatograms were collected over 9 days during which the radioimmunoconjugate was incubated in serum

substantial size shift upon binding the radiolabeled antibody (Fig. 9.12a). An advantage of using SEC for the immunoreactivity assay is that the injection of the radiolabeled antibody alone is required. Thus, this radiochromatogram will serve as an indication of the purity of the radiolabeled antibody as well. In some cases, the method of radiolabeling may increase the odds of aggregation, which can be easily observed and calculated from the radiochromatogram. In most cases, aggregation should be kept below 5–10%; if the radioimmunoconjugate contains aggregates >5–10%, it may be necessary to remove the aggregates on a preparative SEC column.

Another IND requirement is the determination of the serum stability of the radioimmunoconjugate. This can be performed via repeat ITLC assays at various time points after radiolabeling. For most studies, a stability of >95% out to 24–48 h should be sufficient. Alternatively, serum stability measurements can be performed by incubating the radioimmunoconjugate with human serum at 37 °C and assaying the construct's integrity over time via SEC. An example of an acceptable serum stability by SEC for ^{225}Ac-labeled DOTA-daratumumab is shown in Fig. 9.12b.

In addition to the studies above, animal studies demonstrating in vivo targeting are often required when filing an IND application. In the case of cancer studies, animals bearing human xenografts must be studied by both imaging and tissue biodistribution. In vivo targeting—that is, the antigen-mediated accumulation of radioactive signal in the target tissue (xenograft)—can be observed over time. Antigen specificity should be confirmed by including a blocking control (i.e., via the co-injection of excess cold antibody) or by including an antigen-negative xenograft or a non-specific antibody (isotype) control group. This is shown in Fig. 9.13, in which the anti-CD20 cys-diabody (^{124}I-GAcDb) demonstrates high uptake in a CD20-positive B-cell lymphoma, resulting in high-contrast images at early time points [40]. The addition of excess blocking antibody and the antigen-negative tumor control groups show significantly lower uptake, confirming the specificity of this radiotracer.
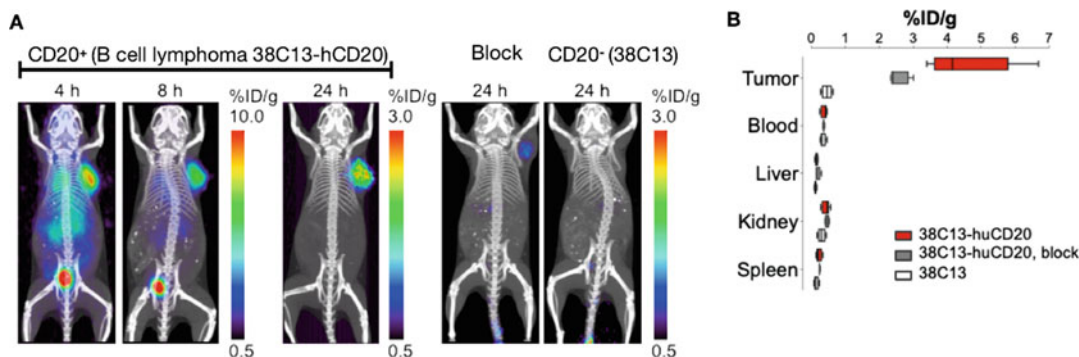
Fig. 9.13 In vivo targeting specificity. (**a**). Serial imaging of [124]I-labeled anti-CD20 cys-diabody antibody in mice bearing huCD20 transfected 38C13 tumors with and without a blocking injection of unlabeled anti-CD20. (**b**). The biodistribution of the radioimmunoconjugate 24 h after injection in mice bearing xenografts of antigen-expressing cells (38C13-huCD20), xenografts of cells that do not express antigen (38C13-huCD20), and antigen-expressing xenografts after blocking (block)
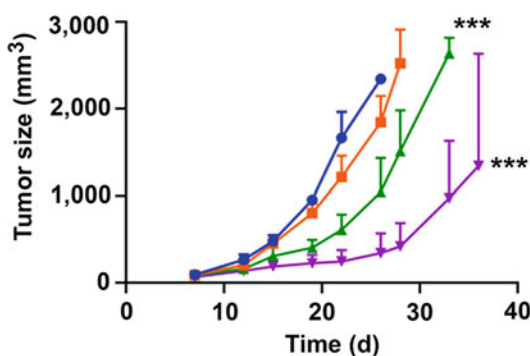

Fig. 9.14 Dose response of CEA positive tumors to [225]Ac-DOTA-anti-CEA M5A. Murine breast tumors transfected with CEA and implanted in the mammary glands of CEA Tg mice ($n = 6$ per group) were untreated (blue) or treated with 3.7 kBq (orange), 7.4 kBq, (green), or 11.1 kBq (purple) of [225]Ac-labeled DOTA-anti-CEA-M5A. Tumor growth curves were analyzed ANOVA, ***$p < 0.001$

For therapeutic radioimmunoconjugates, the preclinical demonstration of therapeutic efficacy is also essential prior to any attempts at clinical translation. An example of the dose-dependent inhibition of tumor growth by an [225]Ac-labeled DOTA-anti-CEA M5A is shown in Fig. 9.14. In the study, the lowest dose of radioimmunoconjugate has a minimal effect on tumor growth compared to the untreated saline control. The increasing doses exhibit statistically significant reductions in tumor growth that suggest even higher doses may be effective.

Since treatment of mice with [225]Ac-labeled antibody could have hematological toxicity due to circulating radiolabeled antibody, selected animals were euthanized at 12 days post-injection to probe for evidence of early toxicity, and the remainder were analyzed after the terminal time point. The transient depression of white blood cell (mainly neutrophils) and platelet levels were observed, with complete recovery at the terminal time point (Fig. 9.15).

IND applications usually include an estimate of radiation doses extrapolated from an animal study using programs such as OLINDA [41]. This can be accomplished by choosing a single dose of radioimmunoconjugate and performing a biodistribution study in tumor-bearing mice over a time period that covers one to two half-lives of the radionuclide and/or circulating antibody. A typical biodistribution study using the same [225]Ac-labeled antibody is shown in Fig. 9.16. In this case, counting the alpha emissions from Ac-225 is difficult, so the gamma emissions from its final daughter radionuclide—Bi-213—were used.

These data clearly show that the accumulation of radioactivity in the tumor increases over time. By integrating the activity concentration in each organ over time, it is possible to obtain total doses per organ and extrapolate these doses to human organs. It is also important to note that the relative biological effect (RBE) of different particle
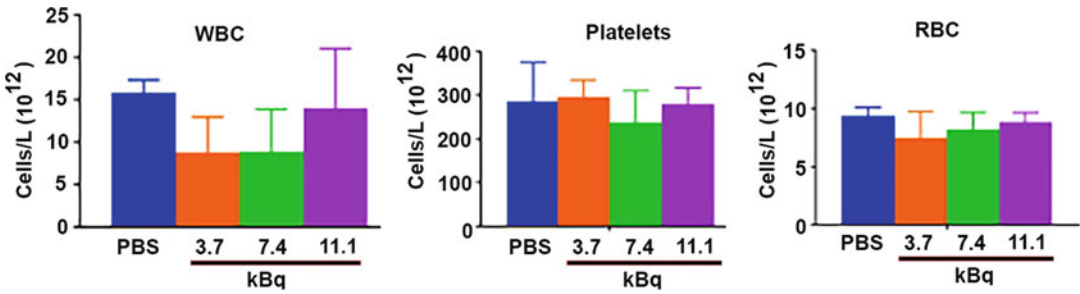
Fig. 9.15 Hematological toxicity of [225]Ac-DOTA-anti-CEA m5A in tumor-bearing mice. Tumor-bearing animals treated or not with [225]Ac-DOTA-anti-CEA M5A were euthanized at the terminal time point (Fig. 9.12), and blood was collected and analyzed for white blood cells (WBC), platelets, and red blood cells (RBC)
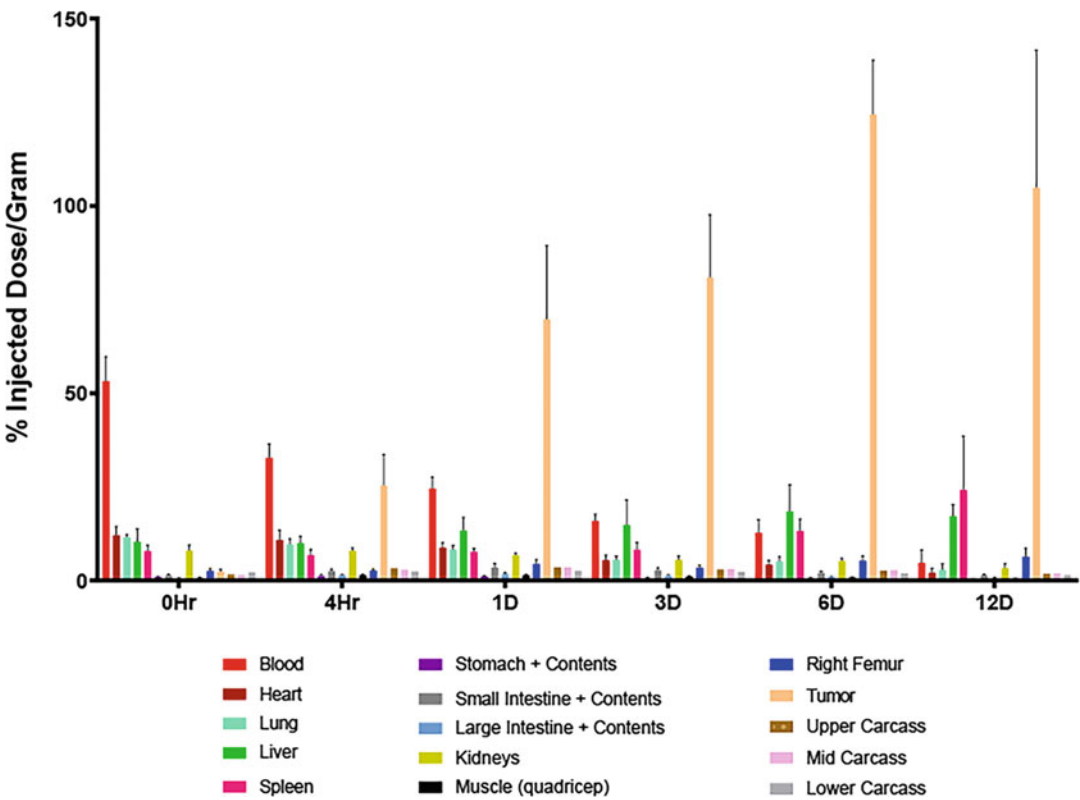

Fig. 9.16 Tissue biodistributions of [225]Ac-DOTA-anti-CEA M5A. Biodistribution data collected from nude mice bearing CEA positive LS174T that were treated with 11.1 kBq of [225]Ac-labeled anti-CEA M5A (30 μg, 6 mice per group) and euthanized at the indicated times

emissions must be considered. For example, the RBE of gamma and beta emissions are taken as 1.0, while alpha emissions have a much higher RBE [42]. Yet these data, while useful, cannot substitute for actual measurement in patients. In this respect, we were able to extrapolate human organ doses from our previous imaging studies with an ^{111}In-labeled variant of the radioimmunoconjugate in colorectal cancer patients. A comparison of the results obtained

Table 9.3 Dosimetry of ^{225}Ac-DOTA-anti-CEA M5A[a]

Organ	Animal biodistribution	In-111 patient imaging
Heart wall	65	1020
Kidneys	150	607
Liver	3004	3292
Lungs	63	108
Red marrow	119	181
Osteogenic cells	833	1281
Spleen	1959	1936
Total body	**149**	**205**

[a]Mean doses in mSv/MBq with the biological effect of the alpha emission as 5.0

using these two methods is shown in Table 9.3. There was good agreement between the methods for the liver and spleen, the two healthy organs with the highest uptake of intact antibodies. In contrast, higher doses were calculated for heart wall, red marrow, and kidneys from the clinical In-111 data. Based on these analyses, we are planning a phase 1 trial for ^{225}Ac-DOTA-M5A in rectal cancer.

Clinical Considerations for Radiopharmaceutical Therapy The first Food and Drug Administration (FDA)-approved radioimmunoconjugate was Zevalin, a ^{90}Y-labeled anti-CD20 antibody approved in 2002 for the treatment of patients with non-Hodgkin's lymphoma [43]. Since then, the number of FDA-approved radioimmunoconjugates remains low despite many phase 1–2 trials with radiotherapeutics bearing beta-emitting radionuclides. However, there is renewed interest in arming antibodies with alpha-emitting radionuclides that have high linear energy transfer compared to beta-emitters. Whether or not these studies will lead to new FDA-approved drugs remains to be seen.

Once the necessary characterization and preclinical studies are completed, the starting points for a phase 1 radioimmunotherapy human trial are patient selection, choosing the starting dose, planning the dose escalation, and deciding on safety protocols. Patient selection typically includes a biopsy or blood test to determine if they are positive for the antigen of interest. The patients in a phase I RPT trial will have likely failed standard-of-care therapies and may have low performance indices that may affect their ability to withstand expected toxicities. Since the expected toxicities of a radioimmunoconjugates are hematological, a patient's platelet and WBC counts should be within the normal range before starting therapy and then monitored throughout the trial. The starting dose for the trial can be extrapolated from the animal dosimetry studies and/or similar published trials. The overall goal will be to test safety and determine the maximum tolerated dose (MTD). A standard trial design may include at least three doses with three patients at each dose until adverse effects are observed. An additional three patients may be added at the final dose to accrue more data. The increments of the dose escalation may be 1.5–2.0 times the starting dose depending on the expected toxicity in the patient population selected.

During the trial, regular blood draws are essential to monitor the pharmacokinetics of the radiolabeled antibody, the potential generation of an immune response to the antibody, changes in biomarker levels, and the hematological toxicity (if any) of the treatment. Response to therapy can be monitored by standard radiological imaging. This can be accompanied by radioimmunoimaging if the therapeutic radioimmunoconjugate also produces "imageable" emissions or if a variant of the radioimmunoconjugate labeled with a different radionuclide suitable for imaging is available. Decreasing levels of serum biomarkers—especially the antigen of interest—often represents an additional important readout for response to therapy.

Table 9.4 Therapeutic radionuclides suitable for radiolabeled antibodies

Radionuclide	Particle	Emax (MeV)	Range max	Half-life	Gamma emissions
Cu-67	Beta	0.58	2 mm	2.6 d	185, 93 keV
Y-90	Beta	2.28	120 mm	2.7 d	n/a
I-131	Beta	0.60	2 mm	8.0 d	364 keV
Lu-177	Beta	0.50	0.6 mm	6.7 d	208 keV
Pb-212	Alpha	7.8	0.09 mm	10.6 hr	239 keV
Ac-225	Alpha	8.4	0.09 mm	10.0 d	(435 keV Bi-213)

Examples of commonly used therapeutic radionuclides as well as their emissions and energy characteristics are given in Table 9.4. A general rule for choosing a radionuclide is to match its half-life with the biological half-life of the immunoglobulin vector. Most intact humanized antibodies have a half-life of 10–12 days in the circulation [44] that can be confirmed by collecting regular blood collections and counting radioactivity starting from the time of infusion. It should be noted that blood clearance times will be affected by the presence of circulating antigen levels that may vary from patient to patient. As mentioned in an earlier section, the blood residence time of a radioimmunoconjugate can be changed by using smaller antibody fragments or engineering the Fc region of the antibody to manipulate its interaction with FcRn receptors [45]. Based on these general guidelines and the need to deliver the maximum amount of radionuclide to the target tissue, intact antibodies are often the first choice for therapeutic radioimmunoconjugates, since their longer residence time translates into higher target tissue uptake. Nonetheless, this feature is offset by increased hematological toxicity, since the radiolabeled antibody can irradiate the bone marrow during its extended circulation in the body. The doses to both the target and non-target tissues—calculated as described in the previous section—will also strongly depend on the tissue pathlength of the emission. Indeed, there are several choices of beta-emitting radionuclides that vary in tissue penetration. Y-90 exhibits the greatest tissue pathlength and thus—all other things being equal—will have more hematological toxicity than Cu-67, I-131, or Lu-177. I-131 and Lu-177 are commercially available, as is (more recently) Cu-67 [46, 47]. Alpha emitters, with their short tissue

penetration but high linear energy transfer (LET), were originally thought to be suitable only for the treatment of hematological malignancies but have more recently enjoyed success in treating solid tumors, presumably due to their cytotoxic effects on tumor vasculature [48]. Pb-212 and Ac-225 are available from the DOE and at least one commercial supplier. As their use increases, their availability can be expected to increase as well.

A large number of therapeutic clinical trials with radiolabeled antibodies have been performed. No attempt will be made to review them all, since most have the same overall goal: delivering a maximum dose with minimal toxicity. Examples of beta radionuclide therapies shown in Table 9.5 indicate a range of about 0.1–6.7 Gy delivered to tumors. In most cases, MTDs were reached with hematologic dose limiting toxicities. The best responses were observed in lymphomas, while radiation resistant solid tumors were less responsive to therapy. The treatment of solid tumors was often improved by multiple cycles [49] or the addition of radiosensitizers [50] or chemotherapeutics [51].

As mentioned earlier, most trials have employed intact monoclonal antibodies or larger bivalent fragments. Since it is well known that full-length antibodies penetrate only a few cell diameters beyond the tumor vasculature of solid tumors [52], it is likely that the tissue penetration of the antibody and its radionuclide emission do not play as large a role in tumor killing as once thought. Thus, alpha emitters with their low tissue penetration and high LET may have a pronounced effect on tumor vasculature (TV) by binding to the tumor cells in contact with the TV. The mechanisms of cytotoxicity to the TV may also include the production of ROS [53].

Table 9.5 Examples of endoradiotherapy trials and tumor doses

Radiolabeled antibody	Tumor type	Tumor dose (cGy/cycle)	Ref
^{131}I-CC49	Prostate, ovary	208–1083	[54]
^{131}I-NP4 F(ab')2	Colorectal, lung, pancreas, thyroid	511–6476	[55]
^{131}I-chL6	Breast	120–3700 (~1300 mean)	[56]
^{131}I-cMOv18	Ovary	600–3800	[57]
^{186}Re-NR-CO-2 F(ab')2	Lung, colorectal, breast, ovary, renal	500–2100	[58]
^{186}Re-hu anti-CD44v66	Head and neck	380–7610 (1240 median)	[59]
^{90}Y-BrE-3	Breast	442–1887	[60]
^{90}Y-chT84.66	Colorectal, breast	46–6400 (1320 mean)	[61]
^{131}I-huA33	Colorectal	1173–3273 (2119 mean)	[62]
^{90}Y-2B8	Non-Hodgkin's lymphoma	580–6700 (1700 median)	[63]
^{131}I-anti-B1	Non-Hodgkin's lymphoma	795 mean	[64]
^{131}I-anti-B1	Non-Hodgkin's lymphoma	141–2584 (925 mean)	[65]
^{131}I-Lym-1	Non-Hodgkin's lymphoma	16–1485 (241 median)	[66]
^{131}I-LL2	Non-Hodgkin's lymphoma	166–861	[67]

Beyond phase 1 safety trials in which determining the MTD is the major goal, many trials include clinical correlates, including monitoring changes in tumor volume, changes in biomarkers, and organ toxicities. In the case of the trials with our ^{90}Y-labeled anti-CEA chimeric antibody, serum CEA levels were used as a reliable biomarker. In a trial with the addition of the radiation sensitizer 5-FU, an MTD of 614 MBq/m^2 combined with 1000 mg/m^2/day 5-FU was reached, with patients eligible to receive up to three cycles of the combination treatment every 6 weeks. Radiological stable disease of 3–8 months duration was observed in 11/21 patients with progressive disease entering the study, while one patient demonstrated a mixed response [61]. In a more recent study with the humanized anti-CEA antibody M5A in which 16 patients received ^{90}Y-DOTA-M5A, the maximum doses were one patient at 614 MBq/m^2 with gemcitabine (150 mg/m^2 days 1 and 3), three patients at 518 MBq/m^2 with gemcitabine, six patients at 440 MBq/m^2 without gemcitabine, and six patients at 370 MBq/m^2 without gemcitabine. Prolonged cytopenias resulted in the discontinuation of dose escalation with gemcitabine. A single agent MTD of 370 MBq/m^2 was established based on the dose-limiting hematopoietic toxicities, and a human anti-human antibody response was observed in 2 of 16 patients (12.5%). Stable disease at 3 months was seen in 10 patients, and 2 patients demonstrated an 88 and 64% decrease in serum CEA levels. In two patients that had concurrent ^{111}In-DOTA-M5A imaging, previously unknown brain metastases were revealed.

9.3   The Future

The future of radiolabeled antibodies for therapy remains bright. Given the importance of antibody therapies in so many areas of cancer research, it seems obvious that their use as vectors for the delivery of radionuclides will be explored. The advantages of radioimmunotherapy over other targeted treatments include the ability to tailor the radionuclide half-life and emissions to the disease and the ability to calculate doses, especially when the radionuclide or a surrogate radionuclide has gamma emissions. This advantage cannot be over-estimated because calculating doses is difficult for most types of biologically based therapies.

9.4   Bottom Line

- Antibodies are promising vectors for the delivery of therapeutic radionuclides to tumor tissue due to their exquisite selectivity and affinity for their molecular targets.
- Full-length immunoglobulins have long circulation half-lives. This can result in high

radiation dose rates to healthy tissues, so smaller format antibody fragments with more rapid pharmacokinetic profiles—i.e., minibodies, diabodies, etc.—have also been explored as vectors for radioimmunotherapy.

- When designing a radioimmunoconjugate, care must be taken with respect to the selection of the radionuclide and the approach to radiolabeling.
- A wide variety of chemical characterization, biological characterization, and preclinical in vivo evaluation steps must be performed as a radioimmunoconjugate is ushered toward clinical translation.
- Radioimmunoimaging studies can complement both the preclinical development and the clinical deployment of therapeutic radioimmunoconjugates.
- Although patients have been treated with FDA-approved radiolabeled antibodies for over 20 years, the number of approved therapeutic radioimmunoconjugates remains low. There is optimism that this may change in the coming years, as new antibodies radiolabeled with high LET alpha emitters are evaluated in clinical trials.

References

1. Lu RM, Hwang YC, Liu IJ, Lee CC, Tsai HZ, Li HJ, et al. Development of therapeutic antibodies for the treatment of diseases. J Biomed Sci. 2020;27(1):1.
2. Yazaki PJ, Sherman MA, Shively JE, Ikle D, Williams LE, Wong JY, et al. Humanization of the anti-CEA T84.66 antibody based on crystal structure data. Protein Eng Des Sel. 2004;17(5):481–9.
3. Freise AC, Wu AM. In vivo imaging with antibodies and engineered fragments. Mol Immunol. 2015;67 (2 Pt A):142–52.
4. Wagener C, Clark BR, Rickard KJ, Shively JE. Monoclonal antibodies for carcinoembryonic antigen and related antigens as a model system: determination of affinities and specificities of monoclonal antibodies by using biotin-labeled antibodies and avidin as precipitating agent in a solution phase immunoassay. J Immunol. 1983;130(5):2302–7.
5. Wagener C, Yang YH, Crawford FG, Shively JE. Monoclonal antibodies for carcinoembryonic antigen and related antigens as a model system: a systematic approach for the determination of epitope specificities of monoclonal antibodies. J Immunol. 1983;130(5):2308–15.
6. Neumaier M, Shively L, Chen FS, Gaida FJ, Ilgen C, Paxton RJ, et al. Cloning of the genes for T84.66, an antibody that has a high specificity and affinity for carcinoembryonic antigen, and expression of chimeric human/mouse T84.66 genes in myeloma and Chinese hamster ovary cells. Cancer Res. 1990;50(7):2128–34.
7. Tsai SW, Li L, Williams LE, Anderson AL, Raubitschek AA, Shively JE. Metabolism and renal clearance of 111In-labeled DOTA-conjugated antibody fragments. Bioconjug Chem. 2001;12 (2):264–70.
8. Wu AM, Chen W, Raubitschek A, Williams LE, Neumaier M, Fischer R, et al. Tumor localization of anti-CEA single-chain Fvs: improved targeting by non-covalent dimers. Immunotechnology. 1996;2 (1):21–36.
9. Li L, Olafsen T, Anderson AL, Wu A, Raubitschek AA, Shively JE. Reduction of kidney uptake in radiometal labeled peptide linkers conjugated to recombinant antibody fragments. Site-specific conjugation of DOTA-peptides to a Cys-diabody. Bioconjug Chem. 2002;13(5):985–95.
10. Kenanova V, Olafsen T, Williams LE, Ruel NH, Longmate J, Yazaki PJ, et al. Radioiodinated versus radiometal-labeled anti-carcinoembryonic antigen single-chain Fv-Fc antibody fragments: optimal pharmacokinetics for therapy. Cancer Res. 2007;67 (2):718–26.
11. Hu S, Shively L, Raubitschek A, Sherman M, Williams LE, Wong JY, et al. Minibody: a novel engineered anti-carcinoembryonic antigen antibody fragment (single-chain Fv-CH3) which exhibits rapid, high-level targeting of xenografts. Cancer Res. 1996;56(13):3055–61.
12. Muyldermans S. Nanobodies: natural single-domain antibodies. Annu Rev Biochem. 2013;82:775–97.
13. Yang EY, Shah K. Nanobodies: next generation of cancer diagnostics and therapeutics. Front Oncol. 2020;10:1182.
14. Caserta E, Chea J, Minnix M, Poku EK, Viola D, Vonderfecht S, et al. Copper 64-labeled daratumumab as a PET/CT imaging tracer for multiple myeloma. Blood. 2018;131(7):741–5.
15. Wong JY, Chu DZ, Williams LE, Yamauchi DM, Ikle DN, Kwok CS, et al. Pilot trial evaluating an 123I-labeled 80-kilodalton engineered anticarcinoembryonic antigen antibody fragment (cT84.66 minibody) in patients with colorectal cancer. Clin Cancer Res. 2004;10(15):5014–21.
16. Tsai WK, Zettlitz KA, Dahlbom M, Reiter RE, Wu AM. Evaluation of [(131)I]I- and [(177)Lu]Lu-DTPA-A11 minibody for radioimmunotherapy in a preclinical model of PSCA-expressing prostate cancer. Mol Imaging Biol. 2020;22(5):1380–91.
17. Mortimer JE, Bading JR, Park JM, Frankel PH, Carroll MI, Tran TT, et al. Tumor uptake of (64)Cu-DOTA-

Trastuzumab in patients with metastatic breast cancer. J Nucl Med. 2018;59(1):38–43.

18. Wong JY, Thomas GE, Yamauchi D, Williams LE, Odom-Maryon TL, Liu A, et al. Clinical evaluation of indium-111-labeled chimeric anti-CEA monoclonal antibody. J Nucl Med. 1997;38(12):1951–9.

19. Krishnan A, Adhikarla V, Poku EK, Palmer J, Chaudhry A, Biglang-Awa VE, et al. Identifying CD38+ cells in patients with multiple myeloma: first-in-human imaging using copper-64-labeled daratumumab. Blood Adv. 2020;4(20):5194–202.

20. Chomet M, van Dongen G, Vugts DJ. State of the art in radiolabeling of antibodies with common and uncommon radiometals for preclinical and clinical immuno-PET. Bioconjug Chem. 2021;32(7):1315–30.

21. Gupta S, Batra S, Jain M. Antibody labeling with radioiodine and radiometals. Methods Mol Biol. 2014;1141:147–57.

22. Boschi A, Uccelli L, Martini P. A picture of modern Tc-99m radiopharmaceuticals: production, chemistry, and applications in molecular imaging. Appl Sci (Basel). 2019;9(12):2526.

23. Wangler C, Wangler B, Lehner S, Elsner A, Todica A, Bartenstein P, et al. A universally applicable 68Ga-labeling technique for proteins. J Nucl Med. 2011;52 (4):586–91.

24. Grunberg J, Novak-Hofer I, Honer M, Zimmermann K, Knogler K, Blauenstein P, et al. In vivo evaluation of 177Lu- and 67/64Cu-labeled recombinant fragments of antibody chCE7 for radioimmunotherapy and PET imaging of L1-CAM-positive tumors. Clin Cancer Res. 2005;11 (14):5112–20.

25. Dearling JL, Paterson BM, Akurathi V, Betanzos-Lara S, Treves ST, Voss SD, et al. The ionic charge of copper-64 complexes conjugated to an engineered antibody affects biodistribution. Bioconjug Chem. 2015;26(4):707–17.

26. Cooper MS, Ma MT, Sunassee K, Shaw KP, Williams JD, Paul RL, et al. Comparison of (64)Cu-complexing bifunctional chelators for radioimmunoconjugation: labeling efficiency, specific activity, and in vitro/in vivo stability. Bioconjug Chem. 2012;23 (5):1029–39.

27. Rinne SS, Leitao CD, Mitran B, Bass TZ, Andersson KG, Tolmachev V, et al. Optimization of HER3 expression imaging using affibody molecules: influence of chelator for labeling with indium-111. Sci Rep. 2019;9(1):655.

28. Kang L, Jiang DW, Ehlerding E, Barnhart T, Ferreira C, Wang RF, et al. Safe and dosimetry evaluation of radimmunotherapy using Lu-177-labeled antibodies in lymphoma. J Nucl Med. 2019;60

29. Crow DM, Williams L, Colcher D, Wong JYC, Raubitschek A, Shively JE. Combined Radioimmunotherapy and chemotherapy of breast tumors with Y-90-labeled anti-Her2 and anti-CEA antibodies with Taxol. Bioconjug Chem. 2005;16 (5):1117–25.

30. Ahlgren S, Orlova A, Rosik D, Sandstrom M, Sjoberg A, Baastrup B, et al. Evaluation of maleimide derivative of DOTA for site-specific labeling of recombinant affibody molecules. Bioconjug Chem. 2008;19(1):235–43.

31. Vugts DJ, Klaver C, Sewing C, Poot AJ, Adamzek K, Huegli S, et al. Comparison of the octadentate bifunctional chelator DFO*-pPhe-NCS and the clinically used hexadentate bifunctional chelator DFO-pPhe-NCS for (89)Zr-immuno-PET. Eur J Nucl Med Mol Imaging. 2017;44(2):286–95.

32. Pentlow KS, Graham MC, Lambrecht RM, Daghighian F, Bacharach SL, Bendriem B, et al. Quantitative imaging of iodine-124 with PET. J Nucl Med. 1996;37(9):1557–62.

33. Kim EJ, Kim BS, Choi DB, Chi SG, Choi TH. Improved in vivo stability of radioiodinated rituximab using an iodination linker for radioimmunotherapy. Cancer Biother Radiopharm. 2016;31(8):287–94.

34. Wadas TJ, Wong EH, Weisman GR, Anderson CJ. Copper chelation chemistry and its role in copper radiopharmaceuticals. Curr Pharm Des. 2007;13 (1):3–16.

35. Liu S, Li Z, Conti PS. Development of multi-functional chelators based on sarcophagine cages. Molecules. 2014;19(4):4246–55.

36. Hafeez U, Parakh S, Gan HK, Scott AM. Antibody-drug conjugates for cancer therapy. Molecules. 2020;25:20.

37. Guillou A, Earley DF, Klingler S, Nisli E, Nuesch LJ, Fay R, et al. The influence of a polyethylene glycol linker on the metabolism and pharmacokinetics of a (89)Zr-radiolabeled antibody. Bioconjug Chem. 2021;32(7):1263–75.

38. Takashima H, Koga Y, Manabe S, Ohnuki K, Tsumura R, Anzai T, et al. Radioimmunotherapy with an (211) At-labeled anti-tissue factor antibody protected by sodium ascorbate. Cancer Sci. 2021;112 (5):1975–86.

39. Zettlitz KA, Tavare R, Knowles SM, Steward KK, Timmerman JM, Wu AM. ImmunoPET of malignant and normal B cells with (89)Zr- and (124)I-labeled obinutuzumab antibody fragments reveals differential CD20 internalization in vivo. Clin Cancer Res. 2017;23(23):7242–52.

40. Zettlitz KA, Tavare R, Tsai WK, Yamada RE, Ha NS, Collins J, et al. (18)F-labeled anti-human CD20 cys-diabody for same-day immunoPET in a model of aggressive B cell lymphoma in human CD20 transgenic mice. Eur J Nucl Med Mol Imaging. 2019;46 (2):489–500.

41. Stabin MG, Sparks RB, Crowe E. OLINDA/EXM: the second-generation personal computer software for internal dose assessment in nuclear medicine. J Nucl Med. 2005;46(6):1023–7.

42. Sgouros G, Roeske JC, McDevitt MR, Palm S, Allen BJ, Fisher DR, et al. MIRD Pamphlet No. 22 (abridged): radiobiology and dosimetry of

alpha-particle emitters for targeted radionuclide therapy. J Nucl Med. 2010;51(2):311–28.

43. Forero A, Lobuglio AF. History of antibody therapy for non-Hodgkin's lymphoma. Semin Oncol. 2003;30 (6 Suppl 17):1–5.

44. Saunders KO. Conceptual approaches to modulating antibody effector functions and circulation half-life. Front Immunol. 2019;10:1296.

45. Lobo ED, Hansen RJ, Balthasar JP. Antibody pharmacokinetics and pharmacodynamics. J Pharm Sci. 2004;93(11):2645–68.

46. Novak-Hofer I, Schubiger PA. Copper-67 as a therapeutic nuclide for radioimmunotherapy. Eur J Nucl Med Mol Imaging. 2002;29(6):821–30.

47. Keinanen O, Fung K, Brennan JM, Zia N, Harris M, van Dam E, et al. Harnessing (64)Cu/(67)Cu for a theranostic approach to pretargeted radioimmunotherapy. Proc Natl Acad Sci U S A. 2020;117(45):28316–27.

48. Morgenstern A, Apostolidis C, Kratochwil C, Sathekge M, Krolicki L, Bruchertseifer F. An overview of targeted alpha therapy with (225)Actinium and (213)Bismuth. Curr Radiopharm. 2018;11(3):200–8.

49. Vallabhajosula S, Goldsmith SJ, Kostakoglu L, Milowsky MI, Nanus DM, Bander NH. Radioimmunotherapy of prostate cancer using 90Y- and 177Lu-labeled J591 monoclonal antibodies: effect of multiple treatments on myelotoxicity. Clin Cancer Res. 2005;11(19 Pt 2):7195s–200s.

50. Chang JE, Khuntia D, Robins HI, Mehta MP. Radiotherapy and radiosensitizers in the treatment of glioblastoma multiforme. Clin Adv Hematol Oncol. 2007;5(11):894–902, 7–15.

51. Magnes T, Wagner SM, Melchardt T, Weiss L, Rinnerthaler G, Huemer F, et al. Postoperative chemoradiotherapy with cisplatin is superior to radioimmunotherapy with cetuximab and radiotherapy alone : analysis of the Austrian head and neck cancer registry of the AGMT. Wien Klin Wochenschr. 2021;133(21–22):1131–6.

52. van Dongen G. Improving tumor penetration of antibodies and antibody-drug conjugates: taking away the barriers for Trojan Horses. Cancer Res. 2021;81(15):3956–7.

53. Behling K, Maguire WF, Di Gialleonardo V, Heeb LE, Hassan IF, Veach DR, et al. Remodeling the vascular microenvironment of glioblastoma with alpha-particles. J Nucl Med. 2016;57(11):1771–7.

54. Meredith RF, Bueschen AJ, Khazaeli MB, Plott WE, Grizzle WE, Wheeler RH, et al. Treatment of metastatic prostate carcinoma with radiolabeled antibody CC49. J Nucl Med. 1994;35(6):1017–22.

55. Juweid ME, Sharkey RM, Behr T, Swayne LC, Dunn R, Siegel J, et al. Radioimmunotherapy of patients with small-volume tumors using iodine-131-labeled anti-CEA monoclonal antibody NP-4 F(ab')2. J Nucl Med. 1996;37(9):1504–10.

56. Denardo SJ, O'Grady LF, Richman CM, Goldstein DS, O'Donnell RT, Denardo DA, et al.

Radioimmunotherapy for advanced breast cancer using I-131-ChL6 antibody. Anticancer Res. 1997;17 (3B):1745–51.

57. van Zanten-Przybysz I, Molthoff CF, Roos JC, Plaizier MA, Visser GW, Pijpers R, et al. Radioimmunotherapy with intravenously administered 131I-labeled chimeric monoclonal antibody MOv18 in patients with ovarian cancer. J Nucl Med. 2000;41(7):1168–76.

58. Breitz HB, Weiden PL, Vanderheyden JL, Appelbaum JW, Bjorn MJ, Fer MF, et al. Clinical experience with rhenium-186-labeled monoclonal antibodies for radioimmunotherapy: results of phase I trials. J Nucl Med. 1992;33(6):1099–109.

59. Postema EJ, Raemaekers JM, Oyen WJ, Boerman OC, Mandigers CM, Goldenberg DM, et al. Final results of a phase I radioimmunotherapy trial using (186)Re-epratuzumab for the treatment of patients with non-Hodgkin's lymphoma. Clin Cancer Res. 2003;9 (10 Pt 2):3995S–4002S.

60. DeNardo SJ, Kramer EL, O'Donnell RT, Richman CM, Salako QA, Shen S, et al. Radioimmunotherapy for breast cancer using indium-111/yttrium-90 BrE-3: results of a phase I clinical trial. J Nucl Med. 1997;38 (8):1180–5.

61. Wong JY, Shibata S, Williams LE, Kwok CS, Liu A, Chu DZ, et al. A Phase I trial of 90Y-anti-carcinoembryonic antigen chimeric T84.66 radioimmunotherapy with 5-fluorouracil in patients with metastatic colorectal cancer. Clin Cancer Res. 2003;9(16 Pt 1):5842–52.

62. Chong G, Lee FT, Hopkins W, Tebbutt N, Cebon JS, Mountain AJ, et al. Phase I trial of 131I-huA33 in patients with advanced colorectal carcinoma. Clin Cancer Res. 2005;11(13):4818–26.

63. Wiseman GA, White CA, Stabin M, Dunn WL, Erwin W, Dahlbom M, et al. Phase I/II 90Y-Zevalin (yttrium-90 ibritumomab tiuxetan, IDEC-Y2B8) radioimmunotherapy dosimetry results in relapsed or refractory non-Hodgkin's lymphoma. Eur J Nucl Med. 2000;27(7):766–77.

64. Kaminski MS, Zasadny KR, Francis IR, Fenner MC, Ross CW, Milik AW, et al. Iodine-131-anti-B1 radioimmunotherapy for B-cell lymphoma. J Clin Oncol. 1996;14(7):1974–81.

65. Vose JM. Bexxar: novel radioimmunotherapy for the treatment of low-grade and transformed low-grade non-Hodgkin's lymphoma. Oncologist. 2004;9 (2):160–72.

66. Lamborn KR, DeNardo GL, DeNardo SJ, Goldstein DS, Shen S, Larkin EC, et al. Treatment-related parameters predicting efficacy of Lym-1 radioimmunotherapy in patients with B-lymphocytic malignancies. Clin Cancer Res. 1997;3(8):1253–60.

67. Vose JM, Wahl RL, Saleh M, Rohatiner AZ, Knox SJ, Radford JA, et al. Multicenter phase II study of iodine-131 tositumomab for chemotherapy-relapsed/refractory low-grade and transformed low-grade B-cell non-Hodgkin's lymphomas. J Clin Oncol. 2000;18(6):1316–23.

Michael R. McDevitt

10.1 The Fundamentals

Monoclonal antibodies (mAb) are well suited to serve as biomolecular targeting vectors for the delivery of cytotoxic α-emitting radionuclides to cancer cells. Metallic radionuclides are appended to mAb via bifunctional chelators that securely coordinate the metal ion during its in vivo transit to the tumor. In most cases, chelators are small molecular weight organic molecules with functional groups that form covalent bonds with the radiometallic cation. In the case of bifunctional chelators, a second reactive functionality (hence "bi") is responsible for covalently linking the chelator-radiometal complex to the biomolecule itself. The stepwise assembly of the mAb + the bifunctional chelator + the radiometal ultimately yields the final active drug construct: the radioimmunoconjugate (Fig. 10.1).

Inorganic coordination chemistry describes the fundamental steric and electronic parameters that govern the chelation of metal ions. The stable coordination of a radiometal becomes an especially complicated proposition in the complex biological milieu of the body, as the chelator is faced by a wide variety of molecules and conditions that challenge its binding to the radionuclide cargo. Yet, the *in vivo* stability of a radioimmunoconjugate is crucial to ensure the delivery of as much its radionuclide cargo to the tumor as possible while limiting the accumulation of the isotope in healthy tissues.

Generally speaking, the mAb delivery platform dictates the pharmacokinetic trafficking of the radioimmunoconjugate in vivo. Relatively long biological half-lives are typical of intact immunoglobulin G (IgG). Furthermore, the internalization of the radioimmunoconjugate by tumor cells maximizes the probability that the α-particle decay will occur within the target cell (in contrast to surface-bound constructs that undergo extracellular decay). Internalization also has a key role in controlling the fate of the parent nuclides isotopic daughters (i.e., progeny), increasing the probability that all of the radioactive decays occur inside of the target cell. The process methods that we developed to synthesize clinical grade ^{225}Ac-lintuzumab are rigorous and well vetted, and our radiosynthetic protocols are applicable for any mAb and this has been evaluated in numerous preclinical studies.

10.2 The Clinical Development Process

The final destination of this story—the use of α-emitting ^{225}Ac-lintuzumab for the radiopharmaceutical therapy (RPT) of human leukemia—was the culmination of a decade of effort focused on (i) the development of a high affinity mAb

M. R. McDevitt (✉)
Department of Radiology, Memorial Sloan Kettering Cancer Center, New York, NY, USA
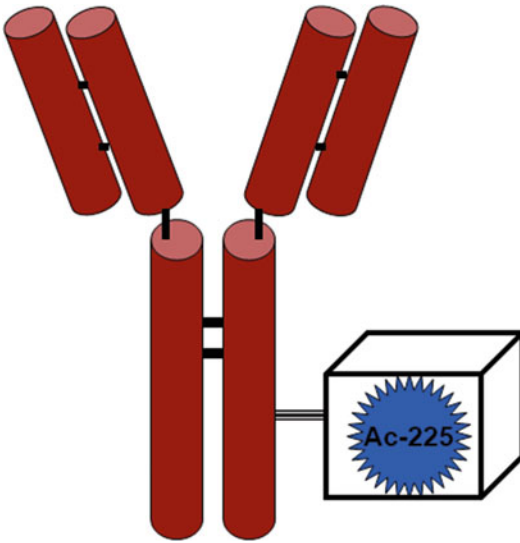e-mail: mcdevitm@mskcc.org

Fig. 10.1 The anatomy of a ^{225}Ac-labeled radioimmunoconjugate showing the antibody framework in red; the DOTA chelator as a box that is attached to the antibody; and the ^{225}Ac in blue

with high specificity for human CD33; (ii) the clinical evaluation of the safety, pharmacokinetic profile, and pharmacodynamics of radioiodinated murine M195 (^{131}I-M195) and radioiodinated humanized HuM195 (^{131}I-huM195) in patients with leukemia; (iii) the transition from the use of a radionuclide (i.e., ^{131}I) with low-linear energy transfer (LET) to one with high-LET (i.e., ^{225}Ac) in order to increase potency and minimize non-specific radiation doses to off-tumor normal tissues; and (iv) the development of novel radiopharmaceutical chemistry in order to optimize the attachment of the α-emitting radiometals to the mAb.

10.2.1 Reengineering the Antibody Platform

M195 is a murine IgG2a mAb that was cloned from a mouse immunized with live human leukemic myeloblasts. M195 exhibited reactivity to the human CD33 antigen, a 67 kDa glycoprotein that is expressed on the surface of myeloid cells, acute non-lymphoid leukemia cells, and monocytic cells (Fig. 10.2) [1]. M195 labeled with the

β-emitting radiohalogen iodine-131 (^{131}I) was advanced to the clinic, and the radioimmunoconjugate effectively reduced the leukemia burden in patients with relapsed acute promyelocytic leukemia while exhibiting toxicity limited to myelosuppression. It should be noted that disease is present in the bone marrow. Using doses of 50 or 70 mCi/m^2, the median disease-free survival was 8 months (range, 3--14.5 months), and the overall survival was 28 months (range, 5.5–43+ months) [2].

Soon after this first clinical experience, the murine IgG was humanized to address the potential for immunogenicity that could arise during repeat administrations of the radioimmunoconjugate. To this end, a humanized variant of M195 was designed that contained the complementarity-determine regions (CDR) of the murine mAb alongside a human framework and constant regions. The human framework was chosen to maximize homology with the M195 V domain sequence [3]. Furthermore, humanized mAb of the IgG1 and IgG3 isotypes exhibited greater apparent binding affinity for CD33 than their IgG2a-based M195 forerunner. The radioiodinated variant of the humanized IgG1 clone—^{131}I-HuM195—was shown to effectively target acute myeloid leukemia and demonstrated potent anti-tumor activity in humans [2].

10.2.2 Arming the Antibody with ^{213}Bi

The decision to arm HuM195 with the short-lived, high-LET radiometal ^{213}Bi for clinical use marked a strategic advance in radiopharmaceutical therapy. Traditionally, radiotherapeutics were labeled with radionuclides (like ^{131}I) that emitted low-LET β-particles. Several problems, however, hampered the use of radioiodinated therapeutics: (i) the catabolic loss of iodine after the cellular internalization of the drug, (ii) the loss of immunoreactivity upon radioiodination due to the high tyrosine content within the CDRs of many mAb [4], and (iii) radiotoxicity due to non-specific radiation dose to bystander tissues arising from the relatively long range of high energy β-particles.
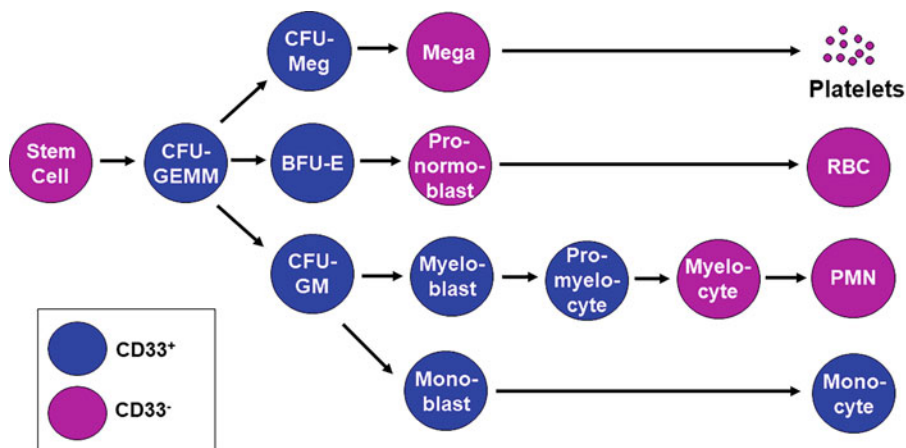
Fig. 10.2 Profile of CD33-positive and CD33-negative myeloid cell types. CD33 expressing cells include common myeloid progenitor cells that generate granulocytes, erythrocytes, monocytes, and megakaryocytes (CFU-GEMM); colony-forming unit-megakaryocytes (CFU-Meg); burst-forming unit erythroid cells (BFU-E); granulocyte–macrophage progenitors (CFU-GM); myeloblasts; monoblasts; pro-myelocytes; and monocytes. Cells that do not express CD33 include stem cells; megakaryoblasts (Mega); pronormoblasts; myelocytes, red blood cells (RBC); polymorphonuclear neutrophils (PMN); and platelets

For the radioimmunoconjugate at hand, the acyclic bifunctional chelator CHX-A″-DTPA ([(R)-2-amino-3-(4-isothiocyanatophenyl)propyl]-trans-(S,S)-cyclohexane-1,2-diamine-pentaacetic acid) was covalently attached to HuM195 and used to chelate the ^{213}Bi cation [6]. The ^{213}Bi itself was produced using a novel ^{225}Ac generator in which the parental ^{225}Ac ion was distributed throughout the resin in order to minimize the radiolytic damage that could severely limit the operational lifetime of the generator [5]. The short half-life of Bi-213 necessitated the on-site elution of the generator, restricting its use to medical laboratory facilities that could perform the radiochemistry, formulation, quality control, and administration of ^{213}Bi-HuM195 to the patient in less than 30 min.

A phase I trial of ^{213}Bi-HuM195 was conducted at Memorial Sloan Kettering Cancer Center in patients with acute or chronic myelogenous leukemia. *This trial marked the first use of an α-emitting mAb radiotheranostic in humans.* This field-changing clinical trial data demonstrated safety, feasibility, and specific anti-leukemic effect of an alpha particle emitting radioimmunotherapeutic drug. Furthermore, the

^{213}Bi γ-emission at 440 keV was used to quantitate the pharmacokinetics and dosimetry of this drug and serves as a diagnostic marker that in combination with the therapeutic alpha particle contribution yields a unique theranostic drug. These relapsed/refractory patients presented with up to a kilogram (10^{12} cells) of leukemia burden, and, as a consequence, no complete remissions were observed. A phase I/II trial ensued in which the patients were treated first with cytarabine to reduce tumor burden and then with escalating doses of ^{213}Bi-HuM195. At the first two activity levels—18.5 and 27.8 MBq/kg (0.5 and 0.75 mCi/kg)—there were no remissions. However, at doses of 37 and 46.25 MBq/kg, complete remissions lasting up to 12 months were observed, highlighting the importance of the cytoreduction of the large leukemia burden prior to α-RPT [7].

10.2.3   Making the Switch to ^{225}Ac

During the course of these ^{213}Bi-HuM195 trials, we began exploring the radiochemistry of ^{225}Ac

in anticipation of the logistical issues caused by the short half-life of ^{213}Bi. Interestingly, in vitro cytotoxicity assay data showed that ^{225}Ac-HuM195 was 1000-fold more potent against leukemia cells than ^{213}Bi-HuM195 on an activity basis. This enhancement is explained by the significantly 313-fold longer half-life of ^{225}Ac ($t_{1/2}$ = 10 d; compared to 45.6 min for ^{213}Bi) as well as its emission of 4 total α-particles during its decay (compared to 1 for ^{213}Bi) [8]. At this time, the radiopharmaceutical chemistry of ^{225}Ac was relatively unexplored, so the development of robust chelators for this rare actinide became particularly important for use in vivo. The need to address the in vivo fate of the radiometal's daughters attracted attention as well.

^{225}Ac decay produces six radionuclide daughters in a cascade that concludes with stable ^{209}Bi (Fig. 10.3). As shown in Fig. 10.3, the decay of ^{225}Ac ($t_{1/2}$ = 10 d; 6 MeV α-particle) produces a total of 4 α- and 3 β-particles, most of rather high energy. These progenies are ^{221}Fr ($t_{1/2}$ = 4.8 m; 6 MeV α-particle and 218 keV γ-emission); ^{217}At ($t_{1/2}$ = 32.3 ms; 7 MeV α-particle); ^{213}Bi ($t_{1/2}$ = 45.6 m; 6 MeV α-particle, 444 keV β-particle, and a 440 keV γ emission); ^{213}Po ($t_{1/2}$ = 4.2 μs; 8 MeV α-particle); ^{209}Tl ($t_{1/2}$ = 2.2 m; 659 keV β-particle); ^{209}Pb ($t_{1/2}$ = 3.25 h; 198 keV β-particle); and stable ^{209}Bi. The γ-emission from ^{213}Bi (440 keV) was used for single-photon emission computed tomographic (SPECT) imaging of ^{213}Bi-HuM195 in patients and yielded pharmacokinetic data that was used to describe the biodistribution and dosimetry of this drug in man [9].

An effective chelator is essential for the in vivo sequestration, stabilization, and transport of ^{225}Ac. Initially, it was thought that the chelator should be suitable for both ^{225}Ac *and* several of its decay progeny [10]. Consequently, early efforts explored both flexible acyclic and large cavity cyclic chelators in order to accommodate the range of properties of these radionuclides. The actinium(III) ion has a radius of 0.111 nm [11]. The hydrolysis of ^{225}Ac was determined by measuring the cation's electromigration in free electrolyte, and a plot of the velocity of the ^{225}Ac ion in the pH 4–10 range produced a constant value of 5.4×10^{-4} cm^2/Vs, indicating that no hydrolytic processes occurred until a pH of 10 [12]. Presumably, the rather large ionic radius of ^{225}Ac^{3+} can accommodate a number of coordinated water molecules while limiting hydroxide formation.

Chemical screens involving radiolabeling, in vitro stability, and in vivo biodistribution experiments were undertaken to identify promising chelators for Ac(III). These data revealed that acyclic chelators (e.g., ethylenediaminetetraacetic acid (EDTA) and CHX-A″-DTPA) exhibited poorer stability with the radiometal compared to macrocyclic chelators (e.g., 1,4,7,10,13-pentaazacyclopentadecane-N,N′,N″,N‴,N⁗-pentaacetic acid (PEPA), 1,4,7,10-tetraazacyclododecane-N,N′,N″,N‴-tetraacetic acid (DOTA), and 1,4,7,10,13,16-hexaazacyclohexadecane-N,N′,N″,N‴,N⁗,N′⁗-hexaacetic acid (HEHA)) [13]. In these screens, all of these ^{225}Ac-chelator complexes rapidly cleared the blood, but the degree to which released ^{225}Ac^{3+} accumulated in healthy tissue decreased as follows: acetate > EDTA > CHX-A″-DTPA ~ PEPA > DOTA > HEHA [13]. Surprisingly, however, in vivo data using ^{225}Ac-labeled radioimmunoconjugates with each chelator suggested that <50% of [^{225}Ac]HEHA-IgG remained intact at 48 h. In contrast, the in vivo stability of [^{225}Ac]DOTA-IgG constructs was markedly higher than the corresponding HEHA-bearing constructs. Clearly, the Ac^{3+} was more easily challenged and lost from HEHA than from DOTA.

The macrocyclic DOTA chelator contains four tertiary amine and four carboxyl moieties that bind to the Ac^{3+} cation in solution. In an effort to optimize the stability of the chelator, we next evaluated several structurally similar macrocycles (Fig. 10.4): 1,4,8,11-tetraazacyclotetradecane-1,4,8,11-tetraacetic acid (TETA), 1,4,7,10-tetraazacyclododecane-1,4,7,10-tetrapropionic acid (DOTPA), 1,4,8,11-tetraazacyclotetradecane-1,4,8,11-tetrapropionic acid (TETPA), and 1,4,7,10-tetraazacyclododecane-1,4,7,10-tetra methylenephosphonic acid (DOTMP). Interestingly, DOTA proved the best chelator of the group for Ac^{3+}. The next most stable with Ac^{3+} was DOTMP, in which a phosphonic acid is

Fig. 10.3 Decay scheme of ^{225}Ac to stable ^{209}Bi
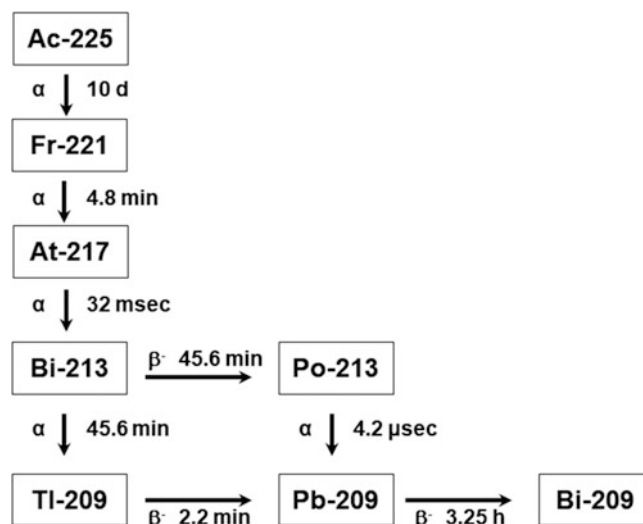
substituted for the carboxylic acid moiety. However, the difference between the two was too large to consider the latter for use in vivo. Finally, the other chelators contained different ring and arm sizes that essentially destabilized their coordination environments for Ac^{3+} relative to DOTA and were not pursued.

The next step in the process was finding a suitable bifunctional variant of DOTA in order to synthetically couple the chelator to the protein. A comparison of two amine-reactive, isothiocyanate-bearing variants of DOTA demonstrated that 2-(*p*-isothiocyanatobenzyl)-1,4,7,10-tetraazacyclododecane-1,4,7,10-tetraacetic acid (2B-DOTA-NCS) and α-(5-isothiocyanato-2-methoxyphenyl)-1,4,7,10-tetraazacyclodo- decane-1,4,7,10-tetraacetic acid (MeO-DOTA-NCS) were comparable as platforms for the coordination of $^{225}Ac^{3+}$. For the synthesis of the radioimmunoconjugate, we devised a two-step radiolabeling scheme in which the bifunctional chelator is first radiolabeled with $^{225}Ac^{3+}$ and then coupled to the immunoglobulin. For Step 1, we reported the synthesis of radiochemically pure [^{225}Ac]DOTA-SCN in yields of 93% ± 8% ($n = 26$). For Step 2, we obtained the pure radioimmunoconjugate in 95% ± 5% ($n = 27$). Ultimately, we opted to move forward with 2B-DOTA-NCS as the bifunctional chelator [14].

Managing the in vivo fate of ^{225}Ac's radioactive daughters is difficult using a single chelator. First, the periodicity of the daughters ranges from the alkali metals (i.e., ^{221}Fr) to the halides (i.e., ^{217}At), and DOTA is not an appropriate chelator for them (except ^{213}Bi). Second, the recoil energy produced by the decay of ^{225}Ac makes it quite difficult to repurpose DOTA for the coordination of any of the metallic progeny. That said, we demonstrated that if [^{225}Ac]DOTA-IgG is internalized by a target cell, then the daughters produced by the decay of ^{225}Ac also remain within the cell [8]. This biologic phenomenon gives rise to the "nanogenerator effect" in which the DOTA only needs to stably coordinate the ^{225}Ac cation until it decays within the cell (Fig. 10.5). The daughters that are produced inside the cell remain there, and the α-particles that they emit contribute to the cytotoxic effects of the initial α-particle form ^{225}Ac. This effect allows us to take full advantage of the therapeutic potential of ^{225}Ac and its radionuclidic progeny. Furthermore, controlling the loss of the daughters from the radioimmunoconjugate and the target tissue reduces their accumulation in non-target tissues and thereby mitigates their radiotoxicity to healthy tissues.
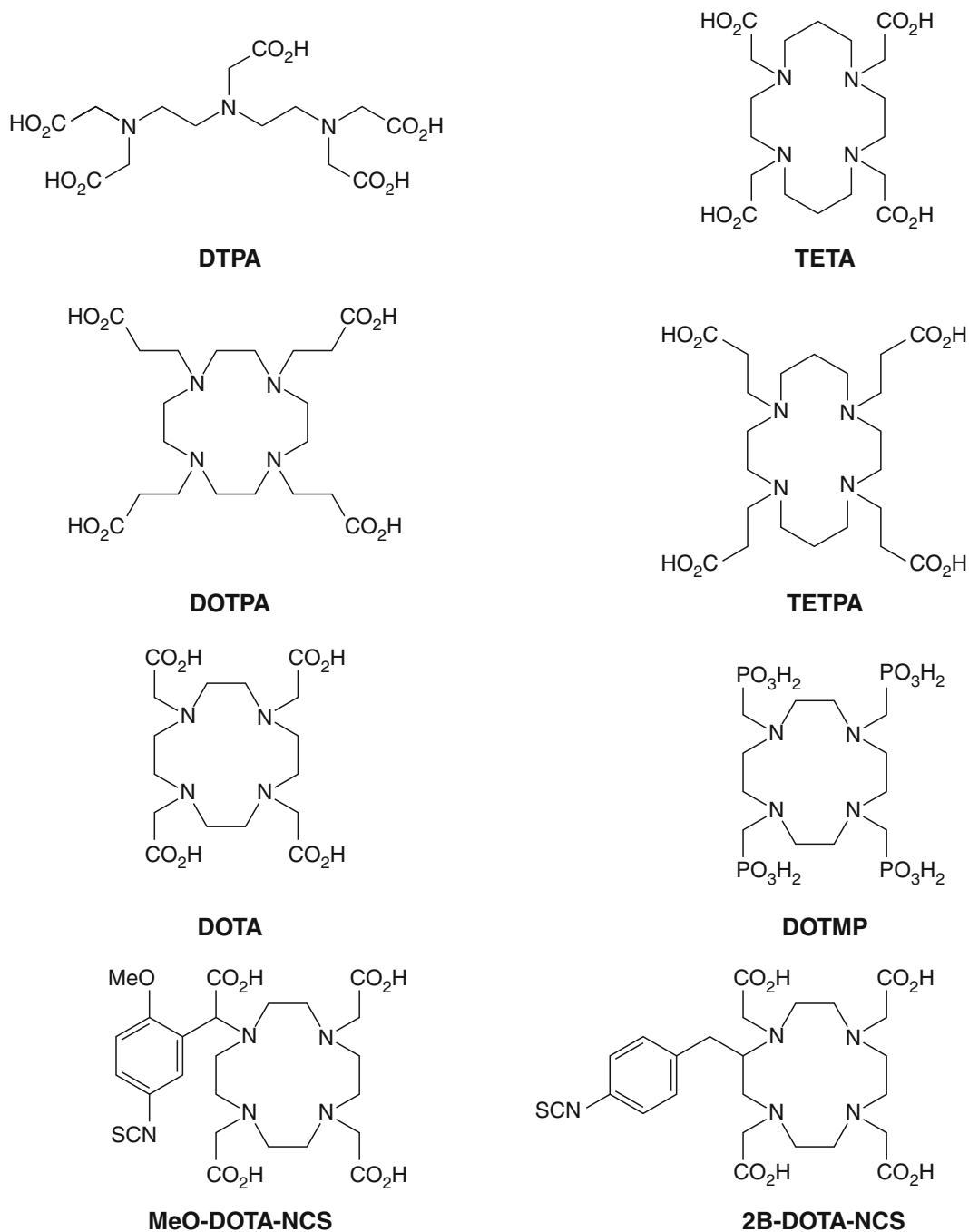
Fig. 10.4 Structures of chelators assayed for the coordination of $^{225}Ac^{3+}$

10.2.3.1 In the Clinic

A report of the first clinical radiopharmaceutical therapy study with ^{225}Ac-lintuzumab was recently published [15]. These phase 1 trial data established that RPT with ^{225}Ac-lintuzumab against AML was feasible, safe, and had potent
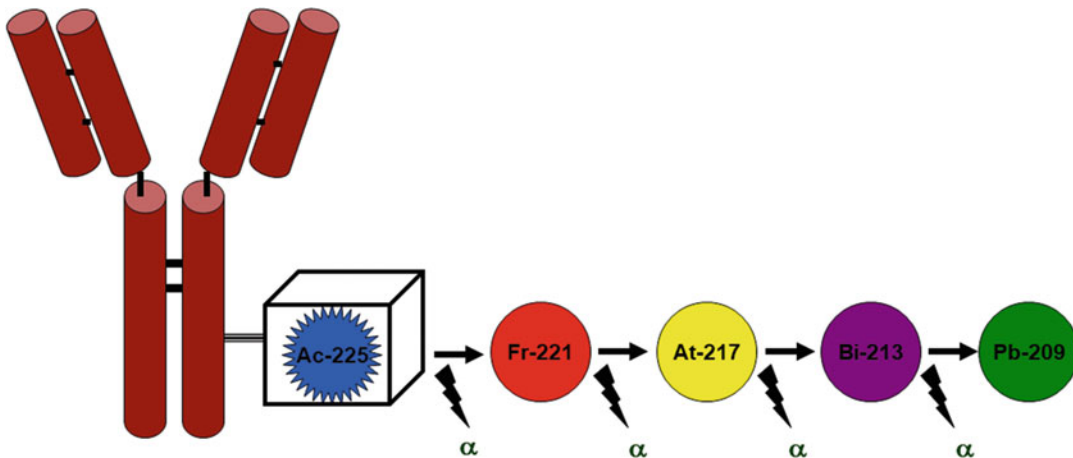
Fig. 10.5 An illustration of the ²²⁵Ac-Lintuzumab nanogenerator. The mAb, DOTA chelator, and ²²⁵Ac radionuclide are illustrated as in Fig. 10.1, and now the several alpha particle emitting progeny are included

anti-cancer activity. The elimination of circulating blasts and/or reductions in marrow blasts was observed at all dose levels. Briefly, 18 patients—median age = 64 years; range = 45–80 years—with relapsed or refractory AML received a single dose of 18.5–148 kBq/kg ²²⁵Ac-lintuzumab. Because AML is found in the bone marrow, myelosuppression was the dose-limiting toxicity. The maximum tolerated dose was 111 kBq/kg. No renal toxicity was observed, and extramedullary toxicities were limited to transient grade 3 liver function abnormalities. Peripheral blasts in circulation were eliminated in 10/16 evaluable patients (63%) but only at doses of ≥37 kBq/kg. Blastic disease in the bone marrow was minimized in 10/15 evaluable patients (67%); 3 of these patients had marrow blasts reduced to ≤5%, and 1 patient was morphologically leukemia-free. Two-phase elimination kinetics were determined for ²²⁵Ac-lintuzumab via gamma spectroscopic counting of ²¹³Bi and ²²¹Fr in samples of whole blood, plasma, and urine at secular equilibrium; the mean plasma $t_{1/2}$ (α) and $t_{1/2}$ (β) values were 1.9 and 38 h, respectively.

An ensuing multicenter phase 1 trial of ²²⁵Ac-lintuzumab was conducted in combination with low-dose cytarabine (LDAC, 20 mg administered twice daily for 10 days every 4–6 weeks for up to 12 cycles). In this study, αRPT was investigated in 18 patients (median age = 77 years; range = 68–87 years) that were diagnosed with untreated AML [16]. Cytarabine was administered prior to ²²⁵Ac-lintuzumab to cytoreduce disease burden. The objective was to conduct a dose-escalation trial and determine the MTD, biological activity, and toxicity of ²²⁵Ac-Lintuzumab in combination with LDAC. In this trial, 2 fractions of ²²⁵Ac-lintuzumab were administered 1 week apart at 4–7 days after the first cycle of LDAC. Four dose levels of ²²⁵Ac-lintuzumab—18.5 ($n = 3$), 37 ($n = 6$), 55.5 ($n = 3$), and 74 ($n = 6$) kBq/kg/fraction—were examined using a 3 + 3 trial design. Bone marrow blasts were reduced in 11/14 evaluable patients (79%) evaluated after cycle 1, and the mean blast reduction was 66% (range = 19–100%). Hematologic toxicities included grade 4 neutropenia ($n = 5$) and thrombocytopenia ($n = 9$). However, the MTD was not reached, and 74 kBq/kg/fraction was selected as the phase II dose in order to minimize prolonged myelosuppression. DLT (grade 4 thrombocytopenia with marrow aplasia for >6 weeks following therapy) was observed in one patient in the 37 kBq/kg/fraction cohort and in one patient in the 74 kBq/kg/fraction cohort.

All patients responded after receiving at least 37 kBq/kg/fraction following 1 cycle of LDAC therapy compared to data for LDAC alone which showed that the median time to response was 3 cycles. Two complete remissions (CR), 1 CR with incomplete platelet recovery (CRp), and 2 CR with incomplete blood count recovery (CRi), were seen for an overall response rate (ORR) of 28%. The median response duration was 9.1 months (range = 4.1–16.9 months); the median progression-free survival (PFS) for all patients was 2.7 months (range = 1.0–16.9-months); and the median overall survival (OS) was 5.6 months (range = 1.6–32+ months).

This clinical study showed that the administration of ^{225}Ac-lintuzumab in a fractionated-dose scheme could be safely used in combination with LDAC. Furthermore, it induced remissions in patients ≥60 years of age with untreated AML. Interestingly, the peripheral blood blast count titer proved to be a robust predictor of response to ^{225}Ac-lintuzumab. In this and the initial phase 1 trial (a total of n = 36 patients), responses were observed in 8/19 patients (42%) with blast counts <200/µL compared with 0/17 patients with blast counts >200/µL (P = 0.002). A higher titer of circulating blasts seems to accumulate more of the drug, thereby limiting the dose available to marrow targets.

10.3 Something Extra

The quantification of ^{225}Ac radioactivity must consider whether the sample is in secular equilibrium with the decay progeny. The activity of ^{225}Ac can be measured using a Squibb CRC-17 Radioisotope Calibrator (E.R. Squibb and Sons, Inc., Princeton, NJ) with the dose calibrator potentiometer set at 775 and multiplying the displayed activity value by 5. The ^{225}Ac activity can be measured when it achieves secular equilibrium with its several daughters, which can take approximately 20 h (though reasonable estimates can be achieved by 6 h; Fig. 10.6). Similarly, counting assays that rely upon instant thin layer chromatography (ITLC) or high-performance liquid chromatography (HPLC) must be performed

at secular equilibrium since the parent and daughters may have different retention factors (R_f). If a high purity germanium (HPGe) radiation detector with pulse height multi-channel analysis is available, the ^{221}Fr or ^{213}Bi γ-emissions can be used when either of these radionuclides are in equilibrium with the parent. The counting efficiency of the HPGe detector for these γ-emissions needs to be determined from a plot of counting efficiency^{-1} vs. the γ-energy of standard radionuclide sources.

10.4 Conclusions and Future Direction

^{225}Ac-lintuzumab has been clinically established as a treatment for AML and is the first study in humans to demonstrate the feasibility of targeted cancer therapy with an in vivo α-particle generator. This CD33-targeting α-particle generator effectively eliminated circulating blasts and reduced the number of marrow blasts across all dose levels. ^{225}Ac-lintuzumab has an acceptable safety profile, exhibiting toxicity limited to myelosuppression. However, it should be noted that disease is present in the bone marrow. Moving forward, it is anticipated that ^{225}Ac-lintuzumab could be best used in combination with cytotoxic chemotherapies that aim to reduce the disease burden prior to the administration of ^{225}Ac-lintuzumab.

10.5 The Bottom Line

- Lintuzumab is an optimized CD33-targeted mAb that was humanized to eliminate immunogenicity and thus be acceptable for repeat human use.
- Novel chelator technology and radiosynthetic methods were developed to attach ^{225}Ac to the mAb for in vivo use.
- The in vivo fates of the ^{225}Ac and its several radioisotopic progeny are managed by the stable chelation with DOTA and the internalization of the mAb in targeted disease, respectively.
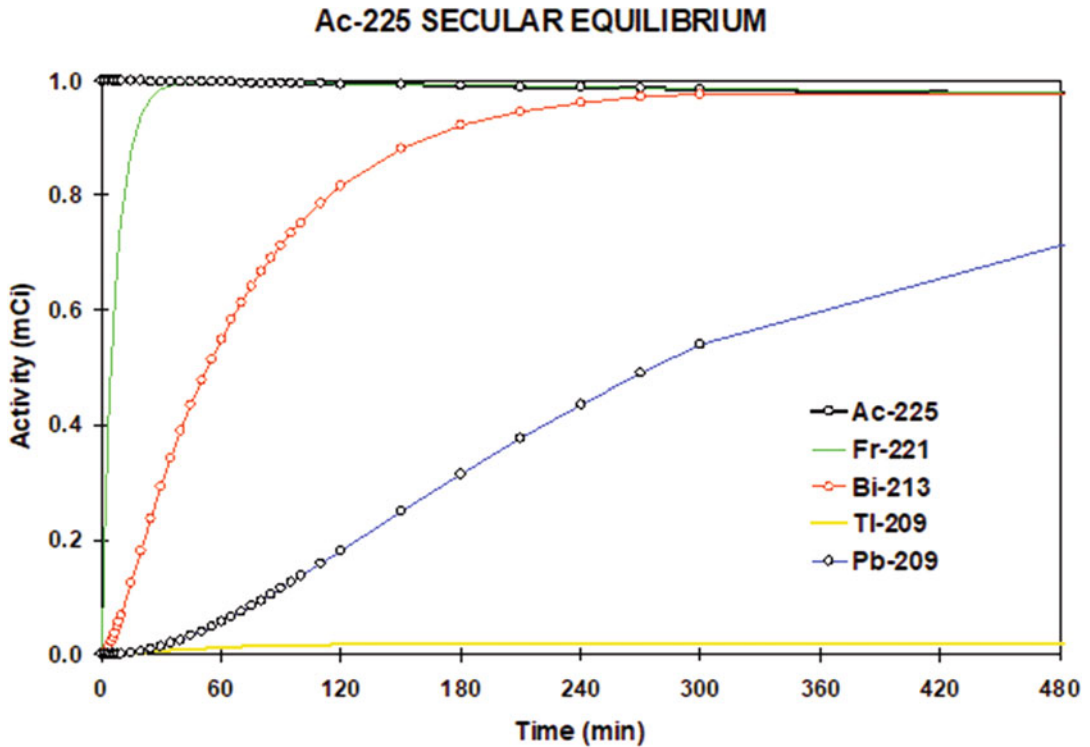
Fig. 10.6 Graphical illustration of the growth of [221]Fr, [213]Bi, [209]Tl, and [209]Pb as these daughters approach secular equilibrium with [225]Ac

- Leukemia presents with tumor burdens as large as 1 Kg and pre-RPT cytoreduction strategies are necessary to minimize disease burden.
- Myelosuppression is the dose-limiting toxicity because AML is found in the bone marrow. No renal toxicity was observed, and extramedullary toxicities were limited to transient grade 3 liver function abnormalities.
- A path has been laid out for the wider use of [225]Ac radiotherapeutics in other cancers using different targeting molecules.

References

1. Tanimoto M, Scheinberg DA, Cordon-Cardo C, Huie D, Clarkson BD, Old LJ. Restricted expression of an early myeloid and monocytic cell surface antigen defined by monoclonal antibody M195. Leukemia. 1989;3(5):339–48.
2. Jurcic JG, Caron PC, Nikula TK, Papadopoulos EB, Finn RD, Gansow OA, Miller WH Jr, Geerlings MW, Warrell RP Jr, Larson SM, et al. Radiolabeled anti-CD33 monoclonal antibody M195 for myeloid leukemias. Cancer Res. 1995;55(23 Suppl):5908s–10s. PMID: 7493368.
3. Co MS, Avdalovic NM, Caron PC, Avdalovic MV, Scheinberg DA, Queen C. Chimeric and humanized antibodies with specificity for the CD33 antigen. J Immunol. 1992;148(4):1149–54. PMID: 1737932.

4. Nikula TK, Bocchia M, Curcio MJ, Sgouros G, Ma Y, Finn RD, Scheinberg DA. Impact of the high tyrosine fraction in complementarity determining regions: measured and predicted effects of radioiodination on IgG immunoreactivity. Mol Immunol. 1995;32 (12):865–72. PMID: 7565813.

5. McDevitt MR, Finn RD, Sgouros G, Ma D, Scheinberg DA. An 225Ac/213Bi generator system for therapeutic clinical applications: construction and operation. Appl Radiat Isot. 1999;50 (5):895–904. PMID: 10214708.

6. Brechbiel MW, Gansow OA. Synthesis of C-functionalized Trans-cyclohexyldiethylene-triaminepenta-acetic acids for labeling of monoclonal antibodies with the bismuth-212 a-particle emitter. J Chem Soc Perkin Trans. 1992;1:1173–8.

7. Rosenblat TL, McDevitt MR, Mulford DA, Pandit-Taskar N, Divgi CR, Panageas KS, Heaney ML, Chanel S, Morgenstern A, Sgouros G, Larson SM, Scheinberg DA, Jurcic JG. Sequential cytarabine and alpha-particle immunotherapy with bismuth-213-lintuzumab (HuM195) for acute myeloid leukemia. Clin Cancer Res. 2010;16(21):5303–11. PMID: 20858843.

8. McDevitt MR, Ma D, Lai LT, Simon J, Borchardt P, Frank RK, Wu K, Pellegrini V, Curcio MJ, Miederer M, Bander NH, Scheinberg DA. Tumor therapy with targeted atomic nanogenerators. Science. 2001;294(5546):1537–40. PMID: 11711678.

9. Sgouros G, Ballangrud AM, Jurcic JG, McDevitt MR, Humm JL, Erdi YE, Mehta BM, Finn RD, Larson SM, Scheinberg DA. Pharmacokinetics and dosimetry of an alpha-particle emitter labeled antibody: 213Bi-HuM195 (anti-CD33) in patients with leukemia. J Nucl Med. 1999;40(11):1935–46. PMID: 10565792.

10. Lambrecht RM, Tomiyoshi K, Sekine T. Radionuclide Generators. Radiochim Acta. 1997;77:103–23.

11. Yamana H, Mitsugashira T, Shiokawa Y, Sato A, Suzuki S. Possibility of the existence of divalent actinium in aqueous solution. J Radioanal Chem. 1983;76 (1):19–26.

12. Kulikov EV, Novgorodov AF, Schumann D. Hydrolysis of ^{225}Actinium trace quantities. J Radioanal Nucl Chem. 1992;164(2):103–8.

13. Sgouros G, Roeske JC, McDevitt MR, Palm S, Allen BJ, Fisher DR, Brill AB, Song H, Howell RW, Akabani G, SNM MIRD Committee, Bolch WE, Brill AB, Fisher DR, Howell RW, Meredith RF, Sgouros G, Wessels BW, Zanzonico PB. MIRD Pamphlet No. 22 (abridged): radiobiology and dosimetry of alpha-particle emitters for targeted radionuclide therapy. J Nucl Med. 2010;51(2):311–28. PMID: 20080889.

14. McDevitt MR, Ma D, Simon J, Frank RK, Scheinberg DA. Design and synthesis of 225Ac radioimmunopharmaceuticals. Appl Radiat Isot. 2002;57(6):841–7. PMID: 12406626.

15. Rosenblat TL, McDevitt MR, Carrasquillo JA, Pandit-Taskar N, Frattini MG, Maslak PG, Park JH, Douer D, Cicic D, Larson SM, Scheinberg DA, Jurcic JG. Treatment of Patients with Acute Myeloid Leukemia with the Targeted Alpha-Particle Nanogenerator Actinium-225-Lintuzumab. Clin Cancer Res. 2022;28 (10):2030–7. PMID: 35247915.

16. Jurcic J, Levy M, Park J, Ravandi F, Perl A, Pagel J, Smith B, Orozco J, Estey E, Kantarjian H, Dragan Cicic D, Scheinberg D. Phase I trial of alpha-particle immunotherapy with 225Ac-lintuzumab and low-dose cytarabine in patients age 60 or older with untreated acute myeloid leukemia. J Nucl Med. 2017;58(supplement 1):456.

Nai-Kong V. Cheung, Kim Kramer, Shakeel Modak, Brian H. Kushner, Mahiuddin Ahmed, Brian Santich, Sarah Cheal, and Steven Larson

11.1 Introduction

GD2-targeting monoclonal antibodies have shown utility in the treatment of high-risk neuroblastoma [1, 2]. These include murine 3F8 [2], hu14.18-K322A [3], ch14.18 (Dinutuximab) [1], and humanized 3F8 (hu3F8, Naxitamab) [4], with the latter two already approved by the United States Food and Drug Administration (FDA). A wide variety of GD2-targeting tools have been developed for preclinical and clinical trials, including radiolabeled antibodies, bispecific antibodies, drug conjugates, nanoparticles, and chimeric antigen receptor (CAR) modified T cells [5]. Beyond neuroblastoma, ganglioside GD2 is expressed on many types of stem cells as well as a range of pediatric and adult solid tumors, including astrocytoma, retinoblastoma, Ewing sarcoma, rhabdomyosarcoma, osteosarcoma, leiomyosarcoma, liposarcoma,

fibrosarcoma, small cell lung cancer, melanoma, and breast cancer. GD2 has a number of advantages for targeted therapy, chief among them the high density of the antigen on several tumor types and its restricted expression on normal tissues [6, 7]. More recently, its potential as a target for a cancer vaccine was demonstrated in high-risk neuroblastoma [8, 9]. In 2009, GD2 was ranked as the 12th most important cancer antigen by a National Cancer Institute pilot program that sought to prioritize cancer antigens based on a variety of factors including their therapeutic function, immunogenicity, role in oncogenicity, expression level, and prevalence among human cancers [10].

11.2 Disialoganglioside GD2

In 1942, a German biochemist Ernst Klenk isolated a new group of carbohydrate-rich glycolipids from ganglion cells and named them "gangliosides" [11]. Gangliosides are composed of glycosphingolipid and sialic acids (i.e., N-acetylneuraminic acid, Neu5Ac, or NANA). They are found on the cell surface of the nervous system in vertebrates. Lower vertebrates such as fish and amphibians have more polysialogangliosides containing 4 to 5 NANA residues, whereas the gangliosides of higher vertebrates (i.e., reptiles, birds, and mammals) have only 1 to 3 NANA residues.

N.-K. V. Cheung (✉) · K. Kramer · S. Modak
B. H. Kushner · S. Larson
Memorial Sloan Kettering Cancer Center,
New York, NY, USA
e-mail: cheungn@mskcc.org

M. Ahmed
Vitruviae, Nutley, NJ, USA

B. Santich
Y-mAbs Therapeutics, New York, NY, USA

S. Cheal
Molecular Imaging Innovations Institute, Department of Radiology, Weill Cornell Medicine, New York, NY, USA
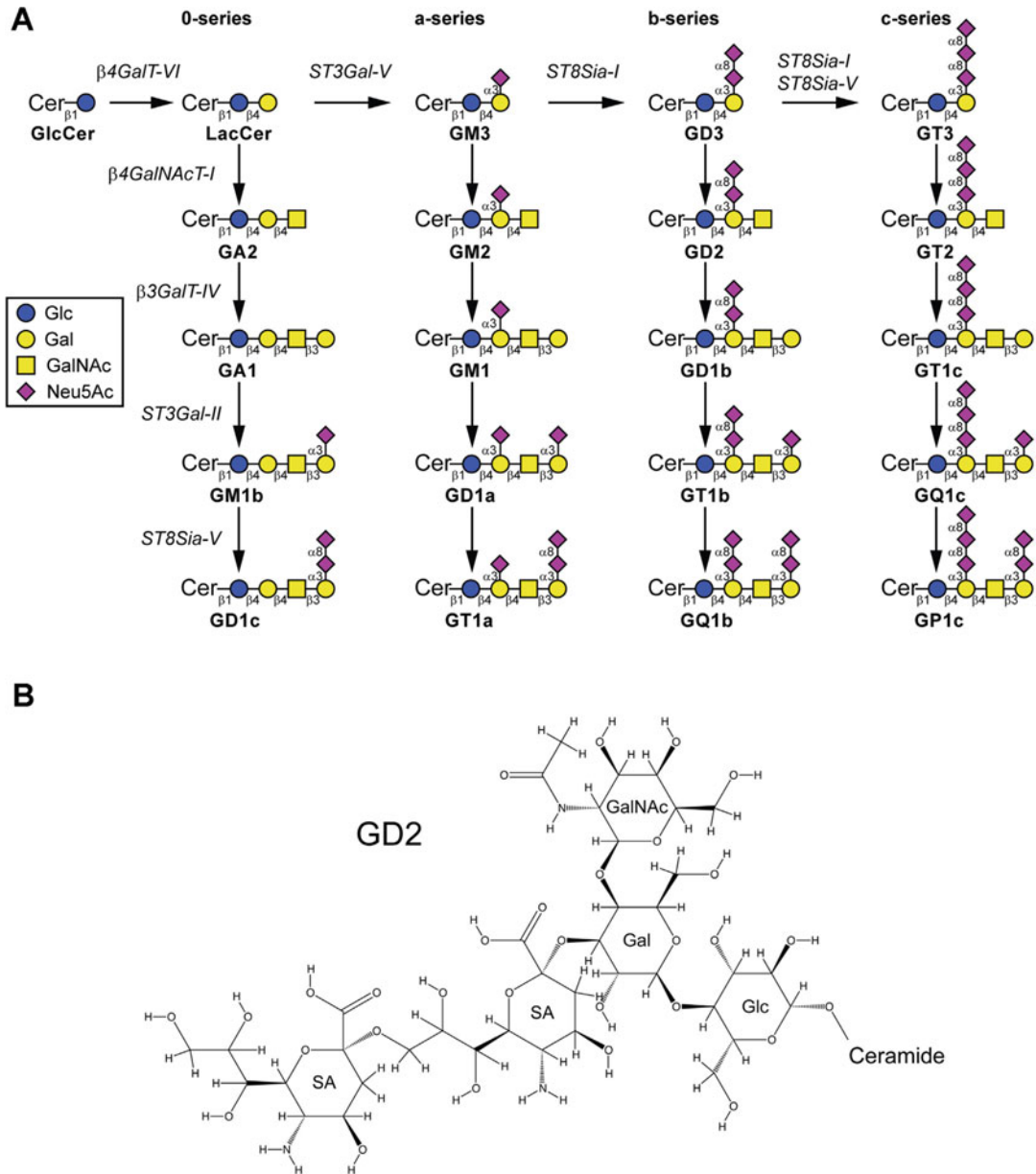
Fig. 11.1 (**a**) The biosynthesis of gangliosides by the stepwise addition of monosaccharides to ceramide. The sequential enzyme actions of ST3Gal V (GM3 synthase), ST8Sia I (GD3 synthase), and ST8Sia V (GT3 synthase) create the precursors for a-, b-, and c-series gangliosides, respectively, while the 0-series gangliosides are directly derived from Lactosylceramide. The nomenclature of gangliosides follows that of Svennerholm. (adapted from http://www.frontiersin.org/Journal/10.3389/fonc.2015.00300/abstract. (**b**) The structure of GD2. (Adapted and modified with permission from a version that appears in Ahmed et al. [33])

The nomenclature of gangliosides is based on the number and position of the NANA residues. GD2 has two NANA—an alpha-2,8 bound sialic acid and an alpha-2,3 bound sialic acid—and is derived from GD3 via the addition of Gal-NAc by GM2/GD2 synthase (β1,4-N-acetylgalactosaminyltransferase) (Fig. 11.1). Interestingly, GM2/GD2 synthase has been

proven to be a highly sensitive and specific marker of residual neuroblastoma in the bone marrow, with major prognostic impact on patient survival [12]. The terminal penta-oligosaccharide carries the epitope of GD2 to which most specific antibodies are directed. As depicted in the synthesis pathways for gangliosides, the epitope neighborhood for GD2 could be clearly defined. For example, GD3 and GD1b are the most common cross-reactive gangliosides recognized by anti-GD2 antibodies. This cross reactivity is critical, since GD3 and GD1b are expressed in many healthy human tissues and could thus divert therapies intended for GD2 besides and increase bystander toxicity. A derivative of GD2 with a 9-O-acetyl modification on the terminal sialic acid is called O-acetyl-GD2. While most anti-GD2 antibodies cross-react with O-GD2, some do not; in addition, anti-O-GD2 antibodies with no cross-reactivity with GD2 had less cross-reactivity with normal neurons [13].

GD2 is expressed on a number of stem cells—including neural, mesenchymal, and peripheral sympathoadrenergic progenitors—but its function in neural differentiation and proliferation remains uncertain. Postnatal somatic expression of GD2 is restricted to the central nervous system (CNS), predominantly neuronal cell bodies, mesenchymal stem cells (MSCs), and peripheral nerves, though skin melanocytes express low levels of the antigen as well. GD2 is thought to play a role in the maintenance and repair of nervous tissues via the regulation of complement activation and subsequent inflammation, although the exact immunologic mechanism remains obscure. Like other disialogangliosides, GD2 could interact with siglec7, functioning as a "do not eat me" ligand [14].

GD2 is highly expressed on a variety of embryonal cancers (i.e., neuroblastoma, brain tumors, retinoblastoma, Ewing sarcoma, rhabdo-myosarcoma), bone tumors (i.e., osteosarcoma, Ewing sarcoma), soft tissue sarcomas (i.e., leiomyosarcoma, liposarcoma, fibrosarcoma), neural crest derived tumors (i.e., small cell lung cancer and melanoma), and breast cancer [7, 11,

15]. The cell biology of GD2 was previously summarized [11]. Soluble GD2 has been reported to be immunosuppressive for human dendritic cells [16] and T cells [17] (probably through myeloid-derived suppressor cells [18]) as well as regulatory T cells [19]. As a biomarker, both the detection and pharmacokinetics of cell-free GD2 in plasma have been extensively studied [20], but its interference with GD2-directed therapies in patients has not been reported.

11.3 GD2 as a Target for Antibodies for Cancer Diagnosis and Therapy

In this chapter, we will retrace the evolution of the diagnostic and therapeutic applications of the murine anti-GD2 mAb 3F8, from radioimmunodiagnosis (RID) to radioimmunotherapy (RIT), from systemic administration to compartmental administration, from mouse studies to clinical trials, and from a murine immunoglobulin (IgG) to humanized bispecific antibody created to optimize pretargeted radioimmunodiagnosis (PRID) and radioimmunotherapy (PRIT).

Murine anti-GD2 monoclonal antibodies (mAb) were first described in the early 1980s. Since then, a wide variety of notable advances have been made using these antibodies for cancer therapy. Anti-GD2 mAbs can detect GD2-posisitve tumor cells via immunocytology and GD2-posisitve tumors in patients via radioimmunoscintigraphy [21, 22]. For some tumors, like neuroblastoma, GD2 is an ideal target because of its abundance—upwards of 10^7 copies per cell [23]—as well as its surface retention after binding to an antibody [21]. Although GD2 is expressed in neurons, the human brain is protected from parenteral anti-GD2 mAbs by the blood-brain barrier [21]. Furthermore, GD2 antigen loss from tumors is uncommon as an escape mechanism after antibody targeted therapy [24]. In addition to inducing apoptosis and reducing invasiveness, anti-GD2 mAbs can arm human leukocytes to perform

Fc-dependent tumor lysis via antibody-dependent cell-mediated cytotoxicity (ADCC) and monocyte-macrophage mediated phagocytosis [25]. Granulocytes and natural killer (NK) cells carry Fc-receptors—FcγRIIA (CD32) and FcγRIIIA (CD16A), respectively—on their cell surface. When these Fc-receptors are engaged by the mAb bound to the tumor cells, cytotoxic granules and cytokines are released, killing the tumor cells via ADCC [25]. These Fc-receptors can also mediate phagocytosis by activating monocytes and macrophages [25], even when they are forced into M2 macrophages by macrophage colony stimulating factor (M-CSF) [26, 27]. When complement C1q binds to the Fc of tumor-bound mAb, it initiates a complement activation cascade leading to the formation of membrane attach complex, creating pores in the cell membrane [25] and lysing tumor cells, a process called "complement-mediated cytotoxicity" (CMC).

11.4 Murine Anti-GD2 Monoclonal Antibodies

The murine IgG3 antibody 3F8 was initially tested in a first-in-human phase I clinical trial in patients with neuroblastoma and malignant melanoma in the late 1980s [28]. The study showed that its major side effects—pain, fever, hypertension, and urticaria—were severe but controllable. Pain was unexpected and did not correlate with the dose of 3F8 or the duration of the 3F8 infusion. Furthermore, selective tumor uptake was demonstrated using radioimmunoscintigraphy with ^{131}I-labeled 3F8, with no uptake in the brain or spinal cord and no non-specific uptake in the reticuloendothelial system (liver, spleen, lymph nodes) [28]. Serum human-anti-mouse antibody (HAMA) levels were detected in >80% of patients with repeated infusions, and those with HAMA during 3F8 infusion no longer had pain [28].

Subsequently phase II studies demonstrated the anti-tumor effects of 3F8, especially when the mAb combined with granulocyte-macrophage colony stimulating factor (GM-CSF). The combination of 3F8 + GM-CSF appeared to improve the long-term survival in patients with high risk (HR) neuroblastoma; indeed, few relapses were seen after follow-up beyond 10 years [2]. When myeloid cells were analyzed, granulocyte activation by GM-CSF could be quantified via their CD11b activation epitope CBRM1/5, which correlated with treatment outcome [29]. When NK cells were analyzed, the missing ligand for inhibitory killer immunoglobulin-like receptor (KIR) was significantly associated with better tumor control [2, 30, 31]. ME36.1 and 14.G2a are two other murine anti-GD2 mAbs of the IgG2a subclass that exhibited lower affinities for GD2 (K_D = 19 nM and 77 nM, respectively) compared to mouse 3F8 (K_D = 5 nM) [32, 33]. 14. G2a was tested in clinical trials and produced similar side effects and anti-tumor activity as mouse 3F8 [15]. Anti-GD2 mAbs have also been used to target various types of payloads to tumors, including radionuclides, drugs, cytokines, and nanoparticles [5]. GD2 has also been an effective target for bispecific antibodies [34, 35] chimeric antigen receptor (CAR) modified T cells [36, 37], and—as we will see later in this chapter—pretargeted radioimmunotherapy [38, 39].

11.5 GD2 as a Target for Radioimmunodiagnosis and Radioimmunotherapy Using Full 3F8 IgG

3F8 has nanomolar affinity for GD2 [32], shows no reactivity with blood or bone marrow cells, and—unlike antibodies against GD3—does not activate T cells [40, 41]. More importantly, 3F8's murine IgG3 Fc domain has low affinity for human and mouse FcRs unless the antibody is bound to its target [42]. In xenograft models, the absence of the uptake of 3F8-based radioimmunoconjugates in the RES has facilitated highly specific and sensitive radioimmunodiagnosis (RID) as well as effective radioimmunotherapy (RIT).

11.6 Preclinical Studies with [131]I-3F8

Neuroblastoma 125 μg of 3F8 conjugated to 50 μCi radioactive iodine (4 mCi of ^{131}I per mg of antibody) administered intravenously exhibited selective localization in GD2-positive human neuroblastoma (NB) xenografts (5 PDXs, IMR-6, LAN1, NMB7) compared to two control xenografts (Ewing sarcoma and Hela cells) with low GD2 expression [21]. Furthermore, the uptake of the radioiodinated 3F8 was specific for 3F8 when compared to pooled mouse IgG or irrelevant IgG3 control (N-S.7) (Table 11.1). Both small (50 mg) and large tumors (>2 g) showed radiolocalization. While the effective half-life of the radioactivity in the tumor was 86 h, all the other organs exhibited relatively rapid washout with effective half-lives of <20 h until the end of the second day (one exception: a 29 h half-life for the brain). After 48 h, the half-life of the radioimmunoconjugate in both the tumor and normal organs was similar: ~60 h. Radioactivity circulating in the blood was protein-bound and TCA-precipitable. Robust and specific uptake of [131]I-3F8 in tumor tissue over normal organs was rapid (within 24 h) and persistent (through >96 h) (Table 11.2). The activity concentration of the radioimmunoconjugate in the tumor (typically expressed as percent injected dose per gram; % ID/g) ranged from 8% to 50% and was inversely correlated with tumor size. Assuming 10^7 GD2 molecules/cell, 1 mg of 3F8 was needed to saturate 1 g of tumor, hence the low %ID/g with large tumors. Optimal tumor-to-normal tissue activity concentration ratios were reached by 24–48 h. Critically, there was no abnormal uptake in the reticuloendothelial system or in the brain. Based on the radioactivity area under the curve (AUC), the relative radiation dose to normal organs was estimated to be 1–20% of the tumor dose, with the blood receiving the highest background dose. In light of these data, [124]I-3F8 was soon developed for quantitative scintigraphy in rats (Fig. 11.2) [43].

Table 11.1 Groups of mice bearing human NB IMR-6 tumors ($n = 5$), control Hela tumors ($n = 4$), or Ewing sarcoma tumors ($n = 8$) were injected with 50 μCi of ^{125}I-labeled 3F8 and 50 μCi of ^{131}I-labeled control antibody N-S.7

Tumor specificity of 3F8 biodistribution tumor to nontumor ratios						
	NB		HELA		Ewing	
Tissues	3F8	N-S.7	3F8	N-S.7	3F8	N-S.7
Blood	27.6	0.5	1.4	0.6	1.4	0.3
Lung	27.1	0.9	2	1.5	3.1	0.8
Skin	28	1.1	1.6	1.7	3.5	0.9
Kidney	39.1	1.4	3	2	4.7	1.1
Heart	64.9	1.6	4.1	2.8	4.8	1.1
Stomach	39.6	2.5	2.2	3.1	7.1	2.3
Spleen	24.2	2.3	1.3	1.9	5.7	1.6
Liver	59	2	2.7	1.7	7.8	1.8
Small bowel	79.7	2.8	2.8	3.5	9.4	2.9
Bone	121	4	3.9	3.8	11.6	2.9
Muscle	130	4.4	7.4	5.5	14.1	2.9
Large bowel	28.3	3.2	5.8	5.2	18	5.5
Brain	403	12.3	26.7	16	36.2	14.8

Mice were sacrificed 4 days after the administration of the radioimmunoconjugates for biodistribution studies. The radioactivity per gram tissue was calculated, and the tumor-to-non-tumor activity concentration ratios were tabulated for each organ. Selective uptake was seen in human NB xenografts compared with Hela and Ewing sarcoma xenografts. 3F8 distributed in NB xenograft-bearing mice with an average tumor-to-non-tumor activity concentration ratio (excluding the brain) of 56, and a ratio of 403 for the brain. For Hela tumor xenografts, the respective values were 3.2 and 26.7, and for Ewing sarcoma xenografts, 7.6 and 36.2. The biodistribution of the irrelevant antibody N-S.7 produced corresponding ratio values of 2.2/12.3 for NB, 2.8/16 for Hela, and 2/14.8 for Ewing sarcoma xenografts Reprinted from Ref. [21]

Table 11.2 The tissue distribution kinetics of 50 μCi of ^{131}I-3F8 intravenously administered to nude mice bearing NB PDX and sacrificed 24, 48, and 96 h thereafter

Kinetics of tumor and tissue radioactivity (%ID/g)			
Hours after MoAb injection			
Tissue	24	48	96
Tumor	25.0 ± 7.7	22.7 ± 8.0	15.1 ± 6.1
Blood	12.8 ± 1.0	4.9 ± 2.1	3.6 ± 2.0
Lung	6.5 ± 0.7	2.6 ± 1.1	1.8 ± 0.8
Skin	5.3 ± 1.6	2.4 ± 0.9	1.9 ± 0.9
Kidney	4.4 ± 0.3	1.7 ± 0.7	1.1 ± 0.6
Heart	4.0 ± 0.6	1.5 ± 0.6	1.1 ± 0.6
Stomach	4.1 ± 0.9	1.4 ± 0.2	0.4 ± 0.1
Spleen	3.3 ± 0.9	2.0 ± 0.7	1.7 ± 0.3
Liver	3.1 ± 0.8	1.4 ± 0.4	0.8 ± 0.3
Small bowel	2.0 ± 0.4	0.7 ± 0.2	0.5 ± 0.2
Bone	2.0 ± 0.5	1.0 ± 0.4	0.7 ± 0.1
Muscle	1.7 ± 0.3	0.7 ± 0.2	0.4 ± 0.2
Large bowel	1.4 ± 0.2	0.5 ± 0.2	0.3 ± 0.2
Brain	0.3 ± 0.01	0.2 ± 0.1	0.2 ± 0.1

The %ID/g values were calculated and corrected for radioactive decay. While the effective half-life of radioactivity in the tumor was 86 h, all the other organs (exception: 29 h for the brain) exhibited rapid washout with effective half-lives of <20 h until the end of the second day. 48 h following the injection of the radioimmunoconjugate, both tumor and normal organs had similar decay half-lives of about 60 h. All radioactivity circulating in the blood was TCA precipitable, i.e., protein bound. %ID/g values are expressed as mean ± SD (n = 3 at 24, 48, 96 h)
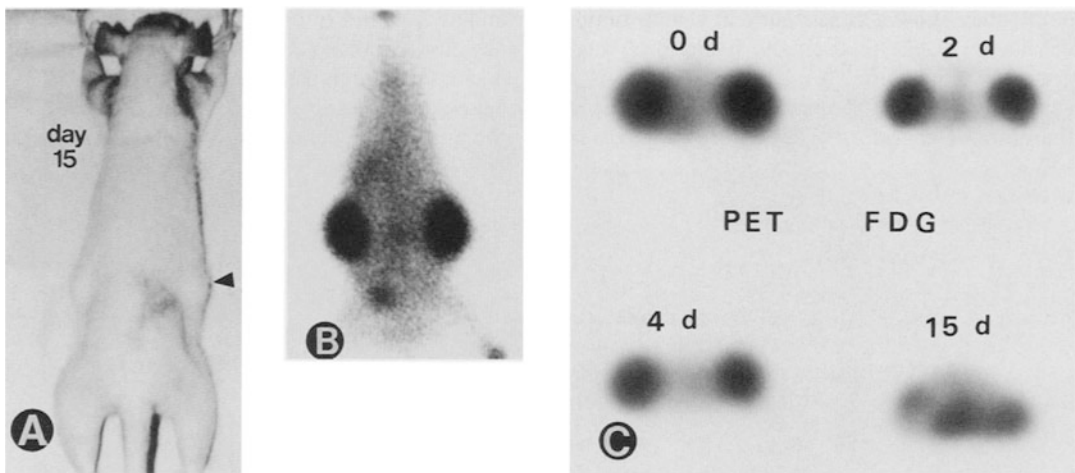Reprinted from Cheung et al. [21]

Fig. 11.2 PET scans for the measurement of changes in glucose metabolism following ^{131}I-3F8 therapy. (**a**) Photograph of nude rat with bilaterally implanted neuroblastoma tumors (depicted by arrow) 15 days post-injection of ^{131}1-3F8. At this time, tumor size was considerably reduced, almost 90% below their original volume. (**b**) Pinhole gamma camera image of a xenograft-bearing rat 24 h after the administration of ^{131}I-3F8. (**c**) ^{18}F-FDG PET images on days 0, 2, 4, and 15 following ^{131}I-3F8 therapy. The level of the transaxial slices shown by arrow in (**a**). The radiation dose from ^{131}I-3F8 was ~5800 cGy. The decreases in ^{18}F-FDG metabolism relative to day 0 were 31%, 50%, and 64% on days 2, 4, and 15, respectively. (Reprinted from Ref. [43])
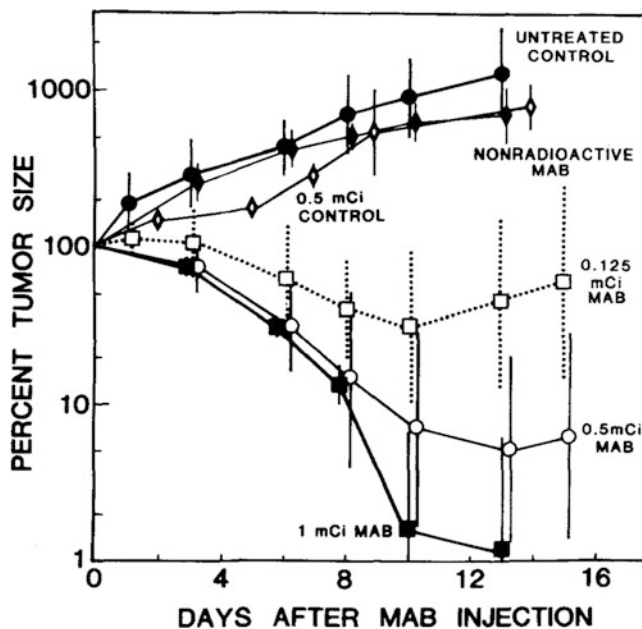
Fig. 11.3 In vivo treatment of mice (n = 3–7 per group) bearing human NB xenografts. Mice bearing established NB xenografts were treated intravenously with ^{131}I-3F8 (l00 µg 3F8, carrying 0.125 mCi, 0.5 mCi, and 1 mCi of ^{131}I). The tumor response over time (in days) was expressed as a percent of the original tumor volume at the beginning of the experiment. Data points represent experimental replication in groups of 3–7 mice. The geometric means ± SD of the percent tumor sizes are depicted. The control group (• sold circle) did not receive any treatment. The non-radioactive mAb group (♦) received 100 µg of unlabeled 3F8. The 0.5 mCi group (◦) received 0.5 mCi of a ^{131}I-radiolabeled control antibody (N-S.7) iv. (Reprinted from Ref. [44])

To test the therapeutic benefit of ^{131}I-3F8, 0.125–1.0 mCi (~230–1840 MBq/kg) of the radioimmunoconjugate were administered intravenously to mice bearing NB xenografts (5 PDXs as well as LAN1 and NMB7 tumors) (Fig. 11.3). The tumoral activity concentration over time was calculated from scintigraphy, and the radiation dose to individual tumors was calculated. While the untreated control tumors enlarged by tenfold, the treated tumors shrank by 95% over 12 days. Both the rate of shrinkage and the duration of tumor response were dose dependent. Calculated doses to the tumor of more than 10,000 rad could be achieved, and only tumors that received more than 4200 rad were completely ablated without recurrence (Fig. 11.4). Recurrent tumors were not antigen negative or radioresistant, did not lose GD2 by IHC, and usually responded again to treatment with ^{131}I-3F8 [44]. The radiation doses to normal organs as percentages of tumoral dose were favorable but not ideal: blood >20%; lung,

20%; skin, 17%; spleen, 15%; kidney, 12%; heart, 11%; stomach, 10%; liver, 8%; small bowel, 6%; femur, 5%; muscle, 5%; brain, <1%. The total-body radiation dose—calculated on the basis of the serial gamma imaging of mice receiving 0.5 mCi ^{131}I-3F8—was between 110 and 380 cGy. This dose decreased linearly with increasing uptake in the tumor (Fig. 11.5), raising the concern that toxicity could substantially increase in the absence of tumor tissue as an antigen sink.

All the mice treated with 0.5–1 mCi ^{131}I-3F8 lost up to 20% of their weight during the first 20 days of the study, but this weight loss was reversible in most animals after 2 weeks. Necropsies at 1 month or more after 0.5 mCi ^{131}I-3F8 did not show detectable radiation damage to any of vital organs compared to untreated normal nude mice or untreated xenograft-bearing mice. However, all the mice given 1 mCi ^{131}I-3F8 showed bone marrow hypoplasia.
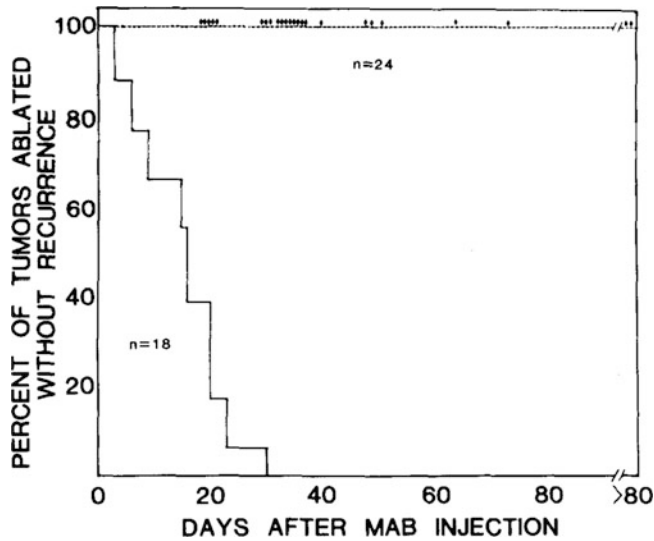
Fig. 11.4 The relationship between remission and radiation dose delivered. The y-axis shows the percent of tumors in remission. The x-axis shows the number of days after the injection of ^{131}I-3F8. Eighteen tumors with radiation doses of <3900 rad recurred within 30 days of treatment; 24 tumors with radiation dose of >4200 rad had no detectable tumor recurrence. Each solid diamond (◆) represents an individual treated tumor at the time of autopsy or necropsy. mAb = ^{131}I-3F8. (Reprinted from Ref. [44])

Fig. 11.5 Radiation dose (in cGy) delivered to NB xenograft as a function of the injected ^{131}I-3F8 in mCi per g tumor. A total of 28 mice were analyzed, with $r = 0.97$ and $P < 0.001$. Open circle (O) = mice with tumors ablated; Solid circle (•) = mice with recurrent tumors: Open square (□) = mice with 1 tumor ablated and 1 tumor recurrent. The weighted mean radiation dose is used. mAb = ^{131}I-3F8. (Reprinted from Ref. [44])
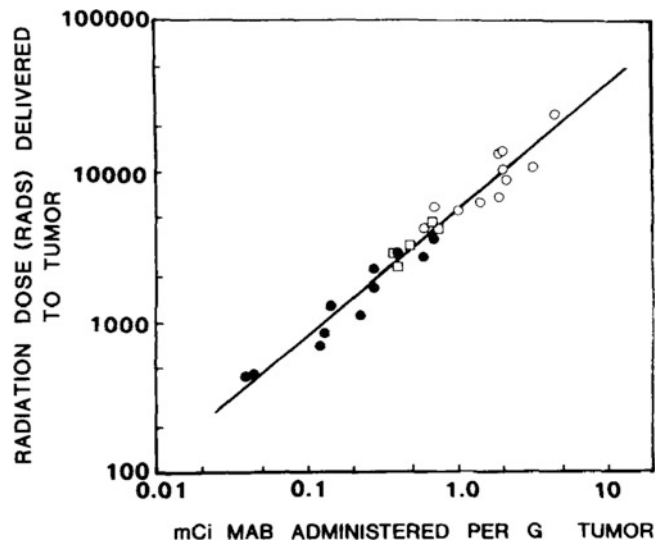
Osteosarcoma Radiotargeting was next investigated in human osteosarcoma (OS) in which GD2 expression is weaker and more heterogeneous [7]. The in vivo performance of the native mAb (3F8) as well as an F(ab′)$_2$ fragment (p-3F8) was tested in athymic nude mice bearing human osteosarcoma xenografts. To this end, mice were sacrificed for biodistribution 24 and 96 h after the administration of 25–50 uCi of either ^{131}I-3F8 or ^{131}I-p-3F8 or (6 mCi/mg of protein). Tumor-to-brain tissue activity concentration ratios of 2.7-58:1 and 1.4-82:1, respectively, were observed after 24 h. These ratios changed to 10-163:1 and 6.0-75:1 after 96 h (Table 11.3). Not surprisingly, the intact IgG-based radioimmunoconjugate produced

Table 11.3 Tumor versus normal tissue activity concentration ratios

Day 1

Organ	Osteoblastic osteosarcoma						Ewing sarcoma		
	3F8	114	SI[a]	p3F8	p-114	p-SI	p-3F8	p-114	p-SI
Blood	2.7[b]	0.5	5.5	6	1	6.8	3.4	0.9	4.1
Heart	6	1.8	4	12	2.2	6.2	8	2.4	3.4
Lung	3.6	1	3.4	5.9	1.2	5.6	2.9	1.1	2.9
Liver	7.5	2	4.7	12	2.1	6.1	3	1.1	2.9
Spleen	6	2	2.7	9.6	1.9	6	2.1	0.7	2.9
Kidney	4.5	1.7	3.1	9.9	0.1	93	5.7	0.1	50
Adrenals	8	2	3.8	11	1.8	11	6.4	2.1	3
Ovaries	5.6	1.7	3.1	8.4	1.8	5.5	8.3	2.6	3.4
Bladder	5.8	3.1	1.8	7.3	1.6	5.2	6.9	2.1	3.2
Stomach	4.8	3.1	1.8	3	0.7	5.2	1.1	0.4	2.5
Stomach contents	7.4	8.3	0.9	14	0.3	5.2	0.3	0.1	2.7
Small bowel	8.3	3.2	2.8	15	3.1	5.5	7	2.9	2.4
Large bowel	7.9	3.1	2.8	14	3.1	6	7.8	3	2.7
Muscle	9.8	3.6	3.7	22	4.5	5.3	17	5.6	3
Femur	9.2	3	3.5	16	3.3	5.7	9.4	3	3.2
Spine	8.9	2.5	3.9	14	2.6	6	8.3	2.7	3.2
Brain	58	15	4.3	82	16	5.4	36	13	2.8
Skin	4.5	1.8	2.5	6.2	1.6	5.1	3.4	1.4	2.6
%ID/g[c]	12.7			1.6			0.35		

Day 4

Organ	Osteoblastic osteosarcoma						Ewing sarcoma		
	3F8	114	SI[a]	p3F8	p-114	p-SI	p-3F8	p-114	p-SI
Blood	10	0.6	17	12	0.8	12	1.4	0.3	5.8
Heart	31	2.7	13	24	2.3	9.3	4.8	1.1	4.7
Lung	15	1.5	11	12	1.3	9	3.1	0.8	4.5
Liver	36	3.6	9.7	11	1.4	6.7	7.8	1.8	4.7
Spleen	18	3.2	5.5	9	1.2	8.8	5.7	1.6	3.6
Kidney	20	2.8	7.6	6	0.8	7.4	4.7	1.1	4.7
Adrenals	29	2.5	11	10	1.3	9	5.4	1.3	4.6
Ovaries	27	2.3	11	12	1.7	7.6	3.9	0.9	4.2
Bladder	14	2	7.5	16	2.4	8.3	2.8	0.7	4.3
Stomach	21	4.9	4	14	2	5.4	7.1	2.3	3.2
Stomach contents	14	10	1.3	12	2.2	4.4	13	7.1	1.8
Small bowel	36	5.3	6.7	25	3.2	6.6	9.4	2.9	3.7
Large bowel	41	602	608	25	3.4	6.8	13	3.5	3.5
Muscle	63	7.3	8.8	51	6.1	7.9	14	2.9	4.5
Femur	50	5.3	9.7	24	3.3	7.7	12	2.9	4.5
Spine	35	3.2	12	27	3.1	8	8.1	1.7	4.7
Brain	163	19	9.6	75	9.6	7.3	36	15	3.8
Skin	17	1.9	9.5	12	1.5	7.5	3.5	0.9	3.9
%ID/g[c]	8.3			0.4			3.7		

Reprinted from Ref. [45]

[a]The values of selective index (SI) are the arithmetic means of individual SI values for each organ for the mice in each experimental group. P3F8 = F(ab')$_2$ of 3F8. p-114 = F(ab')$_2$ of a control antibody TIB114)

[b]Each number represents the arithmetic mean of the T/NT activity concentration ratios for each organ of the mice in the experimental group
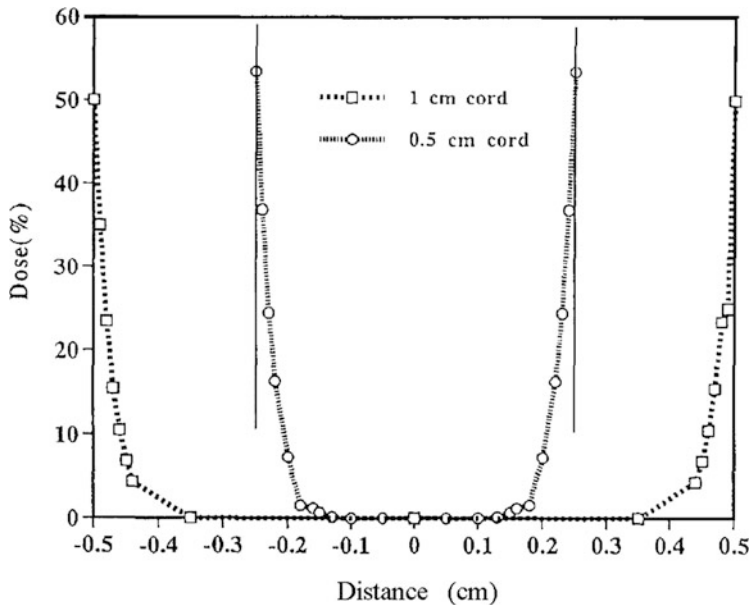
[c]Percentage of injected dose per gram of tumor

Fig. 11.6 Dose profile across the spinal cord from ^{131}I-beta rays. The estimated dose profile across the spinal cord—expressed as the percentage of the CSF dose—varied from about 50% at the cord edge to zero in the cord center. In these calculations, the cord was assumed to be a right circular cylinder measuring 1 cm in diameter at the cervical region and 0.5 cm at the level of the lumbar vertebrae in cynomolgus monkeys. It is expected that at the CSF doses calculated in this study, the dose to the spinal cord will be far below the tolerance dose (40–45 Gy) derived from external beam estimates (Kun LE, Moulder J: General principles of radiation therapy. In: Pizzo PA, Poplack DG (eds) Principles and Practice of Pediatric Oncology. J.B. Lippincott Co., Philadelphia 291, 1993) (Figure reprinted from Ref. [46])

higher tumoral activity concentrations than the F(ab')$_2$ fragment, but the former's longer tissue half-life degraded its tumor-to-healthy tissue activity concentration ratios [45].

Leptomeningeal Metastasis Model GD2(+) tumors including neuroblastoma that are metastatic to the leptomeninges are mostly incurable despite the current array of aggressive treatment modalities. The pharmacokinetics and toxicities of intraventricular [131]I-3F8 (20.35–37.80 mCi total dose) were studied in eight cynomolgus monkeys, whose patterns of GD2 expression in the CNS are similar to those of humans [46]. Four animals were immunized with intravenous 3F8 2 to 4 weeks prior to the administration of multiple doses of [131]I-3F8 (5 mCi of ^{131}I per mg of antibody 3F8). The first subject underwent a pilot study of four incremental injections of 1, 3, 5, and 7 mCi [131]I-3F8, while seven subjects received

5, 6, 7, or 8 sequential doses of 5 mCi of [131]I-3F8. Toxicities included mild weight loss, fever, and CSF leukocytosis. One animal developed a left-sided hemiparesis following its seventh injection, presumably due to local drug accumulation in the setting of an intermittently patent catheter. The estimated radiation dose to the CSF was 1900–4800 cGy in the immunized animals and 1900–8200 cGy in the non-immunized animals, and the radiation doses to the blood were 11–98 cGy and 29–203 cGy, respectively. Importantly, the calculated radiation dose to the spinal cord was well below tolerance (Fig. 11.6). Histopathology revealed chronic reactive changes adjacent to the region of catheter placement and focal vasculitis in 2 animals. Peripheral blood counts and bone marrow examinations remained normal. Because of the blood-brain barrier, monkey-anti-mouse antibody titers in the CSF were 14- to 22-fold below than

Fig. 11.7 The relationship of CSF MAMA to serum MAMA. CSF and serum samples were drawn at the same time. Only those with measurable CSF MAMA titers are included in this regression analysis ($R = 0.77$, $p < 0.01$). The 95% confidence limits of the mean are also calculated. Regression analysis yielded a ratio between serum and CSF of 14-22-to-1. (Reprinted from Ref. [46])
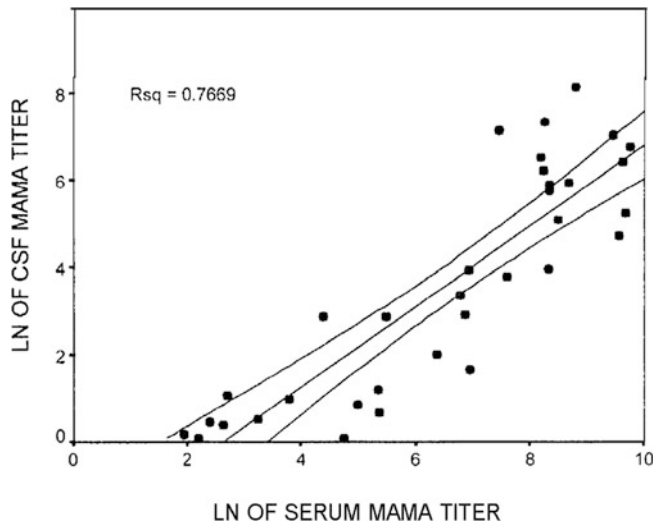
those in the serum (Fig. 11.7). While the clearance of radioactivity from the CSF was similar in all of the animals, clearance from the blood was substantially accelerated in the 3F8-immunized animals. Correspondingly, the ratio of the radiation dose to the CSF to the radiation dose to the blood was improved 1.3- to 6.6-fold (mean 3.5) in the immunized primates. These studies showed that the intraventricular administration of ^{131}I-3F8 was tolerable in non-human primates, delivering very high doses of radiation to the CSF space with minimal toxicity to the blood and bone marrow. Furthermore, serum anti-mouse antibodies accelerated the clearance of ^{131}I-3F8 in the blood and may therefore improve therapeutic indices.

11.7 Clinical Studies: ^{131}I-3F8 and ^{124}I-3F8 for RID

Neuroblastoma In a pilot study of six patients with neuroblastoma, 3–5 mCi of ^{131}I-3F8 was injected intravenously, nuclear imaging was carried out using a Searle (Chicago) large-field-of-view camera fitted with a high-energy collimator, and the information was acquired simultaneously on film and a Medical Data Systems (Ann Arbor,

Mich.) computer [47]. With the camera set for the 364 gamma peak with a 20% window, each region was scanned in at least two views and, whenever possible, in two orthogonal views (Fig. 11.8). For any one patient, the geometry on successive scans was reproduced so that the relative activity of any region as a function of time could be followed. The approximate volume of organs or tumors was estimated from the images on the computer monitor or by computed tomography (CT). An ^{131}I-filled water phantom was used for calibration and attenuation correction [48]. When consistently applied, dosimetry estimates based on tissue sampling and gamma imaging suggested therapeutic potential but also dose-limiting toxicities to critical organs (Table 11.4). These estimates were consistent with the intense accumulation of ^{131}I-3F8 in tumors as well as the lack of significant uptake in normal brain, liver, spleen, or adrenal glands. Tumor-to-nontumor activity concentration ratios varied but were approximately 10:1–20:1. This ratio yielded good contrast for visualization. Time-activity curves showed that the half-life of radioactivity was 13–20 h in the blood, 60 h in tumor tissue, and somewhere in between (~40 h) in normal tissues (Fig. 11.9). Significant gastric secretion of free iodine was consistent with the
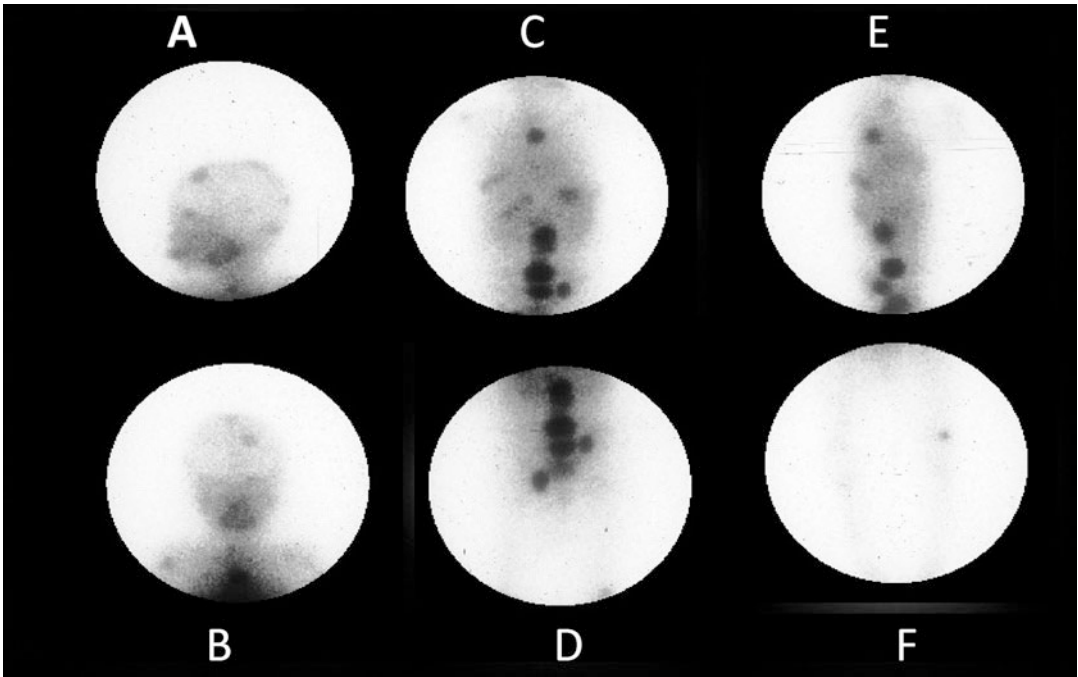
Fig. 11.8 Gamma-camera scan of a child with recurrent stage 4 neuroblastoma imaged 48 h after the injection of ^{131}I-3F8 and showing diffuse metastases in the skull and axial and appendicular skeleton. Also notable is the absence of non-specific uptake in liver or spleen.

Figures show the uptake of ^{131}I-3F8 in (**a**) the left lateral skull, (**b**) the anterior skull, (**c**) the posterior chest and abdomen, (**d**) the posterior abdomen and pelvis; (**e**) the lateral torso; and (**f**) the lower extremities

Table 11.4 Estimated tumor and organ radiation dose in Gy

Average I-131 radiation dose in Gy		
Tumor	36.6	(100)
Blood	3.4–5.2	(9.2–14.1)
Brain	0.6	(1.6)
Kidney	3.3	(8.9)
Liver	2.1	(5.7)
Lung	1.5	(4.1)
Muscle	2	(5.4)

Note: the numbers in parentheses are doses in Gy/MBq $\times$ 10^{-4}
Reprinted from Ref. [47]

dehalogenation of ^{131}I-3F8. No clinical toxicities were observed in this pilot study. These preliminary results supported further clinical development of ^{131}I-3F8 for both the imaging and therapy of human neuroblastomas [47].

Imaging with ^{131}I-3F8 was next compared with magnetic resonance imaging (MRI) in detecting marrow metastases in the spine, pelvis, and femurs of five children with disseminated

NB. While MRI identified all the skeletal disease sites detected by ^{131}I-3F8, several diffuse and multifocal marrow changes in MRI were not corroborated by bone scan, CT or biopsy, raising the question if these MRI findings could be non-specific [49]. ^{131}I-3F8 (0.5 mg of protein with 2 mCi of ^{131}I) detected more abnormal sites (n = 283) than either ^{131}I-metaiodobenzylguanidine (^{131}I-MIBG; 1 mCi
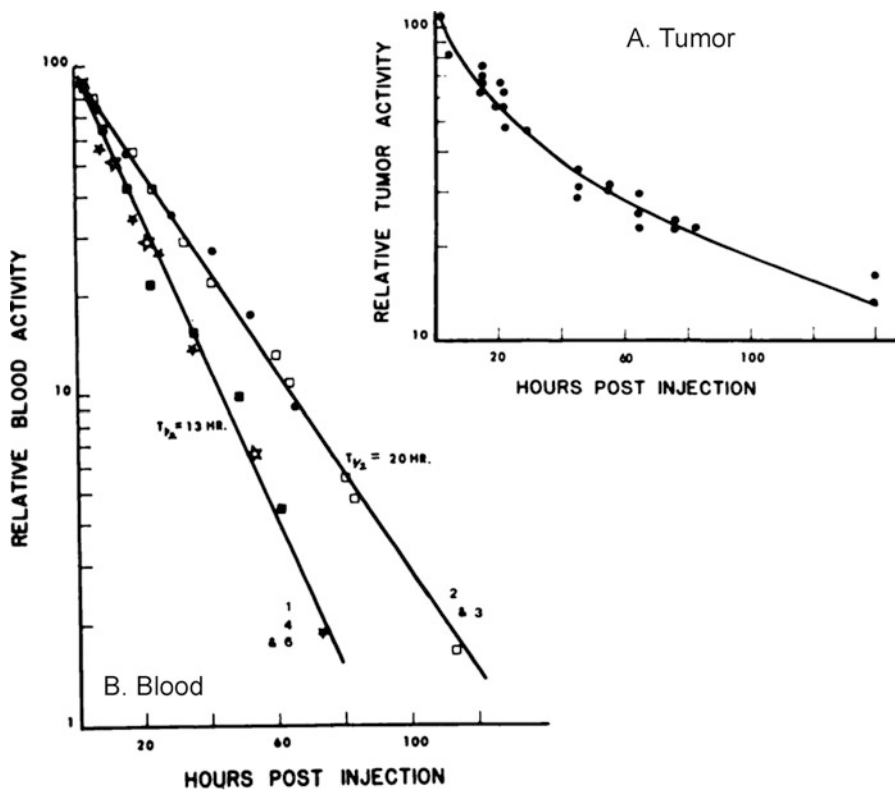
Fig. 11.9 The pharmacokinetics of [131]I-3F8: (**a**) Normalized tumor clearance of [131]I-3F8. Data from eight tumors in two patients (patients 1 and 4) and normalized 15 h after injection. (**b**) Normalized blood clearance of [131]I-3F8. Patients 2 and 3 had small tumor burdens (tumor $t_{1/2} = 20$ h), while patients 1, 4, and 6 had large tumor burdens ($t_{1/2} = 13$ h). (Reprinted from Ref. [47])

per l.7 m^2; $n = 138$) or ^{99m}Tc-methylene diphosphonate bone scans (^{99m}Tc-MDP; 25 mCi per 70 kg; $n = 69$) especially in patients with extensive disease (Tables 11.5 and 11.6) [50]. In 20 patients with soft-tissue tumors demonstrated by CT/MRI, [131]I-3F8 detected the disease in 18 (Table 11.7). Upon surgical resection, two tumors interpreted as negative with [131]I-3F8 imaging revealed either ganglioneuroma or microscopic foci of neuroblastoma. The soft tissue tumors identified with [131]I-3F8 were all confirmed histologically as neuroblastomas. In 26 patients with evidence of marrow disease by [131]I-3F8 scans, 14/26 were confirmed by iliac crest marrow aspirate/biopsy examinations [50]. Finally, no major pain or toxicities from [131]I-3F8 were observed.

ImmunoPET with [124]I-3F8 was carried out in one patient with advanced chemo-resistant neuroblastoma presenting as a large abdominal mass and bone marrow replacement [51]. Positron emission tomography (PET) imaging was performed at 72 h post-injection using a BGO-based Cyclotron Corporation PC4600 head scanner modified to accommodate pediatric patients. Based on time activity curves and on MIRD (Medical Internal Radiation Dosimetry) calculations, a radiation absorbed dose of 7.55 rad/mCi was found for the most antibody-avid lesions. The maximum uptake in the intramedullary disease site was 0.059% injected dose/gm with a biological half-life of 24.7 h. The dose to the abdominal mass was 1.9 rad/mCi,

Table 11.5 Comparison of imaging modalities

Comparison of imaging modalities: Average number of lesions detected per person			
Average number of lesions detected per patient			
Clinical status	131I-3F8	[131I]MIBG	99mTc-MDP
Progressive disease with positive BM (13)[c]	13.6 ± 9.0[a] (177)[b]	7.1 ± 6.2 (82)	3.4 ± 3.9 (44)
Progressive disease with negative BM (5)	10.8 ± 10.8 (54)	4.0 ± 4.5 (20)	2.0 ± 1.9 (10)
Active but stable disease (7)	5.1 ± 3.6 (36)	3.1 ± 2.9 (22)	1.1 ± 1.2 (8)
Complete remission (16)	1.0 ± 2.2 (16)	0.25 ± 0.58 (4)	0.44 ± 0.89[d] (7)

Radioimmnodetection of neuroblastoma with [131I]I-3F8: Correlation with biopsy, [131I]metaiodobenzylguanidine (MIBG), and standard diagnostic modalities
Reprinted from Ref. [50]
[a]Mean ± s.d.; BM = bone marrow test
[b]Total number of abnormal sites of uptake
[c]Numbers in parentheses = total number of patients in each category
[d]Abnormal 99mTc-MDP uptake disappeared in two patients without treatment. One patient had increased. 99mTc-MDP uptake after iliac crest biopsy, and another one at the surgical site after marrow harvesting

Table 11.6 The correlation between [131I]I-3F8 and [131I]MIBG imaging in 41 patients

Correlation between [131I]I-3F8 and [131I]MIBG[a] imaging in 41 patients			
		[131I]MIBG	
		+	−
131I-3F8	+	24	4
	−	0	13

Likelihood of agreement = 90% ±9% (95% confidence limits)
Reprinted from Ref. [50]
[a]Iodine-131-MIBG images were obtained within 1 wk. prior to the antibody study in 19 patients and within 1 mo in 22 patients (mean 26 days, median 21 days)

Table 11.7 The evaluation of chest, abdomen, and pelvic soft-tissue masses: correlation between [131I]I-3F8 imaging and CT/MRI in 42 patients

Evaluation of chest/abdomen/pelvic soft-tissue masses: correlation between 131I-3F8 imaging and CT/MRI in 42 patients			
		CT/MRI	
		+	−
131I-3F8	+	18	1[a]
	−	2[b]	21

Likelihood of agreement = 93% ±8% (95% confidence limits)
Reprinted from Ref. [50]
[a]This patient had a "hot spot" on [131I]MIBG in the presacral soft tissue on repeated studies. Both 131I-3F8, bone scan, and laparotomy failed to reveal any evidence of tumor
[b]False-negative: first patient had abdominal ganglioneuroma and scattered foci of neuroblastoma. Second patient had ganglioneuroma

while the dose to the remainder of the body was estimated to be no more than 0.4 rad/mCi.

Brain Tumors Radioiodine-labeled 3F8 was administered intravenously to 12 patients with brain tumors—4 glioblastoma (GBM), 5 high-grade anaplastic astrocytoma (AA), 2 low-grade AA, and 1 metastatic melanoma—for RID [52]. Six patients received 2 mCi (0.74 Bq) of [131I]I-3F8, five patients received 10 mCi (3.7 Bq) of [131I]I-3F8, and one patient received 2.6 mCi (0.96 Bq) of [124I]I-3F8. All four GBM patients, 4 of 5 high-grade AA patients, and the single metastatic melanoma patient showed localization of the antibody in the tumor tissue, with the best tumor delineation on single-photon emission tomography (SPECT) following 10 mCi (3.7 Bq)/1.73 m^2/dose. No non-specific uptake
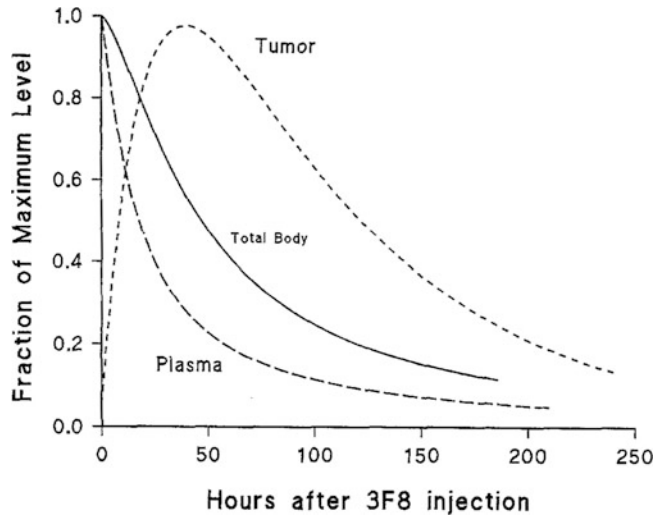
Fig. 11.10 Clearance of plasma, total body, and tumor radioactivity based on pooled patient data. Plasma clearance was based on 8 patients, total body on 1 patient, and tumor on 6 patients. Tumor radioactivity was estimated from conjugate planar images and combined with measurements from surgical samples. Half-lives were plasma $= 18$ h ($r^2 = 0.97$); total body $= 47$ h ($r^2 = 0.97$); and tumor $= 62$ h ($r^2 = 0.81$). Tumor uptake peaked at 39 h after the administration of the radioimmunoconjugate. (Reprinted from Arbit E et al. European Journal of Nuclear Medicine: 22: 419–426, 1995)

was detected in the normal craniospinal axis. There was no difference in the pharmacokinetics of the low-dose and higher-dose groups: the plasma and total-body half-lives were 18 and 49 h, respectively. Surgical sampling and time-activity curves based on quantitative imaging showed peak uptake in high-grade glioma at 39 h with a half-life of 62 h (Fig. 11.10). Tumor uptake at the time of surgery averaged 3.5×10^{-3}%ID/g, and the peak activity by the conjugate view method averaged 9.2×10^{-3}%ID/g (3.5–17.8×10^{-3}). Mean radiation absorption dose was 3.9 cGy/mCi (range 0.7–9.6) or 10.5 cGy/Bq (range 1.9–26). There was agreement on positive sites when RID was compared with ^{99m}Tc-glucoheptonate or ^{99m}Tc-DTPA planar imaging, thallium-201 SPECT, and ^{18}FDG-PET. Within hours of the injection of ^{99m}Tc-glucoheptonate or ^{99m}Tc-DTPA, clear tumor delineation was seen. An off-target non-specific EPR (enhanced permeability and retention) effect could account for the initial uptake of ^{131}I-3F8 in these brain tumors. However, the persistence of the ^{131}I-3F8 uptake and the steady improvement in the tumor-to-normal brain

activity concentration ratio over time suggest the specific interaction of the radioimmunoconjugate with the tumor. The highest activity concentration in the tumor was observed between 20 and 75 h. The tumor-to-normal brain activity concentration ratio was consistent for primary high-grade brain tumors (4.4–6.2) but increased in the case of metastatic melanoma (23). The tumor %ID/g values for the radioimmunoconjugate were comparable to those achieved in gliomas using an anti-tenascin antibody (0.6–4.3×10^{-3}%ID/g) and antibody UJ13A (0.36–1.8×10^{-3}). No pain or major toxicities were observed. Overall, while the radioimmunoconjugates produced tumor-selective uptake and exhibited potential for RID, the calculated TI were insufficient for therapeutic benefit (Tables 11.8 and 11.9).

11.8   Clinical Studies: ^{131}I-3F8 for RIT

Systemic Injection In a phase I dose escalation trial, twenty-four patients (12 male and 12 female, 0.3–24.2 years of age at diagnosis) with refractory neuroblastoma (23 metastatic, 1 localized)

Table 11.8 Athymic nude mice bearing NB LAN-1 xenografts (0.5–0.8 cm diameter) were injected intravenously with 5F11-SA, followed 24 h later by the intravenous injection of sCA biotin-LCNM-(Gal-NAc)$_{16}$ and then 4 h later by the intravenous injection of 2.5 ug ^{111}In-DOTA-biotin

Relationship of T/NT ratio and dose of scFv-SA			
Dose of 5F11-scFv-SA (µg)			
Tissue	100	300	900	2400
---	---	---	---	---
Adrenal	19.7 ± 5.5	65.3 ± 20.3	124.6 ± 20.9	193.1 ± 7.1
Bladder	22.8 ± 4.3	29.1 ± 3.8	145.2 ± 44.4	92.1 ± 7.6
Blood	139.4 ± 30.3	160.9 ± 17.3	1121.3 ± 306	621.4 ± 61.5
Brain	170.9 ± 12.6	503 ± 100.6	1187 ± 268	901.6 ± 157.4
Femur	67.3 ± 11	169.4 ± 27.1	405.2 ± 38.1	288.8 ± 41.9
Heart	34.3 ± 4	110.8 ± 13.3	265 ± 30.9	269.7 ± 11
Kidney	1.1 ± 0.3	2.7 ± 0.6	10.6 ± 2.9	7.1 ± 0.2
L intestine	3.7 ± 1	17.4 ± 3.9	15.9 ± 3.2	10.2 ± 1.7
Liver	10 ± 1.6	18.5 ± 2.6	50.3 ± 11.9	37 ± 1.5
Lung	19.8 ± 3.1	21.8 ± 3.4	62.8 ± 21.5	23.1 ± 2.3
Muscle	35.8 ± 6.1	160.7 ± 22.9	467 ± 61.4	429 ± 39
Skin	13.3 ± 1.9	23.6 ± 4.4	51.4 ± 3.9	56.6 ± 8.3
S intestine	37.4 ± 7	66 ± 9.2	135.6 ± 33.1	114.3 ± 24.9
Spine	49.2 ± 5.9	130.8 ± 4.1	425.4 ± 58.8	338.6 ± 27.2
Spleen	14.8 ± 2.2	30.8 ± 4.1	118.2 ± 12.3	120.2 ± 5.8
Stomach	48.2 ± 14.9	94.7 ± 12.4	181.7 ± 30.7	70.6 ± 5.2
Tumor %ID/g	1.9 ± 0.5	3.1 ± 0.9	6.5 ± 1.5	7.4 ± 0.5

Mice were sacrificed for biodistribution studies 24 h after the administration of ^{111}In-DOTA-biotin. Four dose levels of 5F11-SA were tested: 100, 300, 900, and 2400 ug (n = 5 mice per group). The dose of sCA was 50% (weight ratio) of the 5F11-scFv-SA dose. Tumor-to-healthy organ activity concentration ratios are summarized for each organ as an arithmetic mean ± SEM
Reprinted from Ref. [39]

were treated with ^{131}I-3F8 at 7 dose levels: 6, 8, 12, 16, 20, 24, or 28 mCi/kg. Twenty out of twenty four patients were rescued with cryopreserved autologous bone marrow; one patient received GM-CSF; and one died of progressive disease before marrow reinfusion. Among 10 evaluable patients, 2 achieved complete remission of marrow disease, and 2 had partial responses of soft tissue tumors. The average tumor dose was 150 rad/mCi/kg, and the cumulative blood radiation dose averaged 2000 cGy. Sixteen of twenty-four patients have subsequently progressed and died of neuroblastoma, while another six died of septic complications. Two patients were long-term survivors: 78+ and 54+ mos from the time of ^{131}I-3F8 treatment.

Acute toxicities of ^{131}I-3F8 treatment included grade 4 myelosuppresion (24/24), ≥2 pain during the infusion (20/24), fever (20/24), hyperbilirubinemia (8/24), pulmonary (1/24),

and mild diarrhea. All 24 patients required autologous bone marrow rescue. Interestingly, the pain side effects were generally much milder than those observed for non-radiolabeled 3F8 [2, 28]. Chemical hypothyroidism developed in 3/11 patients despite oral saturated solution of potassium iodide (SSKI) and 1/10 patients despite oral SSKI plus synthroid or cytomel. Among 6 patients followed for more than 20 months after antibody treatment, no extramedullary toxicities were encountered. Although significant extra-medullary toxicities were not evident, the late effects of this treatment modality could not be assessed because of the short follow-up.

In this phase I dose escalation trial, serial whole-body dose rate measurements were obtained on patients receiving 2.5 GBq dose of ^{131}I-3F8 (range 1–8.14 GBq) every 2–4 days for up to 9 treatment cycles [53]. Whole-body retention fractions were derived and fitted exponentially for each treatment cycle to determine both

Table 11.9 Athymic nude mice ($n = 4$ to 5 per group) bearing GD2-negative human lymphoma (Daudi), GD2-negative human colon carcinoma (Colo205), GD2-negative human rhabdomyosarcoma (HTB82), and GD2-positive NB (SK-N-LP, SK-N-JD, LAN-1) xenografts as well as C57Bl/6 mice autografted with GD2-negative melanoma (B16) and GD2-positive melanomas (B16D14, B16D14Kb, B16D14KbKd) were studied using 900 µg of 5F11-scFv-SA, 450 µg of sCA, and 2.5 µg of ^{111}In-DOTA-biotin

Relationship of T/NT ratio and tumors with different GD2 expression

| | GD2-negative cell line | | | | | GD2-positive murine cell line | | | | | GD2-positive human cell line | | | |
| | Colo-205 | Daudi | HTB82 | B16 | Mean ± SEM[a] | MOLT-4 | B16-D14 | B16-D14Kb | B16-D14KbKd | Mean ± SEM*2 | SK-N-LP | SK-N-JD | LAN-1 | Mean ± SEM*3 |
Tissue	H	H	H	M		H	M	M	M		H	H	H	
Adrenal	7	1	5	4	4.1 ± 1.4	3	24	11	28	16.4 ± 5.8	245	91	74	136.7 ± 54.5
Bladder	10	1	3	2	4.1 ± 2.0	3	10	2	22	9.2 ± 4.5	162	85	97	114.4 ± 24.0
Blood	6	11	72	28	29.2 ± 14.9	30	169	33	190	105.4 ± 43.1	667	701	442	603.6 ± 81.3
Brain	59	37	43	64	50.7 ± 6.4	66	294	100	427	222.0 ± 85.0	541	1919	929	1129.9 ± 410.4
Femur	9	4	18	7	9.6 ± 3.0	7	38	14	52	27.9 ± 10.6	342	741	221	434.9 ± 157.1
Heart	7	2	8	6	5.6 ± 1.4	8	23	8	30	17.5 ± 5.7	231	244	190	221.6 ± 16.2
Kidney	0	0	0	0	0.2 ± 0.1	0	1	0	1	0.5 ± 0.2	5	6	5	5.2 ± 0.3
Large bowel	0	1	1	0	0.9 ± 0.3	0	2	0	2	1.3 ± 0.6	15	12	31	19.4 ± 6.1
Liver	1	0	1	1	1.2 ± 0.3	2	7	3	6	4.3 ± 1.3	59	37	37	44.4 ± 7.5
Lung	2	1	1	1	1.3 ± 0.4	1	3	2	6	3.2 ± 1.1	29	73	41	48 ± 13.3
Muscle	12	6	16	14	11.8 ± 2.3	8	40	16	80	35.9 ± 16.2	451	425	225	366.9 ± 71.5
Skin	1	1	4	2	2.0 ± 0.8	1	7	3	21	8.2 ± 4.7	32	72	73	59.1 ± 13.5
Small bowel	4	3	7	5	4.8 ± 0.9	2	16	2	45	16.2 ± 10.3	174	243	197	204.6 ± 20.1
Spine	10	4	19	9	10.5 ± 3.1	10	36	15	45	26.6 ± 8.4	330	376	131	279.3 ± 75.2
Spleen	3	1	3	2	2.2 ± 0.4	3	10	4	15	8.1 ± 2.9	174	120	71	122 ± 29.7
Stomach	3	3	21	3	7.7 ± 4.4	7	20	5	42	18.6 ± 805	109	197	784	363.4 ± 211.6
GD2 (%LAN-1)[b]	2	4	3	4	3.3 ± 0.5	17	22	32	12	20.8 ± 4.3	289	77	100	155.4 ± 67.2

At 20–28 h, the mice were sacrificed, and the radioactivity in each of their organs was measured. The %ID/g for the blood and various organs was measured, and the T/NT activity concentration ratio was calculated for each organ

Reprinted from Ref. [39]

[a]Mean ± SEM denotes arithmetic mean ± SEM across cell lines in each tumor group

[b]GD2 (% LAN-1) relative mean fluorescence, indirect fluorescent staining with anti-GD2 antibody 3F8. It is calculated using the mean fluorescence channel of the cell line divided by the mean fluorescence channel of the NB cell line LAN-1. H = human, M = murine

Fig. 11.11 Patients with high-risk neuroblastoma (stage 4 diagnosed at >18 months of age or with tumor MYCN amplification) achieved first remission after induction chemotherapy and received 3F8 antibody consolidation without (protocol N6) or with (protocol N7, clinicaltrials.gov NCT00002634) [131]I-3F8 (20 mCi/kg) followed by stem cell rescue
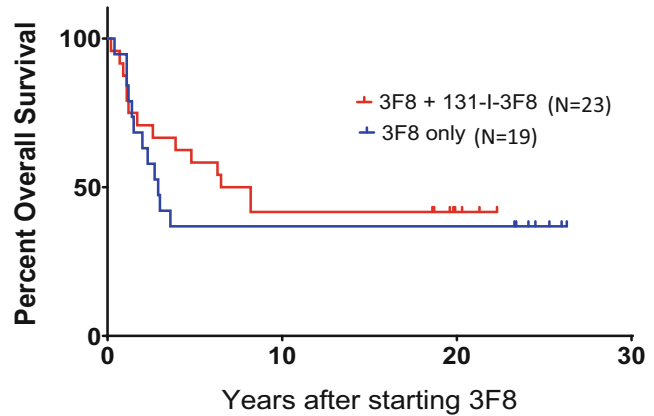
the effective half-lives and the corresponding clearance fractions. The calculated mono-exponential effective clearance half-life time was variable, with a mean of 26.4 h (range, 12.4–45.5 h). This slow clearance was responsible for the myelotoxicity encountered, and the half-time variability supports the need for patient-specific dosimetry in order to optimize treatment efficacy and toxicity as well as decision making vis a vis radiation safety precautions.

In a phase II trial using [131]I-3F8 (20 mCi/kg, 740 MBq/kg) to consolidate patients in remission following induction chemoimmunotherapy (clinicaltrials.gov NCT00002634), all patients received marrow rescue following RIT, and all patients successfully recovered their blood counts within 2 months of marrow rescue. As in the phase 1 study, the toxicities included pain, myelosuppression, fever, and hypothyroidism, with no extramedullary toxicity. Median time to achieve an absolute neutrophil count of 500/L was 16 days, and the median time to achieve a platelet count of 20,000/L was 41 days. One patient died of complications from infection. The absorbed doses were calculated using the DOSCAL program developed at Memorial Sloan–Kettering Cancer Center that implements S-factor. Based on the tracer dosimetry, the average doses for the liver, spleen, red marrow, lung, and tumor were 0.06, 0.07, 0.06, 0.05, and 0.37 cGy/MBq, respectively [54]. Progression-free survival and overall survival were not significantly improved when compared to historical control patients not receiving [131]I-3F8

(Fig. 11.11). Even at these high mCi doses, [131]I-3F8 was unable to eliminate microscopic residual NB. The only reassuring finding was the relative lack of additional toxicity from [131]I-3F8 after a long-term follow-up of more than 20 years. There were no late side effects attributable to RIT; no neuropathy either sensory or motor, central, or peripheral; no obvious deficit in cognition; and no major organ deficit.

11.9 Clinical Studies: [131]I-3F8 for Compartmental Radioimmunotherapy (cRIT)

IntraOmmaya cRIT Intra-Ommaya [131]I-3F8 was tested in patients with leptomeningeal disease in a phase I trial (NCT00003022) [55]. Adequate CSF flow was confirmed by pretreatment ^{111}In-DTPA studies. Fifteen patients received a tracer (1 to 2 mCi) followed by a therapeutic injection 4–7 days later (10 to 20 mCi) of intra-Ommaya [131]I-3F8. The pharmacokinetics of [131]I-3F8 were studied by serial CSF and blood samplings. Dosimetry calculations were based on pharmacokinetics and region-of-interest (ROI) analyses using whole body gamma camera scans. Tumor response was determined by clinical, radiographic, and cytologic criteria. The dose to the CSF was used as a surrogate for the dose to free floating tumor cells in the CSF. CSF half-life of the radioimmunoconjugate by tissue sampling was 3 to 12.9 h. The total absorbed dose to the CSF was 112–1300 cGy via sampling and

100–1370 cGy via ROI analysis. The average ratio (± standard deviation) of therapeutic dose to tracer dose in Gy/(MBq administered) was 0.88 (± 0.58) and 1.08 (± 0.66) by CSF counting and ROI analysis, respectively. Considering preferential tumor uptake and geometric enhancement factors, the tumor dose could be substantial [46]. Animal studies have shown that the radioactivity AUC ratios for tumor deposits versus CSF ranged from 5 for melanoma to more than 30 for neuroblastoma [56]; hence, a CSF dose of 100–1000 could translate into a tumor dose >500–30,000 cGy. Toxicities included self-limited headache, fever, and vomiting were observed, but no systemic pain or neuropathy was reported. Dose-limiting toxicity was reached at the 20 mCi dose, when transient elevations in intracranial pressure and chemical meningitis were seen. Three of 13 assessable patients achieved objective radiographic and/or cytologic responses. No late toxicities were seen in two patients who remained in remission off therapy for more than 3.5 years. Based on these results, giving [131]I-3F8 into a small compartment greatly improved its tumor-to-systemic tissue (e.g., blood) radiation dose ratio, and tracer studies reliably predicted the therapeutic dose to the CSF.

Modeling cRIT A pharmacokinetic model to evaluate the role of kinetic and transport parameters in cRIT was built to maximize the therapeutic ratio, i.e., the ratio of the area under the curve for the concentration of GD2-bound radioimmunoconjugates over time (AUC [CIAR]) to that for unbound radioimmunoconjugates over time (AUC[CIA]) [57]. A single compartment was used for the CSF space, and [131]I-3F8 was assumed to bind to antigens on tumor cells lining the surface of the CSF space. Mass conservation was applied to set up the equations for CIAR, CIA, and other pharmacokinetic variables, and a Runge-Kutta method was used to solve the equations. The model agreed with the measured data in 10 of 14 patients in the phase I trial of intra-Ommaya [131]I-3F8. Based on the model, increasing the affinity of antibodies to antigens should greatly increase AUC(CIAR) but not AUC(CIA); for the same amount of radionuclide administered, reducing the antibody dose and increasing the specific activity should improve the therapeutic ratio. When the $t_{1/2}$ half-life of the radioimmunoconjugate was 0.77 h, increasing the antibody's association constant enhanced AUC(CIAR) much more than decreasing its dissociation constant, even if its overall affinity was unchanged. When the $t_{1/2}$ of the radioimmunoconjugate reached 240 h, decreasing the dissociation constant would slightly enhance AUC(CIAR). Other predictions were that (1) decreasing the CSF bulk flow rate would increase AUC(CIAR) with 3 mL/h being optimal; (2) at holding the amount of antibody constant, one could improve AUC(CIAR) by up to 1.8- and 1.7-fold by continuous infusion and split administrations, respectively, compared to a single bolus administration; and (3) for an antibody affinity of 10^{-8} M, increasing the $t_{1/2}$ of the radioimmunoconjugate from 0.77 h up to 64 h could greatly enhance the therapeutic ratio.

By adopting a two-compartment model to simulate the lateral ventricle (where the Ommaya catheter was placed) and the rest of the CSF space, the fitting of CSF kBq/mL data was robust (R = 0.95 ± 0.03) [58]. Correlations were substantially better when compared to the one-compartment model (R = 0.92 ± 0.11 versus 0.77 ± 0.21, p = 0.005). New predictions included (1) Increasing the immunoreactivity of [131]I-3F8 from 10% to 90% increased both the (AUC[CIAR]) and the therapeutic ratio ([AUC [CIAR]/AUC[CIA]] by 7.4-fold; (2) if [131]I-3F8 could be split into 4 doses of 1.4 mg each and given at ≥24 h apart, an antibody K_D of 4×10^{-9} at 50% immunoreactivity was sufficient to deliver ≥10,000 cGy to tumor cells while keeping normal CSF exposure to <1000 cGy.

[131]I-3F8 cRIT of Medulloblastoma (MB)

Patients with high-risk or recurrent MB and adequate CSF flow by [111]IN-DTPA received 2 mCi [124]I-3F8 or [131]I-3F8 for nuclear imaging, followed by up to four therapeutic (10 mCi/ dose) doses of [131]I-3F8 (clinicaltrials.gov NCT00058370) [59]. Dosimetry estimates were based on serial CSF and blood samplings over

48 hr. plus region-of-interest analyses using serial PET (^{124}I-3F8) or SPECT (^{131}I-3F8) imaging. Forty-three patients received a total of 167 injections, and 42 patients were evaluable for outcome. No treatment-related deaths occurred. Toxicities related to the administration of the drug included acute bradycardia with somnolence, headache, fatigue, and CSF pleocytosis consistent with chemical meningitis and dystonic reaction. The total CSF absorbed dose was 1453 cGy (350–2784). Median overall survival from the first dose of cRIT was 24.9 months (95% CI 16.3–55.8). Patients treated in radiographic and cytologic remission were at a lower risk of death compared to patients with radiographically measurable disease (hazard ratio: 0.40, 95% CI: 0.18–0.88, P = 0.024). In light of these data, cRIT with ^{131}I-3F8 was deemed safe with favorable dosimetry to the CSF.

Late Effects from ^{131}I-3F8 cRIT Radionecrosis is a potentially devastating complication of external beam radiotherapy (XRT). Ninety-six patients with metastatic CNS neuroblastoma (NB) and medulloblastoma (MB) treated with cRIT using ^{131}I-3F8 or ^{131}I-8H9 (specific for B7-H3) were studied for late effects (NCT00058370, NCT00445965, and NCT00089245) [60]. Ninety-four patients received both craniospinal radiation (CSI-XRT) and cRIT, and two received cRIT alone. The median follow-up was 41.5 months (6.5–124.8 months). Mean CSI-XRT dose was 28 Gy (boost to the primary tumor site up to 54 Gy) in the MB cohort, and the CSI-XRT dose was 18–21 Gy (boost to 30 Gy for focal parenchymal mass) in the NB cohort. For MB patients, 20% had focal re-irradiation for a second or more subsequent relapses, and the mean repeat-XRT dose was 27.5 Gy; seven patients with NB had additional focal XRT. The median CSF cRIT dose was 18.6 Gy in the MB cohort and 32.1 in the NB cohort. One asymptomatic patient underwent resection of 0.6-cm hemorrhagic periventricular white-matter lesion confirmed to be necrosis and granulation tissue 2.5 years after XRT. The risk of radionecrosis in children treated with XRT and cRIT appeared

minimal (~1%). No neurologic deficits secondary to radionecrosis have been observed in long-term survivors treated with both modalities, including patients who underwent re-XRT. These data suggest that the administration of cRIT could safely proceed in patients treated with conventional radiotherapy without appearing to increase the risk of radionecrosis.

11.10 GD2 as a Target for PRID and PRIT Using Recombinant scFv-Streptavidin

IgG-based radioligand therapy (RLT) (e.g., murine 3F8) has consistently shown unintended dose-limiting toxicities due to poor therapeutic indices. This typically results in patients receiving subtherapeutic doses of treatment followed invariably by disease progression. Even with tumor-specific targets, conventional 1-step delivery systems typically have TI below 10:1. While many protein-based therapies benefit from long terminal half-lives, the delivery of highly cytotoxic payloads is inevitably dose-limited by such platforms, which reduces antitumor efficacy. However, rapidly clearing antibody fragments might not be the solution either, due to their reduced bioavailability and insufficient tumor uptake, Likewise, peptides suffer from renal retention that limits dose escalation. Multi-step targeting strategies in which tumor-targeting agents are delivered separately from their therapeutic payloads (e.g., chelated radionuclides) could improve Tis [61]. This is particularly relevant in the context of pediatric patients in which acute toxicity and late effects of treatment are major concerns. Biotin-streptavidin offers a convenient platform for pretargeted radioimmunodiagnosis (PRID) and pretargeted radioimmunotherapy (PRIT). Furthermore, the replacement of radioiodine with a radiometal should broaden the versatility and utility of RIT. 5F11scFv (scFv, single-chain variable fragment) was constructed from the V_H and V_L domains of the anti-GD2 IgM hybridoma 5F11 and ligated to full-length streptavidin for expression in

Escherichia coli [39]. Purified 5F11-scFv-streptavidin (5F11-scFv-SA) is a homotetramer and showed a 30-fold improvement in affinity over monomeric 5F11 scFv (5F11 scFv has 13-fold lower affinity compared to 3F8 scFv [62]).

The biodistribution of 5F11-scFv-SA was studied in nude mice bearing LAN-1 neuroblastoma xenografts. Twenty-four hours after the intravenous injection of 300–900 μg of 5F11-scFv-SA, 150–450 μg of a thiogalactoside-containing clearing agent— $(Gal-Nac)_{16}-\alpha-SC_5H_{10}-NH-LC-N-Me-biotin$ (molecular weight = 8.6 kDa)—were administered intravenously followed 4 h later by ~2.5 μg (1.85–3.7 MBq) ^{111}In-1,4,7,10-tetraazacyclododecane-1,4,7,10-tetraacetic acid-biotin (^{111}In-DOTA-biotin) intravenously (t = 0). Tumoral uptake at 2 h after the administration of the radioligand was 7%ID/g and decayed with a half-life of 72 h, whereas the activity concentration in the blood rapidly decreased to ~1/500th of the tumor's value after 24 h. The median tumor-to-non-tumor (T/NT) activity concentration ratio at 72 h post-injection was 106, with a low value for the kidney (3.4) and a high value for the blood (1660). The therapeutic index (radioactivity AUC of tumor vs normal) was favorable for blood (162) but less so for kidney (4.8). When human and murine tumors were surveyed, the T/NT activity concentration ratios for ^{111}In-DOTA-biotin correlated with their levels of GD2 expression as determined via flow cytometry. Biotinylated polypeptides—bovine serum albumin and vasointestinal peptides—also produced selective tumor targeting when the multistep strategy was applied. The dramatic improvement in the T/NT ratios, especially for the blood, highlights the clinical potential of PRID and PRIT compared to RID and RIT. In addition, since haptenated (e.g., biotinylated) polypeptides were rendered tumor-selective, a large repertoire of haptenated payloads could potentially be explored. Yet multistep targeting strategies using biotin and streptavidin faced significant clinical limitations when they were first trranslated to the clinic in the 1990s, namely the high immunogenicity of avidin proteins, the

potential for competition with endogenous biotin within the body, the need for clearing agents to remove unbound antibodies from circulation, and the unfavorable TI for the kidneys. These limitations forced the exploration of less immunogenic multistep targeting strategies.

11.11 GD2 as a Target for PRID and PRIT Using Recombinant IgG-[L]-scFv

To overcome limitations of streptavidin and biotin discussed above, a 2 + 2 IgG-[L]-scFv BsAb format was engineered in which both carboxyl ends of the hu3F8 light chains were fused to C825 scFvs that conferred high affinity for 1,4,7,10-tetraazacyclododecane-1,4,7,10-tetraacetic acid (DOTA) complexed with β-particle-emitting radiometals such as ^{177}Lu and ^{90}Y (Fig. 11.12) [38]. A three-step regimen—including the administration of hu3F8-C825, a dextran-based clearing agent, and *p*-aminobenzyl-DOTA radiolabeled with ^{177}Lu ($t_{1/2}$ = 6.7 days)—was optimized in immunocompromised mice carrying subcutaneous human GD2(þ) neuroblastoma (NB) xenografts. The absorbed doses to the tumor and normal tissues were approximately 85 cGy/MBq and ≤ 3.7 cGy/MBq, respectively, yielding therapeutic indices of 142 for the blood and 23 for the kidneys (Fig. 11.13). A therapy study (n = 5/group; tumor volume, 240 ± 160 mm^3) with three successive PRIT cycles (total ^{177}Lu: ~33 MBq; tumor dose ~3400 cGy) produced complete tumor response in all animals with no recurrence up to 120 days after treatment. Tumor ablation was confirmed histologically, and normal organs showed minimal overall toxicities. All non-treated mice required sacrifice within 3 weeks (>2.0-cm^3 tumor volume). Using DOTA-Bn as the handle for PRID or PRIT, Tis could finally be reached to allow a wide therapeutic window. One remaining hurdle of this approach, however, was the need for a clearing agent which may be difficult to titrate because of differences in tumor load and antibody clearance in individual patients.
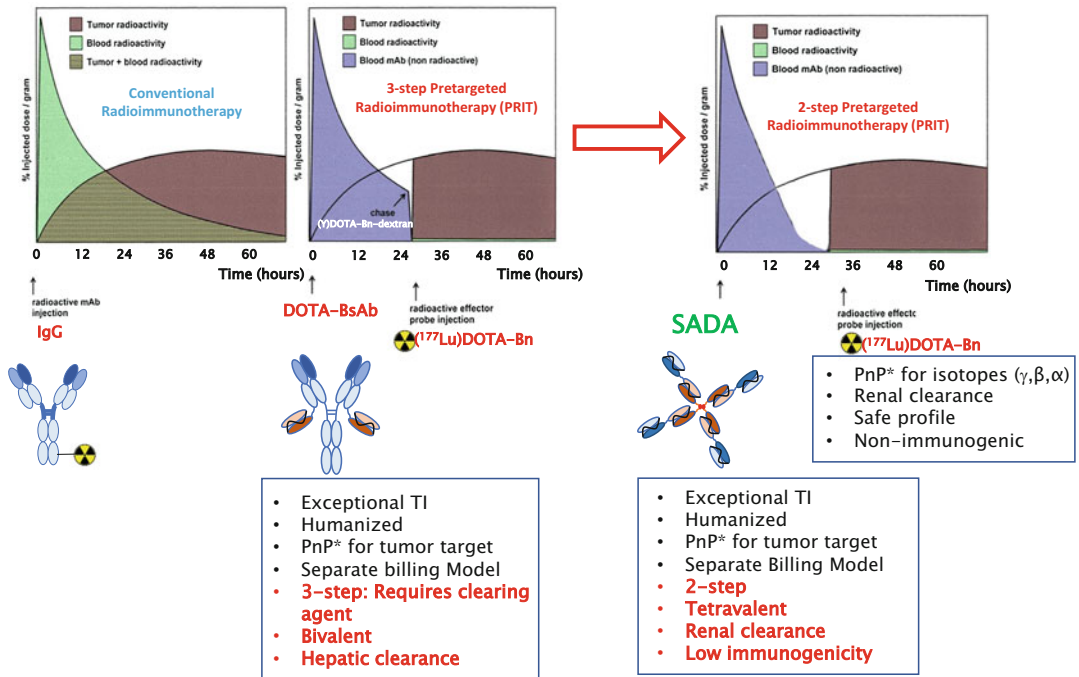
Fig. 11.12 Comparison of single step RIT, 3-step pretargeted radioimmunotherapy (PRIT), and 2-step PRIT using S-2-(4-aminobenzyl)-1,4,7,10-tetraazacyclododecane tetraacetic acid (DOTA) as a hapten. *PnP = plug-and-play

11.12 GD2 as a Target for PRID and PRIT Using Recombinant Self-Assembling Dis-Assembling (SADA) Bispecific Antibodies

To overcome these final challenges, a novel multimerization platform that rapidly removes tumor-targeting proteins from the blood was developed to substantially improve therapeutic indices (Fig. 11.12). The platform was designed as a fusion protein that combines a self-assembling and disassembling (SADA) domain with a tandem single-chain bispecific antibody (BsAb, anti-ganglioside GD2 anti-DOTA[Lu]) [63]. SADA-BsAbs were assessed in vivo with multiple tumor models to evaluate their tumor uptake, dosimetry, and antitumor responses. SADA-BsAbs self-assembled into stable tetramers (220 kDa) but could also disassemble into dimers or monomers (55 kDa) that rapidly cleared via renal filtration with substantially reduced immunogenicity in mice. When used in a multistep targeting strategy with rapidly clearing DOTA-coordinated PET isotopes, SADA-BsAbs yielded promising tumor localization, dosimetry, and imaging contrast by PET/CT (Fig. 11.14). When combined with therapeutic isotopes, two-step SADA-PRIT safely delivered high doses of DOTA-bound alpha-emitting (^{225}Ac, 1.48 MBq/kg) or beta-emitting (^{177}Lu, 6660 MBq/kg) payloads to tumors, ablating tumors without any short- or long-term toxicities to the bone marrow, kidneys, or liver (Fig. 11.15). The SADA–BsAb platform can safely deliver large doses of radionuclides to tumors and demonstrated no toxicities to the bone marrow, kidneys, or liver. Because of its modularity, SADA-BsAbs could be adapted to most tumor antigens, tumor types, or drug delivery approaches to improve therapeutic indices and maximize radiation doses to the tumor.

^{177}Lu IgG[L]-scFv PRIT (3-step) of neuroblastoma

hu3F8-C825 [t = -28 h]

CA [t = -4 h] and 11.1 MBq (^{177}Lu)DOTA-Bn [t = 0 h]

Total 33 MBq = 0.9 mCi

Tissues	cGy/MBq	cGy/mCi	AUC Tumor/tissue ratio
Blood	0.6	22	142
Tumor	84.9	3141	1
Heart	0.7	26	121
Lung	3.5	129	24
Liver	2.1	78	40
Spleen	2	74	42
Stomach	0.9	33	94
Sm. Intestine	0.8	30	106
Lg. Intestine	2.1	78	40
Kidneys	3.7	137	23
Muscle	5.5	203	15
Bone	0.7	26	121
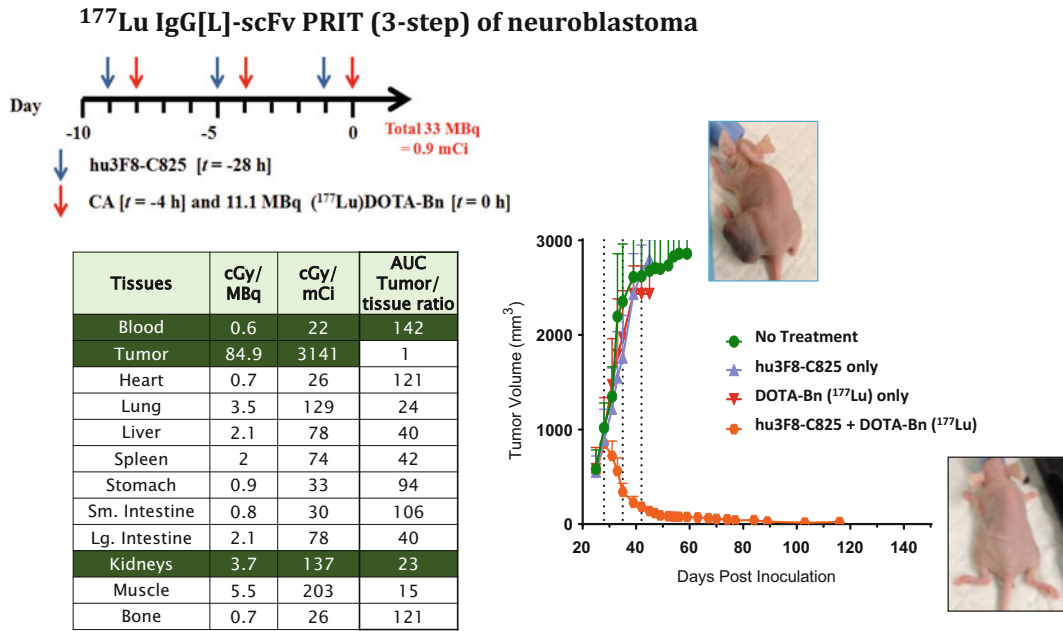
Fig. 11.13 PRIT when applied to GD2 in neuroblastoma: (**a**) PRIT treatment schedule. Groups of mice bearing GD2 (+) IMR32 NB tumors (n = 5 per group) received either three successive cycles of 1.75 mg of hu3F8-C825, CA [250 g; 14% (w/w) of (Y)-DOTA-Bn/dextran], and approximately 11.1 MBq (60 pmoles) of ^{177}Lu-DOTA-Bn with 68 h between each cycle or no treatment. (**b**) summary table of tumor-to-tissue radiation absorbed dose ratios, (**c**) comparison of tumor volumes of treated or non-treated groups of animals up to 118 days after therapy. (Adapted from Cheal et al. [38])

11.13 Conclusion

Despite its promising preclinical efficacy, IgG-based RIT directed at GD2 was crippled by its dose-limiting myelotoxicity. PRIT is a paradigm shift. As the antibody formats evolved from IgG to scFv-streptavidin to scFv-IgG to SADA, Tis have improved not just for select organs but for all critical organs, allowing for the delivery of doses of >10,000 cGy to GD2(+) tumors while sparing normal tissues, even when there is no tumor to act as an antigen sink (Table 11.10). With the SADA platform, high doses of β- and α-particles can be delivered to eradicate tumors with nearly zero critical organ toxicities. These fully humanized constructs should reduce immunogenicity, and their fast renal (instead of hepatic) clearance should further minimize the production of anti-drug antibodies. The next frontiers for SADA-PRIT are reducing on-target off-tumor side effects and leveraging rapidly internalizing antigens that are not easily amenable to pretargeting strategies. Finally, the clinical potential of SADA-PRIT (and its limitations) will soon be revealed in a first-in-human trial.

11.14 The Bottom Line

- GD2 is expressed on a number of stem cells including neural, mesenchymal, and peripheral sympathoadrenergic progenitors but is limited to the central nervous system after birth.
- GD2 is highly expressed on a variety of embryonal cancers (i.e., neuroblastoma, brain tumors, retinoblastoma, Ewing sarcoma, rhabdomyosarcoma), bone tumors (i.e., osteosarcoma, Ewing sarcoma), soft tissue sarcomas (i.e., leiomyosarcoma, liposarcoma, fibrosarcoma), neural crest derived tumors (i.e., small cell lung cancer and melanoma), and breast cancer.
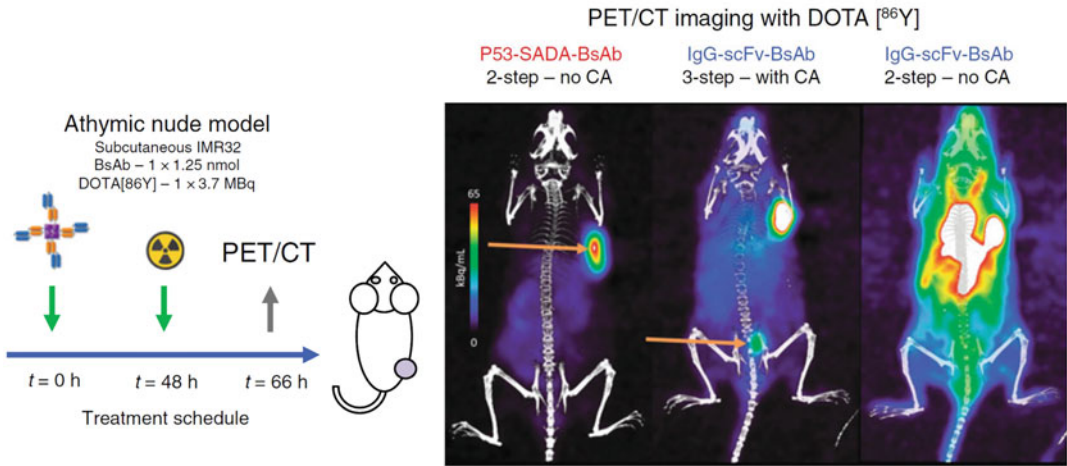
Fig. 11.14 ^{86}Y-DOTA and self-assembling disassembling antibody (SADA) system for the pretargeted radiodiagnosis (PRID) of GD2(+) neuroblastoma IMR32: (A) PET/CT using SADA-PRID. Representative schematic (left) and images (right). Mice were injected with SADA-BsAb or IgG-scFv-BsAb [with and without clearing agents (CA)] followed by DOTA-Bn [^{86}Y] (green lines correspond to each injection). Eighteen hours after the administration of the DOTA hapten, mice were imaged for 30 min (gray arrow). Representative images are normalized using the same scale. Orange arrows point to the subcutaneous tumor (left) or the bladder (middle). (Adapted from Ref. [63])

Fig. 11.15 ^{177}Lu-DOTA SADA PRIT of GD2(+) neuroblastoma. Each dose of SADA BsAb (1.25 nmol, triangle) was followed 48 h later by one dose of DOTA-Bn[^{177}Lu] (18.5 MBq, star). Each solid line represents one treatment group (n = 10 per group). Tumor averages were calculated until at least one mouse had to be euthanized. (Adapted from Ref. [63])
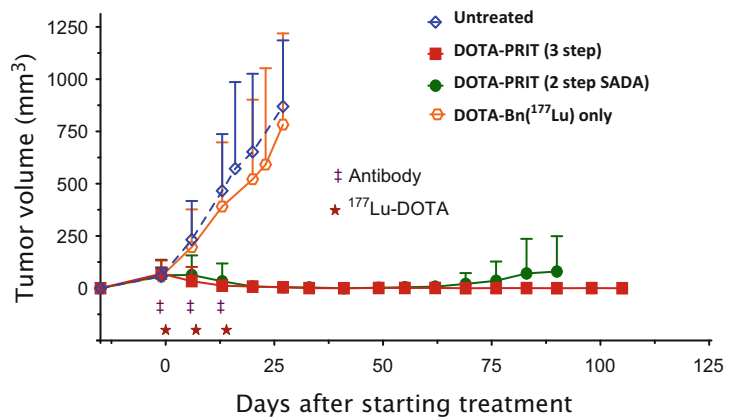
Table 11.10 A comparison of RIT using IgG, scFv-streptavidin-PRIT, IgG-scFv PRIT, and SADA PRIT

Antibody form	Points to consider	Potential issues	Advantages	Impact on clinical translation
mIgG (RIT)	Tumor ablation	–	–	Not curative
	Myelotoxicity	Suboptimal TI	–	Disabling
	Renal toxicity	Suboptimal TI	–	–
	Immunogenicity	Anti-drug antibody	–	Disabling
	Metabolism of unbound	Hepatic + RES	–	Retained systemically
	Target valency	–	2	–
	Billing model	Nuclear medicine referral	–	Disabling
scFv-streptavidin (3-step PRIT)	Renal toxicity	Suboptimal TI	–	Disabling
	Immunogenicity	Anti-drug antibody	–	Disabling
	Clearing agent	Additional drug and step	–	Complexity
	Endogenous biotin	Degrading TI	–	Undesirable
	Metabolism of unbound	Hepatic		–
	Target valency	–	4 + 4 (1st + 2nd specificity)	–
	Billing model	–	Nuclear medicine + oncology	–
IgG-scFv (3-step PRIT)	Clearing agent	Additional drug and step	–	Complexity
	Metabolism of unbound	Hepatic	–	Retained systemically
	Target valency	–	2 + 2 (1st + 2nd specificity)	–
	Billing model	–	Nuclear medicine + oncology	–
SADA (2-step PRIT)	Metabolism of unbound	–	Fast renal clearance	–
	Target valency	–	4 + 4 (1st + 2nd specificity)	–
	Billing model	–	Nuclear medicine + oncology	–

- GD2-targeting monoclonal antibodies have shown utility and safety in the treatment of high-risk neuroblastoma as evidenced by the US FDA's approval of ch14.18 (dinutuximab) and humanized 3F8 (hu3F8, naxitamab).
- The exceptional tumor selectivity of murine 3F8 in preclinical models quickly translated into clinical studies with ^{131}I- and ^{124}I-labeled 3F8 in the early 1990s, building a strong clinical rationale for RIT based on its binding domains.
- To achieve a curative therapeutic index (TI, AUC_{tumor} vs. $AUC_{normal\ organs}$), compartmental intraommaya ^{131}I-3F8 was developed with modest success in patients with leptomeningeal indications.
- Pretargeted radioimmunotherapy (PRIT) targeting GD2 has shown promise by combining the tumor targeting properties of immunoglobulins with the rapid pharmacokinetic profiles of small payloads.

- Unlike 3-step PRIT that requires a clearing agent, SADA DOTA-PRIT is a 2-step, fully humanized platform built on tandem scFv and DOTA payloads. Each step can potentially be optimized separately to further improve therapeutic indices and thus avoid myeloid, renal, hepatic, and gut toxicities.

References

1. Yu AL, Gilman AL, Ozkaynak MF, et al. Anti-GD2 antibody with GM-CSF, interleukin-2, and isotretinoin for neuroblastoma. N Engl J Med. 2010;363:1324–34.

2. Cheung NK, Cheung IY, Kushner BH, et al. Murine anti-GD2 monoclonal antibody 3F8 combined with granulocyte-macrophage Colony-stimulating factor and 13-cis-retinoic acid in high-risk patients with stage 4 neuroblastoma in first remission. J Clin Oncol. 2012;30:3264–70.

3. Navid F, Sondel PM, Barfield R, et al. Phase I trial of a novel anti-GD2 monoclonal antibody, Hu14.18K322A, designed to decrease toxicity in children with refractory or recurrent neuroblastoma. J Clin Oncol. 2014;32:1445–52.

4. Kushner BH, Cheung IY, Modak S, et al. Humanized 3F8 anti-GD2 monoclonal antibody dosing with granulocyte-macrophage Colony-stimulating factor in patients with resistant neuroblastoma: a phase 1 clinical trial. JAMA Oncol. 2018;4:1729–35.

5. Park JA, Cheung NV. Targets and antibody formats for immunotherapy of neuroblastoma. J Clin Oncol. 2020;38:1836–48.

6. Lammie G, Cheung N, Gerald W, et al. Ganglioside gd (2) expression in the human nervous-system and in neuroblastomas – an immunohistochemical study. Int J Oncol. 1993;3:909–15.

7. Dobrenkov K, Ostrovnaya I, Gu J, et al. Oncotargets GD2 and GD3 are highly expressed in sarcomas of children, adolescents, and young adults. Pediatr Blood Cancer. 2016;63:1780–5.

8. Kushner BH, Cheung IY, Modak S, et al. Phase I trial of a bivalent gangliosides vaccine in combination with beta-glucan for high-risk neuroblastoma in second or later remission. Clin Cancer Res. 2014;20:1375–82.

9. Cheung IY, Cheung NV, Modak S, et al. Survival impact of anti-GD2 antibody response in a phase II ganglioside vaccine trial among patients with high-risk neuroblastoma with prior disease progression. J Clin Oncol. 2021;39:215–26.

10. Cheever MA, Allison JP, Ferris AS, et al. The prioritization of cancer antigens: a national cancer institute pilot project for the acceleration of translational research. Clin Cancer Res. 2009;15:5323–37.

11. Suzuki M, Cheung NK. Disialoganglioside GD2 as a therapeutic target for human diseases. Expert Opin Ther Targets. 2015:1–14. https://doi.org/10.1517/14728222.2014.986459.

12. Cheung IY, Lo Piccolo MS, Kushner BH, et al. Early molecular response of marrow disease to biologic therapy is highly prognostic in neuroblastoma. J Clin Oncol. 2003;21:3853–8.

13. Terme M, Dorvillius M, Cochonneau D, et al. Chimeric antibody c.8B6 to O-Acetyl-GD2 mediates the same efficient anti-neuroblastoma effects as therapeutic ch14.18 antibody to GD2 without antibody induced allodynia. PLoS One. 2014;9:e87210.

14. Theruvath J, Menard M, Smith BAH, et al. Anti-GD2 synergizes with CD47 blockade to mediate tumor eradication. Nat Med. 2022;28:333–44.

15. Dobrenkov K, Cheung NK. GD2-targeted immunotherapy and radioimmunotherapy. Semin Oncol. 2014;41:589–612.

16. Shurin GV, Shurin MR, Bykovskaia S, et al. Neuroblastoma-derived gangliosides inhibit dendritic cell generation and function. Cancer Res. 2001;61:363–9.

17. Lee HC, Wondimu A, Liu Y, et al. Ganglioside inhibition of CD8+ T cell cytotoxicity: interference with lytic granule trafficking and exocytosis. J Immunol. 2012;189:3521–7.

18. Wondimu A, Liu Y, Su Y, et al. Gangliosides drive the tumor infiltration and function of myeloid-derived suppressor cells. Cancer Res. 2014;74:5449–57.

19. Jales A, Falahati R, Mari E, et al. Ganglioside-exposed dendritic cells inhibit T-cell effector function by promoting regulatory cell activity. Immunology. 2011;132:134–43.

20. Balis FM, McCully CL, Busch CM, et al. Pharmacokinetics of the disialoganglioside, G(D2), a circulating tumor biomarker for neuroblastoma, in nonhuman primates. J Circ Biomark. 2021;10:26–9.

21. Cheung NK, Neely JE, Landmeier B, et al. Targeting of ganglioside GD2 monoclonal antibody to neuroblastoma. J Nucl Med. 1987;28:1577–83.

22. Jin HJ, Nam HY, Bae YK, et al. GD2 expression is closely associated with neuronal differentiation of human umbilical cord blood-derived mesenchymal stem cells. Cell Mol Life Sci. 2010;67:1845–58.

23. Wu ZL, Schwartz E, Seeger R, et al. Expression of GD2 ganglioside by untreated primary human neuroblastomas. Cancer Res. 1986;46:440–3.

24. Cheung NK, Saarinen UM, Neely JE, et al. Monoclonal antibodies to a glycolipid antigen on human neuroblastoma cells. Cancer Res. 1985;45:2642–9.

25. Cheung NK, Dyer MA. Neuroblastoma: developmental biology, cancer genomics and immunotherapy. Nat Rev Cancer. 2013;13:397–411.

26. Munn DH, Cheung NK. Antibody-dependent antitumor cytotoxicity by human monocytes cultured with recombinant macrophage colony-stimulating factor. Induction of efficient antibody-mediated antitumor cytotoxicity not detected by isotope release assays. J Exp Med. 1989;170:511–26.

27. Munn DH, Cheung NK. Phagocytosis of tumor cells by human monocytes cultured in recombinant macrophage colony-stimulating factor. J Exp Med. 1990;172:231–7.

28. Cheung NK, Lazarus H, Miraldi FD, et al. Ganglioside GD2 specific monoclonal antibody 3F8: a phase I study in patients with neuroblastoma and malignant melanoma. J Clin Oncol. 1987;5:1430–40.

29. Cheung IY, Hsu K, Cheung NK. Activation of peripheral-blood granulocytes is strongly correlated with patient outcome after immunotherapy with anti-GD2 monoclonal antibody and granulocyte-macrophage Colony-stimulating factor. J Clin Oncol. 2012;30:426–32.

30. Tarek N, Le Luduec JB, Gallagher MM, et al. Unlicensed NK cells target neuroblastoma following anti-GD2 antibody treatment. J Clin Invest. 2012;122:3260–70.

31. Delgado DC, Hank JA, Kolesar J, et al. Genotypes of NK cell KIR receptors, their ligands, and Fcgamma receptors in the response of neuroblastoma patients to Hu14.18-IL2 immunotherapy. Cancer Res. 2010;70:9554–61.

32. Cheung NK, Guo H, Hu J, et al. Humanizing murine IgG3 anti-GD2 antibody m3F8 substantially improves antibody-dependent cell-mediated cytotoxicity while retaining targeting in vivo. Oncoimmunology. 2012;1:477–86.

33. Ahmed M, Cheung NK. Engineering anti-GD2 monoclonal antibodies for cancer immunotherapy. FEBS Lett. 2014;588:288–97.

34. Yankelevich M, Kondadasula SV, Thakur A, et al. Anti-CD3 x anti-GD2 bispecific antibody redirects T-cell cytolytic activity to neuroblastoma targets. Pediatr Blood Cancer. 2012;59:1198–205.

35. Xu H, Cheng M, Guo H, et al. Retargeting T cells to GD2 pentasaccharide on human tumors using bispecific humanized antibody. Cancer Immunol Res. 2015;3:266–77.

36. Pule MA, Savoldo B, Myers GD, et al. Virus-specific T cells engineered to coexpress tumor-specific receptors: persistence and antitumor activity in individuals with neuroblastoma. Nat Med. 2008;14:1264–70.

37. Majzner RG, Ramakrishna S, Yeom KW, et al. GD2-CAR T cell therapy for H3K27M-mutated diffuse midline gliomas. Nature. 2022;603:934.

38. Cheal SM, Xu H, Guo HF, et al. Preclinical evaluation of multistep targeting of diasialoganglioside GD2 using an IgG-scFv bispecific antibody with high affinity for GD2 and DOTA metal complex. Mol Cancer Ther. 2014;13:1803–12.

39. Cheung NK, Modak S, Lin Y, et al. Single-chain Fv-streptavidin substantially improved therapeutic index in multistep targeting directed at disialoganglioside GD2. J Nucl Med. 2004;45:867–77.

40. Cheung NK, Heller G, Kushner BH, et al. Detection of metastatic neuroblastoma in bone marrow: when is routine marrow histology insensitive? J Clin Oncol. 1997;15:2807–17.

41. Welte K, Miller G, Chapman PB, et al. Stimulation of T lymphocyte proliferation by monoclonal antibodies against GD3 ganglioside. J Immunol. 1987;139:1763–71.

42. Xu H, Guo H, Cheung IY, et al. Antitumor efficacy of anti-GD2 IgG1 is enhanced by fc Glyco-engineering. Cancer Immunol Res. 2016;4:631–8.

43. Miraldi F. Monoclonal antibodies and neuroblastoma. Semin Nucl Med. 1989;19:282–94.

44. Cheung NK, Landmeier B, Neely J, et al. Complete tumor ablation with iodine 131-radiolabeled disialoganglioside GD2-specific monoclonal antibody against human neuroblastoma xenografted in nude mice. J Natl Cancer Inst. 1986;77:739–45.

45. Heiner JP, Miraldi F, Kallick S, et al. Localization of GD2-specific monoclonal antibody 3F8 in human osteosarcoma. Cancer Res. 1987;47:5377–81.

46. Kramer K, Cheung NKV, DiResta G, et al. Pharmacokinetics and acute toxicology of intraventricular I-monoclonal antibody targeting disialoganglioside in non-human primates. J Neuro-Oncol. 1997;35:101–11.

47. Miraldi FD, Nelson AD, Kraly C, et al. Diagnostic imaging of human neuroblastoma with radiolabeled antibody. Radiology. 1986;161:413–8.

48. Nelson AD, Miraldi F, Cheung NKV. Biodistribution and dosimetry of 3F8 neuroblastoma monoclonal antibody. Am J Phys. 1989;4:143–50.

49. Fletcher BD, Miraldi FD, Cheung NKV. Comparison of radiolabeled monoclonal antibody and magnetic resonance imaging in the detection of metastatic neuroblastoma in bone marrow: preliminary results. Pediatr Radiol. 1989;20:72–5.

50. Yeh SD, Larson SM, Burch L, et al. Radioimmunodetection of neuroblastoma with iodine-131-3F8: correlation with biopsy, iodine-131-metaiodobenzylguanidine and standard diagnostic modalities. J Nucl Med. 1991;32:769–76.

51. Larson SM, Pentlow KS, Volkow ND, et al. PET scanning of iodine-124-3F8 as an approach to tumor dosimetry during treatment planning for radioimmunotherapy in a child with neuroblastoma. J Nucl Med. 1992;33:2020–3.

52. Arbour KC, Mezquita L, Long N, et al. Impact of baseline steroids on efficacy of programmed cell Death-1 and programmed death-ligand 1 blockade in patients with non-small-cell lung cancer. J Clin Oncol. 2018;36:2872–8.

53. Dauer LT, St Germain J, Williamson MJ, et al. Whole-body clearance kinetics and external dosimetry of 131I-3F8 monoclonal antibody for radioimmunotherapy of neuroblastoma. Health Phys. 2007;92:33–9.

54. Larson SM, Divgi C, Sgouros G, et al. Monoclonal antibodies: basic prniciples – radioisotope conjugates. In: DeVita VT, Hellman S, Rosenberg SA, editors. Biologic therapy of cancer – principles and practice. Philadelphia: J.B. Lippincott Co.; 2000. p. 396–412.

55. Kramer K, Humm JL, Souweidane MM, et al. Phase I study of targeted radioimmunotherapy for leptomeningeal cancers using intra-Ommaya 131-I-3F8. J Clin Oncol. 2007;25:5465–70.

56. Bergman I, Pohl CR, Venkataramanan R, et al. Intra-thecal administration of an anti-ganglioside antibody results in specific accumulation within meningeal neo-plastic xenografts in nude rats. J Immunother. 1999;22:114–23.

57. Lv Y, Cheung NK, Fu BM. A pharmacokinetic model for radioimmunotherapy delivered through cerebrospi-nal fluid for the treatment of leptomeningeal metastases. J Nucl Med. 2009;50:1324–31.

58. He P, Kramer K, Smith-Jones P, et al. Two-compartment model of radioimmunotherapy delivered through cerebrospinal fluid. Eur J Nucl Med Mol Imaging. 2011;38:334–42.

59. Kramer K, Pandit-Taskar N, Humm JL, et al. A phase II study of radioimmunotherapy with intraventricular 131 I-3F8 for medulloblastoma. Pediatr Blood Cancer. 2017;65 https://doi.org/10.1002/pbc.26754.

60. Kramer K, Pandit-Taskar N, Zanzonico P, et al. Low incidence of radionecrosis in children treated with conventional radiation therapy and intrathecal radioimmunotherapy. J Neuro-Oncol. 2015;123:245–9.

61. Larson SM, Carrasquillo JA, Cheung NK, et al. Radioimmunotherapy of human tumours. Nat Rev Cancer. 2015;15:347–60.

62. Cheng M, Santich BH, Xu H, et al. Successful engi-neering of a highly potent single-chain variable-frag-ment (scFv) bispecific antibody to target disialoganglioside (GD2) positive tumors. Onco Targets Ther. 2016;5:e1168557.

63. Santich BH, Cheal SM, Ahmed M, et al. A self-assembling and disassembling (SADA) bispecific anti-body (BsAb) platform for curative two-step Pretargeted Radioimmunotherapy. Clin Cancer Res. 2021;27:532–41.

Case Study #3: Antibody Fragments in Radiopharmaceutical Therapy

12

Cyprine Neba Funeh, Parinaz Asiabi, Matthias D'Huyvetter, and Nick Devoogdt

12.1 Introduction

Since the approval of Zevalin® in 2002 by the United States Food and Drug Administration (FDA) as the first radiolabeled monoclonal antibody (mAb) for radiopharmaceutical therapy (RPT) of refractory B-cell non-Hodgkin lymphoma, the field of RPT has witnessed remarkable growth, with hundreds of preclinical and clinical trials underway. While mAbs have been explored most often as vectors for delivering lethal payloads to cancer cells, the intrinsic limitations of mAbs as vectors for RPT have fueled interest in other vectors with interesting properties with breakthrough results [1].

An antibody (Ab) or immunoglobulin (Ig) is an affinity protein produced by white blood cells as a key component of humoral immunity, specifically the elimination of pathogens or foreign particles [2]. The efficacy of mAbs is linked with their ability to bind to their targets with high affinity and specificity. Upon binding, they can neutralize the pathogen or function as adaptor molecules which serve an effector function in recruiting other immune cells. In addition to the above-mentioned functions, recombinantly-produced mAbs are harnessed in nuclear medicine as vectors for the delivery of radionuclides to cancer cells for imaging and therapy.

12.1.1 The Structure of an Antibody

There are five different classes of Abs that exhibit diverse functions: IgA, IgD, IgE, IgM, and IgG. IgG is the most abundant of all the Abs (representing ~75% of the total pool of Abs in circulation) and the class commonly used as vectors for RPT. In humans, four subclasses of IgG exist; IgG_1, IgG_2, IgG_3, and IgG_4, each with a specific function [3]. However, the structure of these subclasses is highly conserved. As shown in Fig. 12.1, IgG is a Y-shaped molecule with a molecular weight of about 150 kDa comprised of two identical heavy (H) and light (L) chains. Both the heavy and light chains are in turn composed of constant (C) and variable (V) domains. Each light chain (25 kDa) contains one constant (C_L) and one variable (V_L) domain, while each heavy chain (50 kDa) contains one variable (V_H) and 3 constant (C_H1, C_H2, C_H3) domains. The nature of the heavy chain determines the antibody class and subclass. The two polypeptide chains that make up the Y-shape structure are held together by disulfide bridges at the hinge region and between the C_L and C_H1 domains.

Based on structure and function, mAbs are divided into a Fab region (fragment antigen binding) and an Fc region (fragment crystallizable).

C. N. Funeh · P. Asiabi · M. D'Huyvetter
N. Devoogdt (✉)
Department of Medical Imaging, Laboratory for In Vivo Cellular and Molecular Imaging, Vrije Universiteit Brussel, Brussels, Belgium
e-mail: nick.devoogdt@vub.be

Fig. 12.1 Structure and different functional domains of a monoclonal antibody: Fab region, Fc region, hinge, light (L) and heavy (H) chains, variable (V), and constant (C) regions
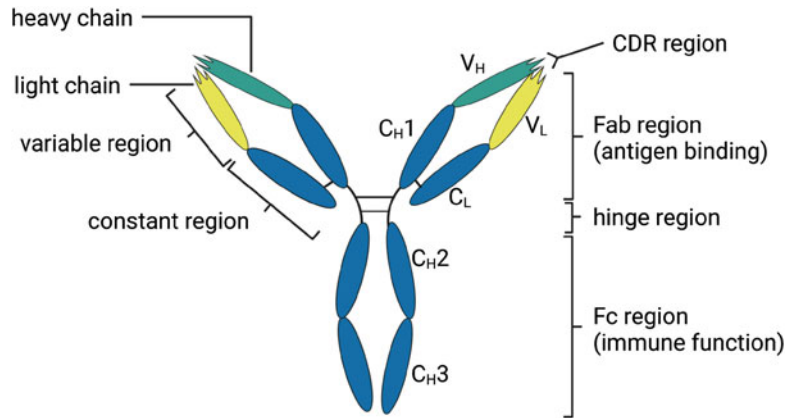
The Fab is made of the variable domains along with C_H1 and C_L, and functions as a region that recognizes and binds to antigens via six hypervariable loops called complementarity determining regions (CDRs), 3 in each variable domain. The Fc region on the other hand is made of the constant domains C_H2 and C_H3, and executes the effector function of mAbs in recruiting immune cells and complement proteins via Fc receptors [2, 3], and regulates the blood half-life of the immunoglobulin through interactions with the neonatal Fc receptor (FcRn). With respect to the latter, the FcRn receptor is found in the endosomes of endothelial cells and monocytes [4]. During circulation, mAbs are taken up via pinocytosis or receptor-mediated endocytosis. Subsequently, FcRn in the endosomes binds to the Fc region of the antibody and protects the Ab from lysosomal degradation. The FcRn-bound Ab then migrates to the cell surface where it is released back into circulation. This mechanism is mediated by changes in pH inside the cell, the low pH of endosomes (pH 6.0) increases the affinity of FcRn for the Fc. Back at the cell surface, the neutral pH (pH 7.0) decreases the affinity of FcRn for Fc, leading to the release of the Ab into circulation [4].

12.1.2 The Concept of RPT

In a key and lock model, an Ab binds to its antigen with high affinity and specificity. This has spurred scientists to generate radiolabeled mAbs that target membrane proteins that are specifically (over-)expressed on cancer cells. The resulting radioimmunoconjugates are injected into a patient, circulate throughout the body, and specifically bind to their targets expressed on cancer cells. Depending on the radionuclide employed, the emitted particles facilitate either imaging via positron emission tomography (PET) or single-photon emission computed tomography (SPECT), or therapy (RPT). In an approach dubbed "thera(g)nostics," nuclear imaging and therapy are used in conjunction, with the former helping to select patients likely to respond to the latter. Furthermore, when using thera(g)-nostic pairs with similar pharmacokinetic profiles (e.g., a single antibody labeled with either a diagnostic or therapeutic radionuclide), imaging can be used to estimate the appropriate radioactive dose for treatment.

12.1.3 Types of Radiations Used in Imaging and RPT

In nuclear medicine, different radionuclides are typically employed for imaging and therapy. For imaging, gamma (γ)-emitting isotopes (e.g., technetium-99 m and indium-111) are used for SPECT, while positron (β^+)-emitting isotopes (e.g., copper-64 and zirconium-89) are used for PET. In contrast, beta (β^-)-emitters (e.g., lutetium-177 and iodine-131), alpha (α)-emitters (e.g., actinium-225 and bismuth-213), and Auger electron-emitters (e.g., gallium-67 and iodine-

125) are used for RPT [5–7]. Therapeutic radionuclides can be differentiated by their decay properties and the linear energy transfer (LET) of the particles they emit. LET is defined as the amount of energy deposited by a particle per unit length along its ionizing track. Simply put, the LET of a particle determines its biological impact on cells: at the same dose, high LET radiation is more toxic than low LET radiation and therefore has a higher likelihood of causing toxicity to healthy tissues if not delivered carefully. Generally speaking, β^--particles exhibit low LET (~0.2 keV/μm), Auger electrons medium LET (between 5–30 keV/μm), and α-particles high LET (from 50–230 keV/μm) [6]. Of note, some radionuclides (e.g., lutetium-177 and iodine-131) emit both γ-rays and β^- particles and are often used in thera(g)nostic applications, as the same radiopharmaceutical can be used for both imaging and therapy [7, 8]. More in-depth examinations of the radionuclides used in RPT can be found in Chaps. 3 and 5.

12.1.4   Radionuclide-Antibody Conjugation Strategies

The selection of a radionuclide and the appropriate bioconjugation chemistry (i.e., bifunctional chelator/prosthetic group and linker) for a radiopharmaceutical should carefully consider the targeting vector to be employed. This is particularly important given that this link can subsequently affect the biological behavior and stability of the compound in vivo. mAb-based radiopharmaceuticals are typically labeled with radionuclides with longer physical half-lives (e.g., zirconium-89) that dovetail with the extended serum residence time of the immunoglobulin [7]. Each mAb has about 30 lysines and about 12 cysteines within their framework which can be exploited to attach radionuclides to the mAb. Depending on the type of radionuclide, a link between the radionuclide and the mAb must be established using a bifunctional chelator or a prosthetic group. For radiometals, a chelator such as diethylenetriamine-pentaacetic acid (DTPA) or tetracyclodecane-tetraacetic acid (DOTA) is often

used [7, 9, 10]. Bifunctional variants of these chelators coordinate the radiometals to prevent their inadvertent release from the conjugate *and* contain moieties that form a stable covalent bond with lysines (or other amino acids) within the targeting vector. In contrast, mAbs can be radiolabeled with radiohalogens like iodine-131 via the direct electrophilic substitution of tyrosine residues within the immunoglobulin. This method is fast, cheap, and straightforward but usually has poor stability in vivo due to deiodination and the subsequent nonspecific accumulation of radioactivity in off-target organs. As a result, more robust radiohalogenation strategies have been developed, including the use of prosthetic groups such as *N*-succinimidyl 4-fluorobenzoate (SFB) and *N*-succinimidyl guanidinomethyl iodobenzoate (SGMIB). In a direct labeling strategy, the antibody is initially pre-modified with a precursor (prosthetic group), followed by the radiolabeling of the immunoconjugate with the radiohalogen of choice. This strategy is frequently used for astatine-211. In an alternative two-step procedure, the prosthetic group is radiolabeled *first* and then conjugated to lysine or cysteine residues within the mAb. Still, more radiohalogenation methods have been developed that harness biorthogonal click chemistry [10].

12.1.5   The Rise of Antibody Fragments for RPT

To date, the use of mAbs as vectors for RPT has proven especially beneficial in the treatment of hematological malignancies, with the approval of Zevalin® (^{90}Y-Ibritumomab tiuxetan) and Bexxar® (^{131}I-tositumomab) for the treatment of refractory non-Hodgkin lymphoma by the US-FDA and European medicines agency (EMA) in the early 2000s [11]. Yet the success of mAbs as vectors for the RPT of solid tumors has remained limited. Both tumor-related factors and the characteristics of the vector play important roles. On the side of the tumor, the dense and fibrous nature of the tumor microenvironment, the availability of the target antigen, and the degree of vascularization of the tumor represent three

prominent factors. The main limiting characteristic of mAbs as vectors stems from their large size and interaction with FcRn, which combine to create a long circulatory half-life that in turn produces myelotoxicity and limits the effective dose that can be safely administered to a patient. Moreover, the large size of mAbs leads to poor tumoral penetration and a heterogeneous distribution within the tumor, rendering them less effective [11]. This is exacerbated by the poor vascularization of solid tumors [1, 13]. A detailed overview of mAbs as vectors for RPT can be found in Chap. 11.

Researchers have explored several strategies to overcome the intrinsic limitations of mAbs, including intra-compartmentalized administration, pre-targeting, and reducing the size of intact mAbs to smaller fragments through recombinant cloning or enzymatic cleavage [1, 13]. In this chapter, we will focus on the latter approach: the use of Ab fragments to build therapeutic radiopharmaceuticals. Indeed, researchers have been able to exploit the structural and functional modularity of IgG to generate smaller, customizable Ab fragments with desirable characteristics as vectors in nuclear medicine [2]. These include Fabs, single chain variable fragment (scFv), single domain antibodies (sdAb), F(ab′)$_2$ fragments, diabodies (Db), and minibodies (Mb). In each case, several core properties are altered, including target affinity, tissue penetration, circulatory half-life, and biodistribution [14]. The use of these fragments has opened a new horizon for the treatment of cancer using RPT—especially in the context of solid tumors—as evidenced by a growing number of preclinical and clinical trials. Fig. 12.2 shows a preclinical example of the tumor targeting of radiolabeled sdAbs compared to mAbs.

In the remainder of this chapter, we will explore the use of Ab fragments in RPT. We will examine the need for Ab fragments, describe the pros and cons of each commonly used Ab fragment, describe the production of these probes as well as important preclinical results, and finally explore a handful of clinical trials using fragment-based radiopharmaceuticals.

12.2 The Use of Antibody Fragments in RPT

Ab fragments have several advantages over mAbs as vectors for nuclear medicine. Indeed, the former boast a straightforward production method that makes use of microbial expression systems that are faster, provide high yields, and are cost-effective. Furthermore, due to their small size (ranging from 12 to 110 kDa), antibody fragments can bind to challenging epitopes with cryptic conformations, penetrate deep into tumors, have a shorter serum half-life, and can be cleared faster from circulation through renal or hepatic routes compared to full-length mAb [13]. The lack of a functional Fc domain may also make them safer than mAb-based probes due to the lack of immune-related adverse effects [4].

Despite these clear advantages, it is also important to note that the small size and lack of a functional Fc domain of some Ab fragments can result in low thermostability, increased susceptibility to aggregation, and a shorter half-life due to the absence of FcRn-mediated recycling. Antibody fragments with a molecular weight of less than 65 kDa (the threshold for glomerular filtration) are rapidly cleared from circulation by renal filtration. This rapid clearance of radiolabeled Ab fragments may be associated with their retention in the kidney cortex, a phenomenon mediated by a reuptake mechanism that occurs in the proximal tubuli of the kidneys. Although not yet completely understood, this reuptake mechanism is thought to be mediated by electrostatic interaction between charged patches on the Ab fragments with those on megalin and cubilin receptors in the proximal tubules. In any case, if the retention of the radiolabeled fragments is extensive, it may pose a risk for nephrotoxicity, making the kidneys potential dose-limiting organs for RPT [15, 16]. Several properties of radiolabeled fragments influence the extent of this kidney retention: (i) the presence of charged patches on the structure of the fragment, (ii) the type of radionuclide, and (iii) the bifunctional chelator or prosthetic group used for
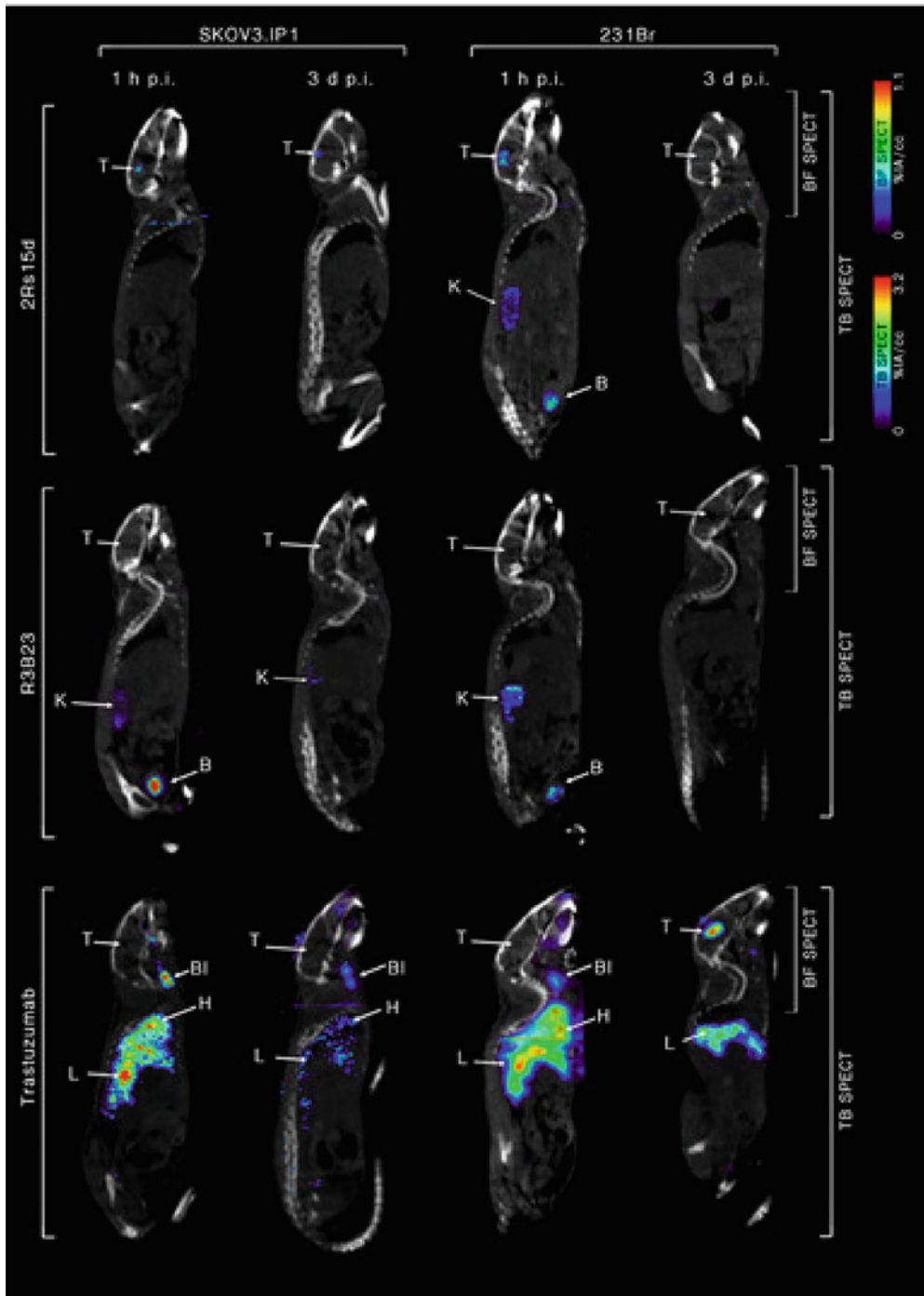
Fig. 12.2 Comparison of the tumor targeting of an ^{111}In-labeled anti-HER2 sdAb, ^{111}In-labeled trastuzumab, and an ^{111}In-labeled control sdAb (R2B23) in the brain metastases of mice bearing SKOV3 and 231Br xenografts. Images taken at 1 h and 3 days post-injection. (Reproduced from J. Puttemans et al., Preclinical targeted α and β[−] radionuclide therapy in HER2 positive brain metastasis using camelid single domain antibodies; vol 12, 1017; Cancers 2020)

radiolabeling the vectors. For example, radiometals are highly residualized (i.e., trapped within cells) compared to radiohalogens [17]. Also, some prosthetic groups used for radiohalogenation (e.g., SGMIB) have been observed to result in fast-clearing catabolites upon renal filtration, which significantly reduces the renal retention of cytotoxic radiation [18]. A handful of methods have been investigated to reduce kidney retention and are highlighted in the section of sdAbs below. In addition, several methods have been studied to modify the pharmacokinetics of Ab fragments and enhance their circulatory half-life, including multimerization, conjugation with polyethylene glycol (PEG), and the fusion of albumin-binding domains. However, some of these modifications can affect the binding affinity and specificity of the fragments as well as reduce their pharmacokinetic and dosimetric benefits over full-length mAbs [13].

Radionuclides emitting Auger electrons, α-particles, and β⁻-particles have all been investigated as radionuclides for Ab fragment-based radiotherapeutics. The short circulatory half-life of Ab fragments facilitates the use of short-lived radionuclides that would normally be incompatible with full-length IgG, including astatine-211 ($t_{1/2}$ = 7.2 h), bismuth-213 ($t_{1/2}$ = 42 min), and lead-212 ($t_{1/2}$ = 10.6 h) [7]. Both random and site-specific approaches have been used for the bioconjugation and radiolabeling of Ab fragments [19]. Along these lines, Ab fragments (like mAb) are commonly radiolabeled via conjugation to lysine residues, but the smaller size of the fragments increases the odds that the radiolabeling strategy could interfere with the binding properties of the vector. As a result, the development of site-specific bioconjugation strategies is an area of intense research, as reviewed elsewhere [19]. Table 12.1 highlights the different Ab fragments—including Fab, scFv, F(ab′)₂, Mbs, Dbs, and sdAbs—that have been investigated in preclinical and clinical studies for the imaging and RPT of cancer. Due to the promising nature of sdAbs for RPT, they are discussed separately in Sect. 12.3.
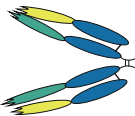
12.2.1 Fab Fragments

In the 1960s, Rodney R. Porter (who later won the Nobel Prize in Medicine in 1972 for his work) demonstrated the possibility of using enzymatic digestion to produce Fab fragments from full-sized mAbs. He showed that these fragments are 3 times smaller than full-size mAbs yet retained the mAb's antigen-binding affinity and specificity at the expense of lower avidity [20]. While affinity is the strength of the interaction between a single Ab binding site (paratope) and a single antigenic epitope, avidity is the combined strength of the interaction between the multiple binding sites of a mAb and the antigenic epitopes. Fab fragments with single binding sites thus tend to have reduced avidities compared to their parental bivalent Ab.

A Fab is a monovalent fragment with a molecular weight of 50–55 kDa [15]. They are the oldest form of Ab fragments used as therapeutics. Initially, they were produced by the enzymatic cleavage of full-sized mAbs using the protease papain [13]. But with advancements in genetic engineering, they can also be recombinantly generated and expressed using bacteria or other expression systems. Structurally, Fab fragments are composed of one light chain ($V_L + C_L$) along with the variable and constant ($V_H + C_H1$) domains of a heavy chain. The two chains are linked together by a disulfide bond between the C_L and C_H1 domains to form a monovalent species that retains the binding affinity and specificity of the parent mAb [2, 13]. With a molecular weight 3 times smaller than mAb and the absence of the Fc domains, Fab fragments have numerous advantages as vectors for RPT over mAbs, first and foremost a greatly reduced blood half-life of 12–20 h.
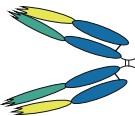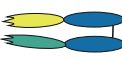
Fab fragments have been proven successful as vectors for RPT in many preclinical studies. For example, a Fab fragment of the mAb nimotuzumab targeting the cancer-associated membrane antigen EGFR was successfully labeled with yittrium-90 (⁹⁰Y) to obtain [⁹⁰Y]Y-DOTA-Fab. Subsequently, its biodistribution, specificity, and pharmacokinetic profile were

Table 12.1 Properties, advantages, and disadvantages of various Ab fragments used as vectors in RPT [2, 12, 16, 20, 21]

Properties	F(ab′)₂	Minibody	Fab	Diabody	scFv	sdAb
Molecular weight (kDa)	110	80	55	55	25	15
Valency	Bivalent	Bivalent	Monovalent	Bivalent	Monovalent	Monovalent
Serum half-life (hours)	8–10	5–10	12–20	5–6	2–4	0.5–1
Mode of production	Enzyme cleavage (papain)	Recombinant (expressed in CHO/HEK cells)	Recombinant and enzyme cleavage (expressed in CHO/HEK cells)	Recombinant (expressed in yeast cells)	Recombinant (expressed in E. coli and yeast)	Recombinant (expressed in E. coli and yeast)
Route of elimination	Hepatic	Hepatic	Renal	Renal	Renal	Renal
Advantages	Low production cost High overall tumor uptake due to low blood clearance Does not require repeated administration due to low blood clearance Low risk of nephrotoxicity due to low blood clearance and hepatic routes elimination High avidity due to its bivalent construct	High avidity due to bivalent construct High overall tumor uptake due to low blood clearance Low risk of nephrotoxicity due to long blood circulation and hepatic route elimination Does not require repeated administration compared to Fab, scFv, sdAbs Lower propensity for aggregation due to presence of the CH3 domain	Low production cost Rapid blood clearance Deep tumor penetration Rapid biodistribution	Increase avidity due to its bivalent construct Rapid biodistribution Rapid blood clearance Deep tumor penetration	Low production cost Rapid blood clearance Deep tumor penetration Rapid biodistribution	Low production cost and high yield (mg/L) High hydrophilicity Refolding capabilities after chemical or thermal degradation High thermal, pH, and shelf-life stability High affinity and specificity Rapid blood clearance Low immunogenicity due to sequence similarity to human VH Low degree of aggregation Deep tumor penetration Rapid biodistribution Access to hidden epitopes

(continued)

Table 12.1 (continued)

Properties	F(ab')2	Minibody	Fab	Diabody	scFv	sdAb
						using an extended CDR3 loop Can be radiolabeled and conjugated with diverse payloads
Disadvantages	Low tumor penetration due to large sizes Risk of off target irradiation and hematoxicity due to long circulatory half-life Increased propensity for aggregation	Engineering is time consuming and production yield is low High production cost Reduced stability after radiolabeling Lower tumor penetration relative to scFv, diabody, sdAb and Fab, due to large size	Low overall tumor uptake due to rapid clearance Risk of nephrotoxicity due to kidney retention Require repeated administration due to rapid blood clearance High propensity of aggregation	High propensity for aggregation Risk of nephrotoxicity due to rapid clearance via the kidney resulting in high renal Engineering is time consuming Reduce affinity and stability after radiolabeling Low overall tumor uptake as a result of rapid blood clearance thus requires repeated administration	High propensity for aggregation Low overall tumor uptake due to rapid blood clearance Require repeated administration due to rapid clearance Risk of nephrotoxicity due to rapid clearance via the kidney resulting in high renal retention Reduced stability and affinities after radiolabeling	Increased propensity for kidney retention, due to rapid clearance and reabsorption in kidney tubules Risk of reduce binding affinities after radiolabeling. Therapy requires repeated administration due to rapid clearance

compared to that of [^{90}Y]Y-DOTA-nimotuzumab in normal rats [16]. Higher uptake values in the liver, lungs, and heart were observed for the full-length radioimmunoconjugate compared to the Fab. However, the ^{90}Y-labeled Fab yielded significantly higher accumulation in the kidney compared to the radiolabeled mAb.

12.2.2   F(ab′)$_2$ Fragments

F(ab′)$_2$ fragments are bivalent constructs composed of two Fab fragments joined together at the hinge region by a disulfide bond. They have a molecular weight of approximately 110 kDa and can be generated via the pepsin digestion of a parent mAb [13]. They can also be produced by recombinant methods and expressed in mammalian cells. Though the tissue penetration of F(ab′)$_2$ fragments is reduced compared to that of Fab fragments due to the former's larger size, it is nonetheless superior to that of full-length mAb [13]. The bivalent nature of the F(ab′)$_2$ fragments give them the advantage of increased avidity and retention in tumors, potentially making them more suitable for RPT than Fab fragments. Considering their intermediate size and lack of an Fc region, the blood half-life of F(ab′)$_2$ fragments is longer than that of Fab fragments but shorter than that of full-size mAbs. Furthermore, the molecular weight of F(ab′)$_2$ fragments (110 kDa) is above the 65 kDa cutoff for glomerular filtration, meaning that they are eliminated via the hepatobiliary system and thus exhibit low renal retention. However, the glomerular cutoff of 65 kDa is not an absolute value and is quite an old paradigm. This means that compounds with larger molecular weights have the tendency of being filtered through the kidneys in relatively low amounts compared to smaller molecules. Nonetheless, F(ab′)$_2$ fragments pose a lower risk for kidney irradiation when used as vectors for RPT compared to Fab and scFv. This change is a double-edged sword, however, as the risk of radiotoxicity shifts to the intestines.

F(ab′)$_2$ fragments are the most used fragment in RPT, with numerous preclinical studies and the highest number of clinical trials. Indeed, the only

commercially approved fragment-based radiotherapeutic is an ^{131}I-labeled F(ab′)$_2$ fragment of the anti-CD147 mAb metuximab for the treatment of metastatic hepatocellular carcinoma (commercialized as Licartin®). Produced via the pepsin cleavage of parent CD147-targeting mAb HAb18, the ^{131}I-labeled metuximab F(ab′)$_2$ fragment demonstrated a blood half-life of 34.6 h in a pharmacokinetic study in BALB/c mice. In a biodistribution study in murine model of human hepatocellular carcinoma, the absorbed tumor-to-non-target tissue dose ratios of ^{131}I-metuximab F(ab′)$_2$ ranged between 2.5 ± 0.7 and 18.6 ± 2.1. With a 50% effective dose of 370 Mbq/kg for mice and a non-toxic dose of 277.5 MBq/kg in rats, ^{131}I-metuximab F(ab′)$_2$ demonstrated safety and efficacy in targeting hepatocellular carcinoma (HCC). This led to a preliminary clinical study in 9 HCC patients and later a phase I/II trial [21]. After demonstrating these promising efficacy and therapy profiles, the drug was approved by the Chinese FDA for the treatment of metastatic refractory hepatocellular carcinoma [22]. Also, the F(ab′)$_2$ fragment of the mAb chCE7 has been radiolabeled with ^{177}Lu- and ^{67}Cu- for RPT of L1-CAM-expressing tumors [23]. Both radioimmunoconjugates produced higher tumor-to-background activity concentration ratios and lower systemic radiation doses compared to the parent mAb but showed higher renal retention as well. In a therapy study in mice bearing colorectal cancer xenografts, 4 and 8 MBq doses of [^{177}Lu]Lu-DOTAGA-F(ab′)$_2$-cetuximab produced a significant reduction in tumor volume compared to the non-targeting F(ab′)$_2$ control [23].

12.2.3   Single Chain Variable Fragments (scFv)

ScFvs are 25 kDa molecular weight fragments composed of the variable domains of parent heavy and light chains (V$_L$, V$_H$). These chains are genetically linked to each other by a flexible glycine and serine-rich linker [13]. This linker resists protease degradation and allows the fragment to retain a similar specificity and affinity to

the parent mAb [13]. The length of the linker is commonly 12–13 residues and must be individually optimized because it can affect the affinity and stability of the scFv. scFvs are produced by genetic engineering techniques and selected via phage or ribosomal display [16].

Several scFvs have been produced and radiolabeled for the nuclear imaging and RPT of cancer. Haylock et al. [25] generated two scFvs—CD44v6-scFv-A11 and CD44v6-scFv-H12—and labeled these with ^{111}In and ^{125}I for the SPECT imaging of CD44v6-expressing neck and head mouse xenograft tumor models. They observed specific tumor targeting and tumor-to-blood ratios above 5 after 24 h for both the ^{111}In and ^{125}I compounds. At the 48-h time point, the tumor-to-blood activity concentration ratios for the ^{111}In-labeled compounds ([^{111}In]In-DTPA-A11 and [^{111}In]In-DTPA-H12) were greater than 31 (36.9 $\pm$ 13.0, 31.6 $\pm$ 4.3), while those of the ^{125}I compounds ([^{125}I]I-A11, [^{125}I]I-H12) were greater than 18 (18.2 $\pm$ 2.0, 18.9 $\pm$ 2.6, respectively) [24]. In another study, Ueda et al., 2015, radiolabeled an anti-HER2 scFv with [^{68}Ga]Ga-desferal for the non-invasive imaging of tumor-bearing mice treated with the chemotherapeutic 17-DMAG. They reported high tumoral accumulation in HER2-positive xenografts and that the imaging helped visualize changes in HER2 expression after therapy. Also, a scFv trimer against CEA was labeled with ^{131}I and evaluated for the treatment of metastatic colorectal carcinoma, ultimately producing convincing enough results to lead a Phase I clinical trial in 2011 [24]. In a cohort of 17 patients, repeated injections of 0.3 mg or 1 mg of radioiodinated CIGB-M3 scFv with activities ranging between 185–259 MBq produced low off-target toxicities coupled with lower immunogenicity compared to patients who received a single dose of 1 mg of a radioimmunoconjugate based on the parental CB-CEA-1 antibody containing the same amount of activity [22]. Although most of the preclinical data with radiolabeled scFvs involve imaging, they have demonstrated good tumor uptake and favorable pharmacokinetics, which increase the likelihood that they can also be radiolabeled with therapeutic radionuclides for use in RPT.

12.2.4 Diabodies (Dbs)

A Db is a bivalent fragment formed when two scFvs are linked together by a flexible linker of about 5–8 amino acids. Dbs are engineered to be either monospecific (two binding sites for the same antigen) or bispecific (two binding sites targeting different antigens). The linker that holds each scFv is shortened so that it prevents the scFv from self-pairing, thereby orientating the two scFvs to form a cross-pair that targets two distinct epitopes in a trans orientation [25]. With a molecular weight of 55 kDa, they have a serum half-life of approximately 5 h. Radiolabeled Dbs have been successfully studied for nuclear imaging and RPT in preclinical studies. For example, a HER2 targeting diabody [^{90}Y]Y-DTPA-C6.5K-A slowed down the growth of breast cancer xenografts compared to non-targeting control [26].

12.2.5 Minibodies (Mbs)

Minibodies—also called small immunoproteins or SIPs—are bivalent, 80 kDa Ab fragments composed of two scFv linked to a C_H3 domain (scFv-C_H3) of IgG. In some cases, however, the scFv is linked to the C_H4 domain of an IgE. The fusion of the scFv to the C_H3 or C_H4 domains is done either via a 2–3 amino acid spacer that forms a non-covalent dimer or via the IgG1 hinge and a flexible linker-peptide that forms a covalent dimer [26]. Mbs are produced by recombinant engineering, are expressed in mammalian cells, and can be engineered to be mono- or bispecific [15]. Unfortunately, Mbs sometimes show decreased thermal stability under clinical conditions due to weak VH-VL interactions. However, some studies have demonstrated that the elongation of the VH-VL linker increases their thermal stability [15].

Mbs have been successfully radiolabeled and studied for both nuclear imaging and RPT. For example, L19-SIP, a Mb targeting fibronectin, was radiolabeled with ^{131}I and evaluated for its therapeutic potential in mice bearing teratocarcinoma tumors. The radiolabeled Mb boasted
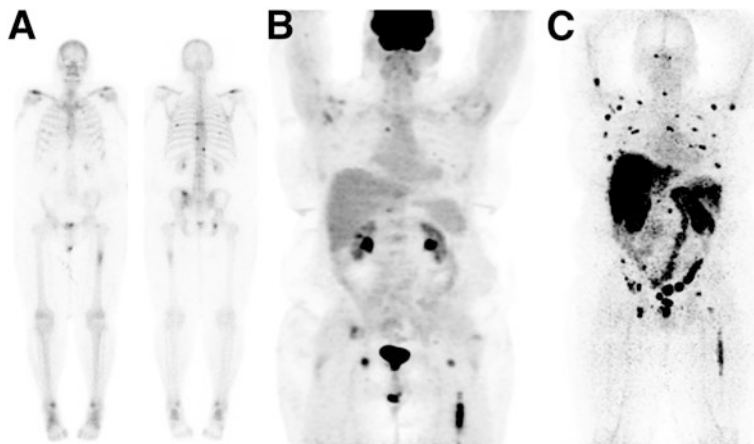
Fig. 12.3 Comparison of the tumor uptake of ^{89}Zr-IAB2M (an anti-PSMA minibody) and ^{18}F-FDG in a patient with metastatic prostate cancer. (**a**) ^{99m}Tc-MDP scans showing uptake in the vertebrae and ribs, (**b**) ^{18}F-FDG PET scans showing uptake in the left femur and low uptake in the vertebral lesions, (**c**) ^{89}Zr-IAB2M SPECT scans showing more uptake in the femur, ribs, and vertebral lesions. (Reproduced with permission from Ref. [27])

superior therapeutic efficacy compared to an analogous ^{131}I-labeled scFv [26]. In addition, a ^{89}Zr-labeled Mb targeting PSMA [^{89}Zr]Zr-DFO-IAB2M was explored for PET in mice bearing prostate cancer xenografts. The promising tumor targeting and the resulting high tumor-to-background contrast prompted the evaluation of the tracer in phase I clinical trial in patients with metastatic prostate cancers (NCT01923727) [27]. No adverse side effects were observed in a cohort of 18 patients, demonstrating the safety of the compound. With an effective dose of 0.41 mSv/MBq, both skeletal and nodal metastasis lesions were detected, and the best visualizations were obtained 48 h after the administration of the radioimmunoconjugate (Fig. 12.3).

12.3 Single Domain Antibodies as Promising Vectors for RPT

One of the most fascinating moments in the last 30 years in the study of antigen binding molecules was the 1993 discovery of single domain antibody fragments (sdAbs) by Hamers et al. [28]. sdAbs are naturally occurring binding domains of heavy-chain-only antibodies (HCAbs) found in the serum of *Camelidae* (alpacas, Ilamas, dromedaries, camels, guanacos, and vicunas). Compared to conventional antibodies that have two heavy and two light chains, HCAbs have a molecular weight of 95 kDa, consisting of only heavy chains without a C_H1 domain, and possess a single antigen-binding domain in their variable regions called a VHH. The VHH domain is similar in amino acid sequence to the VH domain of human antibodies but contains 3 CDR loops instead of the 6 in Ab-fragments derived from V_H/V_L-containing conventional Abs [29, 30] (Fig. 12.4). This VHH is also called a single domain antibody fragment (sdAb) or a nanobody® (the latter by Ablynx a spin-off company of the Vrije Universiteit Brussel that is now part of Sanofi). SdAbs can be recombinantly produced against almost any antigen. While they typically retain the binding affinity and specificity of their parent antibody, they do (inevitably) exhibit reduced avidity due to their monovalent nature. Finally, sdAbs are the smallest naturally occurring antigen-binding molecule with a molecular weight of 12–15 kDa, a prolate shape with a size of 2.5 × 3 nm, and a serum half-life of 30–60 min.

Fig. 12.4 Structure of a heavy chain only antibody (HCAb) with a single domain antibody fragment [sdAb, also called variable domain of a heavy-chain-only antibody (VHH)]
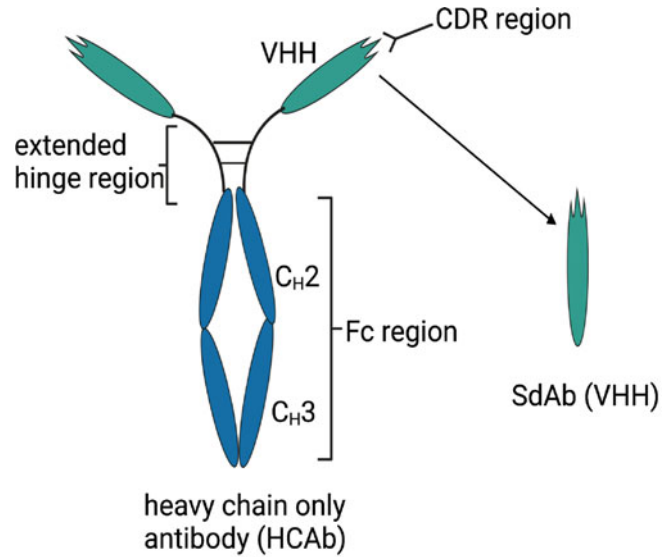
Interestingly, sharks also produce HCAbs called new antigen receptors (NAR) that contain a single antigen-binding domain (V-NAR). Their variable binding domains share some similarities to VHHs, but they differ in structural conformity. Unlike VHHs that share sequence similarities with human VH domains, V-NAR and human VH are much more divergent [30]. To the best of our knowledge, no V-NARs has been investigated for nuclear imaging or RPT.

The increasing interest in the use of sdAbs in diagnostic and therapeutic applications is predicated on their diverse applications and favorable properties. Due to the robustness and versatility of sdAbs, they attracted a lot of attention as potential vectors for RPT. Several sdAbs radiolabeled with therapeutic radionuclides have been preclinically validated with overall good efficacy results and safety profiles. This has led to the approval of some ongoing clinical trials. For example, a radioiodinated sdAb targeting HER2 for the treatment of metastatic brain tumors that express the antigen is currently being evaluated in a multicenter phase Ib/II trial (NCT04467515).

As vectors for RPT, sdAbs are easy and cheap to produce in high yield, and they have high hydrophilicity, making them highly soluble. Furthermore, sdAbs have high thermal, acidic, and shelf-life stability as well as high binding affinity and specificity for their target. Moreover, with a molecular weight of ≈15 kDa, they exhibit a rapid pharmacokinetic profile, penetrate deep into tumors, and are rapidly cleared from circulation through the kidneys. They have a low tendency for aggregation and can be radiolabeled with diverse payloads. Finally, their extended CDR3 loops can access "hidden" antigen epitopes [29]. A detailed example of the preclinical validation and clinical translation of a radiolabeled variant of the HER2-targeting sdAb 2Rs15d for RPT is detailed in a case study in Sect. 12.7.1. The advantages and disadvantages of using sdAbs as vectors for RPT are detailed in Table 12.1.

Preclinical RPT studies with radiolabeled sdAbs have highlighted the risk of nephrotoxicity due to the kidney retention of the radioimmunoconjugates. However, increasing evidence from human trials suggests otherwise [31, 32]. The mechanism of kidney retention of radiolabeled sdAbs is common for all Ab fragments and is explained above. Many mechanisms have been investigated to reduce the kidney retention of sdAbs, including the administration of a solution of positively charged amino acids before and during treatment, the infusion of a plasma expander (gelofusine) [33], and the modulation of the overall charge of sdAbs. Other mechanisms include the

introduction of an albumin-binding domain to the sdAb to slow down its blood clearance and the addition of linkers between the radionuclide and the targeting vector that can be cleaved by kidney brush border enzymes [34]. Using these mechanisms—especially the co-infusion of the radioconjugate with gelofusine—we have previously reported a reduction in kidney uptake by over 40% in preclinical models [33]. In the same study, we observed a 25.1 + 7.3% reduction in kidney uptake when the tracer (^{99m}Tc-7C12) was co-administered with lysine solution, and about a 45% reduction in uptake from the combined co-administration of lysine and gelofusion [33]. In another study, we investigated the effects of the C-terminal polarity of sdAbs on kidney retention. Here, Myc-his-tagged, his-tagged, and untagged ^{111}In-labeled 2Rs15d sdAb ([^{111}In]In-DTPA-2Rs15d) produced kidney uptake values of 52.4 ± 4.7, 36.5 ± 4.3, and 18.2 ± 1.7%IA/g, respectively, in Winster rats [35].

The in vivo cellular and molecular imaging laboratory (ICMI) Brussel has been amongst the pioneers in the use of sdAbs for nuclear imaging and RPT. They have moved three distinct sdAbs (targeting HER2, CD206, and VCAM1) into the clinic through six different clinical trials (NCT03924466, NCT03331601, NCT02683083, NCT04467515, NCT04168528, NCT04483167) for imaging or RPT. Table 12.2 summarizes the different sdAbs that have been preclinically used as vectors for RPT. However, several other sdAbs have been characterized for imaging and could easily be applied to RPT. These imaging studies are described elsewhere [12, 36].

12.4 The Identification of Antibodies and Antibody Fragments

Generally, there are two main methods to generate and identify antibodies and antibody fragments for imaging or RPT. The oldest method relies on hybridoma technology for the production of mAbs that can then be used to generate Fab and F(ab′)$_2$ fragments via enzymatic digestion. After the amino acid sequence of the mAb variable regions is known, recombinant DNA technology can be used to reformat the sequences into smaller fragments that are then expressed in appropriate expression systems (as described in Sect. 12.5). This method is being used to generate Mbs, Dbs, Fab, and scFv. The second method—display technology—involves the selection of individual Ab fragments from large Ab fragment libraries by display technologies and biopanning procedures. This methodology has frequently been used to identify Fab, scFv, and sdAb directly. Recombinant DNA technology can subsequently be used to reformat these fragments into other Ab fragments of interest or even mAbs.

12.4.1 Hybridoma

The development of hybridomas is one of the oldest methods used to generate mAbs. Developed in 1975 by George Köhler and César Milstein, hybridoma technology is based on the fusion of immunized mouse spleen cells with myeloma cells (hybridomas), thereby immortalizing the antibody-producing B lymphocytes. Next, the hybridoma clones are screened via ELISA or flow cytometry to obtain the mAbs with the desired antigen affinity. Hybridomas allow for the production of highly sensitive mAb binders at an affordable cost. Subsequent PCR amplification and sequencing of the V_H and V_L domains of the mAbs identified allow for the generation of Ab fragments via recombinant DNA technology and production in an appropriate host system [37].

There are, however, several drawbacks to using hybridomas to identify mAbs and Ab fragments. First, the process is time-consuming and takes between 6 and 8 months to obtain a reasonable number of mAbs. And second, the murine origin of the mAbs necessitates humanization before translation, which incurs additional costs. In light of these limitations, hybridomas have been progressively replaced by faster and more efficient techniques called display technologies.

Table 12.2 Radiolabeled SdAbs described in preclinical RPT

SdAbs	Target antigen	ERT compound	Disease model
2Rs15d	HER2	[^{131}I]I-SGMIB-2Rs15d	Breast and ovarian cancers (SKOV3-IP1, BT474/M1) (D'Huyvetter et al. 2017, Clin Cancer Res, PMID: 28751451)
		[^{177}Lu]Lu-DTPA-2Rs15d	Breast cancer (D'Huyvetter et al. 2014, Theranostics, PMID: 24883121)
		[^{225}Ac]Ac-DOTA-2Rs15d	Breast and ovarian (SKOV3) (Pruszynski M. et at. 2018, Mol Pharm, PMID: 29502411)
		[^{213}Bi]Bi-DTPA-2Rs15d	Breast (SKOV3) (Dekempeneer et al. 2020, Mol Pharm, PMID: 32787284))
		[^{211}At]At-SGMTB-2Rs15d	Breast (SKOV3) (Dekempeneer et al. 2019, Mol Pharm, PMID: 31268724)
		[^{131}I]I-SGMIB-2Rs15d [^{225}Ac]Ac-DOTA-2Rs15d	HER2$^+$ Brain metastasis (SKOV3-IP1) orthotopic (Puttemans J. et al. 2020, Cancers, PMID: 32326199) HER2$^+$ Brain metastasis (MDA-MB-231Br) orthotopic (Puttemans J et al. 2020, Cancers, PMID: 32326199)
VHH_1028		[^{131}I]I-SGMIB-VHH_1028	Breast and ovarian (SKOV3 & BT474) (Feng Y., Meshaw, R., MacDougald, D. et al. 2022, Sci Rep, doi: 10.1038/s41598-022-07006-9
5F7		[^{211}At]At-SGMIB-5F7 [^{131}I]I-SGMIB-5F7	Breast cancer (BT474-M1) (Choi J et al. 2017, Nucl Med Biol, PMID: 29031230) Breast cancer (B7474-M1) (J Choi et al. 2017 Nucl Med Biol, PMID: 29031230)
1E2 6E10	HGFR	[^{89}Zr]Zr-Df-Bz-NCS-1E2 [^{89}Zr]Zr-Df-Bz-NCS-6E10	Glioblastoma (U87-MG) (Vosjan J.W.D Maria et al. 2012, Mol Cancer Ther, PMID: 22319202)
9079	CD20	[^{177}Lu]Lu-DTPA-9079	Melanoma (human-CD20 transfected B16) (Ertveldt et al. 2022, Mol Cancer Ther, PMID: 35499391)
9079	CD20	[^{177}Lu]Lu-DTPA-9079	Non-Hodgkin lymphoma (Daudi & hCD20$^+$ B16) (Krasniqi et al. 2017, Mol Cancer Ther, PMID : 29054987)
JVZ-007	PSMA	[^{177}Lu]Lu-DTPA-JVZ-007	Prostate cancer (PC295) (Eline A M Ruigrok et al. 2020, Eur J Nucl Med Mol Imaging, PMID: 33094433)
2F8	CD38	[^{177}Lu]Lu-DTPA-2F8	Multiple Myeloma (RPMI 8226) (Duray et al. 2021, J Hematol Oncol, PMID : 34727950)
α-MMR	MMR	[177Lu]Lu-DTPA- αMMR	Mammary adenocarcinoma (TS/A) (Bolli, Evangelia, et al. 2019, J control Release, PMID: 31626860)
mCS-1	CS-1	[^{225}Ac]Ac-DOTA-mCS-1	Multiple Myeloma (5T33MM) (K. DE VEIRMAN et al. 2021, Oncoimmunology, PMID : 34777914)
R3B23	M-protein	[^{177}Lu]Lu-DTPA-R3B23	Multiple Myeloma (5T2MM) (Lemaire M. et al. 2014, Leukemia, PMID : 24166214)

HER2 Human epidermal growth factor receptor 2, *HGFR* Hepatocellular growth factor receptor, *CD20* a cluster of differentiation 20, *PSMA* Prostate-specific membrane antigen, *MMR* Macrophage mannose receptor, *CS-1* Cell surface glycoprotein, *M-protein* Monoclonal protein

12.4.2 Display Technologies

Newer methods for identifying antigen-binding mAbs rely on the screening of Ab-fragment libraries that are displayed on a "selectable" biological entity such as bacteriophage, bacteria, yeast, or ribosomes. The principle of these display technologies is to create a "phenotype/genotype linkage." This means that a displayed Ab-fragment protein is physically connected to a DNA fragment coding for the amino acid sequence of the Ab-fragment. When one selects

a displayed Ab-fragment by an affinity screening (the so-called biopanning procedure), the identity of the Ab-fragment can be easily obtained by sequencing the connected DNA fragment [37].

The most common display technology is phage display. In phage display, *Escherichia coli* bacteriophages are attached to their viral coat an Ab fragment (scFv, Fab, or sdAb), while a DNA fragment that encodes for the Ab fragment is contained within their phage genome (inside the viral coat). The Ab-fragment-displaying bacteriophage is generated by infecting *E. coli* cells that contain Ab-encoding phagemids in their cytoplasm with helper phages. Typically, large Ab-fragment *E. coli* libraries are displayed that contain between 10^6 and 10^{10} different Ab variants. These Ab-fragment libraries are made via the high-throughput DNA cloning of the variable regions of Abs from the B lymphocytes of immunized animals in phagemids and transforming *E. coli* cells (so-called "immune" Ab-fragment libraries). Nowadays, Ab-libraries are made synthetically (i.e., "synthetic" Ab-fragment libraries) without the need for animal immunization by randomizing CDRs of humanized Ab-fragments [37].

The antigen-specific Ab-fragments are selected from these phage-displayed libraries by a "biopanning" procedure. This is an in vitro process of repeated cycles: (i) incubating the phages to bind the Ab-fragment library repertoire to an immobilized antigen; (ii) washing to eliminate the non-specific binders, and (iii) eluting and amplifying to obtain the Ab-fragments that specifically bind to the antigen. This procedure is repeated 2–4 cycles to select the best binders from the library that are then sequenced. The most powerful advantages of phage display are its ease of use, low cost, versatility, and speed (a couple of weeks) [37].

12.5 The Production of Antibodies and Antibody Fragments

E. coli was the first bacterial system used to produce Ab fragments that are not glycosylated.

One-third of approved protein therapeutics by the FDA and EMA are produced by either cytoplasmic or periplasmic *E. coli* expression systems [38]. However, the production of large recombinant proteins containing multiple disulfide bonds in *E. coli* is challenging [39]. These proteins need then to be re-folded after purification, which can be time-consuming, inefficient, and costly. Therefore, the *E. coli* host is used as an expression system only for sdAb, scFv, and Fab. Eukaryotic cells have developed an advanced folding, post-translational, and secretion apparatus which enhances the secretory production of Abs (including full immunoglobulins) compared to bacteria. Yeasts combine the short generation time and ease of genetic manipulation of eukaryotic cells with the robustness and simple medium requirements of unicellular microbial hosts. *Pichia pastoris* and *Saccharomyces cerevisiae* represent the predominant yeast strains used for recombinant Ab fragment production. However, yeast lacks the correct human-type glycosylation for mAb production. While glycosylation is not only essential for the proper folding and biological activity of the Fc domain of the mAb, it also ensures stability in circulation. As a result, mammalian cells which allow human-like glycosylation are currently used to produce mAbs. However, mammalian cells have several drawbacks when it comes to bioprocessing and scale-up, resulting in long processing times and elevated costs. Chinese hamster ovary (CHO) and human embryonic kidney 293 (HEK293) cells are the two most popular mammalian hosts for the production of mAbs and larger Ab fragments such as $F(ab')_2$, minibodies, and diabodies [37, 38].

In addition to recombinant protein expression methods, the production of Ab fragments such as Fab and $F(ab')_2$ can be easily produced from their parent mAb via enzymatic cleavage using commercially available enzymes. While papain cleaves just above the hinge region to produce two Fab fragments and a hinge-C_H2-C_H3 fragment, pepsin cleaves just below the hinge region to produce a $F(ab')_2$ and an Fc fragment [13].

12.6 The Purification of Antibodies and Antibody Fragments

The purification of Ab fragments is more complicated than the purification of full-sized mAbs. This is because of the lack of an Fc domain that facilitates efficient purification by Protein A or Protein G affinity chromatography, which is commonly used for the efficient purification of mAbs. To overcome this limitation, Protein L has been developed and is commonly used for the purification of Ab fragments. Protein L is a cell wall-associated protein isolated from *Peptostreptococcus magnus* that binds strongly to the kappa light chain (V_L) region of certain Ab fragments, such as scFv's, Fab, and sdAbs. Since Protein L interacts with the kappa light chain subtypes, it has no immunoglobulin class restrictions and offers a broadly useful affinity ligand. To extend the usage of Protein L chromatography even further, Protein L has been fused with other Protein G and Protein A, to generate highly versatile affinity ligands with broad binding specificity. This allows it to be used for the purification of Ab fragments containing lambda light chains as well.

At present, Ab fragments are purified using several combinations of chromatographic and non-chromatographic techniques. In light of this, during the production of recombinant Ab fragments, they can be genetically engineered to display affinity tags such as hexa-histidine (6HIS), glutathione-S transferase (GST), or mannose-binding protein (MBP) [40, 41]. These affinity tags offer alternatives to Protein L chromatography and allow for purification via immobilized metal affinity chromatography (IMAC) or other affinity-based methods such as GST-C. However, affinity tags are generally relied upon only for the purification of fragments used in preclinical research. For human applications, affinity tags are rarely included because of the need to remove the potentially immunogenic tags later in production. Instead, secondary chromatography methods are used for purification, such as size exclusion chromatography, ion-exchange chromatography, and mixed-mode chromatography [41].

12.7 The Clinical Translation of Antibody Fragments

While RPT with fragment-based probes has shown great promise in murine models of disease, the successes of Ab fragments as vectors for RPT have not been limited to preclinical studies. Several phases I and II RPT clinical trials with Ab fragments-based radiotherapeutics are underway, as summarized in Table 12.3. As discussed above, one $F(ab')_2$ fragment-based radiopharmaceutical has received regulatory approval for RPT. Licartin® ($[^{131}I]$I-metuximab HAb18G) is a pepsin-digested $F(ab')_2$ fragment of the murine mAb metuximab that targets CD147 and is radiolabeled with iodine-131. It is used for the post-surgical treatment of recurrent metastatic hepatic carcinoma was approved by the Chinese FDA in 2015 [22]. Even though this drug has yet to be approved by EMA and USA-FDA, it nonetheless marks a significant breakthrough for the application of Ab fragments for RPT. At present, most ongoing clinical trials underway involve sdAbs and $F(ab')_2$ fragments. Indeed, the versatility of sdAbs has fueled increased interest in their use for RPT, and the past decade has witnessed rapid progress in the development and validation of radiotherapeutics based on these fragments. Below we detail the background of the most advanced sdAbcurrently in a clinical trial for RPT.

12.7.1 Case Study: The Clinical Translation of sdAb 2Rs15d for RPT

In 2011, our research group reported the generation and characterization of an anti-HER2 sdAb for non-invasive imaging of HER2$^+$ tumors [42]. The human epidermal growth factor receptor 2 (HER2) is a transmembrane receptor that is overexpressed in about 20–30% of breast cancer patients and at lower frequencies in gastric, ovarian, and colon carcinoma, making it a good target for RPT [35]. This HER2-targeting sdAb, referred to as 2Rs15d, demonstrated highly specific binding to its target with nanomolar

Table 12.3 Different antibody fragments in a clinical trial for RPT of cancer

Fragment	Target	Compound	Trial number	Phase	Status	Disease
2Rs15d	HER2	[^{131}I]I-SGMIB-2Rs15d	NCT02683083	I	Completed	Metastatic HER2$^+$ Breast cancer
2Rs15d	HER2	[^{131}I]I-SGMIB-2Rs15d	NCT04467515	I/II	Recruiting	Metastatic HER2$^+$ breast, gastric, gastro-esophageal cancer
NM-02	HER2	[^{188}Re]Re-NM-02	NCT04674722	I	Recruiting	Breast cancer
MX35 F (ab)$_2$	NaPi2b	[^{211}At]At-MX35 F(ab)2	NCT04461457		Completed	Ovarian cancer
F19SIP Minibody	Fibronectin (domain B)	[^{131}I]I-F19-SIP	NCT01125085	II	Completed	Solid tumor brain metastasis
F16SIP F (ab)$_2$	Tenacin-C	[^{131}I]I-F16SIP (Tenarad)	EudraCT2007-007259-15	I/II	Completed	Refractory Hodgkin's lymphoma
CIGB-m3 ScFv	CEA	[^{131}I]I-CIGB-M3		I	Completed	Metastatic colorectal cancer
HAb18g metuximab F(ab)$_2$	CD147	[^{131}I]I-metuximab HAb18G / CD147 (Licartin®)	ChiCTR-TRC-08000250	P	Completed	Metastatic hepatocellular carcinoma
			NCT00819650	II	Completed	Metastatic hepatocellular carcinoma
			NCT00829465	III	Completed	Metastatic hepatocellular carcinoma
			ChiCTR-TRC-10000837	III	Completed	Metastatic hepatocellular carcinoma

HER2 Human epidermal growth factor receptor 2, *CEA* Carcinoembryonic antigen, *CD147* Cluster of differentiation 147, *NaPi2b* sodium-dependent phosphate transporter 2b, *P* prospective

affinities. Radiolabeled with technetium-99 m, 2Rs15d displayed high tumor uptake and tumor-to-background activity concentrations with limited kidney uptake in a HER2$^+$ mouse tumor model. Furthermore, the binding of 2Rs15d was shown not to compete with the HER2-targeting mAbs trastuzumab and pertuzumab, suggesting the possibility of combination therapies. Due to its targeting potential, 2Rs15d was subsequently radiolabeled with gallium-68 to obtain [^{68}Ga]Ga-NOTA-2Rs15d and preclinically validated for immunoPET in a murine model of HER2-expressing breast cancer [43]. Based on its high tumor-to-background contrast, good tumor-targeting, and lack of toxicity in mice, [^{68}Ga]Ga-NOTA-HER2 was studied in a first-in-human trial evaluating its safety, biodistribution, dosimetry, and targeting potential (Fig. 12.5) [31]. The phase I safety results led to its approval for a phase II trial (NCT03924466) focused on repeatability uptake assessment, whereby its accuracy for the diagnosis of HER2+ breast cancer lesions is assessed by performing repeated imaging procedures on the same patient. A second phase II trial is evaluating the uptake of the radiotracer in the brain metastases of patients with breast cancer (NCT03331601).

Based on the specific tumor targeting of 2Rs15d, D'Huyvetter et al. labeled the fragment with ^{177}Lu and evaluated its biodistribution, tumor targeting, and therapeutic efficacy in a HER$^+$ mouse tumor model [35]. We observed that the therapy resulted in the efficient blockade of the growth of the HER2$^+$ tumors as well as a significant difference in overall survival compared to a control group. These data opened the door for the preclinical evaluation of RPT with 2Rs15d radiolabeled with other β$^-$- or α-emitters as shown in Table 12.3. For example, we evaluated the biodistribution, therapeutic efficacy, and potential toxicity of 2Rs15d labeled with iodine-131 ([^{131}I]I-GMIB-2Rs15d; CAM-H2) in two HER2$^+$ xenograft mouse models [18]. We observed high tumor uptake that surpassed the kidney accretion levels at 3 h post-administration, low uptake in non-target
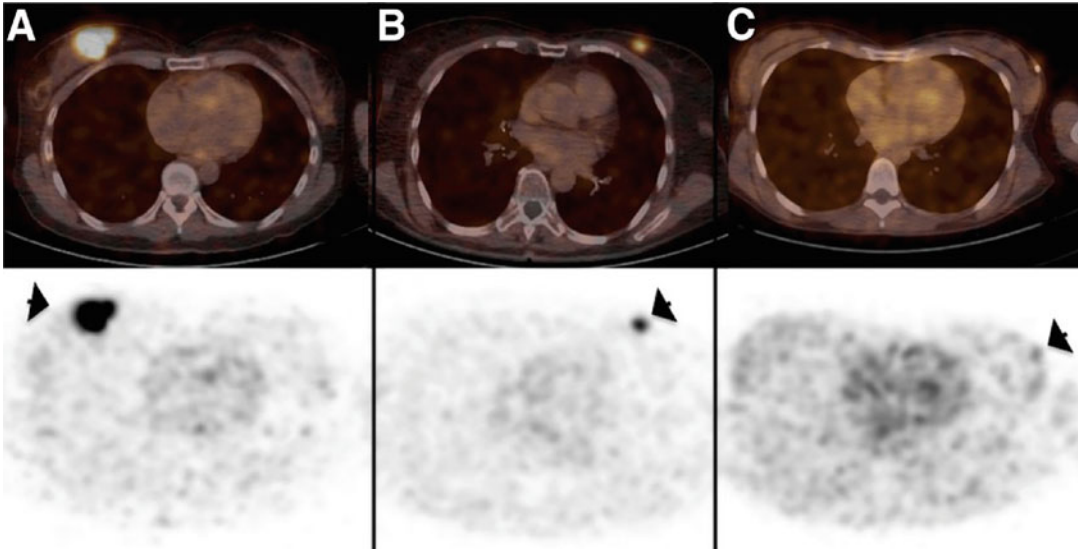
Fig. 12.5 Clinical images (PET/CT: top panel and PET: bottom panel) obtained with a ^{68}Ga-HER2 nanobody in 3 patients with primary breast cancer lesions. (**a**) highest tracer uptake (SUV$_{mean}$,11.8), (**b**) Moderate lesion uptake (SUV$_{mean}$, 4.9), and (**c**) no uptake (SUV$_{mean}$, 0.9). (Reproduced from Ref. [31])

organs and tissues, and a significant extension of median survival in the treated mice compared to controls. The preclinical efficacy and safety profile of CAM-H2 led to a first-in-human clinical trial in 2016 (NCT02683083). This phase I trial, which was completed in 2018, evaluated the biodistribution, dosimetry, safety, and tumor imaging of CAM-H2 in 6 healthy adults and 3 patients with metastatic HER2$^+$ breast cancer [32]. The trial data revealed that the radioimmunoconjugate was safe (with no drug-related adverse events in both patients and healthy volunteers), produced focal uptake in metastatic lesions (Fig. 12.6), and was rapidly cleared from circulation via the kidneys.

These results led to the approval of a phase Ib/II clinical trial for CAM-H2 in 2021 (NCT04467515; sponsored by PRECIRIX, formerly known as CAMEL-IDS). This trial is a multicenter clinical trial that evaluates the safety, tolerability, efficacy, and dosimetry of CAM-H2 in 70 patients with metastatic HER2$^+$ breast, gastric, or gastroesophageal junction cancer. This trial is expected to be completed by January 2025. Table 12.3 provides an overview of the various Ab fragments completed or in active clinical trials.

12.8 Conclusion and the Future

In this chapter, we sought to provide insight into the use of Ab fragments for RPT, from preclinical validation to clinical translation to the approval of the first Ab fragment for the RPT of metastatic hepatocellular carcinoma. These fragments have shown great potential as alternative vectors for RPT that overcome many of the limitations of mAbs. All that said, there are still several facets of Ab fragments that remain areas of attention, including their potential for high kidney retention, reduced affinities after radiolabeling, and lower absolute tumor uptake compared to mAbs. We expect that the efficacy and safety of Ab fragment-based radioimmunoconjugates for RPT will increase as interest in these vectors fuels research into novel radiochemical strategies that help optimize their stability and affinity after radiolabeling, and methods to reduce their uptake and retention in the kidneys. In the early 2000s, the clinical translation of Ab fragments for RPT proceeded at a slow pace. However, the recent rise in Ab fragment-based radiotherapeutics entering clinical trials demonstrates hope for the future.
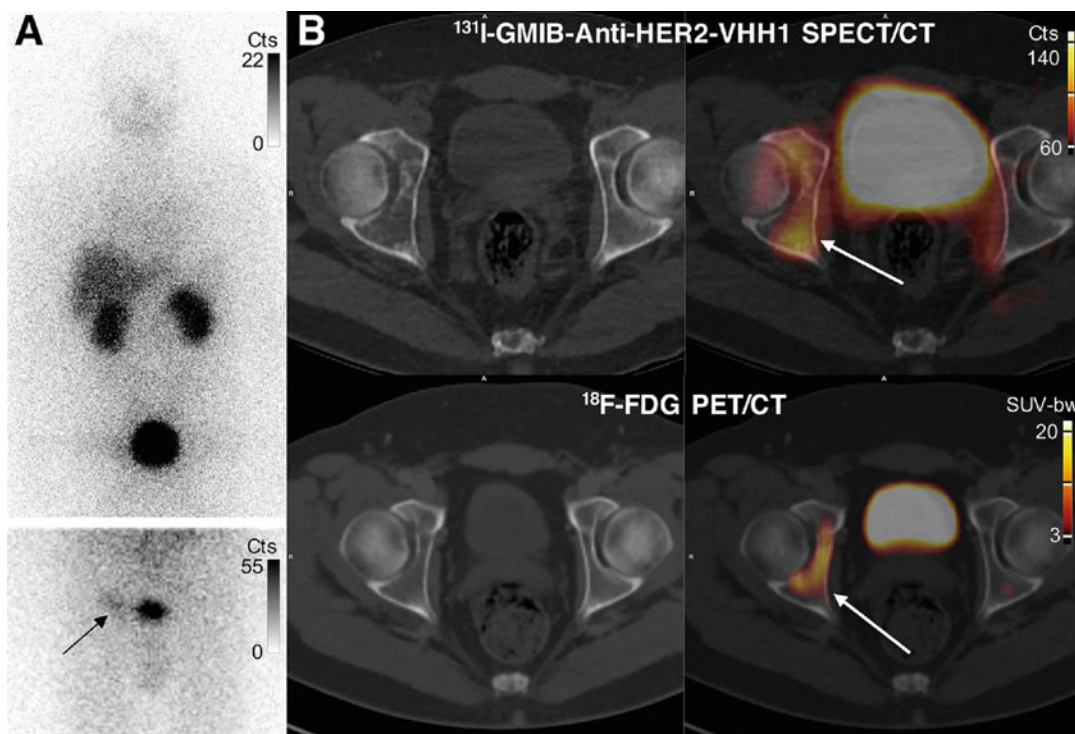
Fig. 12.6 Clinical images of ^{131}I-GMIB-anti-HER2 VHH1 in a patient with bone marrow breast cancer metastasis. (**a**) anterior whole body planar uptake images obtained 2 h post-injection, with the top image showing pronounced bladder activity due to the excretion of the compound and the bottom image depicting a significant drop in activity after urination. (**b**) SPECT/CT (top) and PET/CT images showing increased uptake of the compound in the right acetabular bone at 2.5 h post-injection for ^{131}I-GMIB-anti-HER2 VHH1 and 1-h post-injection for ^{18}F-FDG. *Cts* counts, *SUV-bw* standard uptake value-body weight. (Reproduced from Ref. [32])

12.9   The Bottom Line

- Ab fragments are small (12–110 kDa), maintain antigen affinities similar to that of their parent mAbs, and can be easily, efficiently, and inexpensively generated in microbial expression systems.
- Most Ab-fragments have a short blood half-life, exhibit rapid tumor accumulation, penetrate deep into tumors, and are rapidly eliminated from the body with better safety profiles than full-size mAbs.
- SdAbs have emerged as particularly versatile vectors for RPT, with superior properties compared to other Ab fragments. Several radiolabeled sdAbs have been preclinically validated, and the number of clinical trials

with sdAb-based radioimmunoconjugates has increased over the last decade.
- The kidney retention observed after the rapid clearance of low molecular weight Ab fragment-based radioimmunoconjugates (i.e., Fab, scFv, and sdAb) remains a point of attention and poses a risk for nephrotoxicity.
- The past decade has played witness to an increasing number of clinical trials with Ab fragment-based radiotherapeutics, and even more are expected in the coming years.

References

1. Wong KJ, Baidoo KE, Nayak TK, Garmestani K, Brechbiel MW, Milenic DE. In vitro and in vivo pre-clinical analysis of a F(ab′)2 fragment of panitumumab for molecular imaging and therapy of

HER1-positive cancers. EJNMMI Res. 2011;1
(1):1–15.

2. Alibakhshi A, Abarghooi Kahaki F, Ahangarzadeh S, Yaghoobi H, Yarian F, Arezumand R, et al. Targeted cancer therapy through antibody fragments-decorated nanomedicines. J Control Release. 2017;268:323–34.

3. Tiller KE, Tessier PM. Advances in antibody design. Annu Rev Biomed Eng. 2015;17:191–216.

4. Liu L. Pharmacokinetics of monoclonal antibodies and Fc-fusion proteins. Protein Cell. 2018;9(1):15–32.

5. Maloth KN, Velpula N, Ugrappa S, Kodangal S. Radioisotopes: an overview. Int J Case Rep Image. 2014;5(9):604.

6. Dekempeneer Y, Keyaerts M, Krasniqi A, Puttemans J, Muyldermans S, Lahoutte T, et al. Targeted alpha therapy using short-lived alpha-particles and the promise of nanobodies as targeting vehicle. Expert Opin Biol Ther. 2016;16(8):1035–47. https://doi.org/10.1080/14712598.2016.1185412.

7. Carter LM, Poty S, Sharma SK, Lewis JS. Preclinical optimization of antibody-based radiopharmaceuticals for cancer imaging and radionuclide therapy—model, vector, and radionuclide selection. J Labelled Comp Radiopharm. 2018;61(9):611–35.

8. D'Huyvetter M, Xavier C, Caveliers V, Lahoutte T, Muyldermans S, Devoogdt N. Radiolabeled nanobodies as theranostic tools in targeted radionu-clide therapy of cancer. Expert Opin Drug Deliv. 2014;11(12):1939–54.

9. D'Huyvetter M, Aerts A, Xavier C, Vaneycken I, Devoogdt N, Gijs M, et al. Development of 177Lu-nanobodies for radioimmunotherapy of HER2-positive breast cancer: evaluation of different bifunctional chelators. Contrast Media Mol Imaging. 2012;7 (2):254–64.

10. Navarro L, Berdal M, Chérel M, Pecorari F, Gestin JF, Guérard F. Prosthetic groups for radioiodination and astatination of peptides and proteins: a comparative study of five potential bioorthogonal labeling strategies. Bioorg Med Chem. 2019;27(1):167–74.

11. Bartholomä MD. Radioimmunotherapy of solid tumors: approaches on the verge of clinical applica-tion. J Labelled Comp Radiopharm. 2018;61 (9):715–26.

12. Debie P, Lafont C, Defrise M, Hansen I, van Willigen DM, van Leeuwen FWB, et al. Size and affinity kinet-ics of nanobodies influence targeting and penetration of solid tumours. J Control Release. 2020;317:34–42.

13. Bates A, Power CA. David vs. Goliath: the structure, function, and clinical prospects of antibody fragments. Antibodies. 2019;8(2):28.

14. Xenaki KT, Oliveira S, van Bergen en Henegouwen PMP. Antibody or antibody fragments: implications for molecular imaging and targeted therapy of solid tumors. Front Immunol. 2017;8:1287.

15. Kholodenko RV, Kalinovsky DV, Doronin II, Ponomarev ED, Kholodenko IV. Antibody fragments as potential biopharmaceuticals for cancer therapy:

success and limitations. Curr Med Chem. 2019;26 (3):396–426.

16. Alonso Martínez LM, Xiques Castillo A, Calzada Fal-cón VN, Pérez-Malo Cruz M, Leyva Montaña R, Zamora Barrabí M, et al. Development of 90Y-DOTA-nimotuzumab Fab fragment for radioimmunotherapy. J Radioanal Nucl Chem. 2014;302(1):49–56.

17. Chitneni SK, Koumarianou E, Vaidyanathan G, Zalutsky MR. Observations on the effects of residualization and dehalogenation on the utility of N-succinimidyl ester acylation agents for radioiodination of the internalizing antibody trastuzumab. Molecules. 2019;24(21):3907.

18. D'Huyvetter M, De Vos J, Xavier C, Pruszynski M, Sterckx YGJ, Massa S, et al. 131I-labeled anti-HER2 camelid sdAb as a theranostic tool in cancer treatment. Clin Cancer Res. 2017;23(21):6616–28.

19. Massa S, Xavier C, Muyldermans S, Devoogdt N. Emerging site-specific bioconjugation strategies for radioimmunotracer development. Expert Opin Drug Deliv. 2016;13(8):1149–63.

20. Kitten O, Martineau P. Antibody alternative formats: antibody fragments and new frameworks. Medecine/ Sciences. 2019;35(12):1092–7.

21. Chen ZN, Mi L, Xu J, Song F, Zhang Q, Zhang Z, et al. Targeting radioimmunotherapy of hepatocellular carcinoma with iodine (131I) metuximab injection: clinical phase I/II trials. Int J Radiat Oncol Biol Phys. 2006;65(2):435–44.

22. Rondon A, Rouanet J, Degoul F. Radioimmunotherapy in oncology: overview of the last decade clinical trials. Cancers. 2021;13(21): 5570.

23. Grünberg J, Novak-Hofer I, Honer M, Zimmermann K, Knogler K, Bläuenstein P, et al. In vivo evaluation of177Lu- and 67/64Cu-labeled recom-binant fragments of antibody chCE7 for radioimmunotherapy and PET imaging of L1-CAM-positive tumors. Clin Cancer Res. 2005;11 (14):5112–20.

24. Haylock AK, Nilvebrant J, Mortensen A, Velikyan I, Nestor M, Falk R. Generation and evaluation of anti-body agents for molecular imaging of CD44v6-expressing cancers. Oncotarget. 2017;8 (39):65152–70.

25. Tsai WTK, Wu AM. Aligning physics and physiology: engineering antibodies for radionuclide delivery. J Labelled Comp Radiopharm. 2018;61(9):693–714.

26. Olafsen T, Wu AM. Antibody vectors for imaging. Semin Nucl Med. 2010;40(3):167–81.

27. Pandit-Taskar N, O'Donoghue JA, Ruan S, Lyashchenko SK, Carrasquillo JA, Heller G, et al. First-in-human imaging with 89Zr-Df-IAB2M anti-PSMA minibody in patients with metastatic prostate cancer: pharmacokinetics, biodistribution, dosimetry, and lesion uptake. J Nucl Med. 2016;57(12):1858–64.

28. Hamers-Casterman C, Atarhouch T, Muyldermans S, Robinson G, Hammers C, Songa EB, et al. Naturally

occurring antibodies devoid of light chains. Nature. 1993;363(6428):446–8.

29. Piramoon M, Khodadust F, Jalal S. BBA - reviews on cancer radiolabeled nanobodies for tumor targeting : from bioengineering to imaging and therapy. BBA – Rev Cancer. 1875;2021(2):188529.

30. Muyldermans S. A guide to: generation and design of nanobodies. FEBS J. 2021;288(7):2084–102.

31. Keyaerts M, Xavier C, Heemskerk J, Devoogdt N, Everaert H, Ackaert C, et al. Phase i study of 68Ga-HER2-Nanobody for PET/CT assessment of HER2 expression in breast carcinoma. J Nucl Med. 2016;57 (1):27–33.

32. D'Huyvetter M, De Vos J, Caveliers V, Vaneycken I, Heemskerk J, Duhoux FP, et al. Phase I trial of 131I-GMIB-anti-HER2-VHH1, a new promising candidate for HER2-targeted radionuclide therapy in breast cancer patients. J Nucl Med. 2021;62(8):1097–105.

33. Tchouate Gainkam LO, Caveliers V, Devoogdt N, Vanhove C, Xavier C, Boerman O, et al. Localization, mechanism and reduction of renal retention of technetium-99m labeled epidermal growth factor receptor-specific nanobody in mice. Contrast Media Mol Imaging. 2011;6(2):85–92.

34. Chigoho DM, Bridoux J, Hernot S. Reducing the renal retention of low- to moderate-molecular-weight radiopharmaceuticals. Curr Opin Chem Biol. 2021;63:219–28.

35. D'Huyvetter M, Vincke C, Xavier C, Aerts A, Impens N, Baatout S, et al. Targeted radionuclide therapy with a 177Lu-labeled anti-HER2 nanobody. Theranostics. 2014;4(7):708–20.

36. Harmand TJ, Islam A, Pishesha N, Ploegh HL. Nanobodies as: in vivo, non-invasive, imaging agents. RSC Chem Biol. 2021;2(3):685–701.

37. Arslan M, Karadağ D, Kalyoncu S. Protein engineering approaches for antibody fragments: directed evolution and rational design approaches. Turk J Biol. 2019;43(1):1–12.

38. Ferrer-Miralles N, Domingo-Espín J, Corchero J, Vázquez E, Villaverde A. Microbial factories for recombinant pharmaceuticals. Microb Cell Factories. 2009;8:1–8.

39. Gaciarz A, Khatri NK, Velez-Suberbie ML, Saaranen MJ, Uchida Y, Keshavarz-Moore E, et al. Efficient soluble expression of disulfide bonded proteins in the cytoplasm of Escherichia coli in fed-batch fermentations on chemically defined minimal media. Microb Cell Factories. 2017;16(1):1–12.

40. Spadiut O, Capone S, Krainer F, Glieder A, Herwig C. Microbials for the production of monoclonal antibodies and antibody fragments. Trends Biotechnol. 2014;32(1):54–60.

41. Rodrigo G, Gruvegård M, Van Alstine JM. Antibody fragments and their purification by protein L affinity chromatography. Antibodies. 2015;4(3):259–77.

42. Vaneycken I, Devoogdt N, Van Gassen N, Vincke C, Xavier C, Wernery U, et al. Preclinical screening of anti-HER2 nanobodies for molecular imaging of breast cancer. FASEB J. 2011;25(7):2433–46.

43. Xavier C, Vaneycken I, D'Huyvetter M, Heemskerk J, Keyaerts M, Vincke C, et al. Synthesis, preclinical validation, dosimetry, and toxicity of 68Ga-NOTA-anti-HER2 nanobodies for iPET imaging of HER2 receptor expression in cancer. J Nucl Med. 2013;54 (5):776–84.

Ryan A. Davis, Tanushree Ganguly, Sven H. Hausner,
and Julie L. Sutcliffe

13.1 The Fundamentals

The Nature of Peptides In their most basic form, peptides are short linear chains of α-amino acids. The basics of amino acids, peptides, and proteins are discussed exhaustively in virtually every biochemistry textbook. As a result, we will only touch on a few key points here. A typical peptide may contain anywhere from two amino acids to a few dozen. These amino acids are named α-amino acids because both the amine and the carboxylate groups are connected to the same (α)-carbon and are identified according to a third group attached to this α-carbon: the side chain (*a. k.a.* the R-group). Because the fourth moiety attached to the α-carbon is typically a hydrogen, α-amino acids are chiral by nature (except for glycine, in which the side chain is also a hydrogen). In a peptide, the individual amino acids are joined by peptide (i.e., amide) bonds formed via a condensation reaction between the amine and carboxylate groups of neighboring amino acids (Fig. 13.1). Peptides span an important pharmaceutical space between small organic molecules and large biomolecules, offering high selectivity and binding affinity for disease-associated receptors with applications in both diagnostic imaging and targeted therapy ([1, 2]) (Fig. 13.2).

The Importance of Peptides as Pharmaceuticals With annual sales exceeding 50 billion US$, peptides account for about 5% of the 1.2 trillion US$ global pharmaceutical market ([3]), and the successful development, approval, and introduction of peptide-based pharmaceuticals to the pharmaceutical market is only accelerating (Fig. 13.3). By 2017, the United States Food and Drug Administration (USFDA) had approved over 60 peptide-based pharmaceuticals (i.e., peptides with up to 100 amino acids) [1]. By 2020, about 80 were marketed globally [3]. Finally, in 2021 alone, eight peptides—as well as two antibody drug conjugates (ADCs) with peptide-based drugs—were approved by the USFDA [4]. Perhaps not surprisingly, considerably more are currently in development both in the laboratory and the clinic, [3], though estimates vary since counts often include closely related compounds such as peptidomimetics. The latter issue highlights that limiting our discussion of peptide-based pharmaceuticals to compounds composed strictly of natural L-α-amino acids is an artificial

R. A. Davis · T. Ganguly
Department of Biomedical Engineering, University of California, Davis, CA, USA

S. H. Hausner
Department of Internal Medicine, Division of Hematology/Oncology, University of California, Davis, CA, USA

J. L. Sutcliffe (✉)
Department of Biomedical Engineering, Department of Internal Medicine, Division of Hematology/Oncology and Center for Molecular and Genomic Imaging, University of California, Davis, CA, USA
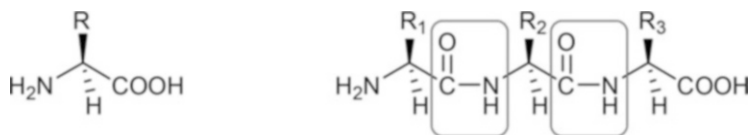e-mail: jlsutcliffe@ucdavis.edu

Fig. 13.1 Left: schematic of an L-α-amino acid with R representing the side chain; right: schematic of a tripeptide comprised of three L-α-amino acids with the amide bonds highlighted
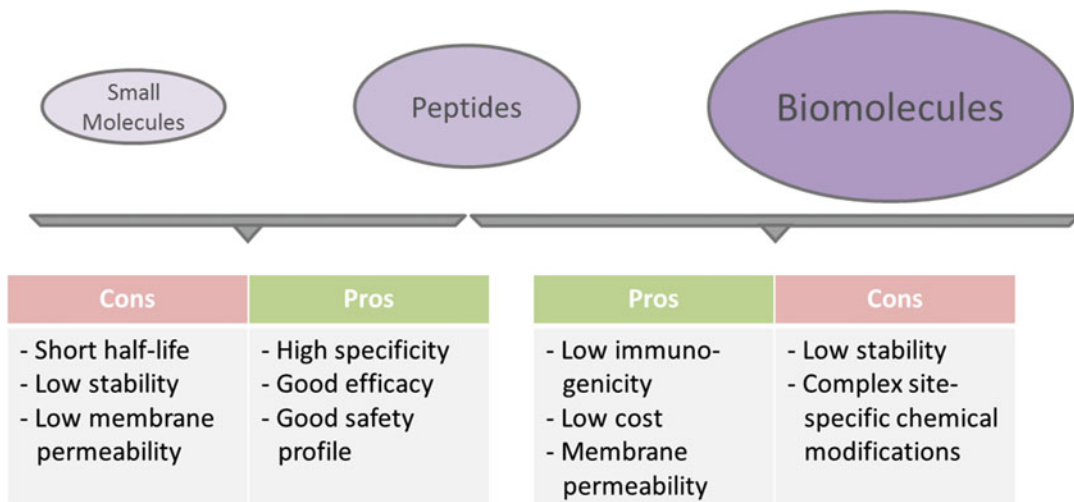

Fig. 13.2 Typical peptide-based pharmaceuticals, depending on their size, can combine many of the advantages of both small molecule and large biomolecular pharmaceuticals. (Figure adapted from Ref. [2])

constraint that does not necessarily reflect nature's complexity. An interesting example that is particularly relevant to this chapter is the urea-based peptidomimetic pharmacophore at the core of PSMA-targeting radiopharmaceuticals for the detection (i.e., [^{68}Ga]Ga-gozetotide a.k.a. [^{68}Ga]Ga-PSMA-11 *a.k.a.* LOCAMETZ®) and treatment (i.e., [^{177}Lu]Lu-vipivotide tetraxetan *a.k.a.* [^{177}Lu]Lu-PSMA-617 *a.k.a.* PLUVICTO™) of prostate cancer that were approved by the USFDA as a theranostic pair in early 2022. In this book (see Chap. 18) and much of the literature, these agents are classified as small molecules, though both have pronounced peptide/peptidomimetic characteristics, as highlighted in Fig. 13.4.

The Use of Peptides for Radiopharmaceutical Therapy Within the multi-billion market for peptide-based pharmaceuticals, peptide-based

*radio*pharmaceuticals are currently a very specialized segment. A notable distinction between peptides used for radiopharmaceutical therapy (RPT)—also referred to as peptide receptor radionuclide therapy (PRRT) agents—compared to those used for traditional targeted therapies is that while the former also depend on binding to receptors in the target tissue, they do not necessarily rely on a specific (i.e., agonistic or antagonistic) biological interaction with the receptor for their therapeutic efficacy [5]. Instead, the receptor primarily serves as an anchor for the peptide to ensure that the therapeutic dose of radiation is delivered to the target tissue. As is the case for all RPT agents, major concerns for the study and widespread adoption of peptide-based radiotherapeutics include the limited availability and high cost of high-purity radionuclides such as the β-emitter lutetium-177 and the α-emitter actininium-225 [6, 7].
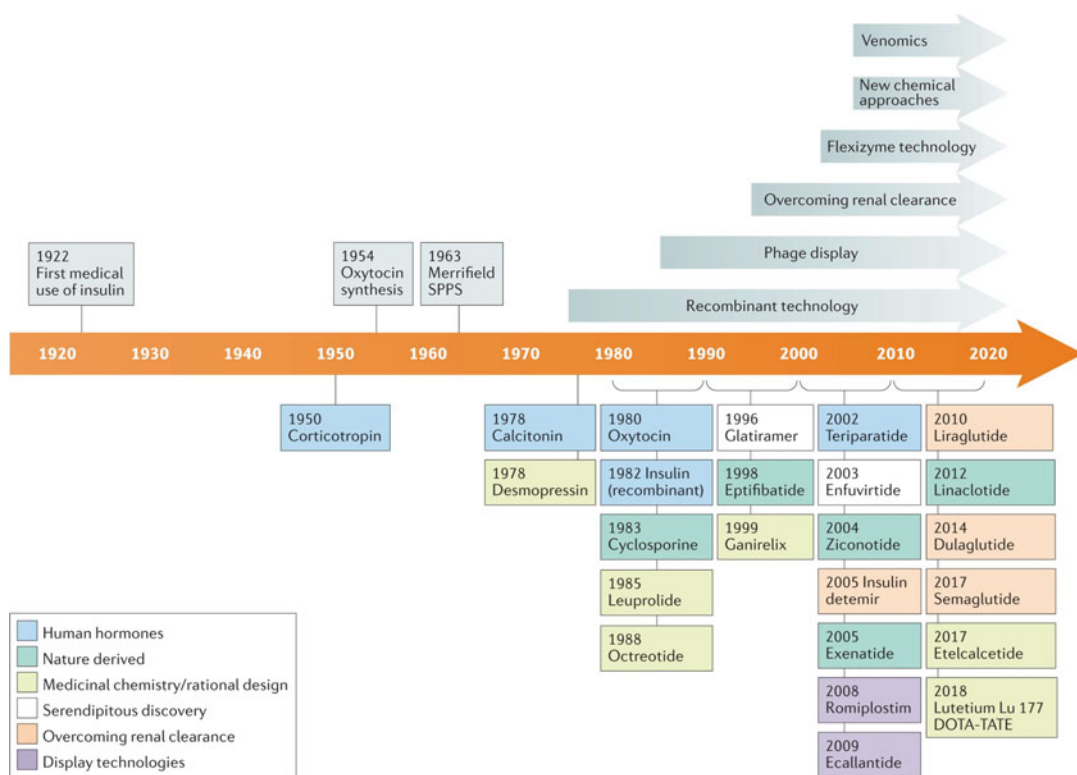
Fig. 13.3 Historical timeline of key milestones, developments, and drug approvals of peptide-based therapeutics. For a detailed review beyond the scope of this chapter, see Muttenthaler et al. [3]. (Reproduced from Ref. [3] with permission)
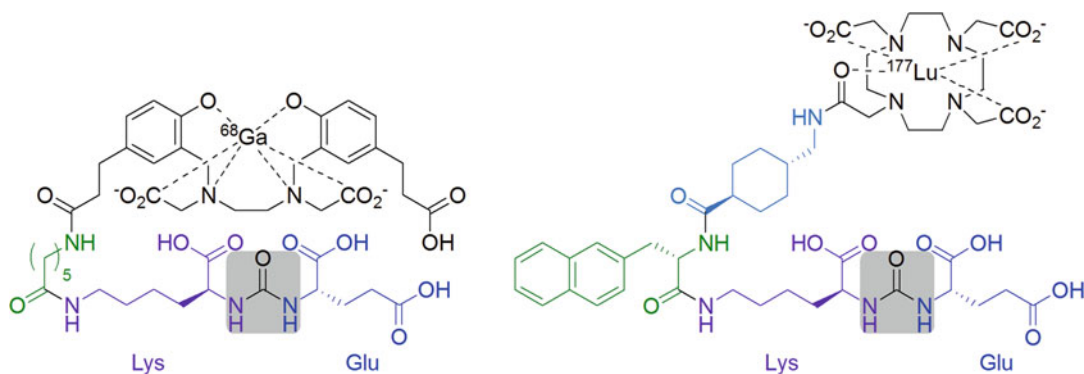

Fig. 13.4 The peptidomimetics [^{68}Ga]Ga-gozetotide and [^{177}Lu]Lu-vipivotide tetraxetan. In the former, the gallium-68 is coordinated by a HBED-CC chelator, while in the latter, the lutetium-177 is coordinated by a DOTA chelator. The amino acids are drawn in color, while the urea moiety is highlighted in gray

Peptide Synthesis and Modifications To appreciate the unique advantages of peptide chemistry, a brief look at peptide synthesis is warranted. Fortunately, the tedious days of solution phase peptide synthesis are long gone, replaced in the 1960s by solid-phase peptide synthesis (SPPS) in which the peptide is assembled in a standardized, stepwise process on a solid resin support bearing a cleavable linker (Fig. 13.5). While SPPS continues to be refined with new reagents, resins,
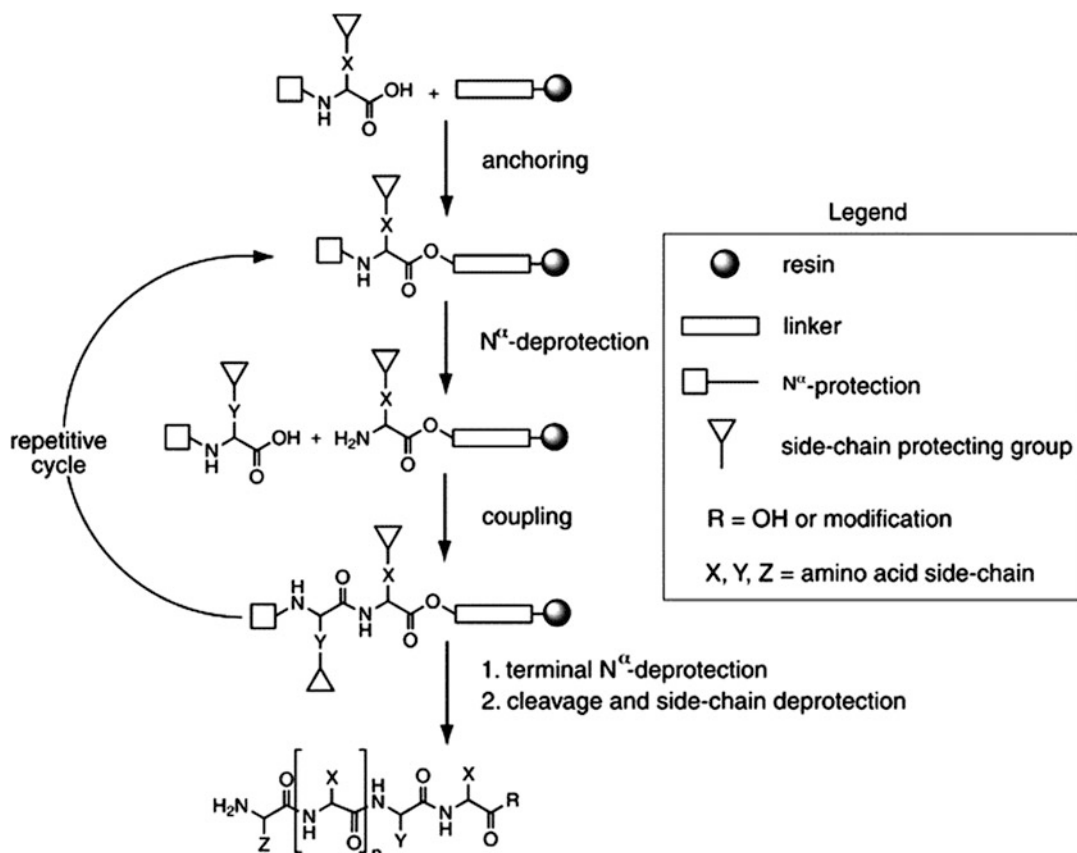
Fig. 13.5 Schematic of solid-phase peptide synthesis (SPPS) highlighting the stepwise assembly of a peptide using amino-acid building blocks. SPPS allows for the incorporation of standard L-α-amino acids as well as unnatural amino acids, pharmacokinetic modifiers, and chelators. Further modifications of the peptide are also possible after terminal deprotection and cleavage. (Reproduced from Ref. [12] with permission)

and specialized protocols, the tried-and-tested standard basic protocols work astoundingly well for the manual or automated synthesis of a large fraction of small to moderately sized peptides (up to ~30–40 amino acids) [8–11]. Amongst the major advantages of SPPS, especially for research labs, are the low setup cost for manual synthesis, the wide range of published standard protocols, and the numerous suppliers offering high-quality reagents.

Once a promising receptor-targeting peptide has been identified—whether via rational design (computational modeling), the screening of phage or chemical libraries, or the use of a known sequence from a protein, antibody, or virus—this peptide must often undergo an iterative optimization process to yield a final optimized radiolabeled peptide [13–16]. Fortunately, thanks to their modular structure, peptides can be modified chemically at specific sites (often using standard off-the-shelf protocols) during SPPS with (i) different standard L-α-amino acids and related amino acids (appropriately Fmoc-N^α-amine and side-chain protected); (ii) amino acids that are handles for site-specific modifications, including branching, post-cleavage cyclization, or the introduction of pharmacokinetic modifiers (e.g., PEG, albumin binders); (iii) metabolic stabilizers (e.g., D-amino acids, *N*-methylation, capping); and (iv) chelators (e.g., DOTA) for post-cleavage radiolabeling [3, 17–21] (Fig. 13.6).

Fig. 13.6 Representation of common modifications made to peptides to improve their selectivity, affinity, stability, and overall pharmacokinetic characteristics. (Reproduced from Ref. [17] with permission)
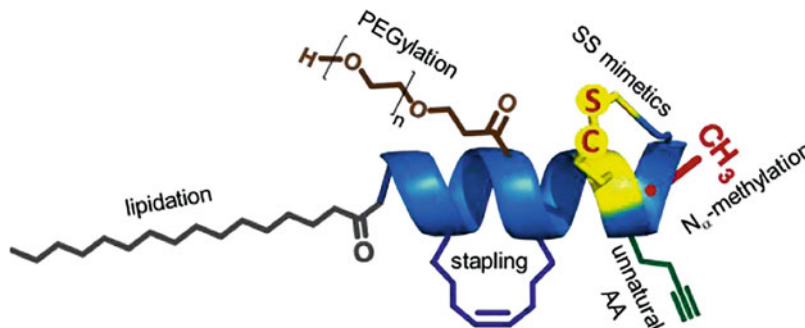
13.2 The Details

13.2.1 Optimizing the Performance of Radiotherapeutic Peptides: A Balancing Act

The success of peptides as diagnostic positron emission tomography (PET) or single-photon emission computed tomography (SPECT) imaging agents stems from both their ability to target disease specific cell surface receptors with binding affinities and selectivities rivaling those of antibodies and their low toxicity (including little to no immunogenicity) [20]. Due to their relatively small size, peptides typically clear rapidly from the blood and most non-target tissues, thereby producing high target-to-background imaging contrast within minutes to an hour [22, 23]. However, this rapid clearance from the blood stream can be problematic in the context of RPT, in which prolonged circulation is advantageous to facilitate high and persistent uptake in (and thus therapeutic radiation dose to) the target tissue. Therefore, when developing a peptide for RPT, it is critical to strike a fine balance: if clearance from the blood is too rapid, then the target uptake and resulting therapeutic efficacy will be sub-optimal; but if blood clearance is too slow, then increased off-target radiotoxicity can be observed. In addition to fine-tuning a peptide's structure to optimize its uptake and clearance profile, peptide modifications for RPT also aim to increase target affinity, specificity, and proteolytic (serum) stability. This is typically done by addressing the questions discussed in the following sections.

13.3 Long Story Short: What Is the Optimal Size and Shape of the Peptide?

Once a lead peptide has been identified, a common starting point is to reduce the number of amino acids to the minimum number required for good affinity and selectivity. This shortens the synthesis of the peptide and, more importantly, reduces the number of possible cleavage sites for proteolytic degradation. For example, as further discussed below, somatostatin—the lead peptide for the somatostatin receptor-targeting peptides [^{68}Ga]Ga-DOTA-TATE (NETSPOT®) and [^{177}Lu]Lu-DOTA-TATE (LUTATHERA®) —had a 14 amino acid cyclic peptide core with a severely limiting in vivo half-life of under 3 min due to its rapid enzymatic degradation [24]. Alongside several critical amino acid substitutions, shortening the peptide to 8 amino acids (*octreo*tide) was key to increasing its serum half-life to 1.5 h while maintaining its receptor affinity (Fig. 13.7) [24, 25].

Cyclization increases rigidity of a peptide and can help to improve its affinity, specificity, and metabolic stability by reducing the number of conformers that can interact with a binding site or be degraded by proteolytic enzymes [26]. In some cases, lead peptides are already cyclic (as in somatostatin), but if not, cyclization is often explored early in the optimization process. Fig. 13.8 shows several approaches to the cyclization of peptides, including two particularly popular routes: the formation of amides and disulfides [26]. Overall, the constraints introduced by cyclization result in a three-dimensional structure that

is more similar to larger proteins and can thus provide higher overall free binding energies compared to their linear counterparts. However, cyclization can also result in reduced or lost target affinity if an unfavorable conformation is locked into place, so the sites used for cyclization must be chosen carefully. Furthermore, the advantages of cyclization come at the cost of increased synthetic complexity. It is indeed important to note that cyclization may not be an essential feature for a successful radiotherapeutic peptide, as illustrated by 5G and NeoBOMB1 (both discussed below).
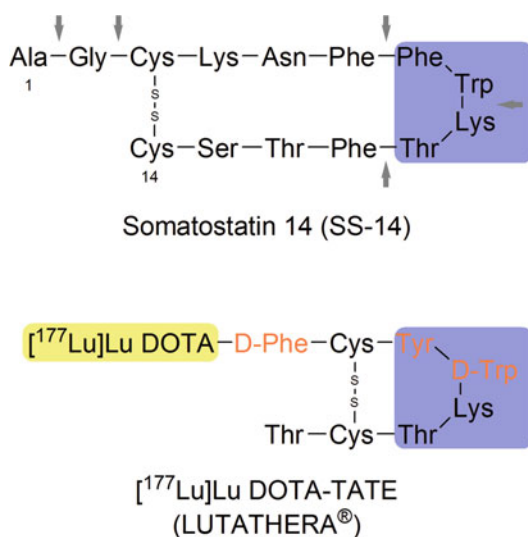
Fig. 13.7 Comparison between the structure of somatostatin and that of [^{177}Lu]Lu-DOTA-TATE, highlighting the binding motif (blue), amino-acid substitutions (orange), the radiolabeling group (yellow), and major metabolic cleavage sites on the original somatostatin (arrows)

13.3.1 Going from Good to Better—Which Residues *Really* Matter?

Modifications to the amino acid sequence of a radiotherapeutic peptide can significantly improve its affinity, selectivity, metabolic stability, and—especially significant in the context of RPT—circulation time. These modifications often make use of D- or unnatural amino acids (including β-amino acids and analogs), N-terminal caps (e.g., acetyl groups), polyethylene glycol chains (i.e., PEGylation), and albumin-binding moieties (ABMs) among others. These modifications are compatible with standard SPPS protocols and are therefore typically easy to perform (Figs. 13.5 and 13.9). Many of the common (natural) amino acid sequences attacked by endoproteases (*a.k.a.* cleavage sites) have been mapped and are incorporated in searchable databases, though the in vivo confirmation of a peptide's stability (or lack thereof) is still recommended because conformational restraints such as cyclization or modifications such as PEGylation can significantly affect stability [27, 28]. In the following pages, we will address these modifications and discuss how they can be used to improve the in vivo performance of radiotherapeutic peptides. We will then offer a look at some notable examples of radiotherapeutic peptides incorporating these modifications.

Good to Better #1: For Stability, Please Do Tell, D or L?

One of the most common modifications to enhance the stability of a peptide is the replacement of susceptible amino acid sequences—and terminal amino acids due to possible attack by
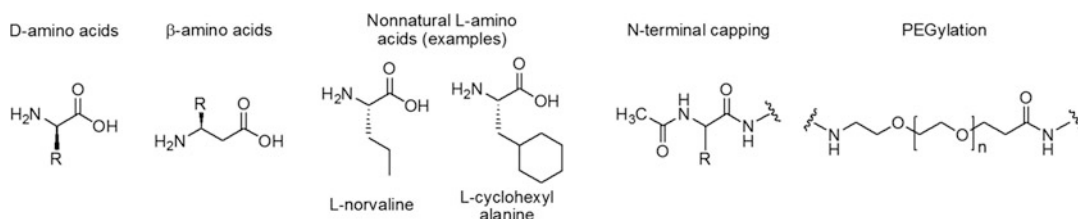

Fig. 13.8 Common approaches to the cyclization of peptides

Fig. 13.9 Examples of common substitutions, additions, and modifications to radiotherapeutic peptides

exoproteases—with D- and/or unnatural amino acids [25]. A large variety of D- and unnatural amino acids are commercially available for SPPS, and the introduction of D-amino acids in particular has often been shown to improve stability and increase the serum half-life of therapeutic peptides [29]. Examples of peptides that have undergone D-amino acid substitutions include DOTA-TATE (Fig. 13.7), the chemokine receptor (CXCR4)-targeting peptides Pentixafor and Pentixather, and the bombesin receptor-targeting peptide NeoBOMB1 (all discussed below) [24, 25, 30].

Good to Better #2: Put a PEG on for a Leg up?
PEGylation is a common modification that can increase a peptide's stability and circulation time by increasing its mass and hydrodynamic volume; help reduce the accumulation of a peptide in the kidneys, lung, and liver; and reduce immunogenicity by masking a peptide from the immune system [20, 31, 32]. PEGylation can be easily achieved during SPPS at either terminus, the side chain ε-amine of lysine, or another amino acid such as cysteine (using maleimide thiol conjugation). Importantly, the blood circulation time and renal and hepatic clearance properties of a PEGylated peptide can be tuned to some degree by changing the molecular weight of the PEG chain [33, 34]. Interestingly, the placement of a PEG chain within the amino acid sequence can also significantly affect a peptide's pharmacokinetic profile. A particularly good example of this phenomenon is provided by the integrin $\alpha_v\beta_6$-targeting peptide A20FMDV2, a linear 20-mer peptide comprised entirely of natural amino acids in which *bi-terminal* PEGylation reduced kidney retention, enhanced tumor accumulation, and improved stability substantially to 80% at 1 h in mouse serum [32].

Good to Better #3: Can Glycosylation Bring Sweet Rewards?
Glycosylation can improve the pharmacokinetic profile of a peptide by increasing its circulation time, accelerating its renal clearance, and reducing its lipophilicity (which in turn reduces its accumulation in the liver and intestines) [35, 36]. The attachment of large polysaccharide chains is much more difficult than PEGylation because the sugar polymers have multiple attachment sites and, as in the case of dextran, must be modified for attachment to the peptide [35]. The addition of mono-, di-, and trisaccharides increases the bioavailability, stability, and tumor accumulation of peptides while decreasing their intestinal and liver accumulation, as demonstrated by the conjugation of glucose, maltose, and maltotriose to octreotide [36, 37] as well as by the attachment of *N*-acetyl glucosamine and galacturonic acid to the cyclic 5-mer peptide cRGDfK in the integrin $\alpha_v\beta_3$-targeting galacto-RGD peptide (note: in this notation, the 'c' is indicative of cyclization, rather than a D-Cys) [38, 39].

Good to Better #4: Hitching a Ride on Albumin?
An increasingly popular modification, particularly for radiotherapeutic peptides, is the addition of albumin binding moieties (ABMs, Fig. 13.10) [40–42]. ABMs are small groups that can be easily added to a peptide during SPPS. They bind reversibly to serum albumin (the most abundant protein in blood) and, thus, prolong the peptide's circulation time and also facilitate renal recycling. This results in increased accumulation and retention in the tumor and can produce particularly striking effects for small, rapidly clearing peptides. However, care must be taken to avoid overly extending the circulation time of a
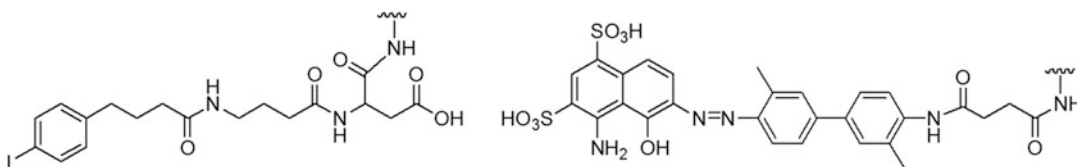
Fig. 13.10 Two widely used albumin binding moieties used to prolong the blood circulation and increase the tumor accumulation of radiotherapeutic peptides: an example of a 4-(*p*-iodophenyl)butyryl-based group (left) and a fragment of the Evans blue dye (right)

radiotherapeutic peptide, as this could result in unacceptable hematotoxicity. Typically, one of the two most widely reported ABMs—a major fragment of the Evans blue (EB) dye or a 4-(*p*-iodophenyl)butyryl (IP) group in close proximity to a carboxylate group—are incorporated. Examples of peptides modified with ABMs include octreotide, cRGDfK, and integrin $\alpha_v\beta_6$-targeting peptides, among others [41]. Of these two ABMs, IP appears to yield lower accumulations in the kidneys and is particularly attractive because it is comprised solely of low-cost, off-the-shelf amino-acid building blocks.

Good to Better #5: More Is Better?
Multimerization can improve the affinity of a peptide for its target, prolong blood circulation time, increase tumor accumulation and retention, and improve metabolic stability by increasing the size of the construct as well as harnessing multiple binding effects (avidity) [43, 44]. As seen for the cRGDfK-peptide dimer [18F]Alfatide and its more stable PEGylated (PEG_4) form [18F] Alfatide II, multimerzation can produce constructs with tumor accumulations enhanced by 2-10-fold [43, 44]. A particularly thoroughly studied example of multimerization involved a comparison of a monomer, dimer, tetramer, and octamer of a cRGD peptide (note: the "c" is again indicative of cyclization, rather than a D-Cys). In this case, little benefit was observed upon going above a dimer, as the tetramer and octamer produced similar tumor accumulation but increased off-target uptake in the intestines, liver, kidney, and muscle [43, 44]. Generally, to maximize the benefits of multimerization, the spacing between the monomers must be evaluated during the synthesis of the construct in order to achieve optimal avidity and tumor internalization while also maintaining a balance with the peptide's overall pharmacokinetic properties [44].

13.3.2 Getting Down to Business: Radiolabeling Peptides for RPT

Business #1: Decay the Right Way: Picking the Appropriate Radionuclide
As discussed in detail in the Fundamentals section of this textbook, the selection criteria for a therapeutic radionuclide include its type and energy of emission, half-life, cost, availability, and ease of labeling (Table 13.1) [45]. Furthermore, the choice of a radionuclide should be informed by the mode of action of the peptide to which it will be attached (i.e., an β^--emitter may be preferable if the peptide remains on the cell surface, while an α-emitter may be preferable if it is internalized), the penetration depth of the emitted particles (Auger: 100 nm, α: 50–100 μm, β^-: 0.05–12 mm), and—for α-emitters—the possibility of forming toxic daughter radionuclides [46]. As peptides are often rapidly taken up in the tumor and have relatively short circulation half-lives (several hours), therapeutic radionuclides with short radioactive half-lives such as terbium-149 ($t_{1/2}$ = 4.1 h) and astatine-211 ($t_{1/2}$ = 7.2 h) can be considered for RPT as well. Choosing a radionuclide that can be used for imaging (or a therapeutic radionuclide that can be paired with a chemically similar diagnostic radionuclide) can also enable image-guided dose estimation, staging, and treatment monitoring

Table 13.1 Selected therapeutic radionuclides along with their companion diagnostic radionuclides [48]

Therapeutic radionuclide	Half life	Decay mode (%)	Imaging radionuclide	Half life
Radiohalogens				
^{125}I	60.1 d	EC (100%) Auger	^{123}I	13.2 h
			^{124}I	4.2 d
^{131}I	8.0 d	β⁻ (100%)	^{123}I	13.2 h
			^{124}I	4.2 d
^{211}At	7.2 h	α (42%) EC (58%)	^{123}I	13.2 h
			^{124}I	4.2 d
Radiometals				
^{67}Cu	2.58 d	β⁻ (100%)	^{64}Cu	12.7 h
^{90}Y	2.67 d	β⁻ (100%)	^{68}Ga	68 min
			^{111}In	2.8 d
^{149}Tb	4.1 h	α (17%) EC (83%)	^{152}Tb	17.5 h
^{161}Tb	6.9 d	β⁻ (100%) Auger	^{152}Tb	17.5 h
^{177}Lu	6.7 d	β⁻ (100%)	^{68}Ga	68 min
			^{111}In	2.8 d
^{225}Ac	10 d	α (100%)		

(Table 13.1) [22, 46]. Finally, as is the case for all radiopharmaceuticals, availability is a major factor in determining why certain radionuclides are preferred. At present, many α- and β-emitting radionuclides remain in limited supply, a fact that has led to the overwhelming use of yttrium-90 and lutetium-177 in both the laboratory and the clinic [47].

Business #2: Getting It On—Picking the Appropriate Approach to Radiolabeling

Many of the radiolabeling chemistries described in Chaps. 6 and 7 of this book can be used with peptides. Furthermore, unlike antibodies and small molecules, peptides can be modified for site-specific radiolabeling relatively easily with little to no effect on their targeting efficacy. Briefly, the attachment of a radionuclide to a peptide can be achieved using indirect or direct radiolabeling approaches (Fig. 13.11). Indirect radiolabeling is best when a peptide is highly susceptible to degradation or unstable at the elevated temperatures required for radiolabeling with a selected radionuclide [49, 50]. Indirect methods employ a prosthetic group that is radiolabeled first and *then* attached to the peptide under mild conditions. Generally speaking, radiohalogens—the radioisotopes of iodine and

astatine-211—are the most likely candidates for indirect radiolabeling via prosthetic groups [49].

Direct radiolabeling is by far the most common approach to radiolabeling with radiometals (Fig. 13.11) and can be carried out with commercially available chelators such as DOTA via incubations in pH 4–6 buffers at 80–100 °C for 10–60 min [22, 51]. Most peptides can tolerate these conditions, making direct radiolabeling a simple and highly efficient approach that often requires only minimal purification (e.g., by solid phase cartridge extraction). In some cases, the procedures are compatible with fully automated radiolabeling kits, which are considered best practice for current Good Manufacturing Practices (cGMP) clinical productions.

Radiolysis can be a significant concern when radiolabeling peptides with high activities of therapeutic radionuclides in small volumes and at high temperatures because the radioactive emissions within the reaction mixture produce superoxide, hydroxyl, and hydrogen radicals that can damage the peptide via reaction or direct energy transfer. Generally speaking, the most radiosensitive amino acids are those that contain sulfhydryl or thioether groups (i.e., cysteine and methionine), those that contain aromatic moieties
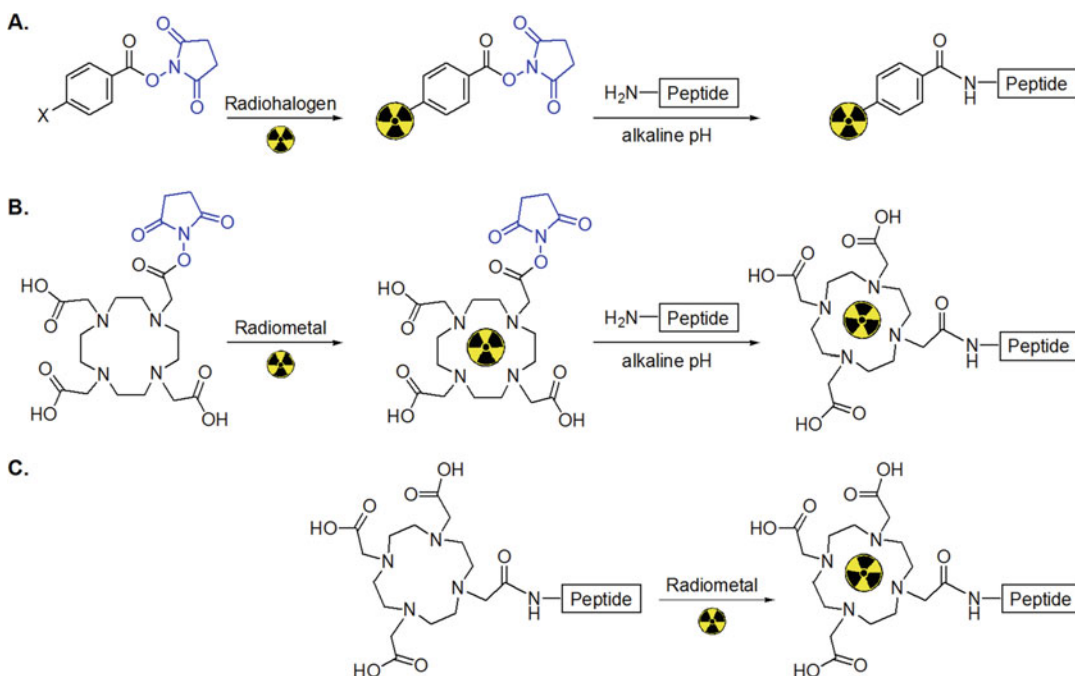
Fig. 13.11 Two examples of indirect approaches to the radiolabeling of a peptide (**a**, **b**) as well as one example of direct radiolabeling (**c**). The indirect examples shown use a prosthetic group with an activated ester—a succinimidyl ester—leaving group (blue)

(i.e., histidine, tyrosine, tryptophan, and phenylalanine), and, to a lesser extent, lysine and arginine [52]. To prevent radiolysis, alcohols (ethanol) and other antioxidants (e.g., L-ascorbic and gentisic acid) are used as additives at concentrations of tens-of-milligrams/milliliter for quenching of the free radicals [53]. Radioprotectants are also a common part of the final formulation of radiotherapeutic peptides to suppress radiolysis during storage.

13.3.3 Peptides for Radiotherapy— Particularly Important Examples

13.3.3.1 Peptide Receptors and Their Clinical Relevance

The answer to the question of whether a given peptide receptor is a good target for RPT is found in biochemistry, physiology, and medicine. Indeed, the suitability of a receptor depends on its selectivity for diseased tissue (i.e., is it expressed exclusively, or at least much more highly, in the malignant target?), its relevance for therapy (i.e., do the expression levels correlate to the severity of disease?), its prevalence within diseased tissue and within a tumor type (i.e., what is the percentage of lesions that express the receptor? What is the percentage in the patient population?), and its distribution within diseased tissue (i.e., is it homogeneously or heterogeneously distributed within each lesion?). Once a promising target has been selected, the optimization of a candidate peptide ligand becomes the priority.

Many cancer-associated cell surface receptors have been identified and targeted with radiolabeled peptides for imaging and, increasingly, for therapy. In the sections that follow, we describe receptors that have risen to prominence in RPT thanks to their important roles in oncology as well as the progress made in developing radiolabeled peptides that target them. These

examples highlight how—at least to date—the optimization of radiotherapeutic peptides has relied upon the strategies described above, including shortening of the amino-acid chain, substituting natural amino acids with D- and unnatural amino acids, cyclization, and so on.

Notable Example #1: Somatostatin Receptors
Somatostatin receptors hold a particularly prominent place in the world of peptide-based RPT due to their important role in many cancers and the trailblazing success of several octreotide-based radiopharmaceuticals, most notably NETSPOT® ([^{68}Ga]Ga-DOTA-TATE) and LUTATHERA® ([^{177}Lu]Lu-DOTA-TATE) (Fig. 13.7 and Chap. 14). Somatostatin receptors (SSTR; SSTR1-5) are inhibitory G protein-coupled receptors present in both normal and cancer cells. SSTRs, specifically SSTR2, are overexpressed in most neuroendocrine tumors (NETs), pancreatic tumors, and breast and colon adenocarcinomas, making them a promising target for imaging and therapy. The endogenous ligand for SSTR2, somatostatin, is a cyclic disulfide peptide containing 14 amino acids (SST-14) that was discovered in hypothalamic extract and first described in 1973 [54]. While somatostatin's sub-3 min plasma half-life may be advantageous for a peptide hormone, it is much too short for a (radio)pharmaceutical. Consequently, somatostatin was optimized in a large-scale collaborative effort that prepared and screened libraries of analogs in an effort to increase its stability and affinity [15]. These efforts ultimately yielded octreotide, an 8-amino acid peptide that retains somatostatin's (shortened) binding loop and disulfide-based cyclization, has short (1-amino acid) *C*- and *N*-terminal extensions beyond the minimal required core, and features two D-amino acids. Taken together, these traits increased octreotide's biological activity and lengthened its plasma half-life (~ 2 h) compared to somatostatin.

Non-radioactive octreotide was first approved as a hormone drug by the USFDA in 1988 and remains in use today. However, its potential as a vector for nuclear imaging and RPT was recognized as soon as it was discovered, as

illustrated by the development of an ^{123}I-labeled variant of Tyr^3-octreotide ([^{123}I-Tyr^3]octreotide) for SPECT imaging in 1987 [16]. The promise of more widely available radionuclides and easier radiolabeling motivated the development of radiometal analogs, culminating in the USFDA approval of [^{111}In]In-DTPA-octreotide (^{111}In-Octreoscan) [55] as the first peptide radiopharmaceutical in 1994. High doses of [^{111}In]In-DTPA-octreotide were also evaluated for RPT, but this approach was largely superseded by variants of the peptide labeled with radiometals possessing more favorable therapeutic emissions, for example ^{90}Y-labeled OctreoTher®. As the advent of SSTR2-targeting radiopharmaceuticals continued, the peptide structure was further fine-tuned via the conversion of the *C*-terminal alcohol in octreotide to a carboxylic acid (TATE) and the replacement of the phenylalanine at position 3 with a tyrosine (Y3-TATE). The resulting peptide formed the core of a theranostic pair of radiopharmaceuticals—[^{68}Ga]Ga-DOTA-TATE (NETSPOT®) and [^{177}Lu]Lu-DOTA-TATE (LUTATHERA®)—that were approved by the USFDA in 2016 and 2018, respectively, for the detection and treatment of SSTR-positive NETs (see Chap. 14). Intriguingly, while TATE-based agents act as SSTR *agonists* and are internalized (a behavior long believed to be required for efficacy), several studies using an SSTR *antagonist*—JR11—have produced promising results as well [5]. Radiotherapeutics based on SSTR antagonists, including JR11, are discussed in Chap. 16.

Notable Example #2: Chemokine Receptor
The C-X-C chemokine receptor 4 (CXCR4) is a G protein-coupled receptor that plays a key role in the invasion and metastasis of several cancers through its interaction with its natural ligand, CXCL12, a 72-amino acid extracellular chemokine [56]. Through efforts that beautifully highlight the breadth and depth of natural sources for peptide lead structures (and their potential applications), a pair of CXCR4-binding peptides—the bicyclic 17-mer Tachyplesin I and the 18-mer Polyphemusin II—were identified in
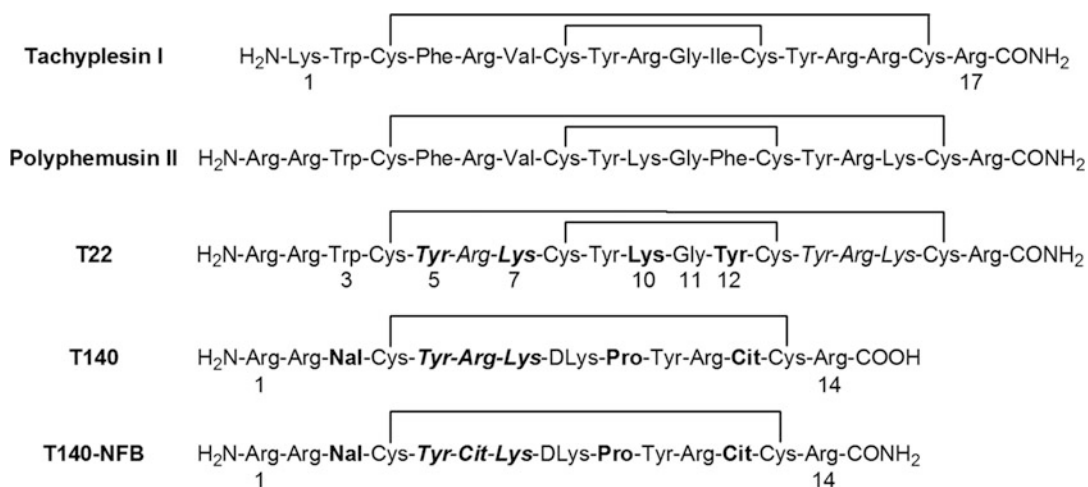
Fig. 13.12 Amino-acid sequences of notable peptidic CXCR4 inhibitors. Some key amino acids discussed in the text have been highlighted in **bold** or *italics*

horseshoe crabs and initially pursued for their strong anti-HIV activity mediated by CXCR4/fusin (Fig. 13.12) [57]. Subsequently, a library of synthetically modified variants of these peptides was generated to decrease cytotoxicity and improve their anti-HIV binding [58]. Of the 16 analogs evaluated, an 18 mer-peptide—T22—stood out for its dramatically increased anti-HIV activity. T22 retains the rigid two disulfide bond structure of Polyphemusin II but replaces three amino acids with more polar/charged analogs: Phe^5 to Tyr^5, Phe^{12} to Tyr^{12}, and Val^7 to Lys^7. Extensive study of T22's binding to CXCR4 ultimately uncovered two important traits: (1) of the peptide's two Tyr-Arg-Lys repeats, Tyr^5-Arg^6-Lys^7 was more important for its anti-HIV activity and (2) only the Cys^4-Cys^{17} disulfide linkage was imperative for the peptide's β-sheet structure. As a result, the Cys^8-Tyr^9 and Tyr^{12}-Cys^{13} residues could be omitted from the structure without loss of activity, which led to the shortening of the peptide chain to 14-amino acids. Subsequently, four more critical observations were also made: (i) the replacement of the aromatic amino acid Trp^3 with Nal^3 (L-2-naphthylalanine) resulted in a fivefold increase in potency; (ii) the +1 charge on Lys^{10} (of T22) was indispensable for the peptide's activity and conformation stability; (iii) the replacement of Gly^{11} with Pro^{11} further

strengthened the β-sheet turn; and (iv) the toxicity of T22 may be due to its positively charged basic residues (five Arg and three Lys) [59]. Changes based on these observations led to the creation of two 14-mer peptides—T140 (Cit^{13}) and T140-NFB (Cit^6 and Cit^{13})—with significantly improved cytotoxicity (Fig. 13.12). This highly condensed, slightly head-spinning summary exemplifies many of the important steps in the optimization of peptides and highlights both the simplicity *and* complexity of the peptide pharmaceutical space. Of particular interest to the RPT community, a variant of T140-NFB modified with NOTA and radiolabeled with gallium-68 was successfully used to image glioma tumors and has shown potential for the diagnosis and treatment planning of patients with CXCR4(+) tumors [60].

But wait, there's more! The chemokine receptor-targeting peptide story continues with another peptide evolution branching off from T140. Based on the extensive structure-activity relationship studies, the residues Arg^2, Nal^3, Tyr^5, and Arg^{14} of T140 were identified as responsible for the peptide's bioactivity. In this case, further amino acid deletions as well as the use of D-amino acids and backbone modifications resulted in the development of a series of cyclic
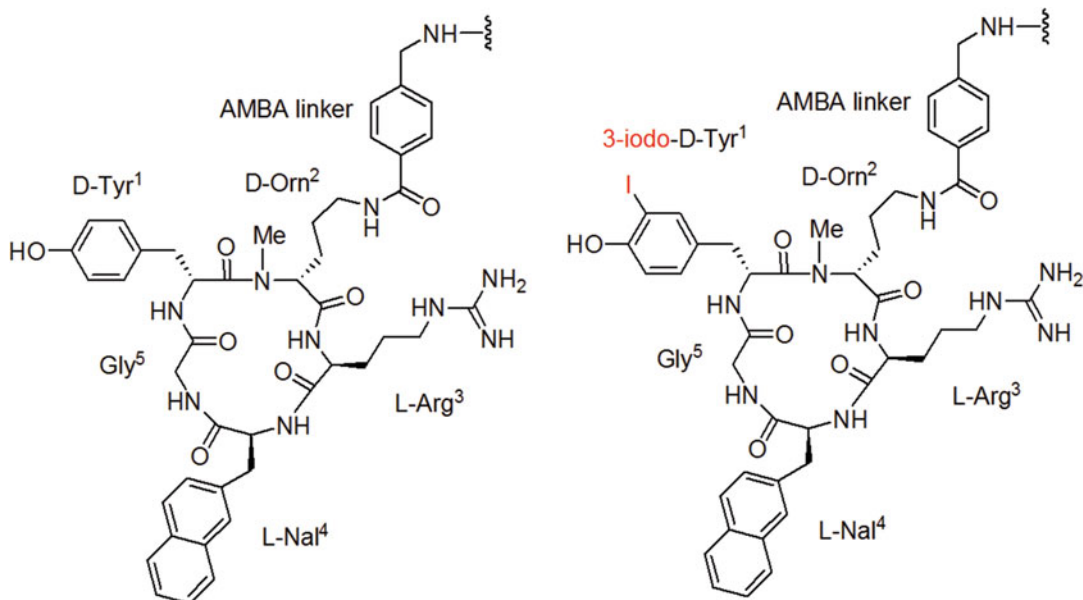
Fig. 13.13 Peptide core structures of Pentixafor (left) and Pentixather (right) pentapeptides. Chelators for radiolabeling can be added to the AMBA linker

pentapeptides designed to have high stability and high affinity for CXCR4 [61]. Two very similar peptides within this library—c(D-Tyr[1]-**Arg**[2]-Arg[3]-NaI[4]-Gly[5]) and c(D-Tyr[1]-**D-Arg**[2]-Arg[3]-NaI[4]-Gly[5])—exhibited affinities comparable to that of T140. Further modifications of these peptides, such as the replacement of Arg[2] (or D-Arg[2]) with the non-natural amino acid ornithine (Orn) and the *N*-methylation of the peptide bond between D-Try[1] and D-Orn[2], eventually resulted in the formation of a highly potent cyclic pentapeptide in which the extension of the D-Orn[2] amino acid with a 4-(aminomethyl) benzoic acid (AMBA) linker facilitated the addition of chelators (Fig. 13.13). The radiolabeling of a DOTA-modified variant of this peptide with gallium-68 yielded ^{68}Ga-Pentixafor [c(DTyr[1]-[*N*Me]-DOrn[2]-[AMBA-[^{68}Ga]Ga-DOTA]-Arg[3]-2NaI[4]-Gly[5])] [62]. ^{68}Ga-Pentixafor has been proven highly effective in detecting CXCR4 overexpressing lesions in patients with advanced multiple myeloma, with comparable or superior PET results compared to [^{18}F]FDG [63].

Finally, in an attempt to leverage the peptide for RPT, Pentixafor was modified with different chelators and radiolabeled with several different therapeutic radionuclides. Unfortunately and unexpectedly, however, the radiolabeled peptide exhibited a significant loss in CXCR4 binding affinity when the radiometal was simply swapped from Ga[+3] to Lu[+3] or Y[+3] (despite the fact that all three metals carry +3 charges!), highlighting that the precise geometry of a radiometal-chelator moiety *can* sometimes affect a peptide's affinity for its target receptor [64]. Consequently, several analogs of Pentixafor with D-Tyr[1] substitutions were evaluated for their CXCR4 affinity when labeled with Lu[+3], Y[+3], and Bi[+3]. It was demonstrated that the replacement of the original D-Tyr[1] with *3-iodo*-D-Tyr[1] (Fig. 13.13)—a deceptively minor change at a seemingly distant site—allowed for efficient radiolabeling with both [^{177}Lu]Lu[+3] and [^{90}Y]Y[+3] and yielded products that retained high affinity for CXCR4. The resulting compounds (dubbed ^{177}Lu/^{90}Y-Pentixather) have produced promising therapeutic results in patients with advanced multiple myeloma, diffuse large B cell lymphoma, and acute myeloid leukemia [65–67]. Although encouraging clinical outcomes have already been achieved with the ^{68}Ga-Pentixafor/^{177}Lu-Pentixather theranostic pair, further modifications

are being explored to further increase their tumor-to-background activity concentration ratios for more sensitive imaging and improved therapy [13].

Notable Example #3: Gastrin Releasing Peptide Receptor or Bombesin Receptor

The gastrin releasing peptide receptor (GRPR), or bombesin receptor subtype-2, is a G protein-coupled receptor expressed in various organs including the GI tract and the pancreas. Importantly, it is known to be overexpressed in many cancers, including prostate, breast, and pancreas cancer [68]. Because GRPR is internalized upon the binding of its agonist ligand, it is considered a promising target for both nuclear imaging and RPT. Natural GRPR ligands like the 14-mer peptide bombesin (BBN)—which, interestingly, was isolated from skin extracts of the European fire-bellied toad—or the 27-mer GRP peptide (isolated, somewhat less exotically, from porcine stomach) have served as a launching point for the development of GRPR-targeting peptides [69, 70].

Several familiar optimization strategies were leveraged to improve these peptides and eventually yielded success in a more linear fashion. Due to its metabolic instability in humans, BBN was truncated to produce an analog that retained the 8 *C*-terminal amino acids (BBN 7–14; Fig. 13.14). This peptide had improved binding affinity and in vivo stability and was developed into GRPR-targeted nuclear imaging agents and radiotherapeutics [71, 72]. Amongst them, one agonist based on the *N*-terminal modification of BBN 7–14, AMBA (DOTA-Gly-4-aminobenzoyl-**Gln-Trp-Ala-Val-Gly-His-Leu-Met**-CONH$_2$), stood out. [^{68}Ga]Ga-AMBA has proven effective for the imaging of several cancers [73], and [^{177}Lu]Lu-AMBA has demonstrated high uptake in GRPR(+) tumors, high therapeutic ratios in mouse models, and promising outcomes in phase 1 clinical trials [74].

Although several GRPR agonists were extensively pursued for clinical translation because of their rapid internalization upon binding to the receptor, it was subsequently demonstrated that some *antagonists* also exhibited high binding to GRPR(+) tumors as well as more favorable pharmacokinetics than their agonist cousins [75]. Several radiotracers based on GRPR antagonists have been developed, including [^{68}Ga]Ga-RM2 (^{68}Ga-BAY86-7548, [^{68}Ga]Ga DOTA-linker-D-Phe-**Gln-Trp-Ala-Val-Gly-His-Sta-Leu**-CONH$_2$) and [^{68}Ga]Ga-NeoBOMB1 ([^{68}Ga]Ga DOTA-linker-D-Phe-**Gln-Trp-Ala-Val-Gly-His**-NH-CH(*iso*butyl)$_2$). The structure of RM2 was derived from the parent peptide RM26 which features a critical backbone modification—the incorporation of the γ-amino acid statine [Sta; (3S,4S)-4-amino-3-hydroxy-6-methylheptanoic acid]. RM26 exhibits high affinity for GRPR in vitro and in vivo and is stable to enzymatic degradation. The RM26 structure was initially modified for radiolabeling via the addition of a DOTA-Gly-amino-benzoyl group to the *N*-terminus, yielding the RM1 peptide. A subsequent replacement of the Gly-amino-benzoyl linker with a positively charged 4-amino-1-carboxymethyl-piperidine linker then yielded RM2 (Fig. 13.14) [76]. [^{68}Ga]Ga-RM2 has been evaluated in prostate and breast cancer patients with promising outcomes, and first-in-human dosimetry studies with [^{177}Lu]Lu-RM2 suggest that it is suitable for the RPT of metastatic castration-resistant prostate cancer (mCRPC) with therapeutically relevant absorbed doses to the tumor as well as rapid clearance from normal organs [77].

The second clinically relevant theranostic pair of GRPR antagonists that stem from the bombesin lineage is ^{68}Ga/^{177}Lu-labeled NeoBOMB1. As in the previous case, NeoBOMB1 retains a significant portion of BBN(7-14) unchanged. In this case, however, a series of peptides with *both C-* and *N*-terminal capping were evaluated to protect against proteolytic degradation, and **Ac**-His-Trp-Ala-Val-Gly-His-NH-**CH(*iso*butyl)$_2$** was identified as a highly potent and metabolically stable candidate [78]. Subsequently, D-Phe-**Gln-Trp-Ala-Val-Gly-His**-NH-CH(*iso*butyl)$_2$ was coupled to DOTA via a *p*-aminomethylaniline-diglycolic acid linker to yield NeoBOMB1. Initial clinical studies with [^{68}Ga]Ga-NeoBOMB1 illustrated
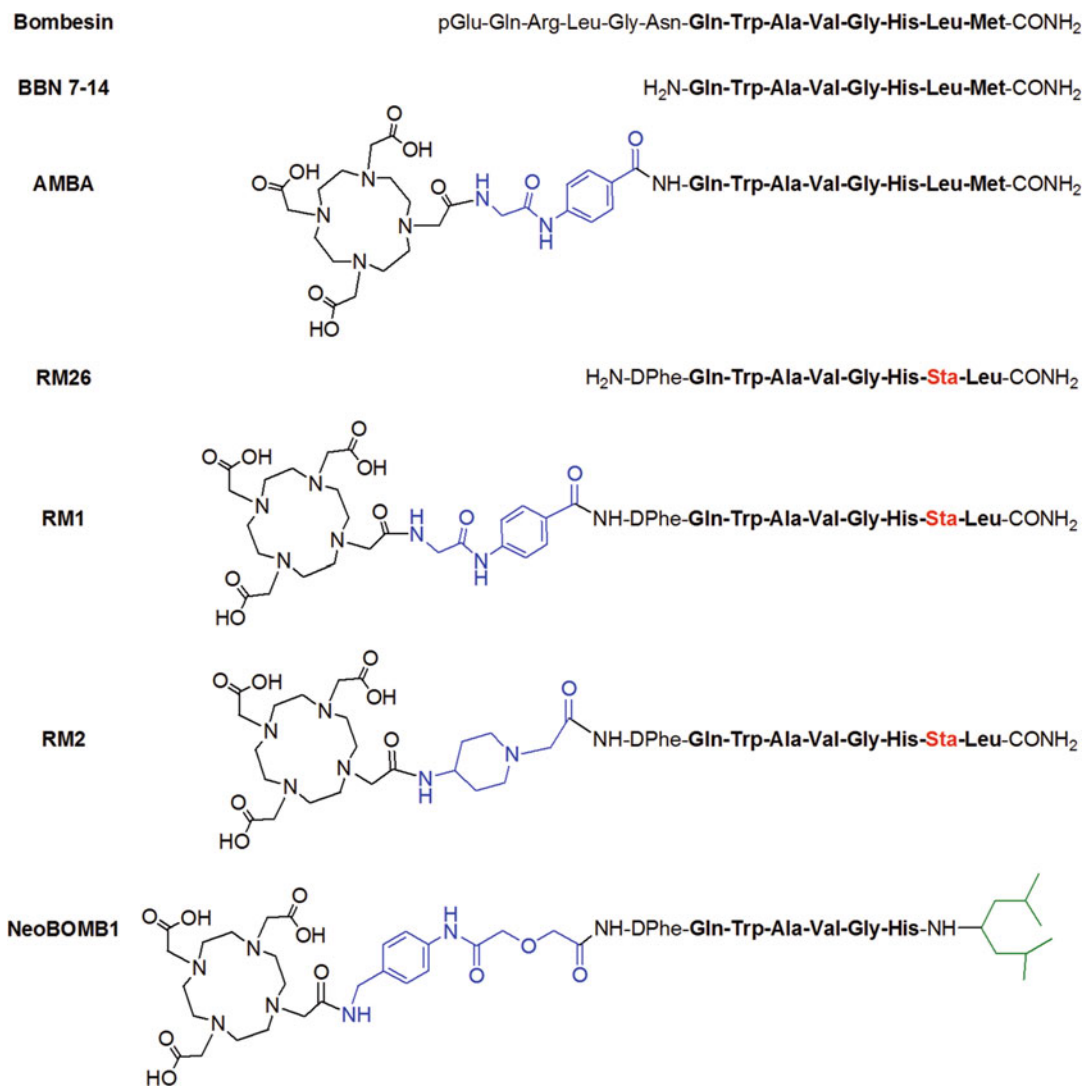
Bombesin pGlu-Gln-Arg-Leu-Gly-Asn-**Gln-Trp-Ala-Val-Gly-His-Leu-Met**-CONH₂

BBN 7-14 H₂N-**Gln-Trp-Ala-Val-Gly-His-Leu-Met**-CONH₂

AMBA NH-**Gln-Trp-Ala-Val-Gly-His-Leu-Met**-CONH₂

RM26 H₂N-DPhe-**Gln-Trp-Ala-Val-Gly-His-Sta-Leu**-CONH₂

RM1 NH-DPhe-**Gln-Trp-Ala-Val-Gly-His-Sta-Leu**-CONH₂

RM2 NH-DPhe-**Gln-Trp-Ala-Val-Gly-His-Sta-Leu**-CONH₂

NeoBOMB1 NH-DPhe-**Gln-Trp-Ala-Val-Gly-His**-NH

Fig. 13.14 Structures of selected GRPR agonists and antagonists. Important backbone core amino acids discussed in the text are highlighted in **bold**, the linkers in blue, the γ-amino acid statine in red, and the *C*-terminal -CH(*iso*butyl)₂ cap in green

that the peptide could successfully detect both primary and metastatic lesions in prostate cancer patients, and the theranostic pair of [^{68}Ga]Ga- and [^{177}Lu]Lu-NeoBOMB1 has advanced to phase I/II clinical trials for the detection and RPT of GRPR-expressing tumors [79].

Example #4: Integrin Receptors
The last group of peptide-binding receptors we would like to highlight are the integrins. Integrins

are a diverse family of cell surface receptors that play key roles in angiogenesis, leukocyte function, tumor development, and metastasis. Of the 24 know members, the integrin $\alpha_v\beta_3$—also known as the vitronectin receptor—is the most studied. It is up-regulated in melanoma, breast, and head and neck cancer as well as in neo-angiogenic blood vessels. Peptide-based agents predicated on a core $\alpha_v\beta_3$—binding arginine-glycine-aspartic acid (RGD) motif have

been used extensively for nuclear imaging and, to a much lesser extent, RPT [80]. Originally discovered from a phage display library as ACD**RGD**CFCG, small cyclic analogs with a c (RGDxX) motif were favored for further development due to the low affinity and stability of linear RGD peptides (note: the "c" is indicative of cyclization, rather than a D-Cys, and the x and X represent exchangeable D- and L-amino acid residues, respectively). The pentapeptides c (RGDfV), c(RGDyK), and c(RGDfK) were developed with the help of computational analysis, and further advanced to yield cilengitide [RGDf(*N*Me)V with an *N*-methylated valine for improved metabolic stability]. With three of the five amino acids required for binding and the fourth and fifth highly restricted, the options for radiolabeling were limited. Fortunately, the presence of a D-tyrosine enabled radioiodination and permitted SPECT imaging with iodine-125 [81]. For PET imaging, a variant in which the lysine is indirectly radiolabeled with fluorine-18 was evaluated in humans [82, 83]. Further modifications were introduced over time to optimize the platform, notably glycosylation (i.e., galacto-RGDfK) to reduce the liver accumulation, and multimerization and PEGylation to increase circulation in blood and tumor uptake (e.g., in [c(RGDfK)]$_2$) [84]. By now, the approaches to peptide optimization that have been used in this context should be familiar: sequence shortening, cyclization, introduction of D-amino acids, and use of pharmacokinetic modifiers (e.g., glycosylation).

Given the extensive study of imaging agents based on cyclo-RGD peptides, the comparative scarcity of complementary radiotherapeutics is somewhat surprising, though RPT with ^{90}Y- and ^{177}Lu-labeled RGD peptides has been explored in preclinical models with some promising outcomes [85, 86]. These studies include work with a group of ABM-bearing c(RGDfK) peptides that showed up to tenfold enhanced tumor accumulation compared to the analogs lacking ABM, and the ^{90}Y-labeled ABM-bearing c(RGDfK) peptide proved efficacious in murine tumor models [87]. To our

knowledge, however, no clinical data on $\alpha_v\beta_3$-targeted RPT have been reported to date.

Another member of the integrin family, the integrin $\alpha_v\beta_6$, has also garnered attention as both a diagnostic and therapeutic target. Integrin $\alpha_v\beta_6$ is a cell surface receptor that is significantly upregulated in a wide range of epithelial-derived cancers, including pancreas, colon, non-small cell lung, ovarian, breast, and prostate cancer, as well as oral squamous cell carcinoma [88, 89]. Peptides targeting the integrin $\alpha_v\beta_6$ often share a common RGDLXXL motif that confer selectivity for $\alpha_v\beta_6$ over other α_v-integrins such as $\alpha_v\beta_3$. Several groups of $\alpha_v\beta_6$-targeted peptides have been discovered separately and radiolabeled. For example, the linear 20-mer A20FMDV2 peptide (NAVPNL**RGDL**QVL**A**QKVART) was originally derived from a coat protein of the foot-and-mouth disease virus (FMDV) which uses the $\alpha_v\beta_6$ receptor to anchor itself on the cell before entering [90]. A20FMDV2 has been modified via amino acid substitution (Lys to Arg) and PEGylation to increase serum stability and tumor uptake (yielding $\alpha_v\beta_6$-BP) and labeled with fluorine-18 for clinical PET imaging trials [91]. Similarly, ^{68}Ga and ^{177}Lu-labeled versions of the 5G and ABM-5G peptides—both PEGylated linear 21-mer peptides with the latter bearing an albumin binding moiety—are currently in first-in-human clinical trials for imaging and therapy as [^{68}Ga]Ga DOTA-5G and [^{177}Lu] Lu DOTA-ABM-5G, respectively [92]. Another group of $\alpha_v\beta_6$-targeting peptides is based on multiply cyclized knot peptides, or knottins, that contain the 3 disulfide bridges. One such knottin, R$_0$1-MG, was labeled with fluorine-18 and gallium-68 and has been used in clinical imaging trials [93]. A third group of $\alpha_v\beta_6$-targeted peptides identified via sunflower trypsin inhibitor-based phage display includes SFITGv6 (GCGRF**RGDL**MQ**L**CYPD) and SFLAP3 (GRCTG**RGDL**GR**L**CYPD), and both have been used in the clinic as platforms for ^{68}Ga-PET. Finally, another imaging agent—[^{68}Ga]Ga-Avebehexin—was created by attaching three c(**FRGDL**AF**p(NMe)**K) cyclic nonapeptides to a TRAP chelator core and

labeling with gallium-68. The probe had to be further modified due to non-specific uptake in the intestines and liver by replacing the phenylalanines with more hydrophilic tyrosines [c(**Y**RGDLA**Y**p(NMe)K)]. The resulting agent, ^{68}Ga-Trivehexin, has also advanced to clinical studies [94] and, depending on the compatibility of TRAP with therapeutic radiometals, might also be considered for RPT.

13.4 Final Thoughts

A tremendous amount of energy and effort is currently dedicated to the development of peptide-based pharmaceuticals. In the area of peptide-based *radio*pharmaceuticals, most of the effort in the past has been focused on diagnostic (imaging) agents. Yet the increasing availability of high-quality therapeutic radionuclides as well as the growing understanding of the clinical value of RPT has fueled a dramatic surge in the preclinical study and clinical evaluation of peptide-based radiotherapeutics. That said, it is critical that more of these agents move beyond "promising results" in clinical trials toward widespread benefit for patient populations, following the footsteps of NETSPOT® and LUTATHERA®. On the scientific side, peptide-based agents are particularly attractive because they can target a wide range of disease-associated receptors and because they are based on amino acid scaffolds that can be precisely tailored using flexible, established, and robust methods to improve their chemical and biological properties. As the examples in this chapter have shown, researchers will undoubtedly continue to advance this science and uncover an increasing array of optimization strategies. From the healthcare perspective, the field of peptide-based RPT—*a.k.a.* PRRT—would certainly benefit from more standardized metrics for evaluating safety and efficacy, strategies for dose optimization, and the education and involvement of clinicians and even healthcare administrators who should be aware of the capabilities (and limitations) of these new medicines [95]. In the end, collaboration between basic scientists, clinicians, entrepreneurs, and patients will be critical for the growth and success of peptide-based RPT.

13.5 The Bottom Line

- Peptide drugs are an important segment of the global pharmaceutical market. Within this segment, peptide *radio*pharmaceuticals are a specialized sub-group with most currently used for diagnostic nuclear imaging (PET and SPECT).
- Peptides are typically comprised of α-amino acid building blocks and can be viewed as protein fragments. Peptide pharmaceuticals target disease-specific cell surface receptors with binding affinities and selectivities rivaling those of antibodies and exhibit low toxicity (including little to no immunogenicity).
- Many standard protocols exist for the efficient, step-wise synthesis of peptides as well as for site-specific modifications that can help improve a peptide's pharmacokinetic profile. These modifications include amino acid substitutions and deletions, branching, cyclization, the incorporation of metabolic stabilizers, and the attachment of pharmacokinetic modulators (e.g., PEG, albumin binders).
- Particularly important targets for which notable peptide RPT agents are being developed include the somatostatin, chemokine, bombesin, and integrin receptors.
- Recent key events in the advent of peptide-based nuclear imaging and radiopharmaceutical therapy (RPT, a.k.a. peptide receptor radionuclide therapy—PRRT) were the USFDA's approvals of the PET imaging agent ^{68}Ga-labeled NETSPOT® in 2016 and its ^{177}Lu-labeled therapeutic twin LUTATHERA® in 2018.
- Moving forward, improvements to standardized metrics for safety and efficacy, strategies for dose optimization, and the education and involvement of clinicians will all be critical to ensuring that peptide-based RPT will deliver the greatest possible benefit for patients.

References

1. Sang Q-XA, Usmani SS, Bedi G, Samuel JS, Singh S, Kalra S, et al. THPdb: Database of FDA-approved peptide and protein therapeutics. PLoS One. 2017;12 (7):e0181748.

2. Wang L, Wang N, Zhang W, Cheng X, Yan Z, Shao G, et al. Therapeutic peptides: current applications and future directions. Signal Transduct and Target Ther. 2022;7(1):48.

3. Muttenthaler M, King GF, Adams DJ, Alewood PF. Trends in peptide drug discovery. Nat Rev Drug Discov. 2021;20(4):309–25.

4. Al Shaer D, Al Musaimi O, Albericio F, de la Torre BG. 2021 FDA TIDES (Peptides and Oligonucleotides) harvest. Pharmaceuticals. 2022;15 (2):222.

5. Fani M, Nicolas GP, Wild D. Somatostatin receptor antagonists for imaging and therapy. J Nucl Med. 2017;58(Supplement 2):61S–6S.

6. Bruchertseifer F, Kellerbauer A, Malmbeck R, Morgenstern A. Targeted alpha therapy with bismuth-213 and actinium-225: Meeting future demand. J Labelled Comp Radiopharm. 2019;62(11): 794–802.

7. Morgenstern A, Apostolidis C, Bruchertseifer F. Supply and Clinical Application of Actinium-225 and Bismuth-213. Semin Nucl Med. 2020;50(2): 119–23.

8. Hansen PR, Oddo A. Fmoc solid-phase peptide synthesis. Methods Mol Biol. 2015;1348:33–50.

9. Behrendt R, White P, Offer J. Advances in Fmoc solid-phase peptide synthesis. J Pept Sci. 2016;22(1):4–27.

10. Coin I, Beyermann M, Bienert M. Solid-phase peptide synthesis: from standard procedures to the synthesis of difficult sequences. Nat Protoc. 2007;2(12):3247–56.

11. Howl J. Peptide synthesis and applications. 2nd ed. Totowa: Humana Press; 2013. 1–253 p

12. Stawikowski M, Fields GB. Introduction to peptide synthesis. Curr Protocols Protein Sci. 2012;69 (1) https://doi.org/10.1002/0471140864.ps1801s69.

13. Osl T, Schmidt A, Schwaiger M, Schottelius M, Wester H-J. A new class of PentixaFor- and PentixaTher-based theranostic agents with enhanced CXCR4-targeting efficiency. Theranostics. 2020;10 (18):8264–80.

14. Eychenne R, Bouvry C, Bourgeois M, Loyer P, Benoist E, Lepareur N. Overview of Radiolabeled Somatostatin Analogs for Cancer Imaging and Therapy. Molecules. 2020;25(17):4012.

15. Pless J. The history of somatostatin analogs. J Endocrinol Invest. 2005;28(11 Suppl International):1–4.

16. Levine R, Krenning EP. Clinical history of the theranostic radionuclide approach to neuroendocrine tumors and other types of cancer: historical review based on an interview of Eric P. Krenning by Rachel Levine. J Nucl Med. 2017;58(Supplement 2):3S–9S.

17. Erak M, Bellmann-Sickert K, Els-Heindl S, Beck-Sickinger AG. Peptide chemistry toolbox – Transforming natural peptides into peptide therapeutics. Bioorg Med Chem. 2018;26(10):2759–65.

18. Chatterjee J, Gilon C, Hoffman A, Kessler H. N-Methylation of Peptides: A New Perspective in Medicinal Chemistry. Acc Chem Res. 2008;41(10): 1331–42.

19. Jwad R, Weissberger D, Hunter L. Strategies for Fine-Tuning the Conformations of Cyclic Peptides. Chem Rev. 2020;120(17):9743–89.

20. Lewis J, Windhorst AD, Zeglis BM. Radiopharmaceutical chemistry. Springer, 2019.

21. Zorzi A, Linciano S, Angelini A. Non-covalent albumin-binding ligands for extending the circulating half-life of small biotherapeutics. MedChemComm. 2019;10:1068.

22. Rangger C, Haubner R. Radiolabelled peptides for positron emission tomography and endoradiotherapy in oncology. Pharmaceuticals. 2020;13(2):22.

23. Marin JFG, Nunes RF, Coutinho AM, Zaniboni EC, Costa LB, Barbosa FG, et al. Theranostics in nuclear medicine: emerging and re-emerging integrated imaging and therapies in the era of precision oncology. Radiographics. 2020;40(6):1715–40.

24. Werle M, Bernkop-Schnurch A. Strategies to improve plasma half life time of peptide and protein drugs. Amino Acids. 2006;30(4):351–67.

25. Evans BJ, King AT, Katsifis A, Matesic L, Jamie JF. Methods to enhance the metabolic stability of peptide-based PET radiopharmaceuticals. Molecules. 2020;25(10):2314.

26. Ali AM, Atmaj J, Van Oosterwijk N, Groves MR, Dömling A. Stapled peptides inhibitors: a new window for target drug discovery. Comput Struct Biotechnol J. 2019;17:263–81.

27. Li F, Leier A, Liu Q, Wang Y, Xiang D, Akutsu T, et al. Procleave: predicting protease-specific substrate cleavage sites by combining sequence and structural information. Genomics Proteomics Bioinformatics. 2020;18(1):52–64.

28. Shahinian H, Tholen S, Schilling O. Proteomic identification of protease cleavage sites: cell-biological and biomedical applications. Expert Rev Proteomics. 2014;10(5):421–33.

29. Powell MF, Grey H, Gaeta F, Sette A, Colón S. Peptide stability in drug development: a comparison of peptide reactivity in different biological media. J Pharm Sci. 1992;81(8):731–5.

30. Diao L, Meibohm B. Pharmacokinetics and pharmacokinetic-pharmacodynamic correlations of therapeutic peptides. Clin Pharmacokinet. 2013;52 (10):855–68.

31. Cheng T-L, Chuang K-H, Chen B-M, Roffler SR. Analytical measurement of PEGylated molecules. Bioconjug Chem. 2012;23(5):881–99.

32. Hausner SH, Bauer N, Hu LY, Knight LM, Sutcliffe JL. The effect of Bi-terminal PEGylation of an integrin

$\alpha_v\beta_6$–targeted ^{18}F peptide on pharmacokinetics and tumor uptake. J Nucl Med. 2015;56(5):784–90.

33. Pasut G, Guiotto A, Veronese FM. Protein, peptide and non-peptide drug PEGylation for therapeutic application. Expert Opin Ther Pat. 2004;14(6): 859–94.

34. Harris JM, Chess RB. Effect of PEGylation on pharmaceuticals. Nat Rev Drug Discov. 2003;2(3): 214–21.

35. Ekladious I, Colson YL, Grinstaff MW. Polymer–drug conjugate therapeutics: advances, insights and prospects. Nat Rev Drug Discov. 2019;18(4):273–94.

36. Wester H-J, Schottelius M, Scheidhauer K, Reubi J-C, Wolf I, Schwaiger M. Comparison of radioiodinated TOC, TOCA and Mtr-TOCA: the effect of carbohydration on the pharmacokinetics. Eur J Nucl Med Mol Imaging. 2002;29(1):28–38.

37. Schottelius M, Wester H-J, Reubi JC, Senekowitsch-Schmidtke R, Schwaiger M. Improvement of Pharmacokinetics of Radioiodinated Tyr3-Octreotide by Conjugation with Carbohydrates. Bioconjug Chem. 2002;13(5):1021–30.

38. Haubner R, Kuhnast B, Mang C, Weber WA, Kessler H, Wester H-J, et al. [18F]Galacto-RGD: synthesis, radiolabeling, metabolic stability, and radiation dose estimates. Bioconjug Chem. 2004;15(1):61–9.

39. Haubner R, Wester H-J, Burkhart F, Senekowitsch-Schmidtke R, Weber W, Goodman SL, et al. Glycosylated RGD-containing peptides: tracer for tumor targeting and angiogenesis imaging with improved biokinetics. J Nucl Med. 2001;42(2):326.

40. Chen H, Wang G, Lang L, Jacobson O, Kiesewetter DO, Liu Y, et al. Chemical conjugation of evans blue derivative: a strategy to develop long-acting therapeutics through albumin binding. Theranostics. 2016;6(2): 243–53.

41. Davis RA, Hausner SH, Harris R, Sutcliffe JL. A comparison of Evans blue and 4-(p-Iodophenyl) butyryl albumin binding moieties on an integrin $\alpha_v\beta_6$ binding peptide. Pharmaceutics. 2022;14(4):745.

42. Liu Z, Chen X. Simple bioconjugate chemistry serves great clinical advances: albumin as a versatile platform for diagnosis and precision therapy. Chem Soc Rev. 2016;45(5):1432–56.

43. Sun X, Li Y, Liu T, Li Z, Zhang X, Chen X. Peptide-based imaging agents for cancer detection. Adv Drug Deliv Rev. 2017;110–111:38–51.

44. Liolios C, Sachpekidis C, Kolocouris A, Dimitrakopoulou-Strauss A, Bouziotis P. PET diagnostic molecules utilizing multimeric cyclic RGD peptide analogs for imaging integrin $\alpha_v\beta_3$ receptors. Molecules. 2021;26(6):1792.

45. Brechbiel MW. Agent optimization: absorption, distribution, metabolism, excretion, dose, and decay. J Nucl Med. 2021;62(4):455–6.

46. White JM, Escorcia FE, Viola NT. Perspectives on metals-based radioimmunotherapy (RIT): moving forward. Theranostics. 2021;11(13):6293–314.

47. Kassis AI. Therapeutic radionuclides: biophysical and radiobiologic principles. Semin Nucl Med. 2008;38 (5):358–66.

48. Zoller F, Eisenhut M, Haberkorn U, Mier W. Endoradiotherapy in cancer treatment--basic concepts and future trends. Eur J Pharmacol. 2009;625(1–3):55–62.

49. Guérard F, Gestin J-F, Brechbiel MW. Production of [211At]-astatinated radiopharmaceuticals and applications in targeted α-particle therapy. Cancer Biother Radiopharm. 2012;28(1):1–20.

50. Bhattacharyya S, Dixit M. Metallic radionuclides in the development of diagnostic and therapeutic radiopharmaceuticals. Dalton Trans. 2011;40(23): 6112–28.

51. Yang H, Wilson JJ, Orvig C, Li Y, Wilbur DS, Ramogida CF, et al. Harnessing α-emitting radionuclides for therapy: radiolabeling method review. J Nucl Med. 2022;63(1):5–13.

52. Minkoff BB, Bruckbauer ST, Sabat G, Cox MM, Sussman MR. Covalent modification of amino acids and peptides induced by ionizing radiation from an electron beam linear accelerator used in radiotherapy. Radiat Res. 2019;191(5):447–59.

53. Liu S, Edwards DS. Stabilization of 90Y-labeled DOTA-biomolecule conjugates using gentisic acid and ascorbic acid. Bioconjug Chem. 2001;12(4): 554–8.

54. Burgus R, Ling N, Butcher M, Guillemin R. Primary structure of somatostatin, a hypothalamic peptide that inhibits the secretion of pituitary growth hormone. Proc Natl Acad Sci U S A. 1973;70(3):684–8.

55. Kwekkeboom DJ, Mueller-Brand J, Paganelli G, Anthony LB, Pauwels S, Kvols LK, et al. Overview of results of peptide receptor radionuclide therapy with 3 radiolabeled somatostatin analogs. J Nucl Med. 2005;46(Suppl 1):62s–6s.

56. Scala S. Molecular pathways: targeting the CXCR4-CXCL12 Axis–untapped potential in the tumor microenvironment. Clin Cancer Res. 2015;21(19):4278–85.

57. Murakami T, Nakajima T, Koyanagi Y, Tachibana K, Fujii N, Tamamura H, et al. A small molecule CXCR4 inhibitor that blocks T cell line-tropic HIV-1 infection. J Exp Med. 1997;186(8):1389–93.

58. Masuda M, Nakashima H, Ueda T, Naba H, Ikoma R, Otaka A, et al. A novel anti-HIV synthetic peptide, T-22 ([Tyr5,12,Lys7]-polyphemusin II). Biochem Biophys Res Commun. 1992;189(2):845–50.

59. Tamamura H, Imai M, Ishihara T, Masuda M, Funakoshi H, Oyake H, et al. Pharmacophore identification of a chemokine receptor (CXCR4) antagonist, T22 ([Tyr(5,12),Lys7]-polyphemusin II), which specifically blocks T cell-line-tropic HIV-1 infection. Bioorg Med Chem. 1998;6(7):1033–41.

60. Wang Z, Zhang M, Wang L, Wang S, Kang F, Li G, et al. Prospective study of 68Ga-NOTA-NFB: radiation dosimetry in healthy volunteers and first application in glioma patients. Theranostics. 2015;5(8):882–9.

61. Fujii N, Oishi S, Hiramatsu K, Araki T, Ueda S, Tamamura H, et al. Molecular-size reduction of a potent CXCR4-chemokine antagonist using orthogonal combination of conformation- and sequence-based libraries. Angew Chem Int Ed Engl. 2003;42(28): 3251–3.

62. Gourni E, Demmer O, Schottelius M, D'Alessandria C, Schulz S, Dijkgraaf I, et al. PET of CXCR4 expression by a ^{68}Ga-labeled highly specific targeted contrast agent. J Nucl Med. 2011;52(11): 1803–10.

63. Philipp-Abbrederis K, Herrmann K, Knop S, Schottelius M, Eiber M, Lückerath K, et al. In vivo molecular imaging of chemokine receptor CXCR4 expression in patients with advanced multiple myeloma. EMBO Mol Med. 2015;7(4):477–87.

64. Poschenrieder A, Schottelius M, Schwaiger M, Kessler H, Wester HJ. The influence of different metal-chelate conjugates of pentixafor on the CXCR4 affinity. EJNMMI Res. 2016;6(1):36.

65. Herrmann K, Schottelius M, Lapa C, Osl T, Poschenrieder A, Hänscheid H, et al. First-in-human experience of CXCR4-directed endoradiotherapy with [177]Lu- and ^{90}Y-labeled pentixather in advanced-stage multiple myeloma with extensive intra- and extramedullary disease. J Nucl Med. 2016;57(2): 248–51.

66. Schottelius M, Osl T, Poschenrieder A, Hoffmann F, Beykan S, Hänscheid H, et al. [^{177}Lu]pentixather: comprehensive preclinical characterization of a First CXCR4-directed endoradiotherapeutic agent. Theranostics. 2017;7(9):2350–62.

67. Lapa C, Hänscheid H, Kircher M, Schirbel A, Wunderlich G, Werner RA, et al. Feasibility of CXCR4-directed radioligand therapy in advanced diffuse large B-cell lymphoma. J Nucl Med. 2019;60(1): 60–4.

68. Moreno P, Ramos-Álvarez I, Moody TW, Jensen RT. Bombesin related peptides/receptors and their promising therapeutic roles in cancer imaging, targeting and treatment. Expert Opin Ther Targets. 2016;20(9):1055–73.

69. Stott Reynolds TP, Bandari RP, Jiang Z, Smith CJ. Lutetium-177 labeled bombesin peptides for radionuclide therapy. Curr Radiopharm. 2015;9(1):33–43.

70. Anastasi A, Erspamer V, Bucci M. Isolation and structure of bombesin and alytesin, two analogous active peptides from skin of european amphibians bombina and alytes. Experientia. 1971;27(2):166–7.

71. Reynolds TS, Bandari RP, Jiang Z, Smith CJ. Lutetium-177 labeled bombesin peptides for radionuclide therapy. Curr Radiopharm. 2016;9(1):33–43.

72. Varshney R, Hazari PP, Fernandez P, Schulz J, Allard M, Mishra AK. ^{68}Ga-labeled bombesin analogs for receptor-mediated imaging. Recent Results Cancer Res. 2013;194:221–56.

73. Baum RP, Vikas, Mutloka N, Frischknecht M, Maecke H, Reubi J. Molecular imaging of bombesin receptors in various tumors by Ga-68 AMBA PET/CT: first results. J Nucl Med. 2007;48(Supp 2):79P.

74. Maddalena ME, Fox J, Chen J, Feng W, Cagnolini A, Linder KE, et al. ^{177}Lu-AMBA biodistribution, radiotherapeutic efficacy, imaging, and autoradiography in prostate cancer models with low GRP-R expression. J Nucl Med. 2009;50(12):2017–24.

75. Gorica J, De Feo MS. Gastrin-releasing peptide receptor agonists and antagonists for molecular imaging of breast and prostate cancer: from pre-clinical studies to translational perspectives. Expert Rev Mol Diagn. 2022;22(11):991–6.

76. Mansi R, Wang X, Forrer F, Waser B, Cescato R, Graham K, et al. Development of a potent DOTA-conjugated bombesin antagonist for targeting GRPr-positive tumours. Eur J Nucl Med Mol Imaging. 2011;38(1):97–107.

77. Kurth J, Krause BJ, Schwarzenböck SM, Bergner C, Hakenberg OW, Heuschkel M. First-in-human dosimetry of gastrin-releasing peptide receptor antagonist [^{177}Lu]Lu-RM2: a radiopharmaceutical for the treatment of metastatic castration-resistant prostate cancer. Eur J Nucl Med Mol Imaging. 2020;47(1):123–35.

78. Heimbrook DC, Saari WS, Balishin NL, Fisher TW, Friedman A, Kiefer DM, et al. Gastrin releasing peptide antagonists with improved potency and stability. J Med Chem. 1991;34(7):2102–7.

79. Dalm SU, Bakker IL, de Blois E, Doeswijk GN, Konijnenberg MW, Orlandi F, et al. [68]Ga/^{177}Lu-NeoBOMB1, a novel radiolabeled GRPR antagonist for theranostic use in oncology. J Nucl Med. 2017;58 (2):293–9.

80. Liu Z, Wang F, Chen X. Integrin targeted delivery of radiotherapeutics. Theranostics. 2011;1:201–10.

81. Haubner R, Wester HJ, Reuning U, Senekowitsch-Schmidtke R, Diefenbach B, Kessler H, et al. Radiolabeled alpha$_v$beta$_3$ integrin antagonists: a new class of tracers for tumor targeting. J Nucl Med. 1999;40(6):1061–71.

82. Haubner R, Wester HJ, Weber WA, Mang C, Ziegler SI, Goodman SL, et al. Noninvasive imaging of alpha$_v$beta$_3$ integrin expression using ^{18}F-labeled RGD-containing glycopeptide and positron emission tomography. Cancer Res. 2001;61(5):1781–5.

83. Haubner R. Alphavbeta3-integrin imaging: a new approach to characterise angiogenesis? Eur J Nucl Med Mol Imaging. 2006;33(Suppl 1):54–63.

84. Jackson IM, Scott PJH, Thompson S. Clinical applications of radiolabeled peptides for PET. Semin Nucl Med. 2017;47(5):493–523.

85. Janssen ML, Oyen WJ, Dijkgraaf I, Massuger LF, Frielink C, Edwards DS, et al. Tumor targeting with radiolabeled alpha$_v$beta$_3$ integrin binding peptides in a nude mouse model. Cancer Res. 2002;62(21): 6146–51.

86. Zhao L, Chen H, Guo Z, Fu K, Yao L, Fu L, et al. Targeted radionuclide therapy in patient-derived xenografts using ^{177}Lu-EB-RGD. Mol Cancer Ther. 2020;19(10):2034–43.

87. Chen H, Jacobson O, Niu G, Weiss ID, Kiesewetter DO, Liu Y, et al. Novel "Add-On" molecule based on Evans blue confers superior pharmacokinetics and transforms drugs to theranostic agents. J Nucl Med. 2017;58(4):590–7.

88. Niu J, Li Z. The roles of integrin $\alpha_v\beta_6$ in cancer. Cancer Lett. 2017;403:128–37.

89. Färber SF, Wurzer A, Reichart F, Beck R, Kessler H, Wester HJ, et al. Therapeutic radiopharmaceuticals targeting integrin $\alpha_v\beta_6$. ACS Omega. 2018;3(2):2428–36.

90. Logan D, Abughazaleh R, Blakemore W, Curry S, Jackson T, King A, et al. Structure of a major immunogenic site on foot-and-mouth-disease virus. Nature. 1993;362(6420):566–8.

91. Hausner SH, Bold RJ, Cheuy LY, Chew HK, Daly ME, Davis RA. Preclinical development and first-in-human imaging of the integrin $\alpha_v\beta_6$ with [^{18}F]$\alpha_v\beta_6$-binding peptide in metastatic carcinoma. Clin Cancer Res. 2019;25(4):1206–15.

92. Ganguly T, Bauer N, Davis RA, Foster CC, Harris RE, Hausner SH, et al. Preclinical evaluation of ^{68}Ga- and ^{177}Lu-labeled integrin $\alpha_v\beta_6$-targeting radiotheranostic peptides. J Nucl Med. 2023, 64:639-644

93. Nakamoto R, Ferri V, Duan H, Hatami N, Goel M, Rosenberg J, et al. Pilot-phase PET/CT study targeting integrin $\alpha_v\beta_6$ in pancreatic cancer patients using the cystine-knot peptide–based ^{18}F-FP-R01-MG-F2. Eur J Nucl Med Mol Imaging. 2021;50(1):184–93.

94. Quigley NG, Steiger K, Hoberück S, Czech N, Zierke MA, Kossatz S, et al. PET/CT imaging of head-and-neck and pancreatic cancer in humans by targeting the "Cancer Integrin" $\alpha_v\beta_6$ with Ga-68-Trivehexin. Eur J Nucl Med Mol Imaging. 2022;49(4):1136–47.

95. Lu X, Lu C, Yang Y, Shi X, Wang H, Yang N, et al. Current status and trends in peptide receptor radionuclide therapy in the past 20 years (2000–2019): a bibliometric study. Front Pharmacol. 2021;12:624534.

Case Study #4: Lutathera, a Gold Standard for Peptide Receptor Radiopharmaceutical Therapy

14

Giuseppe Danilo Di Stasio, Lighea Simona Airò Farulla, Francesca Botta, Laura Gilardi, and Chiara Maria Grana

14.1 The Fundamentals

14.1.1 Neuroendocrine Tumors

Neuroendocrine tumors (NETs) originate from neuroendocrine cells distributed throughout the human body. These tumors most commonly stem from the neuroendocrine cells of the gastrointestinal system, giving rise to their alternate name of gastroenteropancreatic neuroendocrine tumors (GEP-NETs). One of the most relevant characteristics of neuroendocrine tumor cells is their relatively high expression levels of somatostatin receptors (SSTRs), which facilitate nuclear imaging and therapy using radiolabeled somatostatin analogues (SSAs). Among the five subtypes of SSTRs, NETs usually express SSTR2 and SSTR5, though different tumor types present with considerable variability in expression [1].

14.1.2 Peptide Receptor Radionuclide Therapy (PRRT)

Peptide receptor radionuclide therapy (PRRT) is a subgenre of radiopharmaceutical therapy (RPT) that is based on the systemic administration of peptides labeled with therapeutic radionuclides that specifically target tumor cells. Radiolabeled SSAs are ideal candidates for PRRT because the receptor–peptide complex is internalized via endocytosis, and the radionuclide is selectively retained by the receptor-expressing tumor cells [2]. This process may eventually lead to cell death, as the β-particles emitted by ^{177}Lu induce DNA single-strand breaks. In addition to the direct effects of the radiation on the cell that has taken up the peptide, the β-particles can also affect cells in the vicinity of the target cell via so-called "cross-fire effect" and "bystander effect." The former can be explained by the higher range of β-particles compared to the diameter of the cell [3]. The latter is related to the induction of biological effects in cells that are not directly exposed to ionizing radiation but are in close proximity to such cells; in essence, the cells "behave" as if they had been directly hit. Both of these additional effects play pivotal roles in improving the efficacy of PRRT, especially in cases of increased tumor heterogeneity [4].

G. D. Di Stasio
Nuclear Medicine Unit, Department of Precision Medicine, University of Campania Luigi Vanvitelli, Naples, Italy

L. S. A. Farulla · F. Botta · L. Gilardi
Nuclear Medicine Division, European Institute of Oncology—IRCCS, Milan, Italy

C. M. Grana (✉)
Radiometabolic Therapy Unit, Nuclear Medicine Division, European Institute of Oncology—IRCCS, Milan, Italy
e-mail: chiara.grana@ieo.it

Fig. 14.1 Schematic representation of the molecular structure of [^{177}Lu]Lu-oxodotreotide ([^{177}Lu]Lu-DOTA-TATE, Lutathera®) illustrating the radiometal (^{177}Lu), the chelating agent, (DOTA), and the peptide with biological activity (TATE)

14.1.3 Functional Imaging

One of the most important advantages of PRRT compared to chemotherapy or external beam radiation therapy is the possibility of combining diagnosis and therapy in a "theranostic" approach. It is, in fact, possible to non-invasively assess in vivo the overexpression of SSTRs by both the primary tumor and metastatic lesions prior to commencing PRRT. This is typically achieved via nuclear imaging, historically with single-photon emission computed tomography (SPECT) using [^{111}In]In-DTPA-Octreotide (OctreoScan®) and currently with positron emission tomography (PET) using [^{68}Ga]Ga-DOTA-TOC, SomaKit TOC®) [5] In particular, tracer uptake in tumor tissue has to be higher than normal liver uptake (i.e., a Krenning score ≥2 in the case of [^{111}In]In-DTPA-Octreotide) [6]. It should be noted that the same scale—albeit adapted from and not validated by Krenning—is commonly also used for PET. As a result, PRRT offers a highly precise and personalized approach to cancer therapy with a lowered risk of side effects for the patient [7].

In this context, the current clinical indication of [^{177}Lu]Lu-oxodotreotide ([^{177}Lu]Lu-DOTA-TATE, Lutathera®) (Fig. 14.1) in Europe is the treatment of unresectable or metastatic, progressive, and well-differentiated (G1 and G2 grade) SSTR-positive gastroenteropancreatic neuroendocrine tumors (GEP-NETs) in adults [8]. Before starting a treatment with Lutathera®, a thorough cross-sectional anatomic and molecular imaging examination is required in order to assess the tumor burden and the overexpression of SSTRs [9]. The recommended treatment schedule for RPT with Lutathera® is described in detail in product monographs and consists of four infusions of 7.4 GBq (200 mCi) Lutathera®
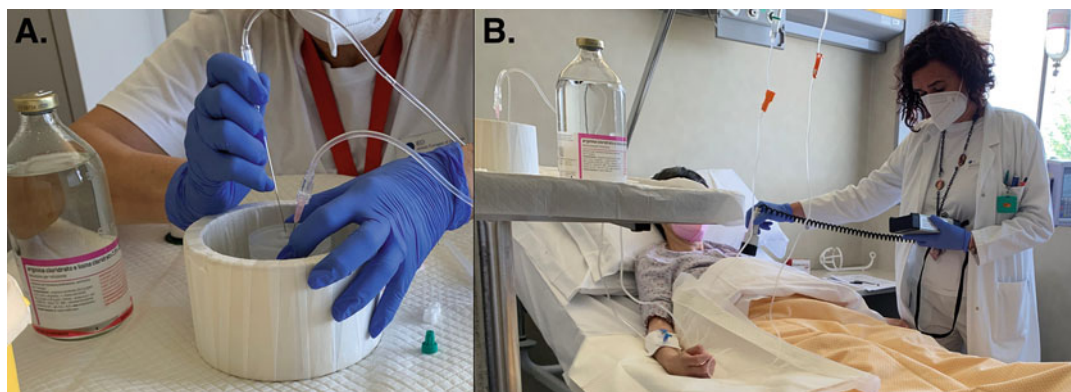
Fig. 14.2 The administration is monitored with a Geiger–Müller counter. The probe is initially placed above the patient in correspondence with the heart to verify the presence of the radiopharmaceutical in the bloodstream. Subsequently, the radiopharmaceutical container is measured with the probe to guarantee that the entire prescribed activity has been administered

Table 14.1 Administration procedure timeline of antiemetic, aminoacid solution and Lutathera©

Administered agents	Start time (min)	Infusion rate (mL/h)	Duration
Antiemetic (Granisetron 3 mg or alternative)	0	–	Bolus
2.5% Lys-Arg amino acid solution (1 L)	30	250	4 h
Lutathera™ with sodium chloride 9 mg/mL (0.9%) solution for injection	60	400	20–30 min

every 8 weeks intervals that can be extended up to 16 weeks when dose-modifying toxicity occurs [10]. The critical organs in terms of toxicity are bone marrow and kidneys. The latter, however, represents a relatively easy problem to solve, as the slow infusion of amino acids (L-lysine and L-arginine) before, during, and after the administration of the radiopharmaceutical can reduce the radiation dose to the kidneys by up to 60% (Fig. 14.2). This infusion could cause nausea and vomiting; therefore, the concomitant administration of antiemetic drugs is recommended (Table 14.1). With respect to the bone marrow, the recommended cumulative dose of 29.6 GBq (4 × 7.4 GBq) did not cause significant hematological toxicity in the majority of the NETTER-1 population, as grade 3 or 4 neutropenia, thrombocytopenia, and lymphopenia were reported in 1%, 2%, and 9% of patients, respectively, in the Lutathera® group (as opposed to no patients in the control group). Nonetheless, before the administration of each dose of Lutathera®, liver and kidney function as well as hematological parameters have to be checked, since findings of toxicity should prompt a prolongation of the treatment interval, a reduction in the administered activity, or even the permanent discontinuation of the treatment itself [11, 12] (Fig. 14.3).

14.2 The Details

In order to understand how to approach a patient with a neuroendocrine tumor and the multidisciplinary discussion needed to face the hidden difficulties of these tumors, we will now follow the clinical case of a patient affected by hepatic, abdominal lymph node, and pararectal (mass) localizations of a well-differentiated non-functioning neuroendocrine tumor of gastrointestinal origin (rectum), Ki-67 8% (G2, [13]), treated with SSA, PRRT, and surgery at the European Institute

Fig. 14.3 Proposed standardized PRRT scheme for Lutathera® (on the left) and patient PRRT scheme for Lutathera® (on the right). *IV* intravenous, *SSA* somatostatin analogue, *SSTR* somatostatin receptor, *LAR* long-acting release, *PRRT* peptide receptor radionuclide therapy, *PD* progressive disease, *PR* partial response

of Oncology (IEO), IRCCS, Milan, Italy as part of an internal clinical trial for which the patient provided written consent. In particular, we will alternately report in *italics* the clinical history of the patient and in **bold** commentary on our choices in the context of PRRT.

The patient is a 52-year-old female with no relevant previous medical history who began to complain of episodes of pain and the sensation of weight in the pelvic region in 2010 for which she was followed by a proctologist without any significant result. In May 2018 she underwent an abdominal ultrasound that demonstrated multiple liver lesions that were subsequently confirmed by a whole-body CT scan, a 6.4 × 4.2 cm solid right pre-sacral lesion posterior to the rectum, and pathologically enlarged bilateral iliac lymph nodes. In June 2018, a liver biopsy showed "localization of a neuroendocrine tumor with low-grade morphological characteristics. Ki67 <2%". At the same time, [^{68}Ga]Ga-DOTA-TOC PET/CT revealed multiple lesions with intense tracer uptake in the liver as well as the presacral mass and bilateral internal iliac nodes. (Fig. 14.4).
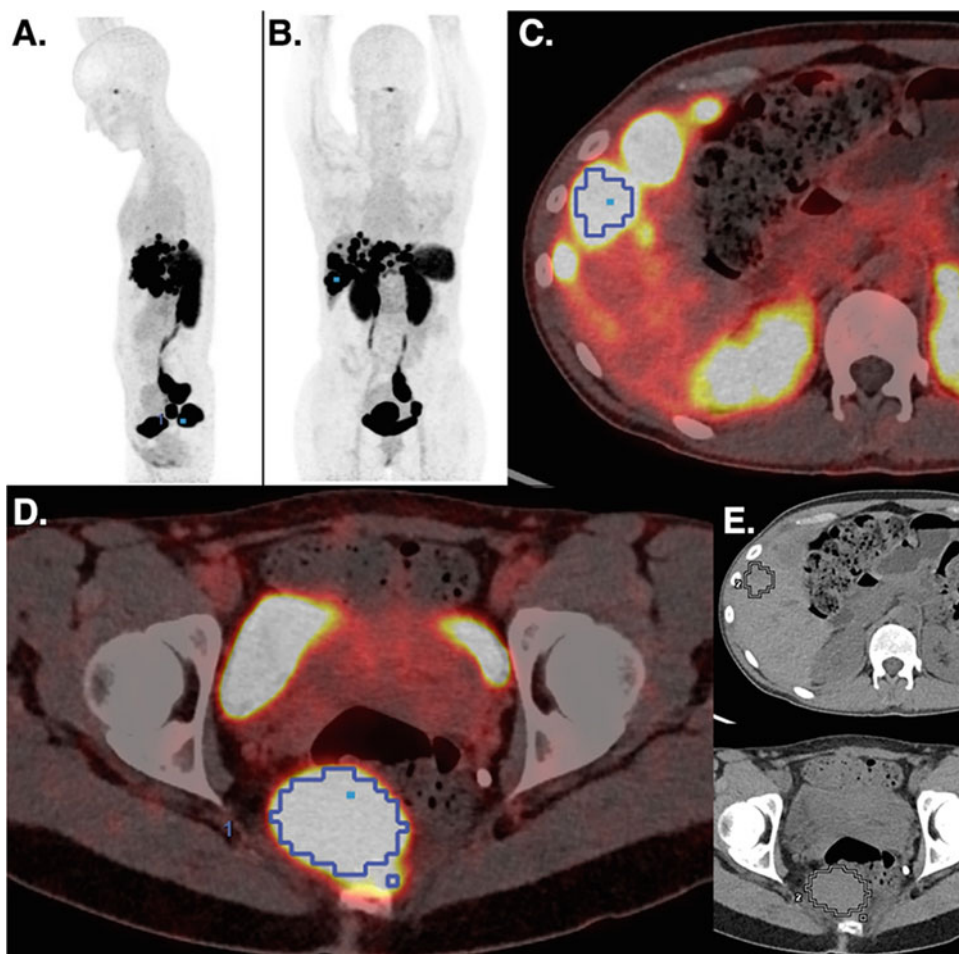
Fig. 14.4 Basal [^{68}Ga]Ga-DOTA-TOC PET/CT demonstrating uptake in the liver (**c**), the right pararectal region (**d**), and the left internal iliac area. (**a**) Whole body maximum intensity projection (MIP) lateral view of [^{68}Ga] Ga-DOTA-TOC PET/CT; (**b**) Whole body MIP anterior view of [^{68}Ga]Ga-DOTA-TOC PET/CT; (c-d) Fused PET and CT axial slices at the liver and pararectal levels; (**e**) Axial CT scan only at the liver and pararectal levels

This scan was done in compliance with the Delphic expert consensus on molecular imaging and theranostics in neuroendocrine neoplasms [7]. According to this, a [^{68}Ga]Ga-DOTA-TOC PET/CT should be performed in addition to diagnostic contrast-enhanced CT or magnetic resonance imaging (MRI) for both initial staging (even with metastatic disease and unknown primary tumor site) and for restaging after surgery (either curative or palliative). The SSTR PET scan allows for the evaluation of the extent of disease and may allow for the localization of the site of the primary tumor. In addition, it allows for the evaluation of the SSTR expression for qualification for PRRT. However, it is important to note that a positive SSTR scan is not, per se, diagnostic of NET, since there are cases of non-NE tumors as well as sites of infection/inflammation that express SSTRs. More recently, in addition to contrast-enhanced CT or MRI and [^{68}Ga]Ga-DOTA-TOC PET/CT, many authors have suggested performing [^{18}F]FDG PET/CT to detect more aggressive tumor cell clones. This approach might be unnecessary in the context of low-grade NETs (as in the case of our patient). However, as discussed in the guidelines provided by the major societies (i.e., EANM and ENETS), performing [^{18}F]FDG PET/CT in patients with higher grade G2 (e.g., Ki-67 10–20%) and G3 NETs and NECs could be useful to provide a complete biological characterization of the tumor [14, 15]. Importantly, [^{18}F]FDG PET/CT also offers a chance to identify mismatched lesions—i.e., lesions that are ([^{68}Ga]Ga-DOTA-TOC negative and [^{18}F]FDG positive—that could reduce the efficacy of PRRT [16].

After the initial staging, the case was discussed at the weekly multidisciplinary NETs tumor board (July 2018). The determination of the board was to schedule a rectal ultrasound endoscopy with biopsy and to commence somatostatin analogue therapy. Rectal-EUS with biopsy of the para-rectal lesion confirmed its neuroendocrine nature: "neoplastic proliferation of neuroendocrine cells in solid-trabecular disposition with low proliferative index (<1) without significant nuclear atypia, in the absence of mitosis and necrosis in the material under examination. CD56 +, Synaptophysin +, CDx2 -, and TTF1 -" (Fig. 14.5). *After an abdominal and pelvic MRI in September 2018 that confirmed stability of the disease, the tumor board opted to schedule "a multidisciplinary meeting (oncologist, nuclear medicine physician, and surgeon) to discuss with the patient the possible future therapies (PRRT for cytoreductive purposes or direct surgery approach)."*

As already stated, NETs are heterogeneous neoplasms that can arise anywhere in the body and thus exhibit extensive variation in their disease symptomatology and clinical presentation. Therefore, with such a complex disease, a multidisciplinary approach is crucial to better address the needs of the patient. This strategy leads to reduced morbidity and mortality, improved patient quality of life, efficient access to the best treatment options, and reduced costs [17, 18].
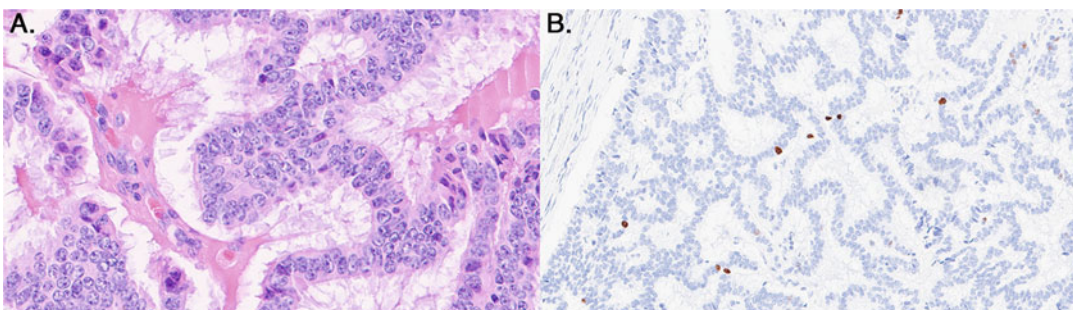

Fig. 14.5 Hematoxylin and eosin stain (**a**) and Ki-67 immunohistochemical staining (**b**) of tissue samples of our patient proving the neoplastic proliferation of neuroendocrine cells. The fraction of Ki-67-positive tumor cells is strictly associated with cell proliferation and is often correlated with the clinical course of cancer

The subsequent discussion leaned toward direct surgery. Surgery was performed in February 2019, during which a right lymph node mass (a) and two liver nodules (b) were removed. Interestingly, the histopathological analysis described rather homogenous disease with (a) lymph- and perilymph nodal metastasis of well differentiated G2 neuroendocrine tumor, mitotic index <1/10 HPF and Ki-67 of 8% and (b) liver metastases of well differentiated G2 neuroendocrine tumor, mitotic index <1/10 HPF and Ki-67 5%.

After almost a year of stable disease as confirmed by a whole-body CT scan performed in July 2019, the follow up CT scan in January 2020 showed mildly increased liver disease with stable left iliac adenopathy and a right para-rectal lesion. Therefore, the oncological visit resulted in the following assessment: "Current exams and visit show stable disease. Treatment with octreotide LAR 30 mg/28 days is well tolerated. We therefore confirm current treatment and will see the patient again in 6 months with MR abdomen-pelvis and labs, as per our internal guideline. The case will then be rediscussed at our tumor board."

As good practice in our institute, after a scheduled oncological visit, we present a brief clinical update at the next weekly tumor board meeting (February 2020) in order to discuss possible alternatives in the therapeutic strategy. In our patient's case, the multidisciplinary team opted for a revision of the histology to evaluate a possible gastroenteropancreatic origin and to repeat PET/CT with [68Ga]Ga-DOTA-TOC for consideration of PRRT. Both decisions proved to be correct. The bioptic specimen revision concluded a possible gastrointestinal origin of the metastasis, and the [68Ga]Ga-DOTA-TOC PET/CT scan showed clear progression of disease with increase in number and extent of the tracer avid liver and node lesions. Therefore, at the subsequent visit with the nuclear medicine team, the patient was deemed eligible for PRRT with [177Lu]Lu-oxodotreotide (Lutathera®). During the visit, we spoke with the patient and her husband about the possible benefits and side effects; the patient understood and agreed with the plan.

To provide context, these were the days of the beginning of COVID-19 pandemic, and northern Italy—where the hospital is located—was the first region hit by the pandemic after China. There, as in any other place hit by COVID-19, the infrastructure was not prepared for such an emergency. Therefore, we decided to postpone the beginning of therapy by a few weeks while we were devising a contingency plan for patients with neuroendocrine tumors [19]. In the meantime, the patient continued to receive a long-acting somatostatin analogue. The experience of this patient illustrates that the final indication for PRRT needs to be tailored for each patient and discussed in a multidisciplinary setting with specialists such as oncologists, nuclear medicine physicians, radiologists, radiation oncologists, endocrinologists, surgeons, gastroenterologists, and endoscopists. In this framework, the patient and clinicians have the opportunity to consider other available treatment options and define the most appropriate treatment sequence [20].

Finally, on March 23, 2020, the patient received the first cycle of PRRT with Lutathera®: 7.4 GBq (200 mCi) along with standard renal protection with amino acids (commercial solution 25 g/25 g arginine hydrochloride/lysine hydrochloride). The treatment was well tolerated with mild nausea in the following days and modest hematological toxicity to leukocytes (G2) in the next few weeks. In consideration of the hematological toxicity and in light of the ongoing pandemic, the 2nd cycle was administered at a reduced dosage [3.6 GBq (98 mCi) on May 25th, 2020] in order to reduce the risk of toxicity and vulnerability to viral infection. Since the patient continued to present moderate leukopenia after the 2nd cycle (G2 with values ranging between 3.2 and 2.84 × 10^9/L in conjunction with gingival inflammation), we asked for a hematological consultation and an interim restaging with abdominopelvic MRI. The hematologist indicated that the reduced neutrophil count was likely related to the slow recovery after therapy. However, since the neutrophil count was >1500, there was no contraindication to the continuation of PRRT. Compared with October 2018 MRI and January 2020 CT, the

MRI showed a volumetric reduction in the bilobar hepatic metastases and the left iliac adenopathy, indicating a response to treatment. Therefore, with cautious optimism, we proceeded with the third cycle of PRRT on September third, 2020 with 5.34 GBq (144 mCi) of Lutathera. We maintained this reduced dosage in consideration of the current (3.58×10^9/L) and previous leukocyte values, the COVID-19 pandemic, and the results of the MRI. From September to November 2020, after an initial and expected drop in white blood count (WBC) (2.7×10^9/L), lab assessments showed a significant recovery (WBC 3.6' 10^9/L), which prompted us to proceed with the fourth and last cycle of PRRT on November 17th, 2020 with 5.52 GBq (149 mCi) of Lutathera®.

As we have mentioned, the kidneys and bone marrow represent the healthy organs that must be considered with respect to potential PRRT toxicity. However, definitive thresholds for the absorbed doses to these tissues have yet to be determined. In clinical practice, maximum absorbed dose thresholds between 23 and 29 Gy for the kidneys [21–23] and 2 Gy for the red marrow [24] are generally recommended to reduce the probability of late nephrotoxicity (within 5 years) below 5% and avoid hematotoxicity.

In the case of our patient, the cumulative absorbed dose to the kidneys for the whole treatment (4 cycles) was estimated to be 15.6 Gy (11.7–19.6 Gy, 95% confidence interval), while the absorbed dose to the red marrow was not assessed (details about the methods adopted for dosimetry are reported in Table 14.2). Our patient did not experience any significant nephrotoxicity, although a G2 leukopenia after the 1st cycle of PRRT forced a prolongation of the interval between treatments (15 weeks between the 2nd and the 3rd cycle) and a slight reduction in the total activity administered (21.8 GBq versus the 29.6 GBq of a standard four-cycle treatment) (Fig. 14.6). We tailored the four-cycle treatment on a clinical basis to reduce the impact of leukopenia, but individualized dosimetry during the course of treatment is also possible thanks to the physical properties of ^{177}Lu, which 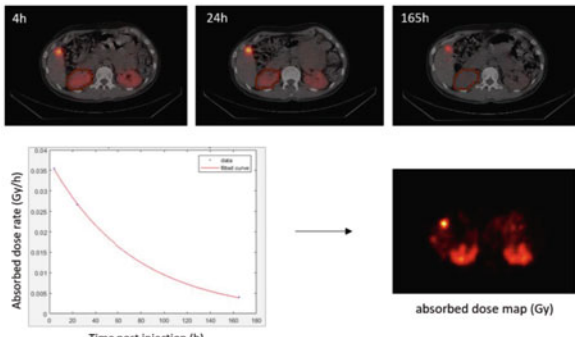decays with the emission of both β-particles (for therapy) and γ-rays (for imaging). In this sense, Lutathera® allows for scintigraphic imaging during therapy that facilitates following the in vivo distribution of the radionuclide and enables personalized dosimetric evaluations [25].
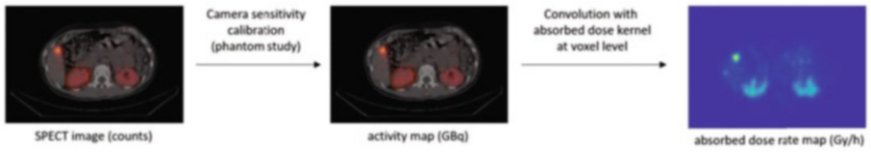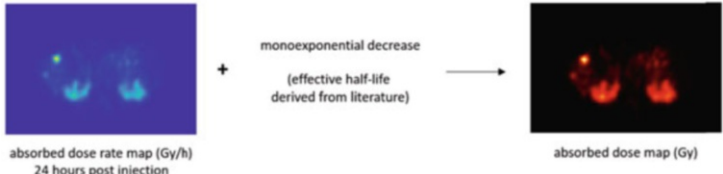
During the February 2021 nuclear medicine visit, it was noted that the patient was in good general condition, with no limitations to the activities of daily life, which included also moderate physical activity. The patient reported markedly improved bowel symptomatology, with considerably decreased episodes of pain and diarrhea. Her weight was stable (58 kg), and she continued to receive Sandostatin LAR 30 mg every 28 days. The physical examination was unremarkable. At this point, she had recently performed: (1) an abdomino-pelvic MRI that showed response to treatment with a decrease in the size of liver lesions, lymph nodes, and pararectal lesion; and (2) a PET/CT with [^{68}Ga]Ga-DOTA-TOC that revealed partial response to treatment with decreased number, extent, and intensity of uptake in the hepatic lesions, lymph nodes, and left pararectal lesion. (Fig. 14.7).

The symptoms of NET patients are principally related to either tumor growth or hormone production, and long-acting somatostatin analogues are typically used for their control. In our case study, the patient mainly experienced constipation and para-rectal pain due to the rectal localization of the primary tumor mass, whereas no carcinoid syndrome—i.e., the direct release of hormones such as serotonin and prostaglandins into systemic circulation, leading to skin flushing, diarrhea, abdominal pain, fast heart rate, and bronchospasm—was reported (Figs. 14.8, 14.9, and 14.10). Finally, in terms of quality-of-life (QoL) improvements after PRRT, our patient demonstrated good results reporting a "normal way of life, moderate physical activity; bowel situation markedly improved" at the first nuclear medicine visit after the end of treatment [26, 27] (Figs. 14.11 and 14.12).

The follow-up continued after the end of PRRT with a new tumor board discussion in March 2021. In consideration of the metastatic stage, the lack of symptoms, and the invasiveness of

Table 14.2 Settings and methods adopted for kidneys dosimetry based on SPECT images. SPECT acquisition, reconstruction, quantification [22, 25] and conversion into absorbed dose rate map [26]. Absorbed dose calculation based on single SPECT acquisition 24 h post injection (cycles 1, 2 and 4) [27] or serial SPECT acquisitions at three time points after injection (cycle 3)

SPECT acquisition	Emission energy window: 208 keV ± 10% Scatter energy windows: 176.8 keV 6% 239.2 keV ± 4% Angular step 3°, 15 s frame duration
SPECT reconstruction	OSEM iterative algorithm, 4 iterations, 10 subsets, no filter Attenuation correction based on CT data, scatter correction with triple window method, resolution recovery
SPECT quantification	
Kidneys absorbed dose calculation (cycles 1, 2, 4)	
Kidneys absorbed dose calculation (cycle 3)	

primary tumor resection, the team decided that there was no indication for surgery but rather for continuing follow-up with abdomino-pelvic MRI with hepatospecific contrast medium, PET/CT with [^{68}Ga]Ga-DOTA-TOC, blood tests, and nuclear medicine visits every 6 months. The patient returned to visit in September 2021 after undergoing the prescribed abdomino-pelvic MRI that confirmed a further reduction in liver lesions and adenopathy with dimensional stability of the pararectal lesion (47 × 33 vs 44 × 35 mm). On this occasion, the nuclear medicine physician reported good general conditions, an active life, a negative clinical examination, a stable WBC count (2.97 × 10^9/L), and no significant problems

in the past months. Similarly, in March 2022, a PET/CT scan with [^{68}Ga]Ga-DOTA-TOC reported further partial response to PRRT (Fig. 14.13) as well as stable clinical conditions. The patient is now awaiting the next visit, and abdominopelvic MRI scheduled in May 2023.

After the end of the four-cycle Lutathera® treatment, the patient began a regular follow-up with nuclear medicine visits every 4–6 months and subsequent multidisciplinary discussions at our tumor board to report on the outcome of therapy and to be updated in case of progressive disease (Fig. 14.14). Fortunately, our patient showed a significant improvement both in terms of morphologic and functional imaging as well as
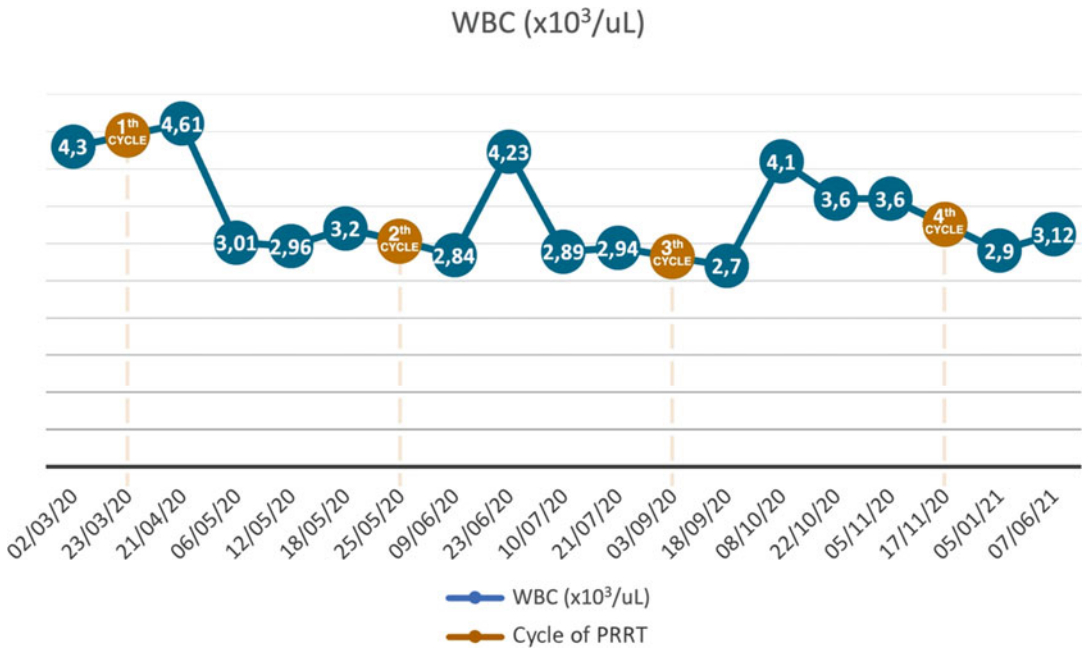
WBC (x10^3/uL)

Fig. 14.6 White blood cell (WBC) count before and after every cycle of PRRT with Lutathera®

clinical outcomes, with markedly improved bowel symptoms with good general conditions and regular lifestyle. The follow-up continues. The take home message from this case study can be found in Fig. 14.15.

14.3 Something Extra: Particularly Important Works

PRRT has been studied in numerous single-arm clinical trials in heterogeneous patient populations that have demonstrated that radiolabeled SSAs deliver targeted radiation with a high therapeutic index to tumors that express somatostatin receptors and thus provide high response rates and long durations of median progression-free survival (PFS). However, the real game-changer for the widespread application of PRRT has been the organization of the first multicenter, randomized, controlled, two-arm, Phase III clinical trial—named NETTER-1—that published its preliminary results in 2017 [10]. The study compared PRRT with [177Lu] Lu-DOTA-TATE plus best supportive care [including 30 mg octreotide LAR (long-acting

release) for the control of symptoms] to treatment with a high dose of the "cold" octreotide LAR (60 mg) in patients with well-differentiated, progressive GEP-NETs. The primary objective of the trial was to determine PFS, and the results confirmed a highly significant difference between the two groups, with longer PFS and significantly higher response rates with [177Lu]Lu-DOTA-TATE than high-dose octreotide LAR (18% vs. 3%; $p < 0.001$). In particular, 65% of patients in the former group were living and free of progression at 20 months compared to only 11% in the latter. The secondary end points included overall survival (OS), safety, and the side-effect profile. In this sense, the final analysis of OS occurred 5 years after the last patient was randomly assigned with a median follow-up period of 76 months for both groups. The PRRT group showed a median OS of 48.0 months versus 36.3 months in the control group, although it is important to consider the adjusted median overall survival for control group patients who crossed over to receive PRRT was 30.9 months.

In terms of safety, the trial demonstrated that treatment with [177Lu]Lu-DOTA-TATE was safe and well tolerated and provided significant
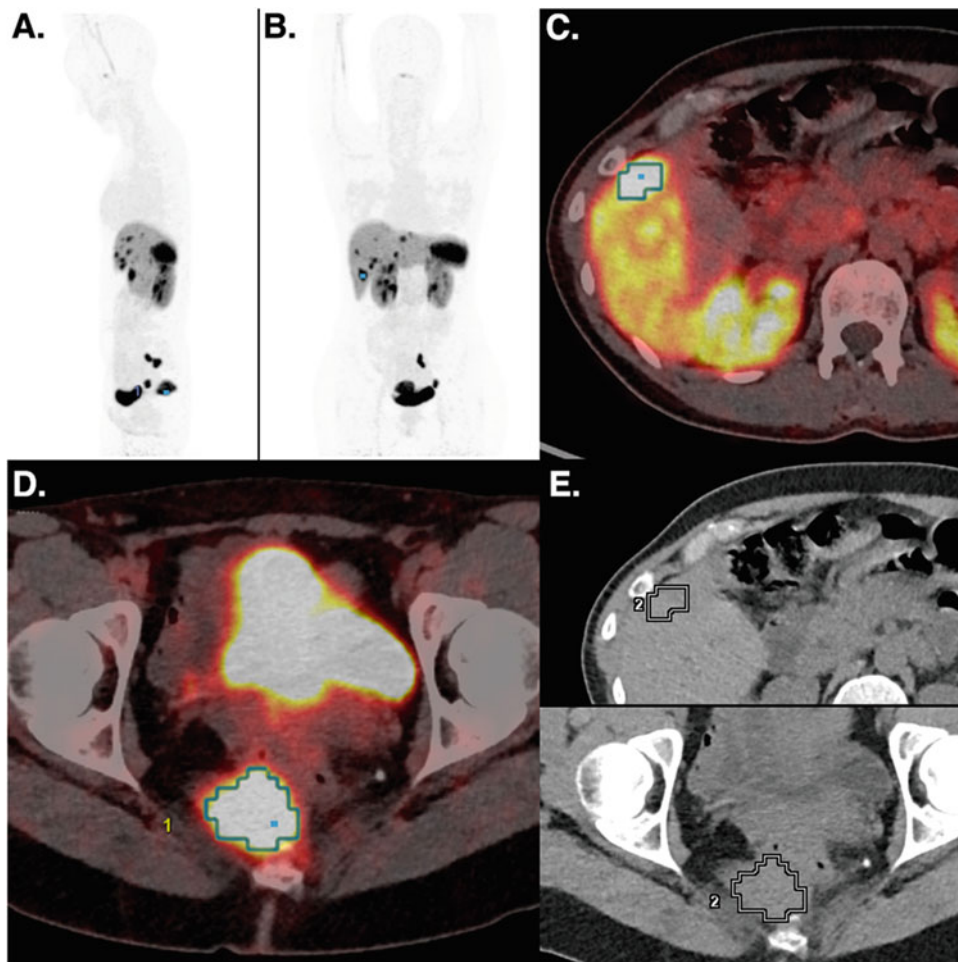
Fig. 14.7 [^{68}Ga]Ga-DOTA-TOC PET/CT after four cycles of PRRT, demonstrating reductions in both the hepatic uptake (**c**) and the right pararectal lesion (**d**). (**a**) Whole body MIP lateral view of [^{68}Ga]Ga-DOTA-TOC PET/CT; (**b**) Whole body MIP anterior view of [^{68}Ga]Ga-DOTA-TOC PET/CT; (c-d) Fused PET and CT axial slices at the liver and pararectal levels; (**e**) Axial CT scan only at the liver and pararectal levels

benefits in terms of QoL compared with high-dose octreotide. The concomitant administration of amino acids as renal-protective agents was pivotal for preventing radiation damage to the kidneys, while PRRT was associated with low rates of grade 3 or 4 hematologic toxic effects (indicating that the doses to the red marrow were not dangerously high). Following the publication of the preliminary results of NETTER-1 in the *New England Journal of Medicine,* the international scientific community started to acknowledge the promise of PRRT. Since then, PRRT with Lutathera® has been approved by the United States Food and Drug Administration (FDA) and the European Medicines Agency (EMA) in patients with SSTR-positive well-differentiated GEP-NETs at a recommended fixed dosage of 7.4 GBq (200 mCi) every 8 weeks for a total of four cycles [8].

The approval of Lutathera® in the US and Europe led to updates to the treatment guidelines, which at this point are focused more on determining whether PRRT should be used before or after chemotherapy in cases of radiographic
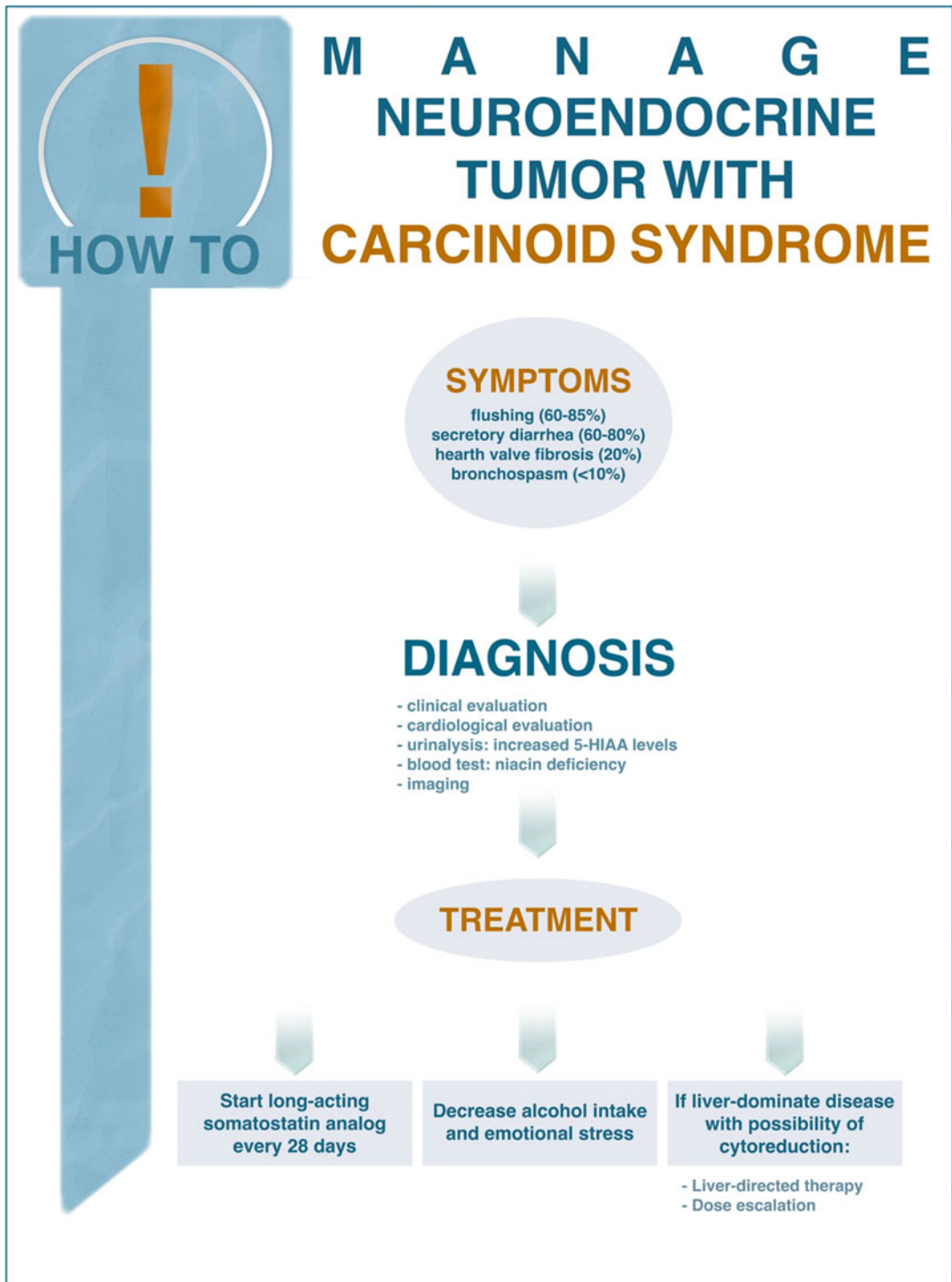
Fig. 14.8 Clinical manifestations, diagnosis, and treatment of carcinoid syndrome in patients with neuroendocrine tumors
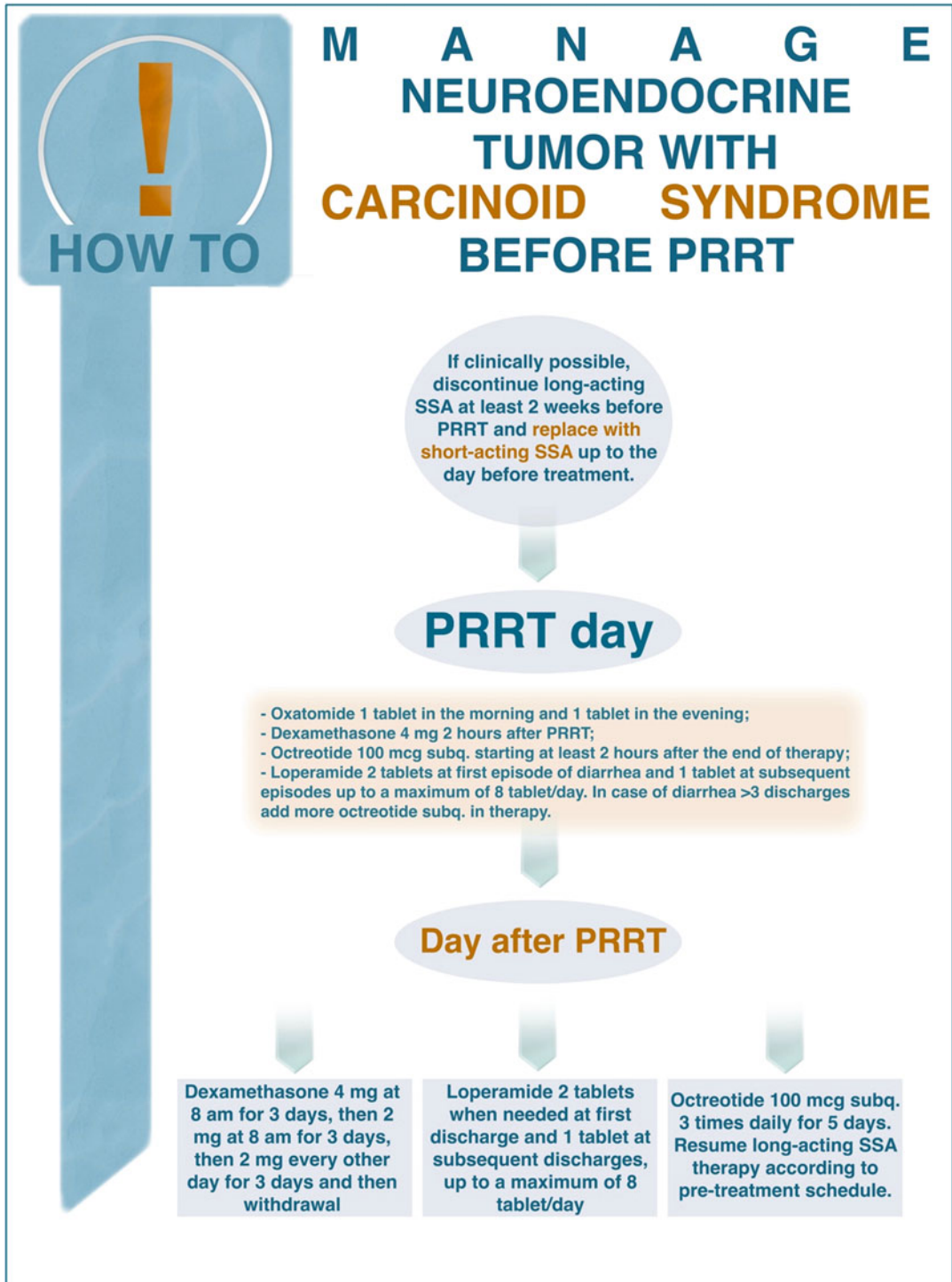
Fig. 14.9 Management of carcinoid syndrome in patient with neuroendocrine tumors before PRRT
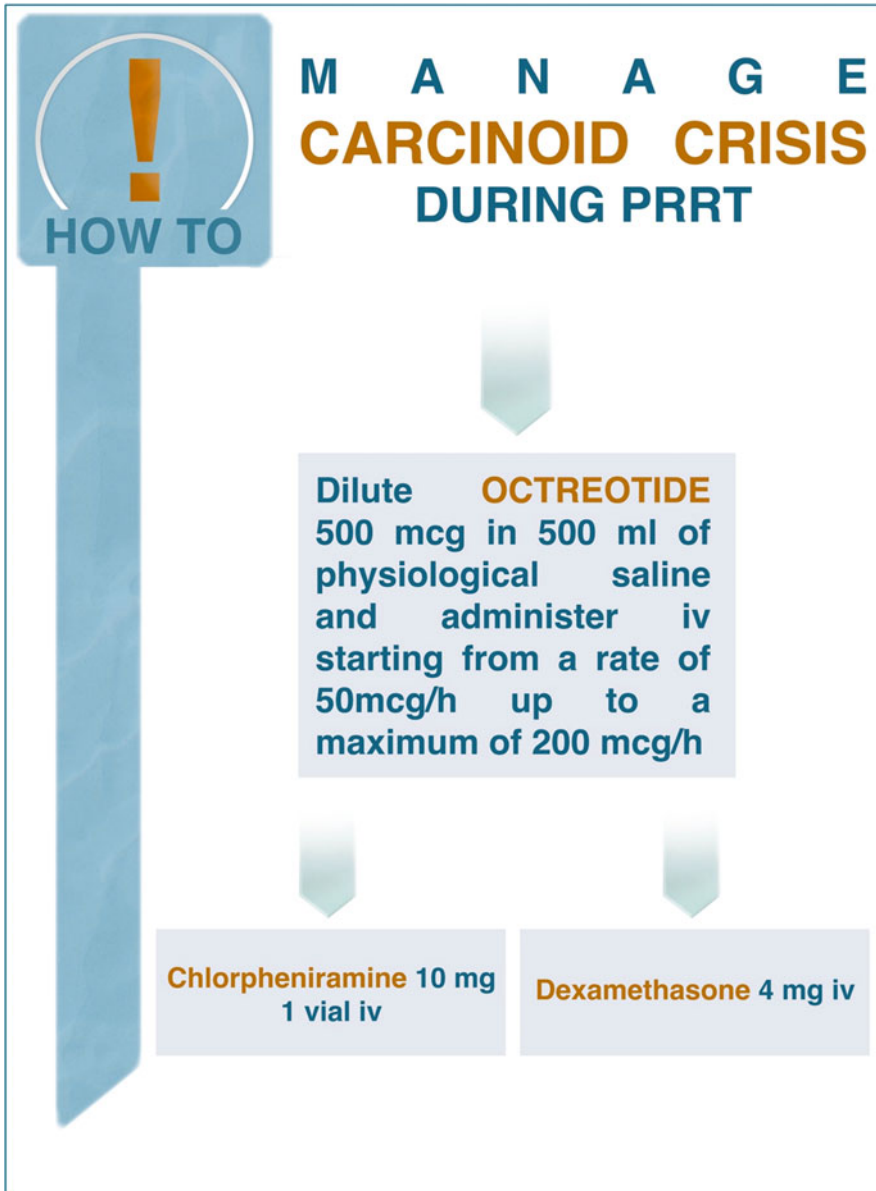
Fig. 14.10 Management of carcinoid crisis during PRRT

progression on first-line SSAs, especially in patients with G2-G3 GEP-NETs. In particular, the ESMO (European Society for Medical Oncology) recommends SSAs for G2 GEP-NETs (with Ki-67 < 10%), with everolimus to be used in progressive G1/G2 P-NETs with or without prior chemotherapy. Specifically, systemic therapies such as CAPTEM or STZ/5-FU are recommended as first-line therapy in case of

G2/G3 P-NETs or in case of SSTR-negative P-NETs, with everolimus or sunitinib recommended as second-line therapy but only within a clinical trial setting. PRRT is recommended in SSTR-positive tumors after the failure of these treatments, although the guideline does highlight that PRRT should be considered earlier in the treatment algorithm, especially in the case of P-NETs. The use of systemic
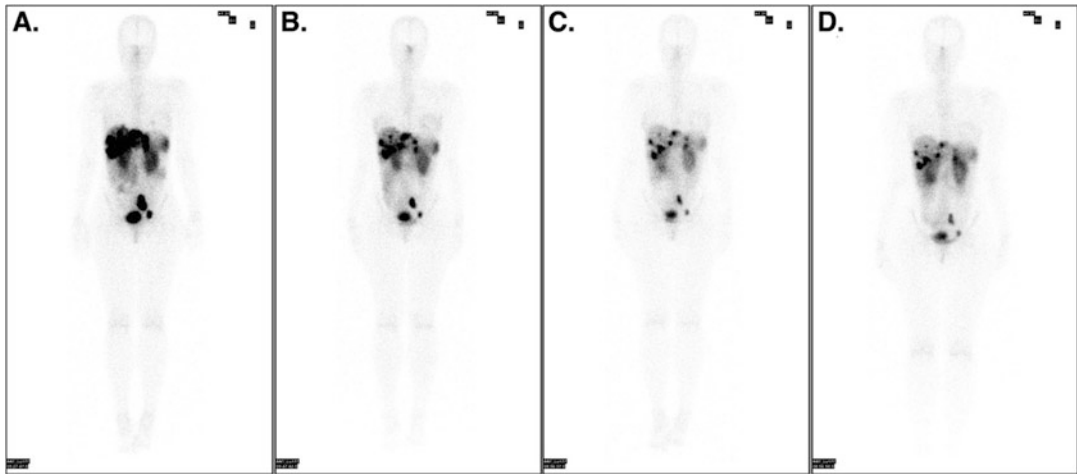
Fig. 14.11 The 24 h post-treatment whole body anterior scans acquired after the first (**a**), second (**b**), third (**c**), and fourth (**d**) cycle of therapy demonstrating the uptake of Lutathera® in the liver, the right pararectal region, and the left internal iliac area
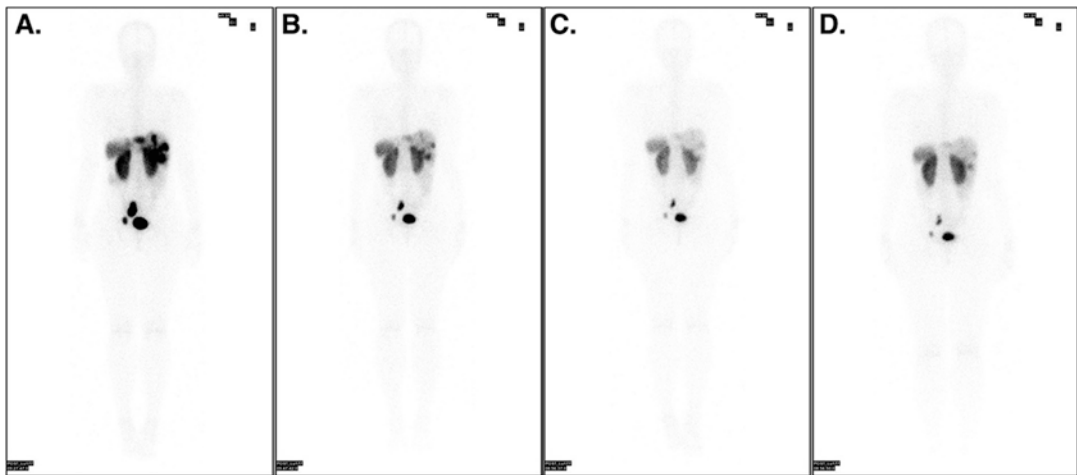
Fig. 14.12 The 24 h post-treatment whole body posterior scans acquired after the first (**a**), second (**b**), third (**c**), and fourth (**d**) cycle of therapy demonstrating the uptake of Lutathera® in the liver, the right pararectal region, and the left internal iliac area

chemotherapy in advanced P-NETs and in G3 NETs of any site is also recommended; PRRT may be considered in selected cases, although it showed best results only in patients with a Ki-67 < 55% [28]. The NCCN (National Comprehensive Cancer Network) Version 2.2021 suggests octreotide or lanreotide as front-line therapy if the patient is SSTR-positive and/or has hormonal symptoms but specifically states that PRRT may be considered after progression on SSAs as an alternative therapeutic option to everolimus or cytotoxic chemotherapy [29].

Guidelines from other relevant societies include those from the European Neuroendocrine
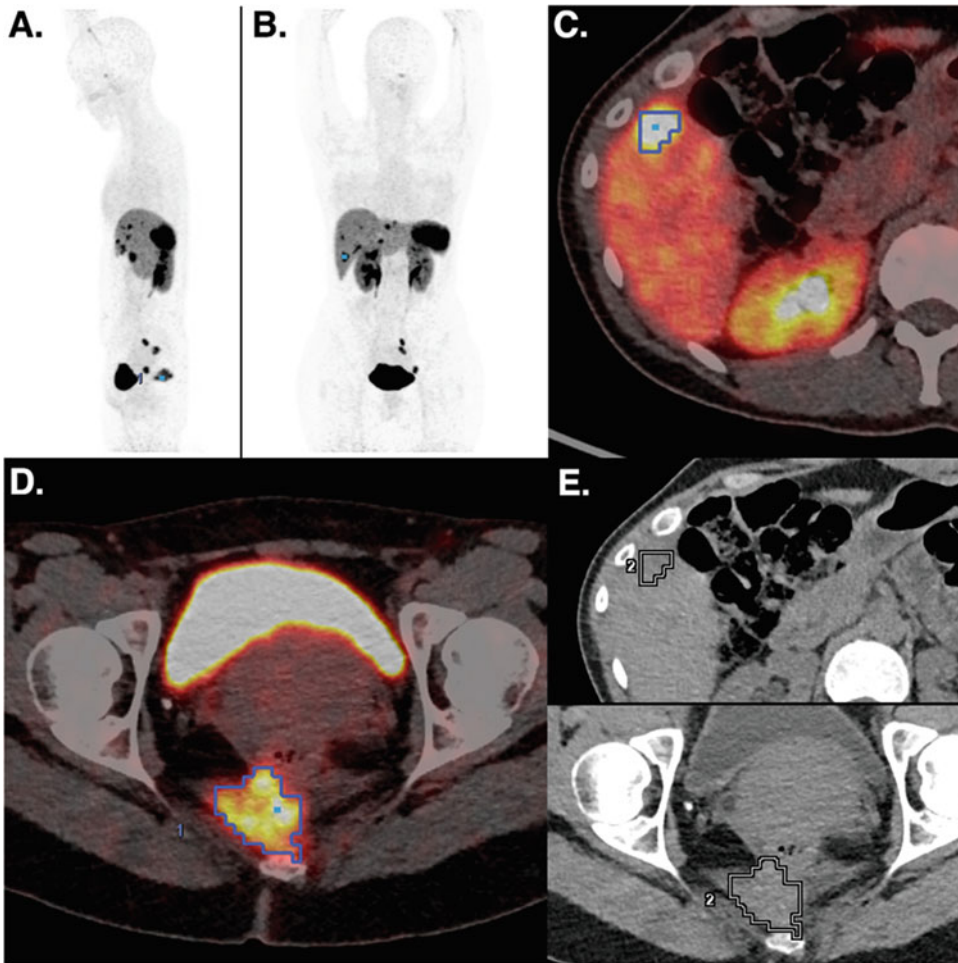
Fig. 14.13 [^{68}Ga]Ga-DOTA-TOC PET/CT performed 1 year after the PRRT, demonstrating further reductions in both the hepatic uptake (**c**) and the right pararectal lesion (**d**). (**a**) Whole body MIP lateral view of [^{68}Ga] Ga-DOTA-TOC PET/CT; (**b**) Whole body MIP anterior view of [^{68}Ga]Ga-DOTA-TOC PET/CT; (c-d) Fused PET and CT axial slices at the liver and pararectal levels; (**e**) Axial CT scan only at the liver and pararectal levels

Tumor Society (ENETS) and the North American Neuroendocrine Society (NANETS). In its 2016 consensus guidelines for high-grade GEP-NECs, ENETS asserted that although a subgroup of tumors express SSRs, there are no data to support the use of SSAs or PRRT. Therefore, this therapeutic strategy is generally not successful. Instead, for patients with localized high-grade disease, a combination of platinum-based chemotherapy with local treatment consisting of surgery, radiotherapy, or both probably offers the greatest likelihood of long-term survival [30]. Finally, the NANETS Consensus Guidelines for Surveillance and Medical Management of Midgut Neuroendocrine Tumors 2017 support the use of everolimus (for non-functioning midgut NETs) after radiographic progression on first-line SSAs, whereas PRRT is recommended as a second-line treatment in patients with SSTR+ midgut NETs compared to IFN-α (in combination with SSAs) or the embolization of liver metastases (for patients with liver-predominant disease and suboptimal control of carcinoid syndrome) [31].

Fig. 14.14 Whole body MIP of [^{68}Ga]Ga-DOTA-TOC PET/CT performed before (**a**), after (**b**) and 1 year after (**c**) PRRT demonstrating the gradual reduction of the pathological uptake in the liver and in the pelvic lesions
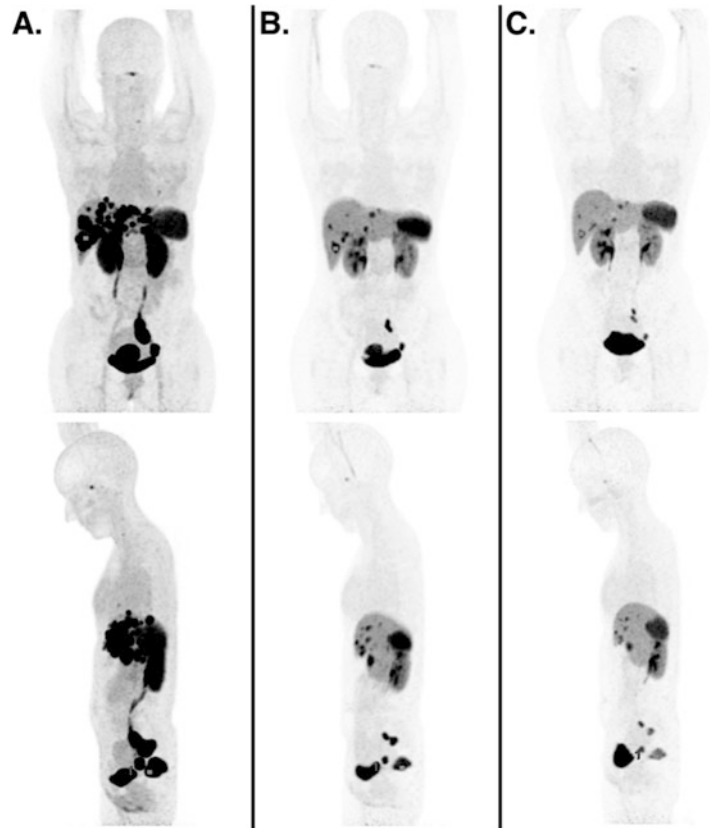
14.4 The Future

Although the NETTER-1 trial represents an important milestone in the field of RPT, many crucial points must still be addressed. For example, as medicine moves toward personalized therapies, the impact of individualized dosimetric evaluations on treatment scheduling and organization should be evaluated. A recent prospective observational study by Garske-Roman et al. [32] investigated the impact of a dosimetry-guided study protocol on outcome and toxicity in 200 patients with advanced NETs. Each treatment cycle, as per standard clinical practice, consisted of 7.4 GBq of Lutathera® with the co-infusion of a mixed amino acid solution. The cycles were, however, repeated until the absorbed dose to the kidneys reached 23 Gy or until other reasons to stop the therapy arose. In the majority of patients (68.5%), the intended absorbed dose of 23 Gy to

the kidneys was reached *after* more than four cycles, and significantly longer PFS and OS were observed compared to the group of patients that had to stop therapy before reaching 23 Gy—median PFS = 33 vs. 15 months and median OS = 54 vs. 25 months—as well as a higher frequency of complete and partial responses. No major radiation-induced nephrotoxicity was observed, and no patient reached the 2 Gy threshold for the irradiation of the bone marrow. In light of these results and in consideration of the intra- and interindividual variability in the absorbed radiation doses observed for the same administered activity, we believe that the implementation of individualized dosimetry in clinical practice could positively impact the total administered activity and the number of therapy cycles and thus significantly improve the current standard set by the NETTER-1 trial. This concept is being further investigated in several ongoing clinical trials (NCT03454763, NCT04917484).
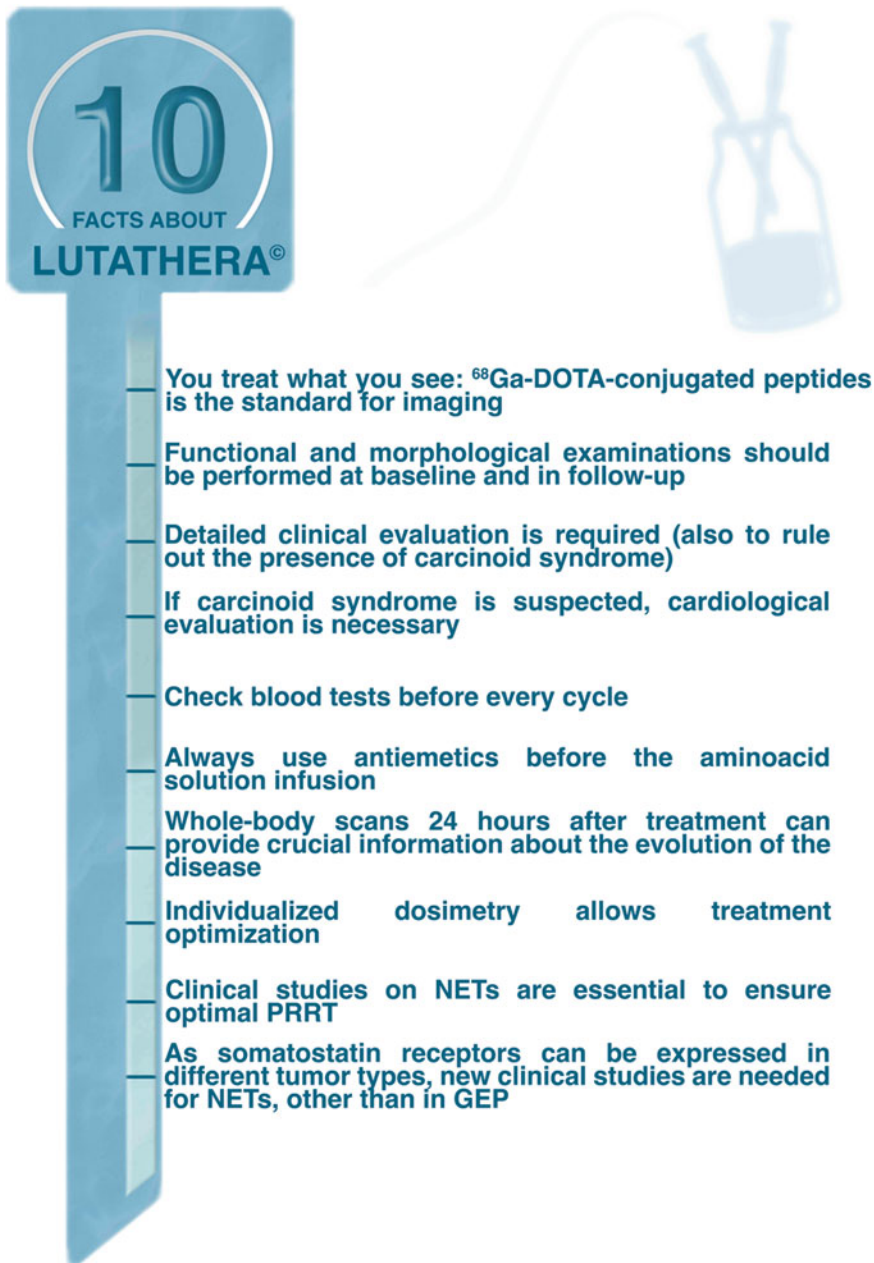
Fig. 14.15 Ten key concepts about the PRRT of neuroendocrine tumors with Lutathera®

Two additional lines of investigation have been proposed to further improve the efficacy of PRRT, and both have produced promising results: the use of SSAs labeled with α-emitting radionuclides (such as ^{212}Pb, ^{213}Bi, and ^{225}Ac) and the use of radiolabeled SSTR-*ant*agonists. The use of α-emitters is attractive due to their

higher linear energy transfer, which induces a higher number of double strand DNA breaks and thus increases their cytotoxicity. Moreover, the very short range of soft tissue penetration (~40–100 μm) of α-emitters attenuates the irradiation of normal tissues and opens the door for the administration of PRRT as an outpatient therapy

[33]. However, it is important to note both the limited availability of α-emitters and the scarcity of literature data on the efficacy and toxicity of PRRT with α-emitters. With respect to the former, there is currently an ongoing phase I trial of [^{212}Pb]Pb-DOTA-TATE in treatment-naïve NET patients (NCT03466216) [34]. Furthermore, we can report the results of a first-in-human study conducted in eight patients with progressive NETs refractory to both "cold" SSA and tandem therapy with [^{90}Y]Y/[^{177}Lu]Lu-DOTA-TOC that have been treated with [^{213}Bi]Bi-DOTA-TOC via either intra-arterial administration into the common hepatic artery ($n = 7$) or systemic administration ($n = 1$). In these patients, [^{213}Bi]Bi-DOTA-TOC was able induce long-term tumor remission (therefore overcoming resistance to β-PRRT) while keeping both nephrotoxicity and acute hematotoxicity within acceptable ranges [35].

Despite the minimal internalization of antagonist-receptor complexes into tumor cells, SSTR antagonists have shown promising pharmacokinetic properties compared to SSTR agonists, most notably higher tumor uptake values (thanks to the ability to occupy more binding sites with a lower dissociation rate), longer retention times in tumor tissue, and shorter retention times in healthy organs [36]. The most often employed antagonist-based radiopharmaceuticals currently undergoing clinical trials are [^{111}In]In-DOTA-SST-ANT, [^{177}Lu]Lu-DOTA-BASS, and [^{177}Lu]Lu-OPS201. In a pilot study of four patients with advanced NET and chronic grade 2 or 3 kidney disease, the latter displayed higher tumor uptake and longer tumoral residence time compared to [^{177}Lu]Lu-DOTA-TATE, resulting in tumor doses up to 10 times higher [37, 38]. Finally, Baum et al. recently reported the first-in-human study with the SSTR antagonist [^{177}Lu]Lu-DOTA-LM3 in 51 patients with advanced and progressive NETs [39]. Although their study population was heterogeneous—i.e., 69% of cases had already been treated with either [^{177}Lu]Lu-DOTA-TOC or [^{177}Lu]Lu-DOTA-TATE—a high disease control rate of 85% was observed alongside low rates of hematological

toxicity and no nephrotoxicity. Interestingly, baseline [^{68}Ga]Ga-DOTA-TOC or DOTA-TATE PET/CT imaging displayed no or low SSTR2 agonist binding in 37 of 51 patients (72.5% of patients), suggesting that PRRT with [^{177}Lu]Lu-DOTA-TOC or [^{177}Lu]Lu-DOTA-TATE would not be possible in these patients. However, theranostic imaging with [^{68}Ga]Ga-NODAGA-LM3 revealed tumoral uptake greater than the uptake in the normal liver parenchyma in all patients. Finally, several clinical trials have sought to combine these two promising avenues by using SSTR antagonists labeled with α-emitting radionuclides, but these data are still very preliminary.

Ultimately, while it is clear that the preliminary data on PRRT using α-emitting radionuclides and/or SSTR antagonists are promising, further analysis in larger groups of patients with longer follow-up times is needed.

14.5   The Bottom Line

- Peptide receptor radionuclide therapy (PRRT) is a subgenre of RPT. The most frequent target for PRRT in clinical practice is the somatostatin receptor (SSTR), which is overexpressed in neuroendocrine tumors (NETs).
- A multidisciplinary approach is crucial to the effective management of patients with NETs since different specialists are needed to consider all available treatment options and to define the most appropriate treatment sequence, including PRRT.
- NETTER-1 is a multicenter phase-III clinical trial that proved the superiority of PRRT with Lutathera® ([^{177}Lu]Lu-DOTA-TATE) compared to treatment with high doses of octreotide LAR in patients with SSTR-positive GEP-NETs.
- Lutathera® is the first approved radiopharmaceutical for PRRT at a recommended fixed dose of 7.4 GBq (200 mCi) every 8 weeks for a total of four cycles.
- The kidneys and bone marrow represent the most likely sources of radiation-related

toxicity during PRRT. Dosimetric evaluation during therapy allows for the personalization of treatment regimens.

- The use of peptides labeled with α-emitting radionuclides represents a promising avenue for improving PRRT, as does the use of SSTR *ant*agonists rather than agonists. However, more data are needed to properly evaluate the efficacy and toxicity of these strategies.

References

1. Kwekkeboom DJ, Kam BL, van Essen M, Teunissen JJ, van Eijck CH, Valkema R, et al. Somatostatin-receptor-based imaging and therapy of gastroenteropancreatic neuroendocrine tumors. Endocr Relat Cancer. 2010;17(1):R53–73.
2. Bodei L, Pepe G, Paganelli G. Peptide receptor radionuclide therapy (PRRT) of neuroendocrine tumors with somatostatin analogues. Eur Rev Med Pharmacol Sci. 2010;14(4):347–51.
3. Prise KM, O'Sullivan JM. Radiation-induced bystander signalling in cancer therapy. Nat Rev Cancer. 2009;9(5):351–60.
4. Murray D, McEwan AJ. Radiobiology of systemic radiation therapy. Cancer Biother Radiopharm. 2007;22(1):1–23.
5. Baum RP, Kulkarni HR. THERANOSTICS: from molecular imaging using Ga-68 labeled tracers and PET/CT to personalized radionuclide therapy - the Bad Berka experience. Theranostics. 2012;2(5):437–47.
6. Di Stasio GD, Buonomano P, Travaini LL, Grana CM, Mansi L. From the magic bullet to Theragnostics: certitudes and hypotheses, trying to optimize the somatostatin model. Cancers (Basel). 2021;13(14):3474.
7. Ambrosini V, Kunikowska J, Baudin E, Bodei L, Bouvier C, Capdevila J, et al. Consensus on molecular imaging and theranostics in neuroendocrine neoplasms. Eur J Cancer. 2021;146:56–73.
8. Hennrich U, Kopka K. Lutathera((R)): the first FDA- and EMA-approved radiopharmaceutical for peptide receptor radionuclide therapy. Pharmaceuticals (Basel). 2019;12(3):114.
9. Ahmadi Bidakhvidi N, Goffin K, Dekervel J, Baete K, Nackaerts K, Clement P, et al. Peptide receptor radionuclide therapy targeting the somatostatin receptor:

basic principles, clinical applications and optimization strategies. Cancers (Basel). 2021;14(1):129.
10. Strosberg J, El-Haddad G, Wolin E, Hendifar A, Yao J, Chasen B, et al. Phase 3 trial of (177)Lu-Dotatate for midgut neuroendocrine tumors. N Engl J Med. 2017;376(2):125–35.
11. Levart D, Kalogianni E, Corcoran B, Mulholland N, Vivian G. Radiation precautions for inpatient and out-patient (177)Lu-DOTATATE peptide receptor radionuclide therapy of neuroendocrine tumours. EJNMMI Phys. 2019;6(1):7.
12. Chantadisai M, Kulkarni HR, Baum RP. Therapy-related myeloid neoplasm after peptide receptor radionuclide therapy (PRRT) in 1631 patients from our 20 years of experiences: prognostic parameters and overall survival. Eur J Nucl Med Mol Imaging. 2021;48(5):1390–8.
13. Nagtegaal ID, Odze RD, Klimstra D, Paradis V, Rugge M, Schirmacher P, et al. The 2019 WHO classification of tumours of the digestive system. Histopathology. 2020;76:182–8. https://doi.org/10.1111/his.13975
14. Sundin A, Arnold R, Baudin E, Cwikla JB, Eriksson B, Fanti S, et al. ENETS consensus guidelines for the standards of care in neuroendocrine tumors: radiological, nuclear medicine & hybrid imaging. Neuroendocrinology. 2017;105(3):212–44.
15. Bodei L, Mueller-Brand J, Baum RP, Pavel ME, Horsch D, O'Dorisio MS, et al. The joint IAEA, EANM, and SNMMI practical guidance on peptide receptor radionuclide therapy (PRRNT) in neuroendocrine tumours. Eur J Nucl Med Mol Imaging. 2013;40(5):800–16.
16. Evangelista L, Ravelli I, Bignotto A, Cecchin D, Zucchetta P. Ga-68 DOTA-peptides and F-18 FDG PET/CT in patients with neuroendocrine tumor: a review. Clin Imaging. 2020;67:113–6.
17. Metz DC, Choi J, Strosberg J, Heaney AP, Howden CW, Klimstra D, et al. A rationale for multidisciplinary care in treating neuroendocrine tumours. Curr Opin Endocrinol Diabetes Obes. 2012;19(4):306–13.
18. Bertani E, Fazio N, Botteri E, Chiappa A, Falconi M, Grana C, et al. Resection of the primary pancreatic neuroendocrine tumor in patients with unresectable liver metastases: possible indications for a multimodal approach. Surgery. 2014;155(4):607–14.
19. Panzuto F, Maccauro M, Campana D, Faggiano A, Massironi S, Pusceddu S, et al. Impact of the SARS-CoV2 pandemic dissemination on the management of neuroendocrine neoplasia in Italy: a report from the Italian Association for Neuroendocrine Tumors (Itanet). J Endocrinol Investig. 2021;44(5):989–94.
20. Burkett BJ, Dundar A, Young JR, Packard AT, Johnson GB, Halfdanarson TR, et al. How we do it: a multidisciplinary approach to (177)Lu DOTATATE peptide receptor radionuclide therapy. Radiology. 2021;298(2):261–74.
21. Garkavij M, Nickel M, Sjogreen-Gleisner K, Ljungberg M, Ohlsson T, Wingardh K, et al. 177Lu-[DOTA0,Tyr3] octreotate therapy in patients with disseminated neuroendocrine tumors: Analysis of

dosimetry with impact on future therapeutic strategy. Cancer. 2010;116(4 Suppl):1084–92.

22. Sandstrom M, Garske-Roman U, Johansson S, Granberg D, Sundin A, Freedman N. Kidney dosimetry during (177)Lu-DOTATATE therapy in patients with neuroendocrine tumors: aspects on calculation and tolerance. Acta Oncol. 2018;57(4):516–21.

23. Ljungberg M, Celler A, Konijnenberg MW, Eckerman KF, Dewaraja YK, Sjogreen-Gleisner K, et al. MIRD pamphlet no. 26: joint EANM/MIRD guidelines for quantitative 177Lu SPECT applied for dosimetry of radiopharmaceutical therapy. J Nucl Med. 2016;57(1):151–62.

24. Pandit-Taskar N, Iravani A, Lee D, Jacene H, Pryma D, Hope T, et al. Dosimetry in clinical radiopharmaceutical therapy of cancer: practicality versus perfection in current practice. J Nucl Med. 2021;62(Suppl 3):60S–72S.

25. Santoro L, Mora-Ramirez E, Trauchessec D, Chouaf S, Eustache P, Pouget JP, et al. Implementation of patient dosimetry in the clinical practice after targeted radiotherapy using (177)Lu-[DOTA0, Tyr3]-octreotate. EJNMMI Res. 2018;8(1):103.

26. Strosberg J, Wolin E, Chasen B, Kulke M, Bushnell D, Caplin M, et al. Health-related quality of life in patients with progressive midgut neuroendocrine tumors treated with (177)Lu-Dotatate in the phase III NETTER-1 trial. J Clin Oncol. 2018;36(25):2578–84.

27. Strosberg JR, Srirajaskanthan R, El-Haddad G, Wolin EM, Chasen BR, Kulke MH, et al. Symptom diaries of patients with midgut neuroendocrine tumors treated with (177)Lu-DOTATATE. J Nucl Med. 2021;62:1712.

28. Pavel M, Oberg K, Falconi M, Krenning EP, Sundin A, Perren A, et al. Gastroenteropancreatic neuroendocrine neoplasms: ESMO clinical practice guidelines for diagnosis, treatment and follow-up. Ann Oncol. 2020;31(7):844–60.

29. Shah MH, Goldner WS, Benson AB, Bergsland E, Blaszkowsky LS, Brock P, et al. Neuroendocrine and adrenal tumors, version 2.2021, NCCN clinical practice guidelines in oncology. J Natl Compr Cancer Netw. 2021;19(7):839–68.

30. Garcia-Carbonero R, Sorbye H, Baudin E, Raymond E, Wiedenmann B, Niederle B, et al. ENETS consensus guidelines for high-grade Gastroenteropancreatic neuroendocrine tumors and neuroendocrine carcinomas. Neuroendocrinology. 2016;103(2):186–94.

31. Strosberg JR, Halfdanarson TR, Bellizzi AM, Chan JA, Dillon JS, Heaney AP, et al. The north American neuroendocrine tumor society consensus guidelines for surveillance and medical Management of Midgut Neuroendocrine Tumors. Pancreas. 2017;46(6):707–14.

32. Garske-Roman U, Sandstrom M, Fross Baron K, Lundin L, Hellman P, Welin S, et al. Prospective observational study of (177)Lu-DOTA-octreotate therapy in 200 patients with advanced metastasized neuroendocrine tumours (NETs): feasibility and impact of a dosimetry-guided study protocol on outcome and toxicity. Eur J Nucl Med Mol Imaging. 2018;45(6):970–88.

33. Ballal S, Yadav MP, Bal C, Sahoo RK, Tripathi M. Broadening horizons with (225)Ac-DOTATATE targeted alpha therapy for gastroenteropancreatic neuroendocrine tumour patients stable or refractory to (177)Lu-DOTATATE PRRT: first clinical experience on the efficacy and safety. Eur J Nucl Med Mol Imaging. 2020;47(4):934–46.

34. Delpassand E, Tworowska I, Esfandiari R, Torgue J, Hurt JD, Nunez R. Phase I dose-escalation study of AlphaMedix for targeted-alpha-emitter therapy of PRRT-naive neuroendocrine patients. Wolters Kluwer Health; 2021.

35. Kratochwil C, Giesel FL, Bruchertseifer F, Mier W, Apostolidis C, Boll R, et al. (2)(1)(3)Bi-DOTATOC receptor-targeted alpha-radionuclide therapy induces remission in neuroendocrine tumours refractory to beta radiation: a first-in-human experience. Eur J Nucl Med Mol Imaging. 2014;41(11):2106–19.

36. Fani M, Nicolas GP, Wild D. Somatostatin receptor antagonists for imaging and therapy. J Nucl Med. 2017;58(Suppl 2):61S–6S.

37. Nicolas GP, Mansi R, McDougall L, Kaufmann J, Bouterfa H, Wild D, et al. Biodistribution, pharmacokinetics, and dosimetry of (177)Lu-, (90)Y-, and (111)in-labeled somatostatin receptor antagonist OPS201 in comparison to the agonist (177)Lu-DOTATATE: the mass effect. J Nucl Med. 2017;58(9):1435–41.

38. Wild D, Fani M, Fischer R, Del Pozzo L, Kaul F, Krebs S, et al. Comparison of somatostatin receptor agonist and antagonist for peptide receptor radionuclide therapy: a pilot study. J Nucl Med. 2014;55(8):1248–52.

39. Baum RP, Zhang J, Schuchardt C, Muller D, Macke H. First-in-humans study of the SSTR antagonist (177)Lu-DOTA-LM3 for peptide receptor radionuclide therapy in patients with metastatic neuroendocrine neoplasms: dosimetry, safety, and efficacy. J Nucl Med. 2021;62(11):1571–81.

Case Study #5: CXCR4-Targeted Radiotherapeutics

15

Andreas K. Buck, Heribert Hänscheid, Sebastian E. Serfling, Takahiro Higuchi, Leo Rasche, Hermann Einsele, and Rudolf A. Werner

15.1 The Fundamentals

15.1.1 C-X-C Motif Chemokine Receptor 4 (CXCR4)—*A Remarkable Theranostic Target*

The G-protein coupled receptor C-X-C motif chemokine receptor 4 (CXCR4) and its ligand—stromal cell-derived factor-1 (C-X-C motif chemokine 12 [CXCL12])—play a pivotal role in orchestrating the angiogenesis and dissemination of tumors [1]. A growing body of work has revealed the overexpression of CXCR4 in more than 23 different cancer subtypes, including but not limited to renal, prostate, and breast cancer as well as melanoma [1]. Interestingly, the CXCR4/CXCL12 axis is also involved in resistance to various therapeutic regimens by recruiting myeloid cell types in the bone marrow (BM) to promote the on-set of metastatic spread [2]. Given their importance in tumor biology, the disruption of the interplay between the two moieties can reduce tumor growth in tumor-bearing mice, and thus CXCR4 and CXCL12 have attracted attention as therapeutic targets [3].

In light of these data, it is perhaps not surprising that several single photon emission tomography (SPECT) and positron emission tomography (PET) radiotracers have been developed to provide a non-invasive read-out of CXCR4 expression on a tumor cell level [4]. To date, [^{68}Ga]Ga-PentixaFor is the most extensively investigated CXCR4-targeted PET tracer (Fig. 15.1) [4]. In addition, in a manner reminiscent of the somatostatin receptor-targeted theranostics, the gallium-68 in [^{68}Ga]Ga-PentixaFor has been replaced with the ß-emitting radiometals yttrium-90 and lutetium-177 to create radiotherapeutics. Indeed, [^{177}Lu]Lu-/[^{90}Y]Y-PentixaTher have already been used in patients with several subtypes of hematological neoplasms [4]. In an acute setting, these therapies exhibited manageable side effects if proper pretherapeutic workup was conducted (e.g., prophylaxis of tumor lysis syndrome [TLS] and pretherapeutic dosimetry) and achieved complete remissions (CMR) in selected cases (e.g., in T-cell lymphoma [TCL]) [5].

As CXCR4 is also crucially involved in gradient-dependent stem cell mobilization and migration [6], [^{177}Lu]Lu- and [^{90}Y]Y-PentixaTher also mediate BM eradication, a

A. K. Buck (✉) · H. Hänscheid · S. E. Serfling
T. Higuchi
Department of Nuclear Medicine, University Hospital Würzburg, Würzburg, Germany
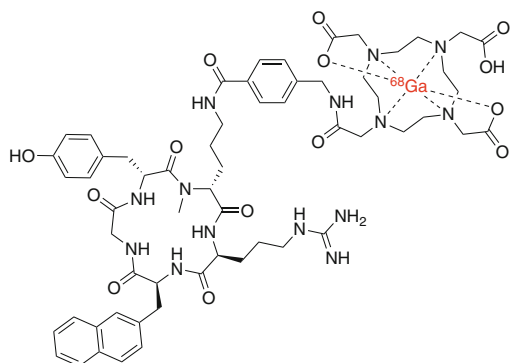e-mail: buck_a@ukw.de

L. Rasche · H. Einsele
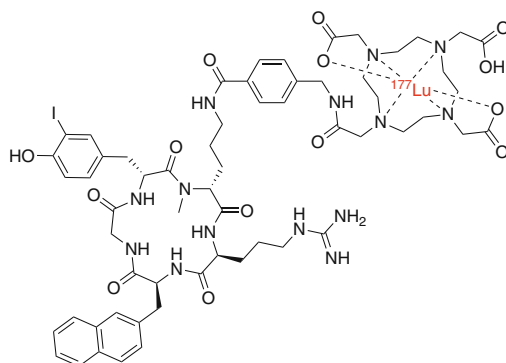Department of Internal Medicine II, University Hospital Würzburg, Würzburg, Germany

R. A. Werner
Department of Nuclear Medicine, University Hospital Würzburg, Würzburg, Germany

Johns Hopkins School of Medicine, The Russell H Morgan Department of Radiology and Radiological Science, Baltimore, MD, USA

[68Ga]Ga-PentixaFor

[177Lu]Lu-PentixaTher

Fig. 15.1 The structures of [^{68}Ga]Ga-Pentixafor and [^{177}Lu]Lu-PentixaTher. It is important to note that structures of PentixaFor and PentixaTher, while very similar, are not identical: the latter contains an iodotyrosine residue in the place of the former's tyrosine residue. This change was made due to the fact that there is a tyrosine moiety in the peptide sequence and thus, iodine can be

easily introduced through direct radioiodination. Later, a series of candidates with or without iodine was tested both in vitro and in-vivo. The activity at CXCR4 is not only reserved after the introduction of iodine, but also showed highest uptake and internalization, both factors which may be advantageous for therapy [52]

desirable phenomenon in patients that per se require hematopoietic stem cell transplantation (HSCT) as an integral part of their treatment plan [4]. As such, beyond an anti-lymphoma effect, CXCR4-targeted RPT can be used alongside high-dose chemotherapeutic regimens to facilitate autologous or allogeneic HSCT [5]. This dual purpose—i.e., helping patients achieve durable anti-lymphoma effects and preparing them for subsequent HSCT—makes PentixaTher-based RPT an attractive therapeutic approach in patients with advanced blood cancer. This complex strategy, however, requires the coordinated interplay of a variety of disciplines, including hemato-oncology, gastroenterology, endocrinology, nuclear medicine, radiology, medical physics, radiochemistry, technicians, and nursing.

In this chapter, we will present recent efforts in the field, including the use of [^{68}Ga]Ga-PentixaFor and its therapeutic counterparts [^{177}Lu]Lu-/[^{90}Y]Y-PentixaTher in solid tumors and hematological neoplasms. In particular, we will highlight the team effort required to provide excellent patient care by initiating CXCR4-RPT at the right time in the most appropriate clinical scenarios.

15.2 The Details

15.2.1 *Gotta Catch 'Em All?*— Interrogating CXCR4-Targeted PET in Solid Tumors

[^{18}F]FDG is the most commonly used PET radiotracer to assess tumor spread [7]. Despite its widespread adoption for cancer care, [^{18}F]FDG also provides false-negative findings, particularly in patients with cardiomyopathies, inflammation, infection, or degenerative joint disease [8, 9]. Those limitations, however, may be addressed by developing novel "pan-tumor" radiotracers for imaging, i.e., PET radiopharmaceuticals that can be applied in virtually every tumor subtype [10]. The ideal "pan-tumor" PET tracer would target a (sub)cellular structure that is overexpressed on different tumor types and could be applied for both staging and restaging. Along these lines, histological analyses in recent years have provided evidence of the upregulation of CXCR4 in a wide variety of solid tumors [1, 10, 11]. As a result, the CXC4-targeted radiopharmaceutical [^{68}Ga]Ga-PentixaFor has been applied to retrospective

"basket" studies including patients with breast, liver, and small-cell lung carcinoma (SCLC); melanoma; cancer of unknown primary (CUP); and brain cancer (glioblastoma). Ultimately, these trials suggested that [^{68}Ga]Ga-PentixaFor possesses good read-out capabilities for SCLC and CUP [12].

CXCR4-directed molecular imaging has also been extensively investigated in neuroendocrine neoplasms (NEN). Weich and coworkers showed that measuring [^{68}Ga]Ga-PentixaFor uptake in dedicated NEN cell lines (BON, QGP1, and MS-18) is feasible and that the accumulation of the radiotracer can be increased by modulating the Wnt/ß-catenin signaling pathway [13], which is involved in regulating tumor growth in NEN patients [14, 15]. To wit, the Wnt activator lithium chloride led to the upregulation of CXCR4 and Wnt, which in turn increased the uptake of [^{68}Ga]Ga-PentixaFor in cell assays [13]. While [^{68}Ga]Ga-PentixaFor seems to be specific to CXCR4 on the NEN cell surface, its uptake can be modified by modulating signaling pathways [13]. Such an approach may be relevant both for nuclear imaging or for radiosensitization to therapeutics such as [^{177}Lu]Lu- or [^{90}Y]Y-PentixaTher. These in vitro studies were followed by a small pilot study including NEN patients. [^{68}Ga]Ga-PentixaFor produced substantial uptake in highly proliferative neuroendocrine neoplasms (G3, Ki67 > 20%; Fig. 15.2) but ultimately proved less sensitive in G1/G2 tumors, [16]. These data may be explained by previous immunohistochemical analyses that demonstrated that CXCR4 upregulation is accompanied by decreasing SSTR expression in G3 NEN [17]. A systematic follow-up study performed a head-to-head comparison between [^{18}F]FDG and [^{68}Ga] Ga-PentixaFor in newly diagnosed neuroendocrine carcinoma patients and [^{68}Ga]Ga-PentixaFor did not reveal superior findings on CXCR4-directed PET [18]. Nonetheless, research on the application of PentixaFor to NENs may offer a treatment option in poorly differentiated NENs since, unlike ^{18}F]FDG, PentixaFor has a theranostic companion.

Yet another retrospective basket study of [^{68}Ga]Ga-PentixaFor investigated whether ex vivo findings using immunohistochemistry are linked to in vivo PET results. Among several cancer types—including NEN, cholangiocarcinoma as well as pancreas, hepato-cellular, renal cell, prostate, and ovarian carcinomas—adequate correlations were observed between histologically-derived CXCR4 expression and the uptake of the radiotracer in sites of disease [19]. Nonetheless, only cholangiocarcinoma provided intense uptake, with a maximum standardized uptake value (SUV$_{max}$) of 16 [19]. A recent study also investigated 10 subjects with esophageal adeno- or squamous cell carcinoma and reported heterogenous findings relative to [^{18}F]FDG (flip-flop phenomenon) in selected cases [20], with 50% of the lesions classified as [^{18}F]FDG negative but PentixaFor positive. In primary or recurrent breast cancer patients, [^{18}F]FDG also exhibited higher SUV$_{max}$ values when compared to [^{68}Ga] Ga-PentixaFor. In addition, only moderate correlation coefficients were observed for comparing CXCR4-specific uptake with clinically established prognostic factors such as estrogen or progesterone receptor status [21]. Adrenocortical carcinoma (ACC) has been extensively investigated using [^{68}Ga]Ga-PentixaFor [22]. Blümel et al. reported equal findings relative to the reference radiotracer ([^{18}F]FDG), and a substantial fraction of patients were still considered suitable for therapy using ß-emitting, CXCR-targeted radiotherapeutics [22]. Finally, a recent study investigated CXCR4-targeted PET/CT in 145 subjects with 27 different cancers and aimed to determine whether varying splenic uptake may provide prognostic information, but the authors reported no associations between radiotracer accumulation and clinical outcome [23].

Taken together, these data suggest that in the vast majority of solid tumors, [^{68}Ga]Ga-PentixaFor PET/CT is not well suited to provide clinically relevant findings. This conclusion is supported by a recent bicentric study investigating 690 patients scheduled for
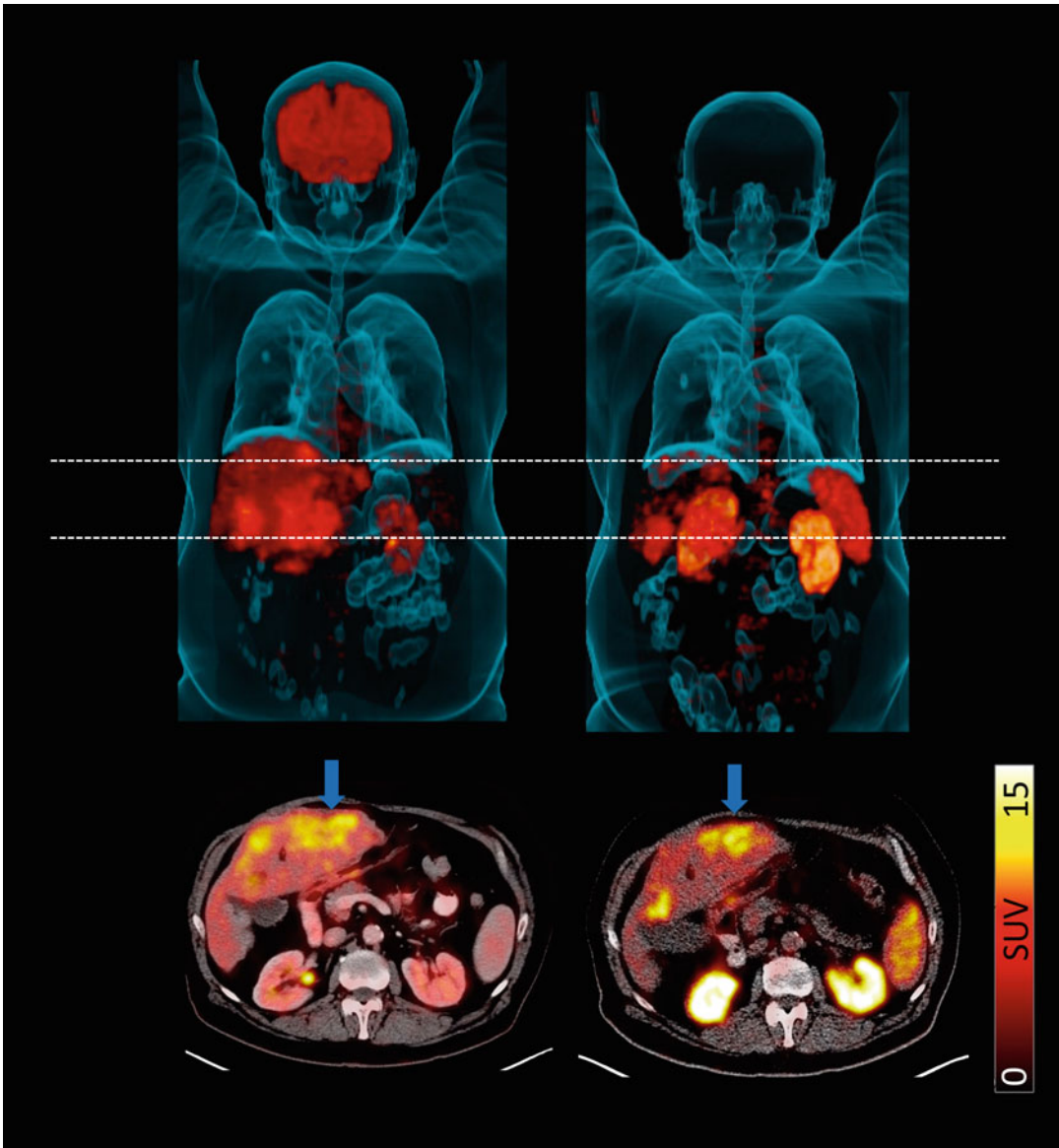
Fig. 15.2 CXCR4-directed molecular imaging in a highly aggressive neuroendocrine neoplasm. Patient affected with G3 neuroendocrine tumor and liver metastases who underwent [18]F[FDG] (left) and CXCR4-directed [68Ga]Ga-PentixaFor (right) PET/CT. Hypermetabolic metastases in the liver demonstrated moderate [68Ga]Ga-PentixaFor uptake (blue arrows). (Modified from Ref. [16])

777 [68Ga]Ga-PentixaFor PET/CT scans. In alignment with previous results, only SCLC and ACC showed relevant SUV_{max} and increased target-to-background ratios (TBR) when compared to other solid tumors [24]. Relative to solid tumors, however, [68Ga]Ga-PentixaFor exhibited the highest TBR and SUV_{max} in patients with hematological malignances such as multiple myeloma, suggesting that CXCR4-targeted PET/CT appears to be most clinically relevant in hemato-oncology (Fig. 15.3) [24]. This brings us to our next section.
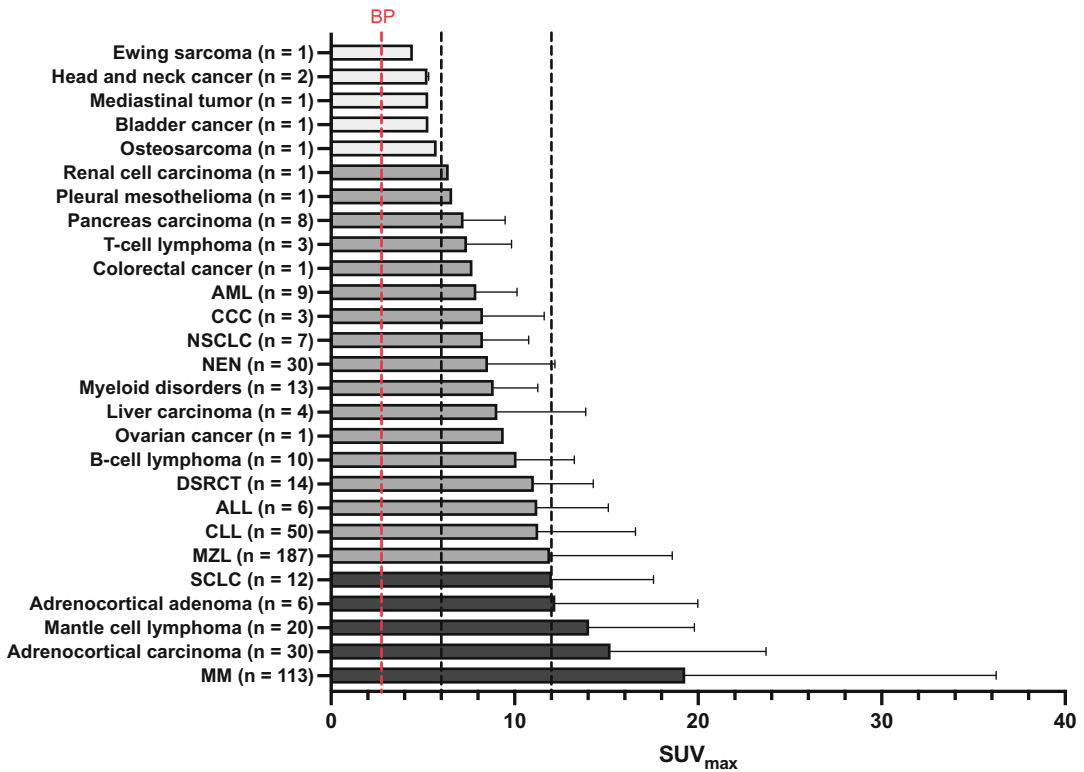
Fig. 15.3 Bar chart displaying average maximum standardized uptake values (SUV$_{max}$) for 690 patients imaged with CXCR4-directed molecular imaging using [^{68}Ga]PentixaFor PET/CT. Black dotted lines represent SUV$_{max}$ of 6 and 12, respectively. *BP* blood pool (indicated by a red dotted line), *AML* acute myeloid leukemia, *CCC* cholangiocarcinoma. *NSCLC* non-small cell lung carcinoma, *NEN* neuroendocrine neoplasm, *DSRCT* Desmoplastic Small Round Cell Tumor, *ALL* acute lymphoblastoid leukemia, *CLL* chronic lymphocytic leukemia, *MZL* marginal zone lymphoma, *SCLC* small cell lung carcinoma, *MM* multiple myeloma, *Adrenocortical adenoma* aldosterone-producing adrenocortical adenoma. (Modified from Ref. [24]). © by the Society of Nuclear Medicine and Molecular Imaging, Inc.)

15.2.2 *Seek and Destroy*— CXCR4-Directed Theranostics in Hematological Neoplasms

15.2.2.1 CXCR4-Targeted Molecular Imaging in Hematological Neoplasms

Among hematological neoplasms, [^{68}Ga]Ga-PentixaFor has been extensively used not only in leukemia, multiple myeloma (MM), and marginal zone lymphoma (MZL) but also in other lymphoma subtypes, such as mantle cell lymphoma [25–28]. In the ensuing section, we will review the application of CXCR4-targeted PET in several of these contexts.

Leukemia: Herhaus and coworkers were among the first to present translational work describing the CXCR4-directed imaging of mice with CXCR4-positive and -negative leukemia xenografts and in patients with active acute myeloid leukemia (AML). In a murine setting, [^{68}Ga]Ga-PentixaFor was only taken up in CXCR4-positive xenografts. More importantly, four out of nine patients with active AML were rated positive on [^{68}Ga]Ga-PentixaFor PET, with comparable findings on magnetic resonance [28].

Multiple Myeloma: Flow cytometry of BM samples showed that more than 40% of MM patients express CXCR4 and that CXCR4-

related phenotypes are linked to survival, suggesting that CXCR4 could have potential as a prognostic biomarker [29]. Philipp-Abbrederis then used [^{68}Ga]Ga-PentixaFor in both mice bearing CXCR4-expressing xenografts and patients with MM. The radiotracer exhibited excellent specificity in the murine model of disease. In the clinic, 10 of 14 MM patients showed radiotracer accumulation on [^{68}Ga]Ga-PentixaFor PET in their manifestations, which was almost comparable to [^{18}F]FDG (9/14 rated positive) [30]. Lapa et al. then performed a head-to-head comparison with both radiotracers in a cohort of 19 MM patients, demonstrating that [^{68}Ga]Ga-PentixaFor was superior to [^{18}F]FDG in 21% of the investigated subjects. The latter tracer, however, identified more manifestations in 37% of patients (with equal findings in the remaining 42%). Nonetheless, the CXCR4-avid lesions were linked to outcome (including disease progression and death), suggesting that beyond diagnostic imaging, [^{68}Ga]Ga-PentixaFor PET may emerge as a risk stratification tool to identify patients that require more intense treatment [27]. Shekhawat et al. evaluated 34 treatment-naïve MM patients and reported that [^{68}Ga]Ga-PentixaFor produced approximately twofold higher TBR compared to [^{18}F]FDG along with a higher number of upstaged patients due to CXCR4-targeted imaging. The authors also speculated that heterogenous findings using a dual-radiotracer approach may also have prognostic value, i.e., that PentixaFor-positive but FDG-negative findings are linked to outcome [31]. The value of [^{68}Ga]Ga-PentixaFor for outcome prediction has recently demonstrated in 17 MM patients, with total BM uptake linked to overall survival, serum beta-2 microglobulin levels, and CRAB score (which represents end organ damage in advanced disease) [32]. Finally, a recent case study showed that in MM under CAR-T cell therapy, [^{68}Ga]Ga-PentixaFor can differentiate between relapse and pulmonary sarcoidosis (a potential treatment-related off-target effect; Fig. 15.4) [33].

Marginal Zone Lymphoma: Samples collected from patients with extranodal MZL of mucosa-associated lymphoid tissue lymphoma revealed that CXCR4 is overexpressed in more than 90%, while SSTR2a—another relevant theranostic target—was present in only 27% [34]. In a prospective study, Mayerhoefer et al. investigated [^{68}Ga]Ga-PentixaFor PET/MR in gastric MZL after first-line eradication of *Helicobacter pylori* and reported an accuracy of 97% for the detection of residual gastric disease. Furthermore, SUV$_{max}$ values showed acceptable correlation with immunohistochemistry-derived CXCR4-positive cell counts, highlighting the potential of CXCR4-directed imaging for therapeutic monitoring [35]. Subsequently, Duell and coworkers investigated [^{68}Ga]Ga-PentixaFor PET/CT for staging changes and impact on oncological management in patients with MZL and reported that CXCR4-targeted PET/CT is superior to the routine diagnostic work-up that includes CT, BM biopsy, and gastrointestinal endoscopy. Notably, more than half of the subjects in this study were reclassified—10/22 were upstaged; 3/22 were downstaged—and changes in management were prompted in one-third of the patients: escalation in 6 subjects and de-escalation in 2 [25]. Taken together, these data underscore the diagnostic value of [^{68}Ga]Ga-PentixaFor as well as its potential implications for changing management in a substantial fraction of patients.

Introducing CXCR4-Directed RPT: The increasing use of [^{68}Ga]Ga-PentixaFor in patients with solid and hematological neoplasms triggered a retrospective study pooling data from Würzburg and Vienna University. This evaluation of 690 subjects provided an overview of the most promising applications for CXCR4-directed PET/CT (Fig. 15.3). As we have discussed, hematological neoplasms exhibited higher in vivo chemokine receptor expression levels compared to solid cancers. Among
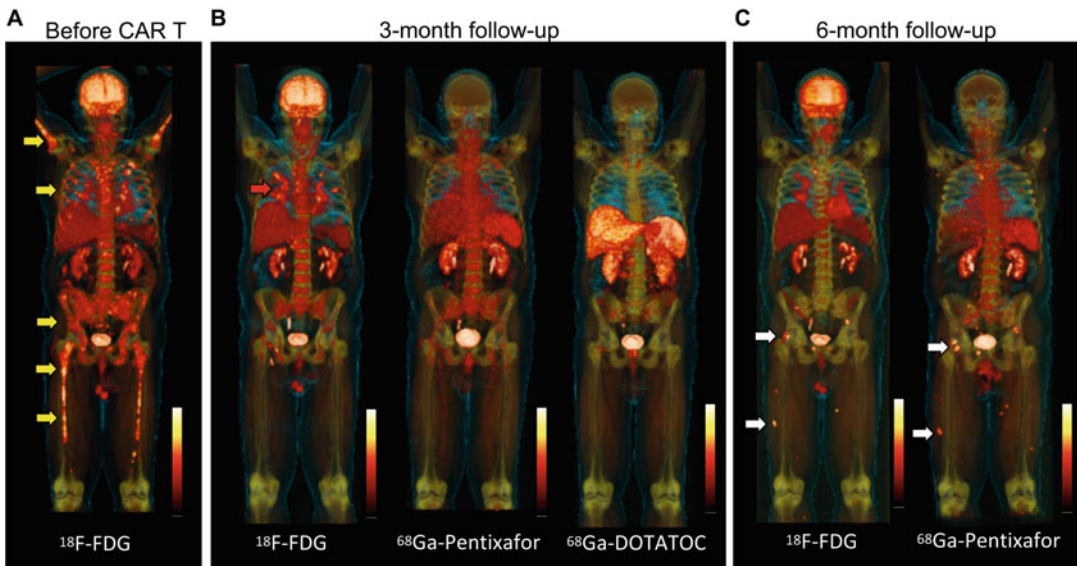
Fig. 15.4 CXCR4-directed PET/CT can differentiate between relapse and autoimmune phenomenon after Idecabtagen Vicleucel (Ide-cel), a BCMA targeting CAR-T cell therapy. (**a**) At baseline, [^{18}F]FDG revealed multiple lesions in the skeleton (yellow arrows). (**b**) 3 months after CAR-T cell therapy, full resolution of focal osseous lesions was observed, along with residual [^{18}F]FDG uptake in the lung (red arrow). Corresponding [^{68}Ga]Ga-PentixaFor and [^{68}Ga]Ga-DOTATOC PET revealed no pulmonary uptake along with clearance of osseous lesions (comparable to [^{18}F]FDG at that time). Single-cell RNA sequencing obtained in specimen from bronchoalveolar lavage then identified Th17.1(+) T-cells, which have been advocated to play a role in autoimmune diseases including sarcoidosis [53]. (**c**) 6 months after therapy, [^{68}Ga]Ga-PentixaFor and [^{18}F]FDG identified novel manifestations in the pelvis and lower limbs (white arrows), indicative for extramedullary relapse. One of those lesions was then biopsied, showing >99% malignant plasma cells with relevant CXCR4 expression. As such, CXCR4-targeted PET/CT may differentiate between side effects and relapse under novel CAR-T cell therapies. (Modified from Ref. [33]. http://creativecommons.org/licenses/by/4.0/)

these, MM (but also mantle cell lymphoma or TCL (Fig. 15.5)) was characterized by intense uptake of [^{68}Ga]Ga-PentixaFor in sites of disease, thereby providing a roadmap for the hematological malignancies that may benefit most from CXCR4-targeted imaging and therapy [24].

Ongoing and recently launched prospective clinical trials will shed further light on the clinical utility of this radiotracer as a pan-hematological tumor agent. For example, a Phase III study including 500 patients with varying lymphomas is expected to start recruiting in the near future [36]. Last, the clinical adoption of [^{68}Ga]Ga-PentixaFor PET/CT also led to an increased use of the agent's therapeutic cousins: [^{177}Lu]Lu- and [^{90}Y]Y-PentixaTher [4]. Along these lines, administering the appropriate amount of activity

is crucial to optimizing the radiotherapeutic's anti-lymphoma and myeloablative efficacy [37]. In the ensuing sections, we first present the concept of peritherapeutic dosimetry (*Part I*) and then offer an overview of the current status of CXCR4-mediated RPT in hematological neoplasms, including its relevance for subsequent HSCT (*Part II*).

15.2.2.2 CXCR4-Directed RPT Part I: Dosimetry

Given the substantial uptake of [^{68}Ga]Ga-PentixaFor in many hematological neoplasms, it is not surprising that the platform has been harnessed for CXCR4-targeted RPT. Along these lines, two β-emitting radiometals—^{90}Y (E_{max} = 2.28 MeV) and ^{177}Lu (E_{max} = 0.497 MeV)—have been harnessed to
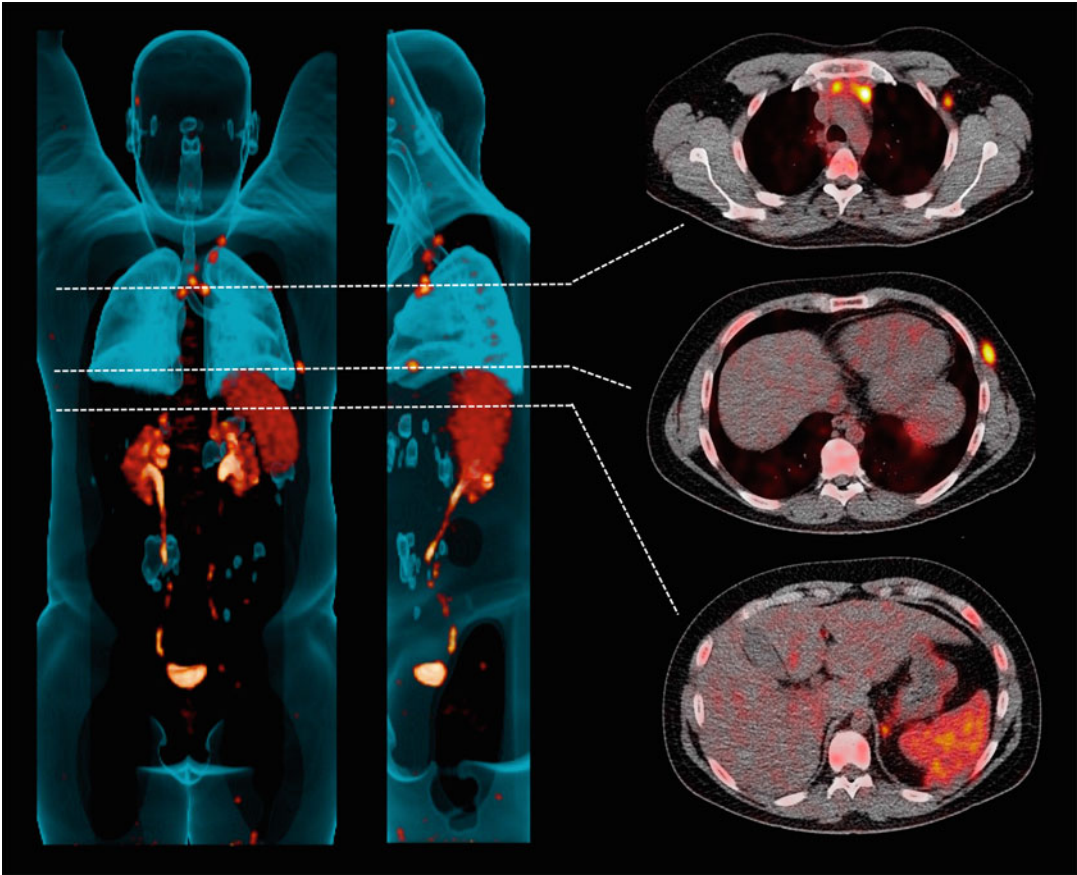
Fig. 15.5 CXCR4-directed molecular imaging using [^{68}Ga]PentixaFor PET/CT in T-cell lymphoma. In this 27-year-old patient, restaging with CXCR4-directed [^{68}Ga]PentixaFor PET/CT was conducted due to suspicion of relapse after allogeneic hematopoietic stem cell transplantation. Multiple subcutaneous, lymphonodal, and intramuscular disease manifestations were identified on maximum intensity projections on the left. Transaxial PET/CT displayed CXCR4-expressing lymph node manifestations in the mediastinum (top), intramuscular manifestations in close proximity to the left upper thorax (middle), and moderate uptake in the enlarged spleen (bottom)

create [^{90}Y]Y- and [^{177}Lu]Lu-PentixaTher. To date, a head-to-head comparison on the anti-lymphoma efficacy between both compounds has not been conducted. Nonetheless, the shorter half-life of ^{90}Y (2.67 days vs ^{177}Lu, 6.7 days) renders it more suitable for CXCR4-targeted RPT as it allows for an earlier initiation of HSCT, thereby reducing the duration of the aplastic phase.

As with any radiotherapeutic, delivering the appropriate dose is crucial. After intravenous administration, [^{177}Lu]Lu-PentixaTher shows high metabolic stability, adhering primarily to serum albumin. In addition to uptake in CXCR4-expressing malignant tissues, scintigraphically detectable accumulation is visible in the kidneys, liver, spleen, and red bone marrow (Fig. 15.6). Furthermore, CXCR4-mediated binding to leukocytes and platelets accounts for about 4% of the administered activity [38]. Since various cells in the red marrow express CXCR4, myelosuppression is the dose-limiting side effect of CXCR4-directed RPT. When high activities of [^{177}Lu]Lu- or [^{90}Y]Y-PentixaTher are used for myeloablation in combination with autologous stem cell transplantation,

Fig. 15.6 Example of activity time functions in a patient with multiple myeloma during pre-therapeutic dosimetry with 0.20 GBq [^{177}Lu]Lu-PentixaTher. Activity retention measurements as well as fit functions are shown for the whole body (black), per liter of whole blood (grey), red bone marrow (red), liver (green), kidneys (purple), and spleen (blue). The long-lasting activity retention in the bone marrow explains the increased doses to this organ during CXCR4-directed RPT that cause substantial myeloablative efficacy for subsequent stem cell transplantation. (Modified from Ref. [37]. © by the Society of Nuclear Medicine and Molecular Imaging, Inc.)
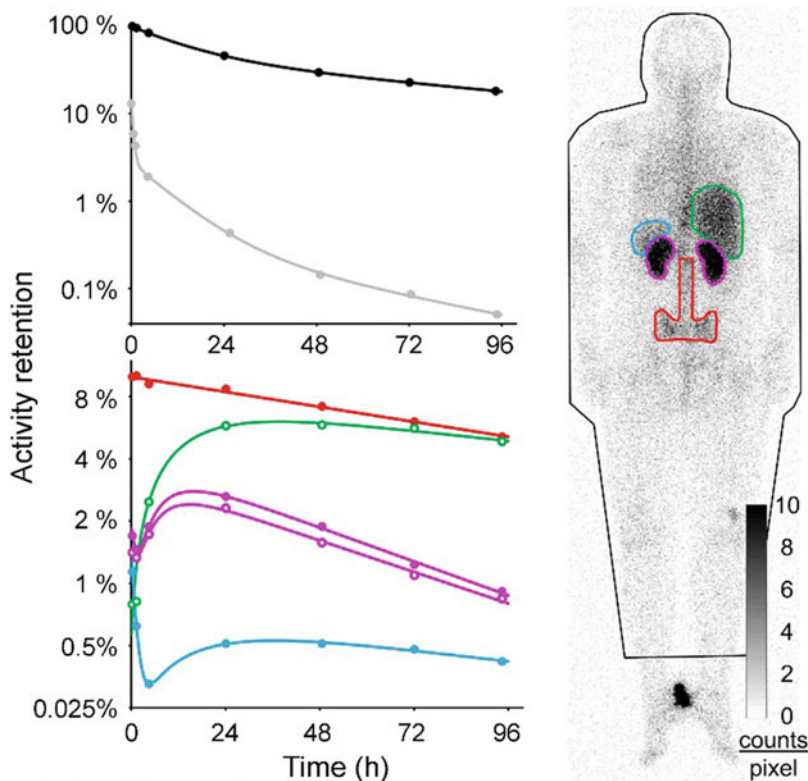
the kidneys most often represent the next dose-limiting organ [37]. Along these lines, the activity is retained in the renal parenchyma, which may result in the radiation-induced loss of renal function [37, 39].

The radiation-absorbed dose per unit administered activity of a radiopharmaceutical in tissues of interest can be determined by dosimetry, i.e., by assessing a patient's individual biokinetics and determining the fractions of the administered activity that decay in each of their tissues. As the therapeutic nuclide ^{177}Lu emits both ß$^-$ and γ-radiation, biokinetics can be measured via the scintigraphy of [^{177}Lu]Lu-PentixaTher. While an activity of 200 MBq of ^{177}Lu is sufficient for the pre-therapeutic dosimetry of kidneys, liver, spleen, and larger tumor lesions, the dosimetry of the red marrow is less reliable, even after the administration of much higher activities [37]. Dosimetry is ideally performed using multiple planar scintigraphic images or multiple SPECTs acquired over several days to determine the time course of the activity in tissues of interest. These data are fitted using reasonable time functions, typically bi- or tri-exponential decay functions. At least one SPECT image with simultaneous CT (SPECT/CT; to correct for the scatter and attenuation of the ^{177}Lu photons) is required for the absolute quantification of the activity concentration at the time of measurement. After the normalization of a decay function to the absolute activity concentration measured via SPECT/CT, the resulting time function of the activity in the tissue can be integrated over time to deduce the total number of decays and—by extension—the radiation-absorbed dose to the tissue [39]. Measurements over 4–5 days should be performed if [^{177}Lu]Lu-PentixaTher is the radiotherapeutic, while measurement over 3–4 days are sufficient if the patient is to be treated with the more rapidly decaying [^{90}Y]Y-PentixaTher [37].

Dosimetric studies in patients prior to treatment with [^{177}Lu]Lu-PentixaTher have revealed

large inter-individual differences in the uptake of the radiotherapeutic as well as the half-life of the activity in accumulating tissues [37]. In the kidneys, the dose-limiting organ during myeloablative therapy, average radiation absorbed doses of about 0.9 Gy/GBq [^{177}Lu]Lu-PentixaTher (corresponding to ~3.8 Gy/GBq [^{90}Y]Y-PentixaTher) were measured, with ^{177}Lu activity decreasing with an effective half-life of ~1.7 days. However, these values may be up to a factor of 3 higher in some cases. Thankfully, with PentixaTher, as with other radiopeptide therapies, a significant reduction in renal absorbed doses can be achieved via a protective infusion of amino acids that significantly reduces the retention of the peptide in the renal tubules [40]. Absorbed doses to the liver and spleen typically hover around 0.6–0.7 Gy/GBq [^{177}Lu]Lu-PentixaTher and almost always remain below 2 Gy/GBq. Since these organs are also less sensitive to radiation, they usually do not limit the activity that can be administered [37]. Furthermore, dosimetric assessments suggest that the absorbed doses to malignant tissues average about 2 Gy/GBq [^{177}Lu]Lu-PentixaTher (6 Gy/GBq [^{90}Y]Y-PentixaTher), which explains the good therapeutic effect in the very radiosensitive target tissues of hematologic origin.

15.2.2.3 CXCR4-Directed RPT Part II: RPT and HSCT

A variety of hematological neoplasms have been treated with [^{177}Lu]Lu-/[^{90}Y]Y-PentixaTher, mainly in small pilot studies. In many of those patients, HSCT is needed, and the myeloablative efficacy of CXCR4-targeted RPT can assist in preparing patients for stem cell transplantation [4, 5]. Here, we will discuss the use of CXCR4-targted RPT for treatment and myeloablation in several hematological neoplasms.

Multiple Myeloma: Initially, MM patients have been treated with CXCR4-targeted RPT on a compassionate use basis when no other suitable treatment option was available. Herrmann et al. first observed a remarkable clinical response to CXCR4-targeted RPT with a concomitant decrease in [^{18}F]FDG uptake upon short-term re-assessment [41]. Lapa and coworkers then further expanded this first-in-human experience by including 8 MM patients and reported one complete metabolic response (CMR), partial remission (PMR) in 5 subjects, and death in the remaining two subjects (one patient succumbed to tumor lysis syndrome [TLS] and another patient to sepsis during aplasia following eradication of the stem cell niche) [42]. This study highlighted two relevant side effects of CXCR4-targeted RPT: (a) aplasia after initiation and (b) TLS. To address the former, most studies switched to [^{90}Y]Y-PentixaTher due to its shorter physical half-life (2.7 d compared to 6.7 d for ^{177}Lu). After the injection of [^{90}Y]Y-PentixaTher, conditioning therapies and HSCT can be started earlier, thereby reducing the time frame of life-threating aplasia. Nonetheless, this switch in radionuclide had no impact on myeloablative efficacy, as levels of cytopenia were comparable between patients treated with [^{90}Y]Y- and [^{177}Lu]Lu-PentixaTher [43]. To overcome the latter, dedicated TLS prevention protocols have been implemented in the pretherapeutic algorithm [4].

Acute Myeloid Leukemia (AML) and Diffuse Large B-Cell Lymphoma (DLBLC): Habringer and coworkers reported on three AML patients suffering from refractory disease after first allogeneic HSCT that exhibited leukemia clearance after RPT with [^{177}Lu]Lu-PentixaTher. After a (second) allogeneic HSCT, successful engraftment was recorded [44]. Relapsed DLCBL patients were investigated by Lapa and coworkers, who reported on CXCR4-targeted RPT that was combined with radioimmunotherapy in selected cases. While 2/6 of these patients died of infectious complications, PMR was recorded in another 2 (those treated with additional

radioimmunotherapy), and mixed response in the remaining two subjects. Again, [^{177}Lu]Lu-PentixaTher also led to desired BM ablation that prepared the patients for HSCT, and successful engraftment was observed in 5/6 subjects after a median of 11 days [45].

T-Cell Lymphoma: A recent case series reported on favorable outcomes in four patients affected with heavily pretreated and relapsed TCL treated with [^{90}Y]Y-PentixaTher. All of those individuals were subject to pretherapeutic dosimetry, indicating lymphoma-absorbed doses of >33 Gy under treatment. One patient ultimately succumbed to sepsis, while engraftment was observed in the remaining three patients. During follow-up, PMR was achieved in one patient, while CMR was observed in two others. Again, those with the best response had also been treated with additional radioimmunotherapy, suggesting an additive effect. In addition, lactate dehydrogenase served as a surrogate marker of response in these patients: after an increase immediately

following RPT, a decrease was observed, suggesting that CXCR4-targeted RPT exhibits direct anti-lymphoma efficacy independent from subsequent (chemotherapeutic) conditioning regimens which are also applied prior to HSCT (Fig. 15.7) [5].

15.2.3 A Bright Future for CXCR4 and Cancer Care!

15.2.3.1 Prospects of CXCR4-Directed RPT in Non-hematological Malignancies

Beyond its use for hematological malignancies, CXCR4-directed RPT may also be used in patients affected with solid cancers. For instance, in patients with ACC, 70% of the patients were considered eligible for treatment with [^{90}Y]Y-PentixaTher based on [^{68}Ga]Ga-PentixaFor PET/CT [22]. In this context, however, strategies for the reduction BM exposure and myeloablation would be important. This could be achieved via
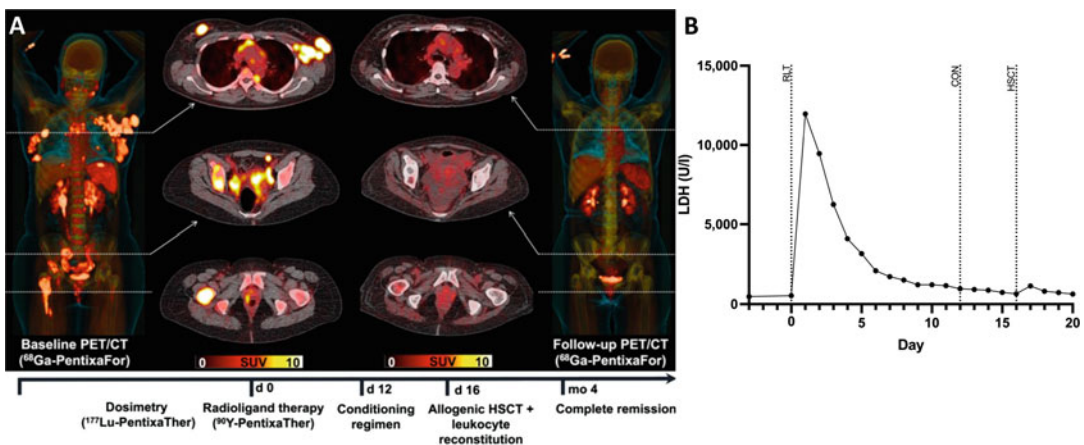

Fig. 15.7 Complete metabolic response after CXCR4-directed RPT in a 43-year-old patient with T-cell lymphoma. Conditioning regimen (CON) and allogeneic hematopoietic stem cell therapy (HSCT) were also initiated after RPT, leading to successful engraftment. (**a**) Maximum intensity projections and transaxial CXCR4-directed [^{68}Ga]PentixaFor PET/CT scans prior to (left) and 4 months after (right) RPT using [^{90}Y]PentixaTher. Prior to therapy, patient demonstrated multiple CXCR4-positive sites of disease, including nodal, peritoneal, and

osseous manifestations, while post-RPT imaging revealed complete response. The timeline of treatment is also displayed, including subsequent therapeutic steps, such as CON and HSCT. (**b**) Time-course of lactate dehydrogenase (LDH, in U/l) levels as a surrogate marker of early response to CXCR4-directed RPT. An initial increase in LDH was observed followed by a decrease, indicating an immediate response to CXCR4-directed RPT independent from CON. (Modified from Ref. [5] © by the Society of Nuclear Medicine and Molecular Imaging, Inc.)

pretherapeutic dosimetry, which would allow for the injection of an appropriate amount of activity that would still exert anti-tumor effects without eradicating the BM niche.

15.2.3.2 Improving CXCR4-Targeted Read-Out: Enhancing CXCR4 Expression and Introducing Second-Generation Radiotracers

While hematological neoplasms clearly benefit from CXCR4-directed molecular imaging, solid tumors seem less suited for [^{68}Ga]Ga-PentixaFor PET/CT [24]. In the latter group of patients, diagnostic read-out may be improved with drugs designed to increase CXCR4 expression, as suggested by Weich and coworkers' work on modulating the Wnt pathway [13]. Another approach to improving CXCR4-targeted PET may be to turn to radiofluorination. The higher positron yield, lower positron energy, and improved spatial resolution of fluorine-18 may increase the diagnostic accuracy of CXCR4-targeted PET probes [46]. Indeed, similar effects of radiofluorination have already been observed in other PET agents, including tracers targeting PSMA or SSTR [46, 47]. Brickute et al. recently reported a cyclam-based ^{18}F-radiolabeled CXCR4-targeting agent: [^{18}F]MCFB [48]. The comprehensive preclinical (or even clinical) evaluation of this compound could shed light on whether a second-generation, CXCR4-targeting radiotracer could offer improvements over [^{68}Ga]Ga-Pentixafor in solid tumors.

15.2.3.3 Improving Patient Selection for CXCR4-Targeted RPT in Patients with Hematological Neoplasms

Despite precautions in patient preparation—including TLS prevention protocols and the use of short-lived radionuclides—a substantial fraction of patients treated with CXCR4-targeted RPT as a last-line approach still dies due to septicemia or tumor cell lysis [4, 5]. Furthermore, there are also patients who do not adequately respond to RPT or do not achieve successful engraftment. As such, it is clear that risk stratification needs to be optimized: It is critical to identify individuals prone to later (lethal) events and those who will experience relevant anti-lymphoma efficacy (which may also increase the likelihood of clinically relevant TLS). In the context of other approaches to RPT (e.g., PSMA-targeted regimens), a growing body of evidence shows that both pretherapeutic PET and clinical parameters can help identify high-risk individuals prone to treatment failure or relevant off-target effects [49–51]. Such outcome studies should also be conducted for CXCR4-directed theranostics, for example by quantifying radiotracer uptake during pretherapeutic [^{68}Ga]Ga-PentixaFor PET or investigating other clinical variables available at baseline (e.g., LDH or ß2-microglobulin).

15.3 Conclusions—CXCR4-Targeted Theranostics as a Multidisciplinary Team Approach

CXCR4-directed theranostic imaging agents provide a platform to improve diagnostic accuracy and identify candidates eligible for CXCR4-directed RPT. This approach appears to be particularly promising in a broad range of hematological neoplasms; in contrast, among solid tumors, only SCLC and ACC seem to be enticing candidates for CXCR4-targeted theranostics. In a diagnostic setting, [^{68}Ga]Ga-PentixaFor has already provided benefits in therapeutic decision-making, for example, by differentiating between relapse and off-target effects in patients undergoing novel CAR-T cell therapies and by changing the management of patients with MZL. The radiotherapeutics [^{177}Lu]Lu- and [^{90}Y]Y-PentixaTher have also achieved durable anti-lymphoma and myeloablative efficacy in refractory hematological malignancies. Indeed, the myeloablative activity of these radiotherapeutics is an integral part of the treatment algorithm, as patients received HSCT after RPT with successful engraftment in most of the cases. In the end, CXCR4-targeted theranostics is a team effort that requires various imaging and internal medicine experts to provide excellent care prior to, during, and after RPT.

15.4 The Bottom Line

- $[^{68}Ga]$Ga-PentixaFor and $[^{177}Lu]$Lu-/$[^{90}Y]$Y-PentixaTher provide a theranostic platform for CXCR4-targeted imaging and RPT.
- Preliminary findings indicate that CXCR4-targeted molecular imaging is not well suited for solid cancers (except for adrenocortical and small cell lung carcinoma) but provides excellent read-out capabilities in patients with hematological neoplasms.
- Imaging with $[^{68}Ga]$Ga-PentixaFor in patients with hematological neoplasms has led to upstaging and changes in oncological management.
- CXCR4-directed RPT with $[^{90}Y]$Y-PentixaTher based on pretherapeutic PET/CT and dosimetry achieved complete or partial remissions in heavily pretreated and refractory T-cell lymphoma. An integral part of this therapeutic approach is that RPT-mediated myeloablation also prepares patients for hematopoietic stem cell transplantation.
- CXCR4 imaging and RPT are team efforts that require experts in imaging and internal medicine, physicists, radiochemists, technicians, and trained nurses.

Ongoing and future clinical trials will shed light on the most promising opportunities for CXCR4-targeted imaging and RPT, with patients with hematological malignancies the most likely to benefit.

References

1. Chatterjee S, Behnam Azad B, Nimmagadda S. The intricate role of CXCR4 in cancer. Adv Cancer Res. 2014;124:31–82. https://doi.org/10.1016/B978-0-12-411638-2.00002-1.
2. Duda DG, Kozin SV, Kirkpatrick ND, Xu L, Fukumura D, Jain RK. CXCL12 (SDF1alpha)-CXCR4/CXCR7 pathway inhibition: an emerging sensitizer for anticancer therapies? Clin Cancer Res. 2011;17(8):2074–80. https://doi.org/10.1158/1078-0432.CCR-10-2636.
3. Righi E, Kashiwagi S, Yuan J, Santosuosso M, Leblanc P, Ingraham R, et al. CXCL12/CXCR4 blockade induces multimodal antitumor effects that prolong survival in an immunocompetent mouse model of ovarian cancer. Cancer Res. 2011;71(16):5522–34. https://doi.org/10.1158/0008-5472.CAN-10-3143.
4. Buck AK, Serfling SE, Lindner T, Hanscheid H, Schirbel A, Hahner S, et al. CXCR4-targeted theranostics in oncology. Eur J Nucl Med Mol Imaging. 2022;49(12):4133–44. https://doi.org/10.1007/s00259-022-05849-y.
5. Buck AK, Grigoleit GU, Kraus S, Schirbel A, Heinsch M, Dreher N, et al. C-X-C motif chemokine receptor 4-targeted radioligand therapy in patients with advanced T-cell lymphoma. J Nucl Med. 2023;64(1):34–9. https://doi.org/10.2967/jnumed.122.264207.
6. Ratajczak MZ, Serwin K, Schneider G. Innate immunity derived factors as external modulators of the CXCL12-CXCR4 axis and their role in stem cell homing and mobilization. Theranostics. 2013;3(1):3–10. https://doi.org/10.7150/thno.4621.
7. Taveira M. Comparison of (68)Ga-FAPI versus (18)F-FDG PET/CT for initial cancer staging. Radiol Imaging Cancer. 2021;3(2):e219007. https://doi.org/10.1148/rycan.2021219007.
8. Shreve PD, Anzai Y, Wahl RL. Pitfalls in oncologic diagnosis with FDG PET imaging: physiologic and benign variants. Radiographics. 1999;19(1):61–77; quiz 150-1. https://doi.org/10.1148/radiographics.19.1.g99ja0761.
9. van der Geest KSM, Treglia G, Glaudemans A, Brouwer E, Jamar F, Slart R, et al. Diagnostic value of [18F]FDG-PET/CT in polymyalgia rheumatica: a systematic review and meta-analysis. Eur J Nucl Med Mol Imaging. 2021;48(6):1876–89. https://doi.org/10.1007/s00259-020-05162-6.
10. Roustaei H, Kiamanesh Z, Askari E, Sadeghi R, Aryana K, Treglia G. Could fibroblast activation protein (FAP)-specific Radioligands be considered as pan-tumor agents? Contrast Media Mol Imaging. 2022;2022:3948873. https://doi.org/10.1155/2022/3948873.
11. Furusato B, Mohamed A, Uhlen M, Rhim JS. CXCR4 and cancer. Pathol Int. 2010;60(7):497–505. https://doi.org/10.1111/j.1440-1827.2010.02548.x.
12. Vag T, Gerngross C, Herhaus P, Eiber M, Philipp-Abbrederis K, Graner FP, et al. First experience with chemokine receptor CXCR4-targeted PET imaging of patients with solid cancers. J Nucl Med. 2016;57(5):741–6. https://doi.org/10.2967/jnumed.115.161034.
13. Weich A, Rogoll D, Gawlas S, Mayer L, Weich W, Pongracz J, et al. Wnt/beta-catenin signaling regulates CXCR4 expression and [(68)Ga] pentixafor internalization in neuroendocrine tumor cells. Diagnostics (Basel). 2021;11(2) https://doi.org/10.3390/diagnostics11020367.
14. Jin XF, Spoettl G, Maurer J, Nolting S, Auernhammer CJ. Inhibition of Wnt/beta-catenin signaling in neuroendocrine tumors in vitro: antitumoral effects. Cancers

(Basel). 2020:12(2). https://doi.org/10.3390/cancers12020345.

15. Jiang X, Cao Y, Li F, Su Y, Li Y, Peng Y, et al. Targeting beta-catenin signaling for therapeutic intervention in MEN1-deficient pancreatic neuroendocrine tumours. Nat Commun. 2014;5:5809. https://doi.org/10.1038/ncomms6809.

16. Werner RA, Weich A, Higuchi T, Schmid JS, Schirbel A, Lassmann M, et al. Imaging of chemokine receptor 4 expression in neuroendocrine tumors – a triple tracer comparative approach. Theranostics. 2017;7(6):1489–98. https://doi.org/10.7150/thno.18754.

17. Kaemmerer D, Trager T, Hoffmeister M, Sipos B, Hommann M, Sanger J, et al. Inverse expression of somatostatin and CXCR4 chemokine receptors in gastroenteropancreatic neuroendocrine neoplasms of different malignancy. Oncotarget. 2015;6 (29):27566–79. https://doi.org/10.18632/oncotarget.4491.

18. Weich A, Werner RA, Buck AK, Hartrampf PE, Serfling SE, Scheurlen M, et al. CXCR4-Directed PET/CT in patients with newly diagnosed neuroendocrine carcinomas. Diagnostics (Basel). 2021;11 (4) https://doi.org/10.3390/diagnostics11040605.

19. Werner RA, Kircher S, Higuchi T, Kircher M, Schirbel A, Wester HJ, et al. CXCR4-directed imaging in solid tumors. Front Oncol. 2019;9:770. https://doi.org/10.3389/fonc.2019.00770.

20. Linde P, Baues C, Wegen S, Trommer M, Quaas A, Rosenbrock J, et al. Pentixafor PET/CT for imaging of chemokine receptor 4 expression in esophageal cancer – a first clinical approach. Cancer Imaging. 2021;21(1):22. https://doi.org/10.1186/s40644-021-00391-w.

21. Vag T, Steiger K, Rossmann A, Keller U, Noske A, Herhaus P, et al. PET imaging of chemokine receptor CXCR4 in patients with primary and recurrent breast carcinoma. EJNMMI Res. 2018;8(1):90. https://doi.org/10.1186/s13550-018-0442-0.

22. Bluemel C, Hahner S, Heinze B, Fassnacht M, Kroiss M, Bley TA, et al. Investigating the chemokine receptor 4 as potential theranostic target in adrenocortical cancer patients. Clin Nucl Med. 2017;42(1): e29–34. https://doi.org/10.1097/RLU.0000000000001435.

23. Lewis R, Habringer S, Kircher M, Hefter M, Peuker CA, Werner R, et al. Investigation of spleen CXCR4 expression by [(68)Ga]Pentixafor PET in a cohort of 145 solid cancer patients. EJNMMI Res. 2021;11 (1):77. https://doi.org/10.1186/s13550-021-00822-6.

24. Buck AK, Haug A, Dreher N, Lambertini A, Higuchi T, Lapa C, et al. Imaging of C-X-C motif chemokine receptor 4 expression in 690 patients with solid or hematologic neoplasms using (68)Ga-Pentixafor PET. J Nucl Med. 2022;63(11):1687–92. https://doi.org/10.2967/jnumed.121.263693.

25. Duell J, Krummenast F, Schirbel A, Klassen P, Samnick S, Rauert-Wunderlich H, et al. Improved primary staging of marginal-zone lymphoma by addition of CXCR4-directed PET/CT. J Nucl Med. 2021;62(10):1415–21. https://doi.org/10.2967/jnumed.120.257279.

26. Mayerhoefer ME, Raderer M, Lamm W, Pichler V, Pfaff S, Weber M, et al. CXCR4 PET imaging of mantle cell lymphoma using [(68)Ga]Pentixafor: comparison with [(18)F]FDG-PET. Theranostics. 2021;11 (2):567–78. https://doi.org/10.7150/thno.48620.

27. Lapa C, Schreder M, Schirbel A, Samnick S, Kortum KM, Herrmann K, et al. [(68)Ga]Pentixafor-PET/CT for imaging of chemokine receptor CXCR4 expression in multiple myeloma – comparison to [(18)F]FDG and laboratory values. Theranostics. 2017;7(1):205–12. https://doi.org/10.7150/thno.16576.

28. Herhaus P, Habringer S, Philipp-Abbrederis K, Vag T, Gerngross C, Schottelius M, et al. Targeted positron emission tomography imaging of CXCR4 expression in patients with acute myeloid leukemia. Haematologica. 2016;101(8):932–40. https://doi.org/10.3324/haematol.2016.142976.

29. Bao L, Lai Y, Liu Y, Qin Y, Zhao X, Lu X, et al. CXCR4 is a good survival prognostic indicator in multiple myeloma patients. Leuk Res. 2013;37 (9):1083–8. https://doi.org/10.1016/j.leukres.2013.06.002.

30. Philipp-Abbrederis K, Herrmann K, Knop S, Schottelius M, Eiber M, Luckerath K, et al. In vivo molecular imaging of chemokine receptor CXCR4 expression in patients with advanced multiple myeloma. EMBO Mol Med. 2015;7(4):477–87. https://doi.org/10.15252/emmm.201404698.

31. Shekhawat AS, Singh B, Malhotra P, Watts A, Basher R, Kaur H, et al. Imaging CXCR4 receptors expression for staging multiple myeloma by using (68) Ga-Pentixafor PET/CT: comparison with (18)F-FDG PET/CT. Br J Radiol. 2022;95(1136):20211272. https://doi.org/10.1259/bjr.20211272.

32. Kuyumcu S, Isik EG, Tiryaki TO, Has-Simsek D, Sanli Y, Buyukkaya F, et al. Prognostic significance of (68)Ga-Pentixafor PET/CT in multiple myeloma recurrence: a comparison to (18)F-FDG PET/CT and laboratory results. Ann Nucl Med. 2021;35 (10):1147–56. https://doi.org/10.1007/s12149-021-01652-1.

33. Leipold AM, Werner RA, Dull J, Jung P, John M, Stanojkovska E, et al. Th17.1 cell driven sarcoidosis-like inflammation after anti-BCMA CAR T cells in multiple myeloma. Leukemia. 2023;37:1–9. https://doi.org/10.1038/s41375-023-01824-0.

34. Stollberg S, Kammerer D, Neubauer E, Schulz S, Simonitsch-Klupp I, Kieswetter B, et al. Differential somatostatin and CXCR4 chemokine receptor expression in MALT-type lymphoma of gastric and extragastric origin. J Cancer Res Clin Oncol. 2016;142(11):2239–47. https://doi.org/10.1007/s00432-016-2220-6.

35. Mayerhoefer ME, Raderer M, Lamm W, Weber M, Kiesewetter B, Rohrbeck J, et al. CXCR4 PET/MRI

for follow-up of gastric mucosa-associated lymphoid tissue lymphoma after first-line Helicobacter pylori eradication. Blood. 2022;139(2):240–4. https://doi.org/10.1182/blood.2021013239.

36. www.ezag.com/home/press/press_releases/detail/?tx_ttnews%5Btt_news%5D=1722&cHash=4b09b542e039cc242d000565ce81a186. Eckert & Ziegler Receives Green Light for Phase III Study with PENTIXAFOR. Last assessed Februar 21, 2023.

37. Hanscheid H, Schirbel A, Hartrampf P, Kraus S, Werner RA, Einsele H, et al. Biokinetics and dosimetry of (177)Lu-Pentixather. J Nucl Med. 2022;63 (5):754–60. https://doi.org/10.2967/jnumed.121.262295.

38. Schottelius M, Osl T, Poschenrieder A, Hoffmann F, Beykan S, Hanscheid H, et al. [(177)Lu]pentixather: comprehensive preclinical characterization of a first CXCR4-directed Endoradiotherapeutic agent. Theranostics. 2017;7(9):2350–62. https://doi.org/10.7150/thno.19119.

39. Hanscheid H, Lapa C, Buck AK, Lassmann M, Werner RA. Dose mapping after Endoradiotherapy with (177) Lu-DOTATATE/DOTATOC by a single measurement after 4 days. J Nucl Med. 2018;59(1):75–81. https://doi.org/10.2967/jnumed.117.193706.

40. Bodei L, Mueller-Brand J, Baum RP, Pavel ME, Horsch D, O'Dorisio MS, et al. The joint IAEA, EANM, and SNMMI practical guidance on peptide receptor radionuclide therapy (PRRNT) in neuroendocrine tumours. Eur J Nucl Med Mol Imaging. 2013;40 (5):800–16. https://doi.org/10.1007/s00259-012-2330-6.

41. Herrmann K, Schottelius M, Lapa C, Osl T, Poschenrieder A, Hanscheid H, et al. First-in-human experience of CXCR4-directed Endoradiotherapy with 177Lu- and 90Y-labeled Pentixather in advanced-stage multiple myeloma with extensive intra- and extramedullary disease. J Nucl Med. 2016;57 (2):248–51. https://doi.org/10.2967/jnumed.115.167361.

42. Lapa C, Herrmann K, Schirbel A, Hanscheid H, Luckerath K, Schottelius M, et al. CXCR4-directed endoradiotherapy induces high response rates in extramedullary relapsed Multiple Myeloma. Theranostics. 2017;7(6):1589–97. https://doi.org/10.7150/thno.19050.

43. Maurer S, Herhaus P, Lippenmeyer R, Hanscheid H, Kircher M, Schirbel A, et al. Side effects of CXC-chemokine receptor 4-directed Endoradiotherapy with Pentixather before hematopoietic stem cell transplantation. J Nucl Med. 2019;60(10):1399–405. https://doi.org/10.2967/jnumed.118.223420.

44. Habringer S, Lapa C, Herhaus P, Schottelius M, Istvanffy R, Steiger K, et al. Dual targeting of acute leukemia and supporting niche by CXCR4-directed

theranostics. Theranostics. 2018;8(2):369–83. https://doi.org/10.7150/thno.21397.

45. Lapa C, Hanscheid H, Kircher M, Schirbel A, Wunderlich G, Werner RA, et al. Feasibility of CXCR4-directed Radioligand therapy in advanced diffuse large B-cell lymphoma. J Nucl Med. 2019;60 (1):60–4. https://doi.org/10.2967/jnumed.118.210997.

46. Werner RA, Derlin T, Lapa C, Sheikhbahaei S, Higuchi T, Giesel FL, et al. (18)F-Labeled, PSMA-targeted radiotracers: leveraging the advantages of radiofluorination for prostate cancer molecular imaging. Theranostics. 2020;10(1):1–16. https://doi.org/10.7150/thno.37894.

47. Ilhan H, Todica A, Lindner S, Boening G, Gosewisch A, Wangler C, et al. First-in-human (18) F-SiFAlin-TATE PET/CT for NET imaging and theranostics. Eur J Nucl Med Mol Imaging. 2019;46 (11):2400–1. https://doi.org/10.1007/s00259-019-04448-8.

48. Brickute D, Braga M, Kaliszczak MA, Barnes C, Lau D, Carroll L, et al. Development and evaluation of an (18)F-radiolabeled monocyclam derivative for imaging CXCR4 expression. Mol Pharm. 2019;16 (5):2106–17. https://doi.org/10.1021/acs.molpharmaceut.9b00069.

49. Hartrampf PE, Seitz AK, Weinzierl FX, Serfling SE, Schirbel A, Rowe SP, et al. Baseline clinical characteristics predict overall survival in patients undergoing radioligand therapy with [(177)Lu]Lu-PSMA I&T during long-term follow-up. Eur J Nucl Med Mol Imaging. 2022;49(12):4262–70. https://doi.org/10.1007/s00259-022-05853-2.

50. Gafita A, Calais J, Grogan TR, Hadaschik B, Wang H, Weber M, et al. Nomograms to predict outcomes after (177)Lu-PSMA therapy in men with metastatic castration-resistant prostate cancer: an international, multicentre, retrospective study. Lancet Oncol. 2021;22(8):1115–25. https://doi.org/10.1016/S1470-2045(21)00274-6.

51. Widjaja L, Werner RA, Ross TL, Bengel FM, Derlin T. Comparison of pretherapeutic osseous tumor volume and standard hematology for prediction of hematotoxicity after PSMA-targeted radioligand therapy. Eur J Nucl Med Mol Imaging. 2021;48 (12):4077–88. https://doi.org/10.1007/s00259-021-05412-1.

52. Osl MT. Development of cyclic pentapeptide ligands for chemokine receptor targeting – doctoral thesis submitted to Fakultät für Chemie der Technischen Universität München, Germany. 2016.

53. Ramstein J, Broos CE, Simpson LJ, Ansel KM, Sun SA, Ho ME, et al. IFN-gamma-producing T-helper 17.1 cells are increased in sarcoidosis and are more prevalent than T-helper type 1 cells. Am J Respir Crit Care Med. 2016;193(11):1281–91. https://doi.org/10.1164/rccm.201507-1499OC.

Case Study #6: [177Lu]Lu-DOTA-JR11: A Somatostatin Receptor Subtype 2 Antagonist for Radiopharmaceutical Therapy

16

Damian Wild and Melpomeni Fani

16.1 The Fundamentals

Neuroendocrine tumors (NETs) are a group of tumors that arise from neuroendocrine cells and are most commonly found in the stomach, intestines, and pancreas (gastroenteropancreatic neuroendocrine tumors; GEP-NETs) as well as in the lungs (lung NETs) [1, 2]. As the majority of NETs are slowly growing tumors with almost no symptoms, up to 50% of cases are metastatic at diagnosis [3]. Somatostatin receptors (SST) have played a key role as molecular targets for both the diagnosis and treatment of NETs for almost 30 years. To date, five somatostatin receptor subtypes have been identified: SST_{1-5}. Somatostatin receptor subtype 2 (SST_2) is the predominant subtype. It is highly expressed in GEP-NETs and is expressed at lower levels in several other tumor types, including small cell lung cancer, lung NETs, breast cancer, renal cell carcinoma, non-Hodgkin lymphoma, paraganglioma, pheochromocytoma, medullary thyroid cancer, and meningioma [4].

Peptide receptor radionuclide therapy (PRRT) is a special type of radiopharmaceutical therapy (RPT) predicated on the use of radiolabeled peptides such as the ^{177}Lu-labeled SST_2 agonists [^{177}Lu]Lu-DOTA-TOC and [^{177}Lu]Lu-DOTA-TATE (Lutathera™). Although PRRT is one of the most efficient treatments for the management of NETs, it predominantly stabilizes—rather than cures—the disease [5]. There is thus an unmet need to improve PRRT with more effective radiopharmaceuticals. Until recently, it was thought that the internalization of the radiolabeled agonists was required for SST-targeted RPT. Yet in 2006, Ginj et al. proposed the paradigm shifting idea that radiolabeled SST antagonists may perform better than agonists despite their lack of internalization [6]. Indeed, there is compelling evidence that ^{177}Lu-labeled SST_2 *ant*agonists—e.g., [^{177}Lu]Lu-DOTA-JR11 = [^{177}Lu]Lu-OPS201 = [^{177}Lu]Lu-satoreotide tetraxetan—bind to many more SST_2 sites on the cell surface [7], resulting in much higher tumor doses and thus greater treatment potential than ^{177}Lu-labeled SST_2 agonists [8–10].

16.2 The Details

16.2.1 A Short History of Peptide Receptor Radionuclide Therapy (PRRT)

After its introduction in the early 1990s, PRRT was gradually improved through a series of steps

D. Wild (✉)
Division of Nuclear Medicine, University Hospital Basel, Basel, Switzerland

Center for Neuroendocrine and Endocrine Tumors, University Hospital Basel, Basel, Switzerland
e-mail: damian.wild@usb.ch

M. Fani
Division of Radiopharmaceutical Chemistry, University Hospital Basel, Basel, Switzerland

to enhance the treatment outcomes of patients with GEP-NETs:

1. The introduction of PRRT with radiolabeled SST agonists such as $[^{111}In]In$-DTPA-octreotide and, subsequently, the advent of improved SST agonists labeled with β-emitting radionuclides, primarily $[^{90}Y]Y$- and $[^{177}Lu]Lu$-DOTA-TOC as well as $[^{177}Lu]Lu$-DOTA-TATE (Lutathera™) [11, 12].

2. The invention of SST-targeted scintigraphy and, later, SST-targeted single photon emission computed tomography/computed tomography (SPECT/CT) and positron emission tomography/computed tomography (PET/CT) with radiolabeled SST agonists such as $[^{111}In]In$-DTPA-octreotide (for scintigraphy and SPECT/CT) and $[^{68}Ga]Ga$-DOTA-TOC and $[^{68}Ga]Ga$-DOTA-TATE (for PET/CT). SST imaging allows for the sensitive detection of NETs as well as the identification of patients who will benefit from PRRT [13]. Along these lines, PRRT became one of the best examples of clinical theranostics, the use of one radiopharmaceutical (e.g., $[^{68}Ga]Ga$-DOTA-TATE) to identify tumors with high SST_2 expression and a second based on the same vector (e.g., $[^{177}Lu]Lu$-DOTA-TATE) to deliver a therapeutic payload.

3. The evaluation of PRRT in the NETTER-1 study: a randomized, controlled phase III trial with both an intervention arm—$[^{177}Lu]Lu$-DOTA-TATE (Lutathera™) plus high-dose somatostatin analog octreotide LAR—and a control arm (only high-dose somatostatin analog octreotide LAR). The NETTER-1 study demonstrated the superiority of PRRT relative to treatment with octreotide LAR [14]. Based on the NETTER-1 study, PRRT with Lutathera™ was approved by the FDA (U.S. Food and Drug Administration) and EMA (European Medicines Agency) for the treatment of patients with GEP-NETs.

4. The introduction of radiolabeled SST antagonists that are able to recognize more bindings sites on SST-expressing tumor cells show favorable pharmacokinetics and produce

higher radiation doses to tumor tissue than agonists despite their very poor internalization rates [6, 8].

16.2.2 Preclinical Development of Radiolabeled SST Antagonists

SST antagonists were initially developed both for studying the pharmacology and mechanism of the natural hormone somatostatin and for enhancing the secretion of hormones such as growth hormone and insulin. Their design was based on modifications of the cyclic octapeptide octreotide. Octreotide is a truncated and stabilized version of the natural peptide somatostatin-14 (SS-14, Fig. 16.1) that activates SST receptors upon binding and internalizes inside cells as part of a peptide-receptor complex. Critically, the majority of the known radiolabeled SST peptide agonists are based on octreotide. The main structural features of octreotide—D-Phe²-c(Cys³-Phe⁷-D-Trp⁸-Lys⁹-Thr¹⁰-Cys¹⁴)-Thr(ol)¹⁵ (the amino acid numbers correspond to those for SS-14)—are as follows:

1. The tetrapeptide Phe⁷-D-Trp⁸-Lys⁹-Thr¹⁰ is essential for the biological activity of SS-14, but L-Trp has been replaced by D-Trp to stabilize the peptide vis a vis enzymatic degradation (Fig. 16.1).

2. As in SS14, the disulfide bridge protects the conformation of the active tetrapeptide.

3. The D-Phe further protects the enzymatically vulnerable N-terminus of the peptide while a hydroxyl functionality lies at the C-terminus.

Certain modifications to this structure have been identified as critical for turning a given peptide from an agonist into an *ant*agonist, thereby inhibiting (or entirely preventing) internalization. Specifically, the following characteristics have been determined to favor antagonism:

1. The inversion of chirality of amino acids 2 and 3 (i.e., from D-Phe² to L-Phe² and from L-Cys³ to D-Cys³) (Fig. 16.1) [15].
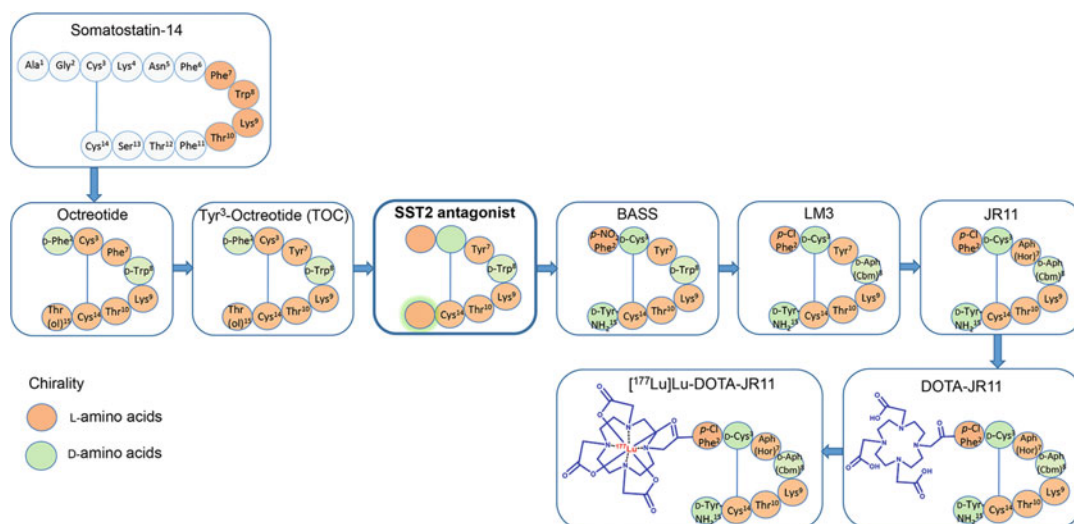
Fig. 16.1 The evolution of [^{177}Lu]Lu-DOTA-JR11. In the somatostatin-14 sequence, the red amino acids indicate the essential amino acids for receptor recognition. The color code also indicates chirality: red for L-amino acids and green for D-amino acids. The blue structure shows the DOTA chelator

2. The introduction of a substituted phenylalanine—e.g., p-NO$_2$-Phe^2 or p-Cl-Phe^2—in the first position.
3. The introduction of large hydrophobic aromatic amino acids—e.g., 2Nal^{15} (3-(2-naphthyl)alanine) or Tyr^{15} (both L- or D-configuration)—at the C-terminus [16, 17].

Taken together, these combinations contribute to antagonistic properties by weakening biological efficacy while maintaining high SST$_2$ affinity. The first SST$_2$ antagonist, namely BASS—(AcNH-p-NO$_2$-Phe^2-cyclo(D-Cys^3-Tyr^7-D-Trp^8-Lys^9-Thr^{10}-Cys^{14})-D-Tyr^{15}-NH$_2$—came out of such a combination.

A number of different modifications have been made to BASS to tune its affinity, SST selectivity, and stability. Two particularly enticing modifications were the inclusion of [1] a carbamoyl functionality (the literature suggested that amide bond-rich moieties are favorably recognized by G-protein coupled receptors) and [2] a urea functionality (which provides structural stabilization via an increase in intra- and intermolecular hydrogen bonds) [18]. A dipeptide bearing both of these modifications—Aph(Hor)-D-Aph(Cbm), in which H-Aph(Hor)-NH$_2$ = 4-amino-phenylalanine(L-hydroorotic acid) and H-D-Aph(Cbm)-NH$_2$ = D-4-amino-phenylalanine(carbamoyl)—was used in the development of gonadotropin releasing hormone (GnRH) antagonists [18]. The question, of course, was whether these functionalities could be implemented in SST antagonists? In BASS, the amino acids 2, 3 14, and 15 were already "tailored" to antagonism. This left only the tetrapeptide (i.e., Tyr^7-D-Trp^8-Lys^9-Thr^{10}) in which these new inserts could be tried. Along these lines, amino acid 7 (position 3 in octreotide) has shown tolerability in terms of substitution, with a number of high affinity SST agonists arising out of its substitution [19]. In the case of the antagonists, the substitution of Tyr^7 with carbamoyl-residues did not alter binding affinity and selectivity for SST$_2$ but did improve hydrophilicity. Furthermore, the substitution of D-Trp^8 by D-Aph(Cbm) clearly improved affinity as well as selectivity for SST$_2$ [20]. A series of antagonists were developed with various combinations of the aforementioned characteristics [20]. The analog featuring the substitution of D-Trp^8 with D-Aph(Cbm) as well as p-Cl-Phe^2 in the first position—i.e., p-Cl-Phe^2-c(D-

Cys^3-Tyr^7-D-$Aph(Cbm)^8$-Lys^9-Thr^{10}-Cys^{14})D-Tyr^{15}-NH_2—is known as LM3 [21]. In contrast, the analog with amino acids 7 and 8 replaced with the dipeptide Aph(Hor)-D-Aph(Cbm) as well as p-Cl-Phe^2 in the first position—p-Cl-Phe^2-cyclo [D-Cys^3-$Aph(Hor)^7$-D-$Aph(Cbm)^8$-Lys^9-Thr^{10}-Cys^{14}]-D-Tyr^{15}-NH_2—is known as JR11 [20]. JR11 was conjugated to DOTA via its N-terminus and labeled with lutetium-177 (Fig. 16.1) [22].

16.2.3 The Preclinical Evaluation of [^{177}Lu]Lu-DOTA-JR11

DOTA-modified JR11 was initially complexed with various (radio)metals, including as indium, yttrium, lutetium, gallium, and copper [21, 22]. These early studies clearly demonstrated the high affinity of the JR11 conjugates for SST_2 (Table 16.1). The affinities of Lu- and Y-DOTA-JR11 (IC_{50} = 0.73 ± 0.15 and 0.47 ± 0.05 nM, respectively) were comparable to that of DOTA-JR11 alone (IC_{50} = 0.72 ± 0.12 nM). However, both In- and Cu-DOTA-JR11 exhibited reduced affinities for the receptor (IC_{50} = 3.8 ± 0.7 and 29 ± 2.7 nM, respectively). Ga-DOTA-JR11 also displayed a reduced affinity, but this value could be improved by employing the NODAGA chelator to create Ga-NODAGA-JR11 (IC_{50} = 1.2 ± 0.2 nM) [22]. Biodistribution experiments in mice bearing SST_2-expressing xenografts—i.e., a human embryonic kidney cell line transfected with human SST_2 HEK-SST_2)—further underscored the importance of the radiometal [23]. To wit, [^{177}Lu]Lu-DOTA-JR11 ($β^-$-and γ-emitter; mean energy = 149 keV, Table 16.2) was assessed head-to-head with

[^{90}Y]Y-DOTA-JR11 ($β^-$emitter; mean energy = 934 keV, Table 16.2) and [^{111}In]In-DOTA-JR11 (γ emitter, a frequent imaging surrogate for ^{90}Y. The two therapeutic variants—[^{177}Lu]Lu-DOTA-JR11 and [^{90}Y]Y-DOTA-JR11—showed very similar biodistributions and pharmacokinetic profiles. As expected, [^{90}Y]Y-DOTA-JR11 delivered a higher tumor dose due to the higher energy of its $β^-$ particles. However, the long tumor retention of DOTA-JR11 is better suited for the longer half-life of ^{177}Lu ($t_{1/2}$ = 162 h). Interestingly, significant differences were observed between the biodistributions of [^{90}Y]Y-DOTA-JR11 and [^{111}In]In-DOTA-JR11,

Table 16.1 Affinity data (IC_{50} = half maximal inhibitory concentration) of SST antagonists and agonists for somatostatin receptor subtype 2 (SST_2)

Compounds	SST_2 affinity
SST antagonists	
DOTA-JR11[a]	0.72 ± 0.12
[^{nat}Lu]Lu-DOTA-JR11[b]	0.73 ± 0.15
[^{nat}Y]Y-DOTA-JR11[b]	0.47 ± 0.05
[^{nat}Cu]Cu-DOTA-JR11[b]	16.0 ± 1.2
[^{nat}In]In-DOTA-JR11[b]	3.8 ± 0.7
[^{nat}Ga]Ga-DOTA-JR11[b]	29.0 ± 2.7
NODAGA-JR11[b]	4.1 ± 0.2
[^{nat}Ga]Ga-NODAGA-JR11[b]	1.2 ± 0.2
DOTA-LM3[b]	0.39 ± 0.05
[^{nat}Ga]Ga-DOTA-LM3[c]	12.5 ± 4.3
[^{nat}In]In-DOTA-LM3[b]	1.3 ± 0.1
[^{nat}Ga]Ga-NODAGA-LM3[c]	1.3 ± 0.2
SST agonists	
[^{nat}Lu]Lu-DOTA-TATE[d]	2.0 ± 0.8
[^{nat}Ga]Ga-DOTA-TATE[e]	0.2 ± 0.04

[a]Data from Cescato et al. [20], [b]Data from Fani et al. [22], [c]Data from Fani et al. [21], [d]Data from Schottelius et al. [37], [e]Data from Reubi et al. [38]. All data represent IC_{50} ± SEM in nM except [^{nat}Lu]Lu-DOTA-TATE data, which is IC_{50} ± SD in nM

Table 16.2 Physical properties of radionuclides for PRRT

Radionuclide	Half-life	Decay	Mean energy	LET	Maximum tissue penetration range
Yttrium-90[a]	67 h	$β^-$	934 keV	~ 0.2 keV/μm	12.0 mm
Lutetium-177[a]	160 h	$β^-$/(γ)	149 keV	~ 0.2 keV/μm	3.0 mm
Terbium-161[b]	165 h	$β^-$/(γ) Auger electrons	154 keV 19 keV	~ 0.2 keV/μm ~ 20 keV/μm	3.0 mm <0.002 mm
Actinium-225[a]	240 h	α	6800 keV	~ 100 keV/μm	0.06 mm
Lead-212	11 h	α	7800 keV	~ 100 keV/μm	0.07 mm

[a]Data from Kong et al. [39], [b]Data from Muller et al. [40]. Abbreviations: *LET* linear energy transfer, *γ* γ-emitter which can be used for imaging and dosimetry studies

both with respect to their accumulation in tumor tissue and healthy organs such as stomach, pancreas, and adrenals. Taken together, these data suggest that ^{111}In-DOTA-JR11 may not be a suitable companion imaging agent for ^{90}Y-DOTA-JR11. The most notable result of these studies, however, stemmed from the head-to-head comparison between [^{177}Lu]Lu-DOTA-JR11 and [^{177}Lu]Lu-DOTA-TATE (Fig. 16.2a–c) [23]. [^{177}Lu]Lu-DOTA-JR11 showed significantly higher tumor uptake than [^{177}Lu]Lu-DOTA-TATE at all time points (from 1 h to 7 d post-injection). Yet even more importantly, the former exhibited a longer residence time in the tumor than the latter. Together, these phenomena resulted in 2.5 times higher tumor radiation dose

for [^{177}Lu]Lu-DOTA-JR11 compared to [^{177}Lu]Lu-DOTA-TATE (Fig. 16.2a).

Two critical aspects of the therapeutic use of radiopharmaceuticals are their renal and hematological toxicity. The higher radiation dose to the tumor of [^{177}Lu]Lu-DOTA-JR11 in the aforementioned study was accompanied by a 1.8-fold higher radiation dose to the kidneys and a 1.5-fold higher radiation dose to the bone marrow [23]. To wit, the tumor-to-kidney radiation dose ratio remained higher (by a factor of 1.3) for [^{177}Lu]Lu-DOTA-JR11 compared to [^{177}Lu]Lu-DOTA-TATE (Fig. 16.2b), while the tumor-to-bone marrow dose ratio was also in favor of [^{177}Lu]Lu-DOTA-JR11 by a factor of 1.7. Importantly, the escalation of the mass of injected peptide from
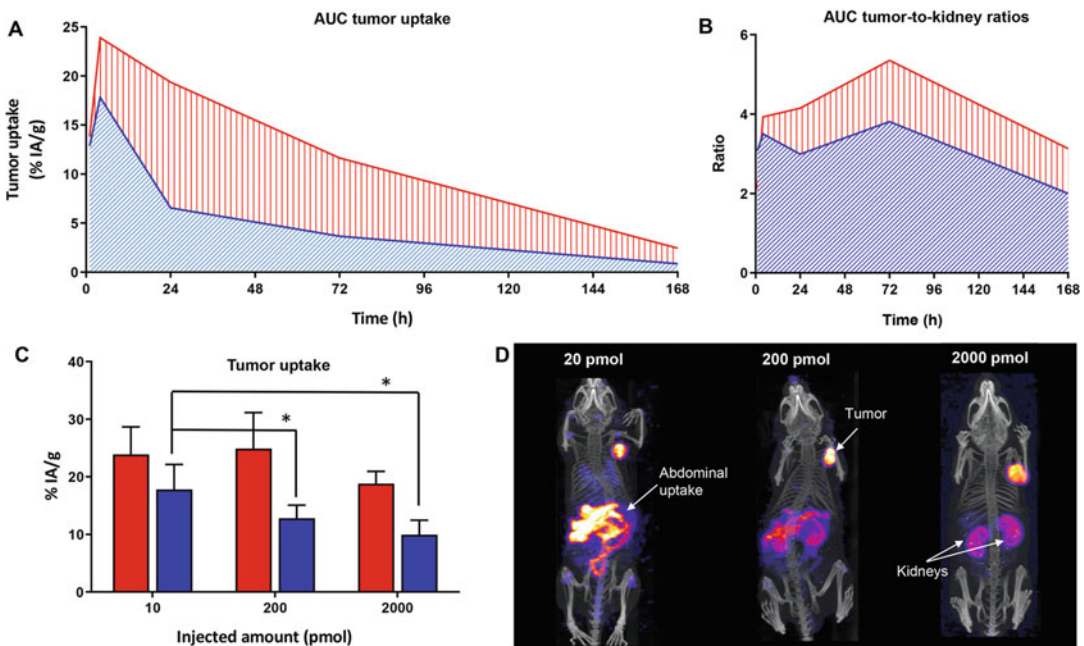
Fig. 16.2 In vivo comparison of [^{177}Lu]Lu-DOTA-JR11 and [^{177}Lu]Lu-DOTA-TATE in nude mice bearing HEK-SST$_2$ xenografts (Human Embryonic Kidney cells transfected with the human somatostatin receptor subtype 2). (**a**) AUC (area under the curve) of [^{177}Lu]Lu-DOTA-JR11 (red) and [^{177}Lu]Lu-DOTA-TATE (blue). The AUC represents the tumor uptake integrated over time, which is directly proportional to the radiation dose to the xenograft. The tumor uptake is given as % injected activity per gram tumor tissue (%IA/g). (**b**) tumor-to-kidney ratios integrated over time for [^{177}Lu]Lu-DOTA-JR11 (red) and [^{177}Lu]Lu-DOTA-TATE (blue). Pharmacokinetic data for A and B were generated from parallel independent biodistribution data collected 1, 4, 24, 72 and 168 h after the injection of [^{177}Lu]Lu-DOTA-JR11 and [^{177}Lu]Lu-DOTA-TATE. (**c**) The impact of the amount of injected peptide of [^{177}Lu]Lu-DOTA-JR11 (red) and [^{177}Lu]Lu-DOTA-TATE (blue) on tumor uptake. *$p \leq 0.05$. (**d**) [^{177}Lu]Lu-DOTA-JR11 nanoSPECT/CT images 4 h after the injection of different amounts of peptide (20, 200 and 2000 pmol)

10 pmol to 200 pmol to 2000 pmol significantly suppressed the background uptake of both [^{177}Lu]Lu-DOTA-JR11 and [^{177}Lu]Lu-DOTA-TATE, especially in SST_2-expressing tissues such as the stomach, pancreas, and bone marrow primarily due to the saturation of the receptors in these tissues. Surprisingly, this mass dose escalation did not affect the tumoral uptake of [^{177}Lu]Lu-DOTA-JR11 but significantly reduced that of [^{177}Lu]Lu-DOTA-TATE (Fig. 16.2c). Ultimately, increasing the amount of peptide injected produced excellent tumor-to-background activity concentration ratios for [^{177}Lu]Lu-DOTA-JR11 (Fig. 16.2d). Consequently, increasing the amount of peptide administered with [^{177}Lu]Lu-DOTA-JR11 may improve its safety profile in the clinic by reducing its accumulation (and thus radiation dose) in the bone marrow and other organ healthy tissues.

16.2.4 Preclinical Therapy Studies with [^{177}Lu]Lu-DOTA-JR11

The therapeutic efficacy of [^{177}Lu]Lu-DOTA-JR11 and [^{177}Lu]Lu-DOTA-TATE was compared in mice bearing H69 human small cell lung cancer xenografts [24]. The mice were given only a single 30 MBq dose (300 pmol) of each radiotherapeutic. The higher tumor uptake of [^{177}Lu]Lu-DOTA-JR11 compared to [^{177}Lu]Lu-DOTA-TATE in this tumor model as well as the former's longer tumoral residence time combined to produce a tumor radiation dose for [^{177}Lu]Lu-DOTA-JR11 (1.8 ± 0.7 Gy/MBq) 4.4 times higher than that of [^{177}Lu]Lu-DOTA-TATE (0.36 ± 0.07 Gy/MBq). Treatment with [^{177}Lu]Lu-DOTA-JR11 also resulted in a higher median survival rate (71 days vs 61 days) and a 1.4 times greater delay in tumor growth than [^{177}Lu]Lu-DOTA-TATE, thought the latter was not statistically significant (Fig. 16.3a, b).
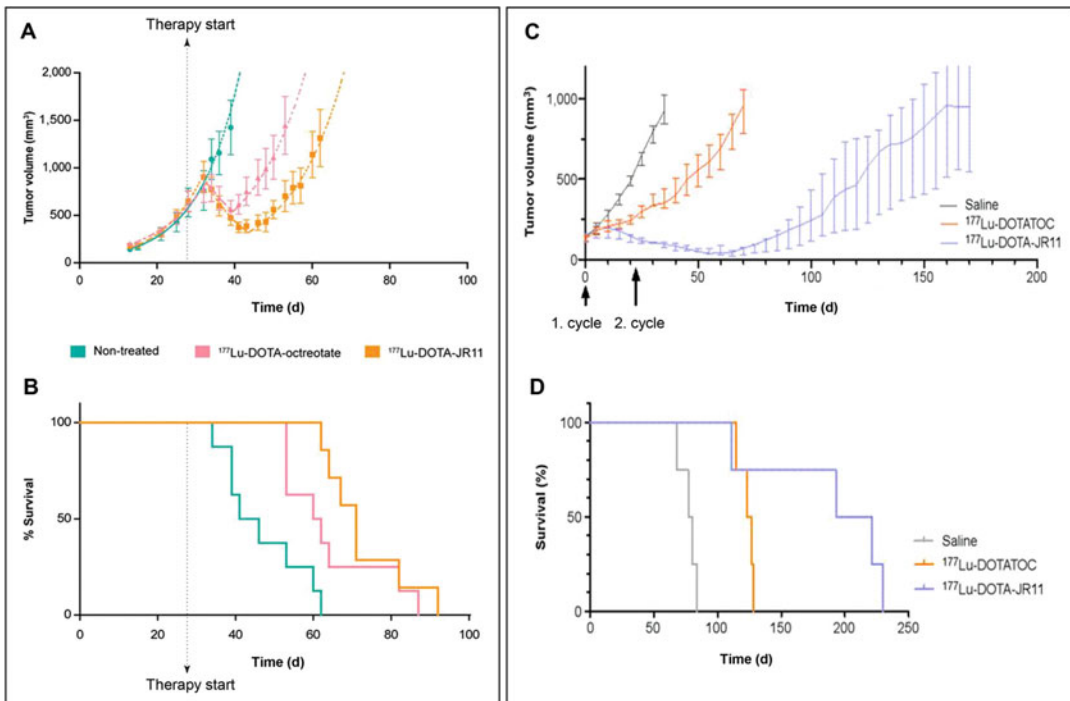
Fig. 16.3 Outcome of nude mice bearing H69 xenografts after treatment with 30 MBq [^{177}Lu]Lu-DOTA-JR11 (**a**) or 30 MBq [^{177}Lu]Lu-DOTA-TATE (**b**). Data are from Dalm et al. [24]. (**c**) and (**d**) Outcome of nude mice bearing BON-SST$_2$ xenografts after treatment with 2 × 20 MBq [^{177}Lu]Lu-DOTA-JR11 (**c**) or 2 × 30 MBq [^{177}Lu]Lu-DOTA-TOC (**d**). Data are from Albrecht et al. [25]. (**a**) and (**c**) show tumor growth. (**b**) and (**d**) show the corresponding Kaplan–Meier survival curves

In another therapy study, [^{177}Lu]Lu-DOTA-JR11 was compared to [^{177}Lu]Lu-DOTA-TOC in an orthotopic xenograft model using human pancreatic BON cells transfected with the human SST$_2$ (BON-SST$_2$) [25]. The study showed that treatment with [^{177}Lu]Lu-DOTA-JR11 produces a significant tumor growth delay and longer survival compared to [^{177}Lu]Lu-DOTA-TOC (Fig. 16.3c, d). The median survival rate was 1.7 times longer for the mice treated with [^{177}Lu]Lu-DOTA-JR11 compared to those treated with [^{177}Lu]Lu-DOTA-TOC (207 days vs 126 days). Furthermore, the improved therapeutic outcome of [^{177}Lu]Lu-DOTA-JR11 was achieved despite using a 30% reduced therapeutic activity compared to [^{177}Lu]Lu-DOTA-TOC (20 MBq vs 30 MBq per cycle, 2 cycles in an interval of 3 weeks). This reduction in activity was necessary due to the higher toxicity of [^{177}Lu]Lu-DOTA-JR11 compared to [^{177}Lu]Lu-DOTA-TOC. Finally, [^{177}Lu]Lu-DOTA-JR11 showed superior targeting properties compared to [^{177}Lu]Lu-DOTA-TATE in an estrogen receptor-positive patient-derived breast cancer mouse model with endogenous SST$_2$ expression [26]. This study confirmed that the antagonist produces significantly higher tumor uptake than the agonist and suggests breast cancer may be an additional indication for [^{177}Lu]Lu-DOTA-JR11.

Overall, the higher tumoral uptake and longer residence time of [^{177}Lu]Lu-DOTA-JR11 compared to SST$_2$ agonists (i.e., [^{177}Lu]Lu-DOTA-TATE or [^{177}Lu]Lu-DOTA-TOC) produces higher tumor doses, more favorable tumor-to-kidney activity concentration ratios, and an enhanced therapeutic effect [23–25]. Mansi et al. evaluated the characteristics that lead to the observed differences between SST$_2$ antagonists and agonists on a cellular level [7]. While both [^{177}Lu]Lu-DOTA-JR11 ([^{177}Lu]Lu-OPS201) and [^{177}Lu]Lu-DOTA-TATE exhibited comparable dissociation constant (K$_D$) values of 0.15 ± 0.003 and 0.08 ± 0.02 nM, respectively, [^{177}Lu]Lu-DOTA-JR11 recognized four times more binding sites than [^{177}Lu]Lu-DOTA-TATE [maximum binding sites (B$_{max}$) of 0.37 ± 0.02 vs. 0.09 ± 0.001 nM, respectively]. This could explain, at least partially, its higher accumulation in the SST$_2$-expressing tumors. In addition, [^{177}Lu]Lu-DOTA-JR11 showed faster association, slower dissociation, and longer cellular retention than [^{177}Lu]Lu-DOTA-TATE in vitro. These characteristics could further explain the higher tumor uptake and retention that lead to the enhanced therapeutic efficacy of [^{177}Lu]Lu-DOTA-JR11 compared to [^{177}Lu]Lu-DOTA-TATE, regardless of their localization at the sub-cellular level (cell surface vs internalized, respectively). Interestingly, when [^{177}Lu]Lu-DOTA-TATE bound to SST$_2$ was challenged with an excess of either [^{nat}Lu]Lu-DOTA-TATE or [^{nat}Lu]Lu-DOTA-JR11, both non-labelled compounds were able to completely displace the [^{177}Lu]Lu-DOTA-TATE from the receptor and prevent its rebinding. On the contrary, when [^{177}Lu]Lu-DOTA-JR11 bound on SST$_2$ was challenged with an excess of [^{nat}Lu]Lu-DOTA-TATE, the latter was not able to displace it entirely or prevent its rebinding. This could only be prevented by the antagonist itself. These findings indicate that the antagonist binds not only to more SST$_2$ binding sites but also to sites that are not recognized by the agonist. This hypothesis might have a clinical impact, as NETs are often treated with long-acting somatostatin agonists such as octreotide or lanreotide that are commonly interrupted before the administration of radiolabeled somatostatin agonists such as [^{177}Lu]Lu-DOTA-TATE in order to avoid SST$_2$ saturation. This practice is based on the assumption that the two agonists compete for the same somatostatin receptor sites. These observations on displacement/rebinding suggest that the interruption of somatostatin agonists before PRRT (which can worsen patient symptoms) may not be necessary when the radiolabeled somatostatin analog is an antagonist.

There are still other microscopic characteristics that may explain the gain in therapeutic efficacy associated with using antagonists. The therapeutic efficacy of radiopharmaceuticals is linked to radiation-induced DNA damage. The timing and degree of DNA double strand break

(DSB) induction were quantified for [^{177}Lu]Lu-DOTA-JR11 and [^{177}Lu]Lu-DOTA-TATE using the number of p53-binding protein 1 (53BP1) foci per nucleus over time in SST_2-transfected U2OS cells treated with both radiopharmaceuticals [24]. In line with the differences in their cellular uptake, [^{177}Lu]Lu-DOTA-JR11 produced at least 60% more DSBs than [^{177}Lu]Lu-DOTA-TATE, and this increased level remained over time despite the fact that [^{177}Lu]Lu-DOTA-JR11 accumulates primarily on the cell membrane while [^{177}Lu]Lu-DOTA-TATE accumulates mainly in the cytoplasm (i.e., closer to the nucleus and DNA). The radiation effects of [^{177}Lu]Lu-DOTA-JR11 were also assessed by analyzing the cell-cycle distribution of the BON-SST_2 cells after incubation with [^{177}Lu]Lu-DOTA-JR11 or [^{177}Lu]Lu-DOTA-TOC [25]. [^{177}Lu]Lu-DOTA-JR11 caused an activity-dependent increase in the number of cells in the G2/M phase as well as a corresponding decrease in the number of cells in the G0/G1 phase. In contrast, same dose of [^{177}Lu]Lu-DOTA-TOC did not affect the cell cycle. This is in line with the increased number of DNA double-strand breaks caused by [^{177}Lu]Lu-DOTA-JR11 compared to [^{177}Lu]Lu-DOTA-TATE [24].

16.2.5 Potential of Radiolabeled SST Antagonists for Novel Indications of PRRT

The improved tissue binding of radiolabeled SST_2 antagonists compared to agonists was demonstrated using human tumor specimens. Human tissue samples from nine different tumors were analyzed via in vitro autoradiography to compare the binding of [^{125}I]I-JR11 vs. [^{125}I]I-Tyr^3-octreotide [27] and [^{177}Lu]Lu-DOTA-BASS vs. [^{177}Lu]Lu-DOTA-TATE [28]. In all cases, the radiolabeled SST_2 antagonist bound to more SST_2 sites, with an antagonist:agonist binding ratio between 3.8 and 21.8 (Fig. 16.4). Such significantly increased binding is likely to increase the therapeutic efficacy of radiolabeled SST_2 antagonists. Indeed, this increased binding capacity could make tumors other than GEP-NETs targets for SST_2 antagonist RPT despite their relatively low SST_2 expression. These tumors—none of which are currently routinely treated with PRRT—include small cell lung cancer, lung NETs, breast cancer, renal cell carcinoma, non-Hodgkin lymphoma, paraganglioma, pheochromocytoma, medullary thyroid cancer, and meningioma.
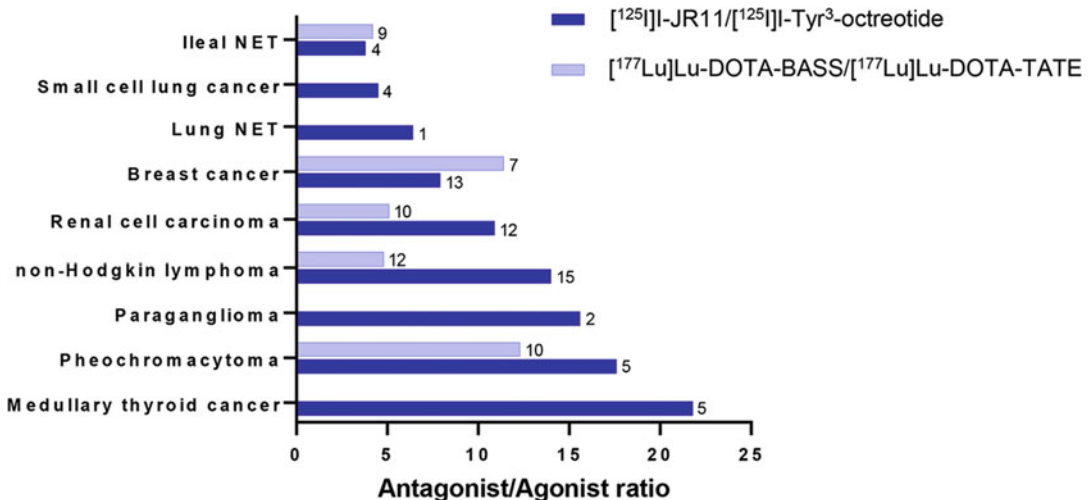
Fig. 16.4 The binding ratio of radiolabeled SST_2 antagonist/agonists to different human tumor tissues. [^{125}I]I-JR11/[^{125}I]I-Tyr^3-octreotide data are from Reubi et al. [27]. [^{177}Lu]Lu-DOTA-BASS/[^{177}Lu]Lu-DOTA-TATE data are from Cescato et al. [28]. Numbers indicate the sample size of tumor tissues

16.2.6 Clinical Translation of Radiolabeled SST Antagonists

As we have noted, there is preclinical evidence that radiolabeled SST_2 antagonists generate higher tumor doses and larger numbers of DNA double strand breaks than agonists, resulting in better treatment efficacy [23, 24]. Yet the question remains: will this difference translate to the clinic? Indeed, the SST_2 antagonist [^{177}Lu]Lu-DOTA-JR11 (a.k.a. [^{177}Lu]Lu-OPS201, [^{177}Lu]Lu-satoreotide tetraxetan) was superior to the agonist [^{177}Lu]Lu-DOTA-TATE in a single-center, prospective first-in-human study (phase 0 study) with 4 patients who had advanced, metastatic NET [8]. The most relevant findings of this study were a 3.5-fold higher median tumor dose for [^{177}Lu]Lu-DOTA-JR11 compared to [^{177}Lu]Lu-DOTA-TATE as well as >twofold higher tumor-to-kidney dose ratios with the former. Furthermore, [^{177}Lu]Lu-DOTA-JR11 produced tumor doses of up to 487 Gy and moderate adverse events, with one grade 3 thrombocytopenia after treatment with 3× ~5 GBq (total 15.2 GBq). The other three patients received two to three cycles with a total administered radioactivity between 5.9 and 13.7 GBq [8]. In another trial, however, Reidy-Lagunes et al. described grade 4 hematotoxicity (leukopenia, neutropenia, and thrombocytopenia) in 4 of 7 patients with NETs treated with 2 × ~7.4 of [^{177}Lu]Lu-DOTA-JR11 (total radioactivity between 10.5 and 15.0 GBq) [9]. As a result, their single-center phase I study (NCT02609737) was suspended, and the protocol was modified to limit the cumulative absorbed bone marrow dose resulting in less bone marrow toxicity. The most important results of this study are summarized in Table 16.3.

[^{177}Lu]Lu-DOTA-JR11 (^{177}Lu-satoreotide tetraxetan) is currently being evaluated in a phase I/II multicenter study (NCT02592707 and NTC05017662) in patients with rapidly progressive NETs [29] and in a retrospective single center study comparing the tumor and organ dosimetry of [^{177}Lu]Lu-DOTA-JR11 and [^{177}Lu]Lu-DOTA-TOC in the same patients with advanced NETs (Fig. 16.5). Based on preclinical findings by Nicolas et al., those studies were performed with 2–4 times higher amounts of peptide than previous studies in order to reduce the radiation dose to SST_2-positive normal tissues [23]. [^{177}Lu]Lu-DOTA-JR11's "sister" compound, [^{177}Lu]Lu-DOTA-LM3, was also evaluated in a single-center compassionate use study [30]. Table 16.3 displays the most important published clinical findings on [^{177}Lu]Lu-DOTA-JR11 and [^{177}Lu]Lu-DOTA-LM3. In summary, [^{177}Lu]Lu-DOTA-JR11 yields several times higher tumor radiation doses than [^{177}Lu]Lu-DOTA-TATE and [^{177}Lu]Lu-DOTA-TOC in

Table 16.3 Summary of clinical study results with radiolabeled SST_2 antagonists

Radiopharmaceutical	Study design, study protocol	Subjects	ORR according to (RECIST 1.1)	1-year DCR	Thrombocytopenia, neutropenia, (CTCAE grade 3/4)
^{177}Lu-DOTA-JR11[a]	Single-center, phase I, 1–2 cycles (5.0–15 GBq)	20 NETs	45%	~75%	20%, 15%
^{177}Lu-DOTA-JR11[b]	Multicenter, phase I/II interims analysis, 3 cycles (~13 GBq)	35 NETs	30%	90%	14%, 6%
^{177}Lu-DOTA-LM3[c]	Single-center compassionate use, 1–4 cycles (6.1–26 GBq)	51 NENs	36%	NA	6% NA

[a]Data are from Reidy-Lagunes et al. [9], [b]Data are from Nicolas et al. [29], [c]Data are from Baum et al. [30]. Abbreviations: *ORR* objective response rate, *RECIST 1.1* response evaluation criteria in solid tumors version 1.1, *DCR* disease control rate, *CTCAE* common terminology criteria for adverse events. Definitions: OOR: percentage of patients with a complete response or partial response to therapy according to RECIST 1.1, 1-year DCR: percentage of patients with progressive, advanced or metastatic tumor disease who have achieved complete response, partial response or stable disease at 1 year after therapy start
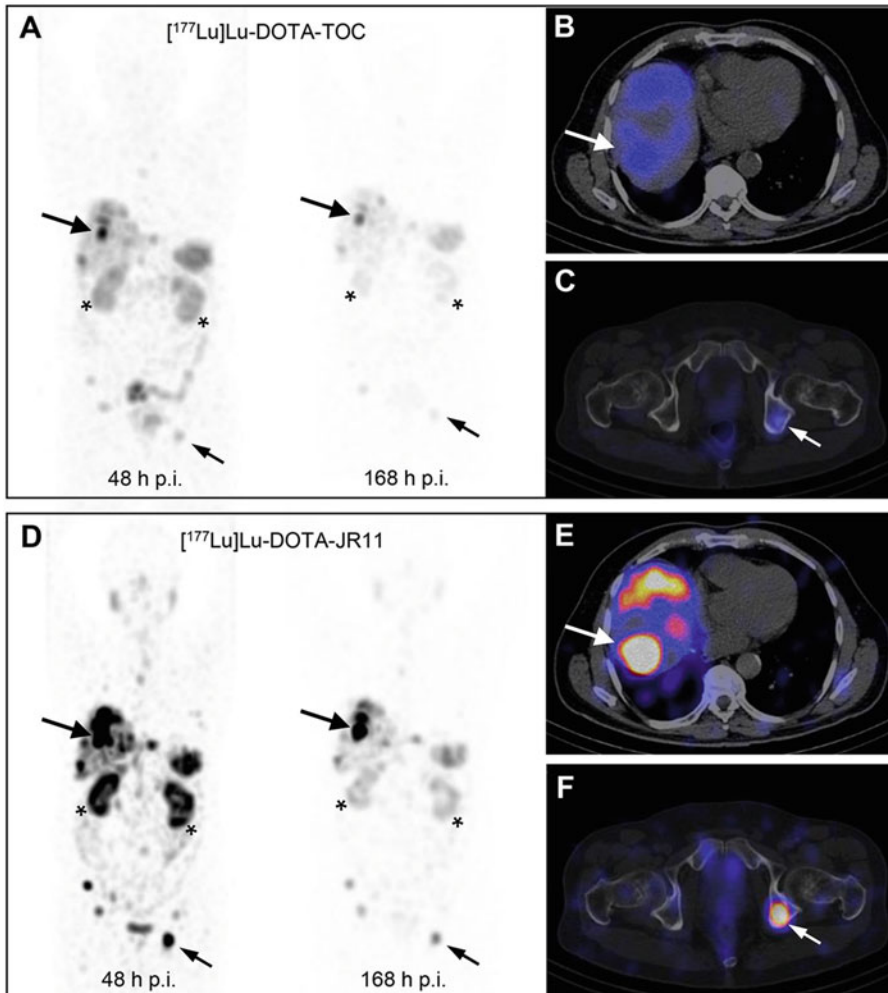
Fig. 16.5 Patient with advanced metastatic lung NETs who received [^{177}Lu]Lu-DOTA-TOC and [^{177}Lu]Lu-DOTA-JR11 treatment at an interval of 10 weeks: (**a**) post-treatment MIP images of quantitative SPECT at 48 and 168 h post-injection as well as (**b, c**) quantitative SPECT/CT images acquired 48 h after the injection of 7.4 GBq [^{177}Lu]Lu-DOTA-TOC. (**d**) Post-treatment MIP images of quantitative SPECT at 48 and 168 h post-injection as well as (E and F) quantitative SPECT/CT images acquired 48 h after the injection of 3.7 GBq [^{177}Lu]Lu-DOTA-JR11. The SUV window threshold was 10 for all images. Large arrows show one liver metastasis in segment VIII (**a, b, d, e**), and small arrows show one bone metastasis in the left acetabulum (**a, c, d, f**). The radiation dose to the liver segment VIII metastasis was 3.4 Gy/GBq with [^{177}Lu]Lu-DOTA-TOC and 12.6 Gy/GBq with [^{177}Lu]Lu-DOTA-JR11. The radiation dose to the left acetabulum metastasis was 1.5 Gy/GBq with [^{177}Lu]Lu-DOTA-TOC and 9.9 Gy/GBq with [^{177}Lu]Lu-DOTA-JR11. The mean radiation dose to the kidneys was 0.3 Gy/GBq with [^{177}Lu]Lu-DOTA-TOC and 0.8 Gy/GBq with [^{177}Lu]Lu-DOTA-JR11. Asterisks indicate kidneys (**a, d**). Half the dose of [^{177}Lu]Lu-DOTA-JR11 was injected relative to the dose of [^{177}Lu]Lu-DOTA-TOC due to the former's higher dose to the kidneys and other organs. Abbreviations: *MIP* maximum intensity projection, *SPECT* single photon emission computed tomography, *SPECT/CT* combined SPECT with computed tomography, *SUV* standardized uptake value

the same patients [8], resulting in objective response rates (ORR) between 30% and 45% and 1 year disease control rates (DCR) between ~75% and 90% (Table 16.3). Yet at the same time [^{177}Lu]Lu-DOTA-JR11 produces higher bone marrow toxicity [9]. Overall, [^{177}Lu]Lu-DOTA-JR11 is a valuable alternative to [^{177}Lu]Lu-DOTA-TATE and [^{177}Lu]Lu-DOTA-TOC.

However, it remains to be evaluated if [^{177}Lu]Lu-DOTA-JR11 improves upon the treatment efficacy and therapeutic indices of its agonist cousins.

16.3 Something Extra

16.3.1 Controversial Issues

Disease control rate and toxicity profile are the main criteria for evaluating the therapeutic performance of a radiopharmaceutical. The main dose-limiting organs of PRRT with radiolabeled somatostatin agonists are the kidneys and the bone marrow, with an accepted upper threshold radiation dose of 23 Gy for kidneys and 2 Gy for the bone marrow. It is worth mentioning, however, that these values originate from external beam radiotherapy. Therefore, the translation of these radiation dose values to radiopharmaceuticals leaves much to be desired, as radiopharmaceuticals irradiate the kidneys and bone marrow for a much longer period of time but with less energy.

So far, [^{177}Lu]Lu-DOTA-JR11 has shown much higher tumor radiation doses compared to [^{177}Lu]Lu-DOTA-TATE and [^{177}Lu]Lu-DOTA-TOC. However, its therapeutic potential seems to be limited by its higher radiation doses to the bone marrow and kidneys. That said, even though [^{177}Lu]Lu-DOTA-JR11 has produced higher radiation doses to the kidneys compared to [^{177}Lu]Lu-DOTA-TATE and [^{177}Lu]Lu-DOTA-TOC, the former's tumor-to-kidney radiation dose ratio remains higher [8] (Fig. 16.5). Furthermore, in most PRRT protocols, amino acid infusions are used in order to reduce renal injury. Taken together, the kidney toxicity profile of [^{177}Lu]Lu-DOTA-JR11 does not seem to raise additional concerns compared to [^{177}Lu]Lu-DOTA-TATE and [^{177}Lu]Lu-DOTA-TOC.

Bone marrow toxicity is a slightly different story, as there is no "bone marrow protection" strategy akin to the infusion of amino acids for the kidneys. In the NETTER-1 study, 3% of the [^{177}Lu]Lu-DOTA-TATE group population showed treatment-related serious adverse events of grade 3 or worse, and 2% developed myelodysplastic syndrome after long-term follow-up [31]. According to the current clinical data, SST_2 antagonists such as [^{177}Lu]Lu-DOTA-JR11 [9] and [^{177}Lu]Lu-DOTA-LM3 (summarized in Table 16.3) produced more hematological toxicity than agonists such as [^{177}Lu]Lu-DOTA-TATE. It has also been shown that human hematopoietic cells express SST_2, especially primitive CD34$^+$ cells [32]. This might be the reason for the more pronounced cytotoxicity of [^{177}Lu]Lu-DOTA-JR11 and [^{177}Lu]Lu-DOTA-LM3, as both compounds show a higher capacity for SST_2 binding than [^{177}Lu]Lu-DOTA-TATE. However, the pathology of higher bone marrow toxicity with radiolabeled SST_2 antagonists is not yet understood.

Finally, to wrap up our consideration of toxicity, it is important to note that the high accumulation of [^{177}Lu]Lu-DOTA-JR11 in tumor cells allows for the administration of lower amounts of radioactivity without reductions in treatment efficacy (Fig. 16.5). This has multiple advantages, including lowering radiation doses to the kidney and bone marrow, reducing radiation exposure to the patient and hospital personnel, reducing the cost of per dose, and limiting the amount of radioactive waste produced.

16.4 The Future

The use of SST antagonists has the potential to offer patients a new and improved theranostic option. Below we have listed four possible future developments for the field:

1. Several tumors other than GEP-NETs are candidates for theranostic studies with SST antagonists, including small cell lung cancer, lung NETs, breast cancer, renal cell carcinoma, non-Hodgkin lymphoma, paraganglioma, pheochromocytoma, medullary thyroid cancer, and meningioma. Along these lines, the evaluation of [^{177}Lu]Lu-DOTA-JR11 in patients with advanced

meningiomas is already planned (NCT04997317).

2. Radiolabeled SST_2 antagonists cause more bone marrow toxicity than agonists, as they likely exhibit more pronounced SST_2 specific binding to hematopoietic cells. But the pathological mechanism of this phenomenon is not fully understood yet. A better understanding of this mechanism would likely aid in the design of radiolabeled SST antagonists that are less toxic to the bone marrow.

3. To date, only lutetium-177 has been used as a radionuclide in conjunction with SST antagonists. The use of alternative radionuclides may decrease bone marrow toxicity and increase tumor toxicity. For example, α-emitters deliver a mean energy of >6000 keV within a maximal range of only 0.06–0.1 mm, resulting in a high linear energy transfer (LET) of ~100 keV/μm (~500 times greater than $β^-$-emitters) (Table 16.2). Due to their high LET, α-emitters principally cause double-strand breaks (DSB) to DNA, the most toxic damage to the cell. Therefore, α-emitters such as actinium-225 and lead-212 are good candidates for use with SST antagonists (Table 16.2).

Auger electron-emitting radionuclides pose yet another option. These radionuclides have high LET, but it is difficult for them to produce DSB unless they are in very close proximity to the cell nucleus. Unfortunately, the specific nuclear accumulation of SST antagonists remains a challenge given their low rate of internalization [33]. However, recent research suggests that the cell membrane is more sensitive to the emission of Auger electrons than the cytoplasm [34]. Therefore, terbium-161—a combined $β^-$- and Auger electron-emitter (Table 16.2)—is also a very promising candidate for the labeling of SST antagonists, as antagonists accumulate mainly on the cell membrane. Indeed, Borgna et al. use clonogenic in vitro assays to demonstrate that [^{161}Tb]Tb-DOTA-LM3 induces a ~100 times higher tumor cell death rate than [^{177}Lu]Lu-DOTA-LM3 [33]. The evaluation of [^{161}Tb]

Tb-DOTA-LM3 in a phase 0 study is ongoing in patients with GEP-NETs (NCT05359146).

4. Several other receptor systems are also likely suitable for the antagonist approach, for example, targeting the gastrin-releasing peptide receptor (GRP) in patients with prostate cancer, breast cancer, small cell lung cancer, and ovarian cancer [35]. In a compassionate use program, a radiolabeled GRP antagonist—[^{177}Lu]Lu-RM2—was successfully evaluated in 4 patients with metastatic castration-resistant prostate cancer [36] and a prospective open-label phase I/II is ongoing using another radiolabeled GRP antagonist: [^{177}Lu]Lu-NeoB (NCT03872778).

5. Last but not least, larger-scale randomized phase II/III studies evaluating radiolabeled DOTA-JR11/DOTA-LM3 and other promising radiolabeled SST antagonists are needed in order to prove their superiority over agonists in patients with GEP-NETs or other tumors with SST_2 expression.

16.5 The Bottom Line

1. Radiolabeled SST antagonists recognize more binding sites on SST-expressing tumor cells than agonists.

2. Several SST_2 antagonists were synthesized for preclinical evaluation. [^{177}Lu]Lu-DOTA-JR11 and [^{177}Lu]Lu-DOTA-LM3 showed the most promising results and were selected for further clinical studies.

3. The SST_2 antagonist [^{177}Lu]Lu-DOTA-JR11 showed several times higher tumor radiation doses in patients than [^{177}Lu]Lu-DOTA-TATE or [^{177}Lu]Lu-DOTA-TOC and produced a high objective response rate between 30% and 45% as well as a 1-year disease control rate of up to 90%.

4. In clinical studies, [^{177}Lu]Lu-DOTA-JR11 produced higher bone marrow toxicity than [^{177}Lu]Lu-DOTA-TATE or [^{177}Lu]Lu-DOTA-TOC.

5. Future developments in this field will include the use of SST_2 antagonists together with α-

and β⁻/Auger electron-emitting radionuclides, the use of radiolabeled SST$_2$ antagonists for RPT in tumors beyond GEP-NETS, and the expansion of the use of radiolabeled antagonists to other receptor systems.

References

1. Kloppel G. Classification and pathology of gastroenteropancreatic neuroendocrine neoplasms. Endocr Relat Cancer. 2011;18(Suppl 1):S1–16.

2. Caplin ME, Baudin E, Ferolla P, Filosso P, Garcia-Yuste M, Lim E, et al. Pulmonary neuroendocrine (carcinoid) tumors: European Neuroendocrine Tumor Society expert consensus and recommendations for best practice for typical and atypical pulmonary carcinoids. Ann Oncol. 2015;26(8):1604–20.

3. Zandee WT, Kamp K, van Adrichem RC, Feelders RA, de Herder WW. Effect of hormone secretory syndromes on neuroendocrine tumor prognosis. Endocr Relat Cancer. 2017;24(7):R261–R74.

4. Fani M, Mansi R, Nicolas GP, Wild D. Radiolabeled somatostatin analogs-a continuously evolving class of radiopharmaceuticals. Cancers (Basel). 2022;14(5):1172.

5. Ambrosini V, Kunikowska J, Baudin E, Bodei L, Bouvier C, Capdevila J, et al. Consensus on molecular imaging and theranostics in neuroendocrine neoplasms. Eur J Cancer. 2021;146:56–73.

6. Ginj M, Zhang H, Waser B, Cescato R, Wild D, Wang X, et al. Radiolabeled somatostatin receptor antagonists are preferable to agonists for in vivo peptide receptor targeting of tumors. Proc Natl Acad Sci U S A. 2006;103(44):16436–41.

7. Mansi R, Plas P, Vauquelin G, Fani M. Distinct in vitro binding profile of the somatostatin receptor subtype 2 antagonist [(177)Lu]Lu-OPS201 compared to the agonist [(177)Lu]Lu-DOTA-TATE. Pharmaceuticals (Basel). 2021;14(12):1265.

8. Wild D, Fani M, Fischer R, Del Pozzo L, Kaul F, Krebs S, et al. Comparison of somatostatin receptor agonist and antagonist for peptide receptor radionuclide therapy: a pilot study. J Nucl Med. 2014;55(8):1248–52.

9. Reidy-Lagunes D, Pandit-Taskar N, O'Donoghue JA, Krebs S, Staton KD, Lyashchenko SK, et al. Phase I Trial of Well-Differentiated Neuroendocrine Tumors (NETs) with Radiolabeled Somatostatin Antagonist (177)Lu-Satoreotide Tetraxetan. Clin Cancer Res. 2019;25(23):6939–47.

10. Fani M, Nicolas GP, Wild D. Somatostatin Receptor Antagonists for Imaging and Therapy. J Nucl Med. 2017;58(Suppl 2):61S–6S.

11. Fjalling M, Andersson P, Forssell-Aronsson E, Gretarsdottir J, Johansson V, Tisell LE, et al. Systemic radionuclide therapy using indium-111-DTPA-D-Phe1-octreotide in midgut carcinoid syndrome. J Nucl Med. 1996;37(9):1519–21.

12. Ambrosini V, Fani M, Fanti S, Forrer F, Maecke HR. Radiopeptide imaging and therapy in Europe. J Nucl Med. 2011;52(Suppl 2):42S–55S.

13. Baumann T, Rottenburger C, Nicolas G, Wild D. Gastroenteropancreatic neuroendocrine tumours (GEP-NET) – imaging and staging. Best Pract Res Clin Endocrinol Metab. 2016;30(1):45–57.

14. Strosberg J, El-Haddad G, Wolin E, Hendifar A, Yao J, Chasen B, et al. Phase 3 trial of (177)Lu-Dotatate for midgut neuroendocrine tumors. N Engl J Med. 2017;376(2):125–35.

15. Bass RT, Buckwalter BL, Patel BP, Pausch MH, Price LA, Strnad J, et al. Identification and characterization of novel somatostatin antagonists. Mol Pharmacol. 1996;50(4):709–15.

16. Raynor K, Murphy WA, Coy DH, Taylor JE, Moreau JP, Yasuda K, et al. Cloned somatostatin receptors: identification of subtype-selective peptides and demonstration of high affinity binding of linear peptides. Mol Pharmacol. 1993;43(6):838–44.

17. Hocart SJ, Jain R, Murphy WA, Taylor JE, Coy DH. Highly potent cyclic disulfide antagonists of somatostatin. J Med Chem. 1999;42(11):1863–71.

18. Jiang G, Stalewski J, Galyean R, Dykert J, Schteingart C, Broqua P, et al. GnRH antagonists: a new generation of long acting analogues incorporating p-ureido-phenylalanines at positions 5 and 6. J Med Chem. 2001;44(3):453–67.

19. Ginj M, Schmitt JS, Chen J, Waser B, Reubi JC, de Jong M, et al. Design, synthesis, and biological evaluation of somatostatin-based radiopeptides. Chem Biol. 2006;13(10):1081–90.

20. Cescato R, Erchegyi J, Waser B, Piccand V, Maecke HR, Rivier JE, et al. Design and in vitro characterization of highly sst2-selective somatostatin antagonists suitable for radiotargeting. J Med Chem. 2008;51(13):4030–7.

21. Fani M, Del Pozzo L, Abiraj K, Mansi R, Tamma ML, Cescato R, et al. PET of somatostatin receptor-positive tumors using 64Cu- and 68Ga-somatostatin antagonists: the chelate makes the difference. J Nucl Med. 2011;52(7):1110–8.

22. Fani M, Braun F, Waser B, Beetschen K, Cescato R, Erchegyi J, et al. Unexpected sensitivity of sst2 antagonists to N-terminal radiometal modifications. J Nucl Med. 2012;53(9):1481–9.

23. Nicolas GP, Mansi R, McDougall L, Kaufmann J, Bouterfa H, Wild D, et al. Biodistribution, pharmacokinetics, and dosimetry of (177)Lu-, (90)Y-, and (111) In-labeled somatostatin receptor antagonist OPS201 in comparison to the agonist (177)Lu-DOTATATE: the mass effect. J Nucl Med. 2017;58(9):1435–41.

24. Dalm SU, Nonnekens J, Doeswijk GN, de Blois E, van Gent DC, Konijnenberg MW, et al. Comparison of the therapeutic response to treatment with a 177Lu-Labeled somatostatin receptor agonist and antagonist in preclinical models. J Nucl Med. 2016;57(2):260–5.

25. Albrecht J, Exner S, Grotzinger C, Prasad S, Konietschke F, Beindorff N, et al. Multimodal imaging of 2-Cycle PRRT with (177)Lu-DOTA-JR11 and (177)Lu-DOTATOC in an orthotopic neuroendocrine xenograft tumor mouse model. J Nucl Med. 2021;62 (3):393–8.

26. Dalm SU, Haeck J, Doeswijk GN, de Blois E, de Jong M, van Deurzen CHM. SSTR-mediated imaging in breast cancer: is there a role for radiolabeled somatostatin receptor antagonists? J Nucl Med. 2017;58(10):1609–14.

27. Reubi JC, Waser B, Macke H, Rivier J. Highly increased 125I-JR11 antagonist binding in vitro reveals novel indications for sst2 targeting in human cancers. J Nucl Med. 2017;58(2):300–6.

28. Cescato R, Waser B, Fani M, Reubi JC. Evaluation of 177Lu-DOTA-sst2 antagonist versus 177Lu-DOTA-sst2 agonist binding in human cancers in vitro. J Nucl Med. 2011;52(12):1886–90.

29. Nicolas GP, Ansquer C, Lenzo NP, McEwan S, Wild D, Hicks RJ. An international open-label study on safety and efficacy of 177Lu-satoreotide tetraxetan in somatostatin receptor positive neuroendocrine tumours (NETs): an interim analysis. Ann Oncol. 2020;31(supplement 4):S771.

30. Baum RP, Zhang J, Schuchardt C, Muller D, Macke H. First-in-humans study of the SSTR antagonist (177) Lu-DOTA-LM3 for peptide receptor radionuclide therapy in patients with metastatic neuroendocrine neoplasms: dosimetry, safety, and efficacy. J Nucl Med. 2021;62(11):1571–81.

31. Strosberg JR, Caplin ME, Kunz PL, Ruszniewski PB, Bodei L, Hendifar A, et al. (177)Lu-Dotatate plus long-acting octreotide versus highdose long-acting octreotide in patients with midgut neuroendocrine tumours (NETTER-1): final overall survival and long-term safety results from an open-label, randomised, controlled, phase 3 trial. Lancet Oncol. 2021;22(12):1752–63.

32. Oomen SP, van Hennik PB, Antonissen C, Lichtenauer-Kaligis EG, Hofland LJ, Lamberts SW, et al. Somatostatin is a selective chemoattractant for primitive (CD34(+)) hematopoietic progenitor cells. Exp Hematol. 2002;30(2):116–25.

33. Borgna F, Haller S, Rodriguez JMM, Ginj M, Grundler PV, Zeevaart JR, et al. Combination of terbium-161 with somatostatin receptor antagonists-a potential paradigm shift for the treatment of neuroendocrine neoplasms. Eur J Nucl Med Mol Imaging. 2022;49(4):1113–26.

34. Pouget JP, Santoro L, Raymond L, Chouin N, Bardies M, Bascoul-Mollevi C, et al. Cell membrane is a more sensitive target than cytoplasm to dense ionization produced by auger electrons. Radiat Res. 2008;170(2):192–200.

35. Cescato R, Maina T, Nock B, Nikolopoulou A, Charalambidis D, Piccand V, et al. Bombesin receptor antagonists may be preferable to agonists for tumor targeting. J Nucl Med. 2008;49(2):318–26.

36. Kurth J, Krause BJ, Schwarzenbock SM, Bergner C, Hakenberg OW, Heuschkel M. First-in-human dosimetry of gastrin-releasing peptide receptor antagonist [(177)Lu]Lu-RM2: a radiopharmaceutical for the treatment of metastatic castration-resistant prostate cancer. Eur J Nucl Med Mol Imaging. 2020;47(1):123–35.

37. Schottelius M, Simecek J, Hoffmann F, Willibald M, Schwaiger M, Wester HJ. Twins in spirit – episode I: comparative preclinical evaluation of [(68)Ga] DOTATATE and [(68)Ga]HA-DOTATATE. EJNMMI Res. 2015;5:22.

38. Reubi JC, Schar JC, Waser B, Wenger S, Heppeler A, Schmitt JS, et al. Affinity profiles for human somatostatin receptor subtypes SST1-SST5 of somatostatin radiotracers selected for scintigraphic and radiotherapeutic use. Eur J Nucl Med. 2000;27(3): 273–82.

39. Kong G, Hicks RJ. Peptide receptor radiotherapy: current approaches and future directions. Curr Treat Options in Oncol. 2019;20(10):77.

40. Muller C, Domnanich KA, Umbricht CA, van der Meulen NP. Scandium and terbium radionuclides for radiotheranostics: current state of development towards clinical application. Br J Radiol. 2018;91 (1091):20180074.

Small Molecules as Vectors for Radiopharmaceutical Therapy

17

Steven P. Rowe, Rudolf A. Werner, Tushar Garg, Andrei Gafita, Andrew F. Voter, Mohammad S. Sadaghiani, Mark C. Markowski, Channing J. Paller, Micheal R. Zalutsky, Lilja B. Solnes, and Martin G. Pomper

17.1 The Fundamentals

17.1.1 Introduction

Despite dramatic improvements in the availability and application of chemotherapeutics, immunologically active agents, and other systemic therapies, few patients with metastatic cancer are cured. Thus, there is an urgent need for new, broadly orthogonal approaches that can extend the quantity and quality of life of patients with metastatic disease. Radiopharmaceutical therapy (RPT) fits this bill, with three United States Food and Drug Administration (FDA)-approved agents currently on the market (Fig. 17.1) [1].

Two of those FDA-approved agents are small molecules: *meta*-[^{131}I]iodobenzylguanidine ([^{131}I]MIBG) (Fig. 17.2) for patients with advanced pheochromocytoma or paraganglioma [2] and [^{177}Lu]Lu-PSMA-617 (Fig. 17.3) for patients with prostate cancer that expresses the prostate-specific membrane antigen (PSMA) [3]. Numerous other agents are in various stages of preclinical and clinical assessment. The emerging dominance of small molecules for RPT can be traced to their rapid pharmacokinetics—which accelerates their uptake in tumors and decreases their circulation time through radiosensitive tissues such as bone marrow—their decreased potential for hypersensitivity reactions (i.e., immunogenicity), and their relatively facile synthesis, purification, and large-scale distribution [4].

S. P. Rowe (✉) · L. B. Solnes · M. G. Pomper
The Russell H. Morgan Department of Radiology and Radiological Science, Johns Hopkins University School of Medicine, Baltimore, MD, USA

Department of Oncology, Sidney Kimmel Comprehensive Cancer Center, Johns Hopkins University School of Medicine, Baltimore, MD, USA
e-mail: srowe8@jhmi.edu

R. A. Werner
The Russell H. Morgan Department of Radiology and Radiological Science, Johns Hopkins University School of Medicine, Baltimore, MD, USA

Department of Nuclear Medicine, University Hospital Würzburg, Würzburg, Germany

T. Garg · A. F. Voter · M. S. Sadaghiani
The Russell H. Morgan Department of Radiology and Radiological Science, Johns Hopkins University School of Medicine, Baltimore, MD, USA

A. Gafita
Ahmanson Translational Theranostics Division of the Department of Molecular and Medical Pharmacology, University of California Los Angeles, Los Angeles, CA, USA

M. C. Markowski · C. J. Paller
Department of Oncology, Sidney Kimmel Comprehensive Cancer Center, Johns Hopkins University School of Medicine, Baltimore, MD, USA

M. R. Zalutsky
Department of Radiology, Duke University Medical Center, Durham, NC, USA

Fig. 17.1 General schema for the mechanism of small-molecule radiotherapeutics. High-affinity binding of the small molecule to a target allows for the localization of cytotoxic radiation which primarily acts via the creation of DNA damage

Radioligand target on cancer cells

Target mediated localization

Radioligand induced cell killing
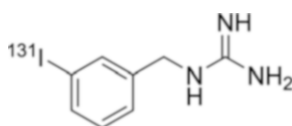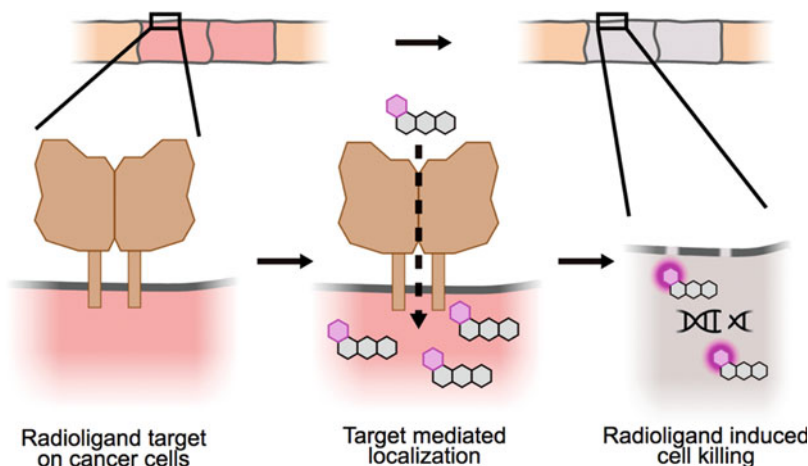
Fig. 17.2 Chemical structure of [^{131}I]MIBG

In this chapter, we will discuss these FDA-approved, small-molecule radiotherapeutics. Particular attention will be paid to [^{177}Lu]Lu-PSMA-617, specifically its path to regulatory approval, the rise of therapy assessment, and current efforts to bring similar molecules to the clinic. We will also cover future directions for small molecule-based RPT agents, including (but not limited to) the fibroblast-activation (FAP)-targeted molecules. We will close with speculation as to the future role of advanced image analysis methods, such as radiomics and artificial intelligence, in selecting patients for RPT and predicting therapeutic response.

17.2 The Details

17.2.1 Agents Approved by the United States Food and Drug Administration

PSMA is a type II integral membrane carboxy-peptidase with limited restriction within normal tissues [5]. It was originally isolated from the serum of patients with prostate cancer by Gerald

Murphy's group at the State University of New York, Buffalo [6]. The 7E11 monoclonal antibody targeting PSMA was radiolabeled with indium-111 and eventually approved by the US Food and Drug Administration (FDA) for the imaging of prostate cancer [7]. However, the epitope for that antibody was intracellular, such that primarily non-viable cells were detected. Eventually, an antibody against an external epitope—J591—was developed by Chang et al. [8] and has been radiolabeled with both imaging and therapeutic nuclides [9–11]. However, antibodies require relatively long circulation times before they clear from the blood pool (often for periods of up to a week) making them challenging to use, particularly within standard clinical workflows. Small molecules, in contrast, can be better manipulated with respect to pharmacokinetics. Accordingly, when it was noted that PSMA was essentially equivalent to glutamate carboxypeptidase II [12] and that small-molecule inhibitors of the latter were under development as neuroprotectants [13, 14], the field began radiolabeling analogs of these small molecules for the imaging and therapy of prostate cancer [15–17].

17.2.1.1 [^{177}Lu]Lu-PSMA-617

Targeting PSMA with small radiolabeled molecules is a highly effective approach to the treatment of castration-resistant prostate cancer (CRPC). A recent meta-analysis on the

Fig. 17.3 The chemical structure of [^{177}Lu]Lu-PSMA-617
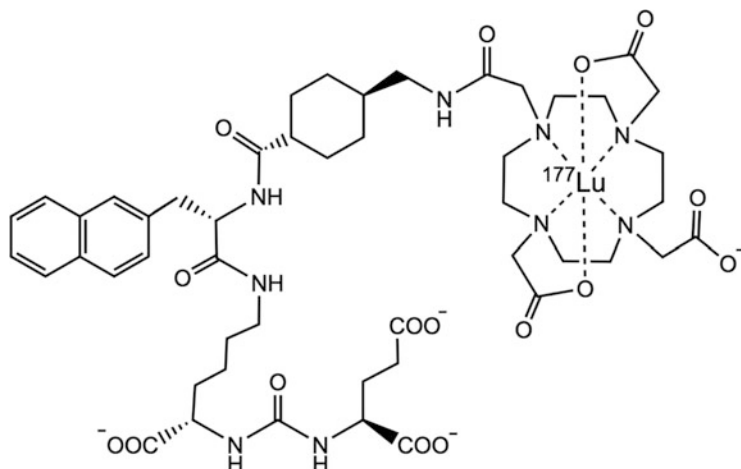
effectiveness of [^{177}Lu]Lu-PSMA-617 in treating CRPC covering 2274 patients from 40 studies showed that a proportion of 0.68 of patients [95% confidence interval (CI): 0.65–0.72] exhibited a decline in prostate-specific antigen (PSA) levels after therapy. Furthermore, a pooled proportion of 0.44 of patients (95% CI: 0.40–0.49) showed ≥50% PSA decline after aggregating the data from 3129 patients of 53 studies (Fig. 17.4). Yet another meta-analysis of six studies showed that the overall survival according to pooled hazard ratios (HRs) for any PSA decline after [^{177}Lu]Lu-PSMA-617 was 0.26 with significance (95% CI: 0.18–0.37, $P < 0.00001$) [18]. With respect to Common Terminology Criteria for Adverse Events (CTCAE) grade 3 or 4 toxicities, anemia was the highest reported adverse event after [^{177}Lu]Lu-PSMA-617 therapy (0.19, 95% CI: 0.06; 0.15) [19].

The clinical factors associated with both positive and negative responses to therapy have been evaluated. For example, elevated levels of alkaline phosphatase and the presence of visceral metastases have been shown as negative predictors of biochemical response after RPT with [^{177}Lu]Lu-PSMA-617 [20]. Another study showed that the presence of visceral metastasis is associated with poor response and survival outcomes [21]. Baseline levels of hemoglobin and serum PSA level also predict survival after treatment. With respect to the former, patients

with normal baseline hemoglobin lived longer that those with anemia. And as for the latter, a study by Rasul et al. showed that those with PSA values of ≤650 μg/L had a significantly longer survival compared to patients with baseline PSA levels of >650 μg/L [22]. It is likely that these only scratch the surface, and there are indeed a large number of other associations between baseline clinical and laboratory characteristics and response to therapy. Along these lines, the adoption of artificial intelligence (AI) algorithms will speed the discovery of clinical biomarkers and aid in the combination of such biomarkers with imaging for optimized nomograms predicting response.

Our understanding of the effectiveness and toxicities of PSMA-targeted RPT is predicated on a large number of single-center (primarily retrospective) studies utilizing multiple different ^{177}Lu-labeled PSMA-targeted radioligands [18, 19]. However, evidence from prospective, multi-center trials is needed for new agents to become standard-of-care. For [^{177}Lu]Lu-PSMA-617, this evidence has arrived in the form of the TheraP [23] and VISION [3] trials (Fig. 17.5).

TheraP was a phase II clinical trial that randomized 200 patients with metastatic CRPC to treatment with [^{177}Lu]Lu-PSMA-617 or cabazitaxel [23]. Patients who were treated with [^{177}Lu]Lu-PSMA-617 had an improved biochemical response (66% vs. 44%) and an improved rate of grade 3–4 adverse events (33% vs. 53%)

Study	Events	Total	Weight (common)	Weight (random)	Proportion [95% CI]
Aghdam, 2019	5	14	0.5%	1.2%	0.36 [0.13; 0.65]
Ahmadzadehfar_1, 2017	38	100	3.3%	2.3%	0.38 [0.28; 0.48]
Ahmadzadehfar_2, 2017	26	49	1.7%	2.1%	0.53 [0.38; 0.67]
Ahmadzadehfar_3, 2017	31	52	1.8%	2.1%	0.60 [0.45; 0.73]
Ahmadzadehfar, 2016	5	10	0.4%	1.1%	0.50 [0.19; 0.81]
Ahmadzadehfar, 2021	232	313	8.5%	2.5%	0.74 [0.69; 0.79]
Ahmadzadehfar, 2021	163	393	13.5%	2.6%	0.41 [0.37; 0.47]
Assadi, 2020	13	21	0.7%	1.5%	0.62 [0.38; 0.82]
Brauer, 2017	24	45	1.6%	2.0%	0.53 [0.38; 0.68]
Calais, 2021	16	43	1.4%	2.0%	0.37 [0.23; 0.53]
Derlin, 2020	14	31	1.1%	1.8%	0.45 [0.27; 0.64]
Derlin, 2020	19	50	1.7%	2.1%	0.38 [0.25; 0.53]
Emmet, 2019	5	14	0.5%	1.2%	0.36 [0.13; 0.65]
Fendler, 2016	9	15	0.5%	1.3%	0.60 [0.32; 0.84]
Ferdinandus, 2016	13	40	1.2%	1.9%	0.32 [0.19; 0.49]
Gadot, 2020	18	52	1.7%	2.1%	0.35 [0.22; 0.49]
Gafita, 2020	22	38	1.3%	1.9%	0.58 [0.41; 0.74]
Grubmüller, 2018	18	38	1.3%	1.9%	0.47 [0.31; 0.64]
Gupta, 2019	5	22	0.5%	1.4%	0.23 [0.08; 0.45]
Hofman, 2018	17	30	1.0%	1.8%	0.57 [0.37; 0.75]
Kalmthout, 2019	17	30	1.0%	1.8%	0.57 [0.37; 0.75]
Kessel 2019	28	87	2.7%	2.3%	0.32 [0.23; 0.43]
Khreish, 2021	16	28	1.0%	1.7%	0.57 [0.37; 0.76]
Khurshid, 2018	4	70	0.5%	1.4%	0.06 [0.02; 0.14]
Kratochwil, 2016	13	30	1.0%	1.8%	0.43 [0.25; 0.63]
Leibowitz, 2020	11	24	0.8%	1.7%	0.46 [0.26; 0.67]
Maffey-Steffan, 2019	16	32	1.1%	1.8%	0.50 [0.32; 0.68]
Marinova, 2020	22	30	0.8%	1.6%	0.73 [0.54; 0.88]
McBean, 2019	22	49	1.7%	2.1%	0.45 [0.31; 0.60]
Michalski, 2021	15	46	1.4%	2.0%	0.33 [0.20; 0.48]
Paganelli, 2020	13	41	1.3%	1.9%	0.32 [0.18; 0.48]
Prasad, 2021	9	38	1.0%	1.7%	0.24 [0.11; 0.40]
Privé 2021	5	10	0.4%	1.1%	0.50 [0.19; 0.81]
Rahbar_1, 2016	45	99	3.5%	2.3%	0.45 [0.35; 0.56]
Rahbar_1, 2017	40	71	2.5%	2.2%	0.56 [0.44; 0.68]
Rahbar_2, 2016	23	74	2.3%	2.2%	0.31 [0.21; 0.43]
Rahbar_2, 2017	34	104	3.2%	2.3%	0.33 [0.24; 0.43]
Rasul, 2020	31	54	1.9%	2.1%	0.57 [0.43; 0.71]
Rasul, 2021	36	61	2.1%	2.2%	0.59 [0.46; 0.71]
Rasul, 2021	18	43	1.5%	2.0%	0.42 [0.27; 0.58]
Rathke, 2017	15	40	1.3%	1.9%	0.38 [0.23; 0.54]
Rathke, 2020	35	100	3.2%	2.3%	0.35 [0.26; 0.45]
Rosasr, 2021	16	22	0.6%	1.5%	0.73 [0.50; 0.89]
Scarpa, 2017	2	10	0.2%	0.8%	0.20 [0.03; 0.56]
Seifert 2020	35	78	2.7%	2.3%	0.45 [0.34; 0.57]
Suman, 2019	17	40	1.4%	2.0%	0.42 [0.27; 0.59]
Tatkovic, 2021	15	66	1.6%	2.0%	0.23 [0.13; 0.35]
Völter, 2021	13	30	1.0%	1.8%	0.43 [0.25; 0.63]
Violet, 2020	32	50	1.6%	2.0%	0.64 [0.49; 0.77]
Widjaja, 2021	34	71	2.5%	2.2%	0.48 [0.36; 0.60]
Yadav 2021	74	121	4.1%	2.4%	0.61 [0.52; 0.70]
Yadav, 2019	29	90	2.8%	2.3%	0.32 [0.23; 0.43]
Yordanova, 2019	6	20	0.6%	1.4%	0.30 [0.12; 0.54]
Total (common effect, 95% CI)		3129	100.0%	--	0.46 [0.44; 0.48]
Total (random effect, 95% CI)			--	100.0%	0.44 [0.40; 0.49]

Heterogeneity: Tau^2 = 0.2645; Chi^2 = 254.81, df = 52 (P < 0.01); I^2 = 80%

Fig. 17.4 Forest plot demonstrating the proportion of patients who had an objective biochemical response to treatment with [^{177}Lu]Lu-PSMA-617 RPT

[23]. The combination of improved efficacy with lower toxicity is indicative of the important emerging role of [^{177}Lu]Lu-PSMA-617 therapy in patients with metastatic CRPC.

Another multicenter effort—the VISION trial—was the basis for the new drug application that led to the FDA approval of [^{177}Lu]Lu-PSMA-617 for use as a standard-of-care agent in the United States in patients with metastatic CRPC who had failed a taxane-based chemotherapy. VISION was a phase III trial in which 831 patients were randomized to receive either

Study or Subgroup	Experimental Events	Total	Control Events	Total	Weight	Odds Ratio M-H, Random, 95% CI	Odds Ratio M-H, Random, 95% CI
Hofman 2021	65	98	37	85	49.9%	2.56 [1.40, 4.65]	
Sartor 2021	177	385	14	196	50.1%	11.06 [6.20, 19.75]	
Total (95% CI)		483		281	100.0%	5.33 [1.24, 22.90]	
Total events	242		51				

Heterogeneity: Tau² = 1.02; Chi² = 12.24, df = 1 (P = 0.0005); I² = 92%
Test for overall effect: Z = 2.25 (P = 0.02)
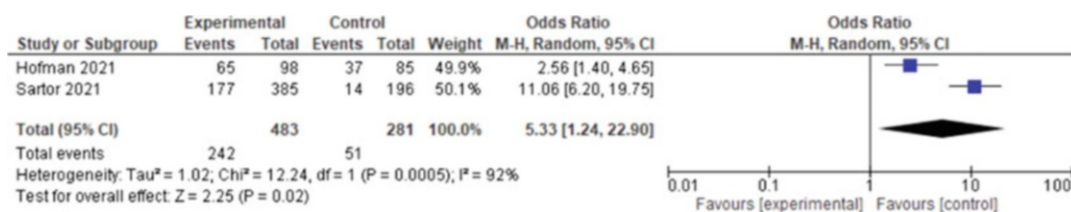
Fig. 17.5 Forest plot of the hazard ratios from the two, multicenter, prospective trials that demonstrated the efficacy of [177Lu]Lu-PSMA-617 RPT to bring about an objective biochemical response relative to pre-determined control therapy

[177Lu]Lu-PSMA-617 plus standard-of-care or standard-of-care alone [3]. With a median follow-up of 20.9 months, the arm that received [177Lu]Lu-PSMA-617 plus standard of care had improved radiographic progression-free survival (8.7 vs. 3.4 months) and improved overall survival (15.3 vs 11.3 months) [3]. Such a gain in overall survival in patients who have been heavily pretreated is remarkable. In an era in which patients are often initially systemically treated with combinations of androgen-deprivation therapy with second-generation antiandrogen agents and/or chemotherapy, the availability of orthogonal therapeutic modalities such as [177Lu]Lu-PSMA-617 is tremendously important for when metastatic patients inevitably progress.

The successful clinical development of [177Lu]Lu-PSMA-617 has opened the door to the use of additional PSMA targeted drugs including radiotherapeutics bearing "next generation" β- and α-emitting radionuclides as well as bispecific T-cell engagers and CAR-T technology [24]. These compounds will undergo clinical testing over the next decade to determine their clinical utility. However, as the use of [177Lu]Lu-PSMA-617 becomes more commonplace in everyday patient care, several clinical questions for treatment teams will need to be addressed.

First, can PSMA-targeted therapy be utilized earlier in the course of treatment for patients with recurrent/advanced prostate cancer? Several studies using 68Ga- and 18F-labeled PSMA-targeting positron emission tomography (PET) agents have demonstrated high rates of prostate cancer detection in patients with biochemically recurrent disease at low PSA values [25, 26]. The expression of PSMA in early-stage disease coupled with the promising detection rates using PSMA-targeted imaging suggest an opportunity for PSMA-targeted RPT prior to novel AR targeted therapy and/or chemotherapy. Although case reports have been published showing preliminary responses in patients with biochemically recurrent disease, several studies in patients with metastatic hormone sensitive disease are ongoing (NCT04443062; NCT04343885; NCT04720157). Ultimately, the implementation of PSMA-targeted RPT earlier in the course of disease must balance efficacy with potential long-term toxicity.

Second, is retreatment with PSMA-targeted RPT safe and feasible? After treatment with [177Lu]Lu-PSMA-617, questions remain regarding the rechallenge of patients with a second course the same or a related PSMA-targeted radiotherapeutics. Preliminary data suggest that retreatment with [177Lu]Lu-PSMA-617 can induce meaningful clinical responses [27]. However, long-term safety remains a concern, so randomized prospective studies will be needed to address this as a potential treatment paradigm. Other PSMA-targeting radiotherapeutics may be an alternative to retreatment with [177Lu]Lu-PSMA-617. To wit, the use of [225Ac]Ac-PSMA-617 after [177Lu]Lu-PSMA-617 showed meaningful clinical activity with moderate toxicity [28]. Future studies will shed additional light on this topic.

And third, what are potential combination treatment strategies with [177Lu]Lu-PSMA-617? Several studies are ongoing testing the combination of PSMA-targeted RPT with stereotactic radiation, PARP inhibition, and immune checkpoint inhibitors. These studies are early phase,

and clinical efficacy—as well as possible additive or synergistic toxicities—remains unknown. Preliminary data combining [^{177}Lu]Lu-PSMA-617 with pembrolizumab showed the combination is safe and produces durable clinical responses [29]. Both preclinical and additional clinical data will be needed to identify appropriate partners for PSMA-targeted radiotherapeutics.

Despite these lingering questions, the RPT of prostate cancer is a budding field. Over the next several years, additional clinical trials will better inform patient care and provide additional life-prolonging agents in the fight against this insidious disease.

17.2.1.2 High-Specific Activity [^{131}I]MIBG

Variants of iodobenzylguanidine, a norepinephrine analog, were initially radiolabeled with iodine-131 to image the canine adrenal medulla [30]. Soon thereafter, similar molecules—particularly the *meta*-isomer of iodobenzylguanidine (MIBG)—were repurposed for myocardial imaging [31]. ^{131}I-labeled MIBG ([^{131}I]MIBG) has been used to treat tumors of neuroendocrine origin, including neuroblastomas, pheochromocytomas, and paragangliomas. The presence of the noradrenalin transporter (NET) seems to play a significant role in the uptake of [^{131}I]MIBG in neuroendocrine tumors [32]. Indeed, the therapeutic uptake of [^{131}I]MIBG through the uptake-1 neuroendocrine transport pathway is much greater than by passive diffusion [33].

RPT with [^{131}I]MIBG is generally indicated for patients with metastatic (stage III or IV) neuroblastoma and unresectable pheochromocytomas and paragangliomas. The European Association of Nuclear Medicine (EANM) guidelines also include metastatic or recurrent medullary thyroid cancer and unresectable carcinoid tumor [34]. However, recent advances in the RPT of unresectable or metastatic midgut neuroendocrine tumors—including the approval of [^{177}Lu]Lu-DOTATATE—limit the role of [^{131}I]MIBG in carcinoid tumors. Prior to therapy with [^{131}I]MIBG, one must document uptake of the agent via imaging using either [^{123}I]MIBG or a low dose of [^{131}I]MIBG.

One of the issues with the conventional preparation of [^{131}I]MIBG is that it contains a significant amount of non-radiolabeled MIBG that will compete with the radiolabeled compound for uptake and thus may reduce the tumor-associated cytotoxicity of the drug [35]. To reduce the amount of unlabeled MIBG administered to patients, a high-specific-activity (HSA, i.e., no-carrier-added) formulation of [^{131}I]MIBG was developed [36]. First-in-human studies demonstrated promising results with increased efficacy over the carrier-added radiopharmaceutical as well as a favorable safety profile [37]. Phase I results of HSA [^{131}I]MIBG in metastatic and/or recurrent pheochromocytomas/paragangliomas also revealed a favorable safety profile, with the majority of adverse events categorized as mild to moderate in severity. A separate analysis suggested that there was a correlation between positive treatment responses and the dose of the radiopharmaceutical that was administered [38].

A subsequent, phase II multicenter trial was performed to assess the safety and efficacy of HSA [^{131}I]MIBG in patients with unresectable or metastatic pheochromocytomas or paragangliomas. This patient population has limited options in terms of treatment at advanced or late stages of disease. The primary endpoint of the study was a 50% reduction in antihypertensive medications following therapy, with secondary endpoints of objective tumor response, biochemical response, overall survival, and safety. Keeping in mind that these are rare tumors, 68 patients received at least one therapeutic dose of HSA [^{131}I]MIBG. Of those patients eligible for analysis, the study demonstrated that 92% of patients had a partial response or stable disease. Additional promising results were reported, including that 25% of patients were able to significantly reduce their antihypertensive medication requirements for at least 6 months following therapy (primary endpoint). The major side effects included nausea (which could be addressed with antinausea medication), myelosuppression, and fatigue [2]. Following the promising results of this study, HSA [^{131}I]MIBG was subsequently approved by the FDA in 2018.

17.2.2 The PSMA RPT Pipeline and Future Directions

17.2.2.1 Other β-Emitting Agents

Beyond [^{177}Lu]Lu-PSMA-617, a number of other scaffolds have been investigated for PSMA-targeted RPT [39–43]. Investigational trials with novel scaffolds have focused on the use of two agents: [^{177}Lu]Lu-PSMA-I&T and [^{177}Lu]Lu-EB-PSMA-617 [19]. Both compounds use the same urea-based pharmacophore to target PSMA as does [^{177}Lu]Lu-PSMA-617; however, the former uses a DOTAGA chelator and a different linker [44], while the latter was designed to increase circulation time by binding to albumin [45].

The efficacy of PSMA-targeted RPT with various ^{177}Lu-labeled agents was investigated in a recent systematic review and meta-analysis [19]. This analysis, which included 24 studies, found that ~44% (39–50%) of patients treated with [^{177}Lu]Lu-EB-PSMA-617 showed a serum PSA decrease of ≥50% with at least an 8-wk interval between therapy and PSA measurement, while 36% (26–47%) of patients showed a similar decrease when treated with [^{177}Lu]Lu-PSMA-I&T [19]. The aggregated response of men treated with more than one cycle of any kind of RPT was 46% (41–51%) for a PSA response of ≥50% [19]. A recent matched-pair study of [^{177}Lu]Lu-PSMA-I&T and [^{177}Lu]Lu-PSMA-617 for the treatment of metastatic castration-resistant prostate cancer patients showed similar median overall survival in both treatment groups (12 months vs 13 months, $P = 0.89$) [46].

With respect to the toxicity of PSMA-targeted RPT, the meta-analysis found that grade 3 and 4 toxicities were generally uncommon [19]. The most common toxicities identified after treatment were 8% (5–12%) for anemia and 1% (0–4%) for nausea, fatigue, diarrhea, and elevated aspartate transaminase levels [19]. In the VISION study, the incidence of toxicities was found to be higher, with grade ≥3 or more toxicities occurring in 52.7% of patients; however, the quality of life in these patients was not adversely affected [3]. In the matched study comparing [^{177}Lu]PSMA-I&T and [^{177}Lu]EB-PSMA-617, the number of grade ≥3 or more toxicities were found to be higher in patients treated with [^{177}Lu]Lu-PSMA-617 (10.9%, 6/55) compared to [^{177}Lu]Lu-PSMA-I&T (1.8%, 1/55). However, the overall toxicity rate was much lower than the VISION study. As such, the results of recent studies support the use of PSMA-targeted RPT with ^{177}Lu-labeled agents for the management of metastatic castration-resistant prostate cancer, which is likely to be further supported as the results of multiple prospective clinical trials become available.

[^{177}Lu]Lu-PSMA-617 is currently also being investigated as a neoadjuvant therapy before radical prostatectomy in the LuTectomy study. The LuTectomy trial is a single-arm study to show safety and potential benefit of RPT, and the initial results presented at the European Association of Urology annual meeting showed positive findings [47]. The UpFrontPSMA and PSMAAddition trials are currently investigating the role of PSMA-targeted RPT in the management of metastatic hormone-sensitive prostate cancer, while the BULLSEYE and ENZA-p trials are investigating its role as a first-line therapy for metastatic castrate-resistant prostate cancer [48–51].

[^{177}Lu]Lu-PSMA-R2 is another urea-based PSMA-targeted small molecular inhibitor that has shown rapid and specific uptake in mice with prostate cancers [52]. A clinical trial (PROter) investigating the use of [^{177}Lu]Lu-PSMA-R2 in patients with PSMA-positive, progressive, metastatic, castration-resistant prostate cancer was halted in Phase I based on a sponsor decision, and no further study results are available [53]. However, the altered biodistribution of [^{177}Lu]Lu-PSMA-R2 compared to other agents (i.e., there is minimal uptake in the salivary glands) may allow the scaffold for [^{177}Lu]Lu-PSMA-R2 to be leveraged for therapy with α-emitting radionuclides.

[^{131}I]I-MIP-1095 is a PSMA-targeted radiotherapeutic that was one of the first agents to be used for treatment of prostate cancer. Iodine-131 is a β-emitting radionuclide with a half-life that is longer (8 days) than lutetium-177; however, it also has more abundant γ emissions that make it more toxic and less safe

[54]. In a study using it for the treatment of patients with CRPC, approximately 61% of the patients showed a PSA decrease of ≥50%, with 25% patients experiencing transient xerostomia and 10.7% experiencing hematological toxicities [54]. A subsequent study showed a PSA response in 70.6% of patients with higher hematological toxicity (13%, grade 3 thrombocytopenia) [55]. In the ARROW trial, the use of [131I]I-MIP-1095 in combination with enzalutamide is being compared to enzalutamide alone in patients with PSMA-avid metastatic castration-resistant prostate cancer who have progressed on abiraterone. Ultimately, [131I]I-MIP-1095 may be a more effective, but also more toxic agent, for PSMA-targeted RPT. At the time of this writing, the agent is no longer being manufactured by the sponsor.

17.2.2.2 α-Emitting Radiopharmaceuticals

The inevitable progression of the vast majority of patients treated with β-emitting targeted radiotherapeutics has sparked interest in the use of compounds bearing radionuclides that emit higher linear-energy-transfer (LET) α-particles. To date, the clinical data with such agents suggest that they are simultaneously more effective *and* more toxic than β-emitting radiotherapeutics.

225Ac-PSMA-617 is the most studied α-emitting, PSMA-targeted agent to date. The first clinical study with 225Ac-PSMA-617 demonstrated complete biochemical and imaging responses to the therapy but with significant xerostomia as a toxicity [56]. The need to balance efficacy with toxicity has become increasingly apparent in larger studies with 225Ac-PSMA-617, in which the toxicities associated with therapy may lead patients to request dose de-escalation or discontinuation despite profound efficacy [57, 58].

The appealing efficacy of 225Ac-PSMA-617 despite its lifestyle-limiting toxicity has spurred exploration into the use of PSMA-targeted radiotherapeutics bearing other α-emitting radionuclides, including bismuth-213. Actinium-225 emits a total of four α-particles during its decay. While this makes it potent, the redistribution of actinium's daughter radionuclides and

their subsequent emission of α-particles in non-target tissues can be problematic. In contrast, other α-particle-emitting radionuclides (such as bismuth-213) emit only a single α-particle per decay, raising the chances that the emission takes place in (and only in) the target tissue. Yet despite the promise of the radionuclide, the first human results with 213Bi-PSMA-617 have been mixed., with higher perfusion-dependent off-target radiation than the corresponding 225Ac-labeled agent Bismuth-213 has been relegated to a secondary radionuclide for PSMA-targeted α-RPT [59]. Along similar lines, Vaidyanathan, et al. have reported on a series of agents that combine efforts to decrease uptake in the lacrimal and salivary glands with the use of the lower-energy, single-α-emitting radionuclide astatine-211 that appear to be promising based on preclinical data [60]. At least for now, it seems that 225Ac-PSMA-617 may still be the best choice for PSMA-targeted α-RPT. Ultimately, whether new generations of scaffolds and new radiometals can reduce toxicity but maintain efficacy will need to be proven in prospective clinical trials.

17.2.2.3 The Development of Response Assessment Criteria

The era of precision oncology has played witness to an exponential growth in the number of targeted treatments. In each case, evaluating early response therapy is essential for the management of the treatment regimen. Initial efforts to develop standardized response evaluation criteria for solid tumors were made by the World Health organization (WHO) in 1979 and resulted in the WHO handbook for reporting results of cancer treatments [61]. In subsequent years, the Southwest Oncology Group (SWOG) developed guidelines to fulfill demands for greater rigor in response and endpoint definitions [62]. In 1994, several organizations involved in clinical research gathered and proposed a new set of guidelines called Response Evaluation Criteria in Solid Tumors (RECIST) 1.0. Those criteria have become widely accepted, which has helped in standardizing the objective recording and reporting of response in solid tumors. In 2009, RECIST 1.0 was updated to version 1.1 [63]. But later, it was demonstrated that the applicability of

RECIST to some malignancies was suboptimal [64]. Fifteen years after the quantitative monitoring of treatment effects with PET was introduced, the first standardized response evaluation criteria for anticancer treatments by PET was proposed: PET Response Criteria in Solid Tumors (PERCIST) [65]. Nevertheless, with the development of new anticancer agents and newer imaging modalities, there is growing evidence that a single response criterion may not fit all malignancies, disease states, and different therapeutic classes.

In metastatic prostate cancer, treatment response is typically evaluated using conventional imaging according to the Prostate Cancer Working Group Criteria 3 (PCWG3) guidelines [66]. The PCWG3 criteria integrates bone a scan (according to the "2 + 2 rule" for skeleton evaluation) and computed tomography (CT) by RECIST 1.1 for soft-tissue evaluation. PSMA-targeted PET/CT is a novel imaging technique that has shown greater detection accuracy in patients with high-risk primary prostate cancer compared to conventional imaging [67]. The FDA has approved the use of [^{68}Ga]Ga-PSMA-11 and [^{18}F]DCFPyL PET/CT in men with prostate cancer in for multiple clinical settings [68]. PSMA PET/CT is increasingly used in clinical practice to monitor the efficacy of various treatments in patients with metastatic prostate cancer. Along these lines, when PSMA PET/CT is performed to evaluate the response to systemic treatments for metastatic CRPC, it is often observed that a decrease in total disease burden can coincide with the appearance of new lesions. This scenario—referred to as a *heterogeneous response*—often leaves the clinician in a dilemma. Around 11% of metastatic CRPC patients treated with ^{177}Lu[Lu]-PSMA exhibit a *heterogeneous response* [69], highlighting the need for standardized response evaluation criteria for PSMA-based imaging.

The first standardized criteria for evaluating the response of metastatic prostate cancer to systemic treatments using PSMA PET/CT was recently proposed: Response Evaluation Criteria In PSMA-imaging (RECIP) 1.0 [69]. RECIP was developed as an evidence-based composite response classification that combines the PSMA-positive total tumor volume (PSMA-VOL) and the occurrence of new lesions. The criteria were developed using a retrospective cohort of 124 men with metastatic CRPC treated with [^{177}Lu]Lu-PSMA who received PSMA-PET/CT at baseline and at 12 weeks after 2 cycles of treatment. The authors found that patients with a response in PSMA-VOL (decline ≥30%) without new lesions had longer survival compared to patients with response in PSMA-VOL and new lesions. On this basis, they classified patients with response in PSMA-VOL and new lesions as having stable disease (RECIP-SD), while patients with response in PSMA-VOL without new lesions as having partial response (RECIP-PR). Further, patients with progression in PSMA-VOL (increase ≥20%) and new lesions had shorter survival times compared to patients with progression in PSMA-VOL without new lesions. On that basis, patients with progression in PSMA-VOL without new lesions were classified as having stable disease (RECIP-SD), while those with progression in PSMA-VOL and new lesions as progressive disease (RECIP-PD). A detailed definition of RECIP 1.0 is provided in Table 17.1.

Table 17.1 Definition of RECIP criteria

RECIP-CR	Absence of any PSMA-uptake on follow-up PET scan
RECIP-PR	≥30% decrease in PSMA-VOL without appearance of new lesions[a]
RECIP-PD	≥20% increase in PSMA-VOL with appearance of new lesions
RECIP-SD	<30% decrease in PSMA-VOL with/without appearance of new lesions *or* ≥30% decrease in PSMA-VOL with appearance of new lesions *or* <20% increase in PSMA-VOL with/without appearance of new lesions *or* ≥20% increase in PSMA-VOL without appearance of new lesions

[a]New lesion on iPET was defined as focal uptake of PSMA-ligand (i) higher than surrounding background, (ii) with tumor SUV_{max} > blood-pool SUV_{max}, (iii) which was not present on bPET (tumor SUV_{max} < blood-pool SUV_{max}), and (iiii) tumor uptake was not attributable to physiological uptake or known pitfalls

Established response criteria such as RECIST [70], PCWG3 [66], and PERCIST [71] were developed prior to the implementation of PSMA-based imaging, so their applicability to PSMA PET has required testing. A multicenter retrospective study investigated the accuracy of five criteria for response evaluation using PSMA PET/CT in men with metastatic CRPC treated with [^{177}Lu]Lu-PSMA [72]. The criteria compared included RECIST 1.1, adapted PCWG3, adapted PERCIST, PSMA PET Progression (PPP) [73], and RECIP. RECIP was found to have highest inter-reader reliability (with 90% agreement) and the highest association with overall survival. RECIP classified a significantly smaller percentage of patients as having PD compared to aPCWG3, aPERCIST, and PPP (32% vs 52–58%). Those results are in keeping with a higher risk of death for PD vs no-PD according to RECIP (HR: 4.2 vs 2.5–2.7). Such findings suggest that PCWG3, PERCIST, and PPP overcall progression. That study also confirmed the limited role of RECIST 1.1, even in patients with late-stage metastatic castration-resistant prostate cancer who are candidates for ^{177}Lu-PSMA RPT. Only 65% of patients had measurable disease, and the number was higher compared to that reported in the VISION trial (i.e., 43% of patients had measurable disease by RECIST 1.1) [3]. This difference relative to VISION was most likely due to the higher prevalence of nodal involvement (81% vs 50% nodal metastases).

Several studies have demonstrated the prognostic value of quantitative changes in PSMA-VOL in PSMA PET/CT on overall survival [74]. As a result, changes in PSMA-VOL were integrated in the initial proposal of RECIP [69]. The manual segmentation of whole-body tumor lesions in the PSMA PET of metastatic CRPC is time consuming. Several semi-automatic and automatic segmentation software tools have been proposed to calculate PSMA-VOL [75, 76]; however, their implementation in clinical practice has not yet been realized. In the meantime, the expanded availability of PSMA-targeted PET radiotracers and the recent US FDA approval of [^{177}Lu]Lu-PSMA-617 will undoubtedly increase the number of patients undergoing PSMA PET/CT for response evaluation.

To meet the need for standardized response criteria in PSMA PET/CT in clinical practice, two different approaches to the RECIP criteria were recently introduced: visual RECIP and quantitative RECIP (Gafita, et al., unpublished). While quantitative RECIP uses the quantitative analysis of changes in PSMA-VOL as initially proposed [69], visual RECIP integrates the visual interpretation of responses in PSMA-VOL by nuclear medicine physicians. The authors found a 95% agreement between quantitative and visual RECIP for the identification of clinically relevant PD vs. non-PD; however, the inter-reader agreement was higher for quantitative RECIP (92%) compared to visual RECIP (83%). Ultimately, the authors concluded that while visual RECIP can be easily incorporated into clinical practice and trials, the use of quantitative RECIP is currently limited to the research environment.

17.2.3 Fibroblast-Activation Protein (FAP) and RPT

Cancer-associated fibroblasts (CAFs) are cells that are involved in the metabolic and immune-mediated modification of the tumor microenvironment (TME), provide resistance to common antitumor strategies, and express large amounts of the cell surface protein fibrinogen-activating protein (FAP) [77]. Given these intriguing roles, investigations into the use of CAF-targeted radiolabeled antibodies emerged as early as the 1990s [78]. These early studies laid the groundwork for the peptide-based CAF-targeted radiotracers that are currently in clinical development [79]. More recently still, small molecule-based FAP-targeting radiotracers have begun trials in human subjects and spurred a dramatic expansion in FAP-targeted theranostics and therapeutics [80]. In the ensuing pages, we will provide a brief overview of the FAP-targeted radiotracers that are currently being explored for the imaging and therapy of a wide spectrum of

solid tumors. We will also briefly discuss recent developments in radiopharmaceutical chemistry that may enhance the efficacy of the FAP-targeted radiotherapeutics in the future.

17.2.3.1 FAP-Targeted Molecular Imaging

One of the first small molecule-based PET radiotracers, [^{68}Ga]Ga-FAPI-04, was developed and preclinically evaluated by the Heidelberg group. The radiotracer demonstrated good stability in human serum and slow excretion. Even more importantly, [^{68}Ga]Ga-FAPI-04 produced excellent tumor-to-blood ratios up to 24 h post-injection in mice bearing FAP-expressing xenografts as well as low renal uptake. The authors also used the tracer to image two patients with breast cancer, demonstrating increased radiotracer accumulation in sites of disease as well as excellent tumor-to-healthy tissue contrast. One patient was also treated using a low dose (2.9 GBq) of a therapeutic counterpart [^{90}Y]Y-FAPI-04, resulting in a reduction in pain medication [81].

Those favorable results triggered further investigations into ^{68}Ga-labeled compounds—most notably ^{68}Ga-labeled FAPI-04 and FAPI-46—with the latter agent achieving markedly higher tumor-to-blood, tumor-to-liver, and tumor-to-muscle activity concentration ratios [82]. Kratochwil and coworkers were among the first to perform FAP-targeted PET in a larger cohort of patients with various solid tumors [83]. High levels of [^{68}Ga]Ga-FAPI-04 uptake were noted in sarcoma, esophageal cancer, cholangiocarcinoma, lung cancer, and breast cancer. Furthermore, given the rather low background uptake of the radiotracer, excellent contrast (i.e., tumor-to-background ratios >6) was achieved as well, suggesting that [^{68}Ga]Ga-FAPI-04 could be used as an imaging agent across a number of cancers [83].

Not surprisingly, ^{68}Ga-FAPI-04 has also been extensively compared to the workhorse in nuclear oncology: 2-deoxy-2-[^{18}F]fluoro-D-glucose ([^{18}F]FDG). FAP PET is less susceptible to false-positive uptake in sites of inflammation, a known pitfall when interpreting [^{18}F]FDG PET

[84]. A head-to-head comparison of 123 patients imaged with both [^{18}F]FDG and [^{68}Ga]Ga-FAPI-04 demonstrated superior detection efficiency of the FAP-targeted agent across multiple cancer types, with the exception of lymphoma and myeloma [85]. These results have fueled considerable excitement for the development and translation of FAP-targeted radiotracers.

The potential advantages of FAP PET over [^{18}F]FDG PET [83] have let to further comparative studies. For example, a direct comparison between both radiopharmaceuticals in patients with head and neck cancer (Fig. 17.1) demonstrated that FAP PET yielded an improved read-out for the malignant primary in cancers of unknown origin upon initial diagnostic workup. Here, one possible explanation may be that chronic inflammation in the Waldeyer's tonsillar ring hampers the precise assessment of the primary tumor with [^{18}F]FDG [86] (Fig. 17.6). Further applications of FAP PET include gastric carcinoma, as certain subtypes such as mucinous (or signet ring) cancers are known to demonstrate almost no uptake of [^{18}F]FDG. Further drawbacks of FDG-PET relative to FAP-PET include greater difficulty in interpreting peritoneal carcinomatosis observed in patients with gastric cancer [86, 87]. Finally, FAP-targeted PET demonstrated a substantially higher detection rate along with capabilities to monitor treatment, rendering FAPI PET/CT a non-invasive biomarker for initial workup and response assessment in certain scenarios for certain tumor types [87].

Targeting CAFs may be particularly useful in primary or secondary liver cancers—such as hepatocellular carcinoma—in which [^{18}F]FDG is less useful due to its high background uptake. To wit, a comparative study of [^{68}Ga]Ga-FAPI-04 and [^{18}F]FDG in 29 patients demonstrated that tumor-to-background contrast was significantly elevated for [^{68}Ga]FAPI-04 and was also tightly linked to tumor size [88]. In a more systematic approach that included guideline-compatible imaging modalities as comparators, Guo and coworkers reported on equivalent read-out capabilities of contrast-enhanced CT and magnetic resonance in patients with primary liver
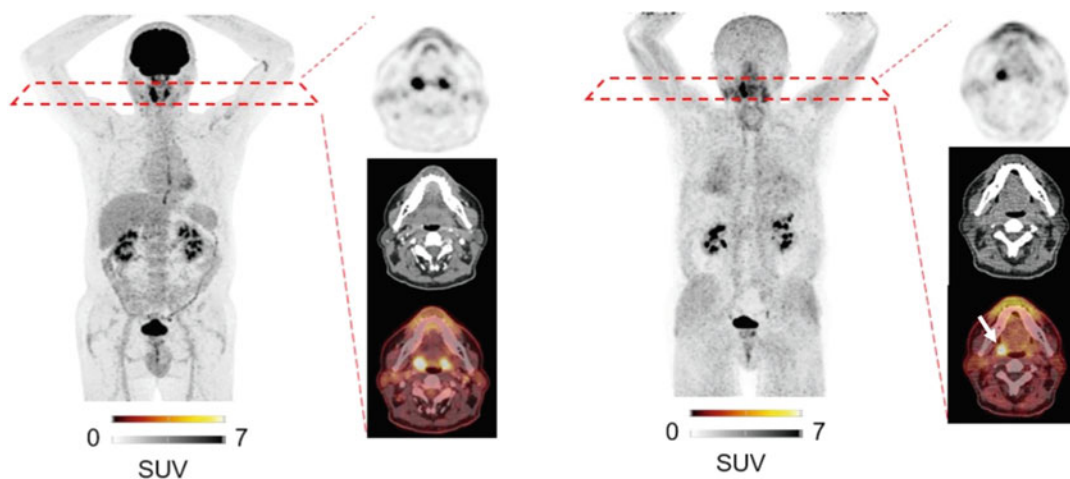
Fig. 17.6 Head-to-head comparison of [^{18}F]FDG and [^{68}Ga]Ga-FAPI-04 in a patient diagnosed with head and neck cancer (palatine tonsil carcinoma). While read-out on [^{18}F]FDG PET/CT was hampered by increased background activity (left), [^{68}Ga]Ga-FAPI-04 (right) allowed for the detection of the primary tumor, as seen on transaxial PET (upper row) and PET/CT (lower row, white arrow). (Modified from [86])

tumors (including hepatocellular carcinoma and intrahepatic cholangiocarcinomas) as well as metastatic lesions [89].

While FAP PET with ^{68}Ga-labeled agents clearly has its advantages, it is nonetheless important to acknowledge some of its drawbacks. Along these lines, several limitations of ^{68}Ga-labeled agents compared to radiofluorinated probes include the longer path of positrons emitted by ^{68}Ga compared to ^{18}F, the injection of less activity with ^{68}Ga-based agents, and the limited ability to use delayed imaging protocols due to ^{68}Ga's 68 min half-life [90]. In light of these factors, several ^{18}F-labeled FAP-directed PET agents have emerged in recent years. For example, Lindner et al. introduced [^{18}F]AlF-FAPI-74 [91] and used to image patients with lung cancer, in which it demonstrated excellent tumor-to-background contrast and produced low radiation dose rates to healthy tissues. Those findings may favor the widespread adoption of ^{18}F-based FAP PET due to the possibility of centralized large-scale production [92].

Despite the increasing use of PET in and even outside of academic centers, PET scanners may not always be available. Therefore, FAP-targeted imaging agents labeled with radionuclides for single-photon emission computed tomography (SPECT) are also needed. For instance, Slania et al. developed ^{111}In-labelled (4-quinolinoyl)-glycyl-2-cyanopyrrolidine-based small molecules for targeting FAP and investigated those compounds in different cell lines and mouse xenograft models, in which they provide good imaging contrast [93]. Moreover, ^{99m}Tc-labeled FAP-targeting compounds (e.g., FAPI-34) could also be used as part of theranostic pairs ^{188}Re-labeled probes [94].

17.2.3.2 FAP-Targeted RPT

Beyond improved read-outs and higher detection rates in patients with a variety of tumors, FAP PET could also help identify potential candidates for RPT with FAP-targeted agents bearing therapeutic radionuclides [19, 95]. Along these lines, FAP-targeted radiotherapeutics labeled with ^{177}Lu, ^{225}Ac, and ^{153}Sm have already been developed and evaluated with preclinical and clinical use [80]. Ballal and coworkers, for example, recently reported on 15 patients with radioiodine-refractory thyroid cancer imaged with [^{68}Ga]Ga-DOTA.SA.FAPi and subsequently treated with [^{177}Lu]Lu-DOTAGA.(SA.FAPi)$_2$. Over 45 treatment cycles, the median

injected activity was 8.2 ± 2.7 GBq, yielding a whole-body effective dose of $1.62E^{-01} ± 1.53E^{-02}$ mSv/MBq. The authors reported a significant drop of thyroglobulin, while disease control included partial response and stable disease in 7/15 patients. Importantly, no grade ≥III events were recorded, suggesting that [177Lu]Lu-DOTAGA.(SA.FAPi)$_2$ may be suitable for patients with radioiodine-refractory disease [96].

The same group also recently reported a case study of a breast cancer patient who had demonstrated progressive disease under all previous treatment lines. After FAP-directed PET demonstrated avidity, the patient received 3.2 GBq [177Lu]Lu-DOTAGA.(SA.FAPi)$_2$. Post-therapeutic dosimetry performed via SPECT demonstrated concordant findings with the pre-therapeutic FAPI-directed PET. Calculated tumor doses were 1.48E mGy/MBq and 3.46 mGy/MBq for the brain lesions, indicating doses of up to 11.07 Gy for the brain metastases. No adverse events up to 4 weeks after therapy were recorded, and the patient reported a decrease of headaches [97].

FAP-targeted radiotherapeutics labeled with 90Y have also attracted attention due the radionuclide's high-energy (2.27 MeV) β-emission which makes it better suited to patients with high tumor burdens. To wit, Ferdinandus et al. reported a feasibility study in which 9 subjects diagnosed with soft-tissue or bone sarcoma with administered [90Y]FAPI-46. Post-treatment bremsstrahlung scintigraphy revealed uptake in the cancerous lesions of 7/9 of subjects. A median dose of 1.28 Gy/GBq to the tumors was recorded with hematopoietic-related grade III or IV events (thrombocytopenia and anemia) [98]. More recently, Fendler et al. screened 119 subjects with FAPI PET, with 21/119 (18%) proving eligible for RPT with [90Y]FAPI-46. The majority of the patients selected for treatment (16/21) were affected with sarcoma, followed by pancreatic ductal adenocarcinoma. After a total of 47 cycles, RECIST assessment revealed disease control in 8/21 (38%) of these patients, including one with partial response and seven with stable disease. The median progression-free survival was 3.4 months; the overall survival was 10 months; and an improved median survival of 14.4 months was noted in subjects achieving stable disease during follow-up. A minority of the subjects (8/21) experienced grade ≥III adverse events, including anemia and thrombocytopenia. Besides progression of disease and the deterioration of the patient's condition, reduced platelets were the main reason for early discontinuation after the first cycle. The authors concluded that FAP-directed RPT must be improved to overcome the high rate of patients experiencing progressive disease or early dropout [99]. Finally, Kratochwil et al. recently expanded upon this idea by administering a 153Sm-labeled variant of FAPI-46 to a sarcoma patient, ultimately leading to disease stabilization [100].

As we have noted, FAP-directed RPT must clearly be optimized to provide a more substantial antitumor effect [99]. There is an urgent need for novel agents that produce longer tumor retention and achieve higher tumor doses [80]. For example, Zhao et al. created a novel dimeric probe bearing two FAP-targeting moieties connected by mini-PEG: [68Ga]Ga-DOTA-2P(FAPI)$_2$. A first-in-human trial of the agent revealed that it produces higher uptake in cancer lesions compared to [68Ga]Ga-FAPI-46 [101]. In theory, radiotherapeutics with the same structure but labeled with different nuclides could exhibit longer intratumoral retention time and thus enhanced therapeutic efficacy. Another recent development in the field is the introduction of FAP-targeted probes bearing the albumin-targeting dye Evans Blue (EB), resulting in prolonged circulation of the molecule. Several EB-bearing FAP-targeted radiotherapeutics have demonstrated excellent in vitro and in vivo for CAFs. [177Lu]Lu-EB-FAPI-B1, for example, produced a reduction in tumor size in a preclinical model, suggesting that it may be a promising candidate to overcome the current limitations of [90Y]Y-FAPI-46 [99, 102].

17.3 Perspective

Though the future is bright for small molecule-based theranostics, significant work remains, including optimization of the use of existing agents and the development of new agents. For

example, the VISION trial demonstrated only a 4 months increase in overall survival for RPT with [^{177}Lu]Lu-PSMA-617 compared to conventional approaches. Furthermore, others are working to exploit new targets—such as neurotensin (touted as "new SSTR") and poly(ADP-ribose) polymerase (PARP)—for RPT with small molecule-based probes, as discussed in several recent reviews. Two generalizable challenges for small-molecule radiotheranostics (as demonstrated by the FAP-targeting probes) are their rapid pharmacokinetic profiles and their brief on-target residence times. Thankfully, small molecules can be readily manipulated and can be optimized through medicinal chemistry. Along these lines, strategies such as the creation of homo- and heterobivalent ligands may enhance tumor residence times. The development of probes containing albumin-binding moieties has also been attempted to increase circulation and tumor residence times, though this may also increase undesired off-target effects.

Another important consideration for RPT—though this does not necessarily only apply to small molecules—is that tumors are heterogeneous and can develop resistance. With respect to the latter, tumors can lose target via de-differentiation (e.g., in the case of PSMA), or the CAFs eliminated by FAP-targeted agents can eventually return to promote tumor maintenance. Consequently, it may be best to treat patients with radiotherapeutics earlier in the course of their disease, before resistance has had a chance to take root. Furthermore, combination therapies in which RPT is paired with, for example, PARP inhibitors or immunotherapies are currently ongoing. The combination of small molecule- and antibody-based radiotherapeutics in an alternating dosing regimen may also warrant exploration, as it could capture the best properties of each. Finally, it will be important to optimize both patient selection and dosing schedules, processes that may be managed using artificial intelligence (a tool that may be used in radiopharmaceutical discovery as well).

In the end, radiotherapeutics enhance quality of life. That has been demonstrated for all of the agents currently in the clinic. Indeed, it was the original charge for ^{223}RaCl$_2$ (Xofigo®), which surprisingly also demonstrated the capacity to prolong life. But that prolongation (as with the PSMA-targeted and other agents discussed above) remains unacceptably brief. Nevertheless, in the coming years—as new targets are uncovered through mining the cancer proteome, radiolabeling strategies continue to improve, novel therapeutic isotopes are increasingly leveraged, and more is understood about the pharmacokinetic effects of chelators and charge—we believe that we will be measuring these improvements to overall survival in years rather than months.

17.4   The Bottom Line

- Given their pharmacokinetic advantages, small molecules are likely to remain an important platform for radiotherapeutics.
- Small-molecule RPT with agents targeting PSMA are now a standard-of-care for patients with metastatic, castration-resistant prostate cancer who have failed chemotherapy.
- There is currently a rich pipeline of PSMA-targeted RPT agents, including several bearing new scaffolds and α-emitting radionuclides.
- Response assessment criteria are evolving for RPT, particularly with respect to PSMA-targeted agents.
- The small-molecule RPT agent [^{131}I]MIBG provides a treatment option for selected patients with metastatic or unresectable neuroblastoma, pheochromocytoma, or paraganglioma.
- RPT agents targeting FAP are currently under investigation and may have efficacy against a range of cancers.
- It will be incumbent upon the field to leverage clinical data and advanced imaging methods to maximize the benefits of RPT with small-molecule radiotherapeutics.

References

1. Solnes LB, Werner RA, Jones KM, Sadaghiani MS, Bailey CR, Lapa C, et al. Theranostics: leveraging molecular imaging and therapy to impact patient management and secure the future of nuclear medicine. J Nucl Med. 2020;61(3):311–8.

2. Pryma DA, Chin BB, Noto RB, Dillon JS, Perkins S, Solnes L, et al. Efficacy and safety of high-specific-activity (131)I-MIBG therapy in patients with advanced pheochromocytoma or paraganglioma. J Nucl Med. 2019;60(5):623–30.

3. Sartor O, de Bono J, Chi KN, Fizazi K, Herrmann K, Rahbar K, et al. Lutetium-177-PSMA-617 for metastatic castration-resistant prostate cancer. N Engl J Med. 2021;385(12):1091–103.

4. Rowe SP, Pomper MG. Molecular imaging in oncology: current impact and future directions. CA Cancer J Clin. 2022;72(4):333–52.

5. Barinka C, Rojas C, Slusher B, Pomper M. Glutamate carboxypeptidase II in diagnosis and treatment of neurologic disorders and prostate cancer. Curr Med Chem. 2012;19(6):856–70.

6. Horoszewicz JS, Kawinski E, Murphy GP. Monoclonal antibodies to a new antigenic marker in epithelial prostatic cells and serum of prostatic cancer patients. Anticancer Res. 1987;7(5B):927–35.

7. Sodee DB, Conant R, Chalfant M, Miron S, Klein E, Bahnson R, et al. Preliminary imaging results using In-111 labeled CYT-356 (Prostascint) in the detection of recurrent prostate cancer. Clin Nucl Med. 1996;21(10):759–67.

8. Chang SS, Reuter VE, Heston WD, Bander NH, Grauer LS, Gaudin PB. Five different anti-prostate-specific membrane antigen (PSMA) antibodies confirm PSMA expression in tumor-associated neovasculature. Cancer Res. 1999;59(13):3192–8.

9. Vallabhajosula S, Kuji I, Hamacher KA, Konishi S, Kostakoglu L, Kothari PA, et al. Pharmacokinetics and biodistribution of 111In- and 177Lu-labeled J591 antibody specific for prostate-specific membrane antigen: prediction of 90Y-J591 radiation dosimetry based on 111In or 177Lu? J Nucl Med. 2005;46(4):634–41.

10. Tagawa ST, Milowsky MI, Morris M, Vallabhajosula S, Christos P, Akhtar NH, et al. Phase II study of Lutetium-177-labeled anti-prostate-specific membrane antigen monoclonal antibody J591 for metastatic castration-resistant prostate cancer. Clin Cancer Res. 2013;19(18):5182–91.

11. Ballangrud AM, Yang WH, Charlton DE, McDevitt MR, Hamacher KA, Panageas KS, et al. Response of LNCaP spheroids after treatment with an alpha-particle emitter (213Bi)-labeled anti-prostate-specific membrane antigen antibody (J591). Cancer Res. 2001;61(5):2008–14.

12. Carter RE, Feldman AR, Coyle JT. Prostate-specific membrane antigen is a hydrolase with substrate and pharmacologic characteristics of a neuropeptidase. Proc Natl Acad Sci U S A. 1996;93(2):749–53.

13. Jackson PF, Cole DC, Slusher BS, Stetz SL, Ross LE, Donzanti BA, et al. Design, synthesis, and biological activity of a potent inhibitor of the neuropeptidase N-acetylated alpha-linked acidic dipeptidase. J Med Chem. 1996;39(2):619–22.

14. Sessions DG, Ogura JH, Ciralsky RH. Late glottic insufficiency. Laryngoscope. 1975;85(6):950–9.

15. Pomper MG, Musachio JL, Zhang J, Scheffel U, Zhou Y, Hilton J, et al. 11C-MCG: synthesis, uptake selectivity, and primate PET of a probe for glutamate carboxypeptidase II (NAALADase). Mol Imaging. 2002;1(2):96–101.

16. Foss CA, Mease RC, Fan H, Wang Y, Ravert HT, Dannals RF, et al. Radiolabeled small-molecule ligands for prostate-specific membrane antigen: in vivo imaging in experimental models of prostate cancer. Clin Cancer Res. 2005;11(11):4022–8.

17. Banerjee SR, Foss CA, Castanares M, Mease RC, Byun Y, Fox JJ, et al. Synthesis and evaluation of technetium-99m- and rhenium-labeled inhibitors of the prostate-specific membrane antigen (PSMA). J Med Chem. 2008;51(15):4504–17.

18. Sadaghiani MS, Sheikhbahaei S, Werner RA, Pienta KJ, Pomper MG, Gorin MA, et al. (177) Lu-PSMA radioligand therapy effectiveness in metastatic castration-resistant prostate cancer: an updated systematic review and meta-analysis. Prostate. 2022;82(7):826–35.

19. Sadaghiani MS, Sheikhbahaei S, Werner RA, Pienta KJ, Pomper MG, Solnes LB, et al. A systematic review and meta-analysis of the effectiveness and toxicities of lutetium-177-labeled prostate-specific membrane antigen-targeted radioligand therapy in metastatic castration-resistant prostate cancer. Eur Urol. 2021;80(1):82–94.

20. Rahbar K, Ahmadzadehfar H, Kratochwil C, Haberkorn U, Schafers M, Essler M, et al. German multicenter study investigating 177Lu-PSMA-617 radioligand therapy in advanced prostate cancer patients. J Nucl Med. 2017;58(1):85–90.

21. Satapathy S, Mittal BR, Sood A. Visceral metastases as predictors of response and survival outcomes in patients of castration-resistant prostate cancer treated with 177Lu-labeled prostate-specific membrane antigen radioligand therapy: a systematic review and meta-analysis. Clin Nucl Med. 2020;45(12):935–42.

22. Rasul S, Hartenbach M, Wollenweber T, Kretschmer-Chott E, Grubmuller B, Kramer G, et al. Prediction of response and survival after standardized treatment with 7400 MBq (177)Lu-PSMA-617 every 4 weeks in patients with metastatic castration-resistant prostate cancer. Eur J Nucl Med Mol Imaging. 2021;48(5):1650–7.

23. Hofman MS, Emmett L, Sandhu S, Iravani A, Joshua AM, Goh JC, et al. [(177)Lu]Lu-PSMA-617 versus cabazitaxel in patients with metastatic castration-resistant prostate cancer (TheraP): a randomised,

open-label, phase 2 trial. Lancet. 2021;397(10276): 797–804.

24. Wang F, Li Z, Feng X, Yang D, Lin M. Advances in PSMA-targeted therapy for prostate cancer. Prostate Cancer Prostatic Dis. 2022;25(1):11–26.

25. Calais J, Ceci F, Eiber M, Hope TA, Hofman MS, Rischpler C, et al. (18)F-fluciclovine PET-CT and (68)Ga-PSMA-11 PET-CT in patients with early biochemical recurrence after prostatectomy: a prospective, single-centre, single-arm, comparative imaging trial. Lancet Oncol. 2019;20(9):1286–94.

26. Rowe SP, Campbell SP, Mana-Ay M, Szabo Z, Allaf ME, Pienta KJ, et al. Prospective evaluation of PSMA-targeted (18)F-DCFPyL PET/CT in men with biochemical failure after radical prostatectomy for prostate cancer. J Nucl Med. 2020;61(1):58–61.

27. Violet J, Sandhu S, Iravani A, Ferdinandus J, Thang SP, Kong G, et al. Long-term follow-up and outcomes of retreatment in an expanded 50-patient single-center phase II prospective trial of (177)Lu-PSMA-617 theranostics in metastatic castration-resistant prostate cancer. J Nucl Med. 2020;61(6): 857–65.

28. Feuerecker B, Tauber R, Knorr K, Heck M, Beheshti A, Seidl C, et al. Activity and adverse events of actinium-225-PSMA-617 in advanced metastatic castration-resistant prostate cancer after failure of lutetium-177-PSMA. Eur Urol. 2021;79(3): 343–50.

29. Aggarwal RR, Sam SL, Koshkin VS, Small EJ, Feng FY, Kouchkovsky ID, et al. Immunogenic priming with 177Lu-PSMA-617 plus pembrolizumab in metastatic castration resistant prostate cancer (mCRPC): a phase 1b study. J Clin Oncol. 2021;39 (15_suppl):5053.

30. Wieland DM, Wu J, Brown LE, Mangner TJ, Swanson DP, Beierwaltes WH. Radiolabeled adrenergi neuron-blocking agents: adrenomedullary imaging with [131I]iodobenzylguanidine. J Nucl Med. 1980;21(4):349–53.

31. Wieland DM, Brown LE, Rogers WL, Worthington KC, Wu JL, Clinthorne NH, et al. Myocardial imaging with a radioiodinated norepinephrine storage analog. J Nucl Med. 1981;22(1):22–31.

32. Koopmans KP, Neels ON, Kema IP, Elsinga PH, Links TP, de Vries EG, et al. Molecular imaging in neuroendocrine tumors: molecular uptake mechanisms and clinical results. Crit Rev Oncol Hematol. 2009;71(3):199–213.

33. Smets LA, Loesberg C, Janssen M, Metwally EA, Huiskamp R. Active uptake and extravesicular storage of m-iodobenzylguanidine in human neuroblastoma SK-N-SH cells. Cancer Res. 1989;49(11): 2941–4.

34. Giammarile F, Chiti A, Lassmann M, Brans B, Flux G. EANM. EANM procedure guidelines for 131I-meta-iodobenzylguanidine (131I-mIBG) therapy. Eur J Nucl Med Mol Imaging. 2008;35(5):1039–47.

35. Kayano D, Kinuya S. Current consensus on I-131 MIBG therapy. Nucl Med Mol Imaging. 2018;52 (4):254–65.

36. Mairs RJ, Russell J, Cunningham S, O'Donoghue JA, Gaze MN, Owens J, et al. Enhanced tumour uptake and in vitro radiotoxicity of no-carrier-added [131I] meta-iodobenzylguanidine: implications for the targeted radiotherapy of neuroblastoma. Eur J Cancer. 1995;31A(4):576–81.

37. Coleman RE, Stubbs JB, Barrett JA, de la Guardia M, Lafrance N, Babich JW. Radiation dosimetry, pharmacokinetics, and safety of ultratrace Iobenguane I-131 in patients with malignant pheochromocytoma/paraganglioma or metastatic carcinoid. Cancer Biother Radiopharm. 2009;24(4):469–75.

38. Noto RB, Pryma DA, Jensen J, Lin T, Stambler N, Strack T, et al. Phase 1 study of high-specific-activity I-131 MIBG for metastatic and/or recurrent pheochromocytoma or paraganglioma. J Clin Endocrinol Metab. 2018;103(1):213–20.

39. Violet J, Sandhu S, Iravani A, Ferdinandus J, Thang S-P, Kong G, et al. Long-term follow-up and outcomes of retreatment in an expanded 50-patient single-center phase II prospective trial of 177Lu-PSMA-617 theranostics in metastatic castration-resistant prostate cancer. J Nucl Med. 2020;61(6): 857–65.

40. Hofman MS, Violet J, Hicks RJ, Ferdinandus J, Thang SP, Akhurst T, et al. [177Lu]-PSMA-617 radionuclide treatment in patients with metastatic castration-resistant prostate cancer (LuPSMA trial): a single-centre, single-arm, phase 2 study. Lancet Oncol. 2018;19(6):825–33.

41. Hofman MS, Emmett L, Sandhu S, Iravani A, Joshua AM, Goh JC, et al. [177Lu] Lu-PSMA-617 versus cabazitaxel in patients with metastatic castration-resistant prostate cancer (TheraP): a randomised, open-label, phase 2 trial. Lancet. 2021;397(10276): 797–804.

42. Schuchardt C, Zhang J, Kulkarni HR, Chen X, Müller D, Baum RP. Prostate-specific membrane antigen radioligand therapy using ^{177}Lu-PSMA I&T and ^{177}Lu-PSMA-617 in patients with metastatic castration-resistant prostate cancer: comparison of safety, biodistribution, and dosimetry. J Nucl Med. 2022;63(8):1199–207.

43. Calais J, Gafita A, Eiber M, Armstrong WR, Gartmann J, Thin P, et al. Prospective phase 2 trial of PSMA-targeted molecular RadiothErapy with 177Lu-PSMA-617 for metastatic Castration-reSISTant Prostate Cancer (RESIST-PC): efficacy results of the UCLA cohort. J Nucl Med. 2021;62 (10):1440–6.

44. Weineisen M, Schottelius M, Simecek J, Baum RP, Yildiz A, Beykan S, et al. 68Ga- and 177Lu-labeled PSMA I&T: optimization of a PSMA-targeted theranostic concept and first proof-of-concept human studies. J Nucl Med. 2015;56(8):1169–76.

45. Zang J, Fan X, Wang H, Liu Q, Wang J, Li H, et al. First-in-human study of (177)Lu-EB-PSMA-617 in patients with metastatic castration-resistant prostate cancer. Eur J Nucl Med Mol Imaging. 2019;46(1):148–58.

46. Hartrampf PE, Weinzierl F-X, Buck AK, Rowe SP, Higuchi T, Seitz AK, et al. Matched-pair analysis of [177Lu] Lu-PSMA I&T and [177Lu] Lu-PSMA-617 in patients with metastatic castration-resistant prostate cancer. Eur J Nucl Med Mol Imaging. 2022;49:1–8.

47. Dhiantravan N, Violet J, Eapen R, Alghazo O, Scalzo M, Jackson P, et al. Clinical trial protocol for LuTectomy: a single-arm study of the dosimetry, safety, and potential benefit of 177Lu-PSMA-617 prior to prostatectomy. Eur Urol Focus. 2021;7(2):234–7.

48. Azad A, Dhiantravan N, Emmett L, Joshua AM, Vela I, Pattison DA, et al. UpFrontPSMA: a randomized phase II study of sequential 177Lu-PSMA617 and docetaxel versus docetaxel in metastatic hormone-naïve prostate cancer (mHNPC). J Clin Oncol. 2021;39(6_suppl):TPS180-TPS.

49. Sartor AO, Tagawa ST, Saad F, Bono JSD, Feng FY, Fizazi K, et al. PSMAddition: a phase 3 trial to compare treatment with 177Lu-PSMA-617 plus standard of care (SOC) versus SOC alone in patients with metastatic hormone-sensitive prostate cancer. J Clin Oncol. 2022;40(6_suppl):TPS210-TPS.

50. Privé BM, Janssen MJR, van Oort IM, Muselaers CHJ, Jonker MA, van Gemert WA, et al. Update to a randomized controlled trial of lutetium-177-PSMA in oligo-metastatic hormone-sensitive prostate cancer: the BULLSEYE trial. Trials. 2021;22(1):768.

51. Emmett L, Subramaniam S, Zhang AY, Martin AJ, Yip S, Crumbaker M, et al. ENZA-p: a randomized phase II trial using PSMA as a therapeutic agent and prognostic indicator in men with metastatic castration-resistant prostate cancer treated with enzalutamide (ANZUP 1901). J Clin Oncol. 2021;39(6_suppl):TPS177-TPS.

52. Kassis AI, Adelstein SJ. Radiobiologic principles in radionuclide therapy. J Nucl Med. 2005;46 (1 suppl):4S–12S.

53. Clinicaltrials.gov. 177Lu-PSMA-R2 in patients with PSMA positive progressive, metastatic, castration resistant prostate cancer (PROter) https://clinicaltrials.gov/ct2/show/NCT034908382022

54. Zechmann CM, Afshar-Oromieh A, Armor T, Stubbs JB, Mier W, Hadaschik B, et al. Radiation dosimetry and first therapy results with a 124I/131I-labeled small molecule (MIP-1095) targeting PSMA for prostate cancer therapy. Eur J Nucl Med Mol Imaging. 2014;41(7):1280–92.

55. Afshar-Oromieh A, Haberkorn U, Zechmann C, Armor T, Mier W, Spohn F, et al. Repeated PSMA-targeting radioligand therapy of metastatic prostate cancer with 131I-MIP-1095. Eur J Nucl Med Mol Imaging. 2017;44(6):950–9.

56. Kratochwil C, Bruchertseifer F, Giesel FL, Weis M, Verburg FA, Mottaghy F, et al. 225Ac-PSMA-617 for PSMA-targeted alpha-radiation therapy of metastatic castration-resistant prostate cancer. J Nucl Med. 2016;57(12):1941–4.

57. Kratochwil C, Bruchertseifer F, Rathke H, Bronzel M, Apostolidis C, Weichert W, et al. Targeted alpha-therapy of metastatic castration-resistant prostate cancer with (225)Ac-PSMA-617: dosimetry estimate and empiric dose finding. J Nucl Med. 2017;58(10):1624–31.

58. Kratochwil C, Bruchertseifer F, Rathke H, Hohenfellner M, Giesel FL, Haberkorn U, et al. Targeted alpha-therapy of metastatic castration-resistant prostate cancer with (225)Ac-PSMA-617: swimmer-plot analysis suggests efficacy regarding duration of tumor control. J Nucl Med. 2018;59(5):795–802.

59. Kratochwil C, Schmidt K, Afshar-Oromieh A, Bruchertseifer F, Rathke H, Morgenstern A, et al. Targeted alpha therapy of mCRPC: dosimetry estimate of (213)Bismuth-PSMA-617. Eur J Nucl Med Mol Imaging. 2018;45(1):31–7.

60. Vaidyanathan G, Mease RC, Minn I, Choi J, Chen Y, Shallal H, et al. Synthesis and preliminary evaluation of (211)At-labeled inhibitors of prostate-specific membrane antigen for targeted alpha particle therapy of prostate cancer. Nucl Med Biol. 2021;94–95:67–80.

61. Organization WH. WHO handbook for reporting results of cancer treatment. World Health Organization; 1979.

62. Green S, Weiss GR. Southwest Oncology Group standard response criteria, endpoint definitions and toxicity criteria. Investig New Drugs. 1992;10(4):239–53.

63. Eisenhauer EA, Therasse P, Bogaerts J, Schwartz LH, Sargent D, Ford R, et al. New response evaluation criteria in solid tumours: revised RECIST guideline (version 1.1). Eur J Cancer (Oxford, England: 1990). 2009;45(2):228–47.

64. Forner A, Ayuso C, Varela M, Rimola J, Hessheimer AJ, de Lope CR, et al. Evaluation of tumor response after locoregional therapies in hepatocellular carcinoma: are response evaluation criteria in solid tumors reliable? Cancer. 2009;115(3):616–23.

65. Wahl RL, Jacene H, Kasamon Y, Lodge MA. From RECIST to PERCIST: evolving considerations for PET response criteria in solid tumors. J Nucl Med. 2009;50(Suppl 1):122s–50s.

66. Scher HI, Morris MJ, Stadler WM, Higano C, Basch E, Fizazi K, et al. Trial design and objectives for castration-resistant prostate cancer: updated recommendations from the prostate cancer clinical trials working group 3. J Clin Oncol. 2016;34(12):1402–18.

67. Hofman MS, Lawrentschuk N, Francis RJ, Tang C, Vela I, Thomas P, et al. Prostate-specific membrane antigen PET-CT in patients with high-risk prostate

cancer before curative-intent surgery or radiotherapy (proPSMA): a prospective, randomised, multicentre study. Lancet. 2020;395(10231):1208–16.

68. FDA approves second PSMA-targeted PET imaging drug for men with prostate cancer 2021. Available from https://www.fda.gov/drugs/drug-safety-and-availability/fda-approves-second-psma-targeted-pet-imaging-drug-men-prostate-cancer

69. Gafita A, Rauscher I, Weber M, Hadaschik B, Wang H, Armstrong WR, et al. Novel framework for treatment response evaluation using PSMA-PET/CT in patients with metastatic castration-resistant prostate cancer (RECIP 1.0): an international multicenter study. J Nucl Med. 2022;63:jnumed.121.263072.

70. Schwartz LH, Litiere S, de Vries E, Ford R, Gwyther S, Mandrekar S, et al. RECIST 1.1-update and clarification: from the RECIST committee. Eur J Cancer (Oxford, England: 1990). 2016;62:132–7.

71. Joo Hyun O, Lodge MA, Wahl RL. Practical PERCIST: a simplified guide to PET response criteria in solid tumors 1.0. Radiology. 2016;280(2):576–84.

72. Gafita A, Rauscher I, Fendler WP, Murthy V, Hui W, Armstrong WR, et al. Measuring response in metastatic castration-resistant prostate cancer using PSMA PET/CT: comparison of RECIST 1.1, aPCWG3, aPERCIST, PPP, and RECIP 1.0 criteria. Eur J Nucl Med Mol Imaging. 2022;49(12):4271–81.

73. Fanti S, Hadaschik B, Herrmann K. Proposal for systemic-therapy response-assessment criteria at the time of PSMA PET/CT imaging: the PSMA PET progression criteria. J Nucl Med. 2020;61(5):678–82.

74. Rosar F, Wenner F, Khreish F, Dewes S, Wagenpfeil G, Hoffmann MA, et al. Early molecular imaging response assessment based on determination of total viable tumor burden in [(68)Ga]Ga-PSMA-11 PET/CT independently predicts overall survival in [(177)Lu]Lu-PSMA-617 radioligand therapy. Eur J Nucl Med Mol Imaging. 2022;49(5):1584–94.

75. Gafita A, Bieth M, Krönke M, Tetteh G, Navarro F, Wang H, et al. qPSMA: semiautomatic software for whole-body tumor burden assessment in prostate cancer using (68)Ga-PSMA11 PET/CT. J Nucl Med. 2019;60(9):1277–83.

76. Seifert R, Herrmann K, Kleesiek J, Schäfers M, Shah V, Xu Z, et al. Semiautomatically quantified tumor volume using (68)Ga-PSMA-11 PET as a biomarker for survival in patients with advanced prostate cancer. J Nucl Med. 2020;61(12):1786–92.

77. Kalluri R. The biology and function of fibroblasts in cancer. Nat Rev Cancer. 2016;16(9):582–98.

78. Scott AM, Wiseman G, Welt S, Adjei A, Lee FT, Hopkins W, et al. A phase I dose-escalation study of sibrotuzumab in patients with advanced or metastatic fibroblast activation protein-positive cancer. Clin Cancer Res. 2003;9(5):1639–47.

79. Zboralski D, Hoehne A, Bredenbeck A, Schumann A, Nguyen M, Schneider E, et al. Preclinical evaluation of FAP-2286 for fibroblast activation protein targeted radionuclide imaging and therapy. Eur J Nucl Med Mol Imaging. 2022;49:3651.

80. Li M, Younis MH, Zhang Y, Cai W, Lan X. Clinical summary of fibroblast activation protein inhibitor-based radiopharmaceuticals: cancer and beyond. Eur J Nucl Med Mol Imaging. 2022;49(8):2844–68.

81. Lindner T, Loktev A, Altmann A, Giesel F, Kratochwil C, Debus J, et al. Development of quinoline-based theranostic ligands for the targeting of fibroblast activation protein. J Nucl Med. 2018;59(9):1415–22.

82. Loktev A, Lindner T, Burger EM, Altmann A, Giesel F, Kratochwil C, et al. Development of fibroblast activation protein-targeted radiotracers with improved tumor retention. J Nucl Med. 2019;60(10):1421–9.

83. Kratochwil C, Flechsig P, Lindner T, Abderrahim L, Altmann A, Mier W, et al. (68)Ga-FAPI PET/CT: tracer uptake in 28 different kinds of cancer. J Nucl Med. 2019;60(6):801–5.

84. Lindner T, Giesel FL, Kratochwil C, Serfling SE. Radioligands targeting fibroblast activation protein (FAP). Cancers (Basel). 2021;13(22):5744.

85. Lan L, Liu H, Wang Y, Deng J, Peng D, Feng Y, et al. The potential utility of [(68) Ga]Ga-DOTA-FAPI-04 as a novel broad-spectrum oncological and non-oncological imaging agent-comparison with [(18)F]FDG. Eur J Nucl Med Mol Imaging. 2022;49(3):963–79.

86. Serfling S, Zhi Y, Schirbel A, Lindner T, Meyer T, Gerhard-Hartmann E, et al. Improved cancer detection in Waldeyer's tonsillar ring by (68)Ga-FAPI PET/CT imaging. Eur J Nucl Med Mol Imaging. 2021;48(4):1178–87.

87. Kuten J, Levine C, Shamni O, Pelles S, Wolf I, Lahat G, et al. Head-to-head comparison of [(68) Ga]Ga-FAPI-04 and [(18)F]-FDG PET/CT in evaluating the extent of disease in gastric adenocarcinoma. Eur J Nucl Med Mol Imaging. 2022;49(2):743–50.

88. Wang H, Zhu W, Ren S, Kong Y, Huang Q, Zhao J, et al. (68)Ga-FAPI-04 versus (18)F-FDG PET/CT in the detection of hepatocellular carcinoma. Front Oncol. 2021;11:693640.

89. Guo W, Pang Y, Yao L, Zhao L, Fan C, Ke J, et al. Imaging fibroblast activation protein in liver cancer: a single-center post hoc retrospective analysis to compare [(68)Ga]Ga-FAPI-04 PET/CT versus MRI and [(18)F]-FDG PET/CT. Eur J Nucl Med Mol Imaging. 2021;48(5):1604–17.

90. Werner RA, Derlin T, Lapa C, Sheikbahaei S, Higuchi T, Giesel FL, et al. (18)F-labeled, PSMA-targeted radiotracers: leveraging the advantages of radiofluorination for prostate cancer molecular imaging. Theranostics. 2020;10(1):1–16.

91. Lindner T, Altmann A, Giesel F, Kratochwil C, Kleist C, Kramer S, et al. (18)F-labeled tracers targeting fibroblast activation protein. EJNMMI Radiopharm Chem. 2021;6(1):26.

92. Giesel FL, Adeberg S, Syed M, Lindner T, Jimenez-Franco LD, Mavriopoulou E, et al. FAPI-74 PET/CT using either (18)F-AlF or cold-kit (68)Ga labeling: biodistribution, radiation dosimetry, and tumor delineation in lung cancer patients. J Nucl Med. 2021;62 (2):201–7.

93. Slania SL, Das D, Lisok A, Du Y, Jiang Z, Mease RC, et al. Imaging of fibroblast activation protein in cancer xenografts using novel (4-quinolinoyl)-glycyl-2-cyanopyrrolidine-based small molecules. J Med Chem. 2021;64(7):4059–70.

94. Lindner T, Altmann A, Kramer S, Kleist C, Loktev A, Kratochwil C, et al. Design and development of (99m)Tc-labeled FAPI tracers for SPECT imaging and (188)Re therapy. J Nucl Med. 2020;61 (10):1507–13.

95. Werner RA, Weich A, Kircher M, Solnes LB, Javadi MS, Higuchi T, et al. The theranostic promise for neuroendocrine tumors in the late 2010s—where do we stand, where do we go? Theranostics. 2018;8(22): 6088–100.

96. Ballal S, Yadav MP, Moon ES, Roesch F, Kumari S, Agarwal S, et al. Novel fibroblast activation protein inhibitor-based targeted theranostics for radioiodine-refractory differentiated thyroid cancer patients: a pilot study. Thyroid. 2022;32(1):65–77.

97. Ballal S, Yadav MP, Kramer V, Moon ES, Roesch F, Tripathi M, et al. A theranostic approach of [(68)Ga] Ga-DOTA.SA.FAPi PET/CT-guided [(177)Lu] Lu-DOTA.SA.FAPi radionuclide therapy in an end-stage breast cancer patient: new frontier in targeted radionuclide therapy. Eur J Nucl Med Mol Imaging. 2021;48(3):942–4.

98. Ferdinandus J, Costa PF, Kessler L, Weber M, Hirmas N, Kostbade K, et al. Initial clinical experience with (90)Y-FAPI-46 radioligand therapy for advanced-stage solid tumors: a case series of 9 patients. J Nucl Med. 2022;63(5):727–34.

99. Fendler WP, Pabst KM, Kessler L, Fragoso Costa P, Ferdinandus J, Weber M, et al. Safety and efficacy of 90Y-FAPI-46 radioligand therapy in patients with advanced sarcoma and other cancer entities. Clin Cancer Res. 2022;28:4346.

100. Kratochwil C, Giesel FL, Rathke H, Fink R, Dendl K, Debus J, et al. [(153)Sm]Samarium-labeled FAPI-46 radioligand therapy in a patient with lung metastases of a sarcoma. Eur J Nucl Med Mol Imaging. 2021;48 (9):3011–3.

101. Zhao L, Niu B, Fang J, Pang Y, Li S, Xie C, et al. Synthesis, preclinical evaluation, and a pilot clinical PET imaging study of (68)Ga-labeled FAPI dimer. J Nucl Med. 2022;63(6):862–8.

102. Wen X, Xu P, Shi M, Liu J, Zeng X, Zhang Y, et al. Evans blue-modified radiolabeled fibroblast activation protein inhibitor as long-acting cancer therapeutics. Theranostics. 2022;12(1):422–33.

18

Case Study #7: PSMA-617

Michael S. Hofman and Narjess Ayati

18.1 The Fundamentals

[^{177}Lu]Lu-PSMA-617 radionuclide therapy is a biomarker-based, precision medicine approach to the treatment of advanced prostate cancer. [^{177}Lu]Lu-PSMA-617 is a radiolabelled small molecule with the ability to bind to prostate-specific membrane antigen (PSMA)-expressing cells and emit beta radiation (Fig. 18.1). Although [^{177}Lu]Lu-PSMA-617 is under 10 years old, it has already contributed to bringing hope to millions of patients around the globe for improved quality and quantity of life. To fully communicate the importance of the subject, we must first provide an overview of advanced prostate cancer.

18.1.1 Why Is Prostate Cancer Important?

Prostate cancer is the second most common cancer in men worldwide. It is not only a main cause of morbidity (especially in the elderly) but also one of the main causes of mortality, the fifth leading cause of death worldwide [2, 3]. It has an annual incidence rate of over 1.2 million cases and accounts for more than 400,000 deaths annually [4]. Currently, approximately 10 million men around the globe are living with this malignancy, and a considerable subgroup of these patients (estimated at approximately 700,000) has advanced disease [5, 6].

The term 'advanced prostate cancer' describes a group of patients who show evidence of disease progression on first-line systemic androgen deprivation therapy (ADT). These patients are also referred to as having 'castration-resistant prostate cancer' (CRPC). The management of this group of patients represents a significant challenge for worldwide health systems, both in terms of the economic burden of the disease and maintaining the patients' well-being and improving their survival. Unfortunately, to date, this subgroup of prostate cancer is considered incurable and fatal. Novel agents are therefore needed to improve patient management and survival.

M. S. Hofman (✉)

Prostate Cancer Theranostics and Imaging Centre of Excellence (ProsTIC); Molecular Imaging and Therapeutic Nuclear Medicine, Cancer Imaging, Peter MacCallum Centre Melbourne, Melbourne, Australia

Sir Peter MacCallum Department of Oncology, University of Melbourne, Melbourne, Australia
e-mail: michael.hofman@petermac.org

N. Ayati
Prostate Cancer Theranostics and Imaging Centre of Excellence (ProsTIC); Molecular Imaging and Therapeutic Nuclear Medicine, Cancer Imaging, Peter MacCallum Centre Melbourne, Melbourne, Australia

Fig. 18.1 Chemical structure of PSMA-617 and PSMA-11. (Reprinted with permission from [1])

18.1.2 How Is Advanced Prostate Cancer Managed?

In general, a broad range of options exist for the management of prostate cancer according to patient status and clinicopathological factors. These options range from active surveillance (for more indolent disease) and watchful waiting (for patients who are not fit for radical treatment) to curative intent local treatments of the primary tumour (mainly radical prostatectomy and/or external beam radiotherapy), metastatic directed therapy (for oligo-metastatic prostate cancer) and systemic therapy (for high-risk or more advanced disease) (Fig. 18.2). Metastatic CRPC (mCRPC) is advanced metastatic prostate cancer, and multi-modal treatment (with an essential part of systemic therapy) is the cornerstone for this subgroup. Before 2004, there was no systemic treatment with proven clinical benefits for advanced prostate cancer. The first agent with proven clinical benefit in the management of advanced prostate cancer (Docetaxel) received US Food and Drug Administration (FDA) approval in 2004. Since then, 9 more agents – including chemotherapeutics from the Taxane family, vaccines androgen receptor pathway inhibitors, bone targeted agents, immune
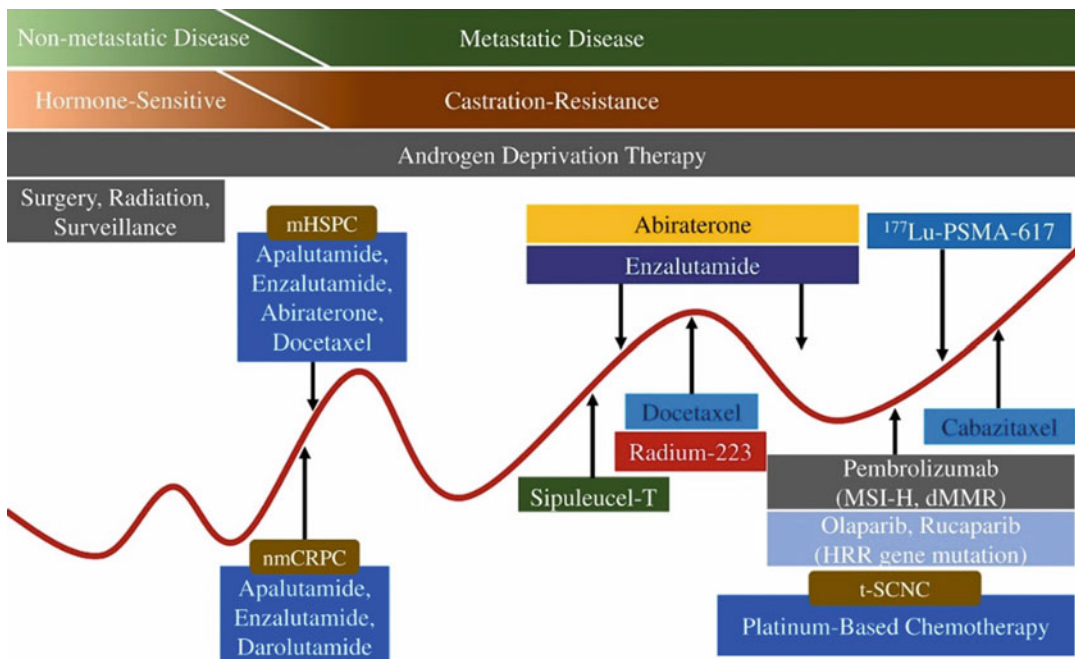
Fig. 18.2 The current landscape of prostate cancer management. (Reprinted from [7] with permission from Elsevier)

checkpoint inhibitors, and Poly-Adenosine diphosphate Ribose Polymerase (PARP) inhibitors – have been approved that have exhibited clinical benefits in increasing the overall survival of patients in phase III clinical trials (Table 18.1) [7]. Lastly, in 2022, the 10th – and probably most powerful – agent in the fight against prostate cancer has received FDA approval: [^{177}Lu]Lu-PSMA-617 [18].

18.2   The Details

18.2.1   PSMA-Targeted Ligands: A Family of Potential Therapeutics

Prostate-specific membrane antigen (PSMA) – also known as glutamate carboxypeptidase II (GCP-II) and folate hydrolase 1 (FOLH1) – is a 750 amino acid type II transmembrane glycoprotein enzyme with a short N-terminal intracellular domain and a large C-terminal extracellular domain [19]. PSMA is highly overexpressed in over 94% of prostate cancer samples, which makes it an excellent theranostic target. It is of note that some other non-prostatic cells express PSMA, including renal, duodenal, lacrimal gland and salivary gland cells. However, the high levels of PSMA expression in prostate cells (up to 100–1000-fold higher than the physiological expression of normal cells) have made it an excellent target for the nuclear imaging and RPT of prostate cancer.

Both small molecule and antibody-based vectors have been leveraged to build PSMA-targeted radiopharmaceuticals. Generally, PSMA-targeted small molecules – mainly derivatives of urea-based ligands with the ability to bind the extracellular domain of PSMA – are considered to have considerable advantages over PSMA-targeted antibodies, including more facile and less expensive manufacturing, rapid clearance kinetics and better target-to-background ratios. Nonetheless, we can consider the monoclonal antibody (mAb) 7E11-C5 (capromab, developed in 1987) to be the first member of this family of PSMA-targeted vectors [20]. Its first well-known radiopharmaceutical derivative

Table 18.1 FDA approved therapeutic agents in the field of advanced prostate cancer prior to the approval of ^{177}Lu-PSMA-617

No.	FDA approval	Therapeutic agent	Clinical trial	Comment
1	2004	Docetaxel (Taxane)	TAX327 [8] SWOG9916 [9]	Prolonged patients' OS (18.9 vs. 16.5 mo, $p = 0.009$ [7] and 17.5 vs. 15.6 mo, $p = 0.02$ [8]) compared with the other study arm and significantly increased QoL in both studies
2	2010	Cabazitaxel (Taxane)	TROPIC [10]	Increased OS (15.1 v. 12.7 mo, $p < 0.0001$) compared with the control arm
3	2010	Sipuleucel-T (Vaccine)	IMPACT [11]	Increased OS (25.8 v. 21.7 mo, $p = 0.03$) compared with the control arm
4	2011	Abiraterone (Androgen Receptor Pathway Inhibitor)	COU-AA-301 [12] COU-AA-302 [13]	Abiraterone plus prednisone increased OS (14.8 v. 10.9 mo, $p < 0.001$), prolonged time to PSA progression, and controlled pain compared with the control arm
5	2012	Enzalutamide (Androgen Receptor Pathway Inhibitor)	AFFIRM [14]	Increased OS (18.4 vs. 13.6 mo, $p < 0.001$), PSA response rate, time to PSA progression, and QoL compared with the control arm
6	2013	[223]Radium[a] (Bone targeted agents)	ALSYMPCA [15]	Increased OS (14.9 vs. 11.3 mo, $p < 0.001$), time to first skeletal event (15.6 vs. 9.8 months, $p < 0.001$), and QoL compared with the control arm
7	2017	Pembrolizumab (Immune checkpoint inhibitor)	KEYNOTE [7]	The first approved biomarker-based pan-cancer therapeutic agent
8	2020	Olaparib (PARP inhibitor)	PROfound [16]	Increased OS (18.5 vs. 15.1 mo, $p = 0.02$) and PFS compared with the other arm
9	2020	Rucaparib (PARP inhibitor)	TRITON2 [17]	Improvement of objective response rate and PSA response rate in mCRPC patients harbouring BRCA alterations

[a][223]Radium has been discussed in detail in the following chapter

OS Overall Survival, *PFS* Progression Free Survival, *QoL* Quality of Life, *mo* month

was ^{111}In-capromab pendetide (ProstaScint®), which was the first FDA-approved molecular imaging agent for prostate cancer in 1996. However, ^{111}In-capromab pendetide's ability to only target the intracellular domain of PSMA limited its binding to dying or dead cells and thus significantly reduced its sensitivity and detection rate.

Since 1996, new generations of PSMA-targeted ligands have been developed and have extended the therapeutic potential of this family. Before discussing ^{177}Lu-PSMA-617, we will review related compounds that have made significant contributions to the field, most notably ^{68}Ga-PSMA-11. The family of PSMA-targeted radiopharmaceuticals has other members whose stories lie beyond the scope of the current chapter, including radiolabelled variants of the PSMA-targeting mAb J591 and ^{177}Lu-PSMA-I&T [20].

18.2.2 ^{68}Ga-PSMA-11: Talented Elder Sister and Fabulous Teammate!

^{68}Ga-PSMA-11 is the most widely used PSMA-targeted positron emission tomography (PET) imaging agent worldwide. In fact, when considering personalized medicine (and RPT), diagnostic and therapeutic agents need to work together. The former works as a companion imaging tool for selecting patients who may benefit from subsequent RPT. In the context of prostate cancer, the most well-known theranostic pair is ^{68}Ga-PSMA-11 and ^{177}Lu-PSMA-617. ^{68}Ga-PSMA-11 was created in 2012 at the University Hospital Heidelberg [21]. In 2020, at only 8 years old, ^{68}Ga-PSMA-11 matured with the results of its first prospective randomized study, known as 'ProPSMA'. This phase III
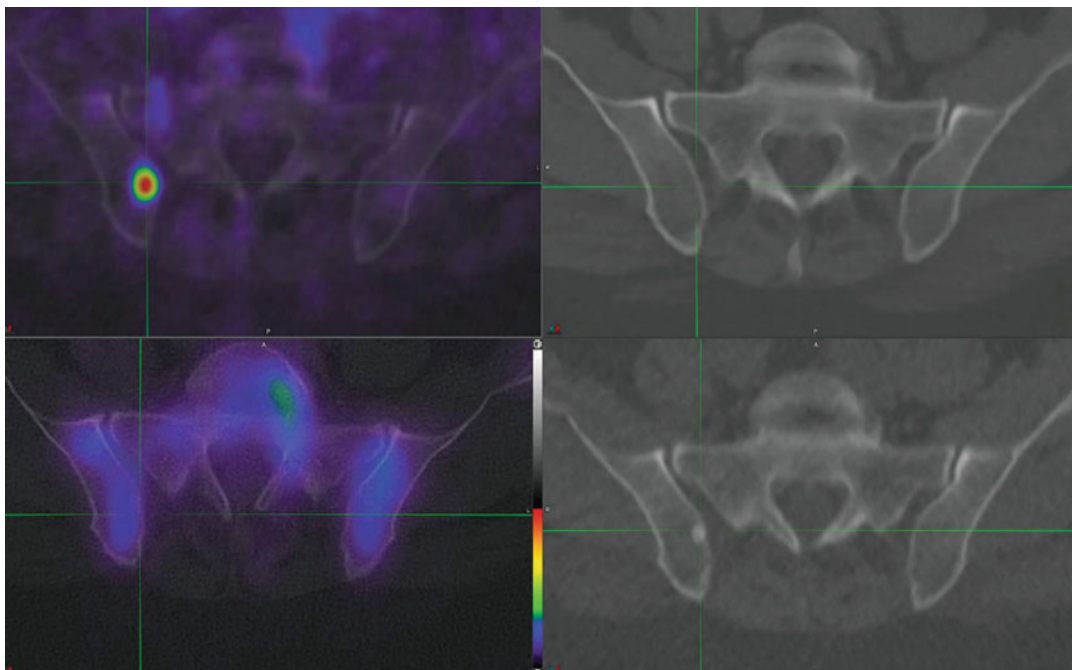
Fig. 18.3 [^{68}Ga]Ga-PSMA-11 PET/CT has higher sensitivity and specificity than conventional imaging. [^{68}Ga]Ga-PSMA-11 PET/CT in a patient with rising PSA level shows a right iliac bone metastasis that was not recognizable on diagnostic CT. Following systemic treatment, the 6-month follow up demonstrates undetectable PSA, complete resolution of PSMA avidity of this lesion, and the development of sclerosis on CT in keeping with complete response to treatment. PSA: prostate-specific antigen, PSMA: prostate-specific membrane antigen. (Reproduced with permission from [22])

multicentre study recruited 300 patients from 10 centres across Australia to investigate the ability of positron emission tomography/computed tomography (PET/CT) with [^{68}Ga]Ga-PSMA-11 to improve the accuracy of staging in men diagnosed with high-risk localized prostate cancer [22]. The patients were randomly assigned to a cohort that received conventional staging using CT and a bone scan or a cohort that received [^{68}Ga]Ga-PSMA-11 PET/CT. The accuracy of [^{68}Ga]Ga-PSMA-11 PET/CT was significantly higher than that of conventional imaging (92% vs. 65%), and its sensitivity and specificity were 85% and 98% compared to 38% and 91% for conventional imaging respectively (Fig. 18.3). Furthermore, PET/CT with [^{68}Ga]Ga-PSMA-11 proved superior to conventional imaging for the detection of both pelvic nodal and distant metastases, changed patient management more often (28% vs. 15%), revealed fewer equivocal findings (7% vs. 23%) and resulted in 10.9 mSv less radiation exposure. This randomized phase 3 study provided compelling evidence that [^{68}Ga]Ga-PSMA-11 PET/CT is a suitable replacement for conventional imaging in the workup of patients with newly diagnosed prostate cancer. The graphical abstract of the study results is shown in Fig. 18.4. According to a subsequent enlarged systematic review and meta-analysis of 4790 patients from 37 studies, the detection rates of [^{68}Ga]Ga-PSMA-11 PET/CT for prostate-specific antigen (PSA) levels ≥ 2, 1–1.99, 0.5–0.99, 0.2–0.49 and <0.2 were estimated to be 95, 75, 59, 45 and 33% respectively [23]. As a result of this strikingly positive data, [^{68}Ga]Ga-PSMA-11 received FDA approval in 2020.
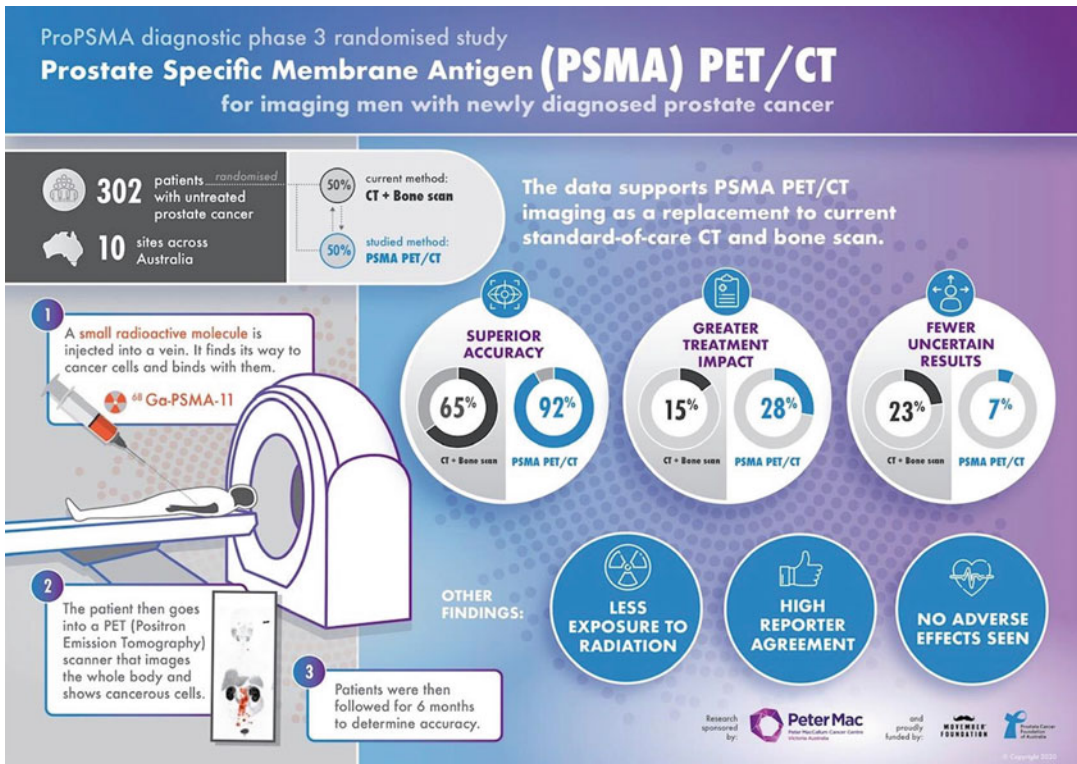
Fig. 18.4 Infographic of the ProPSMA trial. Note the remarkable advantages of [^{68}Ga]Ga-PSMA-11 PET/CT compared to conventional imaging

18.2.3 [^{177}Lu]Lu-PSMA-617

[^{177}Lu]Lu-PSMA-617 is a radiolabelled small molecule with the ability to bind to PSMA-expressing cells and emit beta radiation. This agent – which is a ^{177}Lu-labeled DOTA-bearing derivative of the Glu-urea-Lys motif – has proven safe and effective for the treatment of patients with metastatic castration-resistant prostate cancer (mCRPC) and is the first prostate cancer-specific radiopharmaceutical with FDA approval. [*Author's Note: Let me tell you something interesting! Today, the 26th of March, 2022, I am writing this part of the chapter and our champion – [^{177}Lu]Lu-PSMA-617 – received FDA approval just two days ago (24/3/2022), I feel so excited!*] Although [^{177}Lu]Lu-PSMA-617 is under 10 years old, it has already brought hope for improved quality and quantity of life to millions of patients around the globe.

18.2.3.1 How Is [^{177}Lu]Lu-PSMA-617 Therapy Being Done? The Recipe!

Today, patients are deemed suitable for RPT with [^{177}Lu]Lu-PSMA-617 if they meet the following criteria:

- Diagnosis of mCRPC
- Progression or intolerance on a novel anti-androgen therapy (e.g. abiraterone, enzalutamide, apalutamide, or darolutamide)
- Previous treatment with at least one taxane cytotoxic agent (or evidence of being unfit for that)
- Evidence of clinical, biochemical, or radiological disease progression
- Acceptable haematological, renal and hepatic function
- A performance status of 0–3 on the eastern cooperative oncology group (ECOG) Performance Scale

- A life expectancy greater than 6 months
- Evidence of PSMA-expressing metastases on [^{68}Ga]Ga-PSMA-11 PET imaging
- No evidence of PSMA-negative sites using either contrast-enhanced CT or fluorodeoxyglucose (FDG) PET/CT

18.3   Something Extra

18.3.1   Particularly Important Works: Step by Step, Toward Success!

Herein, we describe the particularly important works in the development of [^{177}Lu]Lu-PSMA-617 radionuclide therapy.

18.3.1.1   Step 1: Preclinical Studies
Prior to the first human experiments, in vitro and in vivo studies were performed to design highly potent ^{177}Lu-labeled PSMA-targeted radioligands and interrogate their safety and efficacy, including their radiolytic stability, tumour affinity, organ distribution and background clearance. These efforts began many years prior to the first human experiment with [^{177}Lu]Lu-PSMA-617 in 2013 [24, 25].

18.3.1.2   Step 2: The First Patient
In Dec 2013, a patient with mCRPC and high PSMA expression on [^{68}Ga]Ga-PSMA-11 PET was treated with 7.4 GBq of [^{177}Lu]Lu-PSMA-617, and follow-up revealed both a PSA response (PSA drop from 38 to 4.6 ng/ml) and a radiological response. This was the first report of RPT with [^{177}Lu]Lu-PMSA-617 and an early indication that this agent could be utilized to improve the clinical management of patients with advanced prostate cancer [26].

18.3.1.3   Step 3: Retrospective Studies Began to Support the Clinical Benefits of [^{177}Lu]Lu-PSMA-617
Three years later, Kratochwil and colleagues retrospectively reported on 30 patients with mCRPC who were treated with 1–3 cycles of [^{177}Lu]Lu-PSMA-617. Twenty-one patients showed a PSA response – with 13 (43%) patients showing reduction of >50% – and 8 patients achieved a durable PSA response (>50%) for over 24 weeks. This PSA response was correlated with radiologic response. Haematological side effects were mild, and xerostomia, nausea and fatigue were observed in less than 10% of patients. Dosimetry showed dose rates of 0.75, 0.03 and 1.4 Gy/GBq to the kidneys, bone marrow and salivary glands respectively, which were irrespective of tumour volume and remained consistent on subsequent cycles [27].

18.3.1.4   Step 4: Further Efforts: Multicentre Retrospective Studies
The following year, a retrospective multicentre study initiated by the German Society of Nuclear Medicine reported on a large cohort of 145 patients from 12 centres treated with 1–4 cycles (2–8 GBq per cycles, 5.9 GBq on average) of [^{177}Lu]Lu-PSMA-617. The overall biochemical response rate (PSA decline $\geq$50%) was 45%, compared to 18% for enzalutamide in a comparable multicentre cohort of mCRPC patients [28]. Grade 3–4 haematotoxicity was observed in 18 (12%) patients, a side effect that was significantly higher in the subset of patients previously treated with ^{223}Ra. A multivariate analysis revealed that an increase in alkaline phosphatase expression and the presence of visceral metastases were negative prognostic factors, and the total number of therapy cycles was a positive predictor of biochemical response. No therapy-related deaths were observed after a total of 284 therapy cycles across 145 patients. This study emphasized the potential effectiveness of this novel therapy and suggested further evaluation of its survival benefit in phase II/III studies [29].

18.3.1.5   Step 5: The First Prospective Clinical Trial on [^{177}Lu]Lu-PSMA-617
In 2018, Hofman et al. published the first prospective phase II clinical trial focused on [^{177}Lu]Lu-PSMA-617 RPT in patients with mCRPC

Fig. 18.5 Waterfall plot of best PSA decline compared with baseline. PSA: prostate-specific antigen. (Reproduced with permission from [29])
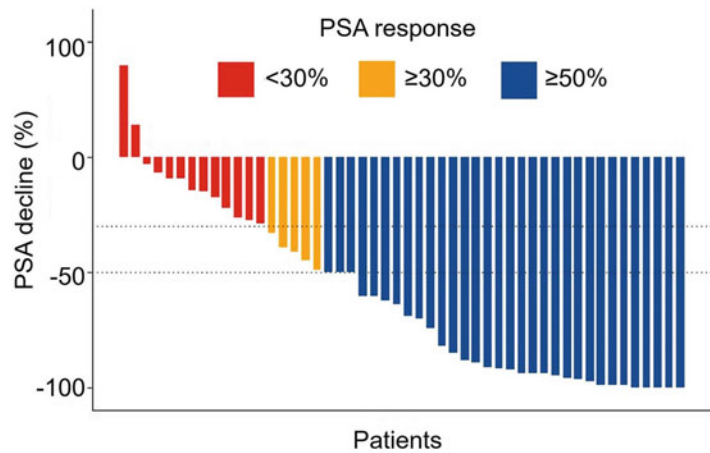
[30]. Thirty eligible men with progressive disease after standard treatments and confirmed high PSMA expression on screening FDG and [^{68}Ga] Ga-PSMA-11 PET/CT were treated with up to 4 cycles of [^{177}Lu]Lu-PSMA-617 (average dose of 7.5 GBq/cycle) with 6-week intervals between cycles. The patients were followed for a median of 25 months. A biochemical response (PSA decline ≥50%) was achieved in 57% of the study population (Fig. 18.5), 97% of the patients (29 of 30) experienced a PSA decline, and a median 7-month PSA progression-free survival was reported. This treatment was well tolerated, with no recorded immediate adverse effects nor treatment-related deaths, and grade 3 or 4 thrombocytopenia was observed in only 4 (13%) patients. Clinically meaningful pain relief in both severity and interference was observed at all-time points.

From these data, the authors concluded that '*LuPSMA resulted in high responses, a low toxicity profile, and improves quality of life parameters especially in men with pain'*. These findings confirmed the retrospective data provided by compassionate access treatments in Germany. Complementary data on longer-term outcomes – including a 20-patient extension cohort – were published later in the *Journal of Nuclear Medicine* [31] (Fig. 18.6).

18.3.1.6 Step 6: The First Randomized Clinical Trial on [^{177}Lu] Lu-PSMA-617: TheraP Trial

It was time for this novel radiopharmaceutical to show its capability in a real battle! In the TheraP study – a multicentre randomized phase 2 clinical trial conducted at 11 centres across Australia in 200 men with mCRPC – [^{177}Lu]Lu-PSMA-617 was compared to the standard of care (cabazitaxel) with respect to improving response rates and the quality of life of patients [32]. The clinical eligibility criteria were adequate hepatic, renal and haematological function as well as satisfactory performance status (i.e. Eastern Cooperative Oncology Group score 0–2). The PET eligibility criteria were evidence of PSMA-expressing disease with no discordant (FDG-positive/PSMA-negative) metastatic lesions (Fig. 18.7). Whilst FDG PET/CT may provide additional information, close correlation of PSMA PET/CT and contrast-enhanced CT provides similar information.

The patients were randomly categorized into two groups to receive either [^{177}Lu]Lu-PSMA-617 (6–8.5 GBq, up to 6 cycles with a 6-week interval between cycles) or cabazitaxel (20 mg/m^2, up to 10 cycles with a 3-week interval between cycles) and were followed for a median of 18.4 months. A biochemical response (>50% decline in baseline
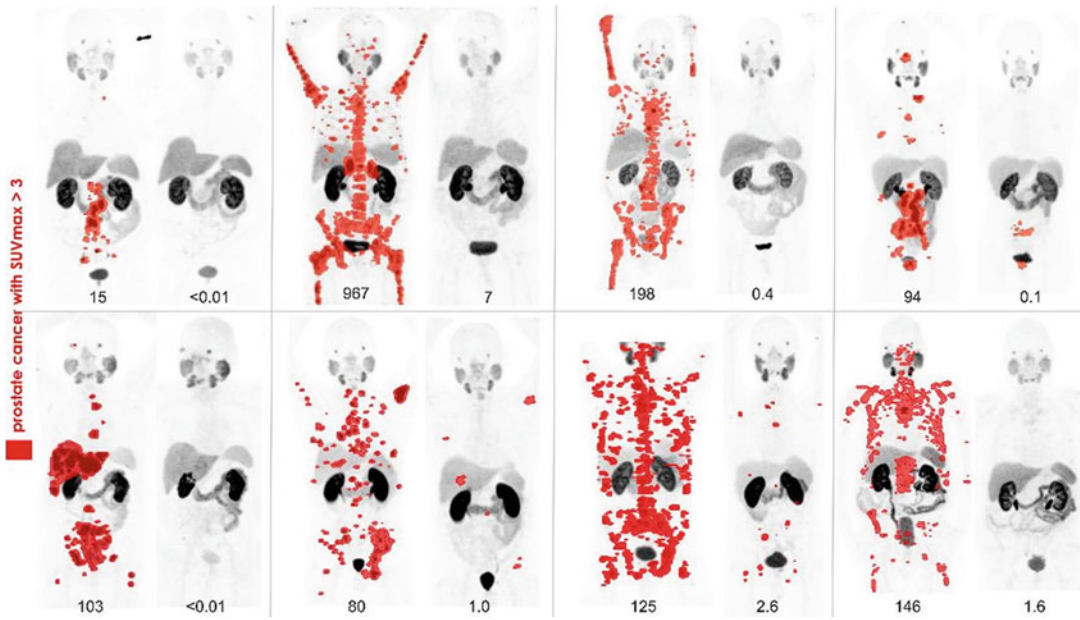
Fig. 18.6 [^{68}Ga]Ga-PSMA-11 PET/CT before and 3 months after therapy in 8 patients with PSA declines of 98% after RPT with [^{177}Lu]Lu-PSMA-617. *PSA* prostate-specific antigen. Image of the Year at 2018 Society of Nuclear Medicine and Molecular Imaging annual meeting. (Reproduced with permission from [29])
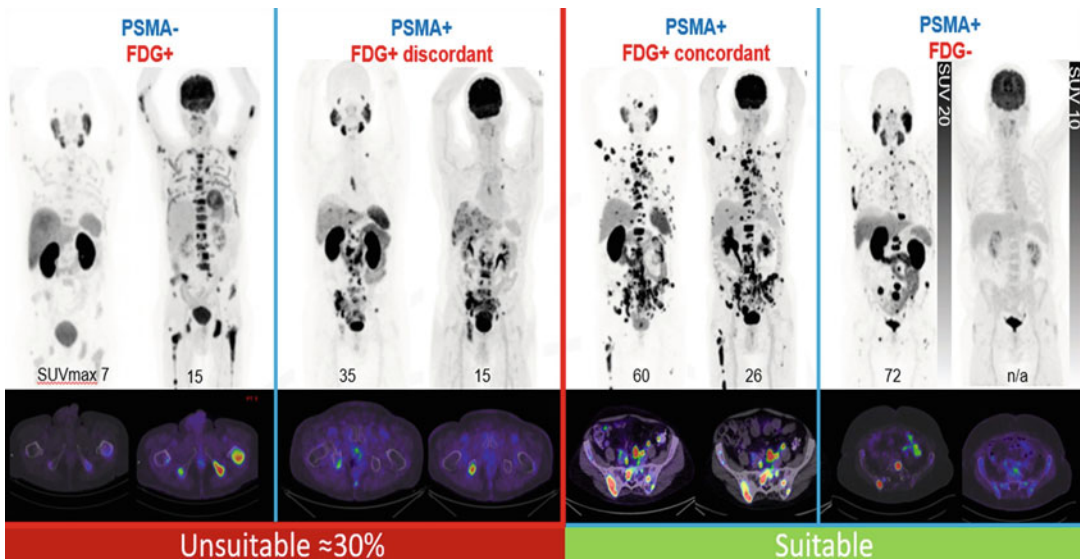
Fig. 18.7 PSMA/FDG phenotypes. Comparing the degree of [^{68}Ga]Ga-PSMA-11 and FDG uptake in metastatic lesions helps select patients with a higher possibility of response to [^{177}Lu]Lu-PSMA-617 RPT
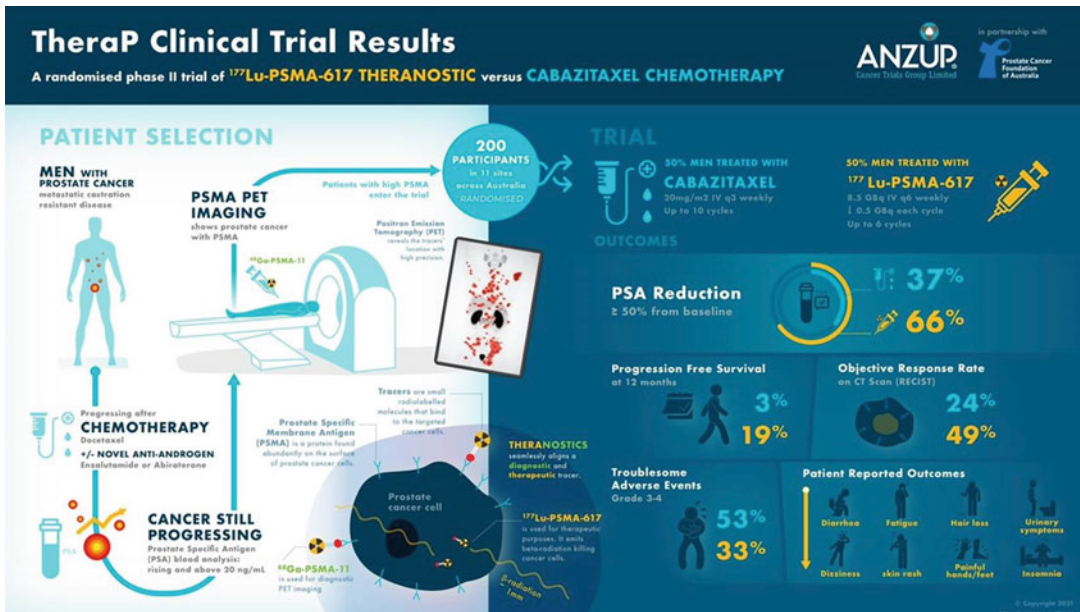
Fig. 18.8 Infographic of the first randomized clinical trial on [^{177}Lu]Lu-PSMA-617

PSA) was seen in 66% of [^{177}Lu]Lu-PSMA-617 patients and 37% of cabazitaxel patients (a 29% difference, $p < 0.0001$). Furthermore, [^{177}Lu]Lu-PSMA-617 delayed progression compared with cabazitaxel (HR 0.63, $p = 0.0028$), and progression-free survival at 12 months was observed in 19 and 3% of these two groups respectively. Severe (grade 3–4) adverse events occurred in 33% of the [^{177}Lu]Lu-PSMA-617 patients versus 53% in the cabazitaxel group, and grade 3 or 4 neutropenia was observed less frequently in the [^{177}Lu]Lu-PSMA-617 arm (4% vs. 13%).

Based on these results (Fig. 18.8), the TheraP trial demonstrated that [^{177}Lu]Lu-PSMA-617 had better activity, safety and patient-reported outcomes than the standard of care in patients with mCRPC [32]. **This was a moment of truth!**

18.3.1.7 Step 7: The Final Match: The International Randomized Phase III VISION Trial

Sartor et al. conducted this study to compare [^{177}Lu]Lu-PSMA-617 with the standard of care in patients with advanced prostate cancer with a view to obtaining approval in the USA from the Food and Drug Administration (FDA). The patients were randomly assigned (in a 2:1 ratio) to receive either [^{177}Lu]Lu-PSMA-617 (7.4 GBq with 6-week intervals, up to 4–6 cycles) plus standard care or protocol-permitted standard care alone. In total, 831 patients entered the study and were followed for a median of 20.9 months. The [^{177}Lu]Lu-PSMA-617 group had significantly longer progression-free (8.7 vs. 3.4 months, $p < 0.001$) and overall survival (15.3 vs. 11.3 months, $p < 0.001$) than the control arm. The comparison of all key secondary endpoints also supported the addition of [^{177}Lu]Lu-PSMA-617 to standard care. The grade 3 or above adverse events were more frequently observed in the [^{177}Lu]Lu-PSMA-617 group; however, quality of life was not adversely affected [18].

As we have seen, the VISION trial demonstrated the clinical benefit of [^{177}Lu]Lu-PSMA-617 in improving patients' overall survival. Based on this study, the FDA reviewed and approved this novel therapeutic agent in patients with mCRPC! Congratulations are in order to every researcher who contributed to this fantastic achievement.

To summarize all of the prior work on this agent, we will briefly discuss a recent systematic review and meta-analysis by Sadaghiani et al. covering the effectiveness and toxicity of [177Lu]Lu-PSMA-617 RPT in patients with mCRPC [33]. According to this study, the proportion of patients who were treated with [177Lu]Lu-PSMA-617 and subsequently demonstrated a ≥50% decline in PSA levels was estimated at 0.44. Based on this study, the overall and progression-free survival according to pooled hazard ratios for >50% PSA reduction were 0.67 and 0.53, respectively. This meta-analysis has been recently updated by the authors with the addition of two randomized controlled trials as well as further retrospective studies [34].

18.3.2 [177Lu]Lu-PSMA-617 in Real Life

To help remind the reader of the human stakes in [177Lu]Lu-PSMA-617 RPT, we thought it would be helpful to include a real personal story associated with the treatment (Fig. 18.9). You can clearly see how this small molecule improves a patient's quality and quantity of life:

From the doctor's notes:

M. F. is a lovely 77-year-old gentleman with castration-resistant prostate cancer. His history of prostate cancer dates back to 2008, when he was diagnosed incidentally through a PSA check. Further investigations showed he had bone, pleural, pulmonary and lymph node metastases at presentation. He had a variety of therapeutic agents, including docetaxel (2013), abiraterone (2014) and enzalutamide (2015). He had further disease progression with PSA elevation to 967 ug/L and clinical symptoms, including fatigue, bone pain, and loss of weight (7 kg in the last 6–9 months). His wife states: 'He is on heavy medication to cope with pain; he spends most of the day asleep, feeling weak and without hope'.

[68Ga]Ga-PSMA-11 PET/CT was performed, demonstrating high PSMA-expression with an SUV_{max} of 55. On 18F-FDG PET/CT, there were no sites of FDG-positive PSMA-negative disease, and the haematological, hepatic and renal profiles were suitable for treatment. We had a detailed discussion about the rationale for [177Lu]Lu-PSMA-617 RPT, the anticipated therapeutic
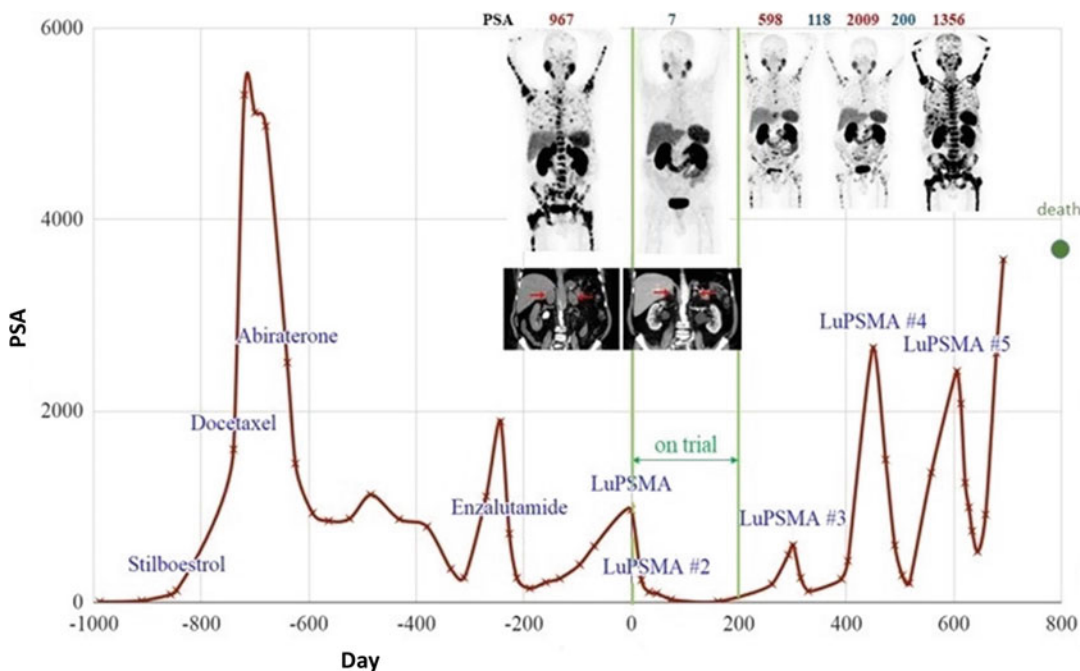
Fig. 18.9 [177Lu]Lu-PSMA-617 in real life. The diagram shows the effect of different therapeutic approaches for controlling a patient's disease (see PSA level). *PSA* prostate-specific antigen

effects, the possible side effects and the appropriate radiation protection precautions. Mr. F. has a supportive wife (who is a retired nurse), and they were both happy to go ahead with [177Lu]Lu-PSMA-617. M. was given 2 cycles of [177Lu]Lu-PSMA-617 with no immediate adverse events and high radionuclide retention within the known sites of metastatic disease. On the post-therapy scan of the second dose, there was a marked reduction in the intensity of uptake at almost all sites of previously extensive metastases.

November 2015 'M. has been feeling extremely well after the second cycle of treatment. He feels more energetic and rarely requires Endone for his bone pain'. A follow-up [68Ga]Ga-PSMA-11 PET/CT was performed after 2 cycles of [177Lu]Lu-PSMA-617. [It should be noted that we do not routinely perform restaging PSMA PET/CT but use it selectively when management might change. This is where you can see how this small molecule can make a difference (Fig. 18.10).]

January 2016 'M. feels extremely well since commencing treatment with [177Lu]Lu-PSMA-617. His bone pain essentially resolved,

and he recently regained approximately 3 kg in weight'. The PSA dropped from 967 to 29 ug/L, and [68Ga]Ga-PSMA-11 PET showed a near complete response to treatment.

March 2016 No clinical symptoms were observed alongside an ongoing near-complete response to treatment. 'M. feels extremely well, ..., His quality of life and energy level has markedly improved.... . His PSA level is now 16.5 ug/L'. His wife reports: 'His energy level has increased, he is doing more around the house, is outside more often and taking occasional walk'.

June 2016 [68Ga]Ga-PSMA-11 PET/CT shows small volume recrudescence of PSMA-expressing bone metastases.

August 2016 Recurrent extensive PSMA-avid bony disease. M. started to feel fatigued. He needs to take Panadol for bone pain but not opioid analgesia. After discussion with the patient, a 3rd cycle of [177Lu]Lu-PSMA-617 was planned for September 2016. I am hopeful there will be favourable response to this cycle of [177Lu]Lu-PSMA-617, but the durability of this response is uncertain.

Fig. 18.10 [68Ga]Ga-PSMA-11 PET/CT before and after 2 cycles of [177Lu]Lu-PSMA-617 therapy. This is how this small molecule make difference!
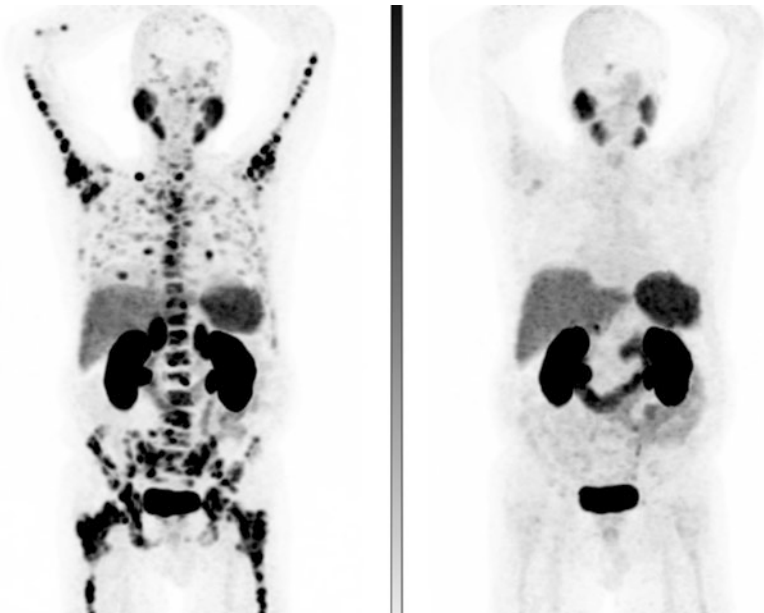
Fig. 18.11 [^{177}Lu]Lu-PSMA-617 in real life

December 2016 After the third cycle: 'M. remains well without pain. His ECOG performance status was 1'. I showed M. and his wife the scans, which demonstrate relatively stable disease with multifocal bony disease but persistent complete response in soft tissue in the adrenal glands and lungs.

February 2017 M. had a further cycle of [^{177}Lu]Lu-PSMA-617.

June 2017 M. was accompanied by his son. Unfortunately, he deteriorated symptomatically, reporting significant loss of appetite and weight. His [^{68}Ga]Ga-PSMA-11 PET/CT showed marked interval disease progression. His pre-existing marrow impairment resulted in two episodes of blood transfusion in the last months. Our tentative plan is to attempt to deliver 2 additional cycles, to try to at least halt or slow down his progressing disease. M. had the third maintenance cycle of [^{177}Lu]Lu-PSMA-617 in June 2017.

Follow-Up Note (June 2017) 'M. in general feels much better since the injection. His family is very supportive of him, and he understands that even though palliative, this treatment will hopefully result in an improvement to his quality of life. It is likely that his life expectancy will be short, given the expansion of red marrow into the arms and legs and replacement with tumour, and the marrow failure is due to marrow replacement rather than radionuclide therapy'.

This was the last visit that M. had in the nuclear medicine department. He passed away in December 2017. This radiolabelled small molecule was a true game changer for him and his family and many patients with similar conditions. The treatment allowed the patient to be pain-free for more than 10 months. This is an achievement, but it is certainly not enough! (Fig. 18.11).

Sir Peter MacCallum (1949) has been quoted as saying: 'Nothing but the best is good enough in the treatment of cancer'. Despite many great efforts that have improved the quality and quantity of thousands of patients' lives, there is room to improve with combination therapies or next generation radiopharmaceuticals that can achieve more durable responses or even cure. More academic, industrial, and clinical efforts are needed.

18.4 The Future

18.4.1 New Eras for [^{177}Lu] Lu-PSMA-617: Upcoming Challenges!

Although the high efficacy and low toxicity of [^{177}Lu]Lu-PSMA-617 RPT have been shown in different retrospective and prospective studies, new clinical trials are needed to achieve higher response rate and more durable effects and to reduce toxicity. The majority of these clinical studies focus on changing the time sequence of RPT, combining [^{177}Lu]Lu-PSMA-617 with other therapeutic agents (e.g. chemotherapeutics and immunotherapy agents), and predicting and reducing unfavourable radiation effects to normal organs. In the following section, some of these important ongoing clinical trials are introduced.

18.4.1.1 Change in Time Sequence

Large randomized clinical trials have demonstrated the efficacy and safety of [^{177}Lu] Lu-PSMA-617. Yet now another important question has been raised: can this agent help prostate cancer patients earlier in the treatment sequence? As seen in Fig. 18.2, the current application of RPT is very near to the end stage of the disease. However, mounting evidence in men with mCRPC with high PSMA expression at earlier stages of the disease supports evaluation for [^{177}Lu]Lu-PSMA-617 RPT earlier in the disease's progression. Consequently, new clinical trials focusing on utilizing PSMA-targeted RPT sooner in the course of patient management have been designed and implemented.

Several trials are now examining the role of [^{177}Lu]Lu-PSMA-617 in men with early manifestations of prostate cancer, when the cancer is not yet castration-resistant but still sensitive to androgen suppression [i.e. so called 'metastatic hormone-sensitive prostate cancer' (mHSPC)]. PSMAaddition (NCT04720157) is an international open-label, randomized, phase III study comparing [^{177}Lu]Lu-PSMA-617 with the standard of care (ARDT + ADT) in patients with metastatic hormone-sensitive prostate cancer (mHSPC) [35]. Another randomized controlled phase II study, BULLSEYE (NCT04443062), aims to assess if [^{177}Lu]Lu-PSMA-617 is an effective treatment in patients with hormone-sensitive prostate cancer with low volume metastatic disease (≤5 metastases) for prolonging progression-free survival [36].

As discussed previously, one of the current inclusion criteria for [^{177}Lu]Lu-PSMA-617 RPT is previous treatment with at least one taxane cytotoxic agent. The PSMAfore (NCT04689828) trial is a phase III, open-label, multicentre randomized trial in patients with progressive mCRPC who have not yet received taxane chemotherapy. The aim of this study is to compare [^{177}Lu]Lu-PSMA-617 treatment to a change of androgen receptor-directed therapy (ARDT) [37].

There are still other ongoing clinical trials looking into the clinical benefit of [^{177}Lu]Lu-PSMA-617 RPT at the time of diagnosis. UpFrontPSMA (NCT04343885) is a phase II randomized clinical trial designed to compare the effectiveness of [^{177}Lu]Lu-PSMA-617 therapy followed by docetaxel chemotherapy versus docetaxel chemotherapy alone in patients with newly diagnosed high volume metastatic hormone naïve prostate cancer (mHNPC) [38]. Another interesting clinical trial is Lutectomy (NCT04430192), which is aimed at evaluating the dosimetry, efficacy and toxicity of [^{177}Lu]Lu-PSMA-617 RPT in patients with high PSMA-expressing localized or locoregional advanced prostate cancer (HRCaP) prior to radical prostatectomy (RP) and pelvic nodal dissection [39].

18.4.1.2 Champions Together

[^{177}Lu]Lu-PSMA-617 has been shown to be effective as a monotherapy, but recent clinical trials have explored whether it may also be effective as a component of combination therapy. For example, the Enza-p study (NCT04419402) is an open-label randomized phase II randomized clinical trial assessing the efficacy of combined [^{177}Lu]Lu-PSMA-617 and enzalutamide compared to enzalutamide alone in patients with
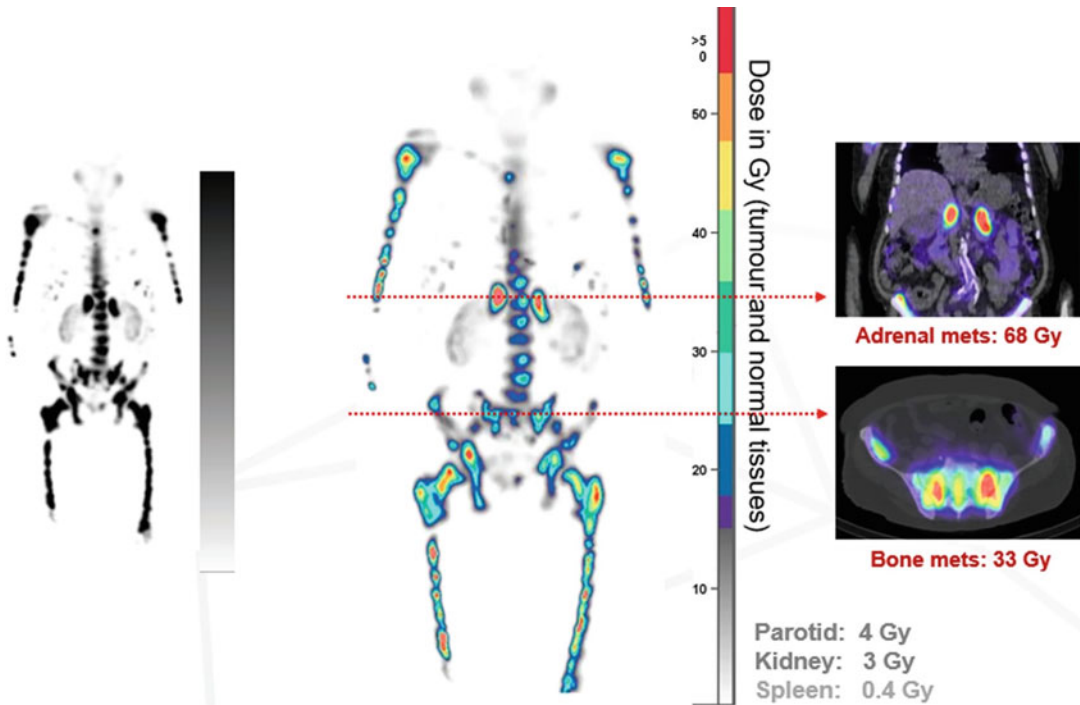
Fig. 18.12 Voxel-based Monte-Carlo dosimetry was determined using three time-point qSPECT/CT imaging following 8 GBq of [^{177}Lu]Lu-PSMA-617. (Reproduced with permission from [45])

mCRPC [40]. Another phase I dose-escalation and dose-expansion single arm study [LuPARP (NCT03874884)] is assessing the safety and tolerability of combined [^{177}Lu]Lu-PSMA-617 and Olaparib, a PARP inhibitor that can act as a radiosensitizer by inhibiting the repair of DNA damage [41]. Finally, the PRINCE trial (NCT03658447) is a phase Ib/II clinical trial focused on assessing the efficacy of combining [^{177}Lu]Lu-PSMA-617 RPT and an immune checkpoint inhibitor (pembrolizumab) [42]. In this single arm trial, all patients will be treated with [^{177}Lu]Lu-PSMA-617 for up to 6 doses and pembrolizumab for up to 35 cycles. This study has primarily completed, and based on the interim report, 73% (27/37) of patients had PSA response >=50% [43]. We expect to see the final report of this important study soon!

18.4.1.3 Radiation Dosimetry in [^{177}Lu] Lu-PSMA-617

RPT is one of the best examples of ways in which medicine can be precisely tuned to individual patients, providing the right therapy at the right dose for the right patient at the right time. The variability in the uptake of [^{177}Lu]Lu-PSMA-617 in target organs and tumour cells between patients stands as the rationale for recent investigations into dosimetry-guided therapy. Dosimetry-guided RPT would provide an opportunity to delineate and save at-risk tissues, to predict treatment failure early, and to improve outcomes via dose escalation in suitable patients (Fig. 18.12). This represents another new opportunity to optimize RPT and revolutionize patient care (see Chap. 8 for a broader discussion of dosimetry in RPT) [44].

18.5 The Bottom Line

- Prostate cancer is the second most common cancer in men worldwide and the fifth leading cause of death worldwide.
- Radiopharmaceutical therapy(RPT) is an essential personalized treatment for advanced prostate cancer.
- Currently, the most commonly-used radiopharmaceutical for the RPT of prostate cancer is [^{177}Lu]Lu-PSMA-617.
- [^{177}Lu]Lu-PSMA-617 is a radiolabelled small molecule with the ability to bind to PSMA-expressing cells and emit beta radiation.
- Recent data has shown the ability of [^{177}Lu] Lu-PSMA-617 to improve the quality and quantity of life in patients with advanced prostate cancer.
- Future studies are needed to achieve more durable response (or even cures) with this novel radiotherapeutic.

References

1. Kopka K, Benešová M, Bařinka C, Haberkorn U, Babich J. Glu-Ureido-based inhibitors of prostate-specific membrane antigen: lessons learned during the development of a novel class of low-molecular-weight theranostic radiotracers. J Nucl Med. 2017;58 (Suppl 2):17S–26S. https://doi.org/10.2967/jnumed.116.186775.
2. Rawla P. Epidemiology of prostate cancer. World J Oncol. 2019;10(2):63–89. https://doi.org/10.14740/wjon1191.
3. Siegel RL, Miller KD, Jemal A. Cancer statistics, 2020. CA Cancer J Clin. 2020;70(1):7–30. https://doi.org/10.3322/caac.21590.
4. Sandhu S, Moore CM, Chiong E, Beltran H, Bristow RG, Williams SG. Prostate cancer. Lancet. 2021;398 (10305):1075–90. https://doi.org/10.1016/S0140-6736(21)00950-8.
5. James SL, Abate D, Abate KH, Abay SM, Abbafati C, Abbasi N, et al. Global, regional, and national incidence, prevalence, and years lived with disability for 354 diseases and injuries for 195 countries and territories, 1990–2017: a systematic analysis for the Global Burden of Disease Study 2017. Lancet. 2018;392(10159):1789–858. https://doi.org/10.1016/S0140-6736(18)32279-7.
6. Foreman KJ, Marquez N, Dolgert A, Fukutaki K, Fullman N, McGaughey M, et al. Forecasting life expectancy, years of life lost, and all-cause and cause-specific mortality for 250 causes of death: reference and alternative scenarios for 2016–40 for 195 countries and territories. Lancet. 2018;392 (10159):2052–90. https://doi.org/10.1016/S0140-6736(18)31694-5.
7. Yamada Y, Beltran H. The treatment landscape of metastatic prostate cancer. Cancer Lett. 2021;519:20–9. https://doi.org/10.1016/j.canlet.2021.06.010.
8. van Soest RJ, de Morree ES, Shen L, Tannock IF, Eisenberger MA, de Wit R. Initial biopsy Gleason score as a predictive marker for survival benefit in patients with castration-resistant prostate cancer treated with docetaxel: data from the TAX327 study. Eur Urol. 2014;66(2):330–6. https://doi.org/10.1016/j.eururo.2013.08.007.
9. Petrylak D, Tangen C, Hussain M, Lara P, Jones J, Talpin M, et al. SWOG 99–16: randomized phase III trial of docetaxel (D)/estramustine (E) versus mitoxantrone (M)/prednisone (p) in men with androgen-independent prostate cancer (AIPCA). J Clin Oncol. 2004;22(14_suppl):3.
10. De Bono JS, Oudard S, Ozguroglu M, Hansen S, Machiels J-P, Kocak I, et al. Prednisone plus cabazitaxel or mitoxantrone for metastatic castration-resistant prostate cancer progressing after docetaxel treatment: a randomised open-label trial. Lancet. 2010;376(9747):1147–54. https://doi.org/10.1016/S0140-6736(10)61389-X.
11. Kantoff PW, Higano CS, Shore ND, Berger ER, Small EJ, Penson DF, et al. Sipuleucel-T immunotherapy for castration-resistant prostate cancer. N Engl J Med. 2010;363(5):411–22.
12. Fizazi K, Scher HI, Molina A, Logothetis CJ, Chi KN, Jones RJ, et al. Abiraterone acetate for treatment of metastatic castration-resistant prostate cancer: final overall survival analysis of the COU-AA-301 randomised, double-blind, placebo-controlled phase 3 study. Lancet Oncol. 2012;13(10):983–92. https://doi.org/10.1016/S1470-2045(12)70379-0.
13. Ryan CJ, Smith MR, Fizazi K, Saad F, Mulders PF, Sternberg CN, et al. Abiraterone acetate plus prednisone versus placebo plus prednisone in chemotherapy-naive men with metastatic castration-resistant prostate cancer (COU-AA-302): final overall survival analysis

of a randomised, double-blind, placebo-controlled phase 3 study. Lancet Oncol. 2015;16(2):152–60. https://doi.org/10.1016/S1470-2045(14)71205-7.

14. Scher HI, Fizazi K, Saad F, Taplin ME, Sternberg CN, Miller K, et al. Increased survival with enzalutamide in prostate cancer after chemotherapy. N Engl J Med. 2012;367(13):1187–97. https://doi.org/10.1056/NEJMoa1207506.

15. Parker C, Nilsson S, Heinrich D, Helle SI, O'Sullivan JM, Fossa SD, et al. Alpha emitter radium-223 and survival in metastatic prostate cancer. N Engl J Med. 2013;369(3):213–23. https://doi.org/10.1056/NEJMoa1213755.

16. de Bono J, Mateo J, Fizazi K, Saad F, Shore N, Sandhu S, et al. Olaparib for metastatic castration-resistant prostate cancer. N Engl J Med. 2020;382 (22):2091–102. https://doi.org/10.1056/NEJMoa1911440.

17. Abida W, Campbell D, Patnaik A, Shapiro JD, Sautois B, Vogelzang NJ, et al. Non-BRCA DNA damage repair gene alterations and response to the PARP inhibitor Rucaparib in metastatic castration-resistant prostate cancer: analysis from the phase II TRITON2 study. Clin Cancer Res. 2020;26 (11):2487–96. https://doi.org/10.1158/1078-0432.CCR-20-0394.

18. Sartor O, de Bono J, Chi KN, Fizazi K, Herrmann K, Rahbar K, et al. Lutetium-177-PSMA-617 for metastatic castration-resistant prostate cancer. N Engl J Med. 2021;385(12):1091–103. https://doi.org/10.1056/NEJMoa2107322.

19. Israeli RS, Powell CT, Fair WR, Heston WD. Molecular cloning of a complementary DNA encoding a prostate-specific membrane antigen. Cancer Res. 1993;53(2):227–30.

20. Miyahira AK, Soule HR. The history of prostate-specific membrane antigen as a theranostic target in prostate cancer: the cornerstone role of the Prostate Cancer Foundation. J Nucl Med. 2022;63(3):331–8. https://doi.org/10.2967/jnumed.121.262997.

21. Afshar-Oromieh A, Haberkorn U, Eder M, Eisenhut M, Zechmann C. [68Ga] Gallium-labelled PSMA ligand as superior PET tracer for the diagnosis of prostate cancer: comparison with 18F-FECH. Eur J Nucl Med Mol Imaging. 2012;39(6):1085–6. https://doi.org/10.1007/s00259-012-2069-0.

22. Hofman MS, Lawrentschuk N, Francis RJ, Tang C, Vela I, Thomas P, et al. Prostate-specific membrane antigen PET-CT in patients with high-risk prostate cancer before curative-intent surgery or radiotherapy (proPSMA): a prospective, randomised, multicentre study. Lancet. 2020;395(10231):1208–16. https://doi.org/10.1016/S0140-6736(20)30314-7.

23. Perera M, Papa N, Roberts M, Williams M, Udovicich C, Vela I, et al. Gallium-68 prostate-specific membrane antigen positron emission tomography in advanced prostate cancer—updated diagnostic utility, sensitivity, specificity, and distribution of prostate-specific membrane antigen-avid lesions: a systematic review and meta-analysis. Eur Urol. 2020;77 (4):403–17. https://doi.org/10.1016/j.eururo.2019.01.049.

24. Wright GL Jr, Haley C, Beckett ML, Schellhammer PF. Expression of prostate-specific membrane antigen in normal, benign, and malignant prostate tissues. Urol Oncol. 1995;1(1):18–28.

25. Hillier SM, Maresca KP, Femia FJ, Marquis JC, Foss CA, Nguyen N, et al. Preclinical evaluation of novel glutamateurea-lysine analogues that target prostate-specific membrane antigen as molecular imaging pharmaceuticals for prostate cancer. Cancer Res. 2009;69:6932–40.

26. Kratochwil C, Giesel FL, Eder M, Afshar-Oromieh A, Benešová M, Mier W, et al. [177Lu] lutetium-labelled PSMA ligand-induced remission in a patient with metastatic prostate cancer. Eur J Nucl Med Mol Imaging. 2015;42(6):987–8. https://doi.org/10.1007/s00259-014-2978-1.

27. Kratochwil C, Giesel FL, Stefanova M, Benešová M, Bronzel M, Afshar-Oromieh A, et al. PSMA-targeted radionuclide therapy of metastatic castration-resistant prostate cancer with 177Lu-labeled PSMA-617. J Nucl Med. 2016;57(8):1170–6. https://doi.org/10.2967/jnumed.115.171397.

28. Brasso K, Thomsen FB, Schrader AJ, Schmid SC, Lorente D, Retz M, et al. Enzalutamide antitumour activity against metastatic castration-resistant prostate cancer previously treated with docetaxel and abiraterone: a multicentre analysis. Eur Urol. 2015;68 (2):317–24. https://doi.org/10.1016/j.eururo.2014.07.028.

29. Rahbar K, Ahmadzadehfar H, Kratochwil C, Haberkorn U, Schäfers M, Essler M, et al. German multicenter study investigating 177Lu-PSMA-617 radioligand therapy in advanced prostate cancer patients. J Nucl Med. 2017;58(1):85–90. https://doi.org/10.2967/jnumed.116.183194.

30. Hofman MS, Violet J, Hicks RJ, Ferdinandus J, Thang SP, Akhurst T, et al. [177Lu]-PSMA-617 radionuclide treatment in patients with metastatic castration-resistant prostate cancer (LuPSMA trial): a single-centre, single-arm, phase 2 study. Lancet Oncol. 2018;19(6):825–33. https://doi.org/10.1016/S1470-2045(18)30198-0.

31. Violet J, Sandhu S, Iravani A, Ferdinandus J, Thang S-P, Kong G, et al. Long-term follow-up and outcomes of retreatment in an expanded 50-patient single-center phase II prospective trial of 177Lu-PSMA-617 theranostics in metastatic castration-resistant prostate cancer. J Nucl Med. 2020;61(6):857–65. https://doi.org/10.2967/jnumed.119.236414.

32. Hofman MS, Emmett L, Violet J, Zhang AY, Lawrence NJ, Stockler M, et al. TheraP: a randomized phase 2 trial of 177 Lu-PSMA-617 theranostic treatment vs cabazitaxel in progressive metastatic castration-resistant prostate cancer (Clinical Trial Protocol ANZUP 1603). BJU Int. 2019;124:5–13. https://doi.org/10.1111/bju.14876.

33. Sadaghiani MS, Sheikhbahaei S, Werner RA, Pienta KJ, Pomper MG, Solnes LB, et al. A systematic review and meta-analysis of the effectiveness and toxicities of lutetium-177-labeled prostate-specific membrane antigen-targeted radioligand therapy in metastatic castration-resistant prostate cancer. Eur Urol. 2021;80 (1):82–94. https://doi.org/10.1016/j.eururo.2021. 03.004.

34. Rahbar K, Bode A, Weckesser M, Avramovic N, Claesener M, Stegger L, et al. Radioligand therapy with 177Lu-PSMA-617 as a novel therapeutic option in patients with metastatic castration resistant prostate cancer. Clin Nucl Med. 2016;41(7):522–8. https://doi. org/10.1097/RLU.0000000000001240.

35. An International Prospective Open-label, Randomized, Phase III Study Comparing 177Lu-PSMA-617 in Combination With Soc, Versus SoC Alone, in Adult Male Patients With mHSPC (PSMAddition). U. S. National Library of Medicine; 2021. https://www.clinicaltrials.gov/ct2/show/ NCT04720157. Accessed 12 Mar 2022.

36. Lutetium-177-PSMA-617 in Oligo-metastatic Hormone Sensitive Prostate Cancer (Bullseye). U. S. National Library of Medicine; 2020. https:// clinicaltrials.gov/ct2/show/NCT04443062. Accessed 12 Mar 2022.

37. 177Lu-PSMA-617 vs. Androgen Receptor-directed Therapy in the Treatment of Progressive Metastatic Castrate Resistant Prostate Cancer (PSMAfore). U. S. National Library of Medicine; 2020. https://www. clinicaltrials.gov/ct2/show/NCT04689828. Accessed 12 Mar 2022.

38. Dhiantravan N, Emmett L, Joshua AM, Pattison DA, Francis RJ, Williams S, et al. UpFrontPSMA: a randomized phase 2 study of sequential 177Lu-PSMA-617 and docetaxel vs docetaxel in metastatic hormone-naïve prostate cancer (clinical trial protocol). BJU Int. 2021;128(3):331–42. https://doi.org/10.1111/ bju.15384.

39. Dhiantravan N, Violet J, Eapen R, Alghazo O, Scalzo M, Jackson P, et al. Clinical trial protocol for lutectomy: a single-arm study of the dosimetry, safety, and potential benefit of 177Lu-PSMA-617 prior to prostatectomy. Eur Urol Focus. 2021;7(2):234–7. https://doi.org/10.1016/j.euf.2020.09.021.

40. Enzalutamide With Lu PSMA-617 Versus Enzalutamide Alone in Men With Metastatic Castration-resistant Prostate Cancer (ENZA-p). U. S. National Library of Medicine; 2020. https:// clinicaltrials.gov/ct2/show/NCT04419402. Accessed 12 Mar 2022.

41. 177Lu-PSMA-617 Therapy and Olaparib in Patients With Metastatic Castration Resistant Prostate Cancer (LuPARP). U.S. National Library of Medicine; 2019. https://clinicaltrials.gov/ct2/show/NCT03874884. Accessed 12 Mar 2022.

42. PRINCE (PSMA-lutetium Radionuclide Therapy and ImmuNotherapy in Prostate CancEr). U. S. National Library of Medicine; 2018. https://clinicaltrials.gov/ ct2/show/NCT03658447. Accessed 12 Mar 2022.

43. Sandhu S, Joshua A, Emmett L, Spain L, Horvath L, Crumbaker M, et al. 577O PRINCE: interim analysis of the phase Ib study of 177Lu-PSMA-617 in combination with pembrolizumab for metastatic castration resistant prostate cancer (mCRPC). Ann Oncol. 2021;32:S626–S7. https://doi.org/10.1016/j.annonc. 2021.08.1090.

44. Violet J, Jackson P, Ferdinandus J, Sandhu S, Akhurst T, Iravani A, et al. Dosimetry of (177)Lu-PSMA-617 in metastatic castration-resistant prostate cancer: correlations between pretherapeutic imaging and whole-body tumor dosimetry with treatment outcomes. J Nucl Med. 2019;60(4):517–23. https:// doi.org/10.2967/jnumed.118.219352.

45. Miyahira AK, Pienta KJ, Babich JW, Bander NH, Calais J, Choyke P, et al. Meeting report from the Prostate Cancer Foundation PSMA theranostics state of the science meeting. Prostate. 2020;80 (15):1273–96. https://doi.org/10.1002/pros.24056.

Luca Pasquini and Michael J. Morris

19.1 The Fundamentals

19.1.1 Prostate Cancer

Prostate cancer is the second most common cancer in men worldwide and the fourth most common cancer overall. It is the second most common cause of cancer-related deaths, with a world age-standardized mortality rate of 7.7/100.000 in 2020 [1]. The American Cancer Society estimates that almost 290,000 new cases of prostate cancer will be diagnosed in 2023 alone, while almost 35,000 men will die of the disease over the same span [2]. The 5-year relative survival rates for prostate cancer according to the Surveillance, Epidemiology, and End Results (SEER) program are >99% for localized disease, >99% for regional disease, and 31% for metastatic cancer [2].

Metastatic prostate cancer typically spreads to the bones, particularly those of the axial skeleton. Under normal conditions, bone function is maintained by a delicate balance between the breakdown and formation of bone, which is managed by osteoclasts and osteoblasts, respectively [3]. Metastatic prostate cancer disrupts this balance by interacting with the bone microenvironment. Cancer cells release growth factors—such as transforming growth factor beta (TGF-b)—that promote osteoblast activity [4, 5]. In turn, osteoblasts release growth factors that promote cancer cell survival, creating a bi-directional positive feedback loop [6]. Furthermore, activated osteoblasts stimulate surrounding osteoclasts by secreting the RANKL protein, which leads to the formation of disorganized bone. Osteoclast-mediated bone resorption releases additional growth factors, which fuel cancer cells and contribute to the vicious cycle of osteoblastic bone metastasis [7, 8]. Taken together, these disruptions to bone metabolism produce pathological bone changes that can have a significant impact on the patient's overall health, leading to decline in function. During the early stages of the disease, bone metastases are often not associated with symptoms, but eventually significant subsets of patients will experience bone pain (35–45%), pathologic fractures (14–22%), and spinal cord compression (3–7%) [9, 10]. For these reasons, bone metastatic disease greatly affects the quality of life of patients with prostate cancer and is a leading cause of mortality [11].

The treatment of patients with newly diagnosed metastatic disease is different from the treatment of patients with localized or regional disease. Metastatic prostate cancer is

L. Pasquini (✉)
Molecular Imaging and Therapy Service, Radiology Department, Memorial Sloan Kettering Cancer Center, New York City, NY, USA
e-mail: pasquinl@mskcc.org

M. J. Morris
Department of Medicine, Memorial Sloan Kettering Cancer Center and Weill Cornell Medicine, New York, NY, USA

typically targeted with androgen deprivation therapy (ADT) using drugs such as gonadotropin-releasing hormone agonists and antagonists, usually in combination with chemotherapeutics such as docetaxel, androgen receptor signaling inhibitors such as abiraterone, or both [12–14]. However, despite initial success, the disease eventually progresses to become metastatic castration-resistant prostate cancer (mCRPC). Certain treatments can still improve survival in these cases, including taxanes [15, 16], androgen receptor signaling inhibitors [17–20], PARP inhibitors (for those with DNA repair deficient disease) [21, 22], immune checkpoint inhibitors (for those with microsatellite instability-high (MSI-H) disease), and cellular adoptive immunotherapy [23, 24].

Radiopharmaceutical therapy (RPT) has been used as part of several different treatment strategies for mCRPC. The palliation of severe pain related to bone metastatic disease was the rationale for the first approved RPTs that employed the beta particle-emitters samarium-153 and strontium-89. Radium-223 dichloride—$[^{223}Ra]RaCl_2$; known commercially as Xofigo®—has been part of the treatment of mCRPC in the United States since its approval by the US Food and Drug Administration (FDA) in 2013. $[^{223}Ra]RaCl_2$ is currently used both alone or in combination therapies for mCRPC with bone involvement and no bulky visceral metastatic disease and has exhibited palliative effects for bone pain as well as proven benefits for overall survival.

19.1.2 The First Radiotherapeutics for Prostate Cancer: Samarium-153 and Strontium-89

Radiopharmaceutical therapy (RPT) is a treatment option for prostate cancer that involves the use of radionuclides to target and destroy cancer cells. Historically, a handful of radionuclides—most notably strontium-89 and samarium-153—have been used for the palliation of symptomatic metastatic prostate cancer, with a primary goal of

decreasing bone pain and improving quality of life [25]. Both of the aforementioned radionuclides emit β⁻-particles that irradiate cancer cells in the bone with relatively limited damage to the surrounding healthy tissues (compared to gamma rays) [26]. Strontium-89 (specifically $[^{89}Sr]Sr^{2+}$) targets bone metastases because it mimics Ca^{2+} and is preferentially absorbed in sites of new bone formation [25, 27]. Samarium-153, on the other hand, is not naturally taken up in bone but rather complexed with ethylene-diamine-tetramethylene-phosphonate (EDTMP), which is incorporated in hydroxyapatite in sites of active bone turnover [28].

Strontium-89 has a half-life of 50.5 days, emits β⁻-particles with a mean energy of 0.58 MeV and a maximum energy of 1.46 MeV, and is administered as strontium chloride in doses of 150 MBq every 90 days. The preferential absorption of strontium-89 in areas of bone formation results in concentrations of the radionuclide ~10 times higher in osteoblastic metastases compared to healthy bone [27]. A systematic review reported that treatment with strontium-89 leads to some degree of pain response in 76% of patients and complete pain relief in 32% of cases [29]. Several studies have explored the effects of strontium-89 when used in addition to or as an alternative to local radiotherapy. Along these lines, a randomized phase III study by Porter et al. found that the group receiving strontium-89 in addition to local radiotherapy had reduced need for pain medication and improved quality of life [30]. Despite these promising results, a large study from the European Organization for the Research and Treatment of Cancer found no difference in progression-free survival between patients treated with a single injection of strontium-89 or palliative local field radiotherapy, although overall survival was improved with external beam radiotherapy [31]. As a result, strontium-89 is reserved to pain palliation and not for its anticancer effects. The side effects of strontium-89 have been reported as low and reversible, with a temporary decrease in white blood cell counts and platelet levels typically occurring 12–16 weeks after treatment [29]. Pain flare lasting up to

4 days has also been reported 1–5 days after the administration of strontium-89, though a previous trial associated the onset of pain flare with good response [29, 32].

Samarium-153 has a half-life of 1.9 days, emits β⁻-particles with a mean energy of 0.69 MeV and a maximum energy of 0.81 MeV, and is administered in a recommended dosage of 37 MBq/kg [28]. Unlike strontium-89, samarium-153 is not naturally absorbed by the bones but is instead complexed by a molecule called ethylenediamine tetramethylene phosphanate (EDTMP) that is responsible for the radiopharmaceutical's ability to target sites of active bone turnover [28]. Sartor et al. conducted a double-blinded, randomized, prospective trial to investigate the effectiveness of [^{153}Sm]Sm-EDTMP by comparing it to a stable placebo, [^{152}Sm]Sm-EDTMP [33]. Patients who received a single administration of 37 MBq/kg [^{153}Sm]Sm-EDTMP reported significant pain relief within 1–2 weeks along with a decrease in opioid use in the following 3–4 weeks. [^{153}Sm]Sm-EDTMP is generally well-tolerated, with limited side effects including transient myelosuppression that predominantly affects platelets and white blood cells but resolves approximately 8 weeks post-treatment [34].

19.2   The Details

19.2.1   The Chemistry, Dosimetry, and Physiology of Radium-223

Radium-223 (^{223}Ra) is a radionuclide that has been extensively studied for the treatment of prostate cancer. Under physiological conditions, radium exists primarily as a dication—Ra^{2+}—that resembles its cationic alkaline earth congener Ca^{2+} [35]. Several studies have shown that [^{223}Ra]Ra^{2+} accumulates in the vicinity of activated osteoblasts and within the surrounding bone matrix, substituting for Ca^{2+} in hydroxyapatite complexes [36, 37]. Furthermore, the skeletal accumulation of [^{223}Ra]Ra^{2+} is dependent on the local blood vessel density [38].

Radium-223 is primarily an α-emitting radionuclide. As the name suggests, α-decay is the

process whereby an unstable nucleus emits an alpha particle consisting of two protons and two neutrons, the structural equivalent to a helium nucleus. Radium-223 has a half-life of 11.4 days and decays via a pathway involving six daughter radioisotopes before reaching stability as lead-207. This protracted decay chain results in the emission of multiple α-particles, which enhances the dose delivered to the target [36, 37, 40, 41]. Indeed, ~95% of the total emitted energy (28.2 MeV) during decay comes from α-particles, compared to ~3% from beta particles and ~2% from gamma emissions [39].

The α-particles produced by radium-223 have high linear energy transfer (LET), meaning that their energy (i.e., a maximum energy of 4.96 MeV) is deposited over a short range of ~100 micrometers. Radionuclides that emit high LET particles cause direct damage to DNA and are thus less reliant on oxygen as a mediator of radiotoxicity and less susceptible to resistance mechanisms than radioisotopes that emit gamma-rays and β-particles [42]. In fact, the DNA damage caused by α-particles—most famously double-strand breaks—is more difficult to repair and thus more cytotoxic than that produced by β-particles, including single-strand breaks, base-pair deletions, substitutions, and crosslinks [42, 43]. For example, while 1000 DNA hits from β-particles are needed to cause cell death, only 1-4 DNA hits from α-particles may be sufficient [42]. In addition, the cytotoxic DNA damage induced by radium-223 in tumor cells promotes apoptosis and disrupts the positive feedback loops between osteoblasts and osteoclasts, thereby breaking the vicious cycle of bone metastases (Fig. 19.1) and potentiating therapeutic effects.

Taken together, the effects of α-particles lead to the inhibition of tumor growth and the stabilization of normal bone structure [44]. In addition, treatment with [^{223}Ra]Ra^{2+} may also enhance the immune system's activity and alter the phenotype of cancer cells, rendering them more susceptible to immune-mediated cell killing [45].

One of the principal advantages of using α-emitting radionuclides like radium-223 is their ability to minimize injury to healthy bone marrow. Because of their high LET, α-emitters have
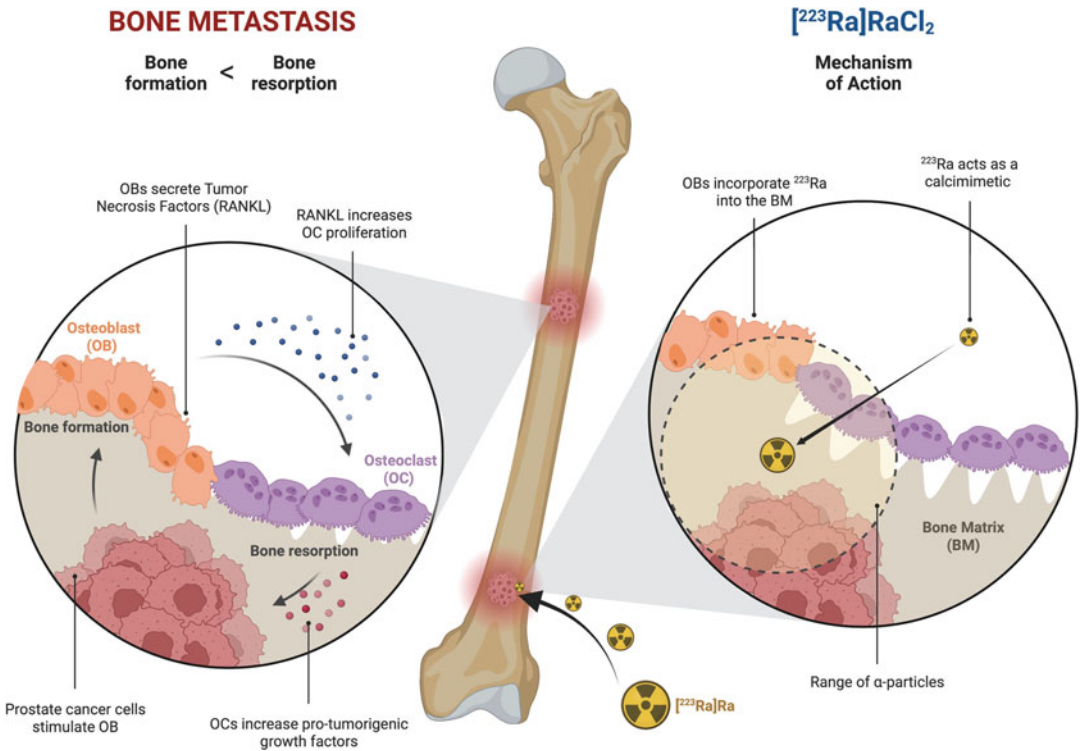
Fig. 19.1 Illustration of the vicious cycle of bone metastases as well as $[^{223}Ra]RaCl_2$'s mechanism of action. Metastatic prostate cancer cells interact with the bone microenvironment, releasing growth factors that promote osteoblast activity. These activated osteoblasts then stimulate surrounding osteoclasts by secreting the RANKL protein, leading to formation of disorganized bone.

$[^{223}Ra]Ra^{2+}$ accumulates within the bone matrix in the vicinity of activated osteoblasts by substituting for Ca^{2+} in hydroxyapatite. It then delivers its therapeutic α-particles, killing cancer cells via radiation-induced DNA damage and thus interfering with the positive feedback loop between osteoblasts and osteoclasts that supports tumor growth

low soft tissue penetration—in the range of 40–90 μm—leading to less dose to the bone marrow compared to β-emitters and thus reduced risk of myelosuppression [46]. This is particularly important in the context of prostate cancer patients, as they are often at a higher risk of developing bone marrow failure due to the disease's predilection for bone metastases.

19.2.2 History of $[^{223}Ra]RaCl_2$: From Clinical Trials to FDA Approval

The first study assessing the suitability of $^{223}Ra^{2+}$ for clinical applications was reported in 2005 [41]. This phase I clinical trial by Nilsson et al. evaluated the safety, tolerability, pain palliation of $[^{223}Ra]RaCl_2$ in patients with breast and prostate cancer with bone metastases. Fifteen prostate cancer and ten breast cancer patients received a single IV dose of $[^{223}Ra]RaCl_2$ and were then monitored for 8 weeks. Five patients were included at each of the dose levels: 46, 93, 163, 213, and 250 kBq/kg. The study reported mild reversible myelosuppression 2–4 weeks after the injection, including grade 1 thrombocytopenia. Two patients had grade 3 neutropenia, and three had grade 3 leucopenia. Ten of the 25 patients experienced mild, temporary diarrhea. Nausea and vomiting were more common in the highest dosage group. Serum markers of bone turnover showed favorable changes in response to treatment, with a decrease of alkaline phosphatase (averages of 29.5% in females and 52.1% in

males). The majority of the patients reported pain relief as early as 7 days. The radium-223 was cleared quickly from the blood pool and was below 1% of its initial level after 24 h, with the primary excretion pathway the intestines. The median survival of the patients was over 20 months [41].

Another phase I study from Carrasquillo et al. assessed the pharmacokinetics, pharmacodynamics, and biodistribution of $[^{223}Ra]RaCl_2$ in ten patients receiving either 50, 100, or 200 kBq/Kg as well as a subgroup of six patients that received a second dose of 50 kBq/kg [47]. Pharmacokinetic analysis indicated the swift removal of radium-223 from the bloodstream, with a median plasma residual of 14% at the end of infusion (range 9–34%), 2% after 4 h (range 1.6–3.9%), and 0.5% after 24 h (range 0.4–1.0%). Biodistribution results showed that a significant proportion of the radium-223 (median of 52%) was excreted through the bowel within 24 h, with a comparatively minor amount (median of 4%) eliminated via urine. Prolonged bone retention was observed, but no dose-limiting toxicity was detected. Observed pharmacodynamic effects included reductions in the levels of alkaline phosphatase and serum N-telopeptides. Overall, administered activities of up to 200 kBq/kg were linked with minimal adverse effects and showed potential to prompt a decrease in serum markers of bone turnover [47].

Additional studies followed these promising results. In a multicenter randomized phase II trial, Nilsson et al. compared the outcomes of 33 mCRPC patients receiving 4 weekly intravenous injections of $[^{223}Ra]RaCl_2$ (50 kBq/kg) and 31 mCRPC patients receiving placebo. The primary outcomes included changes in bone-alkaline phosphatase (ALP) concentration and the time to skeletal-related events (SRE). Secondary outcomes included toxicity, time to PSA progression, and overall survival. The study demonstrated good tolerance of radium-223, with minimal myelotoxicity and significant positive effects on bone-ALP concentrations [48]. Particularly, thrombocytopenia (CTCAE grade 2+) was not observed in the $[^{223}Ra]RaCl_2$ group, while it was recorded in a single placebo patient.

Neutropenia of grade 2+ was found in three patients treated with $[^{223}Ra]RaCl_2$ and none given the placebo, though it was typically transient and occurred primarily during the initial 4 weeks of treatment, with no indication of cumulative myelotoxic effects. No significant differences in hematological toxicity were observed between the two groups, and none of the patients ceased $[^{223}Ra]RaCl_2$ treatment due to treatment-related adverse effects [48].

Another phase II trial evaluated the relationship between the dose of $[^{223}Ra]RaCl_2$ and its pain-relieving effects [49]. The study was conducted with 100 patients with mCRPC and painful bone metastases, with the primary efficacy endpoint the change in pain index (Brief Pain Inventory—BPI [50]) from baseline to weeks 2, 4, 8, 12 and 16. The patients were randomly given a single intravenous dose of 5, 25, 50, or 100 kBq/kg of $[^{223}Ra]RaCl_2$. Results showed a significant dose-response relationship for pain reduction at week 2. By week 8, 40%, 63%, 56%, and 71% of patients in the 5, 25, 50, and 100 kBq/kg groups, respectively, showed improvement in their pain and stable use of pain medication. Additionally, there was a decrease in the level of ALP in the group receiving the highest dose. All doses were found to be safe and well-tolerated.

The phase II non-randomized multicenter open trial by McHugh et al. evaluated pain palliation with $[^{223}Ra]RaCl_2$ standard dosing in patients with mCRPC. The primary endpoint of the study was a >30% decline in BPI score by week 8, confirmed at week 12 [51]. Out of the 29 subjects enrolled, 9 (31%) met this primary endpoint. The median worst pain declined among responders, with a 62% reduction (range 36–100) at week 8 and a 63% reduction (range 38–100) at week 12. The median reduction in pain interference with general activity and sleep at week 12 was 62% (range 18–100) and 53% (range 8–100), respectively. At week 12, the median reduction in worst fatigue was 45% (range 10–85) [51].

The use of $[^{223}Ra]RaCl_2$ for the treatment of mCRPC was approved by the FDA in 2013 as a result of the ALSYMPCA trial [52]. This study

was a randomized double-blinded phase III trial that evaluated $[^{223}Ra]RaCl_2$ versus placebo (in addition to the best standard of care) in patients with mCRPC metastatic to the bones. The study recruited 921 subjects and used overall survival as the primary endpoint. Additional secondary outcomes included time to the first symptomatic SRE as well as multiple biochemical metrics. The analysis confirmed a survival benefit for $[^{223}Ra]RaCl_2$ compared to placebo: median 14.9 months versus 11.3 months (hazard ratio 0.70; 95% CI 0.58–0.83; $P < 0.001$). In addition, the mean time to the first symptomatic SRE was 15.6 months in the $[^{223}Ra]RaCl_2$ and 9.8 months in the placebo group ($p < 0.001$). $[^{223}Ra]RaCl_2$ was also associated with low myelosuppression rates. Indeed, there were fewer patients who experienced adverse events in the $[^{223}Ra]RaCl_2$ group than in the placebo group for all adverse events (558 [93%] vs. 290 [96%]), grade 3 or 4 adverse events (339 [56%] vs. 188 [62%]), serious adverse events (281 [47%] vs. 181 [60%]), and discontinuation due to adverse events (99 [16%] vs. 62 [21%]). Grade 3 febrile neutropenia was reported in one patient (<1%) in the $[^{223}Ra]RaCl_2$ group and in one patient (<1%) in the placebo group. Only one grade 5 hematologic adverse event was deemed possibly related to the study drug, namely thrombocytopenia in a patient in the radium-223 group who died from pneumonia with hypoxemia and no evidence of bleeding. The frequencies of serious adverse events that occurred in at least 5% of patients in either the $[^{223}Ra]RaCl_2$ or the placebo arm, respectively, were as follows: disease progression (11% and 12%), bone pain (10% and 16%), anemia (8% and 9%), and spinal cord compression (4% and 5%). Finally, quality of life was significantly improved in the patients who received $[^{223}Ra]RaCl_2$.

Following FDA approval, the long-term side effects of $[^{223}Ra]RaCl_2$ have been evaluated by two studies: the ALSYMPCA trial follow-up study at 3 years [53] and the ongoing REASSURE study [54]. The ALSYMPCA 3-year follow-up analysis found no correlation between $[^{223}Ra]RaCl_2$ treatment and the development of secondary malignancies such as acute myelogenous leukemia, myelodysplastic syndrome, or new primary bone cancer. Non-treatment-related malignancies occurred at a similar rate in both the $[^{223}Ra]RaCl_2$ and placebo groups. $[^{223}Ra]RaCl_2$ was associated with a low incidence of myelosuppression and low cumulative rates for both hematological and non-hematological adverse events [53]. The other trial, REASSURE, is a global, prospective, non-interventional study to evaluate long-term safety of $[^{223}Ra]RaCl_2$ in patients with mCRPC and bone involvement. The study group published an interim analysis in 2019 [55], reporting data from 583 subjects observed for a median of 7 months. The interim analysis showed that the short-term safety of $[^{223}Ra]RaCl_2$ in routine clinical practice is similar to that reported by other clinical studies regardless of prior chemotherapy use, but hematological adverse events occurred more often in the group that had previously received chemotherapy. This is likely due to decreased bone marrow function from advanced disease and previous cytotoxic therapy. Patients with no prior record of chemotherapy demonstrated less severe disease and a lower rate of discontinuation of $[^{223}Ra]RaCl_2$ treatment.

The encouraging results of the ALSYMPCA trial and the subsequent safety studies have led to the recommendation of $[^{223}Ra]RaCl_2$ in all the main guidelines for the treatment of mCRPC. The guidelines from the National Comprehensive Cancer Network (NCCN) advocate for the use of $[^{223}Ra]RaCl_2$ in patients with mCRPC, symptomatic bone metastases, and no other metastases in the viscera [56]. The American Urological Association (AUA) suggests offering $[^{223}Ra]RaCl_2$ to patients with mCRPC, symptomatic bony metastases, and without known visceral disease or lymphadenopathy >3 cm [57]. The European Association of Urology (EAU) includes $[^{223}Ra]RaCl_2$ as an option for life-prolonging treatment for patients with mCRPC with progression after docetaxel chemotherapy [58]. The Advanced Prostate Cancer Consensus Conference advises for the use of $[^{223}Ra]RaCl_2$ during the course of bone-predominant mCRPC in patients without visceral or bulky lymph node disease [12].

Unfortunately, biomarkers of response for RPT with $[^{223}Ra]RaCl_2$ are lacking in the

literature. Imaging assessment was not performed in the ALSYMPCA trial, so it remains to be clarified whether radiographic or scintigraphic response is an indicator of treatment benefit [52]. PSA is not a reliable biomarker of response during treatment with $[^{223}Ra]RaCl_2$, as it often fails to show any significant decline or demonstrates variable increments ('PSA flares') that do not correlate with treatment efficacy [59]. Sartor et al. conducted an exploratory analyses of the data from the ALSYMPCA trial to assess the prognostic and predictive value of blood levels of ALP, lactate dehydrogenase (LDH), and PSA for treatment with $[^{223}Ra]RaCl_2$ [60]. The authors described noticeable decreases in ALP compared to the placebo group as soon as 4 weeks into therapy with $[^{223}Ra]RaCl_2$. While lower levels of ALP or LDH at the 12-week mark were associated with extended overall survival, they failed to satisfy statistical surrogate criteria. Ultimately, the authors concluded that although tracking the fluctuation of ALP and LDH during $[^{223}Ra]RaCl_2$ treatment could be beneficial for monitoring purposes, these levels cannot be utilized as substitutes for survival prediction [60]. Conversely, however, other authors found a significant association between early treatment-induced changes in ALP after one injection of $[^{223}Ra]RaCl_2$ and overall survival in patients with mCRPC [61]. Based on this evidence, ALP appears to be the closest the field has to a biomarker that indicates treatment benefit. Clearly, further studies are required to find a better candidate to serve this purpose.

19.2.3 $[^{223}Ra]RaCl_2$ and Bone Fracture Risk: The ERA223 and PEACE III Trials

Bone fractures are a relatively common adverse event in patients with bony prostate cancer, with up to 14–22% of treated patients experiencing this complication at some point during the history of their disease [11]. As a result, increased risk of bone fractures is a primary concern in treatments for prostate cancer. To wit, ADT has been linked to loss of bone density at 12 months, with increased predisposition to weight-bearing bone fractures [62]. A recent study analyzed National Cancer Institute Cancer Therapy Evaluation Program (CTEP)-sponsored early phase trials to assess the prevalence of bone fractures amongst patients during or after ADT, with a result of 4.6 per 1000 person-years [63]. Other lines of therapy for mCRPC also carry increased risk of bone fractures, mainly related to their combination with corticosteroids such as prednisone or prednisolone which are well-known inducers of osteoporosis [64].

Treatment with $[^{223}Ra]RaCl_2$ has also been associated with increased bone fracture risk in several studies. The randomized, double-blind, placebo-controlled, phase 3 clinical trial ERA223 evaluated the addition of $[^{223}Ra]RaCl_2$ to abiraterone acetate and prednisone or prednisolone in patients with CRPC metastatic to the bone [65]. The study evaluated a total of 806 patients and was unblinded prematurely due to increased number of skeletal events and death in the $[^{223}Ra]RaCl_2$ group compared to placebo. Particularly, bone fractures occurred in 29% of patients in the $[^{223}Ra]RaCl_2$ group versus 11% in the placebo group, while SRE-free survival was 22.3 months in the $[^{223}Ra]RaCl_2$ group and 26.0 months in the placebo group (hazard ratio 1.122 [95% CI 0.9—17−1.374]; $p = 0.2636$). Therefore, the combination of $[^{223}Ra]RaCl_2$ with abiraterone acetate and either prednisone or prednisolone was not recommended by the ERA223 trial, and it is currently contraindicated by the EMA [66].

On the other hand, in the ALSYMPCA trial, the proportion of patients reporting a pathologic fracture was 4% for the $[^{223}Ra]RaCl_2$ group and 5% for the placebo group. The explanation for these contrasting results remains debated. $[^{223}Ra]RaCl_2$ may increase the risk of fracture if used in combination with other agents with negative effects on bone density, primarily abiraterone and prednisolone. This hypothesis is supported by the correlation between prior corticosteroid use and the risk of fracture in patients treated with $[^{223}Ra]RaCl_2$ [67]. However, other studies—such as the PEACE III trial, an ongoing

Table 19.1 Ongoing clinical trials of combination therapies featuring [^{223}Ra]RaCl$_2$

	Second agent	Mechanism	Trial design	Primary outcomes	Patient characteristics	Estimated completion date	Trial ID
Androgen-receptor signaling inhibitors							
PEACE III trial	Enzalutamide	AR inhibitor	Phase III (vs. enzalutamide only)	Radiological progression-free survival	CRPC with asymptomatic or mildly symptomatic BM ($n = 416$)	December 2025	NCT02194842
Chemotherapy							
DORA trial	Docetaxel	Microtubule inhibitor	Randomized phase III (vs. docetaxel only)	Overall survival	mCRPC ($n = 738$)	December 2024	NCT03574571
Immunotherapy							
	Pembrolizumab	PD-1 inhibitor	Randomized phase II (vs. ^{223}Ra only)	Extent of immune cell infiltration	mCRPC with BM ($n = 45$)	June 2024	NCT03093428
DNA damage response							
COMRADE trial	Olaparib	PARP inhibitor	Randomized phase I/II (vs. ^{223}Ra only)	Maximum tolerated dose of olaparib and 223Ra; radiographic progression-free survival	CRPC with BM ($n = 133$)	November 30, 2023	NCT03317392

randomized phase III clinical trial investigating the combination of $[^{223}Ra]RaCl_2$ with the androgen-receptor signaling inhibitor enzalutamide (Table 19.1)—reported an increased fracture risk in the $[^{223}Ra]RaCl_2$ arm without steroids [68]. As a consequence, anti-androgenic effects may play a pivotal role in rising bone fracture risk independent from steroids.

In the ERA223 trial, the use of bone health agents (BHAs) such as bisphosphonates (zoledronic acid) and denosumab was linked to lower fracture rates in both the $[^{223}Ra]RaCl_2$ (15% with BHAs; 37% without) and placebo (7% with BHAs; 15% without) groups. In addition, the hazard ratios for symptomatic SRE-free survival for the $[^{223}Ra]RaCl_2$ and placebo groups was lower with BHAs (0.932) than without them (1.252) [65]. The ALSYMPCA trial also showed that patients treated with $[^{223}Ra]RaCl_2$ and BHAs had better symptomatic SRE outcomes than those without BHAs [52]. The benefits of BHAs in combination with $[^{223}Ra]RaCl_2$ also emerged from the PEACE III trial [68]. Initially, the trial did not mandate bone protective therapy, resulting in a fracture rate of 13% for the enzalutamide arm and 33% for the $[^{223}Ra]RaCl_2$ + enzalutamide cohort. Following the publication of the ERA223 trial data, however, the trial was amended to mandate the use of BHAs, a pivot which dramatically decreased of the fracture risk in both arms to 0% and 3%, respectively [68]. A recent study on the long-term safety of $[^{223}Ra]RaCl_2$ plus enzalutamide after a median of 22 months did not show any increase in fractures or other adverse events in the combination group with the use of protective bone agents [69]. As a consequence, BHAs are always recommended to maximize treatment benefits of $[^{223}Ra]RaCl_2$ and preserve bone health.

19.2.4 Combination Therapies

The combination of $[^{223}Ra]RaCl_2$ with other therapeutic agents with different mechanisms has been proposed to increase the efficacy of treatments without modifying their tolerability.

The primary agents that have been studied or are currently being explored as combination treatments with $[^{223}Ra]RaCl_2$ include androgen-receptor signaling inhibitors (abiraterone, enzalutamide), chemotherapy agents (docetaxel), immunotherapy agents (atezolizumab, pembrolizumab, sipuleucel-T), and DNA damage response inhibitors (niraparib, olaparib) [66].

19.2.4.1 $[^{223}Ra]RaCl_2$ and Chemotherapy
The rationale for combining chemotherapeutic agents with $[^{223}Ra]RaCl_2$ is to target the tumor and osseous compartment at the same time and to take advantage of the cumulative effects from cross-sensitization [66]. In fact, chemotherapy can increase the uptake of $[^{223}Ra]RaCl_2$ by promoting bone healing and enhancing the deposition of hydroxyapatite [70]. Also, the spatial distribution of $[^{223}Ra]RaCl_2$ in the bone is likely to leave some regions of bone tumors unaffected due to the short range of α-particles, leaving areas that must be targeted by systemic chemotherapy [70].

Docetaxel is an antimitotic chemotherapeutic agent of the taxane class that acts by stabilizing the microtubules of dividing cells [71]. The NCCN and ESMO guidelines recommend docetaxel for mCRPC patients who are symptomatic or have high disease burden [72]. Treatment with docetaxel demonstrated improved overall survival in patients with mCRPC in the TAX327 trial, a randomized multicenter non-blinded phase III study conducted on 1006 patients [15] in which patients treated with docetaxel every 3 weeks and prednisone achieved a median survival of 18.9 months versus 16.5 months compared to patients treated with mitoxantrone and steroids [15, 73]. Cabazitaxel similarly prolongs life in men with mCRPC [16]. Chemotherapy is the preferred treatment modality for patients who have progressed after androgen-receptor pathway inhibitors, following the CARD trial. In that study, the efficacy and safety of cabazitaxel was compared to an androgen-receptor signaling inhibitor (abiraterone or enzalutamide) in patients with mCRPC who had previously received docetaxel and experienced progression while receiving the alternate androgen-receptor

signaling inhibitor [74]. Results after a median follow-up of 9.2 months revealed that 95 out of 129 patients (73.6%) in the cabazitaxel group experienced imaging-based progression or death compared to 101 out of 126 patients (80.2%) inthe androgen-receptor signaling inhibitor group (hazard ratio: 0.54; 95% confidence interval [CI]: 0.40–0.73; $P < 0.001$). Median imaging-based PFS was 8.0 months in the cabazitaxel group versus 3.7 months in the control. Median overall survival was 13.6 months in the cabazitaxel group and 11.0 months in the control group (hazard ratio for death: 0.64; 95% CI: 0.46–0.89; $P = 0.008$) [74].

Given the continued importance of chemotherapy for mCRPC, several studies have explored the combination of $[^{223}Ra]RaCl_2$ and docetaxel-based chemotherapy. For example, a phase 1 dose escalation/randomized phase 2a trial evaluated the combination of $[^{223}Ra]RaCl_2$ and docetaxel in patients with bony mCRPC [75]. The recommended phase 2 dose (RP2D) of $[^{223}Ra]RaCl_2$ for the combination was 5 doses of 55 kBq/kg every 6 weeks alongside 10 doses of 60 mg/m^2 docetaxel every 3 weeks. Full doses of docetaxel—75 mg/m^2—produced an excess of febrile neutropenic events; however, $[^{223}Ra]RaCl_2$ at the full 55 kBq/kg plus docetaxel at 60 mg/m^2 actually yielded less hematologic toxicity than docetaxel alone. Otherwise, the safety profiles of both treatment groups were comparable. The combination arm showed a more sustained suppression of PSA (6.6 vs. 4.8 months median time to progression), ALP (9 vs. 7 months), and markers of osteoblastic bone deposition. Median time to PSA progression was longer in the patients treated with $[^{223}Ra]RaCl_2$ + docetaxel compared to docetaxel alone (7 vs. 5 months). Therefore, the study concluded that the combination was well tolerated, with efficacy data suggesting enhanced antitumoral activity for the $[^{223}Ra]RaCl_2$ + docetaxel compared to docetaxel alone.

The phase III clinical trial DORA is currently investigating the combination $[^{223}Ra]RaCl_2$ + docetaxel versus docetaxel alone in a larger randomized cohort (Table 19.1). In this study, 75 mg/m^2 docetaxel is administered IV every 3 weeks for 10 doses alongside prednisone 5 mg orally twice daily. For the combination arm, 10 doses of 60 mg/m^2 docetaxel are administered IV every 3 weeks as well as 6 doses of 55 kBq/kg $[^{223}Ra]RaCl_2$ administered at 6-week intervals. The primary evaluated endpoint is overall survival. The secondary and exploratory objectives include evaluating progression-free survival, freedom from symptomatic SRE, safety, changes in markers of bone metabolism, alterations in circulating tumor cells and DNA, and patient-reported outcomes [76].

19.2.4.2 $[^{223}Ra]RaCl_2$ and DNA Damage Response Inhibitors

Genomic defects in DNA repair are fairly common in mCRPC and can influence the disease's sensitivity to anti-cancer drugs that cause DNA damage, including inhibitors of DNA repair proteins such as poly(ADP-ribose) polymerase (PARP) [66]. This suggests that administering PARP inhibitors to patients with tumors that have DNA repair defects could exploit a synthetic lethality interaction. Alpha particles cause cell death by causing both single and double-stranded DNA breaks. Hence, blocking various DNA repair pathways with PARP inhibitors may enhance the cytotoxicity of $[^{223}Ra]RaCl_2$. It is also possible that treatment with $[^{223}Ra]RaCl_2$ alone may be more effective in patients whose tumors have genetic defects in DNA repair [70].

Olaparib, a PARP inhibitor, is used to treat advanced ovarian cancer patients with germline BRCA1 or BRCA2 gene mutations [77]. The FDA granted olaparib a breakthrough therapy designation for the monotherapy of BRCA1, BRCA2, or ATM-mutated mCRPC patients who have received prior taxane-based chemotherapy and at least one next-generation anti-hormonal agent (abiraterone or enzalutamide) [78]. The open label multicenter phase I/II trial COMRADE is testing the hypothesis that the combination of $[^{223}Ra]RaCl_2$ with olaparib has anti-tumoral activity in patients with mCRPC regardless of the underlying homologous recombination repair deficiency status (Table 19.1) [79]. An interim communication about phase I of the study reported 12 enrolled patients (age range

59–81 years). Three patients had grade 3–4 treatment-related adverse events at dose level 1 (olaparib 200 mg), including two with G3 anemia and one with G3 thrombocytopenia, not requiring dose reduction. Two patients had G3-4 treatment-related adverse events at dose level 2 (olaparib 300 mg), including one with G3 anemia, one with G4 lymphocytopenia, and one with G3 stroke. Five patients underwent a dose reduction at dose level 2, and there were no grade 5 events. The recommended dose for olaparib was determined to be 200 mg BID when combined with $[^{223}Ra]RaCl_2$. Out of the enrolled patients, two had a PSA response (16.7%) and eight had an ALP response (67%). The median follow-up was 6.5 months with a 6-month rPFS rate of 57% (95% CI 25–80%). The report concluded that olaparib can be safely combined with $[^{223}Ra]RaCl_2$ [80].

A recent Phase I study evaluated the PARP inhibitor niraparib in combination with $[^{223}Ra]RaCl_2$ for the treatment of mCRPC in men without known BRCA mutations [81]. Thirty patients underwent treatment in the combination arm. Out of these, 13 patients received a dose of 100 mg niraparib, 12 received 200 mg, and 5 received 300 mg. There were 6 instances of dose-limiting toxicity, including 2 cases (13%) of neutropenia, 2 cases (13%) of thrombocytopenia, and 1 case each (3%) of fatigue and nausea. Anemia (2 cases; 13%) and neutropenia (2 cases; 13%) were the most common grade 3 side effects. These results showed that the combination of niraparib and $[^{223}Ra]RaCl_2$ was safe in patients with mCRPC, laying the foundation for further randomized trials.

19.2.4.3 $[^{223}Ra]RaCl_2$ and Immunotherapy

Radiation therapy induces immunogenic tumor cell death and can optimize anti-tumor immune responses for maximal therapeutic outcomes [82]. As a result, combining RPT and immunotherapeutics has garnered a great deal of attention. Immunotherapy treatments for mCRPC include immune checkpoint inhibitors (e.g., ipilimumab and tremelimumab), PD-1/PD-L1 inhibitors (e.g. atezolizumab, pembrolizumab,

and nivolumab), and immunostimulants (e.g., sipuleucel-T) [66]. Combination therapies featuring each of these classes and $[^{223}Ra]RaCl_2$ are currently under investigation.

PD-L1 is expressed on cancer cells and immune cells in response to inflammation and inhibits immune activation. Research in mice found that radiation therapy can increase the expression of PD-1 and PD-L1 in the tumor's microenvironment, thereby weakening the immune response [83]. However, the use of inhibitory PD-L1 antibodies at the same time as radiation boosts the effect of radiation via the activation of cytotoxic T cells, creating synergistic effects that block tumor growth [83]. These data establish a compelling rationale for combining of $[^{223}Ra]RaCl_2$ with agents that target the PD-1/PD-L1 axis, such as atezolizumab and pembrolizumab. However, the phase Ib trial NCT02814669 focused on the combination of $[^{223}Ra]RaCl_2$ and atezolizumab in patients with mCRPC and bone and lymph node and/or visceral metastases reported greater toxicity for the combination than either drug alone (regardless of administration schedule) as well as no clear evidence of additional clinical benefit [84]. In addition, the combination of $[^{223}Ra]RaCl_2$ and pembrolizumab is currently under investigation in a randomized phase II trial (Table 19.1) [85]. An interim report of the trial revealed that $[^{223}Ra]RaCl_2$ + pembrolizumab did not increase unexpected adverse events but did not lead to prolonged progression-free survival or overall survival compared to $[^{223}Ra]RaCl_2$ alone [86]. Based on this early evidence, this combination does not improve clinical outcomes to the degree necessary to support its sustained clinical use.

Sipuleucel-T is an FDA-approved autologous cell therapy that generates and increases T cell populations specific to tumor antigens using patient-enriched monocytic cells activated with a recombinant fusion protein (PA2024) [66]. The combination of this treatment with $[^{223}Ra]RaCl_2$ may achieve synergistic therapeutic effects, since sublethal doses of $[^{223}Ra]RaCl_2$ have been shown to make prostate cancer cells more susceptible to lysis by T lymphocytes [87]. A phase II study
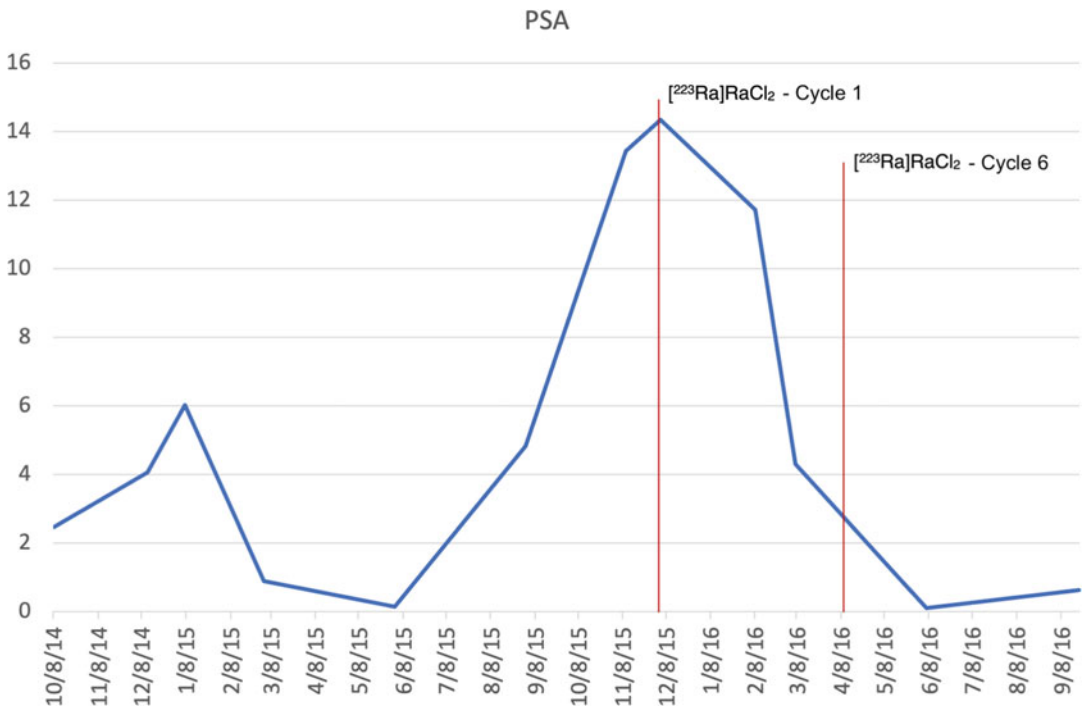
Fig. 19.2 Prostate-specific antigen (PSA) values at the time of $[^{223}Ra]RaCl_2$ administration (first and last cycles indicated as vertical red lines). The patient demonstrated a significant decline in PSA levels after the initiation of RPT with $[^{223}Ra]RaCl_2$. However, PSA decreases are not commonly seen in association with this treatment, as variable blood levels typically offer limited correlation with treatment response

investigated the combination of $[^{223}Ra]RaCl_2$ and sipuleucel-T in patients with mCRPC with asymptomatic or mildly symptomatic bone metastases [88]. In this study, patients in the combination group showed more frequent >50% PSA decline (5 [31%] versus 0 patients; $P = 0.04$), longer PFS (39 vs. 12 weeks; HR 0.32; 95% CI 0.14–0.76), and longer OS (not-reached vs. 2.6 years; HR 0.32; 95% CI 0.08–1.23). The results highlighted the increased clinical efficacy the combination of sipuleucel-T and $[^{223}Ra]RaCl_2$ in men with mCRPC and minimally symptomatic bone disease, despite their seemingly weaker immune responses [88].

19.3 $[^{223}Ra]RaCl_2$ in Clinical Practice

Here we include two clinical case studies to illustrate the power of $[^{223}Ra]RaCl_2$ for the treatment of patients with mCRPC.

19.3.1 Case 1

A 77-year-old male with Gleason 7 (4 + 3) CRPC metastatic to the bones received 6 cycles of $[^{223}Ra]RaCl_2$ treatment with a dose of 50 kBq/ kg. The patient had previously undergone a radical retropubic prostatectomy, and pathology reported negative margins, the focal involvement of the seminal vesicles, and 0/13 positive lymph nodes. He was initially treated with ADT, corticosteroids, and BHAs. He underwent external beam salvage radiation to the prostatectomy bed and seminal vesicles and subsequently to the right pelvis for recurrence. He progressed to mCRPC and was treated with enzalutamide. The patient's prostate-specific antigen (PSA) peaked at a value of 124.21 ng/mL during systemic treatment. After transient normalization followed by the fluctuation of PSA, the value rose again from 0.14 to 14.34 ng/ml (Fig. 19.2), and he was referred to the nuclear medicine service for RPT

Fig. 19.3 Bone scans before (**a**) and after (**b**) RPT with $[^{223}Ra]RaCl_2$, showing slightly decreased uptake of ^{99m}Tc-MPD by the osseous metastases in the latter (red arrows)
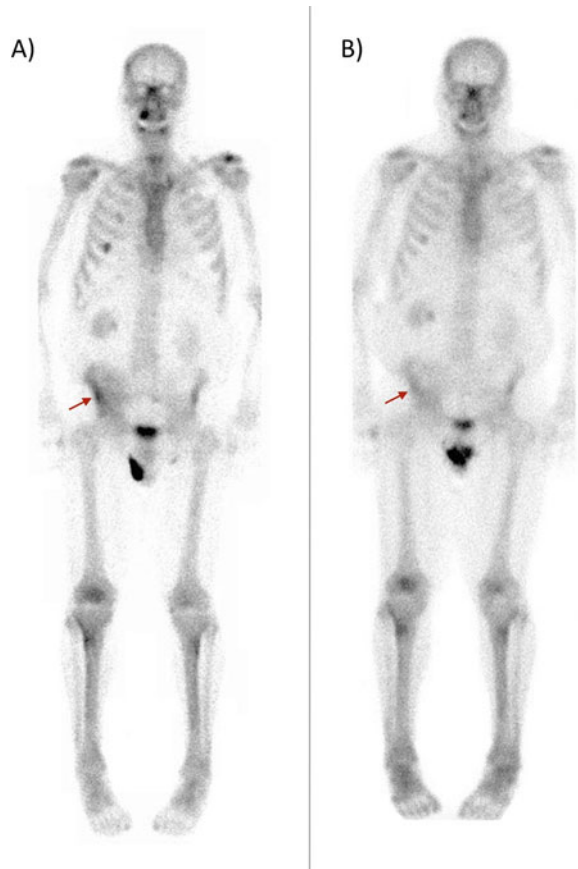
with $[^{223}Ra]RaCl_2$. The pre-treatment ^{99m}Tc-MPD bone scan showed tracer-avid metastases in the right fifth rib and the right iliac bone (Fig. 19.3a). After RPT with $[^{223}Ra]RaCl_2$, the metastases showed decreased avidity on bone scan (Fig. 19.3b), and the PSA levels decreased to 0.1 ng/ml (Fig. 19.2).

19.3.2 Case 2

A 76-year-old male with Gleason 7 (3 + 4) CRPC metastatic to the bones received 6 cycles of $[^{223}Ra]RaCl_2$ with a dose of 55 kBq/kg. The patient had previously undergone a radical retropubic prostatectomy, and pathology reported positive margins, the involvement of the seminal vesicles, and 2/19 positive lymph nodes (stage pT3b). He was initially treated with ADT, corticosteroids, and BHAs. He underwent initial external beam salvage radiation to the prostatectomy bed and pelvis and subsequently palliative radiation to right iliac bone metastasis. He progressed to mCRPC and was treated with enzalutamide. The patient's PSA gradually increased over time from a value of 0.17 ng/mL to 98.57 ng/mL (Fig. 19.4), and he was referred to the nuclear medicine service for RPT with $[^{223}Ra]RaCl_2$. The pre-treatment bone scan showed multiple tracer-avid bone metastases, including the whole spine, bilateral ribs, and right iliac bone (Fig. 19.5a). After RPT with $[^{223}Ra]RaCl_2$, the metastases showed decreased avidity on bone scan (Fig. 19.5b), and the PSA level decreased to 0.7 ng/ml (Fig. 19.4).
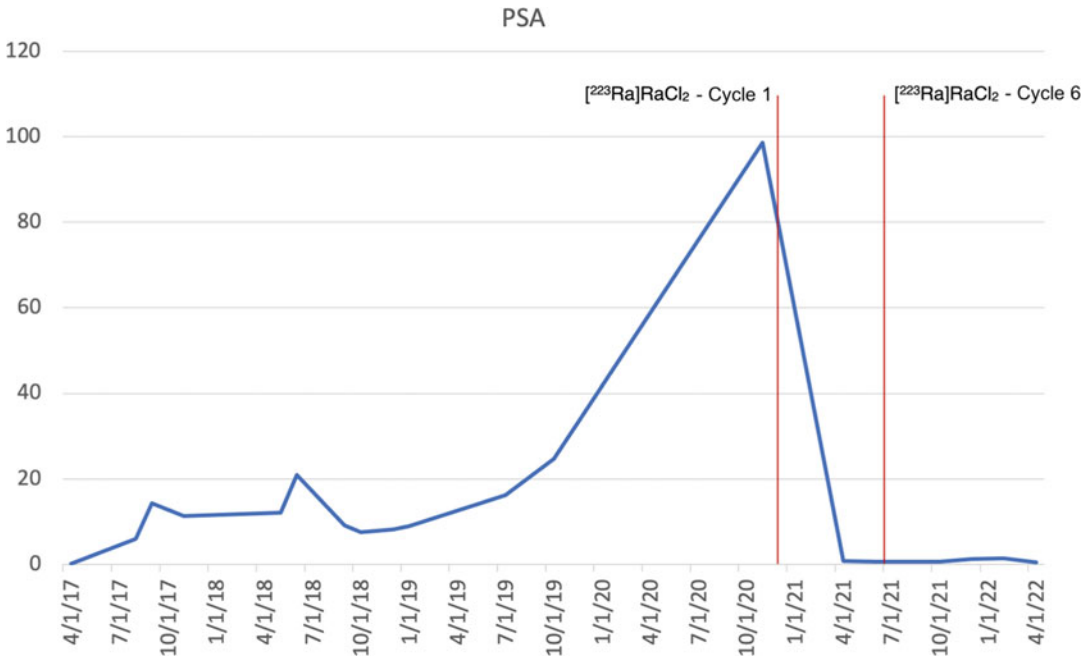
Fig. 19.4 Prostate-specific antigen (PSA) values at the time of $[^{223}Ra]RaCl_2$ administration (first and last cycles indicated as vertical red lines). The patient demonstrated a significant decline in PSA levels after the initiation of RPT with $[^{223}Ra]RaCl_2$. However, PSA decreases are not commonly seen in association with this treatment, as variable blood levels typically offer limited correlation with treatment response

19.4 Future Directions: The Role of $[^{223}Ra]RaCl_2$ in a Field Dominated by PSMA-Targeted Therapies

The panorama of prostate cancer treatment is rapidly changing via the incorporation of recent discoveries in new therapeutic approaches. The use of RPT for mCRPC is growing given the promising results of numerous studies in the recent years. The future direction of α-particle therapy will inevitably be influenced by the recent FDA approval of the β-emitting radiotherapeutic $[^{177}Lu]Lu$-PSMA-617 (Pluvicto). $[^{177}Lu]Lu$-PSMA-617 targets prostate-membrane specific antigen (PSMA), a cell surface marker that is over-expressed by prostate cancer cells (although not specifically) [89–91]. The FDA gave its approval to Pluvicto as a treatment option for adults suffering from mCRPC (including those with bone and viscera metastases) whose tumors exhibit an excessive production of PSMA and who have not responded to standard treatment methods. The FDA's decision was based on the results of the VISION trial, which demonstrated a survival advantage for patients treated with $[^{177}Lu]Lu$-PSMA-617 compared to those who received only standard therapies (median of 15.3 months versus 11.3 months) [92].

PSMA-targeted radiotherapeutics carry the promise of delivering radiation selectively to the tumor, a clear advantage compared to the extant ^{89}Sr-, ^{153}Sm-, and ^{223}Ra-based radiotherapeutics that lack tumor-targeting power. It is important to note, however, that lutetium-177—like strontium-89 and samarium-153—emits β-particles that have low LET and are thus less cytotoxic than α-particles while boasting greater soft tissue penetration, potentially increasing radiation dose to the bone marrow, and causing more adverse events. In this context, $[^{223}Ra]RaCl_2$ represents a model for the advancement of the field. Indeed, the historic success of $[^{223}Ra]$
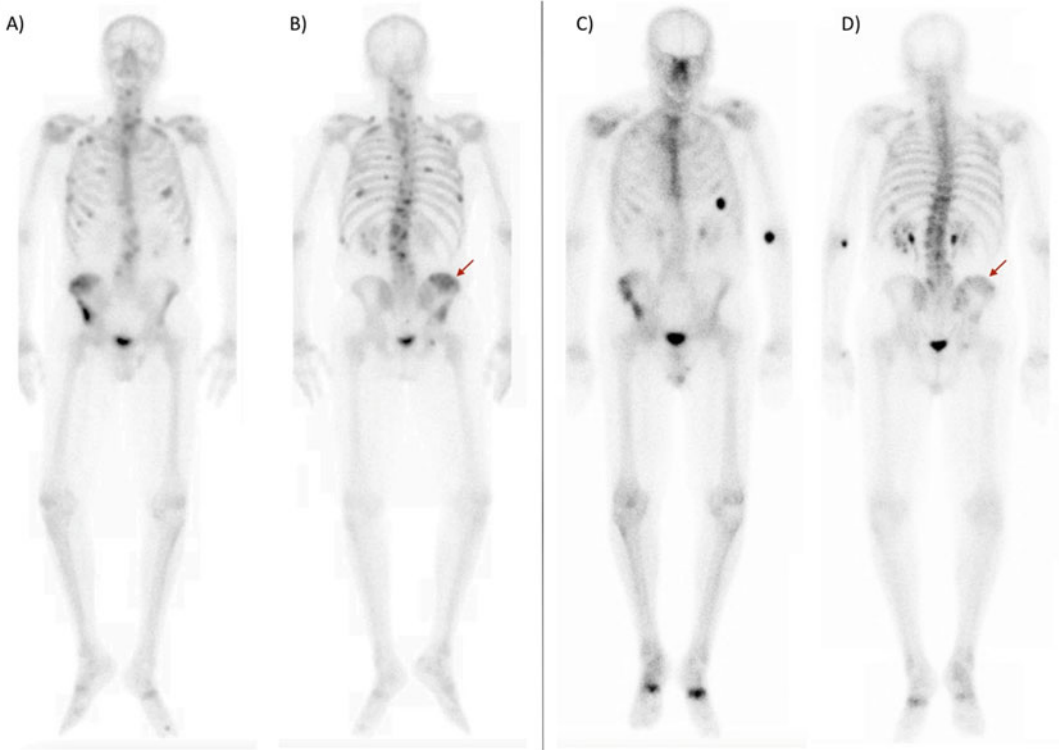
Fig. 19.5 Bone scans before (**a** and **b** show anterior and posterior views, respectively) and after (**b** and **c** show anterior and posterior views, respectively) the administration of $[^{223}Ra]RaCl_2$, showing decreased uptake of ^{99m}Tc-MDP by the osseous metastases in the latter (red arrows). New focal uptake in the left antecubital region in **c** and **d** was related to the accumulation of the imaging agent at the injection site. New focal uptake of ^{99m}Tc-MDP in the left anterior sixth rib in panels **c** and **d** was post-traumatic

$RaCl_2$ RPT in mCRPC highlights the strengths of α-radiation for cancer treatment: high LET particles produce more cytotoxic damage to tumor cells while simultaneously offering both greater control over the local irradiated volume and bone marrow protection. It is our belief that the future of mCRPC treatment will lie with α-emitting, PSMA-targeted radiotherapeutics, which will be able to leverage the combined strengths of all of the currently available tools.

19.5 Bottom Line

- The spread of cancer to the bones is a major cause of mortality for prostate cancer patients.
- Recent advancements have significantly transformed the landscape of prostate cancer treatment. The use of RPT for metastatic castration-resistant prostate cancer (mCRPC) has gained momentum due to promising outcomes in numerous studies.
- $[^{223}Ra]RaCl_2$ is currently employed either as a standalone treatment or in combination therapies for mCRPC with bone involvement, excluding extensive metastasis to other organs.
- The alpha particle-emitting cation $[^{223}Ra]Ra^{2+}$ accumulates near activated osteoblasts and within the adjacent bone structure, irradiating cancer cells while causing minimal harm to the bone marrow.
- RPT with $[^{223}Ra]RaCl_2$ has demonstrated palliative effects on bone pain and has shown substantial benefits in terms of overall survival.

References

1. WCRF. Prostate cancer statistics. 2020. https://www.wcrf.org/cancer-trends/prostate-cancer-statistics/. Accessed 1 Feb 2023.
2. Prostate cancer detection, diagnosis, staging, survival rates. https://www.cancer.org/cancer/prostate-cancer/detection-diagnosis-staging/survival-rates.html. Accessed 1 Feb 2023.
3. Chiechi A, Guise TA. Pathobiology of osteolytic and osteoblastic bone metastases. Metastatic Bone Disease. 2016; https://doi.org/10.1007/978-1-4614-5662-9_2.
4. Dallas SL, Rosser JL, Mundy GR, Bonewald LF. Proteolysis of latent transforming growth factor-β (TGF-β)-binding protein-1 by osteoclasts. A cellular mechanism for release of TGF-β from bone matrix. J Biol Chem. 2002;277:21352–60.
5. Dallas SL, Zhao S, Cramer SD, Chen Z, Peehl DM, Bonewald LF. Preferential production of latent transforming growth factor β-2 by primary prostatic epithelial cells and its activation by prostate-specific antigen. J Cell Physiol. 2005;202:361–70.
6. Fizazi K, Yang J, Peleg S, et al. Prostate cancer cells-osteoblast interaction shifts expression of growth/survival-related genes in prostate cancer and reduces expression of osteoprotegerin in osteoblasts. Clin Cancer Res. 2003;9:2587–97.
7. Brown JM, Corey E, Lee ZD, True LD, Yun TJ, Tondravi M, Vessella RL. Osteoprotegerin and rank ligand expression in prostate cancer. Urology. 2001;57:611–6.
8. Enomoto H, Shiojiri S, Hoshi K, et al. Induction of osteoclast differentiation by Runx2 through receptor activator of nuclear factor-κB ligand (RANKL) and osteoprotegerin regulation and partial rescue of osteoclastogenesis in Runx2-/- mice by RANKL transgene. J Biol Chem. 2003;278:23971–7.
9. Saad F, Gleason DM, Murray R, Tchekmedyian S, Venner P, Lacombe L, Chin JL, Vinholes JJ, Goas JA, Zheng M. Long-term efficacy of zoledronic acid for the prevention of skeletal complications in patients with metastatic hormone-refractory prostate cancer. J Natl Cancer Inst. 2004;96:879–82.
10. Fizazi K, Carducci M, Smith M, et al. Denosumab versus zoledronic acid for treatment of bone metastases in men with castration-resistant prostate cancer: a randomised, double-blind study. Lancet. 2011;377:813–22.
11. Autio KA, Scher HI, Morris MJ. Therapeutic strategies for bone metastases and their clinical sequelae in prostate cancer. Curr Treat Options in Oncol. 2012;13:174–88.
12. Gillessen S, Attard G, Beer TM, et al. Management of patients with advanced prostate cancer: report of the advanced prostate cancer consensus conference 2019. Eur Urol. 2020;77:508–47.
13. Gillessen S, Armstrong A, Attard G, et al. Management of patients with advanced prostate cancer: report from the advanced prostate cancer consensus conference 2021. Eur Urol. 2022;82:115–41.
14. Gillessen S, Bossi A, Davis ID, et al. Management of patients with advanced prostate cancer. Part I: intermediate-/high-risk and locally advanced disease, biochemical relapse, and side effects of hormonal treatment: report of the advanced prostate cancer consensus conference 2022. Eur Urol. 2022;83:267–93.
15. Tannock IF, de Wit R, Berry WR, et al. Docetaxel plus prednisone or mitoxantrone plus prednisone for advanced prostate cancer. N Engl J Med. 2004;351:1502–12.
16. De Bono JS, Oudard S, Ozguroglu M, et al. Prednisone plus cabazitaxel or mitoxantrone for metastatic castration-resistant prostate cancer progressing after docetaxel treatment: a randomised open-label trial. Lancet. 2010;376:1147–54.
17. de Bono JS, Logothetis CJ, Molina A, et al. Abiraterone and increased survival in metastatic prostate cancer. N Engl J Med. 2011;364:1995–2005.
18. Ryan CJ, Smith MR, de Bono JS, et al. Abiraterone in metastatic prostate cancer without previous chemotherapy. N Engl J Med. 2013;368:138–48.
19. Beer TM, Armstrong AJ, Rathkopf DE, et al. Enzalutamide in metastatic prostate cancer before chemotherapy. N Engl J Med. 2014;371:424–33.
20. Scher HI, Fizazi K, Saad F, et al. Increased survival with enzalutamide in prostate cancer after chemotherapy. N Engl J Med. 2012;367:1187–97.
21. de Bono J, Mateo J, Fizazi K, et al. Olaparib for metastatic castration-resistant prostate cancer. N Engl J Med. 2020;382:2091–102.
22. Agarwal N, Azad A, Carles J, et al. TALAPRO-2: phase 3 study of talazoparib (TALA) + enzalutamide (ENZA) versus placebo (PBO) + ENZA as first-line (1L) treatment in patients (pts) with metastatic castration-resistant prostate cancer (mCRPC). J Clin Oncol. 2023;41(6_suppl):LBA17.
23. Kantoff PW, Higano CS, Shore ND, et al. Sipuleucel-T immunotherapy for castration-resistant prostate cancer. N Engl J Med. 2010;363:411–22.
24. (2017) FDA grants accelerated approval to pembrolizumab for first tissue/site agnostic indication. https://www.fda.gov/drugs/resources-information-approved-drugs/fda-grants-accelerated-approval-pembrolizumab-first-tissuesite-agnostic-indication. Accessed 27 Mar 2023.
25. Murray I, Du Y. Systemic radiotherapy of bone metastases with radionuclides. Clin Oncol. 2021;33:98–105.
26. Radiation Basics. https://www.epa.gov/radiation/radiation-basics. Accessed 7 Feb 2023.
27. Robinson RG, Blake GM, Preston DF, McEwan AJ, Spicer JA, Martin NL, Wegst AV, Ackery DM. Strontium-89: treatment results and kinetics in patients with painful metastatic prostate and breast cancer in bone. Radiographics. 1989;9:271–81.
28. Bayouth JE, Macey DJ, Kasi LP, Fossella FV. Dosimetry and toxicity of samarium-153-

EDTMP administered for bone pain due to skeletal metastases. J Nucl Med. 1994;35:63–9.

29. Finlay IG, Mason MD, Shelley M. Radioisotopes for the palliation of metastatic bone cancer: a systematic review. Lancet Oncol. 2005;6:392–400.

30. Porter AT, Mcgowan DG, Powe JE, et al. Results of a randomized phase-III trial to evaluate the efficacy of strontium-89 adjuvant to local field external beam irradiation in the management of endocrine resistant metastatic prostate cancer. Int J Radiat Oncol Biol Phys. 1993;25:805–13.

31. Oosterhof GON, Roberts JT, de Reijke TM, Engelholm SA, Horenblas S, von der Maase H, Neymark N, Debois M, Collette L. Strontium-89 chloride versus palliative local field radiotherapy in patients with hormonal escaped prostate cancer: a phase III study of the European Organisation for Research and Treatment of Cancer Genitourinary Group. Eur Urol. 2003;44:519–26.

32. Laing AH, Ackery DM, Bayly RJ, Buchanan RB, Lewington VJ, McEwan AJB, Macleod PM, Zivanovic MA. Strontium-89 chloride for pain palliation in prostatic skeletal malignancy. Br J Radiol. 1991;64:817–22.

33. Sartor O, Reid RH, Hoskin PJ, Quick DP, Ell PJ, Coleman RE, Kotler JA, Freeman LM, Olivier P. Samarium-153-lexidronam complex for treatment of painful bone metastases in hormone-refractory prostate cancer. Urology. 2004;63:940–5.

34. Sartor O, Reid RH, Bushnell DL, Quick DP, Ell PJ. Safety and efficacy of repeat administration of samarium Sm-153 lexidronam to patients with metastatic bone pain. Cancer. 2007;109:637–43.

35. Henriksen G, Hoff P, Alstad J, Larsen RH, Henriksen G, Larsen RH. 223Ra for endoradiotherapeutic applications prepared from an immobilized 227Ac/227Th source. Radiochim Acta. 2001;89:661–6.

36. Henriksen G, Larsen RH, Henriksen G, Larsen RH, Breistøl K, Fodstad Ø, Bruland ØS. Significant antitumor effect from bone-seeking, α-particle-emitting 223Ra demonstrated in an experimental skeletal metastases model. Cancer Res. 2002;62:3120–5.

37. Henriksen G, Fisher DR, Roeske JC, Bruland ØS, Larsen RH. Targeting of osseous sites with alpha-emitting 223Ra: comparison with the beta-emitter 89Sr in mice. J Nucl Med. 2003;44:252–9.

38. Abou DS, Ulmert D, Doucet M, Hobbs RF, Riddle RC, Thorek DLJ. Whole-body and microenvironmental localization of radium-223 in Naïve and mouse models of prostate cancer metastasis. J Natl Cancer Inst. 2016;108:1–9.

39. Deshayes E, Roumiguie M, Thibault C, et al. Radium 223 dichloride for prostate cancer treatment. Drug Des Devel Ther. 2017;11:2643–51.

40. Pallares RM, Abergel RJ. Development of radiopharmaceuticals for targeted alpha therapy: where do we stand? Front Med (Lausanne). 2022;9: 1–16.

41. Nilsson S, Larsen RH, Fosså SD, Balteskard L, Borch KW, Westlin JE, Salberg G, Bruland ØS. First clinical experience with α-emitting radium-223 in the treatment of skeletal metastases. Clin Cancer Res. 2005;11:4451–9.

42. Sgouros G, Roeske JC, McDevitt MR, et al. MIRD pamphlet No. 22 (Abridged): radiobiology and dosimetry of α-particle emitters for targeted radionuclide therapy. J Nucl Med. 2010;51:311–28.

43. Elgqvist J, Frost S, Pouget JP, Albertsson P. The potential and hurdles of targeted alpha therapy—clinical trials and beyond. Front Oncol. 2014;3:324.

44. Suominen MI, Fagerlund KM, Rissanen JP, et al. Radium-223 inhibits osseous prostate cancer growth by dual targeting of cancer cells and bone microenvironment in mouse models. Clin Cancer Res. 2017;23: 4335–46.

45. Malamas AS, Gameiro SR, Knudson KM, Hodge JW. Sublethal exposure to alpha radiation (223Ra dichloride) enhances various carcinomas' sensitivity to lysis by antigenspecific cytotoxic T lymphocytes through calreticulin-mediated immunogenic modulation. Oncotarget. 2016;7:86937–47.

46. Sartor O, Sharma D. Radium and other alpha emitters in prostate cancer. Transl Androl Urol. 2018;7:436–44.

47. Carrasquillo JA, O'Donoghue JA, Pandit-Taskar N, et al. Phase I pharmacokinetic and biodistribution study with escalating doses of 223Ra-dichloride in men with castration-resistant metastatic prostate cancer. Eur J Nucl Med Mol Imaging. 2013;40:1384–93.

48. Nilsson S, Franzén L, Parker C, et al. Bone-targeted radium-223 in symptomatic, hormone-refractory prostate cancer: a randomised, multicentre, placebo-controlled phase II study. Lancet Oncol. 2007;8:587–94.

49. Nilsson S, Strang P, Aksnes AK, Franzn L, Olivier P, Pecking A, Staffurth J, Vasanthan S, Andersson C, Bruland OS. A randomized, dose-response, multicenter phase II study of radium-223 chloride for the palliation of painful bone metastases in patients with castration-resistant prostate cancer. Eur J Cancer. 2012;48:678–86.

50. Daut RL, Cleeland CS, Flanery RC. Development of the Wisconsin Brief Pain Questionnaire to assess pain in cancer and other diseases. Pain. 1983;17:197–210.

51. McHugh D, Tagawa S, Moryl N, Milowsky M, Heller G, Osborne J, Rathkopf D, Basch E, Pandit-Taskar N, Morris MJ. A phase II, nonrandomized open trial assessing pain efficacy with radium-223 in symptomatic metastatic castration-resistant prostate cancer. Clin Genitourin Cancer. 2021;19:447–56.

52. Parker C, Nilsson S, Heinrich D, et al. Alpha emitter radium-223 and survival in metastatic prostate cancer. N Engl J Med. 2013;369:213–23.

53. Parker C, Zhan L, Cislo P, Reuning-Scherer J, Vogelzang NJ, Nilsson S, Sartor O, O'Sullivan JM, Coleman RE. Effect of radium-223 dichloride (Ra-223) on hospitalisation: an analysis from the

phase 3 randomised Alpharadin in Symptomatic Prostate Cancer Patients (ALSYMPCA) trial. Eur J Cancer. 2017;71:1–6.

54. NCT02141438. https://www.clinicaltrials.gov/ct2/show/NCT02141438. Accessed 1 Feb 2023.

55. Dizdarevic S, Petersen PM, Essler M, et al. Interim analysis of the REASSURE (Radium-223 alpha Emitter Agent in non-intervention Safety Study in mCRPC popUlation for long-teRm Evaluation) study: patient characteristics and safety according to prior use of chemotherapy in routine clinical practice. Eur J Nucl Med Mol Imaging. 2019;46:1102–10.

56. NCCN. National comprehensive cancer network. NCCN guidelines Prostate cancer version 1. 2018. Accessed 1 Feb 2023.

57. AUA American Urological Association. Castration-resistant prostate cancer. 2020. https://www.auanet.org/guidelines/prostate-cancer-castration-resistantguideline.

58. EAU. European Association of Urology. Prostate cancer guidelines. 2019.

59. Castello A, Macapinlac HA, Lopci E, Santos EB. Prostate-specific antigen flare induced by 223RaCl2 in patients with metastatic castration-resistant prostate cancer. Eur J Nucl Med Mol Imaging. 2018;45:2256–63.

60. Sartor O, Coleman RE, Nilsson S, et al. An exploratory analysis of alkaline phosphatase, lactate dehydrogenase, and prostate-specific antigen dynamics in the phase 3 ALSYMPCA trial with radium-223. Ann Oncol. 2017;28:1090–7.

61. van der Doelen MJ, Stockhaus A, Ma Y, Mehra N, Yachnin J, Gerritsen WR, Nilsson S, van Oort IM, Ullén A. Early alkaline phosphatase dynamics as biomarker of survival in metastatic castration-resistant prostate cancer patients treated with radium-223. Eur J Nucl Med Mol Imaging. 2021;48:3325–34.

62. Daniell H, Dunn S, Ferguson D, Lomas G, Niazi Z, Stratte P. Progressive osteoporosis during androgen deprivation therapy for prostate cancer. J Urol. 2000;163:181–6.

63. Myint ZW, Kunos CA. Bone fracture incidence after androgen deprivation therapy-investigational agents: results from cancer therapy evaluation program-sponsored early phase clinical trials 2006–2013. Front Oncol. 2020;10:1–8.

64. Kobza AO, Herman D, Papaioannou A, Lau AN, Adachi JD. Understanding and managing corticosteroid-induced osteoporosis. Open Access Rheumatol. 2021;13:177–90.

65. Smith M, Parker C, Saad F, et al. Addition of radium-223 to abiraterone acetate and prednisone or prednisolone in patients with castration-resistant prostate cancer and bone metastases (ERA 223): a randomised, double-blind, placebo-controlled, phase 3 trial. Lancet Oncol. 2019;20:408–19.

66. Morris MJ, Corey E, Guise TA, Gulley JL, Kevin Kelly W, Quinn DI, Scholz A, Sgouros G. Radium-223 mechanism of action: implications for use in treatment combinations. Nat Rev Urol. 2019;16:745–56.

67. Hijab A, Curcean S, Tunariu N, et al. Fracture risk in men with metastatic prostate cancer treated with radium-223. Clin Genitourin Cancer. 2021;19:e299–305.

68. Gillessen S, Choudhury A, Rodriguez-Vida A, et al. Decreased fracture rate by mandating bone protecting agents in the EORTC 1333/PEACEIII trial combining Ra223 with enzalutamide versus enzalutamide alone: an updated safety analysis. J Clin Oncol. 2021;39 (15_suppl):5002.

69. Maughan BL, Kessel A, McFarland TR, et al. Radium-223 plus enzalutamide versus enzalutamide in metastatic castration-refractory prostate cancer: final safety and efficacy results. Oncologist. 2021;26:1006–e2129.

70. Miyahira AK, Morris M, Soule HR. Meeting report from the Prostate Cancer Foundation Scientific Working Group on Radium-223. Prostate. 2017;77:245–54.

71. Bissery MC, Gueritte-Voegelein F. Experimental antitumor activity of taxotere (RP 56976, NSC 628503), a taxol analogue. Cancer Res. 1991;51:4845–52.

72. Parker C, Gillessen S, Heidenreich A, Horwich A. Cancer of the prostate: ESMO Clinical Practice Guidelines for diagnosis, treatment and follow-up. Ann Oncol. 2015;26:v69–77.

73. Berthold DR, Pond GR, Soban F, De Wit R, Eisenberger M, Tannock IF. Docetaxel plus prednisone or mitoxantrone plus prednisone for advanced prostate cancer: updated survival in the TAX 327 study. J Clin Oncol. 2008;26:242–5.

74. de Wit R, de Bono J, Sternberg CN, et al. Cabazitaxel versus abiraterone or enzalutamide in metastatic prostate cancer. N Engl J Med. 2019;381:2506–18.

75. Morris MJ, Loriot Y, Sweeney CJ, et al. Radium-223 in combination with docetaxel in patients with castration-resistant prostate cancer and bone metastases: a phase 1 dose escalation/randomised phase 2a trial. Eur J Cancer. 2019;114:107–16.

76. Morris MJ, de Wit R, Vogelzang NJ, Tagawa ST, Higano CS, Hamberg P. A phase III trial of docetaxel versus docetaxel and radium-223 (Ra-223) in patients with metastatic castration-resistant prostate cancer (mCRPC): DORA. J Clin Oncol. 2021;37(7_suppl):TPS348.

77. Fong PC, Boss DS, Yap TA, et al. Inhibition of poly (ADP-ribose) polymerase in tumors from BRCA mutation carriers. N Engl J Med. 2009;361:123–34.

78. (2016) Lynparza Olaparib granted breakthrough therapy designation by USFDA for treatment of BRCA1-2 or ATM gene-mutated metastatic castration-resistant prostate cancer. https://www.astrazeneca.com/media-centre/press-releases/2016/Lynparza-Olaparibgranted-Breakthrough-Therapy-Designation-by-USFDA-for-treatment-of-BRCA1-2-or-ATM-gene-mutatedmetastatic-Castration-Resistant-Prostate-Cancer-28012016.html#. Accessed 1 Feb 2023.

79. Shaya J, Xie W, Saraiya B, et al. A phase I/II study of combination olaparib and radium-223 in men with metastatic castration-resistant prostate cancer with bone metastases (COMRADE): a trial in progress. J Clin Oncol. 2021;39(6_suppl):TPS182.

80. McKay RR, Xie W, Ajmera A, et al. A phase 1/2 study of olaparib and radium-223 in men with metastatic castration-resistant prostate cancer (mCRPC) with bone metastases (COMRADE): results of the phase 1 study. J Clin Oncol. 2021;39(15_suppl):e17020.

81. Quinn Z, Leiby B, Sonpavde G, et al. Phase I study of Niraparib in combination with radium-223 for the treatment of metastatic castrate-resistant prostate cancer. Clin Cancer Res. 2023;29:50–9.

82. Gelbard A, Garnett CT, Abrams SI, Patel V, Gutkind SJ, Palena C, Tsang K-Y, Schlom J, Hodge JW. Combination chemotherapy and radiation of human squamous cell carcinoma of the head and neck augments CTL-mediated lysis. Clin Cancer Res. 2006;12:1897–905.

83. Deng L, Liang H, Burnette B, Beckett M, Darga T, Weichselbaum RR, Fu YX. Irradiation and anti-PD-L1 treatment synergistically promote antitumor immunity in mice. J Clin Investig. 2014;124:687–95.

84. Fong L, Morris MJ, Sartor O, et al. A phase Ib study of atezolizumab with radium-223 dichloride in men with metastatic castration-resistant prostate cancer. Clin Cancer Res. 2021;27:4746–56.

85. NCT03093428. https://clinicaltrials.gov/ct2/show/NCT03093428. Accessed 1 Feb 2023.

86. Choudhury AD, Kwak L, Cheung A, et al. Randomized phase II study evaluating the addition of pembrolizumab to radium-223 in metastatic castration-resistant prostate cancer. J Clin Oncol. 2021;39(6_suppl):98.

87. Gameiro SR, Ardiani A, Kwilas A, Hodge JW. Radiation-induced survival responses promote immunogenic modulation to enhance immunotherapy in combinatorial regimens. Onco Targets Ther. 2014;3:e28643.

88. Marshall CH, Fu W, Wang H, et al. Randomized phase II trial of sipuleucel-T with or without radium-223 in men with bone-metastatic castration-resistant prostate cancer. Clin Cancer Res. 2021;26:1623–30.

89. Wright GL, Haley C, Lou BM, Schellhammer PF. Expression of prostate-specific membrane antigen in normal, benign, and malignant prostate tissues. Urol Oncol: Semin Orig Investig. 1995;1:18–28.

90. Heston DW. Characterization and glutamyl preferring carboxypeptidase function of prostate specific membrane antigen: a novel folate hydrolase. Urology. 1997;49:104–12.

91. Chang SS, Reuter VE, Heston WDW, Bander NH, Grauer LS, Gaudin PB. Five different anti-prostate-specific membrane antigen (PSMA) antibodies confirm PSMA expression in tumor-associated neovasculature. Cancer Res. 1999;59:3192–8.

92. Sartor O, de Bono J, Chi KN, et al. Lutetium-177–PSMA-617 for metastatic castration-resistant prostate cancer. N Engl J Med. 2021;385:1091–103.

Part III

Special Topics

Katarzyna M. Wulfmeier, Jordan Cheng, Ines M. Costa,
Alex Rigby, Lefteris Livieratos, Richard Fernandez,
Philip J. Blower, Katherine A. Vallis, Raymond M. Reilly,
Giacomo Pirovano, and Samantha Y. A. Terry

20.1 The Fundamentals

Auger electrons (AEs) were first described by Lise Meitner [1] and Pierre Auger in the 1920s. They arise due to the decay of radionuclides via electron capture or internal conversion. Electron capture occurs when an inner shell electron is drawn into the nucleus of an unstable, positively charged atom, leaving a vacancy in an inner orbital shell. Internal conversion is a non-nuclear decay process in which an excited nucleus interacts electromagnetically with one of the electrons surrounding the nucleus, leading to the ejection of said electron. This too causes a vacancy in an orbital shell. Regardless of the initiating process, the electron shell vacancy is filled via the transition of a higher energy electron to the shell containing the vacancy. This process in turn creates a new shell vacancy that needs to be filled, thereby initiating a cascade of electronic transitions. Ultimately, this phenomenon releases energy that is emitted as an X-ray or imparted on an outer electron (now named an AE) that is ejected from the atom (Fig. 20.1).

Due to the cascade, AEs can be produced in large numbers. Depending on the radionuclide, between 4 and 37 AEs with different energies can be emitted per decay [2]. They are characteristically low in energy, with a maximum energy release of less than 25 keV [2]. However, as this energy is deposited across a short distance – typically less than 0.5 μm in tissue – the linear energy transfer (LET) of AEs is very large: 4–26 keV/μm. This LET value is much larger higher than that of β particles (~0.2 keV/μm) but lower than that of α-particles (50–230 keV/μm). To put this into context, the RPT field has mostly been driven by radiotherapeutics bearing low LET β-emitters, such as [^{177}Lu]Lu-DOTATATE for patients with advanced neuroendocrine tumours and

K. M. Wulfmeier · J. Cheng · I. M. Costa · A. Rigby
P. J. Blower · S. Y. A. Terry (✉)
School of Biomedical Engineering and Imaging Sciences, King's College London, London, UK
e-mail: samantha.terry@kcl.ac.uk

L. Livieratos
School of Biomedical Engineering and Imaging Sciences, King's College London, London, UK

Department of Medical Physics, Guy's and St Thomas' Hospital, London, UK

R. Fernandez
Department of Medical Physics, Guy's and St Thomas' Hospital, London, UK

K. A. Vallis
Oxford Institute for Radiation Oncology, University of Oxford, Oxford, UK

R. M. Reilly
Leslie Dan Faculty of Pharmacy, University of Toronto, Toronto, ON, Canada

Joint Department of Medical Imaging and Princess Margaret Cancer Centre, University Health Network, Toronto, ON, Canada

G. Pirovano
Novartis Institutes for BioMedical Research, Novartis, Italy

Fig. 20.1 A diagrammatic representation of how Auger electrons are generated

[^{177}Lu]Lu-PSMA-617 for patients with advanced prostate cancer. Other effective RPTs based on low LET radionuclides include [^{131}I]I-MIBG for paediatric neuroblastoma, [^{90}Y]Y-anti-CD20 antibodies for non-Hodgkin's lymphoma, [^{90}Y]Y-microspheres for hepatic tumours, and [^{131}I]NaI for thyroid cancer. Although these radiopharmaceuticals can be highly effective in inhibiting and reducing tumour growth, their relatively low LET value and large distance of energy deposition (several millimetres) lead to non-targeted kidney or bone marrow toxicity from a "cross-fire" effect. This in turn limits the amount of radioactivity that can be injected.

This is where AE-emitters – and α-emitters – could be truly valuable. Their high LET could permit highly targeted therapies capable of the precise killing of tumour cells while (theoretically) minimising toxicity to healthy tissues. Also, and rather excitingly, since most of the AE-related energy is deposited within the cell to which the radionuclide is attached or into which it is internalised, AE-emitters could also be uniquely efficient at targeting micrometastases

and single circulating tumour cells, thereby decreasing the risk of cancer recurrence and progression. One important advantage of AE-emitters over many α-emitters is that AEs decay to a stable element: AE-emitters have no daughter products that are radioactive, eliminating the risk of toxicity from these daughters.

Radionuclides that emit AEs usually also emit gamma rays. These can be tracked using single photon computed emission tomography (SPECT) or gamma scintigraphy. As a result, the focus of AE-emitting radionuclides in nuclear medicine has historically been on their use in imaging, such as ^{201}Tl for myocardial perfusion as well as [^{111}In]In-oxine-, [^{99m}Tc]Tc-HMPAO-, [^{99m}Tc]Tc-stannous fluoride colloid-labelled leukocytes or [^{67}Ga]Ga-citrate for infection (Fig. 20.2). The utility of AE emitters in clinical nuclear imaging has made them available for preclinical radiotherapeutic research and enables the development of true theragnostics, agents that combine therapy with diagnostic imaging in a single radiopharmaceutical. These long-distance gamma emissions have downsides as well, however,
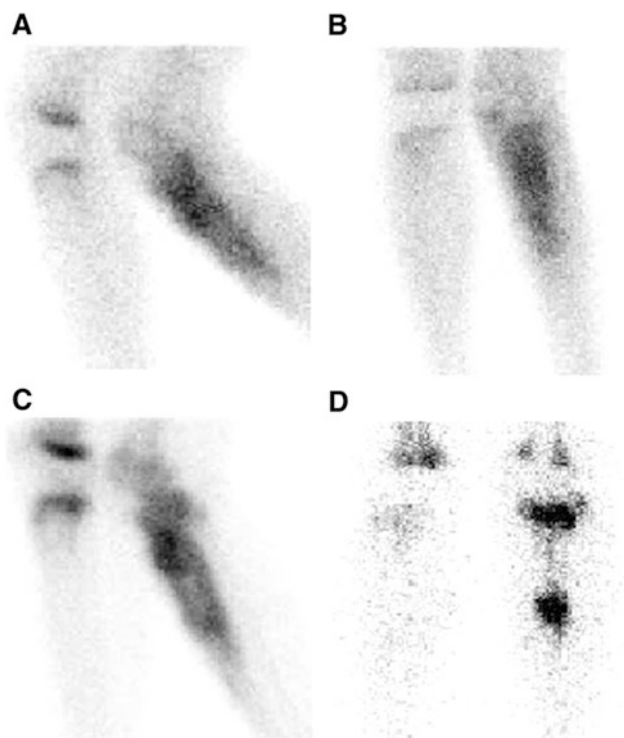
Fig. 20.2 Examples of [^{99m}Tc]-labelled agents used for non-invasive SPECT imaging. (**a** and **b**) [^{99m}Tc]Tc-MDP blood-pool images of regions-of-interest are important in the diagnosis of osteomyelitis. (**c**) Delayed imaging of [^{99m}Tc]Tc-MDP studies can give more detailed localisation information concerning bones involved in the infection process. In addition to [^{99m}Tc]Tc-MDP imaging, radiolabelled leukocytes can be used in diagnostic procedures when investigating osteomyelitis. (**d**) For this patient, [^{99m}Tc]Tc-stannous fluoride colloid was administered 3 days after [^{99m}Tc]Tc-MDP. ^{99m}Tc-stannous fluoride colloid was imaged 3 h after injection. (This research was originally published in JNMT by Hughes [3])

specifically the irradiation of non-target tissues (albeit at a very low LET) and the exposure of caretakers and family members to radiation.

Successful radiotherapy is usually thought to be predicated on the ionisation of DNA at irreparable levels. This DNA-centric approach has also been attributed to AEs: the closer they can be located to the DNA, the more damage will be achieved, the higher the potential for tumour control. This remains correct since chromosomal DNA is a sensitive target of AEs (Fig. 20.3), but the irradiation of other cellular targets – such as the membrane – can lead to cell death as well [4]. This will be described further later in this chapter.

20.2   The Details

20.2.1   Radionuclides Emitting Auger electrons

There is a plethora of radiometals and radiohalogens that emit AEs. Table 20.1 summarises the key properties of several AE-emitting radionuclides. However, for the sake of brevity, we shall describe only the AE-emitters used in biomedical applications.

Gallium-67 (^{67}Ga) is a cyclotron-produced radionuclide with a physical half-life of 3.2 days that has been used in nuclear medicine for over 50 years. Its energetic gamma rays of 93, 184 and 300 keV (39%, 21% and 17% abundance,
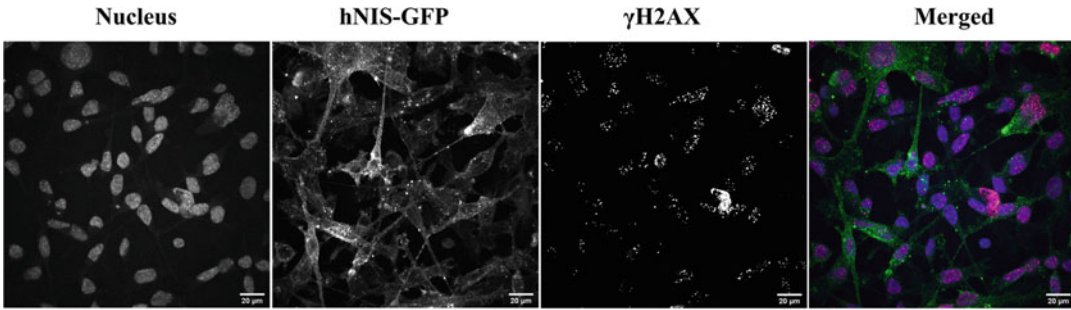
Fig. 20.3 DNA damage in the form of DNA double-strand breaks (γH2AX) imaged after 24 h of incubation with [^{99m}Tc]TcO^{4-}. The uptake of this AE-emitter into triple-negative breast cancer cells is mediated by the human sodium iodide symporter, fused in this case to green fluorescent protein (hNIS-GFP; MDA-MB-231. hNIS-GFP)

Table 20.1 The properties of several AE-emitting radionuclides used in nuclear medicine

Radionuclide	Half-life (days)	Average AEs/decay	Average energy (AE, keV)	Radionuclide	Half-life (days)	Average AEs/decay	Average energy (AE, keV)
^{64}Cu	0.53	1.8	2.1	^{123}I	0.55	14.9	7.4
^{67}Ga	3.26	4.7	6.3	^{125}I	59.4	24.9	12.2
^{77}Br	2.38	6.7	1	^{161}Tb	6.89	0.9	8.9
^{80m}Br	0.18	9.6	8.9	^{195m}Pt	4.02	32.8	23.1
^{99m}Tc	0.25	4.4	0.9	^{197}Hg	2.67	23.2	7.4
^{111}In	2.8	14.7	6.8	^{197m}Hg	0.99	19.4	7.6
^{119}Sb	1.59	23.7	8.9	^{201}Tl	3.04	36.9	15.3

respectively) were initially used to image Hodgkin's disease and lymphomas and later for the detection of infection, inflammation and cancers including lung carcinomas, melanomas and neuroblastoma. The widely available form of gallium-67 is [^{67}Ga]Ga citrate. ^{67}Ga is rapidly released from [^{67}Ga]Ga citrate upon injection and becomes bound by the iron-transporting protein transferrin. Early studies assessing the radiotoxicity of ^{67}Ga for cancer therapy revealed that despite emitting relatively few AEs per decay (Table 20.1), ^{67}Ga causes a significant level of DNA damage and substantially reduced clonogenic survival in vitro. ^{67}Ga therefore presents a promising therapeutic radionuclide [5, 6].

Technetium-99m (^{99m}Tc) is one of the most ubiquitous radionuclides in diagnostic imaging. Several factors have positioned ^{99m}Tc as the gold-standard radionuclide for SPECT, including its moderate energy γ-photons (140 keV), short half-life ($t_{1/2}$ = 6 h), world-wide availability (including the supply via ^{99}Mo/^{99m}Tc generator; Fig. 20.4) and compatibility with an extensive range of chelators and complexes. ^{99m}Tc-labelled phosphates like methyl diphosphonate are most widely used in the clinic to image cancer. The next most prevalent is the use of ^{99m}Tc in myocardial perfusion imaging. Two commercially used radiopharmaceuticals – [^{99m}Tc]Tc-sestamibi and [^{99m}Tc]Tc-tetrofosmin – were developed in the early 1980s for diagnosing ischaemic heart disease, and since then, several more ^{99m}Tc-labelled tracers have been investigated to improve the quality of myocardial perfusion imaging. ^{99m}Tc radiotracers are also very useful for the imaging of infection and play important roles in imaging the brain, detecting apoptosis and hypoxia, visualising tumour and bone pathology, and monitoring drug resistance.
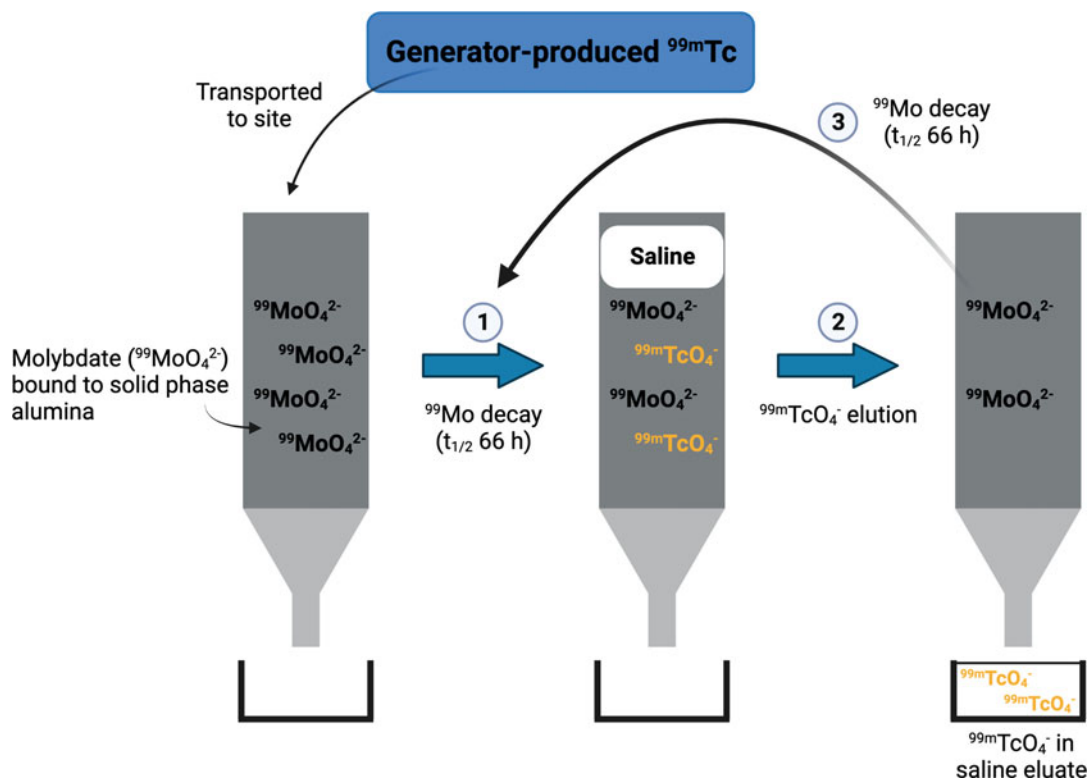
Fig. 20.4 A simplified illustration depicting a [^{99}Mo]MoO$_4$$^{2-}$/[^{99m}Tc]TcO$_4$$^-$ generator (Created in BioRender.com). On-site generators are typically manufactured with [^{99}Mo]Mo in its molybdate form (MoO$_4$$^{2-}$) embedded on a solid-phase alumina support. Following its decay [1], radioactive pertechnetate ([^{99m}Tc]TcO$_4$$^-$) is produced and can be selectively eluted from the generator [2] in saline, leaving behind just the molybdate in the generator. The process can then be repeated once the parent – [^{99}Mo]Mo – has been given sufficient time after the last elution to decay to [^{99m}Tc]Tc [3]. The availability of ^{99m}Tc through generators has greatly influenced its use in the clinic

Only recently has interest in the AEs emitted by ^{99m}Tc emerged. While the radionuclide's dosimetry data and in vitro and in vivo radiotoxicity are encouraging [7–9], more investigation is needed to illuminate the therapeutic potential of ^{99m}Tc.

Indium-111 (^{111}In) is produced in a cyclotron via the proton irradiation of a ^{111}Cd or ^{112}Cd target. It decays to stable ^{111}Cd by electron capture with a half-life of 2.8 days, releasing around 15 AEs and internal conversion electrons per decay. Thanks to its energetic gamma emissions (171 keV and 245 keV, abundance 91% and 94%, respectively), it has been mostly used for radiolabelling peptides and antibodies for the diagnostic imaging of primary and metastatic cancers, such as prostate cancer ([^{111}In]In-anti-PSMA monoclonal antibody, Prostascint) or neuroendocrine tumours ([^{111}In]In-pentetreotide, Octreoscan). Labelling white blood cells with ^{111}In using oxyquinoline and tropolonate ligands plays an important role in detecting infections and inflammatory sites. Recently, ^{111}In gained attention for RPT, showing some promising results in vitro and in vivo, especially when attached to antibodies such as trastuzumab [10] or peptides like human epidermal growth factor (EGF) [11].^{111}In can also be delivered to cancer cells by targeted nanoparticles [12].

Iodine-123 (^{123}I) is produced in a cyclotron from ^{124}Xe and supplied as [^{123}I]I-iodide. The gamma emission of ^{123}I (159 keV, 83% abundance) allows for good-quality imaging, and its convenient half-life of approximately 13 h has contributed to the widespread of [^{123}I]NaI for

thyroid function diagnostic tests. It is also used for detecting and staging thyroid carcinomas and metastatic lesions. [123]I can readily radiolabel different molecules through radioiodination, which further increases its diagnostic potential beyond thyroid imaging. For example, [^{123}I]I-meta-iodobenzylguanidine (MIBG) is used in clinical settings to image neuroendocrine tumours. One example of an investigational agent is 5-^{123}I-iodo-49-thio-29-deoxyuridine (^{123}I-ITdU) which binds DNA during the cell cycle replication phase, causing extensive damage and apoptosis, even in treatment-resistant leukaemia cells [13].

Iodine-125 (^{125}I) is the most widely investigated AE-emitter for RPT due to its availability, long half-life ($t_{1/2} = 59.4$ days) and abundance of AEs emitted per decay. The production of ^{125}I from a [124]Xe target is well established, and it is provided commercially as [^{125}I]I-iodide. During its radioactive decay by electron capture, ^{125}I releases around 25 AEs and demonstrates high relative biological effectiveness. When brought within a short distance of DNA, ^{125}I can cause extensive damage resulting in cellular death. [125]I can be easily incorporated into various organic and biological molecules and is thus used for the radiolabelling of proteins and peptides for biological assays and delivering AEs to nuclear targets [14]. Examples of ^{125}I-based radiotherapeutics include ^{125}I-iododeoxyuridine [15] and ^{125}I-labelled DNA triplex-forming oligonucleotides [16]. However, the long half-life of ^{125}I, its low dose rate and its potential for in vivo deiodination – and subsequent distribution to the thyroid or other sodium-iodide symporter-expression organs – suggest that it may have limited use for RPT in the clinic.

Platinum-195m ([195m]Pt) is a reactor-produced radionuclide with a physical half-life of around 4 days. When incorporated into platinum-based chemotherapeutics such as cisplatin or carboplatin, it could be harnessed for SPECT imaging to assess the pharmacokinetic profiles of the drugs and thus facilitate patient selection and dose optimisation, although this has not been exploited. [195m]Pt decays by isomeric transition, releasing a higher number of AEs per decay (32.8) than most of the other emitters. Radiolabelling platinum anticancer drugs that form DNA crosslinks with purines ensures that the AEs are emitted within close proximity to the DNA, allowing them to cause substantial DNA damage and potentially increasing the cytotoxicity of platinum-based chemotherapy [17].

Thallium-201 (^{201}Tl) is mostly known for its past use in myocardial planar gamma and SPECT imaging (X-ray emission: 67–82 keV; 88% abundance) for the diagnosis of ischaemic heart disease and other cardiac abnormalities. ^{201}Tl-labelled diagnostics were widely used in 1970s and 1980s. However, the low signal-to-noise ratio of the radionuclide, the significant tissue attenuation of its emissions, and dosimetric considerations due to its long half-life compared to ^{99m}Tc have resulted in it being replaced by ^{99m}Tc-labelled myocardial perfusion imaging agents. The production of [201]Tl ($t_{1/2} = 3.04$ days) from a naturally occurring [205]Tl target via cyclotron is well-established, and its decay product is stable [201]Hg. [201]Tl$^+$ mimics potassium in a biological environment and can be transported via sodium/potassium ATPases, accumulating with high efficiency in well-perfused myocytes as well as several tumour tissues. Recent untargeted in vitro studies in a variety of cancer cells have demonstrated the therapeutic potential of thallium-201 [18]. In the end, ^{201}Tl remains a very attractive radionuclide for AE RPT due to its large number of AEs released per decay, but its use remains hampered by the paucity of chelators that can be used to attach the radiometal to biological vectors.

20.2.2 Auger Electron-Emitters in Cell Free Studies

When investigating the cytotoxicity of AEs, cellular studies are a suboptimal way to elucidate their effects on sensitive targets (e.g. DNA) due to cellular barriers that prevent radiopharmaceuticals from reaching these targets. These barriers can include the cell membrane,

cytoplasmic vesicles such as endosomes or lyso-some and the nuclear membrane. Thus, some studies have used isolated DNA to probe the effects of AEs and provide insight into the ability of the particles to create single- and double-strand breaks (SSBs or DSBs).

20.2.2.1 Plasmid-DNA Gel Electrophoresis

The plasmid-DNA gel electrophoresis assay (referred to here as the plasmid assay) is a commonly employed technique to investigate DNA damage from AE-emitting radionuclides. The plasmid assay utilises the resolving power of an agarose gel to separate undamaged, supercoiled plasmids from those containing radiation-induced SSBs and DSBs. The ability to resolve subpopulations of damaged and undamaged plasmids stems from changes in the conformation of the plasmid after SSBs and DSBs that alter its migration through the gel. Specifically, plasmids will undergo a transformation from a supercoiled conformation (undamaged, travels fastest through the gel) to relaxed/open-circular (SSBs, travels slowest through the gel) and linear (DSBs, travels with an intermediate speed) conformations (Fig. 20.5).

A variety of advantages, disadvantages, and caveats with this technique should be discussed (see Table 20.2). One of the major points is that the technique is performed with isolated, "naked" DNA without DNA repair enzymes. While it is thus useful to easily and directly compare the "absolute" amount of damage caused by different radionuclides, this lack of enzymes able to repair the damage – particularly low levels of damage – reduces the relevance of the results, especially if the assay is the only technique used to assess the cytotoxicity of the radionuclide. In contrast, DNA repair is (of course) included in assays involving intact cells, one reason why these assays are more biologically relevant.

Figure 20.6 summarises the general steps for a typical plasmid assay. In brief, the plasmid DNA solution is either incubated with the radionuclide in question for a period of time or, for studies looking at the effects of γ-rays, placed in the radionuclide solution with the plasmid itself housed in a smaller vessel. After incubation, the radionuclide-plasmid mixture is loaded into the wells of an ethidium bromide-containing agarose gel, and the different plasmid conformations are resolved into distinct bands by applying an electrical current. Once run, the gel is imaged (usually
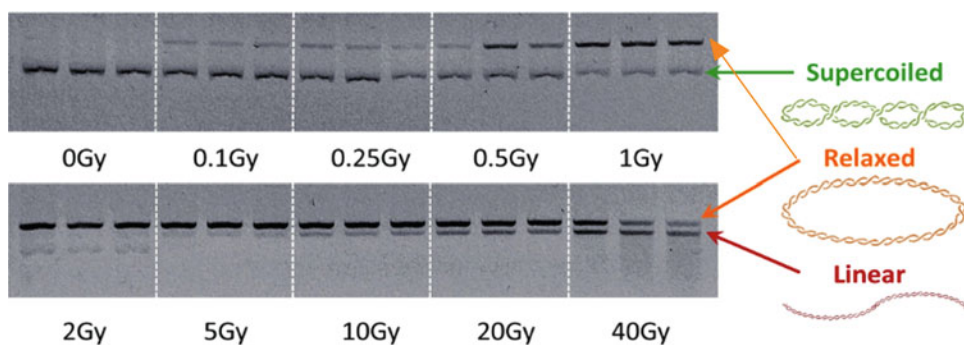
Fig. 20.5 Representative image of triplicate samples of intact, supercoiled plasmid pBR322 irradiated with gamma rays up to a dose of 40 Gy and run on an agarose gel showing the induction of DNA damage as relaxed DNA (i.e. single-strand breaks) and linear DNA (i.e. double-strand breaks). White lines were superimposed, and the samples were run on the same gel. Samples at 0 Gy show a strong supercoiled band, while samples irradiated with 2 Gy reveal a strong relaxed band with faint linear and supercoiled bands. The same setup can be used to study radionuclide-induced DNA damage (Figure from Verger et al. [19] under Creative Commons Attribution 4.0 International License (CC BY 4.0))

Table 20.2 Advantages, disadvantages, and caveats of the plasmid assay

Advantages	Disadvantages	Caveats
No highly specialised equipment needed	Dedicated equipment to prevent radioactive contamination/spread in the lab	Many plasmids available – differing radiosensitivity?
Low skill ceiling	Does not factor in biological radiosensitivity of different cancer types	Cannot directly correlate results to cellular DNA damage
No DNA damage repair to obscure low-level damage	No DNA damage repair	Acidic solutions sometimes required for radiolabelling also cause DNA damage
Direct comparisons between different radiation types	"Naked" plasmid DNA is not representative of DNA in a protective nucleus	DNA damage levels are dependent on initial plasmid concentration
More easily determine contributions from direct and indirect damage	Cannot quantify the number of single- and double-strand DNA breaks	
Can isolate damage contribution from coemitting γ-rays		
Inexpensive reagents		
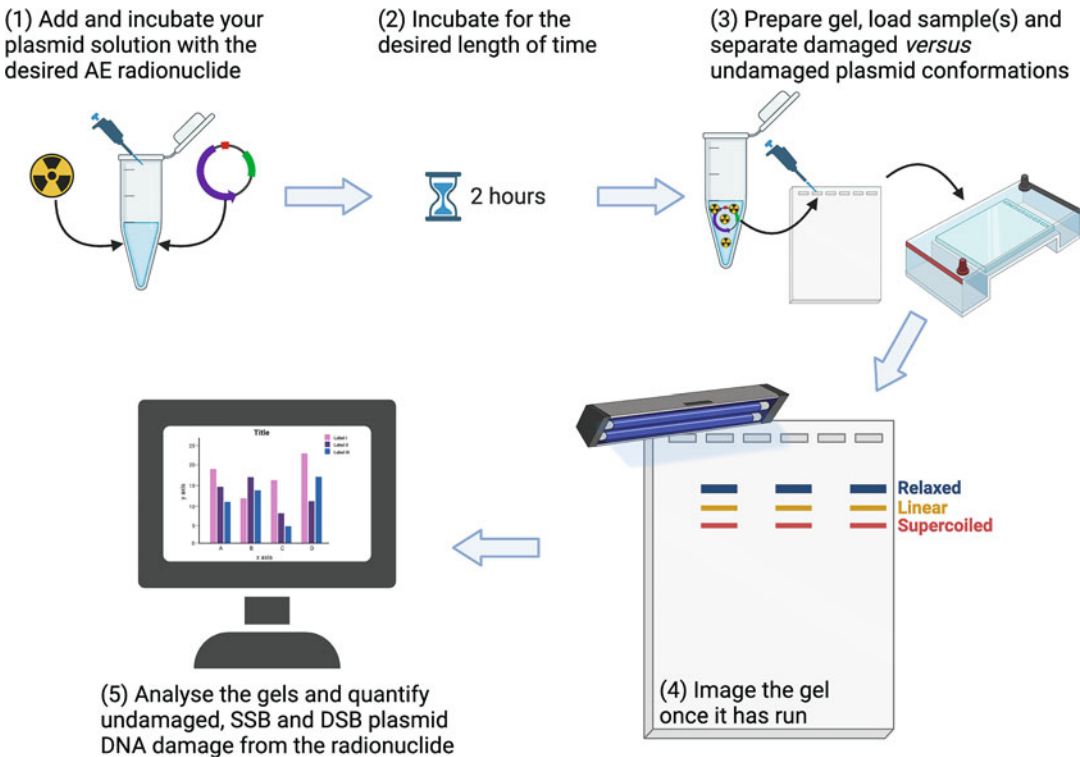
Fig. 20.6 General workflow for the plasmid assay (Created in BioRender.com). A plasmid solution is incubated with the radionuclide/radiopharmaceutical of choice (1) of known activity and incubated for the desired period(s) of time (2). Following incubation, the plasmid mixture is loaded onto an agarose gel (3), and the sample mixtures are separated/resolved by an electric current. Once run, the gel is imaged (4), and damaged versus undamaged subpopulations are quantified (5)

under UV light), and the image is analysed and processed to quantify the distribution of supercoiled, relaxed, and linear plasmids.

While this chapter will not go into a full review of the different approaches to this technique, it is still worth mentioning a few studies that highlight the technique's utility, particularly for research into AE-mediated DNA damage.

Recent work by Verger et al. has shown that the damage caused to plasmids by ^{67}Ga and [111]In (of known activity, Bq) can be directly compared to external beam radiation doses (EBRT, Gy). Mathematical modelling could then be used to identify the combination of radionuclide activity and incubation time that produces DNA damage corresponding to an equivalent dose of EBRT [19]. Work by both Reissig et al. and Pereira et al. have also highlighted the importance and influence of the distance between the AE-emitter and the DNA double helix on the creation DNA damage by radiolabelling the DNA-intercalators pyrene [20] and acridine orange [21]. Both studies showed that a longer linker between the intercalator and the radionuclide resulted in less DNA damage. Furthermore, these works also highlighted the importance of distance on AE-mediated direct DNA damage (i.e. the interaction of emitted AEs with the DNA) versus indirect free-radical-mediated DNA damage (i.e. free radical-mediated DNA interactions following the AE-mediated ionisation of surrounding water molecules) via coincubation with DMSO, a commonly used free-radical scavenger [20, 21]. While the damage created by compounds bearing short linkers resulted primarily from direct AE–DNA interactions, the damage produced by compounds bearing longer linkers stemmed from indirect, free radical-mediated interactions.

20.2.2.2 In Silico Modelling

Another cell-free approach often encountered in the literature is the in silico modelling of AE dosimetry to predict cellular damage. In silico studies focus on modelling the spatial energy deposition of a radionuclide's emitted particles (either for particular particles/energies or its entire emission spectrum) and hence its dosimetry at the single cell and subcellular level, often termed cellular dosimetry (or microdosimetry). A variety of methods and approaches exist, with two standing out:

1. *The Medical Internal Radiation Dose (MIRD) schema for dosimetric calculations from S-values:* This is considered the standard approach. S-values describe the absorbed dose in a target compartment from the cumulative activity in a source compartment in a cell [e.g. Gy/(Bq × sec)]. The source compartments are the compartments in a cell where the activity is located, e.g. the cell membrane, cytoplasm, or nucleus. The target compartments are the locations in the cell that receive the dose, and these may be the same as the source compartments (e.g. nuclear activity depositing dose in the nucleus) or they may be different than the source compartments (e.g. cell membrane-associated activity depositing dose in the nucleus). S-values depend on the physical decay properties of the radionuclide as well as the geometry of the cell, i.e. the dimensions of the cell and nucleus. A comprehensive compendium of S-values for a wide range of radionuclides and different cellular and nuclear dimensions has been published and is constantly updated by the MIRD Committee. S-values are also available for organ dosimetry, which employs similar calculations at the organ level, but for AEs, cellular S-values are the most relevant due to their subcellular range. The absorbed doses to biological targets for a wide variety of radionuclides – ranging from organ-level all the way to cellular-level [22, 23] – are detailed and available for use. Values have been calculated for both generic anatomical models and more realistic models generated from segmented radionuclide scans.

2. *Monte-Carlo (MC) simulation software packages:* It has become increasingly common in recent years to opt for MC-based approaches in favour of the MIRD schema, as the latter does not accurately reflect the consideration of AE energy depositions at the micrometre range and below [22, 24, 25]. Examples of MC software packages/

codes include PENELOPE, FLUKA, and Geant4-DNA. An advantage of MC-based approaches over the MIRD strategy at the single-cell and subcellular levels is the former's ability to account for the wide variety and eccentricity of cellular geometries observed in the real world. MIRD-generated S-values are based on perfectly spherical cells with geometrically centred nuclei, a model that rarely (if ever) holds true, especially given the tight range of cellular dimensions used to calculate them. In addition, the interaction of charged particles with surrounding matter holds some degree of randomness (i.e. is stochastic [26]), which MC approaches replicate well. More important perhaps is that modelling also needs to consider the non-uniformity of the uptake of the radiopharmaceutical and its deposition of energy in tumours and subcellular compartments. MC-based codes model and replicate stochastic processes well, albeit in a cost- and resource-intensive manner. This can pose a potential barrier for accessibility, especially if coupled with a lack of personnel with relevant knowledge and experience. While these models may be good at calculating doses to cells and organelles based on hypothetical distributions, real data on the microscopic distribution of radiopharmaceuticals can be obtained via subcellular fractionation experiments to better inform the parameters used for MC modelling.

20.2.3 Preclinical Cancer Therapy with Auger Electron Emitters

In vitro studies have also been used as proof-of-concept models to study AE-induced toxicity. However, in vivo studies in animal models of cancer are critical to ascertain whether a radiotherapeutic is likely to have a clinical impact. Studies so far have used a variety of targeting moieties including small molecules, antibodies, and nanoparticles.

Radioiodinated 2-deoxyuridine (IUdR) is an example of one of the first successful small molecules used for the in vivo delivery of an AE-emitting radionuclide. It is synthesised via the radiolabelling of a thymidine analogue – IUdR – which is incorporated directly into the DNA (Fig. 20.7, [15]). Sahu et al. showed that the intrathecal administration of 18.5 MBq of ^{125}I-IUdR (given either by single administration, five daily administrations, or continuous 5-day infusion) prolonged the median time before paralysis caused by leptomeningeal gliosarcoma metastases in rats (11.2 ± 0.1, 12.3 ± 0.1 and 15.2 ± 0.4 days, respectively) compared to control mice (9.0 ± 0.1 days) [15].

Other small molecules have also been labelled with ^{125}I, including 2-[3-[1-carboxy-5-(4-[^{125}I] iodo-benzoylamino)-pentyl]-ureido]-pentanedioic acid) and [^{125}I]I-DCIBzL, both of which target the prostate-specific membrane antigen (PSMA). Using a micrometastatic model of

Fig. 20.7 Induction of hind-leg paralysis after intrathecal injection of 18.5 MBq (500 μCi) [^{125}I]I-UdR in rats bearing intrathecal 9 L gliosarcoma. (This research was originally published in JNM; Figure from Sahu et al. 1997;38 [3]: 386–90 [18]. © SNMMI)
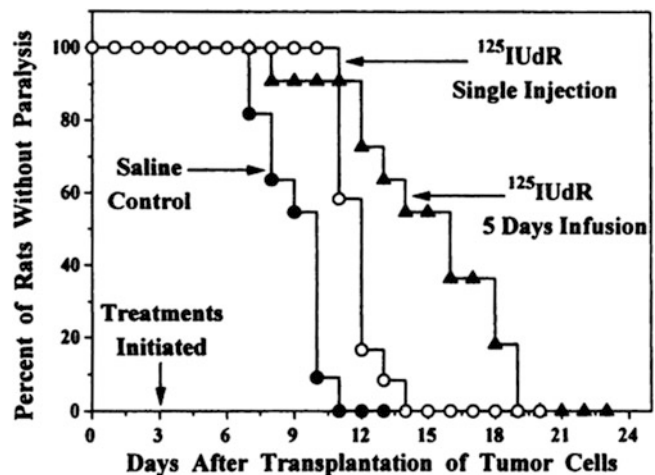
prostate cancer, the intravenous administration of [125I]I-DCIBzL resulted in a significant delay in the development of metastatic disease and an improvement in overall survival [27]. Furthermore, Grudzinski et al. evaluated cancer cell-selective small molecule phospholipid ether analogue radiolabelled with 125I – [125I]I-CLR1404 – for the treatment of triple-negative breast cancer xenografts. An intravenous administration of 74 MBq was estimated to deliver a tumour radiation-absorbed dose of ~19 Gy. Sixty days post-treatment with [125I]I-CLR1404, a 60% reduction in tumour volume was observed compared to a control group without systemic toxicity. Dosimetry calculations revealed that [125I]I-CLR1404 delivered a high absorbed dose to the tumour per MBq (0.261–0.023 Gy/MBq), whereas the bone marrow, generally a dose-limiting organ, received a low absorbed dose (0.063–0.005 Gy/MBq) [28].

Other studies have demonstrated the in vivo therapeutic efficacy of other AE emitters. Nadar et al. showed that a bisphosphonate radiolabelled with platinum-195 m ([195mPt]Pt-BP) accumulated 7.3-fold more than [195mPt]Pt-cisplatin in murine intratibial bone metastatic lesions, resulting in 4.5-fold more DNA damage and over 3.4-fold more apoptosis [29]. In vivo studies also revealed that another platinum AE-emitter ([191Pt]Pt-cisplatin) produced a substantial delay in tumour growth in mice bearing human squamous cell carcinoma tumours compared to non-radioactive cisplatin without inducing toxicity in healthy organs [30]. In addition, despite not being the most promising AE emitter for therapy due to its emission of few AEs, Schipper et al. showed that 99mTc – in the form of 99mTc pertechnetate – induced a substantial reduction of tumour growth in sodium iodide symporter-expressing neuroendocrine tumours [31].

Several radiopharmaceutical research groups have explored the in vivo therapeutic effect of monoclonal antibodies (mAbs) radiolabelled with AEs-emitters. Santoro et al. demonstrated that the intravenous administration of non-internalising [125I]I-35A7 mAb substantially increased the median survival of Swiss nude mice bearing intraperitoneal A-431 tumour cell xenografts compared to controls. Furthermore, the internalisation of [125I]I-m225 mAb resulted in 7.4-fold decrease in the estimated absorbed dose compared to non-internalised [125I]I-35A7 mAb (15.1 Gy vs 111.6 Gy, respectively) [32]. This suggests that the internalisation of radiolabelled mAbs is not necessarily a requirement for successful in vivo radioimmunotherapy with 125I. A study performed by Paillas et al. also described the mechanisms behind how the non-internalising anti-carcinoembryonic antigen (CEA) mAb radiolabelled with 125I induced a radiotherapeutic effect through oxidative stress-mediated, non-targeted effects [4].

Behr et al. also showed that the in vivo therapeutic efficacy of 131I- versus 125I-labelled variants of a non-internalising anti-CEA mAb ([131I]I-F023C5 and [125I]I-F023C5) was not significantly different at equitoxic doses. Also, radiolabelled internalised mAbs [125I]I-CO17-1A and [111In]In-CO17-1A showed greater therapeutic efficacy compared to 131I- and 90Y-radiolabelled CO17-1A in nude mice bearing subcutaneous human colon cancer xenografts [33]. In addition, Costantini et al. demonstrated that the addition of a nuclear-localising sequence (NLS) peptide to [111In]In-trastuzumab ([111In]In-NLS-trastuzumab) resulted in increased tumour uptake with subsequent nuclear translocation. Two separate intraperitoneal administrations of 9.25 MBq [111In]In-NLS-trastuzumab were shown to enhance the survival of tumour-bearing mice compared to mice treated with non-radioactive trastuzumab or control cohorts (>140 days vs 96 and 84 days, respectively) [34].

Radiolabelled modular nanotransporters (MNTs) have also shown promise for the receptor-targeted delivery of AE emitters to the nuclei of targeted cells. Rosenkranz et al. demonstrated the prolonged intratumoural retention of [111In]In-MNTs-EGFR and found that the radiotherapeutic produced a significant tumour growth delay dependent on the local activity infused in xenograft-bearing mice [35]. In addition, Slastnikova et al. synthesised MNTs to deliver 111In to HeLa human cancer xenografts expressing the folate receptor, showing the

enhanced retention of ^{111}In in tumours following intratumoural injection as well as a significant tumour growth inhibition [36]. These studies suggest that MNTs are a potential tool for AE therapy.

Other research groups have used nanoparticles to deliver AEs to cancer cells. The surface of nanoparticles can be modified with vectors that have a high affinity for a target of interest (e.g. peptides or small biologically active molecules). For example, Cai et al. showed that gold nanoparticles modified with polyethylene glycol chains linked to trastuzumab and radiolabelled with [111]In ([^{111}In]In-trastuzumab-AuNP) inhibited up to 80% of tumour growth following intratumoural injection (Fig. 20.8, [37]). In this study, the local intra-tumoural administration of the ^{111}In-labelled gold nanoparticles deposited high absorbed doses in the tumour, while the gold nanoparticles acted as an "anchor" to retain the radioactivity in the tumour and avoid its re-distribution to other tissues, greatly minimising the radiation dose to healthy organs. The local administration of

AE-emitting radiopharmaceuticals is a promising approach that could significantly improve effectiveness while avoiding or minimising normal tissue toxicity. The local administration of AE-emitting radiopharmaceuticals, however, is largely untenable in cases of metastatic disease.

Narmani et al. synthesised a PAMAM dendrimer labelled with the AE-emitter ^{99m}Tc and 5-fluorouracil (5FU): PEG-PAMAM G4-FA-5FU-Suc-[99m]Tc. This nanocomplex was shown to be a highly effective delivery system for the targeting of folate receptors in BALB/C mice bearing breast cancer xenografts, resulting in tumour growth delay and an increase in the survival of the mice [38]. Furthermore, activity-dependent tumour growth delay was observed in athymic nude mice bearing PC-3 PIP tumours following the administration of 5 and 10 MBq of [[161]Tb]Tb-PSMA-617, a β-emitter ($T_{1/2} = 6.96$ days, $E\beta_{average} = 154$ keV) that also emits AEs. The inhibitory effect on tumour growth was greater than previously reported for the same administered activities of [^{177}Lu]Lu-PSMA-617 ($T_{1/2} = 6.65$, days $E\beta_{average} = 134$ keV), an emitter of solely β-particles with similar physical
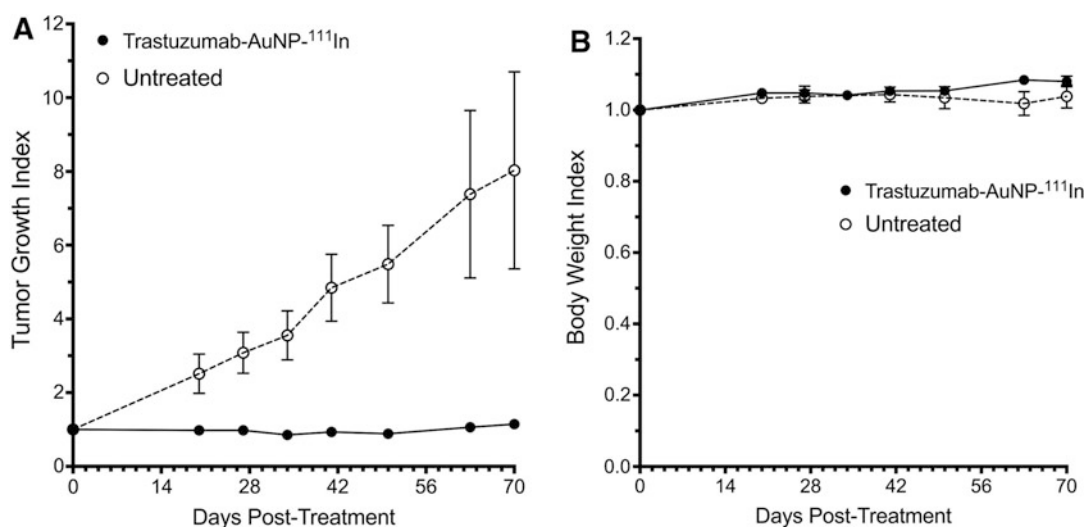
Fig. 20.8 (a) Tumour growth index (described here as the growth relative to starting tumour size, which is normalised to 1) in CD1 athymic mice bearing subcutaneous MDA-MB-361 human breast cancer xenografts injected intratumourally with ^{111}In-labelled and trastuzumab-modified gold nanoparticles (trastuzumab-AuNP-^{111}In; 10 MBq, 0.7 mg, 2.6×10^{12} AuNP) or receiving no treatment. (b) Body weight index for trastuzumab-AuNP-^{111}In-treated and untreated mice. (Figure from Cai et al. [37] under Creative Commons Attribution 4.0 International License (CC BY 4.0))

decay properties to [161]Tb in terms of half-life and β⁻ energy [39]. In addition, Borgna et al. reported that when localising both [161]Tb and [177]Lu – as [[161]Tb] Tb-DOTA-LM3 and [^{177}Lu]Lu-DOTA-LM3 – to the cell membrane in SSTR-positive exocrine rat pancreatic tumours in athymic nude mice, [[161]Tb] Tb-DOTA-LM3 was more effective in delaying tumour growth and prolonging the survival of mice compared to [^{177}Lu]Lu-DOTA-LM3. The therapeutic efficacy of [^{177}Lu]Lu-DOTA-LM3 was in turn superior to [^{177}Lu]Lu-DOTA-TOC and [[161]Tb]Tb-DOTA-TOC that localised both [161]Tb and ^{177}Lu in the cytoplasm, showing that the superior in vivo therapeutic efficacy of [[161]Tb]Tb-DOTA-LM3 may have benefited from both the membrane localisation of the [161]Tb and the additional emission of AEs [40].

Despite the promising in vivo efficacy results, there is a notable lack of in vivo work carried out aimed at determining the relationships between absorbed dose and biological effects using the identical radiopharmaceutical under comparable conditions. This is almost impossible to do, considering that different research groups have disparate focuses *and* the wide range of targeting strategies for AE-emitter-based radiotherapeutics. Likewise, there is a need to perform dosimetry studies in concert with the development of therapeutic radiopharmaceuticals, not after the fact (as it is typically done today). This is particularly true for AE emitters, as differences in subcellular localisation will result in varied radiation absorbed doses that will in turn greatly affect biological outcomes. Therefore, this knowledge is key not only to predicting the therapeutic efficacy of radionuclides but also to developing the therapeutic radiopharmaceuticals themselves. There is also a

lack of work designed to determine dose-response relationships in healthy tissues, which are crucial to elucidating the maximum safe radiation absorbed dose of AEs-emitters to these critical organs (i.e. red marrow, liver, spleen and kidneys).

20.3   Particularly Important Works

The studies below on [^{111}In]In-octreotide, [^{111}In] In-EGF and [^{123}I]I-MAPi (Fig. 20.9) are great examples of what is possible. Hopefully, the stories behind them will inspire and inform future work.

20.3.1   [^{111}In]In-Octreotide

Octreotide is a synthetic version of the natural hormone somatostatin and is used to treat symptoms in patients with advanced neuroendocrine tumours. Recent years have played witness to a surge of effective radiotherapeutics that target the somatostatin receptor, the most prominent being the β-emitter [^{177}Lu]Lu-DOTATATE. However, many of those new to the field of RPT might have missed some early clinical studies of [^{111}In]In-labelled somatostatin analogues, which are still used clinically as diagnostics to inform [^{177}Lu]Lu-DOTATATE treatment but at one point were being considered as AE-emitting radiotherapeutics in their own right.

A 1990s clinical trial in 30 end-stage neuroendocrine cancer patients whose tumours continued to progress first demonstrated that [^{111}In]In-DTPA-D-phe1-octreotide ([^{111}In]In-pentetreotide, Fig. 20.9a) could stabilise disease [42]. Likewise, a case report
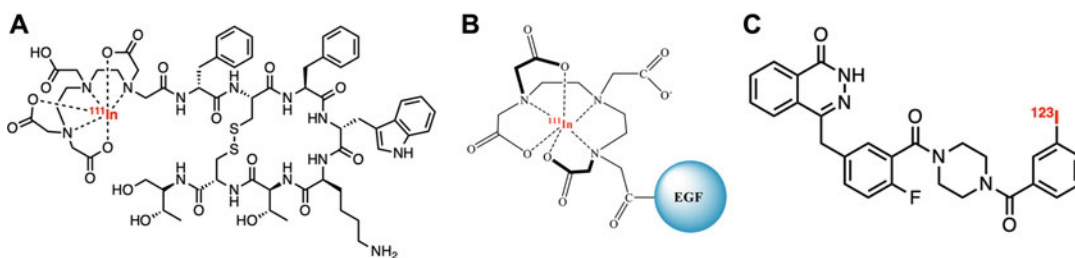
Fig. 20.9   Chemical structures of (**a**) [^{111}In]In-octreotide, (**b**) [^{111}In]In-EGF, and (**c**) [^{123}I]I-MAPi

published a year later first showed that 8 cycles of ^{111}In-pentetreotide (6.66 GBq) in a 35-year-old patient with a highly metastatic atypical carcinoid tumour also led to stable disease for 14 months [43]. Although the patient passed away approximately 18 months after the start of ^{111}In-pentetreotide therapy, this new approach to RPT was deemed a successful alternative to chemotherapy which, in this patient, gave severe gastrointestinal side effects. Similar stabilising effects were seen in other trials of ^{111}In-pentetreotide, including in non-responsive thyroid cancer, and a maximum tolerated activity of 100 GBq was established [44]. Despite a predicted 45 Gy radiation dose to the kidneys – twice the accepted limit for external beam radiation – no signs of kidney toxicity were observed [44]. This may have been due to the distribution of the radionuclide within the kidney.

Although initial studies were very successful (Fig. 20.10, [41]), ^{111}In-labelled somatostatin analogues mostly only improved symptoms and rarely resulted in reductions in tumour size. In addition, the high doses of ^{111}In combined with its moderate energy gamma emissions necessitated radiation protection precautions and restrictions for staff, family members, and the general public. Taken together, these factors meant that ^{111}In-pentetreotide was soon replaced by the β-emitting [90Y]Y-DOTATOC and [177Lu]Lu-DOTATATE, which could be used at lower activities and displayed either lower or no gamma abundance.

20.3.2 ^{111}In-EGF

The story of ^{111}In-EGF (Fig. 20.9b) started at the University of Toronto with then Ph.D. student and now professor Raymond Reilly. There was an interest in developing a novel radiolabelled peptide for the imaging of breast cancer, and it was recognised that the receptor for epidermal growth factor, EGFR, was commonly over-expressed in certain subtypes of breast cancer. EGF is a small peptide that stimulates cell growth and differentiation by binding to its receptors that are often found on the surface of breast cancer cells but also sometimes observed in the nuclei of rapidly proliferating cells. It was reasoned that EGF could be used to transport short-track length AE-emitting radionuclides into the nuclei of EGFR-positive cancer cells, thereby causing DNA damage and cytotoxicity. [111]In was chosen as the radionuclide for this application as it is suitable for SPECT and had previously been noted, in the context of labelling white blood cells, to cause DNA and chromosomal damage [45].

In vitro clonogenic assays with EGFR-expressing breast cancer cells showed that ^{111}In-EGF killed these cells potently and specifically and displayed high nuclear-absorbed radiation doses [46, 47]. Subsequent studies demonstrated that ^{111}In-EGF was effective for treating mice bearing EGFR-expressing MDA-MB-468 human breast cancer xenografts and other tumours at doses that were non-toxic to normal tissues [46, 48]. A collaboration then

Fig. 20.10 Kaplan-Meier survival analysis of neuroendocrine tumour patients receiving one, two, three, or four cycles of high activity ^{111}In-pentetreotide therapy. (Figure from Delpassand et al. [41] under Creative Commons Attribution International License (CC BY-NC 3.0))
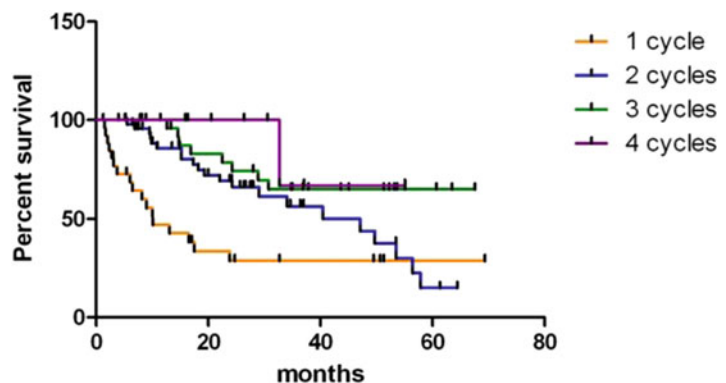
followed with Prof Katherine Vallis at the Princess Margaret Hospital in Toronto focused on the use of GMP-formulated $[^{111}In]$In-EGF [11] for the treatment of patients with EGFR-positive breast cancer. As the nuclear localisation of the EGF receptor is associated with aggressive disease and poor prognosis, exploiting this target for AE radiotherapy was thought to provide a novel treatment option for patients with this aggressive type of breast cancer.

In the 16-patient Phase I trial, the administered amount of $[^{111}In]$In-EGF was escalated and its safety was evaluated. The localisation of $[^{111}In]$In-EGF in tumours and normal tissues was assessed via SPECT, with the ultimate goal of using it as a theragnostic agent for tumour imaging and RPT. The radiopharmaceutical was generally well tolerated and was localised to tumours in about half of the participants (Fig. 20.11, [49]). Little to no bone marrow toxicity was expected, as there is very little expression of EGFR in bone marrow stem cells, and there is no cross-fire effect from the AEs. This was born out in the trial, with only one episode of Grade 3 or 4 haematological toxicity (and in a patient with extensive pre-existing bone marrow infiltration). However, a transient decrease in blood pressure was observed in some patients, thought to stem from the binding of the radiotracer to EGFR on vascular endothelial cells. This observation illustrates the importance of considering not only the radiobiological effects of radiolabelled peptides but also the biological and pharmacologic effects of the carrier peptide itself. For this reason, $[^{111}In]$In-labelled EGFR-targeting monoclonal antibodies may be more suitable for AE-based RPT than $[^{111}In]$In-EGF [50] despite the longer blood circulation time and poorer internalisation of the former. Small peptides such as EGF nonetheless exhibit better tumour penetration than monoclonal antibodies, which is important for AE RPT due to the absence of the cross-fire irradiation of non-targeted cells. At present, the use of EGF or EGFR-targeting mAb as platforms for the AE-based RPT of EGFR-expressing tumours continues to be explored.

20.3.3 $[^{123}I]$I-MAPi

In 2018, the Reiner lab at Memorial Sloan Kettering Cancer Center published a report summarising their efforts at the characterisation of PARP-targeted imaging agents [51]. PARP is a DNA damage repair protein that represents an intriguing target because it can be targeted with
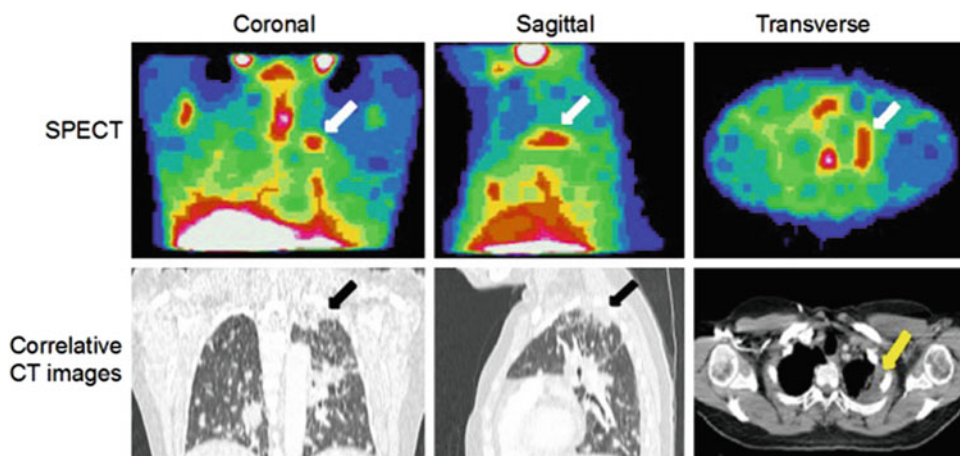
Fig. 20.11 Representative images from Patient 11 showing the tumour accumulation of $[^{111}In]$In-DTPA-hEGF with correlative CT images. Coronal, sagittal, and transverse SPECT images at 24 h post-injection. A tumour deposit present in the left lung apex (arrows) shows ^{111}In uptake. (Figure from Vallis et al. [49] under Creative Commons Attribution International License (CC BY-NC))

small molecule inhibitors. The selective inhibition of PARP leads to cancer cell death when there are no functioning back-up DNA damage repair pathways (i.e. when cells lack BCRA1 DNA repair activity). A panel of clinical PARP inhibitors was used, and their target binding in vitro and in vivo was investigated. The study showed that it was possible to quantify the target engagement of a family of radiolabelled PARP-targeting small molecules using PET imaging with implications for clinical cancer imaging, particularly in the context of probing the capacity of tumours for DNA repair. Interestingly, the in vitro data suggested that different PARP inhibitors have varying residence times in tumour cells, an observation that could explain their diverse treatment efficacies. Based on these findings and others, a question arose: if we can image tumours using radiolabelled olaparib, can we synthesise a theragnostic version to satisfy the theragnostic principle "We see what we treat, and we treat what we see"?

Leveraging previous efforts in producing radioiodinated variants of olaparib [52], a first attempt at theranostic imaging and treatment was performed in a mouse model of glioblastoma (GBM) using ^{123}I-MAPi, a radiolabelled PARP inhibitor (Fig. 20.9c). The treatment of GBM is inherently challenging due to the infiltrative nature of the disease and the blood-brain-barrier's exclusion of many intravenously administered agents. Few advances have been made in the treatment of GBM over the past few decades, most notably the introduction of temozolomide chemotherapy. A major challenge remains the prevention of recurrence due to the inability of the surgeon to safely resect all tumours. Radio-pharmaceutical therapies – particularly those with short-range emissions such as $\alpha-$particles or AEs – may have an important role to play in the future treatment of GBM by irradiating and killing tumour cells at the surgical margins and thus slowing (or even preventing) recurrence.

In their work, Salinas et al. showed that the labelling of the olaparib-based PARP inhibitor with ^{131}I did not perturb its binding specificity or the pharmacokinetic profile of the compound upon intratumoural administration, and significant retention of radioactivity was observed in the tumour if PARP was present [52]. These data were used for preclinical dosimetry, which showed that the tumour received 134.2 cGy/MBq while the major clearance organ, the liver, received a dose of 6.1 cGy/MBq. The intratumoural administration of [^{131}I]I-PARPi to tumour-bearing mice (either a single dose of 14.8 MBq or 3 doses of 14.8 MBq) yielded a significant reduction in tumour growth and improved median survival, suggesting the possibility of targeting PARP via the local administration of radiotherapeutics with little toxicity.

Spatial precision in the delivery of the radioactive payload is needed to effectively damage the DNA of GBM cells without affecting nearby healthy cells. Olaparib is a PARP inhibitor (PARPi) that complexes with its target and docks it onto the DNA – a process called "PARP trapping" – that results in the packing of the inhibitor-target-DNA complex within a 50 Å space. When the inhibitor is labelled with an AE-emitted radionuclide, this packing places the radionuclide and DNA within the radius of action of the AEs. The radiolabelled PARP inhibitors will selectively localise in tumour cells treated with DNA-damaging agents such as chemotherapeutics or radiation due to these cells' recruitment of PARP to sites of DNA damage. In contrast, PARP is only present in the cytosol (i.e. far from the DNA) in non-damaged cells.

The radiosynthesis of [^{123}I]I-PARPi was optimised [53], and the product was named [^{123}I]I-MAPi ($\underline{123}$I-Meitner-Auger PARP inhibitor) [54]. ^{123}I-MAPi was internalised in GBM cells and was found to induce DNA damage with a resulting EC$_{50}$ of 69 nM, a concentration at which olaparib did not show any cytotoxicity. By combining in vitro colony formation assay data and in silico Monte Carlo simulations, cellular-level dosimetry calculations were performed, and a significantly greater relative biological effectiveness was observed for [^{123}I]I-MAPi compared with external beam irradiation of

the same samples. The radiotherapeutic also exhibited a favourable in vivo biodistribution, with a specific tumoural uptake of 33.4 ± 28.0 %ID/g following intratumoural injection and excretion mainly via the liver. In normal liver cells, the localisation of the compound was confirmed to be mainly cytoplasmic (compared to primarily nuclear in cancer cells), significantly reducing off-target toxicity. Mice bearing orthotopic GBM xenografts showed improved survival upon the intratumoural injection of [123I]I-MAPi [54]. The median survival increased to 58 days in mice treated intratumourally (single dose of 0.37–1.11 MBq) compared to 40 days for the untreated cohort. Kaplan–Meier survival plots also confirmed the therapeutic efficacy of [123I]I-MAPi in mice treated with the radiotherapeutic through an osmotic-pump, with a median survival at 72 days as opposed to 48 days for a control cohort.

A study to investigate the safety and efficacy of intravenously administered [123I]I-MAPi (as opposed to intratumoural or osmotic-pump administration) was subsequently performed (Fig. 20.12, [55]). Injections of up to 74 MBq of [123I]I-MAPi showed no signs of toxicity, while a whole-body biodistribution study allowed for the calculation of preclinical dosimetry and the confirmation of ex-vivo tumour DNA damage. Dosimetry calculations confirmed that the liver – i.e. the dose-limiting organ – received an absorbed dose of 4.4 mGy/MBq in mice, a value which translates to 4.2 mGy/GBq in a human. Mice bearing HCT116 human colon carcinoma

xenografts that were injected intravenously with 5 cycles of 74 MBq [123I]I-MAPi showed a statistically significant improvement in survival.

An analogue of [123I]I-MAPi for PET imaging – [18F]F-PARPi – was investigated in brain cancer patients in a first-in-human investigator-initiated clinical trial (NCT04173104) and demonstrated the tumoural accumulation of the radiotracer in humans [56]. This study will also allow for human image-based dosimetry in support of a future clinical package with the theragnostic agent.

In conclusion, [123I]I-MAPi represents an extremely attractive tool for AE-based precision RPT. The biophysical properties of this approach provide clear advantages, such as high linear energy transfer and no crossfire. Furthermore, the isotope's energy deposition topology – confined to a radius of 10–100 nanometers – makes [123I]I-MAPi a precise tool for the direct irradiation of cancer cells. This is particularly compelling in the context of the treatment of GBM.

Taken together, these clinical and preclinical studies have demonstrated that RPT with AE-emitting radionuclides is a promising and scientifically sound approach for the treatment of multiple tumour types if the radiopharmaceuticals are adequately targeted to tumours and subcellular compartments. However, further studies are needed to shed light on the mechanisms of AE-mediated damage to cells to understand if delivery to the nucleus is essential or, alternatively, if targeting the cell membrane would be sufficient. In addition, once the most
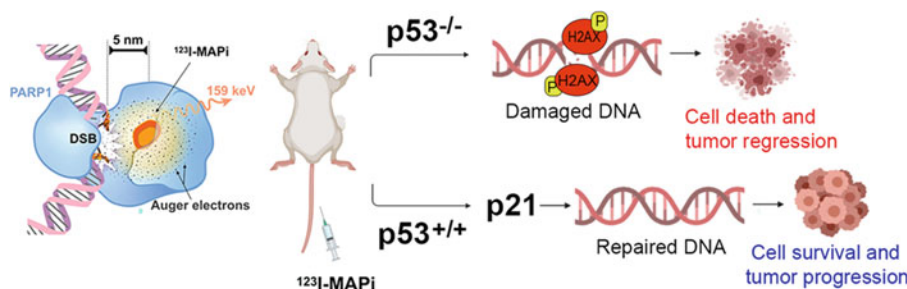
Fig. 20.12 Graphical abstract describing the work carried out by Wilson et al. [55] in which it was shown that p53 status influences the biological effects of [123I]I-MAPi.

(Reprinted with permission from Wilson et al. [55]. Copyright 2021 American Chemical Society)

sensitive intracellular compartments have been identified, further advances in the design of AE-emitting radiopharmaceuticals will be needed to route these agents more efficiently to these cellular compartments. Furthermore, the development of novel AE-emitting radionuclides that have more abundant electron emissions and fewer penetrating γ-photon emissions would improve the potency of AE radiotherapy and further restrict cell killing to the tumour cells targeted by the radiopharmaceuticals. The clinical role of AE-RPT in the management of cancer patients also needs to be better defined: is there a role for these radiotherapeutics in the treatment of large tumours? Or would these radiopharmaceuticals be better suited to the eradication of single cancer cells (e.g. circulating tumour cells) and micrometastases after other forms of cancer therapy?

20.4 The Future

20.4.1 Theragnostics

Radionuclides that emit AEs usually also emit γ-photons that can be imaged via SPECT. Hence, Auger electron-emitting radionuclides have the potential to be theragnostic agents in which the same radiopharmaceutical can be used for diagnostic imaging *and* therapy (Fig. 20.13). In addition, serial imaging can be used to investigate treatment response, and the quantification of the radioactivity uptake in tumours and normal organs can be used to estimate macro-doses. However, as discussed earlier, the most relevant dosimetry for AE-emitting radionuclides takes their subcellular distribution into consideration, which (of course) cannot be quantified by gamma camera imaging. Along these lines, preclinical studies may provide insight into the subcellular distribution and dosimetry of these radiopharmaceuticals in tumours and normal tissues.

20.4.2 Considerations for Successful AE Therapy

20.4.2.1 Photon:Electron Ratios

As mentioned above, AE-emitting radionuclides also often release both γ-rays and X-rays. Whereas AEs have a subcellular penetration, γ-rays are penetrating and travel much farther distances in tissue. While these photons have the advantage of enabling imaging as well as biodistribution, biokinetics and macrodosimetry studies, they can also be a disadvantage from a therapeutic perspective. This is because these photons will irradiate the healthy tissues of patients, resulting in absorbed dose to normal tissues [albeit at low LET ($<$0.2 keV/μm)] that will increase the risk of undesired toxicity to critical organs such as bone marrow, kidneys, liver and spleen. This is particularly true given the high amounts of activity required for AE radiotherapy as discussed earlier [57]. Therefore, the emission of γ-rays is a limiting factor to the maximum amount of radioactivity that can be administered to patients, a phenomenon which has limited the translation of AE-emitting radiotherapeutics to human studies. The release of gamma photons also means patients may decline molecular radiotherapy if significant radiation protection restrictions – e.g. sleeping apart from partners and limiting contact with young children – are necessary.

Improvements in the design of AE-emitting radiopharmaceuticals to route these agents more efficiently to sensitive cellular compartments may enable significant reductions in the amount of activity administered, thereby minimising the effects of the γ-photons on normal tissues. In addition, the use of AE-emitting radionuclides with higher ratios of electrons-to-photons would reduce toxicity to normal tissues. It is interesting, though, that many AE-emitting radiopharmaceuticals have been shown to be effective for treating tumours in mouse models at doses that caused no evidence of normal tissue
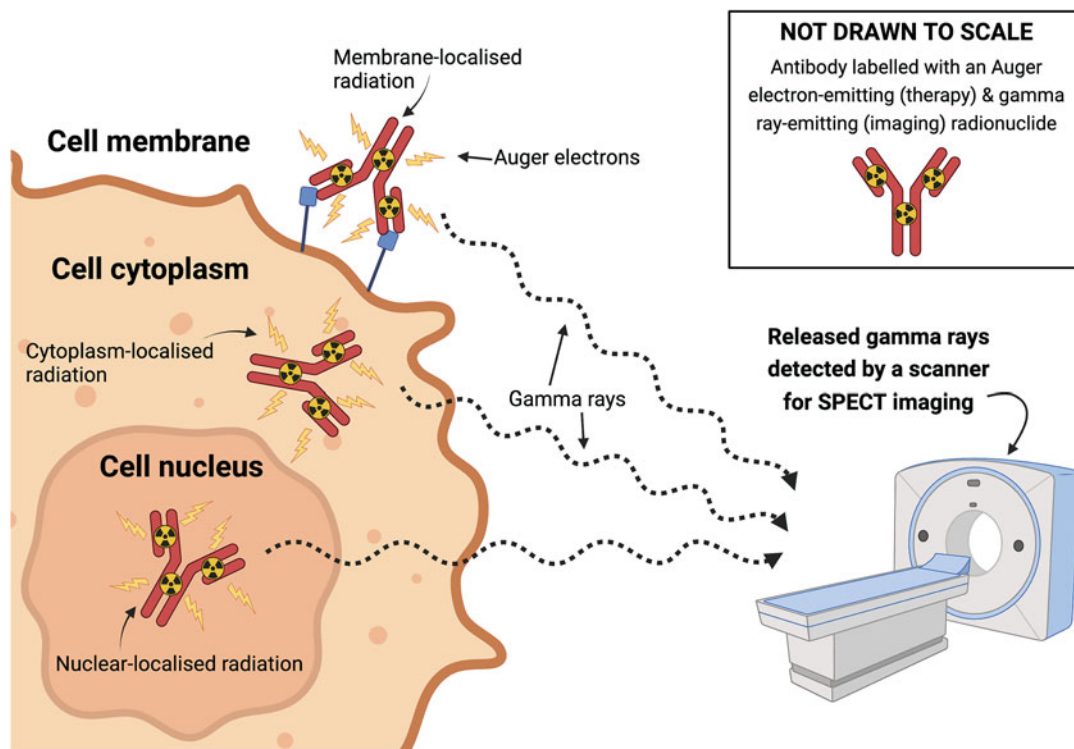
Fig. 20.13 The theragnostic potential of commonly employed SPECT radionuclides (Created in BioRender. com). SPECT commonly uses radionuclides that emit both gamma rays and Auger electrons. As a result, there is great potential for developing "true" theragnostic agents for both therapy via Auger electrons and diagnostic imaging via SPECT

toxicity. The challenge is scaling these amounts to human studies, especially since the tumoural uptake of radiopharmaceuticals in patients is often <0.01 %ID/g compared to 10–20 %ID/g in mouse models.

A model to estimate tumour-to-normal-tissue mean absorbed dose ratios provides insight on how the emission of photons affects the ratio of the absorbed dose to the tumour and normal tissues. Several parameters have been described by Uusijärvia et al. that can affect this ratio, including the type and energy of the emitted particles, the number of photons emitted, the size of the tumours and the subcellular distribution of AEs [57]. For optimal AE-therapy, a low photon:AE emission is desirable to deliver high absorbed dose to tumour while minimising off-target absorbed radiation dose. Currently, most available AE-emitters such as ^{99m}Tc, ^{111}In and ^{123}I have high photon:AE emission ratios (7.8, 11.8 and 6.27 respectively) [57]. These radionuclides thus have a greater likelihood of inducing undesirable radiation effects in normal tissues at the high activity levels administered to humans. Other, less readily available AE-emitters such as ^{195m}Pt and ^{193m}Pt have lower photon/AE emission ratios (0.42 and 0.09, respectively) and thus represent promising "next-generation" AE-emitters for RPT. Another "alternative" radionuclide that is currently more available is ^{201}Tl, which has a photon:AE ratio of 2.15 [57]. However, the use of the radiometal is hampered by the lack of an ideal chelator [58] as well as its emission of a large number of low-energy X-rays that are easily absorbed by tissue. Finally, ^{197}Hg is also an attractive AE emitter due to its low photon:AE ratio of 1.05 [57].

20.4.2.2 Subcellular Localisation

As mentioned above, most AEs travel short distances from the point of decay (<1 μm), which leads to a relatively high LET (between 4 and 26 keV/μm). Historically, nuclear DNA is considered the primary target of radiotherapeutics, including those bearing AE emitters. High energy particulate radiation, i.e. α-particles, can cause direct DNA damage, including single- and double-stand breaks, DNA base damage, and DNA crosslinks. Left unrepaired, these lead to cell death. The same effect can be achieved indirectly via reactive hydroxyl radicals (˙OH) and other reactive oxygen species produced during the radiation-induced radiolysis of water. However, these species may diffuse from the site of their formation to other sensitive molecular targets.

The radiation dose deposited by AE emitters in the nucleus is strongly linked to their subcellular distribution. Theoretical dosimetry calculations have also demonstrated that, for some radionuclides, the majority of the AE energy is deposited within a sphere of 2 nm in diameter [i.e. the diameter of DNA [59]], implying that the distance between the radionuclide and the DNA helix plays an important role in determining the efficacy of the radiotherapeutic. Studies using the plasmid method have shown that ^{99m}Tc and ^{125}I can directly fragment DNA only when in very close proximity (shorter than the 'critical distance'), as predicted by microdosimetry calculations [20, 60]. Moreover, when the radionuclide is placed a little beyond this 'critical distance', one can observe indirect DNA damage. AE emitters located in the nucleus have greater toxic effects than those located in the cytoplasm or the cell membrane. Importantly, this does not mean that the *only* method of killing cancer cells with AEs is through their emission in the nucleus, only that it is highly effective.

Different methods have been established to deliver AE emitters to the nucleus. Most common among them are methods in which the radionuclide is bound directly to the DNA, such as with 5-[^{125}I]-iodo-2′-deoxyuridine (^{125}IUdR) [15] or ^{125}I-labelled oligonucleotides [16]. Radiopharmaceuticals that target nuclear proteins (such as PARP) may be a successful alternative approach. Other AE emitters that target cell surface receptors have been modified with nuclear localisation sequences (NLSs) to facilitate their translocation to the nucleus. Examples include [^{111}In]In-EGF [11, 46], [^{111}In]In-trastuzumab [34], and gold nanoparticles [37]. In some instances, the receptor that binds the radiopharmaceutical may itself have an NLS and mediate nuclear localisation following receptor-mediated internalisation (e.g. EGFR).

An alternative approach to depositing energy in the nucleus lies in the use AE emitters, such as ^{67}Ga, that emit higher energy and longer-range AEs as well as internal conversion electrons. These radionuclides can be attached to tumour-targeting moieties that localise further from the nucleus. For example, Othman et al. used oxine to form neutral lipophilic complexes labelled with ^{67}Ga to deliver these AEs emitters to prostate cancer cells in vitro [5]. Clonogenic assays showed cells treated with ^{67}Ga-oxine exhibited lower clonogenic survival than cells treated with ^{111}In-oxine; to decrease clonogenic survival to 50%, 0.3 Bq/cell of ^{67}Ga and 0.7 Bq/cell of ^{111}In was needed. Based on these promising results, Othman et al. then conjugated ^{67}Ga to trastuzumab via the chelator THP-NCS to form [^{67}Ga]Ga-THP-trastuzumab and compared it to [^{111}In]In-DOTA-trastuzumab [6]. Both radiotracers significantly decreased clonogenicity compared to untreated controls, with [^{67}Ga]Ga-THP-trastuzumab 1.4-fold more toxic than [^{111}In]In-DOTA-trastuzumab.

Although targeting the energy from AE emitters to the nucleus remains the most potent anti-cancer approach, evidence that demonstrates an important role for extranuclear targets is emerging as well (Fig. 20.14). It has been suggested that increased oxidative stress, mostly mediated indirectly by free radicals, in the mitochondria or the cell membrane phospholipid structure [4] can also lead to cell death. This knowledge has greatly expanded the potential areas to which future AE-emitting radiopharmaceuticals could be targeted and remains an important area for future research.
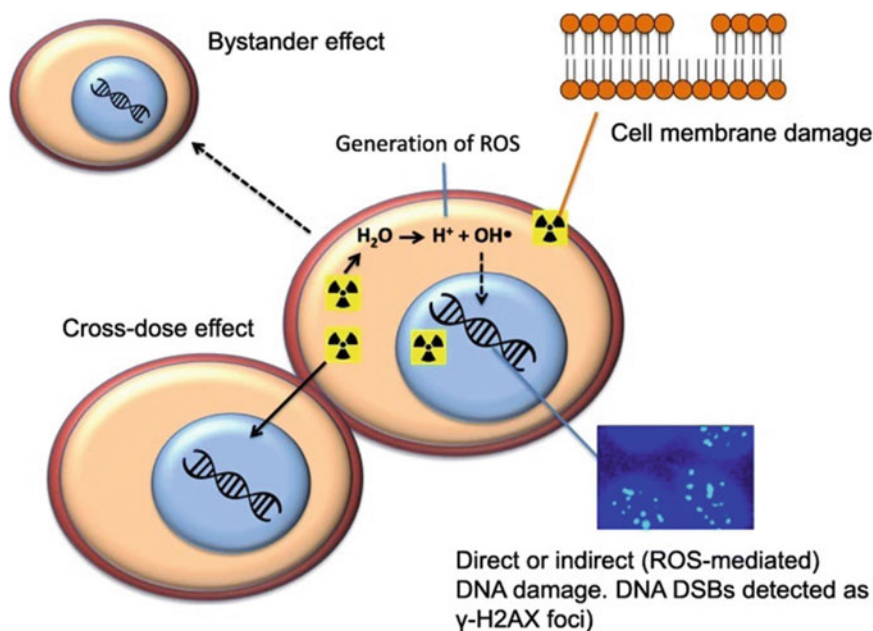
Fig. 20.14 Modes of cell death caused by the emission of AE. AEs may cause DNA double-strand breaks (DSBs) either directly or indirectly via the creation of reaction oxygen species (ROS) from water molecules. MAEs may also cause damage to the cell membrane leading to cell death. There is a localised short-range "cross-dose" effect of AEs on cancer cells which are directly adjacent to the targeted cells and a longer range "bystander" effect on more distant cells. (Figure from Ku et al. [61] under Creative Commons Attribution 4.0 International License (CC BY 4.0))

20.4.2.3 Radionuclides to Watch

As well as the common AE-emitting radionuclides described above, there are a few exciting radionuclides that deserve extra attention, as they will likely prove important players in the future of AE-emitting radiotherapeutics.

^{161}Tb, for example, is an attractive radionuclide for medical applications due to its favourable physical characteristics. ^{161}Tb ($t_{1/2}$ = 6.9 days) decays to stable ^{161}Dy via the emission of low energy β^- particles ($E\beta^-_{av}$ = 154 keV) that have a longer tissue range than AEs and thus enable the treatment of larger tumours and metastases without the need to target each individual cell within a tumour. ^{161}Tb also emits a substantial number of AEs useful for RPT, as well as gamma rays suitable for SPECT. The ability of AEs to initiate a bystander effect or stimulate an abscopal effect on the immune system could also extend their range beyond targeting and killing single cells. From a chemical perspective, ^{161}Tb is similar to ^{177}Lu (i.e. both can be stably coordinated by DOTA). Several in vitro and in vivo studies have explored the use of ^{161}Tb for RPT. For example, in mice bearing prostate and neuroendocrine tumours, ^{161}Tb has been shown to be superior to ^{177}Lu for killing cancer cells and prolonging animal survival while simultaneously limiting cross-dose radiation to healthy tissues [39, 40].

Recent work by Rigby et al. and Osytek et al. have also underscored the therapeutic potential of ^{201}Tl, which emits the highest number of AEs per decay among AE-emitters: 36.9 [18, 58]. The uptake of ^{201}Tl is mediated by the Na$^+$/K$^+$ pump in both breast and prostate cancer cells, with 0.18–0.29 Bq/cell required to achieve a 90% reduction in clonogenicity [18]. Although work carried out by Osytek et al. [18], Othman et al. [5], and Costa et al. [7] were not conducted under fully identical conditions, the number of decays/cells for ^{201}Tl – 1000–1600 decays/cell over 90 min incubation – to obtain 90% reduction of cell survival suggests that it may be more potent

than ^{111}In, ^{67}Ga, and ^{99m}Tc (3240 and 3600 decays/cell, respectively, over a 60 min incubation and 24,430 decays/cell over a 24 h incubation). However, these studies incubated cells with ^{201}Tl in its ionic form (not complexed to a targeting ligand) and it is not known if the ^{201}Tl was deposited in the cell nucleus; this may have amplified its cytotoxic effects.

Mercury-197m (^{197m}Hg) and -197 (^{197}Hg) are γ-photon-emitting radionuclides. ^{197}Hg was previously used many years ago in nuclear medicine as ^{197}Hg-chlormerodrin for evaluating renal function and performing brain scans. Improved methods for the cyclotron-based production of both radionuclides have allowed for high-specific activities to be achieved, limiting concerns about the neurotoxic effects of mercury. Recently, the theragnostic application of both radioisotopes has been explored due to their high yield of AEs and concurrent emission of γ-photons.

One final radionuclide to consider in our discussion is antimony-119 (^{119}Sb). Based on theoretical dosimetry calculations, ^{119}Sb ($t_{1/2} = 1.6$ days) is thought to be one of the most potent AE emitters for RPT. Its physical properties – including its emission of low energy γ-photons (23.9 keV) and around 24 AEs per decay – make it a great candidate for the localised radiotherapy of small tumours and micrometastases. Its cyclotron production, however, is limited, and more studies on both methods for its production and its coordination chemistry are needed.

20.4.2.4 Local Consequences of Auger Electron Decay

The chemical and biological damage caused by radionuclides is almost universally imagined in terms of the trajectory and energy of the emitted electrons (or particles) and their collisions with (and thus ionisation of) molecules in their path. One element missing from this model is the view of events occurring at the site of emission: the decaying atom itself and its immediately surrounding molecules. When a β−emission occurs, a single electron is ejected, and the atomic number of the decaying atom increases by one, a

relatively inconsequential change. Similarly, the emission of an α particle produces an increase of residual negative charge equal to two electrons. In this case, a significant recoil energy is imparted to the decaying atom, which may have locally disruptive consequences. However, when an Auger electron-emitting radionuclide decays – particularly if the number of emitted electrons is large (e.g. ~37 for ^{201}Tl) – the picture may be very different. Let us for the moment continue thinking about ^{201}Tl, whose decay leads to the emission of around 37 electrons. Each of these electrons has its own trajectory, and each deposits energy and imparts damage at a distance. To complete the picture, however, one must also imagine the local consequences of the sudden departure of those 37 electrons(!) To wit, this process leaves behind a local charge of +37, thus creating a disturbance of (molecularly) cataclysmic proportions.

The extraordinarily steep-sided electrostatic potential landscape produced by this event is far more extreme than any encountered in normal chemical and biochemical reactions. What are the likely effects of this remarkable event? This question currently remains unanswered. The least dramatic outcome may be that the molecules immediately surrounding the newly formed ion – such as the water molecules that had been occupying the coordination sphere or the biomolecules bound to it – will experience a highly polarising field that will break hydrogen bonds and other non-covalent interactions. However, far more dramatic consequences are likely: the ionisation energy liberated when such a highly charged ion captures electrons is easily enough to destabilise surrounding molecules and break covalent bonds, devastating the normal chemical order in the immediate vicinity. Such events taking place within a submicrometre radius of a biomolecule such as DNA or a lipid bilayer could therefore be devastating, enough to cause irreparable double-strand breaks in the former or puncture the latter. The extreme nature of these events is dependent not only on the energy of the electrons emitted but also on the number of them and will have extreme consequences that are very localised. This effect might be a significant

contributor to the strong dependence of the extent of chemical damage suffered by DNA (for example) on the distance from the decay event.

The events described above are – for now – a conjecture. And the contribution of this phenomenon to the damage done by AE-emitting radionuclides to biomolecules remains unknown. Modelling it and understanding its role through experiments are challenges that must be addressed to help with the design of Auger-emitting radiotherapeutics.

20.5 The Bottom Line

- There remains great interest in studying the use of Auger electrons for cancer treatment due to their short-distance energy deposition and their likelihood of limited healthy tissue toxicity. However, this enthusiasm needs to be coupled with the pursuit of a greater understanding of the mechanisms by which cell damage and cell killing are induced by AE-emitting radionuclides.
- A plethora of AE-emitting radionuclides can be considered for RPT.
- Several exciting AE-emitting radiopharmaceuticals – including [^{111}In]In-octreotide, [^{111}In]In-EGF, and [^{123}I]I-MAPi – have made it to the translational phase of development with varying degrees of success.
- It is likely that the greatest clinical impact of AE-emitting radiopharmaceuticals will be in the treatment of (micro)metastases or single cancer cells (e.g. circulating tumour cells), although therapeutic effects have been demonstrated in small solid tumours in mice.
- Several points need to be considered when developing novel AE-emitting radiopharmaceuticals, including the physical properties and photon:electron ratio of the radionuclide, the subcellular localisation of the vector, and the impact of the ionised atoms of that remain once they have emitted the electrons.

References

1. Drake R, Terry SYA, Langdon S. Lise Meitner, the scientist who changed medicine by splitting atoms. Front Young Minds. 2022;10 https://doi.org/10.3389/frym.2022.722112.
2. Buchegger F, Perillo-Adamer F, Dupertuis YM, Delaloye AB. Auger radiation targeted into DNA: a therapy perspective. Eur J Nucl Med Mol Imaging. 2006;33(11):1352–63. https://doi.org/10.1007/s00259-006-0187-2.
3. Hughes DK. Nuclear medicine and infection detection: the relative effectiveness of imaging with 111In-oxine-, 99mTc-HMPAO-, and 99mTc-stannous fluoride colloid-labeled leukocytes and with 67Ga-citrate. J Nucl Med Technol. 2003;31(4):196–201. quiz 3-4
4. Paillas S, Ladjohounlou R, Lozza C, Pichard A, Boudousq V, Jarlier M, et al. Localized irradiation of cell membrane by Auger electrons is cytotoxic through oxidative stress-mediated nontargeted effects. Antioxid Redox Signal. 2016;25(8):467–84. https://doi.org/10.1089/ars.2015.6309.
5. Othman MF, Mitry NR, Lewington VJ, Blower PJ, Terry SY. Re-assessing gallium-67 as a therapeutic radionuclide. Nucl Med Biol. 2017;46:12–8. https://doi.org/10.1016/j.nucmedbio.2016.10.008.
6. Othman MFB, Verger E, Costa I, Tanapirakgul M, Cooper MS, Imberti C, et al. In vitro cytotoxicity of Auger electron-emitting [(67)Ga]Ga-trastuzumab. Nucl Med Biol. 2020;80–81:57–64. https://doi.org/10.1016/j.nucmedbio.2019.12.004.
7. Costa IM, Siksek N, Volpe A, Man F, Osytek KM, Verger E, et al. Relationship of in vitro toxicity of technetium-99m to subcellular localisation and absorbed dose. Int J Mol Sci. 2021;22(24) https://doi.org/10.3390/ijms222413466.
8. Imstepf S, Pierroz V, Raposinho P, Bauwens M, Felber M, Fox T, et al. Nuclear targeting with an Auger electron emitter potentiates the action of a widely used antineoplastic drug. Bioconjug Chem. 2015;26(12):2397–407. https://doi.org/10.1021/acs.bioconjchem.5b00466.
9. Tavares AA, Tavares JM. Evaluating 99mTc Auger electrons for targeted tumor radiotherapy by computa-

tional methods. Med Phys. 2010;37(7):3551–9. https://doi.org/10.1118/1.3451117.

10. Costantini DL, Bateman K, McLarty K, Vallis KA, Reilly RM. Trastuzumab-resistant breast cancer cells remain sensitive to the auger electron-emitting radiotherapeutic agent 111In-NLS-trastuzumab and are radiosensitized by methotrexate. J Nucl Med. 2008;49(9):1498–505. https://doi.org/10.2967/jnumed.108.051771.

11. Reilly RM, Scollard DA, Wang J, Mondal H, Chen P, Henderson LA, et al. A kit formulated under good manufacturing practices for labeling human epidermal growth factor with 111In for radiotherapeutic applications. J Nucl Med. 2004;45(4):701–8.

12. Gill MR, Menon JU, Jarman PJ, Owen J, Skaripa-Koukelli I, Able S, et al. (111)In-labelled polymeric nanoparticles incorporating a ruthenium-based radiosensitizer for EGFR-targeted combination therapy in oesophageal cancer cells. Nanoscale. 2018;10(22):10596–608. https://doi.org/10.1039/c7nr09606b.

13. Reske SN, Deisenhofer S, Glatting G, Zlatopolskiy BD, Morgenroth A, Vogg AT, et al. 123I-ITdU-mediated nanoirradiation of DNA efficiently induces cell kill in HL60 leukemia cells and in doxorubicin-, beta-, or gamma-radiation-resistant cell lines. J Nucl Med. 2007;48(6):1000–7. https://doi.org/10.2967/jnumed.107.040337.

14. Michel RB, Castillo ME, Andrews PM, Mattes MJ. In vitro toxicity of A-431 carcinoma cells with antibodies to epidermal growth factor receptor and epithelial glycoprotein-1 conjugated to radionuclides emitting low-energy electrons. Clin Cancer Res. 2004;10(17):5957–66. https://doi.org/10.1158/1078-0432.CCR-03-0465.

15. Sahu SK, Wen PY, Foulon CF, Nagel JS, Black PM, Adelstein SJ, et al. Intrathecal 5-[125I]iodo-2′-deoxyuridine in a rat model of leptomeningeal metastases. J Nucl Med. 1997;38(3):386–90.

16. Dahmen V, Kriehuber R. Cytotoxic effects and specific gene expression alterations induced by I-125-labeled triplex-forming oligonucleotides. Int J Radiat Biol. 2012;88(12):972–9. https://doi.org/10.3109/09553002.2012.702298.

17. Bodnar EN, Dikiy MP, Medvedeva P. Photonuclear production and antitumor effect of radioactive cisplatin (195mPt). J Radioanal Nucl Chem. 2015;205:133–8.

18. Osytek KM, Blower PJ, Costa IM, Smith GE, Abbate V, Terry SYA. In vitro proof of concept studies of radiotoxicity from Auger electron-emitter thallium-201. EJNMMI Res. 2021;11(1):63. https://doi.org/10.1186/s13550-021-00802-w.

19. Verger E, Cheng J, de Santis V, Iafrate M, Jackson JA, Imberti C, et al. Validation of the plasmid study to relate DNA damaging effects of radionuclides to those from external beam radiotherapy. Nucl Med Biol. 2021;100–101:36–43. https://doi.org/10.1016/j.nucmedbio.2021.06.004.

20. Reissig F, Mamat C, Steinbach J, Pietzsch HJ, Freudenberg R, Navarro-Retamal C, et al. Direct and

Auger electron-induced, single- and double-strand breaks on plasmid DNA caused by 99mTc-labeled pyrene derivatives and the effect of bonding distance. PLoS One. 2016;11(9):e0161973. https://doi.org/10.1371/journal.pone.0161973.

21. Pereira E, do Quental L, Palma E, Oliveira MC, Mendes F, Raposinho P, et al. Evaluation of acridine orange derivatives as DNA-targeted radiopharmaceuticals for Auger therapy: influence of the radionuclide and distance to DNA. Sci Rep. 2017;7:42544. https://doi.org/10.1038/srep42544.

22. Falzone N, Lee BQ, Fernandez-Varea JM, Kartsonaki C, Stuchbery AE, Kibedi T, et al. Absorbed dose evaluation of Auger electron-emitting radionuclides: impact of input decay spectra on dose point kernels and S-values. Phys Med Biol. 2017;62(6):2239–53. https://doi.org/10.1088/1361-6560/aa5aa4.

23. Thierens HM, Monsieurs MA, Brans B, Van Driessche T, Christiaens I, Dierckx RA. Dosimetry from organ to cellular dimensions. Comput Med Imaging Graph. 2001;25(2):187–93. https://doi.org/10.1016/s0895-6111(00)00047-1.

24. Arnaud FX, Paillas S, Pouget JP, Incerti S, Bardiès M, Bordage MC. Complex cell geometry and sources distribution model for Monte Carlo single cell dosimetry with iodine 125 radioimmunotherapy. Nucl Instrum Methods Phys Res Sect B Beam Interact Mater Atoms. 2016;366:227–33.

25. Cai Z, Kwon YL, Reilly RM. Monte Carlo N-Particle (MCNP) modeling of the cellular dosimetry of 64Cu: comparison with MIRDcell S values and implications for studies of its cytotoxic effects. J Nucl Med. 2017;58(2):339–45. https://doi.org/10.2967/jnumed.116.175695.

26. Tajik-Mansoury MA, Rajabi H, Mozdarani HA. A comparison between track-structure, condensed-history Monte Carlo simulations and MIRD cellular S-values. Phys Med Biol. 2017;62:N90–106. https://doi.org/10.1088/1361-6560/62/5/N90.

27. Shen CJ, Minn I, Hobbs RF, Chen Y, Josefsson A, Brummet M, et al. Auger radiopharmaceutical therapy targeting prostate-specific membrane antigen in a micrometastatic model of prostate cancer. Theranostics. 2020;10(7):2888–96. https://doi.org/10.7150/thno.38882.

28. Grudzinski J, Marsh I, Titz B, Jeffery J, Longino M, Kozak K, et al. CLR 125 Auger electrons for the targeted radiotherapy of triple-negative breast cancer. Cancer Biother Radiopharm. 2018;33(3):87–95. https://doi.org/10.1089/cbr.2017.2376.

29. Nadar RA, Franssen GM, Van Dijk NWM, Codee-van der Schilden K, de Weijert M, Oosterwijk E, et al. Bone tumor-targeted delivery of theranostic (195m)Pt-bisphosphonate complexes promotes killing of metastatic tumor cells. Mater Today Biol. 2021;9:100088. https://doi.org/10.1016/j.mtbio.2020.100088.

30. Areberg J, Wennerberg J, Johnsson A, Norrgren K, Mattsson S. Antitumor effect of radioactive cisplatin

(191Pt) on nude mice. Int J Radiat Oncol Biol Phys. 2001;49(3):827–32. https://doi.org/10.1016/s0360-3016(00)01419-x.

31. Schipper ML, Riese CGU, Seitz S, Weber A, Behe M, Schurrat T, et al. Efficacy of 99mTc pertechnetate and 131I radioisotope therapy in sodium/iodide symporter (NIS)-expressing neuroendocrine tumors in vivo. Eur J Nucl Med Mol Imaging. 2007;34(5):638–50. https://doi.org/10.1007/s00259-006-0254-8.

32. Santoro L, Boutaleb S, Garambois V, Bascoul-Mollevi C, Boudousq V, Kotzki PO, et al. Noninternalizing monoclonal antibodies are suitable candidates for 125I radioimmunotherapy of small-volume peritoneal carcinomatosis. J Nucl Med. 2009;50(12):2033–41. https://doi.org/10.2967/jnumed.109.066993.

33. Behr TM, Behe M, Lohr M, Sgouros G, Angerstein C, Wehrmann E, et al. Therapeutic advantages of Auger electron- over beta-emitting radiometals or radioiodine when conjugated to internalizing antibodies. Eur J Nucl Med. 2000;27(7):753–65. https://doi.org/10.1007/s002590000272.

34. Costantini DL, McLarty K, Lee H, Done SJ, Vallis KA, Reilly RM. Antitumor effects and normal-tissue toxicity of 111In-nuclear localization sequence-trastuzumab in athymic mice bearing HER-positive human breast cancer xenografts. J Nucl Med. 2010;51(7):1084–91. https://doi.org/10.2967/jnumed.109.072389.

35. Rosenkranz AA, Slastnikova TA, Karmakova TA, Vorontsova MS, Morozova NB, Petriev VM, et al. Antitumor activity of Auger electron emitter (111)In delivered by modular nanotransporter for treatment of bladder cancer with EGFR overexpression. Front Pharmacol. 2018;9:1331. https://doi.org/10.3389/fphar.2018.01331.

36. Slastnikova TA, Rosenkranz AA, Khramtsov YV, Karyagina TS, Ovechko SA, Sobolev AS. Development and evaluation of a new modular nanotransporter for drug delivery into nuclei of pathological cells expressing folate receptors. Drug Des Devel Ther. 2017;11:1315–34. https://doi.org/10.2147/DDDT.S127270.

37. Cai Z, Chattopadhyay N, Yang K, Kwon YL, Yook S, Pignol JP, et al. (111)In-labeled trastuzumab-modified gold nanoparticles are cytotoxic in vitro to HER2-positive breast cancer cells and arrest tumor growth in vivo in athymic mice after intratumoral injection. Nucl Med Biol. 2016;43(12):818–26. https://doi.org/10.1016/j.nucmedbio.2016.08.009.

38. Narmani A, Arani MAA, Mohammadnejad J, Vaziri AZ, Solymani S, Yavari K, et al. Breast tumor targeting with PAMAM-PEG-5FU-(99m)Tc As a new therapeutic nanocomplex: in In-vitro and In-vivo studies. Biomed Microdevices. 2020;22(2):31. https://doi.org/10.1007/s10544-020-00485-5.

39. Muller C, Umbricht CA, Gracheva N, Tschan VJ, Pellegrini G, Bernhardt P, et al. Terbium-161 for PSMA-targeted radionuclide therapy of prostate cancer. Eur J Nucl Med Mol Imaging. 2019;46(9):1919–30. https://doi.org/10.1007/s00259-019-04345-0.

40. Borgna F, Haller S, Rodriguez JMM, Ginj M, Grundler PV, Zeevaart JR, et al. Combination of terbium-161 with somatostatin receptor antagonists-a potential paradigm shift for the treatment of neuroendocrine neoplasms. Eur J Nucl Med Mol Imaging. 2022;49(4):1113–26. https://doi.org/10.1007/s00259-021-05564-0.

41. Delpassand ES, Samarghandi A, Mourtada JS, Zamanian S, Espenan GD, Sharif R, et al. Long-term survival, toxicity profile, and role of F-18 FDG PET/CT scan in patients with progressive neuroendocrine tumors following peptide receptor radionuclide therapy with high activity In-111 pentetreotide. Theranostics. 2012;2(5):472–80. https://doi.org/10.7150/thno.3739.

42. Krenning EP, de Jong M, Kooij PP, Breeman WA, Bakker WH, de Herder WW, et al. Radiolabelled somatostatin analogue(s) for peptide receptor scintigraphy and radionuclide therapy. Ann Oncol. 1999;10 (Suppl 2):S23–9. https://doi.org/10.1093/annonc/10.suppl_2.s23.

43. Meyers MO, Anthony LB, McCarthy KE, Drouant G, Maloney TJ, Espanan GD, et al. High-dose indium 111In pentetreotide radiotherapy for metastatic atypical carcinoid tumor. South Med J. 2000;93(8):809–11.

44. Valkema R, De Jong M, Bakker WH, Breeman WA, Kooij PP, Lugtenburg PJ, et al. Phase I study of peptide receptor radionuclide therapy with [In-DTPA] octreotide: the Rotterdam experience. Semin Nucl Med. 2002;32(2):110–22. https://doi.org/10.1053/snuc/2002.31025.

45. Remy S, Reilly RM, Sheldon K, Gariepy J. A new radioligand for the epidermal growth factor receptor: 111In labeled human epidermal growth factor derivatized with a bifunctional metal-chelating peptide. Bioconjug Chem. 1995;6(6):683–90. https://doi.org/10.1021/bc00036a004.

46. Reilly RM, Kiarash R, Cameron RG, Porlier N, Sandhu J, Hill RP, et al. 111In-labeled EGF is selectively radiotoxic to human breast cancer cells overexpressing EGFR. J Nucl Med. 2000;41(3):429–38.

47. Cai Z, Chen Z, Bailey KE, Scollard DA, Reilly RM, Vallis KA. Relationship between induction of phosphorylated H2AX and survival in breast cancer cells exposed to 111In-DTPA-hEGF. J Nucl Med. 2008;49(8):1353–61. https://doi.org/10.2967/jnumed.108.051805.

48. Chen P, Cameron R, Wang J, Vallis KA, Reilly RM. Antitumor effects and normal tissue toxicity of 111In-labeled epidermal growth factor administered to athymic mice bearing epidermal growth factor receptor-positive human breast cancer xenografts. J Nucl Med. 2003;44(9):1469–78.

49. Vallis KA, Reilly RM, Scollard D, Merante P, Brade A, Velauthapillai S, et al. Phase I trial to

evaluate the tumor and normal tissue uptake, radiation dosimetry and safety of (111)In-DTPA-human epidermal growth factor in patients with metastatic EGFR-positive breast cancer. Am J Nucl Med Mol Imaging. 2014;4(2):181–92.

50. Reilly RM, Kiarash R, Sandhu J, Lee YW, Cameron RG, Hendler A, et al. A comparison of EGF and MAb 528 labeled with 111In for imaging human breast cancer. J Nucl Med. 2000;41(5):903–11.

51. Carney B, Kossatz S, Lok BH, Schneeberger V, Gangangari KK, Pillarsetty NVK, et al. Target engagement imaging of PARP inhibitors in small-cell lung cancer. Nat Commun. 2018;9(1):176. https://doi.org/10.1038/s41467-017-02096-w.

52. Salinas B, Irwin CP, Kossatz S, Bolaender A, Chiosis G, Pillarsetty N, et al. Radioiodinated PARP1 tracers for glioblastoma imaging. EJNMMI Res. 2015;5(1):123. https://doi.org/10.1186/s13550-015-0123-1.

53. Wilson TC, Jannetti SA, Guru N, Pillarsetty N, Reiner T, Pirovano G. Improved radiosynthesis of (123)I-MAPi, an auger theranostic agent. Int J Radiat Biol. 2020;99:1–7. https://doi.org/10.1080/09553002.2020.1781283.

54. Pirovano G, Jannetti SA, Carter LM, Sadique A, Kossatz S, Guru N, et al. Targeted brain tumor radiotherapy using an Auger emitter. Clin Cancer Res. 2020;26(12):2871–81. https://doi.org/10.1158/1078-0432.CCR-19-2440.

55. Wilson T, Pirovano G, Xiao G, Samuels Z, Roberts S, Viray T, et al. PARP-targeted Auger therapy in p53 mutant colon cancer xenograft mouse models. Mol Pharm. 2021;18(9):3418–28. https://doi.org/10.1021/acs.molpharmaceut.1c00323.

56. Young RJ, Demetrio De Souza Franca P, Pirovano G, Piotrowski AF, Nicklin PJ, Riedl CC, et al. Preclinical and first-in-human-brain-cancer applications of [(18)F]poly (ADP-ribose) polymerase inhibitor PET/MR. Neurooncol Adv. 2020;2(1):vdaa119. https://doi.org/10.1093/noajnl/vdaa119.

57. Uusijarvi H, Bernhardt P, Ericsson T, Forssell-Aronsson E. Dosimetric characterization of radionuclides for systemic tumor therapy: influence of particle range, photon emission, and subcellular distribution. Med Phys. 2006;33(9):3260–9. https://doi.org/10.1118/1.2229428.

58. Rigby A, Blower JE, Blower PJ, Terry SYA, Abbate V. Targeted Auger electron-emitter therapy: radiochemical approaches for thallium-201 radiopharmaceuticals. Nucl Med Biol. 2021;98–99:1–7. https://doi.org/10.1016/j.nucmedbio.2021.03.012.

59. Falzone N, Fernandez-Varea JM, Flux G, Vallis KA. Monte Carlo evaluation of Auger electron-emitting theranostic radionuclides. J Nucl Med. 2015;56(9):1441–6. https://doi.org/10.2967/jnumed.114.153502.

60. Balagurumoorthy P, Xu X, Wang K, Adelstein SJ, Kassis AI. Effect of distance between decaying 125 I and DNA on Auger-electron induced double-strand break yield. Int J Radiat Biol. 2012;88:998–1008.

61. Ku A, Facca VJ, Cai Z, Reilly RM. Auger electrons for cancer therapy—a review. EJNMMI Radiopharm Chem. 2019;4(1):27. https://doi.org/10.1186/s41181-019-0075-2.

Pretargeted Radiopharmaceutical Therapy

21

Outi M. Keinänen and Brian M. Zeglis

21.1 The Fundamentals

21.1.1 The Principle of Pretargeted Radioimmunotherapy

While radioimmunotherapy (RIT) has long shown great promise for the treatment of cancer, the prolonged circulation times of radioimmunoconjugates frequently yield high radiation doses to healthy tissues, a complication that has hampered the clinical utility of RIT [1–3]. Pretargeted radioimmunotherapy (PRIT) aims

to leverage the advantages of full-length antibodies while avoiding their dosimetric drawbacks. In PRIT, the antibody and radioactivity are decoupled, the immunoglobulin is injected days before a small-molecule radioligand, and a highly selective ligation is relied upon to drive the in vivo combination of the two components at the tumor site (Fig. 21.1). In this way, the antibody spends most (if not all) of its time in circulation unlabeled and only becomes a *radio*immunoconjugate after it has bound to the tumor and reacts with its rapidly circulating small molecule counterpart. This method—which in essence performs radiochemistry within the body—is thus designed to deliver high doses of radiation to malignant tissue while minimizing the radiation dose to healthy organs. Furthermore, PRIT facilitates the use of shorter-lived therapeutic nuclides (e.g., lead-212, bismuth-213, and astatine-211) that are normally incompatible with vectors such as antibodies with slow pharmacokinetic profiles. Broadly speaking, any approach to PRIT consists of four essential steps (Fig. 21.1): (1) the administration of an immunoconjugate bearing one half of the system's molecular couple; (2) an interval period during which the antibody accumulates at the tumor and clears from the blood; (3) the injection of a small-molecule radioligand containing the *other* half of the system's molecular couple; and (4) the in vivo ligation between the two components followed by the rapid clearance of excess radioligand.

O. M. Keinänen
Department of Chemistry, Hunter College, City University of New York, New York, NY, USA

Department of Radiology, Memorial Sloan Kettering Cancer Center, New York, NY, USA

Department of Chemistry, University of Helsinki, Helsinki, Finland

B. M. Zeglis (✉)
Department of Chemistry, Hunter College, City University of New York, New York, NY, USA

Department of Radiology, Memorial Sloan Kettering Cancer Center, New York, NY, USA

PhD Program in Chemistry, Graduate Center of the City University of New York, New York, NY, USA

PhD Program in Biochemistry, Graduate Center of the City University of New York, New York, NY, USA

Department of Radiology, Weill Cornell Medicine, New York, NY, USA
e-mail: bz102@hunter.cuny.edu
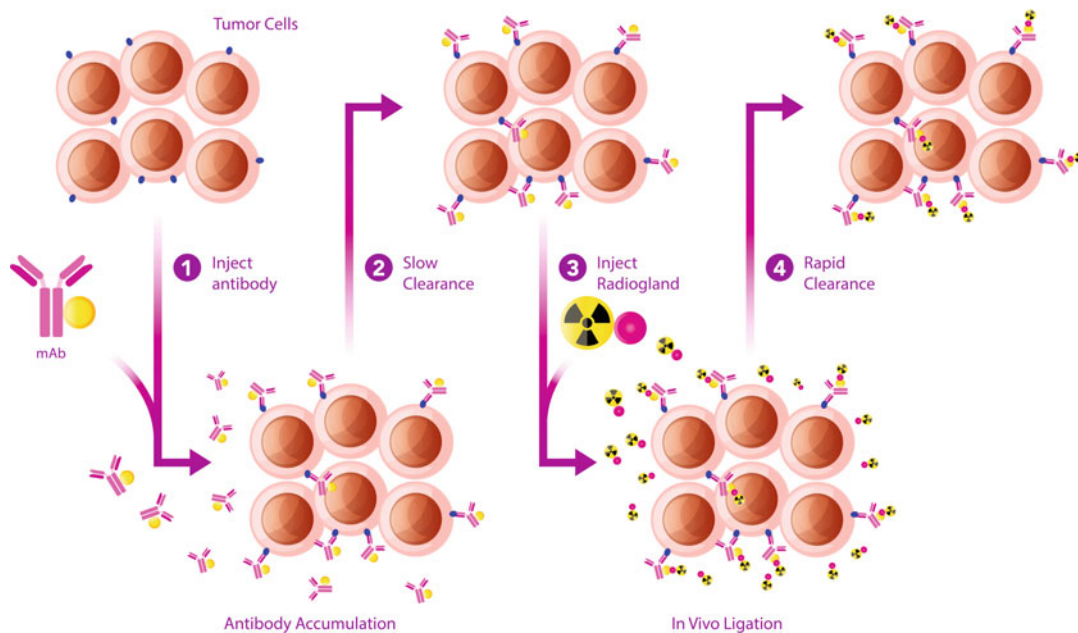
Fig. 21.1 General schematic of in vivo pretargeting

21.1.2 The Anatomy of an Effective Pretargeting System

The essence of any approach to pretargeting is the central molecular couple that undergoes the system's in vivo ligation. Because the body contains an array of different chemical functionalities each with its own reactivity, it is essential that the two components of the molecular couple exhibit selectivity and specificity for—and *only* for—each other, even within a complex biological milieu. The product of the ligation between the two components of the system must also remain stable under physiological conditions, or else the radioactivity will be released from the immunoconjugate and will either redistribute within the body or clear entirely. As we will see, both non-covalent and covalent approaches to this in vivo ligation have been explored, with the latter the clear winner in terms of post-ligation stability. Below, we will address the different molecular couples that have been used for in vivo pretargeting over the last three decades. Before we do, however, we think it is important to address the other core components of any approach to in vivo pretargeting.

Building a good pretargeting system starts with the selection of the antibody. The antibody has to be capable of binding both a cancer antigen and, through an added functionality, the radioligand in question. With respect to molecular targets, many of the same factors that make an antigen a good target for a traditional radioimmunoconjugate will make it a good antigen for pretargeting, namely high extracellular expression by cancer cells and low expression by healthy tissues. Yet for pretargeting systems, the internalization of the antibody—or lack thereof—is a particularly critical consideration. If the antibody is internalized rapidly after binding its target, it will no longer be available to react with its counterpart. Generally speaking, this precludes antibodies that rapidly internalize. Indeed, non-internalizing mAb are best, though antibodies that internalize at more moderate rates—e.g., the CA19-9-targeting mAb 5B1—have been harnessed for pretargeted positron emission tomography (PET) and PRIT to great effect. All that said, interesting work has been done to facilitate the use of internalizing antibodies for in vivo pretargeting by driving the retention of the target antigen at the surface of the

cell. For instance, Pereira et al. have shown that statins slow the caveolae-mediated endocytosis of HER2 after it is bound by pertuzumab and trastuzumab and that the pretreatment of mice with lovastatin (a statin) can enhance the utility of these antibodies for in vivo pretargeting [4].

The other half of the system—the radioligand—must also be carefully designed. The radioligand of a pretargeting system is almost always a small molecule with a rapid pharmacokinetic profile. This speed is essential to ensure that excess radioligand is excreted quickly, thereby reducing the circulation time of the radioactivity and, in turn, the radiation dose to healthy tissues. However, the pharmacokinetic profile of the radioligand cannot be *too* quick, as overly fast clearance (e.g., single-pass renal clearance) will unduly lower the probability of reaction between the two components of the molecular couple. Along these lines, the modularity of radioligands often comes in handy during optimization, as various elements—e.g., chelators, PEG linkers—can be altered to fine-tune the pharmacokinetics of the construct without altering its fundamental reactivity.

Finally, once the fundamental components—i.e., the antibody and radioligand—of a pretargeting system have been selected, several other parameters must often be optimized during the preclinical development of the methodology. These include the amount of immunoconjugate administered, the number of reactive functional groups attached per antibody, the administration route, the interval period between the two injections, the use of a clearing agent, and the amount of radiotracer administered. Changes to any of these parameters can dramatically impact the in vivo performance of a pretargeting strategy, either in terms of the activity concentrations delivered to the tumor or the uptake of the radioligand by healthy organs.

21.2 The Details

21.2.1 Methods of In Vivo Pretargeting

Over the years, a variety of different molecular couples have been used for in vivo pretargeting, including strategies based on streptavidin and biotin, bispecific antibodies (bsAbs), complementary oligonucleotides, and bioorthogonal click chemistry (Fig. 21.2). Each strategy has been extensively validated preclinically, while the
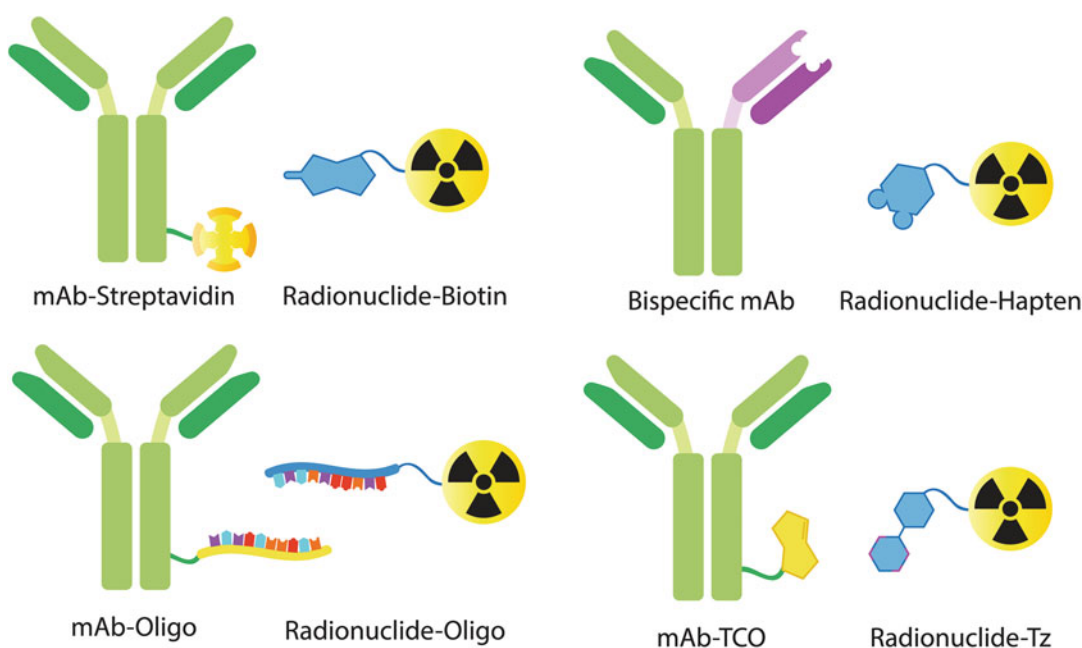
Fig. 21.2 Four different approaches to in vivo pretargeting. *TCO trans*-cyclooctene, *Tz* tetrazine

former pair have been evaluated in clinical trials. In the ensuing pages, we will offer detailed discussions of the preclinical and clinical development of each of these approaches.

21.2.1.1 Streptavidin and Biotin

One of the earliest approaches to in vivo pretargeting was predicated on the extraordinarily high affinity between (strept)avidin and biotin. Streptavidin (60 kDa) and avidin (66 kDa) are tetrameric proteins composed of four identical subunits that each bind to a single biotin, a 244 Da water-soluble small molecule. The affinity between (strept)avidin and biotin is one of the strongest known non-covalent interactions—$K_d = \sim 10^{-15}$ M—and this pair has been exploited in several biotechnological applications, including immunological assays, electron microscopy, affinity chromatography, and nucleic acid hybridization. In theory either member of the molecular couple—i.e., (strept)avidin or biotin—could be conjugated to the antibody while the other is used as a platform for the radioligand. However, biotin's low molecular weight and ease of modification has led the field to use it (most often but not always) as the core of the radioligand. On the other side, streptavidin and avidin have identical binding affinities for biotin, but differences in their pharmacokinetic profiles have influenced the way they are used for in vivo pretargeting. Avidin clears rapidly from circulation via the liver and has therefore been used primarily as a clearing agent (vide infra). In contrast, the high in vivo stability of streptavidin has made it the protein of choice to be conjugated to the antibody.

A variety of protocols have been developed for streptavidin–biotin pretargeting (Fig. 21.3). In the simplest method, the streptavidin-bearing mAb is administered first; it slowly accumulates in the tumor and clears from the blood and is followed—hours or days later—by the injection of the radiolabeled biotin (Fig. 21.3a). This strategy produced promising preclinical results, but the sluggish serum clearance of the high-molecular-weight immunoconjugate (~210 kDa) meant that ligations between the biotin-based radioligand and the mAb-streptavidin in the blood could create circulating radioimmunoconjugates that would raise radiation dose rates to the blood and other healthy tissues. To circumvent this issue, another component—a clearing agent—could be injected prior to the administration of the radioligand to remove excess mAb-streptavidin from the blood (Fig. 21.3b). This galactose-bearing biotin-based clearing agent binds to the circulating mAb-streptavidin and directs the entire complex to the liver, where it is metabolized. This leaves only tumor-bound immunoconjugate to react with the subsequently administered radioligand.

While the addition of a clearing agent addressed the issue of circulating immunoconjugate, it did not surmount another obstacle to this system: endogenous biotin. Natural biotin in the body can block the binding sites of streptavidin and thus prevent the radiolabeled biotin from interacting with the immunoconjugate. To combat endogenous biotin, another approach was developed that flips the script a bit by employing both a biotinylated antibody *and* a biotinylated radioligand (Fig. 21.3c). Here, the mAb-biotin is injected first. After its uptake in the tumor peaks, an avidin-based clearing agent is administered that transports both excess immunoconjugate *and* endogenous biotin to the liver. Next, streptavidin is administered, which either binds to the remaining mAb-biotin at the tumor or clears from the blood. Finally, a biotin-based radioligand is administered that can quickly bind the mAb-biotin-streptavidin complex at the tumor. Despite its complexity, this four-agent approach proved successful in preclinical models by accelerating the blood clearance of the radioligand and increasing the tumor/non-tumor ratios [5–7].

Streptavidin–biotin pretargeting has been evaluated in clinical trials for both nuclear imaging and PRIT [8–18]. The first clinical trials were focused on pretargeted single photon emission computed tomography (SPECT). In 1990, Kalofonos et al. published the first-in-human study in which a streptavidin-functionalized HMFG1 mAb was administered to patients with squamous cell carcinoma three days prior to a ^{111}In-labeled biotin radioligand [8]. SPECT
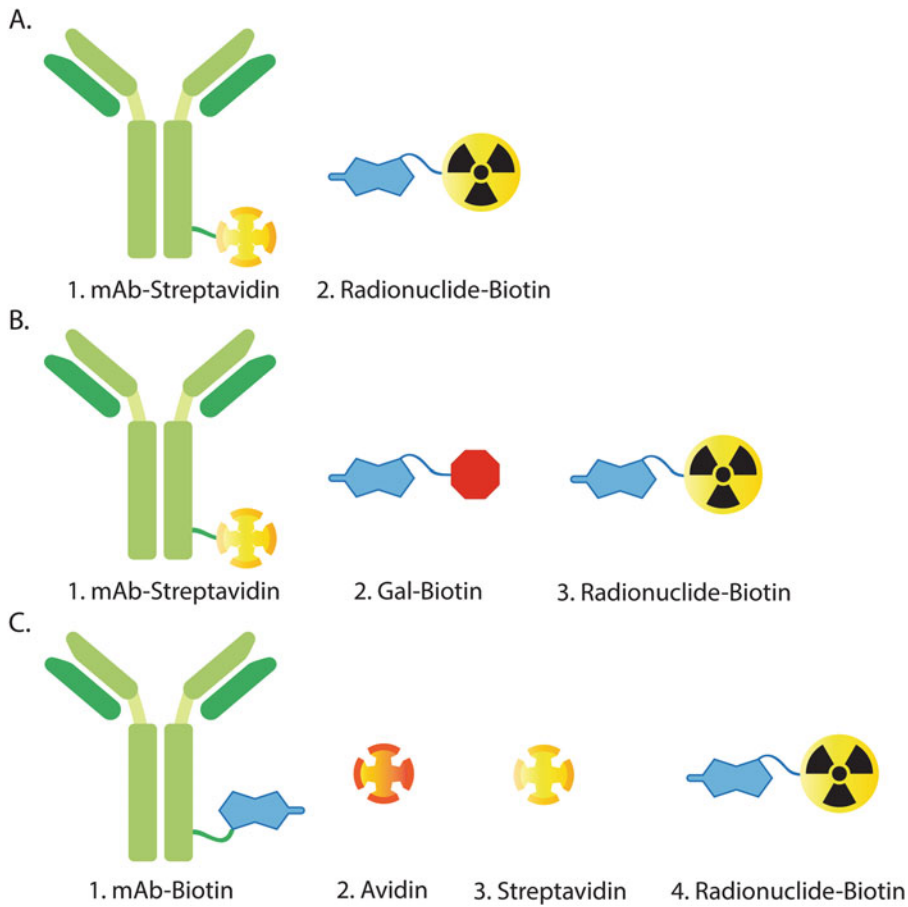
Fig. 21.3 Pretargeting strategies based on streptavidin and biotin. (**a**) In the simplest methodology, a streptavidin-modified mAb is administered before a radiolabeled biotin. (**b**) To decrease the radiation dose to the blood and other healthy tissues, a galactose-bearing, biotin-based clearing agent can be used between the administration of the mAb-streptavidin and the radioligand. (**c**) To prevent natural biotin from blocking the binding sites on streptavidin, a biotinylated mAb and an avidin-based clearing agent have been used. In this approach, a biotin-modified antibody is administered first. Subsequently, avidin is injected to bind circulating biotin and circulating immunoconjugate and rapidly clear both to the liver. Streptavidin is then injected to bind the tumor-associated mAb-biotin immunoconjugate, followed, finally, by a biotin-based radioligand

imaging performed 2 h after the injection of $[^{111}In]In$-DTPA-biotin showed modest improvement in image quality compared to control experiments in which the same patients received $[^{111}In]In$-DTPA-biotin without the pre-injection of streptavidin-mAb. Although no adverse effects were observed, all patients displayed an immune response by developing anti-streptavidin antibodies. Despite this clear immunogenicity, the development of this pretargeting strategy continued.

Almost a decade later, the first clinical PRIT studies were reported with very promising results. In 1999, Paganelli et al. used a biotin-functionalized mAb, an avidin clearing agent, streptavidin, and $[^{90}Y]Y$-DOTA-biotin in patients with glioblastoma and ultimately observed a tumor mass reduction of 25% (Fig. 21.4) [11]. Later, another PRIT study by the same team reported a 25% response rate and significantly prolonged median survival times (33.5 months vs. 8 months) in patients with
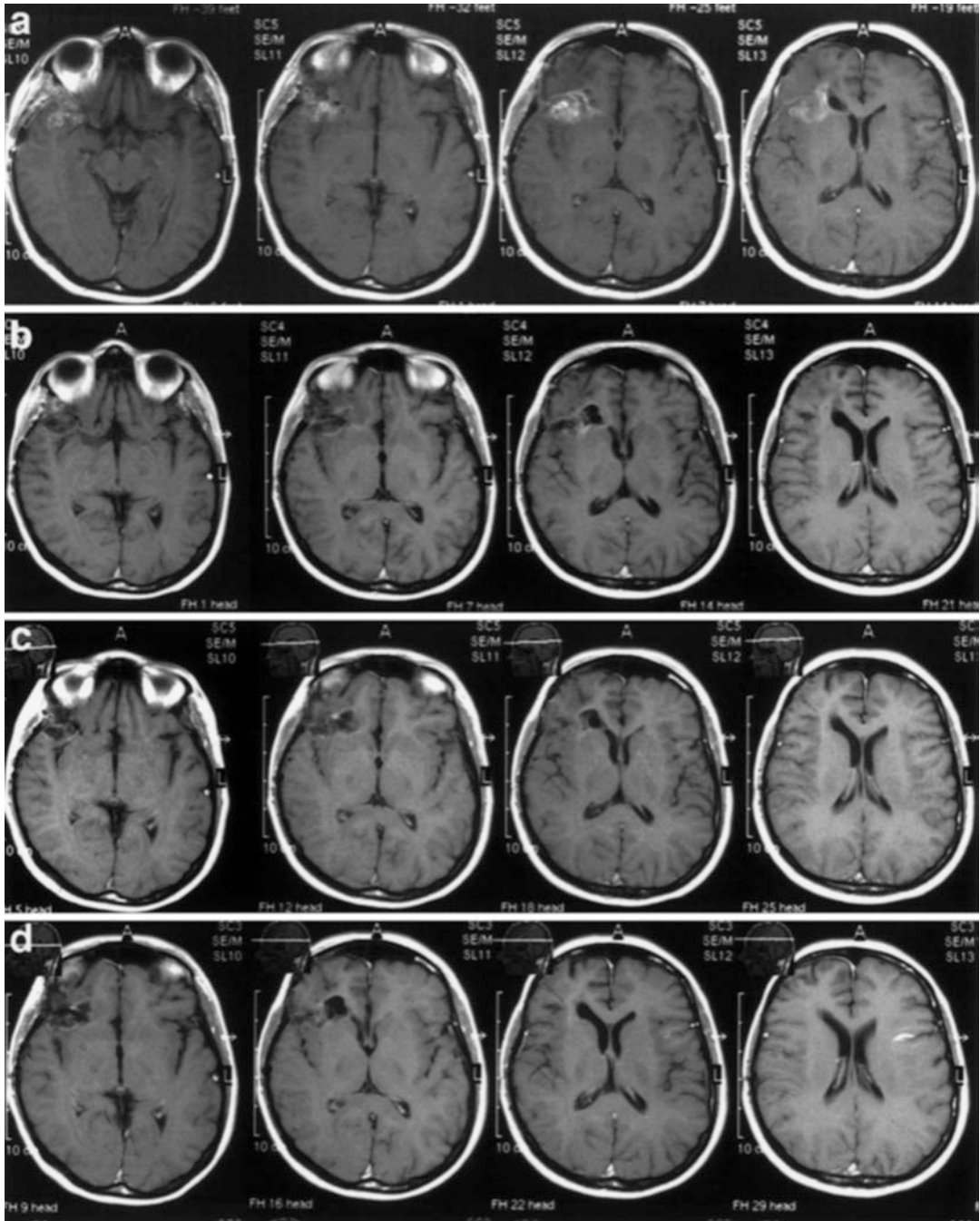
Fig. 21.4 (**a**) Magnetic resonance imaging (MRI) study of a 29-year-old patient who had partial surgery for anaplastic oligodendroglioma followed by pretargeted radioimmunotherapy. Progressive reduction in the tumor is evident at two months (**b**), with complete remission of the disease at five months (**c**) persisting for more than a year (**d**). (Source: Paganelli G. et al. 1999, fig. 4 [11]. Reprinted with permission from *European Journal of Nuclear Medicine and Molecular Imaging*, Springer Nature)

glioma and anaplastic astrocytoma [14, 16]. Around the same time, streptavidin–biotin PRIT was shown to increase the radiation dose to the tumor, limit the radiation dose to healthy tissues, and reduce tumor burden in patients with non-Hodgkin lymphoma [15, 17]. Unfortunately, all these encouraging studies also featured hematologic toxicity and immune responses to the streptavidin-based compounds [10–17]. The former most likely could have been addressed by adjusting the pretargeting parameters, such as the interval time between the injections or the doses of immunoconjugates, clearing agents, or radioligands [12]. But the immunogenicity of (strept)avidin has remained a persistent and seemingly debilitating obstacle that has prompted the

field to shift its interest to other pretargeting methods. Efforts to overcome this limitation are still on-going in preclinical settings, but very few clinical trials have been conducted in the past 15 years.

21.2.1.2 Bispecific Antibodies and Radiolabeled Haptens

The advent of pretargeting methods based on bispecific antibodies (bsAbs) ran almost concurrently to the development of streptavidin–biotin systems. In this technique, bsAbs are genetically or chemically engineered to contain binding domains against both a tumor antigen *and* a small, radiolabeled hapten (Fig. 21.5). The earliest bsAbs for pretargeting consisted of two monovalent Fab fragments: one for a tumor

Fig. 21.5 Pretargeting strategies based on bispecific antibodies and radiolabeled haptens. (**a**) A tumor-specific Fab fragment chemically linked to a radiometal-chelator-specific Fab fragment with a monovalent radiometal-chelator complex used as the radioligand. (**b**) Two chelators linked together with a peptide chain, thereby forming a bivalent radioligand that can bind two bsAbs. (**c**) A tumor-specific Fab fragment chemically linked to an histamine-succinyl-glycine (HSG)-specific Fab fragment. The radioligand consists of two HSG haptens linked together with a peptide chain that contains a functional group to which a chelator or other radiolabeling prosthetic group can be attached. (**d**) A tri-Fab scaffold containing two anti-tumor Fab fragments and one anti-HSG Fab fragment

A. Tumor-specific Fab - chelator-specific Fab — Radiometal chelator hapten

B. Tumor-specific Fab - chelator-specific Fab — Bivalent radiometal chelator hapten

C. Tumor-specific Fab - HSG-specific Fab — Bivalent HSG radionuclide hapten

D. 2 × tumor-specific Fab - HSG-specific Fab — Bivalent HSG radionuclide hapten
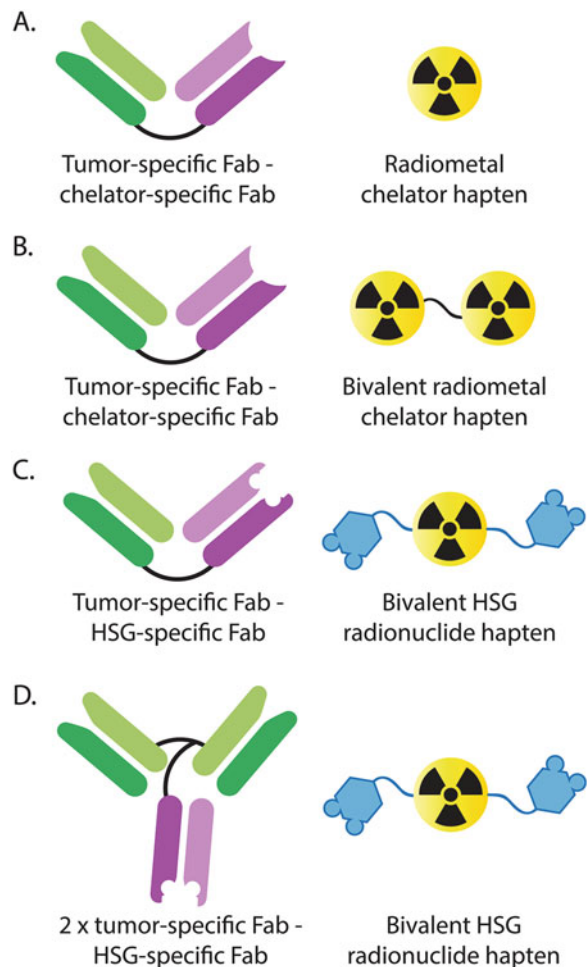
antigen and one for a chelated radiometal. The preclinical and clinical studies with this system showed improved tumor-to-blood and tumor-to-liver activity concentration ratios compared to directly radiolabeled antibodies. However, this system suffered from the rapid release of the non-covalently bound chelators from the tumor-associated immunoconjugate. Consequently, the approach was improved by linking two chelators with a peptide chain, thereby forming a bivalent radioligand that exhibited enhanced tumoral uptake and retention.

Although these early chelator-based systems proved promising, it was soon noticed that the binding affinity of the bsAbs for the radiometallated chelators dropped substantially when different radiometals were used. For example, a given bsAb could have high affinity for [111In]In-DTPA but low affinity for [177Lu]Lu-DTPA. In addition, the use of different chelators would have required the generation of completely new bsAbs. Taken together, these traits significantly reduce the modularity and adaptability of this approach, particularly given the increasing popularity of pairing radionuclides for imaging and therapy. To broaden the flexibility of the system, the anti-chelator Fab was replaced by a Fab that binds a histamine-succinyl-glycine (HSG) hapten with nanomolar affinity. Subsequently, a pair of HSGs were linked together with a short peptide to create a bivalent hapten capable of bridging two different bsAbs. Importantly, this peptide linker could also be modified to contain a functional group to which a chelator or other radiolabeling prosthetic group could be attached.

These bsAb pretargeting systems improved even further as antibody engineering methods evolved. For example, an approach termed "Dock-and-Lock" was used to assemble two anti-tumor Fabs and one anti-HSG Fab in a tri-Fab bsAb scaffold. In preclinical investigations, this tri-Fab system yielded high tumoral uptake and high tumor-to-blood activity concentration ratios and increased the median survival of mice in therapy studies [19, 20]. To date, all clinical trials of bsAb-based pretargeting have used this tri-Fab approach. More recently,

an in vivo pretargeting strategy that leverages self-assembling and disassembling (SADA) domains has proven compelling [21]. In this case, chelator- and tumor-specific antibody fragments are combined with a SADA domain in a 55 kDa SADA-bsAb fusion protein. These SADA-bsAbs self-assemble into stable tetramers when present in high concentrations (i.e., at the tumor) but can disassemble into rapidly clearing dimers or monomers if present in low concentrations in the blood. In murine models of cancer, in vivo pretargeting with SADA-bsAbs has yielded promising tumor uptake, high image contrast, and high therapeutic indices. The clinical translation of a SADA-based pretargeting system is expected in the near future.

In clinical trials, bsAbs pretargeting has been extensively studied for imaging, therapy, and theranostics [22–38]. The first clinical trial using a tri-Fab in tandem with a 111In-radiolabeled HSG-hapten was reported in 2013 [31]. The tri-Fab bsAb in this initial study—"TF2"—targets carcinoembryonic antigen (CEA), an extracellular protein expressed by adenocarcinomas that remains the *only* antigen used for clinical bsAb pretargeting. More recently, TF2 has been used in conjunction with an HSG-based peptide called IMP288 in patients with colorectal and lung cancer [31, 32, 34]. In these studies, pretargeted SPECT with 111In-labeled IMP288 was used as a predictive imaging agent for PRIT with 177Lu-labeled IMP288 (Fig. 21.6a). Pretherapeutic imaging with [111In]In-IMP288 accurately predicted the pharmacokinetic profile and absorbed doses of [177Lu]Lu-IMP288. For example, the calculated radiation dose to the red marrow after the administration of [177Lu]Lu-IMP288 was in good correlation with the predicted dose based on imaging with [111In]In-IMP288 (Fig. 21.6b). Individualized dosing designed to facilitate patient-specific treatment planning and reduce hematological toxicity proved important in these studies due to large interpatient variations in the pharmacokinetics of both TF2 and IMP288. Most importantly, these studies have clearly demonstrated bsAb pretargeting is both feasible and safe in patients. Recent pretargeted PET studies with TF2 and
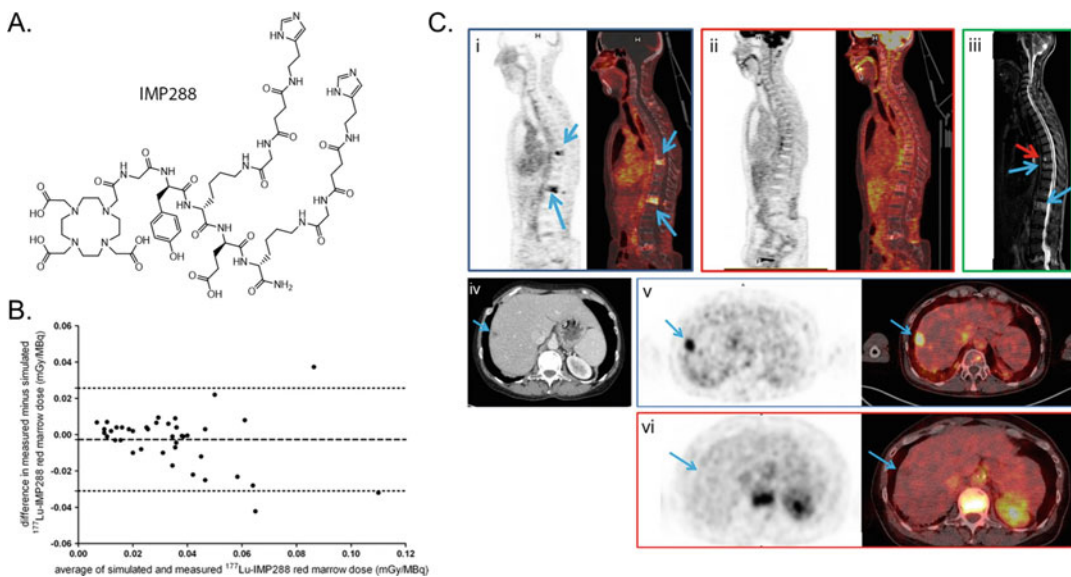
Fig. 21.6 (**a**) The structure of the bivalent HSG hapten IMP288. (**b**) A Bland-Altman plot showing the agreement between the predicted and measured radiation doses from [^{177}Lu]Lu-IMP288. The dashed line is the mean difference (-0.0026 mGy/MBq), while the dotted lines represent the 95% agreement limits (-0.031 and 0.026 mGy/MBq). (Source: Schoffelen R. et al. 2014, fig. 5 [32]. Reprinted with permission from *European Journal of Nuclear Medicine and Molecular Imaging*, Springer Nature). (**c**) In a patient with HER2-negative metastatic breast cancer, pretargeted immunoPET with TF2 and [^{68}Ga]Ga-IMP288 visualizes two vertebral metastases (L1 and T9, arrows) (i), [^{18}F]FDG PET discloses no vertebral abnormalities (ii), and vertebral MRI confirms both lesions (blue arrows) and discloses another (red arrow) at T8 (iii). In another patient with the same malignancy, computed tomography (CT) shows a suspected liver lesion (iv). Pretargeted immunoPET with TF2 and [^{68}Ga]Ga-IMP288 reveals high uptake by the liver lesion (arrow) (v), but it is not seen by [^{18}F]FDG PET (vi). (Source: Rousseau C. et al. 2020, fig. 2 [36]. Reprinted with permission from the Society of Nuclear Medicine and Molecular Imaging, Inc. © 2020 SNMMI)

^{68}Ga-labeled IMP288 in patients with breast cancer and colon cancer have also yielded very promising results [36, 37]. To wit, pretargeted TF2/[^{68}Ga]Ga-IMP288 PET proved to be more sensitive for detecting lesions than ^{18}F-FDG (Fig. 21.6c).

Despite the promise of bsAb pretargeting, some immunogenicity issues have been detected in these clinical trials, specifically the development of antibodies against the bsAb constructs in as high as 61% of patients [24, 27, 28, 30]. In response to this challenge, recent studies have successfully relied upon the pretreatment of patients with antihistamines and corticosteroids to reduce this immunogenic response to 0–16% of patients [36, 37]. Beyond this immunogenicity, the lack of modularity and the complicated engineering required for the production of bispecific antibodies also stand as drawbacks to this strategy. However, the very promising recent clinical reports and the advent of SADA-based pretargeting will hopefully drive the expansion of this technology in the near future.

21.2.1.3 Complementary Oligonucleotides

The high affinity and specificity of the hybridization of oligonucleotides has been leveraged for in vivo pretargeting systems in which one oligonucleotide is attached to the antibody and its complementary strand is radiolabeled. Natural DNA and RNA oligomers are unsuitable for this purpose, as they are rapidly hydrolyzed by nucleases in vivo. Therefore, more stable analogs have been used for pretargeting. In this section, we will focus on pretargeting systems that
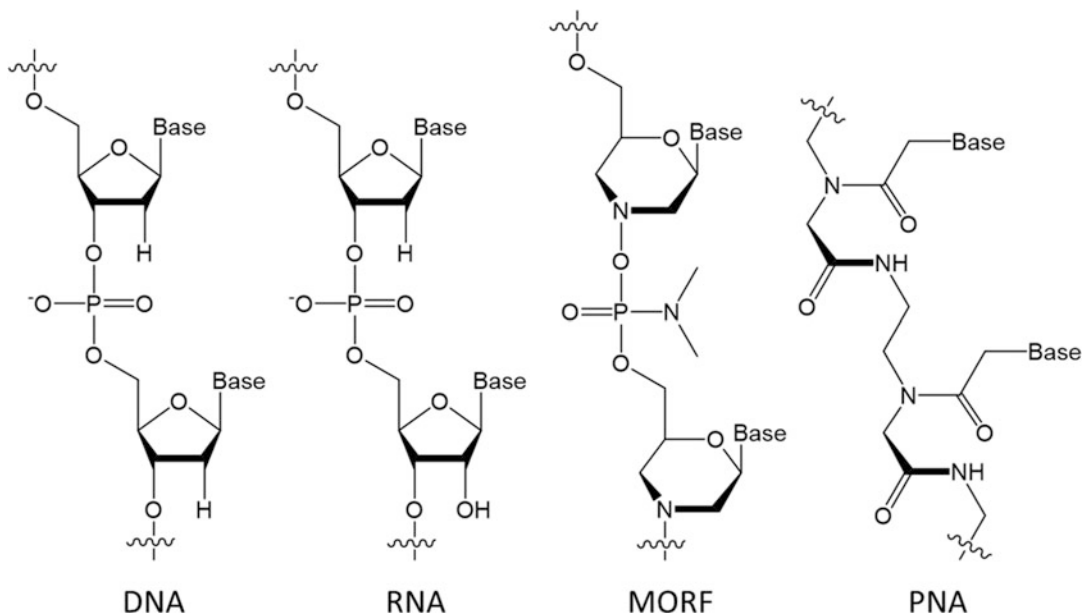
Fig. 21.7 Structures of DNA, RNA, MORF, and PNA oligonucleotides

employ two types of artificial oligonucleotides: phosphorodiamidate morpholino oligomers (MORFs, morpholinos, or PMOs) and peptide nucleic acids (PNAs) (Fig. 21.7). MORFs are synthetic oligomers in which the DNA bases are attached to an achiral, non-ionic backbone comprised of morpholine subunits linked by phosphorodiamidate groups. This backbone replaces the ribofuranose-phosphodiester backbone in DNA and RNA and makes the oligomer resistant to nucleases and proteases. MORFs bind through Watson-Crick base pairing and are water soluble. In PNAs, the sugar-phosphate backbone of natural DNA and RNA is replaced by N-(2-aminoethyl)-glycine units that are connected through amide bonds. Similar to MORFs, PNAs are achiral, non-ionic, enzymatically stable, and able to undergo Watson-Crick base pairing.

The earliest application of MORFs to in vivo pretargeting was performed using nude mice bearing LS174T human colorectal cancer xenografts [39]. An immunoconjugate composed of an anti-CEA mAb linked to a MORF was administered 48 h prior to the injection of ^{99m}Tc-labled MORF with a complementary sequence (cMORF). Compared to a control

cohort in which only the ^{99m}Tc-labeled MORF was administered, the pretargeting system produced significantly higher tumor uptake in the tumor: 1.8 %ID/g vs. 0.1 %ID/g at 3 h p.i. and 1.7 %ID/g vs. 0.1 %ID/g 24 h p.i. A few years later, the first preclinical PRIT study was carried out using the same animal model and immunoconjugate [40]. In this work, a ^{188}Re-labeled cMORF localized rapidly in tumor tissue and cleared quickly from healthy organs. Critically, the ^{188}Re-PRIT strategy produced a statistically significant delay in tumor growth compared to control cohorts, demonstrating the efficacy of the approach. Later, the therapeutic efficacy of MORF-based PRIT was illustrated with another antibody—the anti-tumor-associated glycoprotein 72 (TAG72) mAb CC49—and another radionuclide, ^{90}Y [41]. In this study, a tumoral activity concentration of 7.2 ± 2.2 %ID/g and a tumor-to-blood activity concentration ratio of 25 were achieved. Over the years, several more preclinical studies utilizing MORFs for pretargeted SPECT and PRIT have been published, yet no clinical studies have been reported.

Fig. 21.8 Inverse electron-demand Diels-Alder (IEDDA) cycloaddition between a tetrazine and a *trans*-cyclooctene
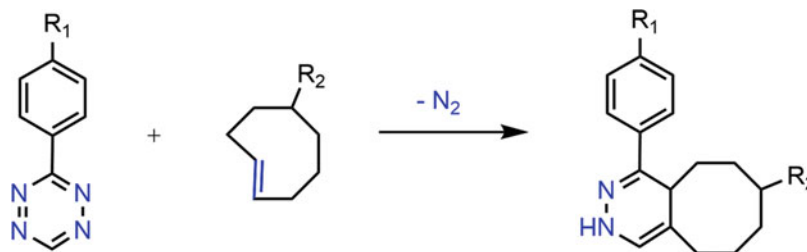
The first exploration of PNA-based pretargeting was reported in 2015 by Leonidova et al. [42]. In this investigation, mice bearing A431 xenografts were administered a PNA-bearing immunoconjugate of cetuximab 24 h prior to the injection of complementary [99mTc]-labeled PNA. SPECT imaging as early as 1 h p.i. revealed that this approach could effectively visualize tumor tissue. Although promising tumor-to-muscle activity concentration ratios of >8 were achieved, the tumor-to-blood activity concentration ratios were disappointing (~0.5) due in large part to the radiolabeled PNA hybridizing with still-circulating immunoconjugate. More recently, Altai et al. investigated the feasibility of PNA-based PRIT using a HER2 targeted affibody [43]. Tumoral activity concentrations of 21 ± 4 %ID/g were observed at 1 h p.i., and the kidney uptake remained low (4 ± 1 %ID/g), ultimately yielding exceptionally high tumor-to-kidney activity concentration ratios for an affibody-based system. The same team has also effectively deployed PNA-based pretargeting for PRIT and theranostic applications [44–47]. While these preclinical results are promising, no clinical data are available yet to assess the feasibility of this technique in patients.

21.2.1.4 Bioorthogonal Chemistry

The term "biorthogonal chemistry" was coined to describe chemical reactions that can occur within biological systems without interfering or perturbing them. A variety of these ligations have been developed over the last two decades, and some of these have—not surprisingly—attracted the attention of those studying in vivo pretargeting. In the next section of this chapter,

we will discuss how three particularly rapid bioorthogonal transformations have been leveraged for in vivo pretargeting: the inverse electron-demand Diels-Alder (IEDDA) reaction, host–guest chemistry, and the strain-promoted sydnone-alkyne cycloaddition (SPSAC).

21.2.1.4.1 The Inverse Electron-Demand Diels-Alder Reaction

The IEDDA ligation occurs between an electron-poor diene (e.g., tetrazine, Tz) and an electron-rich dienophile (e.g., an alkene or an alkyne) (Fig. 21.8). To date, the highest reaction rates have been observed with *trans*-cyclooctene (TCO) as the dienophile, singling the molecular couple of Tz and TCO out as particularly promising for in vivo pretargeting. In IEDDA-based pretargeting, the more stable of the two components, TCO, is attached to the mAb, while the Tz forms the basis of the radioligand. While TCO does isomerize to inactive *cis*-cyclooctene (CCO) in vivo with a half-life of six to seven days, it is nonetheless far more stable under physiological conditions than its partner Tz. Depending on pH and temperature, Tz can decompose within a matter of hours, making it unsuitable as a component of an immunoconjugate but perfect as a scaffold for a radioligand with a serum half-life in the tens of minutes.

The feasibility of IEDDA-based pretargeting was first demonstrated by Rossin et al., who used a TCO-bearing immunoconjugate of CC49 and a [111In]-labeled tetrazine to perform pretargeted SPECT in mice bearing subcutaneous LS174T colorectal cancer xenografts [48]. The CC49-TCO was administered 24 h prior to the [111In]-labeled Tz, and SPECT imaging 3 h after the

injection of the radioligand revealed rapid urinary clearance of the ^{111}In-labeled Tz as well as activity concentrations of ∼3 %ID/g in the tumor. In the years since, several groups—including ours—have developed IEDDA-based pretargeting systems for PET, SPECT, and PRIT [49].

The first foray into IEDDA-based PRIT was published in 2017 [50]. In this investigation, a TCO-modified variant of an anti-CA19.9 antibody (5B1-TCO) was administered to mice bearing BxPC3 pancreatic ductal adenocarcinoma xenografts 72 h prior to the injection of increasing doses (14.8–44.4 MBq) of a ^{177}Lu-labeled Tz ([^{177}Lu]Lu-DOTA-PEG$_7$-Tz). The authors demonstrated a dose-dependent therapeutic response, with a near-complete regression of the tumors at the highest dose. In another study, pretargeted SPECT and PRIT were combined in an orthotopic model of peritoneal carcinomatosis [51]. An anti-CEA immunoconjugate (35A7-TCO) was injected 24 h prior the administration of ^{177}Lu-labeled tetrazine, and subsequent bioluminescence and SPECT imaging confirmed the specific uptake of the radioligand in the disseminated peritoneal tumors. In a longitudinal therapy study, the PRIT regimen slowed tumor growth, and significantly lower ex vivo peritoneal carcinomatosis indices were observed in the radiopharmaceutical therapy (RPT) cohort compared to the control groups. IEDDA-based PRIT has also been combined with α-emitting radionuclides, most notably in an α-PRIT schema employing 5B1-TCO and an [[225]Ac]Ac-DOTA-PEG$_7$-Tz [52, 53]. Finally, recent studies have revealed how following the administration of the immunoconjugate with sequential injections of a single tetrazine radioligand—or, alternatively, two different radioligands—can be harnessed for theranostic imaging or fractionated dosing [54, 55].

In each of the investigations described above, the TCO moieties have been attached to the mAb via the random modification of lysine residues throughout the immunoglobulin. While this approach to bioconjugation is facile, it inevitably creates heterogeneous products that can exhibit suboptimal in vitro and in vivo behavior. In response to these limitations, a wide variety of site-specific and site-selective approaches to bioconjugation have been developed over the years, and two—the use of THIOmAbs and the chemoenzymatic manipulation of the heavy chain glycans—have been applied to IEDDA-based pretargeting [56–59]. THIOmAbs are engineered mAb with free cysteine residues added to their constant domains that can be exploited for bioconjugation using thiol-reactive groups such as maleimides. Mandikian et al. used a maleimide-bearing variant of TCO in conjunction with a series of anti-HER2 THIOmAbs containing increasing numbers of engineered cysteines to create immunoconjugates with varying degrees of labeling with TCO (i.e., 2, 4, or 6 TCO/mAb) [56]. The team injected mice bearing KPL-4 tumors with an ^{111}In-labeled Tz 24 h after the administration of the TCO-modified THIOmAbs. The resultant SPECT images revealed the rapid urinary excretion of excess radioligand as well as specific tumoral uptake that correlated with the degree of labeling of TCO (i.e., immunoconjugates with 6 and 2 TCO/mAb produced tumor activity concentration of 6 and 2% ID/g, respectively). Shifting gears, our laboratory has leveraged a chemoenzymatic approach to site-specific bioconjugation for the construction of TCO-modified mAb. In this strategy, a pair of enzymes are used to install azide-bearing sugars into the heavy chain glycans of an mAb that can then be modified via the strain-promoted azide-alkyne cycloaddition (SPAAC) reaction with dibenzocyclooctyne-bearing synthons. This methodology was used to construct immunoconjugates of huA33 bearing 4 and 8 TCO/mAb, and subsequent pretargeted PET imaging experiments in a murine model of colorectal cancer with a ^{64}Cu-labeled Tz revealed that tumor uptake correlated to the DOL of TCO but that the dendrimers used to achieve a DOL of 8 TCO/mAb increased non-specific uptake in healthy tissues [58, 59].

While clinical trials of IEDDA-based pretargeting have not yet been conducted, the methodology recently made an important preclinical leap from small to large animals. In 2022, Maitz et al. reported the use of a TCO-modified

bisphosphonate and a ^{64}Cu-labeled Tz radioligand for the pretargeted PET imaging of companion dogs with osteodestructive lesions [60]. For more details on this study and its important implications for IEDDA-based pretargeting, please see "Particularly Important Works" in Sect. 21.3 below.

21.2.1.4.2 New Chemistries: Host–Guest Chemistry and the SPSAC Ligation

In the last few years, a new approach to in vivo pretargeting based on host-guest chemistry—specifically the host–guest relationship between cucurbituril and adamantane or ferrocene—has emerged in the literature (Fig. 21.9a) [61–63]. To be fair, only a handful of reports on this method have been published, and all are focused on pretargeted PET rather than PRIT. While the earliest studies by Strebl et al. laid the groundwork for the feasibility of this strategy, the most exciting work has arisen from Jallinoja and coworkers [64–66]. This team has employed a cucurbit[7]uril-modified immunoconjugate of an anti-carcinoembryonic antigen mAb (M5A) in conjunction with a ^{64}Cu-labeled ferrocene radioligand for pretargeted PET in mice bearing BxPC3 xenografts [65, 66]. The system produced specific uptake in the tumor, and the team was able to extend the interval time between injections to a remarkable ten days. Somewhat worryingly, however, the concentration of the radioligand in the tumor decreases over time, perhaps as a result of the non-covalent nature of the host–guest interaction. It remains to be seen if modifications to the system, such as the use of dimeric or multimeric radioligands, can solve this issue.

The most recent molecular couple to be used for in vivo pretargeting emerged in 2019, when Richard et al. reported the use of a novel strain-
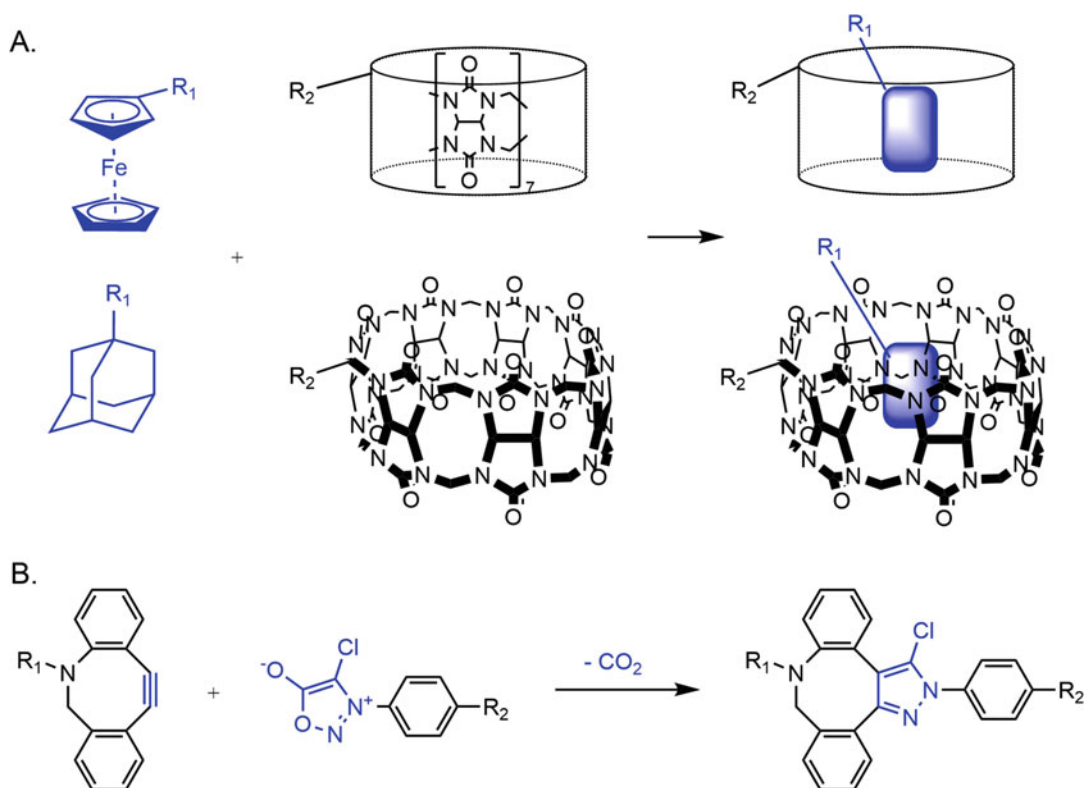
Fig. 21.9 (a) The host–guest interaction between adamantane or ferrocene (blue) and cucurbit[7]uril. (b) The strain-promoted sydnone-alkyne cycloaddition (SPSAC) between a cyclooctyne and a 4-chloro-sydnone

promoted sydnone-alkyne cycloaddition (SPSAC) for pretargeted PET (Fig. 21.9b) [67]. The authors administered a sydnone-bearing cetuximab immunoconjugate 72 h prior to the injection of an ^{18}F-labeled variant of DBCO. A maximum activity concentration of ~2 %ID/g was observed in the tumor 4 h after the administration of the radiotracer as well as modest tumor-to-healthy organ activity concentration ratios. In the absence of follow-up studies, it remains unclear whether these somewhat unimpressive results stem from the internalization of the immunoconjugate or the relatively sluggish kinetics of the SPSAC reaction ($k_2 = 10^2$–10^3 M^{-1} s^{-1}). Clearly, further validation is needed to assess the potential of the SPSAC reaction as a tool for pretargeted imaging and therapy.

21.3 Particularly Important Works

21.3.1 Clinical PRIT with a bsAb-HSG System

In 2013 and 2014, Schoffelen et al. published a pair of reports on their clinical efforts to assess the safety and optimal conditions for HSG-based pretargeting with TF2 and [111]In- or ^{177}Lu-labeled haptens in patients with metastatic colorectal cancer [31, 32]. Both the interval time between injections (1 vs. 5 days) and the amount of immunoconjugate (75–150 mg) and peptide (25–100 μg) were varied to optimize the system. Increasing the interval time from one to five days significantly decreased the radiation dose to the red marrow, but the best tumor targeting was achieved with a one-day interval. Furthermore, it was determined that a high dose of TF2 (150 mg) and a low dose of the peptide (25 μg) produced the best in vivo results: high tumoral uptake as early as 1 h after the injection of the radioligand with tumor-to-tissue activity concentration ratios over 20 at 24 h. Dosimetry calculations revealed low doses to the kidneys and red bone marrow (set as the dose limiting organs in the study), thereby opening the door for repeated administrations of the therapeutic radioligand. The rather high doses of radioactivity used in the study—2.5–7.4 GBq—were well tolerated,

with some manageable reactions during the TF2 infusions and transient thrombocytopenia (grades 3–4) in 10% of the patients (Fig. 21.10).

21.3.2 Performing Bioorthogonal Chemistry in Large Animals

During the preclinical development of IEDDA-based pretargeting over the last several years, some concerns have been raised about whether the click ligation will work in larger blood volume of humans. While clinical trials are an obvious way to answer these questions, large animal studies represent a less expensive alternative. In 2022, Maitz et al. used a bone-seeking, TCO-modified bisphosphonate (TCO-BP) in conjunction with ^{64}Cu-labeled Tz radioligand for pretargeted PET in relatively large (20–55 kg) companion dogs with osteodestructive lesions [60]. The TCO-BP was administered first, followed 1 h later by the ^{64}Cu-labeled Tz. PET images acquired 4 h after the administration of the radioligand unambiguously demonstrated the success of the in vivo ligation, revealing (i) clear delineation of the healthy skeleton, (ii) high focal uptake in osteodestructive lesions, and (iii) low radioactivity levels in background tissues other than the kidneys and bladder. In one of the subjects, for example, lesion-to-bone and lesion-to-background SUV_{mean} ratios of 4.5 and 15.1, respectively, were determined (Fig. 21.11). While translating these data to human studies with a TCO-modified mAb is difficult, these results nonetheless bode well for future clinical studies. Furthermore, efforts are currently underway to adapt this approach for the PRIT of companion dogs with osteosarcoma using the [64]Cu's β-emitting isotopologue of [67]Cu ($t_{1/2}$ ~ 2.6 days).

21.4 The Future

Pretargeting was introduced 40 years ago and has consistently produced promising preclinical and early clinical results. Yet frustratingly, none of the approaches to in vivo pretargeting that we outline here has come close to routine clinical use or regulatory approval. A variety of culprits
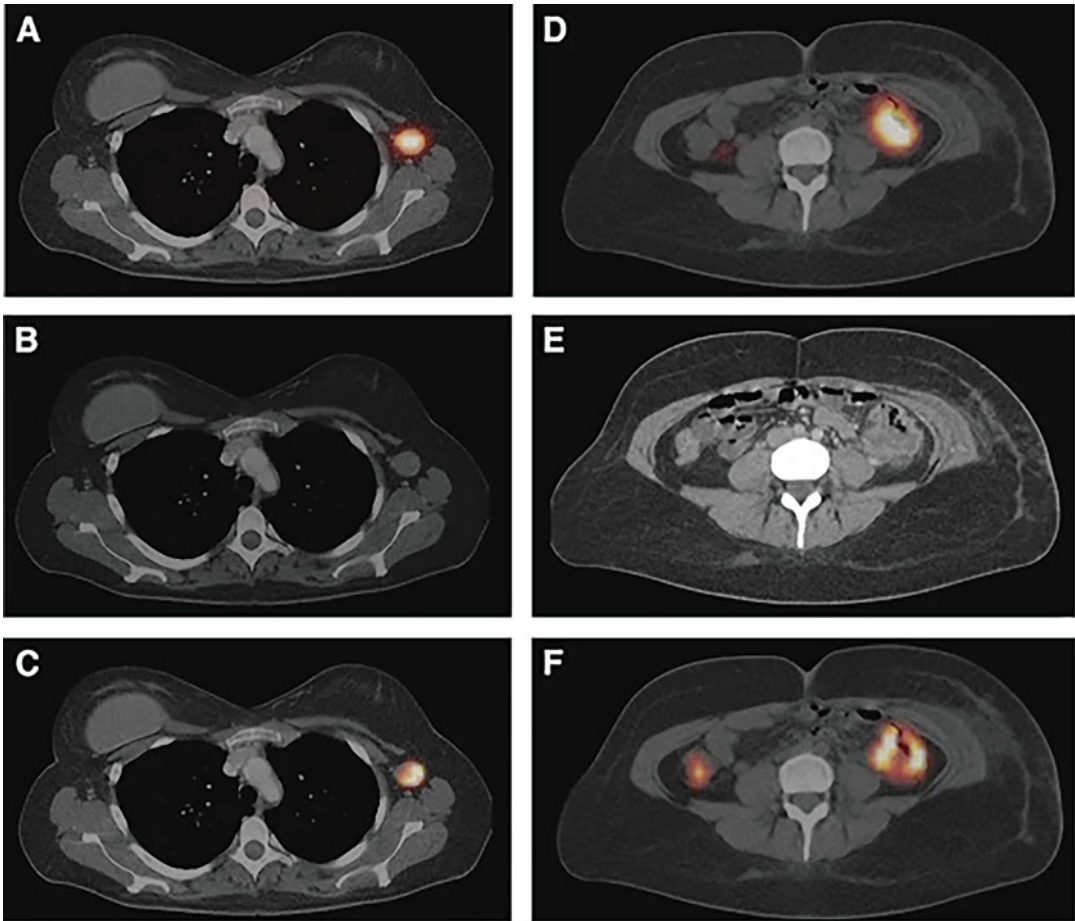
Fig. 21.10 (**a**) SPECT/CT image acquired 24 h after injection of [^{111}In]In-IMP288 (185 MBq, 25 µg) pretargeted with 75 mg TF2 (1-day interval) in a 38-year-old patient with metastatic colorectal cancer, showing very clear targeting of an axillary lymph-node metastasis with very low concentrations of radioactivity in normal tissues. A corresponding contrast-enhanced CT scan and a fused FDG-PET/CT scan are shown (**b** and **c**, respectively). The primary colon tumor also shows highly specific radiotracer uptake in the SPECT image (**d**), as confirmed by the CT scan and FDG-PET/CT (**e** and **f**, respectively). The latter shows non-specific FDG uptake in the ascending colon. (Source: Schoffelen R. et al. 2013, fig. 4, *British Journal of Cancer*, Springer Nature [31]. Licensed under Creative Commons 4.0)

are responsible, ranging from the disqualifying immunogenicity of streptavidin to logistical and regulatory concerns about multicomponent technologies. Yet the elegance and undeniable potential of in vivo pretargeting means enthusiasm remains. In the context of RPT, pretargeting has been shown to dramatically reduce radiation dose rates to healthy tissues and facilitate the use of radionuclides that would normally be incompatible with the full-length antibody vectors. Furthermore, several studies have illustrated how pretargeting could be effectively harnessed for theranostic imaging and RPT. In the end, we are optimistic that pretargeting will one day become an effective tool for clinical RPT, though we acknowledge that careful optimization will be needed to bring this to fruition. As we look to the future, we are eager to see more clinical data, both with the established bsAb systems and with approaches based on the IEDDA ligation and the hybridization of oligonucleotides.
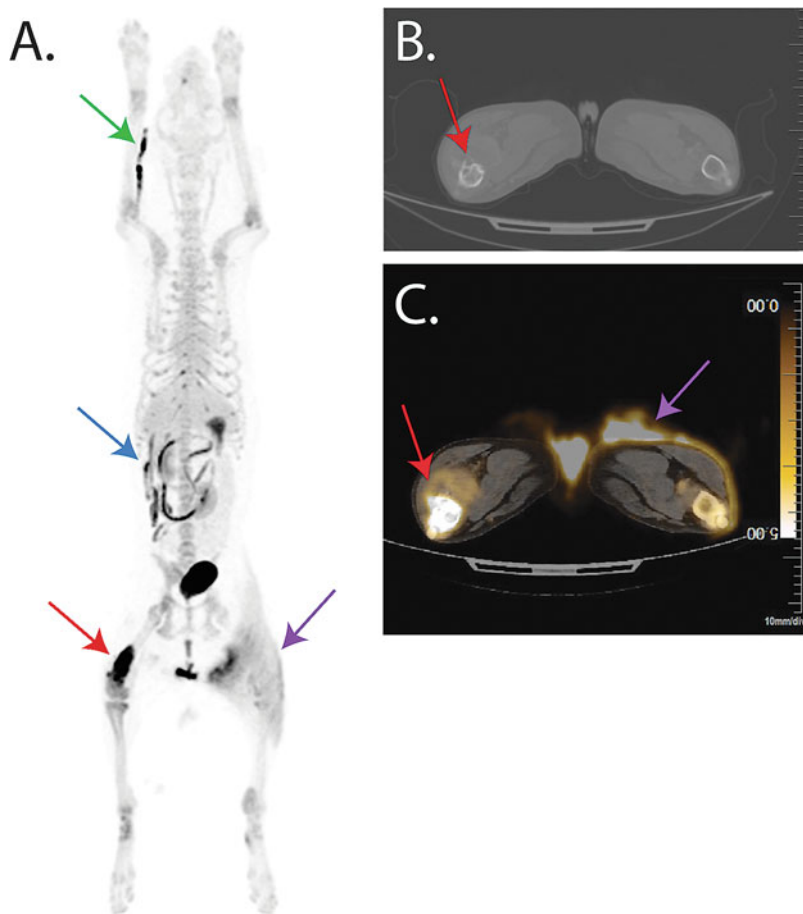
Fig. 21.11 Pretargeted PET and CT images of an osteodestructive lesion in the right femur. The dog was administered TCO-BP (10 mg/kg) followed 1 h later by [^{64}Cu]Cu-SarAr-Tz (6.8 mCi, 251.6 MBq), and scans were collected 4 h after the injection of the radioligand. (**a**) Maximum intensity projection illustrating renal clearance of [^{64}Cu]Cu-SarAr-Tz, moderate uptake in the healthy skeleton, high focal uptake in the osteodestructive lesion (red arrow), and low activity concentrations in healthy tissues. Some moderate uptake can also be seen at the injection site in the right forelimb (green arrow) as well as in the intestinal tract (blue arrow) and left hindquarter (purple arrow) due to the dog excreting activity in the urine and then lying in and consuming it. (**b**) Transverse CT showing osteodestruction (red arrow) in the right femur. (**c**) Coronal PET slice showing the focal uptake in the right femoral lesion (red arrow). This slice also reinforces that the radioactivity seen on the right hindquarter (purple arrow) is on the dog's skin and fur. (Reprinted with permission from Maitz C. et al. 2022, Molecular Pharmaceutics, American Chemical Society [60]. © 2022 American Chemical Society)

21.5 The Bottom Line

- The goal of in vivo pretargeting is to reap the benefits of immunoglobulins as targeting vectors while avoiding the high radiation dose rates to healthy tissues associated with traditional radioimmunoconjugates.

- In vivo pretargeting is predicated on decoupling the antibody and the radionuclide, injecting them sequentially (the former before the latter), and exploiting a selective ligation to facilitate the in vivo combination of the two components.
- Pretargeting systems based on the affinity of streptavidin and biotin showed preclinical and

clinic promise, but the immunogenicity of the former proved problematic.

- Pretargeting systems based on bispecific antibodies and radiolabeled haptens have generated exciting clinical data with both [68]Ga- and ^{177}Lu-labeled radioligands.
- Pretargeting systems based on the IEDDA ligation and the hybridization of complementary oligonucleotides have produced promising preclinical data but are yet to be validated in the clinic.
- Both host–guest chemistry and the SPSAC ligation have been used in a handful of preclinical pretargeting studies, but more data are needed to assess the true potential of these technologies.

References

1. Rondon A, Rouanet J, Degoul F. Radioimmunotherapy in oncology: overview of the last decade clinical trials. Cancers (Basel). 2021;13(21) https://doi.org/10.3390/cancers13215570.
2. Wei W, Rosenkrans ZT, Liu J, Huang G, Luo Q-Y, Cai W. ImmunoPET: concept, design, and applications. Chem Rev. 2020;120(8):3787–851. https://doi.org/10.1021/acs.chemrev.9b00738.
3. Jallinoja VIJ, Houghton JL. Current landscape in clinical pretargeted radioimmunoimaging and therapy. J Nucl Med. 2021;62(9):1200–6. https://doi.org/10.2967/jnumed.120.260687.
4. Pereira PMR, Mandleywala K, Ragupathi A, Carter LM, Goos J, Janjigian YY, et al. Temporal modulation of HER2 membrane availability increases pertuzumab uptake and pretargeted molecular imaging of gastric tumors. J Nucl Med. 2019;60(11):1569–78. https://doi.org/10.2967/jnumed.119.225813.
5. Sinitsyn VV, Mamontova AG, Checkneva YY, Shnyra AA, Domogatsky SP. Rapid blood clearance of biotinylated IgG after infusion of avidin. J Nucl Med. 1989;30(1):66–9.
6. Paganelli G, Pervez S, Siccardi AG, Rowlinson G, Deleide G, Chiolerio F, et al. Intraperitoneal radiolocalization of tumors pre-targeted by biotinylated monoclonal antibodies. Int J Cancer. 1990;45(6):1184–9. https://doi.org/10.1002/ijc.2910450632.
7. Kobayashi H, Sakahara H, Hosono M, Yao ZS, Toyama S, Endo K, et al. Improved clearance of radiolabeled biotinylated monoclonal antibody following the infusion of avidin as a "chase" without decreased accumulation in the target tumor. J Nucl Med. 1994;35(10):1677–84.
8. Kalofonos HP, Rusckowski M, Siebecker DA, Sivolapenko GB, Snook D, Lavender JP, et al. Imaging of tumor in patients with indium-111-labeled biotin and streptavidin-conjugated antibodies: preliminary communication. J Nucl Med. 1990;31(11):1791–6.
9. Paganelli G, Magnani P, Zito F, Villa E, Sudati F, Lopalco L, et al. Three-step monoclonal antibody tumor targeting in carcinoembryonic antigen-positive patients. Cancer Res. 1991;51(21):5960–6.
10. Cremonesi M, Ferrari M, Chinol M, Stabin MG, Grana C, Prisco G, et al. Three-step radioimmunotherapy with yttrium-90 biotin: dosimetry and pharmacokinetics in cancer patients. Eur J Nucl Med. 1999;26(2):110–20. https://doi.org/10.1007/s002590050366.
11. Paganelli G, Grana C, Chinol M, Cremonesi M, De Cicco C, De Braud F, et al. Antibody-guided three-step therapy for high grade glioma with yttrium-90 biotin. Eur J Nucl Med. 1999;26(4):348–57. https://doi.org/10.1007/s002590050397.
12. Breitz HB, Weiden PL, Beaumier PL, Axworthy DB, Seiler C, Su FM, et al. Clinical optimization of pretargeted radioimmunotherapy with antibody-streptavidin conjugate and ^{90}Y-DOTA-biotin. J Nucl Med. 2000;41(1):131–40.
13. Knox SJ, Goris ML, Tempero M, Weiden PL, Gentner L, Breitz H, et al. Phase II trial of yttrium-90-DOTA-biotin pretargeted by NR-LU-10 antibody/streptavidin in patients with metastatic colon cancer. Clin Cancer Res. 2000;6(2):406–14.
14. Paganelli G, Bartolomei M, Ferrari M, Cremonesi M, Broggi G, Maira G, et al. Pre-targeted locoregional radioimmunotherapy with ^{90}Y-biotin in glioma patients: phase I study and preliminary therapeutic results. Cancer Biother Radiopharm. 2001;16(3):227–35. https://doi.org/10.1089/10849780152389410.
15. Weiden PL, Breitz HB. Pretargeted radioimmunotherapy (PRIT) for treatment of non-Hodgkin's lymphoma (NHL). Crit Rev Oncol Hematol. 2001;40(1):37–51. https://doi.org/10.1016/s1040-8428(01)00133-0.
16. Grana C, Chinol M, Robertson C, Mazzetta C, Bartolomei M, De Cicco C, et al. Pretargeted adjuvant radioimmunotherapy with yttrium-90-biotin in malignant glioma patients: a pilot study. Br J Cancer. 2002;86(2):207–12. https://doi.org/10.1038/sj.bjc.6600047.
17. Forero A, Weiden PL, Vose JM, Knox SJ, LoBuglio AF, Hankins J, et al. Phase 1 trial of a novel anti-CD20 fusion protein in pretargeted radioimmunotherapy for B-cell non-Hodgkin lymphoma. Blood. 2004;104(1):227–36. https://doi.org/10.1182/blood-2003-09-3284.
18. Shen S, Forero A, LoBuglio AF, Breitz H, Khazaeli MB, Fisher DR, et al. Patient-specific dosimetry of pretargeted radioimmunotherapy using CC49 fusion

protein in patients with gastrointestinal malignancies. J Nucl Med. 2005;46(4):642–51.

19. Sharkey RM, van Rij CM, Karacay H, Rossi EA, Frielink C, Regino C, et al. A new tri-fab bispecific antibody for pretargeting Trop-2-expressing epithelial cancers. J Nucl Med. 2012;53(10):1625–32. https://doi.org/10.2967/jnumed.112.104364.

20. van Rij CM, Frielink C, Goldenberg DM, Sharkey RM, Lütje S, McBride WJ, et al. Pretargeted radioimmunotherapy of prostate cancer with an anti-TROP-2×anti-HSG bispecific antibody and a (177)Lu-labeled peptide. Cancer Biother Radiopharm. 2014;29(8):323–9. https://doi.org/10.1089/cbr.2014.1660.

21. Santich BH, Cheal SM, Ahmed M, McDevitt MR, Ouerfelli O, Yang G, et al. A self-assembling and disassembling (SADA) bispecific antibody (BsAb) platform for curative two-step pretargeted radioimmunotherapy. Clin Cancer Res. 2021;27(2):532–41. https://doi.org/10.1158/1078-0432.Ccr-20-2150.

22. Stickney DR, Anderson LD, Slater JB, Ahlem CN, Kirk GA, Schweighardt SA, et al. Bifunctional antibody: a binary radiopharmaceutical delivery system for imaging colorectal carcinoma. Cancer Res. 1991;51(24):6650–5.

23. Le Doussal JM, Chetanneau A, Gruaz-Guyon A, Martin M, Gautherot E, Lehur PA, et al. Bispecific monoclonal antibody-mediated targeting of an indium-111-labeled DTPA dimer to primary colorectal tumors: pharmacokinetics, biodistribution, scintigraphy and immune response. J Nucl Med. 1993;34(10):1662–71.

24. Barbet J, Peltier P, Bardet S, Vuillez JP, Bachelot I, Denet S, et al. Radioimmunodetection of medullary thyroid carcinoma using indium-111 bivalent hapten and anti-CEA x anti-DTPA-indium bispecific antibody. J Nucl Med. 1998;39(7):1172–8.

25. Kraeber-Bodéré F, Bardet S, Hoefnagel CA, Vieira MR, Vuillez JP, Murat A, et al. Radioimmunotherapy in medullary thyroid cancer using bispecific antibody and iodine 131-labeled bivalent hapten: preliminary results of a phase I/II clinical trial. Clin Cancer Res. 1999;5(10 Suppl):3190s–8s.

26. Kraeber-Bodéré F, Faivre-Chauvet A, Ferrer L, Vuillez JP, Brard PY, Rousseau C, et al. Pharmacokinetics and dosimetry studies for optimization of anti-carcinoembryonic antigen x anti-hapten bispecific antibody-mediated pretargeting of Iodine-131-labeled hapten in a phase I radioimmunotherapy trial. Clin Cancer Res. 2003;9(10 Pt 2):3973s–81s.

27. Kraeber-Bodéré F, Rousseau C, Bodet-Milin C, Ferrer L, Faivre-Chauvet A, Campion L, et al. Targeting, toxicity, and efficacy of 2-step, pretargeted radioimmunotherapy using a chimeric bispecific antibody and ^{131}I-labeled bivalent hapten in a phase I optimization clinical trial. J Nucl Med. 2006;47(2):247–55.

28. Chatal JF, Campion L, Kraeber-Bodéré F, Bardet S, Vuillez JP, Charbonnel B, et al. Survival improvement in patients with medullary thyroid carcinoma who undergo pretargeted anti-carcinoembryonic-antigen radioimmunotherapy: a collaborative study with the French Endocrine Tumor Group. J Clin Oncol. 2006;24(11):1705–11. https://doi.org/10.1200/jco.2005.04.4917.

29. Aarts F, Boerman OC, Sharkey RM, Hendriks T, Chang CH, McBride WJ, et al. Pretargeted radioimmunoscintigraphy in patients with primary colorectal cancer using a bispecific anticarcinoembryonic antigen CEA X anti-di-diethylenetriaminepentaacetic acid F(ab')2 antibody. Cancer. 2010;116(4 Suppl):1111–7. https://doi.org/10.1002/cncr.24799.

30. Salaun PY, Campion L, Bournaud C, Faivre-Chauvet-A, Vuillez JP, Taieb D, et al. Phase II trial of anticarcinoembryonic antigen pretargeted radioimmunotherapy in progressive metastatic medullary thyroid carcinoma: biomarker response and survival improvement. J Nucl Med. 2012;53(8):1185–92. https://doi.org/10.2967/jnumed.111.101865.

31. Schoffelen R, Boerman OC, Goldenberg DM, Sharkey RM, van Herpen CM, Franssen GM, et al. Development of an imaging-guided CEA-pretargeted radionuclide treatment of advanced colorectal cancer: first clinical results. Br J Cancer. 2013;109(4):934–42. https://doi.org/10.1038/bjc.2013.376.

32. Schoffelen R, Woliner-van der Weg W, Visser EP, Goldenberg DM, Sharkey RM, McBride WJ, et al. Predictive patient-specific dosimetry and individualized dosing of pretargeted radioimmunotherapy in patients with advanced colorectal cancer. Eur J Nucl Med Mol Imaging. 2014;41(8):1593–602. https://doi.org/10.1007/s00259-014-2742-6.

33. Kraeber-Bodéré F, Rousseau C, Bodet-Milin C, Frampas E, Faivre-Chauvet A, Rauscher A, et al. A pretargeting system for tumor PET imaging and radioimmunotherapy. Front Pharmacol. 2015;6:54. https://doi.org/10.3389/fphar.2015.00054.

34. Bodet-Milin C, Ferrer L, Rauscher A, Masson D, Rbah-Vidal L, Faivre-Chauvet A, et al. Pharmacokinetics and dosimetry studies for optimization of pretargeted radioimmunotherapy in CEA-expressing advanced lung cancer patients. Front Med (Lausanne). 2015;2:84. https://doi.org/10.3389/fmed.2015.00084.

35. Bodet-Milin C, Faivre-Chauvet A, Carlier T, Rauscher A, Bourgeois M, Cerato E, et al. Immuno-PET using anticarcinoembryonic antigen bispecific antibody and 68Ga-labeled peptide in metastatic medullary thyroid carcinoma: clinical optimization of the pretargeting parameters in a first-in-human trial. J Nucl Med. 2016;57(10):1505–11. https://doi.org/10.2967/jnumed.116.172221.

36. Rousseau C, Goldenberg DM, Colombié M, Sébille JC, Meingan P, Ferrer L, et al. Initial clinical results of a novel immuno-PET theranostic probe in human epidermal growth factor receptor 2-negative breast

cancer. J Nucl Med. 2020;61(8):1205–11. https://doi.org/10.2967/jnumed.119.236000.

37. Touchefeu Y, Bailly C, Frampas E, Eugène T, Rousseau C, Bourgeois M, et al. Promising clinical performance of pretargeted immuno-PET with anti-CEA bispecific antibody and gallium-68-labelled IMP-288 peptide for imaging colorectal cancer metastases: a pilot study. Eur J Nucl Med Mol Imaging. 2021;48(3):874–82. https://doi.org/10.1007/s00259-020-04989-3.

38. Bodet-Milin C, Bailly C, Touchefeu Y, Frampas E, Bourgeois M, Rauscher A, et al. Clinical results in medullary thyroid carcinoma suggest high potential of pretargeted immuno-PET for tumor imaging and theranostic approaches. Front Med (Lausanne). 2019;6:124. https://doi.org/10.3389/fmed.2019.00124.

39. Liu G, Mang'era K, Liu N, Gupta S, Rusckowski M, Hnatowich DJ. Tumor pretargeting in mice using ^{99m}Tc-labeled morpholino, a DNA analog. J Nucl Med. 2002;43(3):384–91.

40. Liu G, Dou S, Mardirossian G, He J, Zhang S, Liu X, et al. Successful radiotherapy of tumor in pretargeted mice by ^{188}Re-radiolabeled phosphorodiamidate morpholino oligomer, a synthetic DNA analogue. Clin Cancer Res. 2006;12(16):4958–64. https://doi.org/10.1158/1078-0432.Ccr-06-0844.

41. Liu G, Dou S, Liu Y, Wang Y, Rusckowski M, Hnatowich DJ. ^{90}Y labeled phosphorodiamidate morpholino oligomer for pretargeting radiotherapy. Bioconjug Chem. 2011;22(12):2539–45. https://doi.org/10.1021/bc200366t.

42. Leonidova A, Foerster C, Zarschler K, Schubert M, Pietzsch H-J, Steinbach J, et al. In vivo demonstration of an active tumor pretargeting approach with peptide nucleic acid bioconjugates as complementary system. Chem Sci. 2015;6(10):5601–16. https://doi.org/10.1039/C5SC00951K.

43. Altai M, Westerlund K, Velletta J, Mitran B, Honarvar H, Karlström AE. Evaluation of affibody molecule-based PNA-mediated radionuclide pretargeting: development of an optimized conjugation protocol and ^{177}Lu labeling. Nucl Med Biol. 2017;54:1–9. https://doi.org/10.1016/j.nucmedbio.2017.07.003.

44. Westerlund K, Altai M, Mitran B, Konijnenberg M, Oroujeni M, Atterby C, et al. Radionuclide therapy of HER2-expressing human xenografts using affibody-based peptide nucleic acid-mediated pretargeting: in vivo proof of principle. J Nucl Med. 2018;59 (7):1092–8. https://doi.org/10.2967/jnumed.118.208348.

45. Vorobyeva A, Westerlund K, Mitran B, Altai M, Rinne S, Sörensen J, et al. Development of an optimal imaging strategy for selection of patients for affibody-based PNA-mediated radionuclide therapy. Sci Rep. 2018;8(1):9643. https://doi.org/10.1038/s41598-018-27886-0.

46. Tano H, Oroujeni M, Vorobyeva A, Westerlund K, Liu Y, Xu T, et al. Comparative evaluation of novel ^{177}Lu-labeled PNA probes for affibody-mediated PNA-based pretargeting. Cancers (Basel). 2021;13 (3) https://doi.org/10.3390/cancers13030500.

47. Oroujeni M, Tano H, Vorobyeva A, Liu Y, Vorontsova O, Xu T, et al. Affibody-mediated PNA-based pretargeted cotreatment improves survival of trastuzumab-treated mice bearing HER2-expressing xenografts. J Nucl Med. 2022;63(7):1046–51. https://doi.org/10.2967/jnumed.121.262123.

48. Rossin R, Verkerk PR, van den Bosch SM, Vulders RC, Verel I, Lub J, et al. In vivo chemistry for pretargeted tumor imaging in live mice. Angew Chem Int Ed Eng. 2010;49(19):3375–8. https://doi.org/10.1002/anie.200906294.

49. Rondon A, Degoul F. Antibody pretargeting based on bioorthogonal click chemistry for cancer imaging and targeted radionuclide therapy. Bioconjug Chem. 2020;31(2):159–73. https://doi.org/10.1021/acs.bioconjchem.9b00761.

50. Houghton JL, Membreno R, Abdel-Atti D, Cunanan KM, Carlin S, Scholz WW, et al. Establishment of the in vivo efficacy of pretargeted radioimmunotherapy utilizing inverse electron demand Diels-Alder click chemistry. Mol Cancer Ther. 2017;16(1):124–33. https://doi.org/10.1158/1535-7163.Mct-16-0503.

51. Rondon A, Schmitt S, Briat A, Ty N, Maigne L, Quintana M, et al. Pretargeted radioimmunotherapy and SPECT imaging of peritoneal carcinomatosis using bioorthogonal click chemistry: probe selection and first proof-of-concept. Theranostics. 2019;9 (22):6706–18. https://doi.org/10.7150/thno.35461.

52. Shah MA, Zhang X, Rossin R, Robillard MS, Fisher DR, Bueltmann T, et al. Metal-free cycloaddition chemistry driven pretargeted radioimmunotherapy using α-particle radiation. Bioconjug Chem. 2017;28 (12):3007–15. https://doi.org/10.1021/acs.bioconjchem.7b00612.

53. Poty S, Carter LM, Mandleywala K, Membreno R, Abdel-Atti D, Ragupathi A, et al. Leveraging bioorthogonal click chemistry to improve ^{225}Ac-radioimmunotherapy of pancreatic ductal adenocarcinoma. Clin Cancer Res. 2019;25(2):868–80. https://doi.org/10.1158/1078-0432.Ccr-18-1650.

54. Keinänen O, Brennan JM, Membreno R, Fung K, Gangangari K, Dayts EJ, et al. Dual radionuclide theranostic pretargeting. Mol Pharm. 2019;16 (10):4416–21. https://doi.org/10.1021/acs.molpharmaceut.9b00746.

55. Keinänen O, Fung K, Brennan JM, Zia N, Harris M, van Dam E, et al. Harnessing ^{64}Cu/^{67}Cu for a theranostic approach to pretargeted radioimmunotherapy. Proc Natl Acad Sci U S A. 2020;117(45):28316–27. https://doi.org/10.1073/pnas.2009960117.

56. Mandikian D, Rafidi H, Adhikari P, Venkatraman P, Nazarova L, Fung G, et al. Site-specific conjugation allows modulation of click reaction stoichiometry for

pretargeted SPECT imaging. MAbs. 2018;10(8):1269–80. https://doi.org/10.1080/19420862.2018.1521132.

57. Ferreira VFC, Oliveira BL, D'Onofrio A, Farinha CM, Gano L, Paulo A, et al. In vivo pretargeting based on cysteine-selective antibody modification with IEDDA bioorthogonal handles for click chemistry. Bioconjug Chem. 2021;32(1):121–32. https://doi.org/10.1021/acs.bioconjchem.0c00551.

58. Cook BE, Membreno R, Zeglis BM. Dendrimer scaffold for the amplification of in vivo pretargeting ligations. Bioconjug Chem. 2018;29(8):2734–40. https://doi.org/10.1021/acs.bioconjchem.8b00385.

59. Cook BE, Adumeau P, Membreno R, Carnazza KE, Brand C, Reiner T, et al. Pretargeted PET imaging using a site-specifically labeled immunoconjugate. Bioconjug Chem. 2016;27(8):1789–95. https://doi.org/10.1021/acs.bioconjchem.6b00235.

60. Maitz CA, Delaney S, Cook BE, Genady AR, Hoerres R, Kuchuk M, et al. Pretargeted PET of osteodestructive lesions in dogs. Mol Pharm. 2022;19(9):3153–62. https://doi.org/10.1021/acs.molpharmaceut.2c00220.

61. Masson E, Ling X, Joseph R, Kyeremeh-Mensah L, Lu X. Cucurbituril chemistry: a tale of supramolecular success. RSC Adv. 2012;2(4):1213–47. https://doi.org/10.1039/C1RA00768H.

62. Assaf KI, Nau WM. Cucurbiturils: from synthesis to high-affinity binding and catalysis. Chem Soc Rev. 2015;44(2):394–418. https://doi.org/10.1039/C4CS00273C.

63. Barrow SJ, Kasera S, Rowland MJ, del Barrio J, Scherman OA. Cucurbituril-based molecular recognition. Chem Rev. 2015;115(22):12320–406. https://doi.org/10.1021/acs.chemrev.5b00341.

64. Strebl MG, Yang J, Isaacs L, Hooker JM. Adamantane/cucurbituril: a potential pretargeted imaging strategy in immuno-PET. Mol Imaging. 2018;17:1536012118799838. https://doi.org/10.1177/1536012118799838.

65. Jallinoja VIJ, Carney BD, Bhatt K, Abbriano CH, Schlyer DJ, Yazaki PJ, et al. Investigation of copper-64-based host-guest chemistry pretargeted positron emission tomography. Mol Pharm. 2022;19(7):2268–78. https://doi.org/10.1021/acs.molpharmaceut.2c00102.

66. Jallinoja VIJ, Carney BD, Zhu M, Bhatt K, Yazaki PJ, Houghton JL. Cucurbituril-ferrocene: host-guest based pretargeted positron emission tomography in a xenograft model. Bioconjug Chem. 2021;32(8):1554–8. https://doi.org/10.1021/acs.bioconjchem.1c00280.

67. Richard M, Truillet C, Tran VL, Liu H, Porte K, Audisio D, et al. New fluorine-18 pretargeting PET imaging by bioorthogonal chlorosydnone-cycloalkyne click reaction. Chem Commun (Camb). 2019;55(70):10400–3. https://doi.org/10.1039/c9cc05486c.

Theranostic Imaging and Radiopharmaceutical Therapy

22

Heying Duan ⓘ and Andrei Iagaru ⓘ

22.1 Introduction

The term *theranostic* is a portmanteau of the Greek words *therapo* (therapy) and *gnosis* (knowing) [3]. Opinions differ on the proper spelling: *theragnostic* or *theranostic*. We prefer *thera**g**nostic*, as this reflects its linguistic roots best, but the editors of this volume have opted to drop the "g," and they (for better or for worse) have final say. Both spellings, however, are acknowledged and are widely used. The principle of theranostics is easily explained: *see what you treat, and treat what you see*. In other words, theranostics is predicated on two steps: (1) using a targeting vector labeled with a diagnostic radionuclide to image a biological marker of disease, and (2) using the very same vector labeled with a therapeutic radionuclide to treat the disease that had been visualized.

The first attempts at clinical theranostics were made in the early 1930s using phosphorus-32 (^{32}P) in the context of leukemia and bone tumors [4]. The big breakthrough, however, came in the form of Saul Hertz's revolutionary work using iodine-131 (^{131}I) for Graves' disease and thyroid cancer [5]. His discovery that ^{131}I destroys thyroid cells while sparing other cells of the body is

the foundation of radiopharmaceutical therapy (RPT).

Within a theranostic paradigm, imaging is used to assess whether tumor tissue expresses a sufficient amount of a given molecular target relative to healthy tissue for RPT to be effective and safe. This approach also allows for the evaluation of tumor heterogenicity, as more aggressive and advanced cancers typically lose some of their specific tumor markers. In this case, patients may not benefit from RPT. Imaging thus allows for the stratification of responders (who will receive the treatment) and non-responders (who will not). This concept exemplifies personalized precision medicine.

Because molecular changes in the tumor happen before a size difference can be measured on anatomical imaging, molecular imaging can also play a key role in evaluating early response to treatment and in distinguishing true progression from pseudo-progression. The latter is characterized by a size increase on anatomical imaging despite pronounced tumor uptake of the radiopharmaceutical on molecular imaging. Pseudo-progression is believed to be attributed to edema surrounding tumor necrosis, the necrosis itself, or an infiltration of immune cells [6].

The over-arching goal of RPT is the delivery of tumoricidal doses of radiation to cancer cells while minimizing damage of the surrounding healthy tissue. One of the keys to RPT is choosing the right radionuclide, specifically one boasting emissions with high energy but low penetration

H. Duan · A. Iagaru (✉)
Department of Radiology, Division of Nuclear Medicine and Molecular Imaging, Stanford University, Stanford, CA, USA
e-mail: heying@stanford.edu; aiagaru@stanford.edu

range. Radionuclides that emit β-particles are well established, but those that emit heavier α-particles have produced very promising results in recent years. Most interestingly, tumor cells that are refractory to β-emitters have been shown to respond to treatment with α-emitters [7]. Dosimetry calculations can be performed to predict the radiation-absorbed doses to the tumor as well as radiosensitive organs such as the kidneys (through which many radiopharmaceuticals are excreted) and thus ensure the delivery of tumoricidal doses with minimal treatment-related side effects. Several new approaches and software tools—such as voxel-based dosimetry—exist to enable the facile and accurate calculation of dosimetric values [8]. In this context, the goal of theranostics is the use of molecular imaging to facilitate pre-treatment dosimetry calculations that in turn allows for personalized doses and a tailored number of cycles based on the characteristics of a patient's tumors.

22.2 Theranostic Pairs

A lock and key can be used to describe the mechanism of theranostic. In this analogy, the target is the cancer cell, but it is *locked* by a molecular marker such as a receptor or enzyme [9]. The *key* (the ligand or vector) targets the *lock* and must fit perfectly in order to bind to the cell. This *key* comes with a *keyring* (a linker) that holds a *keychain* (the radionuclide) (Fig. 22.1). In one scenario, this radioactive *keychain* will enable the imaging of the *lock*, depicting the tumor's specific molecular marker. In another, it will deliver a highly energetic radionuclide that will therapeutically irradiate the tumor cell.

Taken together, the imaging and therapeutic agents we have discussed above constitute a "theranostic pair." The former can be labeled with a radionuclide that emits either γ-rays that allow for scintigraphy/single photon emission computed tomography (SPECT) or positrons
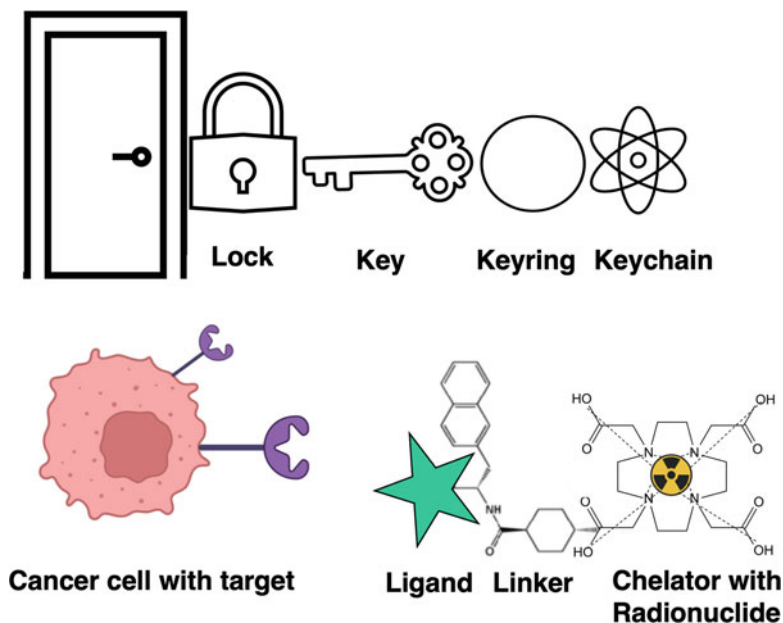
Fig. 22.1 Schematic representation of our *key-lock principle* of theranostics. The target on the cancer cell can be a receptor such as the somatostatin receptor or the human epidermal growth factor receptor-2 (HER-2) or an enzyme such as prostate-specific membrane antigen (PSMA). The

matching ligand (or targeting vector) can be a peptide, antibody, or small molecule linked to the chelator, which acts like a cage holding the radionuclide. The radionuclide is chosen according to its application, i.e., ^{99m}Tc, ^{18}F, ^{68}Ga for imaging and ^{177}Lu, ^{90}Y, ^{223}Ra, ^{225}Ac for treatment

that allow for positron emission tomography (PET). Both emissions are characterized by low linear energy transfer (LET), and long radiation range, traits that are ideal for imaging and result in low radiation exposure to the patient. The therapeutic half of this pair, however, is typically labeled with a radionuclide that emits β- or α-particles and exhibits a long half-life (days to weeks), as these traits maximize damage to tumor cells. The emission range of a therapeutic radionuclide reflects its tissue penetration range and determines the size of the area that is irradiated. In some cases, the crossfire effect further enhances treatment to include cells that are not directly targeted but are in the vicinity of those that are.

The ideal theranostic pair employs either a single radionuclide that boasts both therapeutic and "imageable" emissions *or* two radioisotopes of the same element with suitable properties. In this way, the imaging agent and radiotherapeutic are chemically identical, differ only in their isotopic compositions, and thus will exhibit identical in vivo behavior. Along these lines, radioiodine provides an excellent example: ^{123}I and ^{124}I are γ- and positron-emitters, respectively, and are thus suitable for imaging, while ^{131}I is a β-emitter suitable for RPT. Yet isotopologous theranostics are generally the exception, not the rule. To wit, a very commonly used pair of radionuclides in theranostics is gallium-68 (^{68}Ga) for PET and lutetium-177 (^{177}Lu) for treatment. While they are not chemically identical, both can be stably coordinated by the ubiquitous chelator DOTA (as they are in, for example, [^{68}Ga]Ga-DOTA-TATE and [^{177}Lu]Lu-DOTA-TATE). A theranostic pair that is rapidly gaining in interest is copper-64 (^{64}Cu), a positron emitter, and copper-67 (^{67}Cu), a β- and γ-emitter, due to recent advances in the production of ^{67}Cu and highly stable chelators based on sarcophagines, a bicyclic cage-like metal chelator. Table 22.1 gives an overview of radionuclides that may be used in theranostic pairs as well as their physical properties.

RPT is a systemic cytotoxic treatment and is usually administered intravenously (IV) or orally (in the case of ^{131}I), though radioembolization (RE)—a locoregional treatment for primary or secondary liver tumors that is administered directly into the hepatic artery—falls under the RPT umbrella as well. The most widely used radionuclides in RPT are the β-emitters ^{131}I, ^{177}Lu, and yttrium-90 (^{90}Y). The ionizing radiation from these nuclides causes mainly single-strand breaks in DNA, which may lead to the apoptosis of the cancer cell. α-Emitters such as radium-223 (^{223}Ra) and actinium-225 (^{225}Ac) have higher LET and shorter tissue range (<100 μm) and thus cause DNA double-strand breaks with higher frequency, suggesting that they might have even greater antitumoral activity than their β-emitting brethren.

22.3 Thyroid Diseases

The World Health Organization (WHO) recently published the 2022 classification for thyroid neoplasms. Briefly, malignant follicle-derived thyroid neoplasms consist of follicular thyroid carcinoma (FTC), papillary thyroid carcinoma (PTC), invasive encapsulated follicular variant PTC, oncocytic carcinoma, and anaplastic thyroid cancer; medullary thyroid carcinoma (MTC), in contrast, is a C-cell-derived thyroid carcinoma. The vast majority of thyroid cancers are PTC (85%). The incidence of thyroid cancer is now slowly declining after decades of increases that have been retroactively attributed to the evolution of improved diagnostic tools and the over-diagnosis of mostly small and indolent PTCs.

Radioiodide is well suited for theranostics. It boasts both diagnostic and therapeutic radioisotopes and is (of course) structurally identical to iodide, meaning it exhibits the same physiological organification. As a result, radioiodide is taken up and retained in thyroid cells—including well-differentiated thyroid cancer—allowing for both imaging and therapy. The key to this schema is the sodium-iodide symporter (NIS), a transmembrane protein that transports iodide from the bloodstream against a concentration gradient into follicular thyroid cells. Mediated by pendrin channels, this iodide continues to the follicular lumen where thyroid peroxidase organifies the iodide via oxidation to iodine and its subsequent attachment to thyroglobulin.

Table 22.1 Selected clinical theranostic pairs

Disease	Diagnostic	Target	Energy (keV)	Half-life	Therapy	Energy (keV)	Max range	Half-life
DTC Hyperthyroidism	[123I]I− [124I]I− [99mTc]Tc-O$_4$−	NIS	159; γ, EC 511; β+ 140; γ	13.22 h 4.17 d 6.03 h	131I	364; β−, γ	2.4 mm	8.02 d
Neuroendocrine tumors	[68Ga]Ga-DOTA-TATE [68Ga]Ga-DOTA-TOC [68Ga]Ga-DOTA-NOC [64Cu]Cu-SAR-TATE	SSTR	Mean 890; β+ 660; β+, β−, γ	68 min 12.7 h	[177Lu]Lu-DOTA-TATE [90Y]Y-DOTA-TOC [225Ac]Ac-DOTA-TATE [67Cu]Cu-SAR-TATE	497; β− 2300; β− 5800; α 562; β−	1.7 mm 12 mm <100 μm 2 mm	6.65 d 2.7 d 10 d 2.6 d
Metastatic prostate cancer	[68Ga]Ga-PSMA11 [18F]F-DCFPyL [64Cu]Cu-PSMA [68Ga]Ga-RM2	PSMA GRPR	Mean 890; β+ 511; β+ 660; β+, β−, γ Mean 890; β+	68 min 110 min 12.7 h 68 min	[177Lu]Lu-PSMA [225Ac]Ac-PSMA [67Cu]Cu-PSMA [177Lu]Lu-RM2	497; β− 5800; α 562; β− 497; β−	1.7 mm <100 μm 2 mm 1.7 mm	6.65 d 10 d 2.6 d 6.65 d
Bone metastases	[99mTc]Tc-HDP [99mTc]Tc-MDP [18F]F-NaF	Bone Hydroxyapatite	140; γ 511; β+	6.03 h 110 min	[223Ra]RaCl$_2$ [153Sm]Sm-EDTMP	5000–7500; α 640; β−	<100 μm 3 mm	11.43 d 1.9 d
Neuroblastoma Pheochromocytoma Paraganglioma	[123I]I-mIBG	Norepinephrine transporter	159; γ, EC	13.22 h	[131I]I-mIBG	364; β−	2 mm	8.02 d
Primary or secondary liver tumors	[99mTc]Tc-MAA	Direct accumulation	140; γ	6.03 h	[90Y]Y-microspheres	940; β−	2.4 mm	64.1 h

DTC Differentiated thyroid cancer, *EC* electron capture, *MAA* macroaggregated albumin, *NIS* sodium/iodide symporter

Molecular imaging with a diagnostic isotope of radioiodide can be performed to determine the function of a thyroid nodule (e.g., over-functioning *hot* or non-functioning *cold* nodules [10]) or probe for the presence of hyperthyroidism (Graves' disease, toxic uni- or multinodular adenoma). Imaging with ^{123}I or [124]I can be useful for assessing the radioiodine avidity of thyroid lesions, aiding in treatment planning, and avoiding RPT when high activity concentrations are observed in radiosensitive tissues such as the breast or when the thyroid cancer is non-avid for radioiodine.

22.3.1 Differentiated Thyroid Cancer

Therapeutic isotopes of radioiodine—especially [131]I—are used for a variety of treatments: to destroy toxic goiter; for whole-organ ablation in Graves' disease; for differentiated thyroid cancer (DTC) after thyroidectomy to ablate any (benign) thyroid remnants so that thyroglobulin decreases to undetectable levels and can be used as tumor marker in follow-up; as adjuvant therapy in DTC to destroy any (unknown) microscopic thyroid cancer cells; and to destroy locoregional or distant metastases in DTC to improve progression-free survival (PFS) and overall survival (OS). A 2019 joint statement from the American Thyroid Association, the European Association of Nuclear Medicine (EANM), the Society of Nuclear Medicine and Molecular Imaging, and the European Thyroid Association (ETA) as well as a recently published 2022 consensus statement of the ETA recommended radioiodine treatment for high-risk and selected cases of intermediate-risk DTC. However, the benefit of radioiodine treatment in low-risk DTC patients is still heavily debated [11, 12]. Importantly, low-risk does not mean no-risk. But how to determine which patient will eventually have recurrent disease? Two large randomized clinical trials are underway to evaluate the benefit of low-dose radioiodine therapy with 1.1 GBq vs. no treatment in patients with low-risk thyroid cancer (NCT01837745,

NCT01398085). For high-risk and recurrent disease, a high dose of ≥3.7 GBq ^{131}I is recommended. Post-treatment whole-body scintigraphy (which utilizes the γ-emission of the already administered therapeutic ^{131}I) serves as treatment verification but also shows the true extent of disease and might reveal unsuspected metastases (Fig. 22.2).

Theranostic radioiodine is indispensable for (re-)staging, therapy, and surveillance of DTC. Although DTC has an excellent long-term prognosis—i.e., a five-year survival rate of 97%—recurrence is seen in 5–30% of cases. The treatment of recurrent or metastatic disease becomes problematic when the tumor has lost its functional expression of NIS and is refractory to radioiodine. Unfortunately, efforts to induce redifferentiation with MEK inhibitors such as selumetinib have failed to improve response rate after radioiodine treatment [13].

22.3.2 Medullary Thyroid Cancer

Despite their localization in the thyroid, MTCs are neuroendocrine tumors (NETs) that derive from parafollicular C-cells that arise from the neural crest. After primary treatment surgery, almost 50% of patients show residual or recurrent disease. In advanced, metastatic MTC, treatment options are limited. State-of-the-art multikinase inhibitors have not demonstrated a significant survival benefit but have shown considerable toxicity. As a NET, a fraction of MTC expresses SSTRs that can be targeted by radiolabeled analogs of somatostatin (SSA) for both imaging and treatment. Multiple studies have evaluated peptide receptor radionuclide therapy (PRRT) in MTC and found promising results. Most recently, small studies have shown that [^{177}Lu]Lu-DOTA-TATE produces a high objective response rate (ORR) of 62% and median OS of 26 months [14]. However, PRRT has not yet become clinical routine for MTC given the heterogeneity of the disease and the lack of a unique landmark biological target.
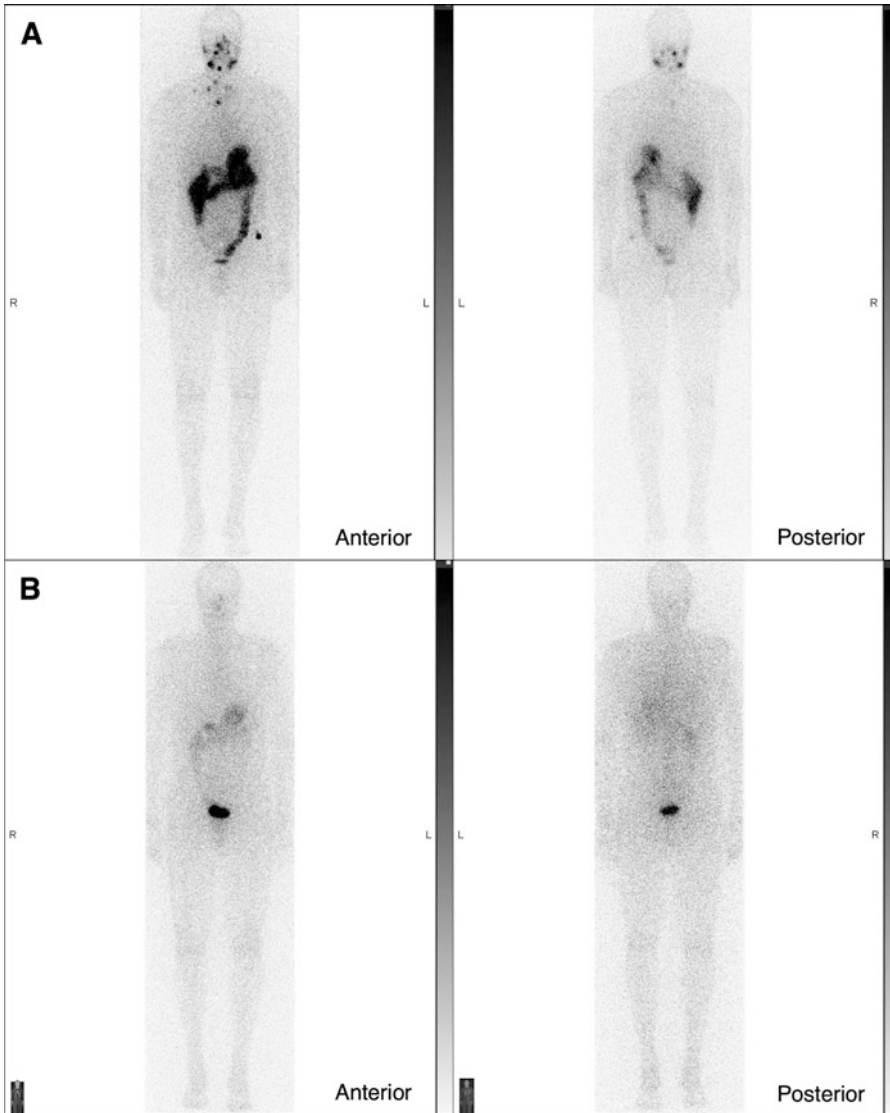
Fig. 22.2 Radioiodine whole-body planar scintigraphy scans of a 34-year-old man with metastatic papillary thyroid cancer. (**a**) After treatment with ^{131}I, multiple foci of uptake in the neck and chest are seen on post-therapeutic imaging. (**b**) In the follow-up diagnostic scintigraphy with ^{123}I, complete response is seen without any pathological uptake

22.4 Neuroendocrine Tumors

NETs derive from neuroendocrine cells and can hence occur in multiple organs, with the majority being gastroenteropancreatic (GEP) and bronchial NETs. These are rare, often slow-growing tumors that are very heterogeneous and only show vague symptoms. Therefore, they are difficult to diagnose, and patients are often misdiagnosed or diagnosed late when the primary tumor has metastasized. Due to the heterogeneity of NETs, their classification and nomenclature is complex. The 2019 WHO classification divides neuroendocrine neoplasia (NEN) into well-differentiated NETs and poorly differentiated

neuroendocrine carcinomas (NECs). NETs can be further stratified by grading based on their mitotic count and Ki-67 index: G1 (Ki67 ≤ 2%), G2 (Ki67 3–20%), and well-differentiated G3 (Ki67 > 20%). NEN can show clinical features that are specific to their organ or cell of origin (e.g., hormone secretion) but can also share characteristics that are independent of the site. Along these lines, all well-differentiated NETs exhibit the overexpression of SSTRs; poorly differentiated NETs and NECs, in contrast, have lesser SSTR expression or have lost it altogether. Five subtypes of human SSTRs have been identified: 1, 2A, 2B, 3, 4, and 5. Most NETs overexpress subtype 2 followed by 5 and 3. The activation of SSTRs results in hormone secretion, thus driving the symptomatic burden of functional NETs. Multiple short- and long-acting SSAs such as octreotide or lanreotide have been developed to target SSTRs and have been shown to relieve NET symptoms and exert an antiproliferative effect [15].

22.4.1 Imaging of NETs

The SPECT imaging of SSTR using [111In]In-octreotide or [99mTc]Tc-hynic-TOC has been largely replaced by SSTR PET paired with computed tomography (CT) or magnetic resonance imaging (MRI) due to the significantly better image quality and detection rate of the latter (as well as patients' convenience). At present, US Food and Drug Administration (FDA)-approved PET imaging agents based on the DOTA-TOC and DOTA-TATE scaffolds are available. Each has a slightly different affinity to the various SSTR subtypes, but both bind to SSTR2 and have equally high diagnostic accuracies. The US Food and Drug Administration (FDA) has approved [68Ga]Ga-DOTA-TATE, [68Ga]Ga-DOTA-TOC, and [64Cu]Cu-DOTA-TATE for PET imaging. All show high sensitivity, specificity, and accuracy without superiority of one over the other. [64Cu] has a longer half-life than [68Ga] (12.7 h vs. 68 min), making its central production with long-haul distribution possible. It also allows for delayed imaging with the potential for pre-treatment dosimetry.

22.4.2 Peptide Receptor Radionuclide Therapy

Once NENs have metastasized, treatment options are limited to SSAs, multikinase inhibitors, chemotherapy, locoregional treatments for liver metastases, and, most notably, PRRT (Fig. 22.3). The same SSAs at the heart of the imaging agents described above can be labeled with β-emitters such as [177Lu] and [90Y] or, more recently, the α-emitter [225Ac] for therapy. While the efficacies of [90Y]Y-DOTA-TOC and [177Lu]Lu-DOTA-TATE are similar, [90Y]Y-DOTA-TOC produces increased nephrotoxicity associated with radiation-induced inflammation and fibrosis stemming from its particularly high-energy β-emission.

[177Lu]Lu-DOTA-TATE is now the most widely used tool for the treatment of SSTR-positive NETs. The FDA-approved therapy schema consists of four IV cycles of 7.4 GBq [177Lu]Lu-DOTA-TATE at intervals of 8 weeks. Dose adjustments can be made in the case of bone marrow depression with borderline hematologic parameters such as thrombocytopenia. An amino acid (arginine/lysine) infusion is given immediately before, during, and after the administration of [177Lu]Lu-DOTA-TATE for nephroprotection. Concurrent treatment with long-acting octreotide should be scheduled after PRRT to ensure that the SSTRs are not saturated with the cold analog. Overall, PRRT is a safe treatment with mild side effects [16, 17]. Kidney failure has been reported in the past, but it has not been a significant concern since the introduction of nephroprotection [18].

Even though PRRT has been employed since the early 1990s and there is a large body of literature showing the efficacy of PRRT, most of the studies were from single centers and retrospective. The NETTER-1 trial was the first prospective, randomized, multicenter phase III trial in which patients with midgut NETs were randomized to either receive a high-dose SSA alone (60 mg octreotide LAR) or [177Lu]Lu-DOTA-TATE with best supportive care (30 mg octreotide LAR) [16]. At data-cutoff date, median
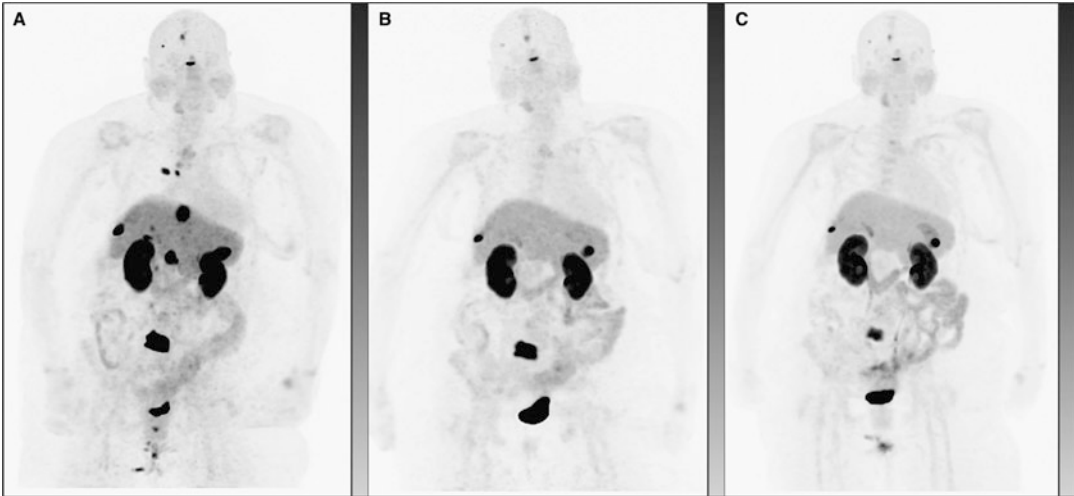
Fig. 22.3 A 69-year-old woman with progressive pancreatic NET, G1. Figures (**a**–**c**) show maximum intensity projections (MIP) of [^{68}Ga]Ga-DOTA-TATE PET: (**a**) pre-treatment evaluation illustrating SSTR overexpression in the primary tumor and metastases; (**b**) interim imaging after two cycles of [^{177}Lu]Lu-DOTA-TATE showing impressive treatment response with markedly decreased tumor burden and resolution of several hepatic and lung lesions; (**c**) imaging after four cycles of PRRT delineating further response in the lumbar vertebra 5 and otherwise stable disease

PFS had not been reached in the PRRT group vs. 8.4 months in the SSA group, which translates to a 79% lower risk of disease progression or death in the PRRT arm. Concordantly, the response rate was significantly higher with [^{177}Lu]Lu-DOTA-TATE (18% vs. 3%). Treatment-related adverse events were higher for PRRT and included nausea and vomiting (attributable to the amino acid infusion), fatigue, abdominal pain, and diarrhea. All were mild and transient. With nephroprotective infusion, grade 3 nephrotoxicity was seen in only 5% (vs. 4% in the control group). Despite similar rates of high-grade adverse events in both groups, neutropenia (1%), thrombocytopenia (2%), and lymphopenia (9%) were unique to PRRT though transient. Patients in the PRRT arm reported a significant improvement in quality of life compared with high-dose SSA. This landmark study led to the 2018 approval of [^{177}Lu]Lu-DOTA-TATE by the FDA and European Medicines Agency for unresectable or metastatic, progressive, well-differentiated, SSTR-positive NETs. The final OS analysis was conducted 5 years after last randomization, with a median observation time of over 6.3 years. Median OS was not statistically significant between both groups: 48.0 months for [^{177}Lu]Lu-DOTA-TATE and 36.3 months for high-dose SSA. However, a high percentage (36%) of patients in the control group crossed over to receive PRRT in follow-up, which may have affected the results for OS. Given that no new long-term toxicity was noted for PRRT with comparable renal toxicity for both groups, the difference of 11.7 months in OS is clinically relevant, therefore favoring PRRT [19].

22.4.3 Theranostics in Advanced Disease

Despite a high Ki-67 index, well-differentiated G3 NETs often still harbor sufficient SSTR for PRRT. Retrospective studies have shown promising results for disease control of up to 72% and PFS of up to 13.1 months [20]. Currently, the NETTER-2 study (NCT03972488) is underway to evaluate the efficacy and safety of [^{177}Lu]Lu-DOTA-TATE as a first-line treatment for well-differentiated but high-grade (Ki67

10–55%) GEP-NETs compared with high-dose octreotide LAR. Other major clinical trials compare PRRT using [^{177}Lu]Lu-edotreotide in high-grade NETs with chemotherapy (NCT04919226) or everolimus (NCT03049189).

The game-changing results with [^{177}Lu]Lu-DOTA-TATE sparked interest in PRRT with α-emitters, particularly in patients who are refractory to [^{177}Lu]Lu-DOTA-TATE despite SSTR-positivity. As the penetration range of α-emitters is short, their toxicity to surrounding healthy tissue is less than that of β-emitters. The first clinical study with [^{225}Ac]Ac-DOTA-TATE was conducted in 32 patients who reached the maximum dosage or failed prior [^{177}Lu]Lu-DOTA-TATE therapy [21]. The interim analysis after a median follow-up of eight months showed a partial response in 63% and stable disease in 37% of the patients who finished two treatment cycles. The toxicity profile was low and similar to [^{177}Lu]Lu-DOTA-TATE: no grade 3 or 4 toxicity was observed. Long-term results of a phase II study with an expanded cohort of 91 patients who received capecitabine as a radiosensitizer prior to [^{225}Ac]Ac-DOTA-TATE with a median follow-up of 24 months showed excellent OS (71%) and PFS (68%) at 24 months as well as response to treatment (3% complete response, 48% partial response, 29% stable disease, 20% progression) [22]. Similar to the pilot study, only minimal toxicities occurred after PRRT. These results warrant future randomized controlled phase III trials comparing [^{225}Ac]Ac-DOTA-TATE and [^{177}Lu]Lu-DOTA-TATE or their sequential administration for the management of NET patients.

22.4.4 Radioembolization of NET Liver Metastases

Up to 91% of GEP-NET patients metastasize to the liver and may develop extensive, bulky disease. As hepatic metastases are the main driver for morbidity and mortality, liver-directed treatment is a local treatment option. Radioembolization with ^{90}Y-microspheres showed a pooled ORR of 51%, estimated disease

control of 88%, and median OS of 32 months [23]. In a first-in-human study, [^{213}Bi]Bi-DOTA-TOC was administered intraarterially to patients with progressive, advanced NET liver metastases refractory to [^{177}Lu]Lu-DOTA-TATE and given systemically to one patient with bone marrow carcinosis [24]. The results were very promising, with partial remission or stable disease in all patients. Nephrotoxicity was moderate, and hematotoxicity was less pronounced than with prior β-PRRT, particularly in the patient who was treated systemically. A combination of [^{177}Lu]Lu-DOTA-TATE and RE with ^{166}Ho-microspheres was also evaluated in a phase II clinical trial with remarkable response in the liver in 43% of patients [25].

22.4.5 SSTR Antagonists

Up until now, only somatostatin agonists have been used for PRRT. Antagonists, however, have been shown to bind to more sites on the SSTR, have a favorable biodistribution, and facilitate better tumor visualization [26]. In a small pilot study, one radiolabeled antagonist—[^{177}Lu]Lu-DOTA-JR11—demonstrated higher tumor radiation doses per administered activity and a seven times higher tumor-to-bone marrow activity concentration ratio compared to [^{177}Lu]Lu-DOTA-TATE [27]. A phase I clinical study evaluated [^{68}Ga]Ga-DOTA-JR11 and [^{177}Lu]Lu-satoreotide tetraxetan ([^{177}Lu]Lu-DOTA-JR11) in patients with advanced SSTR-positive NETs [28]. While the ORR was promising at 45% (including 5% with a complete response), unexpected severe grade 4 hematotoxicity was seen in 4/7 (57%) patients. The reason remains unclear; despite the earliest findings of the pilot study, it cannot be ruled out that the increased binding sites for antagonists, including the bone marrow, result in higher radiation exposure to progenitor cells. A different pair of antagonistic compounds—[^{68}Ga]Ga-NODAGA-LM3 and [^{177}Lu]Lu-DOTA-LM3—have also been evaluated in first-in-human studies [29]. Unlike [^{177}Lu]Lu-DOTA-JR11, only grade 3 thrombocytopenia and lymphopenia were observed in 3/51

(5.9%) and 4/51 (7.8%) patients who were administered [68Ga]Ga-NODAGA-LM3 and [177Lu]Lu-DOTA-LM3, respectively. The mild hematotoxicity might be attributable to the different molecular structure of the two agents or the amount of peptide used in each case.

22.4.6 Other Theranostic Pairs

Another interesting theranostic pair that targets SSTR is [64Cu]/[67Cu]Cu-SAR-TATE. [64Cu]Cu-SAR-TATE PET/CT has demonstrated comparable image quality to [68Ga]Ga-DOTA-TATE 1 h post injection (PI) with high tumor uptake. The lesion-to-liver ratio of [64Cu]Cu-SAR-TATE increased over time, with the highest observed at 24 h PI [30]. The long retention time allows for delayed imaging and therefore pre-treatment dosimetry. [67Cu] is a β-emitter with similar LET to [177Lu] but has a significantly shorter half-life (2.6 days vs. 6.7 days) that provides a higher dose-rate and potentially greater efficacy. [67Cu]Cu-SAR-TATE recently showed promising tumor growth inhibition in a murine model of SSTR-positive cancer [31]. A phase I/II trial is currently evaluating the dose escalation of [67Cu]Cu-SAR-TATE in pediatric patients with high-risk SSTR-expressing neuroblastoma (NCT04023331).

22.4.7 Treatment Sequence

One particularly important question to address is where to place PRRT in the treatment sequence after progression from first-line treatment with SSAs. The guidelines from the three major NET associations—the European Neuroendocrine Tumor Society, the European Society of Medical Oncology, and the North American Neuroendocrine Tumor Society—are similar and recommend PRRT as the second-line treatment for advanced midgut NETs and the third-line treatment in pancreatic NETs due to a lack of prospective trials. Recently, a multidisciplinary focus group of the EANM reached Delphi consensus on PRRT as the second-line treatment for gastrointestinal (GI) NETs, the first-line treatment for non-resectable or disseminated NET with high SSTR expression, and at first progression in G1-G3 GEP-NETs with sufficient SSTR expression [32].

22.5 Primary and Secondary Liver Tumors

Primary liver tumors include hepatocellular carcinoma (HCC) and intrahepatic cholangiocarcinoma (ICC). Secondary liver malignancies are liver metastases derived from other cancers, most commonly colorectal cancer (CRCLM). The theranostic approach to treat these tumors has many names—selective internal radiation therapy (SIRT), transarterial RE (TARE), or simply RE—but all refer to a technique that is unlike the previously mentioned treatment concepts because it is not given systemically but rather locally, directly at the liver tumors. [90Y]-microspheres are administered through a femoral catheter to the tumor-feeding arteries, where the microspheres get trapped as the vessels get smaller and smaller. The tumoricidal effect is induced by internal radiation rather than embolization. The underlying principle is predicated on the dual blood supply to the liver from both the hepatic artery and the portal vein. Liver cells are supplied around 70% by the portal vein and around 30% by the hepatic artery. Liver tumors, however, receive most of their blood from the hepatic artery, which means that a transarterial treatment approach targets liver tumors while sparing normal liver tissue that is mainly provided by the portal system.

Patients with unresectable liver-dominant malignancies with no signs of liver failure (i.e., ascites, elevated total bilirubin level >2 mg/dL), life expectancy of at least 3 months, and Eastern Cooperative Oncology Group Performance Status (ECOG PS) of ≤2 with adequate hepatic arterial flow to the cancer(s) can be evaluated for RE. For treatment planning, patients undergo a "mapping" angiography to outline the hepatic arterial flow and identify the tumor-feeding artery/arteries. In some cases, the prophylactic coil embolization of

the extrahepatic vessels arising from the hepatic artery—the right gastric, gastroduodenal, and cystic arteries—might be necessary. This prevents any extrahepatic deposits of microspheres that can cause severe ulcers and inflammation.

22.5.1 Pre-Treatment Planning

[^{99m}Tc]Tc-macroaggregated albumin (MAA) particles are similar in size to the treatment microspheres, and the former are given to provide an estimate of their distribution of the latter. To this end, [^{99m}Tc]Tc-MAA is administered to the vessel(s) that has been selected for treatment. The position of the catheter depends on the area to be treated: proximal to the tumor-feeding artery in case of a single lesion, proximal of the tumor-bearing hepatic lobar artery in case of a radiation segmentectomy/lobectomy, or distal when the whole liver is treated (liver metastases). Post-interventional scintigraphy is performed to estimate the lung shunt fraction (LSF), the fraction of MAA that has escaped the hepatic vascular bed into the pulmonary circulation. SPECT/CT of the liver shows intrahepatic MAA distribution and allows for dosimetry. There are multiple ways to determine the treatment dose, each with certain limitations. The modified body surface area (BSA) method is easy to calculate and commonly used for whole-liver treatment with resin microspheres. It assumes that a larger BSA correlates with a larger liver but does not account for hepatomegaly, prior hepatic resection, obesity, or cachexia. Thus, it tends to underdose large tumors and large livers and overdose small tumors and small livers. The medical internal radiation dose (MIRD) model is based on a single compartment that contains the tumor and the normal liver and assumes the uniform distribution of microspheres within this compartment. In this case, a hypervascular tumor will absorb a higher dose, potentially resulting in over-treatment. Finally, the partition model is the most accurate, as it divides the lung, tumor, and normal liver into separate compartments to estimate their respective radiation absorbed doses but also relies on the concept of a homogenous distribution of particles per compartment. Its limitation is that it can only be used for clearly defined tumors like HCC. Dedicated dosimetry software can aid in dose calculation and personalization to achieve the desired tumor dose while keeping the radiation absorbed dose to healthy liver tissue low.

The treatment procedure is analogous to the planning angiography in which the treatment dose is administered to the tumor-supplying vessel(s) through the same catheter tip position. For ^{90}Y-microspheres, post-treatment imaging with SPECT/CT is challenging, as the emitted bremsstrahlung radiation—i.e., the energy from β-radiation penetrating through tissue—has a broad energy distribution without a well-defined photopeak and is thus difficult to capture. As the decay of ^{90}Y also produces positrons, PET imaging shows higher image quality compared to bremsstrahlung SPECT/CT even at short imaging times [8]. Post-treatment imaging not only enables treatment verification but also helps scout for potential extrahepatic deposits. As collateral vessels form quickly after coil embolization, RE should be performed within 1 week after treatment planning. A schematic representation of the RE workup and workflow shown in Figs. 22.4 and 22.5 shows pre-treatment planning [^{99m}Tc]Tc-MAA SPECT/CT and post-therapeutic ^{90}Y-microsphere PET/CT.

Overall, treatment-related complications and side effects are low [33, 34]. Immediate adverse events include fatigue, nausea, and abdominal pain. Serious complications arise from inadvertent extrahepatic microsphere deposits and are related to their location (i.e., gastritis, duodenitis). Radiation pneumonitis (high LSF) and severe RE-induced liver disease (REILD) are rare but can occur when more than 30 Gy is given to the healthy lung and liver tissue, respectively.

There are two types of ^{90}Y-microspheres with different properties: resin and glass. Glass microspheres are most commonly used for well-defined primary liver cancer, while resin microspheres are mostly used for liver metastases. In addition, holmium-166 (^{166}Ho)
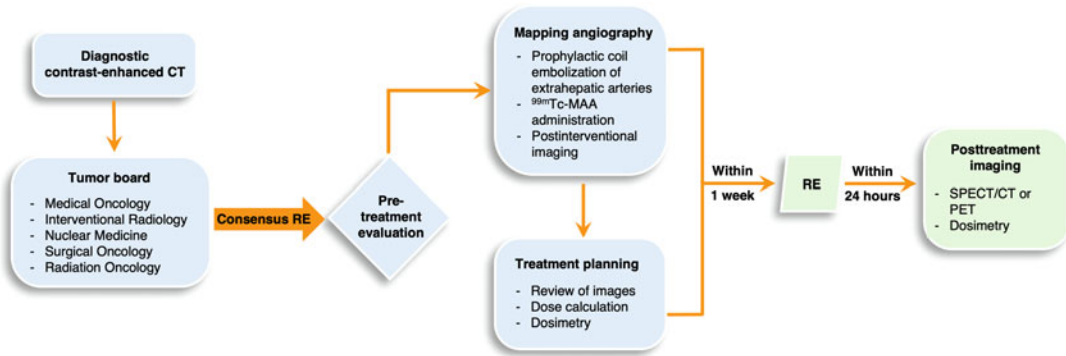
Fig. 22.4 Workup and workflow for radioembolization with ^{90}Y-microspheres
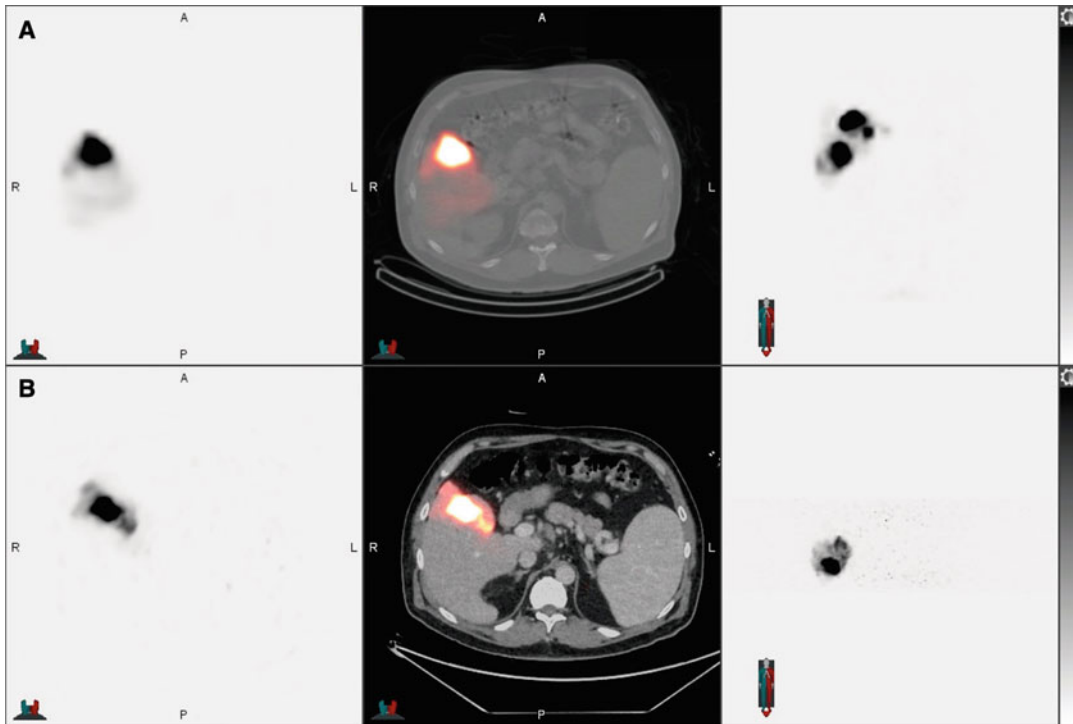
Fig. 22.5 A patient with multifocal HCC presenting for radioembolization of the dominant segment 5 lesion. Pre-treatment planning (**a**) [^{99m}Tc]Tc-MAA SPECT/CT shows MAA distribution in the known tumors in segments 5 and 8 without any extrahepatic deposits. Post-therapeutic (**b**) ^{90}Y-microsphere PET/CT verifies microsphere distribution strictly in the treated segment 5 tumor without any extrahepatic deposits

microspheres are currently under clinical investigation. The benefit in this case is that the β-emitter ^{166}Ho also emits γ-radiation that would allow for therapy planning with the ^{166}Ho-microspheres themselves instead of [^{99m}Tc]Tc-MAA as a surrogate.

22.5.2 Hepatocellular Carcinoma

RE plays a role across all tumor stages of HCC. RE bridges prolonged waiting times to transplantation or downstages to meet Milan criteria for transplantation. This can be achieved by radiation

lobectomy or segmentectomy in which not only the tumor is treated but also hypertrophy of healthy liver is induced. Neoadjuvant RE showed a high ORR of 88% with an OS of 95% and 87% at two years and three years, respectively. Interestingly, survival rates were comparable for patients undergoing subsequent surgery and for those who did not [35]. Long-term follow-up of 15 years in 207 patients who received RE for downstaging or bridging showed a median OS of 12.5 years with a recurrence-free survival of 10 years; only 12% had recurrent disease [36].

In advanced HCC, RE showed a significantly longer time to progression (>26 months) and was better tolerated compared to transarterial chemoembolization (TACE; 6.8 months) [33]. No difference in OS was seen upon comparison to the tyrosine kinase inhibitor sorafenib; however, the reduced toxicity of RE compared to sorafenib affords patients with a higher quality of life and should thus be considered during treatment planning and patient selection [34]. Studies are underway to evaluate the combination of RE and immunotherapy in HCC. RE has been reported to induce the release of tumor-associated antigens that are targeted by antigen-presenting cells. This can lead to a change in the tumor microenvironment (TME) with a potent antitumoral immune response, which could in turn further enhance the efficacy of subsequent immunotherapy. The preliminary results of a trial focused on treatment with nivolumab three weeks after RE revealed favorable tolerability and encouraging response rates [37]. Another randomized trial (NCT04541173) is investigating the safety and effectiveness of RE followed by a combination of atezolizumab and bevacizumab.

22.5.3 Intrahepatic Cholangiocarcinoma

Data on RE in ICC are scarce and involve mostly small cohorts from single centers. A systematic review on RE in treatment-naïve patients showed a prolonged survival, especially when the tumor burden was less than 25% [38]. The combination

of chemotherapy and RE led to a longer median OS of up to 24 months compared to chemotherapy and TACE (up to 17 months) [39]. A retrospective study involving 136 patients showed remarkable results: complete response in 2 patients (1.5%), partial response in 42 patients (32.1%), stable disease in 82 patients (62.6%), and progressive disease in only 5 patients (3.8%), with a median OS of 14.2 months [40]. RE was able to downstage 11 patients (8%) to resection, and 2 participants (2%) were bridged to transplant. After resection, the median recurrence and OS were 26.3 and 39.9 months, respectively. Toxicity ≥ grade 3 was seen in 10 patients (8%), and abdominal pain was the leading side effect.

22.5.4 Colorectal Cancer Liver Metastases

Finally, RE was evaluated in patients with unresectable CRCLM in three randomized controlled phase III trials as an addition to first-line treatment with chemotherapy. Even though a delayed progression in the liver was seen, there was no significant OS benefit [41]. However, the major design flaw of this study was that PFS at *any* site was taken as an endpoint for a liver-directed treatment. Current guidelines recommend RE in the salvage setting in which RE has shown a survival benefit.

22.6 Prostate Cancer

Prostate cancer (PC) is the most common cancer in men in the USA, with one in every eight men diagnosed with PC during their lifetime [42]. Despite advances in its management, PC remains the second leading cause of cancer deaths among men. The tumor biology of PC is very heterogeneous and on a spectrum, ranges from indolent disease (Gleason score 3 + 3) to clinically significant, aggressive cancer (Gleason score ≥ 3 + 4), often with reclassification over time. The ease of screening with prostate-specific

antigen (PSA) has led to a dramatic increase in the diagnosis of PC. The over-diagnosis of often insignificant cancers has resulted in over-treatment with its associated risks of erectile dysfunction and incontinence. Given these potentially life-altering side effects, risk stratification is necessary as studies have shown that low-risk disease and some subsets of intermediate-risk indolent disease will benefit from active surveillance, while aggressive cancers merit therapy.

Prostate-specific membrane antigen (PSMA) is a type II transmembrane glycoprotein that is highly overexpressed in over 90% of PCs. A positive correlation between PSMA expression and disease progression has been reported: for example, higher PSMA expression is associated with more advanced, metastasized, and castration-resistant PC (mCRPC). To be fair, the name "PSMA" is a misnomer, as the protein is in fact an enzyme, not an antigen: glutamate carboxypeptidase II. There are many compounds capable of targeting PSMA ranging from peptides and small molecules to antibodies. That said, [^{68}Ga]Ga-PSMA-11 and [^{18}F]F-DCFPyL are the most widely used (and only FDA-approved) radiopharmaceuticals for the imaging of PC. Indeed, the FDA first approved [^{68}Ga]Ga-PSMA-11 in December 2020 for use only at UCLA and UCSF. [^{18}F]F-DCFPyL was approved for US-wide use in May 2021, while [^{68}Ga]Ga-PSMA-11 was approved for widespread use in December of the same year.

Both [^{68}Ga]Ga-PSMA-11 and [^{18}F]F-DCFPyL exhibit high specificity and high tumor uptake and are well suited for patient selection for RPT as they use the same urea-based moiety as a binding motif for PSMA. ^{18}F-labeled DCFPyL has the advantages of higher spatial resolution and better image quality, and its longer half-life (110 min) allows for better tumor-to-background contrast (since the healthy organs have more time for clearance) and facilitates the commercial distribution of the probe. The theranostic pair of [^{64}Cu]Cu- and [^{67}Cu]Cu-SARbisPSMA has also shown promising results in early clinical studies (NCT04868604).

22.6.1 Metastatic Castration-Resistant Prostate Cancer

Once metastatic PC becomes hormone-refractory, treatment options are limited, and the prognosis is poor. PSMA-targeted RPT produced impressive results in the VISION trial, leading to the recent FDA approval of [^{177}Lu]Lu-PSMA-617 for the RPT of mCRPC. An international, multicenter, open-label phase III study enrolled patients with PSMA-positive mCRPC who had previously failed treatment with a next-generation androgen-receptor-pathway inhibitor (i.e., abiraterone, enzalutamide) and taxane-based chemotherapy, and were randomized in a 2:1 ratio to receive either [^{177}Lu]Lu-PSMA-617 plus standard-of-care (SOC) or SOC alone (no other active cytotoxic treatment) [43]. Then, 7.4 GBq [^{177}Lu]Lu-PSMA-617 was administered IV in four cycles with an interval of six weeks. The treatment arm ($n = 551$) showed a significantly longer radiographic PFS (8.7 vs. 3.4 months), OS (15.3 vs. 11.3 months), and time to first symptomatic skeletal event or death (11.5 vs. 6.8 months) than SOC alone ($n = 280$). The response rates to [^{177}Lu]Lu-PSMA-617 were excellent, with 9.2% (vs. 0%) complete response and 41.8% (vs. 3%) partial response along with concordant PSA decreases of up to 80%. Despite a greater incidence of high-grade ($\geq$ grade 3) adverse events related to bone marrow suppression (12.9% anemia, 7.9% thrombocytopenia, and 7.8% lymphopenia), [^{177}Lu]Lu-PSMA-617 was overall well tolerated. Other side effects included fatigue (43.1%), xerostomia (38.8%), and nausea (35.3%), which were all transient. Complementary to the VISION study is TheraP, a randomized multicenter phase II trial in which patients with mCRPC who failed treatment with docetaxel and for whom cabazitaxel was considered the next treatment option were randomized in a 1:1 fashion to receive either [^{177}Lu]Lu-PSMA-617 ($n = 99$) or chemotherapy with cabazitaxel ($n = 101$) [44]. For treatment eligibility, participants underwent both [^{68}Ga]Ga-PSMA-11 and [^{18}F]F-

FDG PET/CT to ensure high PSMA-avidity without any PSMA-negative lesions. A significantly higher decrease in PSA was seen in the [177Lu] Lu-PSMA-617 arm (66%) compared to 37% with cabazitaxel. Concordantly, the ORR was higher for RPT (49% vs. 24%) as well as the 12-month PFS (19% vs. 3%). Interestingly, [177Lu]Lu-PSMA-617 showed fewer adverse events (33% vs. 53%) and more thrombocytopenia (11% vs. 0%), while the cabazitaxel arm exhibited more neutropenia (13% vs. 4%). Among the participants who had pain at baseline, symptomatic relief was higher with RPT vs. chemotherapy (60% vs. 43%). Patient-reported quality of life was similar for both groups at baseline and improved with [177Lu] Lu-PSMA-617, particularly with respect to diarrhea, fatigue, social functioning, and insomnia.

Both the VISION and TheraP trials showed that [177Lu]Lu-PSMA-617 is safe and effective for the RPT of patients with mCRPC who fail androgen-receptor-directed treatment and taxane-based chemotherapy. A larger decrease in PSA was observed in the TheraP trial compared to the VISION trial, a result that could be attributed to the former's strict inclusion criteria of high PSMA-avidity without PSMA-negative lesions. Multiple trials are now underway to evaluate the use of [177Lu]Lu-PSMA-617 earlier in the treatment sequence (NCT04689828 and NCT04720157), even before docetaxel in men with de novo diagnosed metastatic hormone-sensitive PC (NCT04343885), or in combination with immune checkpoint inhibitors (NCT03658447, NCT03805594) and enzalutamide (NCT04419402). Another PSMA-targeting radiotherapeutic—[177Lu]Lu-PSMA I&T—is also under investigation compared to a next-generation androgen-receptor-pathway inhibitor in a phase III trial (NCT04647526).

22.6.2 Alpha Emitters

As in NETs, the RPT of PC using radiotherapeutics labeled with α-emitters is currently of high interest, particularly for patients who are refractory to [177Lu]Lu-PSMA-617. RPT with [225Ac]Ac-PSMA-617 has shown significant decrease in tumor burden and PSA as well as prolonged PFS of 15.2 months and OS of 18 months. Xerostomia was the single most frequent adverse event, occurring after the first treatment cycle. However, despite the concern that the higher LET might lead to higher toxicity, it was not severe enough to discontinue treatment [45]. In a small cohort of patients with advanced mCRPC who failed previous [177Lu]Lu-PSMA-617 therapy, [225Ac]Ac-PSMA-617 produced significant PSA declines with a PFS of 4.1 months and OS of 7.7 months [7]. A tandem technique combining low-dose [225Ac]Ac-PSMA-617 with standard activities of [177Lu]Lu-PSMA-617 reduced the incidence and severity of xerostomia while maintaining the desired antitumor effect [46].

PSMA-targeted RPT with other α-emitters—such as lead-212 (^{212}Pb) and ^{213}Bi—is currently under investigation. [213Bi]Bi-PSMA-617 was explored in a first-in-human study in patients with progressive mCRPC [47]. After two cycles with a cumulative activity of 592 MBq, a radiographic and biochemical response was observed (PSA decline >80%) [47]. Dosimetry, however, renders [213Bi]Bi-PSMA-617 a second choice compared to [225Ac]Ac-PSMA-617 due to the higher perfusion-dependent off-target radiation of [213Bi]Bi-PSMA-617 in the salivary glands and kidneys [48]. In a preclinical study, PSMA-targeting [212Pb]Pb-NG001 produced significant uptake and therapeutic efficacy in mice bearing xenografts of two human PC cell lines with different degrees of PSMA expression: C4-2 (PSMA +) and PC-3 PIP (PSMA+++). Interestingly, the uptake of the radiotherapeutic was only 1.8-fold higher in the PC-3 PIP cells despite their 10-fold higher PSMA expression [49]. Differences in the cellular internalization of natural PSMA-expressing cells compared to the genetically engineered PC-3 PIP cells may explain this discrepancy. Treatment response was better in mice treated with two cycles vs. one cycle. Future clinical studies are warranted.

22.6.3 Gastrin-Releasing Peptide Receptor

Despite its name, PSMA is overexpressed not only by 90% of PCs but also by various other tissues and cancers, leading to false-positive findings. In addition, 10% or greater of PCs are PSMA-negative. As a result, gastrin-releasing peptide receptor (GRPR) has emerged as a promising target alternative to PSMA. GRPR is significantly overexpressed in PC, while the pancreas is the only healthy tissue with high GRPR expression. Initially, agonists were developed to target the receptor, but side effects caused by their internalization prompted a shift toward antagonists. GRPR antagonists have been found to have more binding sites on PC cells, leading to better tumor-to-normal tissue activity concentration ratios.

Many GRPR antagonists have been developed and evaluated preclinically, but only a few have entered the clinic. Among the most studied clinically is RM2. [^{68}Ga]Ga-RM2 shows high tumor uptake and has an overall favorable biodistribution. Compared to PSMA-targeted compounds, the low physiological uptake of GRPR antagonists makes the delineation of pathological abdominal lymph nodes easier. Figure 22.6 shows the biodistribution of [^{68}Ga]Ga-RM2 compared to that of [^{68}Ga]Ga-PSMA-11. [^{68}Ga]Ga-RM2 has demonstrated high detection rates of PC at initial staging [50] as well as at biochemical recurrence [51]. A first-in-human study of ^{177}Lu-labeled RM2 in four patients with mCRPC showed the highest tumor absorbed doses in metastases of bone, lymph nodes, and soft tissue that were all therapeutically relevant [52]. The highest uptake in healthy tissues was seen in the pancreas, making it the dose-limiting organ. However, current thresholds for radiation toxicity to the pancreas are derived from external beam radiation therapy, and it is unknown whether these are transferable to RPT.

In a first-in-man study, another interesting GRPR antagonist—[^{68}Ga]Ga-NeoB (formerly NeoBOMB1)—demonstrated high uptake in pathological PC lesions in primary localized and metastatic PC [53]. [^{68}Ga]Ga-NeoBOMB1 was also explored in GRPR-expressing metastatic GI stromal tumors (GIST) in which high tumor uptake was seen in the majority of patients alongside an excellent safety profile [54]. The theranostic pair of [^{68}Ga]Ga- and [^{177}Lu]Lu-NeoB has shown high GRPR affinity and cell binding as well as high in vivo stability preclinically [53, 55]. A phase I/IIa open-label, multicenter trial is currently underway to evaluate the biodistribution, dosimetry, safety, tolerability, and antitumoral efficacy of [^{177}Lu]Lu-NeoB in patients with GRPR-expressing metastatic solid tumors (NCT03872778). Shifting gears slightly, ^{64}Cu/^{67}Cu-labeled GRPR antagonists conjugated to a novel derivative of sarcophagine—[^{64}Cu]Cu/[^{67}Cu]Cu-SAR-BBN—have shown high affinity for GRPR preclinically [56, 57]. [^{64}Cu]Cu-SAR-BBN is currently being explored in a phase I clinical trial in men with biochemically recurrent PC who are negative on [^{68}Ga]Ga-PSMA-11 PET (NCT05407311).

No correlation has been found between the uptake of PSMA- and GRPR-targeted radiopharmaceuticals, suggesting a complementary relationship between these probes.

Indeed, the molecular interrogation of *both* targets may best reflect the full extent of disease. Along these lines, bispecific compounds that simultaneously target PSMA *and* GRPR have been explored in preclinical studies. The translation of these tools into the clinic is anticipated after they have been shown to be safe and to exhibit suitable radiopharmacokinetics in healthy volunteers [58].

22.7 Bone Metastases

Almost all cancers can spread hematologically to the skeleton, though the most common to follow this pattern include breast, lung, and particularly castration-resistant PC. Bone metastases are frequently categorized as osteoblastic or osteolytic according to their cell of origin. Both interfere with the normal bone cell cycle, leading to either the pronounced breakdown or aberrant
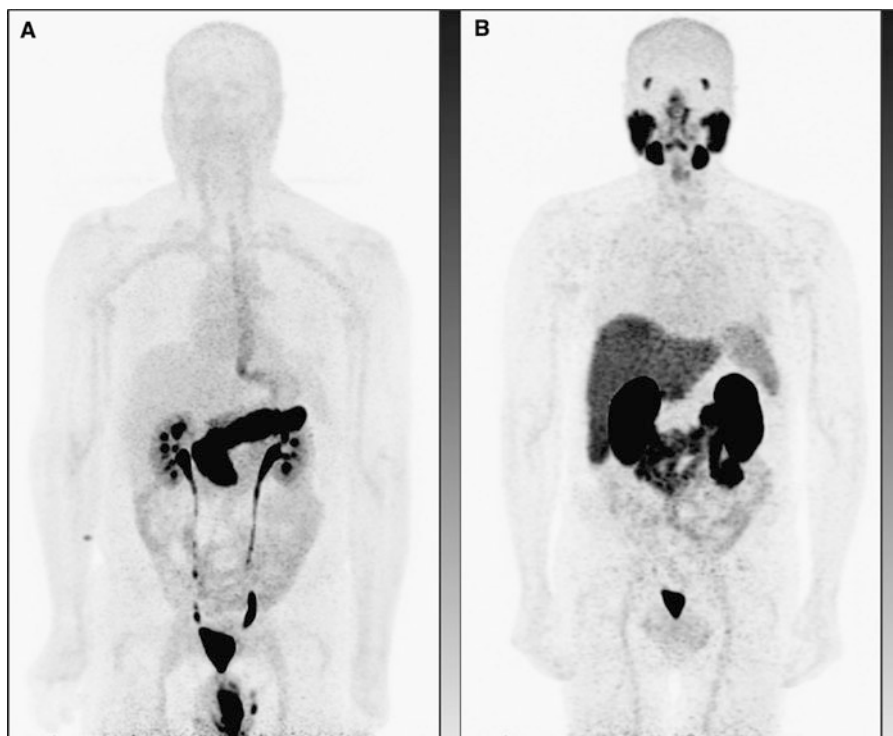
Fig. 22.6 Physiological biodistribution of (**a**) [^{68}Ga]Ga-RM2 and (**b**) [^{68}Ga]Ga-PSMA-11 in a patient with prostate cancer. Most notable is the lower uptake of [^{68}Ga]Ga-RM2 in the gastrointestinal tract. For treatment, the pancreas and the salivary glands are the dose-limiting organs for [^{68}Ga]Ga-RM2 and [^{68}Ga]Ga-PSMA-11, respectively

proliferation of bone tissue. Either process can cause bones to break more easily and can lead to pathologic fractures, pain, hypercalcemia, bone marrow depression, and spinal cord compression. Bone metabolism can be imaged via SPECT with [^{99m}Tc]Tc-bisphosphonates and via PET with sodium fluoride-18 ([^{18}F]F-NaF). Yet since both are bone-seeking agents, only osteoblastic lesions will show uptake. Degenerative skeletal changes are also characterized by enhanced bone activity and can be a differential diagnosis.

Up until the last decade, RPT was only available for bone palliation. Samarium-153 ethylenediamine tetramethylene phosphonate ([^{153}Sm]Sm-EDTMP), a bone-seeking bisphosphonate, produced pain relief within 1–2 weeks along with reduced opioid use and improved quality of life. Despite a delay in skeletal events, however, no significant benefit in OS was seen [59]. As randomized phase III trials were lacking, [^{153}Sm]Sm-EDTMP was not recommended in official guidelines. EDTMP radiolabeled to ^{177}Lu showed promising results for bone palliation in metastatic breast cancer and mCRPC. However, its theranostic partner, [^{68}Ga]-EDTMP, ultimately proved unstable in vivo. The next-generation bisphosphonate zoledronate targets the bone mineral hydroxyapatite and has been radiolabeled with both ^{68}Ga (i.e., [^{68}Ga]Ga-NODAGA^{ZOL}) and ^{177}Lu (i.e., [^{177}Lu]Lu-DOTA-ZOL). In a comparative study of [^{68}Ga]Ga-NODAGA^{ZOL}, [^{68}Ga]Ga-PSMA-11, and [^{99m}Tc]Tc-MDP in patients with advanced PC, [^{68}Ga]Ga-NODAGA^{ZOL} showed better performance in detecting bone lesions at restaging, particularly in patients who failed prior [^{225}Ac]Ac-PSMA-617 treatment. However, [^{68}Ga]Ga-PSMA-11 identified more skeletal metastases at staging at a per-lesion level [60]. [^{68}Ga]Ga-NODAGA^{ZOL}'s therapeutic counterpart, [^{177}Lu]

Lu-DOTA-ZOL, showed high uptake in skeletal metastases and low uptake in the bone marrow in patients with bone metastases secondary to PC [61]. Further prospective studies on the efficacy of treatment with [^{177}Lu]Lu-DOTA-ZOL are warranted.

22.7.1 ^{223}Ra: An Alpha-Emitting Calcium Analog

The α-emitting radiometal ^{223}Ra belongs to the category of calcium analogs that—just like physiological calcium—accumulates in areas of enhanced bone metabolism by forming complexes with the bone mineral hydroxyapatite. The short range of ^{223}Ra's α-particles ($< 100\,\mu m$) allows for high doses to the osteoblastic tumor while sparing surrounding healthy bone marrow. The safety and efficacy of ^{223}Ra-dichloride ([^{223}Ra]RaCl$_2$) was evaluated in the ALSYMPCA study, a randomized, double-blind, placebo-controlled, multicenter phase III trial [62]. Patients with mCRPC to the bone were randomized to receive [^{223}Ra]RaCl$_2$ or placebo in a 2:1 ratio. The treatment group was administered [^{223}Ra]RaCl$_2$ IV every 4 weeks for up to six cycles, while the placebo group received saline. Patients treated with [^{223}Ra]RaCl$_2$ showed a survival benefit of 3.6 months compared to placebo (14.9 vs. 11.3 months) regardless of prior docetaxel treatment. A delay in time to first symptomatic skeletal event of 5.8 months was seen in the [^{223}Ra]RaCl$_2$ group (15.6 vs. 9.8 months) as well as a 30% reduction in risk of death. Bone pain palliation occurred within two weeks. PSA was unreliable in assessing response to treatment, as only 16% (vs. 6% in the placebo group) of patients showed a decrease in PSA. However, alkaline phosphatase significantly decreased or normalized as sign of therapy response, similar to lactate dehydrogenase. Interestingly, adverse events were less frequent in the [^{223}Ra]RaCl$_2$ group (93% vs. 96%) and included hematotoxicity, particularly anemia and thrombocytopenia, nausea, fatigue, and GI reactions. Predictors for hematotoxicity were prior chemotherapies and extended bone disease. Quality of life improved significantly with [^{223}Ra]RaCl$_2$ and showed a slower decline in the post hoc data analysis. This pivotal study led to the 2013 approval of [^{223}Ra]RaCl$_2$ by the FDA for the RPT of symptomatic bone metastases in patients with mCRPC without known visceral metastases.

Because ^{223}Ra has limited γ-emission, post-treatment imaging is technically possible; however, image quality is poor and scan times are long. The advancement of next-generation SPECT/CT systems based on cadmium zinc telluride (CZT) technology might bring a change (Fig. 22.7). Several studies have investigated the combination of [^{223}Ra]RaCl$_2$ with various other treatment agents. While chemotherapy with docetaxel and paclitaxel paired with [^{223}Ra]RaCl$_2$ has been shown to be safe and produced a longer median time to PSA progression [63, 64], the combination of [^{223}Ra]RaCl$_2$ with abiraterone was unfavorable and led to more fractures and deaths when compared to abiraterone alone [65].

The mode of action of [^{223}Ra]RaCl$_2$ suggests that it may be effective against malignant osteoblastic transformations beyond those caused by mCRPC. The bone metastases in breast cancer, for example, are mostly a mix of osteolytic and osteoblastic lesions. The presence of an osteoblastic portion suggests that ^{223}Ra could be a treatment option. This was investigated in a phase II study for patients with hormone receptor-positive, bone-dominant metastatic breast cancer in which [^{223}Ra]RaCl$_2$ was given concurrently with hormonal therapy [66]. A tumor response rate of 54% and a disease control rate of 49% were seen, leading to a median PFS of 7.4 months and a bone-PFS of 16 months. The treatment was well tolerated, with no grade 3 or 4 adverse events. Studies are now comparing [^{223}Ra]RaCl$_2$ vs. placebo in combination with hormonal therapy and everolimus (NCT02258451) or paclitaxel (NCT04090398).
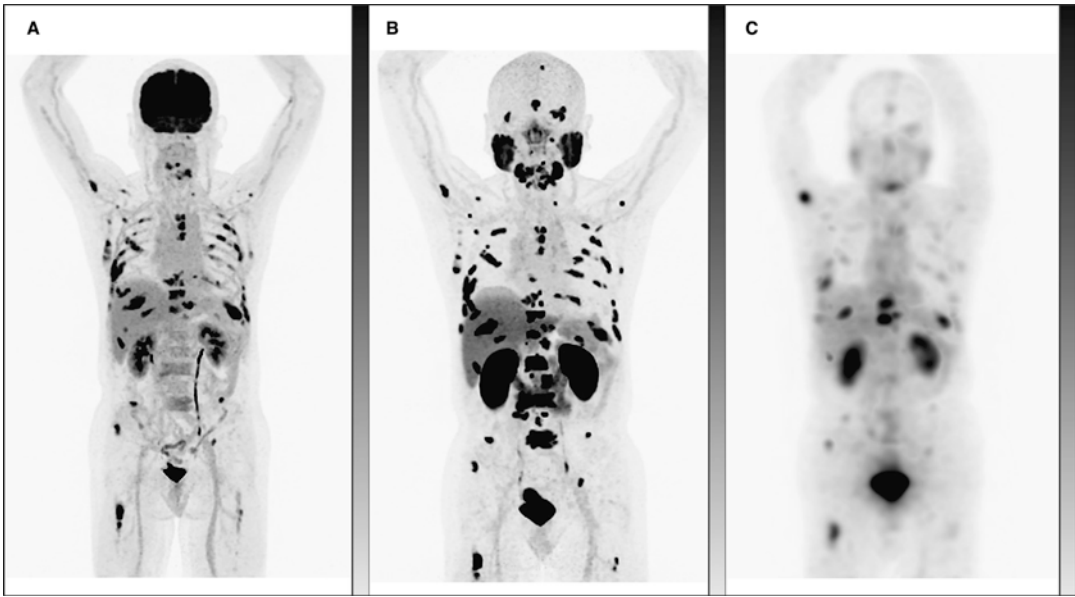
Fig. 22.7 A 66-year-old man with progressive metastatic prostate cancer presenting with PSA 34.7 ng/mL for treatment with [^{177}Lu]Lu-PSMA-617. Pre-treatment [^{18}F]F-FDG PET (MIP, **a**) and [^{18}F]F-DCFPyL PET (MIP, **b**) were performed at 2 min per bed position for a total of 10 min. Both PET scans show an oligometastatic patient with numerous osseous lesions throughout the skeleton. Post-treatment [^{177}Lu]Lu-PSMA-617 SPECT (MIP, **c**) was performed using a next-generation SPECT/CT system based on cadmium zinc telluride technology at 3 min per bed position for four bed positions (12 min total) and shows excellent image quality with high tumor uptake at a significantly reduced acquisition time

22.8 Neuroblastoma, Pheochromocytoma, Paraganglioma

Neuroblastoma, pheochromocytoma, and paraganglioma (PPGL) are orphan diseases (i.e., rare cancers). They are endocrine tumors that arise from neural crest cells, and are characterized by heterogeneous tumor biology. Neuroblastoma is the most common solid childhood tumor and is most commonly found in the adrenal gland. Pheochromocytomas originate from the adrenal medulla, while paragangliomas stem from extra-adrenal, sympathetic (abdomen), or parasympathetic (head and neck) ganglia. Most PPGLs exhibit increased production of catecholamines, leading to hypertension, palpitation, and headache. The tumorigenesis of neuroblastoma and PPGL is characterized by complex molecular pathways with various gene mutations. In unresectable and metastatic cases, treatment options are limited, and the prognosis is poor.

One hallmark of these tumors is the overexpression of the norepinephrine transporter (90% of neuroblastomas, 50–60% of PPGL, and a lower fraction of head and neck paragangliomas). Meta-iodobenzylguanidine (mIBG) is a norepinephrine analog that is actively taken up via norepinephrine transporters, accumulates intracellularly in neuro-secretory granules, and can be radiolabeled with ^{131}I or ^{123}I for theranostic imaging and RPT. [^{131}I]I- or [^{123}I]I-mIBG is typically given first for whole-body imaging to assess the expression of norepinephrine transporters and to determine the extent of disease. Given ^{131}I's long half-life, pre-treatment dosimetry can be performed through serial imaging with [^{131}I]I-mIBG. Subsequent treatment is administered for mIBG-positive tumors for up to two cycles, while post-therapeutic whole-body

scans can be obtained for treatment verification within a week. It is important to note that certain medications (i.e., antihypertensives such as labetalol and calcium channel blockers, antidepressants, tramadol, and pseudoephedrine) should be paused for at least five of their respective half-lives prior to patient evaluation as well as 7 days after diagnostic scans or treatment with [131I]I-mIBG as they interfere with norepinephrine transporters and may cause false-negative scans or a priori transporter saturation. That said, patients should be on an antihypertensive regimen, as worsening hypertension may occur within 24 h of the administration of [131I]I-mIBG. Prophylactic thyroid blockade should also be given at least 24 h prior to treatment and for 10 days afterward, as [131I]I-mIBG usually contains a small quantity of unbound iodine that may be taken up by the thyroid gland otherwise.

In the study that led to the FDA approval of [131I]I-mIBG for PPGL, 68 patients with mIBG-positive, unresectable, or metastatic PPGL with hypertension were treated with one to two cycles of [131I]I-mIBG [67]. Treatment response was seen in 22% of patients after a single cycle and increased to 30% of patients after two cycles. The majority of patients showed stable disease, while 8% progressed. The median OS was 37 months and was longer in patients who received two cycles (44 months vs. 18 months). Symptomatic relief manifested in a ≥50 reduction of all antihypertensive medication for at least 6 months in 25% of patients. A high rate of hematologic adverse events was observed: grade ≥3 hematotoxicity was mostly transient, while 25% required supportive care. Myelodysplastic syndrome was seen in 4% of patients, and secondary leukemias in 3%. A limitation is that patients were not stratified by genetic mutations such as succinate dehydrogenase complex iron sulfur subunit B (SDHB), as the study was designed before their importance was apparent.

Mutations to SDHB are the most common germline mutations in PPGL and a sign of tumor dedifferentiation. Consequently, SDHB mutations are associated with high malignant transformation, metastases, and shorter OS (5-year survival rate 36% vs. 67% in patients without SDHB mutation). The loss of norepinephrine transporter expression is concomitant with tumor dedifferentiation, resulting in false-negative [131I]I-mIBG scans. Furthermore, patients with metastatic, extra-adrenal primaries, and familial PPGL may also exhibit low [131I]I-mIBG avidity. In these patients, SSTR-targeted PRRT might be a viable treatment option (Fig. 22.8).

22.8.1 Peptide Receptor Radionuclide Therapy in Pheochromocytoma and Paraganglioma

Most studies of PRRT in PPGL have been retrospective and comprised of small cohorts. However, an impressive pooled disease control rate of 84% and an ORR of 25% have been reported for PRRT in these patients as well as a more favorable toxicity profile compared to [131I]I-mIBG [68]. Recently, RPT with [225Ac]Ac-DOTA-TATE was evaluated in patients with metastatic paraganglioma refractory to [177Lu]Lu-DOTA-TATE and produced a notably high ORR of 50%, a disease control rate of 88%, and a concordant reduction in antihypertensive drugs. The treatment was well tolerated with improvement in ECOG PS [69]. A study combining [131I]I-mIBG and [90Y]Y-DOTA-TOC is now underway (NCT03044977).

22.8.2 Neuroblastoma

For high-risk and relapsed neuroblastoma, a combination of treatments including chemotherapy, radiotherapy, and autologous stem cell transplantation (ASCT) are commonly employed. Monotherapy with [131I]I-mIBG produced a promising 30–40% response rate, so combination therapies with [131I]I-mIBG alongside chemotherapeutic agents such as topotecan, cisplatin, cyclophosphamide, and melphalan have been
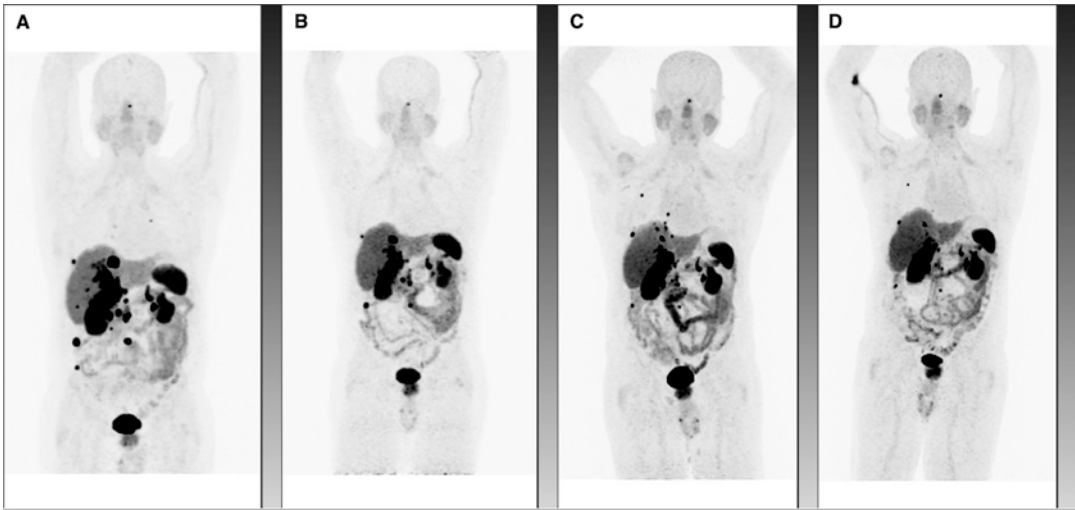
Fig. 22.8 A 73-year-old man with progressive metastatic pheochromocytoma. Figures (**a**–**d**) show maximum intensity projections (MIP) of [^{68}Ga]Ga-DOTA-TATE PET: (**a**) pre-treatment evaluation illustrating SSTR overexpression in all known metastases; (**b**) imaging after four cycles of PRRT with [^{177}Lu]Lu-DOTA-TATE delineating response to treatment with lesional size decreases and the resolution of several hepatic and lung lesions; (**c**) progressive disease with new lesions two years after PRRT; (**d**) after two additional cycles of [^{177}Lu]Lu-DOTA-TATE, favorable treatment response with size decrease in all lesions and the resolution of some hepatic lesions

explored and have yielded response rates ranging from 27 to 80% [70]. [^{131}I]I-mIBG has also produced impressive results in newly diagnosed high-risk neuroblastoma: after two cycles of [^{131}I]I-mIBG combined with topotecan as radiosensitizer followed by standard induction treatment, surgery, and myeloablative therapy with subsequent ASCT, overall ORR was 57%, and the primary tumor showed a response rate of 94% [71]. Hematological adverse effects were most common, often amplified by combined chemotherapy. However, high-risk neuroblastoma patients usually have pre-existing bone marrow disease, which contributes to hematotoxicity.

Patients with neuroblastoma and PPGL should be evaluated for the expression of both norepinephrine transporters and SSTRs. In most cases, a radiopharmaceutical that binds one of these two targets will show a higher degree of uptake and thus should be chosen for subsequent treatment. If both targets are equally overexpressed, the patient's characteristics—most importantly their bone marrow reserve—should drive the selection of the radiotherapeutic RPT.

22.9   Future Developments in Theranostics

By their very nature, theranostics are very specific both to their target and their tumor type. This specificity is advantageous when diagnosing and treating a particular disease, but, in a broader sense, it intrinsically limits RPT to a handful of cancer types. To circumvent this challenge, efforts have been made to identify cancer-specific targets that are expressed across a variety of tumors. One approach aims at the microenvironment of solid tumors, as it contributes to the majority of the tumor mass. The TME consists of a wide variety of cells—ranging from vascular cells to immune cells—but the most abundant are cancer-associated fibroblasts (CAF). These stromal cells overexpress a transmembrane glycoprotein called fibroblast activation protein (FAP) that is associated with tumorigenesis, proliferation, and escape from immunosurveillance. Over 90% of epithelial cancers including colorectal, breast, ovarian, lung, pancreatic, and PC

overexpress FAP. Since its expression in healthy tissue is low, it is suitable as a *broad-spectrum* tumor target.

22.9.1 Fibroblast Activation Protein Inhibitors

FAP inhibitors (FAPI) have been developed for theranostics with promising first clinical results. In a small cohort of patients with sarcoma and pancreatic cancer, [^{90}Y]Y-FAPI-46 showed disease control in 50% of patients as well as a favorable biodistribution profile that could allow for repeat treatment cycles [72]. [^{177}Lu]Lu-FAP-2286 demonstrated high tumor uptake with long retention and reasonable adverse events in patients with metastasized pancreatic, breast, ovarian, and colorectal carcinoma [73]. [^{68}Ga] Ga-FAP-2286 (NCT04621435) and [^{177}Lu]Lu-FAP-2286 (NCT04939610) are currently being evaluated in patients with metastatic FAP-expressing solid tumors to determine their feasibility, efficacy, and safety.

22.9.2 The CXCL12/CXCR-4 Pathway

A distinctive feature of cancer is its ability to evade the immune system. More specifically, it is a disrupted balance of host immunity and tumor growth that leads to tumor progression. In the TME, stromal and immune cells express chemokines that regulate tumor proliferation. The stromal chemokine CXCL12 and its receptor, CXC-chemokine receptor type 4 (CXCR-4), recruit regulatory T-cells that suppress the function of tumor-infiltrating lymphocytes (TILs). TILs, on the other hand, represent host immunity and create a pro-inflammatory environment to kill tumor cells. As cancer is conniving, it upregulates the expression of CXCR-4 on its surface, which in turn stimulates the production of CXCL12 in the TME. The interaction of CXCL12 and CXCR-4 prevents the TILs from deploying their antitumor activity. Thus, the cancer is able to evade the immune system. The activated

CXCL12/CXCR4 axis plays a significant role in tumor development and is associated with aggressive tumors [74]. CXCR-4 is particularly overexpressed in cancers of the hematopoietic system. The CXCR-4-targeted theranostic pair of [^{68}Ga]Ga-pentixafor and [^{177}Lu]Lu−/[^{90}Y]Y-pentixather achieved remarkable early results in the clinic: in heavily pre-treated extramedullary relapsed multiple myeloma, an overall ORR of 83% was reported without any acute adverse events [75]. In addition, successful pre-transplant conditioning with desired bone marrow ablation was seen in three patients with refractory acute myeloid leukemia [76]. Finally, in six patients with relapsed diffuse large B-cell lymphoma, CXCR-4 directed RPT in combination with conditioning chemotherapy or radioimmunotherapy led to successful ASCT [77]. Without question, these very promising initial results warrant future studies of CXCR-4-targeted theranostics in solid tumors expressing the receptor.

22.9.3 Pan-Cancer Theranostics

The trend toward a *pan*-cancer theranostic marker may also be achieved with already familiar targets. As mentioned earlier, both PSMA and GRPR are overexpressed in several cancers beyond PC. PSMA-targeted radiopharmaceuticals have been investigated in glioblastoma multiforme, HCC, and renal cell carcinoma, in which uptake has been found in the tumor-associated neovasculature. Furthermore, novel GRPR-antagonists such as NeoBOMB1 and SAR-Bombesin are now being investigated in metastatic gastrointestinal stromal tumors (GIST) and breast cancer (Fig. 22.9), respectively. Early imaging results have been encouraging; however, there is still a long way to go until a therapeutic agent can be translated to the clinic.

Another target of high interest in breast cancer is human epidermal growth factor receptor-2 (HER-2). Variants of the HER-2-targeting antibody trastuzumab have been labeled with various
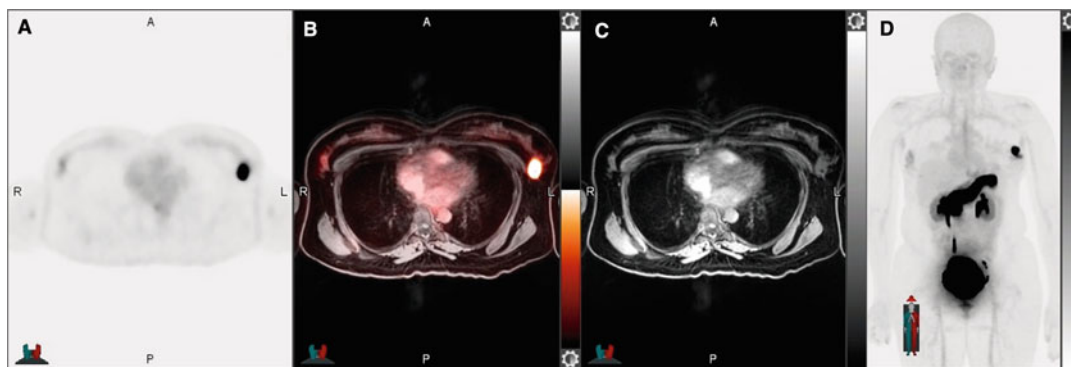
Fig. 22.9 A 36-year-old woman with grade 3 invasive ductal carcinoma. Figures (**a**–**d**) show [^{68}Ga]Ga-RM2 PET/MRI for staging (**a**) axial PET, (**b**) fused axial PET/MRI, (**c**) MRI, and (**d**) maximum intensity projection (MIP) illustrating GRPR overexpression in the left breast mass without evidence for lymph node involvement or distant metastatic disease

positron emitters for imaging such as ^{111}In, ^{124}I, ^{64}Cu, and ^{89}Zr. In a pilot study, a variant of trastuzumab labeled with the therapeutic radionuclide ^{177}Lu has been shown to be well tolerated and has produced high tumor to non-tumor activity concentration ratios as well as satisfactory dosimetry in patients with metastatic HER-2-positive breast cancer [78].

22.9.4 $\alpha_v\beta_6$-Integrin

Another potential target for theranostics is $\alpha_v\beta_6$-integrin, which is overexpressed in epithelial cancers and promotes carcinogenesis. As such, it is found to be markedly overexpressed at the border between tumor and healthy tissue. Many $\alpha_v\beta_6$-targeting compounds have been developed but have also been characterized by high levels of non-specific uptake in the GI system as well as the liver, lungs, and pancreas. A novel, improved compound—[^{68}Ga]Ga-Trivehexin—was recently introduced and has produced promising first results (i.e., high tumor uptake and low non-specific uptake in other organs) in patients with head and neck cancer and pancreatic adenocarcinoma [79].

22.9.5 Moving Forward

In the end, the sheer volume of preclinical studies, clinical studies, and registered new clinical trials on new and established agents bears witness to the high interest and wide range of possibilities of theranostics. Moving forward, future objectives for the field will include the refinement of current therapies with new radiolabeling techniques and chelators to increase the efficacy and safety profile of radiotherapeutics. Furthermore, the best position for many RPTs within the therapeutic sequence needs to be defined, as their value might merit an earlier position in the treatment timeline. Indeed, temporally shifting RPT in this manner may advance it from a palliative to a curative tool. Efforts in dosimetry will allow RPT to move from empiric standardized regimens to personalized treatment doses and cycles. To bring this chapter full circle, we envision that in the future, the language surrounding theranostics in oncology may change from cancer-specific (as in prostate cancer, breast cancer, and neuroendocrine tumors) to molecular phenotype-specific (as in PSMA-expressing, SSTR-expressing, and HER-2-expressing).

22.10 The Bottom Line

- Theranostics is an approach to precision oncology that combines nuclear imaging and radiopharmaceutical therapy using similar targeted radiopharmaceuticals.
- Theranostic radiopharmaceuticals target molecular features on cancer cells for imaging and therapy in an effort to allow clinicians to work according to the maxim "seeing what you treat, and treating what you see."
- Radiotherapeutics produce antitumor activity and symptomatic relief and are ideally characterized by a low-toxicity profile compared to standard chemotherapy, resulting in improved quality of life for patients.
- Prospective clinical trials will pave the way for using RPT earlier in the treatment timeline.

Competing Interests HD and AI declare that they have no conflict of, or competing, interest.

Disclosure Statement The authors have nothing to disclose.

References

1. Bodei L, Herrmann K, Schoder H, Scott AM, Lewis JS. Radiotheranostics in oncology: current challenges and emerging opportunities. Nat Rev Clin Oncol. 2022;19:534–50.
2. Baum RP, Kulkarni HR. THERANOSTICS: from molecular imaging using Ga-68 labeled tracers and PET/CT to personalized radionuclide therapy – the Bad Berka experience. Theranostics. 2012;2:437–47.
3. Frangos S, Buscombe JR. Why should we be concerned about a "g"? Eur J Nucl Med Mol Imaging. 2019;46:519.
4. Erf LA, Lawrence JH. Clinical studies with the aid of radioactive phosphorus. I. The absorption and distribution of radio-phosphorus in the blood and its excretion by normal individuals and patients with leukemia. J Clin Invest. 1941;20:567–75.
5. Hertz S, Roberts A, Salter WT. Radioactive iodine as an indicator in thyroid physiology. Iv. The metabolism of iodine in Graves' disease. J Clin Invest. 1942;21:25–9.
6. Brabander T, van der Zwan WA, Teunissen JJM, et al. Pitfalls in the response evaluation after peptide receptor radionuclide therapy with [(177)Lu-DOTA(0),Tyr(3)]octreotate. Endocr Relat Cancer. 2017;24:243–51.
7. Feuerecker B, Tauber R, Knorr K, et al. Activity and adverse events of Actinium-225-PSMA-617 in advanced metastatic castration-resistant prostate cancer after failure of Lutetium-177-PSMA. Eur Urol. 2021;79:343–50.
8. Duan H, Khalaf MH, Ferri V, et al. High quality imaging and dosimetry for yttrium-90 ((90)Y) liver radioembolization using a SiPM-based PET/CT scanner. Eur J Nucl Med Mol Imaging. 2021;48:2426–36.
9. Jamous M, Haberkorn U, Mier W. Synthesis of peptide radiopharmaceuticals for the therapy and diagnosis of tumor diseases. Molecules. 2013;18:3379–409.
10. Tonacchera M, Viacava P, Agretti P, et al. Benign nonfunctioning thyroid adenomas are characterized by a defective targeting to cell membrane or a reduced expression of the sodium iodide symporter protein. J Clin Endocrinol Metab. 2002;87:352–7.
11. Pacini F, Fuhrer D, Elisei R, et al. ETA Consensus Statement: what are the indications for post-surgical radioiodine therapy in differentiated thyroid cancer? Eur Thyroid J. 2022;2022:11.
12. Tuttle RM, Ahuja S, Avram AM, et al. Controversies, consensus, and collaboration in the use of (131)I therapy in differentiated thyroid cancer: a joint statement from the American Thyroid Association, the European Association of Nuclear Medicine, the Society of Nuclear Medicine and Molecular Imaging, and the European Thyroid Association. Thyroid. 2019;29:461–70.
13. Ho AL, Dedecjus M, Wirth LJ, et al. Selumetinib plus adjuvant radioactive iodine in patients with high-risk differentiated thyroid cancer: a phase III, randomized, placebo-controlled trial (ASTRA). J Clin Oncol. 2022;40:1870–8.
14. Parghane RV, Naik C, Talole S, et al. Clinical utility of (177) Lu-DOTATATE PRRT in somatostatin receptor-positive metastatic medullary carcinoma of thyroid patients with assessment of efficacy, survival analysis, prognostic variables, and toxicity. Head Neck. 2020;42:401–16.
15. Caplin ME, Pavel M, Cwikla JB, et al. Anti-tumour effects of lanreotide for pancreatic and intestinal neuroendocrine tumours: the CLARINET open-label extension study. Endocr Relat Cancer. 2016;23:191–9.
16. Strosberg J, El-Haddad G, Wolin E, et al. Phase 3 trial of (177)Lu-Dotatate for midgut neuroendocrine tumors. N Engl J Med. 2017;376:125–35.
17. Strosberg J, Wolin E, Chasen B, et al. Health-related quality of life in patients with progressive midgut neuroendocrine tumors treated with (177)Lu-Dotatate in the phase III NETTER-1 trial. J Clin Oncol. 2018;36:2578–84.
18. Duan H, Ferri V, Fisher GA, et al. Evaluation of liver and renal toxicity in peptide receptor radionuclide therapy for somatostatin receptor expressing tumors: a 2-year follow-up. Oncologist. 2022;27:447–52.
19. Strosberg JR, Caplin ME, Kunz PL, et al. (177)Lu-Dotatate plus long-acting octreotide versus highdose long-acting octreotide in patients with midgut neuroendocrine tumours (NETTER-1): final overall survival and long-term safety results from an open-label, randomised, controlled, phase 3 trial. Lancet Oncol. 2021;22:1752–63.

20. Raj N, Coffman K, Le T, et al. Treatment response and clinical outcomes of well differentiated high grade neuroendocrine tumors to lutetium-177 DOTATATE. Neuroendocrinology. 2022;112:1177.

21. Ballal S, Yadav MP, Bal C, Sahoo RK, Tripathi M. Broadening horizons with (225)Ac-DOTATATE targeted alpha therapy for gastroenteropancreatic neuroendocrine tumour patients stable or refractory to (177)Lu-DOTATATE PRRT: first clinical experience on the efficacy and safety. Eur J Nucl Med Mol Imaging. 2020;47:934–46.

22. Ballal S, Yadav MP, Tripathi M, Sahoo RK, Bal C. Survival outcomes in metastatic gastroenteropancreatic neuroendocrine tumor patients receiving concomitant (225)Ac-DOTATATE targeted alpha therapy and capecitabine: a real-world scenario management based long-term outcome study. J Nucl Med. 2023;64(2):211–8. https://doi.org/10.2967/jnumed.122.264043

23. Frilling A, Clift AK, Braat A, et al. Radioembolisation with 90Y microspheres for neuroendocrine liver metastases: an institutional case series, systematic review and meta-analysis. HPB (Oxford). 2019;21:773–83.

24. Kratochwil C, Giesel FL, Bruchertseifer F, et al. (2)(1)(3)Bi-DOTATOC receptor-targeted alpha-radionuclide therapy induces remission in neuroendocrine tumours refractory to beta radiation: a first-in-human experience. Eur J Nucl Med Mol Imaging. 2014;41:2106–19.

25. Braat A, Bruijnen RCG, van Rooij R, et al. Additional holmium-166 radioembolisation after lutetium-177-dotatate in patients with neuroendocrine tumour liver metastases (HEPAR PLuS): a single-centre, single-arm, open-label, phase 2 study. Lancet Oncol. 2020;21:561–70.

26. Nicolas GP, Schreiter N, Kaul F, et al. Sensitivity comparison of (68)Ga-OPS202 and (68)Ga-DOTATOC PET/CT in patients with gastroenteropancreatic neuroendocrine tumors: a prospective phase II imaging study. J Nucl Med. 2018;59:915–21.

27. Wild D, Fani M, Fischer R, et al. Comparison of somatostatin receptor agonist and antagonist for peptide receptor radionuclide therapy: a pilot study. J Nucl Med. 2014;55:1248–52.

28. Reidy-Lagunes D, Pandit-Taskar N, O'Donoghue JA, et al. Phase I trial of well-differentiated neuroendocrine tumors (NETs) with radiolabeled somatostatin antagonist (177)Lu-satoreotide tetraxetan. Clin Cancer Res. 2019;25:6939–47.

29. Baum RP, Zhang J, Schuchardt C, Muller D, Macke H. First-in-humans study of the SSTR antagonist (177)Lu-DOTA-LM3 for peptide receptor radionuclide therapy in patients with metastatic neuroendocrine neoplasms: dosimetry, safety, and efficacy. J Nucl Med. 2021;62:1571–81.

30. Hicks RJ, Jackson P, Kong G, et al. (64)Cu-SARTATE PET imaging of patients with neuroendocrine tumors demonstrates high tumor uptake and retention, potentially allowing prospective dosimetry for peptide receptor radionuclide therapy. J Nucl Med. 2019;60:777–85.

31. Cullinane C, Jeffery CM, Roselt PD, et al. Peptide receptor radionuclide therapy with (67)Cu-CuSarTATE is highly efficacious against a somatostatin-positive neuroendocrine tumor model. J Nucl Med. 2020;61:1800–5.

32. Ambrosini V, Kunikowska J, Baudin E, et al. Consensus on molecular imaging and theranostics in neuroendocrine neoplasms. Eur J Cancer. 2021;146:56–73.

33. Salem R, Gordon AC, Mouli S, et al. Y90 radioembolization significantly prolongs time to progression compared with chemoembolization in patients with hepatocellular carcinoma. Gastroenterology. 2016;151:1155–1163 e1152.

34. Venerito M, Pech M, Canbay A, et al. NEMESIS: noninferiority, individual-patient metaanalysis of selective internal radiation therapy with (90)Y resin microspheres versus sorafenib in advanced hepatocellular carcinoma. J Nucl Med. 2020;61:1736–42.

35. Salem R, Johnson GE, Kim E, et al. Yttrium-90 radioembolization for the treatment of solitary, unresectable HCC: the LEGACY study. Hepatology. 2021;74:2342–52.

36. Gabr A, Kulik L, Mouli S, et al. Liver transplantation following Yttrium-90 radioembolization: 15-year experience in 207-patient cohort. Hepatology. 2021;73:998–1010.

37. Chew V, Lee YH, Pan L, et al. Immune activation underlies a sustained clinical response to Yttrium-90 radioembolisation in hepatocellular carcinoma. Gut. 2019;68:335–46.

38. Reimer P, Virarkar MK, Binnenhei M, Justinger M, Schon MR, Tatsch K. Prognostic factors in overall survival of patients with unresectable intrahepatic cholangiocarcinoma treated by means of Yttrium-90 radioembolization: results in therapy-naive patients. Cardiovasc Intervent Radiol. 2018;41:744–52.

39. Cucchetti A, Cappelli A, Mosconi C, et al. Improving patient selection for selective internal radiation therapy of intra-hepatic cholangiocarcinoma: a meta-regression study. Liver Int. 2017;37:1056–64.

40. Gupta AN, Gordon AC, Gabr A, et al. Yttrium-90 radioembolization of unresectable intrahepatic cholangiocarcinoma: long-term follow-up for a 136-patient cohort. Cardiovasc Intervent Radiol. 2022;45(8):1117–28. https://doi.org/10.1007/s00270-022-03183-2

41. Wasan HS, Gibbs P, Sharma NK, et al. First-line selective internal radiotherapy plus chemotherapy versus chemotherapy alone in patients with liver metastases from colorectal cancer (FOXFIRE, SIRFLOX, and FOXFIRE-Global): a combined analysis of three multicentre, randomised, phase 3 trials. Lancet Oncol. 2017;18:1159–71.

42. Siegel RL, Miller KD, Fuchs HE, Jemal A. Cancer statistics, 2022. CA Cancer J Clin. 2022;72:7–33.

43. Sartor O, de Bono J, Chi KN, et al. Lutetium-177-PSMA-617 for metastatic castration-resistant prostate cancer. N Engl J Med. 2021;385:1091–103.

44. Hofman MS, Emmett L, Sandhu S, et al. [(177)Lu]Lu-PSMA-617 versus cabazitaxel in patients with metastatic castration-resistant prostate cancer (TheraP): a randomised, open-label, phase 2 trial. Lancet. 2021;397:797–804.

45. Sathekge M, Bruchertseifer F, Vorster M, et al. Predictors of overall and disease-free survival in metastatic castration-resistant prostate cancer patients receiving (225)Ac-PSMA-617 radioligand therapy. J Nucl Med. 2020;61:62–9.

46. Khreish F, Ebert N, Ries M, et al. (225)Ac-PSMA-617/(177)Lu-PSMA-617 tandem therapy of metastatic castration-resistant prostate cancer: pilot experience. Eur J Nucl Med Mol Imaging. 2020;47:721–8.

47. Sathekge M, Knoesen O, Meckel M, Modiselle M, Vorster M, Marx S. (213)Bi-PSMA-617 targeted alpha-radionuclide therapy in metastatic castration-resistant prostate cancer. Eur J Nucl Med Mol Imaging. 2017;44:1099–100.

48. Kratochwil C, Schmidt K, Afshar-Oromieh A, et al. Targeted alpha therapy of mCRPC: dosimetry estimate of (213)Bismuth-PSMA-617. Eur J Nucl Med Mol Imaging. 2018;45:31–7.

49. Stenberg VY, Tornes AJK, Nilsen HR, et al. Factors influencing the therapeutic efficacy of the PSMA targeting radioligand (212)Pb-NG001. Cancers (Basel). 2022;14(11):2784. https://doi.org/10.3390/cancers14112784

50. Duan H, Baratto L, Fan RE, et al. Correlation of (68)Ga-RM2 PET with postsurgery histopathology findings in patients with newly diagnosed intermediate- or high-risk prostate cancer. J Nucl Med. 2022;63:1829–35.

51. Baratto L, Song H, Duan H, et al. PSMA- and GRPR-targeted PET: results from 50 patients with biochemically recurrent prostate cancer. J Nucl Med. 2021;62:1545–9.

52. Kurth J, Krause BJ, Schwarzenbock SM, Bergner C, Hakenberg OW, Heuschkel M. First-in-human dosimetry of gastrin-releasing peptide receptor antagonist [(177)Lu]Lu-RM2: a radiopharmaceutical for the treatment of metastatic castration-resistant prostate cancer. Eur J Nucl Med Mol Imaging. 2020;47:123–35.

53. Nock BA, Kaloudi A, Lymperis E, et al. Theranostic perspectives in prostate cancer with the gastrin-releasing peptide receptor antagonist NeoBOMB1: preclinical and first clinical results. J Nucl Med. 2017;58:75–80.

54. Gruber L, Jimenez-Franco LD, Decristoforo C, et al. MITIGATE-NeoBOMB1, a phase I/IIa study to evaluate safety, pharmacokinetics, and preliminary imaging of (68)Ga-NeoBOMB1, a gastrin-releasing peptide receptor antagonist, in GIST patients. J Nucl Med. 2020;61:1749–55.

55. Dalm SU, Bakker IL, de Blois E, et al. 68Ga/177Lu-NeoBOMB1, a novel radiolabeled GRPR antagonist

56. Gourni E, Del Pozzo L, Kheirallah E, et al. Copper-64 labeled macrobicyclic sarcophagine coupled to a GRP receptor antagonist shows great promise for PET imaging of prostate cancer. Mol Pharm. 2015;12:2781–90.

57. Huynh TT, van Dam EM, Sreekumar S, et al. Copper-67-labeled bombesin peptide for targeted radionuclide therapy of prostate cancer. Pharmaceuticals (Basel). 2022;15(6):728. https://doi.org/10.3390/ph15060728

58. Rivera-Bravo B, Ramirez-Nava G, Mendoza-Figueroa MJ, et al. [(68)Ga]Ga-iPSMA-Lys(3)-bombesin: biokinetics, dosimetry and first patient PET/CT imaging. Nucl Med Biol. 2021;96-97:54–60.

59. Sartor O, Reid RH, Hoskin PJ, et al. Samarium-153-lexidronam complex for treatment of painful bone metastases in hormone-refractory prostate cancer. Urology. 2004;63:940–5.

60. Lawal IO, Mokoala KMG, Mahapane J, et al. A prospective intra-individual comparison of [(68)Ga]Ga-PSMA-11 PET/CT, [(68)Ga]Ga-NODAGA(ZOL) PET/CT, and [(99m)Tc]Tc-MDP bone scintigraphy for radionuclide imaging of prostate cancer skeletal metastases. Eur J Nucl Med Mol Imaging. 2021;48:134–42.

61. Fernandez R, Eppard E, Lehnert W, et al. Evaluation of safety and dosimetry of (177)Lu-DOTA-ZOL for therapy of bone metastases. J Nucl Med. 2021;62:1126–32.

62. Parker C, Nilsson S, Heinrich D, et al. Alpha emitter radium-223 and survival in metastatic prostate cancer. N Engl J Med. 2013;369:213–23.

63. Morris MJ, Loriot Y, Sweeney CJ, et al. Radium-223 in combination with docetaxel in patients with castration-resistant prostate cancer and bone metastases: a phase 1 dose escalation/randomised phase 2a trial. Eur J Cancer. 2019;114:107–16.

64. Geva R, Lopez J, Danson S, et al. Radium-223 in combination with paclitaxel in cancer patients with bone metastases: safety results from an open-label, multicenter phase Ib study. Eur J Nucl Med Mol Imaging. 2019;46:1092–101.

65. Smith M, Parker C, Saad F, et al. Addition of radium-223 to abiraterone acetate and prednisone or prednisolone in patients with castration-resistant prostate cancer and bone metastases (ERA 223): a randomised, double-blind, placebo-controlled, phase 3 trial. Lancet Oncol. 2019;20:408–19.

66. Ueno NT, Tahara RK, Fujii T, et al. Phase II study of Radium-223 dichloride combined with hormonal therapy for hormone receptor-positive, bone-dominant metastatic breast cancer. Cancer Med. 2020;9:1025–32.

67. Pryma DA, Chin BB, Noto RB, et al. Efficacy and safety of high-specific-activity (131)I-MIBG therapy in patients with advanced pheochromocytoma or paraganglioma. J Nucl Med. 2019;60:623–30.

68. Satapathy S, Mittal BR, Bhansali A. Peptide receptor radionuclide therapy in the management of advanced

pheochromocytoma and paraganglioma: a systematic review and meta-analysis. Clin Endocrinol. 2019;91: 718–27.

69. Yadav MP, Ballal S, Sahoo RK, Bal C. Efficacy and safety of (225)Ac-DOTATATE targeted alpha therapy in metastatic paragangliomas: a pilot study. Eur J Nucl Med Mol Imaging. 2022;49:1595–606.

70. Mastrangelo S, Tornesello A, Diociaiuti L, et al. Treatment of advanced neuroblastoma: feasibility and therapeutic potential of a novel approach combining 131-I-MIBG and multiple drug chemotherapy. Br J Cancer. 2001;84:460–4.

71. Kraal KC, Tytgat GA, van Eck-Smit BL, Kam B, Caron HN, van Noesel M. Upfront treatment of high-risk neuroblastoma with a combination of 131I-MIBG and topotecan. Pediatr Blood Cancer. 2015;62:1886–91.

72. Ferdinandus J, Costa PF, Kessler L, et al. Initial clinical experience with (90)Y-FAPI-46 radioligand therapy for advanced-stage solid tumors: a case series of 9 patients. J Nucl Med. 2022;63:727–34.

73. Baum RP, Schuchardt C, Singh A, et al. Feasibility, biodistribution, and preliminary dosimetry in peptide-targeted radionuclide therapy of diverse adenocarcinomas using (177)Lu-FAP-2286: first-in-humans results. J Nucl Med. 2022;63:415–23.

74. Liu XQ, Fourel L, Dalonneau F, et al. Biomaterial-enabled delivery of SDF-1alpha at the ventral side of breast cancer cells reveals a crosstalk between cell receptors to promote the invasive phenotype. Biomaterials. 2017;127:61–74.

75. Lapa C, Herrmann K, Schirbel A, et al. CXCR4-directed endoradiotherapy induces high response rates in extramedullary relapsed Multiple Myeloma. Theranostics. 2017;7:1589–97.

76. Habringer S, Lapa C, Herhaus P, et al. Dual targeting of acute leukemia and supporting niche by CXCR4-directed theranostics. Theranostics. 2018;8:369–83.

77. Lapa C, Hanscheid H, Kircher M, et al. Feasibility of CXCR4-directed radioligand therapy in advanced diffuse large B-cell lymphoma. J Nucl Med. 2019;60:60–4.

78. Nautiyal A, Jha AK, Mithun S, et al. Analysis of absorbed dose in radioimmunotherapy with 177Lu-trastuzumab using two different imaging scenarios: a pilot study. Nucl Med Commun. 2021;42:1382–95.

79. Quigley NG, Steiger K, Hoberuck S, et al. PET/CT imaging of head-and-neck and pancreatic cancer in humans by targeting the "Cancer Integrin" alphavbeta6 with Ga-68-Trivehexin. Eur J Nucl Med Mol Imaging. 2022;49:1136–47.

The Next Generation of Therapeutic Radionuclides

23

Cornelia Hoehr

23.1 The Fundamentals

23.1.1 The Selection of New Therapeutic Radionuclides

Several therapeutic radionuclides are already in widespread clinical use, including ^{131}I, ^{90}Y, and ^{177}Lu. An additional cohort—notably ^{225}Ac, ^{212}Pb, and ^{211}At—is currently being explored in preclinical and clinical trials [1]. Yet beyond even these, the table of radionuclides contains many more options that could be suitable for radiopharmaceutical therapy (RPT) but are not (yet) produced in quantities sufficient for either preclinical studies or clinical trials (Fig. 23.1).

While a radiopharmaceutical labeled with a given therapeutic radionuclide—for example, [^{177}Lu]Lu-PSMA-617 (PSMA – prostate-specific membrane antigen)—works well in one patient, it may not in another. The therapeutic efficacy of a radiotherapeutic depends on the stage of the disease, the radiosensitivity of the tumor, the proximity of the tumor to other organs (especially radiosensitive ones), and whether the treatment is supposed to be curative or palliative. Ultimately, the selection of the most effective and safest radiotherapeutic for a given patient requires

good diagnostic tools and an extensive library of radionuclides for radiopharmaceuticals.

The selection of a new radionuclide for therapeutic radiopharmaceuticals is an exercise in compromise and balance. Several factors must be considered. For example, the emissions of a new radionuclide (and of any daughter radionuclides) may not entirely be known. Furthermore, nuclear data for the radionuclide may need to be measured more precisely, especially its branching ratios, the energy of its emissions, and its half-life. All this information can then be used to estimate the dose that the radiotherapeutic will deliver to the tumor and other organs (see Chap. 8).

23.1.2 Half-Lives

A core tenet in the development of targeted radiotherapeutics is the importance of considering the physical half-life of the radionuclide in the context of the biological half-life of the radiopharmaceutical as a whole. "Biological half-life" is defined as the amount of time required for 50% of a radiopharmaceutical to clear from a biological system (i.e., a patient), a process typically mediated by the hepatobiliary and renal systems. Along these lines, radionuclides with half-lives of only hours (e.g., ^{149}Tb, $t_{1/2} = 4.1$ h) are often not a good match for radiopharmaceuticals that require much longer to reach the treatment site, as most of the decay will occur before the radionuclide reaches the

C. Hoehr (✉)
Life Sciences Division, TRIUMF, Vancouver, BC, Canada
e-mail: choehr@triumf.ca

Fig. 23.1 Table of isotopes illustrated by different decay mechanisms that result in different emissions. Only a small fraction of these isotopes is currently being used for therapeutic applications, but many more radionuclides may be suitable

- ■ stable nuclides
- ■ β+, EC decay
- ■ β- decay
- ■ α decay
- ■ spontaneous fission
- ■ proton

number of protons

number of neutrons
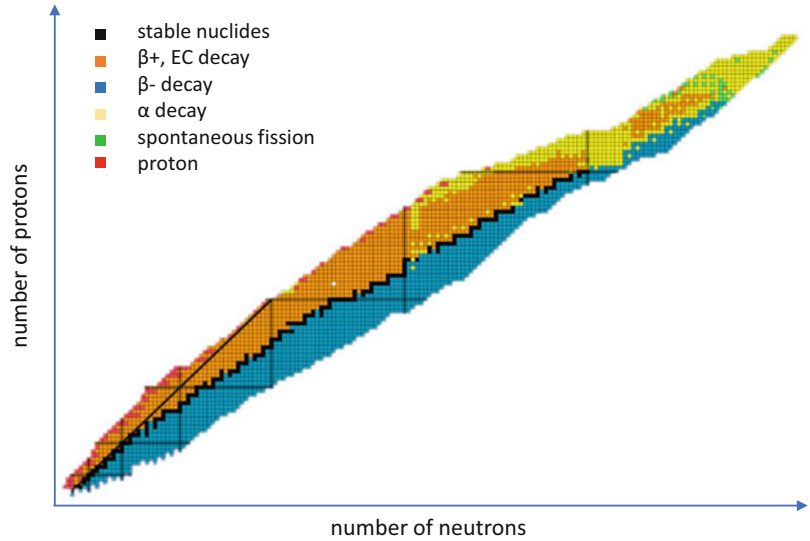
target. On the other hand, radionuclides with very long half-lives (e.g., ^{103}Pd, $t_{1/2} = 17$ days) can also be problematic with both short- and long-lived vectors. With the former, most of the radionuclide's decay may happen after excretion. With the latter, a long-lived radionuclide can result in high levels of background radiation dose to healthy tissues. Aligning these two qualities can truly be a balancing act.

23.1.3 Matching Emission to Cancer Size and Location

Any new radionuclide for a radiopharmaceutical will be chosen with a specific emission in mind, either β-particles, α-particles, or Auger electrons. Each emission exhibits a different range that influences the nature of the radiopharmaceutical itself (Fig. 23.2). A radiotherapeutic labeled with an Auger electron-emitter will most likely need to be internalized not just into the cell but also the nucleus (see Chaps. 5 and 20). In contrast, a radiotherapeutic labeled with a β-emitter will spread its damage over several cells. The range of the emission, its biological effectiveness, and how close the tracer can get to the tumor all affect the efficacy and therapeutic index of the radiotherapeutic (see Fig. 23.3) [2]. If the

- ● ionizing event
- ➡ α particle
- ● β- particle
- ⇨ Auger electron
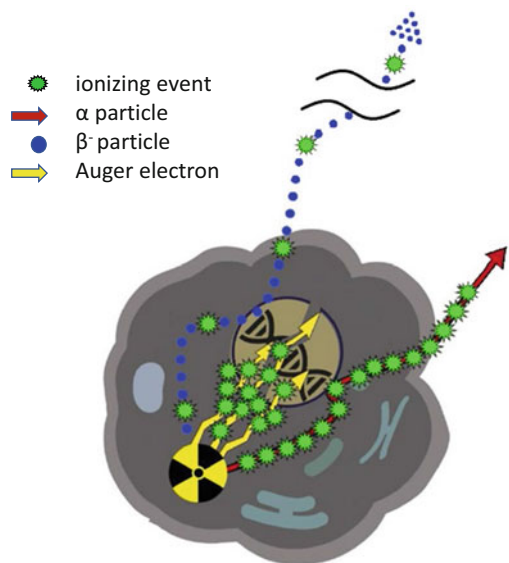
Fig. 23.2 Range of different emissions in comparison to the size of a typical cell

cytotoxicity of the radiotherapeutic is confined to only cancer cells, then higher doses can be given without damaging healthy tissue and causing immediate and long-term side effects. Widening the therapeutic index in this manner dramatically increases the chances of a successful treatment and greater quality of life for the patient.

Fig. 23.3 Visual representation of the therapeutic index. Widening the therapeutic index will allow for more damage to the tumor while maintaining or reducing damage to normal tissue
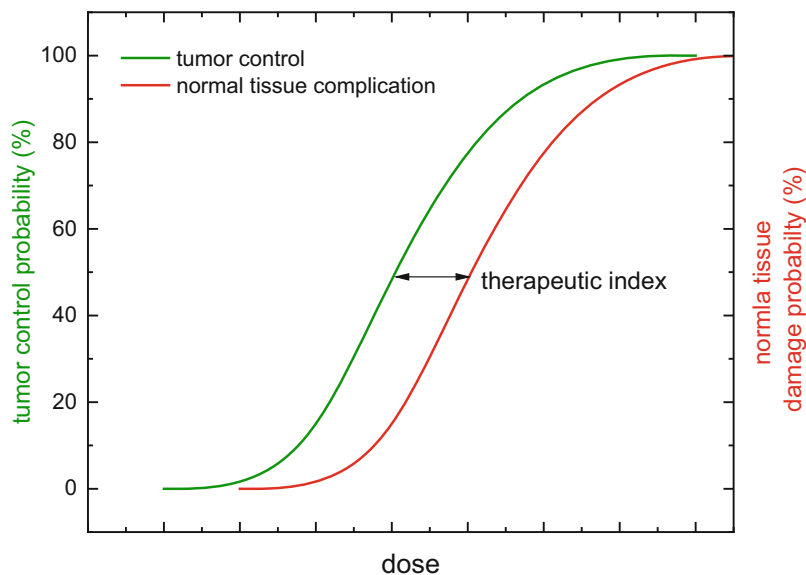
23.2 The Details

23.2.1 Considerations in the Production of New Therapeutic Radionuclides

It is important to take several issues into account during the production of therapeutic radionuclides (see Chap. 4). Each new radionuclide is different and thus needs to be assessed individually to ensure its optimal, safe, and economical production. This is particularly critical for clinical translation, as the path to the clinic is nearly impossible without a steady supply of the central radionuclide. Below we enumerate several considerations that must be balanced during the production of novel radionuclides.

23.2.2 Production Site Availability and Production Frequency

Some promising new radionuclides require large accelerators for their production. For example, ^{225}Ac is produced via the ^{232}Th(p,x)^{225}Ac reaction, which benefits from proton beams with energies >100 MeV. While a handful of sites worldwide can produce beams with such high energies—e.g., Conseil Européen pour la Recherche Nucléaire (CERN) in Switzerland [3], TRIUMF in Canada [5], Los Alamos in the USA [6], or Arronax in France [7]—the shipping radius of radionuclides can be limited by their half-lives or that of their parents (in the case of a generator-produced product). In addition, many of these sites do not operate year-round and can have lengthy planned (or unplanned) shutdown periods. This naturally limits the availability of these radionuclides.

Still other emergent radionuclides can be produced using small (<24 MeV) medical cyclotrons. There are currently hundreds of medical cyclotrons operating throughout the world, and many hospitals with nuclear medicine departments have access to one (Fig. 23.4). While this approach provides wider access to therapeutic radionuclides than high-energy reactors, it still precludes many rural and remote communities. For these areas, generator-based systems with longer-lived parent radionuclides may be the best option. In a generator, the parent radionuclide of the desired radionuclide is produced and loaded onto a column, from which the desired (daughter) radionuclide can be extracted when needed.

Fig. 23.4 Locations of cyclotrons producing medical radionuclides. Some cities have more than one cyclotron. (Data from Ref. [8])

23.2.3 Reaction Cross Section: The Pathway to Maximum Yield

A single radionuclide can often be produced via more than one pathway. ^{225}Ac, for example, can be produced from ^{232}Th via a fission reaction, using the ^{226}Ra(p,2n)^{225}Ac reaction, or via a generator loaded with ^{225}Ra. Each of these pathways have different cross sections (production probabilities), and while the pathway with the highest cross section is desirable, it may be restricted due to the nature of the target material or the equipment needed. For example, the ^{232}Th(p,x) ^{225}Ac reaction has a high cross section but requires a proton accelerator with an energy >100 MeV. In contrast, the cross section of the ^{226}Ra(p,2n)^{225}Ac reaction is much lower (16 MeV), but this pathway can be performed using a medical cyclotron.

23.2.4 Reaction Cross Sections: The Pathway to Minimal Contamination

In the context of nuclear reactions, the radionuclide that is desired is often (unfortunately) not the only radionuclide that is produced. Indeed, contaminant radionuclides can be co-produced from the same starting material or from impurities in the starting material (Fig. 23.5). These contaminants may be difficult to separate and thus lower the specific activity of the desired radiopharmaceutical and/or increase the radiation dose to the healthy tissues of the patient. In some cases, therefore, it may be necessary to discard even efficient production pathways that produce contaminants. In others, the restriction of the accelerator energy may be necessary to avoid the co-production of contaminants.

Contaminants must also be considered in the context of shipping. The useful shipping radius of a radionuclide—or its parent nuclide in the case of a generator—depends primarily on its physical half-life. However, competing decays from co-produced radionuclides may need to be factored in as well, as such contaminants may grow in over time until they comprise a fraction too large for clinical applications due to their additional dose burden.

23.2.5 Theranostic Pairs

In order to optimize the safety and efficacy of RPT, it is often necessary to perform "theranostic" imaging using a companion radiopharmaceutical

Fig. 23.5 Cross sections for the proton irradiation of ^{226}Ra to produce ^{225}Ac and (the contaminate) ^{226}Ac. (Data from Ref. [9])
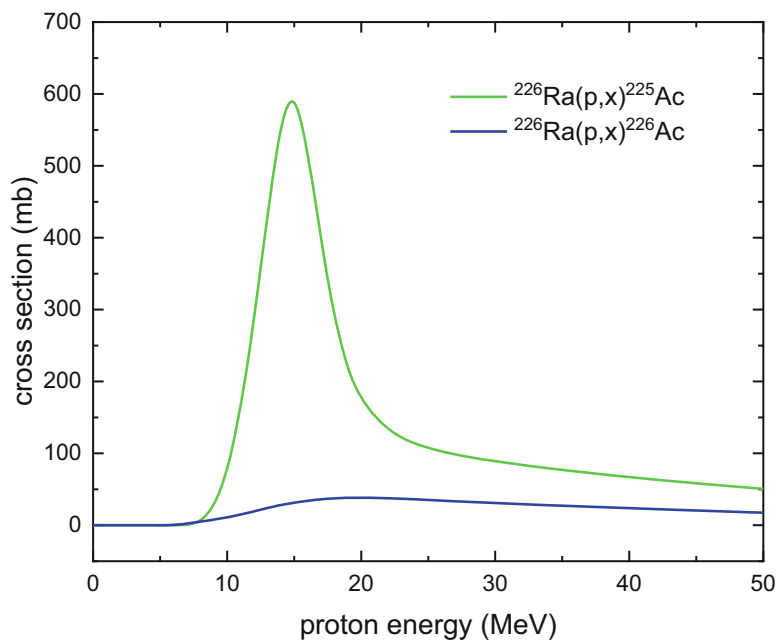
labeled with a radionuclide suitable for positron emission tomography (PET) or single photon emission computed tomography (SPECT) (see Chap. 22). The radionuclide in this theranostic partner should ideally be an isotope of the same element as the therapeutic nuclide or at least have very similar chemical properties so the radiopharmaceutical functions identically—or least very similarly—in the patient's body. This will enable the use of the imaging surrogate to help estimate the dose of the radiotherapeutic to the target organ and other healthy tissues and to monitor the delivered dose during treatment. Unfortunately, some therapeutic radiopharmaceuticals do not have "imaging partners" that are easily available. For example, an imaging partner for ^{225}Ac could be ^{226}Ac (which has emissions suitable for SPECT), but ^{226}Ac is far more difficult to produce than ^{225}Ac. A different element—for example, ^{68}Ga—can of course be chosen as a surrogate for an isotopologous pair, but this has drawbacks in terms of pharmacological behavior. When selecting a new radionuclide for RPT, all efforts should be made to choose a nuclide with a companion isotope (or at least a similar partner) that can be used for theranostic imaging.

23.2.6   Target Material Availability and Cost

When developing production methods for therapeutic radionuclides, it is also important to consider the cost and availability of the starting material. For example, what is the natural abundance of the desired starting isotope? How easy or costly is the enrichment of the target material? It is often not advisable to select a target material that can only be procured from a single company or within a single country, as it makes the production of the radionuclide vulnerable to supply chain issues and regulatory restrictions. On the other hand, the development of production methodologies for an emergent radionuclide may encourage other companies to provide the target material as well.

23.2.7   Target Material Physical and Chemical Properties

Even if a target material is inexpensive and readily available, it still faces a final hurdle as a centerpiece of a production method: its suitability

for irradiation. It may have a melting or evaporation point that would trigger a phase change in the target (although it should be noted that some targets take advantage of this very phenomenon) [10]. Alternatively, the target material may be corrosive, which would make the handling of the target inside the target holder difficult. The target material may also be challenging in the context of separations; for example, its dissolution may require large amounts of very strong acids. Moreover, it may be difficult to separate the radionuclide of interest from other nuclides (both radioactive and non-radioactive) within the target, a state of affairs that would yield a product prone to low specific activity and contamination. Finally, some target materials are themselves radioactive (e.g., ^{226}Ra, ^{232}Th), which makes storing, handling, and machining them challenging. In this scenario, the risk of contamination and down-time due to a target malfunction or a processing failure should be carefully considered.

23.2.8 Radioactive Waste

Another consideration in the production of novel radionuclides is the amount of radioactive waste that is produced during production and separation. The storage and handling of large amounts of radioactive waste—especially liquids—are costly, and this needs to be factored into the selection of a radionuclide and the methodology for its production.

23.2.9 Available Labeling Chemistry

Finally, a radiopharmaceutical labeled with a new radionuclide will have a much better chance at successful clinical translation if methods for the stable, high-yielding incorporation of the nuclide into a radiopharmaceutical are known (see Chaps. 6 and 7). This is especially a concern if the radionuclide in question does not have a stable isotope with which to test new labeling techniques. In these cases, the development of a new radiopharmaceutical can be very slow and

costly, and the anticipated benefits need to be very large to justify the undertaking.

23.3 Something Extra

Several radiopharmaceuticals labeled with new radionuclides are currently being investigated for therapeutic and theranostic applications (Fig. 23.6). These radionuclides can be divided into three categories: Auger electron-emitters, β-emitters, and α-emitters (see Tables 23.1a, 23.1b, and 23.1c).

23.3.1 Example #1: ^{197}Hg

Radiopharmaceuticals labeled with radionuclides that emit Auger electrons—or, more appropriately, "Meitner-Auger electrons" in honor of Lise Meitner's discovery [11] of this process prior to Pierre Auger [12]—are gaining popularity for RPT due to their short range of 1–20 μm and high linear energy transfer (LET) of 4–26 keV/μm [13] (see Chap. 20). One of the easiest Meitner-Auger-emitting nuclides to make on a small medical cyclotron is ^{197}Hg. The physical characteristics of ^{197}Hg are shown in Table 23.1a, and its decay scheme is illustrated in Fig. 23.7. Due to its emission of high LET Meitner-Auger electrons, the therapeutic dose of $^{197m/g}$Hg within a radius of 1 μm is 10 times higher than that of ^{177}Lu [16]. Furthermore, the ground and metastable states of ^{197}Hg combine to emit eight times more gamma rays with energies of >50 keV than ^{177}Lu, creating the possibility for theranostic imaging [15].

This therapeutic radionuclide can be made via the ^{197}Au(p,n)^{197}Hg reaction, by which both the metastable (^{197m}Hg) and ground states (^{197g}Hg) are produced simultaneously. Both cross sections are shown in Fig. 23.8, and while the cross sections are not overly high, the proton energy of the cross-section peaks is in the energy range of small medical cyclotrons. Moreover, Au is naturally 100% ^{197}Au, and the plating of Au to the desired thickness is relatively easy. One
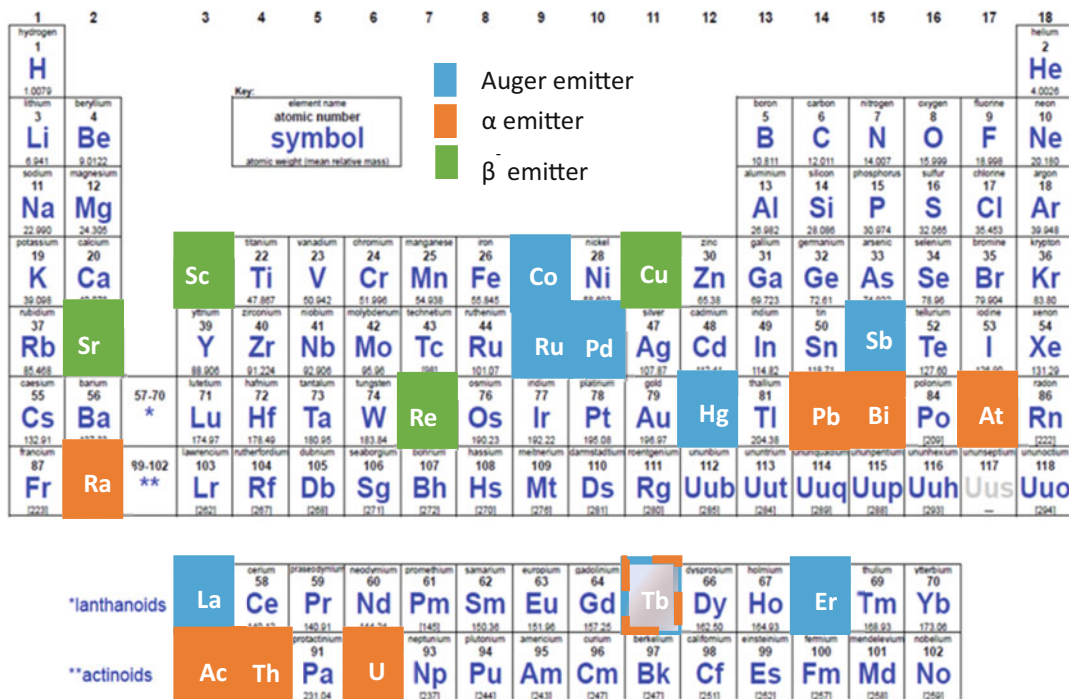
Fig. 23.6 Selection of emergent radionuclides for radiopharmaceutical therapy

Table 23.1a Examples of emergent Auger electron-emitters for targeted radionuclide therapy

Auger electron-emitters		
Radionuclide	Half-life [21]	Conversion Electron (CE) and Auger electron energy (keV) below 50 KeV [17, 20]
^{58m}Co	9.10 h	23
^{103}Pd	16.991 days	44
^{119}Sb	38.19 h	26
^{135}La	19.5 h	6.9
^{161}Tb (also β$^-$-emitter)	6.89 days	29.3
^{165}Er	10.36 h	8
^{197}Hg	64.14 h	13.4

Table 23.1b Examples of emergent β-emitters for targeted radionuclide therapy [21]

β-emitters		
Radionuclide	Half-life	Average β energy (keV)
^{47}Sc	3.3492 days	162.04
^{67}Cu	61.83 h	141.21
^{89}Sr	50.563 days	587.1
^{186}Re	3.7185 days	321.8

Table 23.1c Examples of emergent α-emitters for targeted radionuclide therapy [21]

Radionuclide			
Parent	Daughter	Half-life	Maximum α energy (MeV)
[149]Tb		4.118 h	3.9967
	[145]Pm	17.7 years	2.240
[211]At		7.214 h	5.8695
	[211]Po	0.516 s	7.450
[225]Ac		9.92 days	5.830
	[221]Fr	4.9 min	6.341
	[217]At	32.6 ms	7.0669
	[213]Bi	45.59 min	5.875
	[213]Po	3.706 μs	8.376
[227]Th		18.697 days	6.03801
	[223]Ra	11.43 days	5.8713
	[219]Rn	3.96 s	6.8191
	[215]Po	1.781 ms	7.3861
	[211]Bi	2.14 min	6.6229
[228]Th		1.9116 years	5.42315
	[224]Ra	3.6316 days	5.68537
	[220]Rn	55.6 s	6.28808
	[216]Po	0.145 s	6.7783
	[212]Bi	60.55 min	6.08988
	[212]Po	294.3 ns	8.78486
[230]U		20.23 days	5.8884
	[226]Th	30.57 min	6.3368
	[222]Ra	38 s	6.558
	[218]Rn	33.75 ms	7.1291
	[214]Po	163.46 μs	7.68682
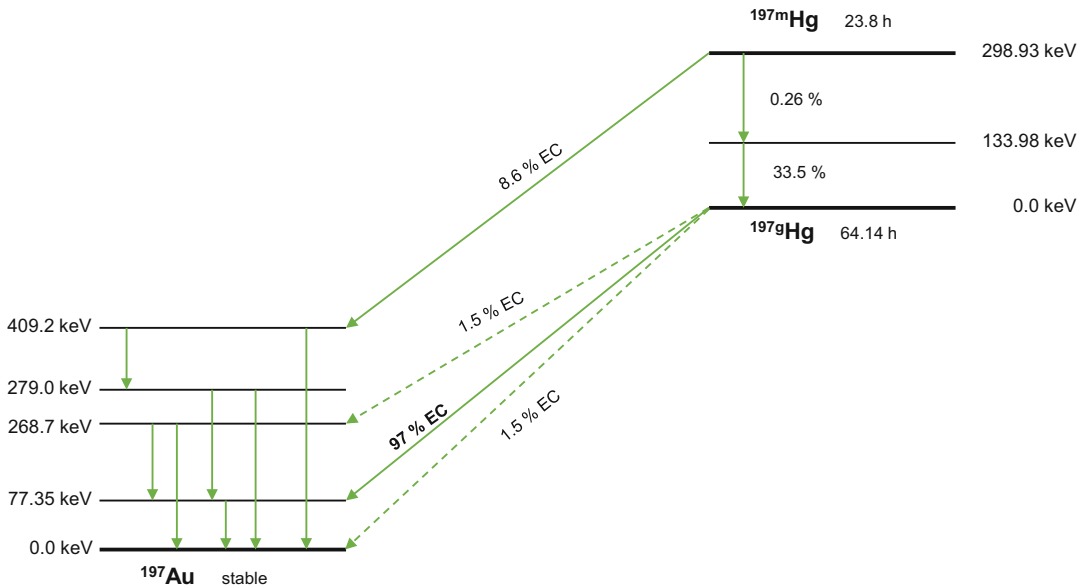
Fig. 23.7 Decay scheme of [197m,g]Hg [18]

Fig. 23.8 Cross sections for the ^{197}Au(p,n)^{197g,m}Hg reactions [9]
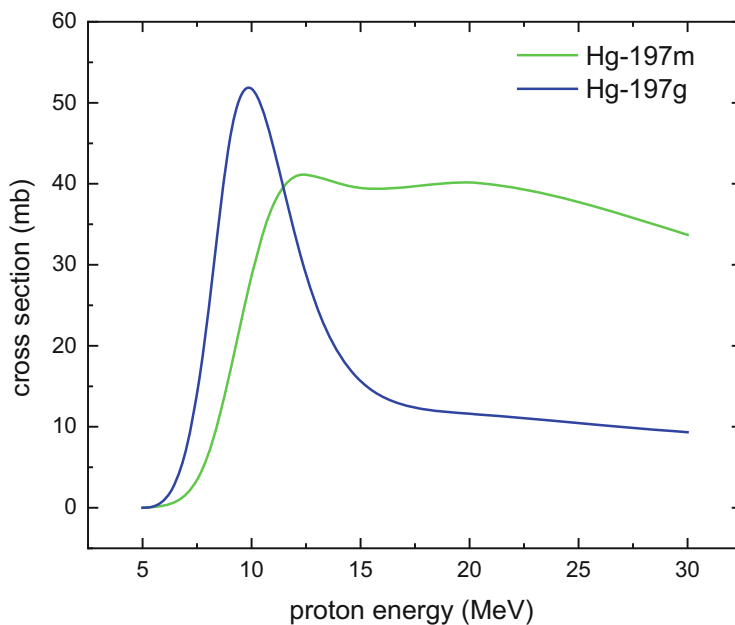
current preclinical application of ^{197}Hg is the treatment of glioblastoma using gold nanoparticles embedded with the radionuclide [14].

23.3.2   Example #2: ^{103}Pd

^{103}Pd is an interesting Auger electron-emitting candidate for RPT since it has long been used for brachytherapy [19]. ^{103}Pd has a very large Auger electron energy (Table 23.1a) and decays mainly to ^{103m}Rh (another Auger electron-emitter), though its half-life of 27 days is a bit on the long side for RPT (Fig. 23.9).

Several reaction pathways can be used to produce ^{103}Pd: ^{102}Pd(n,γ)^{103}Pd, ^{nat}Ag(p,x)^{103}Pd, ^{103}Rh(p,n)^{103}Pd, ^{103}Rh(d,2n)^{103}Pd, ^{100}Ru (α,2n)^{103}Pd, and ^{101}Ru(^{3}He,2n)^{103}Pd. The production of ^{103}Pd in a reactor via the ^{102}Pd (n,γ)^{103}Pd reaction yields a product with low specific activity due to the low abundance of ^{102}Pd. The highest accelerator-driven cross section is for the ^{nat}Ag(p,x)^{103}Pd reaction at ~70 MeV [23]. However, at this energy range, a considerable amount of ^{100}Pd (~50%) is co-produced, which is less than ideal. Thankfully,

the ^{103}Rh(p,n)^{103}Pd reaction on a medical proton cyclotron has a very large cross section at low energies, which makes production simple and convenient (Fig. 23.10). However, the dissolution of a solid, irradiated ^{103}Rh target is very difficult and time consuming, rendering processing and labeling a significant challenge. On the other hand, it is possible to irradiate ^{103}Rh nitrate in a liquid target so that the irradiated product is already in a liquid form and thus no dissolution is required [24].

23.3.3   Example #3: ^{58m}Co

^{58m}Co is yet another interesting Auger electron-emitting radionuclide with potential in RPT. It has a half-life of 9.1 h and decays to ^{58g}Co before decaying into the stable ^{58}Fe; see Table 23.1a and Fig. 23.11.

^{58m}Co can be produced via the ^{58}Fe(p,n)^{58m}Co reaction (see Fig. 23.12) from either a solid [25, 26] or liquid target [28]. The low energy threshold makes this an attractive reaction for medical cyclotrons. However, the natural abundance of ^{58}Fe is only 0.3%, making it necessary to use enriched Fe as target material. One extant
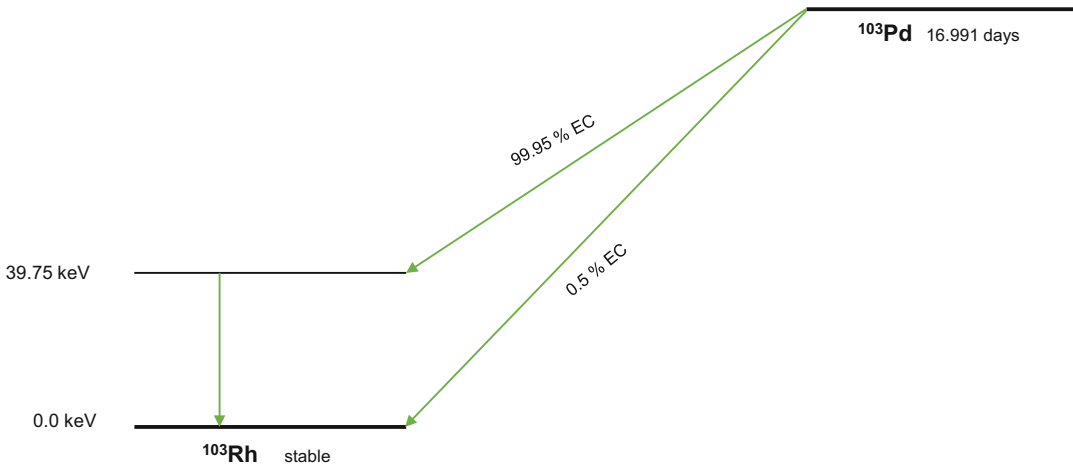
Fig. 23.9 Decay scheme of ^{103}Pd [22]

Fig. 23.10 Cross sections for the ^{103}Rh(p,n)^{103}Pd reaction [9]
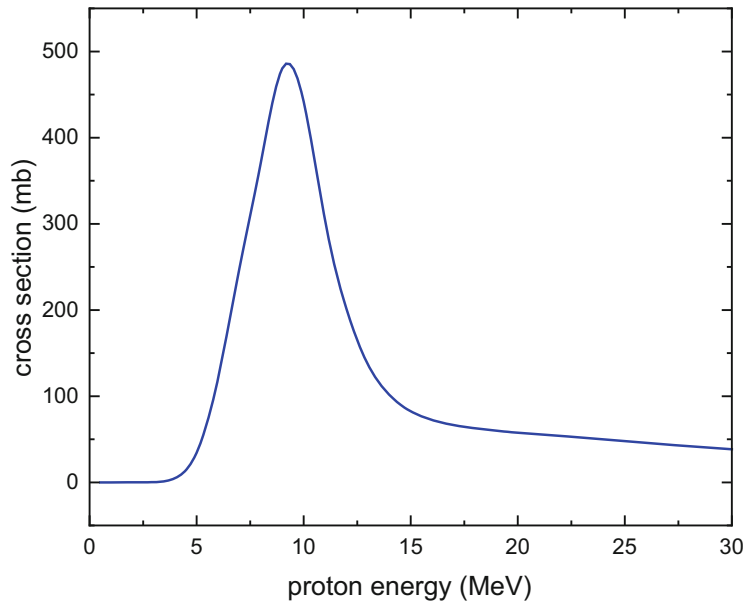
preclinical application of ^{58m}Co is the labeling of DOTATOC ($C_{65}H_{92}N_{14}O_{18}S_2$) to create a radiotherapeutic for somatostatin receptor-expressing neuroendocrine tumors [27].

23.3.4 Example #4: ^{211}At

^{211}At is an α-emitter with a half-life of 7.2 h that emits only a single α-particle during its decay to stable ^{207}Pb (see Table 23.1c and Fig. 23.13). The

nature of ^{211}At's decay abrogates worries over the redistribution of radioactive daughters that plagues radiopharmaceuticals labeled with nuclides like ^{225}Ac that have longer decay chains and emit several α-particles.

While the daughter of one of ^{211}At's decay pathways—^{211}Po—is quite toxic, its short half-life of 0.5 s means that it can only travel about two cell diameters from the initial site of decay, limiting concerns around its redistribution. The daughter of ^{211}At's other decay pathway—^{207}Bi—is a
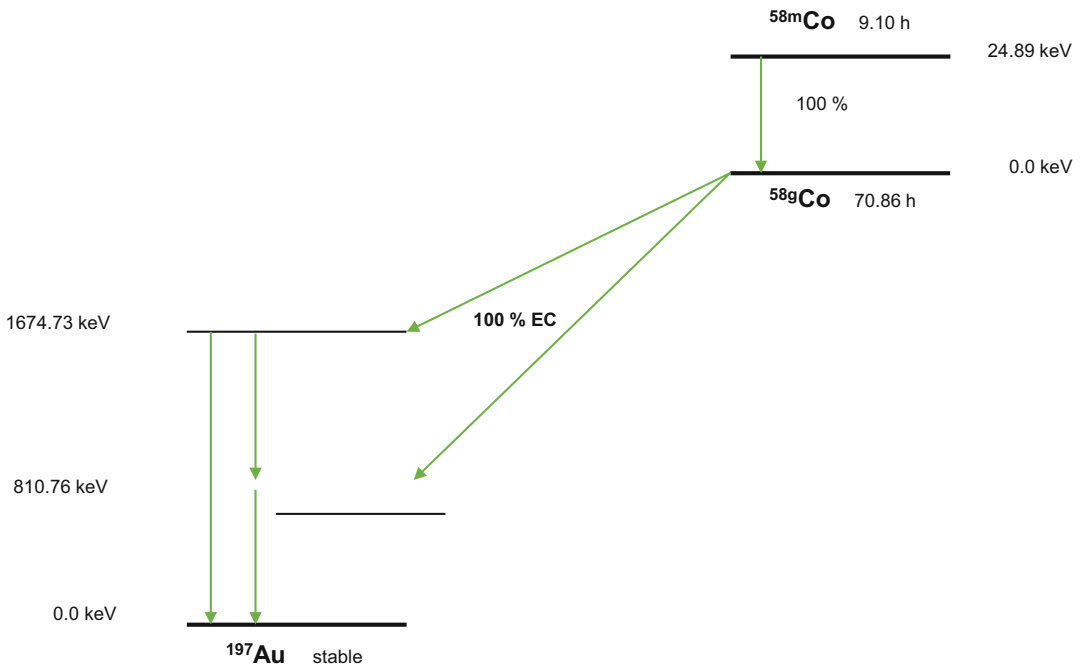
Fig. 23.11 Decay scheme of $^{58m/g}$Co [21]

Fig. 23.12 Cross section for the ^{58}Fe(p,n)^{58m}Co reaction [9]
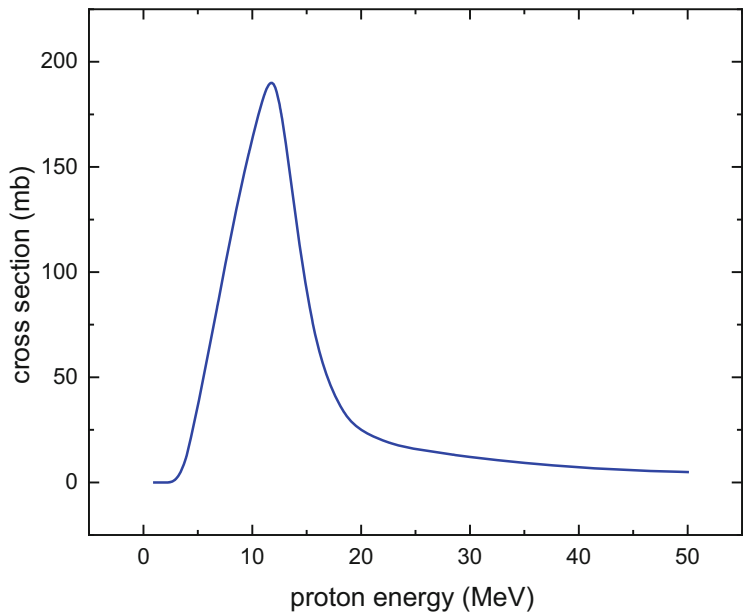
very long-lived one, so much so the burden of secondary damage from its decay is considered negligible. ^{211}At also generates Auger electrons, which might contribute to its cytotoxicity.

The chemical properties of the halogenic ^{211}At make it suitable for the labeling of radiopharmaceutical vectors ranging from small molecules to proteins. Yet despite its potential for RPT, its
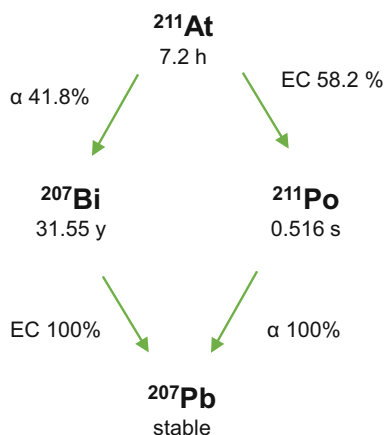
Fig. 23.13 Simplified decay change of ^{211}At. (Adapted from Ref. [29])

widespread application has been constrained by its availability [29]. The most common method for the production of ^{211}At is the ^{209}Bi$(\alpha,2n)^{211}$At reaction (see Fig. 23.14). While the target material, ^{209}Bi, is readily available, α-cyclotrons with the required energy of ~28 MeV are few and far between. As ^{210}At (which decays into the toxic ^{210}Po) is co-produced at energies >30 MeV, most production sites limit the α-beam energy to 28.4 MeV. It also should be noted that the target material, ^{209}Bi, has poor thermal conductivity and a rather low melting point (272°C), making the cooling of the target crucial. An alternative route for the production of ^{211}At is the use of a generator stocked with ^{211}Rn, which can in turn be produced via the ^{209}Bi$(^{6}$Li,4n$)^{211}$Rn reaction, the ^{209}Bi$(^{7}$Li,5n$)^{211}$Rn reaction, or the spallation of actinide target [29].

23.3.5   Example #5: ^{149}Tb

^{149}Tb is a highly promising yet scarcely used α-emitter [31]. Conveniently, Tb has a stable isotope (^{159}Tb) as well as several additional radioisotopes that could be used for other applications, e.g., ^{152}Tb for PET, ^{155}Tb for SPECT, and ^{161}Tb for β-RPT. Furthermore, ^{149}Tb itself emits 730 keV positrons with a

branching ratio of 7.1%, enabling both SPECT imaging and RPT with the same radiopharmaceutical: a true theranostic! The decay characteristics and decay scheme of ^{149}Tb are shown in Table 23.1c and Fig. 23.15.

^{149}Tb has no α-emitting daughters, eschewing ^{225}Ac's issue of having several α-emitters in its decay chain. While these additional α-emitters present the advantage of additional cytotoxicity, the recoil-energy-mediated dislocation of these daughter nuclei from the radiopharmaceutical and their subsequent redistribution throughout the body increase radiation dose to healthy tissues. This phenomenon is avoided with ^{149}Tb, but the potential radiotoxicity of its radiolanthanide daughters should be explored.

^{149}Tb can be produced via several pathways [33]. One possible route is the ^{152}Gd$(p,4n)^{149}$Tb reaction with 50 MeV protons (Fig. 23.16), although the low natural abundance of ^{152}Gd necessitates significant target enrichment. ^{149}Tb can also be produced via the ^{181}Ta(p,spall)^{149}Tb reaction, but this requires an accelerator with even higher energy and can lead to the formation of 100 s of radionuclides that must be separated via costly methods. A third option is the use of irradiation with heavy ions like ^{12}C, either via the direct ^{141}Pr$(^{12}$C,4n$)^{149}$Tb reaction or the indirect ^{142}Nd$(^{12}$C,5n$)^{149}$Dy → ^{149}Tb pathway [4].

23.4   The Future

What is the future of radiopharmaceuticals in oncology? What will a visit to an oncologist entail in the coming years or decades? Hopefully, by then a large library of radiopharmaceuticals bearing therapeutic or diagnostic radionuclides will be available. An imaging scan will clearly show which treatment will be best, and a radiopharmaceutical labeled with the optimal radionuclide for the specific patient will be selected and prescribed. During treatment, the damage to healthy tissue will be monitored via nuclear imaging, and the treatment will be adjusted accordingly to ensure the best outcome for the patient.

Fig. 23.14 Cross section for the ^{209}Bi(α,2n)^{211}At reaction [30]
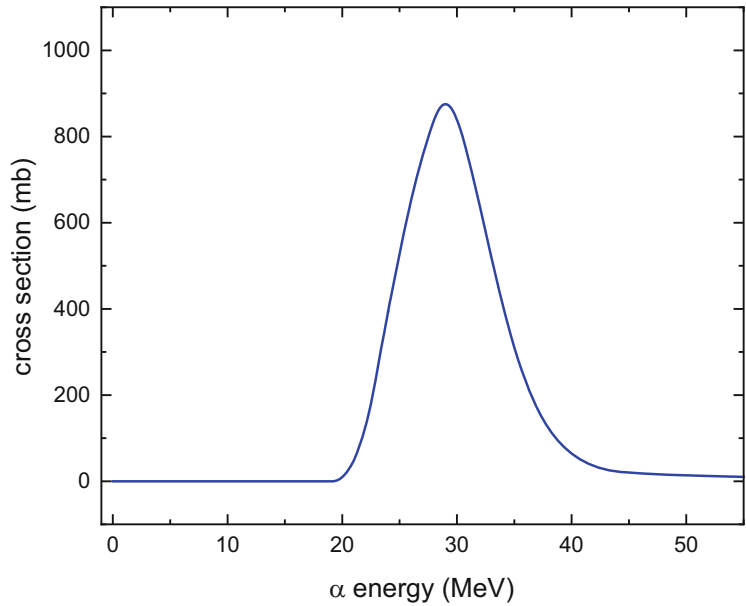
Fig. 23.15 Decay scheme of ^{149}Tb [32]
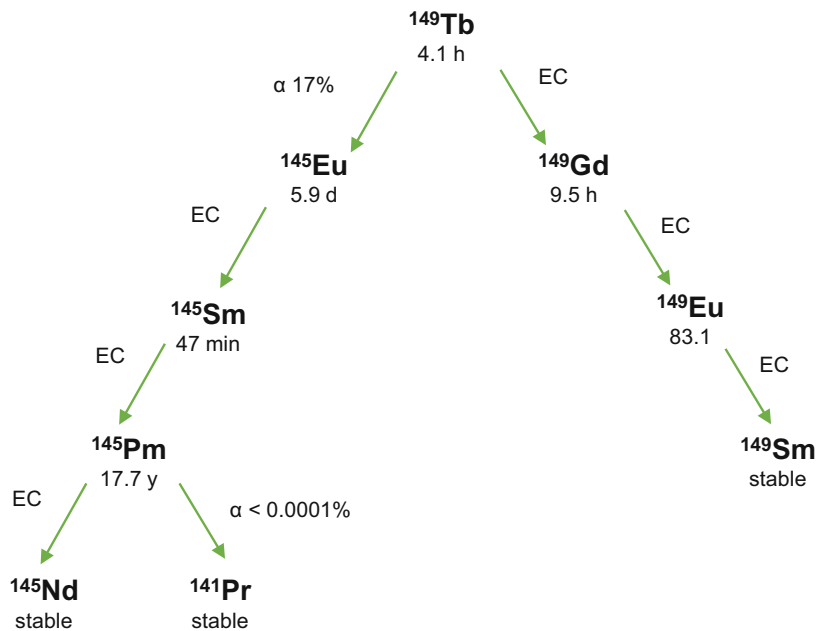
23.4.1 Combining Different Emitters

By combining different radionuclides (or emissions) into a single treatment, more complex tumors that would benefit from the characteristics of different emitters could be treated. Along these lines, radiopharmaceuticals labeled with lower LET β-emitters like ^{177}Lu and higher LET α-emitters like ^{225}Ac could be combined to treat patients with a heterogeneous tumor burden composed of both a larger primary tumor and smaller metastatic deposits. In another form, the field could reap the benefits of multiple emissions by taking advantage of a single

Fig. 23.16 Cross sections for the ^{152}Gd(p,4n)^{149}Tb reaction [9]
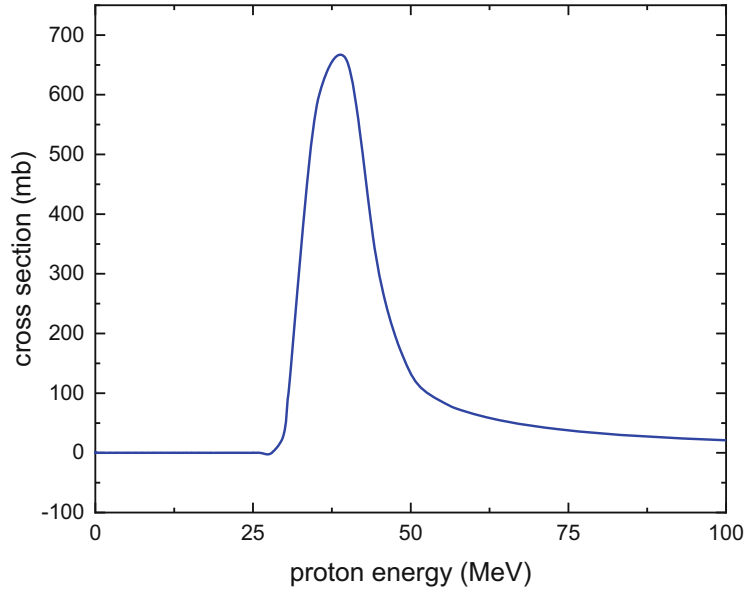
radionuclide—for example, ^{161}Tb—that emits both low LET β-particles and high LET Auger electrons.

23.4.2 Combining Different Treatment Modalities

RPT can also be combined with other forms of radiation therapy, including external-beam radiotherapy using photon, electron, proton, or heavy ion beams. One could envision treating larger tumor sites with an external beam prior to or in tandem with RPT. Furthermore, these radiopharmaceuticals could be combined with nanoparticles that—upon external or internal radiation—produce additional short-range radiation, e.g., gold nanoparticles, or release chemotherapeutics or radiation sensitizers. This approach may even lead to synergistic effects, in which the overall effect of the combination treatment is greater than the sum of the individual therapies.

23.5 The Bottom Line

- Radiopharmaceuticals labeled with emergent radionuclides will soon become available for clinical application, and many more are in the preclinical and clinical pipeline. The table of isotopes is vast, and its exploration can lead to the creation of a library of radionuclides for RPT.
- The clinical success of a radiopharmaceutical labeled with a new radionuclide depends on many factors, including the alignment of the physical half-life of the isotope and the biological half-life of the radiopharmaceutical and the nature of the radionuclide's emissions.
- A radiopharmaceutical labeled with a new radionuclide can only come into the clinic if it can be produced in reasonable quantities in an economical and reliable fashion.
- In the future, RPT will be combined with other treatment modalities, including external-beam radiotherapy and chemotherapy.

References

1. Radchenko V, Morgenstern A, Jalilian A, Ramogida C, Cutler C, Duchemin C, Hoehr C, Haddad F, Buchertseifer F, Gausemel H, Yang H, Osso J, Washiyama K, Czherwinski LK, Pruszynski M, Valzdorf O, Causey P, Schaffer P, Perron R, Maxim S, Wilbur S, Stora T, Li Y. Production and supply of alpha particles emitting radionuclides for Targeted Alpha Therapy (TAT). J Nucl Med. 2021;62:1495.
2. Rösch F. Nuclear-and radiochemistry. Berlin/Boston: Walter de Gruyter GmbH & Company, KG; 2014.
3. Burkhardt C, Bühler L, Viertl D, Stora T. New isotopes for the treatment of pancreatic cancer in collaboration with CERN: a mini review. Front Med. 2021;8:674656.
4. Beyer GJ, Čomor JJ, Daković M, Soloviev D, Tamburella C, Hagebø E, Allan B, Dmitriev SN, Zaitseva NG, Starodub G, Molokanova LG, Vranješ S, Miederer M, the ISOLDE Collaboration. Production routes of the alpha emitting ^{149}Tb for medical application. Radiochim Acta. 2002;90:247.
5. Radchenko V, Hoehr C. Modern alchemy to fight cancer. Nucl Phys News. 2020;30:28.
6. O'Brien EM, Baily S, Birnbaum E, Chapman C, Espinoza E, Faucett J, Hill J, John K, Marroquin P, McCrady R, Norman D, Nortier F, O'Hara J, Olivas E, Patten A, Pieck M, Rybarcyk L, Snyder J, Swensen E, Valicenti R, Vermeulen C, Watkins H, Woloshun K. Novel design and diagnostics improvements for the increased production capacity and improved reliability at the Los Alamos Isotope Production Facility. Nucl Instrum Methods Phys Res A. 2020;956:163316.
7. Haddad F, Barbet J, Chatal J-F. The ARRONAX project. Curr Radiopharm. 2011;4:186–96.
8. https://nucleus.iaea.org/sites/accelerators/Pages/Cyclotron.aspx. Accessed 10 May 2022.
9. Koning A, Rochman D, Sublet J, Dzysiuk N, Fleming M, van der Marck S. TENDL: complete nuclear data library for innovative nuclear science and technology. Nucl Data Sheets. 2019;155:1.
10. O'Brien E. Application and validation of multiphysics coupling to model LAs Alamos National Laboratory's Routine Production RbCl-Rb-Cl-Ga target stack. Disseration, NC State University. 2018.
11. Meitner L. Uber die Entstehung der Strahlspektren radioaktiver Substanzen. Zeitschrift fuer Physik. 1922;9:131–44.
12. Auger P. The auger effect. Surf Sci. 1975;48:1–8.
13. Randhawa P, Olson A, Chen S, Gower-Fry K, Hoehr C, Engle J, Ramogida C, Radchenko V. Meitner-Auger electron emitters for targeted radionuclide therapy: mercury-197m/g and antimony-119. Curr Radiopharm. 2021;14:394–419.
14. Georgiou C, Reilly R. unpublished results. University of Toronto, state:12.01.2022.
15. Walther M, Preusche S, Bartel S, Wunderlich G, Freudenberg R, Steinbach J, Pietzsch H-J. Theranostic mercury: 197 (m) Hg with high specific activity for imaging and therapy. Appl Radiat Isot. 2015;97:177–81.
16. Grünberg J, Lindenblatt D, Dorrer H, Cohrs S, Zhernosekov K, Köster U, Türler A, Fischer E, Schibli R. Anti-L1CAM radioimmunotherapy is more effective with the radiolanthanide terbium-161 compared to lutetium-177 in an ovarian cancer model. Eur J Nucl Med Mol Imaging. 2014;41:1907–15.
17. Ku A, Facca V, Zhongli C, Reilly R. Auger electrons for cancer therapy–a review. EJNMMI Radiopharm Chem. 2019;4:1–36.
18. Huang X, Zhou C. Nuclear data sheets for A = 197. Nucl Data Sheets. 2005;104:283–426.
19. Blasko J, Grimm P, Sylvester J, Badiozamani K, Hoak D, Cavanagh W. Palladium-103 brachytherapy for prostate carcinoma. Int J Radiat Oncol Biol Phys. 2000;46:839–50.
20. Filosofov D, Kurakina E, Radchenko V. Potent candidates for targeted auger therapy: production and radiochemical considerations. Nucl Med Biol. 2021;94-95:1–19.
21. https://www-nds.iaea.org/relnsd/vcharthtml/VChartHTML.html. Accessed Jan 2023.
22. Tárkányi F, Hermanne A, Ignatyuk A, Takács S, Capote R. Upgrade of recommended nuclear cross section data base for production of therapeutic radionuclides. J Radioanal Nucl Chem. 2022;331:1163–206.
23. Hussain M, Sudar S, Aslam N, Shah H, Ahmad R, Malik A, Qaim S. A comprehensive evaluation of charged-particle data for production of the therapeutic radionuclide Pd-103. Appl Radiat Isot. 2009;67:1842–54.
24. Krol V, Mues gennant Koers L, Kurakina E, Hoehr C, Radchenko V. ^{103}Pd production utilizing liquid target set up. WTTC18 abstract (2022).
25. Barrett KE, Houson HA, Lin W, Lapi SE, Engle JW. Production, purification, and applications of a potential Theranostic pair: Cobalt-55 and Cobalt-58m. Diagnostics. 2021;11:1235.
26. Valdovinos HF, et al. Cyclotron production and radiochemical separation of ^{55}Co and ^{58m}Co from ^{54}Fe, ^{58}Ni and ^{57}Fe targets'. Appl Radiat Isot. 2017;130:90.
27. Thisgaard H, Olesen ML, Dam JH. Radiosynthesis of ^{55}Co- and ^{58m}Co-labelled DOTATOC for positron emission tomography imaging and targeted radionuclide therapy: radiosynthesis of ^{55}Co- and ^{58m}Co-labelled DOTATOC'. J Label Compd Radiopharm. 2011;54:758.
28. Mues L, McNeil SW, Radchenko V, Paulssen E, Hoehr C. Production of Co-58m in a siphon-style liquid target on a medical cyclotron. Appl Radiat Isot. under revision.

29. Feng Y, Zalutsky M. Production, purification and availability of ^{211}At: near term steps towards global access. Nucl Med Biol. 2021;100:12.

30. https://tendl.web.psi.ch/tendl_2019/tendl2019.html. Accessed Jan 2023.

31. Müller C, Vermeulen C, Köster U, Johnston K, Türler A, Schibli R, van der Meulen N. Alpha-PET with terbium-149: evidence and perspectives for radiotheragnostics. EJNMMI Radiopharm Chem. 2016;1:5.

32. Müller C, van der Meulen N, Benesova M, Schibli R. Therapeutic radiometals beyond 177 Lu and 90 Y: production and application of promising a-particle, b2-particle, and Auger electron emitters. J Nucl Med. 2017;58(Suppl 2):91S–6S.

33. Eychenne R, Chérel M, Haddad F, Guérard F, Gestin J-F. Overview of the most promising radionuclides for targeted alpha therapy: the "hopeful eight". Pharmaceutics. 2021;13:906.

Artificial Intelligence and Machine Learning

24

Guido Rovera, Piero Fariselli, and Désirée Deandreis

24.1 The Fundamentals

24.1.1 Artificial Intelligence and Machine Learning

Machine learning (ML) is a branch of artificial intelligence (AI) that uses algorithms trained on available observations in order to predict the output of future input data. These ML models can differ greatly in terms of their complexity and predictive capabilities, and models with higher performance tend to be more complex and computationally challenging. Generally, there is also a trade-off between the performance of a model and its interpretability (i.e., the degree to which humans can understand the reasoning behind the predicted values): algorithms with better performance are usually less interpretable.

ML applications need to process large amounts of data such as medical images, histopathologic data, genetic data, laboratory test results, and patients' clinical histories. Each data point within a dataset can have a variable number of attributes or features. The number of features determines the "dimensionality" of a data point in the feature space (i.e., the n-dimensional spatial representation of the collection of properties related to the phenomenon under study). The higher the dimensionality of a dataset, the more computationally challenging it is to visualize the feature space and identify significant patterns. However, this problem can be mitigated by applying dimensionality reduction techniques to reduce the number of features. In ML, data are usually divided into three subsets: training, validation, and testing. Training data teach the model, validation data fine-tune hyperparameters (i.e., variables used to control and optimize the model learning process), and testing data measure the performance of the trained model.

Based on the availability of known outputs in the training data, ML can be classified into two main categories: supervised and unsupervised learning. "Supervised learning" refers to ML models in which the algorithms are fed data containing both the observations *and* the corresponding known output values; the knowledge derived from the training dataset can then be used to predict the classification or output value of previously unseen data points. Depending on the type of predicted outcome, supervised learning can be further divided into two main categories: (i) classification models for categorical variables, and (ii) regression models for

G. Rovera (✉)
Nuclear Medicine, Department of Medical Sciences, AOU Città della Salute e della Scienza di Torino, University of Turin, Turin, Italy
e-mail: guido.rovera@unito.it

P. Fariselli
Computational Biomedicine, Department of Medical Sciences, AOU Città della Salute e della Scienza di Torino, University of Turin, Turin, Italy

D. Deandreis
Nuclear Medicine Division, Gustave Roussy Institute, Villejuif, France

continuous output values. Examples of supervised learning include linear regression, support vector machines (SVMs), random forests, and artificial neural networks (ANNs). On the other hand, unsupervised learning models are able to identify patterns among observations with no prior knowledge of their classification or output. Unsupervised algorithms can thus be used to identify similarities or patterns among the data or to perform data compression and reduce the number of features required for outcome prediction. Examples of unsupervised ML algorithms include *k*-means clustering and principal component analysis (PCA). Fig. 24.1 illustrates a simplified classification of ML algorithms.

24.1.2 Supervised Machine Learning

24.1.2.1 K-Nearest Neighbors

K-Nearest Neighbors (kNNs) is a simple model that stores labeled data points (training data) into an *n*-dimensional feature space and then classifies new unseen observations based on the labels of a *k* number of closest neighbors (Fig. 24.2). That means that in order to classify a new case (e.g., predict the treatment outcome of a patient), the algorithm will find the K closest cases in the training dataset (i.e., the "neighbors" with similar feature values) and look at their classification (i.e., known outcomes): the classification of the new case (i.e., predicted outcome) will then be assigned based on the most frequent value among its K neighbors. Multiple metrics can be used to evaluate the distance between two data points to identify the closest neighbors such as Euclidean, Manhattan, and Minkowski. The Euclidean distance is calculated as the square root of the sum of the squared differences between two vectors, and it can be used for data points with numerical values (floating point or integer values). The Manhattan distance, on the other hand, is calculated as the sum of the absolute differences between two real-valued vectors and is preferably used for vectors in an integer feature space. Finally, the Minkowski

distance is a generalized metric that introduces a parameter *p* (called "order") that allows for different distance metrics to be calculated. When *p* is set to 1, the formula is equal to the Manhattan distance, while when *p* is set to 2, it mirrors the Euclidean distance.

Euclidean

$$d = \sqrt{\sum_{(i=1)}^{n} (x_i - y_i)^2}$$

Manhattan

$$d = \sum_{i=1}^{n} | x_i - y_i |$$

Minkowski

$$d = \left(\sum_{i=1}^{n} |x_i - y_i|^p \right)^{\frac{1}{p}}$$

Although the kNNs model has a low computational cost, it also has some limitations. Specifically, this model cannot learn to identify the most relevant parameters for the prediction of outcomes among all the available features. Therefore, the results will be highly influenced by noise. Furthermore, it scales poorly with the feature and data sizes, making it unsuitable for large or complex datasets.

24.1.2.2 Naïve Bayes Classification

The naïve Bayes classification is a supervised algorithm based on the application of the Bayesian formula for conditional probability in which features are assumed to be conditionally independent of one another. The classification of new items is performed by analyzing their features and computing the class that maximizes a likelihood function. The hyperparameters of this model are represented by the distribution mean and variance of each class. The computational cost for this model is low.

24.1.2.3 Random Forests and Gradient Boosting Frameworks

A random forest is a supervised algorithm that can be used for either classification or regression problems. This model is based on the creation of a series of decision trees by selecting random subsets of cases and features from the training dataset. When new data points are inserted into the model, the final predicted output is
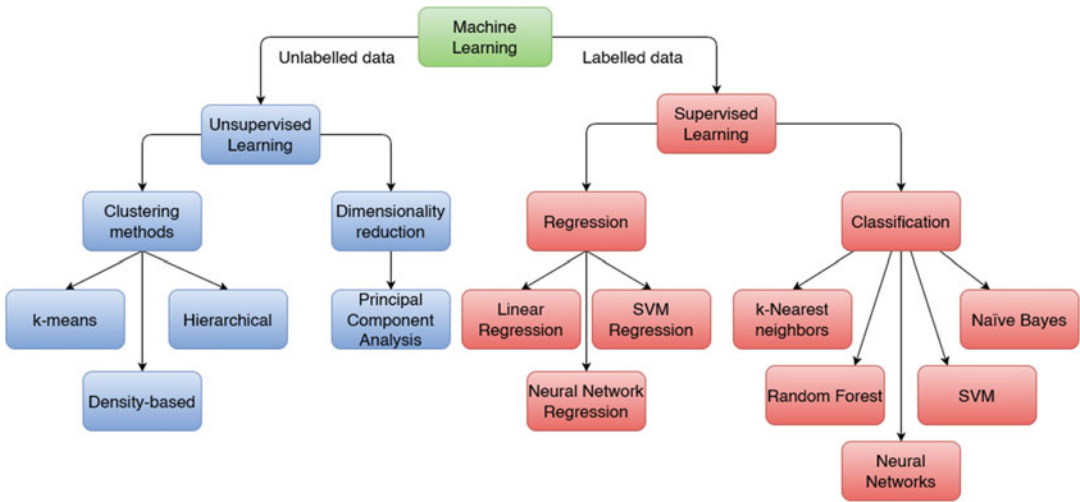
Fig. 24.1 Schematic classification of supervised and unsupervised machine learning models
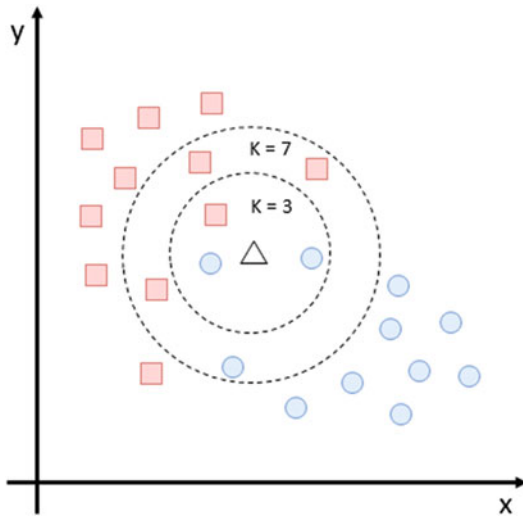
Fig. 24.2 K-nearest neighbors (kNNs) model: a new data point (triangle) is assigned to a category based on the labels of its adjacent neighbors. The results can vary depending on the selected *k*-value (hyperparameter)

represented by the most common result among all decision trees (Fig. 24.3). Model endpoints can be either a label for classification tasks or numeric for regression problems. The number of observations used to generate the decision trees is a model hyperparameter and can be fine-tuned in order to increase the model performance.

Decision trees are not only used by random forest models but also by gradient boosting frameworks. The main difference is that random forest algorithms work by building multiple deep decision trees in parallel exploiting a bagging strategy to reduce overfitting. On the contrary, gradient boosting algorithms such as XGBoost or CatBoost create a multitude of shallow decision trees (weak predictors) in a sequence and improve by learning from the errors of the previous models.

24.1.2.4 Linear Regression

Linear regression models are supervised algorithms that can be used for regression problems and are based on the identification of the *n*-dimensional hyperplane (which corresponds to a line in one dimension) that best fits a training dataset with *n*-dimensional continuous features (Fig. 24.4). The model performance can be evaluated with the mean square error or R^2 between the known outputs and the model predicted values. Regression models tend to have a low computational cost.

24.1.2.5 Support Vector Machines

A support vector machine (SVM) is a supervised algorithm that can be used for either binary
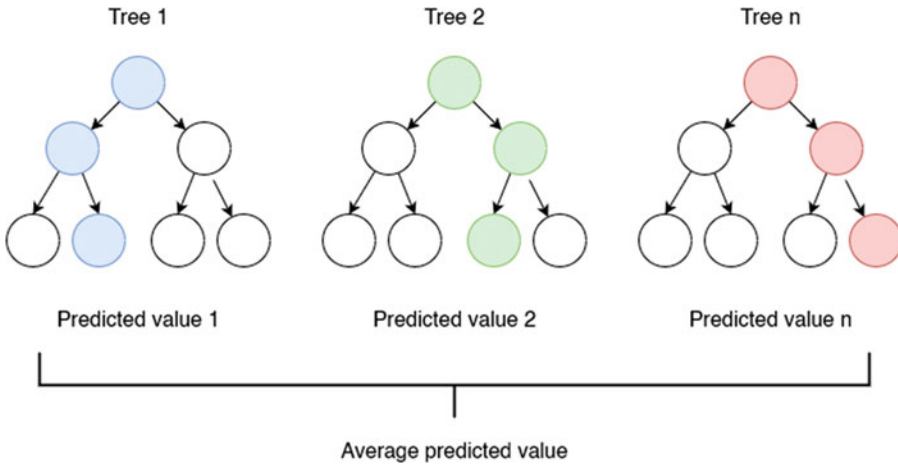
Fig. 24.3 Random forest example. Multiple decision trees are generated after randomly selecting *n* subsets of patients and *k* features from the starting dataset. New observations are then classified according to the majority decision based on the predicted values of each decision tree

Fig. 24.4 Representation of a linear regression model and a nonlinear approach. (**a**) The m_2 linear model has a better fit than the m_1 model since it minimizes the misclassification rate (cost function). (**b**) Data distribution better suited for a nonlinear approach, which reduces misclassification
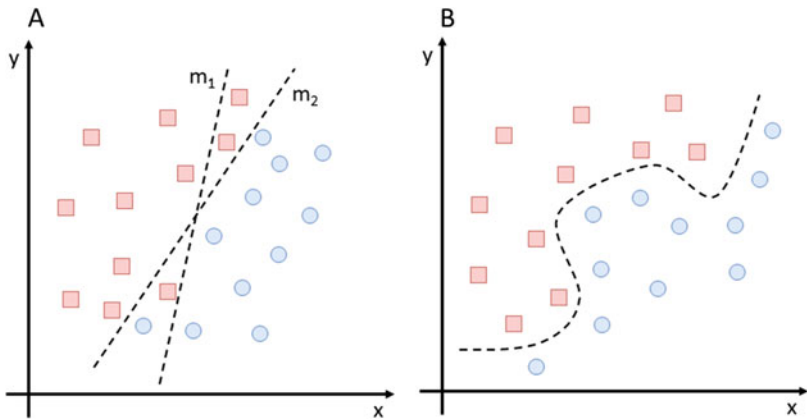
classification or regression problems. The algorithm works by identifying the curve (or hypersurface in case of multidimensional data) that best separates two classes and maximizes the distance from the closest points of each class (Fig. 24.5). After model training is completed, SVMs generally require low computational resources.

24.1.2.6 Artificial Neural Networks

Artificial neural networks (ANNs) are typically supervised models suitable for both classification and regression problems. ANNs consist of many interconnected layers of computational units (neurons) that process input data and send the output on to deeper layers, which in turn propagate the signal to the last output layer (Fig. 24.6). The computation performed at each level involves the summation of weighted inputs followed by the application of a nonlinear activation function (e.g., a sigmoidal function). The simplest ANN architecture is the "feedforward" neural network, in which the information is propagated through the layers from the input up to the output layer, and the system does not retain a memory of its past state. To learn, ANNs exploit gradient-based algorithms—known as backpropagations—a process through which

they can adjust the weights applied at each layer by taking into account the error of the generated output (i.e., the difference between the predicted outcome and the known output). Recurrent neural networks (RNNs) are a type of ANNs dedicated to analyzing sequential data since each system state derives from the combination of the previous state with the current signal.

ANNs are among the most powerful ML models, but they have a high computational cost. The number of hidden layers between the input and output layers differentiates shallow learning systems (with one or a few hidden layers) from deep neural networks (DNNs) with many hidden layers. DNNs can solve complex problems, and each DNN layer can be designed to perform a specific task (e.g., image segmentation, lesion identification). However, DNNs are also more computationally demanding due to their complex structure and require large amounts of training data. Data-augmentation procedures, image dimensionality reduction, and transfer learning techniques can be used to overcome this limitation. Finally, convolutional neural networks (CNNs) represent a type of DNNs that use convolutional layers and are suitable for image-processing applications.

24.1.3 Unsupervised Machine Learning

24.1.3.1 Principal Component Analysis

Medical applications often deal with high-dimensional data (i.e., a high number of features for each data point), as in the case of transcriptomic, metabolomic, proteomic, and other "omics" data. However, working with high-dimensional feature spaces poses some problems for both data visualization and data analysis. In order to mitigate these problems, dimensionality reduction techniques might be applied, such as principal component analysis (PCA) or a neural network-based autoencoder. Dimensionality reduction can compress and filter relevant features that can be used to reconstruct the initial data without significant data loss, while preserving the dataset variability and the relative
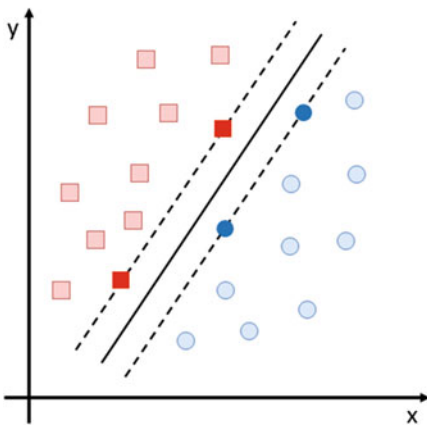
Fig. 24.5 Illustration of a support vector machine model. The solid line represents the hyperplane that maximizes the distance between the "support vectors" (solid colors), defined as the closest data points of each category

Fig. 24.6 Sample structure of an artificial neural network (ANN). Two interconnected hidden layers of four neurons (circles) separate the input and output layers
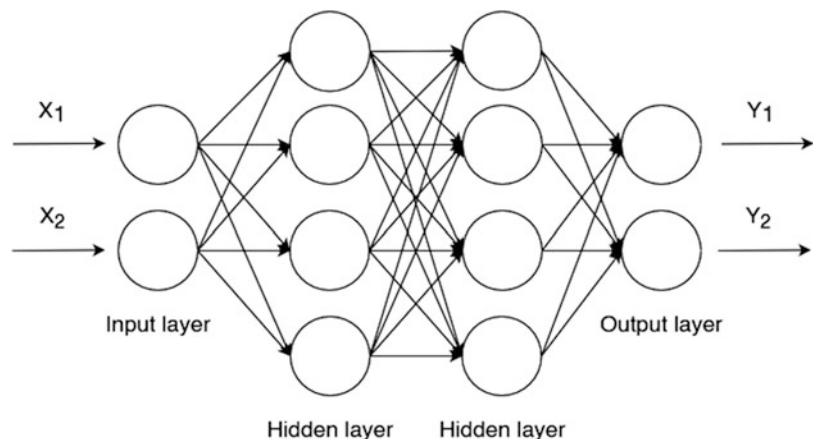
Fig. 24.7 Example of dimensionality reduction with principal component analysis (PCA). (**a**) The highest proportion of the data variability is distributed along the x_1 axis. (**b**) Data dimensionality is reduced by discarding the y_1 feature and compressing the data points along the x_1 axis
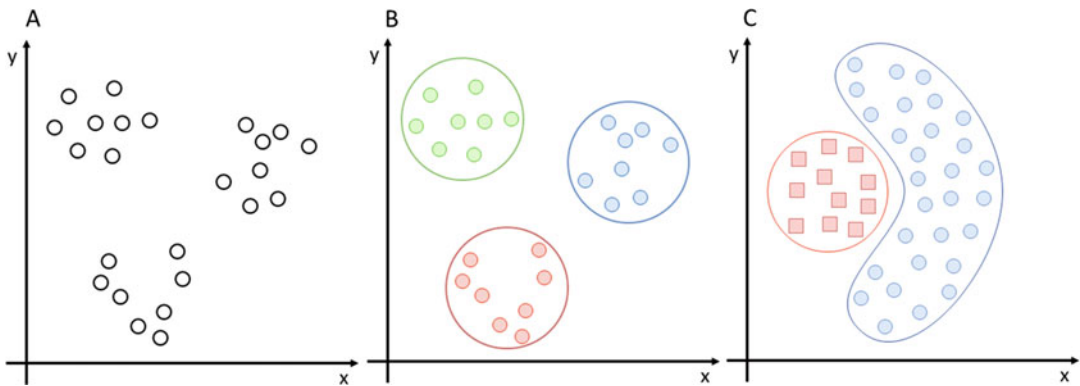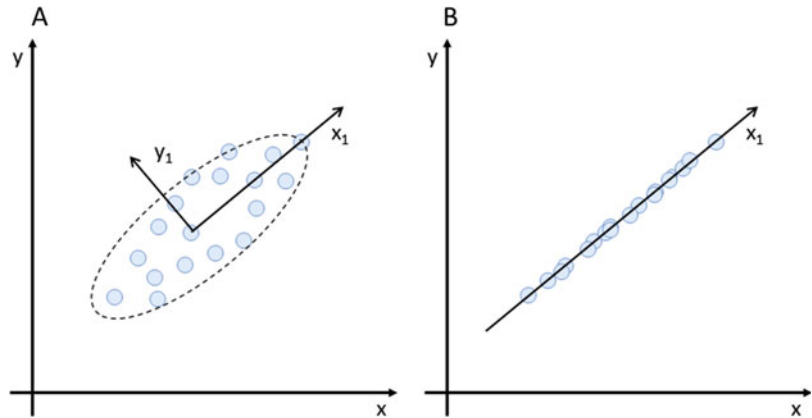
Fig. 24.8 Illustration of clustering algorithms. (**a**, **b**) Distribution of unlabeled data points in the feature space and corresponding k-means clustering classification (k-value $= 3$). (**c**) Representation of a density-based clustering approach, which allows for non-convex clustering without predefining a k-value

distances between adjacent data points (Fig. 24.7). Furthermore, dimensionality reduction can drop non-relevant features and reduce noise, thereby improving the model performance.

24.1.3.2 Clustering

Clustering algorithms group patients in disjoint sets by the similarity of the observed features. They include k-means clustering, density-based clustering, and hierarchical clustering.

K-means clustering works by randomly placing a pre-specified k number of cluster centers in the feature space and then repeatedly assigning data points to the closest cluster center. Finally, the cluster centers' positions are iteratively updated based on the newly assigned data points

until convergence is reached (Fig. 24.8, panes a, b). Despite its simplicity, k-means clustering is strongly influenced by the k parameter, which is often unknown.

Density-based clustering methods—such as density-based spatial clustering of applications with noise—do not require setting a specific number of clusters. Instead, the higher-density regions of the feature space are categorized as clusters, whereas lower-density regions are labeled as noise. Differently from k-means clustering, this approach also allows to create non-convex clusters as seen in Fig. 24.8, pane c.

Finally, hierarchical clustering works by computing the distances between all data points and then iteratively grouping the nearest data points

into pairs and clusters. The resulting tree-like structure is called a dendrogram. Hierarchical clustering is often used to analyze gene expression patterns.

24.1.4 Model Performance

The predictive accuracy of a model can be evaluated with a "cost function" or "loss function" that measures the distance of the predicted values from the known outputs. The performance of ML models also frequently depends on some parameters called "hyperparameters" that can be fine-tuned after initial setup to improve the model predictive accuracy.

24.1.4.1 Model Fitting

Model fitting is a measure of how well a machine learning model generalizes to data similar to the observations with which it was trained. A "well-fitted" model is able to accurately approximate the outcome when it is provided with new unseen input data. On the contrary, both "overfitting" and "underfitting" can lead to poor performance. Overfitting happens when a model learns from the random fluctuations and the noise present in the training data to the point that the model performance on new data is negatively affected. Indeed, since these fluctuations are not representative of the true relationships between input and output variables, this phenomenon will negatively impact the model ability to generalize. Overfitting

may occur when the model's complexity is too high or too many features selected over a small dataset. Overfitting models are also defined as having high variance. Underfitting, in contrast, refers to a model that cannot sufficiently approximate the training data and therefore cannot generalize new data. This can occur when the model is too simple or when the selected features do not have a strong predictive role. In this case, we can also talk about high bias. The underfitting/overfitting problem is also referred to as the bias/variance trade-off, since increasing the model complexity will minimize the predicted error and decrease bias but will also inevitably increase variance. The aim of model fitting is thus to estimate the best model parameters that will minimize the distance between the predicted outcomes and the actual data by minimizing the "loss function" (or "cost function").

Different metrics can be chosen to measure the predictive error of the model and find the optimal value for hyperparameters. For regression models, we typically use the mean squared error. Alternatively, optimization algorithms such as gradient descent can also be used to solve for the best parameter values by iteratively minimizing the cost function by moving in the direction of the steepest descent. For binary classification models, performance metrics can be derived from the "confusion matrix" (Fig. 24.9):

- Precision: The ratio of true positives to the total number of predicted positive values.

Fig. 24.9 Common performance metrics for binary classification problems defined on the confusion matrix

- Recall (true positive rate, TPR): The ratio of correct positive predictions to the total number of positive cases.
- False positive rate (FPR): The ratio of misclassified negative values to the total number of negative values.
- Accuracy: The number of correctly classified cases divided by the total number of cases.
- Area under the curve (AUC): Identifies the parameters that maximize the TPR and minimize the FPR.

24.1.4.2 Cross-Validation

In order to identify the best fitting algorithm, the starting dataset should be divided into three subsets: training, validation, and testing. First, the training subset is used to train multiple ML models, then the validation dataset allows to compare their performance and optimize the hyperparameters, and, finally, the selected models are tested on the test dataset to assess the generalization error (or test error). Although using a fully independent validation dataset is the gold-standard, resampling techniques such as k-fold cross-validation can be used if the sample size of the starting dataset is too low. The k-fold cross-validation method has a single hyperparameter k that corresponds to the number of groups into which the starting dataset is split (after initially putting aside a subset for final testing). For each iteration of the process, the kth group is used once for test while the remaining k-1 groups are combined to form the training dataset, as detailed in Fig. 24.10. After repeating the process k times, the performance scores obtained from each subset are averaged.

24.2 The Details

24.2.1 Radiomics: Machine Learning Applied to Biomedical Imaging

Biomedical imaging is swiftly gaining interest in the context of precision medicine thanks to the potential of radiomic analyses and machine learning techniques for the development of clinical decision support systems (CDSS). Radiomics consists in the extraction of quantitative features from medical images able to provide information on multiple tumor characteristics, such as gene expression/mutational patterns, cancer phenotype, and clinical endpoints like treatment response or prognosis.

A variety of radiomic features can be extracted from medical images, including statistical (histogram-based and texture-based), model-based, transform-based, and shape-based features. A more detailed description is provided in Panel 24.1. After features extraction, post-processing harmonization techniques can be used to balance the effect of different acquisition and reconstruction parameters on the values of radiomic features.

> **Panel 24.1: Schematic overview of radiomic features that can be extracted from medical images**
> *Histogram features* are basic statistical features that include gray-level mean/maximum/minimum, variance, standardized uptake value (SUV) max/mean/peak, and

Fig. 24.10 Illustration of the iterative process of a k-fold cross-validation technique ($k = 5$)

more complicated parameters such as skewness, kurtosis, entropy, and uniformity. For example, skewness quantifies the asymmetry of the data distribution, whereas kurtosis estimates the difference compared to a Gaussian distribution due to outliers

Texture features are based on the absolute gradient (AG), gray-level cooccurrence matrix (GLCM), gray-level run-length matrix (GLRLM), gray-level size zone matrix (GLSZM), gray-level distance zone matrix (GLDZM), neighborhood gray-tone difference matrix (NGTDM), and neighborhood gray-level dependence matrix (NGLDM). AG provides information on the fluctuations of the gray-level intensity across adjacent pixels or voxels. GLCM describes the spatial relationships of pairs of pixels or voxels with a specific gray-level intensity and a fixed distance. GLRLM and GLSZM, instead, reflect the spatial distribution of runs or groups (zones) of adjacent pixels with the same gray-level intensity in the two-dimensional (2D) or three-dimensional (3D) space. Finally, NGTDM and NGLDM express the gray-level differences between a pixel or voxel and its neighboring pixels or voxels

Model-based features are derived from parameterized models fitted to the region of interest (ROI) that depict the signal spatial shape. Examples include the autoregressive approach and fractal analysis

Transform-based features are based on image decomposition through wavelet transforms (e.g., Fourier, Gabor, and Haar). The Haar wavelet transform, for instance, uses high-pass and low-pass filters to emphasize or smooth image details

Shape-based features are used to describe geometric properties of ROIs, such as diameters, compactness, and sphericity

The extracted radiomic features often show a high degree of redundancy, and their inclusion in a predictive model would thus result in overfitting and low performance. Therefore, some of the features need to be discarded or grouped together through dimensionality reduction techniques such as principal component or linear discriminant analysis. Although radiomic features may be analyzed independently, the large amount of information contained in the whole features dataset is best suited to be analyzed as a whole through machine learning techniques. Indeed, radiomic data represent mineable high-dimensional data that can be combined with other data types (such as clinical, laboratory, histologic, and "omics" data) to discover novel disease biomarkers or molecular pathways as well as factors that are predictive or prognostic of patient outcome.

There are several areas in which machine-learning-based analysis of radiomic features extracted from molecular hybrid imaging techniques (e.g., positron emission tomography/computed tomography [PET/CT]) has shown promising results, including radiogenomic cancer profiling, tumor heterogeneity assessment, and clinical outcome prediction.

24.2.1.1 Radiogenomic Studies

Radiogenomics makes use of radiomic features to correlate imaging phenotypes to specific gene expression patterns. Unlike standard tissue sampling procedures for genomic analysis, which require an invasive approach and are limited by tumor heterogeneity, radiomics allows the simultaneous non-invasive evaluation of all tumor lesions and can account for intratumoral heterogeneity. Radiogenomic features could therefore potentially represent independent biomarkers with a predictive and prognostic value [1].

24.2.1.2 Tumor Heterogeneity Assessment

Histological tumor heterogeneity has been proposed as a prognostic factor with an impact on patient survival [2]. Indeed, tumor heterogeneity may be associated with a high mutational load

and, consequently, with a variable degree of treatment sensitivity. In this context, radiomic features can be used to evaluate intratumoral heterogeneity across the entire tumor volume through the exploration of the distribution and uptake of various radiopharmaceuticals [3, 4].

24.2.1.3 Clinical Outcome Prediction

Radiomic features have also been suggested to predict clinical endpoints, such as early treatment response [5] and patients' survival [6]. In this setting, Δ[delta]-radiomics, which quantifies the evolution of radiomic features across multiple imaging scans during treatment, is of particular interest for treatment response assessment [7]. The information provided by radiomic features could thus improve patient stratification and help clinicians select the most appropriate treatment.

Despite these promising results, radiomic analyses are also limited by some technical obstacles. First, radiomic features are influenced by image acquisition parameters and reconstruction algorithms; therefore, there is a need to standardize image acquisition protocols and develop image-processing techniques that account for inter-scanner variability. Second, radiomic features are sensitive to segmentation methods [8], and an accurate description of the segmentation process (whether manual or semi-automatic) should be provided. Moreover, researchers should disclose precise details of the radiomic features extraction process in order to ensure the reproducibility and replicability of radiomics studies. Finally, internal or external validation must be performed in order to ensure the robustness of the extracted radiomic features and the generalizability of the radiomic model.

24.2.2 Machine Learning Applications in Radiopharmaceutical Therapy

24.2.2.1 Peptide Receptor Radionuclide Therapy (PRRT)

Neuroendocrine tumors (NETs) are a heterogeneous group of malignancies and gastroenteropancreatic (GEP) NETs represent the most common subtype (up to 70% of all NETs). Based on clinical behavior, histology, and proliferation rate, NETs can be divided into well differentiated and poorly differentiated forms: this classification is highly relevant for treatment selection since poorly differentiated forms are more aggressive and are associated with a higher risk of distant metastases, faster progression, and a worse long-term prognosis. Targeted molecular imaging of somatostatin receptor expression via ^{68}Ga-based PET/CT (SSTR-PET/CT) has become a valuable diagnostic tool for accurate disease staging, and peptide receptor radionuclide therapy (PRRT) with radiolabeled somatostatin analogues represents an effective treatment strategy in the case of metastatic or inoperable NETs. Yet while PRRT is effective in most cases, up to 15–30% of patients show disease progression due to treatment resistance [9].

Currently, response assessment to PRRT is still suboptimal due to the histological heterogeneity of NETs and the variability in their expression of the somatostatin receptor. Furthermore, innovative approaches such as the neuroendocrine neoplasms test—NETest, a multianalyte liquid biopsy that measures neuroendocrine tumor gene expression in blood—are still limited by high costs and restricted availability. Therefore, the development of new quantitative imaging parameters could not only help to objectively assess PRRT response but also to identify candidates eligible for PRRT based on the predicted treatment outcome, thus avoiding the costs and toxicities of ineffective treatments.

In this context, radiomics and machine learning represent a promising approach to extract quantitative features from hybrid imaging that could support medical decisions by providing information about tumor molecular heterogeneity, the likelihood of PRRT response, and patient outcomes. In a recent study, Laudicella et al. developed a radiomic predictive model of therapy response by analyzing [68Ga] Ga-dodecane tetraacetic acid-octreotide ([^{68}Ga]Ga-DOTA-TOC) PET/CT images collected before and after [^{177}Lu]Lu-DOTA-TOC PRRT in patients with well differentiated, progressive, metastatic GEP NETs [10]. Discriminant analysis and *k*-fold

cross-validation were used to build a classification model based on 65 radiomic features automatically extracted from each lesion and 5 clinical features: tumor grading, number of PRRT cycles, PRRT cumulative activity, and chromogranin A (CgA) values before *and* after treatment. The combination of two PET features (skewness and kurtosis) and one clinical feature (grading) was able to predict the response of lesions to PRRT (progression vs stable disease or partial/complete response) with an area under the curve (AUC), sensitivity, and specificity of 0.74, 66%, and 70%, respectively. The best predictive results were achieved using the skewness feature, which had an AUC, sensitivity, and specificity of 0.75, 81%, and 67%, respectively. On the contrary, the SUV_{max} value of lesions was not a significant predictor of their response to PRRT (AUC 0.52, sensitivity 37%, specificity 63%). At Δ[delta]-radiomics analysis, PRRT response was associated with a mean reduction in skewness and an increase in kurtosis, while progression was associated with an increase in both skewness and kurtosis. The potential role of these features in predicting response to PRRT is in line with the previous evidence acquired by Önner et al. in a cohort of 22 GEP NET patients [11]. Considering 326 lesions, these 2 features were shown to have significantly higher values in non-responder patients, although with only moderate to low accuracies upon Receiver Operating Characteristic (ROC) curve analyses.

Other studies have also investigated the application of radiomics and machine learning to the prediction of response to PRRT [12, 13]. Werner and colleagues investigated the prognostic value of imaging-based heterogeneity assessment in 141 patients with NETs undergoing SSTR-PET/CT and eligible for PRRT [13]. In this study, radiomic features were shown to be significantly different between PRRT responders and non-responders, outperforming the predictive value of conventional PET parameters (e.g., SUV_{max}). Furthermore, the entropy feature was independently associated with progression-free survival (PFS) and overall survival (OS), while skewness was significantly associated with OS.

Although machine learning applications in hybrid imaging analysis have shown promising results, supervised machine learning requires large amounts of high-quality labeled data. However, accurate labeling of clinical data and medical images by experienced nuclear medicine physicians is time and resource consuming. This issue could be partially addressed by using deep convolutional generative adversarial networks (DCGANs) to perform synthetic data augmentation [14]. In DCGANs, one network continuously creates artificial images, while the other network keeps learning to discriminate between artificial and real images and performs data labeling. Therefore, DCGANs could be applied to theranostics to expand existing datasets of conventionally labeled SSTR-targeted PET/CT scans and facilitate machine learning applications.

Besides radiomic features, the analysis of gene expression patterns in pre-treatment blood samples of patients undergoing PRRT has shown great promise for discriminating between responders and non-responders [15–18]. The neuroendocrine neoplasms test (NETest) is a multianalyte liquid biopsy that measures neuroendocrine tumor gene expression in blood, providing a unique signature that precisely defines the biological activity of the tumor in real time. The NETest uses supervised machine learning algorithms—including support vector machines, linear discriminant analyses, *k*-nearest neighbors, and the naïve Bayes algorithm—to provide diagnostic, prognostic, and predictive information. To better predict the efficacy of PRRT, a combination of tumor grading and a specific variant of the NETest gene signature (encompassing growth factor signaling and metabolomic gene expression) called the "PRRT predictive quotient" (PPQ) has been developed. The PPQ reached an AUC of 0.90 ± 0.07 and an accuracy of 94% for predicting PRRT response [17], and its predictive performance was later validated in three independent PRRT-treated cohorts yielding an accuracy of 95% [18].

Machine learning techniques have also been used to personalize PRRT treatments through individualized dosimetry approaches. Götz et al.

investigated a new machine-learning-based dosimetry method to estimate the absorbed radiation dose to the kidneys in 13 patients undergoing PRRT [19]. Full whole-body Monte Carlo simulations were used to train a 3D convolutional U-Net neural network to predict dose voxel kernels (DVK) from given CT-based tissue-specific mass density kernels. The predicted DVKs were then combined with the related time-integrated activity maps to estimate the dose distribution at a voxel resolution. Overall, the deep-learning approach proved to be an accurate and reliable solution to estimate the absorbed radiation dose in critical organs such as the kidneys, showing a faster computing time and a higher spatial resolution compared to complete Monte Carlo simulations.

24.2.2.2 [^{177}Lu]Lu-PSMA-617 and [^{223}Ra] RaCl$_2$ Therapies

Radiopharmaceutical therapy (RPT) with prostate-specific membrane antigen (PSMA)-targeted radiopharmaceuticals is gaining importance in the management of patients with advanced prostate carcinoma. Specifically, [^{177}Lu]Lu-PSMA-617 is an especially promising therapeutic in patients with metastatic, castration-resistant prostate cancer (mCRPC) who have exhausted (or are ineligible for) approved alternative options and have adequate PSMA uptake on the basis of a pre-therapy imaging scan. The advantages of PSMA-based radiopharmaceuticals include high binding affinity, high internalization within tumor cells, prolonged retention time in tumor tissue, and rapid kidney clearance.

Recently, the VISION study—a prospective randomized open-label multicenter phase III study—evaluated the safety and efficacy of [^{177}Lu]Lu-PSMA-617 (7.4 GBq administered by i.v. infusion every 6 weeks for a maximum of 6 cycles) plus investigator-chosen best standard-of-care versus best standard-of-care alone [20]. According to preliminary results, RPT with [^{177}Lu]Lu-PSMA-617 significantly improved both radiographic progression-free survival (median rPFS 8.7 vs. 3.4 months) and overall survival (median OS 15.3 vs. 11.3 months) in a cohort of 831 mCRPC patients with a positive PSMA-PET scan and progression after prior taxane and androgen receptor-directed therapy (ARDT). However, up to 30% of patients showed resistance to PSMA-based RPT and could benefit from alternative treatment strategies. Therefore, efforts should be made to identify predictive factors of treatment response to [^{177}Lu]Lu-PSMA-617 in order to improve patient selection.

A retrospective analysis by Moazemi et al. investigated the use of machine learning models to predict response to treatment with [^{177}Lu]Lu-PSMA-617 based on radiomic features extracted from pre-therapeutic [^{68}Ga]Ga-PSMA-11 PET/CT scans and clinical parameters [21]. The study cohort included 83 patients with advanced prostate cancer eligible for treatment with [^{177}Lu]Lu-PSMA-617 and previously scanned with a [^{68}Ga]Ga-PSMA-11 PET/CT. Results showed that some features of both PSMA-PET and low-dose CT (first-/higher-order statistics and textural features) as well as three clinical parameters (serum alkaline phosphatase, time from first diagnosis, and Gleason score) had strong correlations with prostate-specific antigen (PSA) decrease after treatment and therefore could represent a surrogate marker of therapy response. Among the five tested machine learning algorithms—linear kernel support vector machine (SVM), polynomial kernel SVM, radial basis function (RBF) kernel SVM, extra trees, and random forest—the SVM classifiers showed the most consistent predictive performances. Specifically, the overall best accuracy scores (AUC 80%, sensitivity 75%, and specificity 75%) were obtained applying RBF SVM to the group of radiomic features and clinical parameters reported above. Overall, these results show that a machine learning approach based on [^{68}Ga]Ga-PSMA-11 PET/CT radiomic features could improve the prediction of response to treatment with [^{177}Lu]Lu-PSMA-617, leading to more accurate patient selection. However, the validation of such preliminary results in larger prospective cohorts is still needed.

Another potential application of machine learning to PSMA-targeted RPT is the development of more personalized treatments based on individualized dosimetry. As previously

mentioned, Götz et al. investigated new machine-learning-based dosimetry methods to estimate the absorbed radiation dose in the kidneys of 13 patients undergoing therapy with $[^{177}Lu]$Lu-PSMA-617 (plus 13 patients undergoing $[^{177}Lu]$Lu-DOTA-TOC therapy) [19, 22]. Overall, the deep-learning approach proved to be an accurate and reliable solution to estimate the absorbed radiation dose in critical organs compared to complete Monte Carlo simulations.

Another promising application of artificial intelligence in the field of prostate cancer RPT is the automatic segmentation of pathological lesions in biomedical images and the evaluation of their response to treatment. Artificial neural networks have been used in metastatic prostate cancer patients undergoing RPT to identify skeletal lesions and compute the bone scan index (BSI), a parameter that can quantify the extent of bone involvement and measure treatment response. In this context, Naito and colleagues evaluated the performance of automated BSI in a cohort of 20 mCRPC patients treated with $[^{223}Ra]$RaCl$_2$ [23]. Radium-223 is an alpha-emitting isotope that has been shown to improve overall survival, reduce bone pain, and delay symptomatic skeletal events in patients with metastatic castration-resistant prostate cancer (mCRPC). Automated neural-network-based BSI was proven to be a useful prognostic biomarker, with significantly longer overall survival in patients with a BSI decrease after treatment. This is in line with other literature evidence in which the BSI, calculated with a computer-assisted artificial neural network system, proved to be a significant prognostic factor in metastatic CRPC patients treated with either chemotherapy or RPT [24, 25]. Other evidence also suggests that BSI may not only be a prognostic factor but could also have a role in predicting biochemical response (measured by alkaline phosphatase reduction) to radium-223 therapy based on the pre-therapy bone scan [26].

24.2.2.3 Other Radionuclide Therapies

Artificial intelligence and machine learning techniques have also shown promising results when applied to other targeted radionuclide therapies such as the treatment of well-differentiated thyroid cancer and hyperthyroidism with iodine-131 and the hepatic radioembolization of primary and metastatic liver tumors with yttrium-90 microspheres.

24.2.2.3.1 Radioiodine [^{131}I]I Therapy

Thyroid cancer is one of the most common endocrine malignancies. Differentiated thyroid cancer (DTC) represents more than 90% of all thyroid carcinomas, with 85% of DTC being of papillary histotype. Patients with DTC generally undergo thyroidectomy followed by radioactive iodine (RAI) remnant ablation with iodine-131. Although DTC usually has an excellent prognosis following thyroidectomy and RAI therapy, some patients show RAI resistance and may benefit from different treatment strategies. The identification of factors associated with a higher risk of RAI failure may improve patient risk stratification and subsequent management.

In this context, Lubin et al. developed a machine-learning algorithm with the Python scikit-learn library to determine the clinical factors associated with a higher likelihood of RAI treatment resistance in a cohort of 107 DTC patients who underwent surgical resection and RAI treatment (mean administered activity of 105 mCi) [27]. After a mean follow-up of 15 months, 46/107 patients showed treatment failure defined as persistent elevation of thyroglobulin (Tg) values (i.e., biochemical incomplete response) or persistent loco-regional/distant metastases at follow-up imaging (e.g., RxWBSs or [^{18}F]fluorodeoxyglucose PET/CT) (i.e., anatomic incomplete response). Using a multivariable logistic regression machine learning analysis and a random forest classifier, the following clinical factors were proven to be significantly associated with RAI treatment failure: elevated serum thyroglobulin (Tg) and Tg-antibodies (TgAb) levels before RAI (relative risk [RR]: 1.82), multifocal gland disease involvement (RR: 1.73), advanced stage of disease (RR: 1.91 for lymph node involvement), and administered activities greater than 160 mCi (RR: 2.12). In addition, the machine learning approach allowed for the identification of more predictors

compared to the standard multivariate regression analysis. Specifically, pre-RAI Tg and Tg-antibody levels as well as the administered activity of iodine-131 achieved statistical significance only in the machine learning analysis. Despite the limitations of the study—its retrospective nature and the small sample size (which predisposes to overfitting issues)—these findings could help to better stratify patients for RAI treatment, thus improving their clinical management and quality of life.

Artificial intelligence applications could also be leveraged to develop clinical decision support systems (CDSS) able to guide physicians in performing evidence-based personalized treatment decisions. Watson for Oncology (WFO) is an example of an AI-based CDSS for oncological therapy selection [28]. Kim et al. investigated the accuracy of WFO in recommending postsurgical RAI therapy by comparing its concordance with physicians [29]. The overall concordance rate was only 77%, with significantly lower values in patients with American Thyroid Association (ATA) intermediate-risk and TNM stage III disease compared to those with ATA low-risk and stage I disease. Although these results do not justify the routine adoption of WFO for the screening of patients with DTC, they represent a promising starting point for future CDSS-oriented projects.

In addition to proper treatment selection and recommendation, a more accurate stratification of patients with DTC could help predict the risk of disease recurrence and identify patients that could benefit from a closer follow-up. Indeed, despite the overall good prognosis of DTC, recurrence rates between 12 and 20% have been reported for DTC, and the ATA guidelines describe several factors that can affect the risk of recurrence, including extrathyroidal extension, lymph node involvement, multifocality, and BRAF gene mutation status [30]. Kim and colleagues investigated the use of machine learning to predict the recurrence of thyroid cancer from a combination of clinical parameters: pathological information (cancer size, multiplicity, extrathyroidal extension, nodal involvement, presence of thyroiditis), genetic information

(BRAF gene mutation), laboratory test results (free thyroxine [fT4], thyroid stimulating hormone [TSH], Tg, TgAb, anti-thyroid peroxidase antibodies [anti-TPOAb] before and after surgery), and RAI treatment data [31]. Inductive logic programming (ILP) was applied to a dataset comprised of 785 patients with DTC treated with total thyroidectomy and RAI with a minimum follow-up of at least 5 years. This technique allowed to identify 8 rules to predict the recurrence of DTC, which showed an average accuracy of 95%. In the validation group, the computed algorithm correctly predicted 71% of positive cases and 98% of negative cases. However, despite these promising results, similar predictive tools will first need to undergo extensive validation before routine clinical use.

Similarly to previous studies, machine learning techniques have also been applied to the investigation of hyperthyroid patients treated with RAI. Recently, Duan et al. tested a series of machine learning algorithms for predicting early post-RAI hypothyroidism (<6 months after treatment) in a cohort of 471 patients with Graves' disease (GD) treated with calculated activities of iodine-131 (based on ultrasound determination of the thyroid volume and iodine uptake) [32]. Out of 138 tested clinical and laboratory features, a multivariate model based on age, thyroid mass, 24 h radioactive iodine uptake (RAIU), aspartate aminotransferase (AST), TRAb, thyroid microsomal antibodies (TMA), and neutrophil count demonstrated an AUC of 0.72 (accuracy 71%, sensitivity 75%, specificity 76%) in the training set and an AUC of 0.74 in the validation set (accuracy 71%, sensitivity 71%, specificity 74%). Overall, GD patients with early post-RAI hypothyroidism were found to have significantly higher age, TRAb, TMA, and AST but lower RAIU, thyroid mass, and neutrophil count.

Finally, other potential applications of machine learning in the field of radioactive iodine therapy include the use of artificial neural networks for the automatic recognition of [^{131}I] I-avid lymph nodes on post-ablation whole-body planar scans (RxWBSs) [33] and the prediction of the radiation exposure of patients' family members and caregivers [34].

24.2.2.3.2 Yttrium-90 Radioembolization

Transarterial radioembolization is an effective loco-regional approach for primary and metastatic liver tumors based on the injection of ^{90}Y-containing microspheres into selected hepatic arteries. Pre-treatment planning includes a single-photon emission computed tomography (SPECT/CT) scan after the transarterial injection of ^{99m}Tc-labeled macroaggregated albumin (MAA) to estimate the distribution of the dose in both the tumorous and healthy liver (and to quantify any lung shunt or extrahepatic leak). Post-treatment absorbed dose evaluation is performed using positron emission tomography (^{90}Y-PET/CT).

Currently, treatment protocols cannot accurately predict the dose distribution since they are based on simplified dosimetry methods (partition model and medical internal radiation dose [MIRD] formalism) that assume a uniform yttrium-90 distribution and do not consider patient-specific parameters or potential discrepancies between the distributions of the ^{99m}Tc-MAA and ^{90}Y-microspheres. In order to improve treatment planning, Plachouris et al. investigated the use of a deep-learning model (generative adversarial network [GAN]) to predict the biodistribution of ^{90}Y-microspheres and the absorbed dose in tumorous/healthy liver tissues on the basis of the pre-treatment ^{99m}Tc-MAA SPECT/CT scan [35]. Comparing the real and predicted data, the machine learning model showed an overall good predictive accuracy with average differences of $5.4 \pm 19.3\%$ (8.0 ± 31.4 Gy) and $0.4 \pm 1.6\%$ (0.03 ± 0.3 Gy) for the tumor and the whole liver parenchyma absorbed doses, respectively.

Other potential approaches to improve treatment planning include computational fluid dynamics (CFD) simulations of the hepatic arterial tree [36]. However, similar applications are still limited by their high computational cost. To address this issue, Taebi et al. trained a convolutional neural network model with the CFD results of a patient with hepatocellular carcinoma: the model proved to be significantly faster than CFD simulations in predicting the distribution of yttrium-90, with an average difference between the actual and predicted data lower than 1% [37].

Finally, machine learning techniques have also been used for prognostic stratification of patients treated with yttrium-90 radioembolization. Ingrisch et al. implemented a random forest model to identify prognostic factors for the outcome of yttrium-90 radioembolization based on pre-therapeutic clinical parameters [38]. Among the collected clinical data—cholinesterase, bilirubin, type of primary tumor, age at radioembolization, hepatic tumor burden, presence of extrahepatic disease, and sex—the random forest survival analysis allowed to identify a stronger prognostic role for baseline cholinesterase and bilirubin.

24.3 Something Extra

24.3.1 Open Issues

Machine learning has opened the path toward new approaches for the analysis of medical data and hybrid images (e.g., PET/CT or PET/MR). However, several issues still need to be addressed before its potential application in routine clinical practice. First, machine learning models need to be trained on large volumes of high-quality data. Extensive access to electronic medical records is therefore essential, and privacy regulations need to be reconciled with the need to collect large amounts of medical data. Second, the presence of outliers, missing data, or biases in the training dataset can negatively impact the generalization capability of models. While missing data replacement and over-/under-sampling techniques can help mitigate this problem, such approaches could also lead to overfitting issues. Another problem is the lack of reproducibility of machine learning models when they are applied across different institutions due to the absence of standardized protocols for the acquisition of images and structured procedures for the validation of models and the assessment of generalizability. Finally, a clear legal framework will need to be defined to ensure the safe development and

usage of machine learning systems, and both clinicians and patients will need to understand the intrinsic limitations of these highly complex and not interpretable algorithms.

24.4 The Future

24.4.1 Future Perspectives

Nuclear medicine has grown to play a key role in the diagnostic work-up and treatment of numerous cancers thanks to the continuous development of new radiopharmaceuticals for functional molecular imaging and targeted therapy. The potential role of nuclear imaging (i.e., radiomic features) as an independent biomarker is a good complement to the new possibilities offered by technologies such as big data and artificial intelligence/machine learning, which are particularly well suited for integrating and analyzing different types of data, including biomedical imaging, clinical histories, omics data, laboratory test results, and environmental exposure.

As we have discussed, in the field of radiopharmaceutical therapy, machine learning models have been shown to increase lesion detection, improve the baseline risk stratification for patients, individualize treatment planning, identify predictive factors of treatment response, and discover prognostic factors. All these capabilities of artificial intelligence should be leveraged in the development of "Clinical Decision Support Systems" (CDSS), electronic systems designed to aid physicians in the decision-making process by considering multiple factors, such as the individual characteristics of patients, the cost-effectiveness of treatments, the quality of life of patients, and the risk of adverse reactions. Moreover, the wider diffusion of machine learning applications will also foster a cultural change in physicians toward a data-science approach, leading to closer and more effective collaborations with data scientists.

Although the patient–doctor relationship will always be the cornerstone of care delivery, the quality and cost-effectiveness of medical care is likely to improve in the future thanks to the integration of the insights obtained from machine learning and clinical decision support systems into clinicians' workflows.

24.5 The Bottom Line

- Machine learning (ML) models are trained on available observations in order to predict the output of future input data.
- The ability of ML models to process large volumes of heterogeneous data holds great potential in the fields of theranostics and radiopharmaceutical therapy.
- ML models have shown promising results in predicting the response of neuroendocrine tumors to ^{177}Lu-PRRT based on pre-/post-therapy PET/CT imaging with [^{68}Ga]Ga-DOTA-TOC or [^{68}Ga]Ga-DOTA-octreotate.
- ML models have been used to predict the response of patients with metastatic castration-resistant prostate cancer to treatment with [^{177}Lu]Lu-PSMA-617 based on radiomic features extracted from pre-therapeutic [^{68}Ga]Ga-PSMA-11 PET/CT scans.
- ML could guide the development of "Clinical Decision Support Systems" (CDSS) that could aid physicians in the decision-making process.
- In the future, structured procedures to validate ML models and assess their generalizability will need to be defined.

References

1. Park Y-J, Shin MH, Moon SH. Radiogenomics based on PET imaging. Nucl Med Mol Imaging. 2020;54:128–38. https://doi.org/10.1007/s13139-020-00642-x.
2. Morris LGT, Riaz N, Desrichard A, Şenbabaoğlu Y, Hakimi AA, Makarov V, et al. Pan-cancer analysis of intratumor heterogeneity as a prognostic determinant of survival. Oncotarget. 2016;7:10051–63. https://doi.org/10.18632/oncotarget.7067.
3. Lee JW, Lee SM. Radiomics in oncological PET/CT: clinical applications. Nucl Med Mol Imaging. 2018;52:170–89. https://doi.org/10.1007/s13139-017-0500-y.
4. Bailly C, Bodet-Milin C, Bourgeois M, Gouard S, Ansquer C, Barbaud M, et al. Exploring tumor heterogeneity using PET imaging: the big picture. Cancers

(Basel). 2019;11:E1282. https://doi.org/10.3390/cancers11091282.

5. Chetan MR, Gleeson FV. Radiomics in predicting treatment response in non-small-cell lung cancer: current status, challenges and future perspectives. Eur Radiol. 2021;31:1049–58. https://doi.org/10.1007/s00330-020-07141-9.

6. Arshad MA, Thornton A, Lu H, Tam H, Wallitt K, Rodgers N, et al. Discovery of pre-therapy 2-deoxy-2-18F-fluoro-D-glucose positron emission tomography-based radiomics classifiers of survival outcome in non-small-cell lung cancer patients. Eur J Nucl Med Mol Imaging. 2019;46:455–66. https://doi.org/10.1007/s00259-018-4139-4.

7. Carles M, Fechter T, Radicioni G, Schimek-Jasch T, Adebahr S, Zamboglou C, et al. FDG-PET radiomics for response monitoring in non-small-cell lung cancer treated with radiation therapy. Cancers (Basel). 2021;13:814. https://doi.org/10.3390/cancers13040814.

8. Liberini V, De Santi B, Rampado O, Gallio E, Dionisi B, Ceci F, et al. Impact of segmentation and discretization on radiomic features in 68Ga-DOTA-TOC PET/CT images of neuroendocrine tumor. EJNMMI Phys. 2021;8:21. https://doi.org/10.1186/s40658-021-00367-6.

9. Strosberg J, El-Haddad G, Wolin E, Hendifar A, Yao J, Chasen B, et al. Phase 3 trial of 177Lu-Dotatate for midgut neuroendocrine tumors. N Engl J Med. 2017;376:125–35. https://doi.org/10.1056/NEJMoa1607427.

10. Laudicella R, Comelli A, Liberini V, Vento A, Stefano A, Spataro A, et al. [68Ga]DOTATOC PET/CT Radiomics to predict the response in GEP-NETs undergoing [177Lu]DOTATOC PRRT: the "Theragnomics" concept. Cancers (Basel). 2022;14:984. https://doi.org/10.3390/cancers14040984.

11. Önner H, Abdülrezzak Ü, Tutuş A. Could the skewness and kurtosis texture parameters of lesions obtained from pretreatment Ga-68 DOTA-TATE PET/CT images predict receptor radionuclide therapy response in patients with gastroenteropancreatic neuroendocrine tumors? Nucl Med Commun. 2020;41:1034–9. https://doi.org/10.1097/MNM.0000000000001231.

12. Liberini V, Rampado O, Gallio E, De Santi B, Ceci F, Dionisi B, et al. 68Ga-DOTATOC PET/CT-based radiomic analysis and PRRT outcome: a preliminary evaluation based on an exploratory radiomic analysis on two patients. Front Med (Lausanne). 2020;7:601853. https://doi.org/10.3389/fmed.2020.601853.

13. Werner RA, Lapa C, Ilhan H, Higuchi T, Buck AK, Lehner S, et al. Survival prediction in patients undergoing radionuclide therapy based on intratumoral somatostatin-receptor heterogeneity. Oncotarget. 2017;8:7039–49. https://doi.org/10.18632/oncotarget.12402.

14. Doman K, Konishi T, Mekada Y. Lesion image synthesis using DCGANs for metastatic liver cancer detection. Adv Exp Med Biol. 2020;1213:95–106. https://doi.org/10.1007/978-3-030-33128-3_6.

15. Bodei L, Schöder H, Baum RP, Herrmann K, Strosberg J, Caplin M, et al. Molecular profiling of neuroendocrine tumours to predict response and toxicity to peptide receptor radionuclide therapy. Lancet Oncol. 2020;21:e431–43. https://doi.org/10.1016/S1470-2045(20)30323-5.

16. Liberini V, Huellner MW, Grimaldi S, Finessi M, Thuillier P, Muni A, et al. The challenge of evaluating response to peptide receptor radionuclide therapy in gastroenteropancreatic neuroendocrine tumors: the present and the future. Diagnostics (Basel). 2020;10:E1083. https://doi.org/10.3390/diagnostics10121083.

17. Bodei L, Kidd M, Modlin IM, Severi S, Drozdov I, Nicolini S, et al. Measurement of circulating transcripts and gene cluster analysis predicts and defines therapeutic efficacy of peptide receptor radionuclide therapy (PRRT) in neuroendocrine tumors. Eur J Nucl Med Mol Imaging. 2016;43:839–51. https://doi.org/10.1007/s00259-015-3250-z.

18. Bodei L, Kidd MS, Singh A, van der Zwan WA, Severi S, Drozdov IA, et al. PRRT genomic signature in blood for prediction of 177Lu-octreotate efficacy. Eur J Nucl Med Mol Imaging. 2018;45:1155–69. https://doi.org/10.1007/s00259-018-3967-6.

19. Götz TI, Lang EW, Schmidkonz C, Kuwert T, Ludwig B. Dose voxel kernel prediction with neural networks for radiation dose estimation. Z Med Phys. 2021;31:23–36. https://doi.org/10.1016/j.zemedi.2020.09.005.

20. Sartor O, de Bono J, Chi KN, Fizazi K, Herrmann K, Rahbar K, et al. Lutetium-177-PSMA-617 for metastatic castration-resistant prostate cancer. N Engl J Med. 2021;385:1091–103. https://doi.org/10.1056/NEJMoa2107322.

21. Moazemi S, Erle A, Khurshid Z, Lütje S, Muders M, Essler M, et al. Decision-support for treatment with 177Lu-PSMA: machine learning predicts response with high accuracy based on PSMA-PET/CT and clinical parameters. Ann Transl Med. 2021;9:818. https://doi.org/10.21037/atm-20-6446.

22. Götz TI, Schmidkonz C, Chen S, Al-Baddai S, Kuwert T, Lang EW. A deep learning approach to radiation dose estimation. Phys Med Biol. 2020;65:035007. https://doi.org/10.1088/1361-6560/ab65dc.

23. Naito M, Ukai R, Hashimoto K. Bone scan index can be a useful biomarker of survival outcomes in patients with metastatic castration-resistant prostate cancer treated with radium-223. Cancer Rep (Hoboken). 2019;2:e1203. https://doi.org/10.1002/cnr2.1203.

24. Mitsui Y, Shiina H, Yamamoto Y, Haramoto M, Arichi N, Yasumoto H, et al. Prediction of survival benefit using an automated bone scan index in patients with castration-resistant prostate cancer. BJU Int. 2012;110:E628–34. https://doi.org/10.1111/j.1464-410X.2012.11355.x.

25. Anand A, Trägårdh E, Edenbrandt L, Beckman L, Svensson J-H, Thellenberg C, et al. Assessing radiographic response to 223Ra with an automated bone scan index in metastatic castration-resistant prostate cancer patients. J Nucl Med. 2020;61:671–5. https://doi.org/10.2967/jnumed.119.231100.

26. Roque V, Jessop M, Pereira L, Gape P, Dizdarevic S, Sousa E, et al. Bone scan index as metastatic bone disease quantifier and predictor of radium-223-dichloride biochemical response. Nucl Med Commun. 2019;40:588–96. https://doi.org/10.1097/MNM.0000000000001005.

27. Lubin DJ, Tsetse C, Khorasani MS, Allahyari M, McGrath M. Clinical predictors of I-131 therapy failure in differentiated thyroid cancer by machine learning: a single-center experience. World J Nucl Med. 2021;20:253–9. https://doi.org/10.4103/wjnm.WJNM_104_20.

28. Jie Z, Zhiying Z, Li L. A meta-analysis of Watson for Oncology in clinical application. Sci Rep. 2021;11:5792. https://doi.org/10.1038/s41598-021-84973-5.

29. Kim M, Kim BH, Kim JM, Kim EH, Kim K, Pak K, et al. Concordance in postsurgical radioactive iodine therapy recommendations between Watson for Oncology and clinical practice in patients with differentiated thyroid carcinoma. Cancer. 2019;125:2803–9. https://doi.org/10.1002/cncr.32166.

30. Haugen BR, Alexander EK, Bible KC, Doherty GM, Mandel SJ, Nikiforov YE, et al. 2015 American thyroid association management guidelines for adult patients with thyroid nodules and differentiated thyroid cancer: the American thyroid association guidelines task force on thyroid nodules and differentiated thyroid cancer. Thyroid. 2016;26:1–133. https://doi.org/10.1089/thy.2015.0020.

31. Kim SY, Kim Y-I, Kim HJ, Chang H, Kim S-M, Lee YS, et al. New approach of prediction of recurrence in thyroid cancer patients using machine learning. Medicine (Baltimore). 2021;100:e27493. https://doi.org/10.1097/MD.0000000000027493.

32. Duan L, Zhang H-Y, Lv M, Zhang H, Chen Y, Wang T, et al. Machine learning identifies baseline clinical features that predict early hypothyroidism in patients with Graves' disease after radioiodine therapy. Endocr Connect. 2022;11:e220119. https://doi.org/10.1530/EC-22-0119.

33. Kavitha M, Lee C-H, Shibudas K, Kurita T, Ahn B-C. Deep learning enables automated localization of the metastatic lymph node for thyroid cancer on 131I post-ablation whole-body planar scans. Sci Rep. 2020;10:7738. https://doi.org/10.1038/s41598-020-64455-w.

34. Ebrahimi M, Kardan MR, Changizi V, Pooya SMH, Geramifar P. Prediction of dose to the relatives of patients treated with radioiodine-131 using neural networks. J Radiol Prot. 2018;38:422–33. https://doi.org/10.1088/1361-6498/aa9b9b.

35. Plachouris D, Tzolas I, Gatos I, Papadimitroulas P, Spyridonidis T, Apostolopoulos D, et al. A deep-learning-based prediction model for the biodistribution of 90 Y microspheres in liver radioembolization. Med Phys. 2021;48:7427–38. https://doi.org/10.1002/mp.15270.

36. Roncali E, Taebi A, Foster C, Vu CT. Personalized dosimetry for liver cancer Y-90 radioembolization using computational fluid dynamics and Monte Carlo simulation. Ann Biomed Eng. 2020;48:1499–510. https://doi.org/10.1007/s10439-020-02469-1.

37. Taebi A, Vu CT, Roncali E. Estimation of Yttrium-90 distribution in liver radioembolization using computational fluid dynamics and deep neural networks. Annu Int Conf IEEE Eng Med Biol Soc. 2020;2020:4974–7. https://doi.org/10.1109/EMBC44109.2020.9176328.

38. Ingrisch M, Schöppe F, Paprottka K, Fabritius M, Strobl FF, De Toni EN, et al. Prediction of 90Y radioembolization outcome from pretherapeutic factors with random survival forests. J Nucl Med. 2018;59:769–73. https://doi.org/10.2967/jnumed.117.200758.

The Regulatory Review of Radiotherapeutics: United States of America

25

Serge K. Lyashchenko

25.1 The Fundamentals

In the United States, all radiopharmaceuticals—including therapeutic radiopharmaceuticals—are classified as medicines. Therefore, their clinical development, production, and clinical use are regulated by the United States Food and Drug Administration (FDA) in the same manner as traditional non-radioactive pharmaceuticals. The FDA is responsible for the oversight of all activities related to the use of radiopharmaceuticals in humans. Generally speaking, this oversight is accomplished in three ways: (i) regulations and guidance that specify requirements for the use of radiopharmaceuticals (e.g., conducting clinical trials, manufacturing), (ii) periodic surveillance audits to ensure compliance with the aforementioned rules, and (iii) the regulatory review and approval of new radiopharmaceuticals.

25.2 The Details

25.2.1 The FDA Framework for Therapeutic Radiopharmaceuticals

Therapeutic radiopharmaceuticals hold a unique position within the world of radiopharmaceuticals. Radiotherapeutics share many characteristics with their diagnostic counterparts, including their emission of radioactivity, administration in sub-pharmacologic mass doses, relatively short shelf-lives, and small batch sizes in which quality control samples are homogeneous with entire batches. In the case of diagnostic radiopharmaceuticals, these traits spurred the creation of a special set of regulations. Yet therapeutic radiopharmaceuticals are currently subject to the same regulations as traditional, non-radioactive drugs. The principal reason for this choice is the potential toxicity of radiotherapeutics. Indeed, while the mechanisms of traditional therapeutics and radiotherapeutics are dramatically different (i.e., biochemical action vs. ionizing radiation), the overall safety and efficacy profiles of therapeutic radiopharmaceuticals are much more closely aligned with those of non-radioactive pharmaceuticals than those of diagnostic radiopharmaceuticals. Yet while the rationale for this regulatory framework is clear, the intrinsic differences between drugs that emit ionizing radiation and non-radioactive drugs—as well as the

S. K. Lyashchenko (✉)
Department of Radiology, Memorial Sloan Kettering Cancer Center, New York CityNY, USA
e-mail: lyashchs@mskcc.org

advent of new classes of radiotherapeutics (i.e., α-emitters)—have necessitated a certain amount of regulatory flexibility.

In the United States, this regulatory flexibility is achieved via a combination of federal regulations, FDA-issued guidance documents, and the FDA's direct communication pathways. Because the terms "FDA regulations" and "FDA guidance" are often erroneously used interchangeably, an explanation of these terms is warranted. "Regulations" are laws that contain binding requirements related to the use of pharmaceuticals in humans. In practice, because passing laws is resource intensive and time consuming, regulations typically contain broad requirements that can be applied to all pharmaceuticals, for example, basic rules for the manufacture of medicines. "Guidance," on the other hand, describes the compilation of FDA-issued documents that contain the Administration's "recommendations" on a specific area. These recommendations are much more detailed than regulations yet are likewise designed to be as general as possible. In addition, while the word "recommendations" suggests that they need not be followed, most entities that are subject to FDA guidance recommendations voluntarily choose to do so.

While the use of therapeutic radiopharmaceuticals in humans is governed by the same regulations as non-radioactive drugs, the unique characteristics of the former have required the implementation of non-traditional processes and the generation of radiotherapeutic-specific FDA guidance documents. One extant example is *Oncology Therapeutic Radiopharmaceuticals: Nonclinical Studies and Labelling Recommendations: Guidance for Industry*. This guidance document provides several recommendations specifically related to the clinical translation of therapeutic radiopharmaceuticals, including considerations with respect to the preclinical evaluation of radiotoxicity [1]. Other aspects of the use of therapeutic radiopharmaceuticals are currently covered by additional FDA-issued guidance documents that may also cover diagnostic radiopharmaceuticals and non-radioactive drugs. Finally, it is important to note that FDA guidance—unlike regulations—is not fixed. Therefore, as field of radiopharmaceutical therapy evolves, existing FDA guidance documents may be updated, or new ones may be issued.

25.2.2 The Role of the US Pharmacopeia

In the context of the manufacturing and handling of radiotherapeutics, the FDA may at times rely on published standards from other entities—most notably the US Pharmacopeia (USP)—as well as its own regulations and guidance documents. The USP is responsible for compiling and managing a collection of standards documents, also referred to as "chapters" that can be used by manufacturers of radiopharmaceuticals to demonstrate compliance with established standards. These compendial "chapters" usually contain descriptions of well-established processes and practices related to the production and handling of radiopharmaceuticals. For example, USP <825> *Radiopharmaceuticals-Preparation, Compounding, Dispensing, and Repackaging* sets standards relevant to the dispensing and compounding of radiopharmaceuticals, including radiotherapeutics [2].

It is important to recognize that the USP is not a governmental agency responsible for enforcing standards. Rather, it is a non-profit agency that documents and manages standard protocols that have been generated by expert groups or by the manufacturer of a specific drug. The underlying principle of the USP is that once a process or standard has been included in the USP, it is considered to be "compendial" or "validated." This system offers several benefits to both the regulatory agencies and the manufacturers of radiotherapeutics. Since the methodologies or standards described in the USP are considered to be valid, regulators often rely on USP standards in lieu of generating yet another guidance document. In addition, once a manufacturer has demonstrated that a process is USP-compliant, regulators have a complete understanding of the process being used. This approach saves

regulators effort and resources and ensures that particular aspects of manufacturing are standardized across the industry (at least as much as possible). In turn, manufacturers benefit from relying on the USP because once their manufacturing processes comply with a "compendial method," no additional effort is needed to demonstrate its suitability.

Significant differences exist between the degrees to which American and European manufacturers may rely on pharmacopeia documents for the production of unapproved radiotherapeutics for clinical use. In the EU, a specific non-approved drug monograph may be generated for the EU Pharmacopeia by a group of experts with relatively limited validation data. In this case, the chapter normally contains information on controls that, in the experts' opinion, should be applied during the production and quality control testing of the radiotherapeutic in question. Once published, these chapters allow manufacturers to produce radiopharmaceuticals that have not received regulatory approval on a limited basis for non-investigational treatments in patients under the auspices of nuclear medicine practice. This is often referred to as "in-house production" or "magistral compounding."

In the United States, on the other hand, radiopharmaceuticals cannot be used in patients unless they have been FDA-approved for a specific indication or investigational agents employed under the auspices of an FDA-acknowledged Investigational New Drug (IND) application. This policy eliminates the possibility of "magistral compounding" and means that there is no practical need to create USP monographs for investigational agents. Instead, drug monographs included in the USP are almost exclusively created by the manufacturer of FDA-approved drugs. Once a drug monograph is included in the USP, generic manufacturers of said drug are obliged to follow the published standards. The manufacturing controls for investigational radiopharmaceuticals are normally described in the "Chemistry, Manufacturing, and Controls" (CMC) section of IND applications, allowing the manufacturers of these investigational agents greater flexibility.

25.2.3 Special Considerations in the United States

Two aspects of the regulation of radiopharmaceuticals that are somewhat unique in the United States and that are absolutely essential for efficient regulation are: (1) the operation of a single regulatory agency (i.e., the FDA), and (2) the existence of well-established two-way communication channels between the regulators and those being regulated.

Regulation by a single agency offers several advantages. First, it ensures that the feedback provided by the regulator is both consistent and well informed. Secondly, it allows for the clear delegation of responsibilities within the regulatory agency. Practically, this means that those seeking regulatory advice are able to obtain information from the relevant division of the FDA quickly and easily.

Efficient communication with trained regulators who focus specifically on radiopharmaceuticals is another key factor that facilitates the development and human use of radiotherapeutics in the United States. The division of the FDA that is responsible for the regulation of radiopharmaceuticals is composed of radiochemists, radiopharmacists, medical physicists, and physicians that have a sound fundamental understanding of radiopharmaceuticals and their development. This expertise accelerates the creation of consensus between parties. In addition, the pathways of communication are well established, and initiating communication is easy. Depending on the matter at hand, communication may be written, verbal, in-person, or any combination thereof [3]. In order to ensure an appropriate response, the inquirer should include background on the problem at hand, the proposed solution alongside supportive reasoning, and a specific query as to the regulator's agreement (or lack thereof) with the proposed solution. In general, those developing radiopharmaceuticals are encouraged to contact regulators with questions prior to initiating their work in order to avoid situations in which the completed work does not satisfy regulatory requirements.

Depending on the urgency of the matter and the method of communication, response times vary from several hours to up to 90 days.

25.2.4 The Regulatory Approval Process

In a regulatory sense, radiotherapeutics can be divided into two broad categories: (1) investigational agents used in clinical trials and (2) drugs that have been approved by the FDA for routine clinical use for a specific indication. With respect to both, the FDA's remit is ensuring that the benefits of the therapeutic radiopharmaceutical outweigh its risks. Hence, investigators and clinicians must submit regulatory applications for drugs in each category so the FDA can determine whether all of the requirements for the use of the drug in humans have been met.

For investigational radiopharmaceuticals, this application is called an Investigational New Drug (IND) application. The IND application for therapeutic radiopharmaceuticals normally has several components: (i) information from preclinical non-human studies to provide a preliminary estimate of the drug's expected safety and efficacy, (ii) dosimetry and radiotoxicity estimates, (iii) a description of how the agent will be produced and tested, and (iv) a description of how the radiopharmaceutical will be evaluated in the clinic. Once the IND application is submitted, the FDA review period lasts 30 days. If no deficiencies are found, the FDA acknowledges the IND and allows the investigators to initiate their clinical trial. If deficiencies are found, however, the FDA will advise the applicants on how to remediate these problems.

Once clinical trials have demonstrated that a radiotherapeutic is a safe and effective treatment for a particular indication, another regulatory application—this one called a "New Drug Application" (NDA)—must be filed to receive approval for the use of the drug as part of standard clinical care as well as for its marketing. An NDA normally summarizes safety, efficacy, and pharmacokinetics data collected during clinical trials as well as additional data covering the production

and quality control of the agent itself. Once the FDA grants an NDA approval for a particular drug, clinicians gain more flexibility with respect to how it is used in patients. For example, clinicians may decide to use the drug for "off-label" use beyond its approved indication if they believe their patients will benefit. Along these lines, clinician investigators may conduct a clinical trial of an FDA-approved drug for a different, non-approved indication. In these scenarios, an IND application may be required even though the drug is already FDA-approved. The need to submit an IND in a given situation may be clarified via communication with the FDA.

In general, the regulators in the United States do not allow clinicians to use drugs that have not been approved by the FDA for standard clinical care. As mentioned above, "magistral compounding" is not permitted in the United States. However, there is nonetheless a regulatory mechanism that allows clinicians to treat their patients using investigational (i.e., non-FDA approved) agents under extenuating circumstances. This mechanism—referred to as "expanded access" by regulators but "compassionate use" or "preapproval use" elsewhere— allows clinicians to petition regulators to use investigational agents for the treatment of patients with life-threatening conditions that have no approved therapeutic alternatives [4]. In practice, this approach is typically employed in the context of a single patient with a life-threatening disease who has run out of treatment options. However, it has also been applied to facilitate the treatment of groups of patients with a therapeutic that has already been found to be effective but has not yet received official regulatory approval.

This approach is particularly relevant to therapeutic radiopharmaceuticals because the majority of radiotherapeutics currently used in humans in the United States are investigational and employed in end-stage cancer patients. In this patient population, it is quite common to need emergency treatments for those who have run out of approved treatment options. Unlike magistral compounding, however, expanded access involves a significant degree of regulatory oversight. Since the radiopharmaceuticals used under

the "expanded access" mechanism are still investigational, the requestor must still have an FDA-acknowledged IND in place. Prior to granting approval for "expanded access" requests, regulators must determine that the potential benefits of using an investigational agent in a given patient or group of patients outweigh the risks *and* that granting access will not negatively impact the radiopharmaceutical's eventual case for NDA approval. The timing for granting approvals may vary from several hours to up to 30 days, depending on the urgency of the matter.

25.3 Conclusion

In summary, the last few years have played witness to a dramatic increase in the clinical study and use of therapeutic radiopharmaceuticals. Given the unique characteristics of these drugs, regulators and physicians must work together to ensure that the landscape governing the use of radiotherapeutics in the clinic allows patients adequate access to these valuable medicines while maintaining the appropriate degree of safety.

25.4 The Bottom Line

- Radiotherapeutics possess unique properties that influence the regulatory requirements that are applied to them.
- In the United States, the use of therapeutic radiopharmaceuticals in humans is governed by federal regulations. The US FDA is the government agency responsible for enforcing those regulations.
- The US Pharmacopeia (USP) is a non-governmental agency that issues compendial standards related to the manufacturing of FDA-approved radiopharmaceuticals. At times, the FDA may rely on USP standards in lieu of generating its own requirements.
- Maintaining well-established communication pathways with the FDA is essential for the efficient development of radiopharmaceuticals.
- It is absolutely paramount for regulators to consider possible impacts on the access of patients to radiotherapeutics when implementing new regulatory requirements.

References

1. United States Food and Drug Administration. Oncology therapeutic radiopharmaceuticals: nonclinical studies and labeling recommendations guidance to industry; 2019.
2. United States Pharmacopeia. USP <825>radiopharmaceuticals – preparation, compounding, dispensing, and repackaging; 2020.
3. United States Food and Drug Administration. Formal meetings between the FDA and sponsors or applicants of PDUFA products draft guidance to industry; 2017.
4. United States Food and Drug Administration. Expanded access to investigational drugs for treatment use – questions and answers. guidance for industry; 2017.

The Regulatory Review of Radiotherapeutics: A European Perspective

26

Clemens Decristoforo

26.1 The Fundamentals

26.1.1 The Definition of Therapeutic Radiopharmaceuticals Within the European Framework

Recent years have played witness to the impressive success of radiopharmaceutical therapy (TRT) in Europe. However, the regulatory framework in Europe has not yet addressed these developments; therefore, in some ways, it does not reflect these advances in this field. This chapter primarily focuses on the European Union (EU) as the major regulatory player in Europe, because several states in Europe that are not members of the EU still nonetheless follow the main regulatory directions developed by EU institutions.

The use of external sources of radioactivity or, in a wider context, of ionizing radiation for medical applications is not regulated homogeneously. These applications can generally be divided into three categories: (1) therapies that use an external source of radiation (i.e., external beam radiation); (2) therapies predicated on the internal administration of sealed sources (i.e., brachytherapy); and (3) therapies that rely on the internal administration of unsealed sources (i.e., radiopharmaceuticals). These distinctions are not only technical but also make a difference in the regulatory sense in Europe. There are, of course, considerations with respect to legislation on radiation safety, but a major differentiation is that sealed radioactive sources are considered medical devices and are therefore not being covered by the respective pharmaceutical legislation but rather by the Medical Device Regulation EU MDR 2017/745 [1]. Recent examples of such radioactive therapies are the treatment of liver metastases via the selective intra-arterial administration of ^{90}Y-labeled particles (e.g., SIRT$^{®}$ spheres [2]) or the treatment of non-melanoma skin cancers with the local application of Re-188 [3]. Even though such applications are usually performed in Nuclear Medicine departments, they are in a strict sense not "radiopharmaceutical therapy" and will be excluded from the further regulatory descriptions because they then have to be handled differently in many respects, including licensing pathways and requirements for clinical testing.

Therapies using "unsealed" sources of radioactivity (i.e., targeted radiopharmaceuticals) legally fall under the pharmaceutical legislation [4]. As a result, the radioactive compound is considered and legally defined as a medicinal product, more specifically a radiopharmaceutical. The regulatory consequences of this definition are manifold. Indeed, when dealing with regulatory issues both during the development and ultimate application of radiotherapeutics, a critical first consideration is whether or not the radioactive

C. Decristoforo (✉)
Department of Nuclear Medicine, Medical University Innsbruck, Innsbruck, Austria
e-mail: Clemens.Decristoforo@i-med.ac.at
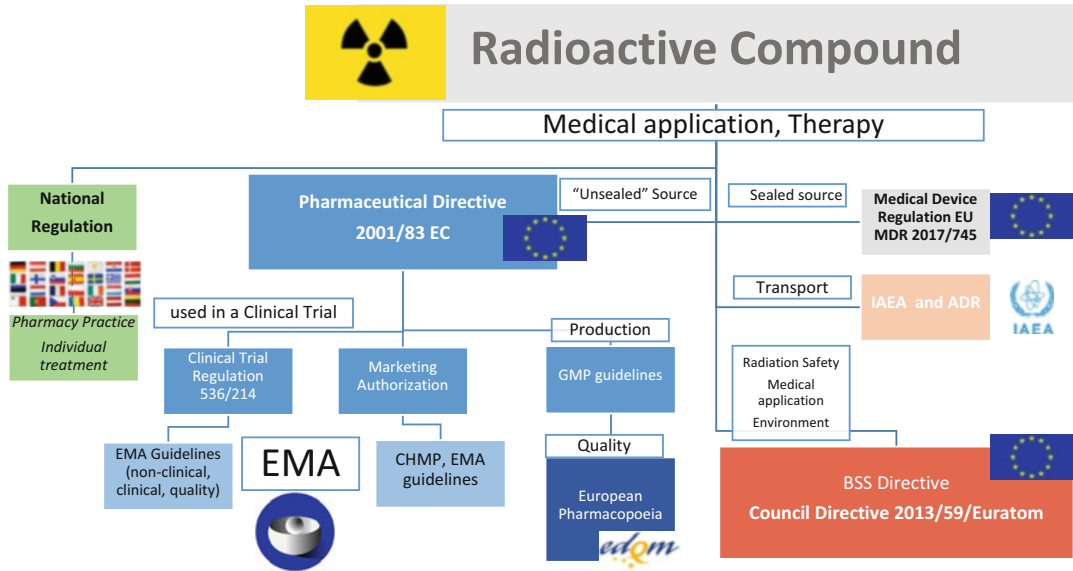
Fig. 26.1 The Regulatory Landscape of Radiotherapeutics in the European Union. Pharmaceutical legislation is shown in blue. Not everything is regulated by the European Union alone; other players involved include the legislatures of member states (green), agencies like the

European Medicines Agency (EMA), the IAEA, and the European Directorate for the Quality of Medicines & HealthCare (EDQM; a body of the Council of Europe). The type of legislation to be applied to a radiotherapeutic also depends on whether or not it is a sealed source

substance is classified as a radiopharmaceutical. An outline of the legislation applicable to radiotherapeutics is provided in Fig. 26.1.

26.1.2 The Interplay Between Radiation Safety and Pharmaceutical Regulations

From a regulatory perspective, radiopharmaceuticals—whether therapeutic or diagnostic—are governed principally by radiation safety and pharmaceutical legislation. Other regulations, e.g., dealing with transport or environmental issues, also impact the use of therapeutic radiopharmaceuticals but are not addressed specifically herein. Radiation safety legislation covers handling, storage, and disposal but also the medical application of the radiopharmaceutical, including therapy. It focusses on ensuring that the radiation exposure of all persons involved remains within acceptable limits. These limits are

dependent upon whether the exposure is to a patient, a healthy volunteer, an occupationally exposed person, or the general public. Legislation considers the effects from both external exposure to radiation and due to contamination. The main regulatory text within the EU is the Basic Safety Standards (BSS) Directive (council Directive 2013/59/EURATOM) [5]. In the context of medical applications, the directive refers to the term radiotherapeutics (thus differentiating from radiodiagnostics) but does not specifically distinguish between external radiotherapy and nuclear medicine applications. Medical applications in general have to be justified and optimized; for radiotherapeutics additional requirements are laid down related to an active role of the Medical Physicist for dose planning and dose verification.

Pharmaceutical legislation in the EU is governed by several legal texts and guidance documents. The basic document is the Pharmaceutical Directive 2001/83 EC [4], which was published more than 20 years ago and has been amended and added to many times since. The

Directive refers to the "medicinal product," in contrast to the United States where the term "drug" is used predominantly. Overall, the legislation aims to ensure that Medicinal Products in the European Union are safe and efficacious over their entire life cycle: from development to routine clinical use. Directive 2001/83 EC clearly includes radiopharmaceuticals and some starting materials (i.e., radionuclide generators, radionuclide precursors, and kits) and brings them under the umbrella of pharmaceutical legislation. It thereby makes no specific distinction between therapeutic and diagnostic applications; therefore, the legislation applies for all types of radiopharmaceuticals. The Pharmaceutical Directive is complemented by other documents, including guidelines. Table 26.1 provides some relevant examples of non-legally binding texts on radiopharmaceuticals. A major player in this context is the European Medicines Agency (EMA), which is under the responsibility of the EU Commission and releases guidance for many pharmaceutical topics despite not having strict legal character. These pharmaceutical guidelines and guidance documents likewise do not, with very few exceptions, differentiate between radiotherapeutics and radiodiagnostics. Of

course, national legislation and guidance exists in addition to EU-based documents; more details on this "web of regulation" with respect to radiopharmaceuticals can be found here [6–9].

Even though radiation safety and pharmaceutical legislation have different scopes and focuses, they nonetheless frequently overlap when it comes to radiopharmaceuticals and particularly their therapeutic applications. Along these lines, conflicting considerations can arise between radiation safety (mainly in relation to the personnel involved in preparing and handling radiotherapeutics) and the measures to ensure the quality of the product (the basis for the safety and efficacy of the radiotherapeutic). There are documents trying to address these conflicts, in particular dedicated texts on radiopharmaceuticals in the pharmaceutical legislation. But recent developments and advances make it challenging to find specific solutions to comply with the current legislation. Some examples of these challenges will be outlined below. The EU has recently announced a push to revise its pharmaceutical legislation, driven in large part by technological advances in drug development over the past 20 years, including advances in the field of radiopharmaceuticals.

Table 26.1 Selected examples of regulatory guidelines and guidance related to radiotherapeutics within the EU (not legally binding)

Document	Topic	Source	Year of release
EMEA/CHMP/QWP/306970	Guideline on radiopharmaceuticals – Quality	EMA	2008
Radiation Protection 99	Guidance on exposure in medical and biomedical research	EU-Commission/Euratom	1998
CHMP/SWP/28367/07 Rev 1	Guideline on "strategies to identify and mitigate risks for first in human and early clinical trials with investigational medicinal products"	EMA	2017
Ph Eur General Chapter 5.19	Guidance for the "extemporaneous preparation of radiopharmaceuticals"	European Pharmacopoeia/EDQM	2014
ICH M3(R2)	Non-clinical safety studies for the conduct of human clinical trials and the marketing authorisation of pharmaceuticals	ICH (EMA)	2013
EMA/CHMP/SWP/686140/2018	Guidance on non-clinical requirements for radiopharmaceuticals	EMA draft	2018

EDQM European Directorate for the Quality of Medicines & HealthCare, *EMA* European Medicines Agency, *ICH* International Council for Harmonisation of Technical Requirements for Pharmaceuticals for Human Use

26.2 The Details

26.2.1 The Regulation of Clinical Trials

The rules for the testing of medicinal products in humans are defined in the Clinical Trial Regulation EU No 536/2014 [10]. This regulation came into force only recently, and its full impact will be seen in the coming years. A major novelty of this regulation is the introduction of a central EU portal for the submission of clinical trials that are then stored in an EU database from which the main data are publicly accessible. This new portal—named Clinical Trials Information System (CTIS) [11]—allows for a single online application of clinical trials, even if they are multicenter and carried out in different member states of the EU. An application for a clinical trial is then reviewed by an assigned national pharmaceutical regulatory body within a very strict time regimen; a separate submission to an ethical committee is no longer required. Overall, this new legislation aims to simplify the application process that, up until now, has been operated at the national level.

The rules for conducting clinical trials are very tightly formulated and are based on the international ICH (International Council for Harmonisation of Technical Requirements for Pharmaceuticals for Human Use) guidelines for Good Clinical Practices (GCP) [12]. GCP includes clear responsibilities for sponsors and investigators in clinical trials and also defines the need for monitoring the trial to ensure data integrity. The required documents for the conduct of a clinical trial include a clinical trial protocol, an informed consent form, case report forms, and Stansard Operation Procedures (SOPs). A medicinal product applied within a clinical trial is termed an "Investigational Medicinal Product (IMP)," a term that can be used to cover both therapeutics and diagnostics, including radiopharmaceuticals. Overall, an IMP must be prepared according to Good Manufacturing Practices (GMP) by a producer with a specific manufacturing authorization for IMPs. However, the new regulation specifies an exemption from

this rule in the case of diagnostic radiopharmaceuticals if the national regulatory framework generally foresees such an exemption from GMP [13]. This exemption is one of the very few examples where regulatory texts specifically differentiate between therapeutic and diagnostic radiopharmaceuticals and implement higher regulatory requirements for the former. The data for the IMP used in a clinical trial have to be compiled in a so-called "Investigational Medicinal Product Dossier (IMPD)." The IMPD has to contain all the data on the quality of the IMP in a specific format, including details on its production, formulation, and quality control. It may be challenging to follow this format for radiopharmaceuticals, so specific guidance has been published [14]. Besides information on the quality of the IMP, and non-clinical and clinical data (pharmacology, toxicology, efficacy) on the radiopharmaceutical must be included. These data also should be summarized in a so-called Investigators Brochure (IB). The process of compiling all these data is elaborate and requires a great deal of expertise [15].

A particular challenge in the context of novel radiopharmaceuticals is toxicity testing. Whereas the radiation-derived toxicity of a candidate IMP can be derived from preclinical dosimetry data, strict guidance is given for the toxicological effects of the "cold" compound. As the amount of substance administered is usually very low, the concept of microdosing has been introduced in the ICH M3 (R2) guideline, reducing some requirements for toxicity testing [9]. Yet this is not applicable in all settings—particularly for radiotherapeutics—and can pose a costly hurdle for the translation of novel radiopharmaceuticals to the clinic [16]. Thankfully, the EMA has recently published specific guidance to allow for a risk-based approach in this setting [17]. The regulatory hurdles in the pharmaceutical legislation in relation to the non-clinical testing of radiopharmaceuticals have recently been summarized [9].

It is important to note that in Europe, not all applications of novel radiopharmaceuticals for radiopharmaceutical therapy have been

conducted as clinical trials following this regulatory framework. In particular, the earliest applications of ^{177}Lu-labeled somatostatin analogs and ligands targeted to the prostate specific membrane antigen (PSMA) were performed outside this regulatory framework. In certain European countries, exceptions exist that give treating physicians a wide berth in selecting treatments for individual patients [7]. That said, applications of novel radiopharmaceuticals leading to marketing authorizations (MAs) have always taken place under the auspices of the European Clinical Trials Regulation.

26.2.2 Marketing Authorization

The licensing of new drugs in the EU is clearly regulated in Directive 2001/83 EC [4]. It describes three pathways through which a drug can be commercially distributed based on a marketing authorization (MA) granted by the pharmaceutical regulatory bodies. Each European country also has national procedures that are widely used for radiodiagnostics and are frequently accepted by other EU member states via the mutual recognition process. This relationship is leveraged in the so-called decentralized procedure described in Directive 2001/83 EC: the applicant chooses the countries in which the MA should be valid but submits to one national lead agency only. Their evaluation then can be directly accepted by regulatory authorities in other member states.

The main pathway for the approval of radiotherapeutics, however, is the Centralized Procedure, in which the application for an MA is submitted centrally to the European Medicines Agency (EMA), which is then in charge of the evaluation. The evaluation results in an opinion from the committee for medicinal products for human use (CHMP) that is the basis for the EU Commission to issue the MA. This centralized procedure is mandatory for novel drugs and also oncological applications, rendering it practically mandatory for new radiotherapeutics. Applying for an MA via this procedure requires the compilation of clinical data from controlled clinical trials (especially Phase III). The EMA can be consulted during the planning of such trials and even on specific issues related to quality or non-clinical safety aspects of the drug (production methods, toxicity requirements, etc.). Such a consultation is formalized in so-called scientific advice and enables the authorities to get involved in the authorization process at an early stage. Not surprisingly, the overall process of MA is time-consuming and resource-intensive. This may not be economically feasible for all applications, especially when indications are rare, as is often the case for radiotherapeutics. To help in these cases, the EMA can grant so-called "orphan drug" designations. For rare indications (which are clearly defined), an applicant can apply for "orphan drug" status, which provides benefits in terms of reduced fees and also ensures market protection for a certain period of time after issuing of an MA. An MA received via this centralized procedure is then immediately valid for all EU member states.

It should be stressed that MA is not just required for finished radiotherapeutic products, i.e., ready-to-use solutions for injection. Directive 2001/83 EC [4] also covers radionuclide precursors, kits, and radionuclide generators. In principle, therefore, the nuclides used for radiolabeling radiotherapeutics can also obtain a marketing authorization, as is the case for [^{177}Lu] Lu-chloride. Non-radioactive kits used for radiolabeling can also fall in this regulatory category, for example the kit for labeling an anti-CD20 antibody with yttrium-90 (Zevalin®).

As already pointed out above, in Europe the clinical use of a given radiotherapeutic is not always based on its MA. Certain national regulations allow for the preparation of radiopharmaceuticals for the direct use in patients either under the responsibility of the physician or within the pharmacy framework of the nation's legislation. This practice, often termed as extemporaneous, or in-house preparation, is a common practice in certain countries, particularly for novel targeted radiotherapeutics; in others, this is not allowed by the national legislation.

Table 26.2 Selected Good Manufacturing Practice topics relevant to radiotherapeutics in the European Regulatory Framework

Part	Chapter	Topic	Year of release of latest version
I Basic Requirements for Medicinal Products	Chapter 1	Pharmaceutical Quality System	2013
	Chapter 2	Personnel	2014
	Chapter 3	Premise and Equipment	2015
	Chapter 4	Documentation	2011
	Chapter 5	Production	2015
	Chapter 6	Quality Control	2014
	Chapter 7	Outsourced activities	2013
	Chapter 8	Complaints and Product Recall	2015
	Chapter 9	Self Inspection	Not available
II Basic Requirements for Active Substances	–	Basic Requirements for Active Substances Used as Starting Materials	2014
III GMP-Related Documents	Various	Site Master file, Batch Record, Quality Risk Management, etc.	Diverse
Annexes	Annex 1	Manufacture of Sterile Medicinal Products	2022
	Annex 3	Manufacture of Radiopharmaceuticals	2011
	Annex 11	Computerised Systems	2011
	Annex 13	Manufacture of Investigational Medicinal Products	2017
	Annex 15	Qualification and Validation	2015
	Annex 16	Certification by a Qualified Person and Batch Release	2016
	Annex 19	Reference and Retention Samples	2005

26.2.3 GMP and Manufacturing

Beyond marketing authorizations (MAs), EU's Pharmaceutical Directive also states that a manufacturing authorization is required for the preparation of medicinal products. This is meant to ensure that the manufacturer follows the principles of GMP [4]. Individual national pathways within Europe may grant exemptions for the in-house preparation of radiopharmaceuticals, thereby removing the requirement of the authorization and (therefore) GMP-focused inspection. To provide guidance for these in-house productions, professional organizations such as the European association of nuclear medicine (EANM) or the pharmaceutical inspection co-operation scheme (PIC/S) have issued guidelines for the preparations of radiopharmaceuticals [18, 19].

General GMP guidelines—which are legally binding for the holder of a manufacturing authorization that distributes radiotherapeutics either

for routine use or clinical trials—can be found in Volume 4 of EUDRALEX. This document is structured in chapters that cover the main aspects of pharmaceutical production, including personnel, resources, quality control, and validation. Specific issues are compiled in annexes to the volume; the contents of EU-GMP are listed in Table 26.2. A dedicated Annex 3 covering radiopharmaceuticals is available, but other annexes are relevant as well; for example, Annex 1 discusses sterile manufacturing, while Annex 13 covers computerized systems. These annexes often contain copious technical details and provide quite a strict framework in which the production of pharmaceuticals can take place. In many documents, however, no particular reference is made to radiopharmaceuticals. Therefore, professional organizations have provided several specific guidance documents covering radiopharmaceuticals in general (though not radiotherapeutics in particular). These cover topics including process validation and

Table 26.3 Relevant texts related to therapeutic radiopharmaceuticals in the European Pharmacopoeia

Type of monograph/text	Name	Pharm Eur number
Finished radiopharmaceutical preparation		
Monograph	Sodium iodide (^{131}I) solution	0281
Monograph	Sodium phosphate (^{32}P) injection	0284
Monograph	Iobenguane (^{131}I) injection for therapeutic use	1112
Monograph	Strontium (^{89}Sr) chloride injection	1475
Monograph	Sodium iodide (^{131}I) capsules for therapeutic use	2116
Radionuclide precursor		
Monograph	Lutetium (^{177}Lu) solution for radiolabelling	2798
Monograph	Yttrium (^{90}Y) chloride solution for radiolabelling	2803
Monograph	Sodium iodide (^{131}I) solution for radiolabelling	2121
Chemical precursor		
Monograph	Iobenguane sulfate for radiopharmaceutical preparations	2351
Monograph	Chemical precursors for radiopharmaceutical preparations	2902
General text related to radiopharmaceuticals		
General monograph	Radiopharmaceutical preparations	0125
General text	2.2.66. Detection and measurement of radioactivity	20266
General text	5.19. Extemporaneous preparation of radiopharmaceuticals	51900
General chapters		
Methods of analysis	2.6.1. Sterility	20601
	2.2.29. Liquid chromatography	20229
General text	5.4. Residual solvents	50400

qualification [20], automated synthesis modules [21], the validation of analytical methods [22], and risk management [23].

26.2.4 The Pharmacopoeia

The European Pharmacopoeia (Pharm Eur) is the main reference document providing the regulatory requirements for the quality of radiopharmaceuticals in general and radiotherapeutics in particular [24]. Unlike in other regions, the main texts of the European Pharmacopoeia (in particular the monographs) are legally binding, and the Pharm Eur also has published more documents related to radiopharmaceuticals than other comparable pharmacopoeias. The Pharm Eur contains monographs for particular radiotherapeutics as well as general texts discussing radioactive preparations, including a general monograph on radiopharmaceutical preparations and a monograph on the detection and measurement of radioactivity. Besides documents on final preparations, monographs on radionuclide precursors (e.g., lutetium-177 solution for radiolabeling) and chemical precursors can be found as well. In addition, there are also several texts that are not specific to radiopharmaceuticals but are nonetheless highly relevant, including sections covering certain tests (e.g., sterility testing or chromatographic methods) or defining certain limits (e.g., of residual solvents). Therefore, Pharm Eur is the main European reference when it comes to defining and testing the quality of radiotherapeutics. Table 26.3 summarizes the texts relevant to therapeutic radiopharmaceuticals. A number of texts relevant to current radiotherapeutics are in preparation and will be released in continuous updates. It should be stressed that almost all European countries (regardless of membership in the European Union) have accepted Pharm Eur as a legally binding document within the European Pharmacopoeia Convention.

26.2.5 BSS Directive and National Regulations

As outlined above, the BSS Directive [5] sets the standards for radiation safety. In the context of nuclear medicine, the radiation exposure of the patient (medical), the medical personnel (occupational), and the environment at large (public) must be considered. Whereas general measures have been created to limit occupational exposure to an annual dose of 20 mSv (with special requirements for local exposures as well as specific groups like students or pregnant personnel), a different approach involving justification and optimization has been applied to exposure in a medical setting. Any radiotherapeutic application, including radiopharmaceutical therapy, requires justification in the sense that the exposure "shows sufficient net benefit" both for the individual and the society. This justification has to be given in advance also for novel applications or individual treatments.

Even if justified, the procedure also has to be optimized. In the context of radiopharmaceutical therapy, this means working to ensure that the maximum dose is delivered to the target tissue while simultaneously limiting the radiation dose to the rest of the body. Furthermore, this optimization includes not only the selection of the radiopharmaceutical, the appropriate quality assurance, and the calibration of the necessary equipment but also the requirement to perform dosimetry calculations to assess the appropriate amount of administered activity.

The radiation dose to members of the public must also not exceed annual dose limits. Protecting the public in this way includes designing facilities for TRT procedures and adopting effective waste management installations but also defining appropriate release criteria for patients receiving radiotherapeutics. In Europe, the limits for radioactive waste and release criteria are typically regulated on a national level, which of course leads to variations between individual member states. Likewise, the procedures for authorizing facilities for TRT and for providing licenses for radionuclides are very much under the auspices of national regulatory bodies. Finally, public exposure can also arise during the transport of radiotherapeutics, both inside and outside treatment facilities. Regulations for the latter are defined in the regulations of the international atomic energy agency (IAEA) on the safe transport of radioactive material that—in Europe—are integrated into the agreement concerning the international carriage of dangerous goods by road (ADR). More details on radiation safety regulations and their interpretation can be found in [25].

26.3 Something Extra

As outlined above, the regulatory environment of radiotherapeutics in Europe is governed by the interrelation between legislations covering pharmaceuticals and radiation safety. The lack of details that specifically address radiopharmaceuticals has understandably caused variability in the interpretation of these regulations. This is exemplified by discussions surrounding the possibility of preparing radiopharmaceuticals—including radiotherapeutics—locally on a small scale for individual patients. This is only possible in a few European countries but has been an essential practice in the development and establishment of novel targeted radiotherapeutics [26]. Another topic that is important to address is the current legal definitions of "radiopharmaceuticals," which also include radionuclide precursors that are considered legally in a manner identical to final preparations. This phenomenon has meant that some producers of radionuclides have to apply for marketing authorizations for their radionuclides even if they are used only as a starting material in a complex radiopharmaceutical preparation [27]. This, of course, adds significant obstacles to the supply of therapeutic radionuclides in particular.

An example of the complex interplay between the legislations covering radiation safety and pharmaceuticals centers on individual dose planning in radionuclide therapy.

Radiopharmaceuticals are legally defined as Medicinal Products and thus have to undergo clinical testing within controlled clinical trials before they receive an MA. In recent years, clinical trials for newly developed radiotherapeutics—e.g., those based on Lu-177—have relied upon a fixed posology. This rigidity was then included in the MA, specifically in the Summary of Product Characteristics (SmPC). A treating physician has to follow these provisions, leading to the practice of fixed administered activities for the treatment. The BSS Directive [5], however, requires that the dose of any type of ionizing radiation for treatment purposes (including therapeutic radiopharmaceuticals) must be optimized. In its own words, "...for all medical exposure of patients for radiotherapeutic purposes, exposures of target volumes shall be individually planned and their delivery appropriately verified.... ." This is contradictory to the SmPC of many therapeutic radiopharmaceuticals and has been a matter of recent debate [28, 29]. Another problem that is very specific to Europe is that even though a common European regulatory framework exists, national regulations can still lead to different practical implementations. This is not only the case for the preparation of radiotherapeutics but also for how TRT is performed. For example, a unified approach to when patients can be discharged after TRT with novel radiotherapeutics (e.g., those based on ^{177}Lu) has not yet been reached, as some countries allow patients to be sent home on the day of the treatment [30] while others require hospitalization for several days [31].

26.4   The Future

The regulatory framework for pharmaceuticals is currently in discussion, and the EU Commission has announced its plans to work on a revision of the relevant legislation. This comes at a time when many novel radiotherapeutics are being implemented into clinical practice or are on the cusp of widespread clinical use. A wide array of probes for TRT may find their way into routine oncologic practice, including radiotherapeutics

based on antibodies, peptides, or small molecules (ligands for fibroblast activation protein are a particularly topical example of the latter) [32]. Yet advances will not only cover new targeting molecules but also novel radionuclides, as TRT with alpha- or Auger electron-emitting radionuclides has recently shown great promise. Of course, new developments in the field will inevitably create new regulatory challenges [33]. For example, no harmonized quality control criteria for alpha-emitting radiotherapeutics have been released.

Guidance documents have been drafted to help both medical professionals and regulators cope with the complex regulatory framework of radiotherapeutics, especially with respect to the development of pharmaceuticals bearing novel radionuclides [34] and in relation to requirements for non-clinical studies [9]. The revision of the pharmaceutical regulations in Europe may also take into account the increasing number of applications involving personalized treatment regimens, a trend that is particularly driven by advanced therapy medicinal products (ATMPs; including gene therapies as well as tissue- and cell-based therapies) that require on-site preparation without classical industrial manufacturing processes. The advent of these regulations may also impact the radiopharmaceutical sphere and lead to a more flexible and adaptive regulatory framework that takes into account rapid developments in the field. However, changes in regulatory processes are slow, and even if they are implemented rapidly, it will take years for the field of TRT to benefit.

26.5   The Bottom Line

- In the European Union, radiotherapeutics are considered Medicinal Products and are therefore covered by pharmaceutical legislation with rare exceptions.
- The regulatory framework for radiotherapeutics within the European Union is characterized by an interplay between legislation covering radiation safety and legislation covering pharmaceuticals.

- The development of novel radiopharmaceuticals for routine clinical use and commercial distribution requires clinical trials to achieve marketing authorization. Clinical trials are very strictly regulated, and legislation has recently been unified throughout the European Union.
- Nation-specific regulations still exist despite a common regulatory framework within the European Union, resulting in variability in practices both with respect to the development of radiopharmaceuticals and with respect to their clinical use.
- Several challenges exist for the regulation of radiotherapeutics in Europe, including addressing inconsistencies between radiation safety and pharmaceutical legislation. Upcoming revisions to the legislation will attempt to adapt to technological advances and in so doing provide a more flexible and adaptive regulatory framework.

References

1. L_2017117EN.01000101.xml [Internet]. [cited 2022 July 23]. Available from: https://eur-lex.europa.eu/legal-content/EN/TXT/HTML/?uri=CELEX:32017R0745&from=de
2. Townsend AR, Chong LC, Karapetis C, Price TJ. Selective internal radiation therapy for liver metastases from colorectal cancer. Cancer Treat Rev. 2016;50:148–54.
3. Castellucci P, Savoia F, Farina A, Lima GM, Patrizi A, Baraldi C, et al. High dose brachytherapy with non sealed 188Re (rhenium) resin in patients with non-melanoma skin cancers (NMSCs): single center preliminary results. Eur J Nucl Med Mol Imaging. 2021;48(5):1511–21.
4. Directive 2001/83/EC of the European Parliament and of the Council of 6 November 2001 on the Community code relating to medicinal products for human use [Internet]. OPOCE; Available from: https://eur-lex.europa.eu/LexUriServ/LexUriServ.do?uri=CELEX:32001L0083:EN:HTML
5. EUR-Lex – 32013L0059 – EN – EUR-Lex [Internet]. [cited 2022 Feb 25]. Available from: https://eur-lex.europa.eu/eli/dir/2013/59/oj
6. Lange R, ter Heine R, Decristoforo C, Peñuelas I, Elsinga PH, van der Westerlaken MML, et al. Untangling the web of European regulations for the preparation of unlicensed radiopharmaceuticals: a concise overview and practical guidance for a risk-based approach. Nucl Med Commun. 2015;36 (5):414–22.
7. Decristoforo C, Penuelas I, Patt M, Todde S. European regulations for the introduction of novel radiopharmaceuticals in the clinical setting. Q J Nucl Med Mol Imaging. 2017;61(2):135–44.
8. Decristoforo C, Lyashchenko SK. Radiopharmaceutical legislation. In: Reference module in biomedical sciences [internet]. Amsterdam: Elsevier; 2021. Available from: https://www.sciencedirect.com/science/article/pii/B9780128229606000685.
9. Korde A, Mikolajczak R, Kolenc P, Bouziotis P, Westin H, Lauritzen M, et al. Practical considerations for navigating the regulatory landscape of non-clinical studies for clinical translation of radiopharmaceuticals. EJNMMI Radiopharm Chem. 2022;7(1):18.
10. Clinical trials – Regulation EU No 536/2014 [Internet]. [cited 2022 July 30]. Available from: https://health.ec.europa.eu/medicinal-products/clinical-trials/clinical-trials-regulation-eu-no-5362014_en
11. EMA. Clinical Trials Information System [Internet]. European Medicines Agency; 2021. [cited 2022 Jul 30]. Available from: https://www.ema.europa.eu/en/human-regulatory/research-development/clinical-trials/clinical-trials-information-system
12. EMA. ICH E6 (R2) Good clinical practice [internet]. European Medicines Agency; 2018. [cited 2022 Jul 30]. Available from: https://www.ema.europa.eu/en/ich-e6-r2-good-clinical-practice
13. Decristoforo C, Penuelas I, Elsinga P, Ballinger J, Winhorst AD, Verbruggen A, et al. Radiopharmaceuticals are special, but is this recognized? The possible impact of the new clinical trials regulation on the preparation of radiopharmaceuticals. Eur J Nucl Med Mol Imaging. 2014;41(11):2005–7.
14. Todde S, Windhorst AD, Behe M, Bormans G, Decristoforo C, Faivre-Chauvet A, et al. EANM guideline for the preparation of an investigational medicinal product dossier (IMPD). Eur J Nucl Med Mol Imaging. 2014;41(11):2175–85.
15. Kolenc Peitl P, Rangger C, Garnuszek P, Mikolajczak R, Hubalewska-Dydejczyk A, Maina T, et al. Clinical translation of theranostic radiopharmaceuticals: current regulatory status and recent examples. J Labelled Comp Radiopharm. 2019;62(10):673–83.
16. Koziorowski J, Behe M, Decristoforo C, Ballinger J, Elsinga P, Ferrari V, et al. Position paper on requirements for toxicological studies in the specific case of radiopharmaceuticals. EJNMMI Radiopharm Chem. 2017;1(1):1.
17. Guideline on the non-clinical requirements for radiopharmaceuticals [Internet]. EMA/CHMP/SWP/686140/2018 Nov 15, 2018 p. 10. Available from: https://www.ema.europa.eu/en/documents/scientific-

guideline/draft-guideline-non-clinical-requirements-radiopharmaceuticals-first-version_en.pdf

18. Pic/S Guide to Good Practices for the Preparation of Medicinal Products In Healthcare Establishments [Internet]. [cited 2021 Feb 9]. Available from: https://picscheme.org/docview/3443

19. Gillings N, Hjelstuen O, Ballinger J, Behe M, Decristoforo C, Elsinga P, et al. Guideline on current good radiopharmacy practice (cGRPP) for the small-scale preparation of radiopharmaceuticals. EJNMMI Radiopharm Chem. 2021;6(1):8.

20. Todde S, Peitl PK, Elsinga P, Koziorowski J, Ferrari V, Ocak EM, et al. Guidance on validation and qualification of processes and operations involving radiopharmaceuticals. EJNMMI Radiopharm Chem. 2017;2(1):8.

21. Aerts J, Ballinger JR, Behe M, Decristoforo C, Elsinga PH, Faivre-Chauvet A, et al. Guidance on current good radiopharmacy practice for the small-scale preparation of radiopharmaceuticals using automated modules: a European perspective. J Labelled Comp Radiopharm. 2014;57(10):615–20.

22. Gillings N, Todde S, Behe M, Decristoforo C, Elsinga P, Ferrari V, et al. EANM guideline on the validation of analytical methods for radiopharmaceuticals. EJNMMI Radiopharm Chem. 2020;5(1):7.

23. Gillings N, Hjelstuen O, Behe M, Decristoforo C, Elsinga PH, Ferrari V, et al. EANM guideline on quality risk management for radiopharmaceuticals. Eur J Nucl Med Mol Imaging. 2022;49(10):3353–64.

24. Council of Europe. European pharmacopoeia commission, european directorate for the quality of medicines & healthcare. 10th ed. European Pharmacopoeia; 2020.

25. Kracmerova T, Holm S. Basics of radioprotection. In: Nuclear medicine and molecular imaging [internet]. St. Louis: Elsevier; 2022. p. 16–29. [cited 2022 July 30]. Available from: https://linkinghub.elsevier.com/retrieve/pii/B9780128229606000508

26. Hendrikse H, Kiss O, Kunikowska J, Wadsak W, Decristoforo C, Patt M. EANM position on the in-house preparation of radiopharmaceuticals. Eur J Nucl Med Mol Imaging. 2022;20:1095–8.

27. Neels O, Patt M, Decristoforo C. Radionuclides: medicinal products or rather starting materials? EJNMMI Radiopharm Chem. 2019;4(1):22.

28. Sjögreen Gleisner K, Spezi E, Solny P, Gabina PM, Cicone F, Stokke C, et al. Variations in the practice of molecular radiotherapy and implementation of dosimetry: results from a European survey. EJNMMI Phys. 2017;4(1):28.

29. Konijnenberg M, Herrmann K, Kobe C, Verburg F, Hindorf C, Hustinx R, et al. EANM position paper on article 56 of the council directive 2013/59/Euratom (basic safety standards) for nuclear medicine therapy. Eur J Nucl Med Mol Imaging. 2021;48(1):67–72.

30. Zhang-Yin J, Guilabert N, Kiffel T, Montravers F, Calais P, Lumbroso J, et al. Patient external dose rate after 177Lu-DOTATATE therapy: factors affecting its decrease and predictive value. Int J Med Sci. 2021;18(12):2725–35.

31. Zippel C, Giesel FL, Kratochwil C, Eiber M, Rahbar K, Albers P, et al. PSMA-Radioligandentherapie könnte Nuklearmedizin vor infrastrukturelle Herausforderungen stellen: Ergebnisse einer Basiskalkulation zur Kapazitätsplanung nuklearmedizinischer Betten im deutschen Krankenhaussektor. Nuklearmedizin. 2021;60(03):216–23.

32. Herrmann K, Kraus BJ, Hadaschik B, Kunikowska J, van Poppel H, N'Dow J, et al. Nuclear medicine theranostics comes of age. Lancet Oncol. 2021;22(11):1497–8.

33. Decristoforo C, Neels O, Patt M. Emerging radionuclides in a regulatory framework for medicinal products – how do they fit? Front Med. 2021;28(8):678452.

34. Decristoforo C, Hayashi SF, Bordeau C, Haddad F, Viertl D, Deville C, et al. Standards for clinical translation; 2022. May 31 [cited 2022 Jul 15]; Available from: https://zenodo.org/record/6599181

The Regulatory Review of Radiotherapeutics: A Japanese Perspective

Tatsuya Higashi

27.1 The Fundamentals

27.1.1 Diagnostic Radiopharmaceuticals in Japan

Diagnostic nuclear medicine is popular and has grown from 1.6 to 1.8 million cases/year over the past 10 years. According to a national survey, the total number of cases in 2018 was about 1.8 million, with ~1.1 million single photon emission computed tomography (SPECT) scans and ~1.1 million positron emission tomography (PET) scans [1]. Although the total number of nuclear medicine examinations has not changed, there is an overall shift from SPECT to PET, as the number of SPECT scans has gradually decreased since 1997. The most utilized radionuclide in Japan for SPECT scans is ^{99m}Tc, followed by ^{201}Tl, ^{123}I, and ^{67}Ga. The latter three are manufactured by accelerators and are stably supplied by two companies: Nihon Medi-Physics (NMP) and PDRadiopharma Inc. ^{99m}Tc, on the other hand, is produced from molybdenum-99 (^{99}Mo), which in turn is made in nuclear reactors abroad. Since there is no medical reactor in Japan that produces ^{99}Mo, the country—which accounts for 14% of the world's ^{99}Mo/^{99m}Tc use—must rely on imports for all ^{99m}Tc radiopharmaceuticals [2].

On the other hand, the increase in the total number of PET scans over the last two decades has been remarkable. PET scans have gradually become widespread since insurance began covering [^{18}F]FDG (fluorodeoxyglucose)-PET in 2002 (Table 27.1). In 2010, [^{18}F]FDG-PET scans began being covered by insurance for *all* malignant tumors, and the procedure is now performed in daily medical care. Radionuclides for PET scans are manufactured domestically, with two methods used to procure [^{18}F]FDG: (1) manufacturing using in-house accelerators and synthesizers, and (2) supply from two private pharmaceutical companies as "insurance-covered radiopharmaceuticals." In a 2018 national survey, the number of PET scans increased by ~25% over 5 years, and the number of [^{18}F]FDG scans using the latter supply route increased significantly [1].

In Japan, ^{11}C, ^{13}N, ^{15}O, and ^{18}F have been designated "the PET4 nuclides." The regulations surrounding their handling have been relaxed due to their short half-lives, and therefore they are particularly widely used for medical purposes. Generally speaking, radiopharmaceuticals employing the PET4 nuclides are supplied using in-house accelerators and synthesizers. As of August 2021, accelerators for the PET4 nuclides have been installed and registered with the Japanese Society of Nuclear Medicine (JSNM) at

T. Higashi (✉)
Department of Molecular Imaging and Theranostics, Institute for Quantum Medical Science (iQMS), National Institutes for Quantum Science and Technology (QST), Chiba-City, Chiba, Japan
e-mail: higashi.tatsuya@qst.go.jp

Table 27.1 Approved radiopharmaceuticals (insurance-listed or marketing-approved) in Japan (after 2000)

Diagnostic or therapeutic	Target	Nuclide	Name of labeled drug	Efficacy	Approval Europe	Approval North America	Approval Japan	Insurance Listed	PubMed First appeared	PubMed First author
Diagnostic	Brain	^{123}I	[^{123}I]-iofetamine	Cerebral blood flow scintigraphy	?	?	July 2002	July 2002	1980	USA
Diagnostic	Brain	^{123}I	[^{123}I]-iomazenil	Epilepsy-focused diagnosis	?	?	June 2004	June 2004	1990	Netherlands
Diagnostic	Tumor, heart, brain	^{18}F	[^{18}F]-fluorodeoxyglucose	Diagnosis of malignant tumor, ischemic heart disease, epilepsy	?	1998 for tumor, 1994 for epilepsy: FDA	August 2005	September 2005	1977	USA
Diagnostic	Tumor	^{111}In	[^{111}In]-ibritumomab-tiuxetan	Low-grade B-cell lymphoma radioimmunotherapy	January 2004: EMA	February 2002: FDA	August 2008	June 2008	2000	USA
Diagnostic	Brain	^{123}I	[^{123}I]-ioflupane	Dopamine transporter scintigraphy	July 2007: EMA	January 2011: FDA	January 2014	November 2013	2003	Italy
Diagnostic	Tumor	^{111}In	[^{111}In]-indium-pentetreotide	Somatostatin receptor diagnosis for neuroendocrine tumors	?	1994: FDA	January 2016	November 2015	1991	Netherlands
Diagnostic	Brain	^{18}F	[^{18}F]-florbetapir	Amyloid imaging agent	January 2013: EMA	April 2012: FDA	August 2017	No	2009	USA
Diagnostic	Brain	^{18}F	[^{18}F]-flutemetamol	Amyloid imaging agent	August 2014: EMA	October 2013: FDA	November 2017	No	2009	Belgium
Diagnostic	Tumor	^{18}F	[^{18}F]-fluciclovine	Diagnosis of brain tumor (glioma)	May 2017: EMA	May 2016: FDA	March 2021	March 2021	1999	USA
Therapuetic	Tumor	Sr-89	[^{89}Sr]-strontium-chloride	Pain relief for metastatic bone tumors	1989: UK	1986: Canada; 1993: FDA	November 2007	September 2007	1942	Belgium
Therapuetic	Tumor	Y-90	[^{90}Y]-ibritumomab-tiuxetan	Low-grade B-cell lymphoma radioimmunotherapy	January 2004: EMA	February 2002: FDA	August 2008	June 2008	2000	USA
Therapuetic	Tumor	Ra-223	[^{223}Ra]-radium-chloride	Castration-resistant prostate cancer with bone metastases	November 2013: EMA	May 2013: FDA	June 2016	May 2016	2003	Norway
Therapuetic	Tumor	Lu-177	[^{177}Lu]-lutetium-oxodotreotide	Somatostatin receptor-positive neuroendocrine tumor	September 2017: EMA	January 2018: FDA	March 2021	March 2021	2001	Netherlands
Therapuetic	Tumor	^{131}I	[^{131}I]-iodine-benzyl guanidine	Pheochromocytoma, paraganglioma	2008: EMA orphan drug for neuroblastoma	July 2018: FDA	March 2021	March 2021	1980	USA

more than 150 facilities nationwide [3]. As mentioned above, [^{18}F]FDG is also delivered to more than 250 PET facilities via a nationwide supply system [3].

In recent years, the use of ^{68}Ga-labeled radiopharmaceuticals has expanded worldwide fueled by the Food and Drug Administration (FDA) and European Medicines Agency (EMA) approvals of [^{68}Ga]Ga-DOTA-TATE (DOTA-octreotate) and [^{68}Ga]Ga-PSMA-11 (prostate specific membrane antigen) [4–6]. However, the response in Japan has been significantly delayed. Indeed, as of 2022, no ^{68}Ga-labeled radiopharmaceuticals have been approved by the Pharmaceuticals and Medical Devices Agency (PMDA; Japanese Pharmaceutical and Medical Device Organization, equivalent to the FDA in the USA), and the supply system is limited. By 2021, only a few physician-led clinical trials using ^{68}Ga-labeled radiopharmaceuticals had begun [7].

27.1.2 Therapeutic Radiopharmaceuticals in Japan

As of 2022, five targeted radionuclide therapies have been approved for reimbursement in Japan: (1) treatment of thyroid disease with radioactive iodine, [^{131}I]NaI, (2) radioimmunotherapy with ^{90}Y-labeled anti-CD20 monoclonal antibody, (3) treatment of metastatic bone tumor with radioactive radium [^{223}Ra]radium chloride, (4) peptide receptor radionuclide therapy (PRRT) with [^{177}Lu]-DOTA-TATE, and (5) treatment of neuroendocrine tumors with [^{131}I] iodobenzylguanidine ([^{131}I]MIBG) (Table 27.1). For each of these radiopharmaceuticals, Japan must rely on imported radionuclides and radiopharmaceuticals. In 2018, National Institutes for Quantum Science and Technology (QST) started a physician-led clinical trial with the National Cancer Center Central Hospital using [^{64}Cu]Cu-diacetyl-bis(N4-methylthiosemicarbazone) ([^{64}Cu][Cu(ATSM)]) (diacetyl-bis (N4-methylthiosemicarbazone) (ASTM)) as a therapeutic radiopharmaceutical [8]. This clinical trial was the first clinical trial in Japan of a domestically produced therapeutic radiopharmaceutical, as we will describe in detail later.

Several α-emitting radionuclides have attracted attention in recent years for radiopharmaceutical therapy (RPT). For example, the remarkable efficacy of [^{225}Ac]PSMA-617 for the RPT of advanced prostate cancer has fueled a surge in interest in ^{225}Ac [9]. Currently, the production of ^{225}Ac is limited to ^{229}Th generators derived from nuclear fuel (i.e., ^{233}U) owned by the USA, Russia, and the EU. For this reason, there is intense interest in the development of alternative production methods for ^{225}Ac, including in Japan [10]. To wit, since 2018, a joint venture by QST and Nihon Medi-Physics (NMP) has worked on developing the accelerator-based production of ^{225}Ac via the proton bombardment of ^{226}Ra [11].

Another α-emitting radionuclide, ^{211}At, has also inspired a great deal of interest in recent years. However, since the production of this α-nuclide requires helium ion irradiation on a medium-sized or larger accelerator, research in Japan has been limited to only a handful of institutes [12]. QST Chiba and QST Takasaki were the first in Japan to explore the production of ^{211}At using a cyclotron and the radiosynthesis of ^{211}At-labeled radiopharmaceuticals [13, 14]. Researchers at Osaka University, Fukushima Medical University, and Riken Wako followed soon thereafter. A clinical trial for the treatment of intractable thyroid cancer using [^{211}At]NaAt started in 2021 at Osaka University [15], and another focused on the RPT of malignant pheochromocytomas using [^{211}At]MABG (astato-benzylguanidine) started in 2022 at Fukushima Medical University. While this work represents a good start, the Japanese infrastructure for the production and manufacturing of α-emitting radiopharmaceuticals remains limited.

Finally, another notable "next-generation" nuclide for RPT is ^{227}Th, which is being developed exclusively by Bayer because it is the parent nuclide of ^{223}Ra. There are several radiopharmaceuticals labeled with ^{227}Th in clinical trials recently [16]. In spite of this, in Japan, all thorium nuclides are subject to the Act on the Regulation of Nuclear Reactors, and their use in medical

institutions is strictly prohibited. Legal issues surrounding the handling of thorium are regarded as a potential problem for the future of RPT in Japan, as discussed below.

27.1.3 Pharmaceutical Affairs Approval and Radiopharmaceutical Development in Japan

Since 2000, a total of 12 radiopharmaceuticals have been approved by the Japanese regulatory authorities, including 7 diagnostic and 5 therapeutic agents (Table 27.1). Please note that the time difference from overseas approval—the so-called "drug lag"—is noticeable in the regulatory approval of these agents. In addition, no diagnostic or

therapeutic radiopharmaceuticals originally developed in Japan have been listed on the Japanese health insurance system to date, and no clinical trials were conducted with a Japan-made radiopharmaceutical until 2018. Indeed, until 2018, all clinical trials of radiopharmaceuticals in Japan were performed using agents that were already approved by the FDA and the EMA and were conducted for the purpose of verification in Japanese patients. As a result, no structure exists for the creation and translation of a Japan-made radiopharmaceutical. In other words, while the PMDA has had a review system for clinical trials of radiopharmaceuticals on humans, they do not have a system to review preclinical studies in animals despite the latter being essential for the regulatory review of radiopharmaceuticals (Fig. 27.1).
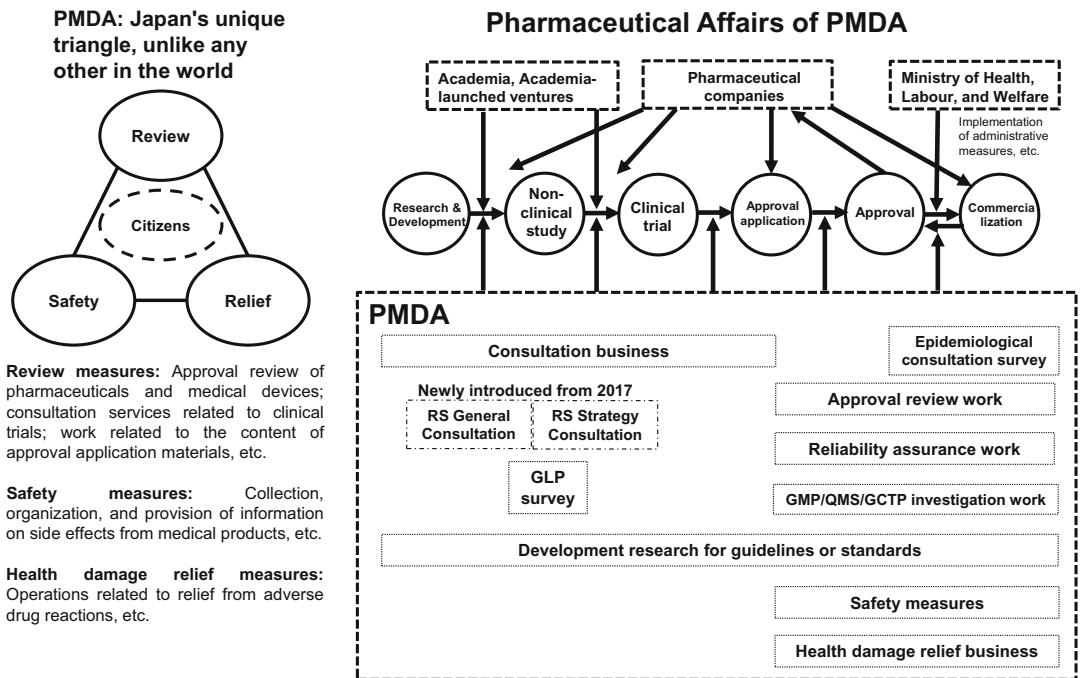
Fig. 27.1 This figure shows the organizational philosophy and the work in pharmaceutical affairs of the Japanese Regulatory Authority for Drugs and Medical Devices: Pharmaceuticals and Medical Devices Agency (PMDA). PMDA is the only public organization in the world that integrates "Japan's unique triangle": the three roles of health damage relief, approval review, and safety measures for pharmaceuticals (left). PMDA conducts

approval review works of submitted documents, reliability assurance works, and GMP/Quality Management System (QMS)/Good Gene, Cellular, and Tissue-based Products Manufacturing Practice (GCTP) investigation works as review-related operations. From 2017, RS General Consultation and RS Strategy Consultation works have also started (right)

Generally speaking, preclinical and clinical studies of pharmaceuticals must be conducted according to Good Laboratory Practice (GLP), Good Manufacturing Practice (GMP), and Good Clinical Practice (GCP) standards as defined by the Organization for Economic Co-operation and Development (OECD), the World Health Organization, and the International Council for Harmonization of Technical Requirements for Pharmaceuticals for Human Use (ICH) [17–19] and enforced based on the Pharmaceuticals and Medical Devices Act in Japan. For both non-clinical studies and the preparation of clinical trials, a non-clinical study implementation system must be established in the form of a GLP "code of conduct." Then at the clinical trial stage, it is necessary to establish a GMP-level manufacturing system for the production of the pharmaceutical. Clinical trials should be performed according to international standards for the manufacturing and quality control of pharmaceuticals and non-pharmaceutical products.

During the research and development (R&D) of radiopharmaceuticals, the situation for non-clinical and clinical studies is different from the production of normal pharmaceuticals because radiopharmaceuticals must be manufactured in controlled areas for radionuclides. While GLP/GMP facilities require positive pressure control, controlled areas for radionuclides require negative pressure control. Therefore, it is not easy to combine the two, especially in Japan, because the regulation of radiation is quite strict. In the development of radiopharmaceuticals, the following things are required to conduct GLP-level non-clinical studies and to manufacture GMP-level radiopharmaceuticals for clinical studies: (1) abundant financial support to construct and maintain special facilities with the controlled areas for radionuclides, (2) expertise in the design and use of such facilities, and (3) an education and training system for professional human resources. Although it is possible to outsource some non-clinical studies to a contractor with GLP-level controlled areas for radionuclides,

very few contractors for this sort of work exist in Japan, and the consignment costs are high. In addition, no contractor in Japan can support α-emitting nuclides at present.

In light of these restrictions, the JSNM has made many guidelines and academic society certification criteria for diagnostic agents labeled with PET4 nuclides produced in-house for the purpose of facilitating PET research under relatively inexpensive conditions [20]. These "academic GLP/GMP" standards are less strict and less expensive than the international GLP/GMP standards and are easier to administer for the clinic. Although the diagnostic PET tracers covered by "academic GLP/GMP" standards can be used for research purposes, they cannot be approved by regulatory affairs as insurance-covered radiopharmaceuticals. Therefore, for the past two decades, most Japanese academia have been focusing on the research using the PET4 nuclides, because deviating from these isotopes would be prohibitively expensive.

For the last 20 years or so, the Japanese economy has endured a long-term economic recession. As a result, national financial support for research has diminished, and shortages of academic research funding have become constant. Therefore, while Japanese nuclear medicine research has been active in clinical research on PET diagnostics, this research has remained limited to studies with the PET4 nuclides. Furthermore, only a few attempts have been made to develop insurance-covered radiopharmaceuticals that require strict and expensive international GLP/GMP standards. These financial challenges also explain why no Japan-made therapeutic radiopharmaceuticals have been developed. For the two domestic radiopharmaceutical companies, preclinical research and development studies are highly risky because the PMDA has never had a review system for preclinical studies. Furthermore, there is a history of delays in the approval of applications for radiopharmaceuticals in Japan, as mentioned below. For academia, it has been impossible to receive sufficient research funding to start and maintain a program focused on the research and development of

radiopharmaceuticals. The research community also cannot rely on private funding. While there is a tendency for venture-funded pharmaceutical companies to take risks and engage in the research and development of radiopharmaceuticals in Europe and the USA, the same amenability to risk does not exist in Japan, probably because of its historical and cultural background. As a result, there has been little to no private investment in the development of novel Japan-made radiopharmaceuticals.

27.2 The Details

27.2.1 Legislation and Policies Related to Radiopharmaceuticals

In Japan, there are major limitations with respect to the preclinical research and development of radiopharmaceuticals. The guidelines discussed within the Application of the Concepts of Exclusion, Exemption, and Clearance by the International Atomic Energy Agency (IAEA) [21] are not applicable in Japan within either the medical field or the development of radiopharmaceuticals. As you may know, a mechanism called a "clearance system" allows for the reuse or disposal of low-level radioactive materials that will have little or no impact on human health as ordinary waste. In Japan, this concept is applicable to nuclear-power-related projects but not to the preclinical development of radiopharmaceuticals. The development of general pharmaceuticals requires a process that includes preclinical studies, clinical trials, and regulatory approval. The development of radiopharmaceuticals requires the same processes, but it should be strictly conducted in controlled areas for radionuclides under the Act on the Regulation of Radioisotopes (RI Regulation Act) and the Medical Care Act. As mentioned above, the PET4 nuclides are exempted from these rules and are thus widely and conveniently used for medical treatment. However, there are strict restrictions on the entry of personnel into controlled areas for radionuclides, the removal of materials from these controlled areas, and the

waste disposal of radionuclides other than the PET4 nuclides.

The RI Regulation Act and the Act on Prevention of Radiation Hazards due to Radioisotopes (Act on RI hazards) do not allow radioactive materials to be taken out of controlled areas of facilities that have permission to use unsealed radionuclides. Under the Act on RI hazards, nuclides other than the PET4 nuclides and their contaminated materials cannot be taken out of the controlled areas for radionuclides *even after* the radioactivity has decayed. Therefore, preclinical studies for the development of novel radiopharmaceuticals cannot be freely conducted in Japan. In other words, if regulatory authorities were to require additional special laboratory analyses or histopathological tests during the preclinical phase of the approval process for a radiopharmaceutical, these tissue (or others) could not be taken out of the controlled areas for radionuclides because they are considered contaminated radioactive materials. Conversely, once special histopathological analyzing equipment is brought into a controlled area for radionuclides, it is considered contaminated with radioactive materials and cannot be taken out(!) Furthermore, when preclinical studies require the use of expensive or specialized animals such as primates, the animals must be kept in facilities within the controlled areas for radionuclides, and, once brought in, they cannot be taken out and must be slaughtered. This is, of course, also a problem from an animal welfare perspective. For these reasons, there are only a few facilities in Japan—including contract research institutes—that can administer radionuclides to primates using isotopes other than PET4 nuclides. Even for small animals, the number of contractors is still small. Furthermore, waste from α-emitting nuclides (except for $[^{223}Ra]$radium-chloride) is currently not allowed out of controlled areas, and thus contaminated materials must be kept inside our own facilities forever.

Obviously, all of these restrictions are major problems for the development of radiopharmaceuticals in Japan. In order to establish a preclinical testing facility for radiopharmaceuticals, a

facility would need to not only be equipped with all of the analytical equipment that would ever be required but also be big enough to keep many animals *and* store radioactive (and decayed) medical waste. This strict regulation based on the RI Regulation Act and the Act on RI hazards—absent the concept of a "clearance system"—has greatly impeded the development of novel radiopharmaceuticals in Japan.

As if the above were not enough, there is still another problem for radiotherapeutics in Japan. In 1998, a Ministry of Health, Labour, and Welfare (MHLW) ordinance based on the Medical Care Act stipulated standards for the discharge of patients from radiotherapy rooms and dictated that the use of ^{131}I requires hospitalization in a radiotherapy room. This guideline is based on international standards for the protection of the general public and is based on the International Commission on Radiological Protection (ICRP) index. However, the standard in Japan, the third strictest in the world after Germany and the UK, is set to 500 MBq, much lower than the ICRP recommended level of 1100 MBq [22]. As a result, there is currently a nationwide shortage of radiotherapy rooms for unsealed radionuclides, and delays in treatment have been reported [23]. This has worsened prognoses for patients with metastatic differentiated thyroid cancer [24]. $[^{90}Y]Y$-ibritumomab-tiuxetan, $[^{89}Sr]$-strontium-chloride, and $[^{223}Ra]$-radium-chloride—all of which were introduced after 2007—are administered at doses below the release criteria, and outpatient treatment is performed. On the other hand, according to the standards of Japanese release criteria, hospitalization in radiotherapy rooms is required for $[^{177}Lu]DOTA$-TATE and $[^{131}I]MIBG$. Furthermore, $[^{177}Lu]PSMA$-617 is being prepared for introduction in Japan and is also expected to require several days of in-patient treatment in a radiotherapy room. Therefore, there are significant concerns about further shortages of radiotherapy rooms for unsealed radionuclides because prostate cancer has a high prevalence among men in Japan.

Thankfully, the MHLW has invested funds to establish a research group to discuss the release criterion for radiopharmaceuticals and to prepare manuals for their proper use in the medical environment [25]. Based on the study of this research group, release criteria were established for $[^{177}Lu]$-DOTA-TATE that consider the non-vaporizing properties of the nuclide ^{177}Lu. In 2021, guidelines were issued under the Medical Care Act allowing for the hospitalization of patients treated with $[^{177}Lu]DOTA$-TATE in a general in-patient room (private room) with appropriate protective measures [26]. This measure eliminates the need for radiotherapy rooms and is expected to contribute to the spread of RPT within the country.

The necessity of establishing a supportive environment for RPT within the medical care system has been discussed by relevant ministries and agencies. In 2018, MHLW issued a notice based on the Basic Plan for the Promotion of Cancer Control establishing the provision of an "RPT" system as one of the requirements for designating hospitals for cancer treatment coordination [27]. Further legislation is expected to contribute to the spread of RPT in Japan in the future.

27.2.2 Research and Development and the Approval Review System for Radiopharmaceuticals

The approval process for radiopharmaceuticals was difficult and time-consuming until the early 2000s. As a result, radiopharmaceutical companies have been unable to actively enter the market in Japan. For example, $[^{89}Sr]$-strontium-chloride—approved in Japan in 2007 for the palliative treatment of bone metastases—was first approved in Canada in 1986, the UK in 1989, and the USA in 1993. The drug insurance application was submitted to the Japanese Pharmaceutical and Medical Device Organization (a predecessor of the PMDA) in 1996, and the approval was finally obtained in 2007 (Table 27.1). This 11-year-long regulatory approval saga makes this radiopharmaceutical a typical example of drug lag in Japan. Ironically, $[^{89}Sr]$-strontium-chloride was subsequently discontinued in 2019

and is no longer available for clinical use. This leaves no palliative radiopharmaceutical for bone metastases in Japan, as no suitable replacement—e.g., a [153]Sm- or [186]Re-labeled radiopharmaceutical—is scheduled to receive approval.

[111]In-pentetreotide, an ^{111}In-labeled somatostatin receptor-targeting radiopharmaceutical for the imaging of neuroendocrine tumors, provides yet another example of the challenges surrounding radiopharmaceuticals in Japan. It was approved in the USA and Europe in 1994, clinical trials were begun in Japan around 1996, and an application for approval was initiated [28]. However, the drug was not approved at that time, and the pharmaceutical company that developed it was forced to withdraw from the Japanese market. After a long interval, the MHLW's "Review Committee on Unapproved Drugs and Off-label Drugs" deliberated on the drug, and another pharmaceutical company submitted a new application that was finally approved by the PMDA in 2015 [29].

In 2001, the PMDA was newly established in response to problems with delays in the review and approval process for pharmaceuticals; hence, the approval process for radiopharmaceuticals is now conducted by the PMDA in the same manner as for general drugs. Recently, improvements in this process have been noted, including the shortening of review periods. The FDA and the EMA approved [[223]Ra]radium-chloride in 2013, while domestic approval was fast-tracked to 2016. In 2021, two new therapeutic radiopharmaceuticals—[^{177}Lu]DOTA-TATE and [^{131}I]MIBG—were approved by the PMDA without significant delays compared to the FDA and the EMA.

On the other hand, the review of diagnostic radiopharmaceuticals continues to be a hurdle for radiopharmaceutical companies. Because the dosage of diagnostic radiopharmaceuticals is only about a microgram (which is considered to be safely administered), the MHLW issued "Guidance for Conducting Microdose Clinical Trials" in 2008 [30]. Therefore, it is relatively easy to start a first-in-human (FIH) study of diagnostic radiopharmaceuticals based on the Clinical Research Act of 2017 [31]. However, in recent

years, diagnostic radiopharmaceuticals have faced difficulties in becoming covered by insurance even if they are effective due to the uncertainty of their prognostic contribution. For example, two amyloid imaging agents, [^{18}F] florbetapir and [^{18}F]flutemetamol, were approved for manufacture and marketing in 2017 by the PMDA but were not listed on the national public insurance due to the uncertainty of their prognostic contribution in dementia.

In industry-controlled clinical trials, PMDA examinations are generally expensive and hold high safety standards for both general drugs and radiopharmaceuticals. Because domestic clinical trials for Japan-made radiopharmaceuticals have never occurred, no detailed information about the preclinical studies required by the PMDA has been provided. As a result, starting preclinical studies for Japan-made radiopharmaceuticals represents a high-risk gamble for the two domestic radiopharmaceutical manufacturers. In contrast, preclinical studies are not needed for radiopharmaceuticals approved overseas, dramatically lowering the hurdles for regulatory approval.

The JSNM has taken the lead in developing guidelines for preclinical studies of diagnostic PET tracers using the PET4 nuclides ("diagnostic GL") [32]. In the "diagnostic GL," safety is the highest priority. Therefore, the "diagnostic GL" requires that four substances must be strictly tested in preclinical studies: the active ingredient, a non-radioactive compound with the same structure as the active ingredient, the compound labeled with an appropriate radionuclide, and the ligand before labeling. In contrast, with therapeutic radiopharmaceuticals, it is necessary to balance the risk of death and the benefit of treatment in patients with refractory cancer. Therefore, there is a question about the need to rigorously verify the four substances described above. Furthermore, the need to test and characterize non-radioactive variants of radiopharmaceuticals can become especially problematic in the context of therapeutic radionuclides for which there are no (or few) stable isotopes. Clearly, guidelines for non-clinical studies on therapeutic radiopharmaceuticals are sorely needed.

The establishment of guidelines for preclinical studies with therapeutic radiopharmaceuticals is now in progress in Europe and the USA. As we have seen, these guidelines are urgently needed in Japan as well. As a first step, Hachisuka et al. published a Japanese translation of the FDA guidance in the *Journal of the Japanese Society of Regulatory Science* [33], and Prof. Hachisuka has obtained research funding to develop guidelines for preclinical studies of therapeutic radiopharmaceuticals in Japan.

27.3   Something Extra

27.3.1   Difficulty in the Domestic Use of ^{68}Ga

Unlike the PET4 nuclides, ^{68}Ga is not produced using an accelerator. Instead, it is supplied by a ^{68}Ge/^{68}Ga generator that is installed in a medical institution. ^{68}Ga is extracted from the generator for each PET scan, and the ^{68}Ga-labeled radiopharmaceutical is manufactured within the medical institution using a labeling kit. Each medical institution purchases an approved generator that can be used for about 1 year because ^{68}Ge has a half-life of about 270 days.

In Japan, the ^{68}Ge/^{68}Ga generator—which is widely used worldwide—has not been approved, and clinical ^{68}Ga PET scans are completely unavailable. This leaves Japan far behind in the world of nuclear medicine. The JSNM has been lobbying for clinical approval of this ^{68}Ge/^{68}Ga generator but has not been able to achieve it for many years, representing a major weakness in clinical nuclear medicine in Japan. One of the reasons for the lack of approval for this generator is a disagreement between the MHLW and the companies trying to introduce the generator to Japanese markets. Unlike the ^{99m}Tc from the ^{99}Mo/^{99m}Tc generator, the extracted ^{68}Ga cannot be administered directly to the patient. For this reason, it was not possible to conclude for more than 10 years whether the ^{68}Ge/^{68}Ga generator is a medical device or a drug under the

Pharmaceutical Affairs Law. This silly debate has caused a significant delay in the medical use of ^{68}Ga use in Japan.

In 2018, the MHLW concluded that the ^{68}Ge/^{68}Ga generator can be "treated as a raw material" like an accelerator or a cyclotron. In response, Hokkaido University issued a press release in 2019, announcing the start of joint research toward the pharmaceutical approval of a [^{68}Ga]PSMA synthesis device. In August 2021, Fukushima Medical University issued a news release on the production of ^{68}Ga using a cyclotron. Future developments, such as the creation of new ^{68}Ga-labeled radiopharmaceuticals and the initiation of physician-led clinical trials, are expected soon.

27.3.2   Thorium and the Nuclear Reactor Regulation Law

In Europe and the USA, Bayer is taking the lead in the development of radiopharmaceuticals labeled with ^{227}Th, and early-stage clinical trials are underway [16]. In most of the world, fissile and non-fissile thorium are considered separately. Although fissile ^{232}Th is converted to nuclear material by neutron irradiation, non-fissionable thorium (^{229}Th, ^{227}Th, ^{226}Th) is typically handled under less stringent controls. For this reason, the medical use of non-fissile ^{227}Th is progressing in Europe and the USA.

In Japan, on the other hand, all thorium is considered nuclear fuel material under the Basic Act on Atomic Energy and the Act on the Regulation of Nuclear Reactors. There is no distinction between fissile and non-fissile thorium. Therefore, in Japan, all thorium is covered under the Basic Act on Atomic Energy and *not* the Medical Care Act. This means that the medical use of ^{227}Th is currently impossible. Thankfully, the Atomic Energy Commission and a research group of the MHLW of Japan are currently engaged in the establishment of a new legal framework and new management guidelines for the radiopharmaceutical use of ^{227}Th.

27.4　The Future

In recent years, new systems have been introduced to the regulatory approval process in Japan, providing a tailwind for the research and development of radiopharmaceuticals. According to the notification of the MHLW in 2017, applications for physician-led clinical trials are subject to the regulatory science general consultation (RS General Consultation: free of charge) and the regulatory science strategy consultation (RS Strategy Consultation) at relatively low costs, unlike very expensive industry-controlled clinical trials (Fig. 27.1) [34]. These RS Consultations are available for the development of pharmaceuticals, medical devices, and regenerative medicines and are primarily meant to provide academia and academia-launched, venture-supported companies with guidance and advice on physician-led clinical trials. The PMDA requirements for preclinical studies tend to be slightly easier, especially when the trial is targeting intractable cases of relatively rare cancers. The goal of this initiative—which is designed to spur innovation in the country's pharmaceutical sector—is to tolerate certain safety risks while encouraging the further development of a wide range of candidate drugs that exist in many academia and academia-launched venture companies. After confirming safety and efficacy in Phase I/II, academia and academia-launched venture companies can then connect with pharmaceutical companies for Phase II/III clinical trials, which of course require much more funding. This system of RS Consultations will be a great help for the research, development, and approval of Japan-made radiopharmaceuticals.

QST—an academic institution with expertise in GMP manufacturing within controlled areas for radionuclides—have developed $[^{64}Cu][Cu(ATSM)]$ as a therapeutic radiopharmaceutical by replacing the central radiometal of $[^{62}Cu][Cu(ATSM)]$, a hypoxia-targeted PET tracer originally developed in Japan [35]. This β- and Meitner-Auger electron-emitting radiopharmaceutical accumulates specifically in hypoxic regions and is expected to be effective for the treatment of intractable malignant brain tumors. $[^{64}Cu][Cu(ATSM)]$ holds one key advantage that positions it well for a clinical trial in Japan: ^{64}Cu emits positrons as well as therapeutic radiations. Therefore, a first-in-human PET imaging study has already been completed in Japan, paving the way for the verification of its safety by reviewers. In 2018, after the review of the preclinical studies by the PMDA, we started a physician-led clinical trial with the National Cancer Center Central Hospital [36]. This trial is the first clinical trial in Japan of a domestically produced therapeutic radiopharmaceutical and also represents the first time a GMP manufacturing system has been established for a domestically produced radiopharmaceutical. Importantly, this trial has also contributed to the establishment of the PMDA approval review system for Japan-made radiopharmaceuticals under the umbrella of international GLP/GMP standards.

Several exciting trials have followed this initial effort. For example, a physician-led clinical trial for the treatment of refractory thyroid cancer using the new α-emitting radiopharmaceutical $[^{211}At]NaAt$ was started in 2021 at Osaka University [37]. At Fukushima Prefectural Medical University, a physician-led clinical trial started in 2022 using $[^{211}At]MABG$ (jointly developed with QST) for the treatment of malignant pheochromocytoma. QST has also started the research and development of radioimmunotherapeutics using an anti-podoplanin (PDPN) antibody labeled with ^{90}Y and ^{225}Ac [38].

27.4.1　A National Action Plan

In November 2021, the Atomic Energy Commission under the jurisdiction of the Cabinet Office established a special subcommittee—"Medical Radioisotope Production and Utilization"—with the aim of achieving full-scale domestic self-sufficiency for the production of medically important radionuclides [39]. On May 31, 2022, this subcommittee deliberated on and summarized a National Action Plan to ensure the secure production and utilization of medical

radionuclides across Japan, with observers from related ministries such as the Cabinet Office, Ministry of Education, Culture, Sports, Science and Technology Ministry of Education, Culture, Sports, Science and Technology (MEXT), MHLW, Ministry of Economy, Trade and Industry, Nuclear Regulation Authority, and Fukushima Reconstruction Agency. As a member of this committee, the author has pointed out Japan's slow progress in the field of nuclear medicine, the research and development of radiopharmaceuticals, and the modernization of pharmaceutical affairs. It has been more than 20 years since the JSNM began lobbying the MHLW to improve the environment in Japan for radiotheranostics, but we have finally established a cross-ministerial subcommittee to address this issue. There is no doubt that the action plan announced in May 2022 will have a positive impact on the future of nuclear medicine in Japan [39].

Japan is the only country whose public has been exposed to radiation multiple times (Hiroshima, Nagasaki, and Fukushima), and many of its citizens have a fear and dislike of radiation. As nuclear medicine moves forward in Japan, it must remain aware of this public perception and strive to gain the public's trust. It is undeniably true that Japan's overzealous regulations have adversely affected nuclear medicine in the country, but the regulatory sciences will nonetheless have an important role to play in gaining public support and trust. While novel radiopharmaceuticals are expected to have a strong therapeutic effect—and α-emitting radiopharmaceuticals are especially promising as breakthrough drugs—the risk of fatal side effects is not zero, so a robust regulatory affairs system will help assuage public anxieties. If physicians, researchers, and regulatory agencies work together, we believe that public acceptance of modern nuclear medicine is possible.

27.4.2 The Bottom Line

- The Japanese nuclear medicine landscape has historically been characterized by strict

examinations of radiopharmaceuticals, significant drug lag, and a very limited number of regulatory approval applications for new radiopharmaceuticals.
- The disposal of low-level radioactive materials and the hospitalization of patients treated with radiopharmaceuticals are strictly regulated by laws, resulting in a shortage of Good Laboratory Practice (GLP) facilities, a dearth of in-patient radiotherapy rooms, and a lack of Japan-made radiopharmaceuticals.
- Since Japan has relied on foreign imports for all its therapeutic radiopharmaceuticals and many of its diagnostic radiopharmaceuticals, the regulatory science needed for preclinical and clinical trials remains underdeveloped.
- Year 2018 played witness to the first physician-led clinical trial of Japan-made therapeutic radiopharmaceutical: [^{64}Cu][Cu(ATSM)].
- In 2022, a government-led action plan aimed at fostering the development of Japan-made radiopharmaceuticals is expected to promote deregulation and advance the regulatory sciences in the field.

References

1. Subcommittee on Survey of Nuclear Medicine Practice in Japan. The present state of nuclear medicine practice in Japan~a report of the 8th nationwide survey in 2017. Radioisotopes. 2018;67:339–87. (in Japanese)
2. Cabinet Office, Government of Japan: Title of subordinate document of Japan Atomic Energy Commission. In: Action plan for "Stable supply of technetium preparations in Japan". 2011. https://wwwa.cao.go.jp/oaep/mo-supply/houkokusho.pdf (in Japanese). Accessed 7 July 2011.
3. Japanese Society of Nuclear Medicine/PET Nuclear Medicine Subcommittee: PET Facility List. https://jcpet.jp/ (in Japanese).
4. RadioMedix, Inc. http://demo.radiomedix.com/news/radiomedix-inc-receives-fda-orphan-drug-designation-for-the-68ga-dotatate-galiomedixtm-for-the-management-of-the-neuroendocrine-tumors/
5. Advanced Accelerator Applications: A Novartis Company. https://www.adacap.com/advanced-accelerator-applications-announces-fda-approval-of-netspot-somakit-tate-a-kit-for-the-preparation-of-gallium-ga-

68-dotatate-for-neuroendocrine-tumor-detection-netspot-w/

6. U.S.A. FOOD & DRUG Administration: https://www.fda.gov/drugs/news-events-human-drugs/fda-approves-second-psma-targeted-pet-imaging-drug-men-prostate-cancer

7. TELIX Pharmaceuticals Japan K.K. https://jp.telixpharma.com/news-media/%e5%89%8d%e7%ab%8b%e8%85%ba%e3%81%8c%e3%82%93pet%e7%94%bb%e5%83%8f%e8%a8%ba%e6%96%ad%e8%96%ac%e3%81%ae%e5%9b%bd%e5%86%85%e5%8c%bb%e5%b8%ab%e4%b8%bb%e5%b0%8e%e6%b2%bb%e9%a8%93%e7%b5%84%e3%81%bf/ (in Japanese).

8. National Institutes for Quantum Science and Technology: Succeeded in formulating a Japanese radiotherapy drug for malignant brain tumors. https://www.qst.go.jp/site/press/1214.html (in Japanese).

9. Kratochwil C, Bruchertseifer F, Giesel FL, Weis M, Verburg FA, Mottaghy F, et al. ^{225}Ac-PSMA-617 for PSMA-targeted α-radiation therapy of metastatic castration-resistant prostate cancer. J Nucl Med. 2016;57(12):1941–4.

10. Radchenko V, Morgenstern A, Jalilian AR, Ramogida CF, Cutler C, Duchemin C, et al. Production and supply of a-particle–emitting radionuclides for targeted a-therapy. J Nucl Med. 2021;62:1495–503.

11. Nagatsu K, Suzuki H, Fukada M, Ito T, Ichinose J, Honda Y, et al. Cyclotron production of 225Ac from an electroplated ^{226}Ra target. Eur J Nucl Med Mol Imaging. 2021;49:279–89.

12. Nagatsu K, Minegishi K, Fukada M, Suzuki H, Hasegawa S, Zhang M-R, et al. Production of (211) At by a vertical beam irradiation method. Appl Radiat Isot. 2014;94:363–71.

13. Ohshima Y, Sudo H, Watanabe S, Nagatsu K, Tsuji AB, Sakashita T, et al. Antitumor effects of radionuclide treatment using α-emitting meta-^{211}At-astatobenzylguanidine in a PC12 pheochromocytoma model. Eur J Nucl Med Mol Imaging. 2018;45:999–1010.

14. Sudo H, Tsuji AB, Sugyo A, Nagatsu K, Minegishi K, Ishioka NS, et al. Preclinical evaluation of the acute radiotoxicity of the alpha-emitting molecular-targeted therapeutic agent (211)At-MABG for the treatment of malignant pheochromocytoma in normal mice. Transl Oncol. 2019;12:879–88.

15. Department of Nuclear Medicine and Tracer Kinetics: Osaka University Graduate School of Medicine. News Release. https://www.med.osaka-u.ac.jp/pub/tracer/about/research/nuclear_01.html (in Japanese).

16. Bayer Development Pipeline: https://www.bayer.com/en/pharma/development-pipeline

17. OECD Good Laboratory Practice (GLP): https://www.oecd.org/chemicalsafety/testing/good-laboratory-practiceglp.htm

18. WHO Health product and policy standards: Good Manufacturing Practices. https://www.who.int/teams/health-product-policy-and-standards/standards-and-specifications/gmp

19. Good Clinical Practice NETWORK. https://ichgcp.net/.

20. The Japanese Society of Nuclear Medicine. General Guidelines for Molecular Imaging and List of Documents Related to Drug Manufacturing. (October 7, 2021). http://jsnm.org/useful/molecule/documents/ (in Japanese).

21. Application of the Concepts of Exclusion, Exemption and Clearance by International Atomic Energy Agency. IAEA Safety Standards Series. STI/PUB/1202 ¦ 92-0-109404-3.

22. ICRP. Release of patients after therapy with unsealed radionuclides. Ann ICRP. 2004;34(2):v–vi.

23. Thyroid RI Treatment Committee of Japanese Society of Nuclear Medicine in Oncology and Immunology. Subcommittee of Japanese society of Nuclear Medicine. Survey report on the operating status of RI treatment rooms in radioiodine internal therapy for thyroid cancer (5th report). Kaku Igaku. 2019;56:107–16. (in Japanese)

24. Higashi T, Nishii R, Yamada S, Nakamoto Y, Ishizu K, Kawase S, et al. Delayed initial radioactive iodine therapy resulted in poor survival in patients with metastatic differentiated thyroid carcinoma: a retrospective statistical analysis of 198 cases. J Nucl Med. 2011;52(5):683–9.

25. Ministry of Health, Labor and Welfare Research Fund/Regional Medical Infrastructure Development Promotion Research Project "Research for establishing standards for radiation protection for new and existing radiation medical care" (19IA1004). https://www.mhlw.go.jp/seisakunitsuite/bunya/hokabunya/kenkyujigyou/hojokin-koubo-2021/gaiyo/19.html (in Japanese).

26. Ministry of Health, Labor and Welfare: Medical Administration: Health Policy Publication No.0819 No. 1 "About the exit of patients who received radiopharmaceuticals". https://www.jrias.or.jp/pdf/iseichihatu0819_01.pdf (in Japanese) (2021). Accessed 19 Aug 2021.

27. Ministry of Health, Labor and Welfare. Health Publication No. 0731No. 1 "Maintenance of Cancer Treatment Cooperation Base Hospitals". https://www.mhlw.go.jp/content/000347080.pdf (in Japanese) (2018). Accessed 31 July 2018.

28. Kimura T, Sakahara H, Higashi T, Honda T, Konishi J, Hosotani R, et al. Survey report on the operating status of RI treatment rooms in radioiodine internal therapy for thyroid cancer (5th report). Kaku Igaku. 2019;56:107–16. (in Japanese)

29. Kurita Y, Kuwahara T, Mizuno N, Okuno N, Matsumoto S, Torisima K, et al. Utility of somatostatin receptor scintigraphy in pancreatic neuroendocrine neoplasms. Suizo. 2019;34:78–85. https://doi.org/10.2958/suizo.34.78. (in Japanese)

30. Ministry of Health, Labor and Welfare: Notification of Chief of Examination and Management Division,

Pharmaceutical and Food Safety Bureau: No. 0603001 "Guidance on the implementation of Microdose clinical trials" (June 3, 2008). https://www.pmda.go.jp/files/000206215.pdf (in Japanese).

31. Ministry of Health, Labor and Welfare. Ministry of Health, Labor and Welfare Ordinance No. 17. "Clinical Research Law Enforcement Regulations" (February 28, 2018). https://www.mhlw.go.jp/web/t_doc?dataId=80ab6260&dataType=0&pageNo=1 (in Japanese).

32. Japanese Society of Nuclear Medicine. "General Guidelines for Molecular Imaging and List of Documents Related to Drug Manufacturing" (October 7, 2021). http://jsnm.org/useful/molecule/documents/

33. Hachisuka A, Higashi T, Hosono M, Ono M, Uehara T, Nishimura N, et al. Japanese translation and supplementary explanation of the FDA guidance "oncology therapeutic radiopharmaceuticals: nonclinical studies and Labeling recommendations guidance for industry". Regul Sci. 2022;12:161–77. https://doi.org/10.14982/rsmp.12.161. (in Japanese)

34. Pharmaceuticals and Medical Devices Agency. Pharmaceuticals and Medical Devices Agency No. 0316001. (March 16, 2017) "Regarding partial revision of the implementation guidelines for regulatory affairs strategy consultation" https://www.pmda.go.jp/files/000217709.pdf (in Japanese).

35. Fujibayashi Y, Taniuchi H, Yonekura Y, Ohtani H, Konishi J, Yokoyama A. Copper-62-ATSM: a new hypoxia imaging agent with high membrane permeability and low redox potential. J Nucl Med. 1997;38 (7):1155–60.

36. National Institutes for Quantum Science and Technology. Title of subordinate document. In: "Succeeded in formulating a Japanese radiotherapy drug for malignant brain tumors". https://www.qst.go.jp/site/press/1214.html (in Japanese).

37. Osaka University. Press release of thyroid cancer treatment with alpha-ray nuclide astatine (NaAt) https://www.med.osaka-u.ac.jp/pub/tracer/about/research/nuclear_01.html (in Japanese).

38. Sudo H, Tsuji AB, Sugyo A, et al. Preclinical evaluation of Podoplanin-targeted alpha-Radioimmunotherapy with the novel antibody NZ-16 for malignant mesothelioma. Cell. 2021;10:2503.

39. Homepage of Japan Atomic Energy Commission. Radioisotope manufacturing and utilization subcommittee for medical use, etc.. http://www.aec.go.jp/jicst/NC/senmon/radioisotope/index.htm (in Japanese).

Radiotherapeutics and Nuclear Pharmacy

28

Akram Hussein

28.1 The Fundamentals

This chapter provides an overview of radiotherapeutics and the role of the nuclear pharmacy in radiopharmaceutical therapy (RPT). Specifically, we will endeavor to answer the following key questions:

- What are radiotherapeutics?
- What is the role of a nuclear pharmacy in RPT?
- What are some common and emergent radiotherapeutic agents?
- How should radiotherapeutics be handled, dispensed, and administered?
- What is the future outlook of work at the intersection of radiotherapeutics and nuclear pharmacy?

28.2 The Details

28.2.1 Overview of Radiotherapeutics

Radiotherapeutics are a special class of radiopharmaceuticals used for the targeted treatment of cancer. Unlike conventional forms of radiation therapy, radiotherapeutics are delivered systemically or locoregionally and target cancerous tissue at the cellular level. In radiotherapeutics, nuclides that emit alpha (α)- or beta (β)-particles are typically used to deliver cytotoxic radiation to tumor cells or tumor-associated targets. This radiation is most often delivered to malignant tissue via the attachment of the radionuclide to a vector that targets tumor cells or the tumor microenvironment (e.g., the binding of $[^{177}Lu]$Lu-DOTA-TATE to somatostatin receptors expressed by neuroendocrine tumor cells) but can also be directed by natural physiological mechanisms (e.g., the accumulation of $[^{131}I]I^-$ in the cancerous thyroid).

Radiotherapeutics have demonstrated significant efficacy as well as minimal toxicity to normal tissues and organs. RPT regimens are also typically shorter and produce fewer severe side effects than traditional chemotherapies. Over the last decade, the widespread recognition of the potential of radiotherapeutics has led to surges in both preclinical research and clinical trials dedicated to exploring the use of new agents for RPT.

28.2.2 The Role of the Nuclear Pharmacy

Nuclear pharmacies—also frequently referred to as radiopharmacies—play a critical role in nuclear medicine and the use of both diagnostic and therapeutic radiopharmaceuticals. Nuclear

A. Hussein (✉)
Department of Nuclear Medicine, The University of Texas MD Anderson Cancer Center, Houston, Texas, USA
e-mail: ABHussein@mdanderson.org

pharmacy is considered a specialty pharmacy practice that focuses on clinical research and patient treatment involving the compounding, preparation, and distribution of radioactive materials. As part of its core functions, a nuclear pharmacy provides radiopharmaceutical management and oversight, including, but not limited to, receipt and storage of radioactive materials, radiopharmaceutical preparation, quality control testing, dispensing, transportation, and radioactive waste disposal. Radiopharmaceuticals must be prepared under the supervision of an authorized user nuclear pharmacist or an authorized user physician. The U.S. Nuclear Regulatory Commission (NRC) is the national regulatory body that oversees and administers authorized user certification [1].

The design, layout, and instrumentation of nuclear pharmacies must be equipped to handle the management and storage of radiopharmaceuticals. This includes specialized areas for the compounding and dispensing of radiopharmaceuticals, the installation of appropriate ventilation systems to ensure clean air environments, and the use of radiation detection instruments to prevent the contamination of work areas and to mitigate radiation exposure to personnel [1]. Nuclear pharmacies are also equipped to safely support the preparation of radiotherapeutics, which require a regulatory-compliant clean room with an ISO 5 vertical Laminar Flow Workbench Area or, at minimum, an ISO 5 vertical Laminar Flow Workbench that is set up away from high traffic areas where drugs are prepared and dispensed. Finally, nuclear pharmacies are subject to federal, state, and local regulatory bodies that oversee their facilities and operations.

Nuclear pharmacists and the personnel staffing a nuclear pharmacy can serve as a source of knowledge and information on the handling, preparation, and dispensing of radiotherapeutics. As such, the nuclear pharmacy is a critical part of—and an essential resource for—the success of the multidisciplinary team (MDT) that manages RPT for patients.

28.2.3 Radiotherapeutic Agents

Radiotherapeutics have been used as an effective treatment for cancer patients for many decades. The following section provides an overview of the US Food and Drug Administration (FDA)-approved radiotherapeutics that are currently used in the clinic. To this end, Table 28.1 provides a list of radiotherapeutic agents, the clinical indications for which they are employed, and their current clinical use status. In the following pages, we will offer more detailed discussions of several of these agents, including information on key clinical trials, their mechanism of action, preparation, shipping and storage, and dispensing and administration.

28.2.3.1 Meta-[^{131}I]Iodobenzylguanidine ([^{131}I]MIBG)

[^{131}I]MIBG has been studied for over four decades for the treatment of certain types of neuroendocrine tumors, including carcinoid tumors, pheochromocytoma, paraganglioma, and neuroblastomas [5]. In 2018, [^{131}I]MIBG became the first and only FDA-approved therapy for non-resectable, locally advanced or metastatic pheochromocytoma or paraganglioma that requires systemic treatment.

28.2.3.1.1 Mechanism of Action
Iobenguane (MIBG) is structurally similar to the neurotransmitter norepinephrine (NE). As a result, MIBG follows the uptake of the NE transporter through the adrenergic nerve terminals, where it accumulates and localizes in adrenergically innervated tissues. Pheochromocytomas and paragangliomas overexpress NE transporters on their cell surface, resulting in [^{131}I]MIBG being taken up within these cancer cells in high-enough concentrations to deliver a cytotoxic dose of radiation.

28.2.3.1.2 Key Clinical Trial
[^{131}I]MIBG was approved based on the results of a pivotal multicenter, open-label phase II clinical trial—"A Phase II Study Evaluating the Efficacy and Safety of Ultratrace Iobenguane I-131 in

Table 28.1 FDA-Approved radiotherapeutics

Drug name	FDA clinical indication	Clinical use status
[^{153}Sm]Samarium-lexidronam	Palliative care of bone metastasis	FDA approved in 1997; production stopped in 2021 due to decline in demand [2]
[^{131}I]I-Tositumomab	Non-Hodgkin's lymphoma	FDA approval withdrawn in 2013 because the post-marketing study intended to verify clinical benefit was not completed [3]
Sodium [^{32}P]P-orthophosphate	Palliative care of bone metastasis; polycythemia vera	No commercially available FDA-approved product since 2009 [4]
[^{89}Sr]Strontium chloride	Palliative care of bone metastasis	FDA approved in 1993; limited utilization
[^{90}Y]Y-Ibritumomab tiuxetan	Non-Hodgkin's lymphoma	FDA approved in 2002; limited utilization
[^{131}I]I-Sodium iodide	Hyperthyroidism and thyroid cancer	FDA approved in 1976; high utilization
[^{223}Ra]radium dichloride	Castrate-resistant prostate cancer with bone metastasis	FDA approved in 2013; high utilization
Meta-[^{131}I] Iodobenzylguanidine	Pheochromocytoma and paraganglioma	FDA approved in 2018; growing in utilization
[^{177}Lu]Lu-DOTA-TATE	Neuroendocrine tumors	FDA approved in 2018; growing in utilization
[^{177}Lu]Lu-vipivotide tetraxetan	Castrate-resistant prostate cancer	FDA approved in 2022; growing in utilization

Patients with Malignant Relapsed/Refractory Pheochromocytoma/Paraganglioma"—that had an enrollment of 74 participants with pheochromocytoma or paraganglioma [6]. The trial focused on two outcomes for the treatment of advanced pheochromocytoma and paraganglioma: a reduction in the need for hypertension medication, and the control of tumor growth. Participants received a dosimetry dose, also referred to as an imaging dose, to confirm that they met the radiological entry criteria and to perform a dosimetry and biodistribution assessment. Sixty-eight patients received at least one therapeutic dose, and 50 received two therapeutic doses. Ultimately, the trial demonstrated strongly positive results: 25% (17 out of 68 patients) receiving at least one therapeutic dose of [^{131}I] MIBG experienced a reduction in the use of antihypertensive medication by 50% or more for 6 months or longer. Even more notable, 22% (15 out of 68 patients) had tumors that were significantly reduced in size [7].

28.2.3.1.3 Preparation
The safe and effective preparation and administration of [^{131}I]MIBG requires a significant amount of time, planning, and coordination.

Fig. 28.1 provides a representative checklist that RPT teams can follow to ensure that a patient is appropriately prepared for the administration of the radiotherapeutic.

- Screen the patient's medications for drug interactions with [^{131}I]MIBG. Discontinue drugs that reduce catecholamine uptake or deplete catecholamine stores for at least five biological half-lives before the administration of either the dosimetry or therapeutic dose.
- Ensure that the patient has no contraindications (i.e., hypersensitivity to iobenguane, iodine allergy, pregnancy, or breastfeeding).
- Prescribe 12 doses of potassium iodide 130 mg or inorganic iodide prior to the administration of [^{131}I]MIBG for thyroid protection. Instruct the patient to take one tablet 24 h prior to each dose of [^{131}I]MIBG, one tablet 1 h prior to injection, and one tablet daily for 10 days following each dose of [^{131}I]MIBG.
- Instruct the patient to increase their fluid intake to at least two liters per day starting at least one day prior to each dose of [^{131}I]MIBG and continue this level of fluid uptake for one week following each dose of [^{131}I]MIBG to decrease radiation exposure to the bladder.

Pre-procedure Interview: ☐ Phone ☐ In person
Scheduled (date/time): _____

☐ Screen the patient's medications for drug interactions with [^{131}I]MIBG. Discontinue drugs that reduce catecholamine uptake or deplete catecholamine stores for at least five biological half-lives before administration of either the dosimetry or therapeutic dose of [^{131}I]MIBG. *Document under follow-up items*

☐ Ensure that the patient has no contraindications [*i.e.* hypersensitivity to iobenguane, iodine allergy, pregnancy or breastfeeding]. *Document under follow-up items*

☐ Prescribe 12 doses of potassium iodide 130 mg or inorganic iodide prior to the administration of [^{131}I]MIBG for thyroid protection. Instruct the patient to take one tablet 24 hours prior to each dose of [^{131}I]MIBG; one tablet one hour prior to injection; and one tablet daily for 10 days following each dose of [^{131}I]MIBG.

☐ Instruct the patient to increase fluid intake to at least two liters per day starting at least one day prior to each dose of [^{131}I]MIBG; continue for one week following each dose of [^{131}I]MIBG to decrease radiation exposure to the bladder.

☐ Review [^{131}I]MIBG injection and imaging time with patient. Fill in below.

Day 1 Injection (date/time): _____   Scan (date/time): _____
Day 2 Scan (date/time): _____
Day 3 Scan (date/time): _____

Follow Up Items:
☐ List Drug Interactions/Contraindications:

_____

Actions Taken

_____

Reviewer: _____ (Initial)

Fig. 28.1 Checklist for the preparation of patient for [^{131}I]MIBG

The preparation of [^{131}I]MIBG may contain free [^{131}I]I. Therefore, as indicated in Fig. 28.1, patients are required to take thyroid-blocking inorganic iodide to reduce the potential radiation exposure to the thyroid and thus decrease the risk of treatment-induced hypothyroidism.

RPT with [^{131}I]MIBG requires dosimetric imaging to determine the patient's ideal therapeutic dose and their receptivity to treatment. The recommended dose for dosimetry varies based on a patient's weight, ranging from 185 to 222 MBq for patients weighing greater than 50 kg and 3.7 MBq/kg for patients weighing 50 kg or less [8]. This dosimetry dose is administered over 60 s, and three SPECT/CT (single photon-emission computed tomography/ computed tomography) images [9] are acquired at 60 min, 1–2 days, and 2–5 days after administration. These images are used to obtain radiation dose estimates to tissues that are then harnessed to calculate the appropriate therapeutic dose for the patient.

28.2.3.1.4 Shipment and Storage

The shipping and storage times for $[^{131}I]$MIBG can vary depending on the location from which the radiotherapeutic agent is shipped. Typically, the pharmaceutical is manufactured the week before a patient's scheduled treatment with a shelf-life of six days after the time of calibration. The dosimetry and therapeutic doses are shipped in 30 mL vials with a total activity of 1110 MBq for the dosimetry dose and 12,488 MBq for the therapeutic dose. The radiotherapeutic agent must be stored at $-70\ °C$ or lower, which requires the use of an ultra-low-temperature freezer that has 24 h temperature monitoring.

28.2.3.1.5 Dispensing and Administration

As described above, RPT with $[^{131}I]$MIBG requires the administration of a dosimetry dose prior to the administration of the therapeutic dose. To administer either the dosimetry or therapeutic dose, the vials must be removed from storage and allowed to thaw to room temperature in a shielded container. The application of a heating source to accelerate warming and/or the refreezing of a vial once it has been thawed are both prohibited, as both acts can impact the safety and efficacy of the radiotherapeutic. The vials containing the therapeutic dose have a significantly larger liquid volume and may take up to 4 h to thaw. The vial containing the dosimetry dose must be diluted with 0.9% NaCl to a concentration of 37 MBq/mL at the time of administration and is dispensed using a 10 mL syringe.

The therapeutic dose is often delivered in multiple vials, making dispensing the therapeutic dose considerably more complex than dispensing the dosimetry dose. To administer the therapeutic dose, the nuclear pharmacy must first identify the administration method that is preferred by the treatment center: vial infusion or syringe pump infusion. Table 28.2 provides a comparison of these two methods.

Patients with pheochromocytes or paragangliomas who weigh more than 62.5 kg may be administered up to 18,500 MBq per cycle, while patients weighing 62.5 kg or less are typically dosed at 296 MBq/kg. Patients are dosed over a span of 30 min at a rate of 100 mL

Table 28.2 Comparison of $[^{131}I]$MIBG administration methods

	Vial infusion	Syringe pump infusion
Procedure steps	1. Transfer the contents of the therapeutic vial (s) to a 50 mL vial. 2. Assay the 50 mL vial in a dose calibrator to determine if the therapeutic dose is above or below the prescribed dose. 3. Remove and dispose off excess activity or add additional activity to the 50 mL vial to achieve the prescribed dose. 4. Add 0.9% NaCl to reach the full volume of 50 mL. 5. Administer the 50 mL vial through an infusion pump.	1. Draw the therapeutic dose in a 50 mL syringe. 2. Assay the syringe in a dose calibrator to determine if the therapeutic dose is above or below the prescribed dose. 3. Remove and dispose off excess activity or add activity to the 50 mL syringe to achieve the prescribed dose. 4. Add 0.9% NaCl to reach the full volume of 50 mL. 5. Administer the 50 mL syringe via syringe pump.
Considerations	*Advantages* The dose remains shielded in the vial during the infusion, limiting unintended radiation exposure. *Challenges* Requires significant preparation time at the patient's bedside (i.e., requires aseptically inserting administration needles). Increased risk of radioactive spills due to vial pressure failures during needle insertions and the 0.9% NaCl flushing after infusion completion.	*Advantages* Decreases the risk of contamination or radioactive spills during infusion time. Minimal preparation time at the patient's bedside. *Challenges* Requires the purchase of radiation protection equipment for the dispensing and shipping of 50 mL radioactive syringes. Treatment facilities must purchase portable syringe pump shields, which are often costly, heavy, and large.

per hour for adults and 50 mL per hour for children. Patients may receive up to two treatment cycles at three-month intervals [8]. After treatment cycle 1, patients must be monitored for adverse reactions. The dose for cycle 2 can then be adjusted (i.e., reduced, withheld, or discontinued) based on the extent and severity of any adverse reactions experienced by the patient [8].

28.2.3.2 [^{177}Lu]Lu-DOTA-TATE

[^{177}Lu]Lu-DOTA-TATE is a radiolabeled somatostatin analog used for the treatment of neuroendocrine tumors that overexpress somatostatin receptor subtype 2 (SSTR2). In January of 2018, [^{177}Lu]Lu-DOTA-TATE was granted FDA approval as the first peptide-based radiotherapeutic.

28.2.3.2.1   Mechanism of Action
[^{177}Lu]Lu-DOTA-TATE is a ^{177}Lu-labeled cyclic peptide that binds to somatostatin receptors (SSTR) expressed on the surface of malignant tumor cells. The radiotherapeutic enters the cancerous cell, and the beta particles that it emits cause radiation damage to the receptor-positive cells as well as neighboring cells [10].

28.2.3.2.2   Key Clinical Trial
The Neuroendocrine Tumors Therapy (NETTER-1) phase III, randomized, open-label, active-controlled international trial paved the way for the FDA approval of [^{177}Lu]Lu-DOTA-TATE. The trial was conducted in patients with progressive, locally advanced and inoperable or metastatic SSTR-positive midgut neuroendocrine tumors. The study compared the outcomes of a cohort ($N = 177$) treated with [^{177}Lu]Lu-DOTA-TATE plus 30 mg octreotide long-acting repeatable (LAR) to a cohort ($N = 114$) treated with 60 mg octreotide LAR alone. The primary endpoint was progression-free survival, though the trial also evaluated objective response rate, overall survival, safety, and treatment side effects [11]. The patients who received [^{177}Lu]Lu-DOTA-TATE demonstrated significantly prolonged progression-free survival compared to patients treated with high-dose octreotide as well as an 11.7 month boost in overall survival.

28.2.3.2.3   Therapy Preparation
A patient is required to have a positive SSTR2-targeted positron emission tomography (PET) or SPECT scan to qualify for RPT with [^{177}Lu]Lu-DOTA-TATE. In preparation for therapy, long-acting somatostatin analogs should be suspended for at least 28 days prior to the start of treatment. Patients may be given short-acting somatostatin analogs as needed to manage disease symptoms up to 24 h prior to start of therapy [10]. Long-acting somatostatin analogs can be initiated again between 4 and 24 h after each infusion cycle of [^{177}Lu]Lu-DOTA-TATE but must be suspended within 28 days of the next [^{177}Lu]Lu-DOTA-TATE cycle.

28.2.3.2.4   Shipment and Storage
[^{177}Lu]Lu-DOTA-TATE is supplied in a 30 mL single dose vial with a shelf-life of 72 h from the time of manufacturing. The single dose vial contains 7.4 GBq at the time of administration in a volume between 20.5 and 25 mL [10]. The drug is temperature-sensitive and must therefore be stored at a temperature below 25°C.

28.2.3.2.5   Dispensing and Administration
Patients are prescribed a standard intravenous (IV) dose of 7.4 GBq of [^{177}Lu]Lu-DOTA-TATE every 56 days for a total of 4 cycles. However, this dosing interval may be extended up to 112 days for the management of dose toxicity. Prior to dispensing [^{177}Lu]Lu-DOTA-TATE, the pharmacy must determine the administration method that the clinic is planning to use. The most common methods used for the administration of ^{177}Lu-labeled radiopharmaceuticals are via gravity with or without an IV pump, via peristaltic pump infusion, and via syringe pump infusion. A comparison of these methods is outlined in Table 28.3.

Notably, [^{177}Lu]Lu-DOTA-TATE is excreted by the kidneys. During excretion, the radiotherapeutic may get reabsorbed in the proximal tubules and deliver unintended radiation dose to the kidneys, resulting in nephrotoxicity. However, the co-administration of amino acids during treatment can reduce this radiation exposure to the kidney by up to 40% [12].

Table 28.3 Comparison of methods for the administration of [^{177}Lu]Lu-DOTA-TATE

	Gravity with or without IV pump	Peristaltic pump infusion	Syringe pump infusion
Procedure steps	1. Assay the 30 mL vial to determine if the therapeutic dose is above or below the prescribed dose (ensure that the vial is placed back into the manufacturer's shield). 2. Using aseptic technique, prepare the vial for infusion by assembling all the necessary equipment (e.g., connect the saline bag to the vial and then connect the vial to the patient). 3. Initiate the infusion by controlling the flow of 0.9% NaCl, either through a manual clamp control or an IV infusion pump[a]. 4. Infuse at a rate of 50–100 mL/h for 5–10 min, then increase the rate to 200–300 mL/h for the next 25–30 min.	1. Assay the 30 mL vial to determine if the therapeutic dose is above or below the prescribed dose (ensure that the vial is placed back into the manufacturer's shield). 2. Prepare the infusion by assembling all necessary equipment. 3. Infuse the dose over 30–40 min.	1. Draw the prescribed dose into a syringe. 2. Assay the dose to determine if the therapeutic dose is above or below the prescribed dose. 3. Prepare the infusion pump. 4. Infuse the dose over 30–40 min.
Considerations	*Advantages* The vial remains shielded during the entire administration. No dose manipulation is needed for the normal dose. *Challenges* Requires significant preparation time from staff at the patient's bedside (i.e., requires aseptically inserting administration needles). Increased risk of radioactive spills due to vial pressure failures during needle insertions and the 0.9% NaCl flushing after infusion completion. Increased risk of misadministration of prescribed dose. Requires calibrated equipment (e.g., an ion chamber) to determine when the administration is complete. A large drug volume is left in the vial, resulting in a higher amount of radioactive waste.	*Advantages* The vial remains shielded during the entire administration. No dose manipulation is needed for the normal dose. Decreased risk of radioactive contamination from drug leaks. *Challenges* Need for a peristaltic pump. Some drug volume is left in the vial. Requires significant preparation time from staff at the patient's bedside (i.e., requires aseptically inserting administration needles).	*Advantages* Decreased risk of radioactive contamination from drug leaks. No drug volume is left in the syringe. Minimal administration preparation time from staff is needed at the patient's bedside. *Challenges* Additional shielding is needed for the syringe pump to prevent radiation exposure. Need for a syringe infusion pump. Dispensing the dose in a syringe may require an ISO 5 class-compliant biological safety cabinet (i.e., must follow regulations regarding sterile drug preparation techniques). Increased exposure to personnel involved in dose preparation.

[a]The transfer of 0.9% NaCl to the vial creates a pressure differential that forces the transfer of the radiotherapeutic dose out of the vial and into the patient

28.2.3.3 [^{177}Lu]Lu-Vipivotide Tetraxetan ([^{177}Lu]Lu-PSMA-617)

[^{177}Lu]Lu-vipivotide tetraxetan, commonly referred to as [^{177}Lu]Lu-PSMA-617, received FDA approval in early 2022 for the treatment of patients with prostate-specific membrane antigen (PSMA)-positive metastatic castration-resistant prostate cancer who have been treated with androgen-receptor-pathway inhibition and taxane-based chemotherapy.

28.2.3.3.1 Mechanism of Action

[^{177}Lu]Lu-PSMA-617 binds to prostate-specific membrane antigen (PSMA) that is highly expressed on the surface of prostate cancer cells and subsequently delivers damaging ionizing radiation.

28.2.3.3.2 Key Clinical Trial

The VISION trial was an international, open-label, phase 3 trial of [^{177}Lu]Lu-PSMA-617 in patients who presented with metastatic castration-resistant prostate cancer who had disease progression on at least one androgen-receptor-pathway inhibitor and one or two taxane regimens [13]. The trial evaluated [^{177}Lu]Lu-PSMA-617 alongside protocol permitted standard care treatment compared to standard care alone. A total of 831 of 1179 screened patients were randomized into the two treatment arms and evaluated for radiographic progression-free survival (rPFS) and overall survival; overall response rate and prostate-specific antigen decline were key secondary end points of the trial. Ultimately, treatment with [^{177}Lu]Lu-PSMA-617 significantly prolonged both rPFS (by 5.3 months) and overall survival (by ~4 months) [13]. Currently, there is great interest in the continuation of trials with [^{177}Lu]Lu-PSMA-617 to demonstrate the efficacy of combining the radiotherapeutic with other approved prostate cancer therapies [14].

28.2.3.3.3 Shipment and Dispensing

[^{177}Lu]Lu-PSMA-617 is supplied in a 30 mL single use vial with a shelf-life of 120 h from the time the drug was manufactured. The vial contains 7.4 GBq at the time of administration in a volume between 7.5 and 12.5 mL. [^{177}Lu]Lu-PSMA-617 is temperature-sensitive and must therefore be stored below 30°C.

28.2.3.3.4 Preparation and Administration

Patients must have a positive PSMA PET scan to qualify for therapy. Patients are prescribed 7.4 GBq IV of [^{177}Lu]Lu-PSMA-617 every 42 days for up to 6 cycles. The dose for a cycle may be reduced by 20% as needed to manage adverse events experienced at any time after a previous cycle. There are several methods that can be utilized for the administration of [^{177}Lu]Lu-PSMA-617: via gravity with or without IV pump, via peristaltic infusion pump, and via a syringe pump. Table 28.4 provides a comparison of these administration methods.

28.2.4 Implementing a Multidisciplinary Approach

A collaborative, multidisciplinary team (MDT) approach is fundamental to delivering RPT safely and effectively. The MDT that underlies patient treatment with radiotherapeutics may differ from institution to institution; however, key team members include those from the nuclear pharmacy, the nuclear medicine or radiation oncology departments, the medical oncology department, the radiation safety department, and nursing. The nuclear pharmacy can serve as the quarterback or the backbone of this MDT, supporting communications and setting the strategy for addressing logistical challenges, including navigating drug shortages, patient scheduling, and drug ordering. Fig. 28.2 highlights the complex workflow that is associated with the treatment of a patient with [^{131}I]MIBG. The nuclear pharmacy and the departments that constitute the MDT all have roles to play in ensuring that each patient achieves the best possible outcome. Putting the patient at the center of care ensures that the members of the MDT are working together toward a common objective and that challenges are dealt with in a collaborative, patient-focused way.

Table 28.4 Comparison of methods for the administration of [^{177}Lu]Lu-PSMA-617

	Gravity with or without IV pump	Peristaltic pump infusion	Syringe pump infusion
Procedure steps	1. Assay the 30 mL vial to determine if the therapeutic dose is above or below the prescribed dose (ensure that the vial is placed back into the manufacturer's shield). 2. Using aseptic technique, prepare the vial for infusion by assembling all the necessary equipment (e.g., connect the saline bag to the vial and then connect the vial to the patient). 3. Initiate the infusion by controlling the flow of 0.9% NaCl, either through manual clamp control or an IV infusion pump[a]. 4. Infuse the dose over 30 min.	1. Assay the 30 mL vial to determine if the therapeutic dose is above or below the prescribed dose (ensure that the vial is placed back into the manufacturer's shield). 2. Prepare the infusion by assembling all necessary equipment. 3. Infuse the dose at a rate of 25 mL/h over 18–30 min.	1. Draw the prescribed dose into a syringe. 2. Assay the dose to determine if the therapeutic dose is above or below the prescribed dose. 3. Prepare the infusion pump. 4. Infuse the dose over 1–10 min.
Considerations	*Advantages* The vial remains shielded during the entire administration. No dose manipulation needed for a normal dose. *Challenges* Requires significant preparation time from staff at the patient's bedside (i.e., requires aseptically inserting administration needles). Increased risk of radioactive spills due to vial pressure failures during needle insertions and the 0.9% NaCl flushing after infusion completion. Increased risk of misadministration of the prescribed dose. Requires calibrated equipment (e.g., an ion chamber) to determine when the administration is complete A large drug volume is left in the vial, resulting in a higher amount of radioactive waste	*Advantages* The vial remains shielded during the entire administration time No dose manipulation needed for a normal dose Decreased risk of radioactive contamination from drug leaks *Challenges* Need for a peristaltic pump Some drug volume is left in the vial Requires significant preparation time from staff at the patient's bedside (i.e., requires aseptically inserting administration needles).	*Advantages* Decreased risk of radioactive contamination from drug leaks. No drug volume is left in the syringe. Minimal preparation time from staff is needed at the patient's bedside. Short dose infusion time can increase the number of patients that can be treated. *Challenges* Additional shielding is needed for the syringe pump to prevent radiation exposure. Need for a syringe infusion pump. Dispensing the dose in a syringe may require an ISO 5 class-compliant biological safety cabinet (i.e., must follow regulations regarding sterile drug preparation techniques). Increased exposure to personnel involved in dose preparation.

[a]The transfer of 0.9% NaCl to the vial creates a pressure differential that forces the transfer of the radiotherapeutic dose out of the vial and into the patient

Fig. 28.2 The clinical workflow for RPT with [^{131}I]MIBG

28.3 Particularly Important Works

The use of radionuclides in medicine dates back nearly a century, and the first ever documented studies of the use of radioactive iodine to treat cancer occurred in the 1940s [15]. In 1942, Dr. Joseph G. Hamilton first explored the use of radioactive iodine to treat thyroid cancer in two patients undergoing thyroidectomy. However, Hamilton and his colleagues found that the radioiodine tracer they had administered did not have significant uptake in the thyroid tumors of their patients [16]. Soon thereafter, in 1946, Samuel Seidlin and colleagues published a study that is often credited for giving rise to the role of radiopharmaceuticals in medicine and paving the way for modern radiotherapeutics. In this work, Dr. Seidlin documented the first successful treatment of metastatic adenocarcinoma of the thyroid with ^{131}I and went on to assemble case studies of 16 patients with thyroid cancer who were responsive to therapy with radioactive iodine [16].

28.4 The Future

As we look to the future, the advent of radiotherapeutics will inevitably transform radiation oncology and nuclear medicine, propelling

the specialty practice of nuclear pharmacy to the forefront of cancer treatment. In just the last decade, there has been a surge in research and clinical trials exploring the efficacy and safety of emerging radiotherapeutics. This relatively new class of radiopharmaceuticals has shown increasing promise in the targeted treatment of cancers, often eschewing the debilitating side effects of more traditional methods of radiation therapy.

The early successes in the use of radiotherapeutics to treat prostate cancer and neuroendocrine tumors has fueled interest in developing radiotherapeutic agents that, in combination with immunotherapies, can significantly enhance the treatment of a wide range of cancers. In fact, the National Cancer Institute launched the Radiopharmaceutical Development Initiative (RDI) in 2019 to further support and promote the clinical evaluation of new theranostic radiopharmaceuticals [17]. The RDI is currently engaged in both early and late phase clinical studies, focusing on cancer treatments in areas of high priority [17].

The growth of radiotherapeutics has also underscored the critical roles of nuclear pharmacies both as educational resources for cancer treatment teams and as the clinical settings that are most equipped to handle, prepare, and dispense these drugs. In thinking about how best to bolster the field in light of the rise of radiotherapeutics, it is important to consider the support needed by the nuclear pharmacy workforce to meet the ever-increasing demand for these novel therapeutics.

28.5 The Bottom Line

- Radiotherapeutics are a special class of radiopharmaceuticals that deliver cytotoxic radiation to cancerous tissue.
- Nuclear pharmacies play a critical role in the clinical use of radiotherapeutics.
- The multidisciplinary clinical teams responsible for RPT must properly consider the handling, storage, dispensing, and administration of radiotherapeutics to ensure their safe and effective delivery.

- The past decade has played witness to a surge in both preclinical research and clinical trials focused on the safe and effective deployment of new radiotherapeutics for the treatment of an ever-expanding array of cancers.

References

1. Saha GB, Saha GB. Nuclear pharmacy Fundamentals of Nuclear Pharmacy. Cham: Springer; 2018. p. 185–202.
2. Manufacturer Letter. Lantheus Medical Imaging; 2021, October 19. http://www.radiopharmaceuticals. info/uploads/7/6/8/7/76874929/quadramet_dc_letter_-_oct_2021.pdf
3. Federal Register. GlaxoSmithKline LLC; Withdrawal of Approval of the Indication for Treatment of Patients With Relapsed or Refractory, Low Grade, Follicular, or Transformed CD20 Positive Non-Hodgkin's Lymphoma Who Have Not Received Prior Rituximab; BEXXAR. A notice by the Food and Drug Administration; 2013, October 23. https://www.federalregister.gov/documents/2013/10/23/2013-24840/glaxosmithkline-llc-withdrawal-of-approval-of-the-indication-for-treatment-of-patients-with-relapsed
4. Mastascusa N. Radiopharmaceuticals in nuclear pharmacy and nuclear medicine.
5. O'Brien SR, Pryma DA. Neuroendocrine tumors: therapy with 131I-MIBG. In: Nuclear oncology: from pathophysiology to clinical applications. Cham: Springer International Publishing; 2022. p. 1461–80.
6. Chin B, Prym D, Olsen J, Jimenez C, Dillon J, Solnes L, Kostakoglu L, Pampaloni M, A study evaluating ultratrace iobenguane I131 in patients with malignant relapsed/refractory pheochromocytoma/paraganglioma (NCT00874614).
7. Pryma D, Chin B, Noto R, Dillon J, Solnes L, White T, Stambler N, Lin T, DiPippo VA, Jensen JD, Mahmood S. Azedra (iobenguane I 131) in patients with malignant, recurrent and/or unresectable pheochromocytoma or paraganglioma (PPGL): updated efficacy and safety results from a multi-center, open-label, pivotal phase 2 study.
8. Azedra [package insert]. New York: Progenics Pharmaceuticals, Inc.; 2018.
9. Bombardieri E, Giammarile F, Aktolun C, Baum RP, Bischof Delaloye A, Maffioli L, Moncayo R, Mortelmans L, Pepe G, Reske SN, Castellani MR. 131 I/123 I-Metaiodobenzylguanidine (mIBG) scintigraphy: procedure guidelines for tumour imaging. Eur J Nucl Med Mol Imaging. 2010;37:2436–46.
10. Lutathera [package insert]. Italy: Advanced Accelerator Applications, S.r.l.; 2018.
11. Strosberg J, El-Haddad G, Wolin E, Hendifar A, Yao J, Chasen B, Mittra E, Kunz PL, Kulke MH, Jacene H, Bushnell D. Phase 3 trial of 177Lu-Dotatate

for midgut neuroendocrine tumors. N Engl J Med. 2017;376(2):125–35.

12. Rolleman EJ, Valkema R, de Jong M, Kooij PP, Krenning EP. Safe and effective inhibition of renal uptake of radiolabelled octreotide by a combination of lysine and arginine. Eur J Nucl Med Mol Imaging. 2003;30:9–15.

13. Sartor O, De Bono J, Chi KN, Fizazi K, Herrmann K, Rahbar K, Tagawa ST, Nordquist LT, Vaishampayan N, El-Haddad G, Park CH. Lutetium-177–PSMA-617 for metastatic castration-resistant prostate cancer. N Engl J Med. 2021;385(12):1091–103.

14. Zhang H, Koumna S, Pouliot F, Beauregard JM, Kolinsky M. PSMA theranostics: current landscape and future outlook. Cancers. 2021;13(16):4023.

15. Rawson RW, Marinelli LD, Skanse BN, Trunnell J, Fluharty RG. Deposition of radioactive iodine in human thyroid tissue. University of California Press; 1948; see also Seidlin SM, Marinelli LD, Oshry E. radioactive iodine therapy: effect on functioning metastases of adenocarcinoma of the thyroid. J Am Med Assoc. 1946;132(14):838–47.

16. Ehrhardt JD Jr, Güleç S. A review of the history of radioactive iodine theranostics: the origin of nuclear ontology. Mol Imaging Radionucl Ther. 2020;29(3):88.

17. National Cancer Institute: Division of Cancer Treatment and Diagnosis. Radiopharmaceutical development initiative (RDI). Cancer Therapy Evaluation Program (CTEP); 2021, April 16. https://ctep.cancer.gov/investigatorResources/radiopharmaceutical_development_initiative.htm

Index